14th International Conference on Clouds and Precipitation

Proceedings — Volume 2

Bologna, Italy

19-23 July 2004

Paper	Table of Contents – Papers	Page

TOPIC 1: AEROSOL-CLOUD INTERACTIONS

1:1	ENTRAINMENT, DRIZZLE, AND STRATOCUMULUS CLOUD ALBEDO *Andrew Ackerman, Michael Kirkpatrick, David Stevens, Owen Toon*	1
1:2	EVIDENCE FOR NATURAL VARIABILITY IN MARINE STRATOCUMULUS CLOUD PROPERTIES DUE TO CLOUD-AEROSOL INTERACTIONS *Bruce Albrecht, Tarah Sharon, Haf Jonsson, Patrick Minnis, J. Kirk Ayers, Mandana M. Khaiyer*	5
1:3	RELATIONSHIP BETWEEN CIRRUS ANVIL ICE CRYSTAL PROPERTIES AND AEROSOL CONCENTRATION, AMBIENT RELATIVE HUMIDITY AND VERTICAL VELOCITY DURING CRYSTAL-FACE *Constantin Andronache, Vaughan Phillips*	9
1:4	COMPARISONS OF MICROPHYSICAL MODEL AND BULK METHOD ESTIMATIONS OF SULFATE AEROSOL WET SCAVENGING RATES *Constantin Andronache*	13
1:5	IN-SITU MASS SPECTROMETRIC MEASUREMENTS OF AIRCRAFT EXHAUST AEROSOL PARTICLES *Stephan Borrmann, S. Henseler, N. Hock, S. Weimer, B. Kärcher, A. Petzold, J. Schneider*	17
1:6	MEASUREMENTS OF CLOUD–AEROSOL INTERACTIONS IN WARM CLOUDS AT THE JUNGFRAUJOCH MOUNTAIN TOP SITE IN SWITZERLAND *Keith Bower, M. R. Alfarra, M. J. Flynn, Martin Gallagher, Hugh Coe, Thomas Choularton, E. Weingartner, C. Corrigan, M. Gysel, U. Baltensperger*	20
1:7	CHANGES IN SIZES AND CHEMICAL COMPOSITION OF CCN IN POLLUTED ENVIRONMENTS AND THE EFFECTS ON CLOUD AND PRECIPITATION DEVELOPMENT *Roelof T Bruintjes, Li Jia, Peter Busek, Vidal Salazar, Daniel Breed , T. Jensen, Kristy Ross, Stuart Piketh*	24
1:8	TEMPORAL AND SPATIAL VARIABILITY OF MINERAL AEROSOLS FROM NORTH AFRICA *Leila Carvalho, Charles Jones, Natalie M. Mahowald, Chao Luo*	28
1:9	SATELLITE OBSERVATION AND RADIATIVE MODELING OF THE INFLUENCE OF AEROSOL PARTICLES FROM BIOMASS BURNING ON CLOUD MICROPHYSICAL PROPERTIES *Elsa Cattani, Vincenzo Levizzani, Ana Maria Silva*	32
1:10	A MODELING STUDY OF AEROSOL IMPACTS ON PRECIPITATION AND CLOUD-RADIATIVE PROPERTIES USING A WARM CLOUD PARAMETERIZATION *Chao-Tzuen Cheng, Wei-Chyung Wang, Jen-Ping Chen*	35
1:11	THE INFLUENCE OF AEROSOL ON THE MICROPHYSICS AND PRECIPITATION FROM MIXED PHASE LAYER AND CONVECTIVE CLOUD. *Thomas Choularton, K. Bower, H. Coe, J. Allan, M. Cubison, M.W. Gallagher, G. McFiggans, D. Grosvenor , P. Clarke , P. Williams*	39
1:12	SIMULATIONS OF ICE CRYSTAL NUCLEATION AND GROWTH: RESULTS FROM THE AIDA CLOUD EXPANSION CHAMBER *Paul Connolly, Paul Field, Ottmar Moehler, S. Büttner, H. Saathoff, A. J. Heymsfield, M. W. Gallagher, T. W. Choularton*	43
1:13	SATELLITE DERIVED CLOUD PROPERTIES RELEVANT FOR CLOUD RADIATIVE FORCING: A CASE STUDY OF INTERACTION BETWEEN CLOUDS AND DUST AEROSOL PARTICLES *M. J. Costa, E. Cattani, A. M. Silva, V. Levizzani*	47
1:14	CONSIDERATION OF CLOUD DYNAMICS EFFECTS ON THE PARAMETERIZATION OF CLOUD RADIATIVE PROPERTIES *Peter Daum, Yangang Liu*	51
1:15	PRELIMINARY STUDY ON TROPOSPHERIC ION-INDUCED NUCLEATION *Raffaella D'Auria, Richard P. Turco*	55
1:16	PHYSICAL AND CHEMICAL IMPACTS ON THE ICE NUCLEATING PROPERTIES OF ATMOSPHERIC PARTICLES *Paul Demott, Daniel Cziczo, Jose Jimenez, Sarah Brooks, Mathews Richardson, Edward Dunlea, Kirsten Koehler, Anthony Prenni, Sonia Kreidenweis, Randy Borys, Daniel Murphy*	59
1:17	HAILSTONE SIZE DISTRIBUTION IN ATMOSPHERIC SAHARAN DUST OUTBREAKS *Jean Dessens, Jose Luis Sanchez, Claude Berthet, Roberto Fraile*	63

1:18 ICE FORMATION IN A BIOMASS BURNING CLOUD: MODEL SIMULATIONS OF DROP FREEZING IN IMMERSION AND CONTACT MODES. 66
Karoline Diehl, Martin Simmel, Sabine Wurzler

1:19 SENSITIVITY OF CONTINENTAL LOW-CLOUDS MICROPHYSICAL PROPERTIES TO CHANGES IN AEROSOL NUMBER CONCENTRATION 70
Régis Dupuy, Paolo Laj

1:20 SMOKE INTERACTIONS WITH CLOUDS 74
Graham Feingold, H. Jiang, J. Y. Harrington

1:21 INVESTIGATION OF THE ICE NUCLEATION ABILITY OF TWO DESERT DUST AEROSOL SAMPLES AT -50C 78
Paul Field, Richard Cotton, Ottmar Mohler, M. Schnaiter, Martina Kramer, P. Connolly, A. J. Heymsfield

1:22 PRECIPITATION INFLUENCE ON PARTICULATE MATTER DISPERSION IN COSENZA (ITALY) 82
Monica Filice, Pierantonio De Luca, Alfonso Nastro

1:23 THE ROLE OF THE AEROSOL PARTICLE CHARACTERISTIC ON DRIZZLE FORMATION 86
Istvan Geresdi, Roy M. Rasmussen

1:24 SEPARATION BETWEEN CLOUD SEEDING AND AIR POLLUTION EFFECTS 90
Amir Givati, Daniel Rosenfeld

1:25 SIMULTANEOUS AIRCRAFT OBSERVATION OF AEROSOL AND CLOUD DROPLET CONCENTRATIONS 94
Toshio Harimaya, Akiko Homma, Akira Sasaki, Yutaka Ishizaka

1:26 PO VALLEY NUCLEATION EVENTS: A SIGNIFICANT SOURCE OF CCN 98
Laura Hiltunen, Jorma Joutsensaari, Maria Cristina Facchini, F. Cavalli, Ari Laaksonen

1:27 LONG-TERM, WINTERTIME CLOUD DROPLET, CONDENSATION NUCLEUS AND PRECIPITATION MEASUREMENTS IN THE NORTHERN COLORADO ROCKIES, USA 100
Edward Hindman, Randolph Borys, Douglas H. Lowenthal

1:28 REEXAMINATION OF THE INFLUENCES OF CARBONACEOUS CHEMICALS ON CLOUD DROP ACTIVATION 104
Wei-Chun Hsieh, Jen-Ping Chen

1:29 ON THE ROLE OF THE GIANT AND SUPER-GIANT PARTICLES IN THE FORMATION OF CONVECTIVE PRECIPITATION AND HAIL 108
B. A. Kamalov

1:30 ON THE PRECIPITATION FORMATION IN DESERT AND NEAR-DESERT REGIONS 111
B. A. Kamalov

1:31 THE CITY INFLUENCE ON PRECIPITATION IN CENTRAL ASIA 113
B. A. Kamalov

1:32 PARAMETRIZATION OF WATER-SOLUBLE VOLUME FRACTION OF ATMOSPHERIC AEROSOL 116
Konrad Kandler, Bernhard Busch, Lothar Schütz

1:33 AEROSOL IMPACTS ON PRECIPITATION FROM CONVECTIVE CLOUDS 119
Alexander Khain, Daniel Rosenfeld, A Pokrovsky

1:34 RESPONSE OF THE COUPLED CLIMATE SYSTEM TO INDIRECT AEROSOL FORCING 123
Jón Egill Kristjánsson, Trond Iversen, Alf Kirkevåg, Øyvind Seland

1:35 THE SEARCH FOR THE OPTIMAL SIZE OF HYGROSCOPIC SEEDING PARTICLES 127
Ronen Lahav, Daniel Rosenfeld

1:36 ADDING SALT TO MINERAL DUST PARTICLES AND THE INTERACTION WITH CLOUDS-A CASE STUDY FROM THE MEIDEX CAMPAIGN 131
Zev Levin, Amit Teller, Eliezer Ganor, Yan Yin

1:37 ANALYSIS OF THE EFFECTS OF ATMOSPHERIC ICE NUCLEI CONCENTRATIONS ON RADIANT PROPERTIES OF COLD CLOUD 135
Juan Li, Jietai Mao, Laiguang You, Zhijin Hu

1:38 REVIEW AND IMPLICATION OF WMO AND IUGG RECOMMENDATIONS CONCERNING THE EFFECT OF AEROSOL POLLUTION AND BIOMASS BURNING ON PRECIPITATION 139
Roland List

1:39 OVERVIEW OF AEROSOL-CLOUD INTERACTIONS IN THE CLIMATE SYSTEM 142
Ulrike Lohmann

1:40 CIRRUS CLOUD MICROPHYSICS AND ITS DEPENDENCY ON AEROSOL TYPE, TEMPERATURE AND COOLING RATE 146
Alexander Mangold, Martina Krämer, Ottmar Möhler, Robert Wagner, Harald Saathoff, H. Teichert, Volker Ebert

1:41 EFFECTS OF AEROSOLS AND THERMODYNAMICS ON THE GLOBAL DISTRIBUTION OF TRMM-DERIVED WARM CLOUD PROPERTIES 150
Toshihisa Matsui, Hirohiko Masunaga, Roger Pielke Sr. , Wei-Kuo Tao

1:43 VARIATIONS OF CLOUD CONDENSATION NUCLEI AND CLOUD DROPLET NUMBER CONCENTRATION DUE TO THE REPRESENTATION OF SIZE DEPENDENT CHEMICAL COMPOSITION OF AEROSOL: A MODELLING STUDY 153
Michaela Mircea, Maria Cristina Facchini, Stefano Decesari, Fabrizia Cavalli, Sandro Fuzzi

1:44 HTDMA MEASUREMENTS AND THERMODYNAMIC MODELLING OF AQUEOUS AEROSOLS CONTAINING ORGANICS: A STUDY OF THE LETOVICITE AND MALEIC ACID SYSTEM 157
Michaela Mircea, Maria Cristina Facchini, Stefano Decesari, Fabrizia Cavalli, Sandro Fuzzi, Jenny Rissler, Erik Swietlicki, Simon Clegg

1:45 FORMATION, GROWTH AND HABIT OF ICE CRYSTALS NUCLEATED ON MINERAL DUST AEROSOL 160
Ottmar Möhler, Robert Wagner, C. Linke, M. Schnaiter, H. Saathoff, Alexander Mangold, Martina Krämer, V. Ebert, L. Schütz, P.R. Field, P.J. Connolly, A.J. Heymsfield

1:46 MODELLING STUDIES OF CIRRUS CLOUDS OBSERVED DURING THE INCA CAMPAIGN, IMPLICATION FOR THE NUCLEATION MECHANISM. 164
Marie Monier, Wolfram Wobrock, Andrea Flossmann

1:47 IMPROVED METHODOLOGY FOR THE COMBINED SPECTROSCOPIC AND CHROMATOGRAPHIC INVESTIGATION OF WATER-SOLUBLE ORGANIC COMPOUNDS IN ATMOSPHERIC AEROSOLS AND FOG 168
Fabio Moretti, Emilio Tagliavini, Stefano Decesari

1:48 MICROPHYSICAL AND CHEMICAL CHARACTERISTICS OF CLOUD DROPLET RESIDUALS AND INTERSTITIAL PARTICLES IN CLEAN CONTINENTAL CLOUDS 171
Kevin Noone, Admir Targino, Gustavo Olivares, Lynn Russell, David Covert, John Ogren, Stephan Borrmann, Frank Drewnick , Johannnes Schneider, S. Henseler, N. Hock, S. Weimer

1:49 EFFECTS OF CLOUD SCAVENGING ON AEROSOL SINGLE-SCATTERING ALBEDO 175
John A Ogren, Elisabeth Andrews, David Covert, Kevin Noone

1:50 SAHARAN DUST AS ICE NUCLEI 177
Riza Gurcan Oraltay, Nejdet Fersiz, John Hallett

1:51 SAHARA DUST IMPACT ON PRECIPITATION IN SEVERE STORM EVENTS OVER WEST – CENTRAL MEDITERRANEAN AREA. 181
Massimiliano Pasqui, Bernardo Gozzini, Francesco Pasi

1:52 HIGH-RESOLUTION SENSITIVITY STUDY OF AEROSOL-CLOUD INTERACTIONS IN MARINE STRATUS CLOUDS 185
Irena Paunova, Henry Leighton

1:53 PREDICTION AND OBSERVATION OF AEROSOL PROCESSING BY A CUMULUS: EVIDENCE FOR PARTICLE REMOVAL AND NUCLEATION IN CLOUDS 189
Justin Peter, Steven T. Siems, Jørgen B. Jensen, John L. Gras, Yutaka Ishizaka, Jörg Hacker

1:54 AEROSOL AND POCKETS OF OPEN CELLS 193
Markus D. Petters, Jefferson R. Snider, Ian C. Faloona

1:55 PREDICTION OF CLOUD DROPLET NUMBER CONCENTRATION FROM CLOUD CONDENSATION NUCLEI DATA 197
Markus D. Petters, Jefferson R. Snider

1:56 PREDICTION OF CLOUD CONDENSATION NUCLEI FROM PARTICLE PHYSICOCHEMICAL DATA 201
Markus D. Petters, Jefferson R. Snider, Cynthia Twohy, James R. Anderson

1:57 MICROTOPS OBSERVATIONS OF COLUMNAR AEROSOL OPTICAL DEPTH, OZONE AND WATER VAPOR OVER GADANKI (13.5^{0}N, 79.2^{0}E) 205
Y. Jaya Rao, Panuganti Devara , Atul Kumar Srivastava, Y. Bhavani Kumar, D. Narayana Rao

Paper	Table of Contents – Papers	Page

1:58 AEROSOL IMPACTS ON PRECIPITATION FROM CONVECTIVE CLOUDS: IN SITU AND REMOTE SENSING OBSERVATIONS 209
Daniel Rosenfeld

1:59 THE EFFECT OF AEROSOL CHEMICAL COMPOSITION ON CLOUD DROPLET NUMBER 213
Kristy Ross, Stuart Piketh, Roelof Bruintjes

1:60 SPATIAL AND SEASONAL VARIATIONS OF CLOUD CONDENSATION NUCLEI AND AEROSOLS IN THE UNITED ARAB EMIRATES 217
Vidal Salazar, Roelof Bruintjes, Daniel Breed, Tara Jensen, Stuart Picketh, Abdulla Al Mandoos, Abdulla Al Mangoosh, K. Ross

1:61 SIMULATION OF EFFECTS OF NATURAL AND SEEDING HYGROSCOPIC PARTICLES ON MICROPHYSICS OF ASCENDING CLOUD PARCELS 221
Yaron Segal, Alexander Khain, Mark Pinsky, Daniel Rosenfeld

1:62 FINGERPRINTING CLOUD CONDENSATION NUCLEI 225
Glen Shaw

1:63 INTEGRATING PHOTOCHEMICAL-AEROSOL-CLOUD PROCESSES INTO A ONE DIMENSIONAL ATMOSPHERIC BOUNDARY LAYER MODEL 227
Chein-Jung Shiu, Jen-Ping Chen, Shaw Chen Liu

1:64 WARM MICROPHYSICS IN AN OROGRAPHIC CLOUD AND PROCESSING OF AEROSOL PARTICLES 231
Martin Simmel, Karoline Diehl, Sabine Wurzler

1:65 EFFECTS OF THE AEROSOL ON THE OPTICAL PROPERTIES OF CLOUDS 235
Sabina Stefan, Gabriela Iorga

1:66 STUDIES OF THE AEROSOL INDIRECT EFFECT IN NCAR CAM2.0 239
Trude Storelvmo, Jón Egill Kristjánsson

1:67 ANALYSIS OF CLIMATE CHANGE BY AEROSOL DIRECT AND INDIRECT EFFECTS WITH AEROSOL TRANSPORT-RADIATION MODEL 243
Toshihiko Takemura, Toru Nozawa

1:68 THE IMPACT OF AEROSOLS ON CLOUD AND PRECIPITATION PROCESSES: CLOUD-RESOLVING MODEL SIMULATIONS 246
Wei-Kuo Tao, Xiaowen Li, Alexander Khain, Joanne Simpson, Danniel Johnson, L. Remer

1:69 SCAVENGING OF CONDENSATION NUCLEI IN CLOUDS: DEPENDENCE OF SIGN OF ELECTROSCAVENGING EFFECT ON DROPLET AND CCN SIZES 248
Brian A. Tinsley

1:70 *MODELLING THE HYGROSCOPIC PROPERTIES OF AEROSOLS* 251
David Topping, Gordon Mcfiggans, Hugh Coe, Michael Cubison

1:71 THE IMPACTS OF SAHARAN DUST ON FLORIDA CONVECTION 253
Susan C. Van Den Heever, William R. Cotton

1:72 THE LEIPZIG AEROSOL CLOUD INTERACTION SIMULATOR: DESCRIPTION AND FIRST RESULTS 257
Heike Wex, Frank Stratmann, Alexei Kiselev, Jost Heintzenberg

TOPIC 2: CLIMATE CHANGE AND PRECIPITATION

2:1 CORRELATION BETWEEN NUMBER OF THUNDER-DAYS AND DURATION OF THUNDERSTORM ACTIVITY IN EASTERN GEORGIA 261
Avtandil Amiranashvili, Bakuri Beritashvili, Irina Mkurnalidze

2:2 SPATIAL-TEMPORARY CHARACTERISTICS OF NUMBER OF DAYS WITH A HAILS IN THE WARM PERIOD OF YEAR IN GEORGIA 265
Avtandil Amiranashvili, Vazha Amiranashvili, Albert Nodia, Tamila Khurodze, A.F. Toronjadze, Tamar Bibilashvili

2:3 INFLUENCE OF THE ANTHROPOGENIC POLLUTION OF THE ATMOSPHERE AND THUNDERSTORMS ON THE PRECIPITATIONS REGIME AND THEIR CHEMICAL COMPOSITION IN ALAZANI VALLEY CONDITIONS 267
Avtandil Amiranashvili, Vazha Amiranashvili, L.L. Bachiashvili, Tamar Bibilashvili, G.D. Supatashvili

2:4 RAINFALL VARIABILITY OVER THE MEDITERRANEAN REGION AND ITS LINKAGE WITH LARGE SCALE FEATURES 269
Marina Baldi, Francesco Cesarone, Giovanni A. Dalu, Giampiero Maracchi, Francesco Meneguzzo

2:5 SATELLITE RAINFALL ESTIMATION USING A FEED FORWARD NEURAL NETWORK : IMPROVEMENTS AND LIMITATIONS 273
Jean Claude Bergès, Franck Chopin

2:6 NORTH ATLANTIC OSCILLATION AND RAINFALL IN CONTINENTAL SPAIN 277
Amaya Castro, Luisa Miguélez, Vera Lucia Fonseca, Roberto Fraile

2:7 CONTRIBUTION OF CHANGES IN SEA SURFACE TEMPERATURE AND AEROSOL LOADING TO THE DECREASING PRECIPITATION TREND IN SOUTHERN CHINA 281
Yanjie Cheng, Ulrike Lohmann, Junhua Zhang, Yunfeng Luo, Zuoting Liu, Glen Lesins

2:8 ANALYSIS OF HEAVY RAINFALL IN VERY HIGH TEMPORAL RESOLUTION IN ITALY DURING LAST 10 YEARS 285
Edmondo Di Giuseppe, Domenico Vento, Stanislao Esposito, Chiara Epifani

2:9 PERSISTENCE OF WET AND DRY SPELLS IN ITALY FIRST RESULTS IN MILANO FROM 1858 TO 2000. 288
Chiara Epifani, Stanislao Esposito, Domenico Vento

2:10 CHANGES IN PRECIPITATION INTENSITY UNDER CLIMATE CHANGE CONDITIONS IN MAJOR CATCHMENTS IN EUROPE 292
Daniela Jacob, Katharina Buelow, Ralf Podzun

2:11 GLOBAL OCCURRENCES OF EXTREME PRECIPITATION AND THE MADDEN-JULIAN OSCILLATION: OBSERVATIONS AND PREDICTABILITY 294
Charles Jones, Duane Waliser, K. M. Lau, W. Stern

2:12 PRECIPITATION IN THE MEDITERRANEAN REGION OBSERVED WITH TRMM MICROWAVE DATA 297
Martina Kaestner, Joerg Steinwagner

2:13 LATENT HEAT FORCING: A NEW CONCEPT IN CLIMATE CHANGE 301
Guy Kelman, Daniel Rosenfeld, Alexander Khain

2:14 ROLE OF RELIEF AND DESERT IN FORMATION OF CLOUDS AND PRECIPITATION AT TIEN SHAN AND THE PAMIRS 305
Vladimir Kurbatkin

2:15 MONTHLY PRECIPITATION ESTIMATE OVER WESTERN CHINA 309
Xiaoyang Liu, Tidiane Diallo, Jietai Mao, Jiantong Li

2:16 A NEW SNOW GROWTH MODEL WITH APPLICATION TO RADAR PRECIPITATION ESTIMATES 313
David Mitchell, A. Huggins, V. Grubisic

2:17 CLIMATE OF CITIES URBAN HEAT ISLAND AND URBAN INDUCED PRECIPITATION, EFFECT ON HUMANITY 317
Olakunle Francis Omidiora

2:18 THE CHEMISTRY OF PRECIPITATION IN THE AMAZON BASIN: A COMPARISON OF PRESERVED AND DISTURBED REGIONS 321
Theotonio Pauliquevis, Paulo Artaxo, Luciene Lara, Norbert Miekeley, , Mariana Gouveia

2:19 PARAMETERIZATION OF THE NITRIC ACID EFFECT ON CCN ACTIVATION 325
Sami Romakkaniemi, Harri Kokkola, Ari Laaksonen

2:20 DIAGNOSTICS OF MESOSCALE AND SYNOPTIC STRUCTURE OF PRECIPITATION ASSOCIATED WITH ATMOSPHERIC CYCLONES 327
Irina Rudeva, Sergey Gulev, Olga Zolina

2:21 DETECTION OF CLIMATE CHANGE OVER NORTH-EAST OF I. R. OF IRAN USING HISTORICAL PRECIPITATION AND AIR SURFACE TEMPERATURE TREND'S PATTERNS 329
Alireza Shahabfar, Javad Bodagh Jamali, Azadeh Ramesh

2:22 CHEMICAL COMPOSITION OF ATMOSPHERIC PRECIPITATION - INDICATOR OF CLIMATIC CHANGES OF ATMOSPHERE ON THE EXAMPLE OF TASHKENT PROVINCE 333
Tatyana Smirnova, Galina Tolkacheva

2:23 CLOUD RESOLVING MODEL SIMULATIONS OF WATER AND ENERGY BUDGETS FOR THE INDIAN OCEAN REGION EFFECTS OF AEROSOLS ON TRADE WIND CUMULI 335
Hailong Wang, Greg M. Mcfarquhar, Wojciech Grabowski

2:24 VERIFICATIONS OF HIGH-RESOLUTION LONG-TERM PREDICTION BY JAPAN METEOROLOGICAL AGENCY – NONHYDROSTATIC MODEL (JMA-NHM) WITH THE SPECTRAL BOUNDARY COUPLING (SBC) METHOD 339
Kazuaki Yasunaga, Teruyuki Kato, Hidetaka Sasaki, Chiashi Muroi, Kazuo Kurihara, Yasuo Sato

2:25 THE SPACE-TIME VARIATIONS OF THE THUNDERSTORM ACTIVITY OVER UKRAINE 343
Tamara Zabolotskaya,, Valentina Podgurskaya, Tatyana Shpital

2:26 THE UNCOMMON STRONG PRECIPITATION AND THE POSSIBLE REASONS OF ITS FORMATION OVER UKRAINE 345
Tamara Zabolotskaya,, Valentina Podgurskaya, Tatyana Shpital

2:27 DETERMINATION OF MESOSCALE AND SYNOPTIC-SCALE PRECIPITATION AND ITS IMPACT ON PRECIPITATION EXTREMES FROM THE SYNOPTIC STATION NETWORK OVER EUROPEAN CONTINENT 347
Olga Zolina, Alice Kapala, Clemens Simmer, Sergey Gulev

2:28 ANALYSIS OF EXTREME PRECIPITATION OVER EUROPE FROM DIFFERENT REANALYSES: A COMPARATIVE ASSESSMENT 350
Olga Zolina, Alice Kapala, Clemens Simmer, Sergey Gulev

TOPIC 3: CLOUD-CLIMATE INTERACTIONS

3:1 INFLUENCE OF CLOUDINESS AND AEROSOL POLLUTION TRENDS ON THE TOTAL SOLAR RADIATION IN SOME NON INDUSTRIAL REGIONS OF GEORGIA 354
Avtandil Amiranashvili, Vazha Amiranashvili, Kukuri Tavartkiladze

3:2 AMELIORATION OF GLOBAL WARMING BY CONTROLLED ENHANCEMENT OF THE ALBEDO AND LONGEVITY OF LOW-LEVEL MARITIME CLOUDS 356
Keith Bower, Tom Choularton, John Latham, Jalil Sahraei

3:3 THE MICROSCALE STRUCTURE OF ENTRAINMENT-MIXING IN BOUNDARY LAYER CLOUDS 360
Frédéric Burnet, Jean-Louis Brenguier

3:4 OPTICAL CHARACTERISATION OF ICE CRYSTALS GROWING AT SIMULATED CIRRUS CONDITIONS 364
Simone Büttner, Martin Schnaiter, Robert Wagner, Claudia Linke, Ottmar Möhler, Paul Field, Paul Connolly

3:5 IFN/CCN AND CLIMATE 367
Gustavo Carrio, Hongli Jiang, William R. Cotton

3:6 RADIATIVE IMPACT OF MIXING PROCESSES IN BOUNDARY LAYER CLOUDS 371
F. Chosson, J.-L. Brenguier, M. Schröder

3:7 EVALUATION OF CLOUD AMOUNT TRENDS AND CONNECTIONS TO LARGE SCALE DYNAMICS 375
Todd Ellis, Graeme L. Stephens, David W. J. Thompson

3:8 SUPER-PARAMETERIZATION: GLOBAL CONTEXT FOR CLOUD-SCALE PROCESSES 379
Wojciech Grabowski, Marat Khairoutdinov, David Randall

3:9 THE EFFECT OF CLOUDS ON THE SHORTWAVE RADIATION BUDGET ON GLOBAL SCALE 383
George Habilomatis, Nikos Hatzianastassiou

3:10 SEASONAL VARIATIONS OF CLOUDS, AEROSOLS AND SHORTWAVE RADIATION OVER CHINA 387
Tadahiro Hayasaka, Kazuaki Kawamoto, Jianqing Xu

3:11 ESTIMATION OF FRACTIONAL SKY COVER, CLOUD TYPE AND CLOUD FORCING EFFECTS AT TERRA NOVA BAY STATION (75°S) FROM BROADBAND RADIATION MEASUREMENTS. 389
Christian Lanconelli, Angelo Lupi, Marianna Nardino, Vito Vitale, Pierfrancesco Calzolari, Franco Evangelisti, Ubaldo Bonafe, Giuliano Trivellone, Daniele Bortoli

3:12 SENSITIVITY STUDIES OF CIRRUS CLOUDS FORMED BY HETEROGENEOUS FREEZING IN THE ECHAM GCM 393
Ulrike Lohmann, Bernd Karcher, Johannes Hendricks

3:13 AN ASSESSMENT OF MULTI-ANGLE IMAGING SPECTRORADIOMETER (MISR) STEREO-DERIVED CLOUD TOP HEIGHTS USING GROUND-BASED MILLIMETER-WAVELENGTH CLOUD RADARS 397
Roger Marchand, Thomas Ackerman

3:14 SINGLE-SCATTERING PROPERTIES OF MIXED-PHASE CLOUDS AT ARCTIC CLOUDS AT SOLAR WAVELENGTHS: IMPACTS ON RADIATIVE TRANSFER 400
Greg M. Mcfarquhar, Stewart G. Cober

3:15 EVALUATION OF THE MULTI-SCALE MODELING FRAMEWORK USING DATA FROM THE ATMOSPHERIC RADIATION MEASUREMENT PROGRAM 404
Mikhail Ovtchinnikov, Thomas P. Ackerman, Roger T. Marchand, Marat Khairoutdinov

3:16 CONVECTIVE ORGANIZATION IN A RADIATIVE-CONVECTIVE EQUILIBRIUM CLOUD RESOLVING MODEL - RADIATIVE AND MOISTURE FEEDBACKS 408
Lyle Pakula, Graeme L. Stephens, Marat Khairoutdinov

3:17 RETRIEVAL OF MICROPHYSICS OF DRIZZLING WATER CLOUDS 412
Nick Schutgens

3:18 VARIOUS APPLICATIONS ON TROPICAL CONVECTIVE SYSTEMS USING A GODDARD CUMULUS ENSEMBLE (GCE) MODEL 413
Chung-Lin Shie, Wei-Kuo Tao, Joanne Simpson

3:19 CLOUDS AND THE EARTH'S CLIMATE: AN OBSERVATIONAL STUDY OF CLOUD FEEDBACKS AND THE REGULATION OF THE HYDROLOGICAL CYCLE OF THE TROPICAL ATMOSPHERE 417
Graeme L. Stephens, Tristan L'Ecuyer

3:20 THE ROLE OF SHALLOW CONVECTION IN THE WATER AND ENERGY CYCLES OF THE ATMOSPHERE 421
Knut von Salzen, Norman McFarlane, Michael Lazare

3:21 CLOUD OBJECT MODELING AND OBSERVATIONS FOR CLIMATE STUDIES 424
Kuan-Man Xu, Bruce Wielicki, Takmeng Wong, Lindsay Parker

TOPIC 4: INTERACTIONS BETWEEN CLOUDS AND ATMOSPHERIC CHEMISTRY

4:1 THE IMPORTANCE OF CLOUD DROP REPRESENTATION ON CLOUD PHOTOCHEMISTRY 428
Mary C. Barth, Roberto Cancel, Kristy Ross, Si-Wan Kim

4:2 TRANSFORMATION AND CLOUD INTERACTION OF ATMOSPHERIC AEROSOLS 432
Hugh Coe, M. Rami Alfarra, J. D. Allan, K. N. Bower, M. Cubison, P. I. Williams, G. Mcfiggans, D. Topping, H. Coe, J. T. Jayne, M. R. Canagaratna, D. R. Worsnop, J. L. Jimenez, S. Fuzzi, M.-C. Facchini, S. Decesari, A. Berner

4:3 THE SURFACE TENSION OF FOG WATER SAMPLES, CLOUD WATER, RAINWATER AND DELIQUESCED AEROSOLS, AND ITS LINKAGE TO THE ORGANIC CHEMICAL COMPOSITION 436
Stefano Decesari, Maria Cristina , Facchini, Mihaiela Mircea, Fabrizia Cavalli, Sandro Fuzzi

4:4 POLAR NIGHT INVESTIGATION OF CHEMICAL COMPONENTS IN FRESH SNOW PARTICLES AND AEROSOL/GAS IN THE ATMOSPHERE AT NY-AELESUND 440
Tatsuo Endoh, Tsuneya Takahashi, Izumi Noguchi, Seiji Koga, Naoyuki Kurita, Noriyuki Tanaka, Makoto Wada

4:5 EFFECT OF ARCTIC SULFURIC ACID AEROSOLS ON WINTERTIME LOW-LEVEL ICE CRYSTALS, HUMIDITY, AND TEMPERATURE OVER THE ARCTIC 444
Eric Girard, Alexandru Stefanof

4:6 CLOUD PROCESSING OF GASES AND AEROSOLS IN A REGIONAL AIR QUALITY MODEL (AURAMS) 448
Wanmin Gong, Ashu P. Dastoor, Véronique S. Bouchet, Sunling Gong, Paul A. Makar, Michael D. Moran, Balbir Pabla, Sylvain Ménard, Louis-Philippe Crevier, Sophie Cousineau, S. Venkatesh

4:7 LABORATORY STUDIES ON THE UPTAKE OF AMMONIA, BTEX AND ALKYLBENZENES BY ICE CRYSTALS 452
Ines Hoog, Subir K. Mitra, Elke Fries, Wolfgang Jaeschke, Stephan Borrmann

4:8 MICROPHYSICS OF PYROCUMULONIMBUS CLOUDS 455
Eric Jensen, Andrew S. Ackerman, Ann Fridlind

4:9 CHANGES IN ACIDITY OF OPENING RAINFALL AND THROUGHFALL IN RELATION TO CANOPY OPENNESS IN FORESTS 458
Katsuhiro Kikuchi, Yoshiaki Sasaki

4:10 DROPLET EVAPORATION: THEORETICAL IMPLICATIONS OF RECENT DATA FOR BINARY NITRIC ACID SOLUTIONS 462
Dennis Lamb, Alfred Moyle, Huiwen Xue

4:11 HOW EFFICIENT IS CLOUD DROPLET FORMATION OF ORGANIC AEROSOLS? 465
Ulrike Lohmann, Keith Broekhuizen, Richard Leaitch, Nicole Shantz, Jonathan Abbatt

4:12 AEROSOL RELATED EXTENDED KESSLER-TYPE PARAMETERIZATION FOR USE IN LARGER SCALE MODELS 469
Frank Müller, Frank Schimmel, Andreas Chlond

4:13 COMPARATIVE STUDY OF THE UPTAKE OF NITRIC ACID TO AEROSOL AND CLOUD PARTICLES IN THE MID AND UPPER TROPOSPHERE 473
Jason Shepherd, Hugh Coe, Gordon Mcfiggans

4:14 DROP-SCALE NUMERICAL MODELING OF CHEMICAL PARTITIONING DURING CLOUD HYDROMETEOR FREEZING 475
Amy L. Stuart, Mark Z. Jacobson

4:15 CHEMICAL EFFECTS ON DROP SPECTRAL BROADENING 479
Huiwen Xue, Graham Feingold

TOPIC 5: WARM CLOUD MICROPHYSICS

5:1 EQUILIBRIUM WET GROWTH/EVAPORATION OF PARTICLES CONTAINING SOLUBLE AND INSOLUBLE KERNELS 483
Vladimir Arkhipov, Mark Pinsky, Alexander Khain

5:2 AIRCRAFT MEASUREMENTS OF HIGH AVERAGE CHARGES ON CLOUD DROPS 487
Kenneth Beard, Harry T. Ochs, Cynthia H. Twohy

5:3 OBSERVATIONS OF REDUCED LIQUID WATER CONTENT IN THE CENTRE OF CUMULUS CLOUD UPDRAFTS 491
Alan M Blyth, Sonia G Lasher-Trapp, William A Cooper

5:4 RELATIONSHIPS BETWEEN WATER VAPOR PATH AND PRECIPITATION OVER THE TROPICAL OCEANS 495
Christopher S. Bretherton, Matthew E. Peters, Larissa Back

5:5 RELATIONSHIP BETWEEN THE HYDROMETEOR SIZE DISTRIBUTION AND CLOUD MICROPHYSICAL PROPERTIES USING DISDROMETRIC DATA 499
Clelia Caracciolo , Franco Prodi, Alessandro Battaglia

5:6 CONDENSATIONAL GROWTH OF DROPLETS IN WARM CUMULUS CLOUDS 503
Alison Coals, Alan Blyth, Jean-Louis Brenguier, Alan Gadian, Wojtek Grabowski

5:7 STUDY OF THE PRECIPITATION IN ATHENS (GREECE) WITH A 2D VIDEO DISTROMETER AND RAINGAUGES 507
Eric Defer, Kostas Lagouvardos, Vassiliki Kotroni, John Kalogiros

5:8 PRECIPITATION AND LIGHTNING ACTIVITY IN ATHENS (GREECE) 510
Eric Defer, Kostas Lagouvardos, Vassiliki Kotroni

5:9 THE EFFECT OF TURBULENT VELOCITY FLUCTUATIONS ON DROP SPECTRUM BROADENING IN STRATOCUMULUS CLOUDS 513
Carynelisa Erlick, Alexander Khain, Mark Pinsky, Yaron Segal

5:10 THE STUDY ON CONVECTIVE CLOUD IN QINGHAI AND SEEDING EXPERIMENT WITH 3D MODEL 517
Wen Fang , Guo Guang Zheng, Guan Fang He

5:11 CLOUD DROPLET COLLISION RATES IN EVOLVING TURBULENT FLOWS 520
Charmaine Franklin, Paul Vaillancourt, M.K. Yau, Peter Bartello

5:12 CLOUD WATER CONTENT AND CLOUD PARTICLE CHARACTERISTICS REVEALED BY DUAL WAVELENGTH CLOUD RADAR OBSERVATIONS 524
Nicolas Gaussiat, Robin Hogan, Anthony Illingworth

5:13 SUPERSATURATION MEASUREMENTS IN A STRATOCUMULUS 528
Hermann Gerber

5:14 PRECIPITATION DEVELOPMENT IN CLOUDS WITH MARITIME VERSUS CONTINENTAL CHARACTERISTICS 530
Sabine Goke, Harry Ochs, Robert Rauber, Neil F. Laird

5:15 RAINDROP SHAPE AND SIZE DISTRIBUTION: IMPACT ON RADAR PRECIPITATION RETRIEVALS 533
Eugenio Gorgucci, V. Chandrasekar , V. N. Bringi, Luca Baldini

5:16 NORMALIZED DROP SIZE DISTRIBUTIONS 537
Jan Handwerker, Winfried Straub, Klaus D. Beheng

5:17 EVALUATION OF QUANTITATIVE PRECIPITATION ESTIMATION (QPE) ALGORITHMS FROM WEATHER RADAR AND RAIN-GAUGE DATA 541
Yuxiang He, Hui Xiao, Shuyan Liu

5:18 THE COMPARISON OF MICROWAVE STATISTICAL ALGORITHMS FOR PRECIPITATION RETRIEVAL OVER LAND 544
Wenying He, Hongbing Chen, Jinli Liu

5:19 OBSERVATIONS OF FLORIDA CONVECTIVE STORMS USING DUAL WAVELENGTH AIRBORNE RADAR 547
Gerald Heymsfield, Andrew Heymsfield, L. Belcher

5:20 THE EFFECTS OF PARTICLE CLUSTERING ON IN-SITU AND REMOTE SENSING MEASUREMENTS OF MEANS AND VARIANCES 551
Art Jameson

5:21 RELATIONSHIP BETWEEN THE LOW-LEVEL CLOUD FIELDS FROM SATELLITES AND PRECIPITATION FROM GROUND OVER CHINA 554
Kazuaki Kawamoto, Tadahiro Hayasaka

5:22 LARGE WATER DROPS IN CONTINENTAL CUMULUS IN THEIR "FIRST-ECHO" STAGE 556
Charles Knight

5:23 ON THE ROLE OF LARGE-SCALE TURBULENCE IN CLOUD MICROSTRUCTURE FORMATION 560
Yefim Kogan

5:24 MODEL SIMULATIONS ON THE FORMATION OF UNACTIVATED FOGS 564
Harri Kokkola, Sami Romakkaniemi, Ari Laaksonen

5:25 DRIZZLE VARIABILITY IN MARINE STRATUS DURING EPIC 2001 566
Pavlos Kollias, Christopher Fairall, Bruce Albrecht

5:26 PARTICLE IMAGE VELOCIMETRY OF CLOUD DROPLETS IN THE PROCESS OF TURBULENT MIXING 570
Piotr Korczyk, Szymon P. Malinowski, Tomasz A. Kowalewski

5:27 RECONSIDERATION OF CERTAIN ASPECTS OF THE Z –R PROBLEM 573
Michael Larsen, Alexander B. Kostinski

5:28 THE SCALING OF DROP SIZE DISTRIBUTIONS AND THEIR NORMALIZATION 576
Gyu Won Lee, Isztar Zawadzki

5:29 TETHERED-BALLOON BORNE MEASUREMENTS IN BOUNDARY LAYER CLOUDS PART II: MICROPHYSICAL PROPERTIES 580
Katrin Lehmann , Sebastian Schmidt, Holger Siebert, Manfred Wendisch

5:30 SIMULATIONS OF STRATOCUMULI CLOUDS WITH A 3D CLOUD MODEL WITH WARM DETAILED MICROPHYSICS 584
Matthieu Leporini, Wolfram Wobrock, Andrea Flossmann

5:31 CLOUD CONDENSATION NUCLEI IN CLEAR AND POLLUTED ATMOSPHERIC CONDITIONS IN THE AMAZONIAN REGION 588
Jorge Martins, Fábio Gonçalves, J.C.P. Oliveira, A.A. Costa, J.B.V. Leal Júnior, M.A. Silva Dias

5:32 OBSERVATIONS OF VERTICAL VARIABILITY OF CLOUD HYDROMETEORS IN STRATIFORM REGIONS BEHIND BOW ECHOES: IMPLICATIONS FOR DOWNDRAFT FORMATION 592
Greg M. Mcfarquhar, Michael S. Timlin, Robert Rauber, Brian Jewett

5:33 ANALYSIS OF DIFFERENT CLOUD MODELS' OUTPUT OF THE SAME STORM FOR CLOUD RADIATION DATABASE GENERATION 596
C.M. Medaglia, Stefano Dietrich, Vassiliki Kotroni, Sabatino Di Michele, C. Adamo, R. Bechini, G.J. Tripoli, K. Lagouvardos

5:34 AN EXAMINATION OF THE IMPACT OF DRIZZLE DROPS ON SATELLITE-RETRIEVED EFFECTIVE PARTICLE SIZES 600
Patrick Minnis, Robert F. Arduini, David F. Young, J. Kirk Ayers, Bruce A. Albrecht, Tarah Sharon, Bjorn Stevens

5:35 MULTIPEAK RAINDROP SPECTRA OBSERVATIONS FROM CONVECTIVE SHOWERS IN MEXICO 604
G. Montero-Martínez, Fernando García-García

5:36 LABORATORY MEASUREMENTS OF THE EFFECT OF TEMPERATURE ON THE COALESCENCE EFFICIENCY OF SMALL PRECIPITATION DROPS 608
Harry T. Ochs, Jennifer Davison, Kenneth Beard, Jeffrey Van Dorn

5:37 CHARACTERISTICS OF DRIZZLING AND NON-DRIZZLING STRATOCUMULUS AS REVEALED BY VERTICAL POINTING CLOUD RADAR AND LIDAR 612
Ewan O'Connor, Robin Hogan, Anthony Illingworth, Jean–Louis Brenguier

5:38 STATISTICAL ANALYSIS OF MICRO RAIN RADAR SPECTRA 616
Igor Petenko, Gerhard Peters

5:39 PROFILES OF MICROPHYSICAL RAIN PARAMETERS AS OBSERVED WITH MICRO RAIN RADARS 620
Gerhard Peters, Bernd Fischer, Hans Münster

5:40 THE MICROPHYSICAL AND THERMODYNAMIC CHARACTERISTICS OF TROPICAL CONVECTIVE CLOUDS BY RESULTS OF MEASUREMENTS ON CUBA 624
Victor V. Petrov, Daniel Martinez, Carlos A. Perez

5:41 RAIN ENHANCEMENT BY SEEDING WITH CHARGED DROPLETS 628
Mark Pinsky, Alexander Khain, Vladimir Arkhipov, Yuri Feldman, Yaroslav Ryabov

5:42 TOWARD THE PARAMETERIZATION OF TURBULENT EFFECTS ON PARTICLE COLLISIONS IN TURBULENT CLOUDS 632
Mark Pinsky, Alexander Khain, B. Grits, Michael Shapiro

5:43 MEASUREMENTS OF PHORETIC VELOCITIES OF AEROSOL PARTICLES IN MICROGRAVITY CONDITIONS 636
Franco Prodi , Gianni Santachiara , Stefania Travaini , Andrei Vedernikov , Frank Dubois , Jean Claude Legros

5:44 EXPERIMENTAL STUDY OF DRIZZLE FORMATION - RESULTS FROM DYCOMS-II 640
Piotr Rasinski, Hanna Pawlowska

5:45 DROPLET GROWTH BY TURBULENT COAGULATION 643
Nicole Riemer, Anthony Wexler

5:46 THEORETICAL STUDY OF COLLISION INDUCED DROPLET BREAKUP PHENOMENA 647
Norbert Roth, Matthias Hase, Bernhard Weigand

5:47 PARTICLE–TURBULENCE INTERACTIONS IN CLOUDS: A MEASUREMENT PERSPECTIVE 651
Raymond Shaw

5:48 OBSERVATIONAL STUDY ON THE MICROPHYSICAL STRUCTURES OF RAINFALL-PRODUCING STRATI-FORM CLOUDS 654
Niu Shengjie, Sun Zhaobo, Fan Shuxian

5:49 CHARACTERISTICS OF RAINDROP SPECTRA OF STRATIFORM-CLOUD PRECIPITATION IN AUTUMN 2002 IN HENAN 657
Aili Shi, Guoguang Zheng, Gen Huang, Yuquan Zhou

5:50 CHARACTERISTICS OF WATER VAPOR CONDITIONS IN AUTUMN STRATIFORM CLOUDS AND THEIR POTENTIAL FOR RAINFALL ENHANCEMENT IN HENAN PROVINCE IN 2002 661
Aili Shi, Guoguang Zheng

5:51 THE BIAS IN MOMENT ESTIMATORS FOR PARAMETERS OF DROP-SIZE DISTRIBUTION FUNCTIONS: SAMPLING FROM EXPONENTIAL DISTRIBUTIONS 664
Paul Smith, Donna Kliche

5:52 THE EFFECT OF SURFACTANTS ON KÖHLER CURVES RECONSIDERED 668
Riikka Sorjamaa, Tomi Raatikainen, Ari Laaksonen

5:53 WHEN IS BETTER TO DETERMINE THE SUPER-SATURATION INTEGRAL FOR A TIME STEP OF THE SIMULATION ? 670
Cristina Stefanof, Alexandru Stefanof, Wanda Szyrmer, Jean-Pierre Blanchet

5:54 A COMPARISON OF THE MICROPHYSICAL AND KINEMATIC CHARACTERISTICS OF MIDLATITUDE AND TROPICAL CONVECTIVE UPDRAFTS 674
Jeffrey Stith, Julie Haggerty, Cedric Grainger, Andrew Detwiler

5:55 ANALYSES OF MICROPHYSICAL AND DYNAMICAL CHARACTERISTICS OF SUMMER CLOUDS IN THE UPPER REACHES OF THE YELLOW RIVER 678
Anping Sun, Lunge Li, Guoguang Zheng, Hengchi Lei, Guanghe Wang

5:56 STORM SYSTEMS AND PRECIPITATION PROCESSES IN EAST ASIAN MONSOON RAIN 682
Tsutomu Takahashi

5:57 EFFECT OF TURBULENCE ON COLLISION EFFICIENCY OF CLOUD DROPLETS 686
Lian-Ping Wang, Orlando Ayala, Scott E. Kasprzak, Wojciech W. Grabowski

5:58 EFFECTS OF STOCHASTIC COALESCENCE AND AIR TURBULENCE ON THE SIZE DISTRIBUTION OF CLOUD DROPLETS 690
Lian-Ping Wang, Yan Xue, Orlando Ayala, Wojciech W. Grabowski

5:59 CLOUD DROPLET SIZE SPECTRAL BROADNESS OF ADIABATIC CLOUDS 694
Seong Soo Yum, James G. Hudson

5:60 THE PHYSICAL CAUSES OF THE VARIABILITY OF DROP SIZE DISTRIBUTIONS 698
Isztar Zawadzki, Gyu Won Lee

TOPIC 6: COLD CLOUD MICROPHYSICS

6:1 A NEW HABIT DIAGRAM AND MASS PARAMETERS FOR ATMOSPHERIC ICE CRYSTALS FROM –20 °C TO – 70 °C 703
Matthew Bailey, John Hallett

6:2 MESOSCALE STRUCTURE OF FRONTAL WINTER CLOUD AND PRECIPITATION SYSTEMS OVER UKRAINE 707
Vladimir Bakhanov, Olexandra Manzhara, Boris Dorman

6:3 NUMERICAL SIMULATION OF CLOUD MICROSTRUCTURE EFFECT ON SATELLITE SIGNAL 711
Vladimir Bakhanov, Oleksiy Kryvobok, Boris Dorman

6:4 PROPERTIES OF SNOWFLAKES OF DIFFERENT RIMING DEGREE AND CRYSTAL TYPES 715
Eszter Barthazy, Raphael Schefold

6:5 HOW DO UPDRAFTS AND EMBEDDED CONVECTION INFLUENCE RIMING? 719
Björn Baschek, Raphael Schefold, Eszter Barthazy

6:6 MONTECARLO COMPUTATIONS OF SOLAR REFLECTANCE FROM ICE AND WATER CLOUDS AT NEAR IR FREQUENCIES 723
Alessandro Battaglia, Simone Mantovani , Franco Prodi, Federico Porcù

6:7 THE SHAPES OF VERY SMALL CIRRUS PARTICLES DERIVED FROM IN SITU MEASUREMENTS 727
Darrel Baumgardner, Helene Chepfer, Graciela B. Raga, Gregory.L. Kok

6:8 10-YEAR STATISTICS ON FREEZING PRECIPITATION ACROSS THE FORMER USSR FROM SURFACE WEATHER OBSERVATIONS 731
Natalia A. Bezrukova, Richard Jeck, Ludmila S. Minina, Marat F. Khalili, Evgeni A. Stulov

6:9 A SYSTEMATIC RETRIEVAL OF ICE CLOUD MICROPHYSICAL AND RADIATIVE PROPERTIES USING A SYNERGETIC RADAR/LIDAR ALGORITHM 735
Dominique Bouniol, Alain Protat, Martial Haeffelin

6:10 SIMULATIONS OF THE JULY 16 AND 21 CRYSTAL-FACE CIRRUS CASES USING A CLOUD-RESOLVING MODEL FORCED BY A ENSEMBLE OF MESOSCALE MODELS 739
Robert Carver, Jerry Harrington, Johannes Verlinde

6:11 A STUDY OF THE EFFECT OF CLOUD DROPLETS ON THE DIFFUSIONAL GROWTH RATE OF ICE PARTICLES 743
Nesvit E. Castellano, Eldo. E. Avila, Clive Saunders

6:12 OBSERVATIONS AND MODELLING OF CIRRUS OUTFLOW FROM HECTOR DURING THE EMERALD-II CAMPAIGN 747
Paul Connolly, T. W. Choularton, M. W. Gallagher, K. N. Bower, M. J. Flynn, J. W. Whiteway

6:13 PARCEL MODELLING OF ICE NUCLEATION IN THE AIDA AEROSOL CHAMBER 751
Richard Cotton, Paul Field, Ottmar Mohler, M. Schnaiter, Martina Kramer, P. Connolly, A. J. Heymsfield

6:14 A WINTER SEASON PHYSICAL EVALUATION OF THE EFFECTS OF CLOUD SEEDING IN THE COLORADO MOUNTAINS USING RAMS 755
William Cotton, Ray McAnelly, Gustavo Carrio

6:15 PRELIMINARY COMPARISON OF AMSR-E OBSERVATION AND NUMERICAL SIMULATION WITH CLOUD RESOLVING MODEL FOR SOLID PRECIPITATION IN WINTER DURING THE WAKASA 2003 759
Hisaki Eito, Kazumasa Aonashi, Guosheng Liu, Chiashi Muroi, Syugo Hayashi , Teruyuki Kato , Masanori Yoshizaki

6:16 HAILSTONE SIZE DISTRIBUTION AND DENT OVERLAP IN HAILPADS 763
Roberto Fraile, Laura López, Covadonga Palencia, Amaya Castro

6:17 THEORY OF HOMOGENEOUS FREEZING NUCLEATION BASED ON NEW SIZE DEPENDENT SURFACE FREE ENERGY AND MEASURED VAPOR PRESSURE OF SUPERCOOLED WATER 767
Norihiko Fukuta

6:18 ASSESSMENT AND TUNING OF THE BEHAVIOR OF A MICROPHYSICAL CHARACTERIZATION SCHEME BASED ON RADAR POLARIMETRIC VARIABLES 771
Michele Galletti, Pier Paolo Alberoni, Vincenzo Levizzani

6:19 MICROPHYSICAL ANALYSIS INSIDE A SUPERCELL 775
Eduardo García-Ortega, Laura López, J.L. Marcos, José Luis Sánchez

6:20 MICROPHYSICAL RELATIONSHIPS IN CRYSTAL-FACE ANVIL CIRRUS 779
Timothy Garrett, Hermann Gerber, Darrel Baumgardner, M. Poellot, Cynthia Twohy, Elliot Weinstock

6:21 CHARACTERIZATION OF MIXED PHASE CLOUD AND PRECIPITATION 782
John Hallet

6:22 MELT CHARACTERISTICS OF FALLING SNOW PARTICLES 786
John Hallet, Gurcan Oraltay

6:23 HOMOGENEOUS ICE NUCLEATION IN TROPICAL CONVECTION AND ITS INFLUENCE ON CIRRUS ANVIL MICROPHYSICS 788
Andrew Heymsfield, Larry Miloshevich, Carl Schmitt, Aaron Bansemer, Cynthia Twohy, Michael Poellot, Ann Fridlind

6:24 3-D NUMERICAL SIMULATION OF HAILSTORMS IN DIFFERENT REGIONS 792
Zhaoxia Hu, Yanchao Hong, Hongyu Li

6:25 EVALUATION OF GROUND-BASED RADAR AND IN-SITU AIRCRAFT DATA COMPARISON IN WINTER STORMS 796
David Hudak, Peter Rodriguez, Mengistu Wolde, Brian Currie, Stewart Cober, Isztar Zawadzki, George Isaac

6:26 USE OF MASS VERSUS VOLUME UNITS FOR CLOUD MICROPHYSICAL PARAMETERS 800
George Isaac, Ismail Gultepe, Stewart Cober

6:27 THE STRUCTURE OF HAIL STORM DEVELOPED AT HANSHIN AREA IN JAPAN 804
Hiroyuki Konishi, Yukari Shusse, Yoshimasa Takaya

6:28 OBSERVATION OF SUBLIMATING ICE PARTICLES IN CLOUDS 808
Alexei Korolev, George A. Isaac

6:29 SUPERSATURATION OF WATER VAPOR IN CLOUDS. 812
Alexei Korolev, Ilia P. Mazin

6:30 NUMERICAL STUDY IMPACT OF SOME BASIS CHARACTERISTICS OF FREEZING NUCLEI ON CLOUD MICROPHYSICS AND PRECIPITATION 816
Svetlana Krakovskaia, Anne Pirnach

6:31 ANALYSIS OF RADAR AND IN SITU MEASUREMENTS OF SNOWFALL IN EASTERN NORTH DAKOTA 820
Paul Kucera, Andrew Newman

6:32 OBSERVATIONS OF QUASI-STATIONARY, SHALLOW OROGRAPHIC SNOW CLOUD: SPATIAL DISTRIBUTIONS OF SUPER LIQUID WATER AND ICE HYDROMETEOR 823
Kenichi Kusunoki, Masataka Murakami, Narihiro Orikasa, Yoshinobu Tanaka, Mizuho Hoshimoto, Yoshinori Yamada, Hakaru Mizuno, Kyosuke Hamazu, Hideyuki Watanabe

6:33 TRANSITION OF LEESIDE PRECIPITATION PROPERTIES OBSERVED BY KA-BAND RADAR AND GROUND-BASED 2D-GREY PROBE 827
Kenichi Kusunoki, Masataka Murakami, Narihiro Orikasa, Yoshinobu Tanaka, Koyuru Iwanami, Masayuki Maki, Park Sanggoon, Ryohei Misumi, Kyosuke Hamazu, Hiroshi Kosuge

6:34 GIANT AND ULTRAGIANT AEROSOL PARTICLES: SOURCE OF LARGE SUPERCOOLED DROPS IN MIXED-PHASE CLOUDS? 831
Sonia Lasher-Trapp, Sarah Bereznicki, Justin Stachnik

6:35 A COMPARISON OF THE MICROPHYSICAL AND RADIATIVE PROPERTIES OF CIRRUS, WAVE AND ANVIL CLOUDS 835
Paul Lawson, Brad Baker, Bryan Pilson

6:36 THE 2D-S (STEREO) PROBE: PRELIMINARY TESTS OF A NEW HIGH-SPEED, HIGHRESOLUTION PARTICLE IMAGING PROBE 839
Paul Lawson, Darren O'Connor, Patrick Zmarzly, Kim Weaver

6:37 SIMULATION OF PRECIPITATION MECHANISM WITHIN TYPICAL COLD-FRONTAL CLOUD SYSTEM 843
Hongyu Li, Yanchao Hong

6:38 NUMERICAL SIMULATION AND SEEDING EXPERIMENTS OF TWO SEVERE CONVECTIVE EVENTS IN BEIJING AREA 846
Shuyan Li, Zhuang Xie

6:39 NUCLEATION IN SYNOPTICALLY FORCED CIRROSTRATUS 850
Ruei-Fong Lin, David Starr, Jens Reichardt, Paul J. Demott

6:40 A CRITICAL OVERVIEW OF AERODYNAMICS AND HEAT AND MASS TRANSFER OF ICE PARTICLES, GRAUPEL AND HAILSTONES 854
Roland List

6:41 THE 1954 INTERNATIONAL CONFERENCE ON EXPERIMENTAL METEOROLOGY IN ZURICH, SWITZERLAND (A HISTORICAL NOTE) 858
Roland List

6:42 CIRRUS CLOUD PROPERTIES DERIVED FROM THE MOMENTS OF MILLIMETER WAVELENGTH DOPPLER SPECTRUM 861
Gerald Mace, Min Deng

6:43 MORPHOLOGY OF ICE CRYSTALS AT LOW TEMPERATURES: LABORATORY MEASUREMENTS AND ATMOSPHERIC MODELING IMPLICATIONS 865
Nathan Magee, Dennis Lamb, Alfred M. Moyle

6:44 EFFECTS OF WIND SHEAR ON CIRRUS: AN LEM AND RADAR CASE-STUDYI 868
J.H. Marsham, S. Dobbie

6:45 CLOUD PHASE STRUCTURE (PARAMETERIZATION, EXPERIMENTAL PROBLEMS) 872
Ilya Mazin

6:45A RETRIEVAL OF CLOUD PHASE AND ICE CRYSTAL HABIT FROM SATELLITE DATA 876
Sally McFarlane, Roger Marchand, Thomas Ackerman

6:46 LABORATORY MEASUREMENTS OF HETEROGENEOUS ICE NUCLEATION: CONTACT NUCLEATION INSIDE-OUT 880
Youshi Mi, Adam Durant, Raymond Shaw

6:47 ON A NATURE OF FORMING OF THE GLORY IN CLOUDS 884
Anatoly N. Nevzorov

6:48 MICROPHYSICAL PROPERTIES OF ANVILS OBTAINED FROM AIRCRAFT MEASUREMENTS DURING X-BAIU-02 FIELD CAMPAIGN 888
Narihiro Orikasa, Masataka Murakami, Kazumasa Mori, Hiroshi Kuroiwa, Haruya Minda

6:49 THE IMPACT OF VARIOUS NUCLEATION PROCESSES ON ANVIL GLACIATION ON A CRYSTAL-FACE THUNDERSTORM 892
Vaughan Phillips, Steve Sherwood, C. Andronache, A. Bansemer, B. Conant, A. Heymsfield, G. Heymsfield, M. Poellot, T. Vanreken

6:50 A CASE STUDY OF TROPICAL CIRRUS ANVIL MICROPHYSICS FROM CRYSTAL-FACE 896
Michael Poellot, Paul Kucera, Andrew Heymsfield, Cynthia Twohy, Hermann Gerber

6:51 NUMERICAL SENSITIVITY STUDIES OF AXIS RATIO CHANGES OF COLLIDING ICE CRYSTALS 900
Rebekka Posselt, Sabine Wurzler, Karoline Diehl

6:52 CLASSIFICATION AND SCATTERING PROPERTIES OF WINTERLY PRECIPITATION PARTICLES 904
Walter Randeu, Franz Teschl, Norbert Witternigg, Michael Schönhuber

6:53 FREEZING DRIZZLE FORMATION OVER THE OREGON CASCADES DURING IMPROVE II 908
Roy Rasmussen, Kyoko Ikeda, Greg Thompson, Istvan Geresdi

6:54 FALL ATTITUDES OF PRISTINE DENDRITIC SNOW CRYSTALS ESTIMATED FROM RADAR DEPOLARIZATION MEASUREMENTS 912
Roger Reinking, Sergey Matrosov

6:55 SENSITIVITY OF CLOUD MICROPHYSICS AND SURFACE PRECIPITATION TO CCN AND GCCN CONCENTRATIONS IN A WINTER STRATIFORM EVENT 916
Stephen Saleeby, William Cotton

6:56 COMBINED MEASUREMENTS OF SNOWFLAKE CHARACTERISTICS IN THE MELTING LAYER 920
Raphael Schefold, Bjorn Baschek, Aaron Bransemer, Eszter Barthazy

6:57 EFFECTS OF COLLISIONAL BREAKUP ON MIXED-PHASE DEEP CONVECTION SIMULATED BY A SPECTRAL (BIN) CLOUD MODEL AND COMPARISON TO DROP SIZE SPECTRA MEASURED AT THE GROUND 924
Axel Seifert, Alexander Khain, Ulrich Blahak

6:58 STATISTICAL PROPERTIES OF VOLUMES SWEPT BY NON-SPHERICAL ICE PARTICLES IN A 3-D TURBULENT FLOW 928
Michael Shapiro, Hod Wirzberger, Mark Pinsky, Boris Grits, Alexander Khain

6:59 GROWTH OF SNOW CRYSTALS FROM FROZEN WATER DROPLETS 932
Chuji Takahashi

6:60 EXPERIMENTAL STUDIES ON THE SUBLIMATION OF A SNOW CRYSTAL 936
Tsuneya Takahashi, Tatsuo Endoh

6:61 COMPARING ICE-CLOUD MICROPHYSICAL PROPERTIES USING CLOUDNET AND ARM DATA 940
Gerd-Jan van Zadelhoff, David P. Donovan

6:62 ICE CRYSTAL BREAKUP ON IMPACT 944
German Vidaurre, John Hallett

6:63 LABORATORY STUDIES ON THE ICE NUCLEATING ABILITY OF POLLEN PARTICLES IN IMMERSION FREEZING AND CONTACT FREEZING MODES 946
Nadine von Blohn, Subir K. Mitra, Stephan Borrmann

6:64 DISCUSSION ON ARTIFICIAL PRECIPITATION ENHANCEMENT CONDITIONS IN CYCLONE 950
Yilin Wang

6:65 A SIMPLE MODEL OF SNOWFLAKE AGGREGATION 954
Chris Westbrook, Robin Ball, Paul Field, Andrew Heymsfield

6:66 THE MICROPHYSICAL AND ELECTRICAL STRUCTURE OF CONVECTIVE ANVILS 957
Paul Willis, J. E. Dye, S. Lewis, W.D. Hall

6:67 HORIZONTAL AND VERTICAL CLOUD STRUCTURE OBTAINED USING W-BAND AIRBORNE RADAR 961
M. Wolde, S. Haimov, D. Marcotte, W. Strapp, G. Vali, G. Isaac

6:68 THE MOLECULAR DIFFUSION OF ICE CRYSTALS OF VARIOUS SHAPES 965
Hyun Youk, Roland List, Theophilus Ola

6:69 SIMULATION AND OBSERVATION ON SUPERCOOLED LIQUID WATER AND ICE CRYSTALS OF PRECIPITATING STRATIFORM CLOUDS IN HENAN PROVINCE 969
Shi Yueqin, Liu Qijun, Liu Weiguo

6:70 THE STUDY OF HAIL IDENTIFICATION CRITERIA 973
Sun Yuwen, Ying Duan , Zhihui Wu, Hai Zhi

6:71 CLOUD MICROSTRUCTURE DETECTION AND ANALYSIS IN BEIJING AND ITS NEIGHBORING AREA 975
Qiang Zhang, Hongyu Li, Lei Zhang

6:72 WIND TUNNEL MEASUREMENTS OF DRAG COEFFICIENTS OF SPHERICAL AND SPHEROIDAL HAILSTONES 978
Guoguang Zheng, Roland List

TOPIC 7: CLOUD ELECTRICITY

7:1 SIMULATION OF THE DEVELOPMENT OF ELECTRIC FIELD IN A 3-DIMENSIONAL WINTER THUNDERCLOUDS FIELD USING THE RAMS MODEL 982
Orit Altaratz, Tamir Reisin, Zev Levin

7:2 LABORATORY INVESTIGATION OF POSITIVE DISCHARGES FROM ICE CRYSTALS: POSSIBLE RELEVANCE TO LIGHTNING INITIATION AND ICE MULTIPLICATION 986
Matthew Bailey, John Hallett, Danyal Petesen, William Beasley

7:3 AN EXPLICIT ELECTRICAL SCHEME FOR USE IN A CLOUD RESOLVING MODEL 990
Christelle Barthe, Jean-Pierre Pinty

7:4 PRECIPITATION AND LIGHTNING ACTIVITY OVER THE MEDITERRANEAN SEA 994
Eric Defer, Kostas Lagouvardos, D. Katsanos, Vassiliki Kotroni

7:5 DERIVATION OF THUNDERSTORM ICE HYDROMETEOR CHARACTERISTICS FROM LIGHTNING MEASUREMENTS 997
Wiebke Deierling, Walter A. Petersen, John Latham, Scott M. Ellis, Hugh J. Christian Jr.

7:6 AIRBORNE OBSERVATIONS OF MICROPHYSICS AND ELECTRIC FIELDS IN ANVILS OF FLORIDA THUNDERSTORMS 1001
James Dye, Sharon Lewis, William Hall, John Willett, Paul Willis, A. C. Grainger, D. Mach, M. Bateman, H. J. Christian

7:7 THE ELECTRICAL FIELD BENEATH THE THUNDERSTORMS AND ITS RELATIONSHIP WITH THE METEOROLOGICAL VARIABLES 1005
Valter Gennaro, Dario B. Giaiotti, Fulvio Stel

7:8 CHARACTERISTICS OF THE PRECIPITATING SYSTEMS DURING THE 2002 DRY-TO-WET FIELD CAMPAIGN IN THE AMAZON REGION 1008
Carlos Augusto Morales, Luiz Augusto Toledo Machado, Maria Assunção Faus Silva Dias, Wando Amorim, Maria Eugenia Baruzzi Frediani

7:9 LIGHTNING BY CAVITY QUANTUM ELECTRODYNAMICS? 1011
T.V. Prevenslik

7:10 CHARACTERISTICS OF WINTER THUNDERCLOUDS IDENTIFIED WITH DUAL POLARIZATION RADAR IN HOKURIKU, JAPAN 1015
Keiichiro Sakashita , Hiroshi Uyada, Takeshi Maesaka, Taro Shinoda, K. Kontani, K. Shinjo

7:11 C-G LIGHTNING ACTIVITIES AND RAINDROP ELECTRIC CHARGE DISTRIBUTIONS OBSERVED DURING BAIU MONSOON SEASON 1019
Kenji Suzuki, Tetsuya Kawano, Masanori Yoshizaki

7:12 THE IMPACT OF LIGHTNING ON A LIFE CYCLE OF CONVECTIVE CLOUDS: A NUMERICAL STUDY 1023
Zlatko Vukovic, Bosko Telenta

7:13 THE RESEARCH ON PRECIPITATION AND LIGHTNING MAP 1027
Xia Wan, Qiang Zhang, Xiaoyun Cai

TOPIC 8: INSTRUMENTATION

8:1 IMPROVED RETRIEVAL OF STRATUS CLOUD MICROPHYSICAL PROPERTIES USING MILLIMETER-WAVE RADAR AND VISIBLE OPTICAL DEPTH 1029
Richard T. Austin, Graeme L. Stephens

8:2 A NEW LOOK AT THE BRIGHT BAND 1033
Kristina Mann Baker, Johannes Verlinde

8:3 CUMULUS CLOUD PROCESSING OF AEROSOL PARTICLES IN THE MEXICAN EAST PACIFIC 1037
Darrel Baumgardner, Jose Carlos Jiménez, Graciela B. Raga

8:4 RAINFALL ESTIMATES OF CONVECTIVE CLOUDS USING METEOSAT-6 RAPID SCAN DATA IN CENTRAL EUROPE 1041
Franz H. Berger

8:5 THOR - CLOUD THICKNESS FROM OFFBEAM LIDAR RETURNS 1044
Robert F. Cahalan, Matthew Mcgill, John Kolasinski, Tamas Varnai, Kenneth Yetzer

8:6 ON THE SENSITIVITY OF MODIS VISIBLE/1.6 μM CHANNELS TO RADAR-MEASURED GROUND PRECIPITATION 1048
Davide Capacci , Alessandro Battaglia, Simone Mantovani , Federico Porcù , Bryan Conway, Franco Prodi

8:7 ANALYSIS OF PLUDIX DISDROMETER PERFORMANCE DURING THE BBC-2 CAMPAIGN 1052
Clelia Caracciolo , Franco Prodi, Remko Uijlenhoet, Stefano Natali

8:8 PHASE-DOPPLER INTERFEROMETRY FOR IMPROVED CLOUD MICROPHYSICAL MEASUREMENTS 1056
Patrick Chuang, William Bachalo

8:9 MEASUREMENTS OF THE DROPLET SPECTRA WITH THE FSSP-100:A STOCHASTIC MODEL OF PROBE FUNCTIONING 1059
Afranio Coelho, Jean-Louis Brenguier, Thierry Perrin

8:10 EVALUATING CLOUD LIQUID WATER IN NWP AND CLIMATE MODELS USING MEASUREMENTS FROM THE BALTEX CLOUD LIQUID WATER NETWORK: CLIWA-NET 1063
Susanne Crewell, Ulrich Löhnert, Erik Van Meijgaard

8:11 POLARIZATION-LIDAR PROBING OF CLEAR AND CLOUDY ATMOSPHERE OVER GADANKI, A REMOTE CONTINENTAL STATION IN INDIA 1066
Panuganti C.S. Devara, Y. Jaya Rao, Atul Kumar Srivastava, Y. Bhavani Kumar, D. Narayana Rao

8:12 IN SITU CLOUD SENSING WITH MULTIPLE SCATTERING LIDAR 1070
K. Franklin Evans, R. Paul Lawson, Pat Zmarzly, Darren O'Connor, Warren J. Wiscombe

8:13 A COMPARISON BETWEEN THE ROSEMOUNT ICING DETECTOR AND THE SMALL ICE DETECTOR 1074
Paul Field, Phil Brown, George Isaac, Walter Strapp, Alexei Korolev, Stewart Cober, Edwin Hirst, Richard Greenaway, Paul Kaye

8:14 A FIELD INTERCOMPARISON OF A PHASE DOPPLER PARTICLE ANALYSER AND FSSP AT THE SPHINX MOUNTAIN LABORATORY. 1078
Mike Flynn, Martin Gallagher, Keith Bower

8:15 AIRBORNE DIGITAL IN-LINE HOLOGRAPHIC DETECTOR FOR CLOUD PARTICLE STUDIES 1081
Jacob Fugal, Ewe Wei Saw, Alex V. Sergeyev, Raymond A. Shaw

8:16 ON THE MEASUREMENT OF RAINDROPS FALL SPEEDS AT THE GROUND USING OPTICAL ARRAY PROBES 1085
Fernando García-García, G. Montero-Martínez

8:17 ASSESSING CLOUD SPATIAL AND VERTICAL DISTRIBUTION WITH INFRARED CLOUD ANALYZER 1089
Iliana Genkova, Chuck Long, Thierry Besnard, Didier Gillotay

8:18 NEPHELOMETER MEASUREMENTS IN FLORIDA THUNDERSTORMS 1092
Hermann Gerber, Timothy Garrett, Andrew Heymsfield, Michael Poellot, Cynthia Twohy

8:19 FLOW FIELD AND PARTICLE TRAJECTORY SIMULATIONS OF A STRATOSPHERIC COUNTERFLOW VIRTUAL IMPACTOR 1095
Måns Håkansson, Kevin Noone, Johan Ström

8:20 MEASUREMENTS OF "LARGE" CCN 1099
James G. Hudson, Seong Soo Yum

8:21 AN AUTOMATED SYSTEM FOR IDENTIFYING TYPES OF SOLID PRECIPITATION BY IMAGE PROCESSING 1103
Masaaki Ishizaka, Toru Shiina, Ken Muramoto, Sento Nakai, Atsushi Sato

8:22 ANALYSIS OF MILLIMETER-WAVE MEASUREMENTS OF FROZEN HYDROMETEORS 1107
Min-Jeong Kim, James Weinman, D.-E. Chang, J.R. Wang, S. Tanelli, J. Roman, S. Sekelsky

8:23 THE COMPACT CLOUD SPECTROMETER AND IMPACTOR 1108
Gregory L. Kok, Cynthia Twohy, Darrel Baumgardner

8:24 SHATTERING DURING SAMPLING BY OAPS AND HVPS 1111
Alexei Korolev, George Isaac

8:25 WARM RAIN PROCESSES OVER THE TROPICAL OCEANS AND IMPLICATIONS FOR CLIMATE 1115
William K. M. Lau, Huey-Tzu Jenny Wu

8:26 AN IMPROVED ALGORITHM FOR IN SITU ICE WATER CONTENT MEASUREMENTS WITH APPLICATIONS TO CIRRUS AND OTHER ICE CLOUDS 1119
Paul Lawson, Brad Baker

8:27 RAINFALL MEASUREMENTS FROM SPACE: WHERE ARE WE? 1123
Vincenzo Levizzani, Alberto Mugnai

8:28 ALL-SKY VISIBLE AND INFRARED IMAGES FOR CLOUD MACRO CHARACTERISTICS OBSERVATION 1127
Daren Lu, Juan Huo, Wenxing Zhang

8:29 MICROPHYSICALLY-BASED RETRIEVAL OF RAINING CLOUDS BY GROUND-BASED MULTISPECTRAL MICROWAVE RADIOMETRY 1130
Frank S. Marzano, Domenico Cimini, Randolph Ware

8:30 FIRST AIRBORNE CLOUD MEASUREMENTS WITH A COUNTERFLOW VIRTUAL IMPACTOR EQUIPPED WITH A PASSIVE WIND TUNNEL FOR OPERATION ON SLOWLY FLYING AIRCRAFT 1134
Stephan Mertes, Alfons Schwarzenböck

8:31 LINK BETWEEN SIZE-RESOLVED HYGROSCOPIC GROWTH MEASUREMENTS OF AEROSOL PARTICLES ENTERING A HILL CLOUD AND NUMBER SIZE DISTRIBUTIONS OF INTERSTITIAL AND CLOUD DROP RESIDUAL PARTICLES MEASURED IN-CLOUD 1138
Stephan Mertes, Katrin Lehmann, Diane Galgon, Andreas Nowak, Andreas Massling, W. Wieprecht

8:32 METEOROLOGICAL SURVEILLANCE TECHNIQUES BASED ON UNMANNED AERIAL VEHICLE SYSTEM 1142
Slobodan Petkovic, Goran Memon

8:33 USE OF DIGITAL HOLOGRAPHY FOR SIZE ESTIMATION OF AEROSOL PARTICLES FROM THEIR BROWNIAN MOTION 1146
Franco Prodi, Gianni Santachiara , Stefania Travaini , F. Belosi, Andrei Vedernikov , Frank Dubois , Jean Claude Legros

8:34 COMPUTATIONAL FLUID DYNAMICS STUDIES OF AN ICE NUCLEUS CHAMBER 1150
David Rogers, Derek Straub, Paul J. Demott

8:35 OXYGEN A-BAND MEASUREMENTS FOR SOLAR PHOTON PATH LENGTH DISTRIBUTION STUDIES 1154
Thomas Scholl, Klaus Pfeilsticker

8:36 THE STUDY OF CLOUD WATER RESOURCES BY DOPPLER RADAR 1158
Lixin Shi , Duan Ying, Zhihui Wu, Dazhang Tang

8:37 AIRBORNE DATA ACQUISITION SYSTEMS 1160
Sergey N. Skuratov, Victor V. Petrov, Victor P. Korneev, Vladimir A. Glushykhin, Vasily V. Volkov

8:38 ASSESSMENT OF SUPERSATURATION IN DIFFUSION CHAMBERS 1163
Jefferson R. Snider, Markus D. Petters

8:39 DEVELOPMENT OF A LOW POWER AND HIGH SENSITIVITY CLOUD PROFILING FM-CW RADAR AT 95 GHZ 1167
Toshiaki Takano, Hiroshi Kumagai, Tamio Takamura, Teruyuki Nakajima

8:40 APPLICATIONS OF PMW RAINFALL ALGORITHMS TO MEDITERRANEAN AREA EVENTS 1171
F Torricella, V Levizzani, V Poli

8:41 USING ICE CRYSTAL ANALOGUES TO VALIDATE CLOUD ICE PARAMETER RETRIEVALS FROM THE CPI ICE SPECTROMETER DATA. 1175
Z Ulanowski, Paul Connolly, Mike Flynn, Martin Gallagher, A.J.M. Clarke, E. Hesse

8:42 RADIATIVE TRANSFER IN SHALLOW CUMULUS CLOUD FIELDS: OBSERVATIONS AND FIRST ANALYSIS WITH THE DIRAM INSTRUMENT DURING THE BBC-2 FIELD CAMPAIGN IN MAY 2003 1179
Han Van Dop, Keith Wilson

8:43 FIRST MEASUREMENTS WITH AN EXPANSION TYPE CCN COUNTER 1183
Stefan Van Ekeren, M. Fierz, U. Baltensperger, H. Burtscher, E. Weingartner

8:44 SATELLITE RAINFALL ESTIMATION OVER SOUTH AMERICA: THE HYDROESTIMATOR TECHNIQUE 1186
Daniel Vila, Alexandra A. Lima

8:45 SMALL-SCALE RAIN NONUNIFORMITY AND ITS EFFECT ON CORRECTION OF NONUNIFORM BEAM FILLING IN SPACEBORNE RADAR RAIN MEASUREMENT 1190
Ling Zhang, Daren Lu, Shu Duan, Jinli Liu

8:46 ONE MEASUREMENT OF CLOUD LIQUID CONTENT BY AN AIRBORNE UP-LOOKING MICROWAVE RADIOMETER 1194
Xiaoqing Zhang, Hengchi Lei

TOPIC 9: APPLICATIONS OF CLOUD PHYSICS

9:1 PHYSICOSTATISTICAL MODEL FOR ROAD ICING FORECAST AND CONTROL 1196
Natalia A. Bezrukova, Evgeni A. Stulov, Marat F. Khalili

9:2 APPLICATION OF A SEMI-SPECTRAL CLOUD WATER PARAMETERIZATION TO COOLING TOWER PLUMES 1200
Emmanuel Bouzereau, Luc Musson-Genon, Bertrand Carissimo, Éric Dupont

9:3 OVERVIEW OF THE RECENT NATIONAL RESEARCH COUNCIL OF THE NATIONAL ACADEMY OF SCIENCES REPORT ON: CRITICAL ISSUES IN WEATHER MODIFICATION RESEARCH 1204
Roelof T Bruintjes, Michael Garstang

9:4 NUMERICAL SIMULATION OF AFFECTING RANGE FOR CLOUD SEEDING WITHIN SUPER-COOLED STRATIFORM CLOUD 1208
Jin Dai, Xing Yu, Peng Fan, Zhengqi Chen

9:5 OBSERVATION STUDY FOR PHYSICAL EFFECT OF LIQUID CARBON DIOXIDE ON CLOUD 1212
Peng Fan, Hong-Tian Chen, Heng-Chi Lei

9:6 FLYING CASE STUDY OF A PRECIPITATION SHEET CLOUDS ARTIFICIAL RAIN ENHANCEMENT MICRO DETECTION ON MAY 9TH, 1995, IN JILIN PROVINCE 1215
Shufang Gu, Jianchun Gao, Dezhen Jin, Jinghong Zhang, Qiang Wei, Zhongming Hu, Zhixin Chen, Zhanzhu Li, Xiaomei Wang, Junmei Guo

9:7 PRECIPITATION CHARACTERISTICS OF CLOUDS OVER THE UNITED ARAB EMIRATES 1218
Tara Jensen, Roelof Bruintjes, Daniel W. Breed, Vidal Salazar, Abdulla Al Mangoosh, Abdulla Al Mandoos

9:8 OBSERVATION EXPERIMENT OF AIRBORNE MICROWAVE RADIOMETER IN WEATHER MODIFICATION 1222
Dezhen Jin, Shufang Gu, Jinghong Zhang, Maolun Li, Xinzhi Chen, Hengchi Lei, Zhong Wei, Zhilai Shen

9:9 THE COMPREHENSIVE OBSERVATION ANALYSIS OF A LC SEEDING MAN-MADE STEERING ICE CRYSTAL EXPERIMENT 1225
Dezhen Jin, Hengchi Lei, Jiaoheng Zheng, Hui Xiao, Lian Cui, Yuxia Wu, Jian Liu

9:10 PRECIPITATION OVER THE SEA IN THE COASTAL AREA OF ISRAEL; A POSSIBLE NEW SOURCE OF WATER 1228
Zev Levin, Joseph Breitgand, David Shtivelman

9:11 DETECTION OF DIFFUSION ON MOUNTAINS OF BEIJING 1232
Ruijie Li

9:12 EFFECT EVALUATION OF SEEDING WITH ROCKETS IN BEIJING REGION 1234
Shuyan Li , Wei Li

9:13 VIL AS AN INDICATOR OF HAIL SIZE 1238
Laura López, Eduardo García-Ortega, Jean Dessens, José Luis Sánchez

9:14 AN ALGORITHM FOR CONTINUOUS EVALUATION OF CLOUD BASE HEIGHT, CLOUD BASE TEMPERATURE, AND CLOUD COVERAGE AT LOCAL SCALE 1242
Esmaiel Malek

9:15 THE MACROSCOPIC AND MULTIPLE PARAMETER MEASURING SYSTEM OF AIRCRAFT PRECIPITATION ENHANCEMENT 1246
Li Maolun, Jin Dezhen

9:16 DIAGNOSIS OF THERMODYNAMIC CONDITIONS REQUIRED FOR OCCURRENCE OF FREEZING RAIN 1249
Hiroki Matsushita, Fumihiko Nishio

9:17 A REAL-TIME SATELLITE-BASED ICING DETECTION SYSTEM 1253
Patrick Minnis, William Smith Jr, Louis Nguyen, Mandana M. Khaiyer, Douglas A. Spangenberg, Patrick W. Heck, Rabindra Palikonda, Ben C. Bernstein, Frank Mcdonough

9:18 COMPARATIVE STUDY OF NUCLEATION BY ALCOHOLIC SOLUTION OF BENZOIN, BENZOIN DUST, AND BENZIL DUST. 1257
Sahana Paul, Anupam Hazra, Utpal Kumar De, Sanjay Bhar, Kushalendu Goswami

9:19 THE SCREEN OF WEATHER MODIFICATION LN MEDIUM 1261
Ying Qi, Xuelin Wang, Jiaoheng Zhen, Feng He, Zhixin Chen, Xiaomei Wang, Junmei Guo, Xiangren Yu

9:20 A THREE-DIMENSIONAL MODELING STUDY OF HAILSTORM SEEDING 1264
Vlado Spiridonov, Lena Jovanovska

9:21 COMPUTATION OF ELECTROMAGNETIC CHARACTERISTICS OF FROZEN HYDROMETEORS AND COMPARISONS WITH MILLIMETER-WAVE MEASUREMENTS 1268
James Weinman, Min-Jeong Kim

9:22 THE DEVELOPMENT OF GROUND-BASE WEATHER MODIFICATION TOOLS IN CHINA 1272
Yuzhong Wu, Guangxue Chen

9:23 STATISTICAL EVALUATION FOR THE PRECIPITATION EFFECTIVENESS OF CLOUD SEEDING IN HENAN COUNTY OF CHINESE QINGHAI PROVINCE 1276
Zhanyu Yao, Chenhai Xu, Hui Xiao, Lijun Wang, Anping Sun, Jiangping Pu

9:24 COMPARISON BETWEEN SIMULATION OF TRANSPORT AND DIFFUSION OF SEEDING AGENT IN PRECIPITATION ENHANCEMENT BY AIRCRAFT WITH NOAA SATELLITE DATA 1278
Xing Yu, Jin Dai, Peng Fan, Zhengqi Chen

9:25 THE RESEARCH OF SEEDING AGENT DIFFUSION TRAIL 1282
Jinghong Zhang , Shufang Gu, Zhixin Chen, Xiaomei Wang

9:26 AN EXPERIMENTAL STUDY OF THE EFFECTS OF EXPLOSION ON A CONVECTIVE ECHO 1285
Hesheng Zhou, Qing Luo, Huanbin Xu, Jianxin Li, Can Xu, Gang Liu, Liyun Yin, Wei Wei, Libing Liu, Qing Wang, Shuguang Meng

TOPIC 10: CLOUD PARAMETERIZATION IN MODELS

10:1 THE EFFECTS OF ADDING SMALL CRYSTALS IN THE ICE PARTICLE SIZE DISTRIBUTION ON THE EVOLUTION OF MIXED-PHASE CLOUD 1289
Faisal Boudala, George Isaac

10:2 A LONG TERM COMPARISON OF CLOUD PROPERTIES OBSERVED BY VERTICALLY POINTING RADAR AND LIDAR WITH THEIR REPRESENTATION IN OPERATIONAL NWP MODELS 1293
Malcolm Brooks, Robin Hogan, Anthony Illingworth

10:3 PARAMETERIZATION OF THE STRATOCUMULUS CLOUD TOPPED BOUNDARY LAYER: EVALUATION OF THE ECHAM BOUNDARY LAYER SCHEME AGAINST LARGE-EDDY SIMULATIONS 1295
Andreas Chlond, Frank Mueller, Igor Sednev

10:4 PARAMETERIZATION OF MICROPHYSICAL PROCESSES IN A NON HYDROSTATIC PREDICTION MODEL 1297
Oxana Drofa, Piero Malguzzi

10:5 PARAMETRIZATION OF MICROPHYSICS FOR CONVECTIVE-SCALE NUMERICAL WEATHER PREDICTION 1301
Richard Forbes

10:6 TEST AND IMPROVEMENTS OF GCM CLOUD PARAMETERIZATION USING THE CCCMA SCM WITH SHEBA DATASET 1304
Qiang Fu, Jian Yuan, Norm Mcfarlane

10:7 MODEL DYNAMIC AND MICROPHYSICAL VERIFICATION OF THE 13-14 DECEMBER 2001 IMPROVE 2 CASE 1308
Matthew Garvert, Christopher Woods, Brian Colle, Cliff Mass, Peter V. Hobbs

10:8 RELATIONSHIP BETWEEN SOLAR RADIATIVE BIASES AND DEEP CONVECTION ANVIL DIMENSIONS 1312
Francesca Di Giuseppe, Adrian Tompkins

10:9 FORECASTING ICING CONDITIONS DURING ALLIANCE ICING RESEARCH STUDY II WITH THE CANADIAN METEOROLOGICAL CENTRE GLOBAL ENVIRONMENTAL MULTISCALE MODEL 1316
Anna Glazer, George Isaac

10:10 CLOUDS AND CLIMATE: PROGRESS AND PROSPECTS 1320
Wojciech Grabowski

10:11 QUANTITATIVE PRECIPITATION FORECASTING OF WINTERTIME STORMS IN THE SIERRA NEVADA: SENSITIVITY TO THE MICROPHYSICAL PARAMETERIZATION 1324
Vanda Grubisic, Ramesh Vellore, Arlen Huggins

10:12 MICROPHYSICAL PARAMETERIZATION AND VARIABILITY FOR MIXED PHASE CLOUDS USING IN-SITU OBSERVATIONS 1326
Ismail Gultepe, George Isaac

10:13 HIERARCHY OF MICROPHYSICAL PARAMETERIZATIONS SUITABLE FOR CLOUD AND MESOSCALE MODELS. 1330
William Hall, Roy M. Rasmussen

10:14 COMPARISON OF OBSERVED CLOUD PROPERTIES AT THREE GROUND BASED SITES WITH THEIR REPRESENTATION IN OPERATIONAL MODELS: THE EU CLOUDNET PROJECT 1334
Anthony Illingworth, Cloudnet Team

10:15 TROPICAL CIRRUS PARAMETERIZATION FOR TRIMODAL SIZE SPECTRA 1337
Dorothea Ivanova, David Mitchell, Greg Mcfarquhar

10:16 SUBGRID-SCALE ACTIVATION OF CCN 1340
Hongli Jiang, William R. Cotton

10:17 REPRESENTING STRATOCUMULUS CLOUDS IN NUMERICAL MODELS: SENSITIVITY TO MODEL PHYSICS AND VERTICAL RESOLUTION 1344
Colin Jones

10:18 USING REMOTE SENSING DATA TO EVALUATE THE LOKAL-MODELL PERFORMANCE 1348
Christian Keil

10:19 CLOUD-RESOLVING MODEL AS A PARAMETERIZATION OF CLOUDS IN A GENERAL CIRCULATION MODEL 1352
Marat Khairoutdinov, David Randall

10:20 ON CHARACTERIZATION OF SUB-GRID VARIABILITY IN STRATIFORM CLOUDS BASED ON MMCR DATA 1354
Zena Kogan, David B. Mechem, Yefim L. Kogan

10:21 DEVELOPMENT OF THE PARAMETERIZATIONS TO PREDICT THE INITIAL SIZE DISTRIBUTION OF CLOUD DROPLETS FOR THE CLOUD MICROPHYSICAL MODEL IN THE GLOBAL OR REGIONAL MODELS – NUMERICAL SIMULATION WITH A HYBRID CLOUD MICROPHYSICAL MODEL – 1358
Naomi Kuba

10:22 DERIVING PROGNOSTIC EQUATIONS FOR CLOUD FRACTION AND LIQUID WATER CONTENT 1362
Vincent Larson

10:23 NEW PARAMETERIZATIONS FOR THE AUTOCONVERSION PROCESS AND THE DISPERSION EFFECT 1366
Yangang Liu, Peter Daum, Robert Mcgraw

10:24 CLOUD PROPERTIES SIMULATED BY A SINGLE-COLUMN MODEL 1370
Yali Luo, Steven Krueger

10:25 SIMULATION OF A SQUALL LINE CONVECTIVE SYSTEM USING SPECTRAL (BIN) MICROPHYSICS AND BULK PARAMETERIZATIONS 1374
Barry H. Lynn, Axel Seifert, A. Khain

10:26 CONVECTIVE CLOUDY BOUNDARY LAYER PARAMETERIZATION USING A MASS FLUX APPROACH 1378
Anne Mathieu, Frederic Hourdin, Alain Lahelle, Martial Haeffelin, Philippe Drobinski, C. Rio

10:27 EXPLICIT PREDICTION OF HAIL USING A TRIPLE-MOMENT BULK MICROPHYSICS SCHEME 1382
Jason Milbrandt, M. K. Yau

10:28 NUMERICAL MODELLING OF RISING THERMAL: APPLICATION FOR CUMULUS CLOUDS PARAMETERIZATION 1386
Georgy Mostovoy, Pat Fitzpatrick

10:29 RESULTS FROM A NEW MAXIMUM SIMPLICATION MODEL OF CLOUD PROPERTIES BENEATH THE MARINE BOUNDARY LAYER 1389
Sungsu Park, Conway Leovy, Margaret Rozendaal

10:30 A STUDY OF DRIZZLE FORMATION FOR GENERAL CIRCULATION MODEL PARAMETERIZATIONS 1393
Hanna Pawlowska, Jean-Louis Brenguier

10:31 A QUASI 2-MOMENT MIXED-PHASE BULK MICROPHYSICAL SCHEME FOR USE IN A CLOUD RESOLVING MODEL 1397
Jean-Pierre Pinty

10:32 STOCHASTIC CONVECTIVE PARAMETERIZATION WITH MULTIPLE PLUMES 1401
Robert Plant, George Craig

10:33 SENSITIVITIES IN MODEL RESULTS DUE TO CHANGES IN THE PARAMETERIZATION OF CLOUD MICROPHYSICS 1404
Thorsten Reinhardt, Ulrike Wacker

10:34 MODELLING CIRRUS CLOUDS IN THE TROPICAL TROPOPAUSE LAYER 1408
Chuansen Ren, A. Robert Mackenzie

10:35 RETRIEVING INHOMOGENEOUS CLOUDS 1412
Ronald Scheirer, Sebastian Schmidt

10:36 A COMPARISON OF SPECTRAL BIN AND TWO-MOMENT BULK MIXED-PHASE MICROPHYSICS 1416
Axel Seifert, Alexander Khain, Andrei Pokrovsky, Klaus D. Beheng

10:37 NUMERICAL SIMULATION OF THE 16TH JULY CRYSTAL-FACE STORM AND COMPARISON WITH OBSERVATIONS 1420
Axel Seifert, Andrew J. Heymsfield, Aaron Bansemer

10:38 USING SUBGRID CLOUD VARIABILITY IN NON LINEAR PRECIPITATION PROCESSES 1424
Adrian Tompkins, Robert Pincus

10:39 A 3D SPECTRAL ICE HABIT PREDICTION SYSTEM FOR IMPROVING CLOUD RADIATION SIMULATIONS 1428
Gregory Tripoli, Tempeii Hashino, Giulia Panegrossi, Sabatino Di Michele, Stefano Dietrich, Alberto Mugnai

10:40 A STATISTICAL ACTIVATION SCHEME FOR TURBULENCE CLOSURE MODELS 1432
Shouping Wang, Jean-Christophe Golaz

10:41 COMPARISON OF MODEL AND RADAR DERIVED CLOUD VERTICAL STRUCTURE AND OVERLAP 1434
Ulrika Willén, S. Crewell

10:42 THE BEHAVIOUR OF DIFFERENT CLOUD PROCESS PARAMETRIZATIONS IN A LARGE-SCALE MODEL 1438
Damian R. Wilson, Amanda Kerr-Munslow, Andrew C. Bushell

10:43 MODELLING CLOUDS AND RADIATION IN THE ARCTIC 1442
Klaus Wyser, Colin Jones, Ulrika Willen

10:44 A QUASI-IMPLICIT CALCULATING SCHEME OF CLOUD MODEL 1446
Shi Yueqin, Hu Zhijin

10:45 A MICROPHYSICAL PARAMETERIZATION FOR CONVECTIVE CLOUDS IN THE ECHAM GCM DESCRIPTION AND FIRST RESULTS 1450
Junhua Zhang, Ulrike Lohmann

10:46 THE DEVELOPMENT OF A NEW EXPLICIT MICROPHYSICAL SCHEME USING IN MM5 1454
Zhen Zhao, Hengchi Lei, Yu-Xia Wu

TOPIC 11: MODELING OF CLOUD-SCALE PROCESSES

11:1 NUMERICAL MODELLING OF MOIST DECAYING TURBULENCE: CLOUD-CLEAR AIR MIXING AT RESOLUTION BETTER THAN 1CM. 1457
Miroslaw Andrejczuk, Wojciech W. Grabowski, Szymon P. Malinowski, Piotr K. Smolarkiewicz

11:2 ADVANCES IN CLOUD ASSIMILATION AT ECMWF USING ARM RADAR DATA 1461
Angela Benedetti, Marta Janisková

11:3 PAFOG - A NEW EFFICIENT FORECAST MODEL OF RADIATION FOG EVENTS 1465
Andreas Bott

11:4 THE SENSITIVITY OF LARGE-EDDY SIMULATIONS OF STRATOCUMULUS TO THE PARAMETRIZATION OF DRIZZLE. 1469
Philip Brown, Glen Richardson, Robert Wood

11:5 MODELLING STUDIES OF ICE CONCENTRATION IN FRONTAL CIRRUS CLOUDS 1473
John Cardwell, T. W. Choularton

11:6 AN ASSESSMENT OF THE MESO-NH CLOUD SCHEME USING SATELLITE OBSERVATIONS FROM THE VISIBLE TO THE MICROWAVES 1476
Jean-Pierre Chaboureau, P. Dubuisson, J. Pardo, C. Prigent, J.-P. Pinty, P. J. Mascart, E. Richard

11:7 MULTIMODEL ENSEMBLE FORECASTS OF PRECIPITATION OVER THE ALPINE REGION DURING THE MAP- SPECIAL OBSERVING PERIOD USING MESOSCALE MODELS. 1480
Federico Ceccarelli, T.N. Krishnamurti, B. Mackey, C.F. Ratto

11:8 IMPLEMENTATION OF A NEW ICE AGGREGATION AND SEDIMENTATION SCHEME IN A BULK-MICROPHYSICAL MODEL, DERIVED FROM AIRCRAFT OBSERVATIONS 1484
Richard Cotton, Paul Field

11:9 COMPARISON OF OBSERVED AND SIMULATED DEEP CONVECTIVE CLOUD OBJECTS 1488
Zachary Eitzen, Kuan-Man Xu

11:10 SENSITIVITY OF SIMULATED WARM RAIN FORMATION TO COLLISION AND COALESCENCE EFFICIENCIES, BREAKUP, AND TURBULENCE COMPARISON OF TWO BIN-RESOLVED NUMERICAL MODELS 1492
Ann Fridlind, Axel Seifert, Andrew Ackerman, Eric Jensen

11:11 NUMERICAL STUDY OF A SEVERE STORM IN BEIJING 1495
Danhong Fu, Xueliang Guo

11:12 UNDERSTANDING OF FOG STRUCTURE, DEVELOPMENT, AND FORECASTING, COST 722 1499
Alan Gadian, Andreas Bott

11:13 CONSTANT SLOPE OR CONSTANT INTERCEPT? THE IMPACT ON PRECIPITATION USING SINGLE-MOMENT MICROPHYSICS 1500
Matthew Gilmore, Susan C. Van Den Heever, Jerry M. Straka, Robert Wilhelmson, William R. Cotton, Erik N. Rasmussen

11:14 SUBGRID-SCALE CCN ACTIVATION 1504
Jean-Christophe Golaz, Shouping Wang, Vincent E. Larson

11:15 NUMERICAL MODELING OF MICROPHYSICAL VARIABLES USING RAMS AT AMAZONIAN REGION, BRAZIL 1508
Fábio Gonçalves, Jorge Martins, M.A. Silva Dias

11:16 RADIATIVE IMPACTS ON THE GROWTH OF DROPS WITHIN SIMULATED MARINE STRATOCUMULUS CLOUDS 1511
Jerry Harrington, Christopher Hartman

11:17 AN IMPROVEMENT FOR LIQUID-PHASE MICROPHYSICS IN JMA-NHM. 1515
Akihiro Hashimoto, Masataka Murakami, Syugo Hayashi, Chiashi Muroi, Teruyuki Kato, Masanori Yoshizaki

11:18 RAPPORT FROM THE WMO INTERNATIONAL CLOUD MODELING WORKSHOP 11-16 JULY 2004 1519
Daniela Jacob, Wojciech Grabowski, Andreas Chlond, Stefan Hagemann

11:19 THE MODELLING OF PROCESS OF RAINFALL FORMATION BY CLOUDS SEEDING 1520
Bakhtior Kadyrov

11:20 THE DERIVATION OF THE GAS DYNAMICS EQUATIONS BY CONSIDERING CHANGES OF THE VELOCITY DISTRIBUTION FUNCTION ON SCALES OF THE MOLECULE FREE PATH 1523
Alexander Kochin

11:21 EVALUATION OF MM5 HIGH-RESOLUTION SUMMERTIME PRECIPITATION FORECASTS OVER THE URBAN AREA OF ATHENS, GREECE 1525
Vassiliki Kotroni, Konstantinos Lagouvardos

11:22 CLOUD WATER AND RAINWATER NUMERICAL SIMULATION WITH LASG-REM MODEL 1529
Shuyan Li, Wenan Xiao, Hengchi Lei

11:23 MULTI-DIMENSIONAL LONGWAVE RADIATIVE FORCING OF PBL CLOUD SYSTEMS 1533
David Mechem, Mikhail Ovtchinnikov, Yefim Kogan, Frank Evans, Anthony Davis, Robert Cahalan, Ezra Takara, Robert Ellingson

11:24 PARAMETERISATION OF NON-INDUCTIVE CHARGING IN THUNDERSTORM REGIONS FREE OF CLOUD DROPLETS 1537
Rumjana Mitzeva, Clive Saunders, Boryana Tsenova

11:25 INNER STRUCTURE AND PRECIPITATION MECHANISM IN OROGRAPHIC SNOW CLOUDS OVER THE COMPLEX TERRAIN IN CENTRAL JAPAN 1541
Masataka Murakami, Narihiro Orikasa, Ken-Ichi Kusunoki, Kazumasa Mori, Akihiro Ikeda, Mitsunori Saitoh

11:26 NUMERICAL STUDY ON STRUCTURE AND MAINTENANCE MECHANISM OF TYPHOON SPIRAL BANDS USING THE CLOUD RESOLVING STORM SIMULATOR 1545
Mitsuharu Nomura, Kazuhisa Tsuboki

11:27 NUMERICAL SIMULATION OF THE WARM-SEASON FRONTAL CLOUD SYSTEMS WITH STRONG PRECIPITATION 1549
Anne Pirnach

11:28 CELL MERGER SIMULATIONS WITH THREE-DIMENSIONAL ENVIRONMENTAL DATA 1553
Diana R. Pozo, Israel Borrajero, Julio C. Marín, Graciela Raga, Daniel Martínez

11:29 MODELING TROPICAL ATMOSPHERIC CONVECTION IN THE CONTEXT OF THE WEAK TEMPERATURE GRADIENT APPROXIMATION 1557
David J. Raymond, Xiping Zeng

11:30 NUMERICAL STUDY ON SNOW CLOUD STREETS IN COLD AIR STREAM OVER THE SEA USING THE CLOUD RESOLVING STORM SIMULATOR 1561
Atsushi Sakakibara, Kazuhisa Tsuboki

11:31 RADIATIVE AND MICROPHYSICAL PROPERTIES OF MIXED-PHASE ALTOCUMULUS A MODEL EVALUATION OF SUPERCOOLING EFFECTS 1565
Kenneth Sassen, Vitaly I. Khvorostyanov

11:32 ON THE DEPENDENCY OF PRECIPITATION FROM MIXED-PHASE CONVECTIVE STORMS ON VERTICAL WIND SHEAR, BUOYANCY AND CLOUD CONDENSATION NUCLEI 1569
Axel Seifert, Klaus D. Beheng

11:33 CLOUD-ENSEMBLE SIMULATIONS OF TROPICAL CONVECTION UNDER DIFFERENT MICROPHYSICAL REGIMES 1573
Antônio Charles Silvério, Alexandre Araújo Costa, José Carlos Parente De Oliveira, Gerson Paiva De Almeida, Sergio Sousa Sombra

11:34 CIRRUS SIMULATIONS OF CRYSTAL-FACE 23 JULY 2002 CASE 1576
David Starr, Ruei-Fong Lin, Belay Demoz, Andrew Lare

11:35 MESOSCALE SIMULATIONS OF CRYSTAL-FACE 23 JULY 2002 CASE 1580
David Starr, Ruei-Fong Lin, Andrew Lare, Belay Demoz, Thomas Rickenbach, Donghai Wang, Lihua Li, G. Thomas Arnold, Yansen Wang

11:36 A COMPARISON OF CONSERVATION PROPERTIES OF MICROPHYSICAL PARAMETERIZATIONS: CONTINUOUS GAMMA DISTRIBUTION FUNCTION WITH FIXED SHAPE PARAMETER 1584
Jerry M. Straka, Mathew S. Gilmore, Erik N. Rasmussen, Katherine M. Kanak

11:37 A MICROPHYSICS PARAMETERIZATION SCHEME FOR RADAR DATA ASSIMILATION 1588
Wanda Szyrmer, Isztar Zawadzki, Stephane Laroche

11:38 FORMATION OF A FIRE-INDUCED CONVECTIVE CLOUD: A MODEL STUDY OF THE CHISHOLM FIRE, 28 MAY 2001 1592
Joerg Trentmann, Tanja Winterrath, G. Luderer, Christiane Textor, Michael D. Fromm, Rene Servranckx, Daniel Rosenfeld, Pao K. Wang, Peter V. Hobbs, Meinrat O. Andreae

11:39 EVALUATION OF CLOUDS AND PRECIPITATION FROM A GLOBAL NWP MODEL 1596
Paul A. Vaillancourt, Stéphane Bélair, Michel Roch, Anne-Marie Leduc

11:40 INCORPORATION OF A 1D ACOUSTIC-ELECTROSTATIC COALESCENCE MODEL INTO THE 3D CLOUD MODEL 1600
Zlatko Vukovic, Mladjen Curic

11:41 THE IMPACT OF EXTREME WATER VAPOR SUPPLY ON OROGRAPHIC-CONVECTIVE-STRATIFORM MIXED CLOUD 1604
Weijia Wang, Xialing Tao

11:42 THREE-DIMENSIONAL NUMERICAL SIMULATION OF TORRENTIAL RAINSTORMS IN WUHAN 1608
Hui Xiao, Xiaobo Wang, Feifei Zhou, Yanchao Hong

11:43 CHARACTERISTIC ANALYSES OF THE CONCENTRATIONS OF ATMOSPHERIC ICE FORMING NUCLEI IN THE SOURCE AREA OF YELLOW RIVER 1612
Hui Xiao, Yuxiang He, Bojie Chen, Zhanyu Yao

11:44 NUMERICAL SIMULATION OF THE INFLUENCE OF ATMOSPHERIC ICE NUCLEI DISTRIBUTION ON CONVECTIVE CLOUD SEEDING EFFECT 1616
Hui Xiao, Shuyan Liu, Zhaoxia Hu, Qiang Zhang

TOPIC 12: CLOUD DYNAMICS AND STRUCTURE

12:1 DETERMINING CLOUD SCALING ANISOTROPY EXPONENTS USING DIRECTIONAL STRUCTURE FUNCTIONS APPLIED TO MODIS SATELLITE IMAGES 1620
Jean-Bernard Addor

12:2 THE LIQUID WATER/ICE CONTENT IN MID-LATITUDE CONVECTIVE STORMS 1624
Ingo Bertram, Axel Seifert, Klaus D. Beheng

12:3 THE DIURNAL CYCLE OF SOUTHEAST PACIFIC STRATOCUMULUS DYNAMICS AND ENTRAINMENT OBSERVED IN EPIC 2001 1628
Christopher S. Bretherton, Peter Caldwell, Robert Wood

12:4 CAN THE FRACTAL DIMENSION OF CLOUDS BE MEASURED? 1632
Joseph Brewer, Larry Di Girolamo

12:5 CHARACTERIZATION OF MESOSCALE FEATURES IN SE PACIFIC STRATOCUMULUS 1636
Kimberly Comstock, Christopher Bretherton, Sandra Yuter, R. Wood

12:6 VELOCITY FIELDS IN CUMULUS DERIVED FROM AIRBORNE DUAL-DOPPLER MEASUREMENTS 1639
Rick Damiani, Samuel Haimov, Gabor Vali

12:7 FACTORS CONTROLLING THE FORMATION AND EVOLUTION OF CUMULONIMBUS ANVILS OVER SOUTHERN FLORIDA 1643
Ann Fridlind, Andrew Ackerman, Eric Jensen

12:8 CHARACTERISTICS OF PRECIPITATING CLOUDS OVER ASIA DURING SUMMER AS DERIVED FROM TRMM PR AND TMI 1646
Yunfei Fu, Rui Li, Guosheng Liu, Jinli Liu, Daren Lu

12:9 CLOUD HOLES 1650
Hermann Gerber, Glendon Frick, Simon Malinowski, Jean-Lui Brenguier, F. Burnet

12:10 CENTRIFUGAL PRECIPITATION TRANSPORT IN TORNADIC SUPERCELLS: AN ALGORITHM CONSISTENT FOR USE WITH BULK MICROPHYSICS SCHEMES 1654
Matthew Gilmore, Robert P. Davies-Jones, Jerry M. Straka, Erik N. Rasmussen, Robert B. Wilhelmson

12:11 SMALL SCALE MIXING PROCESSES AT THE TOP OF A MARINE STRATOCUMULUS - A CASE STUDY. 1657
Krzysztof E. Haman, Szymon P. Malinowski, Joanna Remiszewska, Marcin Kurowski, Hermann Gerber, Jean-Louis Brenguier

12:12 IMPACTS OF UNIFORM FLOW ON THE DIFFUSION OF THE ICE NUCLEI IN STRATUS 1661
Hui He, Wankui Chen

12:13 STRUCTURES OF CLOUDS AND PRECIPITATION PRODUCING MECHANISMS 1665
Peter Hobbs, Arthur Rangno

12:14 A 3D STOCHASTIC CLOUD MODEL FOR INVESTIGATING THE RADIATIVE PROPERTIES OF INHOMOGENEOUS CIRRUS CLOUDS 1669
Robin Hogan, Sarah Kew

12:15 A NUMERICAL STUDY OF THE SNOWFALL AROUND THE NIIGATA REGION 1673
Katsushi Iwamoto, Sento Nakai, Masaaki Ishizaka, Masujiro Shimizu, Atsushi Sato, Toshisuke Maruyama

12:16 INVESTIGATION OF THE EVOLUTION OF RELATIVE HUMIDITY DURING TURBULENT MIXING USING PDF METHODS 1675
Christopher A. Jeffery

12:17 STRUCTURE AND EVOLUTION OF LONG-LIVED SLOW-MOVING LINE-SYSTEM IN MOIST AND WARM ENVIRONMENT IN EAST ASIA. 1679
Sachie Kanada, Teruyuki Kato, Masanori Yoshizaki

12:18 OCEANIC DIURNAL PRECIPITATING SYSTEMS OVER THE TROPICAL WESTERN PACIFIC, NORTH OF NEW GUINEA ISLAND 1683
Masaki Katsumata, Kunio Yoneyama

12:19 THE LIFE CYCLE OF CONVECTIVELY GENERATED STRATIFORM CLOUDS 1687
Steven K. Krueger, Michael A. Zulauf, Yali Luo

12:20 STRUCTURE OF LWC AND TEMPERATURE FIELDS IN SMALL CUMULUS CLOUDS SEEN FROM STATIONARY (TETHERED BALLOON) AND MOVING (AIRCRAFT) PLATFORMS. 1691
Marcin Kurowski, Holger Siebert, Krzysztof E. Haman, Szymon P. Malinowski

12:21 HUMIDITY CHARACTERISTICS IN THE DETRAINMENT REGION OF SMALL CUMULUS 1695
Neil Laird, Robert M. Rauber, Harry T. Ochs

12:22 COMPARISON STUDY OF A TYPHOON PRECIPITATION OVER SOUTH CHINA SEA 1697
Jinli Liu, Gang Zhao, Jiantong Li, Daren Lu, Yong Zhang, Ling Zhang

12:23 NUMERICAL SIMULATION OF RETRIEVING THREE-DIMENSIONAL WIND FIELD FROM DUAL DOPPLER RADAR 1701
Shuyan Liu, Hui Xiao, Yuxiang He

12:24 SIMULATIONS OF MEIYU FRONT WITH A NEW MICROPHYSICS SCHEME 1704
Xiaofeng Lou, Zhijin Hu, Penyun Wang, Xiuji Zhou, Yueqing Shi, Jing Sun

12:25 MIXING OF CLOUD AND CLEAR AIR IN CENTIMETER SCALES OBSERVED IN LABORATORY BY MEANS OF PARTICLE IMAGE VELOCIMETRY 1707
Szymon P. Malinowski, Piotr Korczyk, Tomasz A. Kowalewski

12:26 EFFECTS OF MESOSCALE CONVERGENCE ON CONVECTIVE RAINFALL SIMULATED WITH AN AXISYMMETRIC CLOUD MODEL WITH DETAILED MICROPHYSICS 1711
Ryohei Misumi, Ken-Ichi Maruyama, Masayuki Maki, Koyuru Iwanami, Sang-Goon Park, Mihoko Suto

12:27 AN OBSERVATIONAL STUDY OF THE NIIGATA SNOWSTORM OF 4-6 JANUARY 2003 1715
Sento Nakai, Masaaki Ishizaka, Katsushi Iwamoto, Masujiro Shimizu, Atsushi Sato, Toshisuke Maruyama

12:28 INSIGHTS ON THE UPDRAUGHT EXTINCTION BY SATELLITE OBSERVATIONS AND CLOUD MICROPHYSICAL MODEL 1719
Alvise Papa, Federico Porcù, Alessandro Battaglia, Pao K Wang, Stefano Natali, Franco Prodi

12:29 ANVIL CIRRUS STRUCTURE 1723
Jacob Petre, Johannes Verlinde

12:30 THE INFLUENCE OF MELTING ON THE PRECIPITATION PRODUCTION IN A MARITIME STORM-CLOUD 1726
Vaughan Phillips, Alexander Khain

12:31 EVALUATION OF VERTICAL AIR VELOCITY AND ITS DISTRIBUTION IN FOUR OPERATIONAL FORECAST MODELS USING CONTINUOUS DOPPLER CLOUD RADAR MEASUREMENTS 1730
Alain Protat, Dominique Bouniol, Martial Haeffelin

12:32 STRUCTURE AND LENGTH SCALES OF A STRATOCUMULUS FIELD DEVELOPING UNDER CONTINENTAL INFLUENCE: THE BBC CASE 23.09.01 1734
Markus Quante, Jens Meywerk, Dagmar Nagel

12:33 MAINTENANCE MECHANISM OF CONVECTIVE CELLS WITHIN MESOSCALE CONVECTIVE SYSTEM IN HUMID SUBTROPICAL REGION 1738
Shingo Shimizu, Hiroshi Uyeda, T. Shinoda, K. Tsuboki, H. Yamada, B. Geng, T. Kato

12:34 THE BALTEX BRIDGE CAMPAIGNS – A QUEST FOR CONTINENTAL CLOUD STRUCTURES 1742
Clemens Simmer, V. Venema, M. Diederich, S. Crewell, Arnout Feijt, Jean-Louis Brenguier

12:35 CU OF NORTH-WEST OF RUSSIA (GENERALIZED CHARACTERISTICS) 1746
Andrey Sinkevich, Yulia Dovgaluk, Yury Ponomarev, Vladimir Stepanenko, Nikolay Veremey

12:36 VERTICAL MOTIONS AT CIRRUS ALTITUDES 1750
Johan Ström

12:37 CIRRUS CLOUD OCCURRENCE AS FUNCTION OF AMBIENT RELATIVE HUMIDITY: A COMPARISON OF OBSERVATIONS OBTAINED DURING THE INCA EXPERIMENT 1754
Johan Ström, Marco Seifert, Bernd Kärcher, Joelle Ovarlez, Andreas Minikin, Jean-Francois Gayet, Radovan Krejci, Andreas Petzold, Frederique Auriol, W. Haag, R. Busen, U. Schumann, H. C. Hansson

12:38 AIRBORNE RADAR OBSERVATIONS OF NON-DRIZZLING MARINE STRATOCUMULUS 1758
Gabor Vali

12:39 ITERATIVE AMPLITUDE ADAPTED FOURIER TRANSFORM SURROGATE CLOUD FIELDS 1761
Victor Venema, Steffen Meyer, Sebastián Gimeno García, Clemens Simmer, Susanne Crewell, Ulrich Löhnert, Thomas Trautmann

12:40 SIZE DISTRIBUTIONS OF SNOW AND AEROSOL PARTICLES IN A CONTINUOUS PRECIPITATION WITH A CHANGE OF SURFACE OZONE CONCENTRATION AT NY-ÅLESUND, ARCTIC 1765
Makoto Wada, Hiroyuki Konishi, Shinji Morimoto, Takashi Yamanouchi

12:41 PRECIPITATION TYPE CLASSIFICATION IN THE BALTIC AREA IN RADAR OBSERVATIONS AND IN REMO 1769
Andi Walther, Jürgen Fischer, Ralf Bennartz

12:42 OBSERVATION OF A MESOSCALE CONVECTIVE SYSTEM IN A BAIU-FRONTAL DEPRESSION GENERATED NEAR THE EAST COAST OF THE EURASIAN CONTINENT 1773
Hiroyuki Yamada, Biao Geng, K. Krishna Reddy, Hiroshi Uyeda

TOPIC 13: CLOUD PROCESSES AND THE MESOSCALE

13:1 THE ANALYSIS OF PRECIPITATION CHARACTERISTICS IN HEBEI PROVINCE 1777
Zhihui Wu, Duan Ying, Xiaobin Wang, Lixin Shi , Xinmin Zhang

13:2 MODELLING THE IMPACT OF URBAN AREAS ON PRECIPITATION INITIATION 1781
M.G.D. Carraça, C.G. Collier

13:3 TROPOSPHERIC DRYNESS AND CLOUDS OVER TROPICAL INDIAN OCEAN. 1785
Frédérique Cheruy, Gian-Luigi Liberti, Caterina Iori

13:4 CLOUDS SPACE AND TIME SCALE IN THE MEDITERRANEAN AREA: CLIMATE MODEL AND OBSERVATIONS. 1789
Frédérique Cheruy, Gian-Luigi Liberti

13:5 OBSERVATIONS OF CLOUDS AND PRECIPITATION OVER THE ARCTIC OCEAN BY USING THE RESEARCH VESSEL "MIRAI" 1793
Yasushi Fujiyoshi, Kazuho Yoshida, Hideyuki Kasuya, Osamau Tsukamoto, Hajime Okamoto, Hiroaki Horie

13:6 ENVIRONMENTAL VARIABLES AFFECTING THE HAILSTONE'S SIZE DISTRIBUTION 1796
Dario B. Giaiotti, Fulvio Stel

13:7 A STUDY ON PRECIPITATION FORMATION MECHANISM OF COLD FRONTAL CLOUD SYSTEM IN HENAN PROVINCE 1799
Yanchao Hong, Zhongxiu Liu

13:8 STRUCTURE AND DYNAMICS OF THE DEVELOPMENT AND CLASSIFICATION OF THE HAIL-STORM PROCESSES IN UZBEKISTAN 1803
Kh.A. Imamdzhanov

13:9 A CLIMATOLOGY OF CONVECTIVE PRECIPITATING PATTERNS IN AFRICA 1806
Arlene Laing, Richard Carbone, Vincenzo Levizzani

13:10 ANALYSIS CHARACTERISTIC OF SPRING PRECIPITATION CLOUD IN SHAAXI AND GANSU PROVINCE 1808
Heng-Chi Lei, Yu-Xia Wu, Peng Fan

13:11 STUDY OF A TYPICAL COLD FRONT RAIN BELT MICRO CHARACTERISTICS, PRECIPITATION MECHANISM AND ARTIFICIAL WEATHER MODIFICATION POTENTIAL 1811
Jian Liu, Yong Yu, Tong Jiang, Xinzhi Chen

13:12 CONVECTIVE SYSTEM AREA EXPANSION AND ITS RELATIONSHIP WITH PRECIPITATION INTENSITY 1815
Luiz Augusto T Machado, Henri Laurent

13:13 NUMERICAL SIMULATION OF A SUPERCELL STORM OVER CAMAGÜEY, CUBA. 1818
Daniel Martinez, Diana R. Pozo, Arnoldo Bezanilla, Sadiel Novo

13:14 IMPACT OF TOPOGRAPHY RESOLUTION AND UPPER AIR DATA ON REAL DATA THUNDERSTORM SIMULATION USING RAMS 1822
Parthasarathi Mukhopadhyay

13:15 MESOSCALE AND MICROSCALE STRUCTURES OF PRECIPITATION BANDS ASSOCIATED WITH BAIU FRONT□AIRCRAFT OBSERVATIONS AND NUMERICAL SIMULATIONS 1825
Masataka Murakami, Akihiro Hashimoto, Narihiro Orikasa, Kazumasa Mori, Hiroshi Kuraiwa, Akihide Kamei, Haruya Minda

13:16 THE RELATIONSHIP BETWEEN SOUTH AMERICAN LOW-LEVEL JET EVENTS WITH THE FORMATION AND MAINTENANCE OF MESOSCALE CONVECTIVE SYSTEMS 1829
Matilde Nicolini, Paola Salio, Juan Carlos Torres, Edward J Zipser

13:17 NUMERICAL INVESTIGATION OF THE INTER WAVE-ROTOR STRUCTURE OF FRONTAL CLOUDS AT DIFFERENT STAGES OF THEIR DEVELOPMENT 1833
Ludmila Palamarchuk, Anna Pirnach, Vitaliy Shpyg

13:18 THREE DIMENSIONAL KINEMATIC AND MICROPHYSICAL EVOLUTION OF MAP IOP3B OROGRAPHIC PRECIPITATION 1837
Olivier Pujol, Jean-François Georgis, Michel Chong, Frank Roux

13:19 FORMATION OF THE CONVECTIVE CELL IN SHEET CLOUD AND THE NUMERICAL EXPERIMENTS OF ITS INFLUENCE ON THE PRECIPITATION 1841
Yanbin Qi, Dezhen Jin, Yanli Qi

13:20 DIURNAL CYCLE OF MESOSCALE CONVECTIVE SYSTEMS OVER SOUTHEASTERN SOUTH AMERICA 1844
Paola Salio, Edward Zipser, Matilde Nicolini, Chuntao Liuct

13:21 UNIVERSAL LAWS FOR POSTFRONTAL SHOWER CLOUDS 1848
Michael Theusner, Thomas Hauf

13:22 WRF SIMULATIONS OF RAINFALL COHERENCE OVER THE CONTINENTAL UNITED STATES 1852
Stanley B. Trier, C. Davis, E. Carbone, S. Frederick

13:23 ON THE FORMATION OF LONGITUDINAL CLOUD MODE IN THE WINTER MONSOON OVER JAPAN 1855
Akira Watanabe

13:24 KEY PARAMETERS AND PROCESSES LEADING TO TORRENTIAL RAINFALL EVENTS IN THE SOUTH – EASTERN MASSIF CENTRAL, FRANCE 1859
Wolfram Wobrock, Andrea Flossmann, G. Delrieu, S. Anquetin

13:25 DRIZZLE AND CLOUD STRUCTURE IN SE PACIFIC STRATOCUMULUS 1863
Robert Wood, Kim Comstock, Peter Caldwell, Chris Bretherton, S.E. Yuter

13:26 ON HETEROGENEITY OF DRIZZLE IN A STRATOCUMULUS-TOPPED MARINE BOUNDARY LAYER 1867
Bai Yang, Yefim Kogan

13:27 OROGRAPHIC PRECIPITATIONS. PHYSICAL PROCESSES AND CONTRIBUTION TO THE RAINFALL REGIME OF THE CÉVENNES – VIVARAIS REGION. 1871
Eddy Yates, Sandrine Anquetin, Jean-Martial Cohard

13:28 A CASE STUDY ON THE COLD-FRONT AND CYCLONE CLOUDS WITH THEIR MULTI-SCALE STRUCTURES AND PRECIPITATING MECHANISMS IN CHINA 1875
Yuquan Zhou, Yanchao Hong, Aifang Su, Yimei Huang

TOPIC 14: CLOUD PROCESSES

14:1 PROMINENT FEATURES OF THE GRAVITY WAVES GENERATED BY TROPICAL CONVECTION DETECTED BY VHF DOPPLER RADAR: A CASE STUDY. 1879
S. Abhilash, K. Mohankumar

14:2 IMPACT OF HORIZONTAL MODEL RESOLUTION ON CLOUD PARAMETERS FORECASTED BY A NON-HYDROSTATIC MESOSCALE MODEL 1883
Felix Ament, Susanne Crewell, Clemens Simmer

14:3 RIMING AND OTHER CHARACTERISTICS OF COLUMNS AND ROSETTES OBSERVED IN WAVE CLOUDS 1887
Brad Baker, Paul Lawson

14:4 RADAR CHARACTERISTICS OF PRECIPITATING CLOUDS IN THE UNITED ARAB EMIRATES 1891
Daniel Breed, Roelof Bruintjes, Nancy Rehak, Abdulla Al Mangoosh, Abdulla Al Mandoos

14:5 LOCAL OROGRAPHY INFLUENCE ON VORTICITY INSIDE CB CLOUD 1895
Mladjen Curic, Dejan Janc, Vladan Vuckovic, Dragana Vujovic

14:6 MICROPHYSICS OF PRECIPITATION ASSOCIATED WITH CLOUDBURSTS FORCED BY OROGRAPHY AND LARGE-SCALE SYNOPTIC CONDITIONS IN DIFFERENT CONVECTIVE REGIMES 1899
Someshwar Das, Raghavendra Ashrit

14:7 A PRELIMINARY STUDY ON THE VARIABLE TENDENCY AND PHYSICAL CAUSE OF FORMATION OF THE NATURAL PRECIPITATION OVER HEBEI AREA 1903
Ying Duan, Baodong Yang, Jinping Guo, Zhihui Wu, Laiguang You, Yuegai An

14:8 THE CLOUD PHYSICAL CHARACTERISTICS AND PRECIPITATION OF CONVECTIVE CLOUD SYSTEMS MODIFIED BY URBANIZATION IN BEIJING REGION 1907
Xueliang Guo, Jing Wang, Danhong Fu

14:9 PARAMETERIZATION OF NON-INDUCTIVE CHARGE TRANSFER BASED ON DISCRIMINANT AND REGRESSION ANALYSES OF LABORATORY DATA 1911
Anastasia Kirilova, Rumjana Mitzeva, Boryana Tsenova

14:10 SIMULATION OF CONVECTIVE SYSTEMS USING MESOSCALE MODEL WITH SPECTRAL MICROPHYSICS 1915
Barry Lynn, Alexander Khain, Andrei Pokrovsky, Daniel Rosenfeld, Axel Seifert

14:11 THE INFLUENCE OF RAINDROP CLUSTERING ON NEW REPRESENTATIONS OF COLLISION-INDUCED BREAKUP: IMPLICATIONS FOR RAINDROP SIZE DISTRIBUTIONS 1919
Greg M. Mcfarquhar

14:12 SOME IMPORTANT MULTI-SCALE FEATURES OF VERTICAL MOISTURE TRANSPORT RELATED TO CLOUD STREETS 1923
Mikhail Mezrin, Evgeny Starokoltsev, Y. Fujiyoshi, M. Yoshizaki

14:13 A MODELLING STUDY OF MIXED-PHASE CONVECTIVE CLOUD SEEDING AND ITS EFFECT ON THUNDERSTORM CHARGING 1927
Rumjana Mitzeva, S. Petrova, John Latham

14:14 STRUCTURE AND DEVELOPMENT OF TWO MERGED RAINBANDS ALONG THE BAIU FRONT AND THE "WATER VAPOR FRONT" OVER THE EAST CHINA SEA DURING X-BAIU-99 1931
Qoosaku Moteki, Hiroshi Uyeda, Teruyuki Kato, Masanori Yoshizaki

14:15 FORMATION PROCESS OF AN OROGRAPHIC LINE-SHAPED RAINFALL SYSTEM FROM A VIEWPOINT OF CELLULAR ECHOES ON THE SOUTH OF THE BAIU FRONT IN WESTERN KYUSHU, JAPAN 1935
Ayako Nakamura, Hiroshi Uyeda, Masanori Yoshizaki, Yoshinobu Tanaka, Shuji Shimizu

14:16 SIMULATION OF DEVELOPMENT OF DEEP CONVECTION FROM SHALLOW CLOUDS. 1939
Tomoe Nasuno

14:17 OBSERVATIONAL STUDY OF THE SNOWFALL SYSTEM ASSOCIATED WITH A MESOSCALE LOW FORMED OVER THE SEA OF JAPAN 1943
Tadayasu Ohigashi, Kazuhisa Tsuboki

14:18 APPLICATION OF CLUSTER ANALYSIS TECHNIQUES TO THE VERIFICATION OF QUANTITATIVE PRECIPITATION FORECASTS 1947
Stefano Serafin, Alessio Bertò, Andrea Buzzi, Rossella Ferretti, Dino Zardi

14:19 PRECIPITATION CHARACTERISTICS OF CUMULONIMBUS CLOUDS IN THE SOUTHERN REGION OF THE MEIYU FRONT OVER CHINA CONTINENT 1951
Yukari Shusse, Kazuhisa Tsuboki

14:20 TETHERED-BALLOON BORNE MEASUREMENTS IN BOUNDARY LAYER CLOUDS. PART I:TURBULENCE AND DYNAMICS 1955
Holger Siebert, Katrin Lehmann , Manfred Wendisch, Szymon P. Malinowski

14:21 THE RESPONSE OF HEATING AND MOISTURE IN CONTINENTAL AND OCEANIC MESOSCALE CONVECTIVE SYSTEMS TO THERMODYNAMIC AND DYNAMICAL PROCESSES 1959
Chiharu Takahashi, Hiroshi Uyeda

14:22 EFFECTS OF MOISTURE PROFILE ON THE DYNAMICS AND ORGANIZATION OF SQUALL LINES 1963
Tetsuya Takemi

14:23 STRUCTURE OF HEAVY RAINFALL SYSTEMS ASSOCIATED WITH A MESOSCALE LOW ALONG THE BAIU FRONT 1967
Kazuhisa Tsuboki, Takeshi Maesaka, Miki Hattori, Mitsuharu Nomura, Taro Shinoda, Hiroshi Uyeda

14:24 ORGANIZATION AND RAINFALL CHARACTERISTICS OF MONSOONAL CONVECTION DURING THE SOUTH EAST ASIAN SUMMER MONSOON 1971
Jian-Jian Wang

14:25 OBSERVATION AND NUMERICAL SIMULATION OF CLOUD PHYSICAL PROCESSES ASSOCIATED WITH TORRENTIAL RAIN OF THE MEI-YU FRONT IN SOUTH CHINA 1975
Pengyun Wang, Jing Yang, Xiangqian Gu, Xiaofeng Lou, Jing Sun

Topic	Table of Contents – Topics	No of Papers	Volume	Page
1	Aerosol-Cloud Interactions	72	1	1
2	Climate Change and Precipitation	28	1	261
3	Cloud-Climate Interactions	21	1	354
4	Interactions between Clouds and Atmospheric Chemistry	15	1	428
5	Warm Cloud Microphysics	60	1	483
6	Cold Cloud Microphysics	72	2	703
7	Cloud Electricity	13	2	982
8	Instrumentation	46	2	1029
9	Applications of Cloud Physics	26	2	1196
10	Cloud Parameterization in Models	46	2	1289
11	Modeling of Cloud-Scale Processes	44	3	1457
12	Cloud Dynamics and Structure	42	3	1620
13	Cloud Processes and the Mesoscale	28	3	1777
14	Cloud Processes	25	3	1879

Author Index

Abbatt, J. 465
Abhilash, S. 1879
Ackerman, A.S. 1, 455
1492,1643
Ackerman, T.P. 397, 404
876
Adamo, C. 596
Addor, J.-B. 1620
Al Mandoos, A. 217, 1218
1891
Al Mangoosh, A. 217, 1218
1891
Alberoni, P.P. 771
Albrecht, B.A. 5, 566
600
Alfarra, M.R. 20, 432
Allan, J.D. 39, 432
Altaratz, O. 982
Ament, F. 1883
Amiranashvili, A.G. 261, 265
267, 354
Amiranashvili, V.A. 265, 267
354
Amorim, W. 1008
An, Y. 1903
Anderson, J.R. 201
Andreae, M.O. 1592
Andrejczuk, M. 1457
Andrews, E. 175
Andronache, C. 9, 13, 892
Anquetin, S. 1859,1871
Aonashi, K. 759
Araújo Costa, A. 1573
Arduini, R.F. 600
Arkhipov, V. 483, 628
Arnold, G.T. 1580
Artaxo, P. 321
Ashrit, R. 1899
Auriol, F. 1754
Austin, R.T. 1029
Avila, E.E. 743
Ayala, O. 686
Ayers, J.K. 5, 600

Bachalo, W.A. 1056
Bachiashvili, L.L. 267
Back, L.E. 495
Bailey, M. 703,986
Baker, B. 835, 1119
1887
Baker, K.M. 1033
Bakhanov, V.P. 707, 711
Baldi, M. 269
Baldini, L. 533
Ball, R.C. 954
Baltensperger, U. 20, 1183
Bansemer. A. 788, 892
920, 1420
Bartello, P. 520
Barth, M.C. 428
Barthazy, E. 715, 719
920
Barthe, C. 990
Baruzzi Frediani, M.E. 1008
Baschek, B. 719, 920
Bateman, M. 1001
Battaglia, A. 499, 723
1048, 1719
Baumgardner, D.G. 727, 779
1037, 1108
Beard, K.V. 487, 608
Bechini, R. 596
Beheng, K.D. 537, 1416
1569, 1624
Bélair, S. 1596
Belcher, L. 547
Belosi, F. 1146
Benedetti, A. 1461
Bennartz, R. 1769
Bereznicki, S. 831
Berger, F.H. 1041
Berges, J.C. 273
Beritashvili, B.Sh. 261
Berner, A. 432
Bernstein, B.C. 1253
Berthet, C. 63
Bertò, A. 1947
Bertram, I. 1624
Besnard, T. 1089
Bezanilla, A. 1818
Bezrukova, N.A. 731, 1196
Bhar, S. 1257
Bibilashvili, T. 265, 267
Blahak, U. 924
Blanchet, J.-P. 670
Blyth, A.M. 491, 503
Bonafè, U. 389
Borrajero, I. 1553
Borrmann, S. 17, 171
452, 946
Bortoli, D. 389
Borys, R. D. 59, 100
Bott, A. 1465, 1499
Bouchet, V.S. 448
Boudala, F.S. 1289
Bouniol, D. 735, 1730
Bouzereau, E. 1200
Bower, K.N. 20, 39, 356
432, 747, 1078
Breed, D.W. 24, 217
1218, 1891
Breitgand, J. 1228
Brenguier, J.-L. 360, 371, 503
612, 1059, 1393
1650, 1657, 1742
Bretherton, C.S. 495, 1628
1636, 1863
Brewer, J. 1632
Bringi, V.N. 533
Broekhuizen, K. 465
Brooks, M.E. 1293
Brooks, S. 59
Brown, P.R.A. 1074, 1469
Bruintjes, R.T. 24, 213,217
1204, 1218
1891
Buelow, K. 292
Burnet, F. 360, 1650
Burtscher, H. 1183
Busch, B. 116
Busek, P. 24
Busen, R. 1754
Bushell, A.C. 1438
Büttner, S. 43, 364
Buzzi, A. 1947

Cahalan, R.F. 1044, 1533
Cai, X. 1027
Caldwell, P. 1628, 1863
Calzolari, P. 389
Canagaratna, M.R. 32
Cancel, R. 428
Capacci, D. 1048
Caracciolo, C. 499, 1052
Carbone, R.E. 1806, 1852
Cardwell, J. 1473
Carissimo, B. 1200
Carraça, M.G.D. 1781
Carrió G.G. 367, 755
Carvalho, L.M.V. 28
Carver, R.W. 739
Castellano, N.E. 743
Castro, A. 277, 763
Cattani, E. 32, 47
Cavalli, F. 98, 153
157, 436
Ceccarelli, F. 1480
Cesarone, F. 269
Chaboureau, J.-P. 1476
Chandrasekar, V. 533
Chang, D.-E. 1107
Chen, B. 1612
Chen, G. 1272
Chen, H. 544
Chen, H.-T. 1212
Chen, J.-P. 35, 104, 227
Chen, W. 1661
Chen, X. 1222, 1261
1811
Chen, Zhengqi 1208, 1278
Chen, Zhixin 1215, 1282
Cheng, C.-T. 35
Cheng, Y. 281
Chepfer, H. 727
Chéruy, F. 1785, 1789
Chlond, A. 469, 1295, 1519
Chong, M. 1837
Chopin, F. 273
Chosson, F. 371
Choularton, T.W. 20, 39, 43
356, 747
1473
Christian, H.J. 1001
Christian Jr, H.J. 997
Chuang, P.Y. 1056
Cimini, D. 1130
Clarke, A.J.M. 1175
Clarke, P. 39
Clegg, S. 157
Coals, A. 503
Cober, S.G. 400, 796
800, 1074
Coe, H. 20, 39, 251
432, 473
Coelho, A.A. 1059
Cohard, J.-M. 1871
Colle, B. 1308
Collier, C.G. 1781

Comstock, K. 1636, 1863
Conant, B. 892
Connolly, P.J. 43, 78, 160
364, 747
751, 1175
Conway, B. 1048
Cooper, W.A. 491
Corrigan, C. 20
Costa, M.J. 32, 47
Costa, A.A. 588
Cotton, R. J. 78, 751
1340, 1484
Cotton, W.R. 253, 367
755, 916
1500
Cousineau, S. 448
Covert, D.S. 171, 175
Craig, G.C. 1401
Crevier, L.-P. 448
Crewell, S. 1063, 1434
1742, 1761
1883
Cubison, M. 39, 251, 432
Cui, L. 1225
Ćurić, M. 1600, 1895
Currie, B. 796
Cziczo, D. 59

D'Auria, R. 55
Dai, J. 1208, 1278
Dalu, G.A. 269
Damiani, R. 1639
Das, S. 1899
Dastoor, A.P. 448
Daum, P.H. 1366
Davies-Jones, R.P. 1654
Davis, A.B. 1533
Davis, C.A. 1852
Davison, J. 608
De, U.K. 1257
De Luca, P. 82
Decesari, S. 153,157
168, 432
436
Defer, E. 507, 510,994
Deierling, W. 997
Delrieu, G. 1859
DeMott, P.J. 59, 850, 1150
Demoz, B. 1576, 1580
Deng, M. 861
Dessens, J. 63, 1238
Detwiler, A. 674
Devara, P.C.S. 205, 1066
Di Girolamo, L. 1632
Di Giuseppe, E. 285
Di Giuseppe, F. 1312
Di Michele, S. 596, 1428
Diallo, T.D. 309
Diederich, M. 1742
Diehl, K. 66, 231, 900
Dietrich. S. 596, 1428
Dobbie, S. 868
Donovan, D.P. 940
Dorman, B.A. 707, 711
Dovgaluk, Y.A. 1746
Drewnick, F. 171
Drobinski, P. 1378
Drofa, O.V. 1301
Duan, S 1190
Duan, Y. 973, 1158
1777, 1903
Dubois, F. 636, 1146
Dubuisson, P. 1476
Dunlea, E. 59
Dupont, E. 1200
Dupuy, R. 70
Durant, A.J. 880
Dye, J.E. 957, 1001

Ebert, V. 146, 160
Eito, H. 759
Eitzen, Z.A. 1488
Ellingson, R.E. 1533
Ellis, S.M. 997
Ellis, T.D. 375
Endoh, T. 440, 936
Epifani, C. 285, 288
Erlick, C. 513
Esposito, S. 285, 288
Evangelisti, F. 389
Evans, K.F. 1070, 1533
Facchini, M.C. 98, 153, 157
432, 436
Fairall, C.W. 566
Faloona, I.C. 193
Fan, P 1208, 1212
1278, 1808
Fan, S. 654
Fang, W. 517
Feijt, A. 1742
Feingold, G. 74, 479
Feldman, Y. 628
Ferretti, R. 1947
Fersiz, N. 177
Field, P.R. 43, 78, 160
364, 751, 954
1074, 1484
Fierz, M. 1183
Filice, M. 82
Fischer, B. 620
Fischer, J. 1769
Fitzpatrick, P.J. 1386
Flossmann , A.I. 164, 584
1859
Flynn, M.J. 20, 747
1078, 175
Fonseca, V.L. 277
Forbes, R.M. 1297
Fraile, R. 63, 277, 763
Franklin, C.N. 520
Frederick, S. 1852
Frick, G. 1650
Fridlind, A. 455, 788
1492, 1643
Fries, E. 452
Fromm, M.D. 1592
Fu, D. 1495, 1907
Fu, Q. 1304
Fu, Y. 1646
Fugal, J.P. 1081
Fujiyoshi, Y. 1793, 1923
Fukuta, N. 767
Fuzzi, S. 153, 157
432, 436
Gadian, A.M. 503, 1499
Galgon, D. 1138
Gallagher, M.W. 20, 39, 43
1078, 1175
Galletti, M. 771
Ganor, E. 131
Gao, J. 1215
García-García, F. 604, 1085
García-Ortega, E. 775, 1238
Garrett, T.J. 779, 1092
Garstang, M. 1204
Garvert, M.F. 1308
Gaussiat, N. 524
Gayet, J.-F. 1754
Geng, B. 1738, 1773
Genkova, I. 1089
Gennaro, V. 1005
Georgis, J.-F. 1837
Gerber, H. 528, 779, 896
1092, 1650, 1657
Geresdi, I. 86, 908
Giaiotti, D.B. 1005, 1796
Gillotay, D. 1089
Gilmore, M.S. 1500, 1584
1654
Gimeno García, S. 1761
Girard, E. 444
Givati, A. 90
Glazer, A. 1316
Glushykhin, V.A. 1160
Göke, S. 530
Golaz, J.-C. 1432, 1504
Gonçalves, F.L.T.588, 1508
Gong, S. 448
Gong, W. 448
Gorgucci, E. 533
Goswami, K. 1257
Gouvea, M. 321
Gozzini, B. 181
Grabowski, W.W. 335, 379
503, 686, 1320
1457, 1519
Grainger, A.C. 674, 1001
Gras, J.L. 189
Greenway, R.S. 1074
Grits, B. 632, 928
Grosvenor, D. 39
Grubišić, V. 313, 1324
Gu, S. 1215, 1222
1282
Gu, X. 1975
Gulev, S.K. 327, 347, 350
Gultepe, I. 800, 1326
Guo, Jinping 1903
Guo, Junmei 1215, 1261
Guo, Xueliang 1495, 1907
Gysel, M. 20

Haag, W. 1754
Habilomatis, G.P. 383
Hacker, J. 189
Haeffelin, M. 735, 1378
1730
Hagemann, S. 1519
Haggerty, J. 674
Haimov, S. 674, 961, 1639
Håkansson, M. 1095

Hall, W.D. 957, 1001 1330
Hallett, J. 177, 703 782, 786 944, 986
Haman, K.E. 1657, 1691
Hamazu, K. 823, 827
Handwerker, J. 537
Hansson, H.C. 1754
Harimaya, T. 94
Harrington, J.Y. 74, 739 1511
Hartman, C.M. 1511
Hase, M. 647
Hashimoto, A. 1515, 1825
Hashino, T. 1428
Hattori, M. 1967
Hatzianastassiou, N. 383
Hauf, T. 1848
Hayasaka, T. 387, 554
Hayashi, T. 440
Hayashi, S. 759, 1515
Hazra, A. 1257
He, F. 1261
He, G.-F. 517
He, H. 1661
He, W. 544
He, Y. 541, 1612 1701
Heck, P.W. 1253
Heintzenberg, J. 257
Hendricks, J. 393
Henseler, S. 17, 171
Hesse, E. 1175
Heymsfield, A.J. 43, 78, 160 547, 751, 788 892, 896, 954 1092, 1420
Heymsfield, G.M. 547, 892
Hiltunen, L. 98
Hindman, E.E. 100
Hirst, E. 1074
Hobbs, P.V. 1308, 1592 1665
Hock, N. 17, 171
Hogan, R.J. 524, 612 1293, 1669
Homma, A. 94
Hong ,Y. 792, 843 1608, 1799 1875
Hoog, I. 452
Horie, H. 1793
Hoshimoto, M. 823
Hourdin, F. 1378
Hsieh, W.-C. 104
Hu, Zaoxia 792, 1616
Hu, Zhijin 135, 1446 1704
Hu, Zhongming 1215
Huang, Gen 657
Huang, Yimei 1875
Hudak, D. 796
Hudson, J.G. 694, 1099
Huggins, A.W. 313, 1324
Huo, J. 1127
Ikeda, A. 1541
Ikeda, K. 908
Illingworth, A. 524, 612 1293, 1334
Imamdzhanov, Kh.A. 1803
Iorga, G. 235
Iori, C. 1785
Isaac, G.A. 796, 800 808, 961 1074, 1111 1289, 1316 1326
Ishizaka, M. 1103, 1673 1715
Ishizaka, Y. 94, 189
Ivanova, D.C. 1337
Iversen, T. 123
Iwamoto, K. 1673, 1715
Iwanami, K. 827, 1711

Jacob, D. 292, 1519
Jacobsonr, M.Z. 475
Jaeschke, W. 452
Jamali, J.B. 329
Jameson, A.R. 551
Janc, D. 1895
Janisková, M. 1461
Jayne, J.T. 432
Jeck, R.K. 731
Jeffery, C.A. 1675
Jensen, E. 455, 1492 1643
Jensen, J.B. 189
Jensen, L.T. 1218
Jensen, T. 24, 217
Jewett, B. 592
Jia, L. 24
Jiang, H. 74, 367 1340
Jiang, T. 1811
Jiménez, J.C. 1037
Jimenez, J.L. 59, 432
Jin, D. 1215, 1222 1841 1225 1246
Johnson, D. 246
Jones, C. 28, 294
Jones, C.G. 1344, 1442
Jonsson, H. 5
Joutsensaari, J. 98
Jovanovska, L. 1264

Kadyrov, B.Sh. 1520
Kalogiros, J. 507
Kamalov, B. A. 108, 111 113
Kamei, A. 1825
Kanada, S. 1679
Kanak, K.M. 1584
Kandler, K. 116
Kapala, A. 347, 350
Kärcher, B. 393, 1754
Kasprzak, S.E. 686
Kästner, M. 297
Kasuya, H. 1793
Kato, T. 339,759 1515, 1679 1738, 1931
Katsanos, D. 994
Katsumata, M. 1683
Kawamoto, K. 387, 554
Kawano, T. 1019
Kaye, P.H. 1074
Keil, C. 1348
Kelman, G. 301
Kerr-Munslow, A.M. 1438
Kew, S.F. 1669
Khain, A. 119, 221, 246 301, 483, 513 628, 632, 924 928, 1374, 1416 1726, 1915
Khairoutdinov, M.F. 379, 404 408, 1352
Khaiyer, M.M. 5, 1253
Khalili, M.F. 1196
Khurodze, T.V. 265
Khvorostyanov, V.I. 1565
Kikuchi, K. 458
Kim, M.-J. 1107, 1268
Kim, S.-W. 428
Kirilova, A. 1911
Kirkevåg, A. 123
Kirkpatrick, M 1
Kiselev, A. 257
Kliche, D.V. 664
Knight, C.A. 556
Kochin, A.V. 1523
Koehler, K. 59
Koga, S. 440
Kogan, Y.L. 560, 1354 1533, 1867
Kogan, Z.N. 1354
Kok, G.L. 727, 1108
Kokkola, H. 325, 564
Kolasinski, J. 1044
Kollias, P. 566
Konishi, H. 804, 1765
Kontani, K. 1015
Korczyk, P. 570, 1707
Korneev, V.P. 1160
Korolev, A.V. 808, 812 1074, 1111
Kostinski, A.B. 573
Kosuge, H. 827
Kotroni, V. 507, 510 596, 994, 1525
Kowalewski, T.A. 570, 1707
Krakovskaia, S.V. 816
Krämer, M. 78, 146 160, 751
Kreidenweis, S. 59
Krejci, R. 1754
Krishnamurti, T.N. 1480
Kristjánsson, J.E. 123, 239
Krueger, S.K. 1370, 1687
Kryvobok, O.A. 711
Kuba, N. 1358
Kucera, P.A. 820, 896
Kumagai, H. 1167
Kumar, B.Y. 205, 1066

Kurbatkin, V.P. 305
Kurihara, K. 339
Kurita, N. 440
Kuroiwa, H. 888, 1825
Kurowski, M. 1657, 1691
Kusunoki, K. 823, 827
1541

L'Ecuyer, T. 417
Laaksonen, A. 98, 325
564, 668
Labellec, A. 1378
Lagouvardos, K. 507, 510
596, 994, 1525
Lahav, R. 127
Laing, A.G. 1806
Laird, N.F. 530, 1695
Laj, P. 70
Lamb, D. 462, 865
Lanconelli, C. 389
Lara, L. 321
Lare, A. 1576,1580
Laroche. S. 1588
Larsen, M.L. 573
Larson, V.E. 1362,1504
Lasher-Trapp, S.G. 491, 831
Latham, J. 356, 997
1927
Lau, W.K.M. 1115
Laurent, H. 1815
Lawson, R.P. 835, 839
1070, 1119, 1887
Lazare, M. 421
Leaitch, R. 465
Leal Júnior, J.B.V. 588
Leduc, A.-M. 1596
Lee, G.W. 576, 698
Legros, J.C. 636, 1146
Lehmann, K. 580, 1138
1955
Lei, H. 678, 1194
1212, 1222
1225,1454
1529, 1808
Leighton. H.G. 185
Leovy, C.B. 1389
Leporini, M. 584
Lesins, G. 281
Levin, Z. 131, 982
1228
Levizzani, V. 32, 47
771, 1123
1171, 1806
Lewis, S. 957, 1001
Li, H. 792, 843, 975
Li, Jiantong 309, 1697
Li, Jianxin 1285
Li, Juan 135
Li, Lihua 1580
Li, Lunge 678
Li, M. 1222, 1246
Li, Rui 1646
Li, Ruijie 1232
Li, S. 846, 1529
Li, W. 1234
Li, X. 246
Li, Z. 1215

Liberti, G.L. 1785, 1789
Lima, A.A. 1186
Lin, R.-F. 850, 1576, 1580
Linke, C. 160, 364
List, R. 139, 854
858, 965, 978
Liu, Gang 1285
Liu, Guosheng 759, 1646
Liu, Jian 1225, 181
Liu, Jiinli 544, 1190
1646, 1697
Liu, L. 1285
Liu, Q. 969
Liu, S. 541, 1234
1616, 1701
Liu, S.C. 227
Liu, W. 969
Liu, X. 309
Liu, Y. 51, 1366
Liu, Zhongxiu 1799
Liu, Zuoting 281
Liuct, C. 1844
Lohmann, U. 142, 281
393, 465, 1450
Löhnert, U. 1063, 1761
Long, C. 1089
López, L. 763, 775, 1238
Lou, X. 1704, 1975
Lowenthal, D.H. 100
Lu, D. 1127, 1190
1646, 197
Luderer, G. 1592
Luo, C. 28
Luo, Q. 1285
Luo, Yali 1370, 1687
Luo, Yunfeng 281
Lupi, A. 389
Lynn, B. 1374, 1915

Mace, G.G. 861
Mach, D. 1001
Machado, L.A.T. 1008, 1815
Machey, B. 1480
MacKenzie, A.R. 1408
Maesaka, T. 1015, 1967
Magee, N. 865
Mahowald, N.M. 28
Makar, P.A. 448
Maki, M. 827, 1711
Malek, E. 1242
Malguzzi, P. 1301
Malinowski, S.P. 570, 1457
1650, 1657
1691, 1707
1955
Mangold, A. 146, 160
Mantovani, S. 723, 1048
Manzhara, A.A. 707
Mao, J. 135, 309
Maracchi, G. 269
Marchand, R.T. 397, 404, 876
Marcos, J.L. 775
Marcotte, D. 961
Marín, J.C. 1553
Marsham, J.H. 868
Martínez, D. 624, 1553
1818

Martins, J.A. 588, 1508
Maruyama, K.-I. 1711
Maruyama, T. 1673, 1715
Marzano, F.S. 1130
Mascart, P.J. 1476
Mass, C.F. 1308
Massling, A. 1138
Masunaga, H. 150
Mathieu, A. 1378
Matrosov, S.Y. 912
Matsui, T. 150
Matsushita, H. 1249
Mazin, I.P. 812, 872
McAnelly, R.L. 755
McDonough, F. 1253
McFarlane, N.A. 421, 1304
McFarlane, S.A. 876
McFarquhar, G.M 335, 400
592, 1337
1919
McFiggans, G. 39, 251
432, 473
McGill, M. 1044
McGraw, R. 1366
Mechem, D.B. 1354, 1533
Medaglia, C.M. 596
Memon, G. 1142
Ménard, S. 448
Meneguzzo, F. 269
Meng. S. 1285
Mertes, S. 1134, 1138
Meyer, S. 1761
Meywerk, J. 1734
Mezrin, M.Yu. 1923
Mi, Y. 880
Miekeley, N. 321
Miguélez, L. 277
Milbrandt, J.A. 1382
Miloshevich, L.M. 788
Minda, H. 888, 1825
Minikin, A. 1754
Minina, L.S. 731
Minnis, P. 5, 600, 1253
Mircea, M. 153, 157, 436
Misumi, R. 827, 1711
Mitchell, D.L. 313, 1337
Mitra, S.K. 452, 946
Mitzeva, R. 1537, 1911
1927
Mizuno, H. 823
Mkurnalidze, I.P. 261
Moehler, O. 78, 751
Mohankumar, K. 1879
Möhler, O. 43, 146
160, 364
Monier, M. 164
Montero-Martínez, G. 604, 1085
Morales, C.A. 1008
Moran, M.D. 448
Moretti, F. 168
Mori, K. 888, 1541
1825
Morimoto, S. 1765
Mostovoy, G.V. 1386
Moteki, Q. 1931
Moyle, A.M. 462, 865
Mugnai, A. 1123, 1428

Mukhopadhyay, P. 1822
Müller, F. 469, 1295
Münster, H. 620
Murakami, M. 823, 827
888, 1515
1541, 1825
Muramoto, K. 1103
Muroi, C. 339, 759, 1515
Murphy, D. 59
Musson-Genon, L. 1200

Nagel, D. 1734
Nakai, S. 1103, 1673
1715
Nakajima, T. 1167
Nakamura, A. 1935
Nardino, M. 389
Nastro, A. 82
Nasuno, T. 1939
Natali, S. 1052, 1719
Nevzorov, A.N. 884
Newman, A.J. 820
Nguyen, L. 1253
Nicolini, M. 1829, 1844
Nishio, N. 1249
Niu, S. 654
Nodia, A.G. 265
Noguchi, I. 440
Nomura, M. 1545, 1967
Noone, K.J. 171, 175
1095
Novo, S. 1818
Nowak, A. 1138
Nozawa, T. 243

O'Connor, D. 839, 1070
O'Connor, E.J. 612
Ochs III, H.T. 487, 530
608, 1695
Ogren, J.A. 171, 175
Ohigashi, T. 1943
Okamoto, H. 1793
Ola, T. 965
Olivares, G. 171
Oliveira, J.C.P. 588
Omidiora, O.F. 317
Oraltay, R.G. 177, 786
Orikasa, N. 823, 827
888, 1541
1825
Ovarlez, J. 1754
Ovtchinnikov, M. 404, 1533

Pabla, B. 448
Paiva de Almeida, G. 1573
Pakula, L.A. 408
Palamarchuk, L.V. 1833
Palencia, C. 763
Palikonda, R. 1253
Panegrossi, G. 1428
Papa, A. 1719
Pardo, J. 1476
Parente de Oliveira, J.C. 1573
Park, S. 1389
Park, S.-G. 827, 1711
Parker, L. 424
Pasi, F. 181
Pasqui, M. 181
Paul, S. 1257
Pauliquevis, T. 321
Paunova, I.T. 185
Pawlowska, H. 640, 1393
Perez, C.A. 624
Perrin, T. 1059
Petenko, I.V. 616
Peter, J.R. 189
Peters, G. 616, 620
Peters, M.E. 495, 1163
Petersen, W.A. 997
Petkovic, S. 1142
Petre, J. M. 1723
Petrov, V.V. 624, 1160
Petrova, S. 1927
Petters, M.D. 193, 197
201
Petzold, A. 1754
Pfeilsticker, K. 1154
Phillips, V.T.J. 9, 892, 1726
Pielke Sr. R. 150
Piketh, S.J. 24, 213, 217
Pilson, B. 835
Pincus, R. 1424
Pinsky, M. 221, 483
513, 628
32, 928
Pinty, J.-P. 990, 1397
1476
Pirnach, A.M. 816, 1549
1833
Plant, R.S. 1401
Podgurskaya, V.N. 343, 345
Podzun, R. 292
Poellot, M.R. 779, 788
892, 896
1092
Pokrovsky, A. 119, 1416
1915
Poli, V. 1171
Ponomarev, Y. Ph. 1746
Porcù, F. 723, 1048
1719
Posselt, R. 900
Pozo, D.R. 1553, 1818
Prenni, A. 59
Prevenslik, T.V. 1011
Prigent, C. 1476
Prodi, F. 499, 636
723, 1048
1052, 1146
1719
Protat, A. 735, 1730
Pu, J. 1276
Pujol, O. 1837

Qi, Yanbin 1841
Qi, Yanli 1841
Qi, Ying 1261
Quante, M. 1734
Raatikainen, T. 668
Raga, G.B. 727, 1037
1553
Ramesh, A. 329
Randall, D.A. 379, 1352
Randeu, W.L. 904
Rangno, A.L. 1665
Rao, D.N. 205, 1066
Rao, Y.J. 205, 1066
Rasinski, P. 640
Rasmussen, E.N. 1500, 1584
1654
Rasmussen, R.M. 86, 908
1330
Ratto, C.F. 1480
Rauber, R.M. 530, 592
1695
Raymond, D.J. 1557
Reddy, K.K. 1773
Rehak, N. 1891
Reichardt, J. 850
Reinhardt, T. 1404
Reinking, R.F. 912
Reisin, T. 982
Remer, L. 246
Remiszewska, J. 1657
Ren, C. 1408
Richard, E. 1476
Richardson, G. 1469
Richardson, M. 59
Rickenbach, T. 1580
Riemer, N. 643
Rio, C. 1378
Rissler, J. 157
Roch, M. 1596
Rodriguez, P. 796
Rogers, D.C. 1150
Romakkaniemi, S. 325, 564
Roman, J. 1107
Rosenfeld, D. 90, 119
127, 209
221, 301
1592, 1915
Ross, K.E. 24, 213
217, 428
Roth, N. 647
Roux, F. 1837
Rozendaal, M.A. 1389
Rudeva, I. 327
Russell, L.M. 171
Ryabov, Ya. 628

Saathoff, H. 43, 146, 160
Sahraei, J. 356
Saito, M. 1541
Sakakibara, A. 1561
Sakashita, K. 1015
Salazar, V. 24, 217, 1218
Saleeby, S.M. 916
Salio, P. 1829, 1844
Sánchez, J.L. 63, 775, 1238
Santachiara, G. 636, 1146
Sasaki, A. 94
Sasaki, H. 339
Sasaki, Y. 458
Sassen, K. 1565
Sato, A. 1103, 1673
1715
Sato, Y. 339
Saunders, C.P.R. 743, 1537
Saw, E.W. 1081
Schefold, R. 715, 719, 920
Scheirer, R. 1412

Schimmel, F. 469
Schmidt, S. 580, 1412
Schmitt, C. 788
Schnaiter, M. 78, 160
364, 751
Schneider, J. 171
Scholl, T. 1154
Schönhuber, M. 904
Schröder, M. 371
Schumann, U. 1754
Schutgens, N.A.J. 412
Schütz, L. 116, 160
Schwarzenböck, A. 1134
Sednev, I. 1295
Segal, Y. 221, 513
Seifert, A. 924, 1374
1416, 1420
1492, 1569
1624, 1754
1915
Sekelsky, S. 1107
Seland, Ø. 123
Serafin, S. 1947
Sergeyev, A.V. 1081
Servranckx, R. 1592
Shahabfar, A. 329
Shantz, N. 465
Shapiro, M. 632, 928
Sharon, T. 5, 600
Shaw, G.E. 225
Shaw, R.A. 651, 880
1081
Shen, Z. 1222
Shepherd, J. 473
Sherwood, S. 892
Shi, A. 657, 661
Shi, L. 1158, 1777
Shi, Y. 969, 1446, 1704
Shie, C.-L. 413
Shiina, T. 1103
Shimizu , M. 1673, 1715
Shimizu, S. 1738, 1935
Shinjo, K. 1015
Shinoda, T. 1015, 1738
1967
Shiu, C.-J. 227
Shpital, T.N. 343, 345
Shpyg, V.M. 1833
Shtivelman, D. 1228
Shusse, Y. 804, 1951
Siebert, H. 580, 1691
1955
Siems, S.T. 189
Silva, A.M. 32, 47
Silva Dias, M.A. 588, 1008
1508
Silvério, A.C. 1573
Simmel, M. 66, 231
Simmer, C. 347, 350
1742, 1761
1883
Simpson, J. 246, 413
Sinkevich, A.A. 1746
Skuratov, S.N. 1160
Smirnova, T.Y. 333
Smith, P.L. 664
Smith, Jr., W.L. 1253
Smolarkiewicz, P.K. 1457
Snider, J.R. 193, 197
201, 1163
Sorjamaa, R. 668
Sousa Sombra, S. 1573
Spangenberg, D.A. 1253
Spiridonov, V. 1264
Srivastava, A.K. 205, 1066
Stachnik, J. 831
Starokoltsev , E.V. 1923
Starr, D. 850, 1576
1580
Stefan, S. 235
Stefanof, A. 444, 670
Stefanof, C. 670
Steinwagner, J. 297
Stel, F. 1005, 1796
Stepanenko, V.D. 1746
Stephens, G.L. 375, 408
417, 1029
Stern, W. 294
Stevens, B. 600
Stevens, D. 1
Stith, J.L. 674
Storelvmo, T. 239
Straka, J.M. 1500, 1584
1654
Strapp. J.W. 961, 1074
Stratmann, F. 257
Straub, D. 1150
Straub, W. 537
Ström, J. 1095, 1750
1754
Stuart, A.L. 475
Stulov, E.A. 731, 1196
Su, A. 1875
Sun, A. 678, 1276
Sun, J. 1704, 1975
Sun, Y. 973
Sun, Z. 654
Supatashvili, G.D. 267
Suto, M. 1711
Suzuki, K. 1019
Swietlicki, E. 157
Szyrmer, W. 670, 1588
Tagliavini, E. 168
Takahashi, C. 932, 936
1959
Takahashi, T. 440, 682
Takamura, T. 1167
Takano, T. 1167
Takara, E.E. 1533
Takaya, Y. 804
Takemi, T. 1963
Takemura, T. 243
Tanaka, N. 440
Tanaka, Y. 823, 827
1935
Tanelli, S. 1107
Tang, D. 1158
Tao, W.-K. 150, 246, 413
Tao, X. 1604
Taoyue 1799
Targino, A. 171
Tavartkiladze, K.A. 354
Teichert, H. 146
Telenta, B.T. 1023
Teller, A. 131
Teschl, F. 904
Textor, C. 1592
Theusner, M. 1848
Thompson, D.W.J. 375
Thompson, G. 908
Timlin, M.S. 592
Tinsley, B.A. 248
Tolkacheva, G.A. 333
Tompkins, A.M. 1312, 1424
Toon, O. 1
Topping, D. 251, 432
Toronjadze, A.F. 265
Torres, J.C. 1829
Torricella, F. 1171
Trautmann, T. 1761
Travaini, S. 636, 1146
Trentmann, J. 1592
Trier, S.B. 1852
Tripoli, G.J. 596, 1428
Trivellone, G. 389
Tsenova, B. 1537, 1911
Tsuboki, K. 1545, 1561
1738, 1943
1951, 1967
Tsukamoto, O. 1793
Turco, R.P. 55
Twohy, C.H. 201, 487
779, 788
896, 1092
1108
Uijlenhoet, R. 1052
Ulanowski, Z. 1175
Uyeda, H. 1015, 1738
1773, 1931
1935, 1959
1967
Vaillancourt, P.A. 520, 1596
Vali, G. 961, 1639, 1758
van den Heever, S.C. 253, 1500
van Dop, H. 1179
Van Dorn, J. 608
van Ekeren, J.S. 1183
van Meijgaard, E. 1063
van Zadelhoff, G.-J. 940
Vanreken, T. 892
Várnai, T. 1044
Vedernikov, A. 636, 1146
Vellore, R.K. 1324
Venema, V. 1742, 1761
Venkatesh, S. 448
Vento, D. 285, 288
Veremey, N.E. 1746
Verlinde, J. 739, 1033, 1723
Vidaurre, G. 944
Vila, D.A. 1186
Vitale, V. 389
Volkov, V.V. 1160
von Blohn, N. 946
von Salzen, K. 421
Vučković, V. 1895
Vujović, D. 1895
Vukovic, Z.R. 1023, 1600
Wacker, U. 1404
Wada, M. 440, 1765
Wagner, R. 146, 160, 364
Waliser, D.E. 294

Walther, A. 1769
Wan, X. 1027
Wang, D 1580
Wang, G. 678
Wang, H. 335
Wang, J. 1907
Wang, J.-J. 1971
Wang, J.R. 1107
Wang, L. 1276
Wang, L.-P. 686, 690
Wang, P. 1704, 1975
Wang, P.K. 1592, 1719
Wang, Q. 1285
Wang, S. 1432, 1504
Wang, W. 1604
Wang, W.-C. 35
Wang, Xia 1027
Wang, Xiaobin 1777
Wang, Xiaobo 1608
Wang, Xiaomei 1215, 1261
1282
Wang, Xuelin 1261
Wang, Yansen 1580
Wang, Yilin 1261
Ware, R. 1130
Watanabe, A. 1855
Watanabe, H. 823
Weaver, K. 839
Wei, Q. 1215
Wei, W. 1285
Wei, Z. 1222
Weigand, B. 647
Weimer, S. 171
Weingartner, E. 20, 1183
Weinman, J.A. 1107, 1268
Weinstock, E.M. 779
Wendisch, M. 580, 1955
Westbrook, C.D. 954
Wex, H. 257
Wexler, A.S. 643
Whiteway, J.W. 747
Wielicki, B.A. 424
Wieprecht, W. 1138
Wilhelmson, R.B. 1500, 1654
Willén, U. 1434, 1442
Willett, J.C. 1001
Williams, P.I. 39, 432
Willis, P.T. 957, 1001
Wilson, D.R. 1438
Wilson, K.M. 1179
Winterrath, T. 1592
Wirzberger, H. 928
Wiscombe, W.J. 1070
Witternigg, N. 904
Wobrock, W. 164, 584
1859
Wolde, M. 796, 961
Wong, T. 424
Wood, R. 1469, 1628
1636, 1863
Woods, C.P. 1308
Worsnop, D.R. 432
Wu, H.-T.J. 1115
Wu, Yuxia 1225, 1454
1808
Wu, Yuzhong 1272
Wu, Z. 973, 1158
1777, 1903
Wurzler, S. 66, 231, 900
Wyser, K. 1442

Xiao, Huanbin 1285
Xiao, Hui 541, 1225
1276, 1608
1612, 1616
1701
Xiao, Wenan 1529
Xie, Z. 846
Xu, Can 1285
Xu, Chenhai 1276
Xu, H. 1285
Xu, J. 387
Xu, K.-M. 424, 1488
Xue, H. 462, 479
Xue, Y. 690
Yamada, H. 1738, 1773
Yamada, Y. 823
Yamanouchi, T. 1765
Yang, Bai 1867
Yang, Baodong 1903
Yang, J. 1975
Yao, Zhanyu 1276, 1612
Yasunaga, K. 339
Yates, E. 1871
Yau, M.K. 520, 1382
Yetzer, K. 1044
Yin, L. 1285
Yin, Y. 131
Yoneyama, K. 1683
Yoshida, K. 1793
Yoshizaki, M. 759, 1019
1515, 1679
1923, 1931
1935
You, Laiguang 135, 1903
Youk, H. 965
Young, D.F. 600
Yu, Xiangren 1261
Yu, Xing 1208, 1278
Yu, Y. 1811
Yuan, J. 1304
Yum, S.S. 694, 1099
Yuter, S.E. 1636, 1863

Zabolotskaya, T.N. 343, 345
Zardi, D. 1947
Zawadzki, I. 576, 698
796, 1588
Zeng, X. 1557
Zhang, Jinghong 1215, 1222
1282
Zhang, Junhua 281, 1450
Zhang, Lei 975
Zhang, Ling 1190, 1697
Zhang, Q. 975, 1027
1616
Zhang, W. 1127
Zhang, Xiaoqing 1194
Zhang, Xinmin 1777
Zhang, Y. 1697
Zhao, G. 1697

Zhao, Z. 1454
Zhen, J. 1222, 1225
1261
Zheng, G. 517, 657
661, 678
978, 1875
Zhi, H. 973
Zhou, F. 608
Zhou, H. 1285
Zhou, X. 1704
Zhou, Y. 657, 1875
Zipser, E.J. 1829, 1844
Zmarzly, P. 839, 1070
Zolina, O. 327, 347, 350
Zulauf, M.A. 1687

A NEW HABIT DIAGRAM AND MASS PARAMETERS FOR ATMOSPHERIC ICE CRYSTALS FROM –20 °C TO – 70 °C

Matt Bailey and John Hallett

Desert Research Institute, Reno Nevada, 89512 USA

1. INTRODUCTION

The distribution of mass in crystals of any particular habit determines their scattering properties, e.g. thick versus thin and compact versus spatially extended crystals. While habits are first a function of temperature, and secondly, ice supersaturation, they are additionally modified by sedimentation and changes in growth conditions. These changes have a significant effect on cloud radiative properties in addition to the interpretation of remote sensing retrievals.

Recent in situ studies by Korolev et al. (1999, 2000) and laboratory studies by Bailey and Hallett (2002, 2004) have shown that below –20°C, irregular polycrystals are the dominant habit under most growth conditions for crystals larger than approximately 40 microns in size. Dimensional and mass-dimensional relations for simple ice habits (solid thick plates, columns, single needles) in addition to dendrites and a few more complex forms (sheaths, hopper plates, bunches of needles) derived from in situ observations and replica data can be found in Pruppacher and Klett (2000). However most of these results were derived from habits observed between –4°C and –20°C, a region where single crystal forms appear with much higher frequency than at temperatures below –20°C. While it has been assumed that such results are applicable to colder regions of the atmosphere, the habits are not statistically representative of those found at temperatures below –20°C, a region dominated by complex plate-like polycrystals between –20°C and –40°C and then columnar forms below –40°C Also, sedimentation of cirrus habits into the plate-like region between –20°C and –40°C have resulted in confusion concerning the characterization of ice crystal habit as a function of temperature and altitude.

In the laboratory study of Bailey and Hallett (2004), volume, projected area, and largest dimension growth rates for ice crystals between –20°C and –70°C are presented as a function of ice supersaturation and pressure, along with a comprehensive habit diagram for this temperature range. Laboratory simulations of habit changes due to sedimentation of cirrus habits have been added, resulting in a new habit diagram that explains the vast majority of in situ habit observations over this temperature range. Recent observations of ice crystal habits with a cloud particle imager (CPI) during AIRS II have confirmed these conclusions. The growth results have subsequently been used to calculate effective radius (volume/projected area) and crystal mass-to-maximum dimension relations. These results provide a new basis for the parameterization of ice habits in clouds with temperatures colder than –20°C.

Corresponding author's address: Matt Bailey, Desert Research Institute, 2215 Raggio Parkway, Reno, Nevada 89512 e-mail matt.bailey@dri.edu

2. HABIT DIAGRAM

In the laboratory study, ice crystals were grown in a static diffusion chamber at ice supersaturations ranging from as low as 1% to approximately the largest values that would be experienced by ventilated crystals falling at terminal velocity. Crystals were grown at pressures commensurate with those found in the atmosphere for a particular temperature in order to achieve the vapor diffusivities that would be present under these conditions. These results have been combined with previously established habit results in figure 1.

As can be seen, the habits divide into two distinct regions between –20°C and –70°C, a regime between between –20°C and –40°C dominated by complex plate-like polycrystals and a columnar regime between –40°C and –70°C where bullet rosettes are the dominant polycrystalline habit. These results are representative of what would be expected in the atmosphere for crystals whose growth is restricted to one habit regime or the other, e.g. mid-altitude cumulus and stratiform clouds with cloud tops no colder than –40°C and no overlying cirrus, and cirrus clouds with cloud bottoms no warmer than –40°C, except in the case of low ice supersaturation growth conditions where short columns, thick plates and compact irregular polycrystals would be observed. This is consistent with the majority of in situ habit observations for the conditions described.

Of equal or greater significance is the process depicted at –40°C in figures 1 and 2, the precipitation of columnar forms into the plate-like region at lower altitudes. While bullet rosettes and columns are frequently observed in the mid troposphere at temperatures between –20°C and –40°C, bullet rosettes were never observed in the laboratory results in this temperature range, and columns appeared with low frequency. Additionally, in situ columnar forms observed between –20°C and –40°C are sometimes solid, capped by plates, or partially to mostly hollow (sheath-like). Hollow columns or sheaths were initially observed in the laboratory study at temperatures

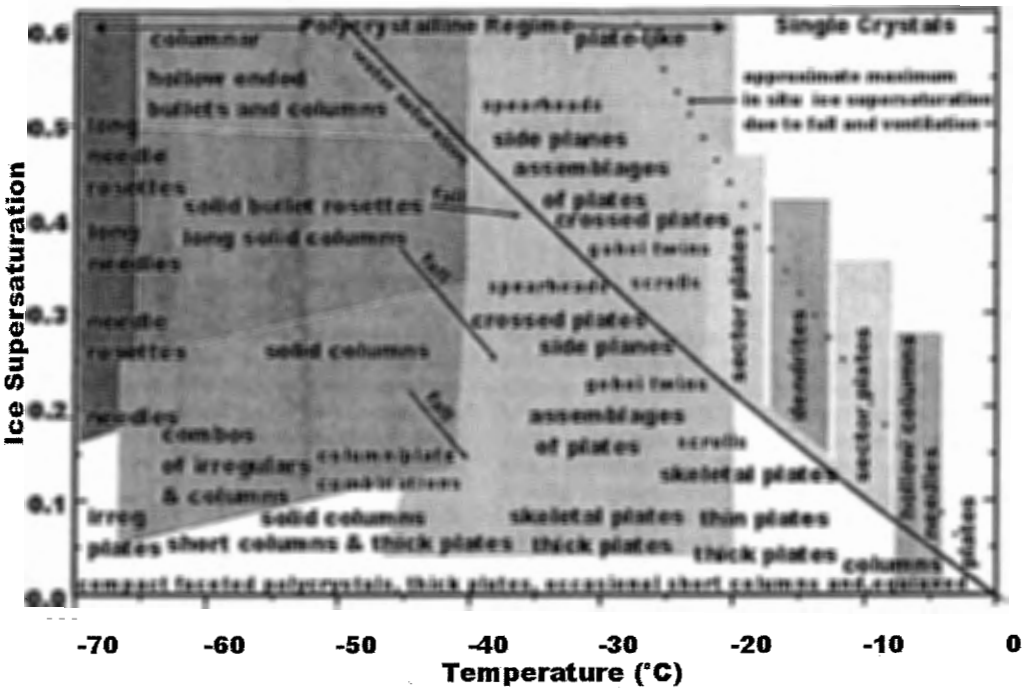

Figure 1 . Habit diagram of ice crystals from the results of Bailey and Hallettt (2004) between -20 °C and -70 °C together with earlier habit results between 0 °C and -20 °C found in Pruppacher and Klett (2002) .

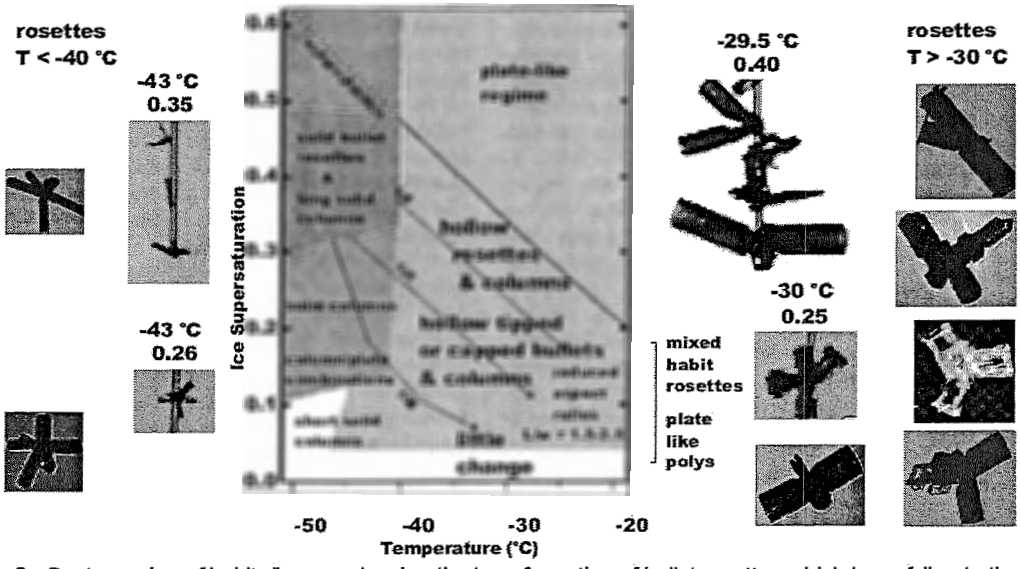

Figure 2. Center region of habit diagram showing the transformation of bullet rosettes which have fallen to the plate-like growth regime warmer than -40 °C. Laboratory crystals on the left growing on substrates initially nucleated and grew at the temperatures and ice supersaturations indicated. Laboratory crystals on the right are the same as those on the left at a later time and under warmer final growth conditions. All other crystals shown are in situ crystals from FIRE ACE (NASA Langley Research Center Atmospheric Sciences Data Center) or from Uyeda and Kikuchi (1979).

below and –40°C, but only at relatively large ice supersaturation and never as plate-capped forms.

The reason for this became clear after viewing thousands of CPI images provided by George Isaac and Alexei Korolev of Environment Canada gathered from a number of field studies where cloud tops were rarely colder than –40°C. In those data sets, bullet rosettes and columnar forms were observed in cumulus and stratiform clouds amongst plate-like forms between –20°C and –40°C whenever overlying cirrus clouds were present. When no overlying cirrus were present and cloud tops were no colder than approximately –40°C, only plate-like forms were observed with a low frequency of single columns as

observed in the laboratory. These results were recently confirmed by the authors in the recent Alliance Icing Research Study (AIRS II). In that study, the altitude of the NASA NCAR C-130 rarely exceeded 8 kilometers and the coldest air temperature at flight level was –37°C. A mix of habits was observed whenever overlying cirrus were present (bullet rosettes sometimes dominating the habit distribution), and on one day in particular, no overlying cirrus were present and only plate-like polycrystalline forms were observed with cloud top temperatures at –37°C.

Subsequent laboratory growth experiments were performed simulating this sedimentation process. Bullet rosettes and columns were nucleated below –40°C and then the growth temperature was raised to –30°C (the pressure was also raised) while the ice supersaturation was varied. Solid bullet rosettes and columns were observed to transform into the hollow forms observed in situ when the relative humidity conditions were near water saturation. For ice supersaturation conditions midway between ice and water saturation, bullets and columns have slightly hollowed tips, are skirted by partial plates, or become solidly capped depending on growth time and decreasing ice supersaturation. Growth at low ice supersaturation leaves habits relatively unchanged. One key indicator of the change in growth conditions for columnar forms which transform under plate-like growth conditions is a significant reduction in aspect ratio, a characteristic also observed in the laboratory.

3. MASS DIMENSIONAL PARAMETERS

In the laboratory study, crystals were grown on rotatable glass fiber substrates and could be viewed at various angles, allowing accurate measurements of crystal dimensions. While some complex shapes had to be estimated, reasonably accurate volumes (and hence masses) and maximum projected areas could readily be determined for most crystals. These have been used to calculate the effective ice crystal radius, defined as volume/(maximum projected area), and the mass-to-maximum dimension values for various types of crystals, examples of which are shown in figures 3 and 4. In both figures, the left side, with sizes smaller than 300 microns, is dominated by results for simple plates (small squares) and columns (short solid bars) while the other symbols represent various plate-like polycrystalline habits. In Bailey and Hallett (2004), exponential fits of volume and maximum projected area growth rates, weighted according to the observed habit frequency, were calculated as a function of temperature. The ratio of these two provide a statistically averaged effective ice radius as a function temperature for crystals restricted to one of the growth regimes previously described and is shown in figure 5. The results are separated according to growth at low ice supersaturation and moderate to high ice supersaturation, reflecting the fact that the low ice supersaturation habit is approximately independent of temperature (see figure 1) and revealing a marked difference between plate-like habits warmer than

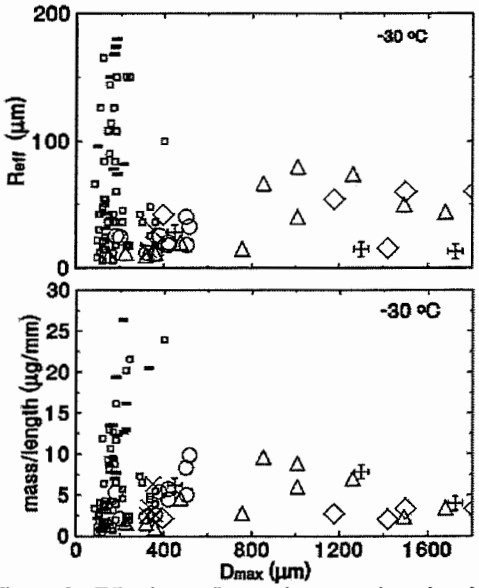

Figure 3. Effective radius and mass to length values for crystals grown at -30 °C.

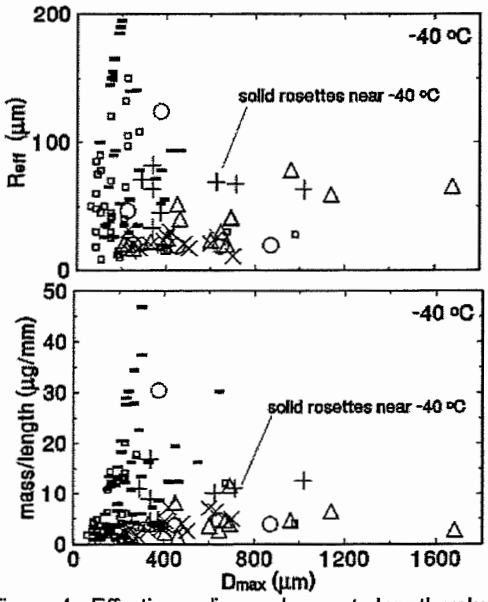

Figure 4. Effective radius and mass to length values for crystals grown at -40 °C.

–40°C and columnar/rosette forms at colder temperatures.

The question of how the laboratory results compare with in situ observations is a valid one since no comprehensive measurements of in situ crystal masses are available. One possible way to answer this question is to compare the observed laboratory dimensional characteristics with in situ results. Korolev and Isaac (2003) analyzed approximately one million CPI images from a number of studies and plotted the results in terms of "roundness", the ratio of the pixel measured projected area to the circular area

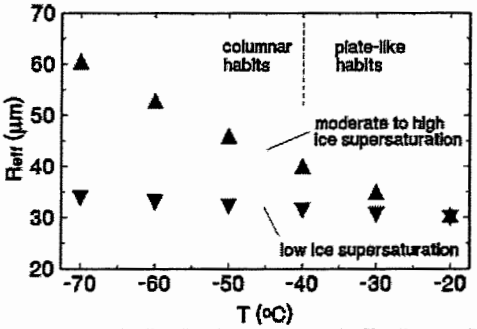

Figure 5. Habit distribution weighted effective radius values for crystals growing between -20 °C and -70 °C.

calculated from the maximum dimension, $pi*D^2_{max}/4$. Examples of these are shown in figure 6 with

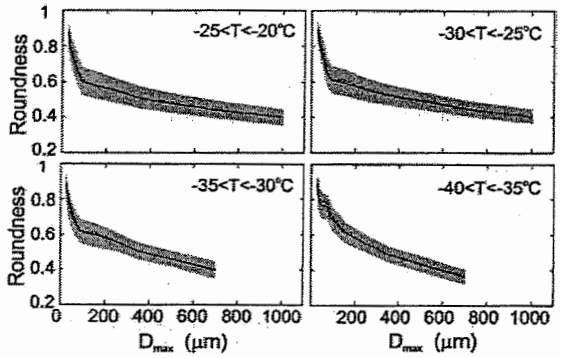

Figure 6. Examples of roundness parameters from Korolev and Isaac (2003); gray band = 1 std. Dev. corresponding results from the laboratory measurements in figure 7. One standard deviations of

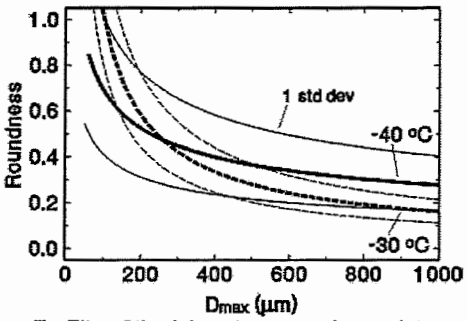

Figure 7. Fits of the laboratory roundness data.

the fits are shown for both. The in situ and laboratory results show very similar behavior, the laboratory results being drawn from a much smaller set of observations, approximately 100 crystals for the two temperatures shown. Furthermore, the laboratory results only include plate-like forms grown under static conditions while the in situ results for the same temperatures contain a mix of columnar habits which have undergone the transitions depicted in figure 2 which increases the "roundness" of columnar forms.

4. CONCLUSION

A full presentation of the laboratory mass-dimensional characteristics is being prepared for publication based on the static growth results presented here. More importantly, further laboratory experiments simulating the habit changes of columnar and plate-like forms which fall to warmer growth regimes are needed since a large portion of glaciated clouds in the atmosphere have radiative characteristics significantly effected by sedimentation processes.

5. ACKNOWLEDGEMENTS

This research was supported by the National Science Foundation, Physical Meteorology Program (ATM-9900560) and NASA (NAGS-7973).

REFERENCES

Bailey, M. and J. Hallett 2004: Growth Rates and Habits of Ice Crystals Between -20 °C and -70 °C. *J. Atmos. Sci.* **61**, 514-54.

Korolev, A.V., G.A. Isaac and J. Hallett, 1999: Ice particle habits in Arctic clouds. *Geophys. Res. Lett.*, **26**, 1299-1302.

Korolev, A.V., G.A. Isaac and J. Hallett, 2000: Ice particle habits in stratiform clouds. *Quart. J.R. Met. Soc.*, **126**, 2873-2902.

Korolev, A. and G. Isaac, 2003: Roundness and aspect ratio of particles in ice clouds. *J. Atmos. Sci.* **60**, 1795-1808.

Pruppacher, H.R. and J.D. Klett, 1997: *Microphysics of clouds and precipitation*, Kluwer Academic Publisher, 954 pp.

Uyeda, H. and K. Kikuchi, 1979: Observations of the Three Dimensional Configuration of Snow Crystals of Combination of Bullet Type. *J. Meteor. Soc. Japan*, **57**, 488-492.

MESOSCALE STRUCTURE OF FRONTAL WINTER CLOUD AND PRECIPITATION SYSTEMS OVER UKRAINE

V.P. Bakhanov, A.A. Manzhara, and B.A. Dorman
Ukrainian Hydrometeorological Research Instiyute (UHRI),
Kyiv-28 , 03028, Ukraine,

1. INTRODUCTION

This paper presents results of numerical simulation of meso-and microstructure of winter stratiform clouds and precipitation fields over Ukraine.

The two-dimensional time-dependent numerical models with detailed microphysics (kinetic equations for size spectra of drops and crystals) and parameterized dynamics were constructed. The detailed description of numerical models was made in our earlier papers (Bakhanov et al.,1989, 1992,1994). Here we shall give a short description of our model.

Consideration is conducted in the coordinate system moving together the front (x – horisontal coordinate perpendicular to front line, z – vertical coordinate). Fields of the pressure p(x,z) , air density ρ (x,z), horizontal and vertical velocities of air flow u (x ,z) ,w (x , z) arenot depended on time in the moving coordinate system. Initial cross-sections of frontal systems were based on rawinsondes and aircraft data received in near one moment. Fields of w (x, z) are calculated from the continuity equation.

In the model the space-time evolution of fields of humidity q (x , z, t), temperature T (x , z ,t), distribution functions of water drops (index 1 f_1 (x ,z ,r_1 ,t) and crystals f_2 (x, z, r_2,t) (index 2) on radii are considerated.

In this paper only one type of crystals (plates which were approximated by rotation ellipsoides) and only one type of ice nuclei (IN, ("condensation –freezing") which are activated at the supersaturation over liquid water $\Delta_1 > 0$) are under consideration.

Vladimir P. Bakhanov, UHRI, 03028,Kyiv-28, Ukraine. E-mail : vpb@zeos.net.

The IN distribution on undercooling has such form (approximation of experimental data):

$$- dN/dT = A_s \exp [B_s (273.15 - T], \quad (1)$$
$$T_0 < T < 273.15,$$

where N – concentration of activated nuclei for temperature T, $A_s = 0.1 \cdot 10^{-4}$ (g grad)$^{-1}$ $B_s = 0.58 \text{grad}^{-1}$, T_0 – a variable parameter, which determines a maximum concentration N_0 of activated IN. The values of other parameters were the same as in our earlier paper(Bakhanov et all., 1992).

We shall consider in the next section some real frontal systems over Ukraine (without riming consideration).

2 MESOSTRUCTURE OF FRONTAL CLOUD and PRECIPITATION SYSTEMS

Our investigations have shown that the fronts under study exhibit a complex system of large-scale whirls occupying the lower layers of troposphere (up to 2...4 km). Efficiency of precipitation formation is to a large extent controlled by the dynamic structurre of a front and its microphysical parameters (particularly concentration of IN and shape spectrums of IN).

Let us consider some examples of frontal systems over Ukraine. The first example – the occluded front of February 17, 1981. There are large scale whirles in the lower troposphere (Fig. 1).

In the prefrontal zone (x<0) there is the vast downdraft region and the connectedwith it region with undersaturation over ice ($\Delta_2 < 0$).

The warm front region (x> 0) has the complex structure of updraft parcels with small values of vertical velocity (till w=+4...+5 cm/s).

In this case tropopause is located very low and temperatures in clouds are quite high (T> -25°C). For this reason the IN of the first type (Mason, 1957) are not active and the maximum concentration of IN is small ($N_o \sim 30$ g^{-1}).

Fig. 2 depicts the state of the system at t=6h of evolution . This figure demonstrates the large liquid water content (LWC) values (q_{L1}>0.3 g/kg), in good agreement with the observation data) and moderate crystal concentrations (maxima n_2 = 5...8 g^{-1}). The precipitation rate is equal 0.4...0.6 mm/ h.

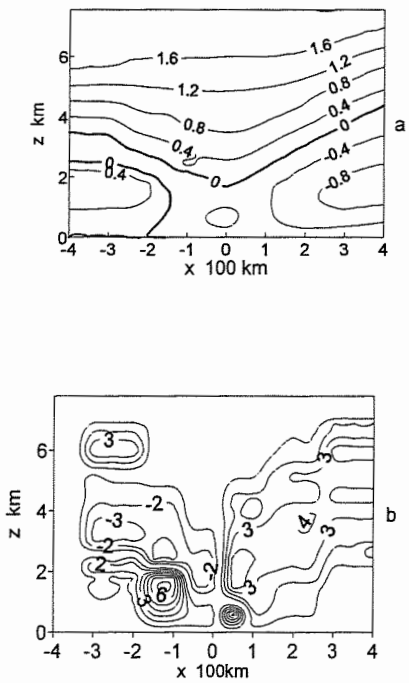

Fig.1. Cross-sections of dynamic structure of occluded front of February !7, 1981;
a) field of stream function in 10^5 g/cm· s units;
b) vertical vellocity values are in cm/s units.

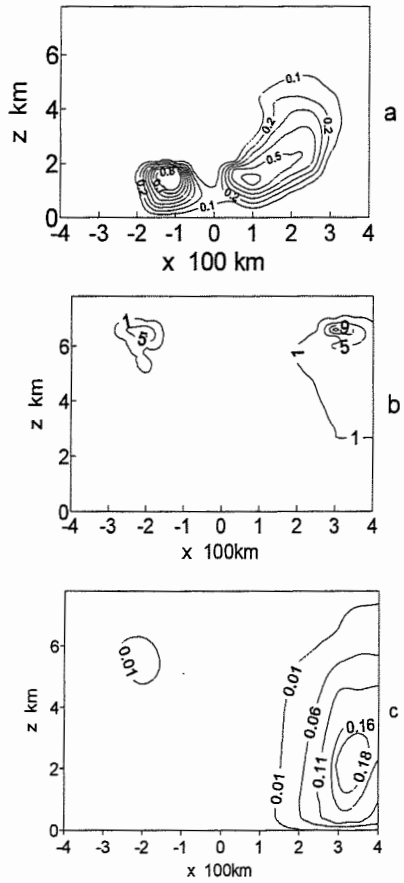

Fig. 2. Cloudiness cross-sections of front of February 17,1981 (for t = 6 h of evolution)
a) – LWC q_{L1} in g/kg ,
b) - n_2 in g^{-1} ,
c) - IWC in g/kg.

The efficiency of precipitation formation in this case is unsufficient , the condition of equality $\overline{j} = \overline{E}$ (the mean in frontal zone quantities of precipitation rate and thermodynamical condensation rate) is reached only after 6...7 hours of cloudiness evolution. The frontal cloud system has all time the mixed phase composition and the great potential for the artificial precipitation enhancement (APE).

The next example is the cold front on December 12 , 1982 . Fig. 3a and 3b show the stream function field and the field of updraft and downdraft . In this case there is also the complex system of large scale whirls and connected with them cells of

updraft and downdraft . The maxima values of updraft velocity reach ~ 20 cm/s.Fig. 4 depicts the vertical cross-sections of the system after 6 hours evolutuon (N= 300 g^{-1}, T_o = - 29 ° C).

It can be seen liquid drop clouds and areas with the high ice water content (IWC) q_{L2} > 0.4 g/kg . Maxima crystal concentrations reach values 45...50 g^{-1}. At t = 2 h the precipitation rate is low (j<< E) , but at t = 6 h a shower rainband emergers in the prefrontal region (maxima values of j ~ 5...7 mm/h). $\overline{j}$ and $\overline{E}$ became near equal after ~ 4...5 hours evolution. After 6...7 hours of evolution clouds became near crystalic and have a small seedability.

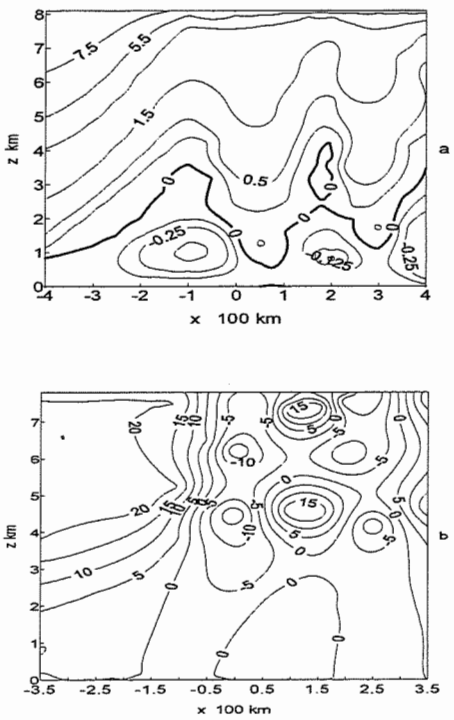

Fig. 3. Cross-sections of the stream functions (a) and vertical velocity (b) for the cold front of December 12 , 1982 . Designations are the same as in Fig 1

In the case of presence of high updraft parcels (T_o < - 31 ° C) and high IN concentrations (more than 3000 g^{-1}) the ice nucleation and precipitation formation ("seeder – feeder" mechanism) processes are very intensive. The condition $\overline{j} = \overline{E}$ is reached in 3...4 hours of evolution, afterwards the complete crystallization takes place. Precipitaton rate values reach tens of mm/h.

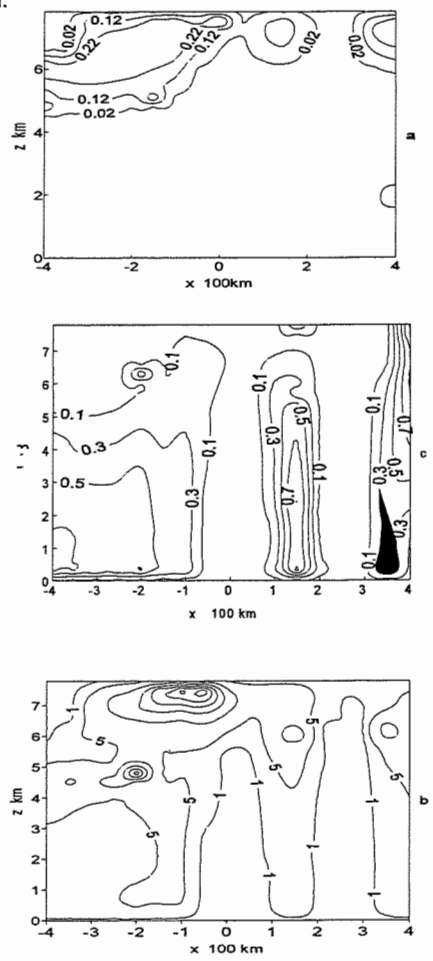

Fig. 4. Cloudiness cross-sections of the front December 12, 1982 . Designations are the same as in Fig. 2.

We have realized also the numerical simulation of solar radiative transfer in model clouds. Investigations have shown that the microstructure of clouds effect very strongly on satellite signal (SS, albedo of clouds) in channels 0.55 – 3.6 μm. The comparison of SS for different wave lenghts gives the possibilty to distinguish regions with great liquid water content and regions with developed crystallization and precipitation.

2. CONCLUSIONS

1) The fronts studied exhibit complex systems of large-scale whirls occyping the lower troposphere (up to 2...4 km).

2) The efficiency of precipitation formation is to a large extent controlled by dynamic structure of front (tropopause hight; presence of above mentioned whirles ; and a consequence thickness and hight of updraft parcels) and characteristics of ice nuclei (IN).

3) When updraft parcels are located at small hights (z < 3...4 km , T> - 25 ° c) the ice nucleation and precipitation formation have insufficient efficiency, the total liquid content can reach 1 mm and such clouds have a cosiderable potential for artificial precipitation enhancement (APE).

4) In a case of hight updraft parcels (z > 5...6 km) and great concentration of IN the ice nucleation and precipitation formation (" seeder-feeder " mechanism) are very intensive. After 3...4 hours of cloudiness evolution the complete crystallization takes place and these clouds have a very small potential for APE.

5) Model Ci- clouds always have mixed phase composition resulting from IN nature ("condensation-freezing ").

6) Numerical simulations of satellite signal (cloud albedo) in the channels λ = 0.55 – 3.6μm shows that the comparison of SS for different wave lengths gives the possibility to distinguish regions with great liquid water content and regions with developed crystallization and precipitation.

4. REFERENCES

Bakhanov, V. P. , Dorman , B. A.. , Kolezhuk , V. T. , and Manzhara , A. A., 1989 : Numerical simulation of frontal mixed stratiform cloud seeding for precipitation enhancement. Proc. 5-th WMO Sci. Conf. Weather Modif. (Beijing), 251-254.

Bakhanov, V.P., Manzhara , A. A., Kolezhuk , V.T., and Zabolotskaya, T.N., 1992 : Numerical simulation of natural and seeded precipitation in frontal cloud systems. Proceedings of the UHRI (Kyiv) , 243,. 39-59 .

Bakhanov, V. P. , Dorman, B.A., Kolezhuk , V.T., Manzhara , A. A., and Zabolotskaya, T. N. 1994 : Natural and seeded precipitation formation in frontal clouds over Ukraine. Proc. 6-th WMO Sci. Conf. Weather Modif. (Paestum), pp. 459-462, 1994.

NUMERICAL SIMULATION OF CLOUD MICROSTRUCTURE EFFECT ON SATELLITE SIGNAL

V.P. Bakhanov, O.A. Kryvobok, and B.A. Dorman,

Ukrainian Hydrometeorological Research Institute,
Kyiv-28, 03028 , Ukraine

1.INTRODUCTION

This paper presents results of consecutive numerical simulation of the satellite signal (SS, cloud reflectance) for frontal model stratiform clouds.The simulation is based on the next models:
a) The time-dependent 1D numerical model of winter mixed frontal stratiform clouds with detailed microphysics and several forms of ice crystals.
b)Models of computation of light scattering by drop and crystal systems in clouds.
c) The discrete ordinate method for simulation of the solar radiation transfer in a not uniform cloud in a visible and near-infrared part of spectrum (for wave lengths λ_1 = 0.55 μm, λ_2= 1.6 μm, λ_3= 3.6 μm) and calculations of satellite signal (SS, cloud reflectance).Further we give the block-diagram of calculations:

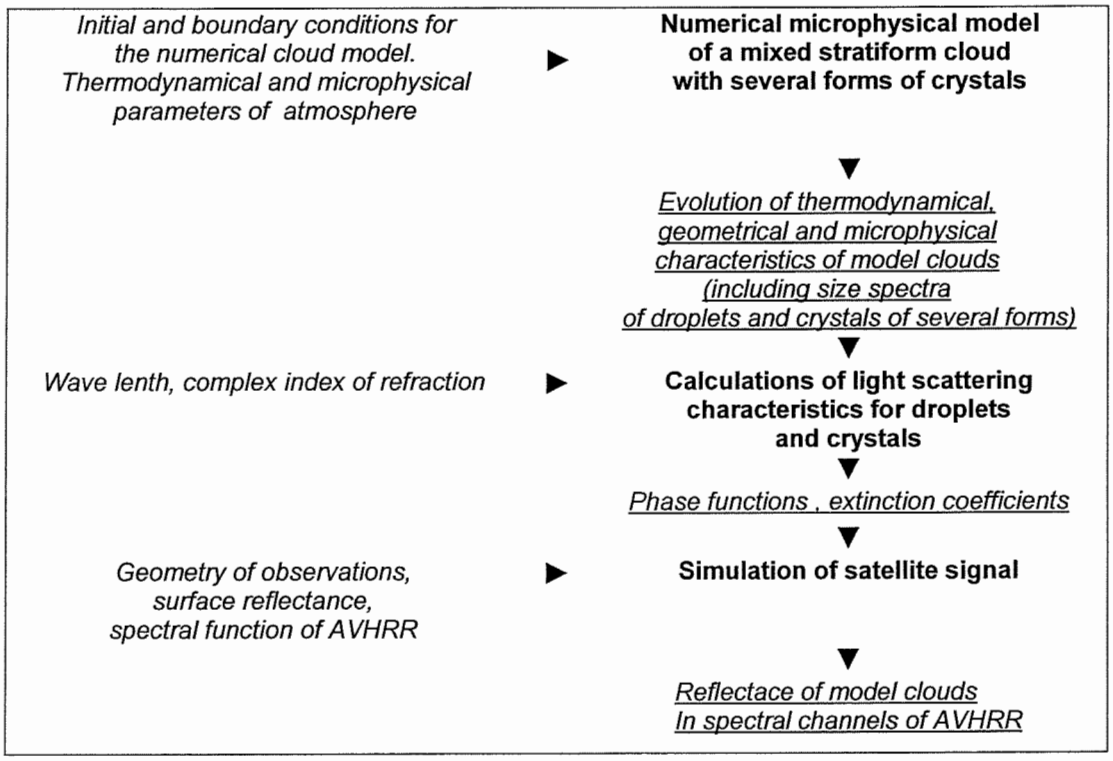

Vladimir P. Bakhanov, Ukrainian Hydrometeorological Research Institute, 03028, Kyiv –28, 37 Avenue of Science, Ukraine. E-mail: vpb@zeos.net.

2. NUMERICAL MICROPHYSICAL MODEL OF FRONTAL CLOUDS

The numerical 1D microphysical model of frontal mixed cloud with several crystal forms (needles, columns, plates) was

described in our previous papers (Bakhanov et al., 1991,1996).

The model equation system consists of equations of heat and vapor transfer and 4 kinetic equations for dimension spectra $f_j(r_j, t, z)$ of drops and crystals (j = 1 – for drops, j = 2 – for needles , j = 3 – for plates, j = 4 – for columns; r_j – the characteristic dimension of particles ; t – time ; z – height).

The cloud dynamics is parameterized : the updraft velocity w = w (z) depends on z parabolically in an interval $z_1 < z_2$ with the maximum velocity w_m (in this presentation w_m = 5 cm/s, z_1 = 0.3 km, z_2=5.7 km).

We will consider so called sorbtion ("condesation – freezing") ice nuclei (IN) which are activated if the supersaturation over water is reached. Distribution of the IN concentration by overcooling has the next form (the approximation of empiric data):

$$-(dN_j/dT)= \mu_j A_S \exp[B_s (T_o -T)],$$

where T –temperature, T_o=0 ° C, B_s=0.2 (° C)$^{-1}$, A_s = 0.015 (g ° C)$^{-1}$ in this presentation.

Temperature intervals for nucleation of different crystal forms are different: for needles - 10 < T < -5 ° C, for columns T < - 25 ° C, for plates –25 < T < - 10 ° C. In these intervals μ_j = 1, outside μ_j = 0.

Since the share of needles in a total concentration of crystals below 0.1% we will not discuss characteristics of needles.

Numerical simulation has been shown that the dynamical structure of a front under study (especially heights and thicknesses of updraft cells) determines the phase composition, crystal form spectra and efficiency of precipitation formation.

The predominate form in snowfalls is plate if the top cloud boundary height less than 4.8 – 5.0 km. These clouds have a very large total liquid water content (TLWC) to 1 mm. If the top boundary has height as isotherm - 34...-35 ° C the predominate crystal form is column, these clouds have the high efficiency of precipitation formation and high ice content (IC).

We will consider in this presentation in detail only one example of the mixed cloud evolution. Fig.1 depicts the time-spatial sections of LWC – liquid water content, $(IC)_3$ – ice content for plates, $(IC)_4$ – ice content for columns. All values are given in g/kg (of air).

It has been seen that the thick cloud

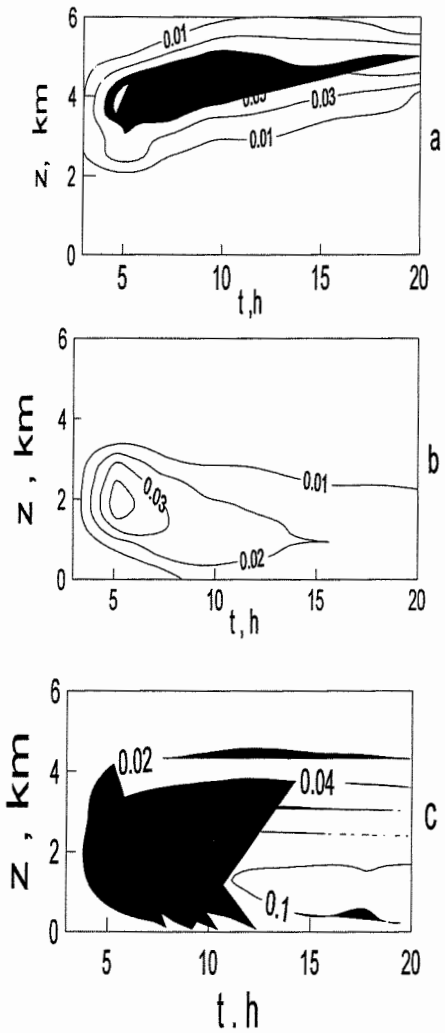

Fig.1 Evolution of a model mixed cloud
a – LWC, b - $(IC)_3$, c – $(IC)_4$ - all in g/kg

has been formed in 3-5 hours of evolution, maxima LWC are more than 0.1 g/kg at 5 h. The further crystallization process leads to abrupt decrease of LWC, increase of $(IC)_3$ and especially $(IC)_4$ at t >10 h (near 0.1 g/kg). Average sizes of plates are more than 600 – 800 μ m and after 10 h the precipitation rate amounts to 0.4-0.5 mm/h.

3.LIGHT SCATTERING CHARACTERISTICS OF A MIXED CLOUD

Simulations of scattering characteristics of liquid drops are based the Mie theory (Deirmendjian ,1969).

Simulations of scattering properties for randomly oriented ice crystals are based on the geometric optics and the far-field diffraction

approximation (Macke et al., 1996).

Fig.2 depicts the time-spatial section of local optical thicknesses (LOT) or else optical thicknesses of thin 300 m layers in our model cloud under study. The section on Fig.2 corresponds to the wave length of satellite radiometer $\lambda_3 = 3.6$ μm.

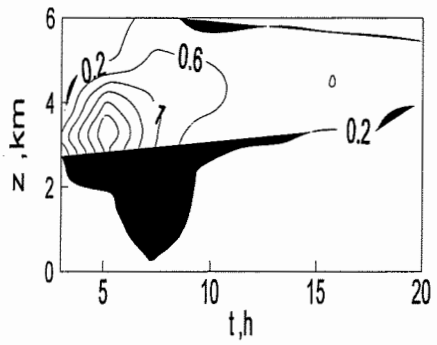

Fig. 2 . The time-spatial section of LOT In the cloud under study, λ_3 =3.6 μm.

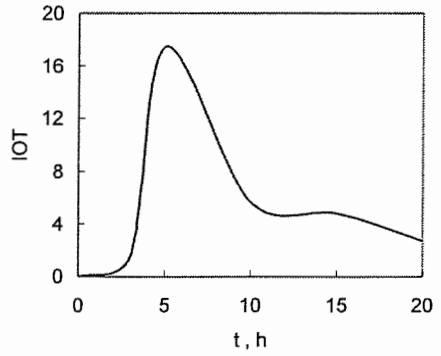

Fig.3. Dependence of integral optical thickness (IOT) of the cloud on time, λ_3=3.6 μm.

Fig.3 depicts the dependence of the integral optical thickness of the model cloud under study on time (λ_3 = 3.6 μm), Dependences of IOT on time for 3 wave lengths (λ_1= 0.55 μm, λ_2 = 1.6 μm, λ_3 = 3.6 μm) under study are close with each other.

It's easy to see from comparison Fig.1 and Fig.2 that LWC determines LOT sufficiently. IOT runs up maximum value ~ 18 at t=5 h and then decreases as a result of crystallization of the cloud and considerable decrease of LWC.

4. SIMULATION OF SATELLITE SIGNAL

Discrete Ordinate Method (DOM, Liou, 1973; Stamnes et all. , 1988) was used for simulation of solar radiation transfer in not uniform clouds and calculation of measured reflected intensity on satellite. This method was slightly modified by one of authors (Kryvobok, 1988). Thick clouds were divided into thin layers with constant microphysical and optical characteristics.

We will determine SS (satellite signal) as a cloud reflectance of solar radiation in visible and near-infrared part of spectrum.

Fig. 4 depicts results of SS simulation for the cloud under study in this presentation.

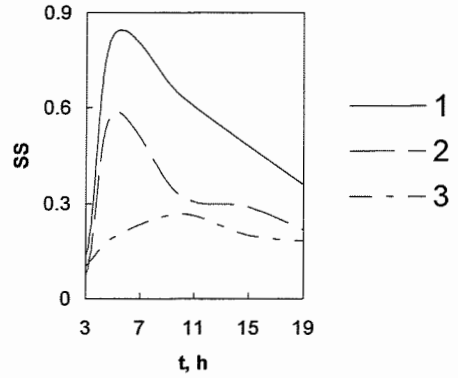

Fig.4 . Satellite signal from the model cloud. 1 – λ_1 = 0.55 μm, 2 – λ_2 = 1.6 μm , 3 – λ_3 = 3.6 μm.

Comparison Fig.3 and Fig.4 shows that reflectances for satellite radiometer channels λ_1 = 0.55 μm and λ_2 = 1.6 μm change synchronously with IOT.The abrupt decrease of IOT and SS at t > 7h is connected with crystallization process and LWC decrease.

SS in the radiometer channel λ_3 = 3.6 μm is less sensible to the optical thickness (more sensible to microphysical and optical characteristics of single scattering).

The important result : $SS_{\lambda 2}$ and $SS_{\lambda 3}$ are very different in a great LWC region: ($SS_{\lambda 2}$ / $SS_{\lambda 3}$)~ 3 , but these signals get close values in a region of significant crystallization and precipitation.

5. CONCLUSIONS

a)The numerical model of mixed frontal clouds with several forms of crystals shows that the phase composition, the crystal form spectra and precipitation formation efficiency are dependent on dynamical structure of front and IN properties.

b) Simulations of satellite signal (cloud albedo) show that $SS_{\lambda 1}$ and $SS_{\lambda 2}$ change synchronously with the integral optical thickness of a cloud. The main contribution to IOT makes LWC .

c) The channel λ_3 =3.6 μm is less sensible to the optical thickness. SS at λ_2 = 1.6 μm and λ_3 = 3.6 μm are very different in a great LWC region but become close in a region of significant crystallization and precipitation.

The preliminary conclusion: the comparison of $SS_{\lambda 1}$, $SS_{\lambda 2}$, $SS_{\lambda 3}$ gives the possibility to distinguish regions with thick LWC layers and regions of highly developed crystallization and precipitation.

6. REFERENCES

Bakhanov,V. P., and Dorman, B. A., 1992 : Natural and seeded precipitation formation in frontal stratiform clouds with several crystal forms. Proceedings of the UHRI (Kyiv), 243, 8-23.

Bakhanov, V.P., and Dorman, B.A. , 1996 : Precipitation formation in winter frontal stratiform clouds with several crystal forms. Proceedings of the 12-th Intern. Conf. on Clouds and Precipitation (Zurich), 846-849.

Deirmendjian, D., 1969 : Electromagnetic scattering on spherical polydispersions. The Rand Corporation (Santa Monica), American Elsevier Publishing Company (New York), 165.

Kryvobok, O. A., 1998: Atmospheric correction of multispectral satellite data. Proceedings of the UHRI (Kyiv), 246, 140-150.

Liou, K.- N., 1973 : A numerical expriment on Chandrasekar's discrete-ordinate for radiative transfer : Applications to cloudy and hazy atmospheres. J. Atm. Sci., 30, 1303-1326.

Make, A., Mueller, J., and Radke, E., 1996 : Single scattering properties of atmospheric ice crystals. J. Atm. Sci., 53, 2813-2825.

Stamnes, K., and Dale, H., 1981: A new look at the discrete-ordinate method for radiative transfer calculations in anisotropically scattering atmospheres.2. Intensity computations. J. Atm. Sci., 38, 2696-2706

PROPERTIES OF SNOWFLAKES OF DIFFERENT RIMING DEGREE AND CRYSTAL TYPES

Eszter Barthazy* and Raphael Schefold

Institute for Atmospheric and Climate Science, ETH Zürich, Switzerland

1 INTRODUCTION

The properties of snow?akes such as their size distribution, fall velocity, axial ratio or their orientation when falling are important in modelling precipitation processes or in interpreting returned radar power, especially of polarized radar. However, literature on shape and fall velocity measurements of snow?akes of different crystal type and riming degree is scarce and rely generally on a very small set of snow?akes. This is a direct consequence of the instrumental dif?culties in measuring properties of single snow?akes.

The Institute of Atmospheric and Climate Science at the ETH has an optical instrument (HVSD, **H**ydrometeor **V**elocity and **S**hape **D**etector) which is capable to measure reliably, with high accuracy and automatically the properties of each single snow?ake falling through a 77 square cm area (Barthazy, 2004). In addition to the geometrical properties, the fall velocity of the snow?akes can be measured.

A large data set of two winter seasons with about 240 hours of snowfall is available. Ice crystal type and riming degree are determined with Formvar slides (Schaefer, 1956). Results on fall velocity and axis ratio of snow?akes consisting of different ice crystal types and of different riming degree are presented.

A second data set of a ?eld campaign in progress (March 2004) will be included and all results together will be presented at the conference.

2 THE INSTRUMENT

A light source is producing a beam of uniform light directed towards an electronic line scan camera. Precipitation particles falling through the light beam in a gap of the housing of the instrument cast a shadow which is measured by the line scan camera with a scan frequency of 9470 Hz. A top and a side view of the instrument is shown in Fig. 1. The camera is sensitive in two horizontal planes, having a vertical distance of 9.45 mm. Therefore, every hydrometeor is recorded twice, with a slight time difference. To calculate the vertical fallspeed and other parameters of hydrometeors, two corresponding images of hydrometeors have to be matched. A program calculates matches on the basis of different characteristics of the images.

* Corresponding author's address: Institute for Atmospheric and Climate Science, ETH Honggerberg HPP, CH–8093 Zurich, e–mail: eszter.barthazy@ethz.ch

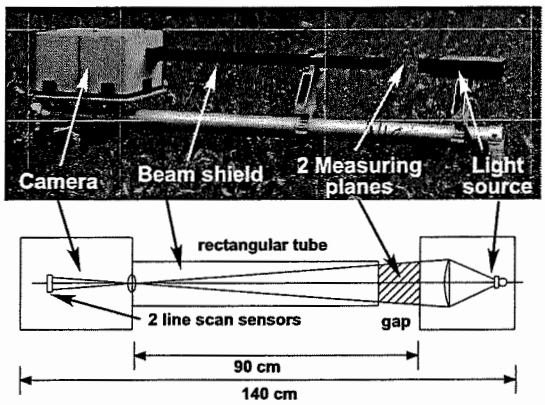

Fig. 1: *Top and side view of the HVSD.*

3 DATA

The HVSD was operated in two winter seasons (2001/02 and 2002/03) during 15 cases with a total of 240 hours of snowfall data and a total of 415 Formvar slides. The Formvar slides have been evaluated with a microscope and for each slide the percentage composition of the crystal types is known as well as the distribution of the riming degree and an average riming degree. The riming degree (rim) of the ice crystals was determined according to Mosimann (1995, see also Table 1).

Riming Degree	Description
0	unrimed
1	lightly rimed
2	moderately rimed
3	densely rimed
4	heavily rimed
5	graupel

Table 1: *Classi?cation of riming with increasing number of frozen up cloud droplets (Mosimann, 1995).*

In order to study the properties of snow?akes of a given crystal type, the data set of the Formvar slides was reduced to those with one dominant crystal type ($\geq$ 50%). 48 out of the 415 Formvar slides could be attributed to either one of the following crystal types: needles, dendrites, plates or graupel. 343 slides were mainly covered with irregular ice crystals and for 24 slides, no predominant crystal type could be attributed (Table 2).

The sampling times of the Formvar slides have been used to identify time intervals from the HVSD data for a given crystal type. For the sampling time t of a Formvar slide, a time interval of $t \pm$ 30 s is chosen to select HVSD data. Depending on the precipitation rate and

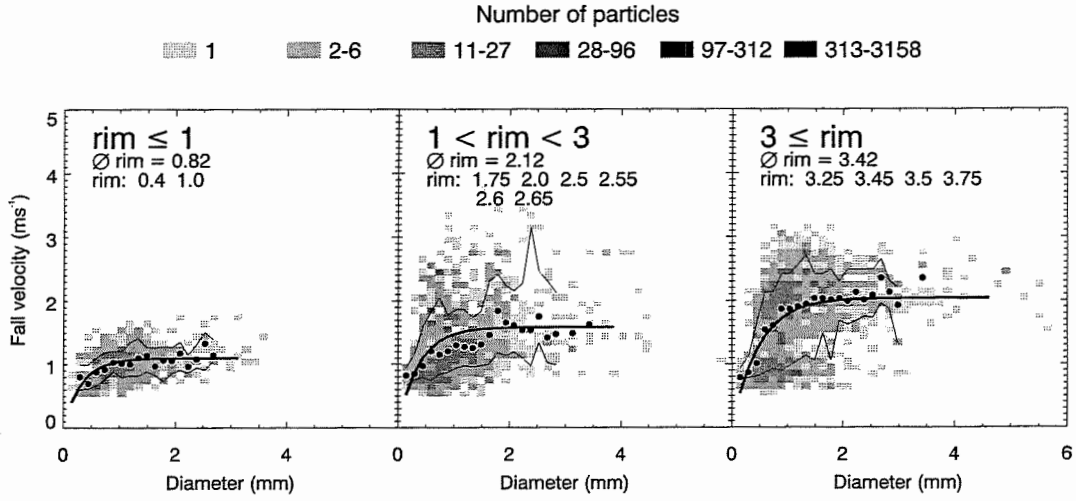

Fig. 2: *Fall velocity versus diameter for snow?akes consisting mainly of needles. The three panels show unrimed, moderately and densly rimed ice particles from left to right. The average riming degree for each subset is printed in each frame as well as the riming degrees of the single Formvar slides contributing to each subset. The thick line shows an exponential ?t to the data, the thin curves are the 17- and 83-percentiles, enclosing 66% of the data. The dots mark the median fall velocity for each size category.*

the number of Formvar samples for each given crystal type, between 800 and 37'000 snow?akes are used for the further investigation.

Crystal type	# formvar slides	# snow?akes (HVSD data)
Needles	16	2'342
Plates	8	1'495
Dendrites	20	1'232
Graupel	4	768
Irreg. crystals	343	36'748

Table 2: *Number of Formvar slides and number of single snow?akes from the HVSD for the ice crystal types investigated.*

4 FALL VELOCITY

The fall velocity behaviour of snow?akes depends on the crystal type they consist of as well as on the riming degree. To study a potential relationship of the fall velocity to the riming degree, snow?ake data have been split up into three riming regimes. Snow?akes with rim$\leq$1, 1<rim<3, 3$\leq$rim are termed hereafter unrimed, moderately and densly rimed, respectively.

4.1 Needles, plates and dendrites

To illustrate the dependence on the riming degree, fall velocity distributions of snow?akes consisting mainly of needles are shown in Fig. 2. The ?gure has three panels, each showing the measured fall velocity for a different riming regime. The gray shaded pixels shown in all three panels of Fig. 2 measure 0.150 mm on the x-axis, which represents the horizontal resolution of the instrument. On the y-axis, the velocity resolution is set to 0.1 ms^{-1}. For each size category, the median fall velocity is marked with a dot, provided that at least ?ve particles were recorded within the size category.

Size-fall velocity relations of snow?akes are usually described by a power law. We have noticed that in most cases an exponential ?t is better suited to approximate the fall velocities of snow?akes, especially when snow?akes are observed of a wide range in size. At small sizes, the fall velocity increases rapidly but after reaching a certain value, fall velocity of snow?akes tend to remain almost constant with increasing snow?ake size. Therefore, the snow?ake data have been ?tted with a function of the form

$$v(D) = a_0(1 - e^{-a_1 D}), \qquad (1)$$

where D is the diameter in mm and a_0 and a_1 are ?t parameters. Then, the velocity $v(D)$ is obtained in ms^{-1}. The ?tted size-fall velocity relationships are drawn in Fig. 2 with a heavy line and Table 3 summarizes the ?t parameters of all crystal types and riming regimes investigated.

More important than an average (?tted) size-fall velocity relationship for snow?akes is the large scatter of fall velocities for a given size. The thin curves in Fig. 2 enclose 66% of the data (17- and 83-percentiles). In case of a normal distribution this would correspond to an interval of $\pm$ one standard deviation. The percentiles are about 0.5 to 1.5 ms^{-1} apart, giving a reasonable variation of snow?ake fall velocity for a given size of $\pm$ 0.3 to 0.7 ms^{-1}. This variablility of the fall velocity can most likely be attributed to the natural variation of snow?ake properties such as the geometrical form of the snow?ake, its density, a certain variability of the riming degree and the ice crystal type composition.

$v(D) =$	unrimed		moderately rimed		densly rimed	
Needles	$1.10\left(1-e^{-3.07\cdot D}\right)$	(0.30–2.7 mm)	$1.59\left(1-e^{-2.65\cdot D}\right)$	(0.15–4 mm)	$2.04\left(1-e^{-2.06\cdot D}\right)$	(0.15–4 mm)
Plates	$1.19\left(1-e^{-2.47\cdot D}\right)$	(0.30–2.7 mm)	$1.47\left(1-e^{-2.49\cdot D}\right)$	(0.30–3.0 mm)	$1.84\left(1-e^{-1.65\cdot D}\right)$	(0.30–2.8 mm)
Dendrites	$0.87\left(1-e^{-10.31\cdot D}\right)$	(0.30–0.8 mm)	$1.29\left(1-e^{-2.01\cdot D}\right)$	(0.30–3.5 mm)	$1.29\left(1-e^{-2.15\cdot D}\right)$	(0.15–3.5 mm)
Irreg. crystals	$1.79\left(1-e^{-1.78\cdot D}\right)$	(0.15–5.0 mm)	$1.57\left(1-e^{-2.18\cdot D}\right)$	(0.15–7.5 mm)	$1.70\left(1-e^{-1.79\cdot D}\right)$	(0.15–7.0 mm)

Table 3: *Size-fall velocity relations for aggregates consisting of different crystal types and of different riming degree. The diameter is in mm, then the fall velocity is in* ms^{-1}.

In respect of the riming degree, the fall velocity of snow?akes consisting of plates shows a similar behaviour as the snow?akes consisting of needles. The fall velocity of the snow?akes increases with the rising riming degree. However, snow?akes consisting of dendrites do not seem to show any dependence of the fall velocity on the riming degree. Both, for dendrites and plates, fall velocities have been ?tted for all three riming regimes with the function given in Eq. 1. Fig. 3 and Table 2 summarize the diameter-fall velocity relationship of aggregates consisting mainly of either needles, plates or dendrites.

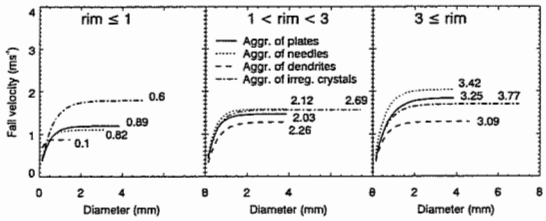

Fig. 3: *Fall velocity versus diameter for snow?akes consisting mainly of needles, plates, dendrites or irregular crystals for the three riming regimes. The numbers at the right of the lines denote the average riming degree of each crystal type and riming regime.*

4.2 Graupel

In 2 of the 15 cases, short episodes of graupel were observed. Four Formvar slides were found where graupel particles were the dominant crystal type and the fall velocities of these particles are shown in Fig. 4. Again, the median fall velocity for each size category is marked with a dot and the 17- and 83-percentiles are marked with thin lines. No ?t has been performed since only few data are available and graupel particles are, to some extent, mixed with snow?akes of a smaller riming degree. Before a ?t is performed, a procedure has to be found to separate the graupel particles from the particles with lower riming. As a comparison, the size-fall velocity relation for lump graupel from Locatelli and Hobbs (1974) is printed with a dashed line in Fig. 4.

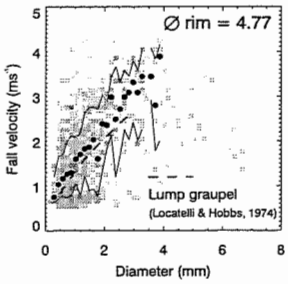

Fig. 4: *Fall velocity versus diameter for graupel particles. Median fall velocities are marked with a dot, the thin lines are the 17- and 83-percentiles.*

4.3 Irregular ice crystals

The fall velocities of snow?akes consisting of irregular ice crystals are shown in Fig. 5. There are obvious differences to the fall velocities of snow?akes of needles (and also of plates and dendrites). Even when unrimed, a considerable amount of small snow?akes have rather high fall velocities. The same can be observed for moderately and densly rimed snow?akes. In addition, when snow?akes are densly rimed, some of the particles are graupel particles, as can be concluded from their fall velocity. However, most of the particles have fall velocities lower than 2 ms^{-1} and median values as well as the ?t-curves are not much different from the size-fall velocity relations of snow?akes consisting of plates, needles or dendrites.

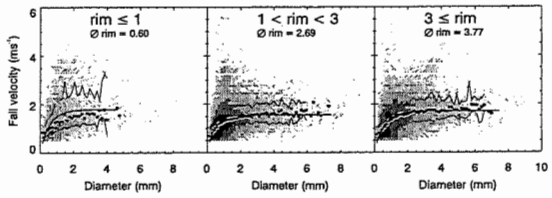

Fig. 5: *Fall velocity versus diameter for snow?akes consisting mainly of irregular ice crystals (as Fig. 2).*

5 AXIS RATIO

The axis ratio as used in this study is de?ned as

$$\mathrm{AR} = \frac{\mathrm{height}}{\mathrm{width}},$$

where height and width are the height and the width of the box enclosing the image of the hydrometeor as shown in Fig. 6. If AR<1, snow?akes are oblate, else prolate.

Fig. 6: *The width and the height of a hydrometeor.*

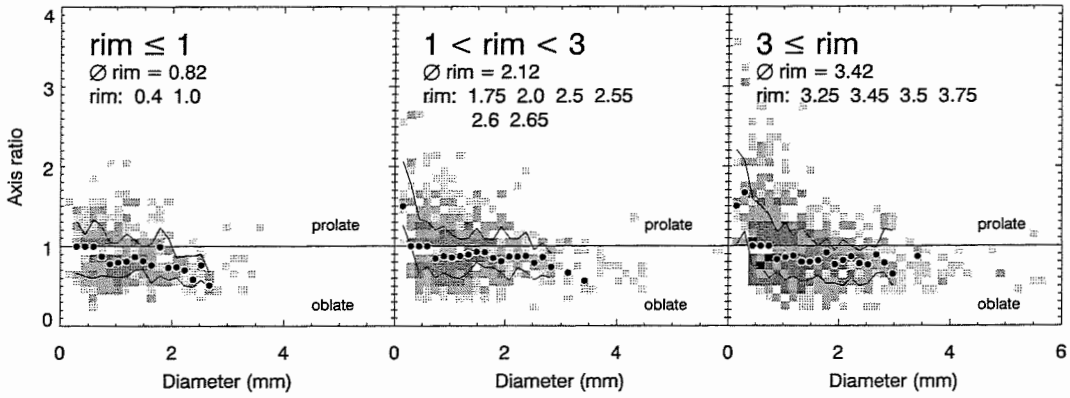

Fig. 7: *Axis ratio versus diameter for snow?akes consisting mainly of needles. The dots mark the median axis ratio for a given size category and the thin lines the 17- and 83-percentiles.*

The axis ratio of snow?akes consisting mainly of needles is shown in Fig. 7. The unrimed snow?akes have median axis ratios of 1 or less, indicating oblate snow?akes. As riming increases, more and more prolate snow?akes can be observed and the median axis ratios rise. The axis ratio versus diameter for snow?akes consisting mainly of plates and dendrites are very similar to the snow?akes of needles shown in Fig. 7. Even the snow?akes of irregular ice crystals show the same behaviour: the higher the riming the more prolate hydrometeors are measured and the higher the axis ratio. Maximum median axis ratios can be observed when graupel particles are measured. Fig. 8 shows that the axis ratio of graupel particles is close to one, as it is expected.

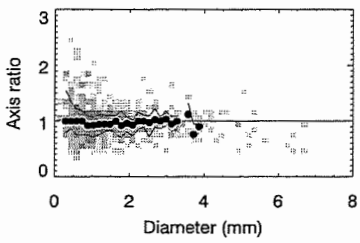

Fig. 8: *Axis ratio versus diameter for graupel particles (as Fig. 7).*

6 CONCLUSION

Shape and fall velocity of single snow?akes have been measured with the optical **H**ydrometeor **V**elocity and **S**ize **D**etector (HVSD). A large dataset of approx. 40'000 snow?akes was investigated. The measured fall velocity in dependence of the size of the snow?akes may be described by an exponential relationship $v(D) = a_0(1 - \exp(-a_1 D))$ where D is the diameter in mm and v is in ms^{-1}. There is a clear dependence of the fall velocity on the riming degree for all snow?akes except those consisting of dendrites. The higher the riming degree, the higher the fall velocity. The ice crystal type does not seem to have a strong in?uence (except dendrites) on the fall velocity of the snow?akes. Size-fall velocity relationships for a given riming regime are very similar for snow?akes consisting of needles, plates or irregular ice crystals.

The knowledge of accurate size-fall velocity relationships of snow?akes is important for precipitation process modelling but even more important is the observed variation of the fall velocity. Some precipitation processes, such as aggregation, are strongly controled by the fall velocity of the involved hydrometeors. It is important to take into account the variation of the fall velocity not only in respect to the size, riming degree and crystal type, but also in respect to the natural variability of the snow?akes when all other variables are ?xed.

The axis ratio of snow?akes was investigated with respect to their size, crystal type and riming degree. There is generally a decrease of the axis ratio with increasing size. No relation of the axis ratio to the ice crystal type could be found. However, there is an increase of axis ratio with increasing riming degree with graupel particles having the largest axis ratio of approximately 1 for all sizes.

7 REFERENCES

Barthazy, E., S. Göke, R. Schefold, and D. Högl, 2004: An optical spectrometer for shape and fall velocity measurements of precipitation size hydrometeors. *J. Atmos. Ocean. Technol.*, submitted.

Locatelli, J. D., and P. V. Hobbs, 1974. Fall speeds and masses of solid precipitation particles. *J. Geophys. Res.*, **79**, 2185–2197.

Mosimann, L., 1995: An improved method for determining the degree of snow crystal riming by vertical Doppler radar. *Atmos. Res.*, **37**, 305–324.

Schaefer, V. J., 1956: The preparation of snow crystal replicas-VI. *Weatherwise*, **9**, 132–135.

HOW DO UPDRAFTS AND EMBEDDED CONVECTION INFLUENCE RIMING?

Björn Baschek*, Raphael Schefold, Eszter Barthazy

Institute for Atmospheric and Climate Science, ETH, Zürich, Switzerland

1. INTRODUCTION

This work is considering two different kinds of phenomena – a microphysical one (riming) and a dynamical one (embedded convection) – and their coupling. Riming is the freezing of super-cooled cloud droplets on snow crystals. It is, besides deposition and aggregation, one of the fundamental snow growing mechanisms. The connection between updrafts, causing condensation, and riming is generally acknowledged. However, experimental observations of the riming degree of ice crystals together with a quanti?cation of updrafts resp. embedded convective cells are scarce. What are suitable means for a quanti?cation of embedded convective cells? What are the relevant time scales, which differ embedded convection from updrafts? What are the correlations to the microphysics of riming? The better understanding of these processes are of interest for, e.g., high resolution weather modelling and the interpretation of radar data.

2. SETUP OF MEASUREMENTS FOR RAMS I

To answer some of the open questions, the ?eld experiment RAMS I (Riming, Aggregation and Mass of Snow?akes) has been taking place at Mount Rigi in the Swiss Alps. This mountain has a steep rising front pointing towards the lowlands and the main weather direction. The setup (Fig. 1) is split up in two locations – one at the bottom and one close to the top. The steepness of the mountain allows to measure variables on different height levels at similar horizontal position.

A precipitating cloud is observed by a mobile vertically pointing X-band Doppler radar with 1 s temporal and 50 m spatial resolution from the foot of the mountain. The radar is at 450 m above sea level, which is usually below the melting layer, and is measuring and saving the full Doppler spectrum of the precipitation particles with 0.125 m/s velocity resolution. For measuring the raindrop size distribution, a Joss-Waldvogel-disdrometer is used. Radio soundings are performed and the wind ?eld around the experimental site is monitored with one resp. two C-band Doppler radars, working in single- resp. dual-Doppler mode. Properties of particles from the same cloud are measured in-situ close to the top of the mountain (1600 m above sea level, 1150 m above the radar). The snowfall is observed with a hydrometeor velocity and shape detector (HVSD, see Schefold (2004) for more details), measuring shapes and the size distribution of the ice particles and their fall velocities, which are in?uenced by the degree of riming. In addition, ice crystals are replicated with the Formvar method to determine their size, type and riming degree. This combination of remote sensing and in-situ measurements gives a multitude of information.

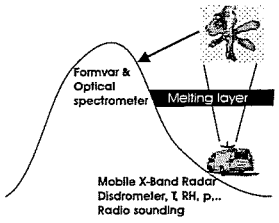

Fig. 1: Setup scheme with two locations, one at the bottom and the second close to the top of the mountain.

3. DEGREE OF RIMING

Different methods and scales exist for the determination of the degree of riming – the amount of accreted super-cooled cloud water on ice crystals. In this study a scale of six classes (Table 1; examples Figure 2), with increasing number of frozen on cloud droplets, has been used (Mosimann et al., 1994). The samples have been achieved with help of the Formvar replication method (Schaefer, 1956). Riming is not only an important growing mechanism, but it is also important for scavenging, the transfer of pollutants from the atmosphere into the snow (Poulida et al., 1998).

Riming Degree	Description
0	unrimed
1	lightly rimed
2	moderately rimed
3	densely rimed
4	heavily rimed
5	graupel

Tab. 1: Classi?cation of riming with increasing number of frozen up cloud droplets (Mosimann, 1995).

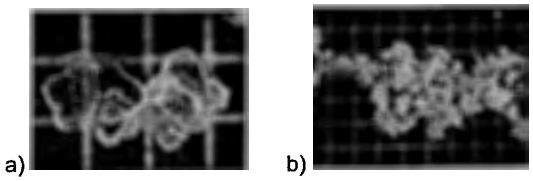

Fig. 2: Formvar replica of an unrimed (class 0) crystal (a) and of a densely rimed (class 3) snow?ake (b)- grid size 1 mm.

4. QUANTIFICATION OF CONVECTION BASED ON RADAR DATA ONLY

Embedded convective cells or "cellular overturning" (Houze and Medina, 2003) in stratiform (Houze, 1997) precipitation could be a reason for riming. The classical separation into stratiform and convective regimes of precipitation is quite rough. A more detailed classi?cation is needed for ?nding a connection between embedded convection and riming and for explaining differences in the degree of riming. Classi?cation of convection has been made before; by, e.g., Mosimann (1995) for vertical X-band radars via the variability

*Corresponding author's address: Institute for Atmospheric and Climate Science, ETH, 8093 Zürich Switzerland; e-mail: Bjoern.Baschek@env.ethz.ch

of the mean Doppler velocity with a convection index,

$$\kappa = \frac{|v - < v >_t|}{< v >_t} \quad , \tag{1}$$

as introduced by Mosimann (1995), which bases on data of vertically pointing radars. The numerator term $|v - < v >_t|$ is a measure of the variability of the Doppler velocity, with v being the Doppler velocity at a certain time and height and $< v >_t$ the average over a period of time (in our study 5 minutes) at constant height. The average velocity as denominator term $< v >_t$, gives smaller absolute changes of κ with ?uctuations for higher average velocities. With the above de?nition the value of κ is becoming negative for negative average Doppler velocities.

The equation provides a value for every height step. If wanting to follow the growth history of a snow crystal and to consider how convective its environment has been during its formation, an integration or averaging of κ over height is a possibility. But for this the above de?nition of κ is not suitable. First because it has a singularity for an average velocity of 0 m/s. Second because negative values of κ, which are describing even more convective situations, could cancel with positive values while averaging. As a straight forward method a modi?ed convection index κ_{mod} (Equation 2) has been chosen:

$$\kappa_{mod} = \begin{cases} \alpha & \kappa \geq \alpha \text{ or } \kappa \leq 0, \\ \kappa & \text{else.} \end{cases} \tag{2}$$

The original κ is cut at a constant value α and the same value α is given to negative κ. For a comparison with riming, convectivity is computed by averaging κ_{mod} over height (Eq. 3; n = number of height steps) and multiplied by a second constant β; with $\alpha \cdot \beta = 5$.

$$\text{Convectivity} = \beta \cdot \left(\sum_{height_0}^{height_1} \kappa_{mod} \right) / n \tag{3}$$

This gives the same value range between 0 and 5, as the riming degree. For the following case studies $\alpha = 0.6$ and thus $\beta = 8.3$ have been chosen. Depending on the time scale for averaging, this convection index is strongly in?uenced by the vertical winds, but only one instrument is needed for its determination.

5. ESTIMATION OF VERTICAL WINDS

The Doppler velocity, measured by a vertically pointing radar, is a combination of particle fall velocity and vertical wind speed. The combination of remote sensing and in-situ measurements gives the possibility to eliminate the in?uence of particle fall velocities, because the HVSD measures the particle fall velocities directly. After a lag time correction through cross-correlation of the data sets of radar and HVSD can thus the vertical winds be estimated (disdrometers could be used in a similar way in rain).

The radar is measuring the re?ectivity and the Doppler spectrum in "free air". The Doppler velocity v_D is de?ned as the ?rst moment of the velocity distribution,

$$v_D = \frac{\int_{-\infty}^{+\infty} z_v \cdot v \cdot dv}{z} \quad . \tag{4}$$

For a vertically pointing radar, the velocity v (Eq. 5) is the sum of the "intrinsic" terminal fall velocity v_T of the particles and the vertical wind speed w (updrafts negative sign; v, v_T positive for falling particles), if assuming, that all particles are equally in?uenced by the vertical wind.

$$v = v_T + w \tag{5}$$

The HVSD is measuring size distribution and velocity of hydrometeors at the ground. With the boundary condition, that vertical winds are zero ($w = 0$) at the ground, the measured velocity is for each particle equal to the intrinsic fall velocity: $v = v_T$.

The particles measured by the HVSD can be split into velocity bins. If the radar re?ectivity is computed separately for these bins, a Doppler spectrum is achieved. For solid ice one could compute the re?ectivity via the "re?ectivity factor" $\sum D^6$, with consideration of the smaller dielectric factor for ice spheres. For other types of ice particles, one has to correct for the lower densities. In this study a mass-size-relation for graupel-like snow of medium density has been chosen (Locatelli and Hobbs, 1974) to compute the re?ectivity - assuming Rayleigh scattering. For the computation of the Doppler velocity via the ?rst moment only the shape of the spectrum is relevant, the scaling has no in?uence. Thus only errors in the exponent of the assumed mass-size-relation play a role. Furthermore, by comparison of the zeroth moment of the Doppler spectrum received from the HVSD with the re?ectivity measured by the radar, a test of the assumptions during the calculation can be performed. Problematic situations with strong vertical wind shear might be recognizable by comparing the computed with the measured Doppler spectra.

Finally, the vertical wind speed above the radar at the height level of the HVSD can be estimated. Therefore, the Doppler velocity, computed via the ?rst moment of the HVSD Doppler spectrum, has to be subtracted from the Doppler velocity, measured by the radar at the equivalent height of the mountain station:

$$w = v_{D,radar} - v_{D,HVSD} \tag{6}$$

Thus, a separation of the in?uence of steady vertical winds from the in?uence of embedded convection on riming can be done for this height level.

6. CASE STUDY

A convective index (see section 4) - based on the X-band radar data - is used to quantify embedded convection in stratiform precipitation. For several case studies, a coupling between the degree of riming and this index resp. vertical winds (estimated by the method described in section 5) is shown. From the case studies, which have been taking place in the winter season 2002/2003, as an example 7 November 2002 has been chosen. Precipitation was caused by an occlusion. In the chosen 7 hour period, the rain rates were relatively low (per minute rain rate up to 7.3 mm/h, with 0.7 mm/h average and 4.7 mm in total). Temperature at the bottom station rose from 4.1° to 6.2° C, falling again for the last half hour. At the top station, the temperature ranged between -1.5° and -2° C. Figure 3 shows the height-time-indicator (HTI) of re?ectivity (a) and of the

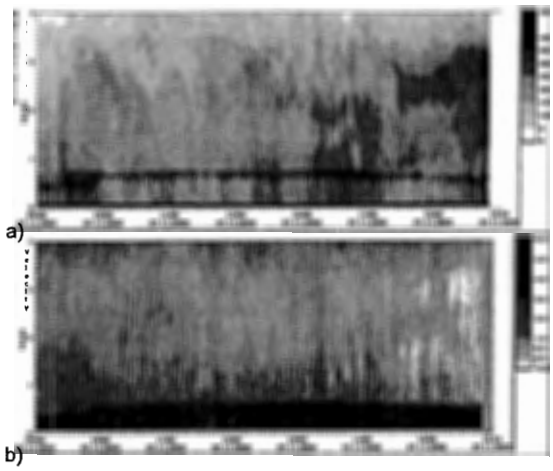

Fig. 3: Height time diagram (HTI) of re?ectivity (a) and Doppler velocity (b) for a 7 hour period on 7 November 2002. An increasing number of embedded convective cells can be seen. (In color at: http://www.iac.ethz.ch/staff/bjoern.)

Doppler velocity (b) for this period. A bright band with varying strength and an increasing number and size of areas with close to zero or negative Doppler velocities – a clear indication of embedded convective cells – can be seen. The increase in cellular structure can even be seen in the re?ectivity HTI.

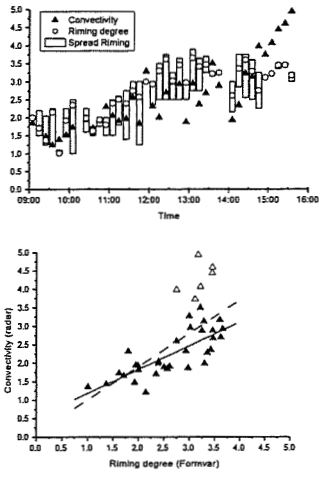

Fig. 4: Change in riming degree and convectivity versus time (a) and scatter plot of convectivity versus riming degree (b). The data points of the last one and a half hours are marked with the empty triangles. The straight lines are ?ts with (dashed) and without (solid) these last data points.

The modi?ed convection index has been computed, applying equation 3, and averaged over the height range 2 km above the height level of the top station. The result is shown in Figure 4a together with riming. The degree of riming is estimated from analysis of the Formvar samples, taken at the top station. At the beginning of the period, the degree of riming has been about 1.5, started then to rise and had at the end of the period a degree of about 3.5. For computing the correlation between riming degree and convectivity, the convectivity has been averaged over the 10 minute periods around the Formvar sampling times (38 in total). A scatter diagram of convectivity versus riming degree is shown in Figure 4b. The computed correlation is 0.67 resp. 0.77 if skipping the last one and a half hours (marked with empty triangles), which had stronger convection.

7. DISCUSSION OF THE CASE STUDY

The correlation between riming and convectivity, deduced from the straight forward modi?cation of the convection index, is quantitatively seen high. If the regions with a negative Doppler velocity are large – as in the last one and a half hours of our case – an increase of convectivity with higher riming can be seen, which is stronger than the slope of the linear ?t. This can possibly be explained by the non-linearity of the riming scale. The increase in rimed mass per riming degree is much smaller for low than for high riming degrees.

Besides, the modi?ed convection index is quite strongly in?uenced by updrafts. Here, the averaging time for the computation of convection index is equivalent to the relevant time scale of the updrafts and could discriminate between different sizes of embedded convective cells. The different behavior for varying averaging times will be looked at in the future. As a ?rst step it has been tried to eliminate the in?uence of the particle fall speed, to directly get the vertical winds and to separate the in?uence of steady vertical winds by the method described in section 5. Results are presented in section 7.

Steady (orographic?) vertical winds are not captured by the convection index. They are likely to have - compared to embedded convective cells - different in?uence on the relative particle velocities, condensation and the residence time of particles in the clouds. Equation 7 ((Klett and Pruppacher, 1997)) is describing the increase in mass of a raindrop (mass m_1, radius a_1) by collecting smaller raindrops (radius a_2) with a collection kernel E_c:

$$\frac{dm_1}{dt} = \frac{4\pi\rho_w}{3}\int E_c \cdot \pi(a_1+a_2)^2 \cdot (\mathrm{v}_{T,1}-\mathrm{v}_{T,2}) \cdot a_2^3 n(a_2)\,da_2. \quad (7)$$

Applying this standard collection equation to riming, it can give us some ideas, what is happening during riming, taking the large collecting raindrop for the ice crystal and the collected smaller raindrops for the supercooled cloud droplets. Besides convectivity and vertical winds, there might be other in?uencing factors, e.g., concentration, size and habit of ice crystals, and size distribution of cloud droplets ($a_2^3 n(a_2)\,da_2$), and wind speed and turbulence, in?uencing the relative velocities ($\mathrm{v}_{T,1}-\mathrm{v}_{T,2}$).

8. EXTENSION TO OTHER CASES

Figure 5a shows a scatter plot of convectivity versus riming for all the cases of RAMS I in winter 02/03. For the determination of the degree of riming, Formvar slides have been selected after the following ?lter rules: the temperature at the top station had to be below -1°C, the rain rate at the bottom station

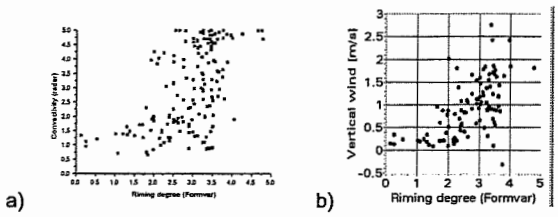

Fig. 5: Scatter plot of convectivity (a)with average time 5 min and vertical winds (b) averaged over eleven one-minute values versus riming degree for 90 Formvar samples of all 9 cases of winter 02/03 of RAMS I.

above 0.1 mm/h and furthermore the lag time had to be below 700 s to make sure, that both measurements where in the same cloud without big developments. The remaining 90 Formvar samples correspond to 900 min of measurements. Also here, an increase of convectivity with higher riming can be seen, which is stronger than the one of the linear ?t in the above case study. Figure 5b shows for these Formvar samples the corresponding scatter plot of the vertical winds. They have been estimated following the method, described in section 4, and are averaged over eleven values, each of which has been computed for one minute. The plot is quite similar to the one with the convectivity, but the convection index has the advantage, that only one instrument namely a radar is needed. The above de?ned convectivity is mainly dominated by the vertical winds and is also depending on the averaging time, which in future will be investigated in more detail.

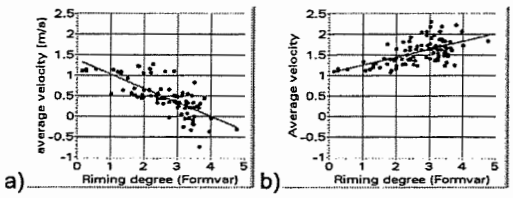

Fig. 6: Averaged Doppler velocity measured by the radar at the height of the top station (a) and Doppler fall velocity measured by the HVSD (b) - both plotted versus degree of riming.

Figure 6a shows the average velocity measured by the radar versus riming degree at the height of the mountain station and 6b the Doppler fall velocity measured by the HVSD. The difference between these two plots corresponds to the vertical winds (Fig. 5b). The terminal fall velocity increases as expected with increasing riming. Interestingly, the Doppler velocity measured by the radar is decreasing with increasing riming. For riming about 3.0 - 3.5 the particles are even in average ?oating at the measuring height.

9. CONCLUSIONS & OUTLOOK

For a case study, a correlation could be found between the degree of riming and convectivity, caused by embedded convective cells. They can be seen in the re?ectivity and Doppler data of the X-band radar – quanti?ed by a convection index. An application to other case studies shows a similar connection, but with a stronger rise of convectivity for higher riming degrees. This might be due to the non-linear character of the riming scale or a too strong weight for negative average velocities in the modi?ed convection index. Further analysis will have to be done carefully, simpler indices will be tested and Meteorological conditions and other microphysical aspects have to be considered. Further plans are e.g. to identify with help of the dual Doppler wind ?elds special synoptic and orographic situations, which are the reason for the generation of embedded convective cells in stratiform winter precipitation and thus creating prerequisites for riming to occur.

With help of a combination of remote sensing and in-situ measurements and a new method, the particle fall velocities can be eliminated from the Doppler radar velocities and the vertical winds can be estimated. This gives a tool, which is more complicated than the convection index because it needs two instruments, but which is also more powerful to analyze the in?uence of either embedded convection or steady vertical winds on riming. First investigations show a spread of the data points, but with a correlation between vertical winds and riming. In future a closer look will be taken especially on the time scales for averaging and thus of the embedded convective cells.

For these case studies, with an increase in riming degree, the fall velocity measured by the HVSD did increase, but the velocity measured by the radar decreased. For a degree of riming of about 3.0 – 3.5 even in average ?oating particles where found in free air at the measuring height. This might be an indicator for orographic effects. By deepening the comparison of radar and HVSD data, whereof re?ectivity is computed, even hypotheses for mass-diameter-relations might be testable. Or can such relations - despite of the many in?uencing factors - even be deduced and thus more information about riming be obtained?

ACKNOWLEDGMENTS

The authors wish to express their appreciation to Markus Stucki for his help with the ?eld campaigns.

REFERENCES

Houze, R. A., 1997: Stratiform precipitation in regions of convection: A meteorological paradox? *Bulletin of the American Meteorological Society*, **78**, 2179.

Houze, R. A. and S. Medina: 2003, Orographic enhancement of precipiation in midlatitudes: Results from map and improve II. *ICAM/MAP*, Brig, Switzerland, 1.

Klett, J. D. and H. R. Pruppacher, 1997: *Microphysics of clouds and precipitation*. Kluwer Academic Publishers, Dordrecht [etc.], 2nd edition.

Locatelli, J. D. and P. V. Hobbs, 1974: Fall speeds and masses of solid precipitation particles. *Journal of Geophysical Research*, **79**, 2185.

Mosimann, L., 1995: An improved method for determining the degree of snow crystal riming by vertical Doppler radar. *Atmospheric Research*, **37**, 305.

Mosimann, L., E. Weingartner, and A. Waldvogel, 1994: An analysis of accreted drop sizes and mass on rimed snow crystals. *Journal of the Atmospheric Sciences*, **51**, 1548.

Poulida, O., M. Schwikowski, U. Baltensperger, J. Staehelin, and H. W. Gaeggeler, 1998: Scavenging of atmospheric constituents in mixed phase clouds at the high-alpine site Jungfraujoch - part II. in?uence of riming on the scavenging of particulate and gaseous chemical species. *Atmospheric Environment*, **32**, 3985.

Schaefer, V., 1956: The preparation of snow crystal replicas. *Weatherwise*, **9**, 132.

Schefold, R., 2004: Messungen von Schnee?ocken: Die Fallgeschwindigkeit und eine Abschätzung weiterer Grössen. *ETH. DISS. Nr. 15431*.

More information: http://www.iac.ethz.ch/staff/bjoern.

MONTECARLO COMPUTATIONS OF SOLAR REFLECTANCE FROM ICE AND WATER CLOUDS AT NEAR IR FREQUENCIES

Alessandro Battaglia[1], Simone Mantovani[2], Franco Prodi[1,2] and Federico Porcu'[1]

[1]University of Ferrara, Dept. of Physics, Ferrara, I-44100, Italy
[2]ISAC-CNR, Bologna, I-40129, Italy

1. INTRODUCTION AND PHYSICAL BACKGROUND

Many cloud remote sensing techniques use solar reflectance for retrieving cloud particle effective radii (r_e). This parameter in fact is a crucial variable in radiative cloud processes studies (Stephens, 1990), in climate modelling and investigations of potential cloud-climate feedbacks, in rain/no rain discrimination (Rosenfeld and Lensky, 1998).

Effective radii are usually extracted by using one of the channels near 1.6 and in the 3.5-4 μm band that are now widely present both on polar and geostationary satellite (SEVIRI on MSG, MODIS on Acqua/Terra, AVHRR/3 on NOAA16-17 for instance). In fact, differently from non absorbing channels (like the VIS 0.6 micron), at these wavelengths, the reflectance depends not only on the optical thickness of the cloud but on the effective radius profile as well (Nakajima and King, 1990) . Thin clouds provide little cumulative absorption to the reflected photons because of the relatively small number of scattering which can occur. As the cloud become thicker the reflectance increases until the absorption causes the NIR reflectance to saturate at a certain optical depth level: photons penetrated down to this level have no chance to be transported upward and still re-emerge from the cloud top without being absorbed.

When very thick clouds are considered only a dependence on particle size remains. At NIR wavelenghts, absorption increases with cloud particle size as shown in fig.1; in fact, for log-normal distributions with greater effective radii, the albedo decreases and it is almost independent on the standard deviation of the size distribution. This is essentially due to the strong increase of the imaginary part of the refractive index of both water and ice in the near IR bands, located atround 1.6, 2.2 and 3.9 μm; for instance the penetration depth passes from 1.6 mm at 1.64 to 75 μm at 3.96 in bulk water and from 0.5 mm to 35 μm in bulk ice. Therefore clouds are much more opaque at the longer wavelengths and for ice-phase in both channels.

Corresponding author's address: Alessandro Battaglia, University of Ferrara, Dept. of Physics, Ferrara, I-44100, Italy; E-Mail: batta@fe.infn.it.

This physical background constitutes the basis of all optical thickness/effective radius retrieval (Nakajima and King, 1990) from satellite-observed bidirectional reflectance distribution function (BRDF). However, because of the strong differential attenuation between 1.6 μm and 3.9 μm channel, absorption-caused saturation occurs quicker at 3.9 μm: as a consequence the satellite radiation sensed at 1.6 μm comes from interactions with deeper layers inside the cloud.

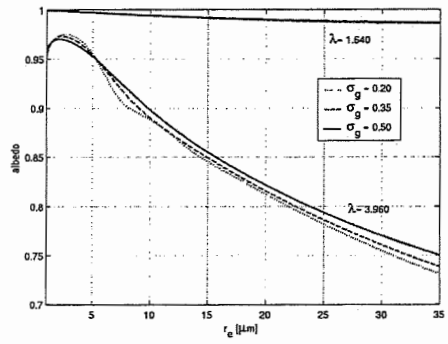

Figure 1: Albedo of a lognormal population of water spheres with different effective radii at 1.6 and 3.9 μm

To evaluate this penetration inside the cloud, Platnick 2000 introduced different weighting functions and concluded that the best suited for r_e retrievals is that based on maximum vertical photon penetrations.

Following these ideas, Chang and Li 2002, proposed a multispectral tecnique (including 1.6 and 3.9 channels) to retrieve r_e profile inside low level, non precipitating marine stratiform clouds characterized by vertical linear-increasing r_e. The retrieval procedure performs better at near-nadir observations at relatively small solar zenith angles.

In this work, we aim at better quantifying the difference between the penetrating capabilities of these two channels, by introducing the center of gravity of the the scattering weighting functions. Moreover, when ice clouds are considered, a preliminary study about the impact of different scattering matrix (correlated to different shape) on BRDF and polarization signal is conducted.

2. FORWARD RADIATIVE TRANSFER COMPUTATIONS

To achieve these goals a polarized forward Monte Carlo radiative transfer code (see Battaglia and Mantovani, 2003) has been developed with biasing techniques to efficiently solve the polarized radiative transfer equation for the full Stokes vector. The code has been adapted to accommodate plane parallel/3-D vertically/horizontally inhomogeneous scattering atmospheres and arbitrary emission sources. For the particular problem under investigation, the sun represents the only source of radiation (we implicitly assume that, at 3.9 μm, the thermal emission is removed from satellite observations by the use of IR channels). Despite a fairly substantial computational penalty, the Monte Carlo approach has the capability of correctly treating complicated phase function and polarization and in evaluating properties of photon transport processes inside clouds.

Monte Carlo computations have been performed to evaluate the reflectance of homogeneous and inhomogeneous clouds with different microphysical characteristics (effective radius, optical thickness, shapes) in presence of a collimated solar for the 1.6 and 3.9 channel for different sensor-sun geometries. All computations are performed in absence of an atmosphere and with an underlying black surface. As an example fig.1 in Capacci et al., ICCP 2004, shows the BRDF for different homogenous clouds.

3. CLOUD DEPTH PENETRATION OF REFLECTED PHOTONS

Evaluation of the contribute to up-welling radiances from the different layers allows to determine which are the levels that principally contribute at the simulated radiance. Generally the weighting functions, defined as

$$w_\lambda(\tau, r_e) = \frac{dR/d\tau}{R}$$

peaks at the top of the cloud for both channels. We compute a center of gravity of each weighting function defined as

$$\tau_{CG}^{\lambda} = \int_{cloud} \tau \, w_\lambda(\tau, r_e) \, d\tau ;$$

this quantity provides a good estimate of the penetration capability of the two channels.

As expected the optical thickness of the center of gravity of the weighting functions (measured from the cloud top downward) is always higher for 1.6μm, and generally decreases as r_e increases (the increase at r_e<5 μm is due to the rescaling of the optical thickness to 0.6μm). The variability in the scatter plot accounts for the variability in the satellite viewing angle, with lower viewing angle sounding deeper in the cloud. With the viewing geometry under investigation, in case of precipitating clouds (r_e>15μm), $\tau_{CG}^{1.6} < 5$ while $\tau_{CG}^{3.9} < 1.5$ with $\tau_{CG}^{1.6} = (3 \div 4) \times \tau_{CG}^{1.6}$.

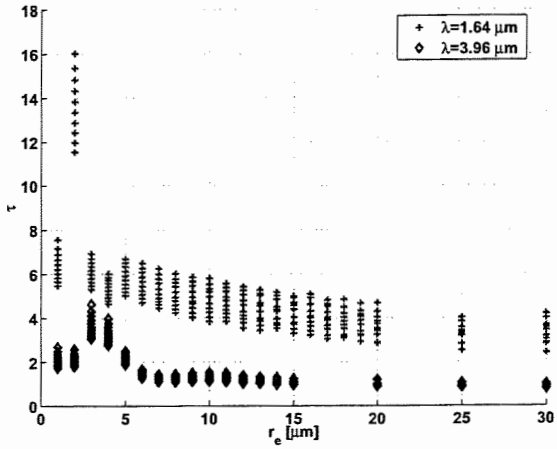

Figure 2: Visible optical thickness of the center of gravity of the weighting function for homogenous glaciated clouds with different effective radii. Viewing geometry: θ_{sun}=63°, 0°<θ_{sat}<45°, Δφ=25°.

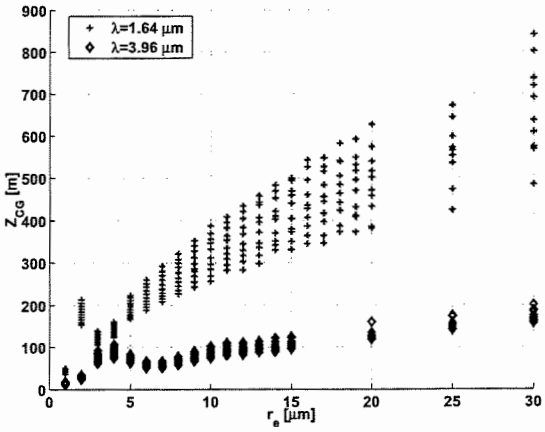

Figure 3: Same as fig.2 but for the height of the center of gravity corresponding to WC=0.1g/m³.

On the other hand for clouds with small droplets/crystals the penetration depth at 1.6μm and 3.9μm can be quite similar. By using the ray-optic approximation:

$$z_{CG}^{\lambda} = \frac{2\rho_L r_e}{3WC}\tau_{CG}^{\lambda}$$

so that, as an exemplification, we have also computed the corresponding height of the center of gravity for a cloud with fixed WC=0.1 g/m^3 (see fig.3).

Because of the r_e factor at the numerator, z_{CG}^{λ} comes out to generally increase with r_e. Therefore, as shown by $z_{CG}^{3.9}$, reflected radiances at 3.9 μm are representative of a shallow layer near the cloud top (the shallower the higher the WC of the cloud) while the radiances at 1.6 μm are generated by photons reflected by cloud particles located 3-4 times deeper in the cloud.

A second analyses is carried out on vertical inhomogeneous clouds with realistic profile of liquid/ice content and of the effective radius as extracted from a field campaign FIRE II-ASTEX over NorthAtlantic startocumulus. Since profiles with high r_e (>15μm) are found in combination with high water content and viceversa, for these study cases $z_{CG}^{3.9}$ and $z_{CG}^{1.6}$ keep lower than 150 m and 300m respectively.

4. IMPACT OF SHAPE ON BRDF

Observation from field campaign have shown that the majority of particles in ice clouds are bullet rosettes, solid and hollow columns, plates and aggregates and only in few cases hexagonal plates and columns. Mishchenko et al., 1996, underlined that this issue has to be addressed when retrieving optical thickness by VIS-channel reflectance.

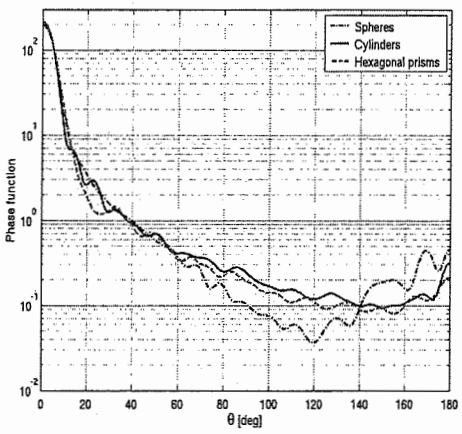

Figure 4: Phase functions for a population of ice particles with r_e=10μm and different shapes at 3.9μm.

Use of the wrong particle model in retrieving the cloud optical thickness from reflectance can result in an underestimation/overestimation of a factor of 3.

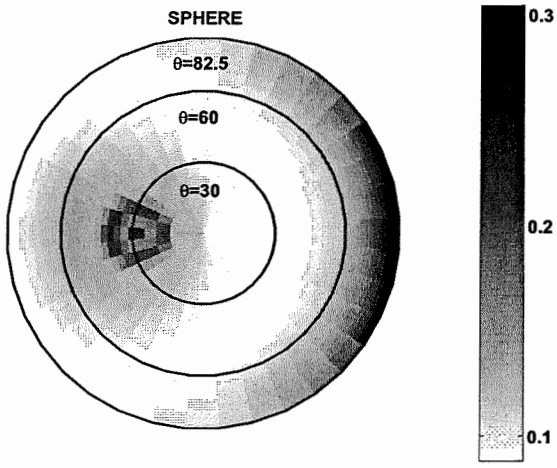

Figure 5: Polar plot (the radial and the azimuthal coordinate represent the sensor viewing angle θ and the azimuthal relative angle between the sun and the sensor) representing the variability of the BRDF with the viewing geometry for a layer of spheres with r_e=10μm and τ=50. The sun position is fixed at θ_{sun}=30° and it is indicated by the square.

Similarly Key et al., 2002 demonstrated that visible BDRFs are strongly dependent both on optical depth and ice crystal shape with solid columns and rough aggregates behaving similarly but systematically larger than plates and spheres. Multiple scattering has a blurring effect but details of the scattering phase function still influence BRDF at very high optical thickness. As an experimental confirmation, measured BRDF of cirrus obtained with the scanning radiometer on board ER-2 presented by Spinhirne, 1996 show that a correct interpretation cannot be done through ice spheres but only by using irregular ice crystals. The same is even truer when considering depolarization signals. We have extended this analysis to 1.6 and 3.96 μm. Fig.4 demonstrates that at near IR randomly oriented cylinders and hexagonal plates scatter less radiation at backscattering and more radiation at intermediate scattering angle than spheres. This different scattering pattern directly affects BRDF. In fact figures 4-5 show different behaviour: cylinders (and hexagons) privilege forward scattering while spheres present a consistent increase of BRDF in the backscattering region. The two BRDF have been computed with the same albedo 0.795 an for an optical thickness equal to 50.

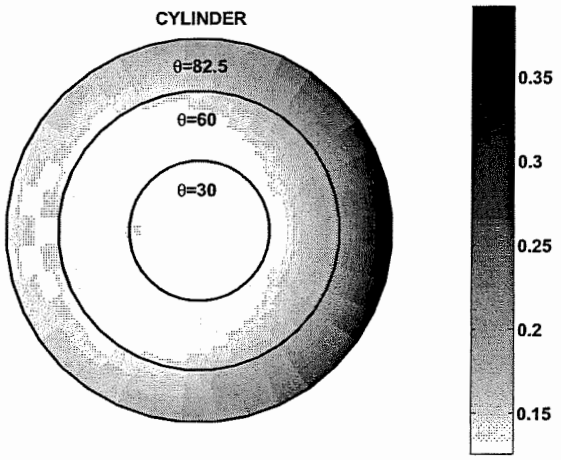

Figure 6: Same as fig.4 but for cylinders.

5. CONCLUSIONS AND FURTHER WORKS

The 1.6 and 3.9 BRDF have been investigated for ice/water omogeneous/inhomogeneous clouds with different sun-sensor geometries. Our findings confirm that NIR reflectances at different wavelengths have variable sensitivity to r_e at different levels inside a cloud layer with higher frequencies channels sounding deeper in the clouds. When high-r_e profiles within homogeneous clouds are considered, the center of gravity of scattering weighting functions at 1.6μm is located 3-4 four time deeper than at 3.9μm. On the other hand when small droplets/ice crystals are considered the penetration capabilities of the two wavelengths is much closer.
In inhomogeneous clouds, the weighting functions depend on the vertical variability of both r_e and liquid water content. In this case general conclusions cannot be drawn but case by case studies are needed. This topic has to be deepened by considering a greater number of realistic r_e/wc profiles derived from in situ measurements (including multi-layered clouds).

Finally for ice clouds, our preliminary study reveals that, even at high optical thickness details of the phase function seem to be relevant for a correct evaluation of the bidirectional reflection function, even at 3.9μm. More simulations are necessary to precise this sentence, by using different shapes and sizes for the ice particles.

The relevance of our results is connected to the fact that the outputs of these simulations can drive bispectral tecniques that use the combination of 1.6 and 3.9 μm to retrieve vertical profiles of effective radii.

5. REFERENCES

Battaglia A. and S. Mantovani, Development of a forward biased MonteCarlo for microwave radiative transfer computations, 2004, MICRORAD2004 Meeting, Rome, Italy.

Chang Fu-Lung and Zhanqing Li, 2002. Estimating the vertical variation of cloud droplet effective radius using multispectral near-infrared satellite measurements, J. Geo. Res., 107, D15.

Key, J. R., P. Yang. B. A. Baum, and S. L. Nasiri, 2002, Parametrization of shortwave ice cloud optical properties for various particle habits, J. Geo. Res., Vol. 107, D13.

Mishchenko, M. I., Rossow, W. B., Macke, A., and Lacis, A.A., 1996, Sensitivity of cirrus cloud albedo, bidirectional reflectance and optical thickness retrieval accuracy to ice particle shape, J. Geophys. Res., 101, 16973-16985

Nakajima, T., and M. D. King, 1990, Determination of the optical thickness and effective particle radius of clouds from reflected solar radiation measurements, J. Atmos. Sci., 47, 1878-1893.

Platnick, S., 2000: Vertical photon transport in cloud remote sensing problems, J. Geo. Res., Vol. 105, 22919-22935.

Rosenfeld, D., and I. M. Lensky, 1998: Spaceborne sensed insights into precipitation formation processes in continental and maritime clouds, Bull. Am. Meteor. Soc., 79, 2457-2476.

Spinhirne, J. D., Hart, W. D., and Hlavka, D. L., 1996, Cirrus infrared parameters and shortwave reflectance relations from observations, J. Atmos. Sci., 53,1438-1458.

Stephens, G.L., S.-C. Tsay, P. W. Stackhouse, and P.J. Flatau, 1990, The relevance of mycrophysical and radiative properties of cirrus cloud to climate and climate feedback, J. Atmos. Sc., 47, 1742-1753.

6. AKNOWLEDGEMENTS

This work has been jointly funded within the framework of EURAINSAT a shared-cost project (contract EVG1-2000-00030) co-funded by the Research DG of the European Commission within the RTD activities (5th Framework Program). Fire II-ASTEX data were obtained from the NASA-LANGLEY Research Center Atmospheric Science Data Center.

THE SHAPES OF VERY SMALL CIRRUS PARTICLES DERIVED FROM IN SITU MEASUREMENTS

D. Baumgardner[1], H. Chepfer[2], G.B. Raga[1] and G.L. Kok[3]

[1]Universidad Nacional Autónoma de México
[2] LMD/IPSL, Palaiseau, France
[3] Droplet Measurement Technologies

1. INTRODUCTION

The uptake of gaseous species and subsequent heterogeneous chemistry occurs on crystal surfaces (*e.g. Gao et al.*, 2004; *Popp et al.*, 2004). Crystal growth and sublimation are also functions of surface area (*Pruppacher and Klett*, 1978). The terminal velocity depends on the drag forces that increases with a crystal's projected area (*Mitchell*, 1994) and the projected area also impacts a crystal's optical properties.

Small cirrus crystals, i.e. those with maximum diameters smaller than 50 μm, occur frequently in high concentrations (*Knollenberg et al.*, 1993; *Heymsfield and McFarquhar*, *Garrett et al.*, 2003). The albedo of cirrus clouds is especially sensitive to the concentration and shapes of this size range of particle (*Arnott et al.*, 1994; *Heymsfield and McFarquhar*, 1996). Very few measurements have been made with sufficient resolution to view the essential features of such small cirrus particles so that an accurate assessment can be made of the particle shape at these sizes. Optical array probes, eg., the PMS-2D probes, have a minimum resolution of 25 μm. Formvar replicators can capture the crystal shape but only a limited number of measurements have been made in cirrus, analysis is tedious and only the projected area can be derived directly. A similar limitation exists with a newer instrument; the Video Ice Particle Sampler captures crystals on a moving 8 mm tape and can resolve sizes down to 30 μm (*Miloshevich and Heymsfield*, 1997). The details of crystal structure can be analyzed and a projected area derived but total surface area must be estimated.

Measurements of ice crystals with the Droplet Measurement Technology cloud and aerosol spectrometer (CAS) are presented here that relate forward to backscattered light to theoretical calculations of light scattering. The measurements suggest that the majority of ice crystals smaller than 45 μm are nearly spherical in shape

Corresponding author's address:
Darrel Baumgardner, UNAM, Mexico City, Mexico,
E-Mail: darrel@servidor.unam.mx

2. MEASUREMENT TECHNIQUE

The CAS collects two cones of light, 4 to 12° and 168° to 176°, scattered from particles that pass through a 680 nm, focused beam produced by a Gaussian mode diode laser (Baumgardner et al., 2001) as shown in Fig. 1. The two cones of light are converted individually into voltage pulses and the peak amplitudes are digitized. The two values are used to decide which of the intensity bins in the forward and backward frequency distributions to increment by one. The threshold of each bin is pre-programmed. The CAS accumulates events over one second periods before storing the results for post-flight analysis. The relationship between scattered light intensity and detector output is established using monodispersed polystyrene latex beads and crown glass beads of known size and refractive index. The average ratio of forward to back scattering is the sum of the 30 forward divided by the sum of the 30 back scattering channels. The size range measured is from 0.5 to 45 μm.

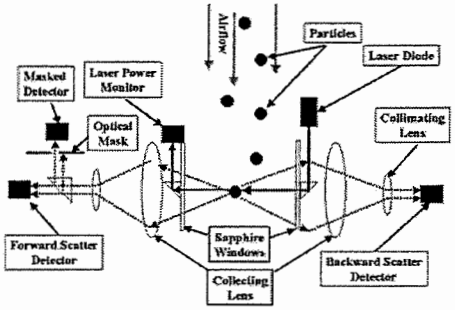

Figure 1

3. PHASE FUNCTION CALCULATIONS

The phase functions were calculated for a number of crystal shapes and mixtures of crystal shapes. These phase functions were then integrated over the same two collection angles as used by the CAS. The ratio of forward and backscattered intensities, Rt, derived from these phase functions is tabulated in Table 1. Some of the phase functions are associated with an ensemble of mono-crystals (MC) having the same size and shape, whereas others are associated with an ensemble of ice crystals with various sizes and shapes. For particles sizes larger than 12.5 μm the

behaviour of the scattering phase function in the forward and backward directions is mainly prescribed by the geometrical optic computations ($X=2\pi r/\lambda > 60$), so that the value of Rt is a signature of a crystal shape that is nearly independent of the size. For particles sizes smaller than 12.5 μm, variations of Rt are associated with changes in both particle size and shape. For small particle sizes (d < 10 μm), Rt tends to increase strongly because diffraction significantly increases the energy scattered in the forward direction. Two exceptions (isccp and modis_rough) have large values of Rt associated with large particle sizes due to the assumed particle roughness in the phase function calculations. This leads to a smoother behaviour of the resulting phase function. The 18 phase functions considered in this study do not reproduce all the possible particle sizes and shapes encountered in reality, but they cover a large range of the available state-of-the-art scattering phase functions in the visible domain, leading to values of Rt ranging between 5 and 183.

4. RESULTS

The CAS was flown on the NASA WB-57F in July 2002 as part of the CRYSTAL-FACE project to study sub-Tropical cirrus clouds (Jensen et al., 2004). Twelve research flights were flown during that period. Flights 2-12 have been evaluated to assess the shapes of small ice crystal as measured by the forward to back scattered ratio (F2BR). The number of events for different values of F2BR was calculated from the 11 flights. The distribution shown in Figure 2A is the number of events as a function of F2BR. The majority of ratios are in the range from < 60, indicating that most of these particles are spherical in shape or mixtures of crystals with shapes corresponding to bullet rosettes, hollow columns and plates.

A number of factors may affect the shapes of small ice crystals, among these are the origin of the ice nuclei, the environmental temperature and the relative humidity with respect to ice (RHI). The ratios were further stratified by these variables. Figures 2B and D show the effect of these conditions on the distribution of F2BRs. Neither temperature nor RHI appear to be significant factors in particle shape since the distribution by F2BR is approximately the same regardless of the temperature or RHI regime in which they were measured.

Figure 2C is a stratification of F2BR frequency with respect to the mean wind direction. The wind was more often from the NE and SE with fewer numbers of instances in which clouds were sampled with SW winds. Particles in clouds with winds from the south had many fewer events with F2BRs greater than 60.

5. DISCUSSION

The shapes of cirrus crystals smaller than 50 μm have been derived from measurements of the forward to backscattering ratios. The range of measured F2BRs is in sensible agreement with the model. The majority of particle shapes are identified as spherical, regardless of the temperature and humidity conditions at the time of measurement. This suggests that the mechanism that formed these crystals is homogeneous nucleation, i.e. the freezing of water droplets. Work is ongoing to further evaluate these measurements in comparison with remote sensors and cloud models.

6. ACKNOWLEDGEMENTS

The authors would like to thank Bruce Anderson at NASA Langley for the CAPS used during CRYSTAL/FACE and for his participation in that program. This work was funded by the NASA Radiation Sciences program.

7. REFERENCES

Arnott, W. P., et al., Role of small ice crystals in radiative properties of cirrus: A case study, FIRE II, November 22, 1991, J. Geophys. Res., 99, 1371–1381, 1994.

Baumgardner, D., et al., 2002: The cloud, aerosol and precipitation spectrometer (CAPS): A new instrument for cloud investigations, *Atmos. Res.*, 59-60, 251-264.

Brogniez, G., Light scattering by finite hexagonal crystals arbitrarily oriented in space, paper presented at the International Radiation Symposium, Lille, France. 18-24 August, 1988.

Garrett, T.J., H. Gerber, D. Baumgardner, C. H. Twohy, E.H. Weinstock, 2003: Small, Highly Reflective Ice Cystals in CRYSTAL-FACE Anvil Cirrus, *Geophys. Res. Lettrs.*, 30, No. 21, 2132, doi:10.1029/2003GL018153.

Gao, R. S.,et al., 2003: Evidence that Ambient Nitric Acid Increases Relative Humidity in Low-Temperature Cirrus Clouds, *Science*, In Press

Heymsfield, A.J. and G.M. McFarquhar, 1996: High albedos of cirrus in the tropical Pacific warm pool: microphysical interpretations from CEPEC and from Kwajalein, Marshall Islands, *J. Atmos. Sci.*, 53, 2424-2451.

Jensen, E., et al., 2004: Mission investigates tropical cirrus clouds. *EOS Transactions*, 84 (5), pp45&50.

Knollenberg, R.G.,et al., 1993: Measurements of ice number density of ice crystals in the tops of tropical cumulonimbus, *J. Geophys. Res.*, 98, 8639-8664.

Macke, A., J. Mueller, and E. Raschke, 1996: Single scattering properties of atmospheric ice crystal. *J. Atmos. Sci.*, 53, 2813-2825.

Miloshevich, L.M. and A.J. Heymsfield, 1997: A balloon-borne continuous cloud particle replicator for measuring vertical profiles of cloud microphysical properties: Instrument design, performance, and collection efficiency analysis, *J. Atmos. and Ocean. Tech.*, 14, 753-768.

Mitchell, D., 1994: Use of mass- and area-dimensional power laws for determining precipitation particle terminal velocities, *J. Atmos. Sci.*, 53, 1710-1723.

Popp P.J., et al., 2003: Nitric Acid Uptake on Subtropical Cirrus Cloud Particles, *J. Geophy. Res.*, In Press

Pruppacher, H.R. and J.D. Klett, 1978: Microphysics of clouds and precipitation, D. Reidel Publishing Co., Boston, MA., 714pp.

Takano, Y., and K. N Liou, Solar radiative transfer in cirrus clouds. Part I : Single-scattering and optical properties of hexagonal ice crystals, *J. Atmos. Sci., 46*, 3-19, 1989.

Yang P., and K. N. Liou, Single scattering properties of complex ice crystals in terrestrial atmosphere, *Contrib. Atmos. Phys.*, **71**, 223-248, 1998.
Yang, et al.,2000: Parameterization of scattering and absorption properties of individual ice crystals, *J. Geophys. Res.*, 105, 4699– 4718, 2000.

Table I
Scattering Phase Functions

Particle shape : CP = hexagonal compacts (Q=1), COL = hexagonal columns (Q=2.5), BR = bullet-rosettes, PL = plates (Q=0.05), HC = hollow columns, AG = aggregates, POL = polycrystals, D = dendrites, S = spheres, MC= Mono-crystals
Computation theory : MT = Mie Theory, GO = Geometric Optic, GOM = Geometric Optic Modified, FDTD = Finite Differential Time Domain, The crystal size corresponds to the effective diameter (□m)

Name	Crystal shape	Crystal Size	Computation method	From	Ratio
Columns MC	COL	40	GO	Brogniez	5
Compacts MC	CP	40	GO	Brogniez	5
Ceres_big_crystal	CP+COL	135	MT+GO	Takano	6
Ceres_nov1	CP+COL	75	GO	Takano	7
Bullet-rosette MC	BR	87	GO	Takano	18
Plates MC	PL	40	GO	Brogniez	25
Ceres_contrail	CP+COL	18	GO	Takano	29
Droxtal		20 to 1	FDTD	Yang	30 to 140
Dendrite	D		GO	Takano	32
Modis_2	BR+PL+HC	33	GO+FDTD	Yang	36
Modis_3	BR+PL+HC+AG	79	GO+FDTD	Yang	37
Modis_1	BR+PL+HC	9	GO+FDTD	Yang	39
Spheres_6	S	12	MT	Mie code	60
Isccp	POL	60	GO	Macke	66
Modis_rough	BR+PL+HC	30	GO+FDTD	Yang	108
Vis 10 - 5	COL(Q=2)	7.5	GO+FDTD	Takano	117
Haze M	S	1.8	MT	Mie code	127
Haze L	S	1.	MT	Mie code	183

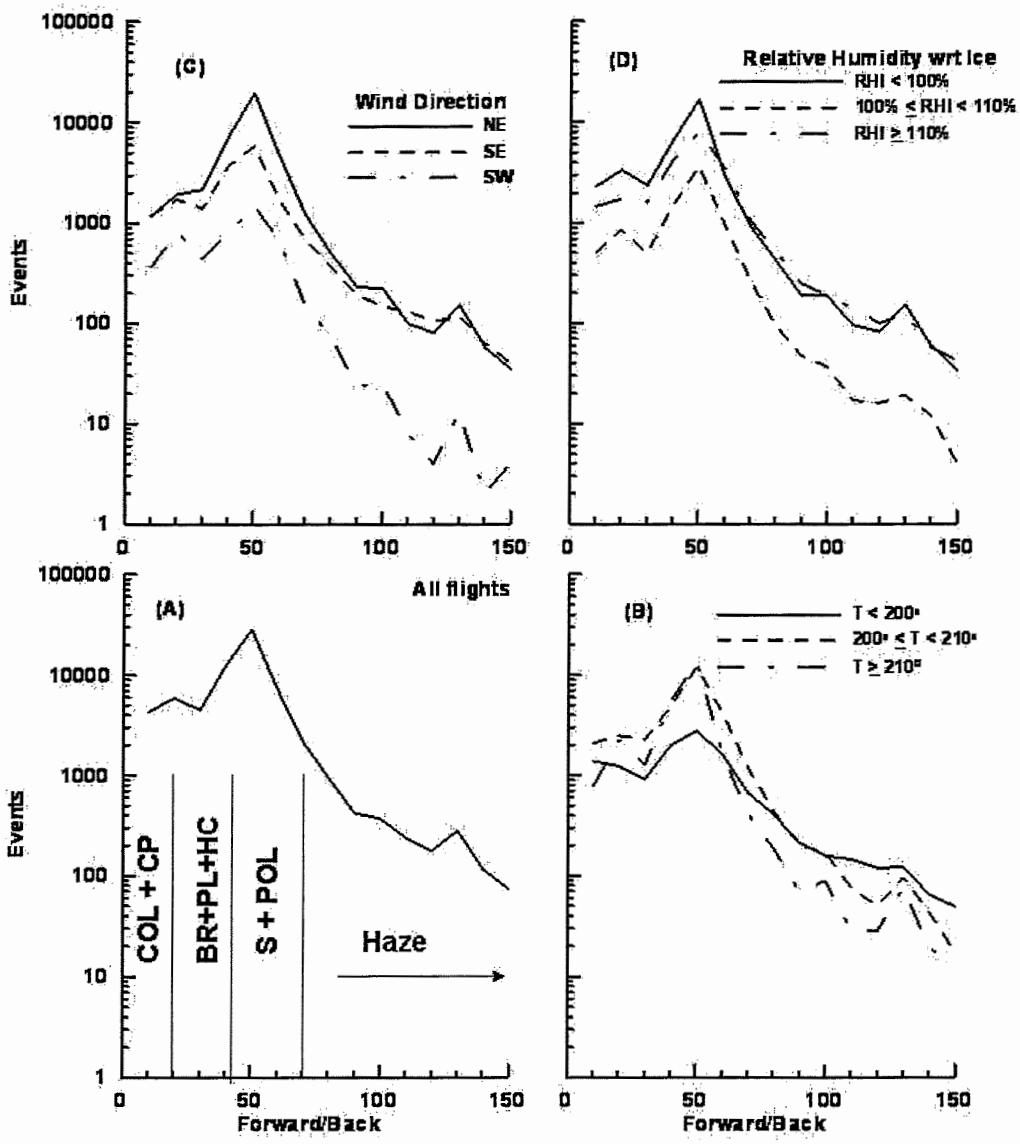
(C)
Wind Direction
NE
SE
SW
(D)
Relative Humidity wrt Ice
RHI < 100%
100% ≤ RHI < 110%
RHI ≥ 110%
(A)
All flights
COL + CP
BR+PL+HC
S + POL
Haze
(B)
T < 200°
200° ≤ T < 210°
T ≥ 210°
Events
Forward/Back
100000
10000
1000
100
10
1
0
50
100
150

Figure 2

10-YEAR STATISTICS ON FREEZING PRECIPITATION ACROSS THE FORMER USSR FROM SURFACE WEATHER OBSERVATIONS

N.A.Bezrukova[1], R.K.Jeck[2], L.S.Minina, M.F.Khalili[3], E.A.Stulov[1]

[1]Central Aerological Observatory, Dolgoprudny, Moscow Region, 141700 Russia
[2]Federal Aviation Administration, Atlantic City, NJ 084057, USA
[3]Moscow State University, Moscow, 119992 Russia

1. INTRODUCTION

This study is a continuation of an earlier climatology investigation on freezing precipitation (FP) over the USSR territory (see Proceedings of 13th ICCP). The study gives exhaustive information about and statistical analysis of the supercooled precipitation events observed over the territory of the former USSR during 10 years.

As a result of recent aircraft accidents or incidents that appear to be associated with flight in freezing rain or freezing drizzle, there is a need to learn more about these conditions on a worldwide basis. The FAA, in the research plan developed in 1997, listed thirteen research tasks, which it agreed to support, centered on the need to ensure flight safety in freezing precipitation. Specifically, Task 13 of the 1997 FAA In-flight Aircraft Icing Plan states that "Records of freezing rain and freezing drizzle from surface observations in many countries...are valuable for assessing the threat worldwide and for determining the opportunities for possible flight tests or additional measurements in (these) conditions." A good climatology for freezing precipitation exists for the U.S. and Canada e.g., Gay&Devis (1993), Strapp et.al(1996), Changnon & Karl (2003), but not over the other areas of the globe where winter icing conditions occur. The purpose of this statistical work is to help fill in that gap by obtaining data and analyses of FP conditions over Russia and the former USSR.

2. BACKGROUND DATA

2.1 Data Sources

The data of ground-based weather stations included in the list approved by the WMO, which are involved in the international exchange of meteorological data, were used. The Monthly Meteorological Tables (1981-90) that contain selected daily surface meteorological observations of FP at 03:00, 09:00, 15:00, and 21:00 from more than 220 stations of the USSR network for a decade served as a basis for our statistics analysis.

Corresponding author's address: Natalia A.Bezrukova, CAO, Pervomayskaya 3, Dolgoprudny, Moscow Region, 141700, Russia; E-Mail: nataly_bez@yahoo.com

Weather characteristics associated with FP phenomena are also collected. Data on FP and weather characteristics were analyzed and mapped for the territory of the former USSR.

2.2 Terminology and Interpretation

In Russian scientific meteorological publications and meteorological vocabularies one can see a double interpretation of FP phenomena: 1) smooth compact deposit of ice, generally transparent, formed by freezing of supercooled drizzle droplets or raindrops on objects with surface temperature below or slightly above 0ºC; and 2) supercooled precipitation drops, which form a coating of glaze on the ground and on exposed objects.

To avoid such distortions, we only collected data in the form of International Weather Codes. All the types of FP events have been subdivided in accordance with the standard WMO categories: freezing drizzle, light (56); freezing drizzle, moderate or heavy (57); freezing rain, light (66); freezing rain, moderate or heavy (67); freezing drizzle or freezing rain observed during the last observation hour (24); fog-deposited rime (48,49). On the whole, all the collected characteristics of Codes 56, 57, 66, 67, 24, 48, and 49 adequately reflect the peculiarities of FP distribution over the territory concerned.

3. DATA CHARACTERISTICS

In particular, the following data were presented for each weather station: location (city) and station number of the weather observation station, date and time of the observation, current weather and weather between observations, temperature, dew point temperature, relative humidity, air pressure, wind speed and direction, visibility, total and low cloud amounts, height of cloud base.

Thus the collected ground observations have formed a data bank of the 11141 FP events reported across the whole territory for a 10-year period. Figure 3.1 shows the distribution by months of all the FP events observed.

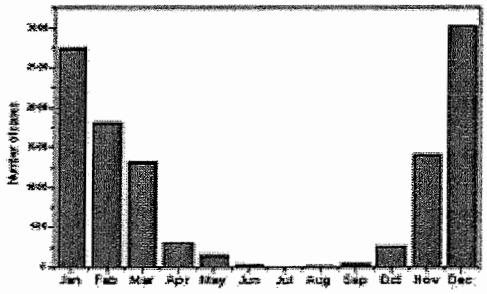

Fig. 3.1 Distribution by months of freezing precipitation events.

4. STATISTICS ON FREEZING PRECIPITATION

4.1 Distribution of cases by weather codes

The distribution of the overall number of freezing precipitation events that are accounted for by each of the WMO standard categories (Codes) is such as is shown in Table 4.1

Table 4.1

Distribution of cases with FP by weather codes

Codes	Count of cases
24	170
48	1998
49	6470
56	1751
57	169
66	533
67	50
Total	11141

The overwhelming majority of FP observations, 1998 and 6470 cases, respectively, are accounted for by Codes 48 and 49 (fog depositing rime). In 1751 cases, Code 56 (freezing drizzle, light) events were observed, while the least number of cases are those designated by Code 67 (freezing rain, moderate or heavy).

4.2 Distribution of cases by regions

The raw data on FP come from 223 stations in the former USSR. These stations are located in various climatic zones, from the Arctic tundra to subtropical deserts. The northern–most station is located at 73º30' N (Ostrov Dikson) and the southern–most (Kushka) at 35º17' N. The western- and eastern–most stations are at 20º37' E (Kaliningrad) and 173º16' W (Buhta Providenia), respectively. The entire territory was divided into 6 principal regions in accordance with their physic-geographical and climatology features. Each of the 223 stations corresponds to one of the 6 regions:

1. ARCTIC. This Region included all the stations located on the Arctic coast and in the northern part of Siberia inside the Polar Circle, with the exclusion of Murmansk and Kandalaksha stations located on the Kola Peninsula.
2. EUROPEAN PART OF THE FORMER USSR. This Region included all the European stations, except the stations located inside the Polar Circle: Hoseda-Hard and Narian-Mar.
3. TRANS-CAUCASUS. This Region included all the stations located south of the Great Caucasus Range.
4. CENTRAL ASIA. This Region included all the stations located in Kazakhstan, Turkmenistan, Uzbekistan, Kirghiz Republic and Tadjikistan.
5. SIBERIA. This Region included all the stations of Western Siberia and Eastern Siberia, excluding the stations located at the Pacific Ocean Coast and Far East Territory.
6. FAR EAST. This Region included all the stations located in Habarovsk Region, Primorsk Region, Kamchatka, Sakhalin and the Sea of Okhotsk coast.

The locations of the stations for the six regions of USSR and total number of cases with freezing precipitation are shown on the map below.

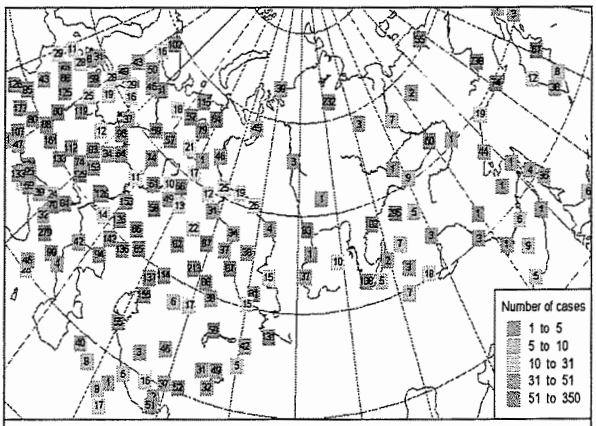

Total number of cases with freezing precipitation (Weather Codes 24, 48, 49, 56, 57, 66, 67) over the USSR territory during 10 years

Table 4.2

Number of stations in the 6 regions of the former USSR

N	Region	Number
1	Arctic	11
2	European part of the former USSR	80
3	Trans- Caucasus	6
4	Central Asia	42
5	Siberia	53
6	Far East	31

Table 4.3

Distribution of cases with freezing precipitation by Weather Codes in different regions of the USSR

Codes		24	48	49	56	57	66	67	Total
Region 1 Arctic	Count	12	327	324	94	5	9	-	771
	%	2	42	42	12	<1	1	-	100
Region 2 European part	Count	127	541	3529	1410	122	423	32	6184
	%	2	9	57	22	2	7	<1	100
Region 3 Trans – Caucasus	Count	-	6	67	-	-	-	-	73
	%	-	8	92	-	-	-	-	100
Region 4 Central Asia	Count	23	351	1514	181	34	72	16	2191
	%	1	16	69	8	2	3	<1	100
Region 5 Siberia	Count	6	635	783	35	4	28	2	1493
	%	<1	42	52	2	<1	2	<1	100
Region 6 Far East	Count	2	138	253	31	4	1	-	429
	%	<1	32	59	7	<1	<1	-	100
Total	Count	170	1998	6470	1751	169	533	50	11141
	%	1.5	18	58	16	1.5	5	0.5	100

4.3 Statistical characteristics of freezing precipitation as related to major meteorological parameters

The frequency of occurrence of FP in the six regions is given in Table 4.3. In general, FP is less frequent in the south and east than in the north and west.

The Arctic region experienced 771 events. As for the other regions, weather types coded 48 and 49 (fog depositing rime) account for 84% of events. Freezing rain and drizzle is rather seldom (16%). In this region, many events were accompanied by very low temperatures (-40º, -50º C) (Fig.4.1) and more high pressure (>1015 hPa).

More than half of all the cases occurred in the European part of the USSR. On the average this region saw 77 events per station during a decade, two thirds of the events being rime events (codes 48, 49).

However, as compared to the Arctic region, freezing rain and drizzle events are more frequent (33%). The majority of events occurred at temperatures above -10^0 C and low pressure (995-1010hPa), with the number of events increasing at temperatures rising to 0^0C. About 40% of events occurred when the height of cloud base was below 100m.

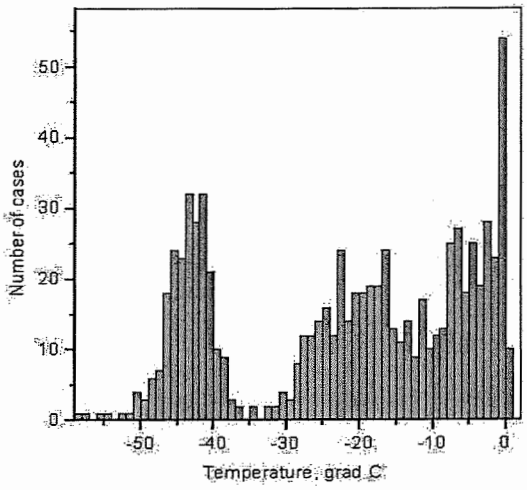

Fig.4.1 Distribution of cases with freezing precipitation versus temperature (Arctic)

In the Trans-Caucasus region, the relations between the parameters concerned, as far as the statistics goes, are the least representative as being hard to compare. Only 73 events (with codes 48 and 49) occurred there, and, besides, 5 out of the 6 stations are located in mountain valleys at different heights. On the average, this region saw 12 rime events per station, which is much less than in the other regions, except the Far East. No freezing rain or drizzle was observed there.

In Central Asia, the occurrence of FP events vs. temperature was the same as in the European part of the former USSR. By the number of events (52) per station, this region holds the third place. The majority of events occur at temperatures 0 –10^{0}C. However, the rate of decrease of the number of cases as temperature goes down is lower.

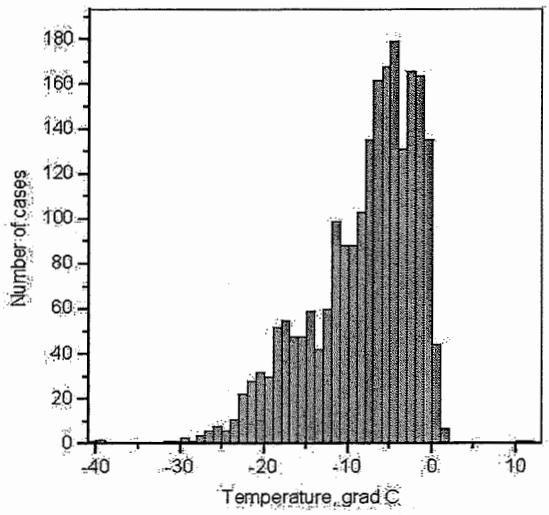

Fig.4.2 Distribution of cases with freezing precipitation versus temperature(Central Asia)

This can be attributed to a more continental climate and to the fact that many stations are located in the Central and North Kazakhstan, where the meteorological conditions are similar to those of Western Siberia. When analyzing the dependence of the frequency of events on pressure, one must bear in mind that some stations are located high above the sea level (e.g., Naryn –2049 m, Khorog –2080 m).

The total number of events at 53 Siberian stations was 1493, or 28 events per station. Fog depositing rime events (codes 48 and 49) contributed 94% of that number. Freezing rain and drizzle occurred in less than 6% of cases. In Siberia (similar to the Arctic), the distribution of FP events versus temperature was typically bimodal (Fig.4.3), with the highest frequency being observed at temperatures from –40 to –45^{0}C, which is characteristic of Siberian winter under anticyclone conditions.

This result is also supported by the distribution of the number of events versus pressure. The majority of cases

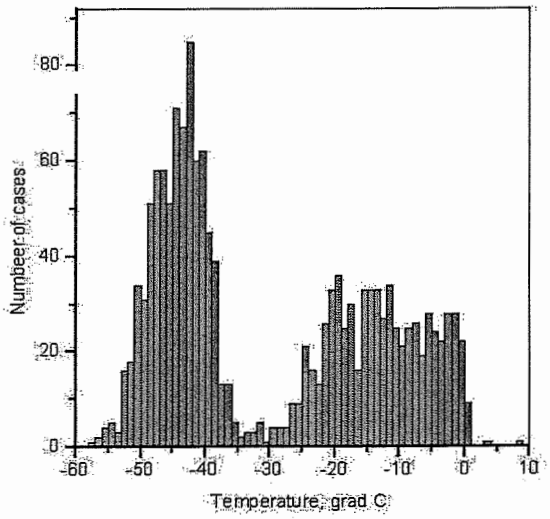

Fig.4.3 Distribution of cases with freezing precipitation versus temperature(Siberia)

were observed at a pressure of 1010-1015 hPa (the majority of the stations in the region are situated several hundred meters above the sea level).

The Far East region includes 31 stations, half of which are located directly on the Pacific coast of Russia. This region is characterized by a small number of FP events. On the average, 13.8 events per station were observed there (429 events all in all). The events with codes 48 and 49 contributed 91% of cases. Their maximum occurrence was observed between 0 and –10^{0}C.

4.4 Resume

The output of this work is an atlas of maps of the monthly occurrence of freezing precipitation (FP) over the territory of the former USSR. This atlas is supplemented with a statistical assessment. This abstract does not permit presenting the work done in sufficient detail.

5. ACKNOWLEDGMENT

This work has been made possible due to the activities implemented under a contract with the FAA with Dr. R.K. Jeck responsible for the technical coordination of the contract.

6. REFERENCES

1. Changnon S.A., Karl T.R., 2003:Temporal and Spatial Variations of Freezing Rain in the Contiguous United States: 1948-2000.J. App. Meteor., 42, 1302-1304.

2. Gay D.A., Davis R.E., 1993: Freezing rain and sleet climatology of the southeastern USA Climate Res.3, 209-220.

3. Strapp J.W., R.A. Stuart, J.A. Isaac, 1996: Canadian climatology of freezing precipitation and detailed study using data from St.John's, Newfoundland, Procc. FAA Int.conf. 6-8, May 1996.

A SYSTEMATIC RETRIEVAL OF ICE CLOUD MICROPHYSICAL AND RADIATIVE PROPERTIES USING A SYNERGETIC RADAR/LIDAR ALGORITHM

Dominique Bouniol[1]*; Alain Protat[1] and Martial Haeffelin[2]

[1]Centre d'étude des Environnemant Terrestre et Planétaire, CNRS, Vélizy, France

[2]SIRTA, IPSL, Palaiseau, France

1. INTRODUCTION

Representation of clouds in climate or forecast model is done (depending on the scale of the model) by using variables such as ice water content or effective radius. On the other hand dynamical variables (such as falling velocity) are used in order to get a realistic cloud life cycle. However due to a lack of observations these parameter can be over/under estimated by a factor of two.

In the framework of the CloudNET project vertically pointing Doppler cloud radar and lidar are continuously operated from three sites in Europe (SIRTA (France), Chilbolton (UK) and Cabauw (Netherlands)) and at the same time outputs of four operational models (ECMWF, UKMO, Météo-France and RACMO) are stored at the measurement points.

A synergetic algorithm, combining radar/lidar measurements (Tinel *et al.*, 2004) in order to obtain an accurate retrieval of microphysical and radiative parameters and algorithms making use of the radar Doppler signal to derive dynamical properties (Protat *et al.*, 2002, Bouniol *et al.*, 2004) have been developped. Since retrieval of dynamical properties (falling velocity and vertical air velocity) is here the subject to another paper, this paper is more focussed on the microphysical an radiative properties determination.

As a first step the principle of radar/lidar synergetic algorithm is recalled, then this algorithm is applied to data collected on one site of the CloudNET project, finally some conclusions and perspectives are given.

2. PRINCIPLE OF THE RETRIEVAL OF MICROPHYSICAL AND RADIATIVE PARAMETERS

The principle of the radar/lidar algorithm is completely described in Tinel *et al.* (2004) for airborne instrument. It has been validated and compared to another algorithm making use of the same measurements (Donnovan *et al.*, 2000) in Hogan *et al.* (2004) for a space configuration. In this paper, it is applied to measurements from ground-based instruments.

This algorithm lies on the hypothesis that the radar reflectivity (Z) and lidar backscattering coefficient (β_a) can be related to each other and then related to microphysical parameter such as ice water content (IWC) and radiative parameter, such as effective radius (r_e) using statistical relationships derived from in-situ measurements. However if one tries to derive a statistical relationship between for instance Z and IWC a large scatter is observed which makes hard a statistical relationship to be derived with accuracy. In order to reduce the dispersion, it is rather looked for relationships between Z/N_0^* and IWC/N_0^* (see Delanoë *et al.* for details), where N_0^* is a normalization parameter of the drop size distribution (see Testud *et al.* (2001) for derivation of this parameter). The set of equations relating the measurements to the parameter to be retrieved and the measurements of the two instruments is called the inverse model. This inverse model as been determined by Delanoë *et al.* (2004) on a large number of microphysical data set and they show that it does not depend of the geographical location of the measurements and of the cloud type or altitude.

The first step of the processing consists in relating the two measurements. This is done by using an integral constraint, written as followed and assuming as a first step a constant profile of $N_0^*(r)$.

$$\int_{r_1}^{r_0} \alpha(s)ds = \int_{r_1}^{r_0} aN_0^*(s)^{(1-b)}Z(s)^b ds \qquad (1)$$

where α is the lidar extinction coefficient, r_0 and r_1 are the upper and lower limits respectively of the common sampling area of radar and lidar and a and b are the coefficients relating α and Z within the inverse model. This equation can be rewritten as $\alpha(r_0) = f(\alpha(r_0))$ and solved. Then the $\alpha(r_0)$ value found is introduced within the Klett (1981) solution rewritten as a function of extinction:

$$\alpha(r) = \frac{\alpha(r_0)\beta_a(r_0)}{\beta_a(r_0) + 2\alpha(r_0)\int_r^{r_0} \beta_a(s)ds} \qquad (2)$$

This leads to a new profile of $\alpha(r)$ and then by using

*Corresponding author address: Dominique Bouniol, CETP/CNRS, 10/12 avenue de l'Europe, 78140 Vélizy, France; *e-mail*: dominique.bouniol@cetp.ipsl.fr

the α/Z law of the inverse model to a new profile of $N_0^*(r)$ which is re-introduced within Eq. 1. This process is carried on up to the convergence to a $N_0^*(r)$ profile. Once this profile is obtained it is introduced within the inverse model and then IWC and r_e profiles are computed.

3. Application to data collected at SIRTA

As mentionned in the introduction a cloud Doppler radar and a lidar are implemented on three sites in Europe and in particular at SIRTA in France. There the RASTA 94GHz Doppler is continuously operated at the same time with the dual-wavelength (532 and 1024 nm) LNA lidar operated in case of dry weather.

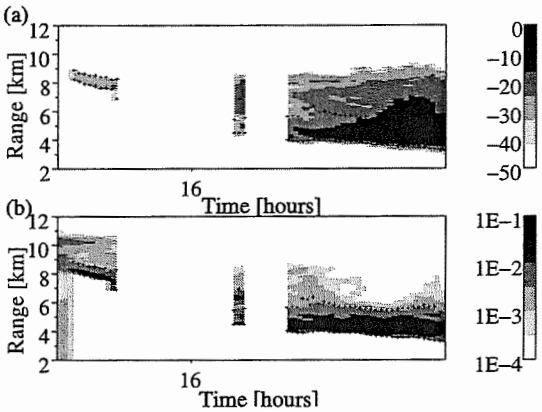

FIGURE 1: Time series of (a) radar reflectivity in [dBZ] and (b) lidar backscatter coefficient in [km^{-1} sr^{-1}] as a function of range in [km] observed at SIRTA on the 13 november 2002. The crosses on both figures delimited the common sampling area of the two instruments.

Figure 1 shows the data collected at SIRTA on the 13 november 2002 by (a) the radar and (b) the lidar. The overlap of the sampling of the two instruments is showed by the crosses on the two figures. These area is determined on lidar data by thresholding the signal. These observations are corresponding to a case of pre-frontal situation, where before 16UTC some cirrus clouds at about 9 km arrive above the site and afterwards the clouds become thicker leading to precipitations within the evening. These data also clearly illustrate the complementarity between radar and lidar observations, with a lidar more sensitive within thin clouds such as within the cirrus clouds. On the other hand when the clouds become thicker the lidar is rapidly attenuated while the radar is able to sample the whole cloud depth. This kind of cloud system is very commonly observed at SIRTA latitude.

These data are ingested within the synergetic algorithm which leads to the results depicted on Fig. 2. Figure 2(a) shows the IWC values obtained

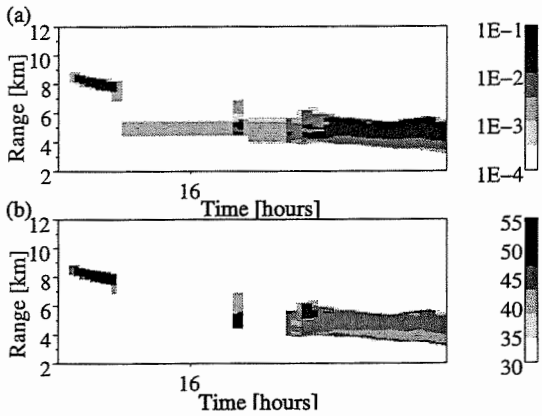

FIGURE 2: Time series of (a) IWC in [g m^{-3}] and (b) r_e in μm as a function of range in [km] deduced from the data showed on Fig. 1 by using the synergetic algorithm.

for this day with values in the range [5 10^{-3} – 1 10^{-1}] g m^{-3}. These values are in agreement with the one obtained by using other instruments such in-situ probes for instance. What can also be observed is that the IWC is decreasing towards the lower cloud edge, which can be explained by the evaporation of ice particles falling within a dryer environment. The corresponding r_e values are shown on Fig. 1(b) and fall within the range [30 – 55] μm which is also the range they are expecting for this kind of cloud.

This algorithm is systematically applied when common measurements are available. As a first step for model/observation comparison, probability density functions are built and are illustrated on Fig. 3. Figure 3(a) shows the probability density function of IWC and Fig. 3(b) of r_e. A first observation, which at this stage cannot be generalized is that the probability density functions seems to be slightly assymmetric with more small values than large for IWC. The shape is inverted for r_e with more large values than small one.

Figure 4 shows the same probability density functions but for another day where a more significant amount of data is present. This case is also for a frontal case and it seems that the same results can be found for IWC but in this case the probability density function for r_e is more symmetric. This result can be partly explained by the fact that on this case the lidar is penetrating deeper within the cloud and smaller r_e are more expected within the upper part of the cloud. For the same reason the range of IWC values is extending toward lower values.

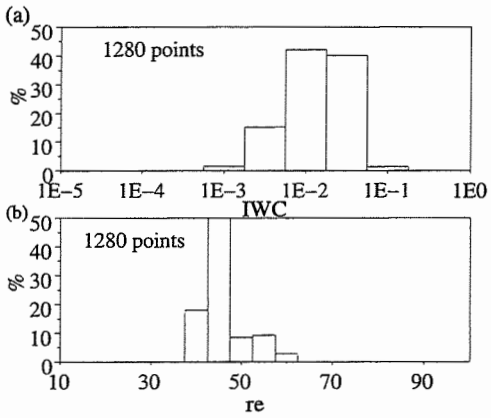

FIGURE 3: Probability density function of (a) IWC in [g m^{-3}] and (b) r_e in μm for the frontal system observed on the 13 november 2002

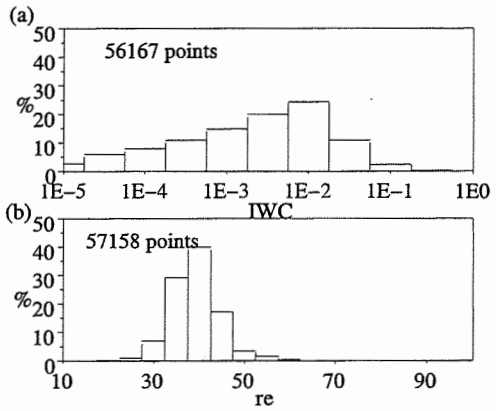

FIGURE 4: Same as Fig. 3 but for the 16 may 2003

4. CONCLUSION

A radar/lidar synergetic algorithm is runned at SIRTA in order to monitor as continuously as possible the microphysical and radiative properties of ice clouds. This algorithm is an iterative process which includes a set of statistical relationships, normalized by the N_0^* parameter, which relies the measurements and the measurements to the parameter to be retrieved. IWC and r_e are then retrieved within the common sampling area. This point needs to improve indeed the common area is often rather small compared to respective amount of data of each instrument. This algorithm should then be completed with two other (one lidar alone and one radar alone) using the results found in the common areas to document the ice cloud properties when only one instrument is available.

Once the microphysical and radiative parameters are determined one can expect to make comparisons with models outups. A first step has been presented here which consists in building probability density functions from the observations. Since this paper was focussed only on two cases, no robust conclusions can be made. The following step is then to compare the obtained distributions to the one coming from models.

Another interesting point is to use the Doppler capability of the radar to retrieve dynamical properties of ice cloud. Studies of dynamical and microphysical/radiative interactions can be performed and parametrisation linking for instance falling velocity to IWC can be derived and compare the existing one, usually derived from in-situ measurements or theoritical works.

5. ACKNOWLEDGEMENT

The RASTA 94 GHz radar was developped with support from Centre National d'Etudes Spatiales and Institut des Sciences de l'Univers. We are all indebted to the technical staffs that helped to develop the radars and conduct the CloudNET operations. This research received funding from the European Union CloudNET project (grant EVK2-CT-2000-00065).

6. REFERENCES

Bouniol, D., R.J. Hogan, A.J. Illingworth et A. Protat, 2004: Eddy dissipation rate from 94 GHz Doppler radar. Submitted to J. Atmos. and Oceanic Technol., March 2004.

Delanoë, J., A. Protat, J. Testud and D. Bouniol, 2004: Statistical properties of normalized ice particle distributios from in-situ microphysical measurements. Part II: Establishment of an "universal" statistical model for radar-lidar inversion techniques. Submitted to J. Appl. Meteor., April 2004.

Donnovan, D.P., A.C.A.P. van Lammeren, H.W.J. Russchenberg and A. Apituley, 2000: Cloud effective particle size and water content profile retrievals using combined lidar and radar observations. Part I: theory and simulations. J. Geophys. Res., **106**, 27425–27448.

Hogan, R.J., D.P. Donovan, C. Tinel, M.A. Brooks, A.J. Illingworth and J.P.V. Poiares Baptista, 2004: Independent evaluation of the ability of spaceborne radar and lidar to retrieve the microphysical and radiative properties of ice clouds. To be submitted.

Klett J.D., 1981: Stable Analytical Inversion for processing lidar returns. Applied Optics, **20**, 2, 211-220

Protat, A., C. Tinel et J. Testud, 2002: Dynamic properties of water and ice clouds from dual beam cloud airborne radar data : the CARL2000 and CARL2001 validation campaign, 11th Conference on Cloud Physics, 3-7 June 2002, Ogden, UT, USA

Testud, J., S. Oury, R.A. Black, P. Amayenc and X.K. Dou, 2001: The concept of "normalized" distribution to describe raindrop spectra: a tool for cloud physics and cloud remote sensing. J. Appl. Meteor., **40**, 1118–1140

Tinel, C., J. Testud, J. Pelon, R. Hogan, A. Protat, J. Delanoë and D. Bouniol,2003 : The retrieval of ice cloud properties from cloud radar and lidar Synergy. Submitted to J. Appl. Meteor, december 2003.

Simulations of the July 16 and 21 CRYSTAL-FACE cirrus cases using a cloud-resolving model forced by a ensemble of mesoscale models

R.W. Carver*, J.Y. Harrington, and J. Verlinde
Department of Meteorology, Penn State University
University Park, PA 16803

1. Background

To understand the role of tropical cirrus in the earth's climate system and to improve cirrus remote sensing, NASA initiated a field project, Cirrus Regional Study of Tropical Anvils and Cirrus Layers (CRYSTAL). CRYSTAL has the following goals (FIRE-IV CRYSTAL Drafting Panel, 2000):

1. It is essential to gain improved knowledge of the global ice water and water vapor fields in the upper troposphere in relationship to the associated global radiative fields and on scales adequate to resolve the dominant physical processes (storm and cloud systems).

2. Improved knowledge and understanding of upper tropospheric cloud generation, regeneration and dissipation mechanisms are critical to formulation and verification of methods to realistically capture these processes in regional and large scale climate models.

In the summer of 2002, NASA carried out the first CRYSTAL field program, Florida Area Cirrus Experiment (CRYSTAL-FACE). As a member of the forecast team, I noted that the 16 July and 21 July flights had good coverage of anvil outflow cirrus and started modeling studies of those clouds. These studies were designed to answer a number of scientific questions:

Q1 How sensitive is anvil outflow cirrus to mesoscale forcing?

Q2 What aspect of large scale forcing (vertical motion, temperature, moisture) is dominant

Q3 How sensitive is anvil outflow cirrus to the parent convection(i.e. amount of condensate and shape of the drop size distributions)

Q4 Does the evolution of anvil outflow cirrus depend on the ambient aerosol concentration?

There are two general strategies in modeling cirrus, one uses bulk ice microphysics and a relatively large grid to capture the spatial evolution of the cloud, Cheng et al. (2001). The other strategy is to use extremely detailed ice microphysics with a one or two dimensional grid that is homogenously initialized to study the role of ice physics in the temporal evolution of the cirrus cloud, Starr et al. (2001) Anvil outflow cirrus presents a unique challenge to numerical modeling since the outflow leaves the parent convection and travels through a mesoscale environment that is spatially and temporally nonhomogenous.

Neither strategy is optimal for solving this problem. Given the wide range of scales involved from the mesoscale environment that produced the deep convection to the buoyantly-driven eddies in the cirrus cloud top, it would be impractical to use a single CRM/LES model with a large grid and bulk microphysics to simulate the evolution of the anvil outflow. The spatial variability of the mesoscale enviroment invalidates the homogenous assumptions of the second approach.

*Corresponding author's address: Robert W. Carver, 503 Walker Building, University Park, PA, 16803, USA

Instead, a dual-model system was devised to simulate the different aspects of the cloud. A mesoscale model, the workstation eta, Janjič (1994), was chosen to simulate the evolution of deep convection and the environment's response. Output from this model was then used to force a CRM/LES model simulation of the evolution of a detached anvil cirrus layer.

A key hurdle in developing this system was calculating the large-scale forcing representing the spatial and temporal variation for the CRM/LES model, RAMS, Cotton et al. (2001). Given that anvil outflow cirrus moves with the upper-level winds, using a time-series of the large scale model at a single grid-point, like Cheng et al. (2001) to represent the changing ambient environment of the cirrus deck would be misleading.

Instead, I developed a Lagrangian parcel trajectory model using the dynamical system of HYSPLIT4 (Draxler and Hess, 1997). This system calculated the trajectories of parcels released at the location of predicted convection in the mesoscale model, simulating the trajectory of anvil outflow. Figure 1 illustrates the predicted trajectories for the 16 July case study. Once the trajectory was determined, vertical profiles of the simulated environment were calculated as a function of time and location along the trajectory. The change in these profiles with time was then used to calculate the large scale forcing tendencies as a function of time. Figure 2 shows how the vertical velocity tendency varied with height and time along the trajectory path.

Addition of the large-scale tendencies to a CRM/LES run initialized using a predicted sounding from the mesoscale model produced some striking differences. In figure 3, it is apparent that the cloud structure of the forced run is less homogenous than that of the unforced run. The structure of the vertical velocity fields were also quite different. The unforced run has a more periodic structure, which is typical at cloud-top radiatively driven circulations. Additionally, the forced run shows broader cells in its lower regions of precipitation.

To assess the overall behavior of the model runs, predicted quantities like total ice mixing ratio and vertical velocity were horizontally averaged to produce time-height profiles of each

Figure 1: The black curved lines represent trajectories of parcels released from a point where convection occured. The color-filled contours represent total cloud coverage.

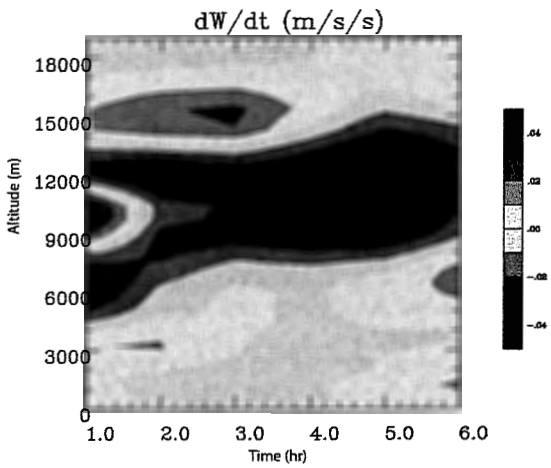

Figure 2: Large scale vertical velocity tendencies derived from vertical profiles taken along the trajectory plotted in figure 1

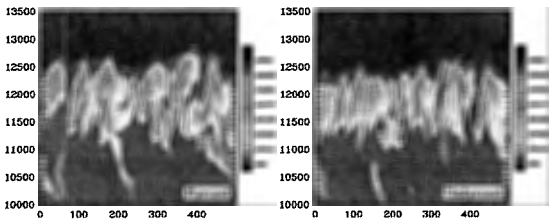

Figure 3: The figure on the left shows total condensate for a CRM that used the forcing in figure 2. The figure on the right is from an unforced CRM run at the same timestep.

run. The difference between these profiles for the forced and unforced run were used to determine the effect of adding mesoscale forcing. Figures 4 and 5 are plots of these differences, and it is apparent that there are distinct differences between the two runs. From fig. 5 it is apparent that the forced run had enhanced sedimentation during the early part of the simulation compared to the unforced run. Figure 4 shows that during the period of enhanced sedimentation, the forced run had negative vertical velocity compared to the unforced run. After this period of settling out, the forced run then had greater positive vertical velocity than the unforced run. This contradicts the vertical velocity forcing illustrated in fig. 2.

If we suppose that

$$\bar{w}_{for}(z,t) = \bar{w}_{un}(z,t) + \frac{dw}{dt}(z,t) + \bar{w}_{response}(z,t), \quad (1)$$

where $\bar{w}(z,t)$ is the the vertical profile of horizontally-averaged vertical velocity and $\frac{dw}{dt}$ is the mesoscale forcing, the then it would be possible to determine the response to the forcing by subtracting the forcing (fig. 2) from the vertical velocity difference (fig. 4). This is shown in fig. 6, and it is apparent that the model has a strong response to vertical forcing. It is probably not a coincidence that the initial downward vertical velocity "pulse" occurs during the period of enhanced sedimentation. This suggests that the positive velocity forcing causes enhanced growth of ice crystals, leading to larger sedimentation velocities, causing a relative descent of the cloud in the forced run.

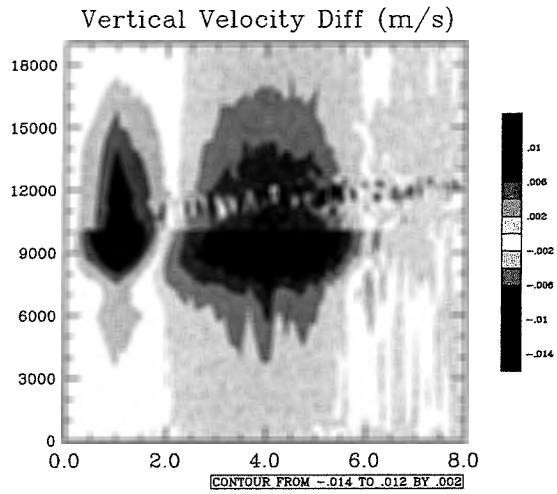

Figure 4: A time-height plot of the difference in horizontally averaged vertical velocity between the forced and unforced runs.

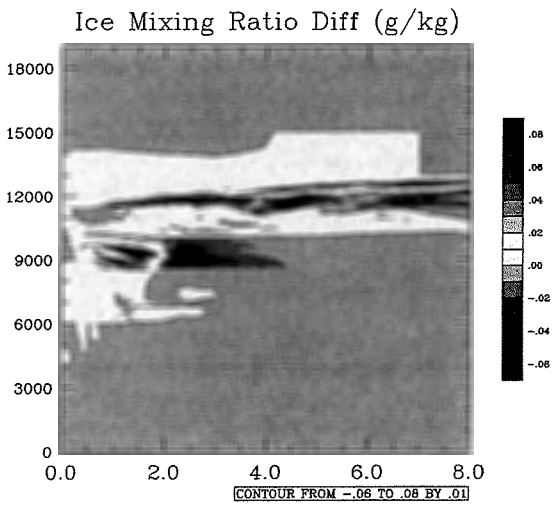

Figure 5: A time-height plot of the difference in horizontally averaged ice mixing ratio between the forced and unforced runs

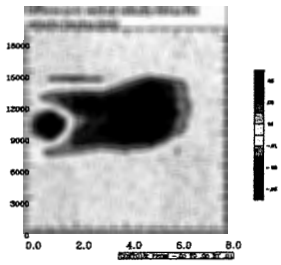

Figure 6: Figure 4 minus the vertical velocity forcing of the forced run.

These results demonstrate the dual-model system's capability to simulate the development and evolution of anvil outflow cirrus. It is obvious that the addition of mesoscale forcing to the CRM/LES model produces a solution that is very different than the unperturbed solution. This suggests that mesoscale forcing plays an important role in the maintenance and evolution of anvil outflow cirrus.

2. Model Verification

The validity of a model run cannot be assesed on the aesthetics of its graphics, but instead must be determined by using the observed atmosphere as a standard. Since the grid spacing of the large scale model is much larger than that of the CRM/LES and parcel models, the large scale model will have to be compared using large scale datasets. Archived satellite imagery and WSR-88D base reflectivity composites will be used to compare the location of predicted convection with the actual storms. The satellite imagery will also be used to compare the simulated anvil cirrus with the observed clouds. Hourly precipitation estimates derived from WSR-88D and rain gauge data (Seo, 1998) will be used to evaluate the strength of simulated convection. Prelimnary comparison of predicted and observed precipitation indicate that the model produces precipitation in the appropriate quantities and location. This suggests that the mesoscale forcing derived from the workstation eta will be reasonably close to what the anvil cloud actually encountered.

3. Bibiliography

Cheng, W.Y.Y., T. Wu, W.R. Cotton, 2001: Large-eddy simulations of the 26 November 1991 FIRE II cirrus case. *J. Atmos. Sci*, **58**, 1017-1034.

Cotton, W.R., R.A. Pielke, Sr., R.L. Walko, G.E. Liston, C.J. Tremback, H. Jiang, R.L. McAnelly, J.Y. Harrington, M.E. Nicholls, G.G. Carrio, J.P. McFadden, 2003: RAMS 2001: Current status and future directions. *Meteor. Atmos Physics*, **82**, 5-29

Draxler, R.R. and G.D. Hess, 1997, *Description of the Hysplit_4 modeling system, NOAA Tech Memo ERL ARL-224*, Dec, 24pp.

FIRE-IV CRYSTAL Drafting Panel, 2000: *CRYSTAL Research Plan*, Availible from FIRE Project Offi ce, Mail Stop 483, NASA Langley Research Center, Hampton, VA 23681.

Janjič, Z. I., 1994: The step-mountain eta coordinate model: Further developments of the convection, viscous sublayer, and turbulence closure schemes. *Mon. Wea. Rev.*, **122**, 927-945.

Seo, D.J., 1998: Real-time estimation of rainfall fi elds using radar rainfall and rain gauge data. *J. of Hydrol.*, **208**, 37-52.

Starr, D.O'C. et al., 2000: Comparison of cirrus models: A project of the GEWEX Cloud System Study Group (GCSS) working group on cirrus cloud systems. 13'th International Conf. on Clouds and Precipitation, Reno, NV, 1-4.

A STUDY OF THE EFFECT OF CLOUD DROPLETS ON THE DIFFUSIONAL GROWTH RATE OF ICE PARTICLES

Nesvit E. Castellano[1], Eldo. E. Avila[1] and Clive P.R. Saunders[2]

[1] Fa.M.A.F, Universidad Nacional de Córdoba, Ciudad Universitaria, 5000 Córdoba, Argentina
[2] Physics Department, UMIST, Manchester, M60 1QD, UK

1. INTRODUCTION

The growth of ice particles in a supercooled water cloud due to the differences between water and ice saturation vapour densities (Bergeron-Findeisen mechanism) is the usual process that occurs in clouds, however this process has not been extensively studied so far. Instead, the usual treatment is based on the classical electrostatic analogy theory of diffusional growth (Mason, 1971; Pruppacher and Klett, 1978) and involves the diffusion of water molecules from a vapour source at infinity towards the ice crystal. The electrostatic analogy theory does not take into account the presence of water droplets surrounding the growing ice particle. However, it is reasonable to assume that their presence could enhance the mass transfer and consequently the growth rate of the ice particle.

A numerical study of the growth rate of ice particles in an array of water droplets is presented here. The model uses the method of electrostatic image charges to determine the vapour density field in which an ice particle grows.

2. MATHEMATICAL MODEL: IMAGE CHARGES METHOD

In order to know the water vapour diffusion to drops or ice particles it is necessary to solve the convective diffusion equation for the water vapour density field (ρ) (Pruppacher and Klett, 1978)

$$\frac{\partial \rho}{\partial t} + \vec{u} \cdot \nabla \rho - \nabla^2 (D\rho) = S_v \qquad (1)$$

where D is the diffusion coefficient or diffusivity of water vapour, $\vec{u}$ denotes the particle fall velocity relative to the air, and S_v represents the vapour sources.

Corresponding author's address:
Eldo E. Avila, Fa.M.A.F, Universidad Nacional de Córdoba, Ciudad Universitaria, 5000 Córdoba, Argentina.
E-Mail: avila@roble.fis.uncor.edu

For the stationary case, the convective diffusion equation becomes identical to Laplace's equation initially worked out for electrostatics:

$$D\nabla^2 \rho = 0 \qquad (2)$$

The model assumes the following:
(a) Steady state conditions exist; the ice particles and droplets do not change shape or size.
(b) The ice particle is represented by a sphere of radius *a*.
(c) A finite 3-D array of droplets of radius *b* uniformly distributed in the space. The separation between droplets is *d*. (Figure 1)
(d) Ambient temperature is uniform (T_a).
(e) Vapour density takes the ice saturation value at the surface of the ice particle (ρ_i) and takes the water saturation value at the surface of the droplets (ρ_w).
(f) Vapour density at an infinite distance from the crystal is ρ_0, which can vary from ρ_i to ρ_w.

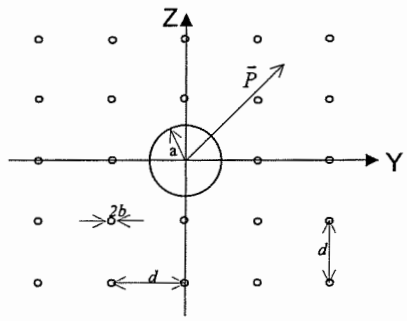

Figure 1. *A view of the ice particle and droplet array in the plane Y-Z (X=0).*

Figure 1 shows the configuration of the ice particle, droplets and nomenclature of the problem. This situation is equivalent to that of a conducting sphere of radius *a* with a constant potential ρ_i, placed among conducting spheres of radius *b* with constant potential ρ_w, with the potential at infinity ρ_0. In order to solve the

problem it is possible to apply the method of successive images (Jackson 1975), which involves locating a number of suitably placed point charges of appropriate magnitude in the region inside the cloud particles. These charges are called image charges and simulate the required boundary conditions. They must be external to the volume of interest between the particles since their potentials must be solutions of the Laplace equation inside the volume.

When n-droplets are present it is necessary to take into account the interaction between the ice crystal with each droplet and the interaction between the droplets with each other. Thus the general solution is given by:

$$\phi(\vec{P}) = \rho_0 + \frac{q_{11}[0]}{|\vec{P}|} + \sum_{j=1}^{n}\left[\begin{array}{l}\dfrac{q_2[0,j]+q'_2[0,j]}{|\vec{P}-\vec{d}[j]|}+\ldots \\ \sum_{i=1}^{\infty}\left(\begin{array}{l}\dfrac{q_{11}[i,j]}{|\vec{P}-P_{11}[i,j]|}+\dfrac{q_{22}[i,j]}{|\vec{P}-P_{22}[i,j]|}+ \\ \dfrac{q'_1[i,j]}{|\vec{P}-P_1[i,j]|}+\dfrac{q'_2[i,j]}{|\vec{P}-P_2[i,j]|}\end{array}\right)\end{array}\right] \quad (3)$$

where:

(1) $q_{11}[0] = a\ (\rho_i - \rho_0)$ is the charge of the ice particle.

(2) $q_2[0,j] = b\ (\rho_w - \rho_0)$ is the charge of the j-th droplet, placed in its centre in the position $\vec{d}[j]$.

(3) $q'_2[0,j]$ is a charge that represents all the image charges arising from the interaction among the j-th droplet with other droplets. This charge is placed in the centre of the j-th droplet.

(4) $q_{22}[i,j]$, $q_{11}[i,j]$, are the i-th image charges of the charge $q_{11}[0]$, placed inside the j-th droplet and ice particle in the positions $P_{22}[i,j]$ and $P_{11}[i,j]$ respectively.

(5) $q'_1[i,j]$ and $q'_2[i,j]$ are the i-th image charges of the charge $q_2[0,j] + q'_2[0,j]$. The charge $q'_1[i,j]$ is placed inside the ice particle in the position $P_1[i,j]$ and the charge $q'_2[i,j]$ is placed inside the j-th droplet in the position $P_2[i,j]$.

The charge $q'_2[0,m]$ in the m-th droplet cancels the potential produced by the rest of the droplets on it. This means that the condition in equation 4 must be satisfied. $q''_1[i,m,j]$ is the i-th image charge of the charge $q'_2[0,m]$ induced inside the j-th droplet in the position $P_1[i,j]$. Therefore, the vapour density can be evaluated at any point in space.

In order to check the performance of the model, the equipotential lines corresponding to $\phi = \rho_i$ and $\phi = \rho_w$ were calculated in a region of 1200×1200 μm^2. These lines reproduce the contours of the particle and droplet surfaces, which means that the vapour density function is adequately represented by Eq. (3). The differences between the contours of the ice particle and droplet surfaces obtained with the model and their real sizes are less than 0.5 %.

$$\frac{q'_2[0,m]}{b} = \sum_{\substack{j=1\\ j\neq m}}^{n}\left[\begin{array}{l}\dfrac{q'_2[0,j]+q_2[0,j]}{|\vec{d}[m]+\vec{b}-\vec{d}[j]|}+ \\ \sum_{i=0}^{\infty}\left(\begin{array}{l}\dfrac{q_{11}[i,j]}{|\vec{d}[m]+\vec{b}-P_{11}[i,j]|}+\dfrac{q_{22}[i,j]}{|\vec{d}[m]+\vec{b}-P_{22}[i,j]|}+ \\ \dfrac{q'_1[i,j]}{|\vec{d}[m]+\vec{b}-P_1[i,j]|}+\dfrac{q'_2[i,j]}{|\vec{d}[m]+\vec{b}-P_2[i,j]|}+ \\ \dfrac{q''_1[i,m,j]}{|\vec{d}[m]+\vec{b}-P_1[i,j]|}\end{array}\right)\end{array}\right] \quad (4)$$

3. RESULTS & DISCUSSION

The mass of vapour flowing per unit time toward the surface of the ice particle (dM/dt) can be calculated as

$$\frac{dM}{dt} = \dot{M} = -D\int_S \nabla\phi . d\vec{S} \quad (5)$$

where the integral is performed over the ice particle surface. It needs to be evaluated numerically, thus the number of cloud droplets involved in the calculation must be finite. One important question was to decide on the adequate number of droplets around the ice particle that we have to take into account in the calculations.

Figure 2 shows the typical behaviour of the quantity $D^{-1}dM/dt$, as a function of the droplet number surrounding the ice particle, involved in the calculation, defined as ng. The calculation was performed for $\rho(\infty)=\rho_w$, T_a= -10°C, a = 75 μm, b = 7.5 μm, and for three different separations between droplets, (d) being 632, 700 and 1209 μm, which corresponds to liquid water contents (LWC) of 7, 5 and 1 g m^{-3} respectively.

Figure 2 shows that the nearest 500 droplets are very important in the calculation of the mass flux, then the value increases slowly tending to a constant value. The calculated value of $D^{-1}dM/dt$ for ng = 2000 differs by less than 0.1% of the value calculated with ng = 4000. In the present work, we chose ng = 2108 as an adequate number of droplets for the calculations, this number corresponds to all the

droplets being placed at a distance less than *8d* from the centre of the ice particle. The temperature was kept constant in this study and equal to -10°C. Figure 3 shows how the presence of cloud droplets can alter the equipotential lines around the ice particle. This figure shows equipotential contours in a region of 400×400 μm^2 centred on the ice

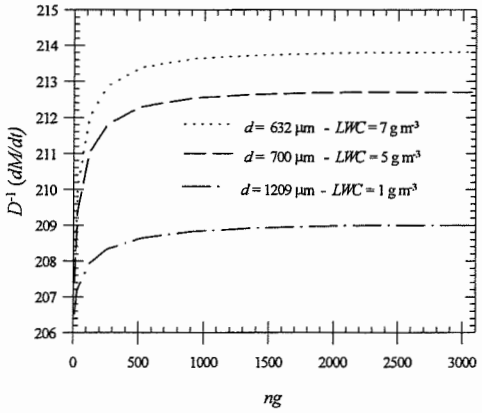

Figure 2. *$D^{-1}dM/dt$ as a function of the droplet number (ng) for T_a= -10°C, a =75 μm, b=7.5 μm, for three different separations between droplets*

particle in the X = 0 plane.

Figure 3(a) shows some equipotential contours for the case without droplets. The vapour density is only a function of the distance (*r*) for this case:

$$\phi(r) = (\rho_i - \rho_w)\frac{a}{r} + \rho_w \qquad (6)$$

the lines in the graph marked as 1, 2, ..., 6, belong to *a/r* = 1, 0.8, 0.6, 0.4, 0.3, 0 respectively. Figure 3(b) shows the contours of the same equipotential lines as Fig. 3(a), but for the case when cloud droplets are present with the following conditions: *a* = 150 μm, *b* = 3 μm, *d* = 253 μm (*LWC* =7 g m^{-3}) and assuming that the vapour density takes the water saturation value (ρ_w) at a distance remote from the particle (at infinity). Comparing both figures, it is evident that the equipotentials have changed with the presence of droplets. Note, for instance, that equipotential 5 is shifted and equipotential 6 does not appear in the case without droplets. This change becomes more and more important when the distance between droplets decreases.

To study the influence of the presence of cloud droplets on ice particle growth, the value of D^{-1} *dM/dt* was determined assuming $\phi = \rho_w$ at infinity and for two different cases: without cloud droplets present: $\frac{dM}{dt} = \dot{M}_o$ and with cloud droplets present: $\frac{dM}{dt} = \dot{M}$. The percentage difference between $\dot{M}$ and $\dot{M}_o$ $\left(\delta = 200\frac{\dot{M} - \dot{M}_o}{\dot{M} + \dot{M}_o}\right)$ is the parameter used to study the cloud droplet influence as a function of the droplet radius *b*, ice particle radius *a* and minimum droplet separation *d*.

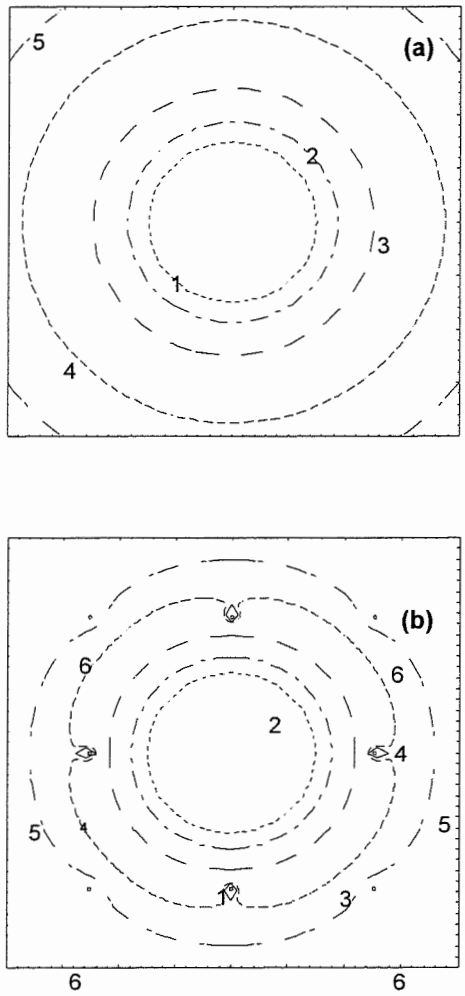

Figure 3. *(a) Equipotential contours for the case without droplets. The lines marked 1, 2, ..., 6, belong to a/r = 1, 0.8, 0.6, 0.4, 0.3, 0 respectively. (b) The contours for the case when cloud droplets are present with a=150 μm, b=3 μm, d=253 μm (LWC=7 g m^{-3}) for vapour density at infinity $\rho(\infty)=\rho_w$.*

The results of the numerical model show that the percentage difference δ increases linearly with a and is proportional to $d^{-1.5}$, $b^{0.5}$. This indicates that when the condition $\rho(\infty)=\rho_w$ is assumed, the percentage difference between $\dot{M}$ and $\dot{M}_o$ can be parameterised as a function of the variables a, b and d as: $\delta \propto \frac{b^{0.5}}{d^{1.5}} a$, or as a function of the liquid water content (*LWC*) as: $\delta \propto LWC^{1/2} ab^{-1}$.

Figure 4 displays the values of δba^{-1} against *LWC* in a log-log graph. The points in the graph belong to all the values calculated with the model. This figure shows that the data can be well fitted by a straight line of slope equal to 0.5, as mentioned previously.

Thus, the percentage difference between $\dot{M}$ and $\dot{M}_o$ can be calculated by using the expression:

$$\delta = C\sqrt{LWC}\,\frac{a}{b} \qquad (7)$$

where $C = 0.134$ %(g m^{-3})$^{-1/2}$.

Figure 4 or Eq. (7) may be used to determine the enhanced growth rate over a range of values of droplet and particle sizes as a function of *LWC*. These calculations have been performed for a temperature of -10°C, for other temperatures, $\dot{M}$ may be multiplied by $(\rho_w(T)-\rho_i(T))/(\rho_w(T_{-10})-\rho_i(T_{-10}))$, which is $(\rho_w(T)-\rho_i(T))/0.219$, to obtain a value appropriate to the new temperature.

Marshall and Langleben (1954) presented a model where an isolated ice particle represented by a spherical particle is growing under the presence of a cloud of water droplets. The model assumes that the cloud droplets are uniformly distributed throughout the volume and each droplet provides vapour only to the ice crystal, thereby it implicitly assumed water saturation at infinity. The authors showed that the ice crystal growth rate is enhanced relative to the electrostatic analogy theory, especially for larger crystals and higher cloud liquid water contents, LWC. The authors presented their results as a function of the parameter $k=(4\pi\ \Sigma\ r_c)^{1/2}$ where $\Sigma\ r_c$ represents the sum of the droplet radii and is related to the liquid water content.

When these new results are compared with those of Marshall and Langleben (1954) it is observed that both theories give similar results for the growth rate enhancement by the presence of water droplets around the ice crystal.

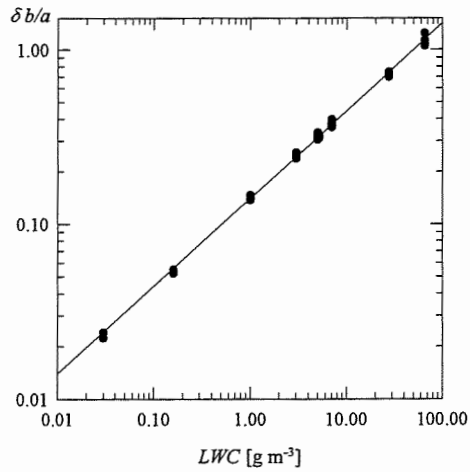

Figure 4. *The percentage difference in growth rates parameterised as a function of LWC and b/a.*

Acknowledgements

This work was sponsored by SECYT-UNC, Argentina and by the Natural Environment Research Council, UK.

References

Marshall J. S. and M. P. Langleben, A theory of snow-crystal habit and growth, J. Met., 11, 104-120, 1954.

Mason B. J. The Physics of Clouds, Oxford Univ. Press, 1971.

Pruppacher, H. R., and J. D. Klett. Microphysics of clouds and precipitation, *Reidel Publishing Corp.* 1978.

OBSERVATIONS AND MODELLING OF CIRRUS OUTFLOW FROM HECTOR DURING THE EMERALD-II CAMPAIGN

P. J. Connolly[1], T. W. Choularton[1], M. W. Gallagher[1], K. N. Bower[1], M. J. Flynn[1], J. W. Whiteway[2].

1. UMIST Manchester UK, 2. University of Aberystwyth Wales UK.

1. INTRODUCTION

The Microphysical properties of cirrus clouds that reside close to the tropical Tropopause influence climate through their interaction with the earth's radiation fluxes and by redistributing water vapour throughout the depth of the Troposphere. The Island thunderstorms occurring in the Maritime Continent produce an extensive cirrus outflow that resides close to the Tropopause. They also often display the most intense thunderstorms to be found any where on the globe and have cloud top heights in excess of 18 km.

The effects of island forcing on the development of tropical convection are complex owing to the chaotic interaction of gust fronts and sea breezes and through the interaction with radiation and surface heat fluxes (Keenan *et al.*, 2000). This has consequences for feedback into the condensed mass aloft within the cirrus outflow layer.

Most climate models are poor at representing the diurnal variation of convection (Lin *et al.*, 2000). CRMs are therefore used to improve the parameterisation of convection in climate and general circulation models. It is therefore important that CRMs themselves are validated by some means.

In November and December 2002, during the second Egret Microphysics Experiment with Radiation, Lidar and Dynamics (EMERALD-II), the Egret high flying research aircraft was employed to measure cirrus outflow from a thunderstorm known as HECTOR that occurs almost daily during these months over the Tiwi Islands, Northern Australia. Particle size distributions and other cloud properties were measured with the suite of instruments that were mounted on the Egret.

In this contribution, a modelling sensitivity study of island size to HECTOR development will be presented for the 2nd December case study during EMERALD-II. The control case of the sensitivity study will be compared to the measured values of Ice water content (IWC) at a time when the simulation and actual storm were both at a similar stage of development.

2. MEASUREMENTS

Measurements used in this study are from the Cloud Microphysics Probes on board the Egret.

Corresponding author's address: Paul Connolly, UMIST, Sackville St. Manchester, ENGLAND; E-mail: p.connolly@postgrad.umist.ac.uk

Particle size distributions in the range 2-47μm were sampled with a DMT modified FSSP. Various researchers have noted degradation in the performance of the FSSP in the presence of large ice crystals (Arnott *et al.*, 2000: Gardiner and Hallett, 1985) and so these measurements were only used during periods when the CPI did not detect any large particles.

Particle size distributions in the range 10-2400μm were sampled with the CPI. Inherent problems with using the CPI to measure particle size distributions in Cirrus outflow are due to the maximum sample rate of the probe, problems with over-sizing of out of focus particles and uncertainties in the sample volume. To overcome these difficulties, a test was made to see whether during a horizontal fight leg the cloud was homogeneous with respect to concentration as in Lawson *et al.*, 2001. The data was then averaged over ten seconds of flight time (a distance of 600m) so that a statistically significant sample was obtained. Laboratory measurements were also made so that the effect of over-sizing and sample volume could be corrected for. Finally, to compute the IWC, the mass-dimension relationship of Heymsfield *et al.*, 2004 was used for particles below 200 μm and those of Mitchell, 1996 for particles greater 200 μm.

Preliminary comparisons of IWC measured by de-facto standard probes and CPI particle spectra have shown that in anvil cirrus, the CPI may underestimate IWC by as much as 30% when uncorrected with errors less than 5% for the corrected data.

Flights were conducted to sample the cirrus outflow at various altitudes and transverse and longitudinal flight patterns were undertaken.

3. CLOUD RESOLVING MODEL

3.1 Model Description

The UK Met Office CRM was used to model the development of HECTOR from cumulus formation, aggregation and development of the cirrus anvil over an isolated island.

The microphysics scheme uses a single moment scheme for liquid water and rain categories and double moment schemes for ice, snow and graupel categories. There are 48 processes for conversion between each hydrometeor class. Particle size distributions are based on modified gamma distributions and the coefficients are chosen to fit observations of particle spectra in tropical clouds.

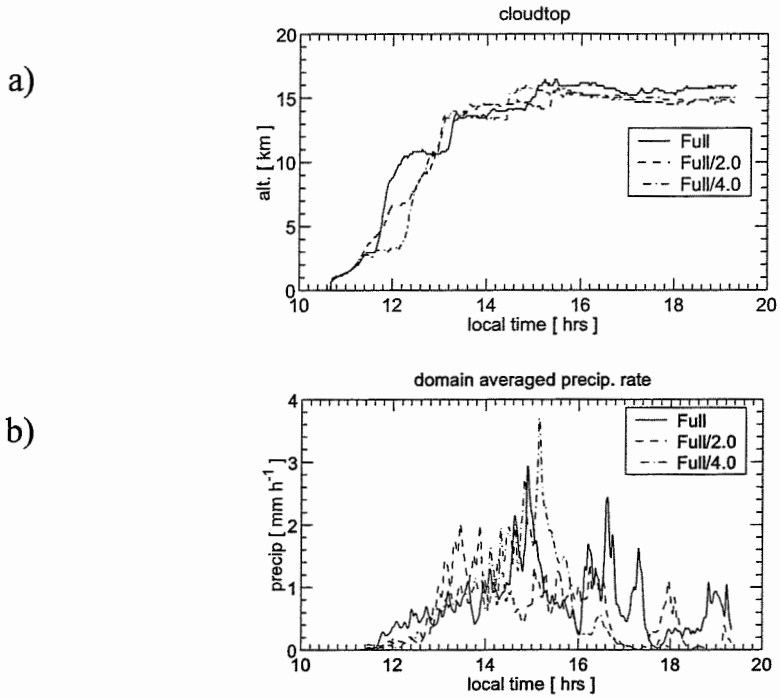

Figure 1. a) Shows the evolution of cloud top height for the three sensitivity tests. Note that the case of the smallest island is slowest to develop initially and then rapidly attains maximum cloud top height. b) Shows the instantaneous precipitation rate averaged over the same sized domain in each case. Solid lines are for the full sized island, dashed lines are for an island half that size and dashed-dotted lines are for an island one quarter of the size.

A coupled radiation scheme that calculates both long and short wave heating from vapour and cloud fields is also used.

4. MODEL SET-UP

The effect of the island sea breeze is crucial to the development and maturing phase of HECTOR. Gust fronts interact with the sea breeze as well as other gust front from neighbouring storms. It is this gust front forcing that results in HECTOR being so strong.

To include these effects as best possible, surface roughness length maps were included in the model by interpreting land use maps supplied by the MODIS satellite and by using the land-use to roughness length conversions given in Zhang *et al.*, 2001. Typical values of sensible and latent for a tropical land and ocean were also used. A horizontal resolution of 200 m was used and the vertical resolution of 50 m stretching to 600m above the Tropopause. To inhibit the reflection of gravity waves, a Newtonian damping layer is used in the highest 2000 m. The domain top is at 22000 m.

4.1 Case study

In this study the sensitivity of the properties of the outflow to island size is explored. Three different island sizes are chosen; 100 km corresponding to the maximum dimension of the islands in an E-W direction, 50 km and 25 km.

The effect of island size on convective strength has important consequences for parameterisations of deep tropical convection at this geographic location. A 1-D heat strip at the centre of a 2-D domain was used to represent the island.

5. RESULTS

5.1 Sensitivity to island size

Changing the island size in two dimensions is analogous to the case of a 2-D island, where peninsulas are in effect acting as smaller islands themselves. Figure 1 shows the results of the three model runs. The effect of reducing the island size was to suppress convection at first, however later on in the clouds development the smaller island size showed more intense updraft velocities and the most rapid ascent of cloud top height (see Figure 1 a)). Visual

a)

b)

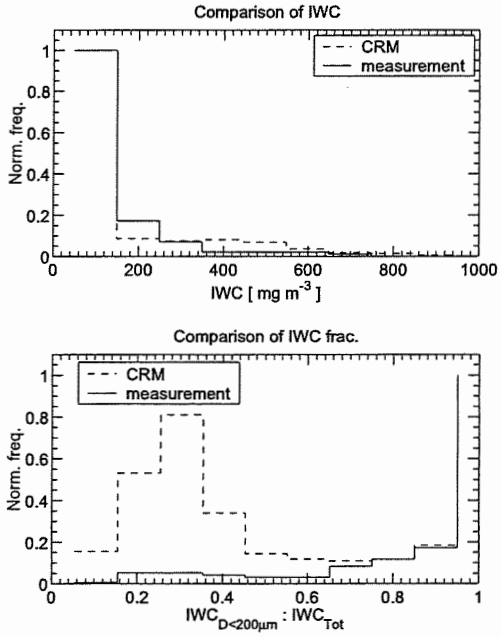

Figure 2. a) Shows the frequency of occurrence of IWC in the simulated anvil and that which was derived from the CPI. b) Shows the fraction of IWC for particles less than 200μm to the total. It is shown that the fraction of the mass that is in contained within crystals smaller than 200μm is miss represented in the model.

inspection of the storms development showed that in the case of the larger island, the cells were more likely to form on the leeward coast initially, while as the island size decreased, there was preferred development on the windward coast. The reason for this is that the roughness length of the large island retards the surface flow promoting development of leeward sea-breeze convergence, whilst for decreasing island size, the smaller island is unable to retard the flow sufficiently for sea breeze convergence.

The rapid development phase in all model runs is due to the confluence of island scale sea breezes near the islands centre fitting the observations of Keenan *et al.*, 2000. This occurs earliest for the smallest island after both windward and leeward sea breezes form and converge. It is interesting to note that the smallest island demonstrates the highest peak precipitation rate (see Figure 1 b)).

5.2 Comparison with observations

A comparison was made with the IWC inferred from both model for the full island size and with the observations over regions that were comparable to the spatial and temporal development of the storm. The method is similar to that employed in Brown and Heymsfield.

Figure 2 a) shows that the IWC from both the model and data agree quite well; both show the highest frequency for IWC below 200 mg m^{-3} with the same trend in low frequency for higher IWC. This is to be expected as deep convection essentially lofts most particles due to the high updraft velocities.

The fraction of ice mass contained in particles smaller than 200 μm to the total is shown in Figure 2 b). It is observed that the CRM shows a higher frequency for ice mass to be distributed in the larger sizes and the observations show that the highest frequency is for ice mass to be distributed in the small sizes.

6. DISCUSSION

The purpose of this study is to gain some idea of how well deep tropical convection is represented in cloud resolving models and to try to explain the observed vertical structure of IWC in HECTOR anvils. It must be noted that there are large room for errors in this approach, however the method is a rather blunt validation test of a CRM against observations.

For each of the three model runs in this sensitivity study, IWC in the anvil region correlates reasonably well with the derived IWC when considering the large room for errors (see Figure 1). This bulk property is expected to correlate well in deep convection owing to high vertical velocities that essentially lofts most particles into the anvil. The fraction of IWC in the small size (less than 200 μm) does not correlate so well. There are many possible reasons for this, however observations of the measured ice particle spectra show that many small ice crystals are present that appear to be fragments of pristine crystals. The

discrepancy of this fraction between model and observations indicates a deficiency in the model microphysics scheme. This may be explained by a number of reasons.

Twohy *et al.*, 2002 observed in-situ formation of new aerosol particles in outflow from storms in the mid-latitudes due to homogeneous bi-molecular nucleation of sulphate particles from surface tracers that are essentially lofted by strong updrafts. These particles could in principle be responsible for homogeneous nucleation of ice in the outflow, however the mass growth rates of small crystals in the anvil is two orders of magnitude lower than larger crystals owing to the low temperatures, so this mechanism may not be responsible for the discrepancy here. Another explanation is that fragmentation is occurring. The laboratory measurements of Latham and Saunders, 1970: Saunders and Wahab, 1975 have shown that under high electric fields, break-up of ice crystals is very efficient. CPI imagery of the crystals during EMERALD-II revealed that many of the crystals appeared to be small fragments. This is to be explored by running more sensitivity tests in the model.

7. CONCLUSIONS

The UK Met Office CRM has been used to simulate the evolution of HECTOR from cloud formation through to dissipating anvils. A sensitivity study to the size of the island shows that the effects of using differential roughness lengths affects development of the sea breeze and therefore HECTOR.

A Comparison of the control experiment with IWC measurements made on this day reveal that the frequency distribution of IWC is well represented in the model. This is to be expected for deep convection, as the fall velocity of ice crystals is negligible compared to the strength of the updraft. The partitioning of IWC by size is less well represented in the model. The CRM has a tendency to show a higher fraction of IWC in ice crystal larger than 200μm in size when compared with the model. This is likely a slightly conservative estimate as the CPI is probably missing the smallest particles. Possible reasons for this are not resolved at present although further sensitivity tests to the microphysics scheme are being carried out.

8. ACKNOWLEDGEMENTS

The author would like to acknowledge help from Dr Phil Brown of the UK Met Office for advise in running the CRM.

Acknowledgement also goes to Airborne Research Australia for their excellent planning and conducting of the flights through cirrus outflow of HECTOR thunderstorms during the EMERALD-II field campaign.

9. REFERENCES

Arnott, W. P., D. Mitchell, C. Schmitt, D. Kingsmill, and D. Ivanova, 2000: Analysis of the FSSP performance for measurement of small crystal spectra in cirrus. *13th ICCP*, Reno, 191-193.

Gardiner, B. A. and J. Hallett, 1985: Degradation of in-cloud forward scattering spectrometer probe measurements in the presence of ice particles. *J. Atmos. Ocean. Tech*, **2,** 171-180.

Heymsfield, A. J., C. Schmitt, A. Bansemer, D. Baumgardner, E. M. Weinstock, J. T. Smith, and D. Sayers, 2004: Effective ice particle densities for cold anvil cirrus. *Geophys. Res. Lett.*, **31,** L02101.

Keenan, T., S. Rutledge, R. Carbone, J. Wilson, T. Takahashi, P. May, N. Tapper, M. Platt, J. Hacker, S. Sekelsky, M. Moncrieff, K. Saito, G. Holland, A. Crook, and K. Gage, 2000: The Martime Continent Thunderstorm Experiment (MCTEX): Overview and Some Results. *Bull. Amer. Meteor. Soc.*, **81,** 2433-2455.

Latham, J. and C. P. R. Saunders, 1970: Experimental measurements of the collection efficiencies of Ice Crystals in Electric Fields. *Q. J. R. Meteorol. Soc*, **96,** 266-272.

Lawson, P., B. A. Baker, C. G. Schmitt, and T. L. Jensen, 2001: An overview of microphysical properties of Artic clouds observed in May and July 1998 during FIRE ACE. *J. Geophy. Res.*, **106,** 14989.

Lin, X., D. A. Randall, and L. D. Fowler, 2000: Diurnal variability of the hydrological cycle and radiative fluxes: Comparison between observations and a GCM. *J. Climate*, **13,** 4159-4179.

Mitchell, D. L., 1996: Use of Mass- and Area-Dimensional Power Laws for Determining Preciptitation Particle Terminal Velocities. *J. Atmos. Sci.*, **53,** 1710-1723.

Saunders, C. P. R. and N. M. A. Wahab, 1975: The Influence of Electric Fields on the Aggregation of Ice Crystals. *J. Met. Soc. Japan.*, **53,** 121-126.

Twohy, C. H., C. F. Clement, B. W. Gandrud, A. J. Weinheimer, T. L. Campos, D. Baumgardner, W. H. Brune, I. Faloona, G. W. Sachse, S. A. Vay, and D. Tan, 2002: Deep convection as a source of new particles in the midlatitude upper troposphere. *J. Geophy. Res.*, **107,** 4560.

Zhang, L., S. Gong, J. Padro, and L. Barrie, 2001: A size-segregated particle dry deposition scheme for an atmospheric aerosol module. *Atmos. Env.*, **35,** 549-560.

PARCEL MODELLING OF ICE NUCLEATION IN THE AIDA AEROSOL CHAMBER

R. J. Cotton,* P. R. Field[1], O. Moehler[2], M. Schnaiter[2], M. Kraemer[3], P. Connolly[4], A. J. Heymsfield[5]

1. Met Office, Exeter, UK. 2. Forschungszentrum Karlsruhe, IMK, Karlsruhe, Germany
3. Forschungszentrum Julich, ICG, Julich, Germany 4. UMIST, Manchester, UK
5. NCAR, Colorado, USA

1. INTRODUCTION

A series of ice nucleation experiments were carried out at the AIDA (Aerosol Interactions and Dynamics in the Atmosphere) aerosol chamber of Forschungszentrum Karlsruhe during September 2003. (See Moehler *et. al.* 2003 for a detailed description of the AIDA chamber, the instruments, and the experimental procedure.) Dust samples from Sahara and Asia were introduced into the chamber. The initial chamber temperature ranged from 2°C to −60°C. During the expansions, the initial formation of ice particles was clearly observed.

The aim of this paper is to establish the ability of the a model to describe the evolving chamber conditions and hence its ability for use as a test bed for different representations of heterogeneous ice nucleation. As examples, expansions using the Asian dust (Exp. 28) and the Saharan dust (Exp. 41), both with a starting temperature −50C° were modeled. The model is a detailed microphysics size-resolving parcel model (modified to account for diabatic heat and moisture interactions with the chamber walls during the expansion).

In both cases, the model predicts that there was first heterogeneous nucleation followed by homogeneous.

2. THE AIDA AEROSOL CHAMBER

AIDA is a large cylindrical chamber made of 2cm thick aluminium walls, within a thermally isolated containment. The chamber is 7m high, has a diameter of 4m and a volume of 84m^3. The interior of the containment can be cooled and maintained to any temperature between ambient and 183K by heat exchangers. This containment defines the initial temperature in the aerosol chamber. Fans within the chamber achieve a well-mixed environment where the temperature inhomogeneity is less than ±0.3K. Two large mechanical pumps, which can be operated at different pumping speeds, are able to evacuate the chamber to 0.01hPa.

The AIDA chamber is extensively instrumented, including pressure, temperature and water vapour sensors, and optical particle counting probes. The gas and chamber wall temperatures (T_g and T_w) are measured with an array of thermocouples. A tunable diode laser hygrometer (TDL) measures the water vapour mixing ratio. A cooled mirror device (MBW) measures the chamber relative humidity but becomes unreliable where there is condensed water, although it can be used to give an estimate of the total water (vapour + condensed) mixing ratio. Particle concentrations and mean particle size are measured using a laser scattering device (SID (small-ice detector) described by Hirst *et al.* (2001)), and a Cloud Droplet Probe (CDP).

The chamber is initially flushed with dry synthetic air which reduces the background concentration of aerosols to below 5 cm^3. The chamber is then filled with dry synthetic air at atmospheric pressure and a controlled amount of water vapour is added. The chamber is then cooled slowly to the experiment starting temperature using the thermal containment heat exchangers. Once the gas temperature is below the frost point temperature, the water vapour deposits onto the chamber walls. The ice coating on the chamber walls means that the vapour pressure immediately next to the wall is the ice saturation vapour pressure, and also that all experiments start at just below ice saturation. (The gas temperature is slightly higher than the wall temperature, due to heat sources in the chamber.) The test aerosol is then added to the chamber and the aerosol characterised. Expansion cooling using mechanical pumps then leads to ice supersaturation conditions. The pumping rate can be varied, but typically the pressure is reduced from 1000hPa to 800 hPa over 5 minutes. Typically there are 4–5 expansions using the same aerosol sample.

The cooling rate deviates from that expected if the expansion was adiabatic. This is caused by the increasing heat flux from the 2 cm thick aluminium chamber walls. The wall temperature remains approximately constant during the pumping due to the large heat capacity. Eventually the gas temperature reaches an equilibrium value where the expansion cooling and the heat flux from the warmer walls balance. During the expansion cooling there is also a water vapour flux from the ice coated chamber walls into the gas volume. Fig 1 shows the chamber pressure and gas temperature, with the equivalent updraft and gas temperature assuming adiabatic expansion, for Exp. 28. This pumping rate equivalent to an updraft of 3–4 m s^{-1}.

3. THE PARCEL MODEL

The parcel model is a detailed microphysics

*Corresponding author: Cloud Physics Research, Met Office, Fitzroy Road, Exeter, Devon, EX1 3PB, UK. e-mail: richard.cotton@metoffice.com

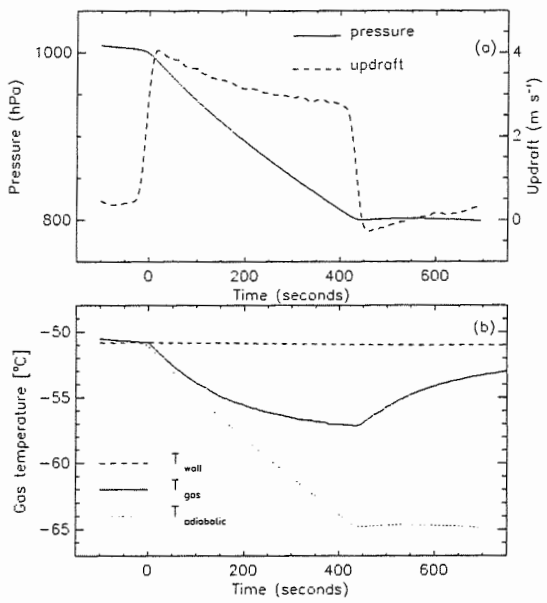

Figure 1: Decrease in chamber pressure and equivalent updraft (a). Resulting gas and wall temperature (b), for Exp. 28

size-resolving model modified to include heat and vapour fluxes from the chamber walls. The unmodified parcel model (described in detail in Cotton and Field (2002)) considers an adiabatic parcel of air containing a conserved mass of water being lifted by a variable updraft. The parcel model was also used in the Cirrus Parcel Model Comparison (CPMC) project as part of the GEWEX Cloud System Studies on cirrus clouds (GCSS WG2) which compared results from various parcel models over a range of updraft velocities and CCN spectrum (see Lin et al. 2002).

The dry CCN size distribution and chemical species are initially specified. The dry CCN are deliquesced to the equilibrium haze particle radii using the Kohler equation. The haze particles are distributed over 40 bins, where each bin carries a radius and number concentration value. The haze particles are not transferable from one bin to another, and number concentration can only be reduced by freezing and transfer to ice bins. Each droplet bin radius is explicitly varied in time using the droplet diffusional growth-rate equation. There are also 40 ice particle bins which are initially empty. The ice particle bin radii are explicitly varied in time using the ice particle diffusional growth-rate equation which contains a capacitance value to represent the ice-crystal habit. A predictor-corrector integration scheme is used, with a time step of 0.01 s.

The homogeneous freezing rate J is calculated by a fit to Jeffery's (1997) formulation,

$$T_e < -65: \quad \log(J) = 25.63$$

$$-65 \geq T_e \geq -30: \quad \log(J) = -243.4 - 14.75T_e - 0.3068T_e^2 - 0.002871T_e^3 - 0.00001021T_e^4$$

$$T_e > -30: \log(J) = -7.63 - 2.996(T_e + 30)$$

where T_e is in °C and J in cm^3 s^{-1}. The solution effect is included by using an effective temperature T_e ($> T_C$), given by

$$T_e = T_g + \lambda\delta T$$

and T_g is the parcel temperature. For $(NH_4)_2SO_4$, $\lambda = 1.7$ and

$$\delta T_j = 0.0220 + 4.12G_j - 1.331G_j^2 + 0.668G_j^3 + 0.125G_j^4 + 0.0083G_j^5$$

where G is the droplet molality. For highly concentrated haze particles the effective temperature T_e is high and freezing is inhibited. As the haze particles grow they become more dilute, and the probability of homogeneous freezing increases. The freezing probability depends on the haze particle molality and temperature with the largest, most dilute haze particles freezing first. Water saturation is not a requirement for the homogeneous freezing of deliquesced haze particles if the temperature is cold enough.

The diabatic terms which represent heat and water vapour fluxes from the chamber walls are formulated using empirically derived constants K_T and K_V. The physics of the heat and vapour diffusion across the boundary layer near the chamber wall is contained within these constants. The heat flux contributes to the rate of change of gas temperature, and is just proportional to the temperature difference between the gas and chamber wall.

$$\left.\frac{dT_g}{dt}\right|_{wallflux} = \frac{K_T}{C_p}\left[T_w - T_g\right]$$

With K_T=4.17 (units), the heating rate of the bulk gas for Exp. 28 is shown in Fig. 2.

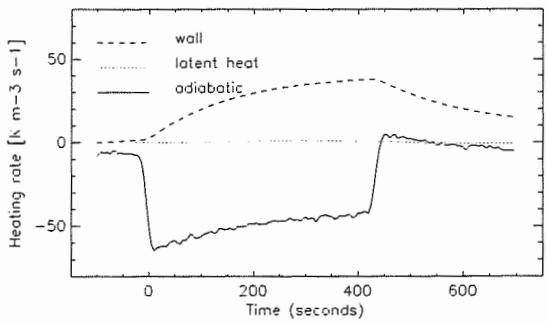

Figure 2: Heating rate contributions to gas, from chamber walls, latent heating and adiabatic cooling, for Exp. 28.

The water vapour flux contributes to the rate of change of total water mixing ratio (q_T), and is proportional to the difference in vapour pressure

just above the chamber wall (which is always at ice saturation) and in the bulk gas,

$$\left.\frac{dq_T}{dt}\right|_{wallflux} = K_V \frac{0.622}{P\rho_{air}} \left[e_{s,i}(T_w) - \sigma_i e_{s,i}(T_g)\right]$$

where $e_{s,i}$ is the ice saturation vapour pressure (Pa) and σ_i is the ice relative humidity fraction (). K_V and K_T can be derived from chamber measurements before the model is run. Integrating the equation for the water vapour flux,

$$q_T(t) - q_T(0) = K_V 0.622 \int_0^t \frac{\left[e_{s,i}(T_w) - \sigma_i e_{s,i}(T_g)\right]}{P\rho_{air}} dt$$

where $q_T(t) - q_T(0)$ is just the increase in total water measured by the MBW. The ice relative humidity σ_i is given by the TDL. Figure 3 shows the increase in q_T as a function of the integrated vapour pressure difference for the chamber expansions. K_V is given by the gradient.

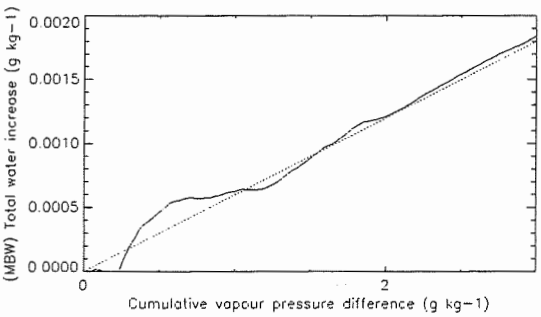

Figure 3: Derivation of water vapour flux from chamber walls for Exp. 28.

4. OBSERVATIONS AND MODEL RESULTS

Observations at all expansions using both the Saharan and Asian dust carried out at a starting temperature of −50C° show two ice formation events (see Field *et al.* (2004) and Mohler *et al.* (2004) for more details).

The two ice formation events can be seen in Fig. 4, which shows particle diameters measured by SID, averaged over 1 second intervals, for Exp. 28. The first nucleation mode occurs near the start of the expansion pumping, where conditions are just above ice saturation. We assume that this is deposition nucleation onto some of the aerosol sample. For simplicity, the model produces exactly 2 cm^{-3} ice particles when the ice relative humidity reaches 105 %. The second nucleation mode occurs later, but still below water saturation. However, because of the cold temperatures, we assume that this is homogeneous freezing of haze particles.

Fig. 5 and 6 show observations and model results for two expansions, using Asian dust (Exp. 28) and Saharan dust (Exp. 41). During Exp. 41, the pumping rate was slowed at 200 s. These figures show that the addition of heat and moisture

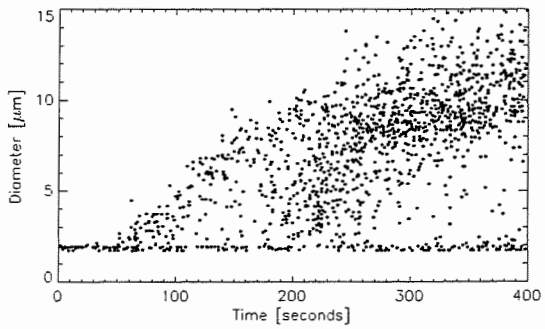

Figure 4: SID particle diameters.

fluxes from the chamber wall to the gas, as described above, allows the model to reproduce the observed temperature and relative humidity.

The CCN species was chosen to be ammonium sulphate, and the size spectrum lognormally distributed, with the number of aerosol per unit volume with radius r to $r + dr$ given by

$$N(r)\,dr = \frac{N_t}{\sqrt{2\pi}\ln\sigma} \exp\left[-0.5\left(\frac{\ln r - \ln r_g}{\ln\sigma}\right)^2\right] d(\ln r)$$

where N_t is the total number concentration of CCN, r_g is the dry mode radius, and σ determines the width of the spectrum.

N_t was set to the observed initial aerosol concentration ($N_t = 36cm^{-3}$ for Exp. 28 and $N_t = 54cm^{-3}$ for Exp. 41). r_g was arbitrarily set to give better agreement with the observed rate of new freezing events ($r_g = 0.007\mu m$). $\sigma = 1.8$. With this small r_g, however, the ammonium sulphate size distribution is much smaller than the observed size range of dust particles (0.2–2.0μm).

5. DISCUSSION AND CONCLUSION .

The AIDA chamber can be modeled using a modified parcel model which contains heat and water vapour fluxes from the chamber walls to the bulk gas. There are two different ice formation events which occur when using both Asian and Saharan dust samples at an expansion start temperature of −50C°. Model results indicate, that the second ice formation, which occurs below water saturation, is homogeneous freezing. However, because the r_g used in the model to describe the CCN dry mode radius is much smaller than the measured dust aerosol size, the dust aerosols are not forming deliquesced haze particles which freeze homogeneously. Rather there might be hygroscopic sites on the dust aerosols, and these sites freeze, initiating ice formation.

REFERENCES.

Cotton, R. J. and Field, P. R., 2002: Ice nucleation characteristics of an isolated wave cloud, *Q. J. R. Meteorol. Soc.*,**128**, 2417–2437

Field, P. R., Cotton, R. J., Moehler, O., Schnaiter, M., M. Kraemer, M., Connolly, P.,

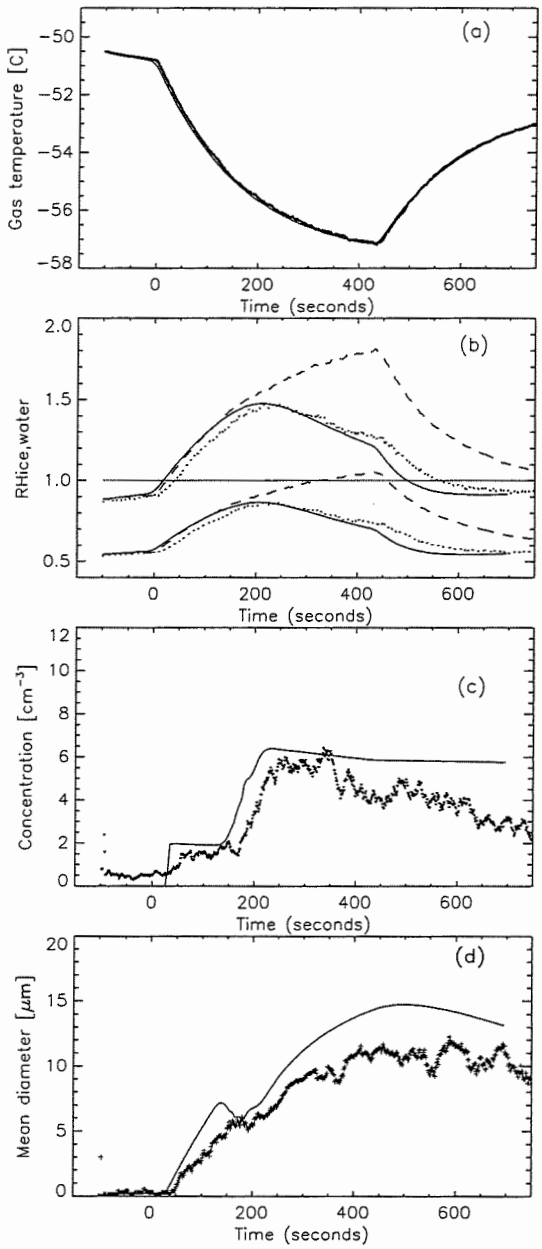

Figure 5: Model-observation comparison for Asian dust (Exp. 28). The model output is the solid line. In Fig. (b), the dashed line is the relative humidity using the total water (MBW), the dotted line using the water vapour (TDL). In Figs. (c) and (d), the points are from the SID, smoothed over 20s.

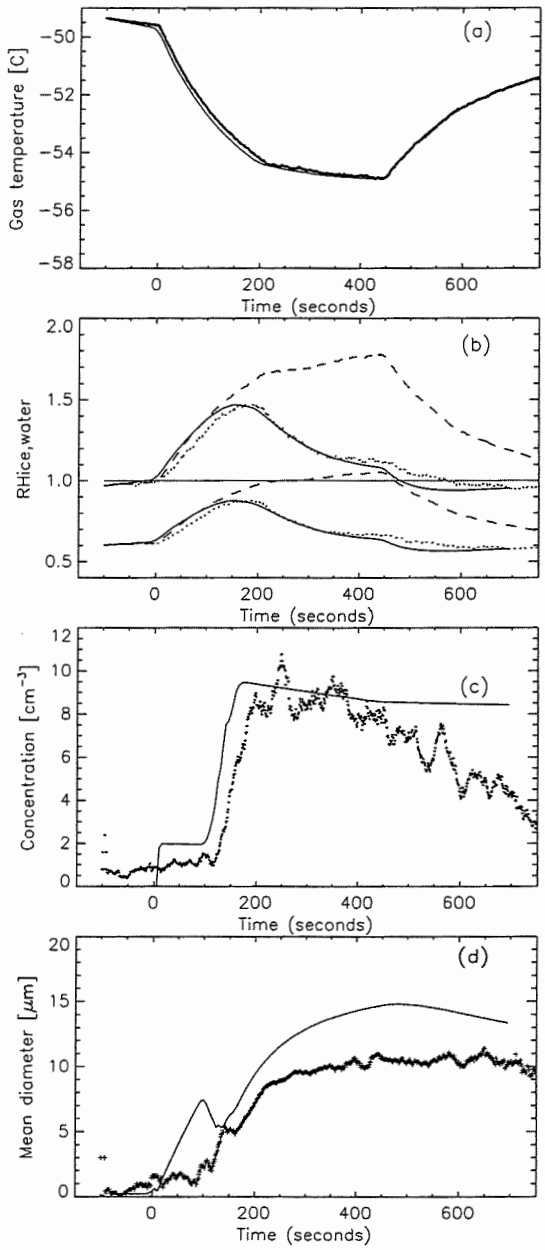

Figure 6: Model-observation comparison for Saharan dust (Exp. 41).

Heymsfield, A. J, 2004: Investigation of the ice nucleation ability of two desert dust aerosol samples at -50°C, *this volume*

Hirst, E., Kaye, P. H., Greenaway, R. S., Field, P. R. and Johnson, D. W., 2001: Discrimination of micrometre-sized ice and supercooled droplets in mixed phase clouds, *Atmos. Environ.*,**35**, 33–47

Moehler, O., Stetzer, O., Schaefers, S., Linke, C., Schnaiter, M., Tiede, R., Saathoff, H., Kraemer, M., Mangold, A., Budz, P., Zink, P., Schreiner, J., Mauersberger, K., Haag, W., Karcher, B. and Schurath, U., 2003: Experimental investigation of homogeneous freezing of sulphuric acid particles in the aerosol chamber AIDA, *Atmos. Chem. Phys.*,**3**, 211–223.

Moehler, O.,/it et al., Formation, growth and habit of ice crystals nucleated on desert dust aerosol, 2004: *this volume*

A WINTER SEASON PHYSICAL EVALUATION OF THE EFFECTS OF CLOUD SEEDING IN THE COLORADO MOUNTAINS USING RAMS

William R. Cotton,* Ray L. McAnelly and Gustavo G. Carrió

Department of Atmospheric Science, Colorado State University, Ft. Collins, CO 80523

1 INTRODUCTION

The Regional Atmospheric Modeling System (RAMS; Cotton et al., 2003) was used during the winter of 2003-04 to provide realtime forecast support for an operational cloud seeding program in the central Colorado Rocky Mountains. The model was also extended to include seeding effects, in order to evaluate the seed vs. no-seed precipitation simulated by RAMS. This paper discusses the seeding operations and realtime forecast simulations, and the ongoing physical evaluation of the seeding effects.

2 SEEDING AND REALTIME FORECAST OPERATIONS

The cloud seeding program took place in the central Colorado Rocky Mountains, primarily during the months of November through February. It was contracted out by the Denver Water Department (DWD) to Western Weather Consultants (WWC), and was one of several seeding programs operating in Colorado this winter [(Colorado Water Conservation Board (CWCB), 2003]. Up to 56 ground-based seeding generators were used to release silver iodide (AgI) during favorable conditions, with the intent being to increase snow precipitation over a target area of ~10,000 km^2.

Our project was a cooperative effort with the DWD/WWC seeding program and CWCB, under separate funding from the U.S. Bureau of Reclamation. Realtime RAMS forecast simulations were run once daily to support the seeding operations, with an inner nested domain covering the seeding target area and a more extensive surrounding area at 3km grid spacing (Fig. 1). A sophisticated two-moment microphysics scheme was used, in which mixing ratios and concentrations are predicted for seven hydrometeor catagories. Graphical forecast products at 2h intervals through the 48h forecast period were available via the internet to assist WWC in the seeding operations (http://rams.atmos.colostate.edu/realtime). Of particular interest to WWC were the high temporal and spatial resolution in the development and evolution of orographic cloud, cloud base, and temperature in the lower cloud layer. These parameters were used to help determine which generators would be utilized, when they would be activated, and at what rate the AgI would be generated.

Originally, it was intended that simulated 24h periods of precipitation from these realtime forecast simulations would be used to establish control, or non-seeded, simulated precipitation for the physical evaluation against the seeded runs (Section 3). However, due to a series of changes in parameters used in the forecast model over the course of the season, and some inconsistencies with the microphysical features that were necessary for the seeded runs, evaluating the sensitivity of seeding effects based on comparison with these realtime control runs would have been difficult because of the other differences. Thus all the realtime forecasts are being rerun using model parameters and microphysical settings that are identical to the seeded runs, except that no AgI effects are included. These rerun forecast simulations provide the daily series of 24h control, or non-seeded, precipitation to be evaluated against the seeded simulations.

3 SEEDED RAMS SIMULATIONS

For evaluation of the seeding program, the model code was extended to include seeding effects. Simulated sources of AgI are included at specified low-level model grid points in accordance with the timing and magnitude of AgI release from each generator as recorded in operational seeding

*Corresponding Author's Address, William R. Cotton, Department of Atmospheric Science, Colorado State University, Fort Collins, CO 80523; E-Mail: citton@atmos.colostate.edu.

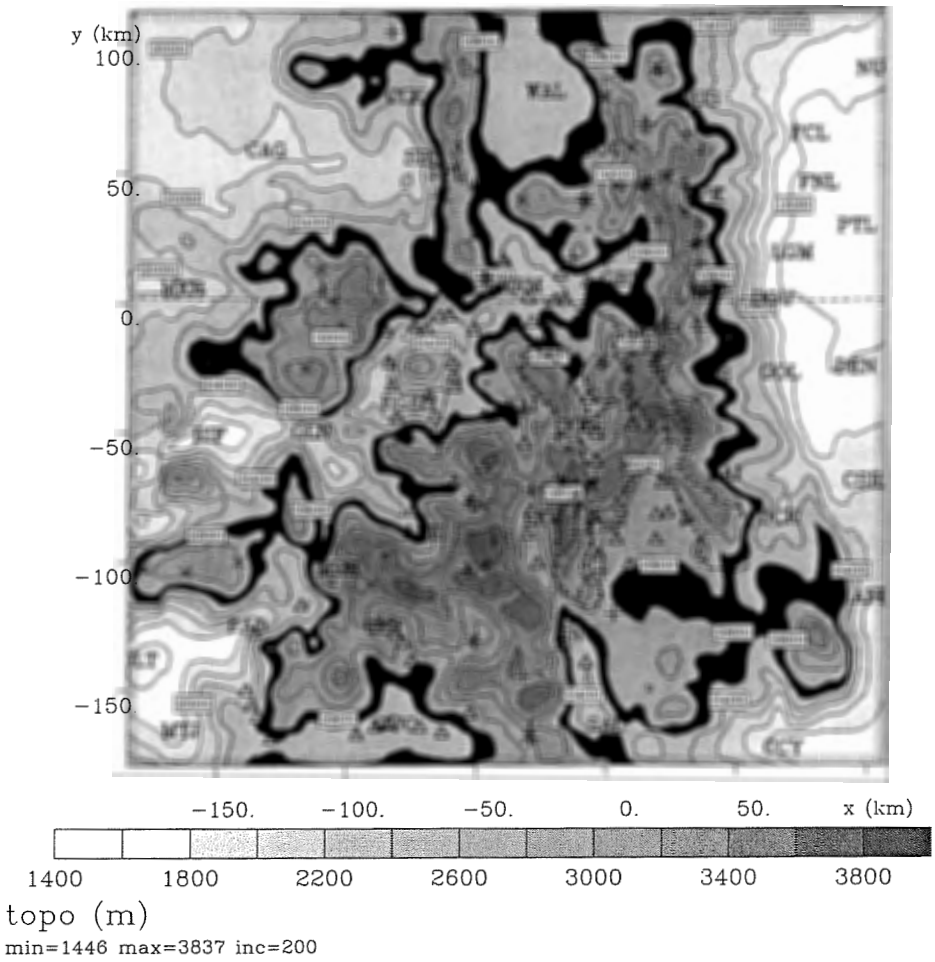

Figure 1: Nested 3km domain for realtime forecast (control) and post-event seeding simulations. Topography is shaded. Included are 3-letter identifiers for towns; the seeding target area (dashed boundary); generators (triangles); SNOTEL sites (X); and snowcourses (+).

logs. The AgI is treated as a second predictive IFN field with its own activation characteristics. This AgI activation law is based on laboratory experiments that used the same types of generators and AgI materials as used by WWC in the current seeding program. As with the standard IFN category, the number of seeded IFN that is activated becomes a source of pristine ice crystals in equal numbers and a corresponding sink of IFN that is available for subsequent activation.

With this seeding model, after-the-fact RAMS simulations are being performed for each 24h period in which seeding operations were conducted. The seeding simulations are set up identically as the control runs, except for the additional IFN category and the seeded AgI. Simulated 24h precipitation in these seeded runs replaces the amounts from the corresponding non-seeded runs to form complete daily, event, monthly and seasonal simulated precipitation totals that include all seeding operations.

An example of a seeded run illustrates how the AgI is introduced into the model. The simulation began at 0000 UTC on 2 Jan 2004, with a broad upper level trough over the western United States. A 24h period of seeding began at 0115 UTC, first using only generators to the west of the target area, then also using generators in the interior of the

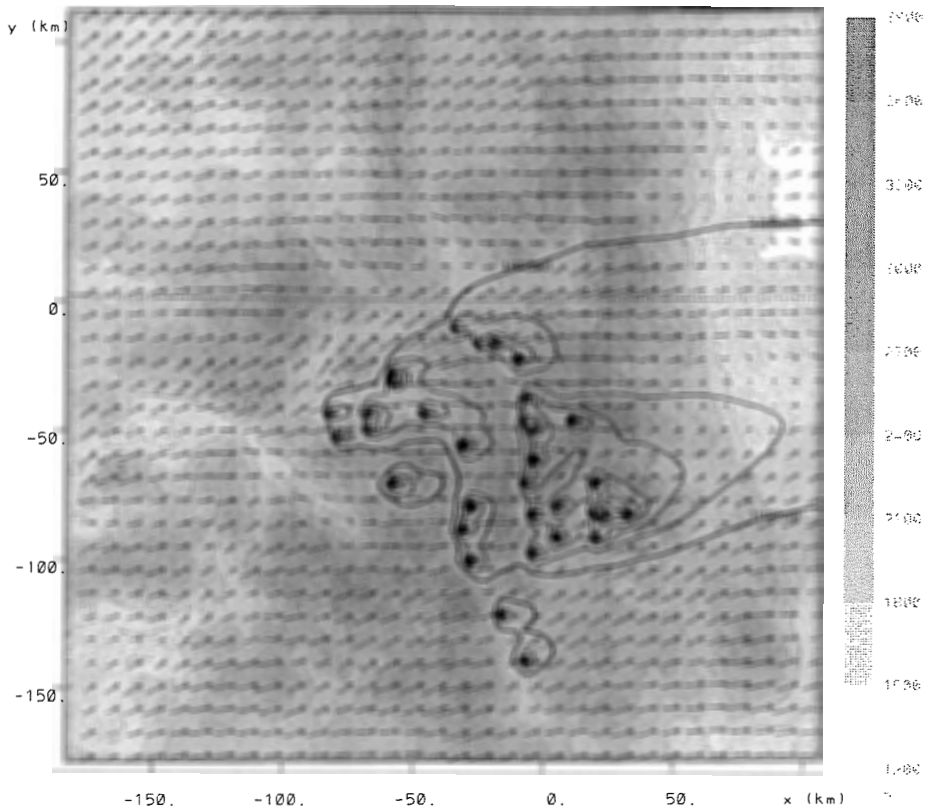

Init 01/02/04 0000 UTC seed		grid 3			
z = 146.4 m	2004-01-02-2000 00 UTC	min	max	inc	lab*
contours	topo (m)	1446.	3537	300.0	1e 0
contours	ifn2-conc (#/kg)	0.000	0.1926E+07	0.2000E+06	1e 0
vectors →	5 m/s horiz	0.2526	23.34		

Figure 2: Seeding simulation: available AgI concentration in lowest model layer (solid contours), on shaded topography.

target area as the cloud system developed further and progressed eastward. In Fig. 2, the available, or non-activated, AgI concentration in the lowest model layer is shown at 2000 UTC. The small maxima show the locations of the active generators, where the AgI is introduced uniformly over the corresponding surface-based grid volume at the rate of release given by the operational seeding logs. (The generators in the southwestern quadrant of Fig. 1 were operated by other seeding programs, and their effects are not included in this study.) Advection and diffusion disperse the seeded material primarily downwind, as shown by the more diffuse plume. Vertical cross sections show that the seeded IFN are restricted to the lowest 1 to 2km AGL as it advects downstream.

A fraction of the available AgI activates when it encounters favorable conditions, given by a temperature and saturation dependent activation algorithm. Figure 3 shows the vertically integrated concentration of activated AgI (and its contribution to pristine ice concentration) at 2000 UTC. Successively larger concentrations develop as activation is enhanced over successive mountain ridges. As with the available AgI in Fig. 2, the activated AgI is concentrated in the lowest 1-2km AGL.

From such seeded and corresponding control simulations, the simulated no-seed and seeded pre-

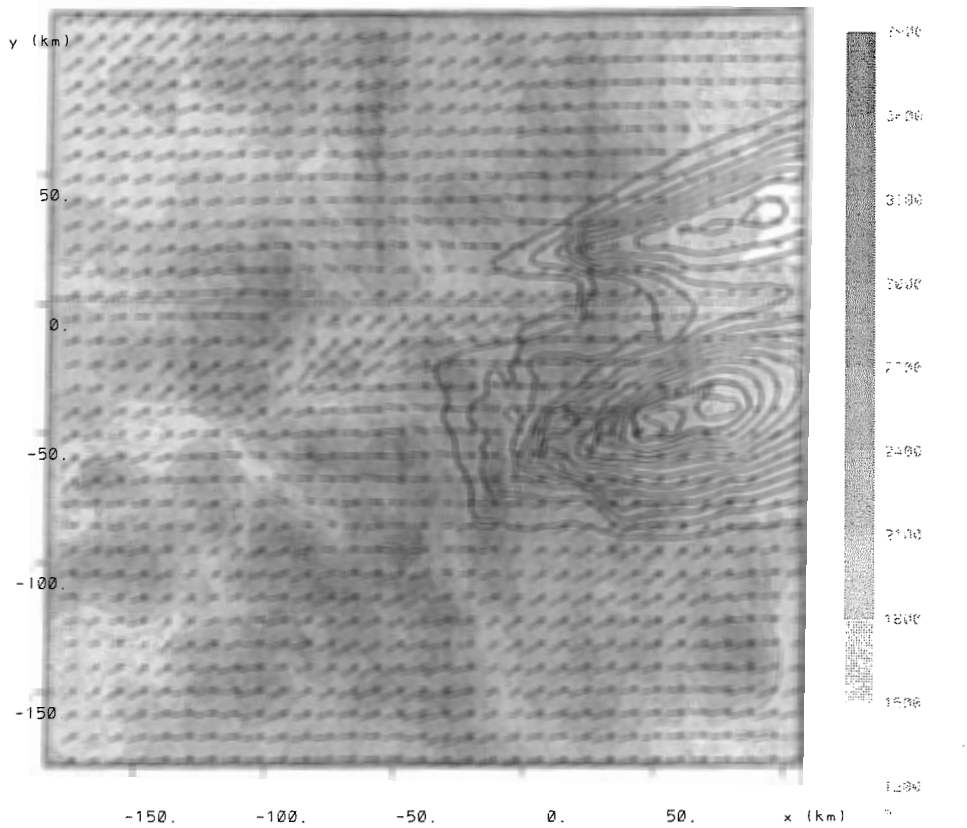

Init 01/02/04 0000 UTC seed		grid 3			
z = 146.4 m	2004-01-02-2000 00 UTC	min	max	inc	lab'
contours	topo (m)	1446	3887.	300.0	1e 0
contours	vertint act2 (#/m 2)	0.000	0.2755E+08	0.2000E+07	1e 0
vectors →	5 m/s horiz	0.2526	23.34		

Figure 3: Seeding simulation: vertically integrated, activated AgI concentration (solid contours), on shaded topography.

cipitation is being evaluated against observed precipitation at numerous SNOTEL sites in both the target area and in areas unaffected by the operational seeding (Fig. 1). A rigorous statistical analysis methodology is used to assess how reliably RAMS simulates no-seeded vs. seeded precipitation, based on 30 seeding days selected over the 4-month seeding season.

4 ACKNOWLEDGMENTS

This research was supported by the U.S. Bureau of Reclamation through the Colorado Water Conservation Board (Contract #C153988).

5 REFERENCES

Colorado Water Conservation Board, 2003: Weather Modification Permitting Program, Status Update March 2003. CWCB, Dept. of Natural Resources, 3pp. [http://cwcb.state.co.us/Weather_Modification/WM_Status_Update_03.pdf]

Cotton, W.R., R. Pielke, R. Walko, G. Liston, C. Tremback, H. Jiang, R.L. McAnelly, G.Y. Harrington, M. Nicholls, G.G. Carrio, and J.P. McFadden, 2003: RAMS 2001: Current status and future directions. *Meteor. And Atmos. Physics*, 82, 5-29.

PRELIMINARY COMPARISON OF AMSR-E OBSERVATION AND NUMERICAL SIMULATION WITH CLOUD RESOLVING MODEL FOR SOLID PRECIPITATION IN WINTER DURING THE WAKASA 2003

Hisaki Eito[1], Kazumasa Aonashi[1], Guosheng Liu[2], Chiashi Muroi[1], Syugo Hayashi[1], Teruyuki Kato[1], and Masanori Yoshizaki[1]

[1]Meteorological Research Institute, Japan Meteorological Agency, Tsukuba, Ibaraki, 305-0052, Japan
[2]Florida State University, Tallahassee, FL 32306-4520, U.S.A.

1. INTRODUCTION

For improving the accuracy of passive microwave solid precipitation retrieval algorithm using the AMSR/AMSR-E, the feild campaign (WAKASA2003) was conducted in the Fukui area, Japan, from January 12 to February 5, 2003. During the WAKASA2003, many active convective snowfall clouds frequently formed over the Sea of Japan due to cold outbreak. On 28-29 January 2003, broad cloud bands extending southeastward from the base of the Korean Peninsula to the Fukui area formed, and developed under the influence of the upper cold low.

In this paper, high-resolution numerical simulations of these cloud bands are performed using a CRM with 1 km horizontal resolution. The expected brightness temperatures simulated by microwave radiative transfer model (MRTM) with CRM-derived atmospheric conditions were compared with AMSR-E observations. Our purposes are to check and improve the cloud microphysics scheme of the CRM, and to supply useful information from the model-derived 3-D structures of precipitation for improving the accuracy of the AMSR-E precipitation retrieval algorithm.

2. OBSERVATIONS

Figure 1 shows the GMS-5 visible imagery at 13 JST on 29 January 2003. Several clouds were found over the Sea of Japan, as a consequence of heat and moisture supply to continental cold air mass. The remarkable cloud bands, where cumulus convections developed, were distributed over the Sea of Japan from the base of the Korean Peninsula to the Tohoku district of Japan. It is well known that these cloud bands form over the low-level convergence zone (Japan Sea Polar-air mass Convergence Zone; JPCZ) between two cold airflows with different property (Nagata et al., 1986; Nagata, 1991; Nagata, 1992). These cloud bands formed in the previous day (28 Jan.), and developed under the influence of upper cold low (Fig. 1).

Figure 2 shows the reflectivity intensity observed by JMA operational radar. High reflectivity areas distribute over the sea and coastal region, showing that many precipitation particles exist. In this time, there are observations of AMSR-E, which is a microwave radiometer aboard AQUA satellite. Figure 3 is the scattering index retrieved from 89 GHz britness temperature of AMSR-E. Colors varying from red to blue correspond to increasing scattering. The areas with large scattering index, where a amount of snow and graupel perticles is large, were distributed over the Sea of Japan. These areas well corresponded to high radar reflectivity intensity areas.

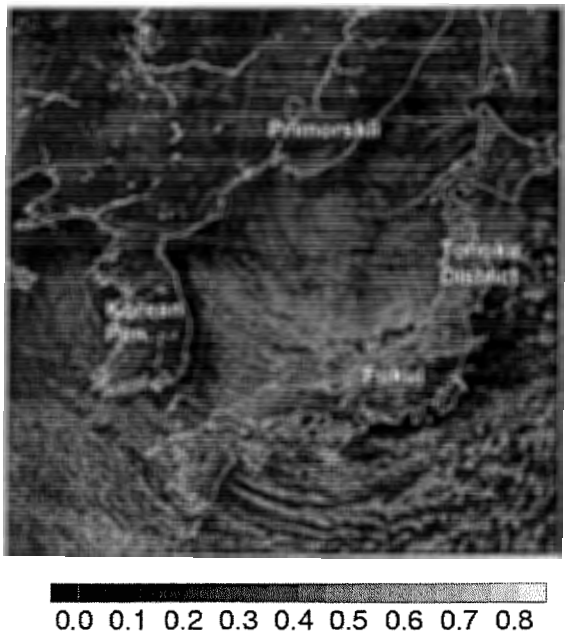

Fig. 1: GMS-5 visible imagery at 13 JST on 29 January 2003. A white solid line shows the flight path of an instrumental aircraft.

Corresponding author's address: Hisaki Eito, Meteorological Research Institute, Japan Meteorological Agency, 1-1, Nagamine, Tsukuba, Ibaraki, 305-0052, Japan; E-Mail: heito@mri-jma.go.jp

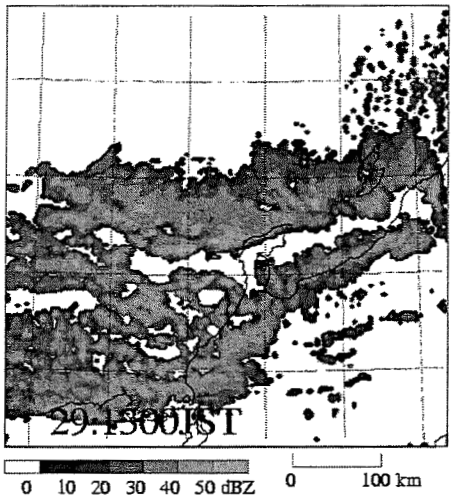

Fig. 2: Radar reflectivity intensity observed by JMA operational radar at 13 JST on 29 January 2003.

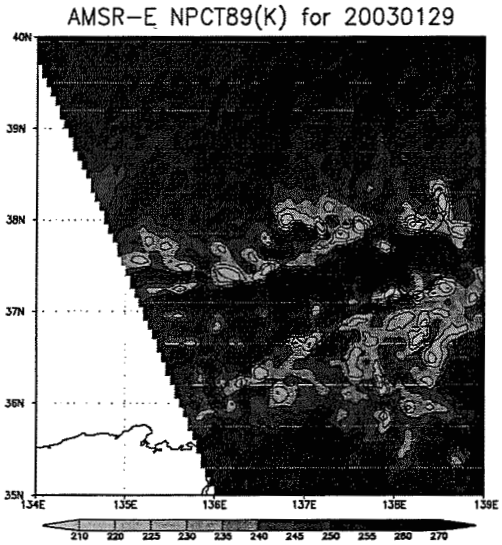

Fig. 3: Scattering index retrieved from 89 GHz data of AMSR-E at 13 JST on 29 January 2003.

3. NUMERICAL MODELS

The CRM developed by Japan Meteorological Agency (JMA) is used in this study (JMANHM: Saito et al., 2001). The fully compressible equations with the conformal mapping are employed as the basic equations of the JMANHM. Primary physical processes such as cloud physics, atmospheric radiation and mixing in the planetary boundary layer are also included in the JMANHM. The bulk cloud microphysics scheme is employed in the JMANHM. This scheme predicts the mixing ratios of six water species (water vapor, cloud water, rain, cloud ice, snow and graupel) and the number concentrations of five condensed water species. The JMANHM has been transferred to the Earth Simulator (ES), which is the fastest supercomputer in the world.

In the present study, the JMANHM has a horizontal grid size of 1km with 2000 x 2000 grid points. The vertical grid with a terrain-following coordinate contains 38 levels with a variable grid interval of 40 m near the surface and 1090 m at the top of the domain. The model top is 20.36 km. The time step interval is 5 seconds. The initial and boundary conditions for the JMANHM are provided from output produced by Regional Spectral Model (RSM). The RSM with a horizontal grid size of about 20km is a hydrostatic model used operationally in JMA.

Radiative transfer calculations are performed with a 4 stream MRTM (Liu, 1998). It includes absorption and scattering by hydrometeors to calculate the expected microwave brightness temperatures corresponding to the atmospheric conditions simulated by the JMANHM.

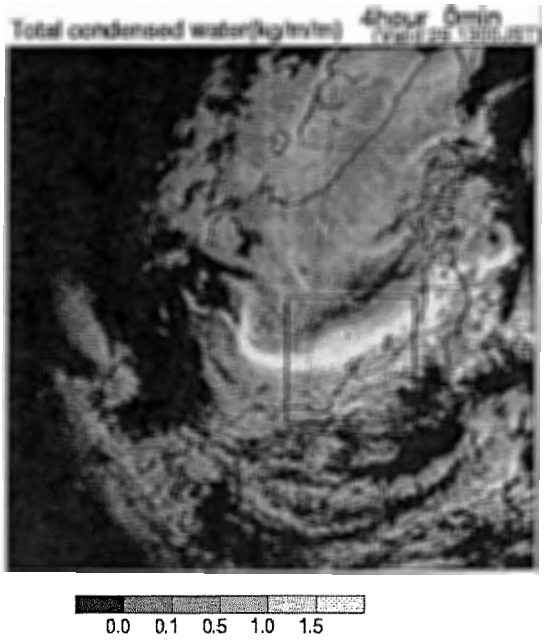

Fig. 4: Horizontal distribution of vertically integrated total condensed water simulated by the JMANHM (4 hour forecast). Black square denotes the drawing area of Fig. 5 and Fig. 6.

4. RESULTS

Figure 4 shows a horizontal distribution of vertically integrated total condensed water simulated by the JMANHM. The JMANHM successfully reproduced features of broad cloud bands. In particular, model-simulated cloud bands resembled observed one (Fig. 1) in shape and location. Detailed features of several cloud streets were also simulated

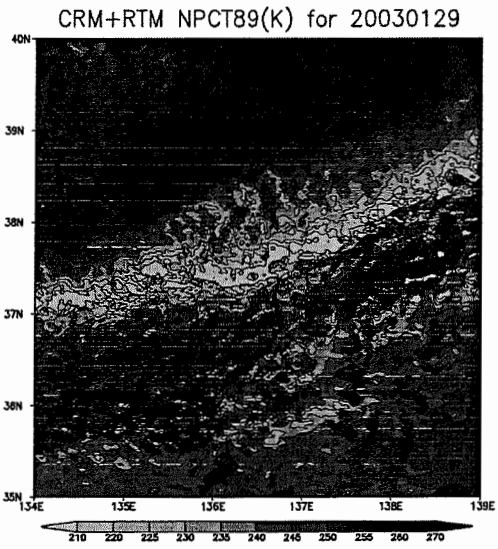

Fig. 5: Scattering index calculated from 89 GHz brightness temperatures simulated by MRTM with JMANHM -derived atmospheric conditions retrieved at 13 JST on 29 January 2003. The drawing area almost corresponds to the black bold square in Fig.4.

around cloud bands. Figure 5 shows a horizontal distribution of scattering index calculated from 89 GHz brightness temperature simulated by JMANHM and MRTM. The spatial structures of the simulated scattering index almost agree with that of AMSR-E observation (Fig. 2). However, the contrast between high and low scattering in simulation is stronger than that in AMSR-E observation. The magnitude of scattering index in simulation is much larger than that in observation. These results indicate that the JMANHM overestimated the amount of solid water particles.

Figure 6 shows the horizontal distributions of vertically integrated values of each solid water particles. Most of model-simulated precipitation particles were snow particles (Fig. 6a). The maximum value of total snow water is ~ 6 kg m^{-2}. This value was almost equivalent to that of total precipitable water. Vertical structures of JMANHM-simulated snow field are shown in Fig. 7. Water contents, number concentrations, and average diameters are shown in upper, middle and lower panel, respectively. Figure 7a shows that a cloud top height is about 6 km, which almost agrees with radar and aircraft observations. In comparison with aircraft observations, JMANHM-simulated number concentrations (~ 100 /l) and averaged diameters (~ 0.5 mm) are almost reasonable. However, an amount of simulated water contents (~ 1.0 gm^{-3}) is larger than that in observation (~ 0.5 gm^{-3}). These gaps in the amount of snow between observation and simulation indicate the necessity of tuning and improvement of the cloud microphysics process in the JMANHM.

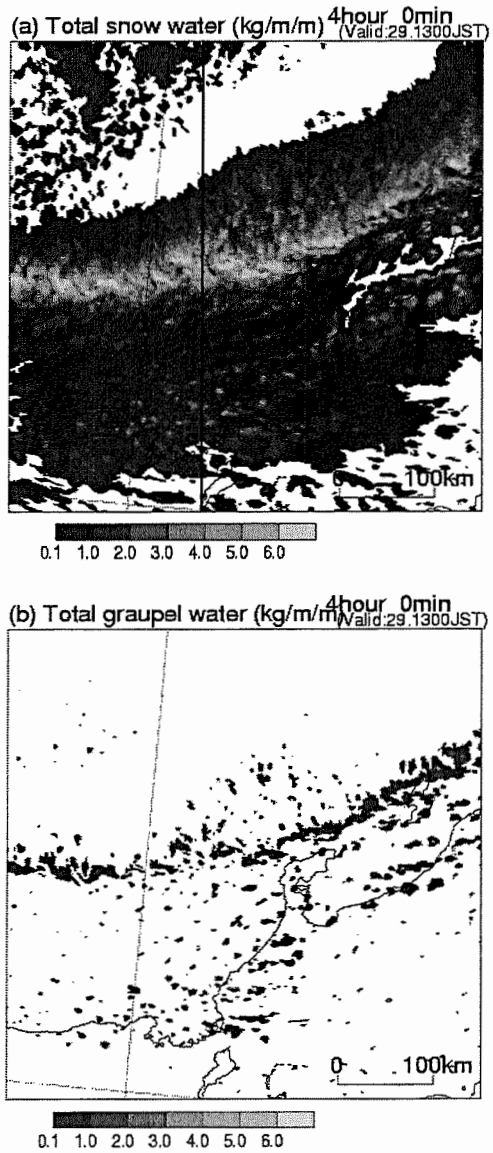

Fig. 6: Horizontal distribution of vertically integrated each solid water particles simulated by the JMANHM (4 hour forecast) in the black bold square on Fig.4. (a) Snow. (b) Graupel. Black solid line denotes the drawing area of Fig. 7.

The same experiment was also conducted on the case in the previous day (not shown). In this case, cloud bands, of which cloud top height was about 3 km, were in the moderate stage. On the comparison of AMSR-E observation and numerical simulation, almost similar aspects shown in the developed case were also found in this case. However, a better agreement about a degree of the scattering was obtained between the simulation and the observation This result indicates that defferences of dvnamic structures such as the intensity of updraft and the cloud top height also

affect the amount of model-simulated solid precipitation particles.

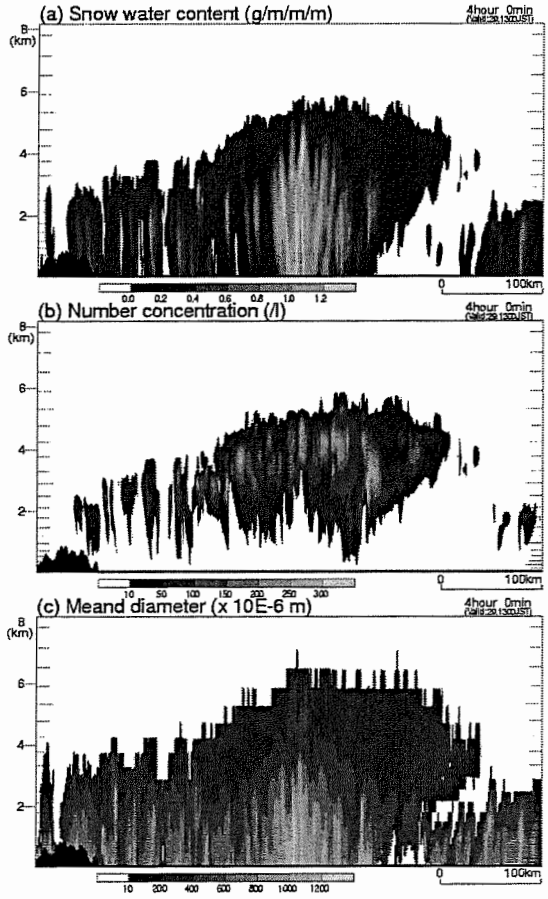

Fig. 7: Vertical cross section of JMANHM-simulated snow field along the black solid line in Fig. 6a. (a) Water contents. (b) Number concentrations. (c) Average diameters.

5. SUMMARY

A high-resolution wide-range numerical simulation of cloud bands observed on the Sea of Japan during the WAKASA2003 was performed using a CRM with 1km horizontal resolution and 2000 x 2000 km calculation domain. Cloud features observed by a meteorological satellite were well reproduced in CRM. Comparison of AMSR-E observation and simulation with CRM and MRTM suggests that CRM overestimates the amount of solid water particles, especially, snow particles. It is necessary to examine the process of cloud microphysics in the model and also to carry out the comparison with the other cases.

ACKNOWLEDGEMENTS

This study was supported by the fund of Japan Science and Technology Corporation - Core Research for Evolutional Science and Technology. The numerical calculations were made by NEC SX-6 on the Earth Simulator.

REFERENCES

Liu G. 1998: A fast and accurate model for microwave radiance calculations. J. Meteor. Soc. Japan, **76**, 335-343.

Nagata M., M. Ikawa, S. Yoshizumi and T. Yoshida, 1986: On the formation of a convergence cloud band over the Japan Sea in winter; numerical experiments. J. Meteor. Soc. Japan, **64**, 841-855.

Nagata M., 1991: Further numerical study on the formation of a convergence cloud band over the Japan Sea in winter. J. Meteor. Soc. Japan, **69**, 419-428.

Nagata, M., 1992: Modeling case study of the Japan-Sea convergent cloud bands in a varying large-scale environment: evolution and upscale effect, J. Meteor. Soc. Japan, **70**, 649-671.

Saito, K., T. Kato, H. Eito and C. Muroi, 2001: Documentation of the Meteorological Research Institute/ Numerical Prediction Division Unified Nonhydrostatic Model. Tec. Rep. MRI, **42**, 133 pp.

HAILSTONE SIZE DISTRIBUTION AND DENT OVERLAP IN HAILPADS

Roberto Fraile, Laura López, Covadonga Palencia and Amaya Castro

Departamento de Física, Instituto de Medio Ambiente, Universidad de León, Spain

1. INTRODUCTION

The hailpad is an easy device that was developed to measure the effects of hailstorms (Long et al., 1980). It has been reported as a useful and effective tool to study hail climatology (Vinet, 2001). The physical parameters from the hailstones are measured by the interaction between the sensitive material in the hailpad and the hailstone.

Due to its simplicity and low cost it will be easy to use as a dense network, in order to study the spatial distribution of hailstorms. Nevertheless, a number of estimations and approximations are needed for the result to be deemed as valid Those approximations will undoubtedly introduce some errors on the measurements; the most important being the overlapping of the hailstone dents.

Both, Long et al (1980) or Rinehart (1983) reported errors from different sources in their earliest hailpad papers. However, to our knowledge, there are no reports on the error on the measurement of hail distribution on a hailpad due to the overlapping of hail stone imprints is reported, even though some authors (Giaiotti et al., 2001) have introduced a correction factor on their analysis of hailpad measurements. We should note that the overlapping error would only be significant when the hailpad is considered "overpopulated" with hits (many impacts). For a few numbers of impacts on the hailpad this error shall be negligible.

In this paper, we will present a study of the hailstone dent overlapping error by the simulation of the effects of a hailstorm on a hailpad. We based our work on the same assumptions used to calibrate hailpads. A side-by-side comparison will be made between the theoretical results and those obtained from a hailpad.

Corresponding author's address: Roberto Fraile, Departamento de Física, Facultad de CC Biológicas y Ambientales, 24071 León, Spain; E-Mail: robertofraile@unileon.es.

2. HAILSTONES AND THEIR MEASUREMENT: HYPOTHESIS.

Once a zone of the hailpad has received the impact of a hailstone, that zone will be unable to measure another impact. This is due to the physical contact between the hailpad and the hailstones. We refer as hailstone dent overlapping error to the impossibility to measure correctly all the hailstone dents on the hailpad.

The main hypotheses used to measure the distribution of on a hailpad are:

- The hailstones are spheres of radius R;
- The imprint of a hailstone on a hailpad is an ellipse where r is the small halfaxis
- There is a known relationship between R and r (calibration curve).

Even if the hailstone is assumed to be a sphere, the dent left on the hailpad will be elliptical. This would be due to the horizontal wind dragging the hailstone while falling. We have assumed that the small semiaxis on the ellipse is wind independent. Hence, the measurement from the hailstone imprint will not give the total kinetic energy but just the energy due to the vertical component of its velocity.

Regarding the hailstone dent: it will only be measurable when the overlapping between dents is a small fraction of them. If the overlapping between them is considerably high, the dents cannot be resolved and therefore are not measurable. In this case, whoever analysed the hailstones prints (researcher or a computer program) will consider only a deformed one since the resolution of both imprints is not possible (Fig. 1).

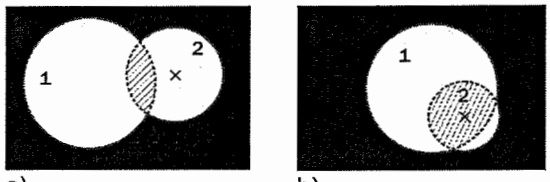

a) b)

Fig. 1. Hailstones imprints a) resolved and b) non-resolved.

The above qualitative criterion is not useful to provide us with any probability. We could draw up a numerical criterion considering the distance between the fresh dents to the previous ones, or we could use the overlapping ratio between the dents, or any other non-qualitative criteria. The authors intend to consider quantitative criteria in a later paper.

Regarding the size distribution, it is generally accepted that the hailstones follow an exponential distribution (Dessens and Fraile, 1994) where the probability density function (PDF) is given by $f(x) = \beta \exp(-\beta x)$ a one variable dependence. In addition, another parameter to take into account is N the total amount of hailstones reaching the hailpad.

3. HAILFALLS SIMULATION.

To check the effect of the dent overlapping in hailpads measurements, several hailstorms of known characteristics were simulated. These hailfalls were simulated over the typical hailpad used on León's network, a 30 cm side square plate (Fraile et al., 1992).

The hailstorm values used were chosen to be common from the data collected on the field. The imprint distributions on 100 hailpads from a hailstorm season in León were measured. The N and β percentile ranks obtained from those measurements can be seen on Fig.2. From those graphs we have chosen the five values used on the simulation and shown on Table 1. It is also important to do those simulations with a high value of N. Although in the chosen hailstorm season the highest number of impacts was 1000, the value of 400 was used. The sizes used on the simulations on monodisperse distributions are also shown on Table 1.

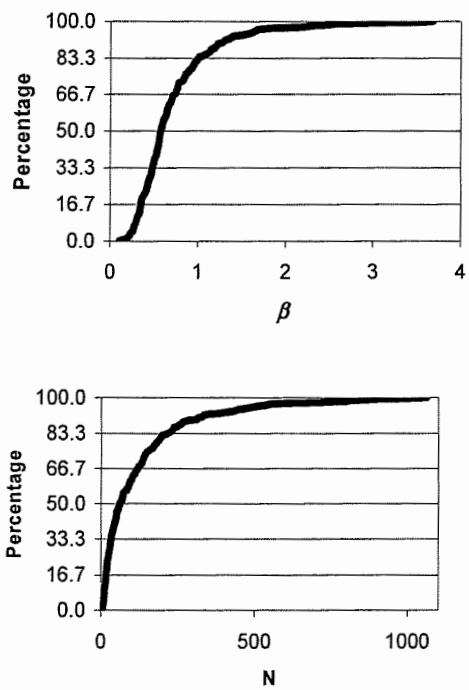

Fig. 2. Percentiles of β y N distributions from actual hailstorms data.

Table 1. N, β and size values used on the computer simulation.

N	20	36	69	123	223	400
β (mm^{-1})	0.35	0.5	0.59	0.75	1.05	
Size (mm)	8	11	14	17	29	

The simulation, a computer model, is based on the generation of N solid circles randomly distributed over the hailpad area: as a monodisperse distribution (all same size circles), or as an exponential size distribution. To construct the dent images both AUTOCAD® and CorelDraw® computer programs were used. Typical results from the computer model (where the values from table 1 were used) are shown in the next figures. Fig. 3 shows monodisperse distributions. Fig.4 shows typical exponential distributions. Five simulations of each distribution were made and we discuss their results in the following paragraph.

4. MEASUREMENTS AND RESULTS

We used IMAGE PRO PLUS® to characterise the images generated by the simulation. This software is widely used in the data processing of hailpads (Dessens et al., 2001). This computer program characterises the white solid circles automatically. It will give their sizes and try to detect a possible overlapping between them. In any case, the best results are obtained with the help of an external technician. The parameter measured is the small semiaxis of the dent on a hailpad. This program will fit this dent to an ellipse.

Firstly we would find the correlation between the total number of generated dents and the number of those measured. Fig 5 shows that those numbers do not correlate. This difference between the measured and the expected N also happens in a real hailstorm. This difference is only due to the overlapping of dents.

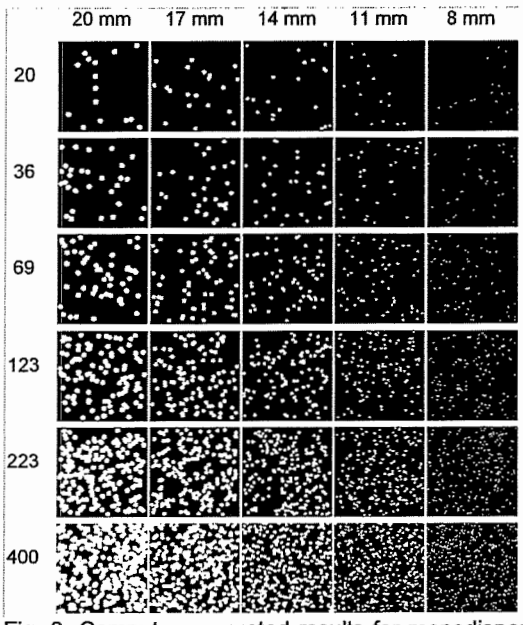

Fig. 3. Computer generated results for monodisperse distributions using different *N* values and sizes.

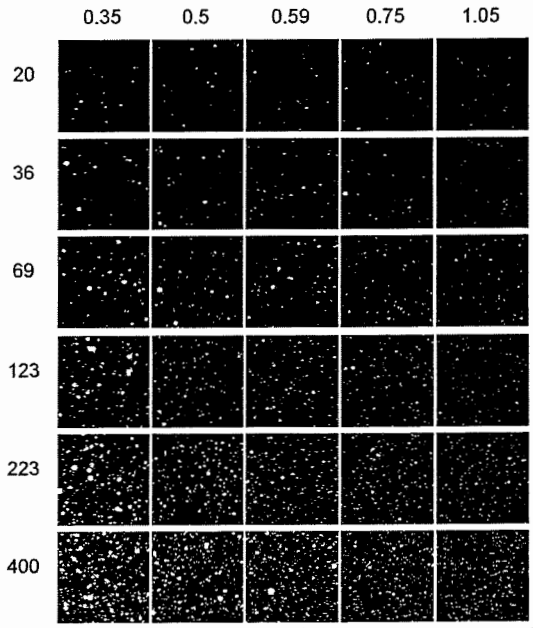

Fig. 4. Computer generated results for exponential distributions using different *N* and β values.

The dent size is measured and the size of the parent hailstone will be deducted from the calibration curve. Subsequently, we calculate their mass and energy. With all the measured data from a hailpad the total number of impacts and the β parameter from the distribution are obtained. Figure 6 shows the comparison between the measured and expected values of the above parameters.

Information is always lost due to the overlapping of the hailstone dents. This effect is more severe when the number of incident hailstones on the hailpad is high. Furthermore, the measured results and the expected results do not match for smaller hailstones.

The overlapping correction should be taken into consideration also when any other parameter (such as the mass or the total energy) is studied. Without this correction the values will be systematically lower than the expected ones. Usually those parameters are important for heavy hailstorms where the amount of hailstones is important. In these cases, the error introduced by the overlapping of their dents is not negligible For instance, in some of our simulations the measure value was less than 60% of the expected total value.

Last but not least, we must study the relation between the estimated errors from the computer model and those from the measurements of the hits on a hailpad. The overlapping is a common phenomenon for the computer simulation and the dents on a real hailpad. Therefore, it is expected that the error in both cases will be of the same order of magnitude. However, the dents on the pads are complex since the real hailstones are not spherical. This fact makes the identification and resolution of dents difficult and therefore the actual error could be considerable higher than the error from the simulation. Besides, the elliptical dents –more similar to the actual case- imply that the hailed area is higher for a given value of *r*. In future papers we will report the relationship between the hailed area and the overlapping of the dents and therefore with the measurement error.

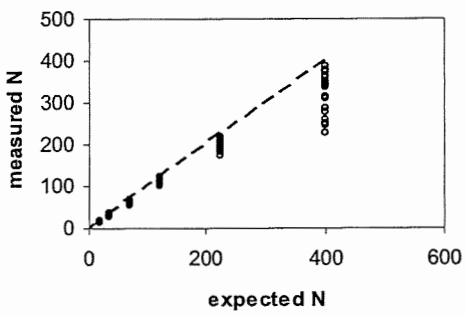

Fig. 5. *N* measured value vs. the expected value (from the computer model).

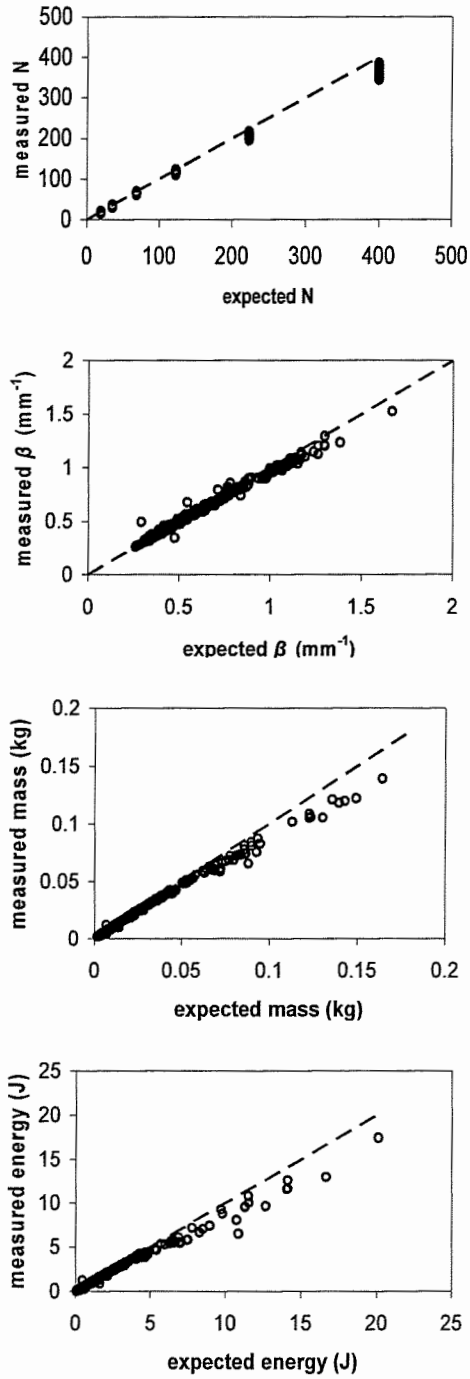

Fig. 6. Measured vs. expected values for *N*, *β*, *M* y *E*.

Last but not least, we must study the relation between the estimated errors from the computer model and those from the measurements of the dents on a hailpad. The overlapping is a common phenomenon for the computer simulation and the imprints on a hailpad. Therefore, it is expected that the error in both cases will be of the same order of magnitude. However, the imprints on the pads are complex since the real hailstones are not spherical. This fact makes the identification and resolution of imprints difficult and therefore the actual error could be considerable higher than the error from the simulation. Besides, the elliptical imprints – more similar to the actual case- imply that the hailed area is higher for a given value of r. In future papers we will report the relationship between the hailed area and the overlapping of the imprints and therefore with the error on the measurement.

5. CONCLUSIONS

- The overlapping of hail prints on a hailpad reduces the number of hail dents measured especially for smaller hailstones.
- The extensive properties (N dependent) such as mass or energy are also smaller -sometimes even much more smaller.
- However, there is not an appreciable variation on the β parameter for the exponential calculated by the method of moments.

ACKNOWLEDGEMENTS

The authors would like to thank Antonio M. Ortín for his help on the computer models and the figures enclosed. We would also like to thank Dr. Pedro Gago, for translate this article into English. The present work was supported by the Junta de Castilla y León (Grant LE53/03).

REFERENCES

Dessens, J. and R. Fraile, 1994: Hailstone size distributions in southwestern France. *Atmos. Res.*, **33,** 57-73.

Dessens, J., R. Fraile, V. Pont and J.L. Sánchez, 2001: Day-of-the-week variability of hail in southwestern France. *Atmos. Res.*, **59-60,** 63-76.

Fraile, R., A. Castro and J.L. Sánchez, 1992: Analysis of hailstone size distributions from a hailpad network. *Atmos. Res.*, **28,** 321-326.

Giaiotti D, E. Gianesini and F. Stel, 2001: Heuristic considerations pertaining to hailstone size distributions in the plain of Friuli-Venezia Giulia. *Atmos. Res.*, **57,** 269-288.

Long, A.B., R.J. Matson and E.L. Crow, 1980: The hailpad - materials, data reduction and calibration. *J. Appl. Meteorol.*, **19,** 1300-1313.

Rinehart, R.E., 1983: Out-of-level instruments: errors in hydrometeor spectra and precipitation measurements. *J. Climate Appl. Meteorol.*, **22,** 1404-1410.

Vinet, F, 2001: Climatology of hail in France. *Atmos. Res.*, **56,** 309-323.

THEORY OF HOMOGENEOUS FREEZING NUCLEATION BASED ON NEW SIZE DEPENDENT SURFACE FREE ENERGY AND MEASURED VAPOR PRESSURE OF SUPERCOOLED WATER

Norihiko Fukuta

Department of Meteorology, University of Utah, Salt Lake City, UT 84112-0110, USA

1. INTRODUCTION

Cirrus clouds are known to form in large amounts during the activity of frontal cumulonimbi through rapid conversion of the cloud droplets into ice crystals via homogeneous freezing nucleation. While the cirrus crystals thus generated are inefficient in generation of precipitation, they contribute significantly to the earth's radiative balance. It is, therefore, important to understand their formation mechanism or homogeneous freezing nucleation, the only mechanism of homogeneous nucleation known to occur naturally in the atmosphere.

Homogeneous nucleation involves interaction between the free energy of the mother phase, and that arises from the change of the total surface free energy, σA, of the nucleation clusters with the size r, where σ is the surface free energy and A the surface area, respectively. The contemporary "Classical Theory" makes use of σ_∞, σ over the flat surface, and the resultant Kelvin equation of monotonic vapor pressure. Use of the equation below the critical size of the nucleus leads to a thermodynamic violation in which the vapor is allowed to spontaneously flow from the low to the high pressure in the case of homogeneous condensation nucleation. Besides, there was no thermodynamic criticality with the theory although it was basically thermodynamic. The only existing size dependence of σ (Tolman, 1949) was shown to be in conceptual error for derivation (Fukuta and Wiśniewska, 1996). In order to resolve these problems the fundamental interactions involved in the formation of the nucleus surface was clarified and a new molecular method was devised to obtain $\sigma(r)$ which led to the theoretical discovery of a maximum of the vapor pressure in universal existence (Fukuta and Guo, 2000). The maximum matched the observed value of homogeneous condensation nucleation and propelled us towards restructuring of the nucleation theory. A new nucleation theory was thus developed after re-examination of the structure of the Classical Theory, identification of the misconception, and correction of the problems (Fukuta, 2004).

In the theory of homogeneous freezing nucleation, the free energy of supercooled water is required as a function of the vapor pressure. The Classical Theory relies on the pressure given in the Smithsonian Meteorological Table, which is an extrapolation from those at high temperatures, therefore, leaving some space of uncertainty. Recently, devising a new method, we have successfully measured the vapor pressure of supercooled water with sufficient accuracy. The result shows significant deviation from the table below -20°C (Fukuta and Gramada, 2003). The new theory was applied to the homogeneous freezing nucleation in consideration with the data of the vapor pressure measurement, and results are reported below.

Corresponding author's address: Norihiko Fukuta, Meteorology Department, University of Utah, 135 S 1460 E Rm 819, Salt Lake City, UT 84112-0110; E-Mail: nfukuta@met.utah.edu

2. PROBLEM OF CLASSICAL NUCLEATION THEORY AND ITS RESTRUCTURING

The Classical Theory of nucleation makes use of the Kelvin equation for the cluster vapor pressure which was the only available formula at the time of the theoretical development and is based on σ_∞. The Kelvin equation gives monotonic increase of cluster vapor pressure with decreasing size. Under the condition of nucleation, the environmental vapor pressure, e_e, matches that of the critical embryo e_{i^*}, with the critical radius, r^*. Below r^*, the environmental vapor has to flow from the low to the high pressure of the clusters in order to grow and nucleate, a violation of the 2nd Law of thermodynamics as mentioned above.

Secondly, the nucleation current was confused with the number flux and further with the increment or the differential for two adjacent clusters, i-1 and i, i being the number of molecules in the cluster (Becker and Döring, 1935). The nucleation current must be a quotient between the total number flux and i^*, i of the critical embryo.

Thirdly, the free energy of critical embryo formation was obtained in the above treatment under the apparent influence of the Boltzmann Factor for energy state distribution whose misconception or non-existence we have recently proved. In a separate approach under the same preconception, the "Exponential Law" of cluster number density was introduced (Dufour and Defay, 1963), which is an apparent mixup between the molecular number density, n, in the chemical potential formula and the number density of the cluster.

With correction of the above three major problems, a new, steady state theory of homogeneous nucleation was

formulated as follows: The nucleation system was viewed like a plant root with hair roots that gather the nutrient molecules everywhere to contribute to the main flow without any bifurcation. As e_e exceeds e_{i*} to let ΔS^*, the critical supersaturation ratio increase, the dammed current at I^* cluster is triggered to flow out. A single dimer flow, therefore, is aligned to the critical embryo flux without bifurcation (Fukuta, 2004).

Then, the nucleation rate was obtained as

$$\begin{aligned} J &= n_{11}\beta_1^I \Delta S^* \\ &= n_{11}\beta_1^I\left[\exp\left(\frac{\Delta\mu_e}{kT}\right) - \exp\left(\frac{\Delta\mu_{i*}}{kT}\right)\right] \\ &= n_{11}\beta_1^I \exp\left(\frac{\Delta\mu_{i*}}{kT}\right)\left[\exp\left(\frac{\Delta\mu^*}{kT}\right) - 1\right], \end{aligned} \tag{1}$$

where

$$\Delta\mu_{i*} = kT\,\ell n\,(e_{i*}/e_\infty),$$

$$\Delta\mu_e = kT\,\ell n(e_e/e_\infty),$$

$$\Delta S^* = \frac{e_e - e_{i*}}{e_\infty} = S_e - S_{i*},$$

and

$$n_{11} = \sqrt{2}\left(\frac{N_1}{2}\right)^2 (2r)^2\sqrt{\frac{8\pi kT}{m}},$$

is the collision frequency of single molecules, N_1, m, k, and T the number density of single molecules, the mass of water molecule, the Boltzmann constant and the absolute temperature, respectively. It should be pointed out that

$$\left[\exp\left(\frac{\Delta\mu^*}{kT}\right) - 1\right] \gtrless 0,$$

or

$$J \gtrless 0.$$

For the free energy of embryo formation, ΔF, the condition $\partial\Delta F/\partial r = 0$ merely corresponds to a local equilibrium or so-called Kelvin particle, and that of the critical embryo in the new theory is given by $\partial^2(\Delta F)/\partial r^2 = 0$ coupled with $\partial\Delta F/\partial r = 0$, or the inflection point, resolving the 2nd Law violation of the Classical Theory.

The rate of homogeneous freezing nucleation may now be expressed as

$$J_f = \frac{n_L kTf}{h}\left[\exp\left(\frac{\Delta\mu_L}{kT}\right) - \exp\left(\frac{\Delta\mu_{i*}}{kT}\right)\right], \tag{2}$$

where n_L, f, and h are the number density of water molecules in the liquid phase, f the resistance factor to establish a steady nucleation current at the dimer and the Planck constant, respectively,

$$\Delta\mu_L = kT\,\ell n\frac{e_w}{e_i}, \tag{3}$$

where e_w and e_i are vapor pressure of supercooled water and that of ice, respectively, and

$$\Delta\mu_{i*} = \frac{\partial(\sigma A)}{\partial V}v_1 \text{ at } i = i^*, \tag{4}$$

where σ, A, v_1 and V are the surface free energy at liquid/solid or L/S interface, the surface area of cluster, the molecular volume in ice phase and the volume, respectively. kT/h is the number of interactions per molecule per second.

3. VAPOR PRESSURE OF SUPERCOOLED WATER

Vapor pressure is a measure of chemical potential whose contribution to the homogeneous freezing nucleation was described above. By means of a specifically designed dewpoint hygrometer, the vapor pressure of supercooled water was measured down to about −38.5°C, the threshold of the homogeneous freezing nucleation (Fukuta and Gramada, 2003). The measured data showed a significant deviation from the table value below about −20°C. The ratio is given in an empirical form as

$$\begin{aligned} e_M/e_T = {} & 0.9992 + 7.113\times10^{-4}\chi - 1.847\times10^{-4}\chi^2 \\ & + 1.189\times10^{-5}\chi^3 + 1.130\times10^{-7}\chi^4 \\ & - 1.743\times10^{-8}\chi^5, \end{aligned} \tag{5}$$

where subscripts M and T stand for measured and table, $\chi = t + 19$, and t is the temperature in degrees Celsius.

Figure 1 shows comparison of the latent heat of fusion, L_f, between the measured and the Smithsonian Meteorological Table values as a function of temperature, and some relevant thermodynamic properties of supercooled water are listed for the temperature range below −20°C in Table 1.

4. NEW THEORY AND MEASUREMENT IN HOMOGENEOUS FREEZING NUCLEATION AND DISCUSSION

The new theory of homogeneous freezing, Eq. (2), may now be tested in the light of the measured vapor pressure data of supercooled water and the temperature threshold of the freezing nucleation. However, σ_{LS}, the surface free energy at water/ice interface in Eq. (4) is expected to vary rather drastically with temperature due to rapid $e_{W,M}$ reduction as T lowers. It is necessary to estimate σ_{LS} from another source. In this regard, Antonow's rule (Antonow, 1907) may be used,

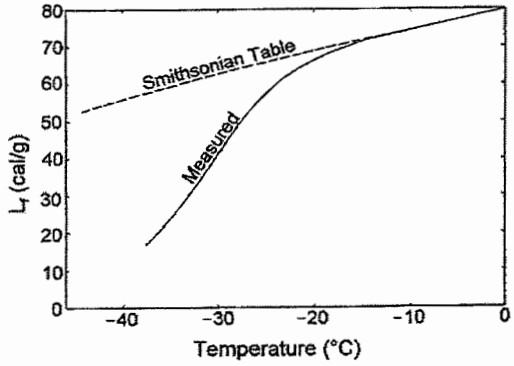

Fig. 1. Comparison of latent heat of fusion between the measured and the Smithsonian Meteorological Table values as a function of temperature.

Table 1. List of thermodynamic properties of supercooled water below -20°C.

T (°C)	$e_{w,M}$ (hPa)	$e_{w,T}$ (hPa)	$e_{i,T}$ (hPa)	$L_{f,M}$ (cal/q)	$L_{f,T}$ (cal/q)
-20	1.250	1.254	1.032	66.4	69.0
-25	0.796	0.807	0.632	58.0	
-30	0.487	0.509	0.380	41.5	63.0
-35	0.288	0.314	0.223	24.1	

$$\sigma \propto L. \tag{6}$$

It is an approximate relationship corresponding to the condition of $\cos\theta = 1$ or $\theta = 0$, θ being the contact angle at the three phase boundary. The rule holds better for temperature variation of $\sigma_{LS} \propto L_f = f(T)$, where subscripts L and S stand for liquid and solid, respectively, and is applied in this mode, with $\sigma_{LS} = 3.48 \times 10^{-2}$J m^{-2} at 0°C.

Secondly, the nucleation rate in Eq. (2) is expressed as an exponential function of $\Delta\mu$, but $\Delta\mu$ and the exponential expression are proportional, non-linear though, so that $\Delta\mu$ can be used to test the trend of two exponential terms, i.e., $\exp(\Delta\mu_L/kT)$ and $\exp(\Delta\mu_{i^*}/kT)$, under a given temperature. $\Delta\mu_{i^*}$ is evaluated based on the properties of the critical embryo of homogeneous condensation nucleation, i.e., the capillary pressure maximum of 2×10^8Pa with $\sigma_\infty = 7.57\times10^{-2}$Jm^{-2}, σ_∞ being σ of flat surface, and $I^* = 13$. $\sigma_{i^*} \approx 0.31\ \sigma_\infty$, $S_{i^*} = 5$.

Figure 2 shows comparison for the chemical potential difference between supercooled water and ice, $\Delta\mu_L$ and that between the critical embryo and the flat surface of ice in water, $\Delta\mu_{i^*}$, as a function of temperature for cases using table (T) and measured (M) values. Both $\Delta\mu_{i^*}$

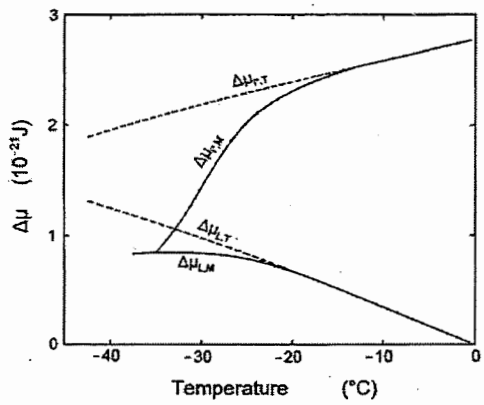

Fig. 2. Comparison of $\Delta\mu_L$ and $\Delta\mu_{i^*}$ computed with table (T) and measured (M) values as a function of temperature.

evaluations are based on the critical embryo conditions, i.e., for hexagonal closest molecular packing with Antonow's rule or the relationship (6) at L/S interface with $L_{f,T}$ for $\Delta\mu_{i^*,T}$ and $L_{f,M}$ for $\Delta\mu_{i^*,M}$.

In the figure, it may be seen that $\Delta\mu_{L,M}$ and $\Delta\mu_{i^*,M}$ intersect each other slightly above the homogeneous freezing point of -38.5°C, while $\Delta\mu_{L,T}$ and $\Delta\mu_{i^*,T}$ appear to cross at around -60°C. The main reason for the former intersection to occur just above the freezing point is rapid decrease of the $\sigma_{LS,M}$ term, with temperature decrease which is estimated from L_f at 0°C by means of Antonow's rule and applied to the new nucleation theory. $\sigma_{LS,\infty}$ taken at 0°C, 3.48×10^{-2}J m^2 should be reasonable in view of the Young-Dupre equation

$$\sigma_{VS} = \sigma_{LS} + \sigma_{VL} \cos\theta, \tag{7}$$

where V stands for vapor, with $\sigma_{VL} = 7.57 \times 10^{-2}$J m^{-2} and $\sigma_{VS} = 10.9 \times 10^{-2}$J m^{-2} (Ketcham and Hobbs, 1969) giving $\sigma_{LS,\infty} = 3.33 \times 10^{-2}$J m^{-2} at the temperature with $\theta = 0$. There are some evidences that θ has a small but finite value which tends to increase this value. A range of $\sigma_{LS,\infty} = 2.4\text{-}3.0 \times 10^{-2}$J m^{-2} is the choice of Pruppacher and Klett (1978) at 0°C.

Application of Antonow's rule to temperature variation of $\sigma_{LS,\infty}$ reduces the value by 70% to 1.05×10^{-2}J m^{-2} at -35°C, and the value for the critical embryo of i*, $\sigma_{LS,i^*} = 0.31\sigma_{LS,\infty} = 0.33 \times 10^{-2}$J m^{-2} which is only 10% of $\sigma_{LS,\infty}$ at 0°C. $\sigma_{LS,\infty}$ at -40°C was previously estimated to be 1.7-2.3 $\times 10^{-2}$J m^{-2} (Pruppacher and Klett, 1978), which obviously did not include the effect of recent vapor pressure measurement of supercooled water (cf. Table 1). Temperature variation of $\sigma_{LS,\infty}$ is parallel to that of L_f, and choice of the former at 0°C hardly shifts the intersection

between $\Delta\mu_{L,M}$ and $\Delta\mu_{i^*,M}$. The match between the intersection and the observed homogeneous freezing point gives a verification for combination of the new nucleation theory and the measurement. This can be seen from the extrapolated intersection between $\Delta\mu_{L,T}$ and $\Delta\mu_{i^*,T}$ within the framework of the new theory which far deviates from the homogeneous freezing point.

The above agreement between the new nucleation theory of homogeneous freezing, combined with the new data of vapor pressure measurement of supercooled water, and the known homogeneous freezing point suggests that homogeneous freezing nucleation of solution droplets may be described along the same line of treatment with chemical potential lowering due to the solute in $\Delta\mu_L$ and accompanying surface free energy variation in $\Delta\mu_{i^*}$. The lack of reliable vapor pressure data of supercooled water below the homogeneous freezing point may present some problems for the effort.

5. CONCLUSION

It is concluded that the agreement between the new nucleation theory of homogeneous freezing incorporating the vapor pressure measurement of supercooled water and the known homogeneous freezing nucleation point gives support for authenticity to both theory and measurement.

Acknowledgements

This study was partially supported by NSF under Grant ATM 0094909.

References

Antonow, G.N., 1907: Sur la tension superficille a la limite de deux couches. *J. Chim. Phys.*, **5**, 372-385.

Becker R., and W. Döring, 1935: Kinetische Behandlung der Keimbildung in übersättigen Dämpfen. *Ann. Phys., Lpz.*, **24**, 719-752.

Dufour, L., and R. Defay, 1963: *Thermodynamics of Clouds*. Academic Press, New York, 255 pp.

Fukuta N., and M. Wiśniewska, 1996: Molecular theory of ultramicro clusters and nucleation. I. The surface free energy. Proc. 14th International Conference on Nucleation and Atmospheric Aerosols, Helsinki, Finland, 26-30 August 1996, 212-215.

Fukuta, N., and G. Guo, 2000: Thermodynamic properties of molecular clusters in nucleation. Proc. 15th Internat. Conf. Nucleation and Atmos. Aerosols, Rolla Missouri, 6-11 August 2000, 233-236.

Fukuta, N., and C.M. Gramada, 2003: Vapor pressure measurement of supercooled water. *J. Atmos. Sci.*, **60**, 1871-1875.

Fukuta, N., 2004: Restructuring nucleation kinetics based on new size-dependent surface free energy. Proc. 16th Internat. Conf. Nucleation and Atmos. Aerosols, Kyoto, Japan.

Ketcham, W.M., and P.V. Hobbs, 1969: An experimental determination of the surface energies of ice. *Phil. Mag.*, **19**, 1161-1173.

Pruppacher, H.R., and J.D. Klett, 1978. *Microphysics of Clouds and Precipitation*, D. Reidel Pub. Co., Boston, 714 pp.

Tolman, R.D., 1949: The effect of droplet size on surface tension. *J. Chem. Phys.*, **17**, 333-337.

ASSESSMENT AND TUNING OF THE BEHAVIOR OF A MICROPHYSICAL CHARACTERIZATION SCHEME BASED ON RADAR POLARIMETRIC VARIABLES

M. Galletti[1], P. P. Alberoni[1], and V. Levizzani[2]

[1] A.R.P.A. Emilia Romagna – Servizio IdroMeteorologico, 40122 Bologna, Italy
[2] ISAC – CNR, 40129 Bologna, Italy

1. INTRODUCTION

Considering the scientific evidence accumulated over the last decade, radar meteorologists made it clear that polarimetry will play a fundamental role in the forthcoming use of weather radars. Polarimetric radar data are relevant and have potential application in many diverse fields from improving quantitative precipitation estimates to identification of scatterers' nature and type, up-to improving initial conditions and constraints in numerical models for short term forecasts. Zrnic and Ryzhkov (1999) give a summary of the state-of-the-art of polarimetry for weather surveillance radar.

A never-ending task such as the best estimation of the rain pattern will benefit from polarimetric information. Indeed, the correct classification of the prevailing bulk hydrometeor type within a radar resolution volume should be a prerequisite of any quantitative rain-retrieving scheme. Further, the classifications is also useful for warning purposes and for validation of non-hydrostatic models where the physical parameterizations are so advanced that major hydrometeor species are represented.

Most of the work in this field is based on the use of S-band data, but the prospects of the deployment of polarimetric radars in Europe motivates the research community to increase work at shorter wavelengths. Radar data taken at C-band or X-band are affected by attenuation and resonance (see among others May et al. 1999, Zrnic et al. 2000). The difficulties in trying to identify the bulk hydrometeor types within a radar resolution volume are amplified by propagation effects at C band. We refer chiefly to incomplete understanding of radar signatures, ambiguities in hydrometeor classes, occurrence of artifacts in the data, and uncertainties in radar calibration.

For this reason particular attention and efforts should be addressed to adapt procedures from S band and validate these at C band. In this paper, we use the scheme developed at the National Severe Storms Laboratory (hereinafter referred to as NSSL scheme), with a reduced set of polarimetric variables (Z, ZDR) collected at C band.

Corresponding author's address: Pier Paolo Alberoni, Servizio Idrometeorologico, ARPA, Bologna, 40122, Italy; E-Mail: palberoni@smr.arpa.emr.it

2 HYDROMETEORS CLASSIFICATION SCHEME

The NSSL scheme is based on fuzzy logic and the reader should refer to Straka et al. (2000) and Zrnic et al. (2001) for an exhaustive introduction to it. In brief, let us say that it is based on a combination of weighting (membership) functions associated with a particular hydrometeor type. These are two-dimensional functions, the first argument being one of the polarimetric variables and the other the reflectivity factor Z. The classification is accomplished by taking the highest value of the combination of weighting functions for each image pixel.

The original version of the NSSL scheme uses four different radar variables plus the temperature profile (to remove certain ambiguities). The variables are: reflectivity (Z), differential reflectivity (ZDR), specific differential phase (KDP) and the cross-correlation coefficient between horizontally and vertically polarized waves (ρhv).

Currently, there are 11 hydrometeor classes that build on the synthesis by Straka et al. (2000):

- Light rain (LR);
- Moderate rain (MR);
- Heavy rain (HR);
- Rain dominated by large drops (LD);
- Rain/hail mixture (RH);
- Graupel and/or small hail (GSH);
- Hail (HA);
- Dry snow (DS);
- Wet snow (WS);
- Horizontally oriented ice crystals (HIC);
- Vertically oriented ice crystals (VIC).

For a fixed Z a trapezoidal membership function over a polarimetric variable describes the valid range associated with each specific bulk hydrometeor type. Finally a weight coefficient defines the relative importance of (confidence in) each variable.

The NSSL scheme is designed to take advantage of the presence of all available polarimetric variables and also to work with a reduced set of these. As discussed in Zrnic et al. (2001), the most discriminating variables are the reflectivity factor and the differential reflectivity. Based on this fact, we expect to obtain reasonable results with our C-band polarimetric radar, which provides the two most significant variables for the classification.

With such a reduced set we are able to study how sensitive the algorithm is to the possible set of the

temperature weight (W_t), to the threshold value (S), and to their interralationship.

3. OVERALL DESCRIPTION OF THE BEHAVIOUR

In order to assess the sensitivity of the scheme to small, if not infinitesimal, variations of the temperature weight and the threshold value, we consider a "representative" convective event. The reflectivity and differential reflectivity are displayed in Fig 1 and Fig 2.

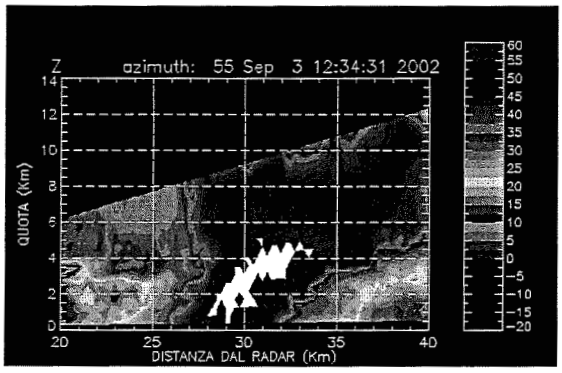

Figure 1 – 3 September, 2002; convective event observed by the SPC radar, the reflectivity is reported in gray scale

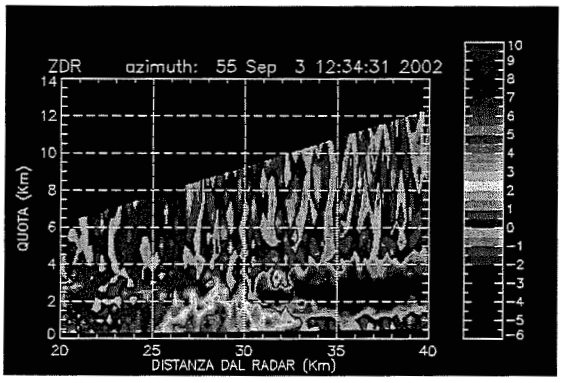

Figure 2 – Same as in Fig. 1, but for the differential reflectivity.

A direct application of the classification scheme with the "natural" values of S (S=0.5) and W_t (W_t=1.0) reproduces well known problems (see Fig. 3) already documented in other works:

- The attenuation cone behind the main convective core is filled with hail;
- Too many ice crystals identified at the highest levels.

These are, of course, not realistic in terms of cloud microphysics. We refer to this type of image as "spurious image" (SI).

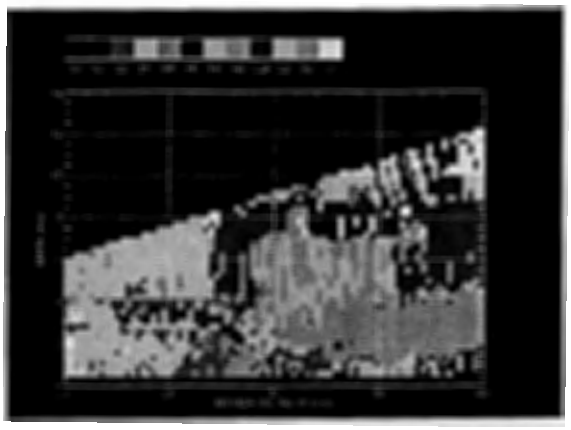

Figure 3 – Hydrometeor classification for the data in Fig. 1 and Fig. 2. (S=0.5, Wt=1.0)

Further, some pixels are assigned hydrometeors that are in contrast with the environmental temperature. Indeed, we note the presence of ice crystals close to the ground and moderate rain at roughly 8km above ground.

A decreasing of the temperature weight causes a transition in the behavior of the algorithm. The attenuated area is now unclassified and also the ice crystal pixels have diminished (see Fig. 4). Note that the pixels which were wrongly classified are now unclassified. On the same stream, also the area close to the base of the convective core is now partially classified as LD and partially unclassified.

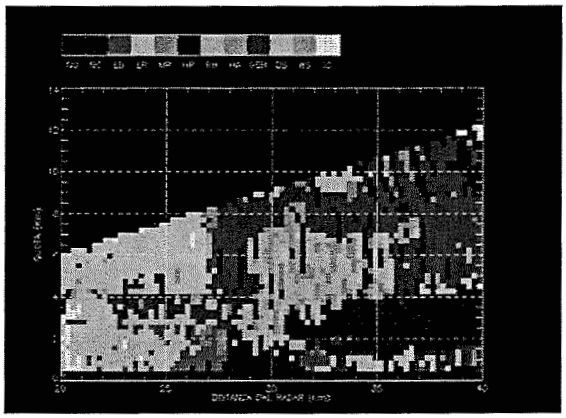

Figure 4 – Hydrometeor classification for the data in Fig. 1 and Fig. 2. (S=0.5, Wt=0.8)

This transition is very sharp and its effect does not increase even when the temperature weight decreases to very low values (Wt=0.4 or lower). If the weight value gets too low the algorithm looses its thermal characterization with obvious negative impact

on the classification itself. We will refer to this behavior as Thermal effect (TE).

These sensitivities and behaviors of the classification algorithm do not depend on the specific image under consideration: similar images for the same couples of S and W_t, were reproduced for convective and stratiform events. This suggests that these observed characteristics are intrinsic properties of the scheme.

4. ANALYSIS OF THE TRANSITION TO SI TYPE

From an analysis of the images produced using a variety of couples of the "driving parameters" it is clear that the transition between a reasonable classification and a classification with the SI characteristics takes place over a well defined sharp boundary. Examples of such a boundary are the couples in Table 1.

	S	W_t
Reasonable	0.48	0.92
SI	0.48	0.93
Reasonable	0.46	0.85
SI	0.46	0.86

Table 1 – Results of the classification scheme with different values of the driving parameters.

A close look to the algorithm reveals that the temperature shape functions are such that for each temperature there is at least one hydrometeor type that could exist in such environment.

As a direct consequence of this constraint there is always some hydrometeor type that gains the maximum score from the thermal component of the algorithm. If in such cases the acceptance threshold, which is the combination between the thermal and the polarimetric components of the algorithm, is lower than the thermal one, we will accept as classified some pixels without any polarimetric agreement. This means that, for examples, if W_t = 1 then we should have $S > 0.5$.

Such behavior could be deducted from the mathematical expression of the algorithm. In this configuration the acceptance threshold could be simplified as:

$$S > \frac{k_2 \cdot Wt}{1 + Wt}$$

where K_2 is the value of the temperature shape function.

In the range of valid temperature [-40, +40] °C we can invert this equation to extract a function that describes the variation of the critical temperature weight as a function of the selected acceptance threshold:

$$Wc = \frac{S}{1 - S}$$

This function is displayed in Fig. 5.

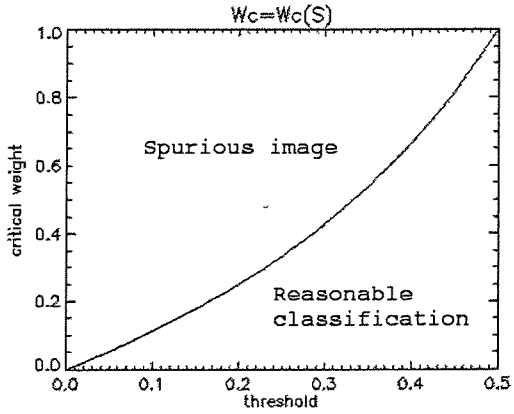

Figure 5 – Boundary of the transition between the SI configuration (upper part of the diagram) and a reasonable classification. The curved boundary represents the variation of the critical temperature weight as a function of the acceptance threshold.

5. ANALYSIS OF THE TRANSITION TO TE TYPE

From the analysis of the images examined so far it can be stated that the TE configuration is always present if the acceptance threshold is below 0.5 regardless of the thermal weight and disappears if we choose a couple like S=0.51 and Wt=1.0.

We need to understand the basic rules of such behavior and further to analyze the TE transition for values of acceptance threshold above 0.5.

For this reason we focused our attention on a convection case using different couples of parameters. As for the SI transition the TE transition happens across a very sharp boundary. Some examples of such transition are displayed in Fig. 6 and Fig 7.

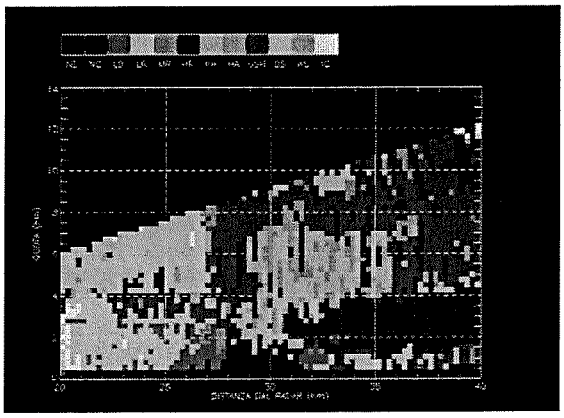

Figure 6 – Hydrometeor classification for the data in Fig. 1 and Fig. 2. (S=0.55, Wt=0.81).

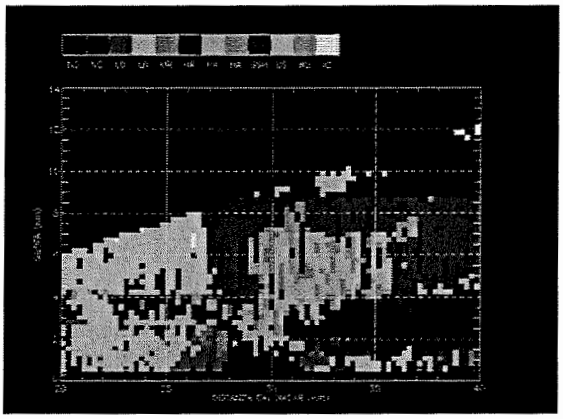

Figure 7 – Hydrometeor classification for the data in Fig. 1 and Fig. 2. (S=0.55, Wt=0.82)

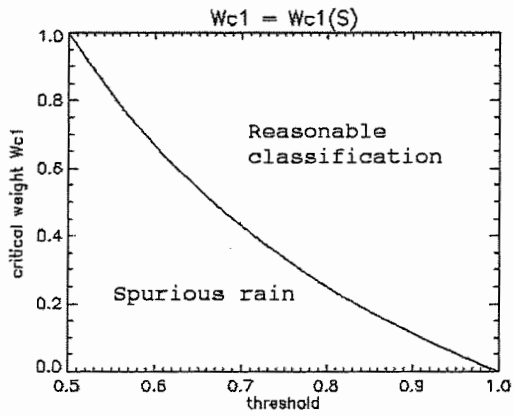

Figure 8 – Boundary of the transition between the TE configuration (lower part of the diagram) and a reasonable classification. The line represents the variation of the critical temperature weight as a function of the acceptance threshold.

In a broad sense the TE configuration is the analog of the SI configuration. In such case some hydrometeors are classified only on the base of the polarimetric component without any contribution from the thermal component. As for the SI case we have to draw upon the mathematical formulation of the algorithm and impose the acceptance threshold be greater than the single polarimetric component. The equation is thus:

$$S > \frac{k_1}{1+Wt}$$

where K_1 is the value of the polarimetric shape function.

If we invert the equation, we obtain the variation of the critical weight as a function of the acceptance threshold for the TE transition (Fig. 8).

6. CONCLUSION

The classification scheme has proved to be robust enough to be used with a reduced set of polarimetric variables provided a careful choice of the parameters is done.

In this configuration a reasonable classification will be obtained. As a counter effect the number of unclassified pixels will increase. It is clear that the correct choice of parameters depends on the type of application and is in the hand of the analyst.

Any sensitivity to the parameters could be avoided by combining the terms with products of them that automatically guarantee the simultaneous contribution of all the terms to the overall acceptance value. This approach, however, has been less investigated in the literature and operational implementations in the US make use of sums rather than products.

7. ACKNOWLEDGEMENTS

This work is partially supported by CARPE DIEM, a research project supported by the European Commission under the 5th FP (Contract N° EVG1-CT-2001-0045), and form the GNDCI through the project RAM.

8. REFERENCES

May, P. T., T. D. Keenan, D. S. Zrnic, L. D. Carey, and S. A. Rutledge, 1999: Polarimetric radar measurements of tropical rain at a 5 cm wavelength. *J. Appl. Meteor.*, **38**, 750-765.

Straka, J. M., D. S. Zrnic, and A. V. Ryzhkov: 2000: Bulk hydrometeor classification and quantification using polarimetric radar data: synthesis of relations. *J. Appl. Meteor.*, **39**, 1341-1372.

Zrnic, D. S., and A. V. Ryzhkov, 1999: Polarimetry for weather surveillance radars. *Bull. Amer. Meteor. Soc.*, **80**, 389-406.

Zrnic, D. S., T. D. Keenan, L. D. Carey, and P. T. May, 2000: Sensitivity analysis of polarimetric variables at a 5-cm wavelengthn rain. *J. Appl. Meteor.*, **39**, 1514-1526.

Zrnic, D. S., A. V. Ryzhkov, J. M. Straka, Y. Liu, and J. Vivekanandan, 2001: Testing a procedure for automatic classification of hydrometeor types. *J. Atmos. Oceanic Technol.*, **18**, 892-913.

MICROPHYSICAL ANALYSIS INSIDE A SUPERCELL

E. García-Ortega, L. López, J. L. Marcos and J. L. Sánchez

Lab. de Física de la Atmósfera. IMA. Universidad de León. Spain.

1. INTRODUCTION

Hail storms are frequent occurrences during the summer months on both sides of the Pyrenees. To the south, the Spanish region known as the Ebro Valley is one of the areas, in Europe, with more cases of severe convective phenomena (figure 1). The temperature of cloud bases in summer storms is usually above 9^oC and the cloud tops are at an altitude where the temperature may be around -50^oC. These storms are of the warm-based cloud type (Sánchez et al. 1999), and consequently, they have a greater potential for producing a significant amount of liquid water content. Strong updrafts may occur inside the feeder clouds, taking the droplets to higher and cooler regions. Some of these storms can develop into supercells. Large size and intensity characterize supercell storms, where the updraft and downdraft circulations coexist in a nearly steady-state form for periods of 30 $min.$ or longer (Cotton and Anthes 1989). Browning (1977) distinguishes between a multicell storm, with growing daugther clouds, and a supercell with no discrete daughter cells, by the visual appearance of feeder cells. Vasiloff et al. (1986) suggest that if the distance between successive updrafts cells is much smaller than the updraft diameter, this is a supercell. This type of storm represents 4% of storms in this region (Castro et al. 1992). However, they are a major contributor to hail damage. Hailstones are formed when either graupel particles or supercooled drops grow by accreting supercooled cloud droplets (Rogers and Yau 1996).

Within the frame of the EURICE Program (EUropean Research on aircraft Ice CErtification), in the summer of 1997 a microphysical analysis inside the flanks of a supercell storm, was carried out in order to study the distributions of supercooled droplets in regions where the temperature was around -5^oC, that is, a zone where water is found both in its liquid and solid phases.

Correponding author's address: José Luis Sánchez, Fac. de CC. BB. y Ambientales. Universidad de León. 24071 León. Spain; e-mail: dfqjsg@unileon.es.

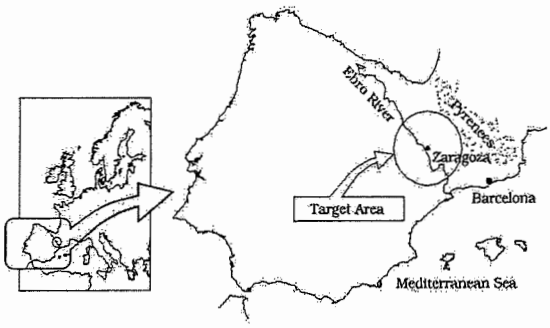

FIG. 1. *Target area*

2. EXPERIMENTAL DESCRIPTION

Observations of aircraft-sampled storm were carried out by a C-212 equipped with a Forward Scattering Spectrometer Probe (FSSP) for measuring cloud droplets in the range $5 - 95$ μm, with 15 channels, each 6 μm wide. In addition, the aircraft was equipped with a PMS Optical Array Probe (OAP) 2D2-C, with 30 channels, used to obtain the hydrometeor distributions, covering diameters from $25 - 1075$ μm, with 35 μm resolution. The results found by Baumgardner and Korolev (1997) and Korolev et al. (1998) show that the concentration values obtained by the OAP for sizes below 100 μm are affected by a high degree of uncertainty. Because of this, the data provided by the first two channels have not been taken into account, thus measuring the spectrum between 95 μm and 1075 μm. This size range provides an extension to the FSSP spectrum. The 2-D image data were registered and classified distinguishing between drops, ice crystals and graupel. Artifacts were removed.

The LWC was measured by means of the PMS CSIRO King. The temperature of the sampling areas was registered by a Rosemont Probe.

A C-band radar located close to Zaragoza allowed for a follow-up the thunderstorms. The information registered by the radar was updated every 3.5 minutes and digitalized. The TITAN radar software (Dixon and Wiener 1993) provided images of the storm cells with a spatial resolution of $1 \times 1 \times 1$ km. The values

of the radar variables were stored for later analysis.

3. OBSERVATIONS

Researchers often refer to supercell storms as severe right storms because the major low-level inflow is on the right flank of the storm relative to its direction of motion (Cotton and Anthes 1989). In the case analyzed here the low-level inflow comes from the east, that is from the Mediterranean Sea, whereas the high-altitude wind comes from southeast. The storm studied was formed 50 km to the SSE of Zaragoza and it lasted for 110 min. The maximum reflectivity factor in the core of the storm, Z_{max}, was over 53 dBZ for more than 90 min, reaching up to 57 dBZ. During its development the storm followed a track towards the north causing intense hail precipitation.

The microphysical measurements were taken during the stage of maturity of the storm, with $Z_{max} = 56\ dBZ$ and the echo top was at 11 km. Consequently, the microphysical measurements were carried out at moments of very active growth processes.

Figure 2 shows a PPI composite image and the track of the aircraft during the process. The sampling has been divided into 7 time intervals according to the microphysical characteristics of the particles detected in the OAP 2-D images.

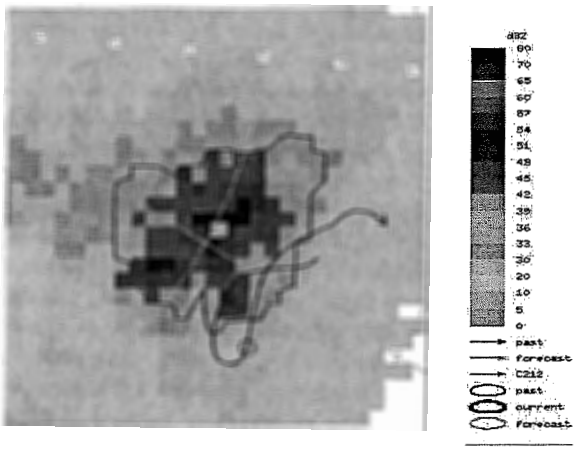

FIG. 2. *PPI composite of supercell area and flight track.*

3.1 Concentration and liquid water content

The top of Figure 3 shows the time series of the cloud droplets concentration measured by the $FSSP(N_t\ FSSP)$ and the hydrometeor concentration measured by the OAP ($N_t\ OAP$). The bottom shows the time series of LWC measured by the CSIRO King (LWC_K) and the LWC estimated using the measurements of the FSSP (LWC_P).

The OAP 2-D images have proved that the concentrations of hydrometeors of any size vary greatly from one region to another. When in a region hydrometeors of $D > 100\ \mu m$ predominate, the presence of droplets is reduced and the value of $N_t\ FSSP$ decreases. Figure 3 shows that when there is an increase in $N_t\ FSSP$ there is a decrease in $N_t\ OAP$. In fact, it has been demonstrated that in the areas where cloud droplets predominate, the OAP 2-D images show an almost complete absence of hydrometeors with a diameter of more than 100 μm.

The results indicate that the spatial distribution of cloud droplets and other larger hydrometeors is not homogeneous in the study zone. There is a heterogeneous distribution of particles with different characteristics. This illustrates the existence of zones where different growth processes predominate and affect water particles in liquid or solid phases.

As far as the liquid water content is concerned, it has been noted that the values measured by the CSIRO King (LWC_K) are consistent with the ones calculated with the FSSP (LWC_P). However, there are some short time intervals where differences have been observed between the two. After analyzing the spectra of these intervals it was noted that there was a high concentration of droplets that are outside the optimal range of the CSIRO King (diameters between $10 - 40\ \mu m$).

Figure 3 shows that when $N_t\ FSSP$ increases, the LWC increases as well. The LWC is proportional to the cube of the diameter of the droplets. Therefore, the increase in LWC may be due either to the presence of cloud droplets with large diameters within the range of the FSSP, or to an important increase in $N_t\ FSSP$, even though the cloud droplets diameter is small. Bearing in mind the agreement between the results of the CSIRO King and the FSSP, it seems that the maximum values of LWC are due to an increase in $N_t\ FSSP$. Figure 3 shows that on several occasions $LWC > 3\ g\ m^{-3}$ with peaks of $4 - 7\ g\ m^{-3}$ in the FSSP.

3.2 FSSP and OAP distributions

The droplet size distributions (DSD) and the hydrometeor size distributions (HSD) were calculated for each interval in the study zone. The DSD fit the gamma distribution put forwards by Ulbrich (1983)

$$n(D) = N_0 D^{\mu} \exp(-\Lambda D) \qquad (1)$$

On the other hand, the HSD fit the exponential distribution (gamma case for $\mu = 0$).

The values of the parameters for DSD and HSD

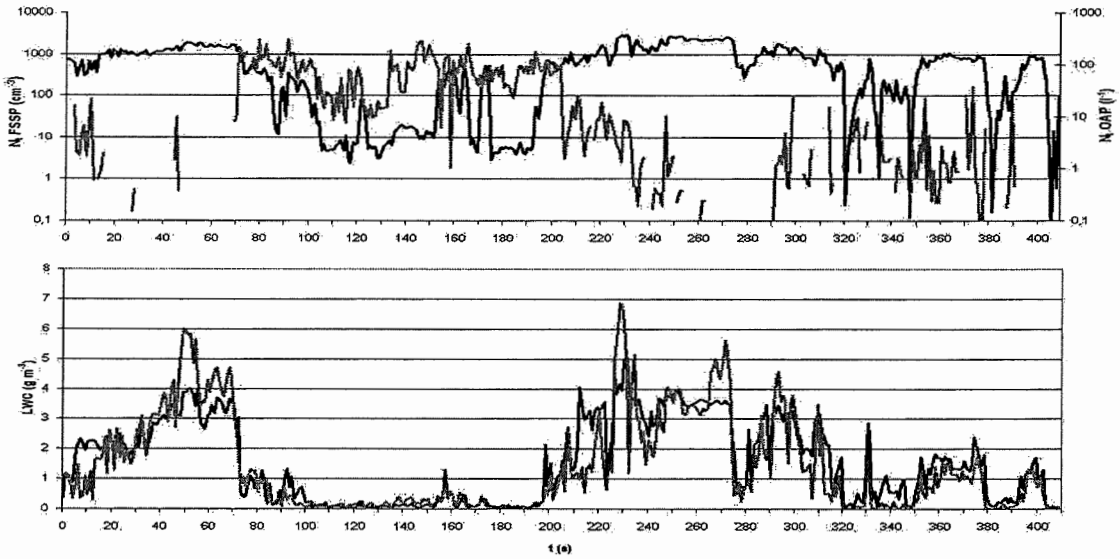

FIG. 3. *Time series of the concentration (upper plot) measured by the FSSP (N_t $FSSP$, cm^{-3}, black color) and the OAP (N_t OAP, l^{-1}, grey color). Time series of liquid water content, $g\ m^{-3}$, (lower plot) measured by the CSIRO King (black color) and the FSSP (grey color).*

TABLE 1. *Parameters of the gamma DSD — FSSP: μ, Λ (μm^{-1}) and N_t (total concentration, cm^{-3})— and exponential HSD —OAP: Λ (mm^{-1}) y N_t (l^{-1})—.*

	gamma DSD			exp. HSD	
case	μ	Λ	N_t	Λ	N_t
1	2.12	0.31	1172	2.78	2
2	1.25	0.27	346	7.14	121
3	0.28	0.11	12	7.14	38
4	0.73	0.28	110	7.69	114
5	1.31	0.40	181	6.67	74
6	3.41	0.49	1419	5.00	33
7	1.61	0.39	405	2.78	2

are shown in Table 1. The liquid water content has been calculated using the DSD,

$$LWC_D = \frac{\pi}{6}\rho N_0 \int_{D_0}^{D_{max}} D^{\mu+3} \exp(-\Lambda D)\, dD \quad (2)$$

The minimum value of LWC_D is 0.08 $g\ m^{-3}$ (case 3) and corresponds to an average FSSP concentration of 12 cm^{-3}, whereas the maximum value is 3.10 $g\ m^{-3}$ (case 1) and the cloud droplets concentration is 1172 cm^{-3}. The mean diameter, D_m, has also been calculated, as well as the medium volume diameter, D_0, defined as

$$2\int_0^{D_0} D^3 n(D)\, dD = \int_0^{D_{max}} D^3 n(D)\, dD \quad (3)$$

The mean diameter takes values between 10.8 μm (case 5) and 16.9 μm (case 3). It can be noted that the variation is small and that the mean diameter of the droplets is always below 17 μm. The medium volume diameter takes values between 14.6 μm (case 5) and 37.4 μm (case 3). In the remaining cases $D_0 < 21$ μm. This value indicates that half of the water volume is contained in droplets with a diameter of less than 21 μm.

The results concerning the sizes of the cloud droplets confirm that, at the altitude at which the measurements were carried out, the dominant growth process is the diffusion of water vapor provided by the updrafts.

4. SUPERCOOLED DROPS AND GRAUPEL PARTICLES

During the first part of the sampling the aircraft crossed a region with a strong updraft. The growth of cloud droplets by water vapour diffusion was studied in this crucial time span. Calculations show that updrafts of approximately 10 $m\ s^{-1}$ are needed to maintain the growth rate. In addition, SLD (Supercooled Large Drops) were found to be grouped in certain accumulation zones (Sánchez et al. 1999). Super-

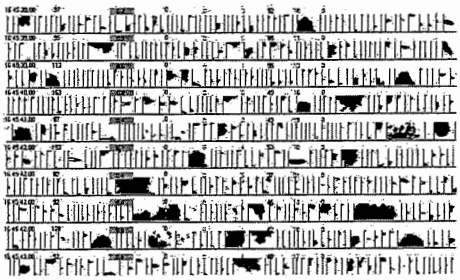

FIG. 4. *OAP 2-D images showing graupel particles (case 4).*

cooled water develops within a parcel of air containing ice crystals when the relative humidity with respect to water exceeds saturation and the condensate supply rate exceeds the bulk ice crystal mass diffusional growth rate. Some results show that the condensate supply rate increases with vertical velocity of air at a given pressure-altitude and temperature (Rauber and Tokay 1991). On the other hand, around these areas are others where important amounts of graupel is found together with small-size ice particles. In these areas, the 2-D images show a great number of ice and graupel particles (figure 4). It is a well-known fact that the presence of high concentrations of supercooled drops and graupel particles favors the formation of hail inside the storms. The 2-D images show the presence of both types of hydrometeors that can favour the hailstone growth.

Acknowledgments. The authors thank Noelia Ramón for translating the paper into proper English and Antonio Martínez for the figures. We would like to express our gratitude to the technical staff of the INTA and CLAEX for operating the C-212 and collecting the data used here. The collaboration of the many colleagues who have contributed to the success of the Project is also acknowledged. This work was supported by the CICYT through the ESP-97/1594/E, REN 2000-1210 CLI and ADV Terres de Ponent.

REFERENCES

Baumgardner, D. and A. Korolev, 1997: Airspeed corrections for optical array probe sample volumes. *J. Atmos. Oceanic Tech.*, **14**, 1224-1229.

Browning, K. A., 1977: The structure and mechanisms of hailstorms. *Meteorol. Monogr.* **16**(38), 1-43.

Castro, A., J. L. Sánchez and R. Fraile, 1992: Statistical comparison of the properties of thunderstorms in different areas around the Ebro Valley (Spain). *Atmos. Res.*, **28**, 237-257.

Cotton, W. R., and R. A. Anthes, 1989: *Storm and cloud dynamics.* Academic Press, 883 pp.

Dixon, M. and G. Wiener, 1993: TITAN: Thunderstorm Identification, Tracking, Analysis and Nowcasting- a radar-based methodology. *J. Atmos. Oceanic Tech.*, **10**, 785-797.

Korolev, A. V., J. W. Strapp and G. A. Isaac, 1998: Evaluation of the accuracy of PMS optical array probes. *J. Atmos. Oceanic Tech.*, **15**, 708-720.

Rauber, R. M., and A. Tokay, 1991: An explanation for the existence of supercooled water at the top of cold clouds. *J. Atmos. Sci.*, **48**, 1005-1023.

Rogers, R. R. and M. K. Yau, 1996: *A short course in cloud physics.* Butterworth-Heinemann, 290 pp.

Sánchez, J. L., E. García, J. L. Marcos and J. Dessens, 1999: Formation of big and giant drops inside Mediterranean convective cells. *Proc. of the EGS Plinius Conf.*, Maratea, Italy, Eur. Geophys. Soc., 57-65.

Ulbrich, C. W., 1983: Natural variations in the analytical form of the raindrop size distribution. *J. Appl. Meteor.*, **22**, 1764-1775.

Vasiloff, S., E. A. Brandes, and R. P. Davies-Jones, 1986: An investigation of the transition from multicell to supercell storms. *J. Climate Appl. Meteor.*, **25**, 1022-1036.

MICROPHYSICAL RELATIONSHIPS IN CRYSTAL-FACE ANVIL CIRRUS

T. J. Garrett*[1], H. Gerber[2], D. G. Baumgardner[3], M. Poellot[4], C. H. Twohy[5], E. M. Weinstock[6]
[1]Meteorology Department, University of Utah, Salt Lake City, Utah, USA
[2]Gerber Scientific Inc., Reston, Virginia, USA
[3]Universidad Nacional Autonoma de Mexico, Mexico City, Mexico
[4]University of North Dakota, Grand Forks, North Dakota, USA
[5]College of Oceanography and Atmospheric Science, Oregon State University, Corvallis, Oregon, USA
[6]Department of Chemistry and Chemical Biology, Harvard University, Cambridge, Massachussetts, USA

1 INTRODUCTION

Compared to water clouds clouds, little is known about relationships between microphysical properties in glaciated clouds such as cirrus. This is due in part to the relative inaccessibility of cold high clouds. But also, important concerns have been raised about how accurately we can measure ice cloud microphysical parameters. Typically, cirrus properties such as ice water content IWC and the extinction coefficient β_{ext} have been derived from size distribution measurements of either ice crystal linear dimension or cross-sectional area. This requires integrating size distributions using questionable assumptions that relate ice crystal size to shape and internal density. Second, estimates of ice crystal total number concentrations N can vary by orders of magnitude, depending on the abilities of probes to measure the smallest ice crystals <100 μm dimension. There is debate over whether high measured concentrations of small ice crystals < 50 μm across are instrument artifacts (Gardiner and Hallett, 1985; Arnott et al., 2000). Estimates of an appropriate ice crystal effective radius r_e are highly sensitive to the extent these small crystals are included in calculations.

Here we circument these issues using direct measurements of IWC and the cloud extinction coefficient β_{ext} obtained in July 2000 during the CRYSTAL-FACE experiment based from Boca Chica Key in Southern Florida. Two aircraft, the University of North Dakota Citation Cessna II and the NASA WB-57F, sampled cloudy air in the anvil ejecta from deep convective storms in an approximate 3° × 3° domain over the southern Florida Penninsula. The highest clouds were sampled at 15.2 km altitude and -78°C . Such extensive simultaneous bulk measurements of IWC and β_{ext} are unprecedented at such high altitude. Based on these measurements, we present relationships between IWC, N and β_{ext}, suitable for cloud models, that fit the parameterization

$$X = kIWC^{\alpha} \tag{1}$$

where, k and α are fitting parameters and X refers to either β_{ext} or N.

2 INSTRUMENTATION

Total ice crystal concentrations N were obtained using a Droplet Measurement Technologies (DMT) Cloud Aerosol and Precipitation Spectrometer (CAPS) (Baumgardner et al., 2002) aboard the WB-57F and combined Particle Measurement Systems (PMS) FSSP-100 and OAP-2D-C probes, and Stratton Park Engineering Company (SPEC) HVPS probes aboard the Citation. The CAPS probe spans the size range 0.5 to 1500 μm diameter. However, derived ice crystal concentrations were truncated to a lower threshold of 2 μm to be consistent with the lower limit of the Citation FSSP-100 probe. The upper measurement limit of the HVPS is 27 mm diameter. Bulk cloud measurements of the extinction coefficient β_{ext} were obtained with a Gerber Scientific Cloud Integrating Nephelometer (CIN) aboard both aircraft (Gerber et al., 2000). Bulk measurements of IWC were obtained using the Harvard University Lyman-Alpha

* *Corresponding author address:* Timothy J. Garrett, 135 S 1460 E, Room 819 Salt Lake City, UT 84112-0110; e-mail: tgarrett@met.utah.edu

Table 1: Fits to Eq. 1 based on measurements obtained in CRYSTAL-FACE anvil cirrus, sorted by 10 °C temperature intervals. A fit to results from prior studies of cirrus (Ryan, 2000) is shown for comparison.

	N			β_{ext}		
T_{mid}	k	α	r^2	k	α	r^2
-10	8.9	1.15	0.84	65	1.11	0.93
-20	11.3	1.02	0.80	116	1.17	0.92
-30	19.0	1.08	0.79	109	1.05	0.86
-40	24.0	1.08	0.83	169	1.19	0.90
-50	49.5	1.25	0.85	275	1.28	0.90
-60	268	0.95	0.90	161	0.91	0.89
-70	141	0.85	0.70	150	0.87	0.91
Ryan (2000)				10	0.67	

Total Water Probe (TWP) aboard the WB-57 (Weinstock, 1994), and the Oregon State University counterflow virtual impactor (CVI) aboard the Citation (Twohy et al., 1997). The estimated uncertainty in all bulk probe measurements was ±15%.

3 OBSERVATIONS

Ten second averages of IWC, N and β_{ext} in CRYSTAL-FACE anvil cirrus were categorized by 10 °C temperature intervals. Measurements at temperatures colder than -55 °C are taken from aboard the WB-57F, whereas measurements within warmer clouds are from aboard the Citation. The data reflect 13 days and 52 hours of in-cloud flight, and 6 days and 8 hours of in-cloud flight from the Citation and WB-57 respectively. Below -55 °C, measured IWC ranged from 0.001 to 0.2 g m^{-3}, and above -55 °C, it ranged from 0.03 to 1.5 g m^{-3}. This wide variation in IWC at a given temperature was principally because cirrus anvils evaporated as they aged (Garrett and coauthors, 2004).

Values for k and α are shown in Table 1. For both N and β_{ext}, fits to Eq. 1 accounted for more than 70% and 85% of the variance in the data, respectively. Additional, over nearly two orders of magnitude in concentration, the value of α was near unity, pointing to a nearly linear relationship between the quantities. As shown by the value of k, the magnitude of N and β_{ext} for a given IWC generally increases with decreasing temperature. By contrast, a summary of previous studies in mid-latitude and tropical clouds give relationships between the extinction coefficient and IWC generally characterized by $k \simeq 10$ and $\alpha \simeq 0.67$ (Ryan, 2000).

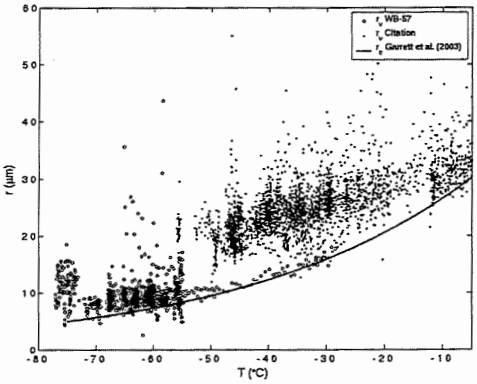

Figure 1: Mean volume radius r_v from the Citation (dots) and WB-57 aircraft (circles), derived from 10 s averages of measurements of N and IWC obtained during CRYSTAL-FACE (Eq. 2). Shown for comparison is a fit to r_e derived by Garrett et al. (2003) explaining 64 % of the variance in the data (Eq. 3) obtained from measurements of β_{ext} and IWC within the same data set.

The derived relationships between N and β_{ext} and IWC are nearly consistent with each other. To illustrate this one may calculate both an effective radius r_e and a mean volume radius r_v

$$r_v = \left(\frac{3IWC}{4\pi\rho_l N}\right)^{1/3} \tag{2}$$

$$r_e = \frac{3IWC}{2\rho_l \beta_{ext}} \tag{3}$$

Fig. 1 shows that both r_v and r_e can be expressed as a function of cloud temperature. Values range from ~5 μm to 30 μm between -75 and 0 °C. As expected, r_v is larger than r_e, but typically by less than a factor of 2. This generally good agreement between r_v and r_e suggests that measurements of bulk probe measurements of IWC and β_{ext}, and size distribution probe measurements of N, form a self-consistent data set. The values for $r_e$are in sharp contrast with many parameterizations currently in use in climate models which give r_e as a function of both IWC and T with values typically close to 30 μm (McFarquhar et al., 2003).

4 DISCUSSION

Here we show that IWC, β_{ext} and N in CRYSTAL-FACE anvil cirrus are linearly correlated at constant temperature. Compared to earlier studies (Ryan, 2000), values of β_{ext} were extremely high for a given IWC. This was because anvil ice crystals were both very small (generally <50 μm across) and numerous (as high as 300 cm^{-3}). The reason we see such comparatively high extinction here might be because low-latiude anvil cirrus are unusual. However, Ryan (2000) also included tropical anvil cirrus (e.g. Heymsfield and McFarquhar (1996)). Also, recent studies have revealed extremely small and numerous ice crystals in mid-latitude clouds (Strom et al., 1997). Instead, the discrepancy might be because earlier studies have tended to discount measurements from optical particle counter (OPC) probes that measure cloud particles <50 μm across (e.g. the FSSP-100) due to concerns about ice crystal shattering on the instrument inlet. Here, we show that OPC measurements of small crystals are remarkably consistent with bulk probe data from instruments that are insensitive to ice crystal breakup. Nearly identical instrumentation to that flown during CRYSTAL-FACE will be used in a field project scheduled for April and May, 2004 directed at Great Plains cirrus. Hopefully, this new data set will show whether similar relationships to those shown in Table 1 are found at mid-latitudes, and help resolve whether numerous small ice crystals indeed dominate the optical extinction of ice clouds.

Acknowledgments This work was supported by the NASA CRYSTAL-FACE program. The support of the NASA WB-57 and U North Dakota Citation flight crews is most gratefully acknowledged.

References

Arnott, W. P., D. Mitchell, C. Schmitt, D. Kingsmill, D. Ivanova, and M. Poellot: 2000, Analysis of the FSSP performance for measurement of small crystal spectra in cirrus. *13th International Conference on Clouds and Precipitation*, 191–193.

Baumgardner, D., H. Jonsson, W. Dawson, D. O'Connor, and R. Newton, 2002: The cloud, aerosol and precipitation spectrometer (CAPS): A new instrument for cloud investigations. *Atmos. Res.*, **59-60**, 251–264.

Gardiner, B. A. and J. Hallett, 1985: Degradation of in-cloud forward scattering spectrometer probe measurements in the presence of ice particles. *J. Atmos. Oceanic Technol.*, **2**, 171–189.

Garrett, T. J. and coauthors, 2004: In situ measurements of the microphysical and radiative evolution of a Florida cirrus anvil. *J. Atmos. Sci.*, submitted.

Garrett, T. J., H. Gerber, D. G. Baumgardner, C. H. Twohy, and E. M. Weinstock, 2003: Small, highly reflective ice crystals in low-latitude cirrus. *Geophys. Res. Lett.*, **30**, doi:10.1029/2003GL018153.

Gerber, H., Y. Takano, T. J. Garrett, and P. V. Hobbs, 2000: Nephelometer measurements of the asymmetry parameter, volume extinction coefficient, and backscatter ratio in clouds. *J. Atmos. Sci.*, **57**, 3021–3034.

Heymsfield, A. J. and G. M. McFarquhar, 1996: High albedos of cirrus in the tropical Pacific warm pool: Microphysical interpretations from CEPEX and from Kwajelein, Marshall Islands. *J. Atmos. Sci.*, **53**, 2424–2451.

McFarquhar, G. M., S. Iacobellis, and R. C. J. Somerville, 2003: SCM simulations of tropical ice clouds using observationally based parameterizations of microphysics. *J. Climate*, **16**, 1643–1664.

Ryan, B. F., 2000: A bulk parameterization of the ice particle size distribution and the optical properties in ice clouds. *J. Atmos. Sci.*, **57**, 1436–1451.

Strom, J., B. Strauss, T. Anderson, F. Schroder, J. Heintzenberg, and P. Wendling, 1997: In situ observations of the microphysical properties of young cirrus clouds. *J. Atmos. Sci.*, **54**, 2542–2553.

Twohy, C. H., A. J. Schanot, and W. A. Cooper, 1997: Measurement of condensed water content in liquid and ice clouds using an airborne counterflow virtual impactor. *J. Atmos. Oceanic Technol.*, **14**, 197–202.

Weinstock, e. a., E. M., 1994: New fast response photofragment fluorescence hygrometer for use on the nasa er-2 and the perseus remotely piloted aircraft. *Rev. Sci. Instrum.*, **65**, 3544–3554.

CHARACTERIZATION OF MIXED PHASE CLOUD AND PRECIPITATION

John Hallett

Desert Research Institute Reno, NV.

1. INTRODUCTION.

Occurrence of the mixed phase as individual particles of water or ice or as a single particle in the process of melting or freezing have long been recognized as a basic reality of many atmospheric processes. For example, the importance of the former scenario lies in rates of phase transition as the process of precipitation by growth of an ice particle from the vapor in the presence of a supercooled water cloud. The importance of the latter scenario lies in the time of persistence of a mix of water and ice present during the freezing of an individual drop either as a single entity or during accretion. The two processes are not mutually exclusive; an assembly of particles as a cloud or region of precipitation may include a fraction of particles themselves having a mix of water and ice.

Application of this knowledge is of importance at a basic level necessary in specifying the removal process through precipitation fallout. It is of major import in remote sensing by radar and satellite surveillance because of differences in dielectric properties of ice and water and the reality that the freezing or melting particle will maintain a temperature close to 0C. Further application lies in the importance of the fraction of supercooled water and ice in graupel growth and mutual electrification following scraping and bouncing of impacting ice crystals, Korolev et al 2003.

Whilst it has long been realized that aircraft icing results from accretion and freezing of supercooled drops as cloud, drizzle and rain, the possible role of mixed phase cloud in the icing process has tended to be ignored. Similarly, the implication of the presence of sequential patches of all ice and of all water along an aircraft track has not been investigated as far as the transitional scale of interfaces between such patches may lead to differing icing condition and different forms of accretion. The problem arises in part from the viewpoint of convenience of averaging over adequate path lengths as determined by the response time and sample volume of different instruments to achieve adequate statistical representation of particles, particularly larger sizes at low concentration which contribute significantly to the total mass. This discussion raises the question of a definition of the concept of a mixed phase assembly of particles in the atmosphere and raises and examines the implication for analysis of data from existing instruments and the design of future instruments for direct measurement of a mixed phase fraction and the specification and structure of the water – ice particle cloud interface.

John Hallett, Desert Research Institute, 2215 Raggio Parkway, Reno NV 89512, USA. hallett@dri.edu

2. DEFINITION AND MEASUREMENT.

Liquid water content is conveniently specified as g/m^3 to be made invariant with pressure by expressing it as a mixing ratio, kg/kg of air, to sufficient accuracy. Hence a relative fraction of ice/water may similarly be defined. Direct measurement of these quantities is nontrivial and has exercised technical skills over the last half century. Particle impaction and measurement by electrical properties as electrical conduction, electrolysis and evaporation latent heat provides direct measurement; integration over shapes and concentration of particles (as from an optical probe), together, for ice, an estimate or direct measurement of density, Hallett and Isaac, 2002. Since the density enters the vertical flux directly through the mass, and the fall velocity through $(\text{density})^{0.5}$, and there is a potential uncertainty in density of about X20 (0.05 to 1.0 compared with water); it is clear that both computed mass and vertical mass flux are significantly sensitive to density as computed from images.

From a different perspective the persistence of completely supercooled, water cloud (as stratocumulus) and all ice cloud (as cirrus) is well documented. Less well documented is the nature of the interface between all supercooled water updraft and all ice down drafts as occurs in strong convection. Similar uncertainties arise in the regions of stratocumulus where weak updrafts tend to be of supercooled water but adjacent downdrafts tend to be of ice, nucleation having occurred in the colder evaporating mixing tops of the weak convection which subsequently descend down shear.

Observations are limited by the dynamic range of available instruments. Water content measurements, as the Johnson-Williams hot wire probe, are limited by heat transfer from the ventilated wire (equivalent to a cylinder < 0.1mm diameter) and within the wire itself, of order 0.01s. The more robust King probe (of order mm diameter) is 0.1s. These times are equivalent to a few meters or tens of meters length scale depending on the detail of the design and the airflow. It is known that such probes are slightly sensitive to the presence of ice depending on the impact characteristics of the ice at the stagnation line. Small particles accrete; large particles break and are mostly shed; really large, dense, particles break the sensor (Hallett et al 1998; Korolev et al 1998, Hallett and Isaac, 2002). Optical probes are limited by volume and depth of field and

artifacts produced by break-up by impact on surrounding geometry, particularly when flow is constrained by a cylinder. Empirical relations for particles density have very limited use. For ice measurement, any collecting surface needs to be constrained by a retro-geometry in order to retain fractured particles, as the inverted cone in a cylinder of the Nevzorov probe (Korolev et al, 1998) and the retro cylindrical geometry of the T probe, designed to preserve collection efficiency for water and ice particles of comparable density. The response time is necessarily related to (diameter)^2. Imaged collecting surfaces as in the cloudscope and the older formvar technique (Hallett 1976) have response times related to collection and recording rates either through video or film transport past a slit. The latter gives a resolution of less than a meter for cloud particles. It shows that, on occasion, a water cloud edge is sharp to less than this distance. The question of the scale of discontinuities inside clouds between water and ice is still open, and known to be less than 100m under some conditions in strong convection in the presence of even a modest shear of horizontal wind in the vertical Hallett, (1999).

3. THE EXPECTATION

Simplistic considerations of the distribution of ice in clouds suggest the following:

a) A near random distribution resulting from ice, having originated as cirrus aloft and been well dispersed, falling into supercooled stratiform cloud below. Less dispersal will give rise to locally changing concentrations.
b) In-situ nucleation of ice crystals during lifting condensation as in the updraft of small and large convective cloud and in frontal regions.
c) The initiation of cloud in a region already containing ice crystals by dynamic or other effects – as the penetration of convection into an overlying anvil or as moist air is lifted over higher terrain in the presence of snow from aloft.
d) The initiation of supercooled water cloud by gravity waves in ice crystals aloft (rendered stable by previous heating below) as in warmer moister air from previous convection below a Cb anvil to different levels.

In these cases, at low concentration of ice, particles grow as individuals first directly from the vapor and subsequently by accretion of droplets. Thus a region around each particle becomes devoid of droplets, up to X10 the size of the particle. As the particle grows further and begins to fall, accretion begins, characterized by the Stokes number (stopping distance/particle dimension) for the accretion, enhanced as the particle falls faster and continues up to a point where the particle fall velocity increases with size only as (diameter)$^{0.5}$. This process is readily demonstrated in the laboratory as becoming important

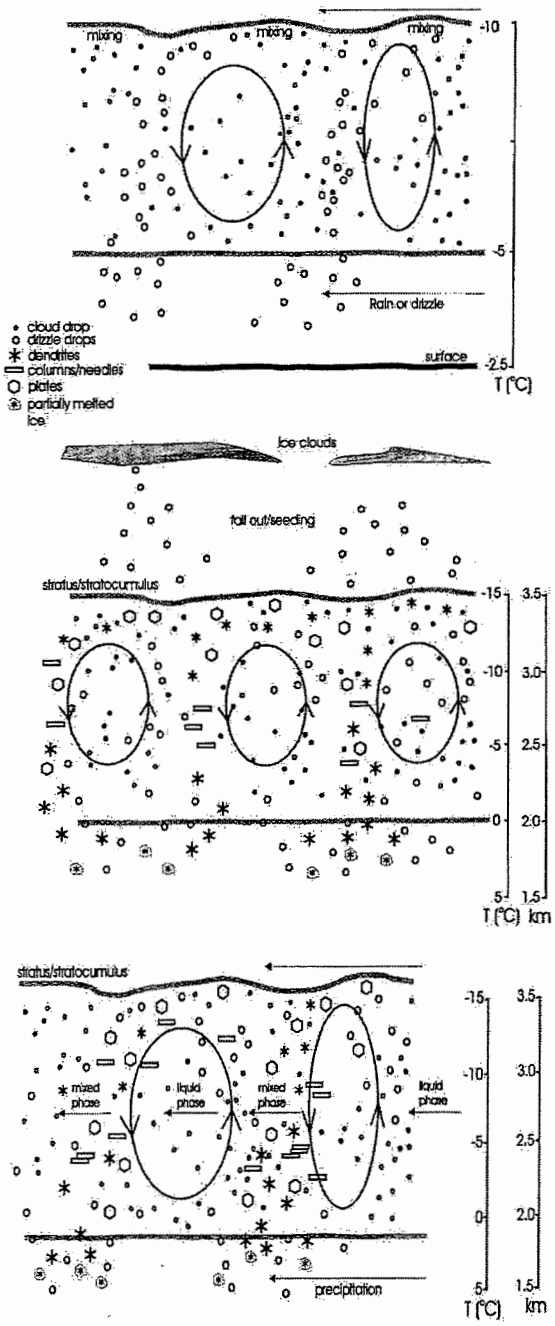

Figures 1, 2, 3. Microphysical Processes

Influence of convection with vertical shear of horizontal wind. Idealization of formation of coalescence precipitation (Fig 1) top, cirrus seeding of a lower stratocumulus layer (Fig 2) and in-situ formation of ice in a stratocumulus layer under inherent overlying shear of horizontal wind with higher wind above from right hand side resulting in sheared convection below (Fig 3).

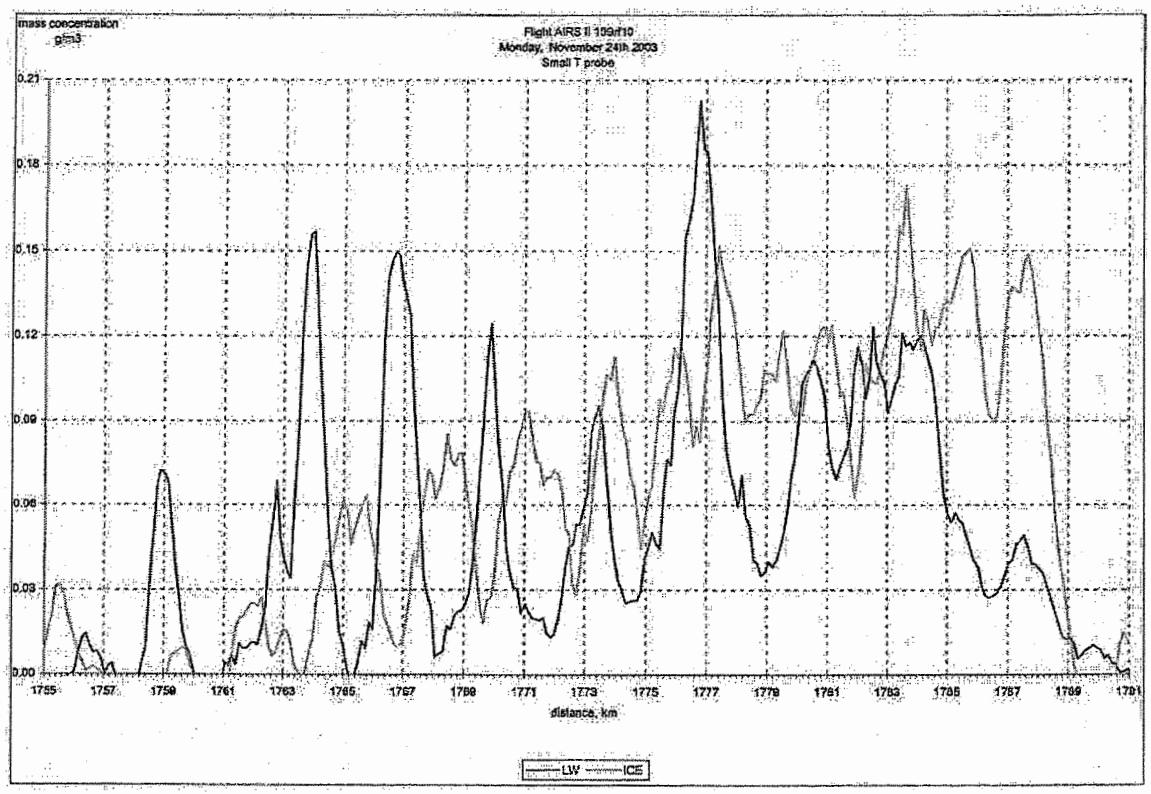

Figure 4. Small T probe ice (max 0.17g/m3) and water concentration (max 0.21 g/m3) during a C-130 1 hour penetration of a mixed phase cloud during AIRS 2, 24 November 2003. The relative locations of ice (faint) and water (full) are clearly shown as are the peaks of each and the inverse relation of ice.

for a fall velocity of >10cm/s, depending on drop size and ice particle porosity. Hence the previous water cloud now contains holes around ice particles and longer wakes following larger falling particles ending as droplets fall into the region to replace those lost. These scenarios are significantly modified should secondary ice be produced by rime splintering, ice particle melt, or ice particle evaporation.

4. THE CHALLENGE

The absence of ice in a given region of cloud is therefore to be considered the condition for the presence and continued existence of the supercooled state, having a potential for ice precipitation, aircraft icing and the separation of electric charge. Such absence may not have to be complete, as pointed out in detail by Korolev and Mazin (2003), depending on the conversion rate processes as determined by dynamical and microphysical considerations. However the measurement of supercooled water in lenticular clouds near -40C and in altocumulus cloud near -35C demonstrates that on occasion, not only the absence of ice nuclei but also the continued absence of ice from nucleation by any process elsewhere. Thus the air trajectory upwind from such supercooled clouds must lack both ice particles and primary ice nuclei and also pre-activated ice nuclei. Thus not only must the air be cleansed of ice by evaporation, it must also be cleansed of pre-activated ice nuclei active at these low temperatures and also of ice nuclei themselves, as conventionally defined. Passage through a scavenging precipitation system and substantial under-saturation over ice must therefore have taken place sometime during its recent history.

During a recent field campaign (AIRS 2, NCAR C-130) a simple observation of difficulties in following regions of stratiform supercooled cloud layers at mid and upper levels became apparent. Shallow layers ideal for studies of cloud properties were selected for penetration and investigation of nuclei above and below. Long continuous regions of supercooled cloud just did not exist; a maximum of some 5 minutes (30km) was practical after which layers disappeared with new layers above, below or both.

5. THE IMPLICATION

It is clear that limitations exist for any instrument and each set of data has limits for its interpretation. Thus wake phenomena, either as clustering or as depletion on the scale of mm diameter and m in length

requires resolution on these scales in the vertical and horizontal for the presence of aerosol or cloud droplets. For a cloudscope, with a field of view of 0.5mm X 0.5mm, and a drop concentration of $100cm^{-3}$, sampled at 1/30 second, 100 drops are sampled sufficient for total but not for bin resolution. For a monodisperse spectrum of particles, 100 drops are necessary for a 10% Poisson uncertainty, a path length of 40m. Similar considerations apply for the interface between an all-water and an all-ice to an all-ice cloud. Should the interface be ideally sharp, the resolution still requires a path length of 30m or greater for 10% statistical evaluation of the sharpness of the interface. In the case of the replicator with a 2mm slit and a film speed of 0.5m/s, the sharp edge is spread over a cm or so of film equivalent to a distance of a few meters. Similar considerations apply to optical instruments. In the case of thermal instruments, an integrated effect of each particle as it evaporates applies to the thermal time constant of the sensor, of order 0.01 to 1 second and depends on the diameter (d) and thermal diffusivity of the construction material (κ) as d^2/κ.

Further considerations apply to the T probe whose inherent design implies a collection efficiency related to sensor cylinder diameter, through the Stokes number, the ratio of probe diameter to particle stopping distance. Thus two probes of different diameter may be selected, the smaller (figure 4) being appropriate for smaller cloud particles and the larger for larger cloud particles. Convenient diameters for maintaining constant temperatures with available power are 2.5mm and 0.9mm. With sufficient precision for our purpose, this size may be used to providing an estimate of differentiation for cloud drops (St = 1, unit density) between 2.5 μm and 5.5μm. Particles larger than 7.5μm and 16.5μm are captured equally; for lower density ice particles larger sizes are relevant. Precipitation as a large snowflake several cm diameter appears to be sliced through, so that the equivalent water content is measured. The Stokes number is a product of true airspeed, (particle diameter)^2 and particle density and is inversely related to sensor diameter. It is convenient to collocate a large format cloudscope with a T probe so that correction can be made for particle size, shape and density and also evaporation latent heat (ice/water) as a second order should either be required.

Initial findings show the importance of high resolution instrumentation in developing insight into ice - water cloud interface structure in application to many problems in clouds in the atmosphere.

6. ACKNOWLEDGEMENTS

This work was supported by a grant from the Physical Meteorology Program, National Science Foundation, Arlington VA; the NCAR -130 flight tests by IDEAS and AIRS 2 Research Program.

7. REFERENCES

Korolev ,A.V., J.W.Strapp, G.A. Isaac and A.N.Nevzorov 1998: The Nevzorov Airborne Hot-wire LWC Probe: Principle of Operation and Performance Characteristics. J.A.O.T. **15** 1495 –1510.

Korolev,A.V., G.A.Isaac, S.G.Cober, J.W.Strapp, and J.Hallett, 2003: Observation of the Microstructure of Mixed Phase Clouds. Q.J.R.M.S. **1 29** 19 –38.

Korolev A.V. and I. P. Mazin, 2003: Supersaturation of water vapor in clouds. J. Atmos. Sci. **60** 2957 – 2974.

Hallett,J, W.P.Arnott, R.Purcell, and C. Schmidt,1998. A Technique for Characterizing Aerosol and Cloud Particles by Real-time Processing. in *PM $_{2.5}$: A fine particle standard.* Proceedings of an International Speciality Conference, sponsored by EPA air and Waste Management Association, Ed J. Chow & P. Koutrakis, **1**, 318 –325.

Hallett,J and G.A. Isaac, 2002: Aircraft Icing in Glaciated and Mixed Phase clouds.40th AIAA Aerospace Sciences Mtg, Reno NV, Paper 2002-0677.

Hallett,J, J.G. Hudson, D.H. Lowenthal, and R. Purcell 2002: Real-time Processing and Characterization of Atmospheric Particulates, AMS 11th Conference on Cloud Physics, 3-7 June 2002,Ogden UT. **(CD) 10.1**

Hallett,J, 1999: Charge Generation with and without Secondary Ice Production. Proceedings of the 11th International Conference on Atmospheric Electricity, 7 –11 June, Guntersville, AL., 355 – 358.

MELT CHARACTERISTICS OF FALLING SNOW PARTICLES

J. Hallett[1] and R.G. Oraltay[2]

[1] Atmospheric Sciences, Desert Research Institute, Reno NV 89512, USA
[2] Environmental Engineering Department, Marmara University, Istanbul, Turkey.

1. INTRODUCTION

As ice particles fall into air with wet bulb temperature above 0C, melting occurs and the resulting liquid becomes distributed over the ice surface as drops or water layers. Such melting results from both heat gain from the environment and also from latent heat from condensation on the ice at 0C; any regions of ice below 0C will grow frost crystals and approach 0C. Continued melting may lead to particle break up, either by the shedding of individual drops or by fracture of the ice at points of weakness as the melting progresses. The shed particles thus may or may not contain ice (Oraltay and Hallett, 1989). The question to be addressed herein is the resulting spatial distribution of this melt water over the ice surface, its evolution during melting (and refreezing) and the physical processes involved. Further questions arise concerning the impact of water drops, above or below 0C, into the melt water or onto existing regions of ice.

2. BASIC CONCEPTS

Water vapour condensing on to a flat surface as liquid retains its flat shape as ordained by a uniform surface tension; condensation on other flat surfaces as solids or non-wetting liquids occurs as individual droplets requiring nucleation. These drops subsequently grow by coalescence. Should such an assembly of droplets be subject to evaporation, each droplet evaporates as an entity. Simple observation of droplets growing and evaporating on a glass substrate shows that these processes are not reversible; there is a hysteresis, nucleation requires a supersaturation whereas evaporation does not. In addition, the contact angle for growth and evaporation differ; for growth the angle is greater than for evaporation. A further instability is evident in as far as the drop periphery is not quite circular but advances and retreats irregularly for growth and evaporation respectively; the drop thus flattens and thickens, approximately as the cap of a sphere of varying diameter depending on overlying supersaturation or undersaturation. The mean contact angle differs between growth and evaporation and depends on the (changing) nature of the interface. Thus a perfectly clean glass surface nucleates a uniform water layer; a hydrophobic surface requires a supersaturation and leads to individual separated drops, each depending on the local surface properties. Drops coalesce sequentially as growth continues. In the case of an ice surface, frost crystals grow at temperatures below 0C; at temperatures at or above 0C a water layer forms, delineating those regions which begin melting first (in reality the temperature is always a little non uniform). Simple experiments of breathing on such surfaces readily demonstrate such effects. In passing it is noted that should water drops accrete, they are incorporated into liquid regions as vortex rings (Hallett and Christensen 1984) and propagate to any underlying ice surface; if they be supercooled some fraction of the supercooling remains (and conversely) depending on layer thickness.

3. APPLICATION

In the case of ice particles the geometry and the nature of the ice surface are highly variable. A large melting hailstone is closest to the ideal, with drops coalescing with a liquid layer and being transferred to the ice below, with the liquid layer carried away in the boundary layer flow. Even here, a cursory observation of a surface suggests some flow instability. For vapour grown crystals things are much more complicated and a re-examination of the geometry is in order. We consider a surface, necessarily in 2 dimensions but as the surface of a 3 dimensional system as crystals of different habits. In a snowflake many crystals intersect and provide a 3 dimensional nest of particles. The geometry can in principle be characterized with flat regions as crystal facets of plates, dendrites and columns, together with interface regions where individual crystals are in contact. The contacts can be characterized as point, linear and planar, the exact fraction of which will be related to the mix (size, habit) of

---

John Hallett, Desert Research Institute, 2215 Raggio Parkway, Reno NV,89512 USA. hallett@dri.edu

crystals in the collection. Thus an overall density and a density variation within the flake, as the contact area is part of the characterization.

To begin, let us consider the melting of a simple approximately one dimensional crystal, as a long thin uniform pencil. It could be a long 'c' axis column or an 'a' axis dorite, or a dendrite having previously lost its arms. let us also consider a hexagonal plate having uniform thickness and an equivalent high aspect ratio. Let us further consider how a thin layer of liquid from the melting process would be distributed over the various geometries, the ideas having been influenced by previous laboratory experiments. Plates size mm tend to become covered with a uniform water layer, top and bottom, become thinner and become smaller from their edges. Ice pencils behave quite differently in that they thin uniformly but the liquid forms as discrete drops along their length. Each drop is separated by a diameter or so from its neighbours; there is an analogy with oil drops on a filament (Carroll, 1976). The ice appears dry between drops. Most important is that the drops have well defined contact angles (40°) with respect to the ice needle, 'c' axis, surface. (Orlatay and Hallett, 2004). There is some evidence that the contact angle changes +/- 10° with the environment conditions. C.V. Boys work on surface tension geometry of bubbles many decades ago showed that fluids tended to develop instabilities based on energy considerations when the aspect ratio of the fluid system was in excess of a few, (2 - 3). Such instabilities lead to break up of layers related to the Laplace excess pressure (2s/r s = surface tension, r = radius of sytem) as with the instability of a vertical flow from a faucet. There should be instability of a flat layer on a horizontal plane at a critical thickness (driven by a temperature gradient); there should be a similar instability of a fluid cylinder on the surface of a central solid cylinder. The relevant temperature differences in the system here are a few degrees above and below 0C over a distance of a mm to a cm, which specifies the Grashoff Number. The classes of fluid instability for a cylindrical geometry involve both an along-axis dimension, and a circumference dimension; the observation that a drop is stable only when skewered by an ice crystal shows that the former is unstable, whereas the latter is stable. It is of interest to speculate that the physical conditions at drop and ice differ and that the ice is at the ice bulb temperature, evaporating, and the drop at the wet bulb temperature, growing, but mainly through the surface transport of a liquid layer from the ice to the drop under the excess pressure of the layer over the narrower ice cylinder compared with the larger drop. From a crude theoretical viewpoint one can consider the equivalence of heat and mass transport equations and the conditions characterized on a plot of vapour density - temperature indicating temperature differences between different parts of the same hydrometeor of a few degrees, depending on the assumptions (Hallett et al 2002).

4. CONCLUSIONS

The sharpness of the drop ice-water interface under these conditions is then to be interpreted in terms of a non-equilibrium situation where the ice just beyond the water interface is just below the equilibrium melting point thus inhibiting the spread of the water and the complete wetting of the ice as might be expected under equilibrium conditions. The transport of melting from the ice needle to the drop is then to be considered as a non steady state and possibly a periodic process. Trace impurity on the ice surfaces cannot be excluded as being of importance.

5. ACKNOWLEDGEMENT

This work was carried out under a Grant from the Physicial Meteorology Program, National Science Foundation, Arlington VA and TUBITAK, via UNISTAR, a United Nations Program for International Exchange.

6. REFERENCES

Carroll,B.J.1976; The Accurate Measurement of Contact Angles, Drop Volume and Laplace Excess Pressure in Drop on Fibre systems. J. Colloid and Interface Sci., **57** 488 – 495.

Hallett,J and L.Christensen, 1984; The Splashing and Penetration of Raindrops into water. Atmos. Res. **18** 226 – 242.

Oraltay R.G. and J. Hallett, Evaporation and Melting of ice crystals: a laboratory Study.1989; Atmos. Res.**24** 169 –189.

Hallett,J., W.P. Arnott, M.P. Bailey,and J.T. Hallett, 2002; *Cirrus.* Ice Crystals in Cirrus, K.D. Lynch, K.Sassen, D.O'C Starr, G. Stepehens (Eds) Oxford Uni. Press NY,Ch 3 41 –77.

Oraltay R.G. and J. Hallett, 2004; The Melting Layer Part I: A Laboratory Study. Submitted for publication.

HOMOGENEOUS ICE NUCLEATION IN TROPICAL CONVECTION AND ITS INFLUENCE ON CIRRUS ANVIL MICROPHYSICS

Andrew J. Heymsfield[1], Larry M. Miloshevich[1], Carl Schmitt[1], Aaron Bansemer[1], Cynthia Twohy[2], Michael R. Poellot[3], and Ann Fridlind[4]

[1]National Center for Atmospheric Research*, Boulder, CO, USA
[2]College of Oceanic and Atmospheric Sciences, Oregon State University, Corvallis, OR, USA
[3]Department of Atmospheric Sciences, University of North Dakota, Grand Forks, ND, USA
[4]NASA Ames Research Center, Moffett Field, CA, USA

1. INTRODUCTION

The poorly understood processes of ice initiation in clouds can lead to large uncertainties in modeled precipitation, with implications for climate change studies. This study investigates factors that control ice initiation through the homogeneous ice nucleation process in deep tropical convective clouds, a possible primary pathway for the initiation of anvil cirrus crystals.

Cirrus ice particles can form on aerosols without the need for ice nuclei, through homogeneous (spontaneous) ice nucleation. At temperatures between -35 and -40^{0}C, cloud droplets of diameter several microns or larger will freeze spontaneously, and at lower temperatures solution droplets smaller than 1 micron in diameter will freeze spontaneously (Heymsfield, 1973; Sassen and Dodd, 1989). The rate of droplet freezing through homogeneous nucleation and the resulting numbers of ice crystals produced homogeneously is strongly influenced by temperature, vertical air velocity, and pre-existing ice particles (which can potentially retard or suppress the homogeneous freezing process due to their effects on depleting water vapor and cloud droplets).

This study examines the homogeneous nucleation process in an environment of vigorous convection with pre-existing large ice particles, a research area not yet studied. The primary observations in this study are from an aircraft penetration of a vigorous convective cell at a temperature near -35°C during the CRYSTAL-FACE project in southern Florida.

2. INSTRUMENTS AND DATA ANALYSIS METHODS

Measurements used in this study were obtained by the University of North Dakota Citation aircraft in July 2002 during the CRYSTAL-FACE project in southern Florida. The focus of this study is an aircraft penetration of a convective core and associated anvil on 18 July 2002 from 1746 to 1750 UTC, at a mean altitude of 9.98 km.

Air temperatures were measured by two deiced Rosemount probes. Water vapor mixing ratio was measured by a tunable diode laser (TDL) hygrometer, then converted to relative humidity with respect to water (RH) using the temperature measurement. The vertical velocity (w) was derived from the corrected aircraft ground speed and position, and from five pressure ports on the radome gust probe that measure the aircraft's airflow attack and sideslip angles. The presence of LW was detected by a Rosemount icing detector (RICE), and the liquid water content (LWC) was measured by a King probe. The RICE output voltage was calibrated for LWC measurement using the method of Mazin et al. (2000). The particle size distribution (PSD) was measured by a PMS 2D-C probe and a SPEC Inc. high volume particle spectrometer (HVPS) imaging probe. The probes span the size range from about 60 μm to 6 cm. Size distributions of droplets and small ice particles between 3.5 and 58 μm diameter, smaller than the size range of the 2D-C probe, were measured by a PMS forward scattering spectrometer probe (FSSP). High-resolution particle images were obtained from the SPEC Inc. Cloud Particle Imager (CPI), with a resolution of about 2 μm and a minimum detectable size of about 20 μm. The condensed water content (CWC), equal to the sum of the LWC and IWC for particles larger than about 8 μm in diameter was measured using a counterflow virtual impactor (CVI, Twohy et al., 1997). Extinction in visible wavelengths was measured directly for sizes above about 5 μm diameter using a cloud integrating nephelometer (CIN) probe (Gerber et al., 2000).

3. AIRCRAFT OBSERVATIONS

The convective cloud focused on in this study formed over land along the east coast of Florida in association with a sea breeze front. The cloud first appeared in GOES-8 visible satellite imagery at 1615 UTC. By 1732 UTC the cloud developed an anvil that streamed southwest, downwind from the convective core. The GOES IR imagery indicated that the cloud had reached the tropopause near 14 km altitude by the time of the aircraft penetration at 1746 UTC.

Corresponding author: Andrew J. Heymsfield, National Center for Atmospheric Research, P.O. Box 3000, Boulder, Colorado, 80307; E-mail: heyms1@ucar.edu
*NCAR is sponsored by the National Science Foundation

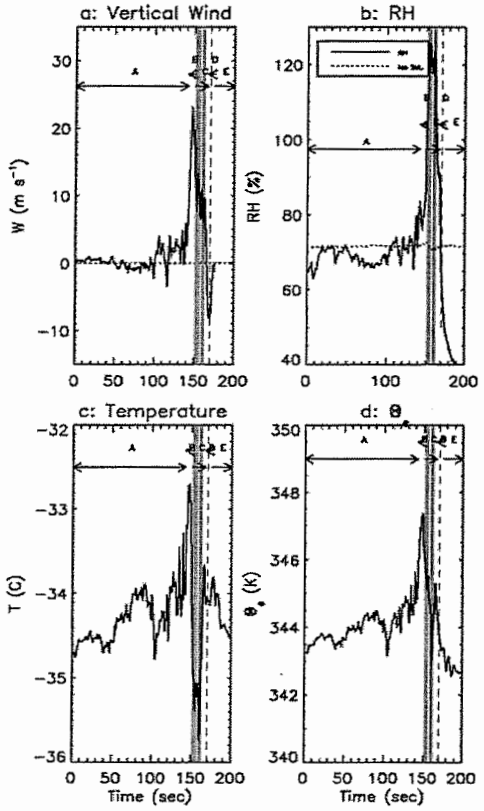

Fig. 1: Citation data from the cloud penetration. a: Vertical winds. b: RH. c: Temperature. d. Equivalent potential temperature. LW regions are shown by vertical shading.

The cloud penetration is separated into four distinct regions as shown in Fig. 1, based on the aircraft measurements of *w* and RH (Figs. 1a and 1b). Proceeding upwind, the aircraft first encountered the anvil (labeled A), which is characterized by relatively weak vertical velocities and RH near ice saturation. Characteristics of the updraft core change markedly in the center of the core. In the downwind portion of the core (B), the vertical velocity is up to 20 m/s and is 5-10% RH supersaturated with respect to ice. However, the upwind portion of the core (C) contains LW and is highly supersaturated with respect to water, despite the lower peak vertical velocity of 10 m/s, indicating that vapor depletion from ice growth in the stronger updrafts far exceeds the depletion in the LW region. The extreme water supersaturation in the LW region is entirely reasonable based on model calculations. The temperature in the LW region, -35.3^{0}C, is at or near the threshold for homogeneous nucleation, and these droplets are either in the process of freezing homogeneously or they will soon do so.

Immediately upwind from the updraft core is a strong downdraft (D), containing ice particles; these particles were presumably carried downward to the aircraft level. Severe turbulence was encountered at the boundary of regions C and D. The equivalent potential temperature (Fig. 1d) decreased through the LW region (C) and is a minimum near the turbulent boundary.

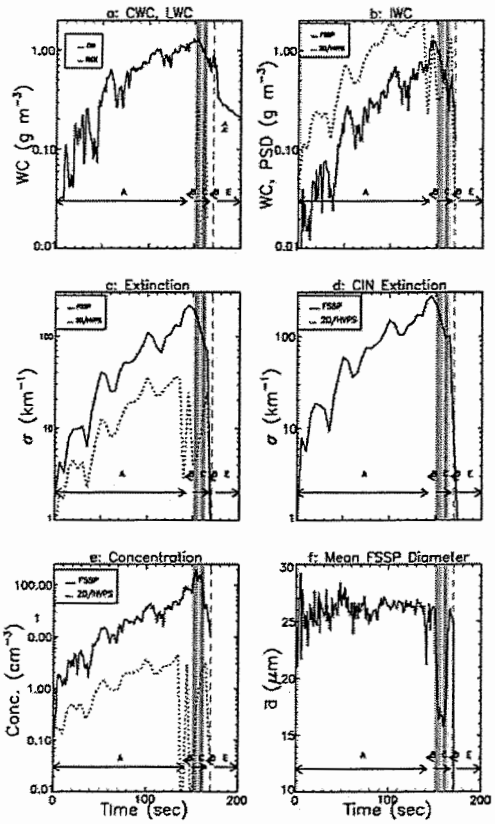

Fig. 2: Microphysical quantities measured during the cloud penetration. a: CWC measured by the CVI and LWC measured by the (RICE). b: IWC in the size range 5-56 μm calculated from FSSP measurements assuming that the particles are solid ice spheres, and IWC above 50 μm from the imaging probe size distributions. c: Extinction from the particle probes. d: Extinction measured by the cloud integrating nephelometer. e: total concentration from the particle probes for their respective size ranges. f: FSSP mean diameter.

The microphysical measurements during the cloud penetration are summarized in Fig. 2. The peak CWC measured by the CVI is about 1.1 g/m^3 in the glaciated portion of the core (Fig. 2a region B), and the CWC decreases with distance both downwind in the anvil and upwind in the LW region (C). The LWC derived from the RICE measurements, about 0.2 g/m^3, is relatively small in comparison to CWC. The IWC as derived from the imaging probes for sizes >50 μm in the anvil (A) is about twice the IWC due to small particles (5-56 μm) calculated from the FSSP measurements. However, in the updraft core (both

regions B and C) the contributions of small particles to the IWC exceeds the contribution of particles > 50 μm measured by the imaging probes. The optical extinction (σ) peaks in regions (B) and (C) and in the updraft core is dominated by FSSP-size particles (Fig. 2c). These σ values were derived from twice the measured total cross-sectional area of the FSSP size distributions (assuming spherical particles) and also from the combined 2D/HVPS size distributions (taking the imaged areas of the particles). Direct measurements of σ from the CIN probe mirror the values derived from the FSSP and further verify that extinction in the updraft core is dominated by contributions from small particles. Figs. 2e and f show that the small (FSSP) particles in the LW region are more numerous (up to 200 cm^{-3} and smaller (17 μm mean diameter) than the small particles in the glaciated region of the core (80 cm^{-3}, 26 μm mean diameter). Whether liquid or ice, the composition of the core is dominated by small particles, unlike the anvil (A).

A composite FSSP and imaging probe size distribution for one 5-s period in the LW region (Fig. 3) shows that the probes agree well in the overlapping portion of their size ranges. The shaded portion of the FSSP size distribution that is assumed to be predominantly droplets is based on the notion that the probability of a given droplet freezing spontaneously increases with its volume. The shaded portion therefore represents the part of the FSSP spectrum that equals the measured liquid water content at this time period. Note that, although the small end of the PSD is liquid, there is a long tail that includes large rimed particles and graupel that are rising with the droplets in the updraft after presumably nucleating heterogeneously at a lower level.

4. HOMOGENEOUS NUCLEATION IN THE UPDRAFTS

We use a 1D parcel model of droplet and ice crystal growth and homogeneous nucleation (Heymsfield and Miloshevich, 1993) to assess whether the aircraft data are consistent with the homogeneous nucleation hypothesis, and to gain insight into its importance in convectively-generated cirrus. The model is initialized with a CCN distribution of the form $N=cS^k$, with N the concentration of CCN at water supersaturation S, and coefficients c=150 cm^{-3} and k=0.3 to yield droplet concentrations comparable to those observed in the LW region. Homogeneous nucleation rates used in the model are given by the chemical activity formulation of Koop et al. (2000). This formulation treats the freezing of solution droplets, and the nucleation rate for the larger (dilute) droplets of concern in this study, and the rates are almost identical to the laboratory measured rates for droplets.

The homogeneous nucleation model has been modified to include an extra vapor depletion term that represents a specified gamma distribution of large ice particles. A gamma-type size distribution, $N(D)=N_0D^{\mu}e^{-\lambda D}$ is specified in terms of a scale factor N_0, the dispersion μ, the slope λ, and minimum and maximum cutoff diameters of 0.01 and 0.3 cm, respectively. Analysis of the aircraft size distribution data suggests the representative values λ=20 cm^{-1} and μ=−1.6. A given initial ice water content (IWC_0), when taken over the size range 0.01 to 0.3 cm assumed for the pre-existing ice, implies a given N_0 for the assumed ice bulk density of 0.15 g/m^3.

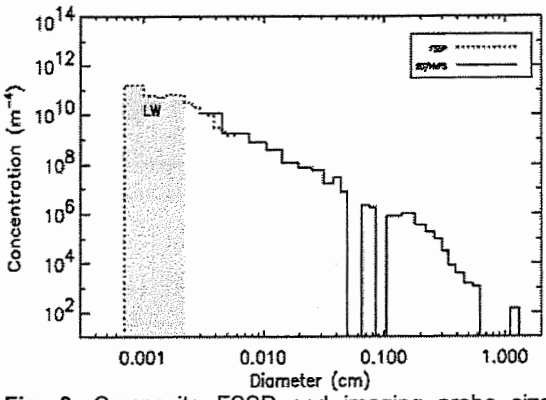

Fig. 3: Composite FSSP and imaging probe size distribution for a 5 second period in the LW region (t=152-157s). The highlighted portion of the FSSP size distribution is the size range presumed to be droplets (see text).

We first address whether droplets can form in a vigorous updraft consisting of pre-existing ice. The dependence of the homogeneously produced ice concentration on the diffusional growth of the pre-existing ice is shown over a wide range of w and IWC_0 conditions in Fig. 4, where the model was initialized at -20°C. The concentration of homogeneously nucleated ice diminishes with increasing IWC_0 and decreasing *w*.

We now address the question of whether it is more likely for cloud droplets to be transported from cloud base to the homogeneous nucleation level. Cloud droplets, lofted in updrafts from cloud base towards the -35°C level, will be depleted either partially or entirely by the pre-existing ice. To examine the fate of the cloud droplets under such conditions which could not be readily considered in the homogeneous nucleation model, graupel growth and droplet collection was examined using the 1D graupel growth model of Heymsfield (1984). The size distributions were taken to be the gamma distributions initialized earlier. Monodisperse cloud droplet size distributions are used to represent the droplet population. For brevity, the results of these calculations are summarized here. Droplet depletion by the large ice is found to increase with decreasing vertical velocity and LWC, and for increasing IWC and droplet size, such that w>10 m/s and LWC>1.0 g/m^3 are required to permit droplets to reach the -350C level with IWC_0>1 g/m^3.

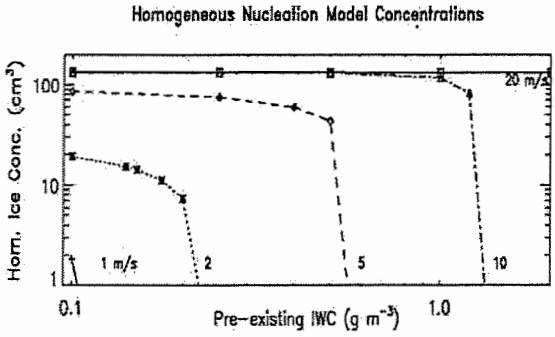

Fig. 4: Ice concentrations formed in the updrafts from the homogeneous nucleation model, with calculations beginning at the -20^0C level, with different vertical velocities and IWC, for PSD slope parameter of 20 cm^{-1}.

5. SUMMARY AND CONCLUSIONS

This study has examined the role of the homogeneous ice nucleation process in a tropical convective cloud updrafts. Our analysis suggests that homogeneous ice nucleation occurs in deep tropical convective updrafts at temperatures between -35.5 and
-37.5^{0}C where the vertical velocities exceed the 5-10 m/s range. In updrafts of such magnitudes, ice particles that develop through non-homogeneous processes at temperatures warmer than -34^{0}C are unable to prohibit some fraction of the droplet population from being lofted to the temperatures where homogeneous nucleation proceeds.

We further conclude that in vigorous deep convection (to heights of the -35^0C level and above), there is a significant population of large ice particles, presumably formed by heterogeneous or secondary ice nucleation, together with a population of homogeneously frozen droplets and a significant population of large ice crystals, that are being lofted to the upper levels of the cloud. The observations for our cloud indicate that the small particles are likely to dominate the radiative (extinction) and ice water content properties of the updrafts. Anvils are therefore comprised of a collection of large particles that were heterogeneously produced (but with relatively little radiative impact) and homogeneously produced (with a large radiative impact). Once in the anvil, aggregation will reduce the radiative and ice water content contributions by the small particles.

REFERENCES

Gerber, H., V. Takano, T. J. Garrett and P. V. Hobbs, 2000: Nephelometer measurements of the asymmetry parameter, volume extinction coefficient, and backscatter ratio in Arctic clouds. *J. Atmos. Sci.*, **57**, 3021-3034.

Heymsfield, A. J., 1973: Cirrus uncinus generating cells, Chapter 5: Ice nucleation and growth of cirrus particles. PhD Dissertation, University of Chicago, 269 pp.

Heymsfield, A. J., 1982: A comparative study of the rates of development of potential graupel and hail embryos in High Plains storms. *J. Atmos. Sci.*, **39**, 2867--2897.

Heymsfield, A. J., and M. Sabin, 1989: Cirrus crystal nucleation by homogeneous freezing of solution droplets. *J. Atmos. Sci.*, **46**, 2252-2264.

Heymsfield, A. J., and L. M. Miloshevich, 1993: Homogeneous ice nucleation and supercooled liquid water in orographic wave clouds. *J. Atmos. Sci.*, **50**, 2335-2353.

Sassen, K., and G. C. Dodd, 1988: Homogeneous nucleation rate for highly superooled cirrus cloud droplets. *J. Atmos. Sci.*, **45**, 1357-1369.

Twohy, C. H., A. J. Schanot, and W. A. Cooper, 1997: Measurement of condensated water content in liquid and ice clouds using an airborne counterflow virtual impactor. *J. Atmos. Ocean. Tech.*, **14**, 197-202.

3-D NUMERICAL SIMULATION OF HAILSTORMS IN DIFFERENT REGIONS

Zhaoxia Hu[1], Yanchao Hong[1] and Hongyu Li[2]

[1]Institute of Atmospheric Physics, Chinese Academy of Sciences, Beijing 100029,China
[2]Beijing Weather Modification Office, Beijing 100089, China

1. INTRODUCTION

Crop losses caused by violent hailstorms threat to food supplies in many agricultural regions around the world. The mechanisms of hail formation have been investigated from many different viewpoints. For example, Browning and Foote (1976) described a supercellular storm and presented a recycling mechanism of hailstone growth. Pflaum (1980) suggested that alternation of low-density riming and wet growth processes play a role in hailstone formation. Such alternation of growth processes has been called microphysical recycling. Miller and Fankhauser (1983) used observations from aircraft, Doppler radars, and surface networks etc. to describe the structure and the evolution of a hailstorm. Foote (1984) discussed an alternative theory of the behavior of hailstorms, and so on. The conceptual model of accumulation zone of supercooled raindrops in a hailstorm was first hypothesized by Sulakvelidze (1969). This hypothesis had been tested in randomized hail suppression experiments such as NHRE in Northeast Colorado in the USA (Foote et al., 1979, Knight et al. 1979) and Grossversuch IV in Switzerland (Federer et al., 1986). In both of above studies, no significant effects of the seeding operations were found and the accumulation zones of supercooled rainwater were not present. In NHRE it turned out that the hailstone embryos were predominantly graupel particles. In Grossversuch IV about half of the embryos were frozen drops. In a hybrid-type hailstorm revealed by polarimetric and Doppler radar measurements, an accumulation zone of big drops did not exist (Holler et al., 1994)

At present, many hail suppression operations are based on the accumulation zone theory in China. The main purpose of this study is to analyze the hail formation mechanisms through comparing hailstorms in three different regions.

2. NUMERICAL MODEL AND SIMULATED CASES

The 3-dimensional, time-dependent hailstorm numerical model (Yanchao Hong, 1999, Zhaoxia Hu et al., 2003) that is non-hydrostatic, fully elastic, and involves detailed microphysical processes for water substance including water vapor, cloud water, rain water, ice crystal, snowflake, graupel particle and frozen drop was used.

The first of three hailstorms simulated was from Lanzhou city, Gansu Province, China on August 9, 1990 (hereafter Lz90809); the second was in Munich, Germany on June 30, 1990 (Holler et al., 1994, hereafter Mun90630); and the last was in Maqu county, Qinghai Province on July 12, 1999 (hereafter Qh99712).

3. RESULTS AND CONCLUSIONS

3.1 Accumulation Zone of Supercooled Raindrops

When the center of supercooled rainwater content is higher than the position of maximum updraft velocity, the accumulation zone exists. According to this definition of accumulation zone of supercooled rainwater hypothesized by Sulakvelidze, the accumulation zone presents in Lz90809 and Qh99712 hailstorms. However it does not exist in Mun90630 hailstorm. The maximum of supercooled rainwater content in above three storms is 8.32g/m^3, 3.67g/m^3 and 7.53g/m^3 respectively.

3.2 Hailstone Embryos

There are two categories of hailstone embryos: frozen embryos and graupel embryos. In the Lz90809 hailstorm, the hail embryos are predominantly frozen drops. In the Qh99712 hailstorm, the hailstone embryos are mainly graupel particles. And in the Mun90630, the number of frozen and graupel embryos is equivalent. The simulating results show that the rainfall of Lz90809 is the largest and that of Qh99712 is the smallest.

In the above three hailstorms, hailstone embryos all formed in the supercooled rainwater area. Fig.1 gives the X-Z cross-section of hailstone embryos, rainwater content and temperature distribution at different times.

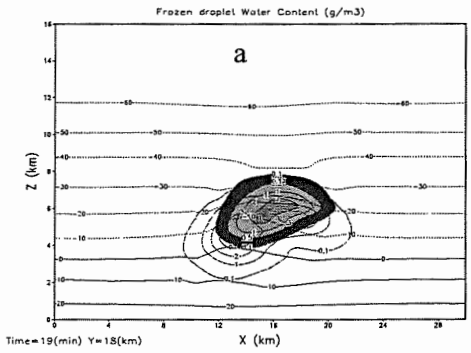

Corresponding author's address: Zhaoxia Hu, Institute of Atmospheric Physics, Chinese Academy of Sciences, Beijing 100029, China; E-mail: huzx@mail.iap.ac.cn

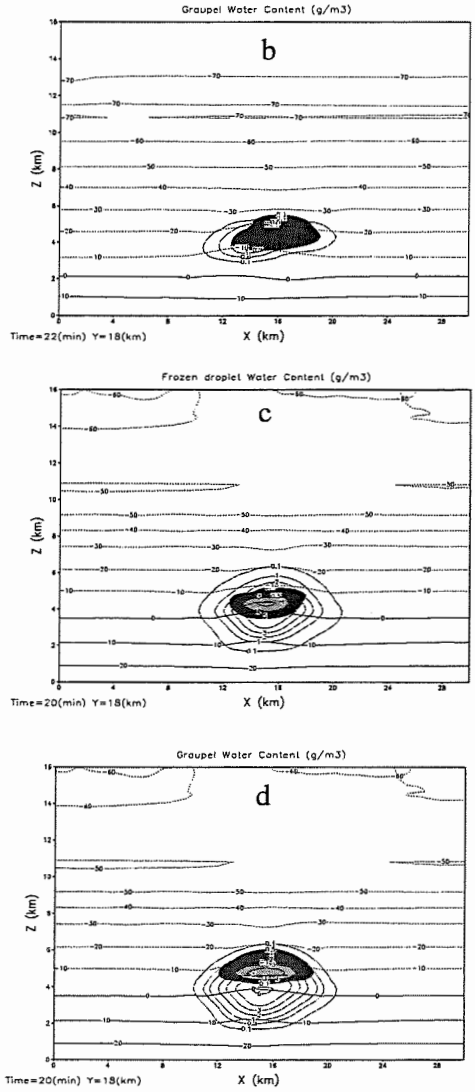

Fig. 1 Vertical cross-section of hailstone embryos (shaded), rainwater and temperature isolines
a: Lz90809 hailstorm (shaded is frozen drops)
b: Qh99712 hailstorm (shaded is graupel particles)
c,d: Mun90630 hailstorm (c: shaded is frozen drops, d: shaded is graupel particles)

3.3 The Mechanism of Hail Formation

In the numerical model there are following four kinds process related to hail growth are considered: the first is the process of ice crystal and snowflake producing, the second is the process of hailstone embryos producing, the third is the process of hailstone embryos growth, and the last one is the hailstone growth.

Fig.2 to Fig.6 indicate that: 1) the producing rate of ice crystal in Lz90809 is the largest and in Qh99712 is the smallest, 2) the snowflake mainly comes from ice

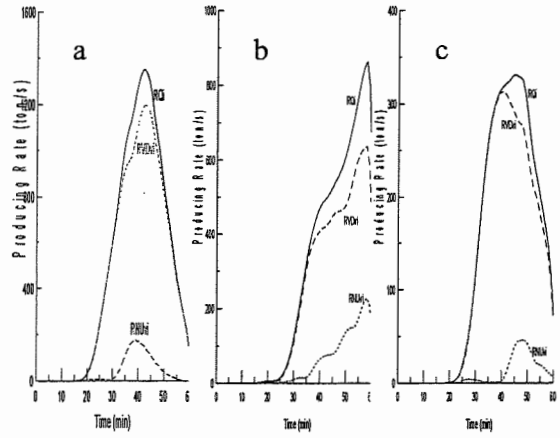

Fig.2 Time series of the producing rate of ice crystal (ton/s) (a: Lz90809, b: Mun90630, c: Qh99712)

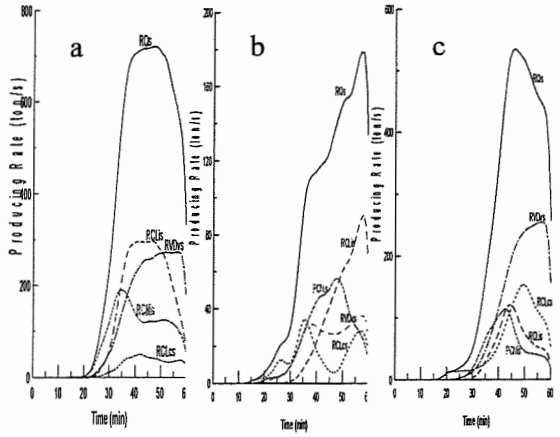

Fig.3 Time series of the producing rate of snowflake (ton/s) (a: Lz90809, b: Mun90630, c: Qh99712)

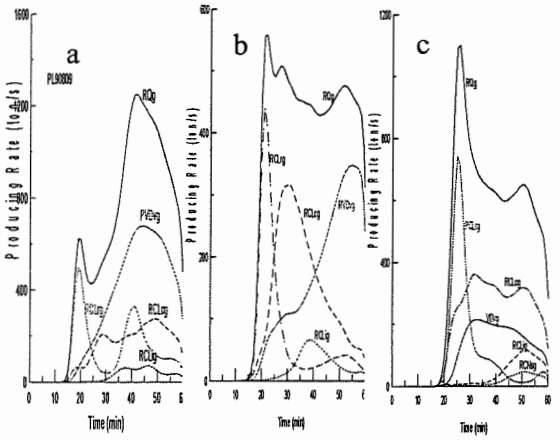

Fig.4 Time series of producing rate of graupel particles (ton/s) (a: Lz90809, b: Mun90630, c: Qh99712)

crystal auto-conversion, 3) in Lz90809 hailstorm, the mass of graupel particles is not small, because of the large number, the mean mass of graupel particles is the smallest. The mean mass of graupel particles in Qh99712 is the largest. Graupel particles grow by accretion with rainwater and cloud water and

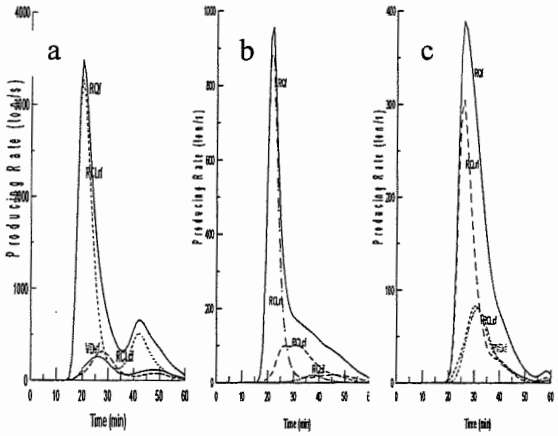

Fig.5 Time series of producing rate of frozen drops (ton/s) (a: Lz90809, b: Mun90630, c: Qh99712)

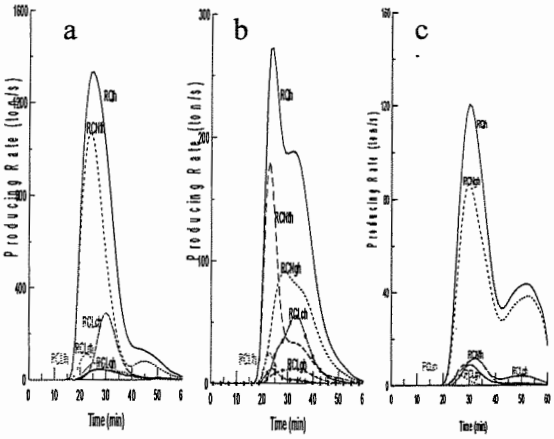

Fig.6 Time series of producing rate of hailstone (ton/s) (a: Lz90809, b: Mun90630, c: Qh99712)

their sublimation. 4) frozen drops grow by accretion with rain water in these three hailstorms. And amount of frozen drops in Lz90809 hailstorm is as 10 times as Qh99712. 5) the mass of hailstone in Lz90809 is the largest and that in Qh99712 is the smallest. Table 1 is the comparison of these three hailstorms

Table 1 Comparison of three hailstorms

	Lz90809	Mun90630	Qh99712
Temperature of cloud base(℃)	14.5	15.2	3.5
Sea level (m)	1346	600	3473
Hailstone embryo	Frozen: 98.0% Graupel: 2.0%	Frozen: 57.5% Graupel: 42.5%	Frozen: 7.8% Graupel: 92.2%
Maximum updraft (m/s)	27.50	19.96	14.23
Maximum observed radar echo (dBZ)	60	65	55
Maximum simulated radar echo (dBZ)	60	70	60
Existence time of AZ (min)	3~4	AZ is not present	5~6
Temperature of AZ (℃)	-4~-10		-12~-20
Depth of AZ (km)	3~4		2-3
Maximum supercooled rainwater (g/m^3)	8.32	7.53	3.67
Rainfall amount at the surface (kt)	2438.0	1297.2	1173.6
Maximum hailfall kinetic energy flux ($Jm^{-2}s^{-1}$)	7.12	1.47	1.28
Observed hailstone on the ground	Frozen drops like eggs	Rain, graupel and hailstone	Mainly graupel particles

AZ: Accumulation Zone of Supercooled Raindrops

Acknowledgements

This research was jointly sponsored by the Natural Science Foundation of China (Grant 40333033) and the Key Project of the Ministry of Science and Technology of China (Grant 2001BA610A-01). We wish to thank Professor Meiyuan Huang of IAP for his suggestions.

References

Browning, K. A and G. B. Foote, 1976: Airflow and hail growth in supercell storms and some implications for hail suppression, Quart. J. Roy. Meteor. Soc., 102, 499-533.

Federer, B., A. Waldvogel et al., 1986: Main results of Grossversuch IV, J. Climate Appl. Meteor., 25, 917-957.
Foote, G. B., 1984: A study of hail growth utilizing observed storm conditions, J. Climate Appl. Meteor., 23, 84-101.
Foote, G. B. and C. A. Knight, 1979: Results of a randomized hail suppression experiment in Northeast Colorado, Part I: Design and conduct of the experiment, J. Appl. Meteor., 18, 1526-1537.
Holler, H., V. N. Bringi et al., 1994: Life cycle and precipitation formation in a hybrid-type hailstorm revealed by polarimetric and Doppler radar measurements, J. Atmos. Sci., 51, 2500-2522.
Knight, C. A., G. B. Foote and P. W. Summers, 1979: Results of a randomized hail suppression experiment in Northeast Colorado, Part IX: Overall discussion and summary in the context of physical research, J. Appl. Meteor., 18, 1629-1639.
Miller, L. J. and J. C. Fankhauser, 1983: Radar echo structure, air motion and hail formation in a large stationary muticellular thunderstorm, J. Atmos. Sci., 40,2399-2418.
Pflaum, J. C., 1980: Hail formation via microphysical recycling, J. Atmos. Sci., 37, 160-173.
Sulakvelidze, G. K., 1969: Rainstorms and hail, Israel Program for Sci. Transl., Jerusalem, pp310.
Yanchao Hong, 1999: Study on mechanism of hail formation and hail suppression with seeding, ACTA Meteor. Sinica, 57, 30-44 (in Chinese).
Zhaoxia Hu, Hongyu Li, et al., 2003: Numerical simulation of hailstorms and the characteristics of accumulation zone of supercooled raindrops in Xunyi county, Climatic and Environmental Research, 8, 196-208 (in Chinese).

EVALUATION OF GROUND-BASED RADAR AND IN-SITU AIRCRAFT DATA COMPARISON IN WINTER STORMS

D. Hudak[1], P. Rodriguez[1], M. Wolde[2], B. Currie[3], S. Cober[1], I. Zawadzki[4] and G. Isaac[1]

[1]Cloud Physics Research Division, Meteorological Service of Canada, Toronto, Ontario, M3H 5T4, Canada
[2]Institute for Aerospace Research, National Research Council of Canada, Ottawa, Ontario, K1A 0R6, Canada
[3]Adaptive Systems Laboratory, McMaster University, Hamilton, Ontario, L8S 4K1, Canada
[4]Department of Atmospheric Sciences, McGill University, Montreal, Quebec, H3A 2K6, Canada

1. INTRODUCTION

There is an increasing synergetic use of remote sensing technology, particularly polarization diversity radars, and in-situ measurements from aircraft to more fully explore cloud and precipitation properties. Studies involve the application of algorithms that use radar data to derive cloud properties that are then compared with direct aircraft in-situ measurements (Ryzhkov et al., 1998). Alternately, they can deal with the modeling of aircraft measurements to derive radar variables that are then compared to ground-based radar measurements (Zrnic et al., 2002). Other similar intercomparison studies involving winter weather include Barthazy et al. (2001) where ground-based in-situ and radar measurements were used and Liao et al. (2003) where aircraft in-situ and radar measurements and ground-based radar measurements were employed. In all these studies, the assessment of the various retrieval algorithms was of a qualitative nature. This was due to uncertainties in the precision of the measurements, space-time sampling discrepancies of the different sensors, the sampling strategy employed in the data collection and the exact nature of the phenomenon being investigated. This study is aimed at exploring these errors as they apply to stratiform winter cloud systems in central North America.

2. METHODOLOGY

The Alliance Icing Research Study I (AIRS I) field project was conducted during the winter of 1999-2000 in the vicinity of Mirabel airport near Montreal, Canada. A key component of the operations plan was to collect a coordinated dataset that combined in-situ aircraft and ground-based radar data. Ground-based radar data were collected by two dual polarized radars, the McMaster University portable X-band radar (IPIX) deployed at Mirabel, and the McGill S-band radar at the Marshall Radar Observatory (MRO) located about 30 km SSE of Mirabel. The IPIX radar scan strategy, limited by other operational constraints, was a series of descending fixed-elevation stares, designed to follow the aircraft The MRO radar employed a fast scanning strategy performing 24-elevation full volume scans every 5 minutes. The NRC Convair-580 aircraft collected in-situ data by performing predetermined sets of maneuvers, the main ones being constant altitude reciprocal runs, termed legs, and spiral ascents/descents, termed spirals. Further details of the data collection and analysis are given in Hudak et al. (2002). In total, approximately 22 hours of in-situ data were collected by the aircraft.

The resultant aircraft microphysical data, averaged to 30 s resolution, included detailed particle spectra for both water and ice as well as a cloud phase determination (liquid, glaciated, or mixed phase) as described in Cober et al. (2001). Radar observables that were derived included reflectivity (Z) following Heymsfield et al. (2002) and differential reflectivity (Z_{DR}) using the T-matrix approach (Wolde et al., 2003). These quantities were then compared with the ground-based radar observations.

The strategy to carry out the comparison is shown schematically in Fig. 1. The horizontal and vertical distance from the centre of the aircraft sample volume to the centre of the radar resolution cell was determined. Correlation statistics were derived as a function of the magnitude of these two offsets as well as of the cloud phase.

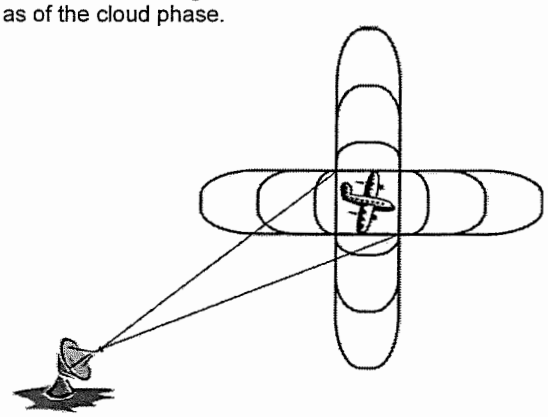

Figure 1: An illustration of the horizontal and vertical offsets of the radar volumes in an expanding window around the aircraft location.

Corresponding author's address: Peter Rodriguez, Meteorological Service of Canada, 14780 Jane Street, King City, Ontario, L7B 1A3, Canada; E-Mail: Peter.Rodriguez@ec.gc.ca.

3. RESULTS

Figure 2 gives the autocorrelation of Z deduced from aircraft data stratified by aircraft maneuver. In a typical 30 s interval, the aircraft would have moved about 2.5 km horizontally during legs or changed altitude by 150 m during spirals. The decrease in autocorrelation with increasing lag is much less for the legs than the spirals. This is an indication of the stratiform nature of these cloud systems.

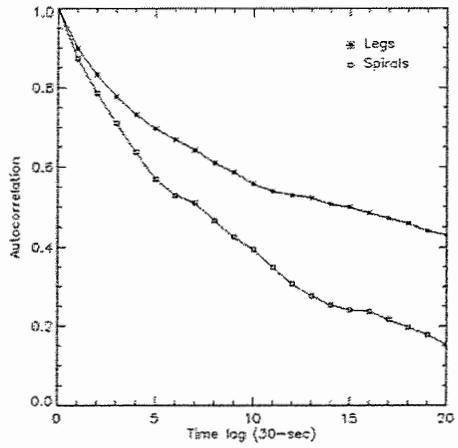

Figure 2: Autocorrelation of aircraft-derived Z by flight maneuver.

The difference in time between the aircraft and coincident radar observation was examined. With the fast scanning of MRO, the maximum Δt possible was 120 s. Within this bound, the correlation statistics showed no sensitivity to the time offset – an indication that these winter cloud system evolve on significantly longer time scales.

Length statistics for portions of the cloud system defined by the three phases based on the aircraft analysis were calculated. For the legs, the median length of continuous cloud phase segments was 3.5 min, 3 min, and 3 min for liquid, mixed phase and glaciated portions of the cloud system. For spirals, the median values were 4.5 min, 4.5 min, and 10.5 min respectively for the three phases. This would suggest that the main difference in the three phases is the limited vertical extent of liquid and mixed phase conditions relative to glaciated conditions.

The MRO data were used to examine the effect of vertical variability on the in-situ – radar comparison. The nature of the volume scanning is such that the horizontal offset would always be less than 2 km. The IPIX data, with its strategy of staring scans, were used to examine the effect of horizontal variability. Figure 3a is an example of the aircraft altitude variation during one event. The level section reflects the legs that were flown in the immediate vicinity of Mirabel. Figures 3b and 3c show the difference in aircraft range and

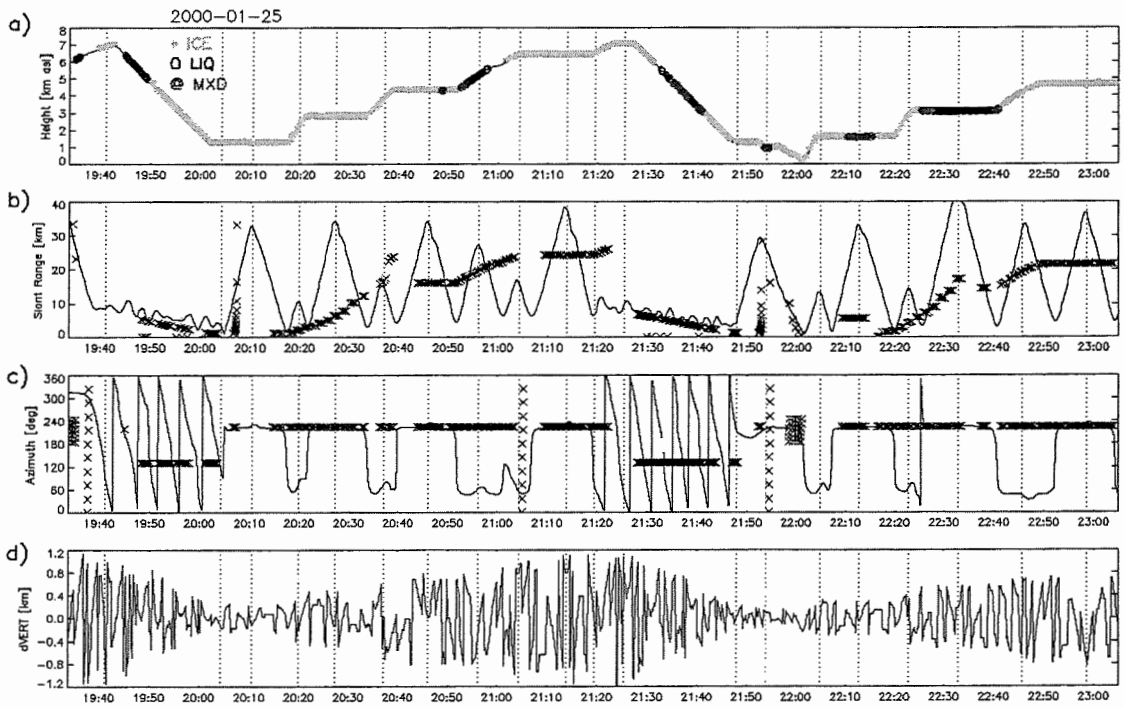

Figure 3: Sample time history of data used in the matching algorithm: a) aircraft altitude and derived cloud phase; b) the range and c) azimuth offset of the aircraft relative to the IPIX beam (see text); and d) vertical offset between aircraft and beam axis of the closest MRO radar volume bin.

azimuth relative to the IPIX beam. The asterisks indicate the range and azimuth of the closest IPIX bin and the line the aircraft position. Where they are close defines regions where the spatial offsets were the least. Figure 3d gives the time history of the variation in the vertical offset of the aircraft data relative to MRO data. It is apparent that MRO will generally have smaller offsets giving a larger number of "close" matches than IPIX.

Figure 4 gives the scatter plot of the Z comparison of the aircraft and MRO data. Table 1 gives the summary of the correlation statistics stratified by vertical offset and cloud phase. Within a vertical offset of 250 m, there is little change in the correlation statistics regardless of the cloud phase. Beyond 500 m, there is a dramatic decrease in the correlation for the glaciated and mixed phase clouds. For the liquid clouds, the decrease begins beyond 250 m. This implies that the liquid layers in these winter cloud systems are of more limited vertical extent than the other two phases. This suggests that beyond a vertical offset of 250 m, the errors due to spatial offsets become dominant. However, with a vertical offset < 250 m, liquid cloud regions had the highest correlations (0.85). This is an indication that the derivation of Z in these cases is less prone to errors, as the measurements are more representative and the retrievals more reliable. The reduction of the correlation from 1.00 would be primarily due to discrepancies in the sampling volumes of the aircraft and radar observations. Further reductions in the correlation in the mixed phase and glaciated cloud conditions reflect the uncertainty in the algorithm retrievals to deduce Z. This would be caused by measurement errors, modeling deficiencies or both.

Figure 5 and Table 2 summarize the results of the horizontal variability analysis using the IPIX data. The correlations are higher here than in the MRO data. Located closer to the aircraft than MRO and using fixed beam scans, the result was better precision in the measurements brought about by more samples per observation, better sensitivity, and smaller resolution volumes. The drawback in this data collection approach is that there was only approximately ¼ the number of "close" matches available for the analysis. An illustration of this is that there were not enough liquid cases on which to carry out a statistical evaluation. The results show that the correlations remained relatively steady and only beyond 3 km do they begin to deteriorate. The correlations are higher in the mixed phase than in the glaciated phase clouds for horizontal offsets > 1 km. This may be an indication that conditions in mixed phase regions were more uniform than in glaciated portions or that the modeling of reflectivity is less prone to errors in mixed phase conditions where better defined ice particles are more likely. In the glaciated phase clouds, more irregular particles that would be more difficult to measure, characterize, and model accurately were present.

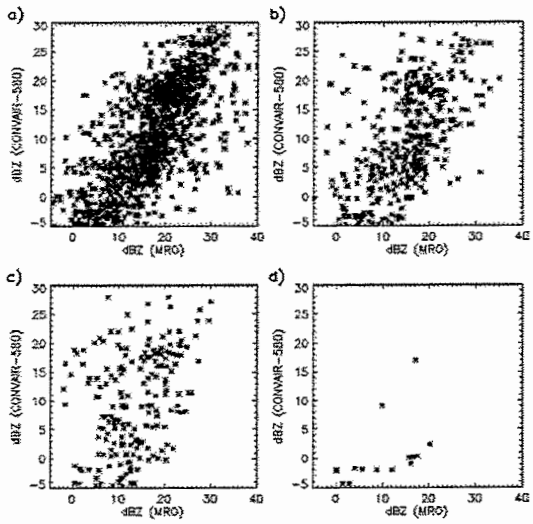

Figure 4: A comparison of Z between MRO and Convair-580 for vertical offset regions a) < 250 m; b) 250 - 500 m; c) 500 - 750 m; and d) 750 - 1000m.

Cloud phase	Vertical offset (m) 0 to 125	125 to 250	250 to 375	375 to 500	500 to 625	625 to 750
All	0.71	0.68	0.59	0.57	0.40	0.30
Ice	0.72	0.72	0.61	0.58	0.37	0.36
Liquid	0.89	0.81	0.45	0.21		
Mixed	0.67	0.60	0.60	0.56	0.32	0.09

Table 1: Correlation coefficient for Z between aircraft and MRO as a function of vertical offset.

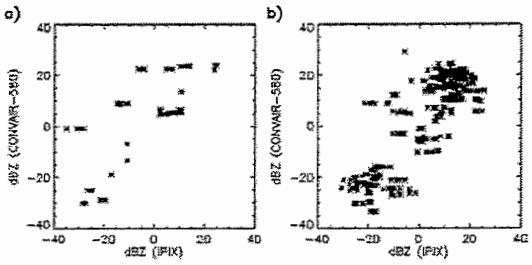

Figure 5: A comparison of Z between IPIX and Convair-580 for a) mixed phase; and b) glaciated conditions.

Cloud phase	Horizontal offset (km) < 0.5	0.5 to 1.0	1.0 to 1.5	1.5 to 2.0	2.0 to 2.5	2.5 to 3.0	3.0 to 3.5
All	0.88	0.92	0.86	0.82	0.80	0.78	0.67
Ice	0.87	0.91	0.57	0.69	0.62	0.68	0.65
Mixed	0.85	0.93	0.92	0.92	0.90	0.86	0.78

Table 2: Correlation coefficient for Z between aircraft and IPIX as a function of horizontal offset.

Wolde et al. (2003) performed a simulation of Z_{DR} for one of the AIRS I flights. For this limited data set, a comparison of the modeled and measured Z_{DR} was carried out. For MRO data, the correlation with a vertical offset < 250 m was lower than with Z, 0.62 vs. 0.70. And beyond 250 m, the Z_{DR} correlations decreased more significantly down to 0.26 vs. 0.58. This is an indication of the difficulty in obtaining in-situ measurements suitable for the modelling of the polarimetric properties using the aircraft data; for example, the inability to provide canting angle information. With IPIX, the Z_{DR} correlations were higher than with MRO, but its trend with vertical opening was the same. There were too few IPIX data points for a statistical assessment. The lack of matching data points with IPIX is further exaggerated since polarimetric data requires a relatively low antenna elevation angle so, unlike MRO which was located away from Mirabel, IPIX was unable to provide any information to correspond to the aircraft observations taken overhead of the airport.

4. SUMMARY AND CONCLUSIONS

This work examined the nature of the errors involved in comparing in-situ aircraft measurements with measurements from two ground-based radars. MRO's fast scanning cycle from a locale removed from Mirabel proved to generate a larger quantity of "close" matches. IPIX on the other hand with its proximity to Mirabel, had better quantitative results. The vertical separation between aircraft position and the centre of the radar bin was a far more sensitive parameter than the horizontal separation. The best correlations occur when the vertical offset is less than 250 m. Beyond 500 m and a horizontal offset of 3 km the errors in the space sampling become a dominant source of error. This is consistent with the matching window of Ellis et al. (2001).

The data were stratified by cloud microphysical conditions. Vertical offset correlation statistics were shown to be dependent on the nature of the cloud system. Liquid cloud areas, with their limited vertical extent, showed a quicker deterioration in their correlation statistics with vertical offset. Correlations were also shown to be dependent on the uncertainty in the retrieval algorithms, either due to measurement or modeling inaccuracies. This effect was also apparent in the retrieval of Z_{DR} that had lower correlations and a stronger sensitivity to vertical offset than Z. Further exploration of the space sampling uncertainties as it applies to polarimetric retrievals using the T-matrix approach will require more advanced aircraft data analysis on the nature of the particles (e.g. Korolev and Sussman, 2000).

5. ACKNOWLEDGMENTS

The authors gratefully acknowledge the financial support given to AIRS by the National Search and Rescue Secretariat, the Department of National Defense, Transport Canada, NASA Glenn, Boeing Commercial Airplane Group, and the US Federal Aviation Administration. We are thankful to Dr. Vivekanandan of NCAR for providing the T-matrix code.

6. REFERENCES

Barthazy, E., S. Goeke, J. Vivekanandan, and S. Ellis, 2001: Detection of snow and ice crystals using polarization radar measurements: comparison between ground-based in situ and S-Pol observations. Atmos. Res., 59-60, 137-162.

Cober, S., G. Isaac, A. Korolev, and J. Strapp, 2001: Assessing cloud-phase conditions. J. Appl. Meteor., 40, 1967-1983.

Ellis, S., J. Vivekanandan, S. Goeke, E. Brandes, J. Stith, and R. Keeler, 2001: In-situ verification of remote aircraft icing detection using S-band polarization radar measurements. 30th Intl. Conf. On Radar Meteorology, Amer. Meteor. Soc., 168-170.

Heymsfield, A.J., S. Lewis, A. Bansemer, J. Iaquinta, and L. Miloshevich, 2002: A general approach for deriving the properties of cirrus and stratiform ice cloud particles. J. Atmos. Sci., 59, 3-29.

Hudak, D., B. Currie, P. Rodriguez, S. Cober, I. Zawadzki, G. Isaac and M. Wolde, 2002: Cloud Phase Detection in Winter Stratiform Clouds using Polarimetric Doppler Radar. ERAD Publication Series, Vol. 1, ISBN 3-936586-04-7, 90-94.

Korolev, A., and B. Sussman, 2000: A technique for habit classification of cloud particles. J. Atmos. Oceanic Technol., 17, 1048-1056.

Liao, L., R. Meneghini, T. Iguchi, and A. Detwiler, 2003: Validation of snow parameters as derived from dual-wavelength airborne radar. 31st Conf. On Radar Meteorology, Amer. Meteor. Soc., 411-414.

Ryzhkov, A., D. Zrnic, and B. Gordon, 1998: Polarimetric method for ice water content determination. J. Appl. Meteor., 37, 125-134.

Wolde, M., D. Hudak, B. Currie, S.G. Cober, P. Rodriguez, I. Zawadzki, G.A. Isaac and D. Marcotte, 2003: Radar Signatures of Winter Clouds from Aircraft In-Situ Data and Ground-Based Radar Observations. 31st Conf. On Radar Meteorology, Amer. Meteor. Soc., 973-975.

Zrnic, D., M. Loney, J. Straka, and A. Ryzhkov, 2002: Enhanced polarimetric radar signatures above the melting level in a supercell storm. IEEE Intl. Geosci. and Remote Sensing Symposium, Toronto, Canada, 296-298.

USE OF MASS VERSUS VOLUME UNITS FOR CLOUD MICROPHYSICAL PARAMETERS

by

G.A. Isaac, I. Gultepe, S.G. Cober

Cloud Physics and Severe Weather Research Division, Meteorological Service of Canada,
Toronto, Ontario, M3H 5T4, Canada

1. INTRODUCTION

It has been common practice to use volume units for characterizing cloud parameters. Textbooks (e.g. Mason, 1971; Rogers and Yau, 1989; Pruppacher and Klett, 1997) usually quote cloud microphysical parameters such as aerosol, ice particle and droplet concentration in number per cm^{-3} or per l^{-1}. Similarly, mass concentrations such as cloud liquid water content, ice water content, etc, are usually quoted in mass per m^{-3}. Even when summarizing measurements from large data sets, usually measurements made at different altitudes (or pressure levels) are combined without regard to referencing them to some common altitude (e.g. Hobbs and Rangno, 1985; Mazin, 1995; Gultepe and Isaac, 1997). This paper will examine the issue of whether cloud microphysical data should be characterized in volume or mass units, or referenced to some common temperature and pressure.

2. DATA ANALYSIS AND RESULTS

Fig. 1 shows the 25%, 50%, 75%, 95% and mean values of liquid water content (LWC) in g kg^{-1} and cloud droplet concentration N_d at sizes < 100 μm in number per g plotted against temperature for measurements made using the National Research Council Convair-580 aircraft in several different field projects. The data points used in this analysis consist of 30 s (approximately 3 km in space scale) averaged values from aircraft penetrations. The data were segregated into 4°C intervals centered on the values indicated. The discrimination of clouds as all liquid, mixed phase or glaciated has been performed using the methods of Cober et al. (2001). The field projects used were the Canadian Freezing Drizzle Experiment (CFDE) I and III, the Alliance Icing Research Study (AIRS) and the FIRE Arctic Cloud Experiment (Isaac et al., 2001; Gultepe and Isaac, 2002). The measurements were made in winter stratiform and Arctic clouds. Figs 2 and 3 show total water content (TWC) in all clouds (liquid, mixed and glaciated) and ice particle number concentration (N_i) for sizes > 100 μm (mixed and glaciated) in mass units g kg^{-1} and number per kg, respectively.

For LWC and TWC, a consistent correlation with temperature is seen in Figs. 1a and 2. N_d shows a maximum values near −10°C (Fig. 1b). However, Fig. 3 shows no increase in N_i with temperature, as one might expect.

Fig. 4 shows the measurement level of all the data from the field projects as a function of pressure and temperature. Figs. 1-3 use subsets of this data, and no data at temperatures warmer than 0°C or colder than -28°C were used. However, Figs. 1-3 contain data, which span the pressure range indicated in Fig. 4.

Table 1 shows the same data as Figs. 1, 2 and 3 but the data were analyzed in their original volume units at the measurement level and in volume units that were referenced to a standard temperature and pressure (STP) level of 0°C and 1013 mb. The STP data presentation is similar to a mass concentration because a simple multiplication factor would convert the numbers to mass units. However presenting the data in this manner allows a direct comparison of the volume and "mass" measurements. It is clearly shown that there can be a factor two between the different methods of presenting the data. The rate of change of LWC and TWC with temperature is less when the data are converted into mass units. This is due to the fact that measurements at colder temperatures were usually taken at lower pressure altitudes (Fig. 4).

3. DISCUSSION

It is known that small changes in cloud parameters within climate models can have a strong influence on the simulations. For example, Slingo (1990) indicated that "the top of the atmosphere radiative forcing by doubled carbon dioxide concentrations can be balanced by modest relative increases of 15-20% in the amount of low clouds and 20-35% in liquid-water path, and by decreases of ~15-

Corresponding author's address:
George A. Isaac
Meteorological Service of Canada
4905 Dufferin Street, Toronto, Ontario, M3H 5T4,
Canada. E-Mail: george.Isaac@ec.gc.ca

20% in mean drop radius. This indicates that a minimum relative accuracy of ~5% is needed, ...to simulate these quantities in climate models. Rotstayn (1999) suggested that a 1% increase in cloudiness, a 6% increase in liquid water path, and a 7% decrease in effective radius (r_{eff}) may result in a radiative forcing of about –2.1 W m^{-2} in the heat budget of the atmosphere. Table 1 indicates that simply changing units between volume and mass units can produce these types of differences in cloud properties.

Mass units for cloud parameters are used in mesoscale models (Myers and Cotton, 1992) and climate models (Yao and DelGenio, 2002; Rash and Kristjánsson, 1998; von Salzen and McFarlane, 2002). Consequently it would seem logical to analyze the data in that manner for the modeling community.

Chemical reactions are usually calculated using mass units, and this provides additional rational for reporting measurements in this manner.

Much of the data for this paper were collected for characterizing the cloud environment to develop guidelines for certifying aircraft for flight into icing conditions. Determining the extreme values is very important. This is one reason the 95% values have been presented. Different results can be obtained if the data are analyzed in volume versus mass units, especially at cold temperatures. This could be important if aircraft icing conditions are being simulated in ground icing wind tunnels.

4. CONCLUSIONS

This paper provides justification for collecting and organizing cloud microphysical data in mass units, or in volume units referenced to a standard temperature and pressure. Table 1 also shows that reporting means or medians can easily give differences that might be important. The variability in cloud parameters is quite large and needs to be considered. Although not discussed in this paper, the scale over which the data are averaged is also important and it should be clearly documented in any summary (see Gultepe and Isaac, 1999). Overall, greater care should be exercised when reporting cloud microphysical data.

5. ACKNOWLEDGEMENTS

This work was funded by the National Search and Rescue Secretariat, Transport Canada, the Panel on Energy Research and Development, as well as Boeing, NASA and the Federal Aviation Authority. The data were collected using the Canadian National Research Council Convair-580 and the authors are grateful to their NRC colleagues for their assistance.

6. REFERENCES

Cober, S.G., G.A. Isaac, A.V. Korolev, and J.W. Strapp, 2001: Assessing cloud-phase conditions. *J. Appl. Meteor.*, 40, 1967-1983.

Gultepe, I., and G. A. Isaac, 1997: Liquid water content and temperature relationship from aircraft observations and its applicability to GCMs. *J. Climate*, **10,** 447-452.

—, and, —, 1999: Scale effects on the relationship between cloud droplet and aerosol number concentrations: Observations and models. *J. of Climate*, 12, 1268-1279.

—, and —, 2002: The effects of air-mass origin on Arctic cloud microphysical parameters during FIRE.ACE. *J. Geophy. Res., 107,* (C10), SHE 4-1 to 4-12.

Hobbs, P. V., and A. L. Rangno, 1985: Ice particle concentrations in clouds. *J. Atmos. Sci.*, **42,** 2523-2549.

Isaac, G.A., S.G. Cober, J.W. Strapp, A.V. Korolev, A. Tremblay, and D.L. Marcotte, 2001: Recent Canadian research on aircraft in-flight icing. *Canadian Aeronautics and Space Journal, 47*, 213-221.

Mason, B.J., 1971: The physics of clouds. 2d ed. Clarendon Press. 671 pp.

Mazin, I. P., 1995: Cloud water content in continental clouds of middle latitudes. *J. Atmos. Res.*, **35,** 283-297.

Meyers, M. P., and W. Cotton, 1992: Evaluation of the potential for wintertime quantitative precipitation forecasting over mountainous terrain with an explicit cloud model. Part I: Two dimensional sensitivity experiments. *J. Appl. Meteor.* 31, 26-50.

Pruppacher, H.R. and J.D. Klett, 1997: Microphysics of clouds and precipitation. Kluwer Academic Publishers. ISBN 0-7923-4211-9.

Rasch, P. J., and J. E. Kristjánsson, 1998: A Comparison of the CCM3 Model Climate Using Diagnosed and Predicted Condensate Parameterizations *Journal of Climate:* Vol. 11, No. 7, pp. 1587–1614.

Rogers, R.R. and M.K. Yau, 1989: A short course in cloud physics – third edition. Buterworth-Heinemann Publications. ISBN 0-7506-3215.

Rotstayn, L.D., 1999: Climate sensitivity of the CSIRO GCM: Effect of cloud modelling assumptions. *J. Climate*, 12, 334-356.

Slingo, A., 1990: Sensitivity of the Earth's Radiation Budget to Changes in Low Clouds. *Nature*, 343, 49-51.

Von Salzen, K. and McFarlane, N.A., 2002: Parameterization of the Bulk Effects of Lateral and Cloud-Top Entrainment in Transient Shallow Cumulus Clouds, *J. Atmos. Sci.:* Vol. 59, No. 8, pp. 1405–1430.

Yao, M-S, and A.D. DelGenio, 2002: Effect of cloud parameterization on the simulation of climate changes in the GISS GCM. Part II: sea surface temperature and cloud feedbacks. *J. Climate*, 15,2491-2503.

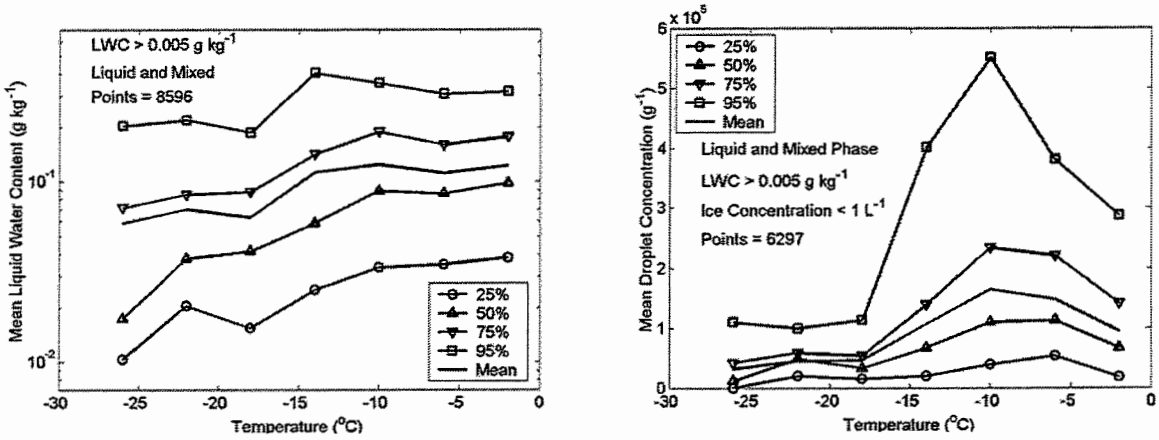

Fig. 1: The 25%, 50%, 75%, 95% and mean 30 s averaged liquid water content (LWC) in g kg^{-1} (left panel) and the droplet number concentration (N_d) at sizes < 100 μm in number per g (right panel) for all liquid and mixed phase clouds with liquid water contents greater than 0.005 g kg^{-1}. For N_d, there is a restriction that the N_i is less than 1 L^{-1}. This reduces errors caused by false counts due to ice crystals (Cober et al., 2001).

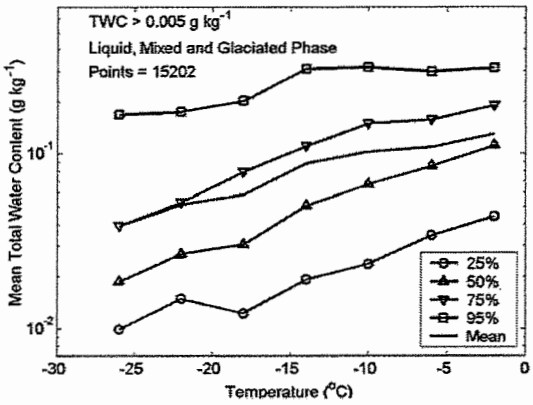

Fig. 2: The 25%, 50%, 75%, 95% and mean 30 s averaged total water content (TWC) as a function of temperature for TWC greater than 0.005 g kg^{-1} in liquid, mixed and glaciated clouds

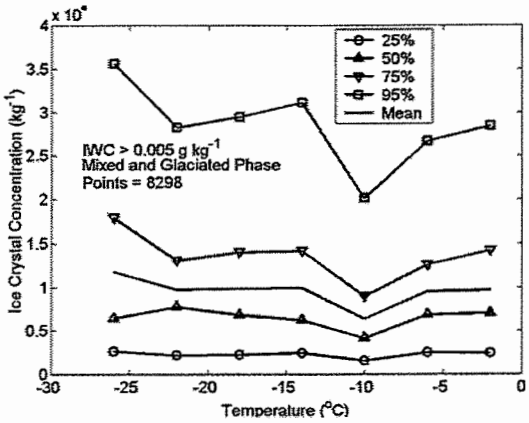

Fig. 3: The 25%, 50%, 75%, 95% and mean 30 s averaged ice crystal concentration (N_i) in number per kg as a function of temperature for ice water contents greater than 0.005 g kg^{-1} in mixed and glaciated clouds. Only particles with sizes > 100 μm were counted for this plot. For the glaciated clouds, all the particles were assumed to be ice, and for the mixed phase clouds, all the non-circular particles were assumed to be ice (Cober et al., 2001).

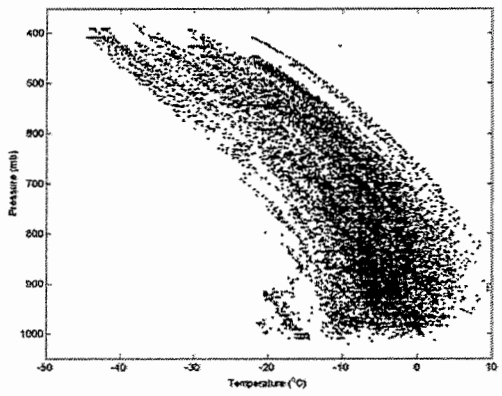

Fig. 4: Pressure versus temperature plot for the location of all the data used in preparation of Figs. 1 to 3, and Table 1.

Liquid Water Content (LWC) Versus Temperature (T)

T [°C]	LWC [g m^{-3}]					LWC [g m^{-3}] at STP				
°C	25%	50%	75%	95%	Mean	25%	50%	75%	95%	Mean
-2	0.04	0.11	0.20	0.35	0.13	0.05	0.13	0.23	0.41	0.16
-6	0.04	0.10	0.18	0.34	0.12	0.05	0.11	0.21	0.40	0.14
-10	0.03	0.10	0.20	0.35	0.13	0.04	0.11	0.25	0.46	0.16
-14	0.02	0.06	0.14	0.41	0.11	0.03	0.08	0.18	0.52	0.15
-18	0.01	0.04	0.07	0.15	0.05	0.02	0.05	0.11	0.24	0.08
-22	0.02	0.04	0.07	0.14	0.05	0.03	0.05	0.11	0.29	0.09
-26	0.01	0.01	0.05	0.15	0.04	0.01	0.02	0.09	0.26	0.08

Total Water Content (TWC) Versus Temperature (T)

T [°C]	TWC [g m^{-3}]					TWC [g m^{-3}] at STP				
	25%	50%	75%	95%	Mean	25%	50%	75%	95%	Mean
-2	0.05	0.12	0.20	0.34	0.14	0.06	0.14	0.25	0.41	0.17
-6	0.04	0.09	0.17	0.32	0.12	0.04	0.11	0.20	0.38	0.14
-10	0.02	0.07	0.15	0.31	0.10	0.03	0.09	0.19	0.41	0.13
-14	0.02	0.04	0.09	0.27	0.08	0.02	0.07	0.14	0.40	0.11
-18	0.01	0.02	0.06	0.15	0.04	0.02	0.04	0.10	0.26	0.08
-22	0.01	0.02	0.04	0.12	0.04	0.02	0.03	0.07	0.23	0.07
-26	0.01	0.01	0.03	0.11	0.03	0.01	0.02	0.05	0.22	0.05

Droplet Number Concentration (N_d) Versus Temperature (T)

T [°C]	N_d [cm^{-3}]					N_d [cm^{-3}] at STP				
	25%	50%	75%	95%	Mean	25%	50%	75%	95%	Mean
-2	22	72	151	329	106	25	87	184	371	123
-6	59	121	240	446	165	70	146	286	492	191
-10	43	120	240	568	173	51	143	303	714	214
-14	18	68	142	437	114	27	88	181	520	139
-18	12	28	52	106	45	20	44	70	147	61
-22	14	38	71	87	43	27	63	77	130	59
-26	0	9	38	98	27	0	16	54	142	42

Ice Particle Concentration (N_i) versus Temperature (T)

T [°C]	N_i [L^{-1}]					N_i [L^{-1}] at STP				
	25%	50%	75%	95%	Mean	25%	50%	75%	95%	Mean
-2	3	8	14	27	10	3	9	18	37	13
-6	3	7	13	26	10	3	9	16	34	12
-10	2	4	9	17	6	2	5	12	26	8
-14	2	5	11	23	8	3	8	18	40	13
-18	2	5	10	20	7	3	9	18	38	13
-22	2	6	9	20	7	3	10	17	36	13
-26	2	5	12	23	8	3	8	23	46	15

Table 1: Parameters shown in Figs. 1, 2 and 3 are given here in the original volume units from the measurement level and volume units at STP (0°C and 1013mb).

THE STRUCTURE OF HAIL STORM DEVELOPED AT HANSHIN AREA IN JAPAN

Hiroyuki Konishi[1], Yukari Shusse[2] and Yoshimasa Takaya[3]

[1]Osaka Kyoiku Univ., Kashiwara-shi, Osaka, 582-8582 Japan
[2]HyARC, Nagoya Univ., Nagoya-shi, Aichi, 464-8601, Japan
[3]Meteorological Research Institute, Tsukuba-shi, Ibaraki 305-0052, Japan

1. INTRODUCTION

A lot of large hailstones fell in a short time at Hanshin area in west part of Japan on May 26, 2002. The hail particles were collected at 3 sites at intervals about 10km along the movement of a hail storm from west to east. The particle diameter was measured and the internal structure of hailstones was observed carefully from the thin section to investigate the development process of the hails in clouds. The formation process of hail was also considered with the data of dual Doppler weather radars. The hail was rare phenomena in that area, which observed only three times in the past five years.

2. PARTICLE DIAMETER OF HAIL

The hailstones were collected at different three sites at Ashiya, Amagasaki, and Suita as shown in Fig. 1. The numbers of collected hailstones are 111, 50-60, and 7 pieces, respectively. They were photographed close and the particle diameter was measured. Since the collection of hailstones was not random, the size distribution shown in Fig. 2 may not show the

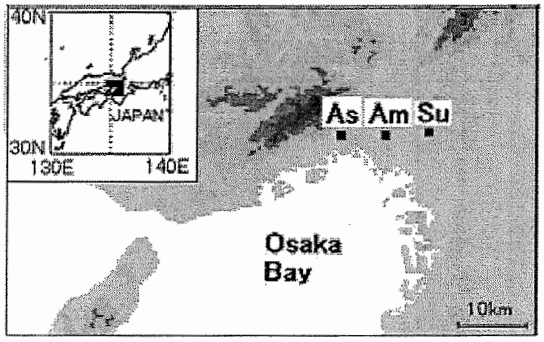

Fig. 1. Location of Hanshi area. The site of Ashiya, Amagasaki and Suita are symbolized as As, Am and Su.

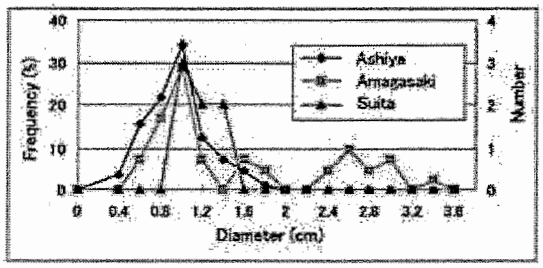

Fig. 2. Size distribution of hailstones observed at Ashiya, Amagasaki, and Suita. The distribution shows the relative frequency at Ashiya and Amagasaki, the actual number at Suita.

Corresponding author's address: Hiroyuki Konishi, Osaka Kyoiku Univ., 4-698-1, Asahigaoka, Kashiwara-shi, Osaka, 582-8582, Japan; E-Mail: konishi@cc.osaka-kyoiku.ac.jp

size distribution of actual hailstones as it is considered that many of large particles were collected. The size distribution show that the mode value of diameter was 1.0cm every site and maximum diameter was 3.2 cm observed at Amagasaki. Due to the hailstones larger than 2cm were recorded only in Amagasaki, it is expected that the clouds were most developed near Amagasaki. Since it is presumed that the diameter of 1cm and the fall speed of 3cm hail are 9 m/sec and 21 m/sec, respectively, the updraft more than this speed would exist in the clouds in which these hailstones were formed.

2. THE STRIPED PATTERN OF HAILSTONES

The total 74 thin sections of hailstones were made and the internal structures were investigated. The shape of hailstones was divided into two types; spherical and conical shape, and the ratio between spherical shape and conical shape was about 6 to 4. Many thin sections of hailstones have alternate opaque and transparent layers. The opaque layer has many small air bubbles and transparent layer has few bubbles. The example of typical thin section of hailstones is shown in Fig. 3. As for the number of stripe (opaque and transparent) patterns, three or more layers occupied 70% in the conical shape as against two or less layers occupied 70% in the spherical shape, Thus it is presumed that the quantity of the supercooled water drop and temperature change largely in clouds when conical hailstones were formed.

The ratio of an opaque layer occupies to the whole was also investigated about spherical

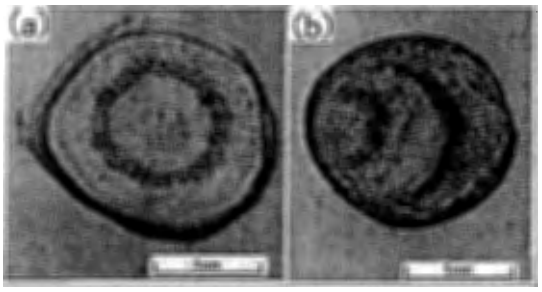

Fig. 3. Striped pattern of typical hailstones. The scale length shows 5mm. (a)Spherical shape (b) Conical shape

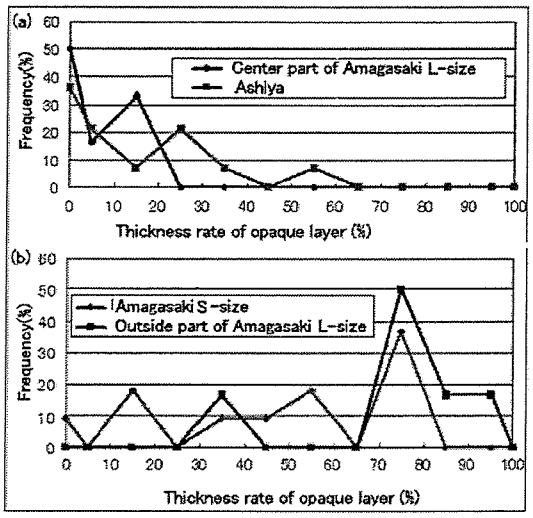

Fig. 4. Rate that opaque layer occupies to the whole. (a) The center part of Amagasaki large hailstones and Ashiya hailstones. (b) The outside part of Amagasaki large hailstones and Amagasaki small hailstones.

shape hailstones collected in Ashiya and Amagasaki. It is thought that a transparent layer is generally formed when temperature goes up or less water content, and an opaque layer is formed when freezing immediately after abundant supercooled water drops adhering under low temperature. Therefore, if the ratio of opaque in hailstone is higher, it will grow up

under low temperature and/or much abundant super cooled water, and if the ratio of transparent is higher, it will be expected that it grew up under high temperature relatively.

Figure 4 (a) and (b) show the frequency distribution of the rate of radial thickness for the opaque layer occupied from the center to outside. The ratio for the hailstone larger than 2cm was measured separately that divided into two parts by a radius of 5mm. As shown in Fig. 4(a), the frequency is similar between the hailstones fallen at Ashiya and the center part of large hailstones fallen at Amagasaki. Their opaque ratio less than 30% is frequent. On the other hand the frequency of the small hailstones at Amagasaki and the outside portion of large hailstones fallen at Amagasaki were similar and they were mainly opaque because of their opaque ratio exceeding 70% is dominant. Therefore the following process is guessed to form the hailstones. First, transparent hail with a diameter of about 1cm is formed with a low altitude, the part comes down to Ashiya, and the remainder is carried by larger updraft to high altitude. The hailstones carried to high altitude attaches to the outside the opaque layer which shows the growth under low temperature with much abundant liquid water, and becomes large to about 3cm. Moreover, hail which newly began to grow simultaneously grows to about 1cm, and it is thought that these came down to Amagasaki.

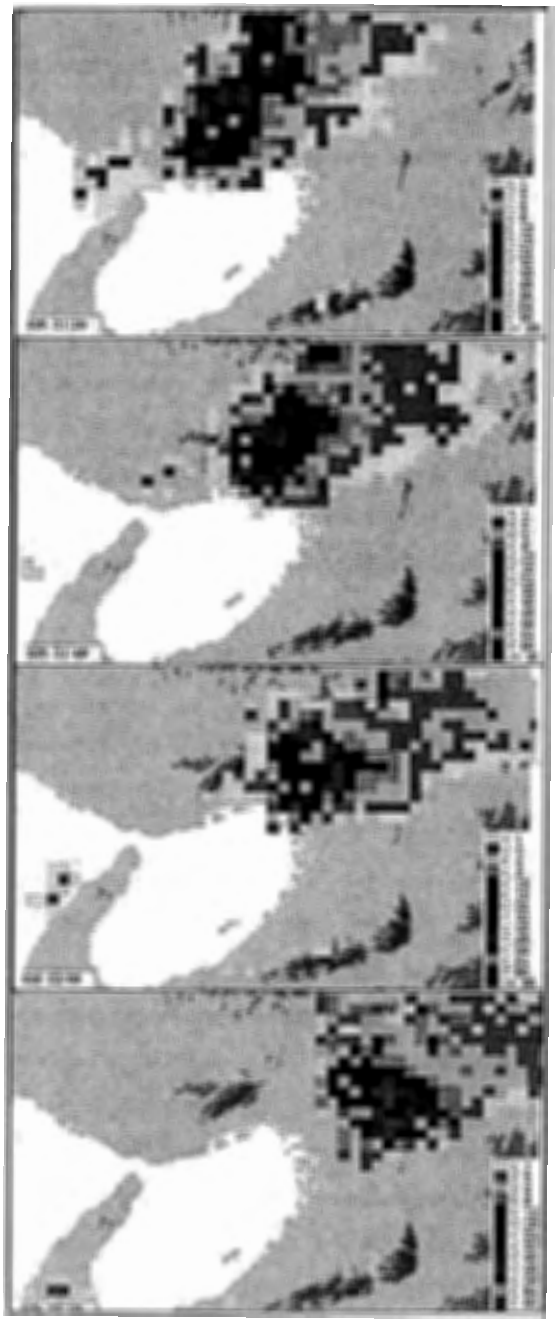

Fig. 5. Change of echo at 20-minute interval of Osaka radar from 21:20 to 22:20 on May 26, 2002. One grid means 2.5km square. The strong echo region where a deep-black portion is equivalent to 80 mm/hr rainfall.

3. THE CLOUDS BROUGHT HAILSTONES

The clouds brought the hailstones had the band structures accompanying the cold front.

Figure 5 shows the time change of the echo observed by JMA Osaka radar. The echo became strong rapidly at the southwest end of the line echo 20km in width extended from the northeast to southwest, moving to east at the rate of about 50 km/h. In spite of there was almost no rain at Kobe 15 km west of Ashiya, the heavy rain and hail was observed Ashiya about 20mm per 10 minutes. It was only for 80 minutes from 21:20 to 22:40 that the strong echo equivalent to 80mm/h rainfalls was observed. The wind from the south or southwest from Osaka Bay would cause an echo develop rapidly along the mountain.

Time change of strong echo considerable strong rain of 80 or more mm/hr and time change of echo intensity of Ashiya, Amagasaki, and Suita are shown in Fig. 6. The strong echo of 80 mm/hr began to be observed at the every site of Ashiya, Amagasaki, and Suita located in a line with east and west at intervals of about 10km, at 21:20, 21:30 and 21:50, respectively. The strong echo area becomes the largest around 22:00

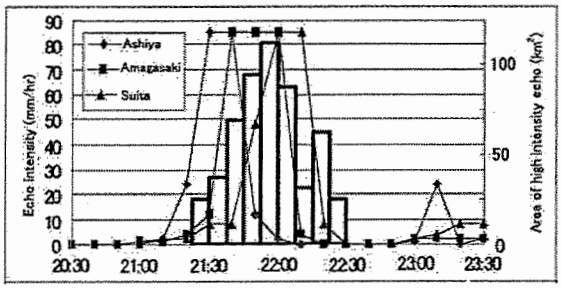

Fig. 6. Time change of area of strong echo considerable rain of 80 or more mm/hr (bar graph) and time change of echo intensity of Ashiya, Amagasaki, and Suita (polygonal line)

near Amagasaki, but continued short duration less than 20 minutes. The area of a strong echo at this time is about 100km^2, and it is expected that the hailstorm was concentrating on the narrow area about 10km square. Thus, the developmental stage of hailstones presumed from the radar echo was well in agreement, and corresponded that guessed from the shape and the internal structure of hailstones from a radar echo.

4. CONCLUSION

The size distribution and the internal structure of hailstones were investigated which was observed between Hanshin area on May 26, 2002. The particle diameter of hailstones was a maximum of 3.2cm, and most of them was about 1cm. The total 74 thin section of hail were made and measured the ratio between transparent and opaque layers. The ratio shows that the hail collected at 3 sites was much different each other. The hail particles observed were mainly transparent at Ashiya where the cloud cell was in a develop stage, however, that was mainly opaque observed at Amagasaki where the cloud cell was in a mature stage. And, hails larger than 2 cm, which were only observed at Amagasaki, were mainly consist of opaque layers in the outside part though transparent in the center part. The formation process of hail presumed from the shape and the internal structure of hailstones is consistency, and corresponded that time change of a radar echo.

Observation of sublimating ice particles in clouds

Alexei Korolev[1] and George A. Isaac[2]
[1] Sky Tech Research Inc., Richmond Hill, ON, L4C 7M6, Canada
[2] Meteorological Service of Canada, Downsview, M3H 5T4, Canada

1. Introduction

In radiative transfer calculations ice particles are usually treated as facetted polyhedrons (e.g. Macke et al. 1996 and others). Sublimation may significantly change ice particle surface topography, resulting in rounding of corners and disappearing facets, eventually changing the scattering properties of the ice particles. Fragmentation of ice particles during sublimation is considered as a possible mechanism of ice multiplication (e.g. Locatelli et al. 1974).

This paper presents the first observational study of sublimating ice particles from in-situ measurements. The main objective of this paper is to investigate the characteristic habits of ice particles subjected to sublimation and estimate the effect of sublimation on ice particle breakup and secondary ice production. The obtained information is important for understanding of the lifecycle of ice in the atmosphere and radiative transfer calculations.

2. Instrumentation

The data presented here were collected with the help of a Cloud Particle Imager (CPI) probe developed by SPEC Inc. (Lawson et al. 2001) an installed on the National Research Council of Canada Convair-580.

The measurements were conducted in winter mid-latitude and polar clouds during three flight projects: CFDE III, FIRE.ACE and AIRS. The temperature of the investigated clouds ranged from 0°C to -40°C. Most of the data were obtained in stratiform clouds (*St, Sc, As, Ac, Ns*) associated with frontal systems.

3. Habits of sublimating ice particles

a. *Definition of sublimating ice particles*

Laboratory experiments of Oraltay and Hallett (1989) and Nelson (1998) showed that sublimation results in rounding of corners and disappearance of ice crystal facets. This observation was used as a basis for identifying sublimating particles in the context of this paper, i.e. ice particles were considered sublimating, if their images had rounded corners and the contours were smooth and sinuous. The corners were classified as rounded if the radius of curvature was no less than about 20μm. Definitions such as this have a number of exclusions, i.e. heavily rimed ice particles, graupel, sleets, and some types of dendrites. Such particles were excluded from the present analysis. The out-of-focus images also having rounded corners were filtered out with the help of CPIVIEW software (SPEC Inc.).

Laboratory experiments by Bailey et al (2002) showed that the characteristic time of re-growth of corners of partially sublimated ice varies from minutes to tens of minutes. Therefore, in the present study, the term "sublimating ice particle" implies that the ice particle was *sublimating at the moment of measurement* or *it had undergone sublimation some time in its recent history.*

b. *Plates*

Figure 1 shows typical shapes of sublimating plates. It was found that a large fraction of evaporating plates have concave basal faces with well distinguished steps (images # 3,6,10,12,14-18,22).

Bacon et al. (1998) found that ice breakup occurs after the formation of a thin neck (3-10μm) between bigger pieces of particles. Neither large nor small sublimating plates exhibit any inhomogeneity on their surfaces that may result in fragmentation during sublimation.

Most of the sublimating particles were sampled in dry air at a relative humidity below 100% and temperature range -28°C<T<-10°C. Some sublimating plates (images #7 and 12) were measured at a supersaturation over ice (RH_i=117%). (Fig.1 captions)

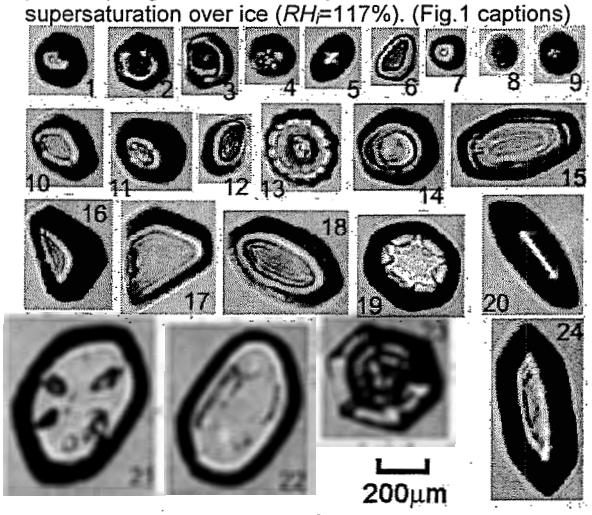

Figure 1. Sublimating ice plates. T(C°)/ RHi(%)/ P(mb) associated with each image: (1)-20/83/550; (2)-20/83/550;(3)-20/92/550; (4)-28/93/510; (5)-10/80/450; (6)-19/88/550; (7)-28/117/500; (8)-19/88/550; (9)-17/98/670; (10)-20/86/550; (11)-20/87/540; (12)-28/117/510; (13)-10/77/450; (14)-20/87/550; (15)-11/83/450; (16)-15/94/640; (17)-15/89/610; (18)-12/84/450; (19)-12/85/450; (20)-12/85/450; (21)-11/83/450; (22)-10/83/450; (23)-20/87/550; (24)-10/83/450;

c. *Columns*

Figure 2 presents images of sublimating columns at the relative humidity between 68%<RH_i<99% and temperatures -38°C <T<-2°C. A large fraction of the columns shown in Fig. 2 transformed into oblate spheroids during their sublimation. The sublimating columns do not show any structures that may result in break up during continued sublimation. Oraltay and Hallett (1989) also found from laboratory observations that columns do not fragment during sublimation.

Corresponding author's address: Sky Tech Research Inc., 28 Don Head Village Blvd., Richmond Hill, ON, L4C 7M6, Canada. E-mail: Alexei.Korolev@rogers.com

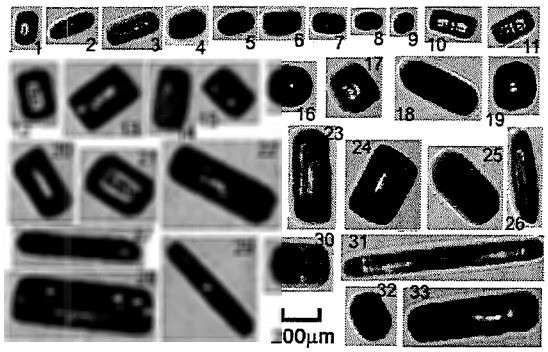

Figure 2. Sublimating columns. T(C°)/ RHi(%)/ P(mb) associated with each image: (1)-27/94/530; (2)-20/74/550; (3)-11/83/450; (4)-20/86/550; (5)-27/94/530; (6)-27/94/530; (7)-20/83/550; (8)-27/94/530; (9)-15/94/700; (10)-27/94/530; (11)-27/94/530; (12)-27/95/530; (13)-11/81/450; (14)-20/84/550; (15)-9/87/690; (16)-15/99/700; (17)-15/99/700; (18)-20/84/550; (19)-13/81/450; (20)-15/96/680; (21)-20/90/550; (22)-20/89/550; (23)-20/93/550; (24)-10/82/453; (25)-20/89/550; (26)-10/83/459; (26)-2/95/570; (28)-10/84/450; (29)-10/88/450; (30)-20/84/550; (31)-2/95/570; (32)-38/98/490; (33)-2/95/570.

d. Dendrites

Figure 3 shows sublimating stellar, dendrites and their fragments collected at 65%< RH_i<114%, and air temperature –17°C <T<-1°C.. It is not clear whether the fragments (images #5-7,10-14,16,18) were originally grown particles or they resulted from fragmentation. The images #8-10,15,17 (Fig. 3) suggests that some stellar particles may not generate fragments during subsequent sublimation and they eventually sublimate as one piece. However, the dendrites having multiple "necks" (images # 1-7,11-13,16,18-20) may result in fragmentation during sublimation. Oraltay and Hallett (1989) observed multiple fragmentation of dendrites during sublimation.

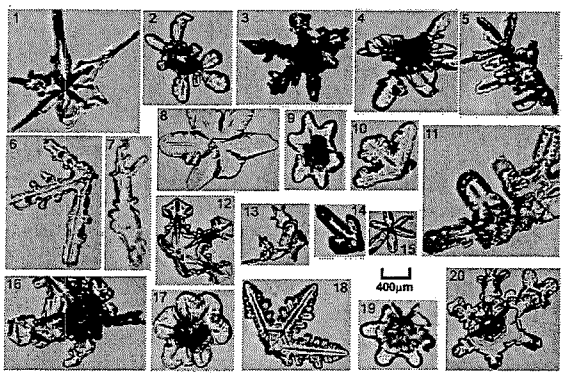

Figure 3. Sublimating stellar, dendrites and their fragments. T(C°)/RHi(%)/P(mb) associated with each image: (1)-11/75/870; (2)-11/84/450; (3)-3/100/750; (4)-4/102/550; (5)-16/75/940; (6)-1/97/760; (7)-2/93/750; (8)-10/91/910; (9)-11/95/940; (10)-12/93/880; (11)-13/76/950; (12)-17/114/790; (13)-11/65/810; (14)-7/103/510; (15)-11/83/450; (16)-3/96/720; (17)-14/86/870; (18)-17/108/800; (19)-12/90/880; (20)-11/93/450.

e. Rosettes of bullets

Figure 4 shows the images of rosettes of bullets, which have undergone partial sublimation. The images were collected at of 53%<RH_i<91%, and -30°C<T<-22°C (captions Fig. 4). Most of the bullets have smooth contours. In some cases bullets in the rosettes are thinning from their center towards the edges (images# 5,6,16,21), whereas the rest of the bullets in the same rosette have shapes similar to single sublimating columns (Fig. 2).

The number of fragments is limited by the number of bullets in a rosette. After separation from the source crystal, each bullet will evaporate as a single particle without fragmentation. It is possible that each rosette will evaporate without fragmentation. The evaporation of each bullet could be directed from the outer edges towards the central part of the rosette and breakup would never occur. This scenario is supported by the higher rate of thinning of the outer edges of the bullets, exposed to higher ventilation compared to the central part of the bullet rosette.

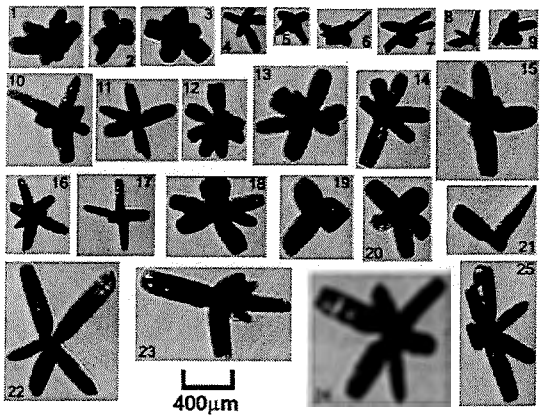

Figure 4 Sublimating rosettes of bullets. T(C°)/RHi(%)/P(mb) associated with each image: (1)-10/81/680; (2)-30/88/440; (3)-29/91/440; (4)-30/86/440; (5)-24/85/560; (6)-29/91/440; (7)-24/85/560; (8)-22/53/580; (9)-24/85/560; (10)-24/85/560; (11)-24/85/560; (12)-25/67/540; (13)-29/87/440; (14)-25/74/540; (15)-24/70/560; (16)-25/73/540; (17)-29/91/440; (18)-30/87/440; (19)-25/73/540; (20)-30/88/440; (21)-24/54/560; (22)-24/54/560; (23)-24/70/560; (24)-24/56/560; (25)-25/74/540.

f. Rosettes of plates

The next group of sublimating ice particles shown in Fig. 5a originated from radiating assemblage of plates or rosettes of plates collected at 70%<RH_i<109%, -25°C<T<-8°C (see caption Fig. 5). The facetted assemblages of plates are shown in Fig. 5b. The sublimation of these particles may result in images similar to that in Fig. 5a. The evaporating assemblage of plates should not be mixed up with evaporating rosettes of bullets, though in many cases their appearance is similar to them. Usually sublimating rosettes of plates have uneven branches growing out of a common center. In most cases the branches sharpen towards the edges.

The assemblages of plates are not expected to produce many fragments during sublimation. The images on the top of Fig. 5a (images#1-9) suggest that the assemblage of plates tends to get a compact shape at the final stage of sublimation.

g. Capped columns

Figure 6 shows sublimating capped columns at 40%< RH_i<102%, and -13°C <T<-4°C. The plates growing on the basal faces of columns appear similar

to single plates as in Fig. 1. However, the columns, which are sandwiched between the plates sublimate differently as compared to isolated columns (Fig.2). Capped columns are thinning toward the center, whereas single columns usually have thicker central parts and thinner edges. The thinning of capped columns becomes most pronounced after the complete evaporation of the side plates (Fig. 6b). Such differences are explained by a specific variation of the ventilation coefficient along the particle surface.

The capped columns are not expected to breakup during sublimation until the very last stage, when the column may produce two pieces.

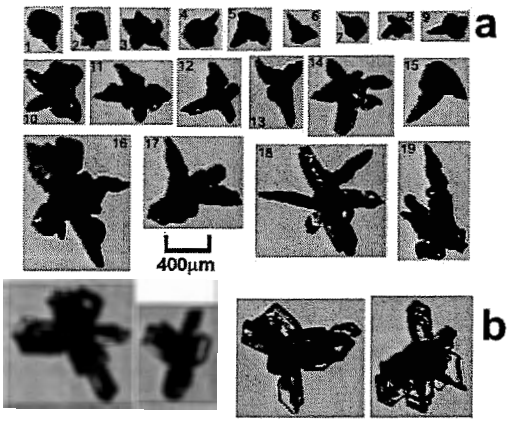

Figure 5. Sublimating radiating assemblage of plates (a); facetted assemblage of plates, which may result in particles like in 'a' after partial sublimation (b). T(C°)/RHi(%)/P(mb) associated with each image: (1)/-19/83/550; (2)-20/86/550; (3)-20/78/550; (4)-20/85/550; (5)-20/85/550; (6)-11/74/660; (7)-20/86/550; (8)-22/80/580; (9)-24/86/560; (10)-11/89/660; (11)-11/83/660; (12)-25/76/540; (13)-8/109/840; (14)-10/81/680; (15)-19/87/550; (16)-19/87/550; (17)-25/70/540; (18)-12/99/450; (19)-25/73/540.

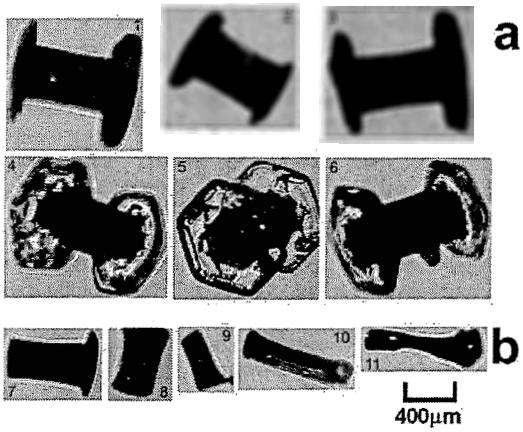

Figure 6. Sublimating capped columns with partially evaporated plates (a); after complete evaporation of the plates (b). T(C°)/RHi(%)/P(mb) associated with each image: (1)-13/81/950; (2)-13/79/950; (3)-12/95/950; (4)-13/85/950; (5)-12/80/950; (6)-13/84/950; (7)-4/58/550; (8)-12/40/980; (9)-7/98/540 (10)-7/102/520; (11)-7/95/540.

h. Irregulars

Figure 7 presents examples of images of irregulars with relatively smooth surfaces. As in the case of particles shown in Figs. 1,2, and 5, there is a tendency towards reduction in surface roughness with the decrease of particle size. The particles in Fig.7 have a low number of surface features that may result in ice breakup during sublimation. The relative humidity and temperature for the particles in Fig.7 vary in the ranges 45%<RH_i<93%, -37°C<T<-2°C.

Examples of irregular ice particles with highly rough surfaces are shown in Fig. 8. Numerous thin necks connecting larger parts suggest that subsequent sublimation may result in multiple fragments. Some of those particles may result in more than 10-20 fragments (e.g. images# 21-28).

There is no clear reason for the peculiar shapes of the particles in Fig. 8. It is possible that the rough surface is related to a low relative humidity, when rapid erosion of the ice surface may take place. Most particles in Fig. 8 were sampled at a relative humidity between 80% to 95%, which is not much different from other cases in Figs. 1-7. However, it is possible that these particles experienced a low humidity some time before the moment of measurement.

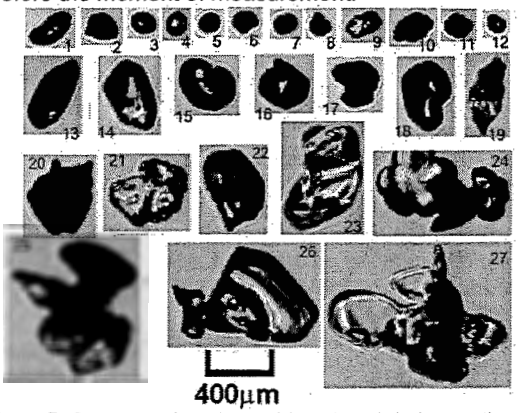

Figure 7. Sublimating irregular particles with relatively smooth surface. T(C°)/ Hi(%)/P(mb) associated with each image: (1)-10/80/450; (2)-10/81/450; (3)-12/91/450; (4)-10/82/450; (5)-10/74/450; (6)-11/71/450; (7)-8/86/700;(8)-10/85/450; (9)-12/94/450; (10)-19/79/560; (11)-13/66/450; (12)-10/81/450; (13)-10/80/450; (14)-12/93/450; (15)-11/91/450; (16)-12/91/450; (17)-20/82/560; (18)-12/88/450; (19)-10/76/450; (20)-19/83/560; (21)-2/82/820; (22)-10/83/450; (23)-37/92/440; (24)-10/83/450; (25)-13/45/960; (26)-8/82/700; (27)-13/89/950.

4. Occurrence of sublimating ice in frontal clouds

Cloud zones with sublimated particles were manually identified from CPI imagery of cloud particles. The total length of the analyzed clouds was 4530 km, and liquid clouds were not included in this analysis. It was found that the cloud fraction with ice particles having modified shapes due to sublimation is approximately 30-40%. The accuracy of this estimate is estimated as no better than 20%. Part of the uncertainty of identifying sublimating zones is related to the presence of clouds, where facetted ice particles were mixed with sublimating ones.

In-situ measurements conducted by Ovarlez et al. (2002) showed that the fraction of cirrus clouds with humidity RH_i<100% for two different projects varied from 33% to 49%. Though this study emphasized different cloud types, the fraction of cirrus clouds undersaturated with respect to ice obtained by Ovarez et al. (2002) supports our estimates.

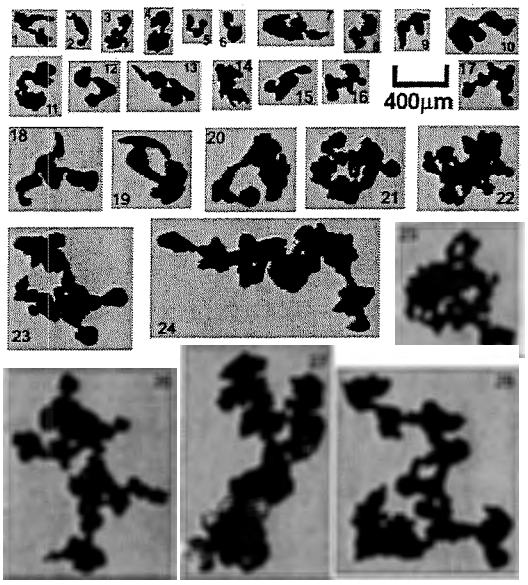

Figure 8. Sublimating irregular particles with highly developed surfaces. T(C°)/RHi(%)/P(mb) associated with each image: (1)-12/80/450; (2)-12/80/450; (3)-12/82/450; (4)-12/68/450; (5)-9/90/630; (6)-12/82/450; (7)-11/86/610; (8)-12/83/600; (9)-28/85/430; (10)-12/36/450; (11)-29/90/440; (12)-9/79/630; (13)-8/79/650; (14)-10/80/450; (15)-6/91/670; (16)-12/64/450; (17)-12/81/450; (18)-12/80/600; (19)-12/83/600; (20)-12/83/590; (21)-30/90/440; (22)-13/88/590; (23)-12/86/600; (24)-13/88/580; (26)-19/98/470; (27)-20/92/470; (28)-15/89/570

5. Discussion and conclusions

The optical effects like halos or sundogs can occur only on ice crystals having well defined facets. Spheroids are not capable of generating such phenomenon. Therefore, halo or sundogs will not occur in cloud regions with hexagonal columns or plates undergoing significant sublimation.

Habit recognition analysis of cloud particle images collected by a PMS OAP-2DC showed that the frequency of occurrence of spherical particles with D>125mm at -25°C <T<-30°C is about 6% (Korolev et al. 2000). As was shown above, ice particles during the final stage of evaporation have a quasi-spherical shape and thus may be misinterpreted as droplets. Polarized lidar studies of cirrus clouds indicated a presence of spherical particles at temperatures below -35°C, which were interpreted as droplets (Sassen 1991). Although these particles could be liquid or frozen droplets, sublimating spherical ice particles might gave a similar backscattering signal.

The following conclusions were obtained here:

1. Sublimation of cloud particles under conditions typical for the troposphere results in smooth surface features, rounded corners and disappearing facets.
2. Different particle habits reveal various capabilities to produce fragments during sublimation and secondary ice production. Plates and columns do not produce fragments at all. Dendrites and some peculiarly shaped particles (Fig. 8) likely have the highest capability for fragmentation during sublimation. This conclusion refers to fragments larger 5-10μm, which can be confidently resolved from the CPI imagery. The images of sublimating ice particles suggest that fragmentation during sublimation in general does not play important role in secondary ice production.
3. The characteristic size of sublimating ice particles, when they turn into spheroids, is about 60-80μm. This size can be considered as a threshold size below which fragmentation does not occur during subsequent sublimation. Korolev and Isaac (2003) found that the majority of small ice particles (D<60μm) in glaciated clouds have a compact quasi-spherical shape, and a large fraction of these particles may result from sublimation.
4. The frequency of occurrence of clouds with ice particles modified by sublimation is estimated as no less than 30-40%. The high occurrence of sublimating ice in the troposphere suggests it should be included in the meteorological classification of cloud ice particles as a separate habit category. The large fraction of sublimating ice particles in clouds should not be overlooked in radiative transfer calculations.

Acknowledgements.
Support for the collection of the data was given by MSC, NRC, the Canadian PERD and NASA Langley. The NSR Secretariat of Canada, Boeing Commercial Airplane Group, Transport Canada, the Canadian Department of National Defense, NASA Glenn and the FAA. The aircraft data were obtained using the NRC Convair-580 and the scientific and technical efforts of many NRC and MSC staff. Alexei Korolev has performed this work under the contract KM175-012030/001/TOR to the Meteorological Service of Canada, with support by the Canadian Climate Action Fund.

Reference list

Bacon, N.J., B.D. Swanson, M.B. Baker and E.J. Davis, 1998: Breakup of levitated frost particles. *J. Geoph. Res.*, **103,** D12, 13763-13774.

Bailey, M., J. Hallett, A. Korolev, and G. Isaac, 2000: Laboratory growth, sublimation, and regrowth of ice crystals. 11th Conf. Cloud Phys, Ogden, Utah, 2-7 June 2000, AMS, P1.4.

Korolev, A., G. A. Isaac and J. Hallett, 2000: Ice particle habits in stratiform clouds. *Q.J.Roy.Meteor.Soc.*, **126**, 2873-2902.

Korolev, A.V., and G.A. Isaac, 2003: Roundness and aspect ratio of particles in ice clouds. *J.Atmos.Sci.,* **60**, 1795-1808.

Lawson, P.R., B. Baker, C.G. Schmitt, and T. Jensen, 2001: An overview of microphysical properties of Arctic clouds observed in May and June 1998 during FIRE ACE, *J. Geoph. Res.*, **106**, D14, 14989-15014.

Locatelli,J.D., P.VHobbs, and K.R.Biswas, 1983: Precipitation from stratocumulus clouds affected by fallstreaks and artificial seeding. *J. Appl. Meteor.* **22**, 1393–1403

Macke, A., J. Mueller, and E. Raschke, 1996: Single scattering properties of atmospheric ice crystals. *J. Atmos. Sci.* **53**, 2813–2825.

Nelson, I., 1998: Sublimating ice particles. *J.Atmos.Sci.*, **55**, 910-919.

Ovarlez, J., J.F. Gayet, K. Gierens, J. Strom, H. Ovarlez, F. Auriol, R. Busen, and U Schmann, 2002: Water vapor measurements inside cirrus clouds in Northern and Southern hemispheres during INCA, *Geoph. Res. Lett.*, **29**, 1813-1817.

Oraltay, R.J. and J. Hallett, 1989: Evaporation and melting of ice crystals: A laboratory study. *Atmos. Res.*, **24**, 169-189

Sassen, K., 1991: The Polarization lidar technique for cloud research: A review and current assessment. *Bull. Amer. Meteo. Soc.*, **72**, 1848–1866

Supersaturation of water vapor in clouds.

Alexei V. Korolev[1] and Ilia P. Mazin[2]
[1] Sky Tech Research Inc., Richmond Hill, ON, Canada
[2] Center for Earth and Space Research, George Mason University, Fairfax, VA, USA

1. Introduction

A theoretical framework is developed to estimate the supersaturation in liquid, ice and mixed phase clouds. An equation describing supersaturation in mixed phase clouds in general form is considered here. The solution for this equation is obtained for the case of quasi-steady approximation, i.e. when particle sizes stay constant. It is shown that the supersaturation asymptotically approaches the quasi-steady supersaturation over time. This creates a basis for the estimation of the supersaturation in clouds from the quasi-steady supersaturation calculations.

2. General equation

Consider a vertically moving adiabatic cloud parcel consisting of a mixture of liquid droplets and ice particles uniformly distributed in space. Assume that the cloud particles move with the air and stay inside the parcel at all times and no nucleation of new cloud droplets and ice particles occur. The water vapor pressure and temperature fields at large distance from cloud particles are considered to be uniform and all cloud particles grow or evaporate under the same conditions.

The changes in the supersaturation in the cloud parcel can be described by an equation (Korolev and Mazin 2003)

$$\frac{1}{S_w+1}\frac{dS_w}{dt} = a_0 u_z - a_2 B_i^* N_i \bar{r}_i - \left(a_1 B_w N_w \bar{r}_w + a_2 B_i N_i \bar{r}_i\right) S_w \qquad (1)$$

Here, $a_0 = \frac{g}{R_a T}\left(\frac{L R_a}{c_p R_v T} - 1\right)$; $a_1 = \frac{1}{q_v} + \frac{L_w^2}{c_p R_v T^2}$;

$a_2 = \frac{1}{q_v} + \frac{L_w L_i}{c_p R_v T^2}$ $B_w = \frac{4\pi \rho_w A_w}{\rho_a}$ $B_i = \frac{4\pi \rho_i c \xi A_i}{\rho_a}$;

$B_i^* = \frac{4\pi \rho_i c}{\rho_a}(\xi - 1) A_i$; $\bar{r}_i$, $\bar{r}_w$ are the average radii of droplets and ice particles; D is the coefficient of water vapor diffusion in the air; k is the coefficient of air heat conductivity; $\xi(T)=E_w(T)/E_i(T)$; E_w, E_i are the saturated water vapor pressures over flat surfaces of water and ice, respectively, at temperature T;

3. Quasi-steady approximation

Assume that the changes in size of the cloud particles can be neglected so that $\bar{r}_w$ and $\bar{r}_i$ are constant, then Eq. 1 yields a solution

$$S_w = \frac{S_{qs\ w} - C_0 \exp(-t/\tau_p)}{1 + C_0 \exp(-t/\tau_p)}$$

Corresponding author's address: Sky Tech Research Inc., 28 Don Head Village Blvd., Richmond Hill, ON, L4C 7M6, Canada, E-mail: Alexei.Korolev@rogers.com

where

$$S_{qs\ w} = \frac{a_0 u_z - b_i^* N_i \bar{r}_i}{b_w N_w \bar{r}_w + b_i N_i \bar{r}_i} \qquad (3)$$

is the limiting supersaturation, and

$$\tau_p = \frac{1}{a_0 u_z + b_w N_w \bar{r}_w + (b_i + b_i^*) N_i \bar{r}_i} \qquad (4)$$

is the time constant characterizing a time of asymptotical approach of S_w to $S_{qs\ w}$. Here $C_0 = \frac{S_{qs\ w} - S_{w0}}{1 + S_{w0}}$; S_{w0} is the supersaturation at t=0; $b_w = a_1 B_w$; $b_i = a_2 B_i$ $b_i^* = a_2 B_i^*$.

Following Squires (1952) and Rogers (1975) $S_{qs\ w}$ will be called "*quasi-steady*", the assumption $\bar{r}_w$ =const and $\bar{r}_i$ =const in Eq. (1), will be called "*quasi-steady approximation*", the constant τ_p herein, will be called *the time of phase relaxation*, following Mazin (1966, 1968).

4. Supersaturation in single-phase clouds.

(a) Liquid clouds

Substituting N_i=0 in Eqs. 2 and 3 gives the expressions for the quasi-steady supersaturation

$$S_{qs\ w} = \frac{a_0 u_z}{b_w N_w \bar{r}_w} \qquad (5)$$

and the time of phase relaxation

$$\tau_p = \frac{1}{a_0 u_z + b_w N_w \bar{r}_w} \qquad (6)$$

For characteristic values of $N_w \bar{r}_{w0}$ and u_z typical for liquid clouds, $b_w N_w \bar{r}_w >> a_0 u_z$. Then neglecting $a_0 u_z$ in Eq. 6, gives

$$\tau_p = \frac{1}{b_w N_w \bar{r}_w} \qquad (7)$$

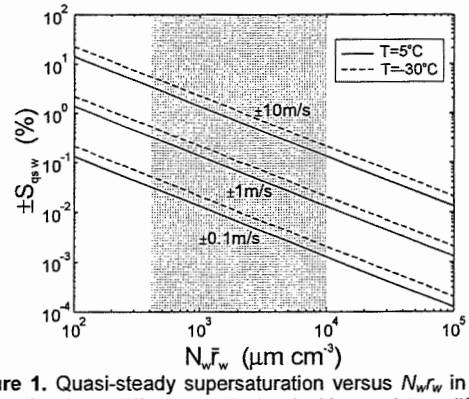

Figure 1. Quasi-steady supersaturation versus $N_w r_w$ in liquid clouds for three different vertical velocities and two different temperatures. Grey color indicates $N_w r_w$ typical for the liquid clouds in the troposphere. P=690mb.

An expression similar to Eq. 5 was originally deduced by Squires (1952), Mazin (1966), and discussed in details in Kabanov et al. (1971). The time of phase relaxation in the form Eq. 5 was first obtained by Squires (1952) and Mazin (1966).

Fig. 1 shows $S_{qs\ w}$ calculated from Eq. 5 for different values of $N_w\bar{r}_w$ and u_z. As seen in Fig. 1 the supersaturation varies between $-5<S_w<5\%$ for vertical velocities $-10<u_z<10$ m/s.

For typical $N_w\bar{r}_w$ the characteristic time of the phase relaxation in liquid clouds is of the order of few seconds as shown in Fig.2. The effect of vertical velocity u_z becomes significant only at small $N_w\bar{r}_w$.

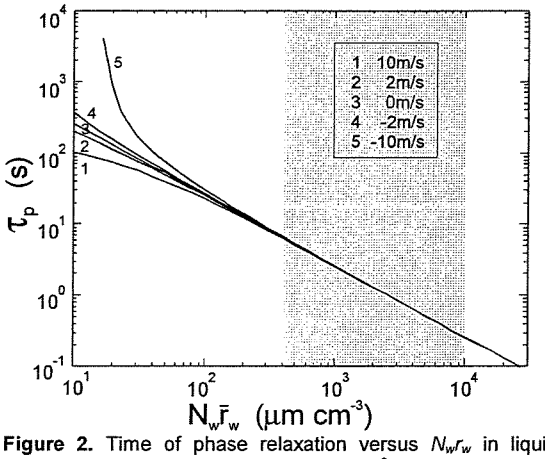

Figure 2. Time of phase relaxation versus $N_w r_w$ in liquid clouds for different vertical velocities. T=0°C, P=680mb. Grey color indicates $N_w r_w$ typical for the liquid clouds in the troposphere.

(b) Ice clouds

Eq.1 can be rewritten for the supersaturation with respect to ice. The solution of this equation yields the quasi-steady supersaturation

$$S_{qs\ i} = \frac{a_0 u_z}{b_{i0} N_i \bar{r}_i} \tag{8}$$

and the time of phase relaxation

$$\tau_p = \frac{1}{a_0 u_z + b_{i0} N_i \bar{r}_i} \tag{9}$$

where $b_{i0} = a_3 B_{i0}$.

Fig. 3 shows $S_{qs\ i}$ calculated from Eq. 8 for different values of $N_i\bar{r}_i$ and u_z. In-situ measurements showed that in glaciated clouds at temperatures $-35<T<0$°C the characteristic size ice particles is about 25-40μm and their concentration is 2-5cm^{-3} (Korolev et al. 2003). As seen from Fig. 3 for u_z=1m/s and for typical $N_i\bar{r}_i$ the supersaturation $S_{qs\ i}$ may range from few to hundreds of percent with respect to ice. However, such a high supersaturation will never be reached in clouds at $T>-40$°C, since an increase it is limited by the saturation over water. Lines 1 and 2 in Fig. 5 show the saturation over water for -5°C and -35°C, respectively.

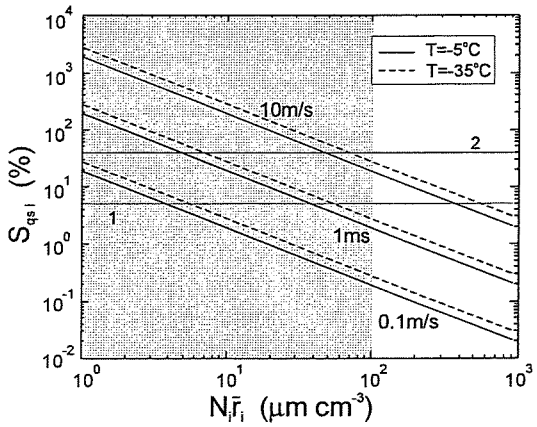

Figure 3. Quasi-steady supersaturation versus $N_i r_i$ in ice clouds for different vertical velocities. Horizontal lines indicate saturation over water at -5°C (1); and at -35°C (2). P=870mb. Grey color indicates $N_i r_i$ typical for the ice clouds.

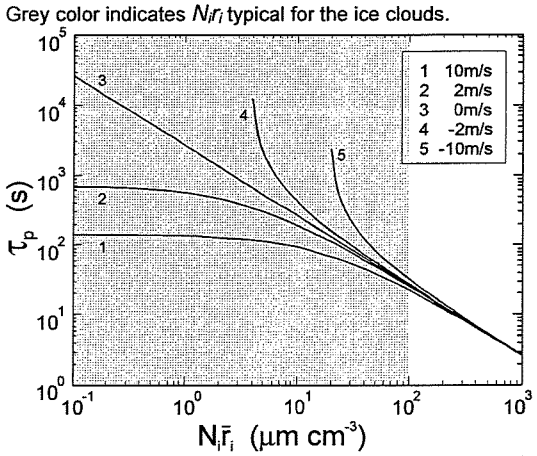

Figure 4. Time of phase relaxation versus $N_i r_i$ in ice clouds for different vertical velocities. T= -10°C; P=680mb. Grey color indicates $N_i r_i$ typical for the ice clouds.

Fig. 4 shows the time of phase relaxation calculated from Eq. 9. For typical $N_i\bar{r}_i$ in ice clouds the characteristic time of the phase relaxation may vary from a few minutes to a few hours.

The ice particles in this section were treated as ice spheres having the "capacitance" c=1. Since for the majority of ice particles c<1, the coefficients B_i and B_i^* will be reduced, and therefore the supersaturation and time of phase relaxation values higher than those shown in Figs. 2 and 4 and.

5. Supersaturation in mixed phase clouds

Since cloud droplets may stay in a metastable liquid condition down to about –40°C, a population of cloud particles below 0°C may consist of a mixture of ice particles and liquid droplets. Such clouds are usually called "mixed" clouds. The behavior of supersaturation in mixed phase clouds is more complex compared to that in single-phase liquid or ice clouds. There are several possible scenarios for the evolution of the three phase colloidal system, depending on the values of u_z, P, T, N_i, r_i, N_w, r_w, the

liquid and ice particles may: (a) both grow, or (b) both evaporate, or (c) ice particle may grow while liquid droplets evaporate.

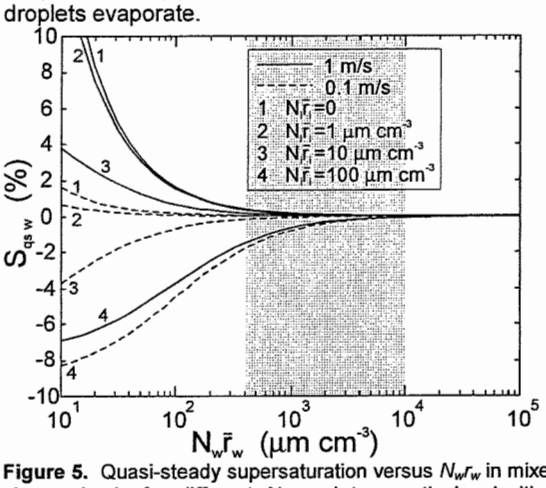

Figure 5. Quasi-steady supersaturation versus $N_w r_w$ in mixed phase clouds for different $N_i r_i$ and two vertical velocities. T=-10°C, P=680mb. Grey color indicates $N_w r_w$ typical for clouds in the troposphere.

Fig. 5 shows quasi-steady supersaturation in mixed phase clouds as a function of $N_w\bar{r}_w$ for different $N_i\bar{r}_i$ for two updraft velocities 0.1m/s and 1m/s calculated from Eq.1. The supersaturation S_w in the ascending mixed phase cloud may be either positive or negative.

Fig. 6 shows the time of phase relaxation in mixed phase clouds for u_z=0. In the mixed phase clouds with typical $N_w\bar{r}_w$ the ice particles do not affect the time of phase relaxation until $N_i\bar{r}_i$ reaches values above 100 μm cm^{-3}. This means that for such clouds the time of phase relaxation is mainly defined by liquid droplets.

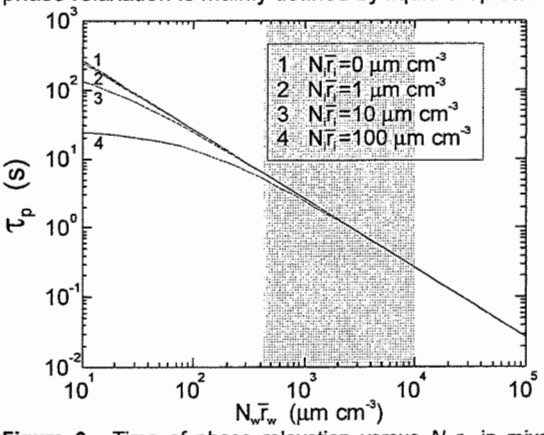

Figure 6. Time of phase relaxation versus $N_w r_w$ in mixed phase clouds for different $N_i r_i$. T= -10°C, P=680mb. Grey color indicates $N_w r_w$ typical for the liquid clouds in the troposphere.

In mixed phase clouds, the droplets would stay in equilibrium, i.e. they will neither grow, nor evaporate, if S_w=0. The ice particles under this condition will keep growing, since S_i>0. Substituting $S_{qs\,w}$=0 in Eq. 3 yields a threshold velocity of ascent when droplets remain in equilibrium

$$u_z^* = \frac{b_i^* N_i \bar{r}_i}{a_0} \qquad (10)$$

The condition for the equilibrium of ice particles, i.e. ice particles neither grow, nor evaporate

$$u_z^o = \frac{(1-\xi) b_w N_w \bar{r}_w}{\xi a_0} \qquad (11)$$

Thus, if $u_z > u_z^*$ both droplets and ice particles grow; if $u_z^o < u_z < u_z^*$ the droplets evaporate, whereas the ice particle grow; if $u_z < u_z^o$ both droplets and ice particles evaporate.

The velocity u_z^* may also be considered as a threshold velocity for the activation of liquid droplets in ice clouds when $u_z > u_z^*$. Basically Eq. 10 defines a condition for maintaining a mixed phase in a cloud. It is worth noting that the threshold velocity u_z^* does not depend on $N_w\bar{r}_w$, and u_z^o does not depend on $N_i\bar{r}_i$.

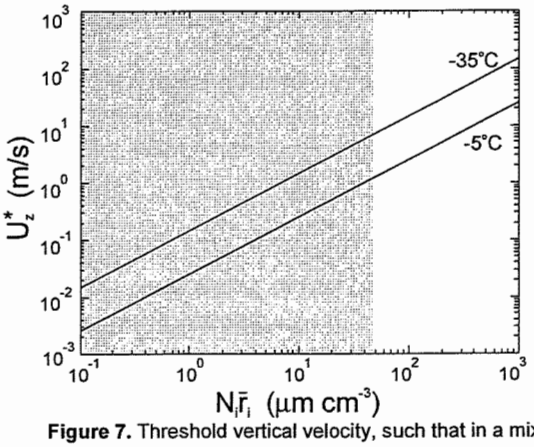

Figure 7. Threshold vertical velocity, such that in a mixed phase cloud at $u_z > u_z^*$ both droplets and ice particles grow. Calculations were done for temperatures -5°C and -35°C; P=680mb. Grey color indicates $N_i r_i$ typical for the ice clouds.

Figure 7 shows the dependence of the threshold velocity u_z^* versus $N_i\bar{r}_i$. The velocity u_z^* does not exceed few meters per second for typical $N_i\bar{r}_i$ (Fig. 7). Such vertical velocities can be generated by turbulence in stratiform clouds or regular convective motions in cumulus clouds. This results in an important conclusion that liquid droplets may be easily activated in ice clouds under relatively small vertical velocities having turbulent or regular nature keeping the cloud in mixed phase condition.

As seen from Fig. 8 for the case u_z=0 for typical $N_i\bar{r}_i$ and $N_w\bar{r}_w$ the supersaturation in mixed phase clouds is close to zero ($|S_{qs\,w}| < 1\%$). It means that in mixed phase clouds the evaporating droplets tend to maintain the water vapor pressure close to saturation over water.

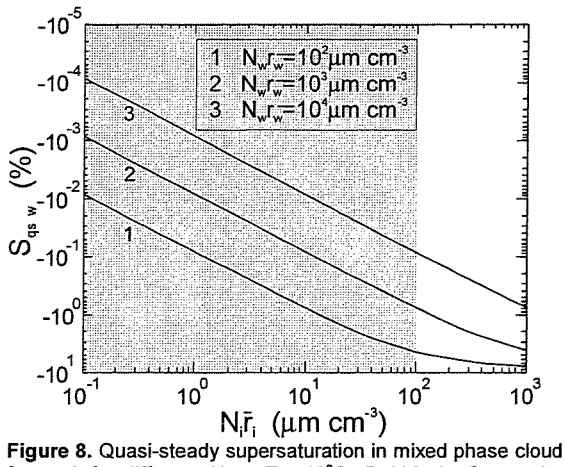

Figure 8. Quasi-steady supersaturation in mixed phase cloud for u_z=0 for different $N_w r_w$. T= -10°C; P=680mb. Grey color indicates $N_i r_i$ typical for the ice clouds.

7. Relation between S and S_{qs}.

Warner (1968) Paluch and Knight (1984), Politovich and Cooper (1988) have estimated the supersaturation in liquid clouds from Eq. 3 based on *in-situ* measurements of u_z and $N_w \bar{r}_w$. So far it is not clear, how accurate is the the estimate of S_w from $S_{qs\ w}$ calculated from measurements of u_z and $N_w \bar{r}_w$. The difference between S_w and $S_{qs\ w}$ can be found by substituting the current values of $r_w(t)$, $N_w(t)$, $e(t)$, $T(t)$, and $P(t)$ calculated from a numerical model into the expression for the quasi-steady approximation (Eq. 5)

$$S_{qs\ w}(t) = \frac{a_0(t) u_z}{b_w(t) N_w(t) \bar{r}_w(t)} \qquad (12)$$

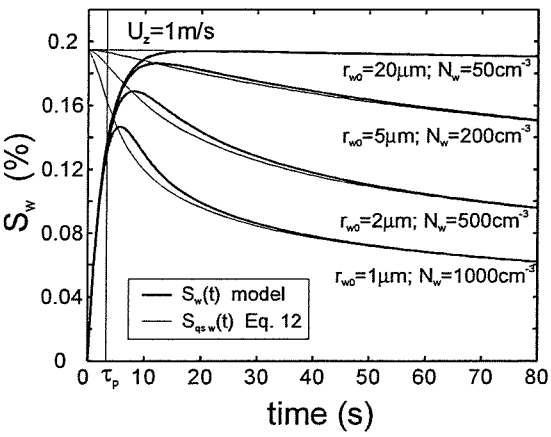

Figure 9. Comparison of the supersaturation $S_w(t)$ and $S_{qs\ w}(t)$ in ascending liquid clouds with the same $N_w r_w$ =1000μm cm⁻³, but different N_w and $\bar{r}_{w0}$. u_z=1m/s, $T(0)$=0°C; $P(0)$=870mb.

A remarkable property of $S_{qs\ w}(t)$ is that it approaches $S_w(t)$ asymptotically over time when u_z=const, i.e.

$$\lim_{t\to\infty}\left(\frac{S_{qs\ w}(t)}{S_w(t)}\right) = 1 \qquad (13)$$

A rigorous mathematical proof of Eq. 13 is not trivial and it goes beyond the scope of this paper. Numerical modeling indicates that Eq. 13 is valid both for liquid, ice and mixed clouds. An example is shown in Figs. 9. The difference between $S_{qs\ w}(t)$ and $S_w(t)$ becomes less than 10% usually within a characteristic time τ_p to $3\tau_p$. Similar results, as in Fig. 9, can be demonstrated for ice and mixed clouds (Korolev and Mazin 2003).

8. Conclusion

In the frame of this study the following results were obtained:

1. An equation for quasi-steady supersaturation and the time of phase relaxation for the general case of mixed phase clouds was obtained here.
2. The supersaturation $S(t)$ in a uniformly vertically moving cloud parcel asymptotically approaches over time the quasi-steady supersaturation $S_{qs}(t)$ calculated for current values of $u_z(t)$, $\bar{r}_w(t)$, $N_w(t)$, $\bar{r}_i(t)$, $N_i(t)$. The characteristic time of the approach is defined by the time of phase relaxation $\tau_p(t)$. This creates a theoretical basis for the use of S_{qs} for estimating supersaturation in clouds from in-situ measurements of $N_w \bar{r}_w$, $N_i \bar{r}_i$ and u_z.
3. Liquid water droplets can be activated in ice clouds with $N_i \bar{r}_i$ <1cm⁻³ at u_z<1m/s. The vertical turbulent and regular motions observed in natural clouds may maintain the cloud in mixed phase for a long time. This may be a possible explanations of the large observed fraction of mixed phase clouds (Korolev et al. 2003).
4. Relative humidity in mixed-phase clouds is close to saturation over water.

References

Kabanov A.S., I.P. Mazin, and V.I. Smirnov, 1971: Water vapor supersaturation in clouds. *Transactions of Central Aerological Observatory (Trudy TsAO*, Gidrometeoiszdat, Moscow), **95,** 50-61.

Korolev, A.V. and I.P. Mazin, 2003: Supersaturation of water vapor in clouds. *J.Atmos.Sci.*, **60,** 2957-2974

Korolev, A.V., Isaac, G.A., Cober, S.G., Strapp J.W., and Hallett, J. 2003 Observation of the Microstructure of Mixed Phase Clouds. *Q. J. R. Meteorol. Soc.*, **129**, 39-66

Mazin, I.P., 1966: On temperature and humidity stratification in clouds. *Transactions of Central Aerological Observatory (Trudy TsAO*, Gidrometeoiszdat, Moscow), **71**, 3-15.

Mazin, I.P., 1968: Effect of phase transition on formation of temperature and humidity stratification in clouds. *Proceedings of the International Conferenve on Cloud Physics*. Toronto, Canada, 132-137

Paluch, I. R. and Ch.A. Knight, 1984: Mixing and evolution of cloud droplet size spectra in vigorous continental cumulus. *J. Atmos. Sci.*, **41**, 1801-1815.

Politovich M.K. and W.A. Cooper, 1988: Variability of the supersaturation in cumulus clouds. *J. Atmos. Sci.*, **45**, 1651-1664.

Rogers, R.R., 1975: An elementary parcel model with explicit condensation and supersaturation. *Atmosphere*, **13**, 192-204

Squires, P., 1952: The growth of cloud drops by condensation. *Aust. J. Sci. Res.*, **5**, 66–86.

NUMERICAL STUDY IMPACT OF SOME BASIS CHARACTERISTICS OF FREEZING NUCLEI ON CLOUD MICROPHYSICS AND PRECIPITATION

S.V. Krakovskaia and A.M. Pirnach

Ukrainian Hydrometeorological Research Institute, Kiev, 03028, Ukraine

1. INTRODUCTION

Cloud and precipitation formation processes are subjects of experimental and theoretical studies in the UHRI in the past half-century. In the presented research the particular attention was devoted to freezing processes that can affect on cloud microphysics and precipitation. In fact, characteristics of freezing nuclei can be modified by aerosol influence, for example, by some biological aerosol particles those are able to act as contact and immersion freezing nuclei or in the artificial seeding experiments.

2. A SHORT DESCRIPTION OF THE METHOD

So-called combined model of the cloudy troposphere, which is a composition of the 3D mesoscale diagnostic LAM and 1D microphysical prognostic numerical model, was used for the research. Only the essential details for a full understanding of the presented results and the principles of models' construction will be described. Reader is referred to Pirnach et al. (1994), Pirnach (1998) and Krakovskaia et al. (1998, 2000) for a detailed presentation of the methodology, sets of equations and numerics.

Thermodynamical state (vertical profiles of temperature, pressure, specific humidity of the air and three projections of wind speed) of the troposphere is obtained from the 3-D mesoscale stationary model. The simulated domain was 1200x800x6.75 km with variable horizontal spacings from 100 km near the edges of domain to 12.5 km near the central point, vertical spacing was 50 m. The inputs for 3-D model were data of 26 sound ascendings of six stations in Ukraine.

In the 1D microphysical model the spectrum of liquid cloud drops is divided into two parts: cloud droplets (radii < 20 μm) and drops (radii > 20 μm). The spectrum of cloud droplets is the result of condensation, turbulent diffusion and dynamical motion. Additionally, the spectrum of drops is determined by the collection of droplets. The size distribution function of the ice particles is assumed to result from sublimation, riming, glaciation (heterogeneous freezing), turbulent diffusion and motion. Coefficients for droplet gravitational collection by drops and ice crystals are variable and depend on cloud particles (CP) radii. For T < -30 °C (T is the temperature of the air) spherical ice crystals transform to plates fell with v_2=30 cm/s (v_i is the fall speed of CP, hereinafter, i=1 is for water or droplets, and i=2 is for ice CP) and collision processes are stopped. The kinetic equation of CP size distribution functions f_i is used in the following form:

$$\frac{df_i}{dt} + \frac{\partial}{\partial r}(R_i f_i) - v_i \frac{\partial f_i}{\partial Z} = I_{\alpha i} \pm I_{fi} - \delta f_i + \Delta f_i , \quad (1)$$

$$I_{fi} = A_f \exp(B_f T_f) r_i^3 f_i \Theta(T_f), \quad T_f = 273.15 - T , \quad (2)$$

where R_i are rates of CP's growths due to condensation (sublimation); δf_i describe the decrease of CP by collection; $I_{\alpha i}$ describe generation of cloud condensation nuclei (CCN) and ice nuclei (IN); I_{fi} describe freezing of droplets; Δf_i describe turbulent transfer; A_f and B_f are the empirical constants (Bujkov et al., 1975); $\Theta(T_f)$ = 1 for T_f > 0 and $\Theta(T_f)$ = 0 for T_f < 0.

The initial profiles of thermodynamic characteristics as inputs for 1D model were got from the diagnostic 3D model and move through the 3D domain. It means, that the vertical column, where cloud microphysics is calculated, moves along horizontal axes opposite to the front displacement at every time step (dt) in 1-D model with variable speeds calculated as Z-averages of horizontal wind projections for the every point of the horizontal grid. One track through the cloud frontal system well-studied previously (Pirnach, 1998, Krakovskaia et al. 1994, Krakovskaia, 1995) was chosen for the numerical study. Initial distributions of thermodynamical characteristics on vertical are presented in Fig.1. There were found updrafs exceeded 40 cm/s in the first two hours of cloud development caused ice (Δ_2) and water (Δ_1) supersaturations, maximums of ice (IC) and liquid water contents (LWC) (Fig.2), and

Corresponding author's address:
Svetlana Krakovskaia, Ukrainian Hydrometeorological Research Institute, Pr. Nauki 37, Kiev-03028, Ukraine
KraSvet@antarc.icyb.kiev.ua, Hanna@ozsol.kiev.ua

following maximums of precipitation. Maximum Δ_2 in the clouds indicates on seeder-zone where ice crystals are generated and grew intensively.

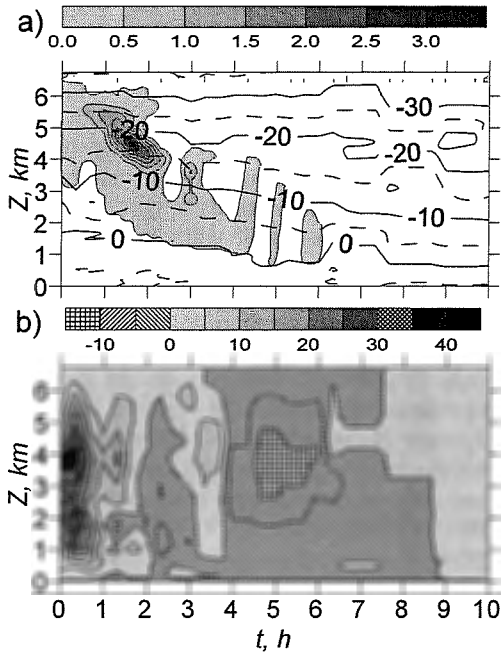

Fig.1. Initial vertical and time development of: (a) temperature (lines, °C) and ice supersaturations (shading, mg/kg); (b) vertical motions (cm/s).

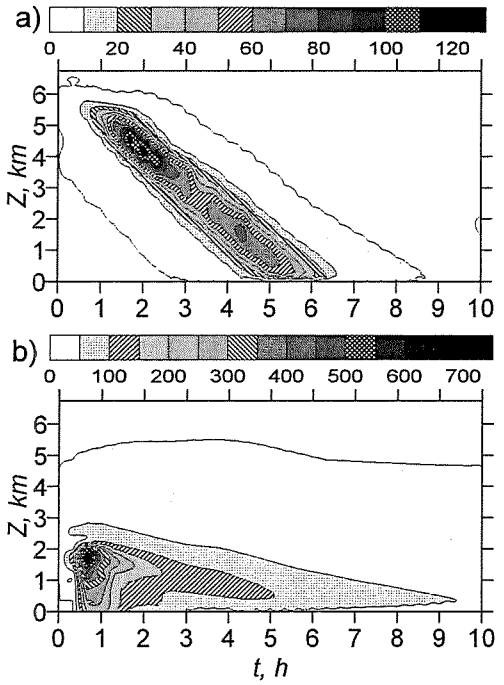

Fig.2. Vertical and time development of (a) ice content (q_2, mg/kg) and (b) liquid water content (q_1, mg/kg) in the run with unmodified freezing.

As it was noted, freezing processes were in the focus of the presented research. Regularly in the model a probability of freezing is a function of distribution of freezing nuclei by supercooling (Eq.2). A new assumption was include in the numerical study that all droplets freeze at temperature T_s and all big drops freeze at temperature T_b. It means that the probability of freezing became equal to 1 at those temperatures and lower, hence liquid CP are transformed to cloud ice crystals.

3. RESULTS AND DISCUSSION

There were performed a few series of numerical experiments on freezing process study. It is known from field experiments that liquid droplets can exist in supercooled clouds even at T < -40 °C. But in chosen case mixed clouds were found at T > -20 °C (see Figs.1, 2). Therefore, all numerical experiments with variable temperatures for freezing of liquid CP started at T = -20 °C.

In the first series of numerical experiments temperature of complete freezing of big drops in the clouds (T_b) was varied and affect on precipitation formation was studied. The results are presented on Figs.3-5. There was found increasing of solid precipitation intensity in general with maximums near T_b equals to -10 °C and -1 °C (Fig.3). It can be explained from initial

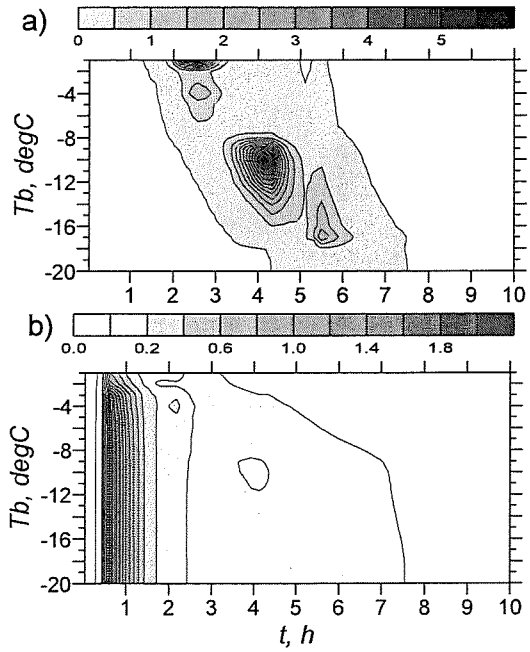

Fig.3. Precipitation intensity (I, mm/h) as function of time and T_b: (a) ice and (b) water phases.

thermodynamical data (Fig.1) and vertical and time development of microphysical characteristic (Fig.2). As it can be seen from Figs.1-3, in the unmodified run the maximum intensity of liquid precipitation I_{liq} = 2.3 *mm/h* near t = 0.5 *h* was caused by maximal updrafts produced ice and water supersaturations. Maximum intensity of solid precipitation I_{sol} < 0.1 *mm/h* was induced by seeder-zone at Z = 4.5 *km* and t = 1.5 *h* with ice supersaturation when cloud ice crystals just fell down with time, partly evaporated and reached the ground after t = 5 *h* (Fig.3a).

When drops freeze (as in these simulations or could be in weather modification experiments), they add huge amount to ice concentration and hence IC. It is clearly illustrated on Figs.4 and 5, where maximum IC appeared near the maximum of updrafts at Z = 3.8 *km* (Fig.4a) and in addition near Z = 2.4 *km* when T_b is higher (Fig.5a). Then cloud ice crystals fell down and reached the ground quicker and precipitation intensities are much higher than in the unmodified simulation (Fig.3a). At the same time cloud ice crystals absorb more free water vapour in the clouds and LWC and water precipitation become lower, that is naturally the most remarkable in Fig.5b when T_b is higher again. Note increasing LWC near t = 3.5 *h* obviously caused by melting of ice precipitation under the 0 °C isotherm (Fig.4b).

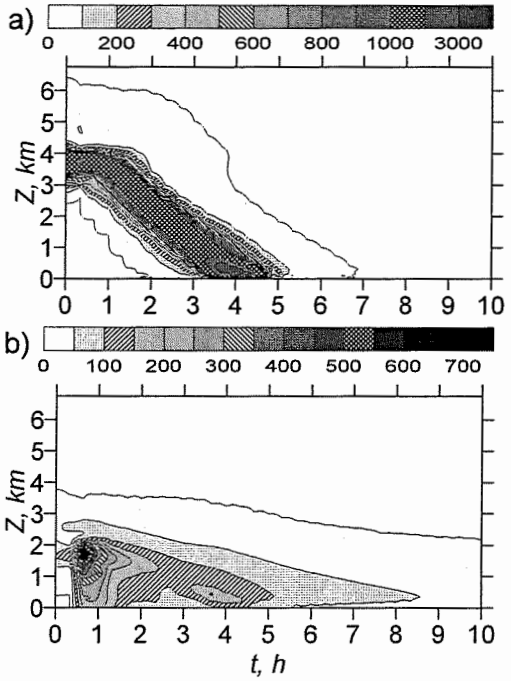

Fig.4. Vertical and time development of (a) ice content (q_2, mg/kg) and (b) liquid water content (q_1, mg/kg) in the run with T_b= -10 °C.

The next series of numerical experiments involve simulations with simultaneous varying of both temperatures: T_b and T_s. The results are presented in Figs.6 and 7 as diagrams for maximum and mean precipitation rates for 10 *h* of the cloud development.

Obviously, situation when $T_s > T_b$ (the left upper corners in the diagrams with maximal precipitation) is unnatural, because the bigger drop the easy it freezes. Nevertheless, it could be imagined that it presents a hypothetic weather modification experiment with injection of highly concentrated aerosol act as activated freezing nuclei. Due to mainly concentration of droplets is higher than concentration of large drops and in the studied case favorable conditions for growth of ice CP exist ($\Delta_i > 0$), maximum precipitation rate exceeded 50 *mm/h* for T_s = -15 °C , $T_s > T_b$.

Except the described situation with $T_s > T_b$, another maximum of solid precipitation (with liquid precipitation maximums due to melting) again corresponds to T_b = -10°C. The reason is explained above and it is in the initial state of the cloudy troposphere (updrafts, T and Δ_i).

Concerning the water precipitation, they notably and naturally decreased when almost all big drops were frozen when freezing temperature T_b > -5 °C and droplets didn't generate and contribute to liquid precipitation formation processes due to absence of water vapour income in absence of updrafts and, hence, Δ_i.

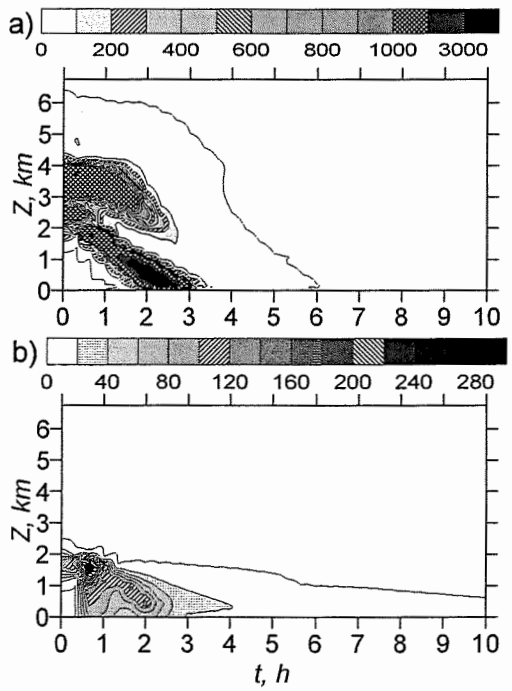

Fig.5. The same as for Fig.4, T_b= -1 °C.

Another numerical study was carried out in this research when empirical constants A_f and B_f from Eq.2 responsible for activation of freezing nuclei in a cloud were varied. Usually, $A_f = 2 \cdot 10^{-3}$ $(cm^3 \cdot s)^{-1}$ and $B_f = 0.26$ $°C^{-1}$ (Bujkov et al., 1975, Pirnach et al., 1994, Krakovskaia et al., 1998). Actually, no remarkable affect on precipitation formation processes was found when varied such coefficients in wide range. It differs from the results obtained in Krakovskaia et al. (1998) where theoretical study was performed and increasing A_f up to 1 $(cm^3 \cdot s)^{-1}$ led to rise precipitation intensity in 2-3 times more than regular values. The explanation can be in the specific features of the studied cloud system which was mixed and relatively warm (Figs.1, 2).

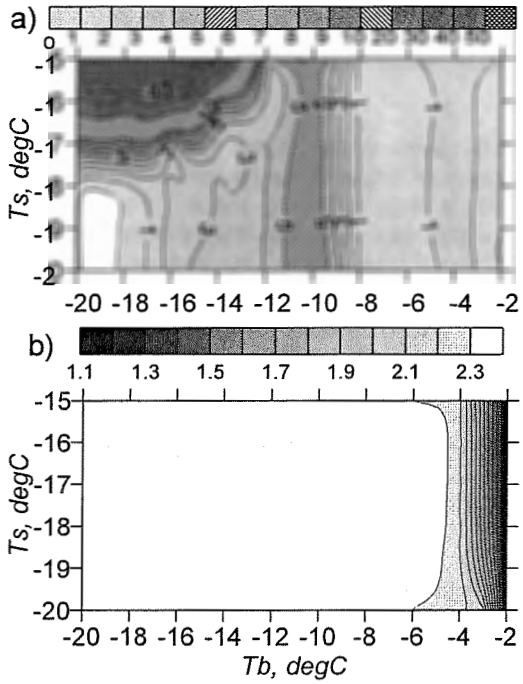

Fig.6. Maximum precipitation rate (I_{max}, *mm/h*) as function of T_s and T_b: (a) ice and (b) water phase.

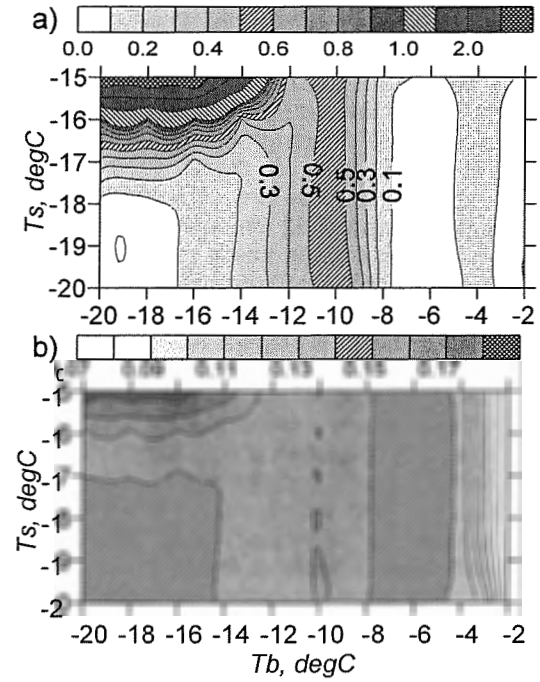

Fig.7. Mean precipitation rate (I_{mean}, mm/h) as function of T_s and T_b: (a) ice and (b) water phase.

4. CONCLUSION

The conducted series of the numerical experiments on the study freezing processes in mixed clouds demonstrate that:

- chosen numerical models and approach are suitable for the research and allow to obtain specific features of studied clouds;
- freezing processes are highly sensitive to the temperature of complete freezing of liquid CP which can notably modify a cloud microphysics and precipitation formation processes;
- in what extend a cloud microphysics and precipitation formation processes will be affected, greatly depends on thermodynamics and the specific features of studied clouds.

5. REFERENCES

Bujkov, M.V. and Pirnach, A.M., 1975. A numerical simulation of precipitation in mixed stratiform clouds taking into account its microstructure. Isv. AS USSR, AO, 2, No.5, 469-480 (in Russian).

Krakovskaia, S.V., 1995. 3-D diagnostic models of frontal rainbands over limited areas of Ukraine. WMO/TD-No.699, 157-162.

Krakovskaia, S.V. and Pirnach, A.M., 1998. Theoretical study of the microphysical structure of mixed stratiform frontal clouds and their precipitation. Atmos. Res., 47-48, 491-503.

Krakovskaia, S.V. and Pirnach, A.M., 2000. Theoretical study formation and development of Antarctic cloudiness under different intensity of ice and cloud droplet nucleation. AIP Press, Melville (NY), 534, 467-470.

Krakovskaya, S.V., Pirnach, A.M. and Suhinsky, A.N., 1994. Simulation of the seeded frontal clouds over Ukraine. WMO/TD-No.596, V. 2, 499-502.

Pirnach, A.M., 1998. The construction and application of numerical models to the study of cloud dynamics and the structure of winter frontal rainbands. Atmos. Res., 47-48, 355-376.

Pirnach A.M., Krakovskaya S.V., 1994. Numerical studies of dynamics and cloud microphysics of the frontal rainbands. Atmos. Res., 33, 333-365.

ANALYSIS OF RADAR AND IN SITU MEASUREMENTS OF SNOWFALL IN EASTERN NORTH DAKOTA

P. A. Kucera[1] and A. J. Newman[1]

[1]Department of Atmospheric Sciences, University of North Dakota, Grand Forks, ND 58202

1. INTRODUCTION

Many attempts to characterize snowflake size distributions along with radar reflectivity-snowfall (Z-S) or equivalent reflectivity-rainfall (Z-R) relationships for snowfall have been made in the past decades. Fujiyoshi et al. (1990) give an extensive list of attempts made to determine Z-S power law relationships and the methods used to obtain the relationships. The first method described by Fujiyoshi et al. (1990) uses surface snowflake size measurements to produce Z-R relationships for snow in the form of a power law (i.e. $Z = aR^b$). The second method described in Fujiyoshi et al. (1990) uses radar reflectivity data along with snowfall accumulation rates made simultaneously on the ground beneath the radar sample volume.

Over the past 10 to 20 years, the development and use of polarimetric radars in the research community has permitted studies to be made concerning hydrometeor identification, bulk distribution retrievals, and polarimetric precipitation estimation.

All these different approaches to determine snowfall accumulation and snowflake properties rely on surface observations as an integral part of the methodology or the means to validate the radar observations. Traditional measurements of snowfall rate and total accumulation are made using devices ranging from a simple yard stick to more sophisticated instrumentation such as a heated tipping bucket rain gauges or highly sensitive electro balances.

When measuring snowfall, any of these methods succumbs to large errors even in light wind conditions. In regions such as the central plains (i.e. Eastern North Dakota) winds during snowfall events can be as high as 20 m/s. This can result in large errors for standard precipitation gauges like a Fischer-Porter gauge. For example, Goodison (1978) reports that a Fischer-Porter gauge achieves only a 40% catch of the actual snowfall with a wind speed of 7 m/s at the gauge height, and this is with a wind shield in place. Fujiyoshi et al. (1990) report undercatchment errors as large as 50%. These errors are unacceptable if one requires the need for accurate estimation of snow depth, water equivalency, total storm snowfall, or even seasonal snowfall accumulation.

Using a video disdrometer developed by Dr. Bliven of the NASA/Wallops Flight Facility, we are beginning to address these errors in the hopes of producing accurate snowflake size distributions that can be used to improve Z-S (Z-R) relationships, estimations of snowfall intensity, accumulation, density and validate polarimetric radar snowfall retrievals.

2. DATA

A video disdrometer, referred to as a Rain Imaging System (RIS), has been deployed at the University of North Dakota's surface validation site, which is located approximately 18 km west of UND. The instrument collected almost continuous precipitation data from December 2003 through April 2004.

The RIS uses a digital CCD grayscale camera with a zoom lens attached that gives a sample volume of 32 mm in width by 24 mm in height. The camera has a resolution of 640 x 240 pixels giving a 0.05 mm resolution in the horizontal and a 0.1 mm resolution in the vertical. The focal plane is two meters from the end of the lens and roughly one meter above ground, while the light source is between one and two meters behind the focal plane. The camera is mounted on a stand inside of a weather proof surveillance camera shelter, while the light source is a 300 W flood lamp mounted on a tripod. An example RIS deployment is shown in Figure 1.

The relatively low cross sectional area of the equipment and relative isolation of the sample volume from camera and light platforms permit this instrument to be much less affected by wind. Only in extreme cases with high winds

Corresponding author's address: Paul A. Kucera, University of North Dakota, Grand Forks, ND, USA; Email: pkucera@aero.und.edu

running directly along the line of sight of the camera will there be disturbances of the snowfall by the instrument itself.

Figure 1: Example cold season setup of a RIS.

The retrieval software grabs images from the camera at a rate of approximately 50 – 60 frames per second and compresses them into hourly files for post-processing. Figure 2 shows an example particle retrieval observed from the RIS. The data processing software currently uses a threshold technique to determine the particle boundaries. By looking at each pixel and comparing it to the threshold value, the software determines if the pixel should be categorized as a valid particle element (black) or background signal (white).

These binary images are then used to produce output ASCII tab delimited text files. Output files contain records of every particle counted, a timestamp, particle location in the x-y plane of the sample volume, and particle size information. The files also contain second and minute summaries from each frame.

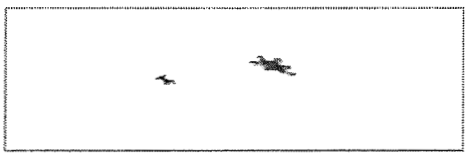

Figure 2: An example grayscale image recorded by the RIS. The image shows the presence of a capped column and dendritic ice particle.

WSR88D Level II archive data were obtained for the Mayville, ND WSR-88D (KMVX) radar through National Climate Data Center (NCDC) archives. The radar is located 43 km due south of the RIS site, which is outside of the clutter maps used by the NWS. The range separation is small enough to avoid overshooting of the radar beam even for shallow wintertime precipitation events. Along with data obtained from the KMVX WSR88D radar, the recently upgraded UND C-band polarimetric Doppler radar was also used in preliminary comparisons with RIS data.

The UND radar transmits at peak power of 290 KW. It has a relatively narrow beamwidth of 1°, polarimetric fields are measured using a simultaneous transmission and receive (STAR) transmission method. The UND radar has a SIGMET RCP08 and RVP08 for antenna control and signal processing, respectively.

3. RESULTS AND DISCUSSION

Using the output files generated by the RIS particle retrieval algorithms, snowflake size distributions were produced for several snowfall events. Snowflake size distributions were generated for various time integration intervals. Figure 3 shows an example snowflake distribution (solid line) for a one hour period during the 25 January 2004 snow event. A modified gamma distribution (dashed line) was fit to the data. The modified gamma distribution we used has the form:

$$N(D) = N_0 D^{\mu} \exp(-\Lambda D), \qquad (1)$$

where N_0 is the intercept parameter, D is the diameter of the particle, μ is referred to as the shape parameter, and Λ is the slope.

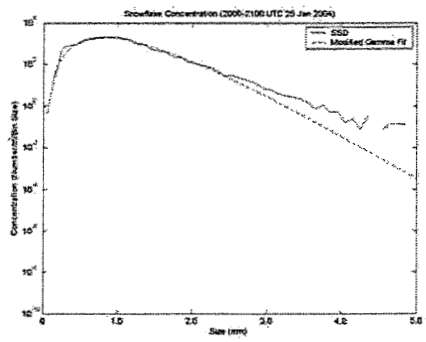

Figure 3: Plot of hourly averaged snowflake size distribution from 21 UTC 25 Jan 2004.

The modified Gamma distribution provides a good fit to the small snow particles (D < 2.5 mm), but diverges from agreement at the larger particle sizes. The decrease in concentrations at the smallest sizes (D < 0.8 mm) is probably due to a decrease in sensitivity of the threshold algorithm to detect the smallest particles. The divergence from a Gamma distribution at the largest particle sizes is most likely from the small sample size (i.e. ~1 particle/m^3 at D > 2.5 mm). An incorrect relationship between sample

volume and particle size for the largest snowflakes could result in an incorrect size distribution. Understanding this relationship is a focus of our current research

Based on previous studies (i.e. Gunn and Marshall (1958), Sekhon and Srivastava (1970), etc.), we expected an exponential size distribution for snow. Recent advancements have been made in the particle retrieval algorithm. Initial results (not shown) do indicate a more exponential snowfall size distribution.

The new algorithm uses an edge detection technique to estimate the size and shape of the hydrometeors. Rainfall observations collected from a RIS at Wallops Island show an excellent agreement with adjacent tipping bucket rain gauge measurements to within 1.5% using the edge detection technique (Bliven, personal communication). We plan to implement the edge detection algorithm in further processing and discuss the results in our presentation.

Nonetheless, we can use the current algorithm to see the relative variability in the snowfall distributions as function of time. Estimate Gamma parameters are shown in Table 1. The parameters are for the period 2000-2359 UTC on 25 January 2004. The parameters are fit at one hour time intervals.

Table 1: Particle size distribution parameters four a four hour period using a modified gamma function.

TIME/ COEF	2000 (UTC)	2100 (UTC)	2200 (UTC)	2300 (UTC)
N_0	5.6×10^5	10.2×10^5	2.1×10^5	1.9×10^5
μ	4.63	5.36	3.84	3.68
Λ	5.76	6.32	4.85	4.78
Correlation	0.986	0.965	0.977	0.983

These results show that at the beginning of the time period the snowflake distribution had a narrower spectrum than later in the event, which indicates the snowfall had potentially more pristine crystals or small aggregates and a lack of larger aggregates. As the event progressed, the distribution widened indicating the presence of larger snowflakes or aggregates.

Preliminary comparisons of RIS estimated reflectivity with coincident reflectivity observations from the KMVX WSR88D radar indicate the RIS estimates were 3-6 dB lower than the radar (reflectivity ranged between 16-18 dBZ). A difference of 2-3 dB can be explained based on the orientation and ZDR signature of the observed pristine ice crystals (see Schuur et al. 2003). The remaining differences are probably due to the threshold retrieval technique and radar sampling errors. A more detailed comparison with the KMVX and UND radars will be presented at the conference.

4. CONCLUSIONS

Because of these preliminary results, we are confident the RIS can provide accurate snowfall measurements. These data will provide estimates of size distributions, snowfall rate, snow depth, and possibly density estimates. Ultimately, the RIS measurements will provide an extensive database for radar algorithm development and verification studies (especially polarimetric) of snowfall retrievals.

5. ACKNOWLEDGEMENTS

The authors thank Dr. Larry Bliven for providing the video disdrometers for our snowfall research. Mr. Newman was partially supported under the ND NASA STaR program.

6. REFERENCES

Fujiyoshi et al., 1990: Determination of a Z-R Relationship for Snowfall Using a Radar and High Sensitivity Snow Gauges. *J. Atmos. Sci.*, **29**, 147-152.

Goodison, Barry E., 1978: Accuracy of Canadian Snow Gage Measurements. *J. Appl. Meteor.*, **17**, 1542-1548.

Gunn, K. L. S and J. S. Marshall, 1958: The distribution with size of aggregate snowflakes. *J. Meteor.*, **15**, 452-466.

Schuur T., A. Ryzhkov, P. Heinselman, D. Zrnic, D. Burgess, and K. Scharfenberg, 2003: Observations and classification of echoes with the polarimetric WSR-88D radar, NSSL, 46 pp.

Sekhon, R. S. and R. C. Srivastava, 1970: Snow size spectra and radar reflectivity. *J. Atmos. Sci.*, **27**, 299-307.

Observations of quasi-stationary, shallow orographic snow cloud: spatial distributions of super liquid water and ice hydrometeor

Kenichi Kusunoki [1*], Masataka Murakami [1], Narihiro Orikasa [1], Yoshinobu Tanaka [1], Mizuho Hoshimoto [2], Yoshinori Yamada [2], Hakaru Mizuno [3], Kyosuke Hamazu [4], and Hideyuki Watanabe [5]

[1] Meteorological Research Institute,Japan
[2] Japan Meteorological Agency, Japan
[3] Meteorological College, Japan
[4] Mitsubishi Electric Corporation , Japan
[5] Tone River Dams Integrated Control Office, Ministry of Land, Infrastructure, and Transport, Japan

1. INTRODUCTION

The Joint Project of Orographic Snow Cloud Modification of 1999 produced observations of orographic snow clouds over the windward slopes along the Japanese coast. The main purpose of the project was the determination of the spatial and temporal distributions of supercooled liquid water (SLW). Such knowledge is basic to understanding precipitation development and efficiency, as well as the potential for increasing precipitation.

On 25 February 1999, orographic snow clouds were observed during a period of weak cold advection due to a winter monsoon after a cyclonic storm had passed over the Japan Sea side (Kusunoki et al. 2004). During the study period, quasi-stationary and shallow orographic clouds prevailed. The typical echo was characterized by a stratiform with a weak embedded convection. The altitude of high relative humidity (above 90%) that follows the cloud regions indicates that the height of the cloud top was 3.5km (temperature -19°C). The echo structure reflected the presence of potential instability in the clouds, which was released partly in the form of weak embedded convections by orographic lifting. In this study, the spatial distributions of the microphysical structures of the snow clouds are examined. The mobile platform in this study is characterized by the main instruments such as microwave radiometer and optical imaging probe (2D-Grey). The platform enabled to provide unique dataset of precipitation particles (e.g., size spectra and shape) in addition to liquid water. The spatial distributions of microphysical properties, by combining vehicle-mounted instruments and a Ka-band Doppler radar, are described in this paper.

2. THE LOCAL TERRAIN OF THE STUDY AREA

Figure 1 shows the locations of the ground-based instruments and the surrounding terrain. The Shimizu Valley is wedge-shaped, elongated southeastward, and terminates at roughly 18km from the entrance to the valley, which faces northwest. Airflows of the monsoon from over the Sea of Japan, which blow nearly parallel to the valley axis, converge and rise on the windward side as a result of the local orography of the valley. Such orographically modified flows develop snow clouds, which form over the sea and/or land upstream of the study area. The deployment of instruments and the mobile measuring route along the Shimizu Valley are suitable for our primary interest, which is to focus on local occurrences of SLW and snow, and, thus, on the nature of the orographically enhanced modifications to snow clouds.

3. MOBILE PLATFORM

In order to investigate quasi-stationary orographic snow clouds, ground-based mobile instruments are appropriate. Note that the concept of mobile observations of orographic snow clouds is not entirely new, but the Desert Research Institute (DRI), Nevada, developed a dual-frequency Mobile Microwave Radiometer (MMR; Huggins 1995). The mobile platform in this study was equipped with a 2D-Grey imaging probe, a microwave radiometer, conventional sensors (thermometer, hygrometer, and anemometer), and a Global Positioning System (GPS) receiver, which gave the vehicle position, heading, and speed (Fig. 2). The mobile measuring route is shown by the bold line in Fig. 1. In this study, the vehicle made four roundtrips between near the Shiozawa site (a height of 190m) and the Shimizu site (a height of 580m). It took about 25 minutes each way. In addition to the mobile instruments, the Ka-band Doppler radar (Hamazu et al. 2003) and rawinsodes were used in this study.

4. SUPERCOOLED LIQUID WATER AND SNOW PARTICLE DISTRIBUTIONS

Figure 3 shows the spatial distributions of wind speeds, the liquid water path (LWP), number concentration of snow particles, and the ice water path (IWP). These spatial distributions are obtained by averaging the data from the mobile instruments and Ka-band radar. The mobile instrument data are averaged over the four round trips between 0842 and 1311 JST. The radar data (reflectivity and Doppler velocity) are averaged over 23 RHI scans (0832 - 1256 JST) around an azimuth of 141.0° as the direction along the valley axis.

* *Corresponding author address:* Kenichi Kusunoki, Meteorological Research Institute, Tsukuba, Japan; e-mail: kkusunok@mri-jma.go.jp.

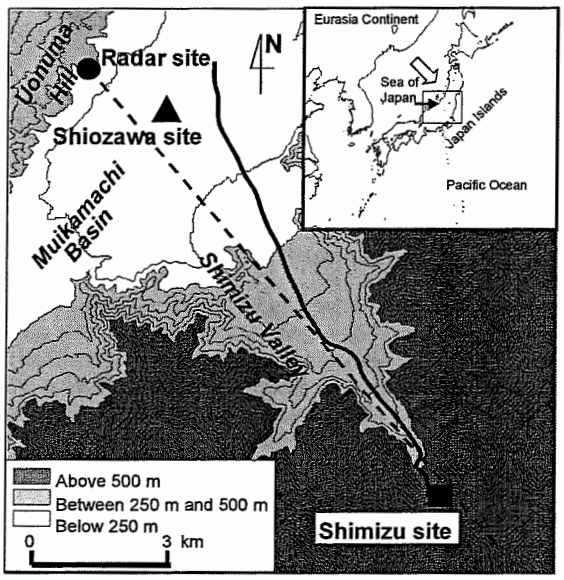

Fig. 1 Topographical map around the study area including geographic names. The locations marked by the symbols are as follows: the radar site of the Ka-band Doppler radar on the Uonuma Hill (circle); Rawinsonde soundings were operated at the Shiozawa site (triangle); the Shimizu site (square). The bold line indicates the mobile measuring route. The radar RHI scan was at the azimuth angle 141° associated with the valley axis (dashed line). The white arrow shows the direction of the monsoon flow. The study area located at the tip of the black arrow.

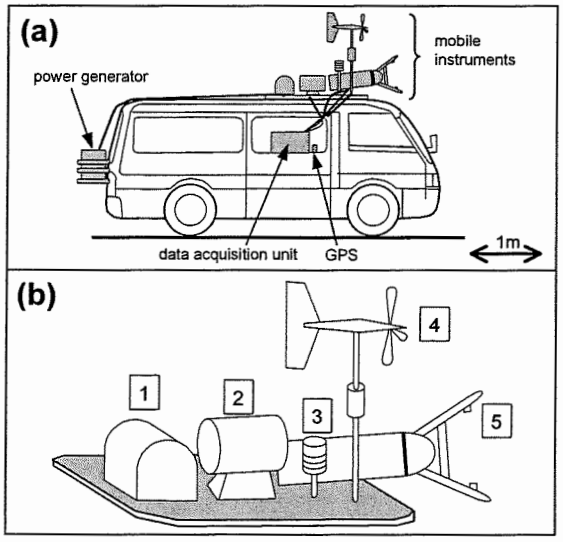

Fig. 2 (a) Illustration of the mobile platform. (b) Rooftop layout, including (1) microwave radiometer, (2) air blower for removing raindrops and snow on the radiometer radome, (3)thermister and hygrometer, (4) anemometer, and (5) 2-D Grey imaging probe.

Figure 3a shows the wind speed distributions observed with the mobile platform. The averaged Doppler velocities, which can be assumed to represent the wind speed up the slope on the Shimizu Valley, are superimposed. The averaged Doppler velocity distribution indicates that the wind speed increased with height. The mobile wind speeds exhibit a trend that is similar to that of the Ka-band radar but is often enhanced by the local terrain forcing associated with the bottlenecks.

Similarly to the wind speeds, the LWP is associated with the terrain height (Fig. 3b). The orographic lifting due to the increase of the wind speed up the slope would lead to generate and increase supercooled cloud droplets. The perturbations of LWP are shown in Fig. 4. Concerning the terrain feature, the perturbations of highest terrain altitudes around the mobile route (i.e., approximately 1-km width of the domain centered on the mobile route) are superimposed. This figure shows that there is a positive correlation between the two variables up the slope. Locally enhanced updrafts may exist where the airflows ascended over the abrupt terrain rises (~3km horizontal scale), and such updrafts may generate supercooled cloud droplets. It is noteworthy that such a small-scale terrain-induced SLW had been reported by Sassen et al. (1990) and Huggins (1995).

Figure 3c shows the distribution of total number concentrations of snow particles derived from the 2D-Grey measurements. Similarly to the wind speed and LWP patterns, the number concentrations (0.1-6.4mm of diameter) are correlated with the altitude. Figure 5 shows the number concentrations for each particle size from the 2D-Grey measurements. This figure indicates that greater concentrations of larger particles tend to appear over the windward slope but not over the bottom of the basin (hereafter BMB). Most of the 2D-Grey particle images exhibit quasi-circular shapes with rounded edges, suggesting significant riming (Fig. 6). From Figs. 3c, 5, and 6, it is considered that ice crystals would generate and/or grow by riming to become larger snow particles with higher altitude downwind of the BMB.

Figure 3d indicates that the IWP increased with terrain height, reached maximum intensity at 14km downwind of the BMB, and then decreased. Figure 7 shows the averaged reflectivity pattern. This figure indicates that the echo tops (-30 dBZ) were about 2.5km and the relatively strong echo region (> -3 dBZ) appeared at 5km downwind of the BMB and extended nearly parallel to the slope. The increase of IWP and the relatively strong echo pattern would reflect snow particle growth during their downwind advection and are consistent with the distributions of size and number of snow particles. The reason for the decrease of the IWP from the mid-barrier

comes from a decrease in the cloud thickness adjacent to the mountain ridge. Note that, although no mobile data were available downwind of the Shimizu site, the LWP adjacent to the mountain ridge would decrease for the same reason as the IWP.

5. SUMMARY AND CONCLUSIONS

The present results are summarized in the schematic diagrams shown in Fig. 8. Downwind of the BMB, the orographic lifting due to the increase of the wind speed up the slope would lead to generate and increase supercooled cloud droplets. Furthermore, small-scale terrains (~3km horizontal scale) enhanced localized updrafts embedded within the larger scale flow and had noticeable impacts on the SLW cloud distribution.

Simultaneously, snow particles grew by riming to become larger with higher altitude. Associated with a high concentration of larger particles, a relatively strong echo region appeared at 5km downwind of the BMB and extended nearly parallel to the slope.

The evolution of the weak cold advection as a result of the winter monsoon described in this paper is a common feature over the Japan Sea side, and, therefore, the case reported here is believed to be representative of a significant fraction of orographic snow clouds over the Japan Sea side.

Acknowledgements

The project is supported by the Ministry of Land, Infrastructure, and Transport of Japan Government.

References

Hamazu, K., H. Hashiguchi, T. Wakayama, T. Matsuda, R. J. Doviak, and S. Fukao, 2003: A 35-GHz scanning Doppler radar for fog observations. *J. Atmos. Oceanic Technol.*, **20**, 972–986.

Huggins, A.W., 1995: Mobile microwave radiometer observations: Spatial characteristics of supercooled cloud water and cloud seeding implications. *J. Appl. Meteor.*, **34**, 432-446.

Kusunoki, K., M. Murakami, M. Hoshimoto, N. Orikasa, Y. Yamada, H. Mizuno, K. Hamazu, and H. Watanabe, 2004: The characteristics and evolution of orographic snow clouds under weak cold advection. *Mon. Wea. Rev.*, **132**, 174-191.

Liao, L., and K. Sassen, 1994: Investigation of relationships between Ka-band radar reflectivity and ice and liquid water content. *Atmos. Res.*, **34**, 231-248.

Sassen, K., A.W. Huggins, A.B. Long, J.B. Snider and R.J. Meitin, 1990: Investigations of a winter mountain storm in Utah. Part II: Mesoscale structure, supercooled liquid water development, and precipitation processes. *J. Atmos. Sci.*, **47**, 1323-1350.

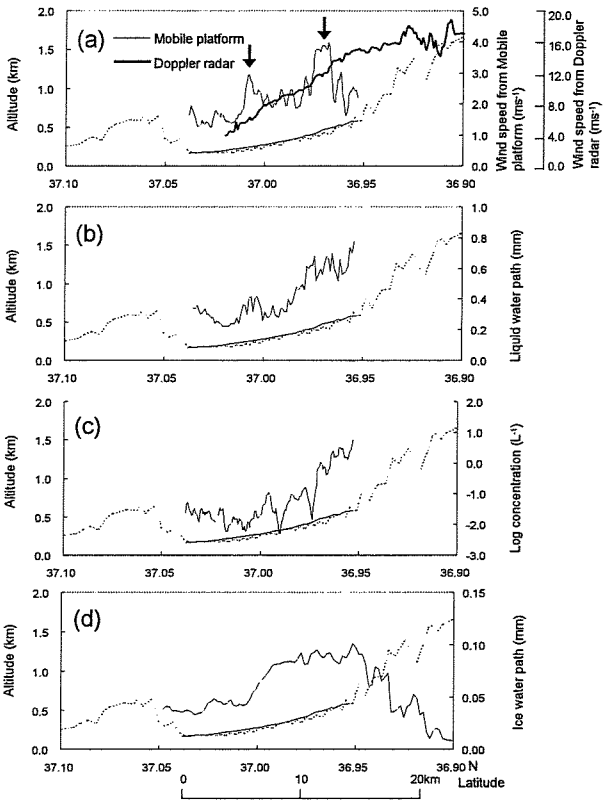

Fig. 3 Time-averaged distributions (0842-1311JST). The terrain heights along the azimuth angle 141° of the radar beam (dashed line) and along the mobile route (solid line) are superimposed. (a) The mobile wind speeds. The averaged Doppler velocities observed by the Ka-band radar are superimposed (0832-1256JST). The arrows indicate the locally enhanced wind speeds. (b) The LWP. (c) The total number concentrations of particles. (d) The IWP.

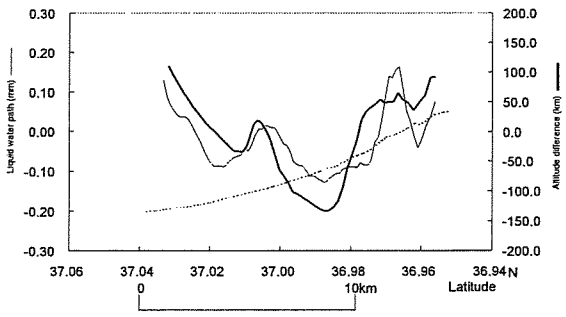

Fig. 4 Time-averaged perturbations of the terrain altitudes and the LWP (0842-1311JST). The linear trend was removed beforehand and smoothed by 2.5 km. The terrain heights along the mobile route (dashed line) are superimposed.

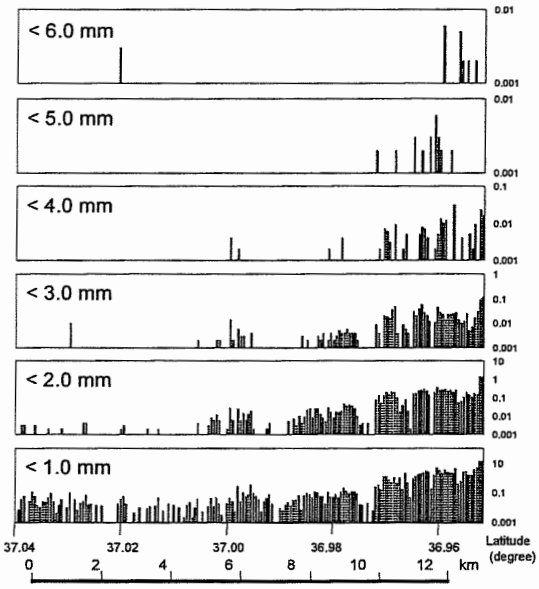

Fig. 5 The number concentrations for each particle diameter from the 2D-Grey measurements.

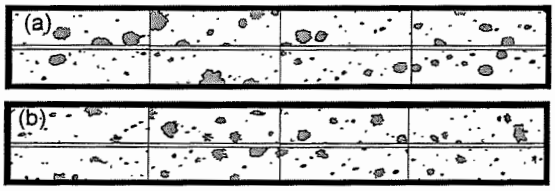

Fig. 6 Example of the 2D- Grey images measured around the Shimizu site. The vertical extent of each strip of images is 6.4 mm. (a) 9:25:55- 9:26:27 JST. (b) 12:29:53-12:30:16 JST.

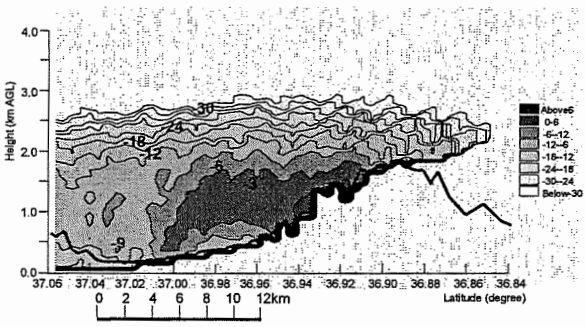

Fig. 7 The averaged reflectivity RHI scan at the azimuth angle 141° along to the valley axis in Fig. 1. The terrain heights are superimposed.

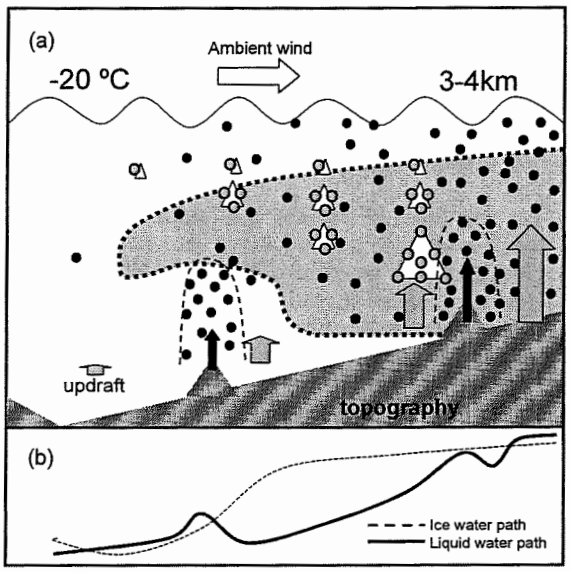

Fig. 8 Schematic of the spatial distributions of cloud droplet and snow particle in orographic snow cloud and how they relate to the LWP and IWP. (a) The terrain (stripe shading), the updrafts associated with the slope (gray-shaded arrows), the locally enhanced updrafts (black arrows), the cloud droplets (black circles), the rimed particles (triangles with gray circles), the dense cloud regions associated with the locally enhanced updrafts (enclosed by thin dashed lines), the relatively strong echo region (shaded area enclosed by a bold dashed line), and the cloud top (wavy line). (b) The horizontal distributions of the LWP (solid line) and IWP (dashed line).

Transition of leeside precipitation properties observed by Ka-band radar and ground-based 2D-Grey probe

Kenichi Kusunoki [1*], Masataka Murakami [1], Narihiro Orikasa [1], Yoshinobu Tanaka [1], Koyuru Iwanami [2], Masayuki Maki [2], Park SangGoon [2], Ryohei Misumi [2], Kyosuke Hamazu [3], and Hiroshi Kosuge [4]

[1] Meteorological Research Institute,Japan
[2] National Research Institute for Earth Science and Disaster Prevention, Japan
[3] Radio Atmospheric Science Center, Kyoto University, Japan
[4] Tone River Dams Integrated Control Office, Ministry of Land, Infrastructure, and Transport, Japan

1. INTRODUCTION

A cold northwesterly monsoon accompanied by a strong Siberian high and the central mountain range of Japan can provide an excellent setting for studying the evolution of orographic snow clouds. In spite of the importance of the microphysical structures of these clouds, most of the studies of orographic snow clouds over the Japan Sea side were oriented toward synoptic and large-scale mesoscale disturbances. This paper documents the flow and leeside particle properties on snow clouds associated with a relatively steady northwesterly monsoon flow interacting with the Mikuni Mountains, Japan. This study utilizes data collected as part of a field campaign which was designed to observe orographic snow clouds and identify seeding opportunities over the windward slopes of the Japan Sea side (e.g., Murakami et al. 2000). One of the most important data sources was a set of two Ka-band Doppler radars, which provided radar reflectivity and Doppler velocity around a steep mountain ridge of the the Mikuni Mountains. Another important instrument was 2D-Grey imaging probe which measured snow particles on the leeward slope.

2. THE STUDY AREA AND INSTRUMENTATION

Figure 1 shows the locations of the instruments and the surrounding terrain. The area consists of mountains, a basin, and a valley, and the elevation varies from about 150m to 2000m. In this study, two Ka-band Doppler radars were deployed on the windward and leeward slopes, respectively (Iwanami et al. 2001, Hamazu et al. 2003). These radars were deployed along the NW-SE line, which corresponded to the direction of the winter monsoon. Composites were constructed from RHI scans oriented toward each other. The distance between both radar sites was 32km.

The ridge of the Mikuni Mountains was at the midpoint between both radar sites. To examine the upstream conditions, rawinsondes were launched 15 km upstream from the ridge at 0827, 1141, and 1520 JST(Japan Standard Time). The 2D-Grey imaging probe was used for precipitation particle measurements (e.g., size spectra and shape) at the leeward radar site which was located 16km in the lee of the mountain ridge.

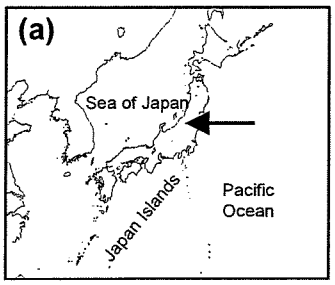

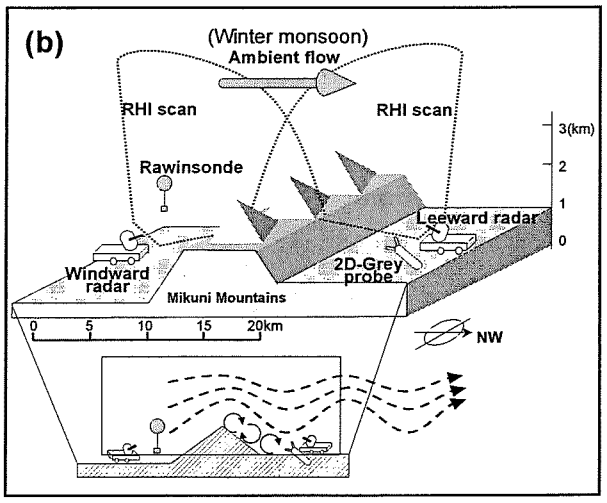

Fig. 1 (a) Map showing the location of the study area (the tip of the black arrow). (b) Schematic illustration of the simplified topography around the Mikuni Mountains.

* *Corresponding author address:* Kenichi Kusunoki, Meteorological Research Institute, Tsukuba, Japan; e-mail: kkusunok@mri-jma.go.jp.

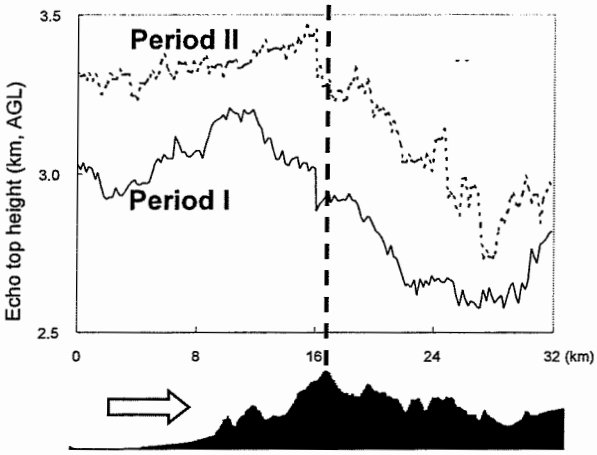

Fig. 2 Variations of the echo top height averaged during Period I (solid line) and Period II (dash line). The arrow shows the direction of the monsoon flow.

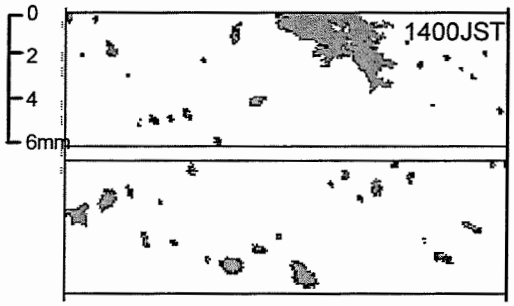

Fig. 3 Example of the 2D Grey images measured on the leeside slope. The vertical extent of each strip of images is 6.4 mm.

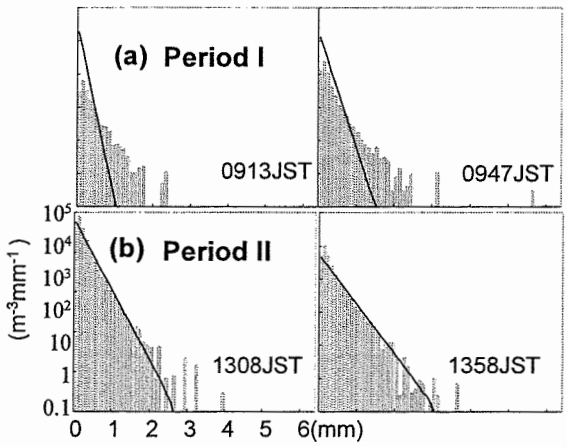

Fig. 4 Size spectra from the 2D-Grey images at the leeward radar site. Gunn-Marshall size distributions (solid lines) are superimposed.

3. LEESIDE PRECIPITATION PROPERTIES

During the study period (December 10, 2001), the upstream soundings indicate that the mean wind direction was northwesterly, which was along the radar sites. The study period was divided into two periods. During the first period (Period I; 0900 - 1300 JST) when the upstream Froude number (Fr) from these soundings was relatively small (< 0.4), radar echo cells moved around the mountain ridge. During the remainder of the study period (Period II; 1300 - 1600 JST), Fr was relatively large (> 0.4) and echo cells moved directly across the ridge. The average echo-top height over the ridge was about 3.0km (Period I) and 3.5km (Period II), respectively (Fig. 2).

According to the 2D-Grey images, snow particle diameters were around 1.0mm during the study period. Most larger particles (> 3mm) were aggregates composed of dendrites, and smaller particles (< 3mm) were usually graupels, rimed dendrites, and dendrites (Fig. 3). Figure 4 shows size spectra from the 2D-Grey images. During Period II, the 2D-Grey images exhibit higher concentrations of small- to moderate-sized (0.1-1 mm) snow particles. The size spectrum during Period II also contains a greater number of large-sized particles than those during Period I. Figure 5 shows the time series of snow water contents, median mass diameters, and number concentrations derived from the 2D-Grey images. These data fluctuated with a timescale of 50-80 minutes, affected by the passage of cloud cells. Overall, regardless of these fluctuations, the snow water contents and the number concentrations were larger during Period II than Period I, while the median mass diameters were relatively constant through the study period. It is consistent with that there are the wider size distributions during Period II than Period I.

Figure 6 shows the NW-SE line at 2.0 km AGL (i.e., the mountain height) versus time series of the Doppler velocity. The transition from the laminar flows to turbulent flows at the ridge is clarified. As described by Kusunoki et al. (2003), the flow over the lee slope suggests that the flow accelerated to a supercritical speed followed by a hydraulic jump-like transition and is qualitatively consistent with the upstream Froude number. Figure 7a shows the turbulence kinetic energy derived from the Doppler velocity. The turbulent area adjacent to the ridge is clarified, and was associated with the precipitation enhancement in the reflectivity on the leeward slope (Fig. 7b).

4. SUMMARY AND DISCUSSION

The present results are summarized in the schematic diagrams shown in Fig. 8. During Period I (relatively small Fr), cloud cells moved around the mountain ridge while echo cells moved directly across the ridge during Period II (relatively large Fr). It is suggested that there would be a higher ice-nucleation activity in the clouds during Period II that had lower cloud-top temperature and stronger upward air motion. Therefore, during Period II, the water vapor could be depleted into numerous ice crystals immediately and considerable mass in the precipitation was due to depositional growth. The increased number of particles and snow water contents during Period II can be attributed to the higher ice-nucleation and aggregation rates. On the lee side, the turbulent wake area existed adjacent to the ridge through the study period. This area was associated with the precipitation enhancement on the leeward slope. A factor contributing to the precipitation enhancement in the turbulent wake flows may be the seeder-feeder effect; that is, the turbulence produced the concentrations of supercooled cloud droplets, and riming growth occurred to lead to snow particles large enough to produce strong radar echoes.

Acknowledgements

The project is supported by the Ministry of Land, Infrastructure, and Transport of Japan Government.

REFERENCES

Kusunoki, K., M. Murakami, N. Orikasa, Y. Tanaka, K. Iwanami, M. Maki, S. Park, R. Misumi, K. Hamazu, and H. Kosuge, 2003: Ka-band radar observations of orographic snow clouds and flows across a steep mountain ridge Preprints, *31th Conf. on Radar Meteorology,* Amer. Meteor. Soc., 104-107.

Iwanami, K. R. Misumi, M. Maki, T. Wakayama, K. Hata and S. Watanabe, 2001: Development of a multiparameter radar system on mobile platform. Proc. Preprinted, *30th Conf. on Radar Meteorology,* Amer. Meteo. Soc., 104-106.

Hamazu, K., H. Hashiguchi, T. Wakayama, T. Matsuda, R. J. Doviak, and S. Fukao, 2003: A 35-GHz scanning Doppler radar for fog observations. *J. Atmos. Oceanic Technol.,* **20**, 972–986.

Murakami, M. , M. Hoshimoto, N. Orikasa, K. Kusunoki, and Y. Yamada, 2000: Microstructure and precipitation processes in a stable orographic snow cloud over the Mikuni Mountains in Central Japan. Preprints, *13th international conference on cloud and precipitation*, 371-374.

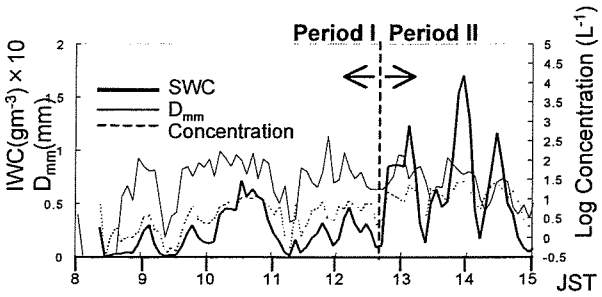

Fig. 5 The snow water contents, median mass diameters, and number concentrations derived from the 2D-Grey images.

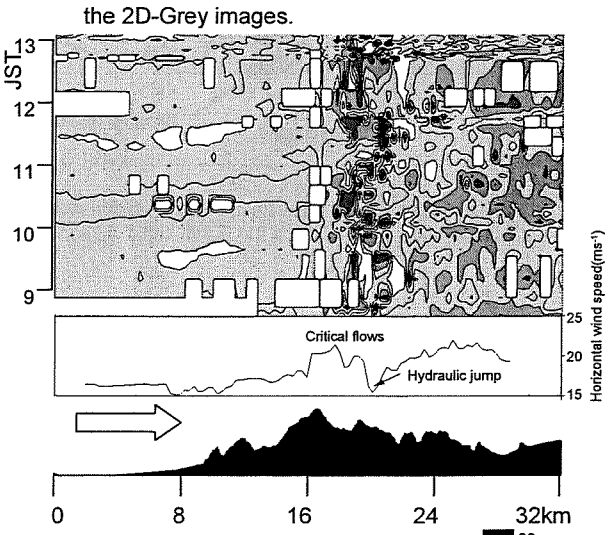

Fig. 6 The NW-SE line at 2.0 km AGL versus time series of the Doppler velocity. The arrow shows the direction of the monsoon flow. Note that the signs of Doppler velocity of the leeward side radar are reversed.

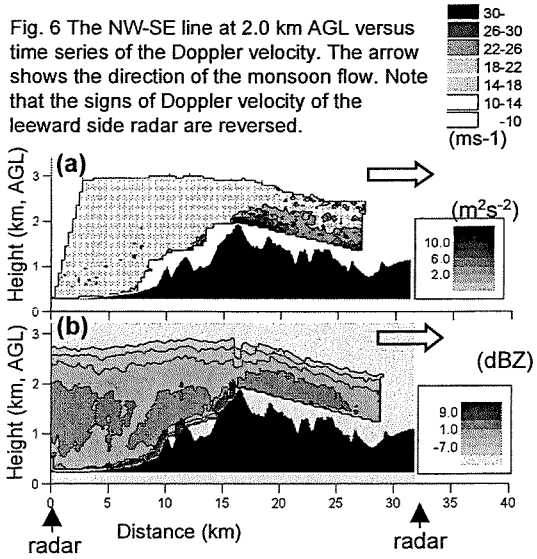

Fig. 7 Composites of (a) turbulence kinetic energy derived from the Doppler velocity and (b) reflectivity along the NW-SE vertical plane. These composites were averaged during the study period. The arrow shows the direction of the monsoon flow.

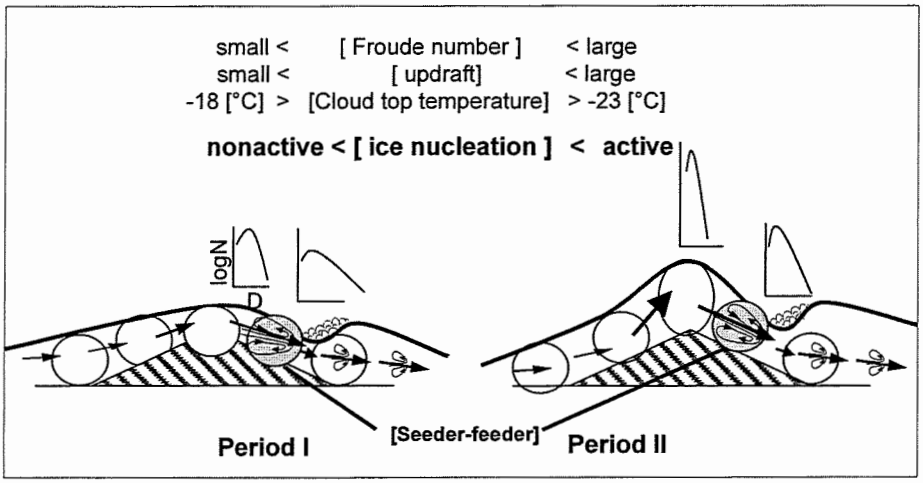

Fig. 8 Schematic of the transition of precipitation properties in orographic snow cloud and how they relate to the flows, cloud motions, and the Froude numbers.

GIANT AND ULTRAGIANT AEROSOL PARTICLES: SOURCE OF LARGE SUPERCOOLED DROPS IN MIXED-PHASE CLOUDS?

Sonia Lasher-Trapp, Sarah Bereznicki and Justin Stachnik

Department of Earth and Atmospheric Sciences, Purdue University, West Lafayette, IN, USA

1. INTRODUCTION AND GOAL

In supercooled clouds or clouds of mixed phase, supercooled large drops (SLD, here defined as having a diameter > 50 μm) can be a major source of aircraft icing. Data collected in numerous field projects to study aircraft icing (e.g. First and Third Canadian Freezing Drizzle Experiment, Winter Icing and Storms Project, Alliance Icing Research Study I) have noted the occurrence of SLD in winter stratiform clouds. The SLD can form by two general mechanisms: warm rain processes (condensation, collision and coalescence), or melting of ice in warm layers with subsequent supercooling in cold layers. If no layer in the cloud or atmosphere is warmer than 0 °C, then the melting mechanism can be eliminated and warm rain processes must be responsible for the SLD. This discrimination of microphysical processes producing SLD has been used to demonstrate that warm rain processes do occur in supercooled wintertime stratiform clouds (e.g. Huffman and Norman 1988, Rasmussen et al. 1992, Strapp et al. 1996, Cober et al. 2001). From several Canadian aircraft icing field experiments, 70-75% of the cases with freezing precipitation were found to involve warm rain processes (Strapp et al. 1996, Cober et al. 2001). While warm rain processes have been shown to be prominent in these mixed-phase stratiform clouds, the formation mechanism of the SLD has not been suitably demonstrated.

In these winter stratiform clouds, it is unclear how the SLD have formed over the long time scales required by condensation growth (on the order of hours) without freezing or otherwise interacting with ice particles. One possibility is that the SLD have grown faster because they originated upon giant (diameter >2 μm) or ultragiant (diameter >20 μm) aerosol particles rather than the smaller sizes of CCN. Giant and ultragiant aerosol particles ingested into a cloud can grow quickly to sizes where coalescence with smaller cloud droplets can be appreciable (even initiating coalescence upon entry into the cloud, if their initial sizes are greater than ~25 μm).

The modeling study of Feingold et al. (1999) showed that giant aerosol particles in stratocumulus could cause 50% more drizzle, and make drizzle form an hour earlier, than if they were absent. This effect was maximized when the cloud particle concentration was high and the cloud liquid water content was low; both characteristics can be met in the wintertime stratiform clouds discussed here.

Numerous other studies have demonstrated the potential for giant and ultragiant aerosol particles to speed rain formation in warm cumuliform clouds (e.g. Johnson 1982, Lasher-Trapp et al. 2001, Blyth et al. 2002), but little has been done to investigate their influence in mixed-phase clouds

The present study reports observations collected during the NCAR C130's participation in the Alliance Icing Research Study II (AIRS II). A preliminary comparison of giant and ultragiant aerosol particle concentrations measured in clear air to observed SLD concentrations within a wintertime mixed-phase stratiform cloud is presented. The comparison is limited to order-of-magnitude estimates due to the preliminary nature of the data set and the instrument uncertainties. The test is straightforward: are the observed giant and/or ultragiant aerosol particle concentrations sufficient to explain the observed concentrations of SLD in a mixed-phase stratiform cloud?

2. NCAR C-130 PARTICIPATION IN AIRS II

The NCAR C-130 aircraft participated during November and December of 2003 within the larger AIRS II field campaign, held during winter 2003-2004 over the Eastern Great Lakes Region to study aircraft icing. The aircraft was based at the NASA -Glenn Research Center hangar in

Corresponding author's address: Sonia Lasher-Trapp, Dept. of Earth & Atmos. Sciences, Purdue University, West Lafayette, IN, 47907; E-Mail: slasher@purdue.edu.

Cleveland, OH. Typical flights included periods of clear-air sampling to measure aerosol particles, CCN and ice nuclei, as well as periods of sampling mixed-phase clouds over the Great Lakes area.

3. PRELIMINARY DATA AND ANALYSIS

All data for this study were collected during the first research flight (RF01) of the NCAR C-130 on 5 November 2003. Clear air and in-cloud sampling were performed over the Lake Erie region. Data, analysis and results presented here are based on the field data, and thus must be considered preliminary until the official release of the calibrated and quality-controlled data set by the NCAR Research Air Facility later in 2004.

3.1 Clear-air Data

Clear-air data over multiple altitudes were collected on 5 Nov 2003. The NCAR Scanning Aerosol Backscatter Lidar (SABL) was operated during the flight, and was used to determine the spatial location of clear-air sampling with respect to overlying clouds. Much of the clear-air sampling was performed below or between layers of clouds, but no significant precipitation falling from the clouds (which would contaminate the clear-air particle estimates) was evident from the SABL data.

Size distributions of the particles measured by the forward scattering spectrometer probe (FSSP-- manufactured by PMS, Inc.) in clear air can be used to determine concentrations of giant and smaller ultragiant aerosol particles, given long enough periods for sampling. At an aircraft speed of ~100 m s^{-1}, the accumulated FSSP sample volume is ~ 3 L min^{-1}. Some examples of size distributions collected on 5 Nov 2003 are shown in Fig. 1.

Nearly all of the particles measured by the FSSP in the clear air were within the "giant" aerosol particle range (2 < D < 20 μm). The scarcity of ultragiant particles is corroborated by data from the 260X, a 1D optical array probe (also manufactured by PMS, Inc.) capable of detecting particles between 10 and 620 μm diameter. The measured ultragiant particles were so few in the time sampled that they are negligible for the goals of this study.

The FSSP clear-air particle size distributions shown are based on the standard response of the FSSP to water droplets. Very small amounts(< 0.02 g m^{-3}) of liquid water was measured by the CSIRO (King) liquid water content probe in the clear air at these times, possibly indicative of deliquesced aerosol particles, although these data are awaiting post-flight instrument callibration. If the particles

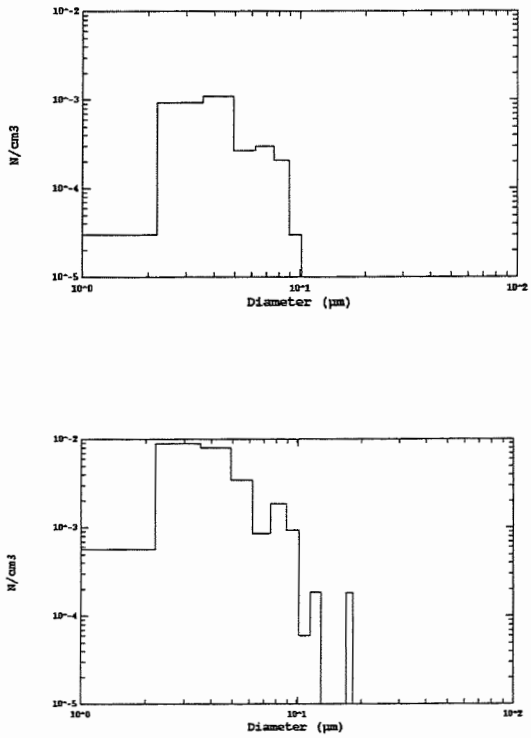

Figure 1. Examples of FSSP particle size distributions measured in clear air for 5 Nov 2003. Top: measured during 600 s of clear-air sampling at 3 km AGL; bottom: measured during 300 s of clear-air sampling at 0.7 km AGL.

measured by the FSSP are instead solid particles having a higher index of refraction than liquid water, the FSSP would underestimate the sizes. Size distributions for solid particles would thus be shifted to the right in Fig. 1, assuming the solid particles could still be approximated as spheres for the Mie scattering relationship.[1]

[1] For ultragiant particles measured in clear air, data from the Cloud Particle Imager (CPI- manufactured by SPEC, Inc.) can be used to determine if the clear-air particles are dry or liquid (deliquesced aerosol particles) and thus help qualify the sizing by the FSSP. The CPI is unable to detect particles smaller than ~ 20 μm diameter, however, and so cannot provide any information on the giant size of particles measured in the clear air for this study.

The clear-air FSSP total particle concentrations as a function of altitude are shown in Fig. 2. The concentration of particles in the clear air decreases exponentially with altitude, ranging from 100 L^{-1} at 0.7 km AGL to less than 0.1 L^{-1} at 5.5 km AGL.

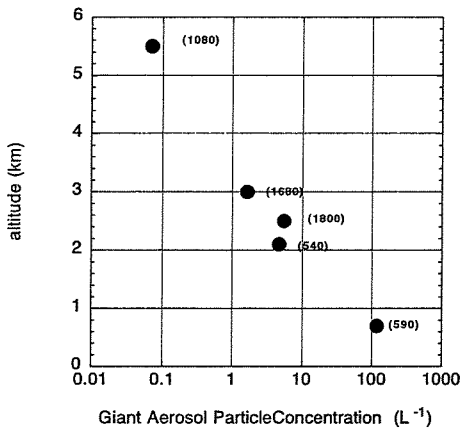

Figure 2. Average concentrations of particles measured by the FSSP in clear air, as a function of height. Averaging intervals are listed by each point (in sec).

3.2 In-cloud Data

A period of aircraft icing (Fig. 3) was encountered from 1958 to 2045 UTC at 4.6 km AGL over the Lake Erie area. The SABL data (not shown) indicate the cloud had a depth of ~ 0.5 km. The cloud formed from slow synoptic-scale ascent; the small updraft speed (~1 m s^{-1} max) and low liquid water content (< 0.5 g m^{-3}) are characteristic of this type of cloud. The buildup of ice on the Rosemont icing detector is indicated by the frequency of the spikes in Fig. 3.

During this period of icing, the 260X probe measured concentrations of particles greater than 50 μm diameter (potential SLD) on the order of 10^{-1} to 1 L^{-1} (Fig. 4), with individual 5 min distributions showing maximum concentrations at these two extremes.

The 260X probe, however, cannot provide any information to distinguish between liquid and ice particles, so the size distribution above includes liquid and ice particles. Because the purpose of this preliminary study is simply to compare order of magnitude estimates of giant aerosol particles with SLD, the peak values in Fig. 4 are of the most importance. Particle images from the 2DC

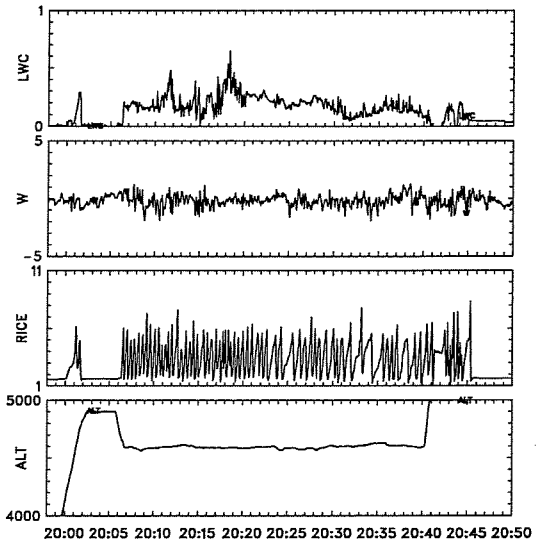

Figure 3. Time period of aircraft icing sampled by the C-130 on 5 Nov 2003; all times are UTC. Data are, from top to bottom, King probe liquid water content (g m^{-3}); air vertical velocity (m s^{-1}); icing detected by the Rosemont icing sensor; and aircraft altitude (m).

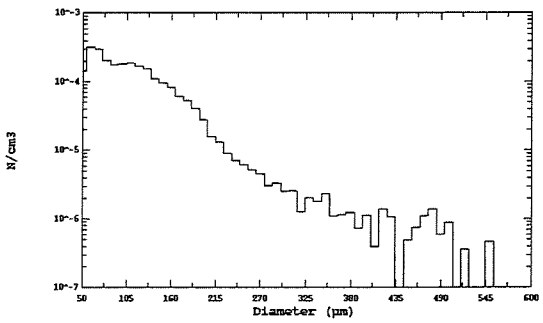

Figure 4. Particles measured in cloud by the 260X during the period of aircraft icing from 1958-2045 UTC on 5 Nov 2003. Total particle concentration (water and ice) is approximately 2 L^{-1}.

(a two-dimensional optical array probe from PMS, Inc. that detects 2D shadows of particles ranging in size from 25 to 800 μm) and the Cloud Particle Imager (CPI- SPEC, Inc.) were used to obtain estimates of the number of liquid particles present in the 260X drop size distribution between 50-150 μm. For the lower part of this range, the CPI images were used to determine the frequency of liquid water versus ice, while at the higher part of this range, the 2DC images were used.

The CPI can display images of particles as small as 20 μm. During the icing period the CPI recorded the most numerous liquid drops at sizes ranging from ~ 20 to 30 μm diameter. The CPI recorded no ice particles at these sizes, but numerous liquid drops at sizes as large as 70 μm, and occasionally drops as large as 130 μm diameter. All ice particle images were larger than 150 μm, and hence outside of the range of interest here. The CPI data thus suggest that all of the smaller particles less than 150 μm in the 260X size distribution shown in Fig. 4 are supercooled droplets.

Data from the 2DC during the period of icing were also surveyed to determine an approximate number concentration of round (here assumed supercooled liquid) particles. Because of the large uncertainty of the sample volumes for 25 and 50 μm particles, as well as the difficulty in labeling a particle of this size as "spherical" with the limited resolution of the 2DC images, concentrations were estimated for particles between 75 and 150 μm, using corrections for the sample volumes at these sizes. From this subjective analysis, the estimated concentrations of particles from 75 - 150 μm diameter ranged from 0.001 to 1 L^{-1} (the latter being rare).

Based on supporting data from the CPI and the 2DC, the peak in the 260X distribution of particle sizes between 50 and 150 μm likely consists of SLD. Maximum total concentrations of SLD are thus on the order of 1 L^{-1}, which is consistent with SLD concentrations found during AIRS I (Cober et al. 2002)

4. RESULTS

The altitude of the mixed-phase cloud containing the SLD was ~ 4.6 km AGL; interpolation between the data values in Fig. 1 suggests that the cloud formed with air containing 0.1 to 1 L^{-1} giant aerosol particles.

From the 260X, 2DC and CPI probes, estimates of SLD in the cloud were a maximum of ~1 L^{-1}. Based on this preliminary analysis, it thus appears that giant aerosol particles may be a sufficient source for SLD occurring in this wintertime stratiform cloud.

Further analysis of the AIRS II data set is needed to support this finding. Checks on the SLD size distribution can be made against data from several liquid and total water content probes. Clear-air data from the "cloudscope" (e.g. Meyers and Hallet 2001) and chemical analysis of particles collected by the Counterflow Virtual Impactor (CVI- Twohy et al. 2001) can be used to interpret the clear-air FSSP measurements and provide information necessary to calculate particle growth times in the cloud. Potential source regions for the giant aerosol particles are yet to be identified. Finally, similar analyses of additional cases from the AIRS II data can provide information on the generality of this result.

5. ACKNOWLEDGEMENTS

The authors wish to acknowledge all of the AIRS II participants, especially the PIs that helped secure the participation of the NCAR C130 in AIRS II: Dr. J. Hallett, Dr. J. Hudson, Dr. C. Twohy, Dr. P. DeMott, their colleagues and students who aided in the data collection, and the staff of the NCAR Research Air Facility. The authors' participation in AIRS II, as well as the data analysis for this study, was funded by NSF grant ATM-0312439.

6. REFERENCES

Cober, S. G., G. A. Isaac, and J. W. Strapp, 2001: Characterizations of aircraft icing environments that include supercooled large drops. *J. Appl. Meteor.*, **40**, 1984-2002.

____, ___, and T. P. Ratvasky, 2002: Assessment of aircraft icing conditions observed during AIRS. AIAA 40th Aerospace Sci. Meeting and Exhibit, Reno, NY, AIAA 2002-0674.

Feingold, G., W. R. Cotton, S. M. Kreidenweis, and J. T. Davis, 1999: The impact of giant cloud condensation nuclei on drizzle formation in stratocumulus: Implications for cloud radiative properties. *J. Atmos. Sci.*, **56**, 4100-4117.

Huffman, G. J., and G. A. Norman, 1988: The supercooled warm rain process and the specification of freezing precipitation. *Mon. Wea. Rev.*, **116**, 2172-2182.

Meyers, M.B. and J. Hallett, 2001: Micrometer-sized hygroscopic particles in the atmosphere: Aircraft measurement in the Artic. *J. Geophys. Res.*, **106 (D24)**, 34,067-34,080.

Rasmussen, R., M. and coauthors, 1992: Winter Icing and Storms Project (WISP). *Bull. Amer. Meteor. Soc.*, **73**, 951-974.

Strapp, J. W., R. A. Stuart and G. A. Isaac, 1996: Canadian climatology of freezing precipitation, and a detailed study using data from St. John's, Newfoundland. FAA International Conference on Aircraft Inflight Icing, Springfield, Virginia, Volume II, DOT/FAA/AR-96/81, 45-55.

Twohy, C.H., and coauthors, 2001: Characteristics of cloud-nucleating aerosols in the Indian Ocean region. *J. Geophysic. Res.*, **106(D22)**, 28,699-28,710.

A COMPARISON OF THE MICROPHYSICAL AND RADIATIVE PROPERTIES OF CIRRUS, WAVE AND ANVIL CLOUDS

R. Paul Lawson, Brad Baker and Bryan Pilson

SPEC Incorporated, Boulder, CO. 80301 USA

1. INTRODUCTION

The relatively recent development of the cloud particle imager (CPI) has led to improvement in measurements of the size and shape of cloud particles. This in turn has led to an improved ability to distinguish water drops from ice particles and to identify the habits of ice crystals (e.g., Korolev et al. 1999; Sassen et al. 2001; Lawson et al., 2001; Heymsfield et al. 2002; Stith et al., 2002). Here we discuss aircraft data collected in wave, cirrus and anvil clouds. The primary research platform used in these studies is the SPEC Learjet, however, limited additional data are presented that were collected by the NASA WB-57 and DC-8, and the University of North Dakota (UND) Citation.

2. WAVE CLOUDS

The wave clouds discussed in this paper were all investigated by the SPEC Learjet along the Front Range of the Colorado Rockies. The basic flight profile was to fly along the wind vector (orthogonal to the ridgeline), making alternating upwind and downwind penetrations through the depth of the cloud. None of the wave clouds exceeded the 45,000 ft msl service ceiling of the Learjet, however, occasionally a requested altitude was unavailable due to restrictions imposed by Air Traffic Control (ATC). Fifteen wave clouds were investigated and 166 horizontal cloud penetrations were executed. The cloud base temperature ranged from –15 C to –40 C and the cloud top temperatures ranged from –17 C to – 60 C.

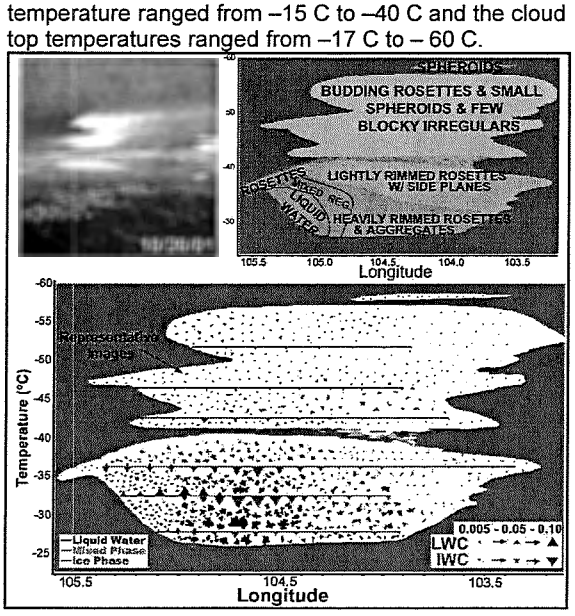

Figure 1. Cross-section showing properties of a typical deep wave cloud investigated by the SPEC Learjet.

Figure 1 shows an *x-z* cross-section of the microphysical characteristics of an example of a deep wave cloud. As shown in the photograph, there are thin regions of clear, or nearly clear air in between what appear to be three distinct wave clouds. The characteristics of this cloud are typical of most of the wave clouds that contained supercooled liquid water and had a cloud top colder than about –37 ° C. The figure shows measurements of liquid water content (LWC), ice water content (IWC) and particle characteristics. IWC is determined by separating ice and water CPI images, computing IWC of the CPI ice images and adding IWC computed from the 2D-C images using the technique described by Lawson et al. (2004).

The cross-section shown in **Figure 1** indicates that SLW is observed as cold as about -35 ° C in this wave cloud, and that the SLW observed at the leading edge of cloud transitioned to mixed-phase about 30 km, and then to glaciated cloud about 50 km downwind of the leading edge. The highest measurement of IWC is found immediately downwind of the mixed-phase region. A vertical profile showing examples of CPI images and microphysical data through this region, at about longitude 104.7 ° in **Figure 1**, is shown in **Figure 2.** The maximum particle size and IWC is found at about -30 ° C, which corresponds to the location shown in **Figure 1**. The maximum (15-km average) ice particle concentration of about 5 cm^{-3} is found slightly higher, around -40 ° C. The maximum 1.5-km ice particle concentration exceeded 20 cm^{-3} in this cloud. The agreement in IWC seen between the Nevzorov probe and the integrated particle size distribution is very good.

Figure 1 suggests a systematic pattern in wave clouds whereby supercooled liquid water formed at the leading edge is followed by a mixed-phase region, then a region with glaciated cloud. Supercooled liquid water (SLW) is only found near the leading edge and up to an altitude where the temperature is –37 ° C. Between –37 ° C and – 50 ° C the particles are mostly budding rosettes. Colder than –50 °C the particles are mostly small spheroidals and irregulars. Downwind of the mixed-phase region is a region with aggregates and complex particles with mostly rosettes that are rimed and/or have sideplanes. Particles in the extreme (> ~ 100 km) downwind region appeared to sublimate and were generally smaller in size than in regions further upwind.

Corresponding Author's Address: Dr. R. Paul Lawson
SPEC Incorporated, 3022 Sterling Circle, Suite 200,
Boulder, CO. 80301 USA plawson@specinc.com

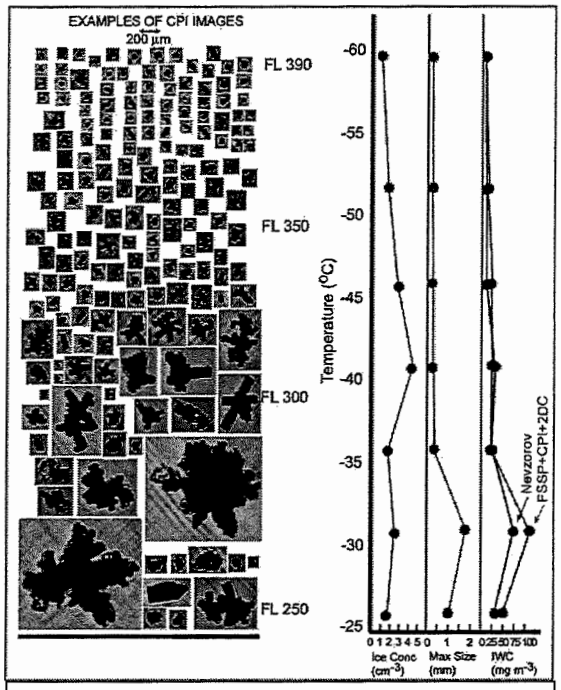

Figure 2. Vertical profile showing examples of CPI images and microphysical data in a wave cloud just downwind of the mixed-phase region (at about longitude 104.4 ° in **Figure 1**).

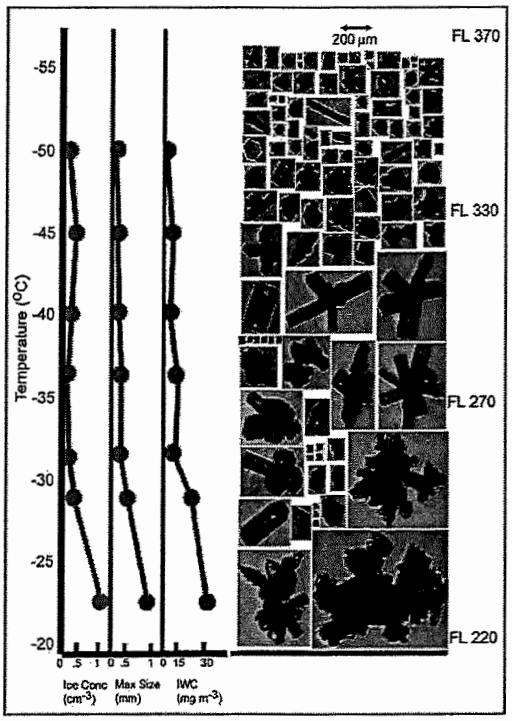

Figure 3. As in **Figure 2**, except for data were collected near Salt Lake City in a deep cirrus cloud on 16 November 1998.

3. CIRRUS CLOUDS

Eleven cirrus clouds were investigated with cloud bases ranging from –20 C to –51 C and cloud tops from –42 C to –62 C. **Figure 3** shows a vertical profile of a deep cirrus cloud. The striking feature of this profile is that it looks very similar to the glaciated region of the wave cloud, except that the particle concentration and IWC are less. As in the wave clouds, the predominant particle type in the composite cirrus data set, when weighted by mass, is the bullet rosette. The similarity in the crystal shapes in the wave and deep cirrus cloud (**Figures 2** and **4**) within the –35 to –55 ° C temperature range suggest that the particles may be undergoing similar microphysical processes. Notable in both types of clouds is the high incidence of bullet rosettes, which presumably form from rapidly frozen water drops (Pruppacher and Klett 1978), implying that the cirrus cloud underwent a nucleation process that involved freezing of SLW and/or solution drops. The microphysics of particle nucleation and the growth process can be followed as air passes over a mountain barrier. In cirrus clouds the process cannot be easily followed. Generally, only the end product is observed, that is, the cirrus cloud with fully developed ice particles.

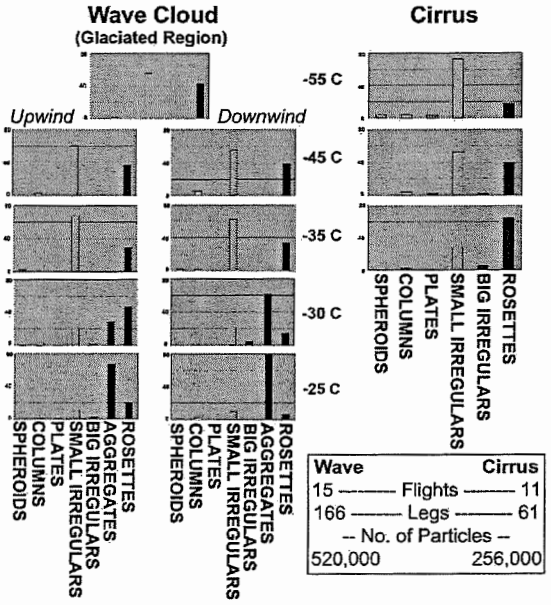

Figure 4. Average particle habit profiles in glaciated regions of wave and cirrus clouds.

4. ANVIL CLOUDS

Here we present some examples of PSDs and particle types in thunderstorm anvils observed by the SPEC Learjet in mid-latitudes, the NASA WB-57 and UND Citation in Florida, the ARA Egrett in Darwin and the NASA DC-8 in Kwajalein. While the particle types in wave clouds and mid-latitude cirrus are strikingly similar, the particle shapes in anvils are very different. Particles observed in the anvils of mid-latitude, Florida and Darwin thunderstorms tend to contain a high percentage of aggregates and chain-like crystals. **Figure 6** shows examples of CPI images and PSDs observed in continental storms in Colorado, Florida, Darwin, and in a maritime tropical storm near Kwajalein.

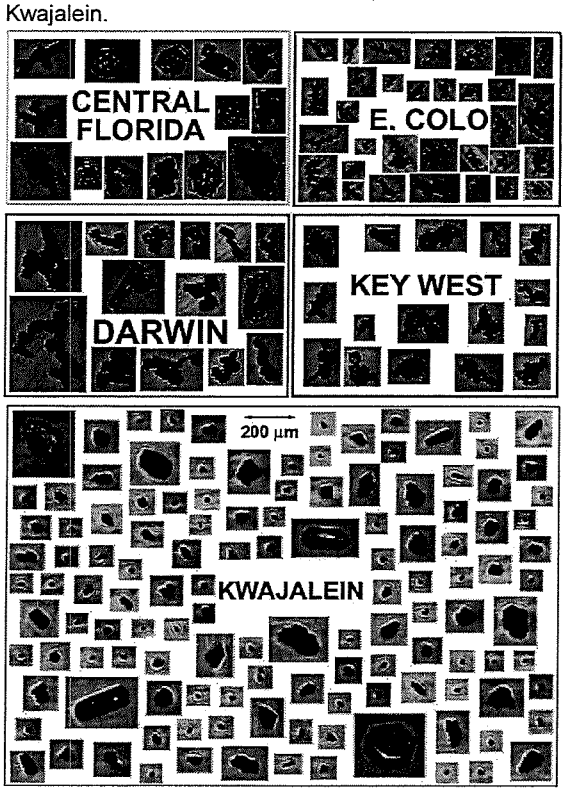

Figure 5. Examples of CPI images from (top four panels) continental anvils and (bottom panel) maritime anvil.

An intensive visual analysis of the images revealed that about 30% of the CPI images in the continental anvils are comprised of aggregates, or complex chains of particles that appear to be aggregates or heavily rimed particles. On the other hand, the large majority of the particles in tropical anvils are single crystals that have irregular, blocky shapes with only occasional hex-shaped crystals and less than 1% of the images in the Kwajalein anvil were aggregates. In addition, about 6% of the images in the continental storms appeared to be chains of small particles. These "chains" are very similar in appearance to chains of ice crystals observed in a cold chamber under a high electric field (Saunders and Wahab 1975).

Regardless of whether the anvils are continental or maritime, the particle shapes in anvils bear virtually little resemblance to the shapes of particles in cirrus and wave clouds. This can be explained through the realization that most of the ice crystals in thunderstorms are nucleated in the updrafts at temperatures > - 30 ° C. The ice particles are then carried up into the anvil. On the other hand, cirrus and wave clouds are formed in situ at temperatures that are generally < - 30 ° C, so polycrystalline structures such as rosettes are expected. The bullet rosette ice particles in cirrus and wave clouds have substantially different phase functions than the blocky ice particles found in maritime anvils and the aggregates and chains found in continental anvils (Lawson et al. 1998).

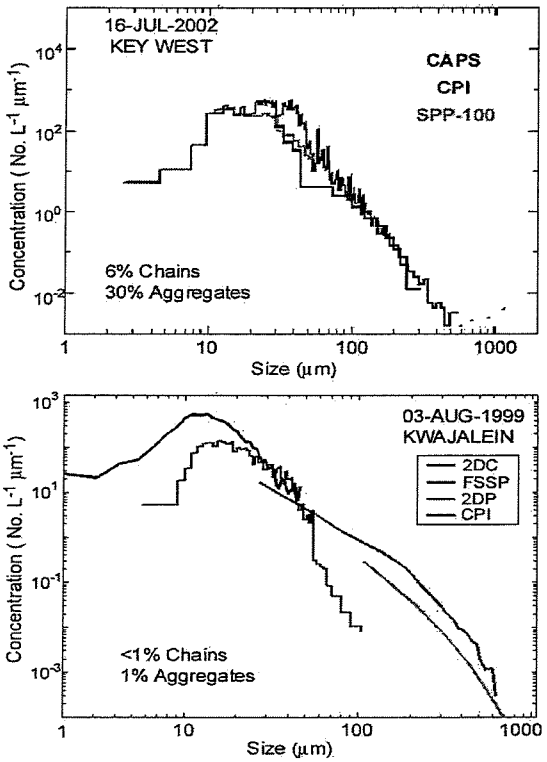

Figure 6. Example Particle Size Distributions from a continental anvil (top panel) and a maritime anvil (bottom panel).

The different phase functions will have a substantial impact on calculations of radiative transfer. For example, Mischenko et al. (1996) have shown that getting the phase function wrong can result in up to a factor of three error in optical depth.

In addition to the striking difference in particle shapes, there are significant differences in particle concentration and the optical properties of anvils compared with wave and cirrus clouds. Very high concentration of small ice, approaching 100 cm^{-3} are observed in both Continental and Maritime anvils, which supports previous observations of small ice with

concentrations approaching 200 cm^{-3} and IWC values in excess of 2 g m^{-3} (Strapp et al. 1999) in both Continental and Maritime anvils.

5. SUMMARY

In situ microphysical measurements of wave clouds, mid-latitude cirrus, continental and tropical anvils are discussed. **Table 3** lists summary properties of each cloud type based on the microphysical measurements discussed in this paper.

Cloud Type	Conc. No. cm^{-3}	IWC g m^{-3}	r_{eff} µm	β_{ext} km^{-}	Particle Type
Wave	10 to 30	0.01 to 0.2	5 to 30	1 to 10	**R, BR & SS @ T < - 50, A, CC @ T > - 37**
Mid-latitude Cirrus	0.1 to 10	0.001 to 0.05	10 to 30	0.1 to 1	R and BR for -55 < T < -35 SS, few C P
Cont. Anvil	5 to 100	0.1 to 2.0	10 to 50	10 to 100	CC, SS, CH
Mari-time. Anvil	5 to 100	0.1 to 1.0	10 to 30	10 to 100	BI, IR, SS, few C & P

Particle Type Abbreviations: R – Rosette; BR - Budding Rosette; SS - Small Spheroids; C – Column; P – Plate; IR - Small Irregular; A – Aggregate; CC - Complex Crystal (Aggregate, Rimed particle, Sideplane); CH - Chain of small particle; BI - Blocky Irregular.

Table 3. Typical values of total particle concentration (Conc.), ice water content (IWC), effective radius (r_{eff}), extinction coefficient (β_{ext}) and particle type for wave clouds, mid-latitude cirrus clouds, Continental and Maritime anvil clouds.

The data in **Table 3** are a departure from number concentrations and particle shapes generally reported in the literature for cirrus and wave clouds. For example, Heymsfield and Platt (1984) report number concentrations from about 10 to 100 L^{-1} in mid-latitude cirrus, and mostly plates and columns, while the data in **Table 3** suggests concentrations an order of magnitude higher with rosettes being predominant in both cirrus and wave clouds. In anvils, particle concentrations are much higher than commonly found in the literature, except for those reported by Strapp et al. (1999). Also, the high incidence of aggregates and particle chains in Continental compared with Maritime anvils is unique to the literature.

Acknowledgements

This research was funded under NSF Grant No. ATM-9904710 and NASA Grant No. NAS5-00244, NAG5-11553.

References

Heymsfield, A.J., and C.M.R. Platt, 1984: A parameterization of the particle size spectrum of ice clouds in terms of the ambient temperature and the ice water content. *J. Atmos. Sci.,* **32,** 799-808.

Heymsfield, A.J., and L.M. Miloshevich, 1993: Homogeneous ice nucleation and supercooled liquid water in orographic wave clouds. *J. Atmos. Sci.,* **50,** 2335-2353.

Heymsfield, A.J., S. Lewis, A. Bansemer, J. Iaquinta, L.M. Miloshevich, M. Kajikawa, C. Twohy and M.R. Poellot, 2002: A general approach for deriving the properties of cirrus and stratiform ice cloud particles. *J. Atmos. Sci.*, **59**, 3-29.

Korolev, A.V., G.A. Isaac and J. Hallett, 1999: Ice particle habits in Arctic clouds. *Geophys. Res. Letters*, **26**, *9,* 1299-1302.

Lawson, R.P., A.J. Heymsfield, S.M. Aulenbach and T.L. Jensen, 1998: Shapes, sizes and light scattering properties of ice crystals in cirrus and a persistent contrail during SUCCESS. *Geo. Res. Let.*, **25**(9), 1331-1334.

Lawson, R.P., B.A. Baker, C.G. Schmitt and T.L. Jensen, 2001: An overview of microphysical properties of Arctic clouds observed in May and July during FIRE.ACE. *J. Geophys. Res.*, **106**, 14,989-15,014.

Lawson, R. P., and B. A. Baker, 2004: An improved algorithm for in situ ice water content measurements with applications to cirrus and other ice clouds. (In this ICCP conference proceedings)

Mishchenko, M.I., W.B. Rossow, A. Macke and A.A. Lacis, 1996: Sensitivity of cirrus cloud albedo, bidirectional reflectance, and optical thickness retrieval accuracy to ice-particle shape. *J. Geophys. Res.*, **101**, D12, 16973-16985.

Pruppacher, H.R., and J.D. Klett, 1978: *Microphysics of Clouds and Precipitation,* D. Reidel Publishing Company, 707 pp.

Sassen, K., J.M. Comstock, Z. Wang and G. Mace, 2001: Cloud and aerosol research capabilities at FARS: the Facility for Atmospheric Remote Sensing. *Bull. Of Amer. Meteorol. Soc.*, **82 (6)**, 1119-1138.

Saunders and Wahab, 1975: The influence of electric fields on the aggregation of ice crystals, *J. Meteor Soc Japan*, **53**, 121-126.

Stith, J.L., J.E. Dye, A. Bansemer, A.J. Heymsfield, C.A. Grainger, W.A. Peterson and R. Cifelli, 2002: Microphysical observations of tropical clouds, *J. Appl. Meteor*, **41**, 97-117

Strapp, J.W., P. Chow, M. Maltby, A.D. Bezer, A. Korolev, I. Stromberg and J. Hallett, 1999: Cloud microphysical measurements in thunderstorm outflow regions during Allied/BAE 1997 flight trials. AIAA 00-0498.

Takano, Y. and K. N. Liou, 1995: Radiative transfer in cirrus clouds; Part III: Light scattering by irregular ice crystals. *J. Atmos. Sci.*, **52**, 818-837.

THE 2D-S (STEREO) PROBE: PRELIMINARY TESTS OF A NEW HIGH-SPEED, HIGH-RESOLUTION PARTICLE IMAGING PROBE

R. Paul Lawson, Darren O'Connor, Patrick Zmarzly and Kim Weaver

SPEC Incorporated, Boulder, CO. 80301 USA

1. INTRODUCTION

The 2D-S (stereo) probe is being built under funding from the U.S. Office of Naval Research (ONR) and has been specifically designed to overcome limitations of existing probes that image cloud particles in the size range from 30 to about 1 mm. First, we discuss briefly the limitations of current imaging probe technology and how the new probe overcomes these limitations. Errors due to electro-optical limitations that are inherent in the design of the Particle Measuring Systems (PMS) model 2D-C and Droplet Measurement Technologies (DMT) model CIP imaging probes have been well documented in the literature. Korolev et al. (1991, 1998) have shown that large counting and sizing errors occur with the PMS 2D-C particle-imaging probe when drops pass outside the optical depth of field (DOF). For example, a 100 μm particle can be oversized by nearly a factor of two, undersized by a factor of four or missed all together. Also, small (e.g., 25 μm) particles have a very small DOF (about 1 mm or 1/60th of the distance between the probe arms) and very large uncertainties in sample volume.

Additional counting and sizing errors occur due to the relatively slow time response of the older probes, resulting from the finite time response of the photodiode array and first stage amplifier. Baumgardner and Korolev (1997), and more recently, Strapp et al. (2001), show that the time response of PMS imaging probes is limited by the time constant of the photodiode array and first stage amplifier, leading to a significant reduction in sensitivity to particles with sizes < ~ 75 μm at airspeeds of 120 m s^{-1} and greater.

2. 2D-S PROBE DESCRIPTION

The new 2D-S probe is designed to minimize errors associated with DOF, sample volume uncertainties and time response. A photograph of the 2D-S probe illustrating its functional aspects is shown in **Figure 1**. Two diode laser beams cross at right angles and illuminate two linear 128-photodiode arrays. The laser beams precisely define a rectangular overlap region in the middle of the probe. The 2D-S simultaneously records two independent images of the same particle in the region where the beams overlap, and single images of all particles outside the overlap region. Since both optical paths have an associated DOF, the overlap of these DOFs defines a region within which all particles that are larger than a predetermined size are in focus. Small particles that are outside the overlap region generate a shadow depth that is too shallow to exceed the threshold level. This is important, because otherwise, high concentrations of small particles would still cause triggering due to coincidence in the regions where the laser beams do not overlap. Large particles that pass outside the laser beam overlap region produce a shadow with sufficient depth to register on only one array. Since larger particles are found in lower concentrations, the probability is much lower that two larger particles will pass simultaneously through the non-overlap regions of the laser beams. Small (< ~ 50 μm) particles are imaged only in the overlap region with a sample volume of 0.2 L s^{-1} at 120 m s^{-1}, which is about three times that of the FSSP. Larger (> ~ 50 μm) particles are imaged when they pass within the overlap region, but also imaged independently by both imaging systems with a sample volume of 15 L s^{-1} at 120 m s^{-1}, which is about 3 times the sample volume of the 2D-C.

The electro-optics used in the 2D-S are on the cutting edge of technology. In order to substantially increase the time response of the photodiode array and first stage amplifier, a new custom 128-element linear photodiode array was built by CentroVision Corporation. Instead of the 200 μm elements in photodiode arrays used in conventional imaging probes, each photodiode in the 2D-S array is 50 μm thereby reducing capacitance and increasing speed. The 128-photodiode array chip is positioned on a 12-layer printed circuit board that is specially designed to reduce lead length and increase speed (**Figure 1**). The 2D-S probe response was tested in the laboratory and compared with the response of a PMS 2D-C probe. **Figure 2** shows digital oscilloscope traces of the time response of the 2D-C and 2D-S probes to a sharp (5 ns fall time) negative-going pulse of laser light (i.e, when the laser beam is blocked corresponding to when a particle occults a photodiode). The 2D-C has a (1/ε) response time constant of 760 ns, while the 2D-S probe has a response of 41 ns, which is nearly 20 times faster than the 2D-C probe. However, the 2D-C probe tested was an older version and some newer probes may have slightly faster response times. For example, Strapp et al. (2001) report an average time constant of 600 ns and Gayet et al. (1993) tested one probe that had a time constant of 280 ns.

An additional test that demonstrates the extremely fast response time of the 2D-S was conducted by Dr. Dagnar Nagel with a unique high-speed spinning glass fiber calibration unit developed and operated by the Institut für Atmosphärenphysik (GKSS). Using the GKSS calibration unit, the 2D-S was able to completely image an 8 μm glass fiber spinning at a velocity of 233 m s^{-1}. **Figure 3** shows a photograph of the GKSS spinning fiber set up and a digital oscilloscope recording of the response of the 2D-S to the 8 μm fiber spinning at 233 m s^{-1}. In comparison, using the same

Corresponding Author's Address: Dr. R. Paul Lawson
SPEC Incorporated, 3022 Sterling Circle, Suite 200,
Boulder, CO. 80301 USA plawson@specinc.com

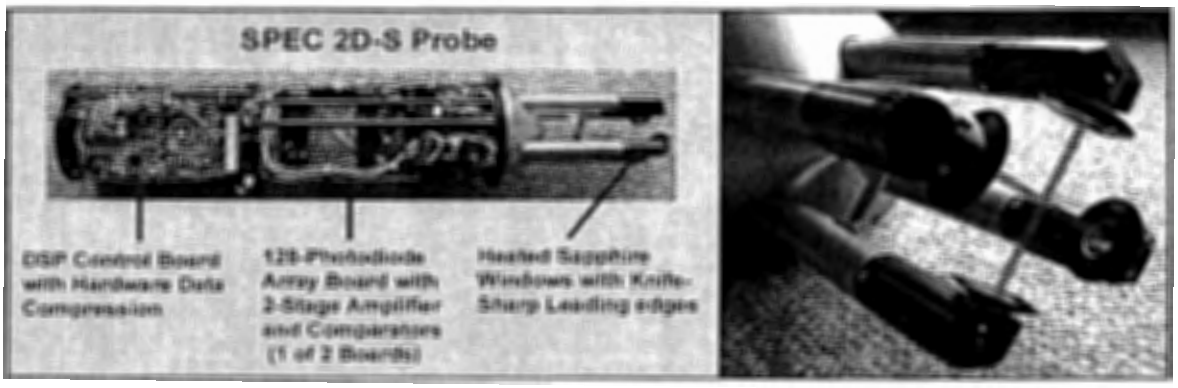

Figure 1. Photographs of the SPEC 2D-S probe. See text for description

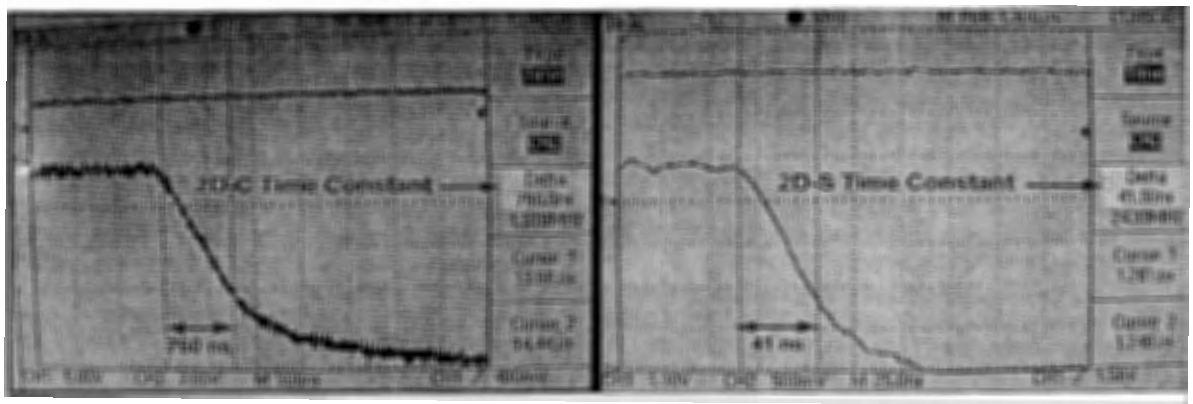

Figure 2. Digital oscilloscope traces and computation of time constants from the front-end amplifiers of (left) PMS 2D-C probe and (right) SPEC 2D-S probe. The response is generated by illuminating each photodiode array with pulsed laser light; the falling edge simulates shadowing by a particle. The $1/\varepsilon$ time constant of the 2D-S is 41 ns, nearly 20 times faster than the 760 ns time constant of the 2D-C (note that the time scale in the 2D-C plot is 500 ns per box and it is 25 ns per box on the 2D-S plot).

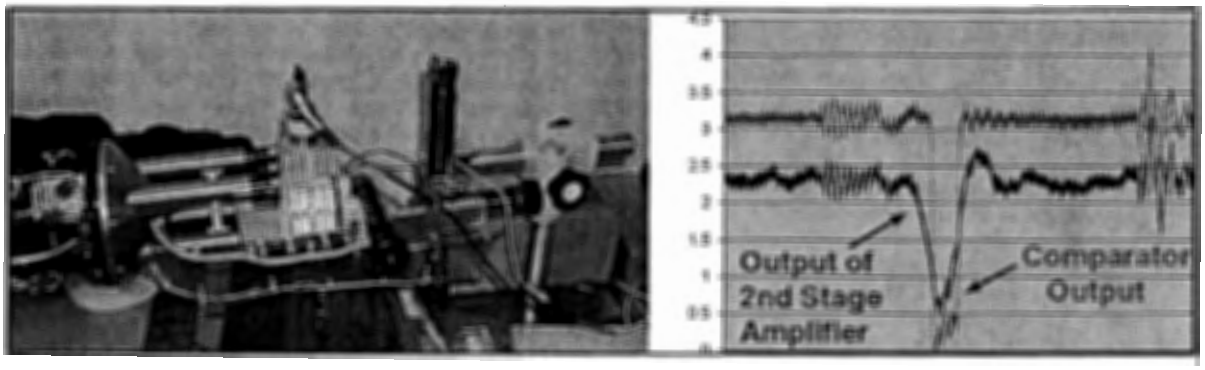

Figure 3. Photograph of GKSS spinning glass fiber calibration unit and oscilloscope-captured electronics waveforms for an 8 μm fiber spinning through the sample volume at 233 m s^{-1}.

GKSS spinning fiber set-up, the best response that the PMS 2D-C and Droplet Measurement Technology model CIP probes could achieve was to image a 75 μm glass fiber at 75 m s^{-1}.

A 12-layer printed circuit board with a 32-bit AD-2192 DSP running at 80 MHz controls very large, ball-grid array Complex Programmable Logic Devices (CPLDs) that perform hardware data compression to handle the extremely high data rates (**Figure 1**). The 2D-S probe outputs data at a maximum rate of 20 million samples per second per 128-photodiode array. This amounts to a maximum "raw" data rate of 1.28 Gbytes s^{-1} Since much of the area is "white space" between particle images, hardware data compression reduces this rate by about a factor of ten to a thousand (depending on particle size and concentration), making it possible to transfer data via a high-speed serial interface. The arrival time of each particle is recorded and the *x-y* position of each particle in the overlap region of the two laser beams is recorded.

Data from the 2D-S are recorded through standard aircraft PMS 2D-C wiring using a HDCL high-speed serial data protocol. The data stream is received by an off-the-shelf HDCL adapter card in a PCI slot of a standard PC computer. SPEC uses a small "brick" computer with a PCI slot, but presumably, when HDCL cards are made for PC laptop adapters, the data could be collected using a laptop computer. Finally, as shown in **Figure 1**, the 2D-S probe is specially designed with non-wetting, heated sapphire windows that have a knife-sharp leading edge to minimize particle bounce and breakup that is suspected to contaminate imaging probes (Jensen and Granek 2002).

3. RESULTS OF PRELIMINARY FLIGHT TESTS

. The 2D-S probe was installed on the SPEC Learjet and flown on four research flights during November-December 2003. Data were collected in cirrus clouds, an all-water wave cloud and during a very brief penetration of a mixed-phase upslope cloud along the Front Range of the Rocky Mountains in Colorado. While there are still a number of areas of 2D-S performance that need attention, these first flight tests demonstrated that the time response and image quality of the 2D-S appears to be commensurate with design parameters and laboratory tests. The areas that require additional attention are addressed in Section 4.

Figure 4 shows examples of 2D-S, CPI and 2D-C data collected at –13 ° C in a mixed-phase upslope cloud east of the Front Range of the Colorado Rocky Mountains. These are examples of in-focus 2D-S images and were selected to be representative of the best-quality images collected during a brief climb through this thin upslope cloud. The 11 μm resolution, 1.28 cm cross-section and ultra-high speed response of the 2D-S probe is unique in that it shows ice particles within a field of cloud droplets. The sample volume of the CPI occasionally shows a few droplets, but is too small to show a representative field of droplets. The 2D-C does not have sufficient resolution to see any of the cloud droplets. The 2D-S, on the other hand, shows some of the intricate detail of the dendritic and stellar ice crystals along with images of the cloud drops.

Figure 5 shows examples of small spheroidal particles and budding rosettes in a cold (- 45 ° C) cirrus cloud. The figure is configured to show the transition from a region of small particles to budding rosettes and highlights how the 2D-S probe sees these particles and the 2D-C barely responds. This is emphasized by the total particle count, where the 2D-S recorded 268,897 particles compared with 264 particles seen by the 2D-C over a 40 s time period. Also, the shapes of many of the larger (> ~ 100 μm) budding rosettes, which are confirmed by the CPI images, are discernable and can be identified as rosettes in the 2D-S imagery, whereas the 2D-C sees only 1 – 5 pixel images whose shape is indistinguishable. **Figure 6** shows another example of small ice particles and budding rosettes in cold (- 50 ° C) cirrus. In this figure, six 2D-S buffers have been aligned horizontally and give a spatial perspective of the particle distribution. Notable in this figure is the large number of small ice particles in the absence of large particles that could have shattered on the probe tips. Observations of high concentrations of small ice particles in cirrus have been reported by some investigators (Lawson et al. 2001; Gayet et al. 2002), but questioned by others as being a possible result of crystal shattering. The 2D-S probe may shed new light on this issue.

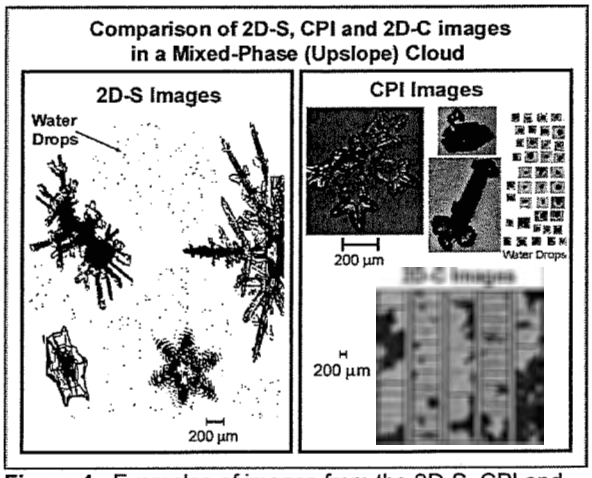

Figure 4. Examples of images from the 2D-S, CPI and 2D-C probes in a mixed-phase upslope cloud investigated by the SPEC Learjet.

4. PRELIMINARY SUMMARY AND FUTURE WORK

Results from the initial laboratory and flight tests show that the 2D-S is capable of recording particle images with <10 μm pixel resolution at jet aircraft speeds. The 2D-S probe sees copious small (< 75 μm) particles when the 2D-C sees few or none. While the

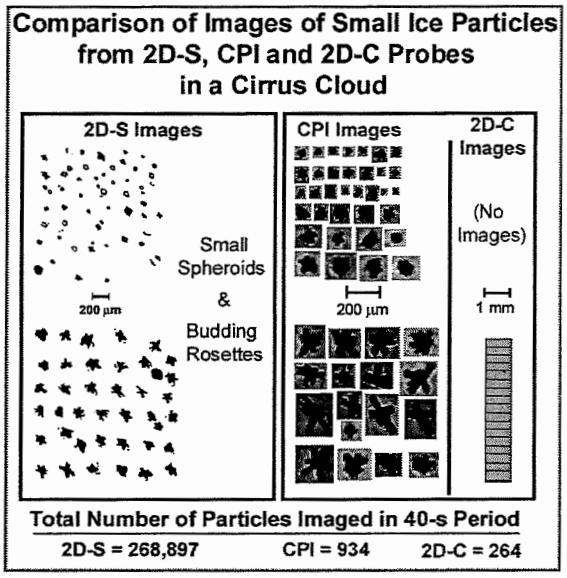

Figure 5. Examples of images from the 2D-S, CPI and 2D-C probes in a cirrus cloud (-45 ° C) investigated by the SPEC Learjet.

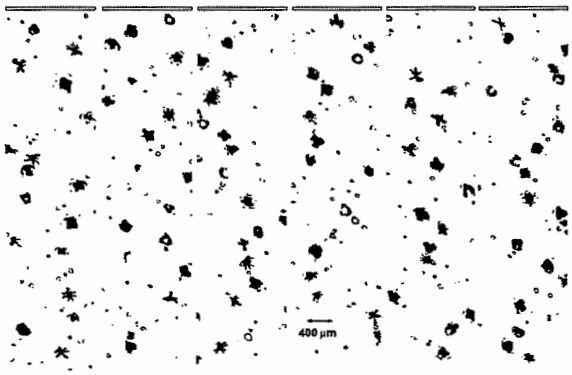

Figure 6. Example of images of budding rosettes, irregular-shaped particles and small particles recorded by the 2D-S during a test flight in a thin cirrus cloud at –50 °C.

sample volume of the CPI limits it from seeing the larger number of small particles recorded by the 2D-S, CPI images confirm the existence of the shapes of the ice particles and water drops seen by the 2D-S. The 2D-S has the unique capability of being able to see small water drops and ice particles along with high-resolution images of large ice particles within a cross-sectional area of 1.2 cm.

While the 2D-S provides a fresh new look at cloud particles, there are still instrumentation issues that need to be resolved, and also post-processing software that needs to be written in order to interpret the images. At this point in the instrument development, the 2D-S has not yet been configured to only record particles in the overlap region of the laser beams. Instead, it currently operates as two independent 2D probes. Also, it is not yet possible to synchronize the image data from both channels so that particles in the overlap region can be identified in post processing. Both of these features are currently being addressed in the laboratory and will be field-tested during the next series of flight tests scheduled the spring of 2004. There are a few pixels on each of the channels that are not functioning due to layout errors on the printed circuit boards, and this will require fabrication of new boards. We will also flight test an "auto masking" algorithm that has been developed to automatically mask any pixels that get "stuck on" due to optical contamination or electrical noise.

Acknowledgements

This work has been funded by the US NAVY Office for Naval Research Center for Interdisciplinary Remotely Piloted Aircraft Studies (CIRPAS) SBIR Contract No. N00014-02-C-0317.

References

Baumgardner, D. and A. Korolev, 1997: Airspeed corrections for optical array probe sample volumes. *J. Atmos. Oceanic Technol.*, **14,** 1224-1229.

Gayet J-F, P. R. Brown and F. Albers: 1993: A comparison on in-cloud measurements obtained with six PMS 2D-C probes. *J. Atmos. Ocean. Tech.*, **10**, 180-194.Gayet, J.-F., and R.G. Soulage, 1992: Observation of high ice particle concentrations in convective cells and cloud glaciation evolution. *Quart. J. Roy. Meteorol. Soc.*, **118**, 177-190.

Gayet, J.F., F. Auriol, A. Minikin, J. Ström, M. Seifert, R. Krejci, A. Petzold, G. Febvre, and U. Schumann, 2002: Quantitative measurement of the microphysical and optical properties of cirrus clouds with four different in situ probes: Evidence of small ice crystals., Accepted for publication in *Geophys. Res. Lettrs.*

Jensen, J.B. and H. Granek, 2002: Optoelectronic simulation of the PMS 260X optical array probe and application to drizzle in a marine stratocumulus. *J. Atmos. and Oceanic Tech.*, **19**, 568-585.

Korolev, A. V., S. V. Kuznetsov, Y. E. Makarov, and V. S. Novikov, 1991: Evaluation of measurements of particle size and sample area from optical array probes. *J. Atmos. Oceanic Technol.*, **8,** 514-522.

Korolev, A.V., J.W. Strapp and G.A. Isaac, 1998: Evaluation of the Accuracy of PMS Optical Array Probes. *J. Atmos. Oceanic Technol.*, **15**, 708-720.

Lawson, R.P., B.A. Baker, C.G. Schmitt and T.L. Jensen, 2001: An overview of microphysical properties of Arctic clouds observed in May and July during FIRE.ACE. *J. Geophys. Res.*, **106**, 14,989-15,014.

Strapp, J. Walter, Frank Albers, Andreas Reuter, A. V. Korolev, Uwe Maixner, E. Rashke and Z. Vukovic, 2001: Laboratory Measurements of the Response of a PMS OAP-2DC. *J. Atmos. and Oceanic Technol.*, **18**, 7, 115

SIMULATION OF PRECIPITATION MECHANISM WITHIN TYPICAL COLD-FRONTAL CLOUD SYSTEM

Hongyu Li[1] and Yanchao Hong[2]

[1]Beijing Weather Modification Office, Beijing, 100089, China
[2]Institute of Atmospheric Physics, Chinese Academy of Sciences, Beijing, 100029, China

1. INTRODUCTION

Microphysical structures and precipitation mechanisms vary distinctly within parts of cold-frontal cloud system (Hobbs et al. 1980) as well as processes and chains through which water vapor transforms into surface precipitation. As a result, there should be different methods of seeding operation for precipitation enhancement. Actually, seeding catalyst according to the 'cloud seeding temperature windows' (Grant and Elliott 1974) or other oversimplified criteria, is only adopted in practice. There leads to much blindness owning to less considering of the diversity of precipitation mechanisms within cloud system. In this article, detailed microphysical processes of each kind of particle's formation and growth and precipitation mechanisms within different parts of the same cloud system are simulated by using a one-dimensional cloud model (Hu 1983, Hong 1996). Both water balance and water budget are analyzed (Braham and Jr. 1952, Foote and Fankhauser 1973, Sui et al. 1994) in the basic research on water resources exploitation and utilization. These help to provide some scientific guidance to practical seeding operation.

2. COLD-FRONT CASE

The low-trough and cold-frontal cloud system which passed through Chinese Henan province during April 4-6 2002 is performed. This kind of cloud system together with stable precipitation occurs frequently in the former area. Because of situ observation data limited in temporal and spatial, we simulated the cloud system earlier than 20pm on April 4. Clouds over sounding stations Zhengzhou and Yinchuan which locate in different parts of the same cloud system are simulated. At the time, Yinchuan station lies behind the frontal cloud system and Zhengzhou locates ahead with about 800km away from the former one. Satellite cloud images show that the frontal cloud system is about 2000km long and spans near 4 or 5 longitude degrees wide. Its main body lies between the two stations.

Corresponding author's address: Hongyu Li, Beijing Weather Modification Office, No.44, Zizhuyuan Road, Haidian District, China; E-Mail: 2000hongyu@sina.com.

3. PRECIPITATION MECHANISM

3.1 Post-frontal clouds

Within post-frontal clouds, ice-phase processes are evident, especially during the early period of clouds evolution. Mass of ice crystals and snows are yielded. Cloud water maintains a very short time. Rain water which forms in the low level and centers in warmer areas increases with the increased snow water and almost all is converted from melted ice-phase particles. After 3 hours, cloud water disappears. An abundance of Ice crystals and snows are produced, with more of them after 5 hours simulation.

Ice crystal chiefly forms through nucleation process and grows through vapor deposition. Snow forms mainly from auto-conversion of ice crystals and grows rapidly through vapor deposition. Snow mass increases fast following the clouds evolution. Aggregation process accelerates its growth. Mostly graupel forms through nucleation of raindrops and conversion of frozen supercooled raindrops, and grows near zero centigrade through collecting snows that dropped from the high level.

3.2 Pre-frontal clouds

Warm-cloud processes within pre-frontal clouds are dominant during its early evolution period. Subsequently, thanks to more and more ice crystals and snows produced, ice-phase processes enhance gradually and become to play an important role in precipitation formation and growth. Cloud water increases rapidly after its being produced. Rain water comes from the conversion of cloud water, on the other hand, it continues to grow through collecting cloud water. Following with the formation and increasing mass of ice-phase particles, amount of rain water enlarges sharply. That also indicates the important role of cold-cloud processes that play in rain water formation. After 5 hours simulation, there produces a large amount of ice crystals in the high level with snows and a small quantity of graupels below. In the low level, there exist much

raindrops, and the maximum level of its amount descends a little than that simulated for 3 hours.

Within pre-frontal clouds there are much multiplicity ice crystals, and they still grow through dominant vapor deposition process. It also grows through riming process. Snow mainly forms from auto-conversion of ice crystals and grows through vapor deposition and aggregation processes. Its riming process is more important than that within post-frontal clouds. Graupel forms chiefly from auto-conversion of snows. Different from that within post-frontal clouds, It grows through riming process as well as aggregation.

4. WATER BUDGET

Amount of cloud water within post-frontal clouds (see Fig.1a) is produced the minimum and much less than that of rain water. Among ice-phase particles, snow is produced the maximum. All these suggest it is ice-phase particles, especially snow, that convert into rain water. Water budget also shows a very low water vapor condensation rate and a high deposition rate. They are about 1.5 percent and 31.1 percent respectively. Among all those condensed and deposited water content, about 39.2 percent is evaporated and 14.4 percent is sublimated. Precipitation efficiency is near 20.8 percent and 25.8 percent of the amount still remains.

Comparing with post-frontal clouds, amount of cloud water within pre-frontal clouds is the most and even more than the total amount of all ice-phase particles together. This suggests cloud water conversion is more important to rain water production. Within pre-frontal clouds, about 32.1 percent of water vapor is condensed with little water vapor deposited. Most of the condensed and deposited water is exhausted through evaporation. The suspending amount is about 13.5 percent, with a less than 10.0 percent precipitation efficiency left.

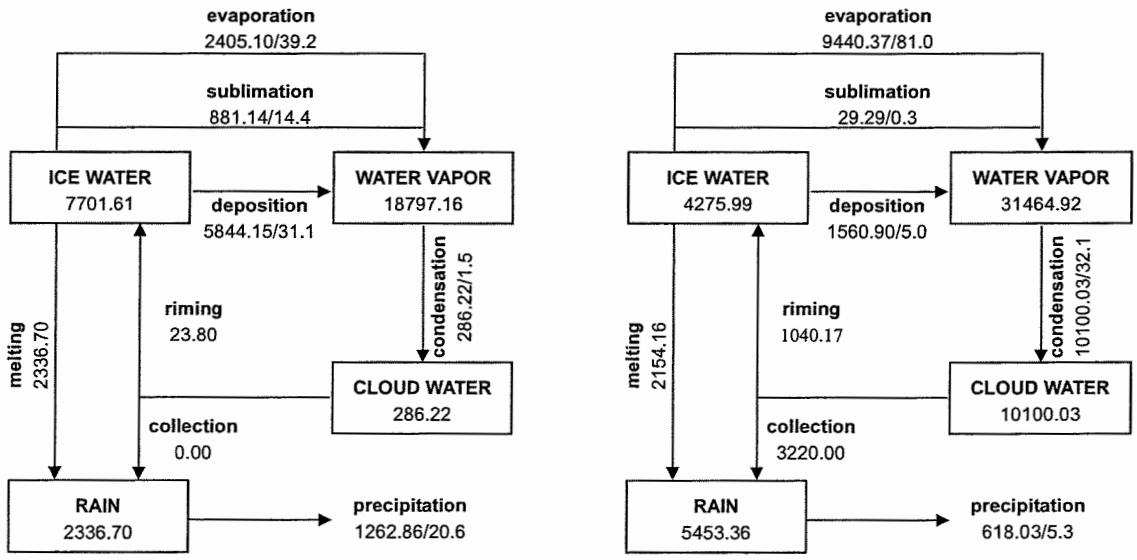

(a) post-frontal clouds **(b)** pre-frontal clouds

FIG.1. Water budget (g/m^2) and some conversion rates (percent, after symbol /) within (a) post-frontal clouds and (b) pre-frontal clouds.

5. CONCLUSION

Simulation of precipitation mechanisms within post-frontal and pre-frontal clouds shows that microphysical structures and precipitation mechanisms vary drasticly with different parts of the cold-front, as well as the processes and chains of water vapor transforming into precipitation.

Most precipitation within post-frontal clouds is yielded through ice-phase processes only, especially through melted snows. Water resources exploitation and utilization is chiefly from water vapor. So, try to augment precipitation by increasing the amount of ice-phase particles like snows is advisable in practical seeding operation. Precipitation enhancement within post-frontal clouds is based mainly on the concept of cold-cloud seeding.

In contrast to post-fontal clouds, precipitation

within pre-frontal clouds is generated through warm-cloud processes and ice-phase processes together. Water resources exploitation and utilization come from liquid water as well as water vapor, and moreover, liquid water can be found throughout the clouds. So precipitation enhancement within pre-frontal clouds can be operated both by influence warm-cloud processes and cold-cloud processes. Different seeding techniques are provided.

REFERRENCE

Braham R. R., and Jr., 1952: The water and energy budgets of the thunderstorm and their relation to thunderstorm development. J.Meteor., **9**, 227–242.

Changon S. A., and Czys R. R., Scott R. W., and Westcott N. E., 1991: Illinois Precipitation Research: A focus on Cloud and Precipitation Modification. Bull.Amer.Meteor.Soc., **72**, 587–604.

Foote G. B., and Fankhauser J. C., 1973: Air flow and moiseture budget beneath a northeast Colorado hailstorm. J.Appl.Meteor., **12**, 1330–1353.

Grant L. O., and Elliott R. E., 1974: The Cloud Seeding Temperature Windows. J.Appl.Meteor., **13**, 355–363.

Herzegh P. H., and Hobbs P. V., 1980: The Mesoscale and Microscale Structure and Organization of Clouds and Precipitation in Midlatitude Cyclones. II: Warm-Frontal Clouds. J.Atmos.Sci., **37**, 597–611.

Hobbs P. V., Matejka T. J., Herzegh P. H., et al., 1980: The Mesoscale and Microscale Structure and Organization of Clouds and Precipitation in Midlatitude Cyclones. I: A case Study of a Cold Front. J.Atmos.Sci., **37**, 568–596.

Hong Y. C., 1996: The numerical simulation study of convective-stratiform mixed cloud. Part I: The model and parameterization of microphysical processes. Acta Meteorological Sinica, **54**(5), 544–557.

Houghton H. G., 1968: On Precipitation Mechanisms and their Artificial Modification. J.Appl.Meteor., **7**, 851–859.

Hu Z. J., Qin Y., and Wang Y. B., 1983: Numerical simulation of cold layer clouds. Acta Meteorological Sinica, **41**(2), 194–203.

Li D. S., et al., 2002: The Current Status and Prospect of Weather Modification. China Meteorological Press.

Orville H. D., 1996: A review of Cloud Modeling in Weather Modification. Bull.Amer.Meteor.Soc., **77**, 1535–1555.

Sui C. H., Lau K. M., Tao W. K., and Simpson J., 1994: The Tropical Water and Energy Cycles in a Cumulus Ensemble Model. Part I: Equilibrium Climate. J.Atmos.Sci., **51**, 711–728.

Takahashi T., and Kuhara K., 1993: Precipitation Mechanisms of Cumulonimbus Clouds at Pohnpei, Micronesia. J.Meteor.Soc.Japan, **71**, 21–31.

NUMERICAL SIMULATION AND SEEDING EXPERIMENTS OF TWO SEVERE CONVECTION PROCESSES IN BEIJING AREA

Shuyan Li[1] and Zhuang Xie[2]

[1]Beijing Weather Modification Office, Beijing, 100089, China
[2]Beijing Meteorological Bureau,100089,China

1. Introduction:

Hail shooting is one of major natural disaster in Beijing and causes large loss of 4～5 billion RMB Yuan every year. Meanwhile it was drought in successive years in beijing, and reservoir had serious water shortage. So how to artificially alleviate hail disaster and enhance convective cloud precipitation is more and more important task in recent years. Our purpose in this paper is to provide theoretical basis for hail suppression and rain enhancement operation, and discuss hail cloud development mechanism. We take severe convective processes on June 13 and June 20,2001 in Beijing as example to analyze physical mechanism of hail cloud and seeding experiments. The model we used is 3-D hail cloud numerical model with non-hydrostatic and full elastic equations, containing more detailed microphysical processes with double-parameter spectrum in the particle-size distribution and bulk-water parameterized microphysics.

2. Numerical simulation of hail cloud

Hail cloud occurring in Beijing on June 13,2001 is simulated by the 3-D hail cloud numerical model to analyze physical mechanism of hail formation.

Shuyan Li: No.44, zizhuyuan road, haidian district Beijing weather modification office., Beijing, 100089, china. e-mail: lw1024@263.net

The surface temperature was 31 ℃ and dew-point temperature 16.8 ℃(sea level elevation is 663m) , and 0℃ layer located in 3km level。The atmospheric stratification was very instable , temperature lapse rate under 10 km level changed from -0.6℃/100m to -1.0℃/100m. There was an inversion layer over 10km level. The atmospheric humidity was much low, the relative humidity in the lower layer under 2km level was only 28～50% ,the specific humidity 7-12g/kg.The wind turned clockwise from northeaster below 2km level and then changed to northwest at 7.5km level. The wind direction over 11.5km level was almost west .On that day the convective cloud developed violently and initial radar echoes and the echo cores in the developing stage of the cloud was situated in about 6-7km height. We describe the physical process of cloud cluster using upper-air detection data at 08(Beijing time) on June 13,2001 in Beijing region as initial field.

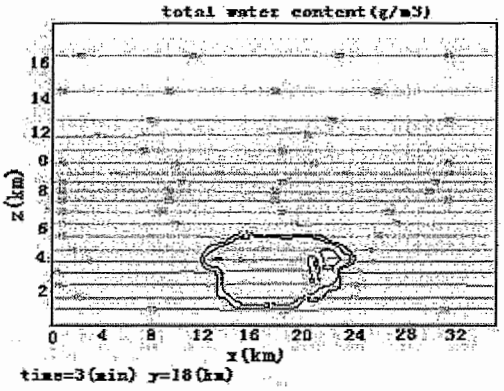

Fig.1 total water content at 3rd minute (unit: g/kg)

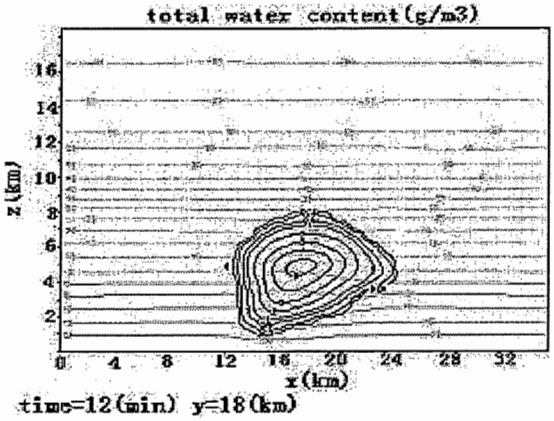

Fig.2 total water content at 12th minute(unit: g/kg)

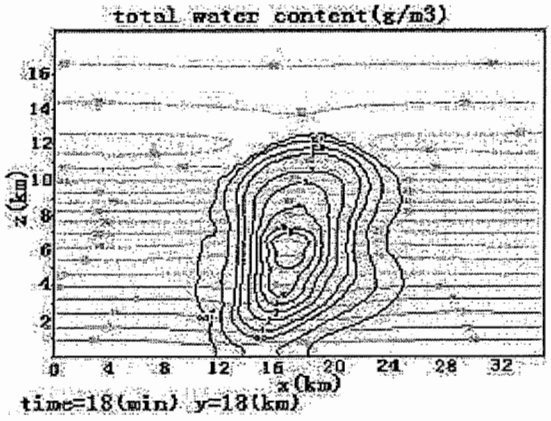

Fig.3 total water content at 18th minute(unit: g/kg)

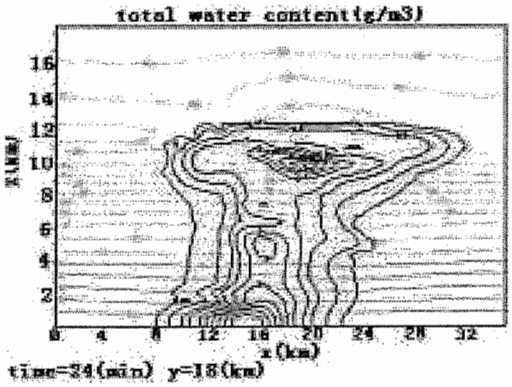

Fig.4 total water content at 24th minute (unit: g/kg)

From figure.1 to figure.4 we can see that cloud water appears over 0°C level, the centre of water content rised from 3km level to 4.5km level at 12th minutes. Then the centre started to rise more quickly, at 18th minute centre of water content had reached 6km and hail began to fall on the ground. At 28th minute, there formed two centres of water content, one centre of water content rised to 10km level, another centre of water content reached the ground and hail shooting intensity maximum and the hail cloud began to weaken after this time.

3. Micro-processes of particle formation in hail cloud

The cores of most hail stones(93%) are frozen drops. Hail also grow by accretion super-cooling water. But types of hail embryo are different in various area. For hail cloud on June 13, 2001, hail embryos of 93% are frozen drops. We take frozen drops as example to illustrate micro-processes. Figure 5 indicate how frozen drops formed. Super-cooling raindrops, due to contacting with ice crystal and snow , freeze into frozen drop (CLrif). In addition, frozen drop may also be formed by raindrop nucleation (Nurf). Frozen drops grow by collecting super-cooling water, first rain water (CLrf) and later cloud water(CLcf). But most of the frozen drops come from Super-cooling raindrops, according to figure 5.

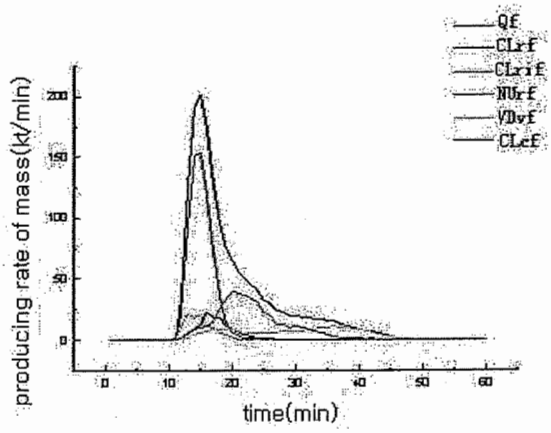

Fig. 5 micro-process of frozen drops

Furthermore, Ice crystals are generated by water vapor nucleation and multiplication, and grew by sublimation. ice crystal and snow are converted to

Graupel and graupel growth mainly depends on accreting super-cooling water.

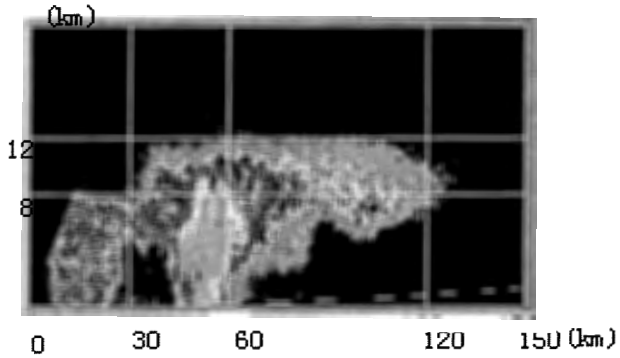

Fig.6 radar echo image during the most intense hail shooting on June 20, 2001.

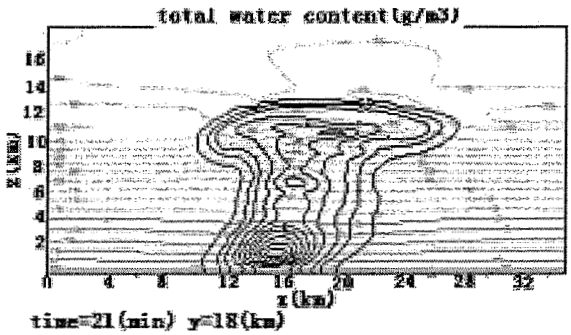

Fig.7 simulated total water content during the most intense hail shooting on June 20, 2001 (g/kg)

We also simulate the hailstorm process on June 20,2001. Figure 6 indicated that centre of water content reached the ground while hail shooting intensity reach maximum. The simulated total water content (figure 7) also indicated the same result. Contrasting figure 6 with figure 7 shows 3-D hail cloud numerical model can simulate convective process well.

4. Seeding experiment:

We also used model to simulate Seeding experiment on June 20,2001. Figure 8 shows change of rain intensity before and after seeding. The rain intensity at first 18 minutes basically remained unchanged, and then reached the first peak at 23min (the rain intensity of non-seeding cloud was 154.380mm/hr and the rain intensity of seeding cloud

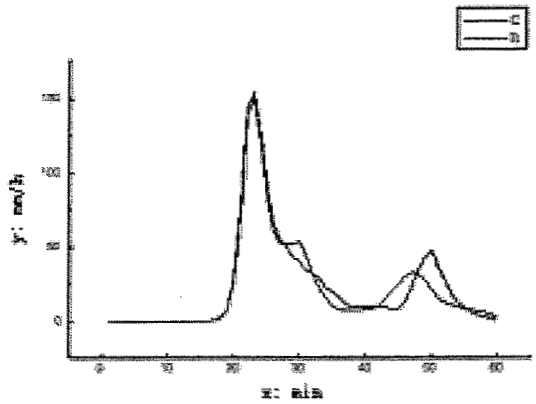

Fig.8 variation of rain intensity with time. B: rain intensity after seeding; C: rain intensity before seeding

was 149.504mm/hr). The rain intensity of seeding cloud strengthen a little at 28minute, and reached a small peak at 30minute, then descend, until 40minute that it began to ascend again but the gradient was small, reached another peak (32.835mm/hr) at 47minute, until 60minute it still remained rain intensity of 3.637mm/hr. For non-seeding cloud, the rain intensity remained weakened trend from 23min to 45min, began to strengthen until 46min, the second peak of rain intensity (47.683mm/hr) occurred at 50min, at 60min rain intensity had fell to 1.287mm/hr.

Seeding experiments for two hailstorm process were carried out at different seeding time, on different seeding height and using different seeding AgI amount. Mechanism of hail suppression is studied by seeding experiment for beijing hail cloud. Table 1 showed that at 9min of hail cloud primary development stage, the seeding material is released uniformly and immediately in the seeding zone, which center is situated at the core of updraft . 200g of seeding AgI amount remain unchanged, seeding heights are from 2.5km、 3km、3.5km、4km、4.5km and 5km with 0.5km interval.

Table 1 Precipitation and hail when seeding AgI in different height

Height (km)	2.5	3	3.5	4	4.5	5
Hail stone(kt)	398.14	390.28	369.45	359.5	358.93	357.65
Rain(kt)	3135.58	3108.74	3174.84	3156.54	3179.43	3142.59

Table 3 indicated that the hail decreased 30.78kt from 3km to 4km, but from 4km to 5km the hail decreased only 1.85kt, the descending velocity became very slow. We can get the reason about why seeding efficiency descend from 4km to 5km by studing updraft velocity, the center of maximal updraft located between 3km and 4km at 9min(-5～0℃), so the seeding efficiency is the highest when we seed cloud on 3.5km height level at 9min. The reason why we select the maximum of height in the seeding test was 5km is: although in practical hail suppression operation, the maximal value of height that seeding artillery can reach theoretically is 4.7km, but the height can't be reached in reality because of effect of wind and air resistance.

Conclusion:

1 The chain of ice phase processes can be described as follows: ice crystal-super-cooling water-hail embryo-hail. Hailstones are formed by conversion from graupels and frozen drops and they all become hail embryos. For beijing hailstorm, most of hail embryos are frozen drops.

2 We carried out seeding experiments at different time, on different height and using different seeding AgI amount, lots of experiment results show that seeding the hail cloud as early as possible is proposed. More catalyst can be saved at suitable time and suitable position. AgI should be delivered into area of the maximun updraft or negative temperature level. For Beijing hail cloud, the best efficiency of hail suppression can be obtained by seeding at the first 3～7min before intense radar hail echo of 35dbz occurred. Suitable amount of catalyst is important for both precipitation enhancement and anti-hail, too much or too little catalyst will cause low efficiency and sometimes even get negative effect.

3 The model can't simulate birth and death of multi-cells, so there exists quite difference between simulated value (maximal precipitation and cumulate precipitation) and real measurement value. Furthermore as terrain hadn't been taken into account in the model, so simulated result was affected to some extent, further work shold be done to the model.

Acknowledgement:
We thank doctor wang hong for her suggestions and help in research.

reference

Kong fanyou, Huang meiyuan, and Xu huaying: Three-dimension numerical simulation of ice phrase microphisics in cumulus clouds, part: Model establishment and ice phrase parameterization. Scientia Atmospheric Sinica, 14(4), 441-453, 1990.

Hong yanchao: A 3-D hail cloud numerical seeding model. Acta Meteorological Sinita, 56(6), 641-651, 1998.

NUCLEATION IN SYNOPTICALLY FORCED CIRROSTRATUS

Ruei-Fong Lin[1], David Starr[2], Jens Reichardt[3], and Paul J. DeMott[4]

[1]Goddard Earth Sciences and Technology Center, University of Maryland, Baltimore County, Baltimore, MD, USA
[2]Laboratory for Atmospheres, NASA/GSFC, Greenbelt, MD, USA
[3]DWD-Meteorological Observatory Lindenberg, Tauche, Germany
[4]Dept. of Atmospheric Sciences, Colorado State University, Fort Collins, CO, USA

1. INTRODUCTION

For synoptically forced cold cirrus, in which the vertical wind speed is less than 0.1 m s^{-1} and temperature is less than -40°C, homogeneous freezing (HF) of aqueous solution particles, and heterogeneous nucleation (HET) via deposition nucleation and/or immersion and contact freezing of aqueous solution particles can be activated. Unless an air parcel is devoid of ice nuclei (IN), it is expected that, as the air parcel ascends and cools, heterogeneous nucleation will be activated first. Depending on the magnitude and duration of forcing, and the number concentration of the activated IN, HF may be partially or completely suppressed.

The detailed formulation for these nucleation modes differs greatly and the heterogeneous nucleation modes are not well understood. From the governing equations to predict the amount of ice particles being generated, the particle number concentration is determined by the activation RH_i and ice particle formation rate $\dot{N}_i$, given forcing and temperature. Testing a fair range of these two controlling factors provides useful insight into the system.

In this study, HF of sulfuric acid haze particles is explicitly formulated by adopting the effective freezing temperature scheme (Sassen and Dodd, 1988; Heymsfield and Miloshevich, 1993). For the formulation of heterogeneous nucleation, we adopted the exponential form

$$N_{IN} = N_0 \exp[\beta(S_i - S_i^*)],$$

where N_{IN} indicates the number concentration of activated IN; N_0 is a small number; S_i and S_i^* are the ice supersaturation ratio and the activation ice supersaturation, respectively; and β is the slope factor for $\log \dot{N}_i$. Parameters β and S_i^* may be functions of IN and aerosol species, temperature, and updraft speed. This formula is the general form of the parameterization scheme for deposition/condensation freezing nucleation of Meyers et al. (1992), hereafter referred to as M92. Parcel simulations of immersion freezing in sulfuric acid haze particles by DeMott indicate that the exponential form may be used to approximate the exact formulation (HF and immersion freezing results shown in Fig. 1), as evidenced by the linear relationship between $\log \dot{N}_i$ and relative humidity with respect to ice (RH_i).

2. 1D CIRRUS MODEL

Ice crystals/H_2SO_4 aerosol particles are grouped into bins according to their ice mass/solute mass to simulate the evolution of particle size distributions (PSD). For a given bin k in any grid box, the mean H_2O mass and number concentration are both recorded. It is assumed that the PSD inside a bin is a piecewise linear function (Chen and Lamb, 1994).

Table 1 shows the values of β and S_i^* used here. Their values derived in M92 are for temperatures between -7°C and -20°C and for S_i^* between 0.02 and 0.25. Here, we test these values although the temperature is colder and humidity is higher in the case studied here. Test M92 is expected to represent the most favorable condition for heterogeneous nucleation. Reasonable values of β and S_i^* may vary by various causes, but should be confined between M92 and HF values (Table 1). The tested values of β are close to DeMott's parcel study of immersion freezing nucleation; about 47 and 60 for the -40°C and -60°C cases, respectively (Fig. 1).

Table 1. Simulation identifiers.

Nucleation Mode	Run ID	$S_i^* \times 100$	β
Heterogeneous nucleation (HET)	M92	~5	~13
	S20β40	20	40
	S30β40	30	40
	S20β60	20	60
	S30β60	30	60
HF	HF	~59.5[a]	~112[a]

[a]For a quick comparison only. These values are derived for the parcel released at z_0=8.822 km.

Corresponding author's address: Ruei-Fong Lin, NASA/GSFC, Mailstop 912, Greenbelt, 20771, USA; E-Mail: lin@agnes.gsgc.nasa.gov

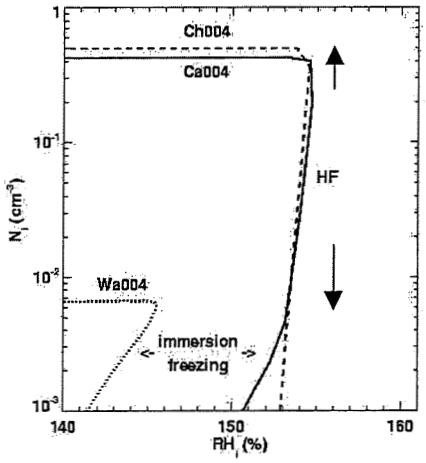

Figure 1. Ice particle number concentration N_i in an ascending parcel as a function of the parcel RH_i. Curves Wa004 and Ca004 (both the HF and immersion freezing modes are included) are parcel simulation by DeMott's model with starting temperature -40°C and -60°C, respectively. For reference, the result of Ch004 (HF only) is also plotted. To learn more about the simulations, see Lin et al. (2002).

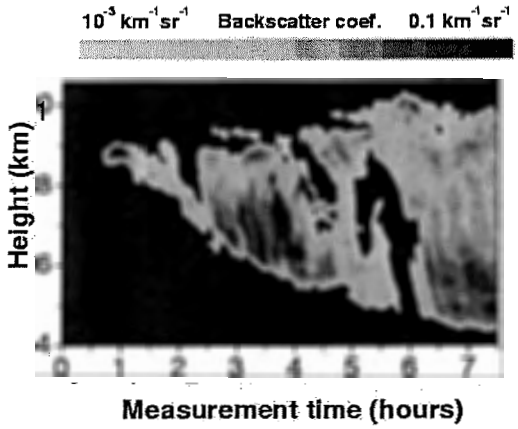

Figure 2. Height versus time display of backscatter coefficient generated from consecutive lidar profiles of the cirrus cloud measured on 16 January 1997 over northern Sweden.

3. CIRRUS EPISODE MEASURED on 16 JANUARY 1997

For our nucleation studies, we simulate the cirrostratus event that was measured with the GKSS Raman lidar (Reichardt et al., 1996) above the research facility Esrange (67.9°N, 21.1°E) near Kiruna, Sweden, on 16 January 1997. The lidar observations are shown in Fig. 2. The cloud started to develop at about 2010 UTC between 8.6-9.0 km. It deepened significantly during the first 3 hours, after which the cloud continued to deepen, but with a slower rate. As time continued, its structure became more complicated. In general, it appeared to be more cellular near the cloud top, possibly corresponding to a generation zone, followed by elongated patterns (fall streaks) that sometimes extended from mid-cloud to cloud base. We assume that the overall cloud top and base heights, as well as the 30-min averaged cloud backscatter coefficient of selected time periods, are in response to the synoptic scale forcing. The aforementioned parameters are used to constrain the values of uncertain parameters (upper tropospheric humidity and vertical wind W). From a series of simulations, it is found that a forcing of $W = 0.05$ m s^{-1} best reproduces the observations.

3. HF SCENARIO

Vertical grid spacings from 100 m to 1 m are tested. Differences in ice water path (IWP) and the column integrated N_i (N_iP) are significant (Fig. 3). By comparing the number of frozen aerosol particle following a given air parcel extracted from the 1D simulation with an independent parcel model simulation, it is confirmed that the 1-m resolution simulation mostly accurately predicts N_i.

The evolution of ice water content (IWC) for the 1-m simulation is plotted in Figure. 4. Two distinct regions of cloud field exist, the fall streak (high IWC) and the cloud-top region (low IWC). The fall streak is generated by ice crystal nucleation that responds to the initially prescribed moist layer of about 100 to 200 m in depth. The trailing region is formed by a continuous cloud-top nucleation zone (about 10 m in depth), which was not captured by previously published numerical studies because of their coarse model resolution. Here, parcels above the initially moist layer progressively achieve nucleation threshold such that the cloud top moves upward more rapidly than W. The undulations in IWP and N_iP of the simulations, in which grid spacing is 100 or 20 m (Fig. 3), are caused by numerical nucleation pulses. These pulses arise because (1) the coarse resolution setup is not able to resolve the cloud-top nucleation zone, and (2) the vertical advection of newly activated ice crystals is not adequately resolved.

The fall streak features greater IWC, ice crystal number concentrations and lower ice supersaturation, while the opposite occurs the cloud-top region. These drastic differences are caused by their differences in the nucleation zone depth (several hundred meters vs. 10 m) indicating that the depth of nucleation zone is an important parameter in predicting cloud properties.

The depth of the nucleation zone in cirrostratus, responding to lifting of a moist layer or its subsequent cloud-top nucleation, is likely to be much shallower

than the upper tropospheric vertical grid spacing of general circulation models (GCMs). Thus, explicit

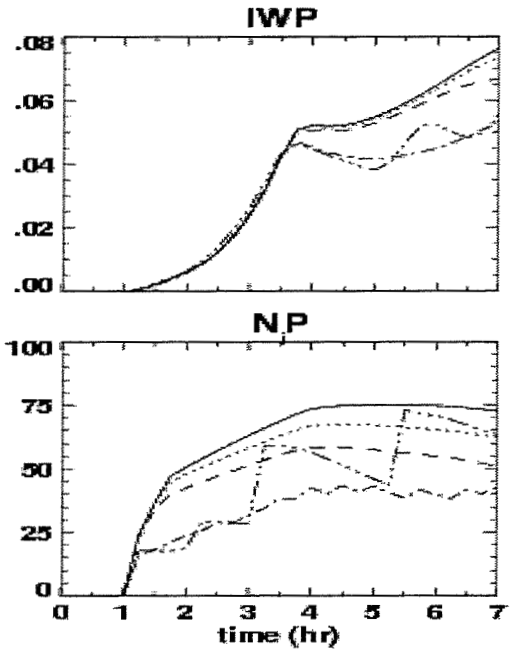

Figure 3. Effects of vertical grid spacing on IWP (kg m^{-2}) and N_iP (10^6 m^{-2}). Solid: 1 m; dotted: 2 m; dashed: 4 m; short-dashed: 20 m; dash-dotted: 100 m.

parametric account of the depth of nucleation zone is needed in a parameterization of ice crystal generation.

4. HETEROGENEOUS NUCLEATION SCENARIO

All simulations including heterogeneous nucleation presented here used a grid spacing of 4 m. Homogeneous nucleation is included, but does not become active because the peak ice supersaturation is too low. Results for IWP and N_iP are shown in Fig. 5.

A prominent feature of the clouds in the HET simulations is the periodic fall streaks, indicated by periods of high IWC and N_i, in comparison with only one dominant fall streak in the HF simulation. Layering of the consecutive fall streaks takes place. In addition to the nucleation responding to the initial moist layer, two other nucleation zones emerge: the continuous cloud-top nucleation region and intermittent mid-cloud nucleation regions.

RH_i in the HET simulations does not decrease significantly (remains highly ice supersaturated) below the cloud-top nucleation zone, which implies that nucleated particles are unable to significantly deplete

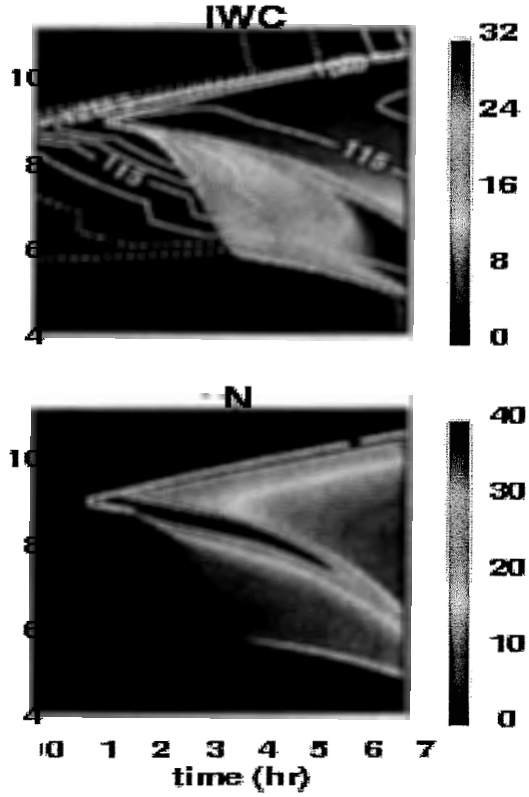

Figure 4. Ice water content (IWC in mg m^{-3}) and N_i ($liter^{-1}$) for the HF scenario with model vertical grid spacing of 1 m. The y coordinate is z in km. The white curves in the upper panel indicate RH_i (dotted: 60 and 80%, solid: 100, 115, 125 135%), while the white curves in the lower panel outlines the nucleation zones.

the excess water vapor as they grow and fall out of the nucleation zone. Mid-cloud nucleation, which is activated when relative humidity is on the rise and IN are available, is a mechanism to increase the cloud efficiency to uptake excess water vapor and to broaden the PSDs. The nucleation pulse mechanism, a cycle of nucleation, growth and decreasing RH_i, particle fallout, increasing RH_i, and new nucleation (e.g., Khvorostyanov et al., 2001), is adequate to explain the formation of the mid-cloud nucleation zones.

For the HET simulations, the cumulative cloud-top contribution to N_iP is less than 50% of the total N_iP (Table 2), reflecting the importance of mid-cloud nucleation. Ignoring the mid-cloud nucleation will result in an underestimate of cloud ice and an overestimate of mid-cloud excess vapor. Furthermore, compared to HF, all of these HET simulations are highly ice supersaturated inside the cloud except near cloud base.

A combination of large S_i^* and extremely large β (HF scenario) results in the complete disappearance of the mid-cloud nucleation zone. In contrast, small S_i^* and small β (Test M92) yields greater contribution by mid-cloud nucleation. The contribution of the mid-cloud nucleation is more sensitive to S_i^* (than β) for the ranges studied here (Table 2).

Table 2. The relative contribution of the cloud-top nucleation to the total particle generation between simulation time 1 to 6 hr.

Run ID	cloud-top/all
M92	38.6%
S20β60	35.4%
S20β40	38.3%
S30β60	45.3%
S30β40	46.0%

5. SUMMARY

The study shows that the complex structure of cirrostratus may result solely from nucleation, particle growth and sedimentation in the absence of turbulence and cloud-scale dynamical processes. This demonstrates the difficulty to parameterize this type of cirriform cloud in GCMs. In particular, we find that the depth of nucleation zone, usually much smaller than the vertical grid spacing for the upper troposphere in GCMs, should be explicitly represented in parametric treatments of ice cloud generation.

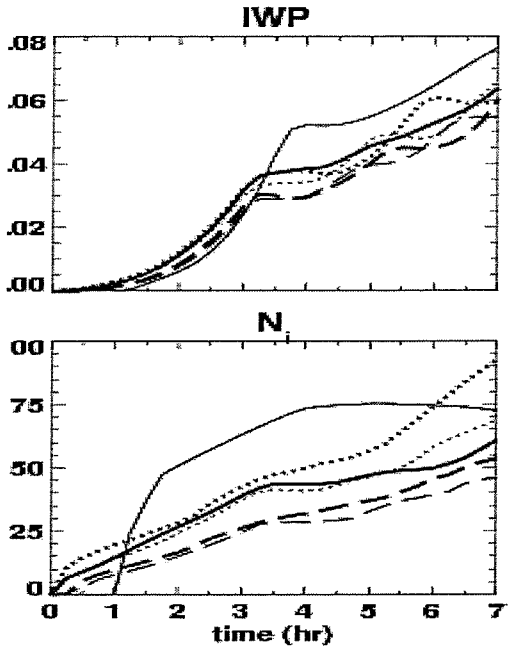

Figure 5. A comparison of IWP (kg m^{-2}) and N_iP (10^6 m^{-2}) of the HF and HET cases. Thin solid: HF; thick solid: M92; thick dotted: S20β60; thin dotted: S20β40; thick dashed: S30β60; thin dashed: S30β40.

6. REFERENCE

1. Chen, J.-P., and D. Lamb, 1994, Simulations of cloud microphysical and chemical processes using a multicomponent framework. Part I: Description of the microphysical model. J. Atmos. Sci., **51**, 3505-3516.
2. Heymsfield, A. J., and L. M. Miloshevich, 1993: Homogeneous ice nucleation and supercooled liquid water in orographic wave clouds. J. Atmos. Sci., **50**, 2335-2353.
3. Khvorostyanov, V. I., J. A. Curry, J. O. Pinto, M. Shupe, B. A. Baker, and K. Sassen, 2001: Modeling with explicit spectral water and ice microphysics of a two-layer cloud system of illustrated and cirrus observed during the FIRE Arctic Clouds Experiment. J. Geophys. Res., **106**, 15099-15112.
4. Lin, R.-F., D. O'C. Starr, P. J. DeMott, R. Cotton, K. Sassen, E. Jensen, B. Kärcher, and X. Liu, 2002: Cirrus parcel model comparison project phase 1. The critical components to simulate cirrus initiation explicitly. J. Atmos. Sci., **59**, 2305-2329.
5. Reichardt, J., U. Wandinger, M. Serwazi, and C. Weitkamp, 1996: Combined Raman lidar for aerosol, ozone, and moisture measurements, Opt. Eng., **35**, 1457–1465.
6. Sassen, K., and G. C. Dodd, 1988: Homogeneous nucleation rate for highly supercooled cirrus cloud droplets. J. Atmos. Sci., **45**, 1357-1369.

A CRITICAL OVERVIEW OF AERODYNAMICS AND HEAT AND MASS TRANSFER OF ICE PARTICLES, GRAUPEL AND HAILSTONES

Roland List

Department of Physics, University of Toronto, Toronto, ON, Canada

1. INTRODUCTION

The aerodynamics and heat and mass transfer [H&M] of atmospheric ice particles from ice crystals to graupel to hailstones have been the subject of 50 years of consistent research by the author and his associates in wind tunnels at the Swiss Federal Institute of Snow and Avalanche Research in Davos (1952-1963) and at the University of Toronto (1963-now). A water tank and a free fall tower were also available at U of T to determine free fall behavior of these particles. The equipment allowed the measurement of particle drag, lift and torque coefficients, Nusselt numbers characterizing the heat transfer and Sherwood numbers describing the mass transfer through the gaseous phase. Insights were gained into the contributions of particle motions such as oscillation, rotation and gyration, and the effects of surface roughness and air turbulence. This present paper sets the frame of how to use the results to parameterize the ice particle evolution over the Reynolds number range 1 < Re < 70000 in a form suitable for a new generation of higher resolution cloud models.

2. PARTICLE PROPERTIES AND INTERACTIONS WITH CLOUD ENVIRONMENT

2.1 Similarity of flow and heat exchange

The particle characteristics are given by the main diameter D, shape, roughness (height of roughness element as fraction of radius), and weight. These factors then help to determine the free fall speed. The surrounding air shall be described by temperature T_a, density ρ_a, liquid water content q_ℓ and water droplet size distribution. Temperature and density determine the inherent molecular viscosity of the air η. Knowing all these parameters, the fall velocity, the type of possible secondary motions, H&M, and particle growth rate can be established by experiment. This has been done and the results are available in the literature.

Similarity theory tells that the aerodynamic behavior, the fall velocity in particular, is determined by the Reynolds number, Re. Based on measurements Re also determines the heat and mass transfer as far as the gas phase is involved and the collection rate for the cloud droplets. The collection of droplets and the "convective" diffusion of vapor to or from the particle determine the particle growth rate (and possible shape changes and free fall properties).

The Reynolds number is defined as $Re=\rho_a V D \eta^{-1}$, where ρ_a stands for air density and η for kinematic viscosity. The key problem for freely falling particles is that V and D are not independent variables. At equilibrium the terminal free fall speed V can be calculated by setting the particle weight equal to the drag force. With ρ_p standing for particle density and C_D for drag coefficient gives

$$V_T = \left[\frac{4}{3}\frac{\rho_p g}{\rho_a C_D} D\right]^{1/2}$$

A new similarity number, the Best number *Be*, can now be defined as

$$Be = C_D \mathrm{Re}^2 = \frac{4}{3}\frac{\rho_a \rho_p g}{\eta^2} D^3$$

Be can be calculated from air and particle properties. This is important because *Be* produces Re and C_D without iterations. Once particle shape and size are chosen with known Re, and C_D, then the H&M can be tackled.

2.2. The heat balance

The physical properties of the ice particles involved, averaged over surface and volume, can be described as follows. ***a)*** The particles are either planar ice crystals or conical graupel, spherical small hail or spherical or spheroidal hailstones. They have a drag coefficient $C_D(D)$, the larger ones also a surface roughness θ and axis ratio α. They have a temperature T_D and a heat capacity C_p; ***b)*** the air is characterized by a temperature T_a , a density ρ_a, a vapor pressure e far away from the particle, a saturation vapor pressure over water at air temperature e_{sv}, a kinematic viscosity and a water vapor diffusivity in air, D_{wa}; ***c)*** the air is assumed to contain cloud droplets q_ℓ (and ice particles) of given size distribution; ***d)*** the latent heats of fusion and evaporation are given by $L_{\ell,s}(T_D)$ and $L_{v,d}(T_a)$ respectively [ℓ for liquid, s solid, v vapor, D deposit.

The most general heat balance equation of an atmospheric particle is composed of four terms, the heat flux by conduction and convection, dQ_{CC}/dt, the flux of water molecules which release latent heat of condensation or deposition at the particle surface, dQ_{ES}/dt the cloud droplet mass flux through the heat content they impart to the particle, the losses created by partial shedding and the latent heat of fusion released at the surface, dQ_{CP}/dt, and the time change of sensible heat content of the particle, dQ_τ/dt. The first three terms have been described by List (1963, 1994). The overall heat transfer is given by the Balance Equation

$$\dot{Q}_{CC} + \dot{Q}_{ES} + \dot{Q}_{CP} + \dot{Q}_\tau = 0$$

where $dQ_\tau/dt = 1/6\,\pi\,\rho_p C_p D^3\, dT_s/dt$.

2.3. The mass accretion rate

The gaseous mass deposition rate is given by the Sherwood number, Sh. The net mass accretion rate by droplet collection is

Corresponding author's address: Roland List, Department of Physics, University of Toronto. Toronto, ON M5S 1A7, Canada. E-Mail: list@atmosp.physics.utoronto.ca

$\dot{M} = \frac{\pi}{4} E\, q_\ell D^2 V$, with E as the collection efficiency; q_ℓ is the cloud liquid water content.

Shedding of precipitation-size raindrops from hailstones also needs to be considered (Garcia-Garcia and List, 1986; Joe et al., 1976, 1980). This aspect will lead to a further complication of the definition of the collection efficiency.

Ice particle growth occurs at the expense of the surrounding water droplets. This in turn reduces the liquid water content of the air. Water vapor will be deposited on the particle or evaporate from the surface. This changes the water vapor content of the air. Further the air will be heated by the always warmer ice particles and momentum will be imparted to the air, following the conservation laws. These feedbacks are of prime importance in modeling the properties and evolution of the cloud.

3. THE GROWTH STAGES

The complexity of the situation suggests that the ice particle growth be split into the different natural growth stages: crystals, graupel, small hail and hailstones. Figures 1 and 2 (both from List 1963) give an overview of the conditions for the different regimes. Figure 1 depicts the saturation water vapor pressure with respect to ice, e_{sp} and water e_{sv} as function of T_D or T_a, respectively. Note that the vapor pressure e in air may not be at water saturation.

There are specific conditions indicating a) no accretional mass growth (pure growth by gaseous deposition), b) mass growth by deposition equals mass growth by accretion (of droplets), c) no mass growth by deposition, followed by d) the region up to T_{0C} where the ice particle looses water vapor by evaporation.

Figure 2 gives an overview of the types of ice growth conditions experienced by a 2 cm diameter hailstone. The diagram would have to multiplied to deal not only with size but also with collection efficiency and liquid water content issues.

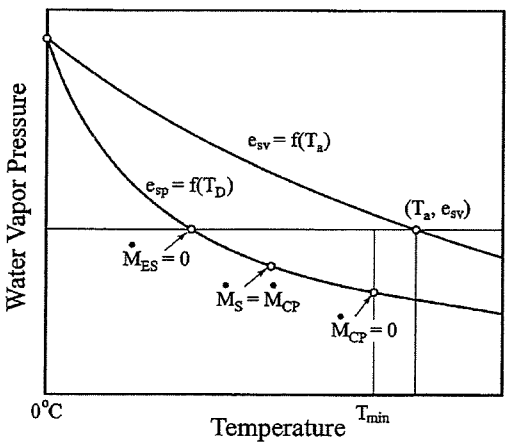

Figure 1. Saturation vapor pressures over cloud droplets in air, e_{sv}, and over ice particles, e_{sp}, as function of air and particle temperatures T; with special growth conditions as given in text.

For modeling purposes it can be assumed that:

Ice crystals grow by deposition of water vapor. Without accretion $dQ_{CP}/dt = 0$. The change in heat capacity of the ice crystal is negligible, rendering $dQ\tau/dt = 0$. Thus, the growth is diffusion limited considering that the diffusion of heat away from the crystal limits the allowable release of latent heat of the phase transition of the accreted water into ice. The original ice crystal shape can be directly associated with its initiation at T_a. It can be assumed that the shape will be conserved as long as the *dominant* growth occurs through deposition. Note that no analytic solution of the diffusion equation exists, but simplifications can be applied.

The crystal stage covers conditions between mass growth points $dM_{CP}/dt=0$ and $dM_S/dt = dM_{CP}/dt$. This growth is also limited by a size D=1 mm.

Graupel, consisting of porous ice and assumed to have conical shape with a rough surface, grow with dominant accretion of droplets up to $e_i = e(_{T0C})$. The graupel stage is terminated either by a size of D = 5 mm or a particle temperature of 0°C.

Small hail particles represent a densification stage of the graupel at $T_D = 0$, where the accreted droplets penetrate into the porous ice frame of the graupel. Once finished this stage is over. This occurs at D = 5 mm. Small hail is assumed to be spherical.

Hail starts to grow once the small hail has densified and a volume growth is resuming. This hail stage is assumed to occur at average $T_D = 0°C$, with deposits either solid or spongy ice (List, 1959), depending on icing conditions. Hailstones are assumed to be spherical up to a size of D = 1 cm, with roughness elements increasing with size. After reaching this critical size the hailstones grow more and more spheroidal and start to gyrate.

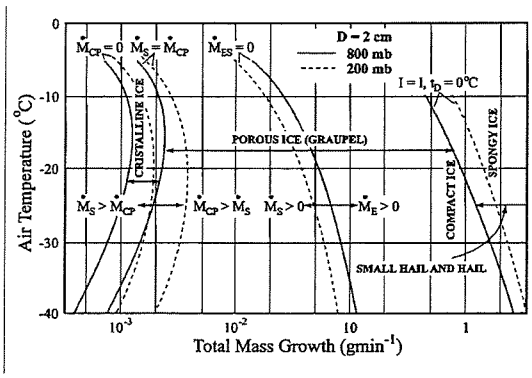

Figure 2. Principal growth conditions for crystalline growth (as for ice crystals, porous ice growth (as for graupel type deposit), and compact and spongy growth (as for small hail and hail. Conditions established for particles 2 cm in diameter can easily be adapted to other conditions.

4. U of T DATA RESOURCES

Aerodynamics. First measurements of drag coefficients of spheres after Prandtl were carried out by Bilham and Relf (1937). Real hailstones were examined by List (1959), a study which was later extended by List and Schemenauer (1971) to ice crystals, graupel and small hail (Figure 3). The issue of hailstones falling while rotating was addressed by List et al. (1971), while Kry and List (1974) produced a theory on the most general free fall motion, the gyration. This concept was later confirmed by Stewart and List (1983).

Roughness effects on drag were addressed by experiment in List et al. (1969), and on H&M by Schuepp and List (1967 and 1969). This work also included the effects of turbulence. Roughness and shape were also studied by List et al. (1994) and Zheng and List (1995).

Accretion was the special topic raised by Lesins et al. (1980) and Joe et al. (1980)., while shedding from hailstones was dealt with by Joe et al. (1976), Garcia-Garcia and List (1986) and Lesins and List (1986).

The heat and mass transfer, H&M was treated in a whole series of papers. Ice crystals and graupel were addressed by Schemenauer and List (1978) and Hyun et al. (2004) [ice crystals only], graupel alone by Cober and List (1992), hailstones by List (1960, 1963, 1994), Schuepp and List (1969), Garcia-Garcia and List (1992), Greenan and List (1995), and in an exhausting fashion by Zheng Guoguang and List, whose main paper of 1995 is listed (see also Figure 4). In their work they addressed rotating and gyrating particles, with and without roughness, and dealt with the heat conduction within the growing hailstone in order to explain the variations in surface temperature.

The above aspects deal with most micro-physical issues of the growth of ice crystal, graupel, small hail and hailstones. There are other aspects which have been left unmentioned, including the theoretical laboring by the author. This paper is a start of a project to integrate all this work into a coherent and consistent formulation of the main aspects of hail growth and a proposal for a. parameterization of the processes for application in more sophisticated cloud models

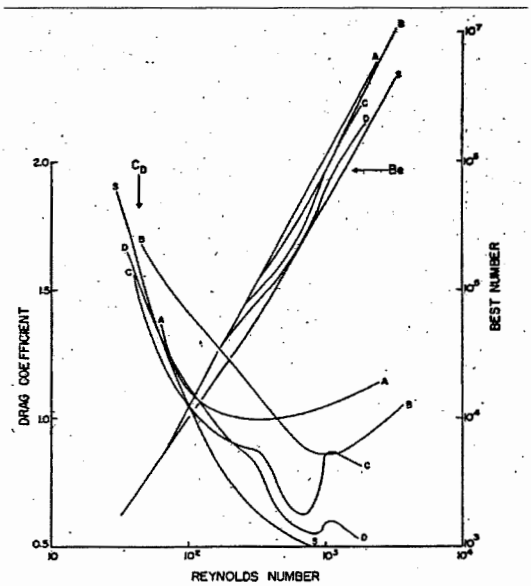

Figure 3. Drag coefficients and Best numbers as function of Reynolds number for conical graupel models released with apex up; A 90° cone-spherical sector, B 70° cone-spherical sector, C 90° cone-hemisphere, D 90° teardrop, S sphere.

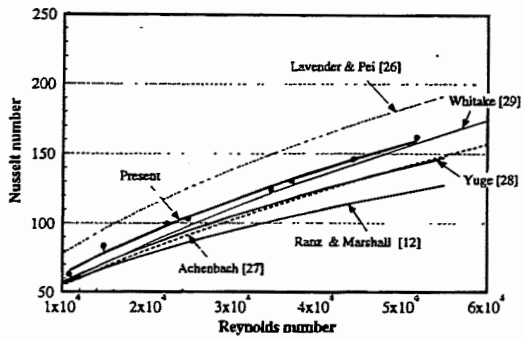

Figure 4. Overall NU f(Re) of rotating spheres as compared to non-rotating particles by other authors (Zheng and List , 1995). Note that "present" studies are placed in the middle of the non-rotating data field. New data ~ 30% higher than Ranz and Marshall.

Acknowledgments. The continuous support by the National Science and Engineering Research Council of Canada and the Meteorological Service of Canada and the Swiss Authorities sponsoring all the research is greatly appreciated. The many graduate students who helped in the development of the facilities and carried out most of the measurements and theoretical interpretations listed deserve my thanks and admiration.

REFERENCES

Bilham, E.G., and E.F. Relf, 1937; Quart. J. R. Met. Soc., 63, 149.

Cober, G.S., and R. List, 1992: Measurements of the heat and mass transfer parameters characterizing graupel growth. J. Atmos. Sci., 50, 1591-1609.

Greenan, B.J.W., and R. List, 1995: Experimental closure of the heat and mass transfer theory of spheroidal hailstones. J. Atmos. Sci., 22, 3797-3815.

Garcia-Garcia, F., and R. List, 1992: Laboratory measurements and parameterizations of supercooled water skin temperatures and bulk properties of gyrating hailstones. J. Atmos. Sci., 49, 2058-2073.

Garcia-Garcia, F., and R. List, 1986: Shedding and related heat transfer of artificial hailstones. Prof. AMS Conf. Cloud Physics, Sept.22-26, Snowmass,CO, 129-132.

Joe, P.I., R. List and G.B. Lesins, 1980: Ice accretions, Part II: Rain accretions, Rain production by icing assisted cloud water conversion. J. Recherches Atmos. 14, 357-364.

Joe, P.I., R. List, P.R. Kry, M.R. de Quervain, P.Y.K. Lui, P.W. Stagg, J.D. McTaggart-Cowan, E.P. Lozowski, M.C. Steiner, J. von Niedrhaeusern, R.E. Stewart, E. Freire and G. Lesins, 1976: Loss of accreted water from growing hailstones. Proc. Int. Cloud Physics Conf. , Boulder, USA, 264-269.

Lesins, G.B., and R. List, 1986: Sponginess and drop shedding of gyrating hailstones in a pressure-controlled wind tunnel. J. Atmos. Sci., 43, 2813-2825.

Lesins, G.G., R. List and P.I. Joe, 1980: Ice accretions, Pt. I: Testing of new atmospheric icing concepts. J. Recherches Atmos., 14, 347-356.

Kry, P.R., and R. List, 1974: Angular motions of freely falling spheroidal hailstone models. Phys. Fluids, 17, No. 6, 1093-1102.

List, R., 1994: Hailstone heat and mass transfer theory and three-component Nusselt numbers. Atmos. Res., 32, 85-93.

List, R., Zheng Guoguang and B. Greenan, 1994: The effects of roughness and shape onb the heat and mass transfer of hailstones. Proc. 6th WMO Scientific Conf. Weather Modification, Paestum, Italy, 30 May – 4 June, 297-300.

List, R., U.W. Rentsch, A.C. Byram and E.P. Lozowski, 1971 The aerodynamics of spheroidal hailstone models. J. Atmos. Sci., 30. 653-661.

List, R.,U.W. Rentsch, P.H. Schuepp, and N.W. McBurney, 1969: The effect of surface roughness on the convective heat and mass transfer of freely falling hailstones. Proc. 6th AMS Conf. Severe Storms, Chicago, Ill., 267-269.

List, R., 1963: General heat and mass exchange of spherical hailstones. J. Atmos. Sci., 20, 189-197.

List, R., and R.S. Schemenauer, 1971: Free fall behaviour of planar snow crystals, conical graupel and small hail. J. Atmos. Sci., 28, 110-115.

List, R., 1960: Zur Thermodynamik teilweise waessriger Hagelkoerner. Z. angew. Math. Phys., 11, 273-306.

List, R., 1959: Wachstum waessriger Hagelkoener im Hagelversuchskanal. Helv. Phys. Acta, 32, 293-296.

List, R., 1959: Zur Aerodynamik von Hagel-koernern. Z. angew. Mathy. Phys., 10, 143-159.

Schemenauer, R.E., and R. List, 1978: Measurements of the convective mass transfer of planar and columnar ice crystals. In Borovikov Memorial Issue: "Some problems of cloud physics" (Collected papers), Academy of Sciences of the USSR, Leningrad, 217-232.

Schuepp, P.H., and R. List, 1969: Mass transfer of rough hailstone models in flows of various turbulence levels. J. Appl. Meteor., 8, 254-263.

Schuepp, P.H., and R. List, 1967: the effect of surface roughness and turbulence on the heat and mass transfer of hailstones. Proc. Severe Local Storms Conf., St. Louis, Missouri, 287-292.

Stewart, R.E., and R. List, 1983: Gyrational motions of disks during free fall. Phys. Fluids., 26, 920-927.

Youk, H., R. List and T. Ola, 2004: The molecular diffusion of ice crystals of various shapes. Proc. Int. Conf. Clouds Precip., Bologna, Italy, July 18-23. pp.3.

Zheng Guoguang and R. List, 1995: Convective heat transfer of rotating spheres and spheroids with non-uniform surface temperatures. Intern. J. Heat Mass Transfer, 39, 1815-1826

THE 1954 INTERNATIONAL CONFERENCE ON EXPERIMENTAL METEOROLOGY IN ZURICH, SWITZERLAND (A HISTORICAL NOTE)

Roland List
Dept. of Physics, University of Toronto, Canada

Historical Environment

In 1950 the Swiss Government decided to form a National Hail Commission to study all aspects of hail formation and to design and lead hail suppression experiments. The activities where around three research topics and field operation: 1) Ice nucleation was studied at ETH under Professor R. Sänger [1895-1962] (later Profs. U. Dütsch and A. Waldvogel). Notable collaborators were U. Katz, G. Barnes, H. Pruppacher, and B. Federer. Topics were: development of ice nuclei chambers and nucleation studies, NMR of the ice nucleation process; later also field program testing of the Russian hail suppression concepts in the fully randomized Grossversuch IV [2 evaluation methods]; radar, cloud micro-physics.

2) Aerosol (CCN) studies at the Osservatorio Ticinese in Locarno Monti under J. C. Thams, later J. Joss. Center of attention: first low supersaturation chambers (H. Wieland); radar (J. Joss); leadership in Grossversuche I-III [GV III with ground generators, fully randomized].

3) Studies of the properties of natural hailstones and artificial ice particles in hail tunnels at the Swiss Federal Institute for Snow and Avalanche Research, Weissfluhjoch-Davos, Director Prof. M. de Quervain (Heads of group R. List, later A. Aufdermaur and O. Buser).

In addition to the directors of these groups notable Commission members were Prof. J. Ackeret (a world leader in aerodynamics, former student of Prandtl, and builder of the first supersonic wind tunnel) and Prof. Berger, Director of the lightning laboratories at ETH and on Monte San Salvatore.

On the hidden agenda of the symposium were discussions about the planned first Hail Tunnel in Davos, for which a funding application had to be prepared. John Mason and Frank Ludlam did not think it was worthwhile. However, Vince Schaefer was enthusiastic about the idea and fully supported it. He realized that new equipment always leads to new science. Thus, we reflected his support in our application and were successful.

Below is a translation of an Article by R. List published in the Technical Section of the leading Swiss newspaper, the Neue Zuercher Zeitung, Nov. 10, Nr. 2787 (114) Blatt 7.

Corresponding author's address: Roland List, Department of Physics, University of Toronto, Toronto, M5S 1A7, Ontario, Canada; E-mail: list@atmosp.physics.utoronto.ca

(INTERNATIONAL SYMPOSIUM ON) EXPERIMENTAL METEOROLOGY, ZURICH, 4 – 8 OCTOBER, 1954

Under the leadership of its President, Professor R. Saenger (Photo), the Swiss Commission for Hail Research and Hail Suppression organized an international symposium for Experimental Meteorology at the Swiss Federal Institute of Technology in Zurich. The main themes were the formation of Precipitation and its artificial modification. The great international participation by scientists from all over the world demonstrated the importance of the conference topics.

Cloud Physics, Natural and Artificial Aerosols

The meeting was opened Prof R. Saenger. The first contribution was by H. Dessens of the Observatoire du Puy-de-Dôme, Clermont-Ferrand. He reviewed the problems investigated by his research team. Photos and films showed the growth of giant hygroscopic nuclei with diameters of 20-30 μm at relative humidities of 93 to 97 % (G. Soulage). Another collaborator of H. Dessens, L. Facy, presented arguments and conclusions about the collection of icing nuclei by droplets - a process of high importance for artificial modification of precipitation. L. Facy came to the conclusion that the force field exerted by the asymmetric collisions of water molecules, later adsorbed by the growing droplets, pushed particles towards the droplets. While

this holds for condensation, no impurities can be imparted on the droplets during evaporation. Under such conditions, aerosol particles would be pushed away. Thus, artificial infusion of AgI particles can only lead to a positive effect in the presence of growing particles. H. Dessens then reported on the artificial formation of precipitation in France. Success with single clouds were supported by slides. No success, however, could be demonstrated over longer periods of time and larger areas.

In another opening talk, B.J. Mason of the Imperial College of Science in London reviewed the physics of rain and hail formation and reviewed the different theories and their evolution.. He accepted as correct the assumptions of Bergeron and Findeisen that precipitation in our latitudes has to go through the ice phase (see also Nr. 1850 of the Neue Zürcher Zeitung, August 29, 1951). He made the point that this had also been confirmed by radar. Only light rain can develop by coalescence of droplets. - using diagrams, B.J. Mason also presented relationships between minimal droplet sizes in a cloud and cloud thickness, liquid water content and updraft.

Prof. Dr. H.R. Byers of the University of Chicago reported about his aircraft measurements of condensation and ice nuclei over the Gulf of Mexico. Of interest were his observations of bigger temperature variations within clouds then observed at the cloud boundary.

The range of effectiveness and concentration of natural ice nuclei was discussed by Dr. W. Rau of the Max-Planck-Institute for Physics of the Stratosphere, Weissenau, Germany. In agreement with Prof. Dr. M. Bossolasco of the Italian Geophysical Institute in Milan, he reported maxima at -4°, -12°, and -19°. W. Rau explained this by the structure of water, considering that the maxima could not be moved by changes of the investigation methods. Dissolved in water the ice nucleus spectrum is displaced according to the lowering of the freezing point. The general assumption that droplets can only be supercooled to -45° was discarded with photos of (liquid) droplets supercooled to -85°. It is surprising that this also occurs in the presence of ice. Rau also reports on experiments allowing an association of the initiation of the freezing process by electrical fields with the droplets.

Ice nuclei and their properties were the topic of a series of papers. However, no apparatus was found acceptable to correctly count ice nuclei. Dr. O Vittori of the Meteorological-Aeronautical Observatory, Monte Cimone, Italy, was, nevertheless, able to present a method to easily identify metallic substances in the atmosphere. The method can also be applied to silver iodide, but the results are not yet satisfactory.

E.M. Fournier d'Albe of the Geophysical Observatory in Quetta (Pakistan) addressed the role of the giant condensation nuclei in the formation of precipitation. In their presence the smaller condensation nuclei are of no importance. Measurements and calculations of concentrations and life expectancy of giant nuclei were shown as function of height.

Ice nuclei-dependent ice structures were discussed by Dr. G. Yamamata of the Geophysical Institute of Tohoku University, Japan, while, in connection with natural nucleation, Prof. C.G. Rossby of the University of Stockholm reported on water analyses over large areas of Sweden. He showed maps of Sodium, Chlorine, Potassium, Calcium and Ammonia, deposited by rain at rates of 1 and 30 kg per hectare (0.01 km^2).

"Cloud Physical Measurements by Aircraft" was the topic of R.J. Murgatroyd of the Meteorological Flight Center in Farnborough, England. He showed slides of a variety of instruments to measure meteorological quantities as flown by his aircraft. Of particular interest were his instruments to measure droplet sizes and liquid water content and the data about these quantities in function of cloud type, cloud thickness and height within clouds. The design of a new instrument to measure cloud liquid water content was presented by Prof. G. Fea of the Italian Ministry of Aeronautical Defense, Rome. - Contrary to Murgatroyd's aircraft measurements, Dr. H.G. Mueller of the German Meteorological Service, Aerological Station, Munich, presented results from radiosonde ascents. After critical comments on measurement accuracy, he moved to the statistics of precipitation and thunderstorms at different average temperatures as function of height.

A collaborator of Prof. Koschmieder, H.V. Tippelskirch of the Technical University of Darmstadt reported on his experiments on convection cells in liquid sulfur. While not directly relevant to the topic of the symposium, this work might become important in the treatment of convection cells in the atmosphere.

Project Skyfire

The "Project Skyfire", a project with a potential for future weather modification applications, was introduced by Dr. V.J. Schaefer of the Munitalp Foundation in Schenectady (USA). The forests of Idaho and surrounding states are often very dry during the summers and susceptible to forest fires caused by lightning. This led to the setup of a substantial network of observers of clouds, the location of their formation and all lightning and lightning strikes (All lightning strike location will all be visited because they are likely to ignite forest fires). The results showed preferred orographic locations for the formation of heavy thunderstorms. Movies showed the evolution of cloud during the days. The conclusion was that the most dangerous thunderstorms produced 200-300 lighting strikes per hour under jet stream conditions aloft. Such situations produced very characteristic cloud forms. Their presence produced fields of layers of electric potentials 10x larger than normal in the air close to the ground. A large mobile laboratory serves for these investigations. However, the studies are not

yet finished.

Cases of Seeding

Findeisen had already reported cases with droplets supercooled to -20° or lower. The supercooling can be limited to -5° by seeding with Silveriodid (among the possible substances). Without these artificial ice crystals precipitation may never have occurred (see Nr. 1810 and Nr. 1862, Neue Zürcher Zeitung 7 and 14 Sept., respectively, 1949). This also led to investigations in Sweden about the conditions under which seeding might be successful. This was reported by F.M. Ludlam of the Imperial College oif Science in London. Two observing stations allowed quick measurement of cloud base, cloud height and distance. Thus, the formation and growth of cumuli producing rain could be documented,
and statistical evaluations of the data allowed conclusions about the cloud distributions. These observations are complemented by the measurement of rainfall of showers. The puzzle resulting from these observations was that iced cloud tops were observed at temperatures higher than -4°. Neither Ludlam nor Rau could explain this observation, considering that the highest known temperatures for nucleus activation are -5° for AgI.

While Ludlam spoke about scientific experimental aspects of nucleation, E. Bollay, a North American Weather consultant from Pasadena (U.S.A.) talked about commercial seeding in the West and Mid-West of America. In these areas artificial rain enhancement is highly desirable considering that a 10% increase in precipitation will augment the farm yield by 50%. But not only farmers see benefits of seeding, this is true also for other industry groups, such as power companies. E. Bollay reported about AgI generators and the measured spreading of the seeding substances. Interesting were also Bollay's critical remarks on the evaluation methods, requiring comparison of seeded regions with unseeded ones, with both regions having closely similar meteorological conditions. The selection of such regions is of prime importance, so is a sufficient duration of seeding activities. E. Bollay estimates that seeding increases rainfall by 20%.

After lively discussions the participants of this international symposium met again at a diner in the "Restaurant zur Weid". On 7. October, interested scientists visited the hail research group at the Swiss Federal Institute for Snow and Avalanche Research in Davos.

Roland List, Weissfluhjoch-Davos

CIRRUS CLOUD PROPERTIES DERIVED FROM THE MOMENTS OF MILLIMETER WAVELENGTH DOPPLER SPECTRUM

Gerald G. Mace and Min Deng

Department of Meteorology, University of Utah, Salt Lake City, Utah, 84112, U. S. A.

1. INTRODUCTION

Millimeter wavelength Doppler radar has been an important instrument for cloud and precipitation studies due to its Doppler capability. However, the small scale air turbulence and volume averaged vertical air motion within the radar sampling volume are a critical source of uncertainty in retrieving cloud and precipitation microphysical information. Recently, several investigations (Gossard, 1994) have suggested approaches to de-convolute the air turbulence from the Doppler Velocity spectrum to retrieve the properties of water clouds or drizzle. However, ice cloud property retrievals from radar moments and Doppler spectra is unique because the quiet air fall velocity and Doppler spectral broadening are of a similar magnitude to the air motions, unlike water clouds where the droplets are very nearly tracers of the air motion.

In this study, a new algorithm that uses the observed Doppler moments and a Z-IWC relationship (Liu and Illingworth, 2002) is developed to retrieve cirrus cloud microphysical properties and the mean and variance of the air motions with estimation of uncertainty. First we state that the observed Doppler spectrum is the convolution of a quiet air reflectivity spectrum with the turbulent PDF (probability density function). Assuming an exponential particle size distribution and an exponential PDF of air turbulence, a set of analytical equations characterizing this convolution that describe the moments of the Doppler spectrum moments is developed. Once these equations are set up, we formalize the retrieval problem into a framework based on estimation theory (Roger, 2000) as Mace (2004) did. The sensitivity study shows that the forward model is sensitive to variables such as size distribution width, air mean velocity and air turbulence width. Finally, this algorithm is tested by in situ measurements. The retrieved results show a good agreement with in situ measurements.

2. FORWARD MODEL DEVELOPMENT

According to Gossard (1994), Dabb (1999), the millimeter cloud radar (MMCR) Doppler spectrum is a broadened spectrum by air turbulence. We call it a convolution of the quiet air reflectivity spectrum with the air motion. In this study, a cloud property and air motion retrieval algorithm is developed only using MMCR moments and IWC-Z relationship.

Corresponding author's address: Gerald G. Mace, Department of Meteorology, University of Utah, Salt Lake City, Utah, E-Mail: mace@met.utah.edu.

2.1 Quiet Air Doppler Spectrum and Radar Moments

First, considering the quiet air radar volume, the water equivalent radar reflectivity factor Z_e is expressed as the integration of radar reflectivity density function.

$$Z_e = \int_0^\infty a_z \times D^{6+b_z} N(D) dD = \int_0^\infty S(D) dD \qquad (1)$$

where the parameters a_z and b_z are found through a power law fit (Mace 2002), and N(D) is the particle size distribution. So the radar reflectivity density function is

$$S_z(D) = a_z \times D^{6+b_z} N(D) \qquad (2)$$

Some researchers have suggested that the particle size versus number concentration spectra can be well represented by one or more exponential regimes. So here we consider a simple exponential droplet size distribution (DSD) function, and then the quiet air spectrum density function is:

$$S_z(D) = a_z \times N_o \times \exp(-\lambda \times D) \times D^{6+b_z} \qquad (3)$$

where the N_o is the drop concentration mode, λ is the exponential slope. However, the observed radar Doppler spectra are a function of Doppler velocity. Fortunately, the relationship between terminal velocities of particles in quiet air versus drop size has been studied (Heymsfield, 2000, Mitchell, 1996), and can be fitted by a power law function according to in situ measurements.

$$D(cm) = a_d \times V_f^{\,b_d}, \qquad (4)$$

where the a_d and b_d are parameters of the power law function, and with

$$Z_e = \int S_z(D) dD = \int S(V_f) dV_f, \qquad (5)$$

the transformed quiet air reflectivity spectral density function as a function of particle fall velocity is:

$$S(V_f) = N_0 \times a_z \times b_d \times a_d^{(7+b_z)} \times V_f^{(b_d \times (7+b_z)-1)} \times \exp(-\lambda \times a_d \times V_f^{\,b_d}) \qquad (6)$$

Through equations (5) and (6), we could calculate radar reflectivity. And the mean Doppler velocity (V_d) and Doppler spectrum width (σ) can also be described (Mace, 2002) by:

$$V_d = \frac{\int_0^\infty S(V_f)\times V_f \times dV_f}{\int_0^\infty S(V_f)\times dV_f} \quad (7)$$

$$\sigma = \frac{\int_0^\infty S(V_f)\times (V_f^2 - V_d^2)\times dV_f}{\int_0^\infty S(V_f)\times dV_f} \quad (8)$$

2.2 Convolution With Air Motion

Next, let's think about the convolution between the quiet air particle motion and air turbulence. The real reflectivity spectrum $S(w_i)$ is composed by convolution of quiet air spectrum $S(V_f)$ with the probability density (PDF) function $G(w_j)$ of air turbulence:

$$S(w_i) = \int_{-\infty}^{\infty} G(w_j)\times S(V_f = (w_i - w_j))\times dw_j \quad (9)$$

For convenience in the integrations, the air turbulence is represented by an exponential PDF given by:

$$G(w_j) = \frac{1}{2\times W_\sigma}\times \exp(-\frac{|w_j - w_m|}{W_\sigma}) \quad (10)$$

where W_m is the mean air velocity and W_σ is the half width of the spectrum. Gossard (1994) had demonstrated that this approach is not very sensitive to the exact functional form chosen for the air turbulence spectrum.

With the convolution model, the observed reflectivity spectra at the i'th velocity bin is a function of N_0, λ, W_m, and W_σ. Substituting equation 10 in equation 9, we have the turbulence-convolved spectrum density function in equations (11) and (12):

$$S_{z1}(w_i) = \frac{1}{2\times w_\sigma}\int_{-\infty}^{w_i} S_0 \times (w_i - w_j)^{b_d(7+b_z)-1}\times \exp(-a_d\lambda(w_i - w_j)^{b_d})\times \exp(\frac{w_j - w_m}{w_\sigma})dw_j, \quad (w_i<w_m) \quad (11)$$

$$S_{z2}(w_i) = \frac{1}{2\times w_\sigma}\{\int_{-\infty}^{w_m} S_0 \times (w_i - w_j)^{b_d(7+b_z)-1}\times \exp(-a_d\lambda(w_i - w_j)^{b_d})\times \exp(\frac{w_j - w_m}{w_\sigma})dw_j + \int_{w_m}^{w_i} S_0 \times (w_i - w_j)^{b_d(7+b_z)-1}\times \exp(-a_d\lambda(w_i - w_j)^{b_d})\times \exp(\frac{w_m - w_j}{w_\sigma})dw_j\} \quad (w_i>w_m) \quad (12)$$

To build up a forward convolution model, we have to assume known value of a_z, a_d, b_z, and b_d and input variables of N_0, λ, W_m, and W_σ. Then from this simulated spectrum we could integrate equations 11 and 12 and calculate the three radar moments. However, to retrieve the two PSD parameters and the PDF parameters, we need additional information. Assuming the IWC (ice water content) can be parameterized (Liu and Illingworth, 2000) using a power law Z-IWC relation,

$$IWC = a_m \times Z_e^{b_m} \quad (13)$$

Table 1. The list of forward model parameters of the power law relationships (units are in cgs)

coefficient	Value
Fall speed power law	
a_d	0.001
b_d	1.1
reflectivity power law	
a_z	4.2e-5
b_z	-1.889
Mass power law	
am	1.2e-5
bm	1.52

where a_m and b_m are the power law parameters, we have a fourth relationship with which to develop our retrieval algorithm. Since we are using estimation theory to invert the system of equations, we will use the Z-IWC relation a loose constraint by imposing large but reasonable uncertainty on the power law coefficients.

3. FORWARD MODEL SENSITIVITY STUDY

A sensitivity study of this forward model allows us to test our basic theory and verify our mathematical deductions. From the above discussion, we know that the forward model expresses our measured variables such as the radar moments and the parameterized IWC from the variables which we are trying to retrieve, such as N_0, λ, W_m, and W_σ. Z and IWC should be dependent on N_0, λ rather than W_m, and W_σ, while Vd and σ are functions of λ, W_m, and W_σ. Besides the input variables, this forward model should be sensitive to power law parameters too. In this sensitivity study, the power law parameters found from papers mentioned above are listed in table 1. Before we come to the numerical results, let's look at the simulated Doppler spectrum with different inputs of W_m, and W_σ

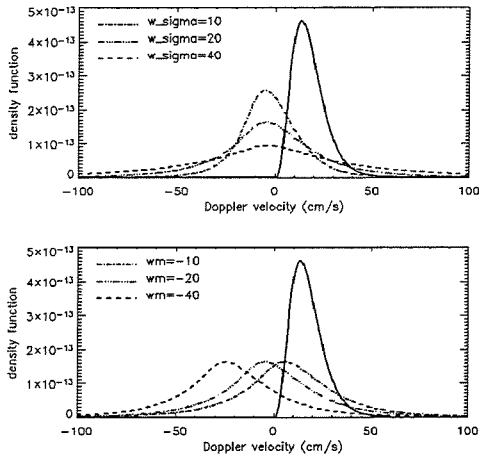

Figure 1. Spectrum simulation with different inputs of W_σ and W_m. The bold black line is the quiet air Doppler spectrum. The air turbulence broadens the quiet air Doppler spectrum; while the air mean velocity shift the quiet air Doppler spectrum toward upward motion. In this simulation, original input are N_0=1.0e5 λ=400, W_m=-20 and W_σ=20, units (cgs)

(Figure 1). This figure shows an obvious impression that the Doppler spectrum is very sensitive to the air mean velocity and air turbulence: the stronger the updraft, the smaller the Doppler velocity (downward motion or toward the radar is positive here); the more turbulent the air motion, the larger the spectrum width.

The sensitivity of forward model to N_0, λ, W_m, and W_σ is plotted in Figure 2. For the radar reflectivity and IWC, they depend nonlinearly on both λ and N_0 rather than air motion. The larger the particle size, the larger the radar reflectivity and IWC. When λ is smaller (large particles), N_0 has little effect on radar reflectivity and IWC; when λ is larger, the radar reflectivity and IWC depend more strongly on No. This shows that both radar reflectivity and IWC are sensitive to large particles.

In this forward model, the Doppler velocity depends little on N_0 and air turbulence width (W_σ), but depends nonlinearly on air mean velocity (W_m) and λ: The larger the air mean velocity, the larger the Doppler velocity (here the downward motion is positive); the larger λ, the smaller the particle size distribution width, the more small particles, then the smaller the Doppler velocity. This could be explained since the Doppler velocity is the mean velocity of the convolution of air motion and quiet air speed. As to the Doppler spectrum width, it depends only on λ and air turbulence width, which determine the particle size variation and air turbulence variation, respectively.

4. ALGORITHM TEST WITH IN SITU MEASUREMENTS

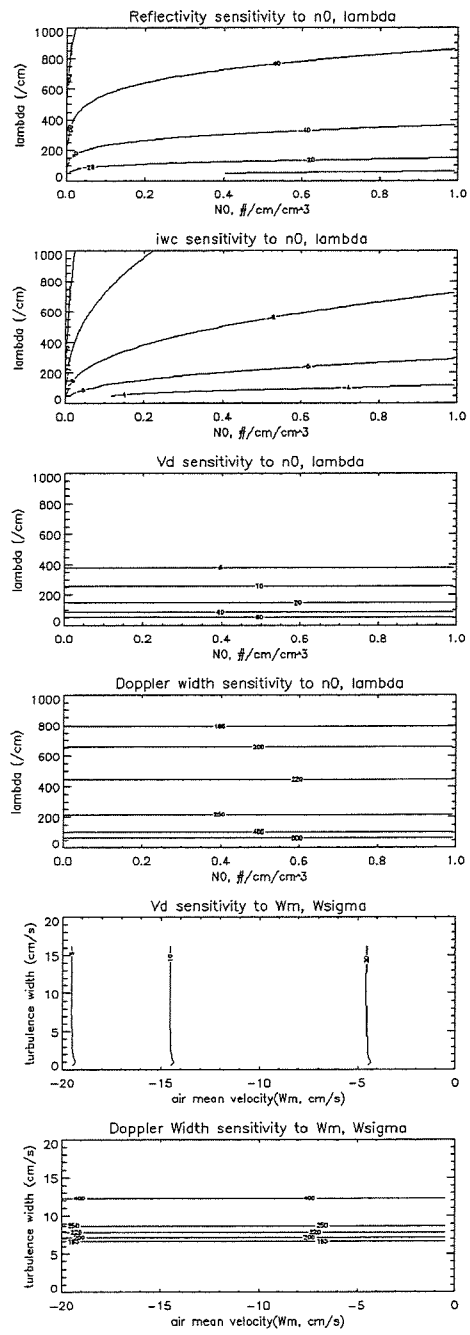

Figure 2. The forward model (Ze, IWC, Vd and σ) sensitivity to inputs (λ, N_0, W_m, and W_σ). The units are in cgs. Power law parameters are listed in Table 1.

In situ data are very useful to validate our retrieval algorithm because of its direct sampling. The citation data provide the DSD and high temporal resolution (25 Hz) air motion. From these data, we build up the Doppler spectrum and hence derive the radar moments and IWC. Then use derived radar moments and IWC as the input to our new algorithm to retrieve the DSD, air mean velocity, and turbulence width. After that the retrieved DSD and air motion is compared with citation data. If they have a good agreement, the algorithm should be reliable to retrieve cirrus cloud and air mean velocity and turbulence width.

Figure 3 is an over-plot of radar reflectivity and the flight of UND (University of North Dakota) citation II weather Research aircraft on Sep. 26, 1997. Particle spectra data files have been generated from the 2D-C probe, which detects particles ranging from 30 to 960 microns. Figure 4 shows a Doppler spectrum simulation from cirrus DSD and 25 Hz air motion PDF at 19:42:52. The DSD is plotted as a function of fall velocity which is derived from particle size and the power law relation. The figure shows a good exponential distribution, even though concentration of very large particles increases a little. The air velocity

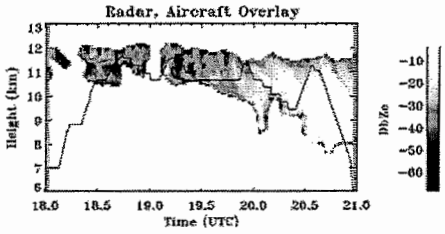

Figure 3 Time-height radar reflectivity and the flight track of the UND (University of North Dakota) citation II weather Research aircraft on Sep. 26, 1997.

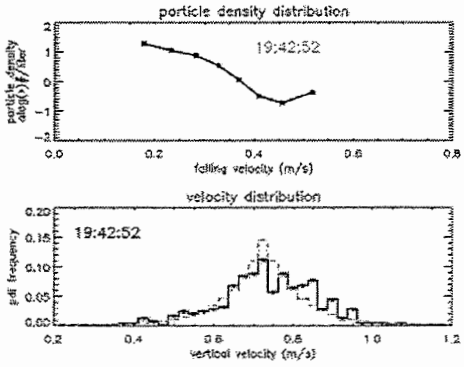

Figure 4 Doppler spectrum simulation from cirrus DSD and air motion PDF which are obtained from citation II at 19:42:52.

PDF is plotted with the exponential fitted PDF, which is in dash-dot line. The simulated Doppler spectrum shows two peaks which may be caused by the concentration of large particles. From this spectrum we can calculate the three radar moments and use that information as input to retrieval algorithm. Preliminary results are encouraging.

5. ACKNOWLEDGEMENTS

This research would not be possible without data collected by the crew of the University of North Dakota Citation led by Mike Poellot. Funding for this work was provided by the Environmental Science Division of the U. S. Department of Energy (Grant DE-FG0398ER62571) and through a NASA EOS Validation Program grant (NAG56458). Data were obtained from the Atmospheric Radiation Measurement Program sponsored by the U. S. Department of Energy, Office of Science, Office of Biological and Environmental Research, Environmental Sciences Division.

6. REFERENCE

Babb, D. M., 1999, Retrieval of could microphysical parameters from 94-GHz radar Doppler power spectra. J. Atmos. Ocean. Tech., **16**, 489-503.

Gossard, E.E., 1994, Measurement of cloud droplet size spectra by Doppler radar. J. Atmos. Ocean. Tech., **11**, 3, 712-726.

Heymsfield, A. J., and J. Iaquinta, 2000, Cirrus crystal terminal velocities, J. Atmos. Sci., **34**, 916-938.

Liu, C, A. J. Illingworth, 2000, Toward more accurate retrievals of ice water content from radar measurements of clouds. J. Appl. Metero., **39**, 1130-1146.

Mace, G, G, 2002: On retrieving the microphysical properties of cirrus clouds using the moments of the millimeter-wavelength Doppler spectrum. J. Geophys. Res. 107, 4815-4831

Mace, G. G., 2004: On retrieving the microphysical properteis of cirus Icoud using the moments of the millimeter wavelength Doppler spectrum, Part II – An analytical framework and formal error analysis. To be submitted to journal of Geophsyical Research 5.2004.

Mitchell, D., 1996, Use of Mass- and area-dimensional power laws for determining precipitation particle terminal velocities. J Atmos. Sci. **53**, 1710-1723.

Roger, C. D. 2000: Inverse methods for atmospheric sounding: Theory and practice (Series on atmospheric oceanic and planetary physics). World scientific.

MORPHOLOGY OF ICE CRYSTALS AT LOW TEMPERATURES: LABORATORY MEASUREMENTS AND ATMOSPHERIC MODELING IMPLICATIONS

Nathan Magee, Dennis Lamb, and Alfred M. Moyle

Department of Meteorology, Pennsylvania State University
University Park, PA, 16802, USA

1. INTRODUCTION

The characteristics of ice crystals at high altitudes is a topic of great relevance in the current landscape of atmospheric science. Cirrus cloud growth, dissipation, and radiative impact are largely governed by the properties of the cloud's constituent particles: small ice crystals, typically of sizes on the order of 100 μm (Heymsfield et al, 2002). It is of particular interest to understand the microphysical composition of cirrus clouds in order that radiation balances can be realistically represented in climate models. High-altitude cloud parameterizations and their related feedbacks currently represent a large source of uncertainty in climate predictions.

Such small, cold ice crystals are also of critical importance to processes of thunderstorm electrification, stratospheric ozone depletion, and contrail formation, not to mention optical phenomena such as halos and sun dogs. Although high-altitude observations are very difficult, radar and in-situ observations have provided some primary information about particle habits and sizes, but these lack the lifetime tracking, close observation, and detail characterization that are possible in the laboratory.

Through use of a unique experimental system, we attempt to contribute new data concerning the nature of ice crystals at conditions closely mimicking the cirrus environment. Time lapse photography provides detailed information for determining growth rates on individual crystal faces under varying conditions of temperature and supersaturation. This type of observation should be conducive to the development of parameterizations for improving cirrus cloud models.

2. THE DEPOSITION COEFFICIENT

The deposition coefficient is defined as the efficiency with which impinging vapor molecules are incorporated into the growing crystal. In measuring the growth rate of crystal surfaces and the ambient supersaturation, we hope to reveal a systematic picture of this growth efficiency as a function of both temperature and supersaturation. Past laboratory studies have measured linear growth rates of ice crystal faces between 0 °C and –30 °C (Lamb and Scott 1974; Takahashi et al 1988), demonstrating that the face-dependant variation in deposition coefficient with temperature results directly in the primary habits of ice at these temperatures. This information is very

Corresponding author's address: Nathan Magee,
503 Walker Bldg., Penn State University, University Park, PA 16802, USA; E-mail: nbm107@psu.edu

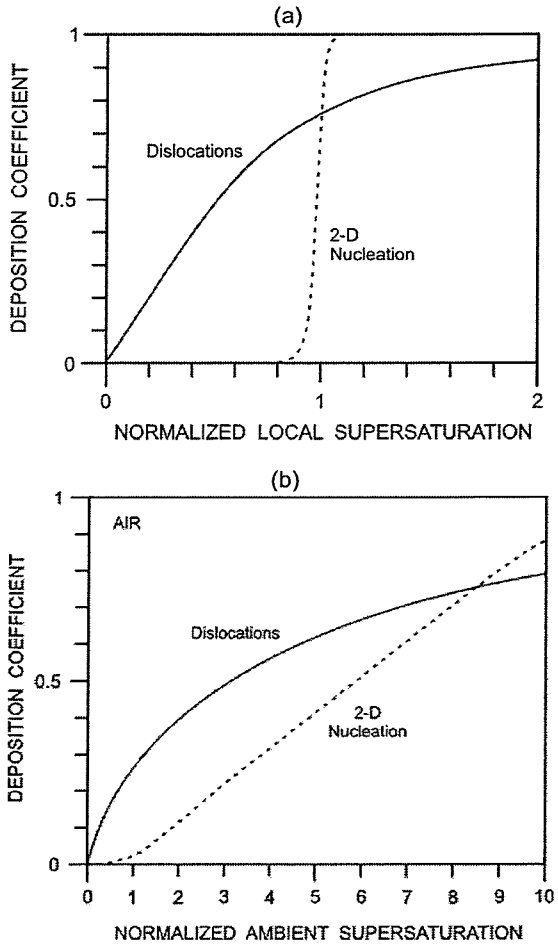

Fig. 1. a) Dependence of the deposition coefficient and local supersaturation on growth mechanism. The dashed line is for m=1, representing growth from screw dislocation step origins and the solid line is for m=30, representing the onset of growth from 2-D island nucleation. b) Dependence of the deposition coefficient on ambient supersaturation in the presence of air (after Lamb 2000)

useful, but most laboratory studies of ice crystal growth rates have been constrained to growth at above –30 °C and at only one saturation ratio (often water-saturation). These studies have established the deposition coefficient as a function of temperature, but they have been unable to validate theoretical prediction of growth efficiency dependence on supersaturation.

Discussion of the incorporation of vapor molecules into the crystal lattice of a growing ice particle often centers upon a debate regarding the specific mechanism of step origin (Fukuta and Lu 1994; Nelson and Knight 1998). In particular, it is often noted that spiral step growth accounts for observed growth at very low supersaturations, whereas 2-D nucleation better explains rapidly growing crystals likely to be relatively defect-free. The focus on the differences between the proposed mechanisms for crystal growth appears to have prevented consensus about implementing the significant commonalties between the two theories in model parameterizations (Lamb 2000). The edge free energy and critical radius for growth are shared between the two theories and both approaches demand that the deposition coefficient approach zero along with the local supersaturation. 2-D nucleation has a very pronounced threshold in a pure vapor environment, but in the presence of air, the influence of volume diffusion tends to mute the difference between the two mechanisms. Equation 1 represents a general theoretical relationship between local supersaturation, s, and the deposition coefficient, α (Nelson and Baker, 1996):

$$\alpha = \left(\frac{s}{s_1}\right)^m \tanh\left[\left(\frac{s_1}{s}\right)^m\right] \qquad (1)$$

The quantity s_1 is the transitional supersaturation which is proportional to the edge free energy (Burton *et al.* 1951), and the parameter m is used to represent the two growth mechanisms. Figure 1a shows the functional dependence of the depositional coefficient with local supersaturation, but some modification needs to be made to represent this dependence as a function of ambient supersaturation in air. Lamb and Chen (1995) and Lamb (2000) have found that equation 1 can be modified for growth in air by balancing the effects of volume diffusion and surface kinetic processes:

$$\alpha = \left(\frac{x}{1+K\alpha}\right)^m \tanh\left[\left(\frac{1+K\alpha}{x}\right)^m\right] \qquad (2)$$

The factor $K\alpha$ is the ratio of growth resistances due to volume diffusion and surface kinetics and $x \equiv s_{ambient}/s_1$. Figure 1 suggests that the presence of air diminishes the distinction between the two growth mechanisms and smoothes the dramatic growth threshold in the case of 2-D nucleation seen in Figure 1a.

Nelson and Knight (1998) have made measurements of the threshold supersaturation for 2-D nucleation growth for prism and basal faces, but little other observational evidence is available regarding the relationship between α and supersaturation. Our laboratory analysis will be directed toward observational confirmation of Figure 1b for varying ambient conditions and for basal and prism faces.

Fig. 2. Photograph of the partially assembled environmental control chamber exposing the resistively-warmed coil coated evenly with 3 mm of ice.

3. THE LABORATORY SYSTEM

The laboratory system is contained within an environmental control chamber that supports the growth of an ice crystal within a vertical wind tunnel. The ice crystal is suspended on a fine glass filament, approximately 10 μm in diameter, in a vertical airstream. The temperature of ambient airflow can is controlled by cooling circulating baths to a minimum temperature of approximately -60°C and differences can be measured by thermocouples to within 0.01°C. Supersaturation of the ambient flow is generated as chilled and saturated air passes over the warmed ice surface of a coil element just before encountering the growing crystal (Fig.2). Figure 3 is a schematic depiction of the process used for manipulating supersaturation. Fine control of ice-supersaturations between zero and slightly above water-saturation can be achieved by varying the electric current used to

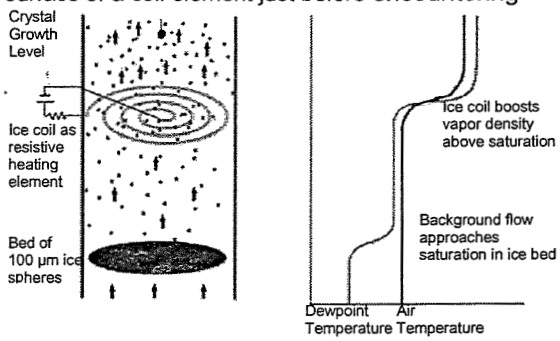

Fig. 3. Schematic of the supersaturation generation mechanism.

warm the ice coil. The conditions surrounding the growing ice crystal are monitored by an array of thermocouples, flow meters, and a manometer. The growing particle is observed optically through a Zeiss stereomicroscope, employing digital images.

4. TOWARD PARAMETERIZATION

Initial experiments have demonstrated the ability to grow crystals under widely varying conditions of temperature and saturation. Figure 4 is an example of a crystal grown in the chamber under a variety of supersaturations. Growth began at –18.4 °C near the lower boundary of the classical regime for plate-like growth and at a supersaturation of approximately 5%. After 20 minutes, the supersaturation was increased to approximately 20%. This change raised the temperature to –14.8 °C and initiated the growth of dendritic arms from the corners of the plate-like crystal. The supersaturation was then reduced to the original level and slower growth occurred for the final 5 minutes prior to the photograph, producing sharply faceted segments along the dendritic arms.

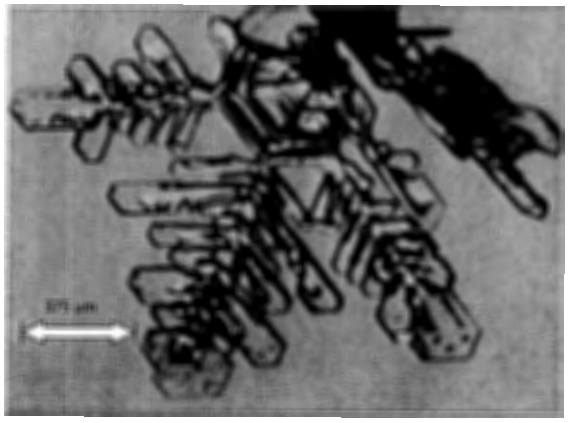

Fig. 4. Photograph of an ice crystal growing in our chamber at a temperature of –18.4 °C. The crystal grew for approximately 20 minutes at very low supersaturation, followed by 2 minutes at water saturation, and then again for 5 minutes at very low supersaturation.

With time-lapse observations of crystal growth like that seen in figure 4, taken at variety of temperatures and supersaturations, it should be possible to reproduce figure 1b with specificity for temperature, supersaturation, and crystal face. Some parameterizations of α(T, crystal habit) are already in use in atmospheric cloud models and have shown promising results (Chen and Lamb 1994; Lin *et al* 2000), but inclusion of a functional dependence for supersaturation and extension to lower temperatures would represent a significant improvement. The improvement would likely be most significant for cirrus conditions, where complicated habits, lower pressures, small crystals, and low supersaturations enhance the influence of surface kinetic processes (Bailey and Hallet 2002).

5. CONCLUSIONS

We have developed a new approach for observing the growth of ice crystals at a wide variety of temperatures and supersaturations. We intend to use the data resulting from this arrangement to extend measurements of growth efficiencies to lower temperatures and a variety of supersaturations. We believe that these data will allow for comparison with the theoretical relationship between growth efficiency and supersaturation. The new measurements will fill holes in crystal observations and allow for an improved parameterization of ice crystal growth, particularly for cirrus-like conditions.

5. ACKNOWLEDGEMENTS

This work is sponsored by NSF Grant ATM-9981511. We thank Raymond Shaw for the initial development of the environmental control chamber and Robert Ziegler for his assistance with laboratory operations.

6. REFERENCES

Bailey, M., and J. Hallett, 2002: Nucleation effects on the habit of vapour grown ice crystals from –18 to –42 °C. *Q.J.R. Meteorol. Soc.*, **128**, 1461-1483.

Burton, W.K., N. Cabrera, and F.C. Frank, 1951: The Growth of Crystals and the Equilibrium Sturcture of their Surface. *Proc. Roy. Soc. London*, **A243**, 299-358.

Chen, J.P., and D. Lamb, 1994: The Theoretical Basis for the Parameterizaiton of Ice Crystal Habits: Growth by Vapor Deposition. *J. Atmos. Sci.*, **51**, 1206-1221.

Fukuta N., and Q.J. Lu, 1994: Surface Microphysical Mechanism for Ice Crystal Growth Habit Development. *Atmos. Res.*, **32**, 31-43.

Heymsfield, A.J., S. Lewis, A. Bansemer, J. IaQuinta, L.M. Milosevich, M. Kajikawa, C. Twohy, and M.R. Pellet, 2002: A General Approach for Deriving the Properties of Cirrus and Stratiform Ice Cloud Particles. *J. Atmos. Sci*, **59**, 3-29.

Lamb, D., and W.D. Scott:: Linear growth rates of ice crystals grown from the vapor phase. *J. Crystal Growth*, **12**, 21-31.

Lamb, D., 2000. Crystal Growth: 2-D or Not 2-D? *Proceedings of 13th Inter. Conf. on Clouds and Precip., Reno, NV.* 1221-1224.

Lin, R.F., D. Starr, P.J. DeMott, R. Cotton, E. Jensen, and K. Sassen, 2000: Cirrus Parcel Model Comparison Project Phase 1. In Proceedings of 13th Inter. Conf. on Clouds and Precip., Reno, NV. 1221-1224.

Nelson, J.T., and M.B. Baker, 1996: New Theoretical Framework for Studies of Vapor Growth and Sublimation of Small Ice Crystals in the Atmosphere. *J. Geophys. Res.* **101**, 7033-7047.

Nelson J., and C. Knight, 1998: Snow Crystal Habit Changes Explained by Layer Nucleation. *J. Atmos. Sci.*, **55**, 1452-1464.

Takahashi, T., T. Endoh, G. Wakahama, and N. Fukuta, 1991: Vapor diffusional growth of free-falling snow crystals between –3 and -23°C. *J. Meteor. Soc. Japan*, **69**, 15-30.

EFFECTS OF WIND SHEAR ON CIRRUS: AN LEM AND RADAR CASE-STUDYI

J.H.Marsham[1] and S.Dobbie[1]

[1]School of the Environment, The University of Leeds, UK

1. INTRODUCTION

Cirrus clouds are a significant source of uncertainty in climate modelling (Liou 1986), largely because of their radiative effects. Improving our understanding of the many complex processes that affect cirrus should allow improvements in cirrus parameterisations and so a better understanding of their effects on climate. Cirrus often form in regions of high wind-shear (either at fronts, near jet-streams or in convective outflow) and many previous modelling studies have referred to the importance of wind-shear, but not investigated its effects (Gu and Liou 2000, Dobbie and Jonas 2001, Liu et al 2003).

In this paper we use the version 2.3 of the Met. Office large-eddy-model (LEM) to investigate the effects of shear. The radiation scheme of Fu and Liou (1992 and 1993) with updated ice (Fu 1996; Fu et al 1998) was added to the LEM (Derbyshire et al 1999 and the LEM documentation). All runs used a 50 km wide and 20 km deep 2D domain, with a horizontal resolution of 100 m and a vertical resolution of 125 m in the cloud layer. This was intended to minimise the effects of the periodic boundary conditions, without the very large computational cost of a 3D domain with a large shear. Studies comparing 2D and 3D simulations, as well as the effects of varying the horizontal resolution, are underway.

The LEM simulations were based on a case of wind-sheared ice-clouds, observed by the Chilbolton radar (51.145 N, 1.437 W) (Hogan and Illingworth 2003). The LEM results show that the shear significantly decreases the ice-water-path (IWP) of the ice clouds, as well as affecting thel distribution of ice by advection and turbulent mixing.

2. THE CASE STUDY

Radiosonde data from Herstmonceux (120 km east of Chilbolton, 11 UTC) was used to initialise the LEM potential temperature and water vapour profiles. The LEM was cooled (at a rate calculated from the observed frontal slope) to give the observed temperature profile after 3 hours, to simulate frontal uplift (Starr et al 2000). This gave an IWC profile similar to that observed, but with too little ice at upper levels (Hogan and Illingworth 2003 describes IWC retrievals from the Chilbolton radar). Varying the scale and magnitude of the initial random perturbations, the cooling rate, or the nucleation rate, did not significantly increase the IWC. However, adding more water vapour and destabilising the initial profile, gave much more convection and an ice water contents (IWC) profile more similar to that observed at Chilbolton, though IWC were still a factor of two too low. Further experiments showed that a similar effect could be achieved by reducing the windspeed during the earlier hours of the simulation. Simulated radar retrievals were produced from the LEM data and Figures 1 and 2 show: (i) convection in the lower-stability low-shear layer (between 7 and 10 km) (ii) fallstreaks below this in the higher-stability high-shear layer, in both the radar and the LEM data.

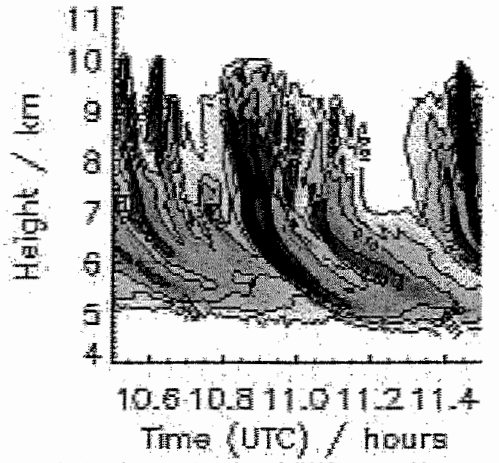

Figure 1: Radar retrievals of IWC from Hogan and Illingworth 2003 Contours of IWC at 0.01, 0.05, 0.1 and 0.2 g/m^3.

3. EFFECTS OF WIND-SHEAR

The shear was varied in the LEM to investigate the effects of wind-shear and the mechanisms by which these effects occurred.

3.1 Suppression of convection by turbulence from Kelvin-Helmholtz wave breaking

The LEM was run with the observed wind, with the shear retained/removed at different levels and with various multiples (0.0 to 1.0) of the observed wind. Figure 3 (top) shows that the shear has a significant

Corresponding author's address: John H. Marsham, School of the Environment, The University of Leeds, Leeds, LS2 9JT,UK

Email: jmarsham@env.leeds.ac.uk

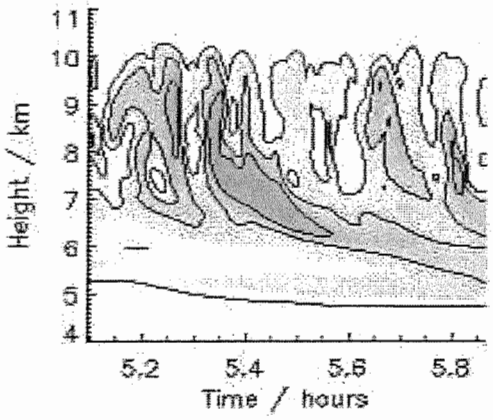

Figure 2: Simulated radar retrievals from the LEM (using the same greyscale and contours of IWC as Figure 1). The vertical distribution of ice is similar to the radar observations, but IWC are approximately half those observed.

effect on the IWC profile, approximately halving the IWC at 9 km. Figure 3 (bottom) shows that it is the strong shear below 7 km that is responsible for the change in IWC at the higher levels, rather than the weaker shear at those levels.

For shears greater than or equal to 0.8 times the observed shear the gradient Richardson number falls below 0.25 in a layer at 7 km, at the base of the convective cells, whereas for lower shears it does not. We expect Kelvin-Helmholtz waves, generated by the strong shear applied to a stable layer, to break for Richardson numbers less than 0.25, generating turbulence (Turner 1973). The turbulence mixes ice downwards from above 7 km, this reduces IWC and so reduces cloud-top cooling. This in turn reduces vertical velocities and so the generation and retention of ice. This effect is very sensitive to the atmospheric stability and shear, which often vary over short vertical intervals in cirrus, giving thin layers of anisotropic turbulence (Smith and Jonas 1996). At certain phases in the wave-cycle gravity waves may also sometimes result in Kelvin-Helmholtz wave-breaking, where we would not otherwise expect it (Smith and Jonas 1996) and the characteristic gravity-wave signature of vertical velocity. perturbations coherently leading potential temperature perturbations by 90 degrees (Axford 1971) was observed in the sheared LEM runs.

The effects of the Kelvin-Helmholtz wave-breaking are clear in the spectral analysis of the horizontal and vertical velocity perturbations. The wave breaking gives peaks (at wavelengths between 0.8 and 3 km) that are not present without shear (such peaks were noted by Smith and Jonas 1996 in aircraft data). The characteristically anisotropic nature of the turbulence can also be seen, with vertical velocities suppressed by the atmospheric stability (Smith and Jonas 1996).

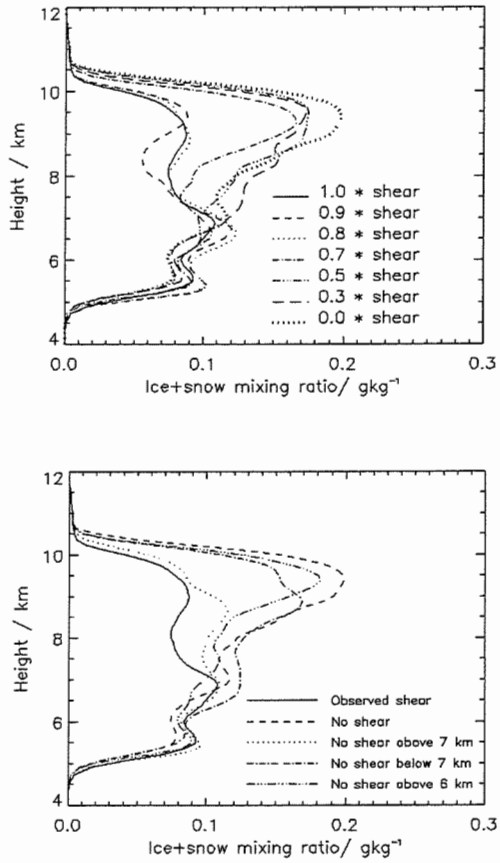

Figure 3: IWC profiles with various multiples (0.0 to 1.0) of the observed shear (top) and the shear retained/removed at different levels (bottom).

3.2 Vertical decorrelation of IWC

Figure 4 shows the mean correlation coefficient of IWC against vertical separation for (i) the sheared LEM case (ii) the zero-shear LEM case and (iii) the radar data (from Hogan and Illingworth 2003). The relationship is linear for small separations, but this is not because of the angle of the wind-sheared fallstreaks, as suggested by Hogan and Illingworth 2003, because there is still a linear fit in the zero-shear LEM data. The gradient of this linear trend does depend on wind-shear however.

In the sheared case oscillations in the correlation coefficient occur at larger separations because of the sheared fallstreaks: the correlation coefficient increases as a streak/gap is advected over a neighbouring streak/gap. For large separations the correlations coefficient tends to zero in the sheared case and a small negative value in the zero-shear case. This occurs because the cloud-top and base are coupled in the zero-shear case and not in the sheared case.

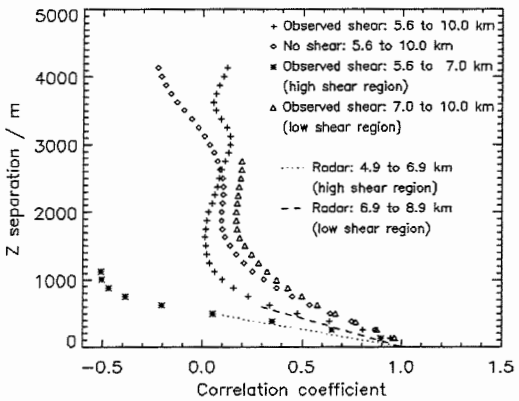

Figure 4: Decorrelation of IWC with vertical separation with and without shear. For separations of less than five to eight hundred metres the trend is linear and the gradient depends on the shear. Oscillations occur at larger separations if there is sufficient shear. Radar results are from Hogan and Illingworth 2003.

3.3 Pdfs of IWCs and total water

There is a move towards cloud schemes that use prognostic probability density functions (pdfs) to represent the water contents within a single GCM grid-cell (Tompkins 2002, Wilson and Gregory 2003). Figure 5 shows that a skewed mono-modal function (as used by Tompkins 2002 and Wilson and Gregory 2003) provides a good fit to both the total water contents and the IWC for this case study, both with and without shear.

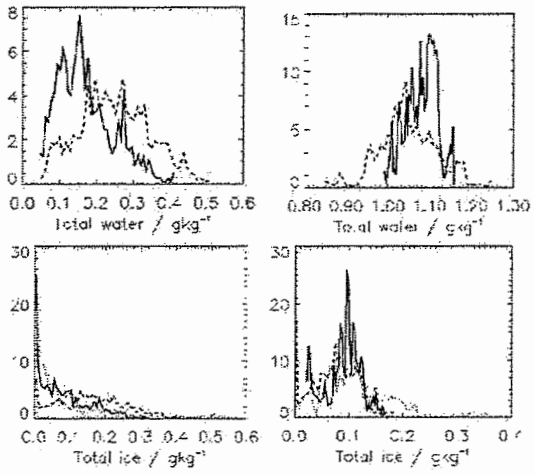

Figure 5: Pdfs of total water (top) and IWC (bottom) at 8500m (left) and 5500 m (right). Solid lines are LEM results with shear, dashed lines without. The dotted lines show the radar retrievals.

Shear has a significant effect on the modelled pdfs (Figure 5) and gives distributions more similar to the radar observations; in particular it gives the monotonically decaying form at 8500 m. Adding a tracer above 10500 m in the LEM shows that this is not because of increased entrainment, but rather because shear gives larger down-draughts, with less turbulence above 7 km, so dry air is less well mixed with air containing ice. At 5500 m shear-induced mixing gives a narrower pdf as expected.

3.4 Conclusions

An LEM case-study, initialised using radiosonde data and IWC observations from the Chilbolton radar, has been used to investigate the effects of wind-shear on ice-clouds. In this case the shear significantly decreases IWC and this was shown to occur because of turbulence from Kelvin Helmholtz wave breaking at the base of the convective cells. This has a significant impact on the clouds radiative properties (reducing the ice water path from 345 g/m^2 to 245 g/m^2).

Shear was also shown to have significant effects on the pdfs of IWC and total water, in particular leading to large dry down-draughts at upper levels and more homogeneous fields at lower levels. The effects of shear on the vertical decorrelation of IWC were also investigated, this showed a linear relationship for small separations, even in the zero-shear case.

In other cases shear-induced turbulence may initiate convection and so increase IWC; this is currently being investigated. The effects of shear are certainly very sensitive to the atmospheric profile, which frequently varies over small vertical distances in cirrus clouds (Smith and Jonas 1996). The potential for using stability numbers, to determine the effects of shear, is being studied.

3.5 Acknowledgements

Robin Hogan, University of Reading, Reading, UK for providing radar data and NERC grant NER/M/S/2002/00127 for funding this work.

3.6 References

Axford, D.N., 1971: Spectral analysis of an aircraft observation of gravity waves, Q.J.R.Meteorol.Soc., **97**, 313-321.

Derbyshire, S.H., Brown, A.R. And Lock, A.P. 1999: The Meteorological Office large-eddy simulation model. *Turbulence and Diffusion Note*, **213**, 1-47

Dobbie, S. and Jonas, P. 2001: Radiative influences on the structure and lifetime of cirrus clouds. Q.J.R.Meteorol.S., **127**, 2663-2682

Fu, Q. and Liou, K.N. 1992: On the correlated {\it k}-distribution method for radiative transfer in nonhomogeneous atmosphere. J. Atmos. Sci. ,**49**, 2139-2156

Fu, Q. and Liou, K.N. 1993: Parameterization of the radiative properties of cirrus clouds. J. Atmos. Sci. , **50**, 2008-2025.

Fu, Q. 1996: An accurate parameterization of the solar radiative properties of cirrus clouds for climate models. J. Climate, **9**, 2058-2082.
Fu, Q., Yang, P. and Sun, W.B.1998: An accurate parameterization of the infrared radiative properties of cirrus clouds for climate models. J. Climate, **11**, 2223-2237.
Gu, Y. and Liou, K.N. 2000:Interactions of radiation, microphysics and turbulence in the evolution of cirrus clouds. J. Atmos. Sci., **57**, 2463-2479.
Hogan, R. J. and Illingworth, A. J. 2003: Parameterizing ice cloud inhomogeneity and the overlap of inhomogeneities using cloud radar data. J. Atmos. Sci., **60**, 756-767.
Liou, K.-N., 1986: Influence of cirrus clouds on weather and climate processes: A global perspective. Mon. Weather Rev., **114**, 1167-1199.
Liu, H.C., Wang, P.K. and Schlesinger, R.E., 2003: A numerical study of cirrus clouds. Part II: Effects of ambient temperature, stability, radiation, ice microphysics, and microdynamics on cirrus evolution. J. Atmos. Sci., **60**, 1097-1119.
Smith, S.A. and Jonas, P.R., 1996: Observations of turbulence in cirrus clouds. Atmos. Res., **43**, 1-29.
Starr, D.O'C., Benedetti, A., Boehm, M., Brown, P.A., Gierens, K.M., Girard, E., Giruad, V., Jakob, C., Jensen, E., Khvorostyanov, V., Koehler, M., Lare, A. Li, R., Maruyama, K., Montero, M., Tao, W., Wang, Y. and Wilson, D. 2000: Comparison of cirrus cloud models: A project of the GEWEX cloud systems study (GCSS) working group on cirrus cloud systems. 13th ICCP , Reno, Italy, 1-4.
Tompkins, A.M. 2002: A prognostic parameterization for the subgrid variability of water vapour and clouds in large-scale models and its use to diagnose cloud cover. J. Atmos. Sci., **59**, 1917-1942.
Turner, J.S., 1973: Buoyancy effects in fluids, Cambridge monographs of mechanics and applied mathematics.
Wilson, D. and Gregory, D., 2003: The behaviour of large-scale model cloud schemes under idealized forcing scenarios., Q.J.R.Meteorol. Soc., **129**, 967-986.

CLOUD PHASE STRUCTURE (parameterization, experimental problems)
14TH INTERNATIONALCONFERENCE ON CLOUDS AND PRECIPITATION

I.P.Mazin

Center for Earth and Space Research, George Mason University, Fairfax, Virginia

1. INTRODUCTION

The cloud phase structure (*CPS*) is one of the most important cloud characteristics. Time is coming for an improved and more reliable *CPS* parameterization in numerical models. Here *CPS* will be characterized by the fraction of ice w_i in the total water content $w_T=(w_i+w_T)$. This value is called *Cloud Phase Index of the third order* $(CPI)_3$.. (Korolev, 1998; Mazin. 1998; 2001).

$$(CPI)_3 = \frac{IWC}{LWC+IWC} = \frac{w_i}{w_w+w_i}.$$

Liquid clouds have $(CPI)_3$=0, *ice* or *glaciated* ones have $(CPI)_3$=1. In *mixed* clouds $0<(CPI)_3<1$. The phase structure in a small part (in a parcel) of a cloud we will call "*local cloud phase structure, LCPS*". The most extensive *CPS* investigations are described in Borovikov and Mazin (1975) and Korolev et al. (2003). These data are reanalyzed here and a parameterization of *CPS* in numerical models is suggested.

2. *CPS* DATA (BOROVIKOV AND MAZIN, 1975; KOROLEV *ET AL.*, 2003)

Borovikov and Mazin (1975) summarized the observational results obtained in the former Soviet Union at aircraft sounding network (*ASN*) operated in 1957-1963. About 55,000 soundings in more than 40,000 clouds had been carried out in that time and more than 70,000 observations of *CPS* had been registered. The quality of these observations was not very high. But the huge amount of collected data, in spite of many reservations, is still of great important. More detailed observations (Korolev et al., 2003) supported some conclusions obtained by Borovikov. The diagram (Fig.1) illustrates the dependence of liquid, mixed, and ice structure frequency of occurrence on temperature in the ensemble of ASN data (bold black lines). Factors, besides temperature, were not accounted for.

Dashed lines indicate the temperature dependence of frequency of occurrence of ice clouds (F_i (T) - areas above upper lines) and of liquid clouds (areas below lower lines) for different cloud types.

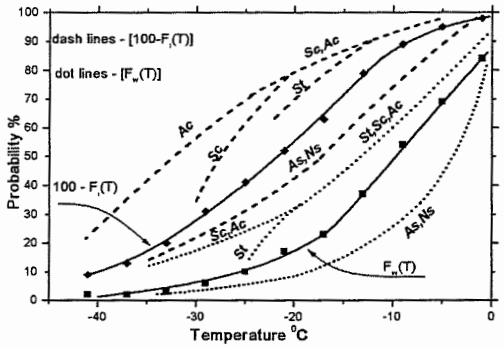

Fig 1. Black lines $F_w(T)$ and $F_{w+m}(T)$ stand for all clouds (Borovikov and Mazin, 1975). Grav lines stand for different cloud

It is seen that the frequency of occurrence of different CPS depends not only on the temperature but on the cloud type as well. All clouds clearly fell into two groups. In one of them (St, Sc, and Ac) the liquid phase occurred more frequently and ice phase less frequently than in the other (As and Ns) group at the same temperature. The authors supposed that it could be caused by the ice particles falling from above, which happens more often in the As and Ns. The differences among the CPS dependencies on temperature in different regions and seasons were insignificant.

The Canadian researchers (Korolev et al., 2003) used different technique to judge about cloud phase structure. They estimated the total (w_T) and the liquid (w_w) water contents using Nevzorov's probe. The scales of averaging (the length of the samples) were about 100m. Large amount of accumulated data allowed them to study the dependence on temperature of the relative amount of the ice mass in individual samples. Korolev kindly provided me with the data shown in the Tab. 1. Here the density of distribution of $(CPI)_3$ at different temperature is presented. When measured values of water content exceeded the threshold values (about 3×10^{-3} g/m^3), the errors in w_T and w_w, according to the authors' estimates, were not exceeding 10÷15%. The accuracy of determining $(CPI)_3$

values was about 0.1. We plotted cumulative distributions of $(CPI)_3$ for different temperature and extrapolated the curves for different T to

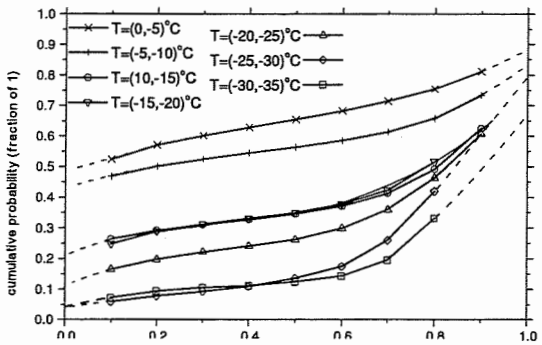

Fig.2. The cumulative distribution of *(CPI)₃*. Markers show the data from Table1

$(CPI)_3=0$ in the left part and to (CPI3=1 in the right part (Fig.2).

The intersection of each curve at a given temperature with the axis $(CPI)_3=0$ indicates the relative frequency of occurrence $F_w(T)$ of the liquid phase. The intersection with axis $(CPI)_3=1$ indicates the 100% minus the relative frequency of occurrence $F_i(T)$ of the ice phase structure. The difference between these intersections is equal to the relative frequency of occurrence of a mixed phase structure at a given temperature (here mixed structure relate to areas where droplets and ice particles coexist.) In the right-hand part of the figure, where $(CPI)_3>0.8$, the cumulative distribution is sharply increased. It is a very interesting phenomenon, which worth more thorough investigation.

Table 1. The density of the *(CPI)₃* frequency of occurrence in different temperature intervals. (Square brackets mean that the corresponding boundary is included in the interval)

	(CPI)₃										
	.0-.1)	[.1-.2)	[.2-3)	[.3-4)	[.4-5)	[.5-6)	[.6-7)	[.7-.8)	[.8-.9)	[.9-1.0	Σ
T °C	Frequency of occurrence (in fraction of one)										
0 –5	.525	.046	.031	.027	.026	.028	.032	.040	.057	.188	1.000
-5-10	.469	.033	.023	.020	.019	.022	.029	.044	.075	.265	0.999
-10-15	.264	.028	.019	.017	.018	.026	.042	.078	.134	.373	0.999
-15-20	.249	.040	.024	.019	.018	.028	.046	.092	.161	.324	1.001
-20-25	.166	.032	.024	.020	.020	.037	.062	.103	.144	.391	0.999
-25-30	.059	.019	.015	.016	.028	.038	.085	.160	.210	.370	1.000
-30-35	.073	.021	.012	.006	.013	.019	.052	.136	.222	.446	1.000

3. COMPARING DATA

There are some noticeably differences between the two sets of data. At least partly this discrepancy may be explained by the CPS dependence on the cloud types whose distribution varies over the compared cloud ensembles. (It is impossible to check it because there is no data about cloud types in Korolev et al.,2003.) The difference in measuring techniques and in the scales of averaging may also have mattered, but we cannot estimate their influences quantitatively. Taking into account the obtained results and keeping in mind that in the interval (-5; -30)°C and when $(CPhI)_3$ <0.8 the Korolev's et al. (2003) data are most reliable, we drew in the Fig.3 smoothed curves for $(CPI)_3=0$ (lower dashed curve) and $(CPI)_3=1$ (upper dashed curve). Presented curves (if observations are not divided according to the cloud types) approximate average dependencies on temperature of the frequency of occurrence of the liquid and ice phase structures.

The geographical effects are hardly responsible for more than 10÷15% deviation from these curves. Here the scale of averaging is about 100m. The increase of the scale of averaging

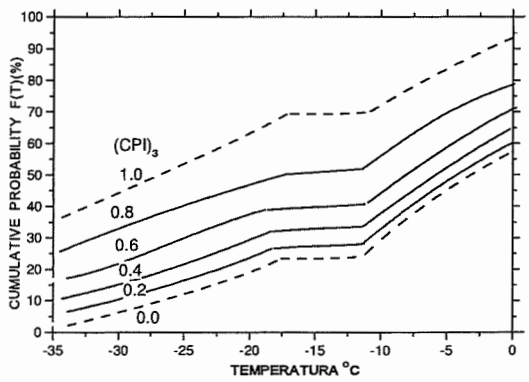

Fig.3. Parameterized dependence of cumulative frequency of *(CPI)₃* occurrence on temperature. Solid lines are given for the intermediate $(CPI)_3$ values.

evidently leads to an increase of the frequency of mixed phase occurrence. In the temperature interval from –12.5 to –17,5°C the distributions of

$(CPI)_3$, actually coincide. Why in that specific temperature interval the cumulative frequency of $(CPhI)_3$ occurrences does not depend on temperature is not quite clear. Some hypotheses are speculated in (Mazin, 2004).

The results of measuring $(CPI)_3$ in different regions where different techniques were used are rather close to each other. This fact increases our confidence in the conclusion that the *CPS* mainly depends on temperature. The dependence changes with changing the scale of averaging. *Additional studies are needed to find the connection between the phase structure and the temperature for different types of clouds and different scales of averaging.*

Procedure of averaging the observational data collected in many clouds and, moreover, the interpretation of the obtained average characteristics must be handled with extreme care. *Generally speaking, the averaged data of $(CPI)_3$ obtained in specific cloud ensembles could not be applied to a separate individual cloud without additional assumptions.* The problem of averaging in cloud physics and particularly of averaging *CPS* data discussed in Mazin, (2004). Comparing summarized observational data obtained in thousands of clouds mainly of stratiform types in mid-latitudes of the former Soviet Union with the results obtained in another region and another techniques allows us to think that situation is not so hopeless. At least today it is reasonable to adopt a hypothesis that the relative fraction of the stratiform cloud space with one or another phase structure is the same if the comparing ensembles of clouds are large enough. We think that it is appropriate to follow that hypothesis until sufficient experimental results will argued against it.

3. PARAMETERIZATION OF THE STRATIFORM CLOUD PHASE STRUCTURE

In real life the experimentalists classify *CPS* as *liquid* if $(CPI)_3$ is close to 0 (not necessarily equal to zero) and as *ice* if it is close to 1. Such a classification makes sense because the physical properties of clouds in these cases are determined by their liquid or ice fraction, respectively. Thus, we, like the above-mentioned authors, will distinguish three local phase structures (Table 2). The data in the Table 2 are satisfactorily approximated by a linear dependence, $F_k(T)=A_k+B_kT$, with standard deviations about 5%. The index k stands for, respectively, w (liquid), m (mixed), and i (ice).

Table 2. Frequency $F_k(T)$% of occurrence of *"liquid"*, *"mixed"*, and *"ice"* phase in stratiform clouds (based on data in Tab. 1).

T °C	*"liquid"* $(CPI)_3$<.1	"mixed" .1<$(CPI)_3$<.8	"ice" $(CPI)_3$ >.8
0, –5	52.5	23,0	24.5
-5,-10	46.9	19,0	34.1
-10,-15	26.4	22.8	50.8
-15,-20	24.9	26.7	48.4
-20,-25	16.6	29.8	53.6
-25,-30	5.9	36.1	58.0
-30,-35	7.3	26.0	66.7

We take into account Borovikov's data (the probability of ice clouds at T>-25 °*C* is lower, but those of mixed and liquid ones are somewhat higher than the probability obtained by Korolev et al.). Thus, we changed slightly the coefficients A_k and B_k obtained according to the Table 2. For stratiform clouds in the interval $0>T>-30°C$ we recommend the linear parameterization of F_k with A_k and B_k. given in Table 3. (See Fig. 4)

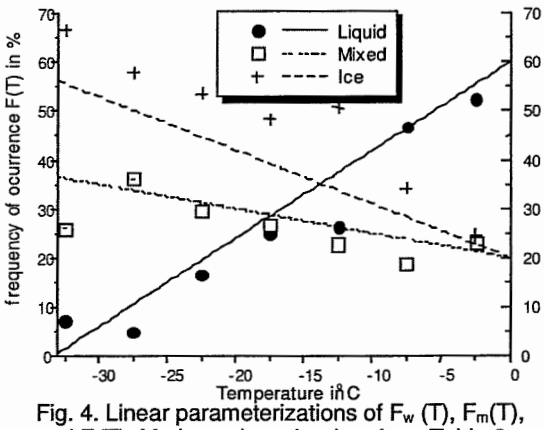

Fig. 4. Linear parameterizations of F_w (T), F_m(T), and F_i(T). Markers show the data from Table 2.

Table 3. A_k and B_k in $F_k(T)=A_k+B_kT$. Here F is in %, T in °*C*.

k	A_k	B_k
w	60	1.6
m	20	-0.5
i	20	-1.1

For using the lognormal parameterization (Mazin, 2004) there is not enough experimental data.

4. FINAL REMARKS AND CONCLUSIONS.

It is evident that the local phase structure depends of the scale of averaging and can be quite inhomogeneous. When speaking about *CPS* it is necessary to distinguish the *local*

phase structure and the *phase structure* of an entire cloud. Unambiguous and clear terminology and its uniformity are of principal importance in considering this problem. In each publication the term *local* need to be clearly defined and the scale of averaging must be indicated.

This work allowed us to come to the following conclusions:

A 1. Comparison of Borovikov's data obtained over former Soviet Union territory with the data of Korolev et al. (2003) obtained in the West hemisphere shows that the geographical effect is not very strong. In clouds with temperatures higher than -10°C and specifically near 0°C it probably leads only to a slight decrease of the frequency of occurrence of the liquid structure in the Western Hemisphere.

2. At any temperature the local phase structure in stratiform clouds (if the length of considered local parcels is about 10^2 m or less) in the most parts of cloud space (in about 70±5%) is single-phase. In fact, only the relative volumes of liquid and ice structures change and the fraction of the mixed phase is about 30% on average and does not change very much with temperature. The space occupied by the liquid structure in clouds is about 60 % of their volume at 0°C, and less than 5% at -30°C. The opposite is true for the ice structure, occupying less than 10% at 0°C and about 60% at -30°C. With increasing the scale of averaging the frequency of occurrence of the mixed phase also increases. These figures are somewhat different for different cloud types. In the wave clouds (Sc, Ac) the probability to find liquid clouds increases and to find ice clouds decreases, in comparison to the values mentioned above. In Ns and As types of clouds this is reversed, liquid clouds are found less and ice clouds more often.

3. The temperature interval (about -12÷-17°C) falls out from the general regularity of gradually changing $(CPI)_3$ with temperature. This unexpected fact maybe not accidental and worth more thorough studies. There are no experimental data to judge about the average local $(CPI)_3$ distribution in a single cloud and we do not know if it coincides with the average distributions for a large amount of the same types of clouds. As a working hypothesis we suggest to accept temporarily that they are the same. A large amount of new observational data is needed to estimate the reliability of such a hypothesis.

B. Suggested parameterization is useful for estimating the role of the uncertainties of the phase structure when solving different applied problems. In this paper a simple linear parameterization of liquid, ice, and mixed phase frequency of occurrence as well as more detailed parameterization of $(CPI)_3$ (Fig.3) are suggested.

The main problems for experimentalists in the coming decade are:

- Studying variability of $(CPI)_3$ in the cloud space and in time and its dependence on temperature, cloud types, and the scale of averaging.
- Getting better understanding of possible shapes of single-phase zones and their size distribution, and also about the scales of the local *CPS* correlation, say, autocorrelation of $(CPI)_3$.

Acknowledgments

I am grateful to A.V. Korolev for providing their data in digital form.

References

Borovikov A.M. and Mazin I.P., 1975: Statistical characteristics of spatial and microphysical structure of clouds. in the Avia-climatological atlas-handbook of USSR. Edited by L.S. Dubrovina, issue 2, part II, v. 1, 127-148; v. 2, 195-226. Moscow, Gidrometeoizdat (in Russian)

Korolev A.V., 1998: About a definition of liquid, mixed, and ice clouds. *Proceedings of the FAA Specialists' workshop on mixed-phase and glaciated icing conditions.* Edited by James T.Riley and Rosemarie McDowall. December 2-3, Atlantic City, NJ, p. 325-326.

Korolev, A.V., Isaac, G.A., Cober, S.G., Strapp J.W., and J. Hallett, 2003: Observation of the microstructure of mixed phase clouds. Quart. J.Roy. Meteor. Soc., 129, 39-66.

Mazin I.P., 1998: Some remarks on mixed phase clouds related to aircraft icing. *Proceedings of the FAA Specialists' workshop on mixed-phase and glaciated icing conditions.* Edited by James T.Riley and Rosemarie McDowall. December 2-3, Atlantic City, NJ, p. 327-332

Mazin I.P., 2001: Cloud classification according to the phase structure. Cloud Phase Index. *Russian Meteorology and Hydrology*, N 11, 5-10.

Mazin I.P., 2004: The phase structure of clouds *Russian Meteorology and Hydrology* , N3. (Accepted for publication)

RETRIEVAL OF CLOUD PHASE AND ICE CRYSTAL HABIT FROM SATELLITE DATA

S. A. McFarlane, R. T. Marchand, and T. P. Ackerman

Pacific Northwest National Laboratory, Richland, Washington, 99352, United States

1. INTRODUCTION

Knowledge of cloud phase (liquid or ice) and crystal habit are of fundamental importance to both remote sensing and climate simulations. Using water droplets instead of ice crystals in retrieving cloud properties from satellite data can lead to errors in retrieval of cloud height, optical thickness, and microphysical properties. Satellite retrievals of cirrus cloud microphysical properties are also influenced by the crystal habit used in the retrieval, either indirectly via an assumed phase function or directly via assumed profiles of ice crystal habits. Realistic treatment of ice cloud radiative and microphysical properties, which depend on crystal habit, is important in climate simulations, especially in tropical anvil regions.

In order to study the variability of crystal habit on a global scale, remote sensing techniques for retrieving crystal habit from satellite instruments need to be developed. The shape of a particle affects the scattering of light such that water droplets and ice crystals of various habits have somewhat different phase functions. Consequently the radiances measured by the Multi-angle Imaging SpectroRadiometer (MISR) instrument (Diner et al., 2002), which observes light scattered from the same cloud at nine different angles, are functions of the crystal shape. In principle, the measured angular radiance pattern can be used to infer the crystal shape. In recent years, several algorithms have been developed to retrieve crystal habit from satellite data at multiple scattering angles (e.g., Baran et al., 1998 and Chepfer et al., 2001). In this work we present initial results from a cloud phase and ice crystal habit retrieval based on a combination of MISR multi-angle measurements in the visible and measurements from the Moderate resolution Imaging Spectroradiometer (MODIS) instrument in the shortwave infrared. The nine angular measurements provided by the MISR cameras allow a wide range of scattering angles to be viewed in a single scene and should provide good sensitivity to particle habit. The presence of the MODIS instrument on the same satellite allows additional information on particle size to be incorporated into the retrievals.

Corresponding author's address: Sally A. McFarlane, Pacific Northwest National Laboratory, P.O. Box 999, Richland, Washington, 99352, United States; E-Mail: Sally.McFarlane@pnl.gov

2. RETRIEVAL ALGORITHM

The MISR and MODIS instruments are both located on the Terra satellite. MISR has 9 cameras with view angles of 0° for the nadir camera and 26.1°, 45.6°, 60.0°, and 70.5° for the forward and aft cameras. Each camera obtains images in four narrow spectral bands. The retrieval is based on reflectance values from MISR channel 1 (centered at .446 μm) due to the low surface reflectance and atmospheric absorption in this channel. A near-infrared MODIS channel (Band 7, centered at 2.1 μm) is also included in the retrieval algorithm. Due to absorption by ice and water particles, reflectance in this channel is primarily a function of particle size, with reflectance increasing as particle size decreases for a given optical depth.

The model reflectance values are calculated using the Spherical Harmonics Discrete Ordinates Method (SHDOM) radiative transfer model (Evans, 1998) in 1D mode. Gaseous absorption is treated with a correlated k-distribution. Rayleigh scattering is included, but aerosol effects are neglected. Single scattering properties of 8 different ice crystal habits are obtained from the calculations of Yang et al., 2000. Bulk scattering properties are obtained by integrating the single scattering properties over a gamma size distribution with a given effective radius and ice water content.

To retrieve particle phase and crystal habit from the MISR and MODIS reflectances, we assume that the dominant phase or habit will be the one that produces the best match between the satellite observations and the model calculations. We define a metric, ξ, which is a measure of the mean relative deviation of the modeled and measured reflectances, to assess how well the modeled reflectances match the observations. This metric is given by

$$\xi(R_e, IWP, H) = \frac{1}{N}\sum_{i=1}^{N}\left[\frac{Sat_i - Mod_i(R_e, IWP, H)}{Sat_i}\right],$$

where N is the number of satellite observations (9 MISR cameras plus MODIS infrared band), Sat_i is the observed reflectance from the given satellite camera, Mod_i is the modeled reflectance, R_e is the effective radius, IWP is the ice water path, and H is the crystal habit. The set of R_e IWP, and H which yields the minimum value of ξ is the retrieved solution. Each satellite observation is weighted equally in the metric.

3. CASE STUDIES

We present two case studies of Terra overpasses: one from the Atmospheric Radiation Measurement (ARM) Program's Southern Great Plains (SGP) site in

Oklahoma and a second from near the Facility for Atmospheric Remote Sensing (FARS) at the University of Utah in Salt Lake City. For each case, we determine cloud boundaries from the ground based instruments and assume a one-layer homogeneous cloud. We average the reflectance for each camera over a 10km x 10km box. For these initial case studies, we ignore the effects of parallax and cloud advection within the MISR observations, although in general these will need to be evaluated carefully.

3.1 Southern Great Plains Case

The first case study is a cirrus cloud that passed over the ARM SGP site on March 6, 2001 (MISR orbit 6471). The ARM millimeter wave radar reflectivity for this day is shown in Figure 1. The dashed line represents the time of the Terra overpass and the black symbols represent cloud base derived from micropulse lidar measurements. The cloud base was approximately 6 km and cloud top was near 10.5 km during the Terra overpass. For this case, the solar zenith angle was 44.6° and the MISR scattering angles ranged from 73.6° to 150.6°. The average optical depth from the MODIS operational retrievals was only 3.5, with a standard deviation of 0.23 and the MODIS average retrieved effective radius was 29.7 μm, with a standard deviation of 1.4 μm. The MODIS IR bi-spectral phase retrieval classified the entire cloud as ice.

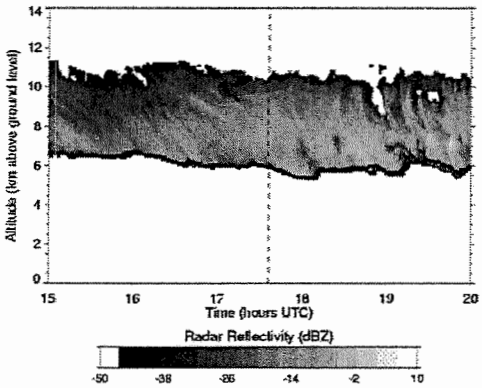

Figure 1. Reflectivity from the ARM radar for the first case study on March 6, 2001.

Figure 2 shows the results of minimizing the mean relative deviation, ξ, between the modeled and measured reflectances for a set of IWP values ranging from 0.005 g/m^2 to 0.2 g/m^2. Each point in Figure 2 represents $\xi(R_e)$, where the IWP and the crystal habit are fixed and the value of R_e which yields the smallest possible value of ξ is plotted against that value of ξ. The same range of IWP is used for all the crystal types and each crystal type is denoted by a different symbol. These results clearly show that water droplets are the worst possible choice to match the MISR reflectance values. This conclusion agrees with the MODIS phase classification. The hollow columns are the best fit to the observed satellite reflectance values. Each particle type shows a clear minimum in the metric, although the location of the minimum for each type varies greatly.

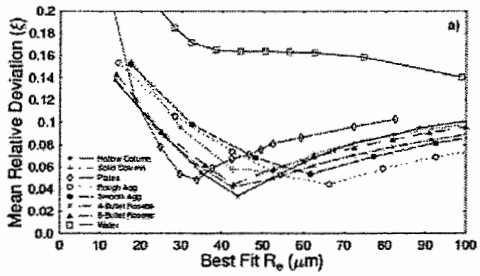

Figure 2. Retrieval metric as a function of best fit effective radius for a range of IWP values for the SGP case.

Table 1 presents the results for the full retrieval in which the metric is minimized to solve for R_e and IWP simultaneously. Hollow columns are the best fit, with a retrieved optical depth of 3.6 and effective radius of 43.2 μm. The retrieved R_e ranges from 32.5 μm for plates to 62.7 μm for rough aggregates and the retrieved optical depth ranges from 2.6 for aggregates to 5.7 for plates. The large differences in the retrieved R_e and τ show that using the correct crystal habit is extremely important in the remote sensing retrievals. Also included in Table 1 are the average MODIS retrievals over the 100 km^2 box centered on the SGP site. The MODIS retrieved IWP and R_e are smaller than any of the MISR retrievals, while the MODIS optical depth is similar to that retrieved using hollow columns. We also retrieve properties of the cloud from the ARM millimeter wave radar using a reflectivity-Doppler moments retrieval algorithm based on the method of Mace et al. (2002). The retrieved values from the radar algorithm, assuming hollow columns, are shown in the bottom row of the table. The retrieved optical depth agrees very well with the MISR and MODIS values, while the radar retrieved effective radius and ice water path are somewhat higher. The radar effective radius profile shows that effective radius decreases in the top 2 km of the cloud. The satellite retrievals are likely more sensitive to the top of the cloud, which may explain the differences in the retrieved effective radius.

3.2 Facility for Atmospheric Remote Sensing Case

Currently there are no cases available at the SGP site in which in situ observations of crystal habit are coincident with a MISR overpass. However, in situ observations were taken by the SPEC Learjet in a cirrus cloud which passed over the FARS site just off the edge of a MISR swath on November 12, 2001. The Polarization Diversity Lidar at the FARS site indicates that the cloud base and top heights were fairly consistent around 9 km and 12 km, respectively, over the period 18:30 to 21:10 UTC.

The aircraft observations were made between 17:57 and 22:13 UTC at roughly 40.8 N, 112 W. Based on radiosondes launched from Salt Lake City at 12:00 GMT on 12 November, 2001 and 00:00 GMT on 13 November, 2001, we estimated the wind speed in the cloud layer to be roughly 25 m/s from a southwesterly direction (239°). This agrees well with the wind speed and direction from the in situ aircraft and the MISR stereo height retrieval, indicating the winds were fairly consistent throughout the region. Based on these wind measurements, a fairly homogeneous cloud region observed at 39.6N, 115W at 19:18 (on the southeastern edge of the MISR swath) would have advected over the FARS site in roughly 3 hours. In this case, the solar zenith angle was 58.0° and there was a very wide range of scattering angles, from 55.1° to 147.9°.

Habit	Metric (ξ)	R_e (μm)	IWP (g/m^2)	τ
Hollow Columns	0.033	43.2	88.3	3.6
Planar Rosettes	0.038	45.1	95.3	3.7
Rough Aggregates	0.041	62.7	103.0	2.9
Spatial Rosettes	0.044	42.5	87.3	3.6
Solid Columns	0.047	47.6	78.8	2.9
Hexagonal Plates	0.047	32.5	107.6	5.7
Smooth Aggregates	0.052	60.0	85.1	2.6
Water Droplets	0.014	100.0	360.0	5.7
MODIS		29.7	77.0	3.5
Radar Retrieval		53.9	110.3	3.4

Table 1. Full retrieval results for the March 6, 2001 cirrus case at SGP. The effective radius and IWP are retrieved simultaneously by minimizing the metric, ξ.

The 1D retrievals for this case using the MISR and MODIS observations are shown in Figure 5. Again, water is the worst fit solution. The two best fits are rough aggregates and smooth aggregates, followed by solid columns and bullet rosettes. The full retrieval results (listed in Table 2) indicate rough aggregates as the best retrieval with a best fit effective radius of 65 μm, optical depth of 2.3 and ice water path of 83.1 g/m^2. Retrievals from a second fairly homogeneous region of the MISR swath at 40.5 N, 115 W (not shown here) also indicated aggregates as the best retrieval type. The average values of the MODIS retrieval in a 100 km^2 box centered on 39.6 N, 115 W are R_e = 24.2 μm, τ = 4.1, and IWP = 71.0 g/m^2. The MODIS retrieval of R_e is significantly smaller than the current retrieval, and the value of τ is higher. The MODIS retrievals assume a size distribution with a mixture of plates, rosettes, and hollow columns when the maximum diameter is less than 70 μm and a mixture of plates, rosettes, hollow columns, and aggregates when the maximum diameter is greater than 70 μm.

Habit	Metric (ξ)	R_e (μm)	IWP (g/m^2)	τ
Rough Aggregates	0.038	61.9	80.1	2.3
Smooth Aggregates	0.052	57.5	57.9	1.8
Solid Columns	0.058	47.2	53.7	2.1
Spatial Rosettes	0.074	42.4	50.1	2.7
Planar Rosettes	0.082	45.9	73.8	2.8
Hollow Columns	0.110	42.5	49.3	2.1
Hexagonal Plates	0.130	32.5	61.8	3.4
Water Droplets	0.17	68.4	152.6	3.6
MODIS		24.2	71.0	4.1

Table 1. Full retrieval results for the FARS case.

Images from the Cloud Particle Imager (CPI) on the in situ aircraft show a mixture of crystal habits, with the primary types being aggregates and bullet rosettes. Also seen were a few columns and a region of quasi-spherical small particles near cloud top. No plates were seen in the CPI images. Many of the bullet rosettes were not pristine, but were beginning to melt and aggregate together. Although the in situ observations and the MISR overpass were not coincident so it is not possible to unambiguously match the retrievals with the in situ properties, the habit type retrieved from the algorithm is consistent with the type of crystals detected in the in situ observations. The results in Table 2 show that the smallest R_e is retrieved when the ice crystals are assumed to be plates. No plates were observed in the CPI images, and plates are shown to be the worst fit (other than water) to the MISR angular reflectance values. In general, a solution based on nadir reflectance which assumes plates when there are none will underestimate the effective radius and overestimate the optical depth.

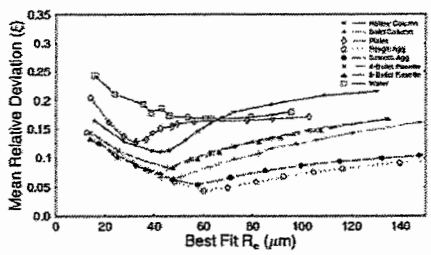

Figure 5. Retrieval results from the FARS case observed on November 12, 2001.

Figure 6 shows the average MISR angular reflectance for the scene as a function of viewing angle. Also plotted is the best fit angular reflectance for plates, liquid water droplets, rough aggregates, and spatial rosettes. Although the aggregates are not a perfect fit to the observed reflectances, they obviously fit the angular characteristics of the scene better than the bullet rosettes (especially for the forward camera

angles), and much better than the plates and water droplets. The inability of the rough aggregates to match the MISR reflectance values at the viewing angles of 26° and 45°, which correspond to scattering angles of 64° and 76.5°, respectively, could be due to a wide range of effects including issues with parallax or cloud advection in the MISR images, variation of the actual crystals from the idealized geometry used in the scattering calculations, or the existence of other habit types within the cloud.

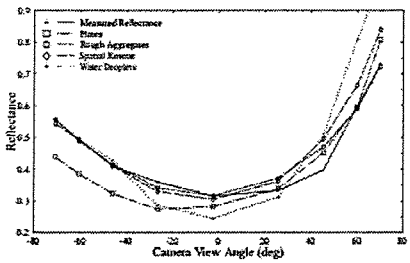

Figure 6. Modeled and observed angular reflectance for the FARS case.

4. CONCLUSIONS

We have presented a new retrieval for cloud phase and crystal habit from MISR and MODIS reflectance values. The case studies presented here demonstrate that we are able to discriminate cloud phase using the MISR angular measurements alone. Since there is currently no phase retrieval from MISR observations, and this method is considerably different from that used in the MODIS phase retrieval, comparisons between the two methods should be instructive in studying mixed phase or multi-layer clouds.

By combining MISR and MODIS measurements, we are able to infer the crystal habit, effective radius and optical depth simultaneously for ice clouds. The initial tests of the algorithm are quite promising. In the first case study, however, the distinction between the retrieved types was fairly small. Future work involving vertical cloud structure, corrections for cloud parallax, and investigations of mixtures of particle habits may improve the results.

The retrieved values of crystal habit and Re will in general only be representative of the particles near the top of the cloud. Simulations, as well as comparisons with in situ data, should be performed to determine whether the retrieval is sensitive to vertical structure in the cloud and to what depth within the cloud the retrieved properties are valid.

Comparison to semi-coincident in situ observations indicates that the retrieved habits are reasonable and consistent with the observations. Future cases of coincident in situ observations for validation will greatly help in assessment of the retrieval. The range of effective radius and optical depth retrieved from the observations using different habits shows the strong dependence of retrieved microphysical parameters on assumed habit, which has implications for current retrievals of cirrus properties from satellite data and ground based radar observations. Comparisons with the MODIS size retrievals for the final case study suggest that the inclusion of hexagonal plates in the MODIS cirrus size distributions might not be valid for all clouds, and might bias the retrieved particle sizes. Future studies will help determine when the MODIS size distributions are applicable.

REFERENCES

Baran, A.J., P.D. Watts, and J.S. Foot, 1998: Potential retrieval of dominating crystal habit and size using radiance data from a dual-view and multiwavelength instrument: A tropical cirrus anvil case. *J. Geophys. Res.*, **103,** 6075-6082.

Chepfer, H., P. Golub, J. Riedi, and J.F. De Haan, 2001: Ice crystal shapes in cirrus clouds derived from POLDER/ADEOS-1. *J. Geophys. Res.*, **106,** 7955-7966.

Evans, K.F., 1998: The spherical harmonics discrete ordinate method for three-dimensional atmospheric radiative transfer. *J. Atmos. Sci.*, **55,** 429-446.

Mace, G.G., A. J. Heymsfield, and M. R. Poellot", 2002: On retrieving the microphysical properties of cirrus clouds using the moments of the millimeter-wavelength Doppler spectrum. *J. Geophys. Res.*, **107,** doi:10.1029/2001JD001308.

Yang, P., K. N. Liou, K. Wyser and D. Mitchell, 2000: Parameterization of the scattering and absorption properties of individual ice crystals. *J. Geophys. Res.*, **105,** 4699-4718.

LABORATORY MEASUREMENTS OF HETEROGENEOUS ICE NUCLEATION: CONTACT NUCLEATION INSIDE-OUT

Y. Mi[1], A.J. Durant[2], and R.A. Shaw[1]

[1]Department of Physics, Michigan Technological University, Houghton, Michigan 49931, USA
[2]Department of Geological Engineering and Sciences, Michigan Technological University, Houghton, Michigan 49931, USA

1. INTRODUCTION

Cloud processes (e.g., lifetime and radiative properties), especially those in cirrus, are sensitive to the competing effects of heterogeneous and homogeneous ice nucleation (Pruppacher and Klett 1997). Tropical cirrus also may be affected by perturbations to the background aerosol, for example due to large volcanic eruptions. Furthermore, the dynamics of volcanic plumes, which are relevant to human health and safety on short time scales and to climate on longer time scales, can be sensitive to the formation of ice (Rose et al. 1995). In order to understand how ice forms in meteorological and volcanic clouds, we have devised a laboratory experiment for studying the mechanisms of heterogeneous ice nucleation, with specific attention given to ice formation on volcanogenic particles. The statistical nature of heterogeneous ice nucleation can yield clues about the physical mechanisms responsible for ice formation. Using a laboratory system capable of measuring the freezing temperature for a single ice nucleus hundreds of times we have obtained detailed estimates of the probability density functions for freezing time (or temperature). The pdf's can be compared to the idealized inhomogeneous Poisson process based on the classical model of heterogeneous ice nucleation. Finally, we have used the laboratory measurements to guide the representation of the ice formation process in a model of volcanic plume dynamics. The laboratory measurements have implications for ice formation in cirrus and volcanic clouds, but here we will concentrate on the broader phenomenon of heterogeneous liquid-solid nucleation.

Corresponding author's address: Raymond A. Shaw, Dept. of Physics, Michigan Technological University, 1400 Townsend Drive, Houghton, MI 49931; E-mail: rashaw@mtu.edu.

2. STATISTICAL NATURE OF NUCLEATION

Experimentally, we observe the number of frozen drops N_f at a given time. For constant temperature (and liquid volume) we may consider, as an idealized model, that nucleation events occur with *perfect randomness* (events are uncorrelated and are statistically homogeneous) so that the number of nucleation events expected in time t is Poisson distributed (Pruppacher and Klett 1997, chap 9; Shaw and Lamb 1998):

$$p(N)=\frac{(\mathcal{J}t)^N e^{-\mathcal{J}t}}{N!},$$

where $\mathcal{J}$ is the *total* nucleation rate for the system (number of nucleation events per unit time). Then the number of 'surviving' drops after time t is $p(N=0)=1-N_f/N_\circ$, such that:

$$\frac{N_f}{N_\circ}=1-e^{-\mathcal{J}t}.$$

Now, according to classical nucleation theory the nucleation rate is a function of temperature. For constant cooling rate the nucleation rate $\mathcal{J}(T)$ varies in a deterministic (non-random) fashion, and we can therefore consider the random number of freezing events to be given by the inhomogeneous Poisson process (Shaw et al. 2002):

$$p(N)=\frac{\left(\int_0^t \mathcal{J}\,dt\right)^N \exp\left(-\int_0^t \mathcal{J}\,dt\right)}{N!},$$

so that the number of frozen drops is

$$\frac{N_f}{N_\circ}=1-\exp\left(-\int_0^t \mathcal{J}\,dt\right).$$

With this theory as motivation, we have designed an experiment to obtain large numbers

of observed freezing events for a single ash particle (this avoids variations in composition, size, morphology, etc., and is the closest we can come to a true ensemble). The purpose is to evaluate the statistical nature of the freezing process, and therefore determine whether the Poisson process model is valid and, in addition, whether the expected temperature dependence from classical nucleation theory is observed.

3. EXPERIMENT

The experimental approach consists of cooling and freezing a single drop containing the same ice nucleus, many, many times. This is the closest we can come, experimentally, to obtaining a statistical ensemble of freezing events: it avoids the difficulties that arise when many ice nuclei are used, such as variations in composition, morphology, and surface area. This approach is in the spirit of work done by Vonnegut and Baldwin (1984; also see Heneghan et al. 2002). The ice nucleus of interest is placed in a small water drop ($r \approx 10^{-4} - 10^{-3}$ m) of ultrapure water (distilled, deionized, filtered, and UV irradiated), which is then immersed in oil, and rests on a platinum resistance thermometer (see Fig. 1). These components are inside an isothermal copper block, which rests on a Peltier cooler/heater; the entire system is housed in an isothermal chamber.

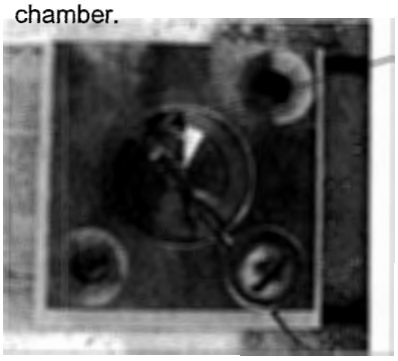

Figure 1: Detail of experimental system, showing the water drop resting on the RTD. The isothermal copper block is resting on the Peltier cooler.

Temperature is decreased linearly with time, with active control to within 0.1 K. When the water drop freezes we detect the enthalpy of freezing directly with the platinum resistance thermometer (see Fig. 2; also see Seeley et al. 1999) The system is fully automated so that we can measure hundreds and even thousands of freezing events on a single ice nucleus.

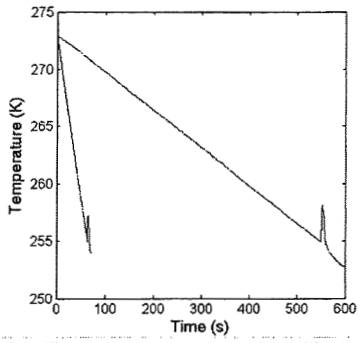

Figure 2. Two cooling curves, illustrating the temperature spikes that are observed when the nucleation event takes place.

Finally, the ice nucleus surface area can be determined through quantitative analysis of SEM stereo pair images of particles investigated in the experiments. This allows us to obtain nucleation rates normalized by nucleus surface area.

4. RESULTS

In this section we illustrate results confirming the robustness of the experimental technique and summarize preliminary results of our experiments. First, in Fig. 3 we have plotted four cumulative probabilities, estimated by counting the fraction of frozen droplets as a function of subcooling temperature. The two middle curves in Figure 4 are for the same ice nucleus in two different water volumes, and confirms that freezing temperature is independent of the drop volume. This is in contrast to most 'bulk water' freezing experiments (e.g., Vali 1971) where the number of ice nuclei presumably is proportional to the volume (see also discussion in chaps. 7 and 9 of Pruppacher and Klett 1997).

Also in Fig. 3 we see that the average subcooling is proportional to the cooling rate, which is in qualitative agreement with classical nucleation theory. The left-most distribution is for the same ice nucleus as the two center distributions, but for cooling rate decreased by a factor of 10. Lastly, the right-most distribution in Fig. 3 confirms that the freezing temperatures for pure water in our system are safely below the observed freezing temperatures for the ice nuclei under consideration.

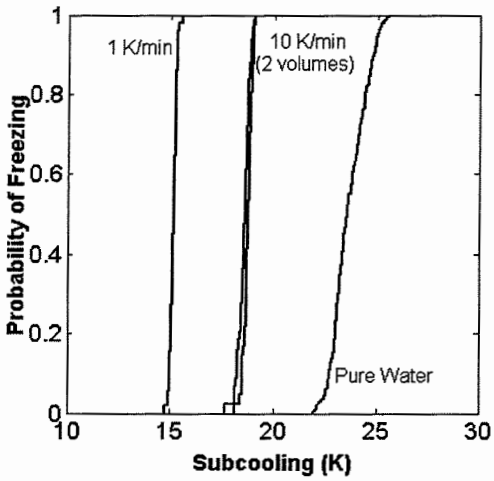

Figure 3. This figure illustrates three concepts. First, the freezing temperature for pure water in the presence of the substrate is below that for the freezing temperatures corresponding to all ice nuclei used in the experiment. Second, for the same ice nucleus, freezing temperature decreases with increasing cooling rate, in qualitative agreement with the classical nucleation theory. Third, the nucleation rate is independent of the volume of water, given that the volumes contain the same ice nucleus (the two water volumes in the figure are approximately 0.5 and 30 μL).

A final observation that was a surprise to us, is the remarkable tendency for the freezing temperature of an ice nucleus to vary between two 'modes' or 'states.' Typically, the freezing temperatures are distributed around some mode, with sporadic, large, positive deviations in freezing temperature. Careful observation has revealed that these positive deviations occur when the ice nucleus migrates within the water droplet (during the repetitive freeze-thaw process) and comes in contact with the water-oil interface. We refer to this as contact nucleation inside-out, and discuss it in greater detail in the following section.

CONTACT NUCLEATION INSIDE-OUT

The enhanced freezing when an ice nucleus contacts the surface of the drop may be a manifestation of surface nucleation (Tabazadeh et al. 2002), so we designed several experiments to investigate the nature of this process. We measured the distribution of freezing temperatures for an ice nucleus in the bulk water only, and at the water-oil interface only. These are the right and left curves in Fig. 4, respectively. The freezing temperature for the surface mode is approximately 5 K higher than that for the bulk-water mode. It should also be noted that the distribution of freezing temperatures is nearly identical in both instances, suggesting that the physical mechanisms for nucleation are not fundamentally different. Finally, in order to understand the influence of the water surface on the nucleation process we devised an experiment in which the water drop is not immersed in oil, but surrounded by air (except for the substrate it rests on). The bulk-water freezing mode is unchanged and therefore is not shown. The surface mode for an ice nucleus at the water-air interface is still enhanced relative to the bulk-water mode, but less so than for the water-oil interface. The distribution of freezing temperatures, however, is strikingly different: it is much broader (see Fig. 4).

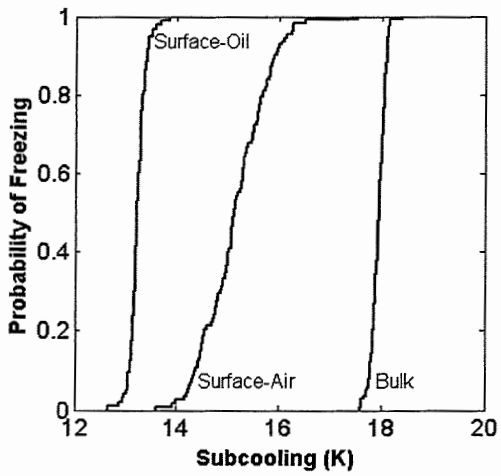

Figure 4. The three curves are for the same ice nucleus in the bulk water volume, away from the droplet surface (right curve), at the droplet surface, immersed in oil (left curve), and at the droplet surface when in air (center curve).

There are at least three common hypotheses for the enhancement in nucleation rate for contact nucleation relative to immersion freezing (see Pruppacher and Klett 1997, chap. 9 for more detail). Briefly they are: 1) partial solubility of the ice nucleus; 2) incomplete adsorption upon contact; 3) movement of water-air interface. Our data can be explained by none of these mechanisms. The first and second mechanisms are rejected outright because the ice nucleus is already immersed in the droplet. Simlarly, the

third mechanism is unlikely because in our experiments there is no rapid movement or collision of the ice nucleus with a droplet. Furthermore, a fourth hypothesis related to the enhancement of contact nucleation relative to deposition nucleation does not apply here because in all cases the ice embryo is being created in the supercooled water, and not in the vapor (Pruppacher and Klett 1997, page 340).

Our data do support the hypothesis that there are distinct interfacial and bulk nucleation rates for water, as suggested by Tabazadeh et al. (2002). That work was related to homogeneous nucleation, but can be adapted to heterogeneous nucleation, at least qualitatively. Specifically, we speculate that the total nucleation rate $\mathcal{J}$ is the sum of a nucleation rate corresponding to the interaction of bulk water with the ice nucleus (J_B) and a nucleation rate corresponding to the interaction of water at the surface of the drop (i.e., interfacial water) and the ice nucleus (J_I). The latter, interfacial nucleation rate J_I presumably would depend on whether that interface is water-air, water-oil, etc. Now we write $\mathcal{J} \propto J_B A_{in,B} + J_I L_{in,I}$, with $A_{in,B}$ being the ice nucleus surface area and $L_{in,I}$ being the total linear extent of the water-ice nucleus-air interface. We will rely on additional, ongoing experiments to evaluate this hypothesis.

Ultimately we hope to gain insight from these experiments that will allow us to make general statements about the mechanism for contact nucleation and perhaps, even the fundamental nature of water and its bulk and interfacial properties. At the very least, we have shown that the process of contact nucleation may be more general than previously thought, because of its ability to operate from the inside-out, as well as the outside-in.

ACKNOWLEDGEMENTS

We thank G. Ernst and W. Rose for providing ash samples and for fruitful collaboration on the volcanic aspects of this work. We thank W. Cantrell, A. Kostinski, and A. Tabazadeh for helpful discussions. This research was supported by NASA NIP (NAG-10568) and NSF (ATM-9984294).

REFERENCES

Heneghan, A. F., P. W. Wilson, and A. D. J. Haymet, 2002: Heterogeneous nucleation of supercooled water, and the effect of an added catalyst. *Proc. Nat. Acad. Sci.*, **99**, 9631-9634.

Pruppacher, H. R., and J. D. Klett, 1997: Microphysics of Clouds and Precipitation. Kluwer Academic Pub., see chaps. 7 and 9.

Rose, W. R., et al., 1995: Ice in the 1994 Rabaul eruption cloud: Implications for volcano hazard and atmospheric effects. *Nature*, **375**, 477-479.

Seeley, L. H., G. T. Seidler, and J. G. Dash, 1999: Apparatus for statistical studies of heterogeneous nucleation. *Rev. Sci. Inst.*, **70**, 3664-3667.

Shaw, R. A., and D. Lamb, 1998: Homogeneous freezing of evaporating cloud droplets. *Geophy. Res. Lett.*, **26**, 1181-1184.

Shaw, R. A., A. B. Kostinski, and M. L. Larsen, 2002: Towards quantifying droplet clustering in clouds. *Quart. J. Roy. Met. Soc.*, **128**, 1043-1057.

Tabazadeh, A., Y. S. Djikaev, and H. Reiss, 2002: Surface crystallization of supercooled water in clouds. *Proc. Nat. Acad. Sci.*, **99**, 15873-15878.

Vali, G., 1971: Quantitative evaluation of experimental results on the heterogeneous freezing nucleation of supercooled liquids. *J. Atmos. Sci.*, **28**, 402-409.

Vonnegut, B., and M. Baldwin, 1984: Repeated nucleation of a supercooled water sample that contains Silver Iodide particles. *J. Clim. Appl. Meteor.*, **23**, 486-490.

ON A NATURE OF FORMING OF THE GLORY IN CLOUDS

Anatoly N. Nevzorov

Central Aerological Observatory, Russia

1. Introduction

The glory as classically defined is an optical phenomenon in the form of iridescent ring surrounding the observer's shadow against sunlight on a cloud top. As any cloud-formed optical phenomenon, the glory carries certain information on the cloud microstructure. Unfortunately, the information thereby offered is still far from being deciphered. Few attempts of physical interpretation of the phenomenon were based on laboratory modeling of like optical effect in a warm fog (van de Hulst, 1957), i. e. under conditions unequal to natural ones. Although today's demands and means make the glory to be objectively attractive for a careful study, no serious scientific interest in this phenomenon is actually being shown at present time. That the glory phenomenon deserves more attention of the cloud physicists may be seen from the simplest example. Namely, since it is universally recognized that the glory originates in spherical particles, it would serve for the most objective identification of mixed clouds. Its applications would be expected to extend even further.

Considered here are both a physical nature of the phenomenon and some of information therein consisted on the cloud composition.

2. Description of the phenomenon

The following description of the glory relies on the most detailed of its published descriptions given by Minnaert (1969), author's own observations, and a series of the glory photographs made from a plane. Our description is composed so that the most characteristic details of the phenomenon are selected.

(i) A basic element of the glory is a shining, rather regular ring, consisting of color circles grading into each other. Its geometrical center is positioned on the shadow projection of the observation point and is usually surrounded by a white aureole.

(ii) The radial sequence of the colors in the glory is somewhat similar to that of well-known rainbow, with the red outer edge. Light of the glory is polarized in the same direction as that of the rainbow.

Corresponding author's address:
Anatoly N. Nevzorov, Central Aerological Observatory, Dolgoprudny, Moscow reg., 141700, Russia.
E-mail: an.nevzorov@mtu-net.ru

(iii) In relatively rare instances, the basic ring is surrounded by one or more much weaker colored rings.

(iv) Though the existing notions of the glory relate its visible proportion with droplet sizes, no certain data on this property are widely available. Our estimations were made from the glory photographic images with the standard image of the sun disc (angular radius 0.268°). The result is that the angular radius of nearly middle (yellow) circle of the basic ring varies from case to case between 1.5° and 3.8°.

(v) Both the visible size and the brightness of the glory have a tendency to rise with clouds being more transparent. Contrariwise, the smallest glories are scarcely discernible and pale-colored and occur in most dense clouds.

(vi) The iridescent glory is formed only in clouds having the top temperatures below 0°C, including those traditionally referred to purely ice ones. The cases were met with where the glory was observed within a transparent cloud simultaneously with such ice-formed effects as the undersun and the halo.

3. Versions

Three rival hypotheses of a nature of the glory phenomenon were touched on in the literature and are to be discussed here:

- An effect of the light diffraction on cloud particles,
- A corona of the backscattering from water droplets,
- A scattering bow formed by water droplets.

The most early diffraction version has been seriously negated by van de Hulst (1957), and we cannot but subscribe to his basic arguments. At the same time, the semi-empirical theory of the back corona advanced by him as well as his criticism of the bow version need a revision in light of the modern knowledge of the cloud physics. Besides, the Mie rigorous theory of light scattering by spheres presents new resources to test former notions.

All the following data of the angular scattering function (scattering indicatrix) were computed (in terms of relative units) from the Mie formulas for the light wavelength λ = 0,575 μm (yellow color). For smoothing, the results were averaged over droplet size spectra described by the gamma-distribution of the power 10, right truncated by $2d_m$, where d_m is the modal diameter. As the characteristic droplet size, the root-mean-square diameter $d_2 \approx 1.15d_m$ is hereinafter used.

4. Is the glory a backscattering corona?

Fig. 1 shows the angular scattering functions at angles close to 180°, calculated from the Mie theory for water droplets (refractive index n = 1,33) of different sizes. Each curve contains a peak with its top angle strongly depending on droplet size. The theory reveals no multiply rings claimed by van de Hulst. The peak angles equal to those of the glory correspond to droplet diameters from ~8 μm to ~20 μm. However, the ensuing relation between the visible size and brightness of an elementary ring is in direct opposition to that observed as for the glory phenomenon. The calculations for different $n(\lambda)$ proper to liquid water have shown that the radial sequence of the colors is identical to that of the glory but with far weaker angle dependence.

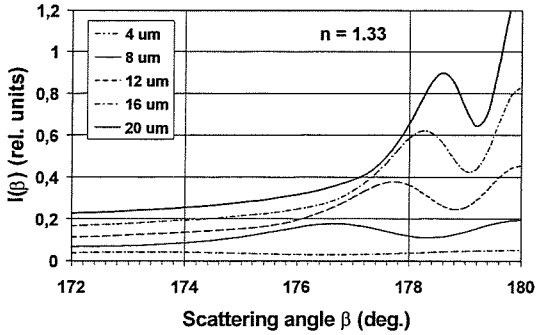

Fig. 1. *The angular functions of relative intensity of the backscattering from droplets of different sizes d_2 of the same concentrations.*

In spite of some formal similarity with the glory, the backscattering peaks produce actually different effect, namely the white aureole around the observer's shadow on the tops of warm clouds. Its corona-shaped image is possible only with very narrow droplet size spectra rather atypical of natural water clouds.

5. The glory as a bow

To refer to the bow version is caused not only by the above rejection of the rest ones. The long-known phenomenon of cloud crystal riming (Pruppacher and Klett, 1978) as well as more recent aircraft measurements (Cober et al., 1996; Mazin et al., 1992) have stated the typical presence in ice-containing clouds of liquid droplets with diameters reaching tens and hundreds micrometers. Nevzorov (1992, 1993, 2000) has found from complex microphysical measurements that the refractive index of those droplets lies between 1.8 and 1.9, and has come to a conclusion that they consist of the water in specific amorphous phase, or A - water. The idea of the bow origin from such kind of particles, capable of existing only at negative temperatures, is in agreement with the last item of the above description.

The visible bow is an image constructed in the observer's eye by certain light rays coming directly from a great number of space-dissipated individual droplets. In reality, observable are the bows formed among the back-scattered light, hence facing both the observer and the light source. The geometrical theory of the bow is presented e.g. by Shifrin (1983). The bow is considered to result from convergence of light rays entering a sphere with the refractive index n from a parallel beam and then leaving it after k internal reflections. The total angle of the turn of the rays forming the k-order bow can be expressed as

$$\gamma^{(k)}(n) = k\pi + 2\arcsin\frac{A}{n} - 2(k+1)\arcsin A, \quad (1)$$

where

$$A = \sqrt{\frac{(k^2+1)^2 - n^2}{k^2-1}}. \quad (2)$$

These rays leave a particle at the angle with the original direction (scattering angle) equal to

$$\beta^{(k)} = \left|\gamma^{(k)} - 2\pi \cdot j\right|. \quad (3)$$

Here $j \geq 0$ is such integer that provides the condition $0 < \beta^{(k)} < \pi$.

As applied to the bow as a visual phenomenon, hereinafter its visible angular radius, or observation angle φ will be used instead of the scattering angle $\beta > \pi/2$:

$$\varphi^{(k)} = \pi - \beta^{(k)} < \pi/2. \quad (4)$$

In case when the dependence $n(\lambda)$ takes place, this results in the dependence $\varphi^{(k)}(\lambda)$ and thereby in the color palette of the bows of all orders.

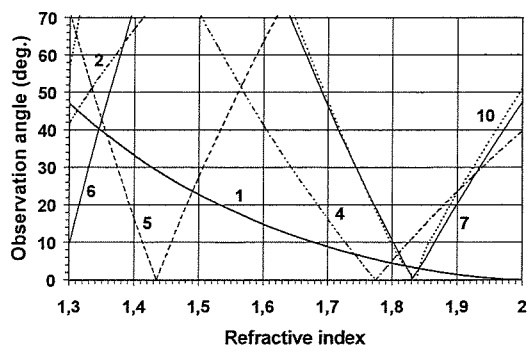

Fig. 2. *Observation angles $\varphi^{(k)}$ of the bows of different orders k (numerals by the curves) against the droplet refractive index n as calculated from the geometrical theory irrespective to droplet size.*

The observation angles of the bows of orders of 1 to 10, calculated from Eqs. (1) – (4), are plotted in Fig. 2 against the refractive index n of scattering spheres. As a support of these theoretical results, at n = 1,33 the mutual angular arrangement of the bows of different orders corresponds to the most complete picture of usual natural rainbow. Thus, the rainbow as a whole consists of four elementary bows of the orders 1, 2, 5, 6.

According to the theoretical results represented in Fig. 2, the actual angle range of the glory (from 1.5° to 3.8°) corresponds to the first order bow from spheres with the refractive index exceeding 1.8. The theory also predicts nearby additional bows of orders 4, 7 and 10. However, all estimations hence issued need corrections for a difference of wave phases of interfering rays, ignored by the geometrical approach. This factor is allowed for by the Mie rigorous theory.

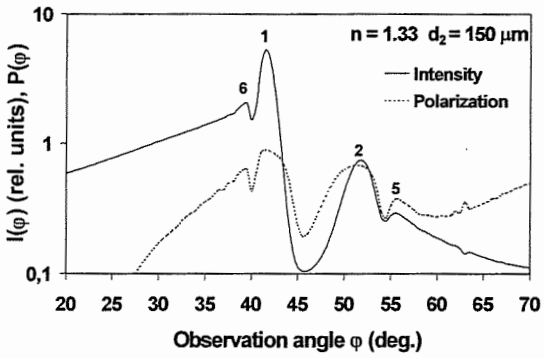

Fig. 3. Angular scattering functions of water droplets with d_2 = 150 μm over the range of the rainbow. The numbers by the peaks denote the bow orders.

To illustrate the reliability of the Mie tool, let us refer again to the example of the rainbow. Fig. 3 represents the angular functions of the intensity, $I(\varphi)$, and of the polarization factor, $P(\varphi)$, of light scattered by the droplets of ordinary water (n = 1,33) with d_2 = 150 μm. The curves exhibit the presence of four distinct peaks corresponding to all bows mapped in Fig. 2, but with angles displaced from their positions in Fig. 2 by ~1° for k = 1 up to 9° for k = 6. These differences increase with droplet size decreasing.

A review of the angular scattering functions calculated at 1.8 < n < 1.9 for d_2 ranging from 4 to 150 μm shows that as d_2 increases, a peak in each curve arises and then becomes higher and narrower as demonstrated in Fig. 4. Its top angle $\varphi_m(n,d_2)$ is at first displaced by ~2° from the curve $\varphi^{(1)}(n)$ of Fig. 2, approaching to this with d_2 increasing.

In Fig. 5 plotted are the curves $\varphi_m(n)$ for different d_2, derived from the curve sets $I(n,\varphi)$ as in Fig. 4. One can see that the "geometrical" curve $\varphi^{(1)}(n)$, also represented in Fig. 5, is the locus of the asymptotes of the peaks angles at $d \to \infty$.

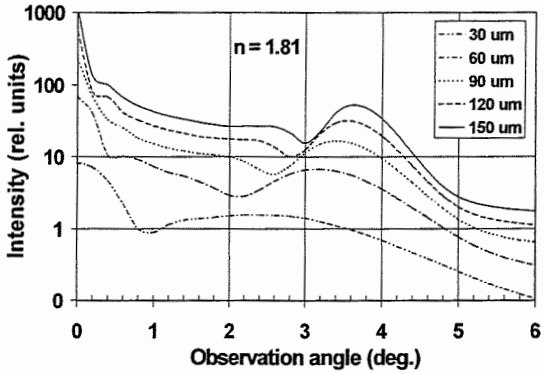

Fig. 4. Deformation of the light scattering peak forming the bow with the droplet size d_2 changing.

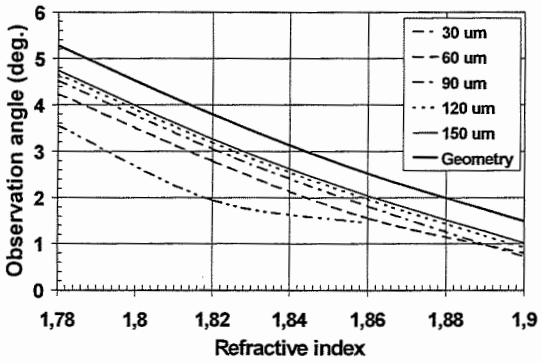

Fig. 5. The bow angle $\varphi^{(1)}$ against the refractive index n calculated from the Mie theory at different droplet sizes d_2 and received from the geometrical theory.

Thus, there is sufficient reason to conclude that the glory (by its classical definition) is the bow formed by spheres with the reflective index much higher than that of the ordinary water. Such spheres existing in cold clouds can be only the droplets consisting of A-water. The Mie theory affirms that both brightness and color contrast of the glory depend directly on sizes of scattering droplets. It can be seen from Fig. 4 that with droplets smaller than 150 μm, the peaks are as wide as comparable with the width of the glory ring. Therefore, the most luminous and sharply multicolored glory can be formed by substantially larger droplets. That such droplets can really occur in cold clouds is certified by Cober et al. (1996) who reported of freezing drizzle droplets reaching almost 0.5 mm in diameter.

Considering all above, one can conclude from Fig. 5 that the natural glories seen at 1.5° to 3.8° radial angle are produced by spheres larger than ~20 μm in diameter with the refractive index lying between 1.81 and 1.82 for the yellow color.

Fig. 4 illustrates the angular functions of intensity around the 1-order bow formed by differently sized droplets with n = 1.81. The width of the glory ring is determined both by the slope of the dependence of the refractive index on the light wavelength and by the width of the droplet size spectrum. In case of wide enough spectra, different colors are mixed within the ring so that its most part other than the red outer edge can look little or not multicolored. One can see that the central aureole is always present in the glory picture, with its width rather weakly depending on droplet sizes.

All attempts have failed to find quite evident signs of the bows of higher orders like those in Fig. 3. This is probably because of smallness of their peaks at $d_2 \leq 150$ μm, or they are so replaced from the position as in Fig. 2 that practically fuse with the central aureole or with the 1-order bow. It is difficult to assume that almost equidistant extra rings surrounding but a part of real glories are the 4-order and 7-order bows formed by substantially bigger droplets. The explanation seems to be more reasonable that they are produced by ice crystals scattering those bow rays that are diametrally opposite to the rays coming directly to the observer. The visible rings stand out against the background-scattered light due to the scattering intensity peaks at definite angles, inherent in ice crystals. The simplest analysis shows that the first extra ring is a possibility when the peak angle is 8° ÷ 9°. In fact, such peak angle responsible for so-called Van Buijsen halo is peculiar to some pyramid-like crystal forms (Volkovitsky et al., 1980). The following rings must be results of consecutive scattering steps to be yet understood.

It is interesting that as calculated from Eqs. (1) – (3), at $n \approx 1.81 \div 1.82$ the forward directed bows of orders 2, 3, 5, 6, 8 and 9 are concentrated between the scattering angles ~40° and ~70°. We believe that such forward bows of least orders are responsible for the effect of irisation of side edges of high clouds exposed to the sunlight, as occurs to be seen from the ground.

6. Conclusion

Presented in this paper are the solutions of two interrelated problems, each of its own significance:

- The optical phenomenon of the iridescent glory is proved to be the bow formed from sunlight rays scattered by spherical particles having the refractive index of 1.81 ÷ 1.82 (for yellow color) and sizes exceeding ~20 μm.
- The convincing corroboration is thereby gained of the existence in cold clouds of liquid water of special phase state, differing in physical properties from the ordinary water and discovered earlier under the term amorphous water, or A-water.

The results here obtained point out that the detailed study of the glory phenomenon is worthy of great interest of the cloud physics, inasmuch as its presences itself as well as its geometrical and photo-chromatic characteristics carry an unique remote information on the phase composition of cold clouds. In particular, the glory observation angle can serve as an indicator of the extent of the right wing of droplet size spectrum.

Acknowledgements. The author is grateful to Dr. Alexander Petrushin for collaboration and to Dr. Alexei Korolev for stimulating discussions as well as for presenting the glory photographs.

References

Minnaert, M., 1969: Light and color in the nature. Moscow, Nauka, 344 pp. (in Russian, translated from English).

Hulst, van de, H. C., 1957: Light scattering by small particles. New York , 570 pp.

Shifrin, K. S., 1983: Introduction to the ocean optics. Leningrad, Gidrometeoizdat, 242 pp. (in Russian).

Cober, S.G., J.W. Strapp, and G.A. Isaac, 1996. A case study of freezing drizzle formed through a collision coalescence process. *J. Appl. Meteor.*, 35, 2250 – 2260.

Mazin, I. P., A. N. Nevzorov, V. F. Shugaev, and A. V. Korolev, 1992. Phase structure of stratiform clouds. *11th Int. Conf. on Clouds and Precipitation, Montreal, Canada*, 332–335.

Nevzorov, A. N., 1992. Permanence, properties and nature of liquid phase in ice-containing clouds. *Ibid.*, 270–273.

Nevzorov, A. N., 1993. Studies into the physics of liquid phase in ice-containing clouds. *Russian Meteorology and Hydrology*, №1, 47–59.

Nevzorov, A. N., 2000. Cloud phase composition and phase evolution as deduced from experimental evidence and physico-chemical concepts. *13th Int. Conf. on Clouds and Precipitation, Reno, Nevada, USA*, 728–731.

Pruppacher, H. R., J. D. Klett, 1978. Microphysics of clouds and precipitation. D. Reidel Publ. Co, 714 pp.

Volkovitsky, O. A., L. N. Pavlova, and A. G. Petrushin, 1984. Optical properties of crystal clouds. Leningrad, Gidrometeoizdat, 198 pp. (in Russian).

MICROPHYSICAL PROPERTIES OF ANVILS OBTAINED FROM AIRCRAFT MEASUREMENTS DURING X-BAIU-02 FIELD CAMPAIGN

N. Orikasa[1] , M. Murakami[1], K. Mori[1], H. Kuroiwa[2] and H. Minda[3]

[1]Meteorological Research Institute, Tsukuba, Ibaraki 305-0052, Japan
[2]Communications Research Laboratory, Koganei, Tokyo 184-8795, Japan
[3]Nagoya University, Nagoya, Aichi 464-8601, Japan

1. INTRODUCTION

Anvils, typically associated with thunderstorms or deep convection system, can affect a significant impact on the radiation balance of the earth. To estimate the radiation budgets properly, the information on their size distributions, crystal habits, and ice water content (IWC) is important to understand the relationships between microphysical and radiation properties. However, both quantity and quality of in situ data on anvil particles are very limited to date (McFarquhar and Heymsfield 1996; Heymsfield and McFarquhar 1996; Heymsfield et al. 2002a). In anvils, there may exist predominant tiny ice particles and it is highly desirable to measure such particles with sufficient accuracy.

We carried out aircraft observations of anvils at southern Japan, as a part of field campaign "East China Sea/Kyushu-BAIU" in June 2002 (X-BAIU-02) (Yoshizaki et al. 2003). One of the purposes in the project is to investigate the inner structures of mesoscale convective systems in Baiu (stationary) front. Such a convective system is accompanied by outflow of cirrus near the core convections. Here we only focused on in situ measurements inside cloud top layers.

In this paper, we present the anvil data measured by in situ instruments which are commonly utilized in aircraft observations and also describe the microphysical characteristics sampled in three cases.

2. DATA OVERVIEW

In June 22, 24, and 28, we flew an instrumented research aircraft (Gulfstream-II) over the Kyusyu southwest ocean. Level flights inside cloud top layers were carried out across Baiu front (100-200 km wide) which moved slowly on each day. Each flight altitude (ambient temperature) was 12.6km (-58C), 13.2km(-61C), 13.2km(-64C), respectively. It is thought that the aircraft often passed through 1-2km below the cloud top, inferred from echo top height and tropopause height.

All microphysical instruments were equipped on the Gulfstream-II; a Particle Measuring Systems (PMS) 2DC, a PMS 2DP, a PMS FSSP-100, and a DMT CAPS probe. We just present the data of 2DC and FSSP, because other instruments did not work sufficiently.

At the high airspeed (Gulfstream-II normally travels at 200 m/s), it is pointed out that estimation of sampling volume in 2DC can have significant uncertainties at detection sizes smaller than ~150μm. Hereafter a $1/D^2$ dependency of depth of field was accounted for particles smaller than 160μm based on the PMS manual. The correction of clock rate was also taken into account in case of TAS > 125 m/s, by adding slice images to reproduce the original particle image.

Corresponding author's address: Narihiro Orikasa, Meteorological Research Institute, Tsukuba, Ibaraki, 305-0052, Japan; E-Mail: norikasa@mri-jma.go.jp.

3. MICROPHYSICAL DATA

3.1 Crystal Habit Classification

Habit classification from the optical array probes was developed among many researchers. Most of the technique was based on the value of area ratio, which is generally the area of a particle divided by the area of its circumscribed circle. However, some area ratio overlaps between different types of particles.

Korolev and Sussman (2002) presented a new algorithm based on the simple geometrical parameter. One advantage is that they introduced two separate parameters for both "complete" and "partial" images from the number of edge pixels.

Another method (unpublished), developed by our group, is compared with the Korolev's method in this study. The flow chart of this algorithm is shown in Fig. 1. We set statistically the range of several factors which were used for classification based on the analysis of each of many ice crystal microphotographs. In two new methods (Korolev, MRI), a tiny particle whose pixels were less than 20 was classified as "Indeterminate".

3.2 Ice Water Content

Based on the above habit classification, we can calculate IWC by the empirical relationships between mass and dimension: "Indeterminate" from Brown and Francis (1995), "Irregular" from the Mitchell et al. (1990), "Column/Needle" from Heymsfield et al. (2002b).

4. RESULTS

4.1 Horizontal Distribution of Ice Crsytal Concentration

Figure 2 shows horizontal distribution of ice crystal concentration sampled on 22 June 2002. All plots except left one in upper panel were measured by the 2DC probe. The number of rejected particles was also plotted in upper panel: "nstrekc" refers to the total number, while "nzeroc" is one of the reject categories which shows particle with zero area (no image).

Shadow-OR counts were plotted in middle panel (right). Their tendency quite resembles the FSSP concentration (upper panel, left) and this was applied to other days. The 2DC concentration on that day was larger than that on other days. Mass-weighted mean diameter (lower panel, left) was typically about 100 μm. In maximum dimension plots (lower panel, right), sometimes particles with sizes larger than 1mm were observed near the core site.

4.2 Size Distributions

Two size distributions by FSSP and by 2DC were compared in each plot in Fig. 3. In Fig. 3(a), quite good agreement was found in both size distributions, while there was a large gap in overlapped size ranges in Fig. 3(c). Poor agreements were sometimes accompanied under coexisting large ice particles like in Fig. 3(b). However that is not the only reason of the discrepancy, similar to the study of McFarquhar and Heymsfield (1996). One possible feature can be found in the number of rejected particles. In Fig. 3(a), relatively strong updrafts were observed at that time. Also on Jun 28 when encountered strongest updrafts among three anvil cases, most of the particles were categorized as rejected.

4.3 Crystal Habit and IWC

A comparison of two habit-classification methods can be seen as time series of IWC (Fig. 4). These two different algorithms made good agreements in IWC estimations.

Figure 5 shows the frequency of classified habit as time series of three cases. 60 to 100 % of particles were "Indeterminate" which was too tiny to distinguish the crystal habit. "Irregular" type was second dominant, however, columnar particles were most dominant in June 28 case by the MRI's method among discriminate types.

Two classification methods had clear difference in mass contribution frequencies in Fig. 6. Based on the MRI's method, the type of bullet rosette could contribute significantly to total IWC.

5. DISCUSSION

Three cases of anvil clouds with low temperatures (about –60C) has been measured with conventional cloud physics probes. It is still unknown and controversial whether such an instrument, like FSSP or 2DC, can reliably detect cirrus particles. Although this study did not include a conclusive statement, rejected particles with the 2DC probe might be a measure that is relevant to this issue, how accurate the 2DC detect tiny particles. Vigorous updrafts, which might cause dominate very tiny particles (<20 μm) or significant amount of coexisting large particles, can be tough conditions in both probes. We did not assess the validity of the FSSP measurements.

A new habit-classification method was proposed in this study. It can be easily improved on the performance in various types of clouds, because the algorithm includes several parameters that are relevant to the shape itself. Such reliable information as shape and IWC derived from empirical relations in each classified type would be necessary to minimize the uncertainty in the radiation budget analysis.

Acknowledgements

This study was supported by CREST of JST (Japan Science and Technology Corporation).

References

Brown, P. R. A. and P. N. Francis, 1995: Improved measurements of the ice water content in cirrus using a total-water probe. J. Atmos. Oceanic Technol., **12**, 410-414.

Heymsfield, A. J., and G. M. McFarquhar, 1996: On the high albedos of anvil cirrus in the tropical Pacific warm pool: Microphysical interpretations from CEPEX and from Kwajalein, Marshall Islands. J. Atmos. Sci., **53**, 2424-2451.

Heymsfield, A. J. and coauthors, 2002a: Observations and parameterizations of particle size distributions in deep tropical cirrus and stratiform precipitating clouds: Results from in situ observations in TRMM field campaigns. J. Atmos. Sci., **59**, 3457-3491.

Heymsfield, A. J. and coauthors, 2002b: A general approach for deriving the properties of cirrus and stratiform ice cloud particles. J. Atmos. Sci., **59**, 3-29.

Korolev, A., and B. Sussman, 2000: A technique for habit classification of cloud particles. J. Atmos. Oceanic Technol., **17**, 1048-1057.

McFarquhar, G. M., and A. J. Heymsfield, 1996: Microphysical characteristics of three cirrus anvils sampled during the Central Equatorial Pacific Experiment. J. Atmos. Sci., **53**, 2401-2423.

Mitchell, D. L., R. Zhang and R. L. Pitter, 1990: Mass-dimensional relationships for ice particles and the influence of riming on snowfall rates. J. Appl. Meteor., **29**, 153-164.

Yoshizaki, M., and coauthors, 2003: A report on field observations of Baiu fronts over East China Sea and Kyushu in 2001 and 2002 (in Japanese). Tenki, **50**, 67-75.

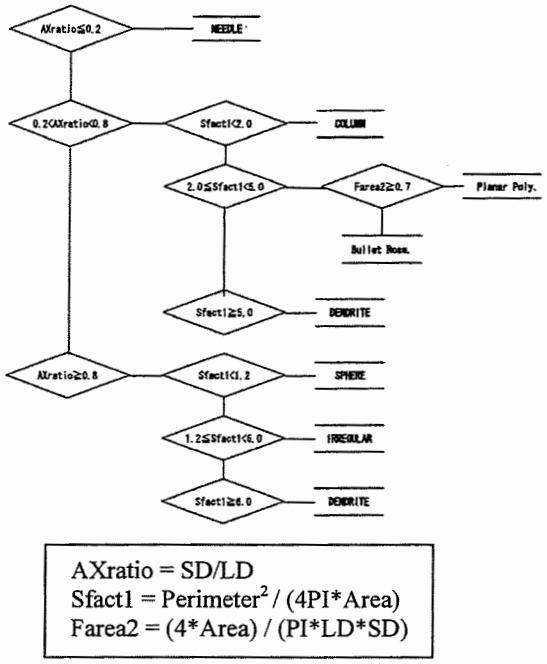

Fig.1 Habit classification developed by the MRI. Seven types are classified in the algorithm.

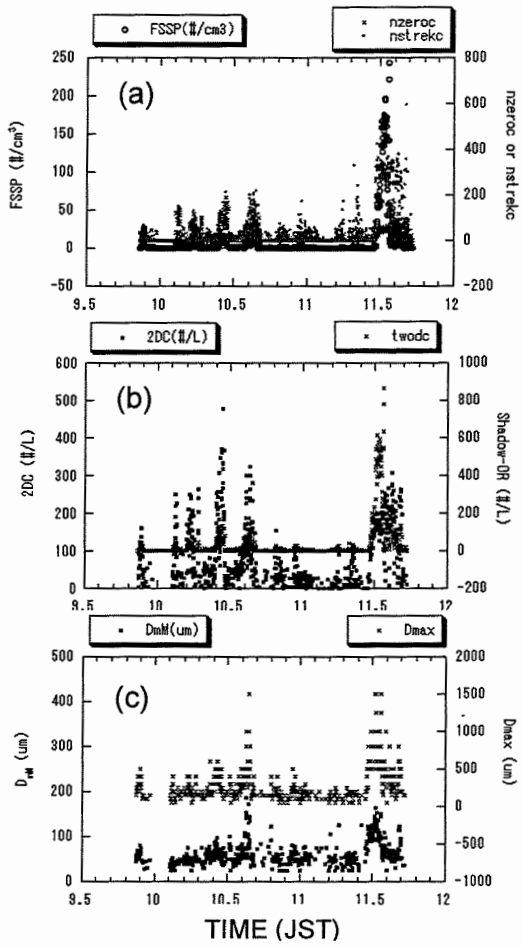

Fig. 2 Horizontal distributions of number concentrations measured by FSSP(panel a, left) and 2DC (panel b, left) sampled on 22 June 2002. In 2DC measurements, shadow-OR counts (panel b, right) and the number of rejected particles (panel a, right) are also plotted. Dimensions are plotted in panel c as mass-weighted mean diameter (left) and maximum diameter (right).

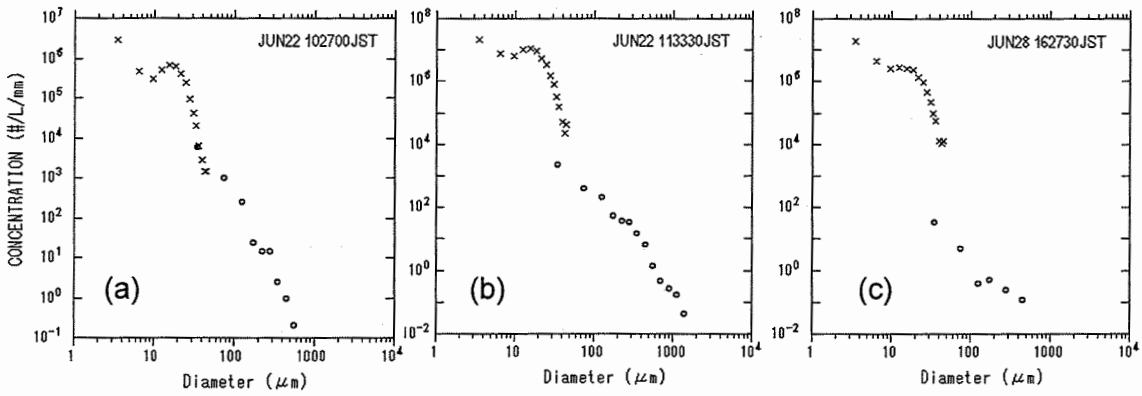

Fig. 3 Examples of size distributions of ice particles. FSSP(cross) and 2DC (circle) data are compared in different sampling time.

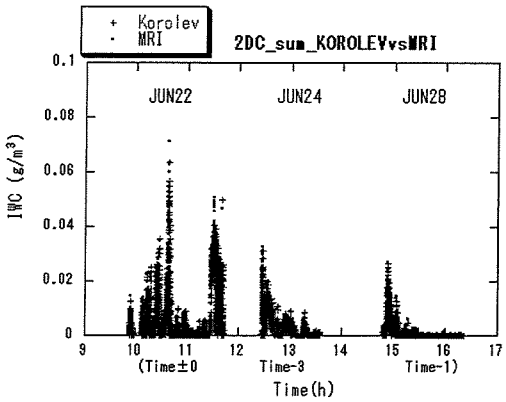

Fig. 4 Time series of derived IWC from habit-classified types in two ways: (a) Korolev's method (plus), (b) MRI's method (circle). The particle image data was obtained from PMS 2DC probe.

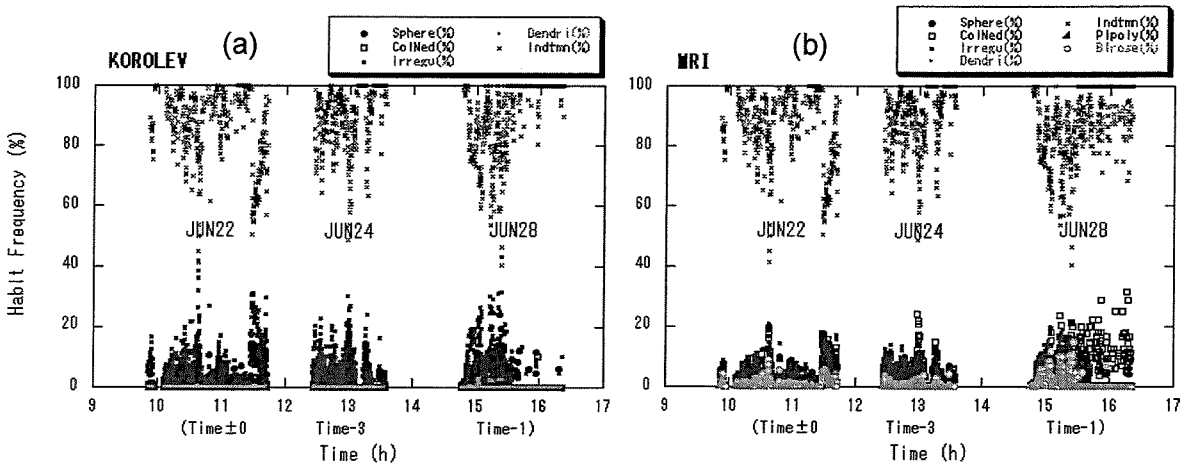

Fig. 5 Time series of presence frequency from habit-classified types in two ways: (a) Korolev's method (left panel), (b) MRI's method (right panel).

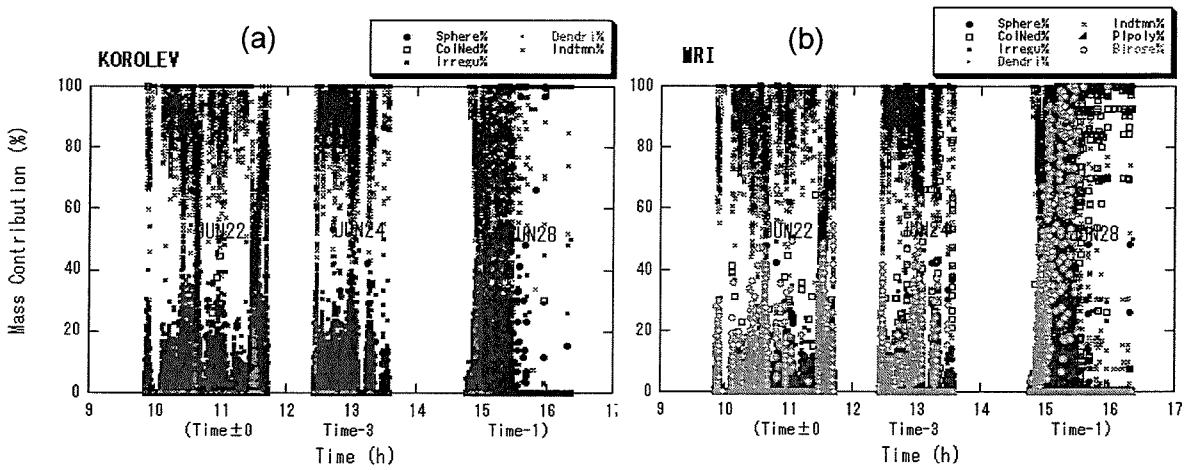

Fig. 6 Same as Fig. 5, but for frequency in mass contribution to the total IWC.

THE IMPACT OF VARIOUS NUCLEATION PROCESSES ON ANVIL GLACIATION ON A CRYSTAL-FACE THUNDERSTORM

V.T.J. Phillips[1], Sherwood, S.[2], Andronache, C.[3], Bansemer, A.[4], Conant, B.[5], Heymsfield, A.[4], Heymsfield, G.[6], Poellot, M.[7] and T. Vanreken[5]

[1] Atmospheric and Oceanic Sciences (AOS) Program , Princeton University, Princeton, USA
[2] Department of Geology, Yale University, Yale, USA
[3]Boston College, Boston, Massachusetts, USA
[4]National Centre for Atmospheric Research (NCAR), Boulder, Colorado, USA
[5] Department of Environmental Sciences and Engineering, Caltech, Pasadena, USA
[6] NASA Goddard Space Flight Centre (GSFC), Greenbelt, USA
[7] University of North Dakota (UND), Grand Forks, USA

1. INTRODUCTION

The Cirrus Regional Study of Tropical Anvils and cirrus Layers – Florida Area Cirrus Experiment (CRYSTAL-FACE) combined measurements of aerosol particles in the troposphere with aircraft observations of Cb clouds and their anvil cirrus. Much cirrus originates from Cb anvils. Globally, cirrus produces a major impact on the radiative budget by:- (1) impacting the upper tropospheric humidity - water vapour is the most important greenhouse gas; and (2) by affecting directly the radiation budget of the climate system by reflection of sunlight to space and the trapping of longwave radiation in the troposphere.

Aerosol particles enabling the formation of activated cloud-droplets (usually referred to as 'droplets') are termed cloud condensation nuclei (CCN). These are emitted by biomass burning and industrial activity, in addition to natural sources such as wave-breaking at sea. Ultimately, CCN may cause the formation of most of the ice particles in the anvil of a Cb storm. All cloud-droplets are nucleated by activation of CCN either at cloud-base ('primary droplet nucleation') or in the interior of the cloud ('secondary droplet nucleation'). Spontaneous ('homogeneous') freezing of all activated drops occurs at temperatures colder than a size-dependent threshold (usually at about -36 degC). Supercooled cloud-droplets and raindrops may also freeze 'heterogeneously' by the activation of IN (a type of 'primary ice nucleation'). Typically a small subset of the population of activated CCN contained inside supercooled drops may act as IN at sufficiently cold temperatures ('condensation-freezing'). In the anvil, unactivated solution droplets (usually referred to as 'haze particles' or CCN) can persist in the supercooled state until they freeze spontaneously at relative humidities intermediate between ice and water saturation ('homogeneous aerosol freezing').

It is expected that microphysical processes occurring in and below the mixed phase region may act to modify the supply to the anvil of frozen and supercooled condensate, of CCN, of IN and of vapour *via* the updraft. Nucleation processes affecting anvil glaciation may not necessarily be confined to the anvil itself.

For the present study, the Explicit Microphysics Model (EMM) is applied to simulate nucleation processes found in a deep convective storm. The EMM was developed by Phillips (2001) and Phillips *et al.* (2001, 2002, 2003). Recent modifications of the EMM have taken advantage of several strands of new research in the literature of cloud microphysics. Firstly, Koop *et al.* (2000) presented a theory for homogeneous aerosol freezing. Secondly, Bott (1998) developed a very accurate scheme for solving the stochastic collection equation. His scheme has been adapted for the variable size-grid framework of the EMM.

In the next Section there is a brief outline of the EMM, including a detailed description of novel features of the model that have enhanced its capability to simulate tropical storms. In Section 3, there is a description of the aircraft observations and how they are used to define the input parameters of the microphysical model. In Section 4, results from sensitivity studies are presented. In the final section some conclusions are presented and discussed.

Corresponding author's address: Vaughan T.J. Phillips, Princeton University, AOS Program, Geophysical Fluid Dynamics Laboratory (GFDL), Princeton, New Jersey, USA; E-Mail: vtp@gfdl.noaa.gov

2. THE MODEL

The EMM is an advanced 1D model with bin microphysics. The size distributions of all types of hydrometeor are explicitly predicted on a variable size-grid. Fully interactive components for vapour, cloud-water, ice and rain, as well as for aggregation of ice,

heterogeneous and homogeneous freezing, melting, simulated radar properties and the evolution of crystal shape (or 'habit') during particle growth are some of the processes incorporated into the EMM by Phillips. Precipitation size-bins are advected in 2-D in the plane that passes through the updraft and downdraft, while cloud-water and vapour are advected in 1-D in the updraft and SCR. An evolving 2-D field of air velocity is prescribed with a simple analytical model, for the tracing of trajectories of hydrometeors.

The dynamical framework of the EMM consists of 1-D vertical channels for the updraft, downdraft and surrounding cloudy region. These channels span the depth of the storm and are divided into many layers of that are about 50 m deep. Each layer has a size distribution associated with it for each type of hydrometeor. Precipitation size categories may fall from one layer to the next, or from one draft to another, following 2-D trajectories traced through the storm. A sequence of thermals initiated at cloud-base ascend through the updraft, as with the model of Blyth and Latham (1997).

In the EMM, there are several basic species of ice particles: (1) homogeneously frozen cloud-ice; (2) primary ice nucleated by condensation/deposition freezing (Meyers *et al.* 1992) between -5 and -30 degC; (3) homogeneously frozen precipitation-particles; (4) H-M splinters emitted from particles in species (2) and (3); and (5) frozen raindrops formed heterogeneously and from collisions with ice in species (2) – (4); and finally, more generations of H-M splinters and raindrops frozen in collisions with these H-M splinters and frozen drops. The observed dependences of the H-M process (Hallett and Mossop 1974) on the riming rate, temperature and droplet size are all represented: 1 splinter is generated for every 200 droplets > 24 μm that are rimed at –5 degC. Homogeneous freezing of droplets in a given size-bin is assumed to be instantaneous, occurring when the temperature falls below the threshold corresponding to their size (see Pruppacher and Klett 1997). The microphysical processes in the EMM are documented in more detail by Phillips *et al.* (2001, 2002, 2003).

There are 33 CCN mass-doubling size-bins, so that droplet nucleation is modeled explicitly. Coalescence and aggregation are represented by solving the stochastic collection equation (SCE) in each layer. Turbulent enhancement of the collision kernels is represented, in the manner of Khain and Sednev (1996). Particle properties, as well as particle number, are transferred between size-bins when the SCE is solved using Bott's method.

3. THE CONTROL SIMULATION

The case simulated by the EMM control simulation is that of the 7th July 2002 from the CRYSTAL-FACE campaign. A vertical profile of the aerosol size distribution was formed from the aircraft measurements, by assuming a power-law CCN activity spectrum. The normalized CCN concentration (at a supersaturation of 1%) was about 1000 cm^{-3} for this activity spectrum. An entrainment rate was selected so as to provide a match of the observed liquid water content with that observed by the Citation aircraft. The peak vertical velocity of about 25 m/s at upper levels measured by the Citation aircraft was used to prescribe the dynamics of the model, while a value of 3 m/s was assumed for the peak updraft speed at cloud-base.

The observed droplet concentration of almost 100 cm^{-3} is adequately predicted. Moreover, there is adequate agreement between the predicted and observed concentration of precipitation-sized particles > 0.5 mm of about 5 L^{-1}.

4. RESULTS FROM SENSITIVITY TESTS WITH EMM

4.1 All Homogeneous Freezing

A run was performed with all homogeneous freezing of droplets, rain and aerosols prohibited (the no-homogeneous freezing case). This run was compared with the control.

The total ice concentration at all levels in the anvil was about three orders of magnitude lower in the no-homogeneous freezing case than in the control. The discontinuity in total ice concentration at the anvil base that had been found in the control was completely eliminated. The ice concentration below the anvil base remained almost unaltered, however. The ice mixing ratio was reduced by about 1 - 2 g/kg at most levels in the anvil in the no-homogeneous freezing case relative to the control. The mixing ratios of rain and cloud-water were increased from zero to values of about 0.1 and 1 g/kg respectively in the anvil when homogeneous freezing was excluded.

About 99.9% of all anvil ice particles are nucleated by homogeneous freezing – mostly of supercooled cloud-droplets at the anvil base – in the control updraft of this particular model cloud. Homogeneously frozen cloud-water also dominates the total mass of ice there.

Consequently, all other nucleation processes can only significantly affect the anvil insofar as they alter the amount of supercooled condensate available for homogeneous freezing in this particular model cloud.

4.2 All Heterogeneous Freezing

A run was performed with all heterogeneous freezing of droplets (ie. primary ice nucleation) and rain prohibited (the no-heterogeneous freezing case).

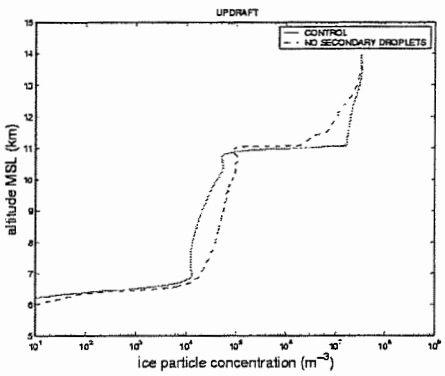

Figure 1. Predicted ice concentration.

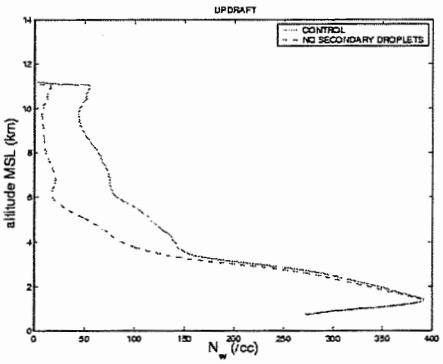

Figure 2. Predicted droplet concentration.

In the mixed phase region below the anvil base, the average concentration and mixing ratio of ice was reduced to zero at all levels in the no-heterogeneous freezing case. This is accompanied by a corresponding increase of 1 – 2 g/kg in the rain mixing ratio relative to the control. In the anvil, the total ice concentration was increased by 40 % relative to the control, due to a similar fractional increase in the concentration of supercooled droplets in the 3 km below the anvil base. The mean ice diameter in the anvil is reduced by about 5 microns in the no-heterogeneous freezing case, due to a lower supersaturation with respect to ice caused by enhanced competition for the available vapour.

In summary, the impact on anvil properties of heterogeneous freezing is much more modest than that of homogeneous freezing, because heterogeneous freezing can only influence the anvil ice concentration indirectly: heterogeneously frozen precipitation sequesters droplets in the mixed phase region by riming, preventing them from freezing homogeneously at the anvil base. Much of this riming is occurring onto raindrops frozen heterogeneously or in collisions with primary ice.

4.3 Secondary Droplet Nucleation

A run was performed with secondary droplet nucleation prohibited (the primary-only case). This run was compared with the control. Secondary droplet nucleation involves the activation of cloud-droplets anywhere in the interior of the cloud, more than 500 m above the cloud-base; primary droplet nucleation refers only to activation of droplets near the cloud-base.

Figures 5 and 6 demonstrate the massive impact that secondary droplet nucleation has on the concentration of anvil ice crystals and supercooled droplets in the storm. Most of the droplets reaching the anvil are clearly generated by secondary droplet nucleation in the control. The droplet concentration is reduced by more than 70 - 80 % at most subzero levels in the primary-only case relative to the control. The cloud-water mixing ratio is reduced similarly. Secondary droplet nucleation is only significant at levels that are more than about 3 km above the cloud-base, because the vertical velocity is lower and the droplet concentration is higher at levels nearer the cloud-base, relative to higher levels. In most of the mixed phase region, the rain mixing ratio is reduced by almost 50 % since the warm rain process is less active in the absence of copious cloud-water. Consequently, rates of raindrop-freezing are lower, and the total ice mixing ratio is about 0.1 g/kg lower, relative to the control.

At the anvil base, the ice concentration is reduced by approximately one order of magnitude because fewer supercooled droplets are available for the homogeneous freezing process in the primary-only case. This difference diminishes with increasing height above the anvil base due to the onset of homogeneous aerosol freezing in the primary-only case. Essentially, the low concentration of crystals near the anvil base promotes a high supersaturation with respect to ice in the primary-only case, exceeding the threshold for homogeneous aerosol freezing.

The mean diameter of anvil crystals is increased by at least 100 % at most levels in the primary-only case relative to the control, due to fewer crystals competing for the available vapour. The predicted crystal properties appear to be quite sensitive to whether the crystals originate from the homogeneous freezing of (unactivated) droplets or of aerosols. In the anvil of the primary-only case, crystals are predicted to be columnar with an average axial ratio of about 3 because they originate as frozen aerosol particles. These become columnar during a period of extended

vapour growth from an initial micron- or submicron-size. In the control simulation, however, the axial ratio is close to unity because most anvil ice particles are nucleated as homogeneously frozen droplets with an initial size of about 30 (m. Also, the predicted bulk density is 50 - 100 kg m-3 higher in the anvil updraft of the primary-only case relative to the control.

5. CONCLUSIONS

In summary, secondary droplet nucleation followed by homogeneous droplet freezing is the primary source of ice particles in most parcels in the anvil updraft of the control simulation. This is because most primary droplets - nucleated near cloud base in the updraft - never reach the anvil base, being depleted by accretion onto precipitation or detrainment. A large fraction of the CCN causing this secondary droplet nucleation appear to originate from the lateral environment.

The shape and bulk density of anvil crystals are quite sensitive to whether homogeneous aerosol freezing or secondary droplet nucleation is their ultimate source.

6. REFERENCES

Blyth, A.M. and Latham, J., 1997: A multi-thermal model of cumulus glaciation via the Hallett-Mossop process. Q. J. R. Meteorol. Soc., **123,** 1185--1198

Bott, A., 1998: A numerical method for the numerical solution of the stochastic collection equation. J. Atmos. Sci., **55,** 2284-2293

Hallett, J., and S.C. Mossop, 1974: Production of secondary ice particles during the riming process. Nature, **249,** 26—28

Khain, A.P., and I.Sednev, 1996: Simulation of precipitation formation in the Eastern Mediterranean coastal zone using a spectral microphysics cloud ensemble model. Atmos. Res., **43,** 77-110

Koop, *et al,* 2000: Water activity as the determinant for homogeneous ice nucleation in aqueous solutions. Nature, **406,** 611-614

Meyers, M.P., DeMott, P.J. and Cotton, W.R., 1992: New primary ice-nucleation parametrizations in an explicit cloud model. *J. Appl. Meteor.*, **31,** 708–720

Phillips, V.T.J., 2001: `Simulations of the glaciation of a New Mexican storm cloud with an explicit microphysics model (EMM)'. PhD Thesis, UMIST, UK

Phillips, V.T.J., Blyth, A.M., Brown, P.R.A., Choularton, T.W. and Latham, J., 2001: The glaciation of a cumulus cloud over New Mexico. *Q. J. R. Meteorol. Soc.*, **127,** 1513--1534

Phillips, V.T.J., Choularton, T.W., Blyth, A.M., and Latham, J., 2002: The influence of aerosol concentrations on the glaciation and precipitation of a cumulus cloud. *Q. J. R. Meteorol. Soc.*, **128,** 951-971

Phillips, V.T.J., Choularton, T.W., Illingworth, A.J., Hogan, R.J., and P.R. Field, 2003: Simulations of the glaciation of a frontal mixed-phase cloud with the Explicit Microphysics Model. *Q. J. R. Meteorol. Soc.,* **129,** 1351-1371

Pruppacher, H.R. and Klett, J.D., 1997: *Microphysics of clouds and precipitation.* Kluwer Academic Publishers, Dordrecht, the Netherlands

A CASE STUDY OF TROPICAL CIRRUS ANVIL MICROPHYSICS FROM CRYSTAL-FACE

M. Poellot[1], P. Kucera[1], A. Heymsfield[2], C. Twohy[3] and H. Gerber[4]

[1]Department of Atmospheric Sciences, University of North Dakota, Grand Forks, ND 58202
[2]National Center for Atmospheric Research, Boulder, CO 80307
[3]Oregon State University, Corvallis, OR 97331
[4]Gerber Scientific, Reston, VA 20190

1. INTRODUCTION

The CRYSTAL-FACE experiment was conducted over the Florida peninsula during July 2002 to study tropical cirrus. Its goal is to better understand tropical clouds and cloud processes leading to improved modeling of tropical clouds and their environment. One key issue is the morphology and lifetime of thunderstorm anvil clouds. This study examines the evolution of the microphysical properties using airborne and remote sensing observations of the cirrus anvil generated by a convective complex on July 16.

2. INSTRUMENTATION

The Citation was equipped to measure cloud microphysics and state parameters. Microphysics instrumentation is described in Table 1. Due to the uncertainty of FSSP measurements in ice clouds, particle concentrations and sizes were derived for this study from the combined spectra of the 2D-C and HVPS probes. Ice water content was determined by a counterflow virtual impactor (CVI) (Ogren et al, 1985; Noone et al, 1988; Twohy et al, 1997), and extinction at 635 nm was observed directly by a cloud integrating nephelometer (Gerber et al, 2000). Water vapor concentrations were measured using a tunable laser diode hygrometer (May, 1998). Environmental winds were derived from a 5-port radome, strap-down gyro and integrated GPS system. The NASA NASA 10 cm polarimetric Doppler radar (NPOL) was operated in a volume scan mode, producing a complete scan of the atmosphere every 10 minutes.

Table 1 – Cloud Physics Probes

Probe	*Parameter*	*Resolution*	*Range*
FSSP	Droplets	3 μm	2-56 μm
2D-C	Cloud	30 μm	30-960 μm
HVPS	Precipitation	200 μm	0.2-51.2 mm
CPI	Images	2.3 μm	20-2000 μm
CVI	Total water	-	-
CIN	Extinction	-	-

Corresponding author's address: Michael Poellot, University of North Dakota, Grand Forks, ND, USA; e-mail:poellot@aero.und.edu

3. OBSERVATIONS

The Citation flight profile consisted of level sampling legs flown along the mean wind direction at several altitudes, first stepping up from 11.3 to 11.9 km, then flying five legs at 11.9 km and finally stepping down from 11.9 to 8.1 km. The temperature ranged from -47 °C at 11.9 km to -19 °C at 8.1 km, relative humidity varied from 30-60%, and the wind speed was approximately 15 m s^{-1} with little shear.

Preliminary examination of cloud particle concentrations at each level found a series of maximum and minimum values along each of the legs (e.g., Fig. 1). Visible satellite images with aircraft flight track overlays revealed that the anvil cloud was generated by a series of individual convective cells. This was verified by constant altitude plan position indicator (CAPPI) radar reflectivity products for 10 and 11 km

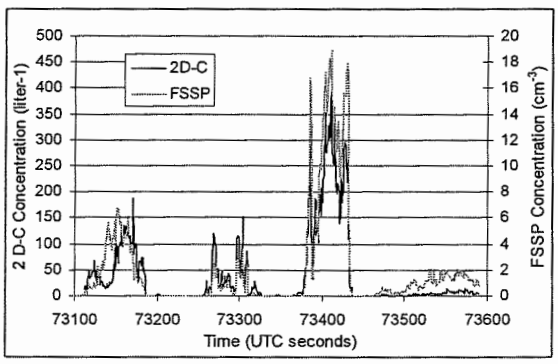

Figure 1. Leg 2 particle concentrations

AGL. Through comparison of the aircraft, satellite and radar data, a total of 10 cells were identified and tracked and the time of generation was approximated.

The Citation made repeated samples of most of these cells at various times and altitudes. To examine the temporal and spatial variability of the anvil microphysics, the following sets of samples were selected: five cells sampled at the same altitude and approximate time after generation; repeated samples of one cell at the same altitude; vertical profiles of three cells; and average values for each level flight leg.

3.1 Intercell Comparison

Mean size and concentrations for five cells sampled at 11.9 km altitude and approximately 60 minutes after generation are presented in Table 2. These are average values for a 45-second period centered around the peak concentration for the cell. This represents a horizontal distance of approximately 5.8 km. The wide range of sizes and concentrations show considerable variability from cell to cell, most likely related to differences in their initial concentrations when the anvils were first generated.

Table 2. Cells sampled at 60 minutes

Cell	Mn D	MVID	MedVolD	2D-C
2	51.2	177	495	345
3	50.6	177	650	683
4	63.6	274	750	435
4p	57.0	216	750	1070
5	52.0	174	525	551

Mn D = mean diameter, MVD = mean volume diameter, MedVolD = median volume diameter, 2D-C = concentration (2D-C + HVPS) in number per liter.

3.2 Time Evolution

The time evolution of the anvil particles over a period of 34 minutes is presented in Table 3. These samples were taken at 11.9 km and are 45-second averages centered on the time of peak concentration. There is a trend in increasing particle size and decreasing concentrations with time, which is indicative of aggregation. This may also be inferred from the decrease in small ice (FSSP concentrations) and decrease in extinction. Also, as the particles aggregate, they fall and reduce the ice water content.

Table 3. Repeated samples of cell 4p at 11.9 km

Time	*MVD*	*2D-C*	*FSSP*	*IWC*	*Ext.*
35	185	3110	47.5	630	170
48	242	1060	31.2	655	122
56	227	1270	31.4	609	122
62	216	1070	22.1	470	92
70	264	561	18.1	408	78

Time = time after generation, MVD = mean volume diameter, 2D-C = concentration (liter^{-1}), FSSP = concentration (cm^{-3}), IWC = ice water content (mg m^{-3}), Ext. = extinction coefficient (km^{-1})

Average particle size distributions for each of the times in Table 3 are shown in Figure 2. These show the decreasing numbers of small particles with time. CPI images are inconclusive as to whether this decrease is due to aggregation or evaporation. Relative humidity averaged approximately 97% of ice saturation, which would cause some evaporative losses.

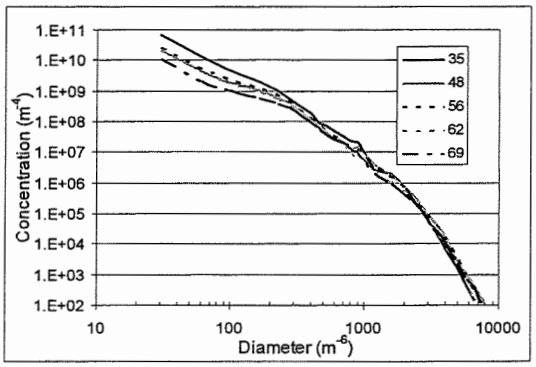

Figure 2. Repeated samples of cell 4p (minutes after generation)

3.3 Vertical Profiles

A vertical profiles of cell 5 is shown in Figure 3

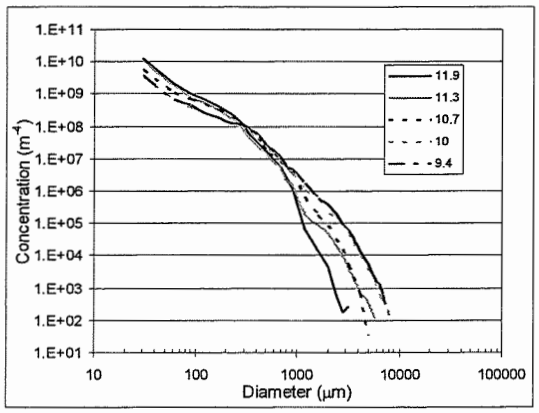

Figure 3. Vertical profile of cell 5 (altitudes in km)

and is typical of several others from this flight. The marked decrease in small particles and increase in large particles downward through the cloud strongly suggests sedimentation and aggregation. Ice water content and extinction also increased downward.

CPI images of particle aggregates and small particles are presented in Figure 4. The three large crystals range from 370-820 μm in diameter. Many of the aggregates throughout the cloud contained plate-type crystals. These plates were apparently formed in the convective cell updrafts and have been noted by other investigators (e.g. Stith et al, 2002).

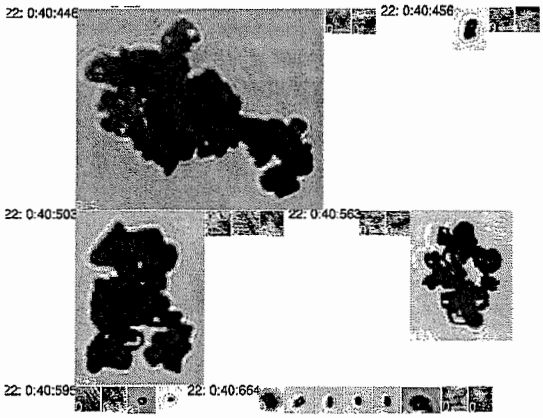

Figure 4. CPI images from cell 5 at 9.4 km

Average values of microphysical parameters for all legs are presented in Figure 5. This represents a profile through the convective complex anvil system. Concentrations generally decrease downward while mean volume diameter increases, again likely due to aggregation and sedimentation. The ice water content also increases downward until near the bottom of cloud, where evaporation into subsaturated air reduces the population of smaller particles. Extinction values are highest in the upper portion of the anvil where high concentrations of small particles exist. There is a secondary maximum in the mid-portion of the cloud with contributions from both small and increasingly large particles.

4.0 DISCUSSION

The in situ sampling of anvil cloud from a convective complex revealed a detailed microphysical structure that resulted from contributions by many individual convective cells. The evolution of the cloud microphysics was apparently the result of a combination of

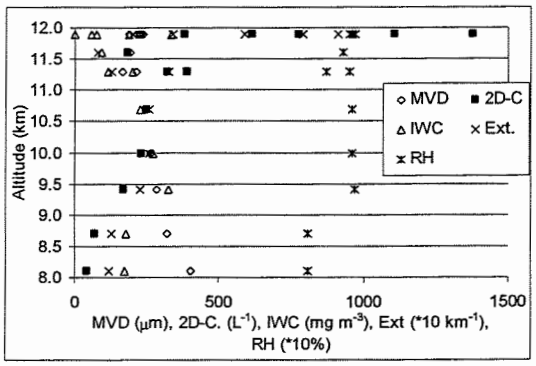

Figure 5. Leg-average values. Variable names as in Table 3. RH = relative humidity (% ice)

aggregation, sedimentation and evaporation. Similar conclusions were reached by McFarquhar and Heymsfield (1996) for anvils sampled over the tropical Pacific. There is still some question as to whether vertical motions internal to the anvil may subsequently affect the ice particle population. There appeared to be some correlation between positive vertical motion, relative humidity and number concentration over the first couple of legs (Fig. 6). Unfortunately, the aircraft radome ports became clogged due to high ice water contents and the vertical winds were not available after leg 3, so the analysis is inconclusive.

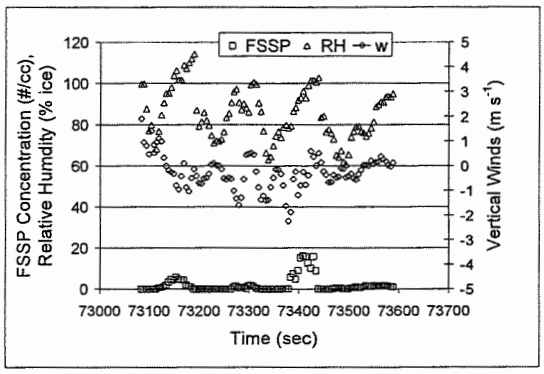

Figure 6. Vertical wind (w), FSSP concentration (FSSP) and relative humidity (RH, ice)

The existence of high concentrations of small particles high in the anvil and relatively soon after generation points toward a homogeneous freezing mechanism in the convective updraft

was consistent with the hypothesis developed by Heymsfield et al. (2004). Their analysis of a convective core penetration also saw evidence of fairly rapid reduction in the small crystal population as the cloud moved downwind in subsaturated air.

The data presented here are part of a larger study to relate cloud microphysics to storm intensity. Radar reflectivity fields will be examined in greater detail to better define the vertical structure of the convective cells.

4.1 Acknowledgements

The authors would like to acknowledge Crystal Paulsen for her assistance in this analysis. This work was supported under NASA Grant NAG5-11509.

4.2 References

Heymsfield, A., L. Miloshevich, et al, 2004: Homogeneous ice nucleation in tropical convection and its influence on cirrus anvil microphysics. Submitted to *J. Atmos Sci.*

May, R., 1998: Open-path, near-infrared tunable diode laser spectrometer for atmospheric measurements of H_2O. *J. Geophys. Res.,* **103**, 19,161-19,172.

McFarquar, G.,and A. Heymsfield, 1996: Microphysical characteristics of three anvils sampled during the Central Equatorial Pacific Experiment. *J. Atmos. Sci.*, **53**, 2401-2423.

Stith, J., J. Dye, et al, 2002: Microphysical observations of tropical clouds. *J. Appl. Meteor.,* **41**, 97-117.

Ogren, J. A., J. Heintzenberg, et al. (1985). "In situ sampling of clouds with a droplet to aerosol converter." *Geophys. Res. Lett.* **12**, 121-124.

Noone, K. J., R. J. Charlson, et al. (1988). "Design and calibration of a counterflow virtual impactor for sampling of atmospheric fog and cloud droplets." *Aer. Sci. Technol* **8**, 235-244.

Twohy, C. H., A. J. Schanot, et al. (1997). "Measurement of condensed water content in liquid and ice clouds using an airborne counterflow virtual impactor." *J. Atmos. Oceanic Tech.* **14**, 197-202.

NUMERICAL SENSITIVITY STUDIES OF AXIS RATIO CHANGES OF COLLIDING ICE CRYSTALS

R. Posselt[1]*, S. Wurzler[2], and K. Diehl[3]

[1]Dalhousie University, Halifax, Nova Scotia, Canada

[2]North-Rhine-Westphalia State Environment Agency, Germany

[3]Institute for Tropospheric Research, Leipzig, Germany

1 INTRODUCTION

Most tropospheric clouds contain ice particles. The number and the size of the ice particles within a cloud determine the optical properties of the cloud (Jiang et al. 2000, Harrington et al. 1999). One type of precipitation produced by these clouds is snow. The formation of snowflakes is the result of collision processes of ice crystals with each other and with their aggregates (Reisin et al. 1996, Wang 2002). The collision process of ice crystals is governed by their shapes and leads dependent on the temperature to a variety of aggregates which may have completely different shapes and hydrodynamical behaviors than the initial ice particles (e.g., Wang 2002). This in turn affects the efficiency of the cloud to produce snow.

In recent years many numerical model studies on the collisions of ice crystals have been carried out (e.g., Pruppacher and Klett 1997, Khain et al. 2000), but most of them did not take into account any changes in the radius ratio and shapes of the collision products. In order to investigate the impact of changes in shape of the aggregates on the collisional growth of ice crystals and their aggregates, an axis ratio relation was developed to describe the collision products. Sensitivity studies with a spectral collectional growth model were carried out to investigate the possible changes in the collision kernel, the ice particle shapes and the time evolution of an ice particle size distribution.

2 METHODS

In order to investigate if changes in ice crystal shape and hydrodynamical properties have significant impact on cloud microphysics the following approach was employed. The axis ratio α was used to evaluate the influence of the changes in the particle shape on the collision process. The axis ratio is defined as the ratio between the length of the axis of symmetry h and the largest length d (diameter) perpendicular to the axis of symmetry:

$$\alpha = \frac{h}{d} \tag{1}$$

Ice plates have an axis ratio of $\alpha < 1$ and ice columns have $\alpha > 1$.

In the atmosphere all different kinds of ice particles collide with each other and form a wide variety of collision products and aggregates. The full range cannot be realized in present cloud models. In order to get a first estimate of the influence of shape variations on the collisional growth of ice particles it was assumed that the collision partners have the same shape, and that the collision product has also that shape. The newly formed particle has the mass of both original particles together and the characteristic length matches that of the larger original particle. For ice plates this is the one with the largest radius perpendicular to the flow and for ice columns it is the one with the largest cylinder height.

For ice plates the axis ratio increases whereas for ice columns the axis ratio decreases. In both cases the boundary value for the changes is an axis ratio of 1.

In order to obtain the new average axis ratio in a size class a mass weighted average of the axis ratio of newly formed particles relocated to this class and particles already present in this class was determined.

Calculations of the time development of ice plates and ice columns were carried out using a sectional cloud model with detailed cloud microphysics. The collisions between different sized ice particles were numerically calculated on the base of the Linear Discrete Method (LDM) developed by Simmel et al. (2002). The collision efficiency was calculated according to Böhm (1999) and Posselt et al. (2004).

In order to make the calculations comparable four different cases of the initial exponential size distribution were considered as the starting point for the simulations.

*Corresponding author's address: Department of Physics and Atmospheric Sciences, Dalhousie University, Halifax, Nova Scotia, B3H 3J5, Canada

In the initial particle size distribution all bins were initialized with the same axis ratio α. In case of the ice plates the axis ratio was 0.05 and in case of the ice columns it was 3. To evaluate the influence of changing shape (represented by the axis ratio), two cases were considered. In the first case the axis ratio was varied. In the second case the axis ratio stayed constant, for ice plates $\alpha = 0.05$ and for ice columns $\alpha = 3$. Both values were taken from literature (e.g., Böhm 1992, 1994) to represent typical axis ratios for these kinds of ice particles.

3 RESULTS

3.1 Changes of axis ratio

Figure 1 shows the axis ratio as function of the ice particle radius for different model times. As long as no collision products were formed the axis ratio stayed constant at a value of 0.05 for ice plates (upper panel of Figure 1) and 3 for ice columns (lower panel of Figure 1). Axis ratio changes set in for particle sizes of about 35 μm for ice plates. For the ice columns changes of the axis ratio were apparent for particle size greater than 30 μm radius. These were the size ranges where the first collision products appeared. Up to a particle size of 150 μm collision products and particles already present in the bin contributed to the new mean axis ratio. Thereby, the respective average axis ratios and masses determined the amount and direction of the axis ratio changes in the bin. The minimum in the axis ratio of ice plates between 100 and 200 μm results from collision products with a smaller axis ratio than the bin particles. If the collision products reached sizes larger than $150 - 200\,\mu m$ they fully determined the axis ratio, as no particles were present there from the initial particle size distribution. Since these quite large particles had undergone a few collision processes their axis ratio had already reached the boundary value of 1.

3.2 Changes in collision kernel

The variation of the axis ratio causes an alteration of the collision efficiency during the simulation. Two main alteration schemes were noticeable. First, the closer the collector particle approached an axis ratio of 1 the smaller the collision efficiency values became for this collector size. Second, the collision efficiency increased for collisions with very small particles ($r_{capt} \lesssim 3\mu m$). These alterations were more pronounced for ice plates than for ice columns.

As result of these changes in the kernel for the different kinds of ice particles the collisional behavior was altered in comparison to the case with a constant axis ratio.

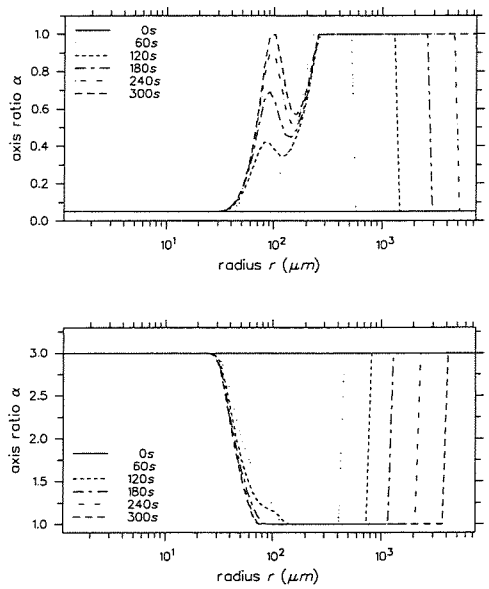

Figure 1: Change of the axis ratio α during the simulation for ice plates (upper panel) and ice columns (lower panel)

3.3 Time evolution of example particle distributions

Two different cases were investigated. In case 1 the axis ratio was changed during the simulation, in case 2 the axis ratio stayed constant.

3.3.1 Ice plates

Figure 2 shows the results for case 1 with the changing axis ratio (upper panel) and case 2 with a constant axis ratio (lower panel). In case 1 large particles were formed earlier but did not reach the sizes present in case 2. The change of the kernel for case 1 allowed smaller particles to take part in collisions and larger particles were formed. However, the collision of these larger particles was delayed by the reduction of the kernel in these size ranges. Therefore, the development of even larger particles was reduced in comparison to case 2.

3.3.2 Ice columns

As the changes in the kernel were very small in the case of ice columns, the time development of the particle distributions did not differ significantly for both cases as can be seen from Figure 3. The slight change of the kernel for collections with very small particles resulted in an enhanced collection of these particles and, therefore, an earlier appearance of larger par-

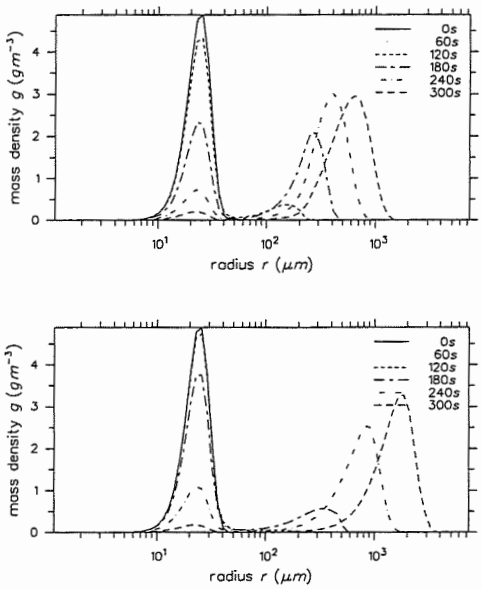

Figure 2: Time development of an ice plate distribution with a changing axis ratio (upper panel) and a constant axis ratio of 0.05 *(lower panel)*

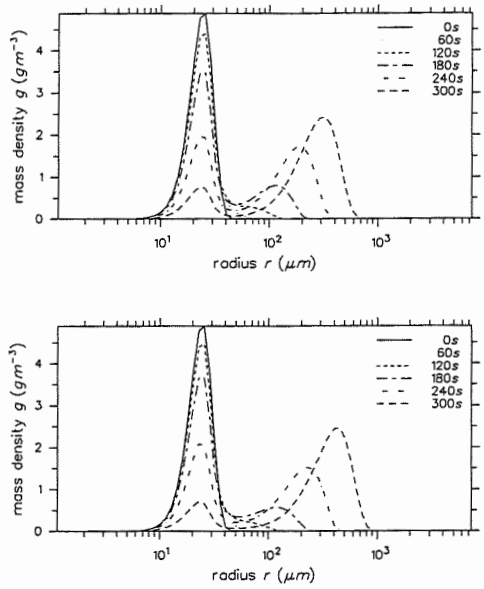

Figure 3: Time development of an ice column distribution with a changing axis ratio (upper panel) and a constant axis ratio of 3 *(lower panel)*

ticles. But similar to the ice plates, the size of the particles at the end of the simulation were smaller in case 1 than in case 2. Still the differences between the two cases were much less than in the cases with the ice plates.

4 CONCLUSIONS

Sensitivity studies were carried out on the changes of the collision kernel, the axis ratio, and the time evolution of ice particle populations by collisional growth. These studies of the collisions of ice particles of one kind (plates or columns) showed that:

- the impact of axis ratio changes are different for ice plates and ice columns,
- the changes in the axis ratio are more pronounced for ice plates than for ice cylinders,
- the effects of a variable axis ratio are more significant for ice plates than for ice columns,
- relatively small changes in the kernel lead to significant changes in the time evolution of the ice particle populations,
- compared to the collisional growth with constant axis ratio, the plates and columns grow faster, but stay smaller when a variable axis ratio is assumed.

From the sensitivity studies one can conclude that changes in the axis ratio of ice crystal collision products should not be neglected. Otherwise the precipitation sized snow production of clouds may be overestimated in cloud models. In addition, small ice crystal numbers may be overestimated owing to underestimating their collision efficiencies. Not much was found in literature on the impact of axis ratio changes of colliding ice crystals. Even with the present results still further model studies as well as field and laboratory investigations are required.

5 REFERENCES

Böhm, J. P., 1992: A general hydrodynamic theory for mixed-phase microphysics. Part I: Drag and fall speed of hydrometeors. Atmos. Res., **27**, 253 – 274.

Böhm, J. P., 1994: Theoretical collision efficiencies for riming and aerosol impaction. Atmos. Res., **32**, 271 – 287.

Böhm, J. P., 1999: Revision and clarification of "A general hydrodynamic theory for mixed-phase microphysics". Atmos. Res., **52**, 167 – 176.

Harrington, J. Y., Reisin, T., and Kreidenweis, S. M., 1999: Cloud resolving simulations of Arctic stratus, II, Transition-season clouds. Atmos. Res., **51**, 45

– 75.

Jiang, H., Cotton, W. R., Pinto, J. O., and Weissbluth, M. J., 2000: Claud resoving simulations of mixes phase Artic stratus observed during BASE: Sensitivity to concentration of ice crystals and large-scale heat and moisture advection. J. Atmos. Sci., **57**, 2105 – 2117.

Khain, A., Ovtchinnikov, M., Pinsky, M., Pokrovsky, A., and Krugliak, H., 2000: Notes on the state-of-the-art numerical modeling of cloud microphysics. Atmos. Res., **55**, 159 – 224.

Posselt, R., Simmel, M., and Wurzler, S., 2004: Comment on Revision and clarification of "A general hydrodynamic theory for mixed-phase microphysics"[Böhm, J.P., 1999,Atmos.Res. 52, 167-176]. Atmos. Res., **(in press)**.

Pruppacher, H. R. and Klett, J. D., 1997: Microphysics of Clouds and Precipitation. Kluwer Academic Publishers.

Reisin, T. G., Levin, Z., and Tzivion, S., 1996: Rain production in convective clouds as simulated in an axissymmetric model with detailed microphysics, II, Effects of varying drop and ice initialization. J. Atmos. Sci., **53**, 1815 – 1837.

Simmel, M., Trautmann, T., and Tetzlaff, G., 2002: Numerical solution of the stochastic collection equation – Comparisons of the linear discrete method with other methods. Atmos. Res., **61**, 137 – 150.

Wang, P. and Lin, H., 1995: Comparison of model results of collection efficiency of aerosol particlesby individual water droplets and ice crystals in a subsaturated atmosphere. Atmos. Res., **38**, 381 – 390.

Wang, P. K., 2002: Ice Microdynamics. Academic Press, Elsevier Science, San Diego, USA.

CLASSIFICATION AND SCATTERING PROPERTIES OF WINTERLY PRECIPITATION PARTICLES

W.L. Randeu[1], F. Teschl[1], N. Witternigg[2] and M. Schönhuber[2]

[1]Institute of Broadband Communications, Graz University of Technology, Austria
[2]Institute of Applied Systems Technology, Joanneum Research GmbH, Graz, Austria

1. INTRODUCTION

Supported by detailed measurements of a large number of natural winterly precipitation particle shapes, sizes and falling velocities, acquired by means of an imaging distrometer (the 2D-Video-Distrometer, Schönhuber et al., 1994), an attempt is undertaken to propose a novel classification of such particles with regard to electromagnetic scattering properties (Teschl, 2003). This classification is based mainly on the material composition and the shapes of particle constituents (ice crystals, water droplets), and on the outer appearance (size, shape) of the whole particle. So far 9 classes with similar scattering and absorption properties to be expected for members of one single class have been defined.

The purpose of this study is to calculate realistic scattering parameters for different classes of winterly precipitation particles including frozen cloud particles. Among the difficulties in this work are stable and accurate scattering calculation tools, able to cope with inhomogeneous material as well as with rather complex particle shapes, as e.g. the case for snow flakes, made up of a large number of elementary crystals, may be interspersed or covered by water.

In the following, results for the Radar Cross Section (RCS) of different precipitation particles, calculated by a Finite Element Method (FEM) are presented.

First radar cross sections of ice spheres and their characteristics at super high frequencies are regarded, as for scattering calculation purposes, spheres are commonly used to approximate actual precipitation particles e.g. ice crystals, graupel, hailstones,...

2. RADAR CROSS SECTIONS OF ICE SPHERES

For spheres an exact scattering solution exists (Mie, 1908). For the following RCS calculations of spheres a Matlab implementation of the Mie-algorithm published in the book of Bohren and Huffmann (1983) was used.

Corresponding author's address: Walter L. Randeu, Institute of Broadband Communications, Graz University of Technology, A-8010 Graz, Austria; E-Mail: randeu@radar.tugraz.at

The real part of the refractive index of ice lies at around 1.78 for the whole radar frequency band. The imaginary part changes significantly with frequency and temperature (Ray, 1972) but is very small. Therefore ice spheres have a backscattering characteristic like non-absorbing spheres.

Figure 1 shows the radar cross section of ice spheres with 8, 10 and 12 mm in diameter at a temperature of –5 °C. (The variation of the refractive index with the frequency is taken into account)

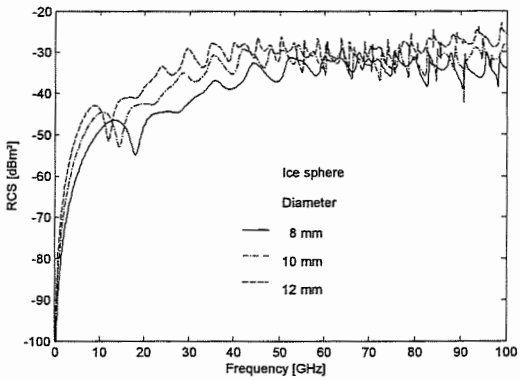

Figure 1: Radar Cross Section of ice spheres

Figure 1 also shows that for a certain frequency ice spheres with different sizes can exhibit the same radar cross section. E.g. at 12.8 GHz the radar cross section equals –47 dBm² for all regarded ice spheres. Therefore radar measurements at this frequency would not be able to distinguish between the different sizes.

3. SCATTERING CALCULATION WITH A FINITE ELEMENT METHOD

The Finite Element Method (FEM) is generally applicable for calculating parameters of arbitrary particles. The particles may have complex shapes and may consist of different materials. The particle however must be approximated by elements (typically tetrahedrons) in a way, that the electromagnetic field does not change significantly within an element.

To find out up to what particle dimensions and up to what frequencies the used FEM program is applicable,

water and ice spheres were modelled and their simulated result for the RCS were compared with the exact Mie-solution.

3.1 Comparison of FEM results with Mie-Solution

Figure 2 shows the RCS of a water sphere with 10 mm in diameter for frequencies up to 100 GHz. For such dimensions this frequency range covers mainly the Mie-region. The FEM results comply with the exact values within a tolerance of ±1dB. However, for frequencies of 100 GHz and higher, a precise computation would require a very fine mesh. Because of the available limited computer power a coarser mesh was used. A higher deviation was the result.

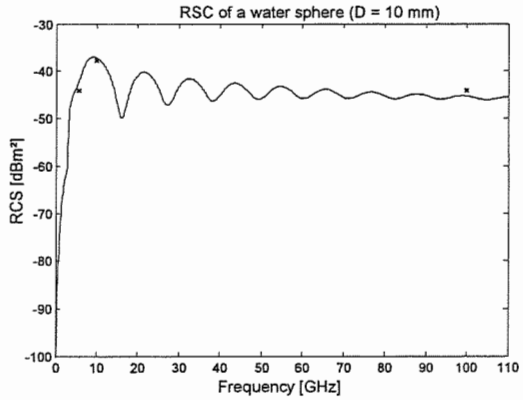

Figure 2: Radar Cross Section of a water sphere with a diameter of 10 mm at 10 °C: exact Mie-Solution and FEM results (x).

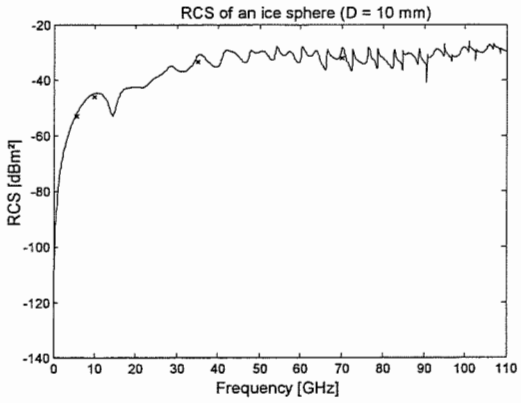

Figure 3: Radar Cross Section of an ice sphere with a diameter of 10 mm at 0 °C: exact Mie-Solution and FEM results (x)

Figure 3 shows the result for an ice sphere with 10 mm in diameter for frequencies up to 100 GHz. The tolerance of the simulation results is, especially at higher frequencies, greater than for water and metal spheres. The reason is the wiggled structure of the RCS curve of an ice sphere. The simulated sphere is not perfectly spherical. Because of the wiggled structure of the RCS curve of an ice sphere minor differences in the circumference can cause significant variations. Figure 4 compares the RCS for two spheres with almost equal diameter (10 mm and 9.9 mm). The differences between the RCS can reach 10 dB for single frequencies in the shown range.

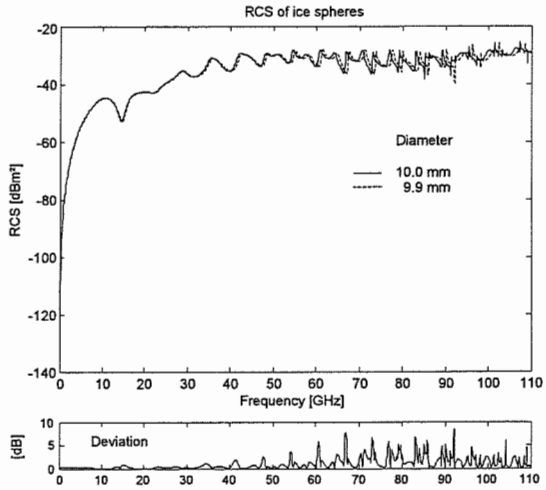

Figure 4: Radar Cross Section of ice spheres with diameters of 10 mm and 9.9 mm. Even small differences in diameter can lead to significant deviations of the RCS.

4. SCATTERING CALCULATION OF SIMPLE ICE CRYSTALS

4.1 Comparison of FEM with FIMHOLT

Witternigg et. al., (2000) calculated scattering parameters trying to cover the range of the most common particles in ice clouds with FIMHOLT, an adaptation of the Fredholm Integral Method. Figure 5 compares FIMHOLT and FEM results for the RCS of an ice crystal (hexagonal plate, aspect ratio = 2, equiv. sphere radius = 0.5 mm, the electromagnetic wave is incident along the particle's longitudinal axis).

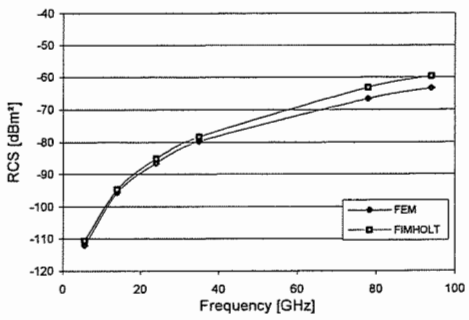

Figure 5: RCS of a hexagonal ice plate determined with FIMHOLT and FEM

FEM yields a lower RCS value for all regarded frequencies. The deviation increases with the frequency. However both results show the same trend. As the FEM models the actual crystal while the FIMHOLT code approximates it by a spheroid, some deviation was to be expected.

4.2 RCS of simple ice crystals

With FEM the RCS of simple hexagonal ice crystals was calculated. The particles were assumed to consist of pure ice at a temperature of –10 °C.

In the following dimensions of the crystals are given as width (w) and height (h) as illustrated in Figure 6 in the form 'w x h mm' (e.g. 1 x 2 mm). The crystals are aligned that the wave is incident along the particle's longitudinal axis. Figure 7 shows the RCS for hexagonal prisms with various dimensions and aspect ratios.

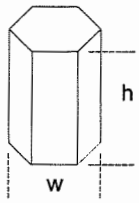

Figure 6: Definition of hexagonal ice crystals' dimension

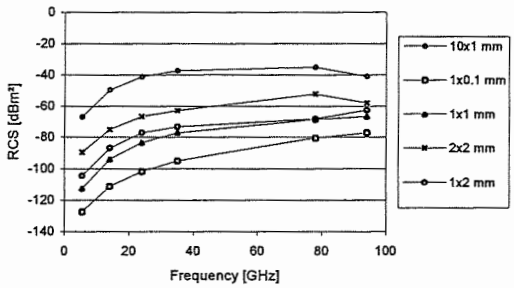

Figure 7: RCS of different hexagonal ice crystals

5. SCATTERING CALCULATION OF SOLID PRECIPITATION PARTICLES OF ARBITRARY SHAPE

With FEM the radar cross section of a real snowflake was determined for several radar frequencies and directions. The snowflake's front and side view (Figure 8) was recorded by the 2D-Video-Distrometer (2DVD). From the 2DVD-data a three-dimensional object was generated in a CAD environment. On this object the calculations were carried out. To simplify object geometry definition the material was assumed to be pure ice at –10 °C. The incident plane wave has vertical polarisation and travels along the positive x-axis (x increases with time).

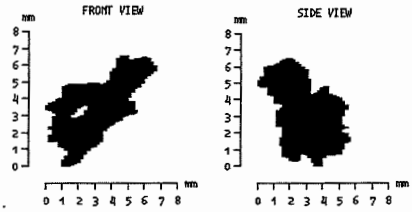

Figure 8: Front and side view of a snowflake

For a radar frequency of 5.6 GHz (Figure 9a) the particle's diameter is small compared to the wavelength. The scattering characteristic is almost equal to dipole excitation. The total RCS is highest for all directions in the xy-plane. In the direction of the positive and negative z-axes the RCS is evanescent.

For 30 GHz (Figure 9b) the wavelength lies in the range of particle's diameter. For wavelength shorter than the particle's diameter the total RCS plot does not show any longer dipole excitation characteristic (Figure 9c-d).

For wavelength small compared to the particle's diameter (Figure 9d) the RCS shows optical scattering behaviour with a lot of local minima and maxima.

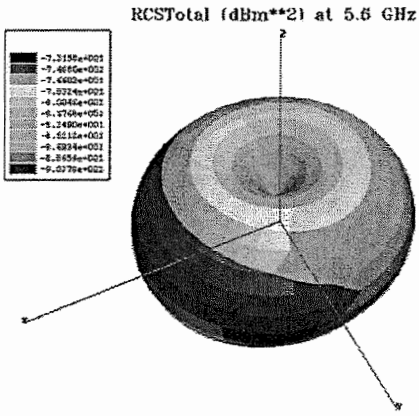

a)

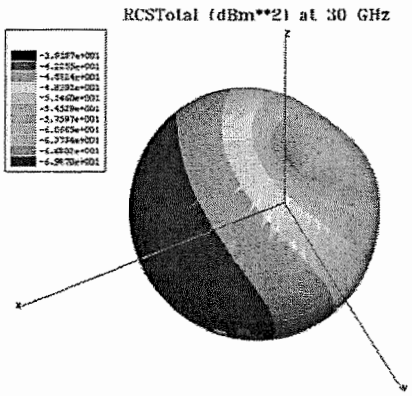

b)

Figure 9 a - b: Scattering behaviour of a snowflake for different radar frequencies

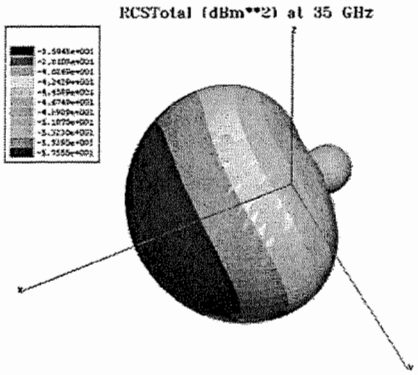

c)

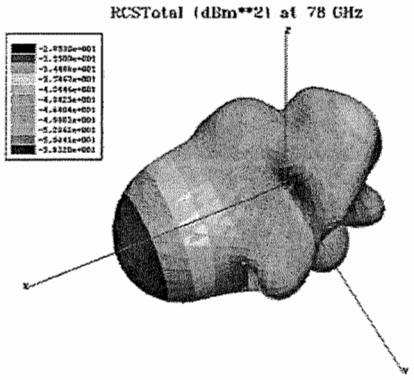

d)

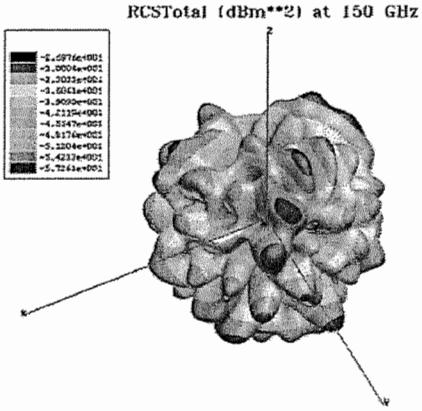

e)

Figure 9 c - d: Scattering behaviour of a snowflake for different radar frequencies

6. CONCLUSION

The FEM showed to be well suited and stable for the scattering calculation of precipitation particles at radar frequencies. For particle dimensions up to 10 mm and frequencies up to 100 GHz the calculations can be carried out with reasonable computing time even on a personal computer.

The main aim of further FEM simulations will be a verification of the proposed precipitation classification, which is now based mainly on the material composition, on the shapes of particle constituents (ice crystals, water drops), and on the outer appearance (size, shape) of the particles. A long term objective is a classification of winterly precipitation particles based on rigorously derived scattering amplitudes even for complicated shapes and mixed-phase constituents – which has turned out to be possible with the existing FEM tool.

7. REFERENCES

Bohren, C. F., and D. R. Huffman, 1983: Absorption and Scattering of Light by Small Particles, Wiley, New York.

Mie, G., 1908: Beiträge zur Optik trüber Medien, speziell kolloidaler Metallösungen. Annalen der Physik, [4] **25**, 377-445.

Ray, P., 1972: Broadband complex refractive indices of ice and water. Appl. Opt., **11**, 1836-1844.

Schönhuber, M., H. Urban, J.P.V. Poiares Baptista, W.L. Randeu and W. Riedler, 1994: Measurements of Precipitation Characteristics by a New Distrometer. Proceedings of Atmospheric Physics and Dynamics in the Analysis and Prognosis of Precipitation Fields, November 15 - 18, 1994, Rome, Italy.

Teschl, F., W . L. Randeu and M. Schönhuber, 2003: A classification of solid and mixed-phase precipitation particles based on scattering properties. EGS-AGU-EUG Joint Assembly, Nice, France, 06 – 11 April 2003, Geophysical Research Abstracts, Vol **5**, 05374

Witternigg, N., and W. L. Randeu, 2000: Scattering calculations and outline specifications for a ground-based cloud profiling radar. Proc. 13th International Conference on Clouds and Precipitation, Reno, Nevada, USA, 14–18 August 2000, 235–238

FREEZING DRIZZLE FORMATION OVER THE OREGON CASCADES DURING IMPROVE II

R.M. Rasmussen[1], K. Ikeda[1], G. Thompson[1], and I. Geresdi[2]

[1]National Center for Atmospheric Research, Boulder, Colorado
[2]University of Pecs, Hungary

1. INTRODUCTION

A number of recent field programs have focused on the meteorological conditions leading to aircraft icing (WISP: Rasmussen et al. (1992), CFDE: Isaac et al. (1999), NASA Glenn, Miller et al. 1998). These programs have primarily focused on aircraft icing conditions over relatively flat terrain (Front Range of Colorado, New Foundland, and Cleveland) in association with cold fronts, warm fronts, and other features associated with mid-latitude cyclones (Bernstein et al. 1997). One of the key results coming out of these and other studies is the significantly higher frequency of freezing drizzle than previous thought (1 – 2% of all icing conditions versus 0.1% previously (Bernstein 2000, Rauber et al. 2000)). Freezing drizzle can be particularly hazardous to aircraft due to the impaction of the larger droplets beyond current deicing boots, leading to a significant reduction in aircraft performance that cannot be alleviated by the activation of ice protection devices such as pneumatic boots. These field programs have also shown that freezing drizzle is mostly formed via a collision-coalescence process rather then melting ice falling into below freezing air (Rasmussen et al. 1995, Cober et al. 1996, Rauber et al. 2000).

Recent climatologies of freezing drizzle by Bernstein (2000) and Stuart and Isaac (1999) have shown that freezing drizzle tends to maximize over continental regions close to large bodies of water, such as the Atlantic or Pacific oceans or the Great Lakes. For instance, freezing drizzle maxima are observed near Nova Scotia, Norway (Ben Bernstein, personal communication), Cleveland, the Pacific Northwest, and Alaska. This result is consistent with conventional thinking in cloud physics that the production of precipitation sized water drops through the collision-coalescence process is relatively rapid in maritime environments in which Cloud Condensation Nuclei (CCN) concentrations are low, leading to rapid broadening of the cloud droplet spectra to sizes at which the collision-coalescence process is rapid.

Corresponding author: Roy Rasmussen, National Center for Atmospheric Research, Boulder, CO, USA rasmus@ucar.edu

The results of icing studies in the above field programs have suggested that icing conditions (either supercooled liquid water or freezing drizzle), tends to be minimized when the radar reflectivity is greater than 5 dBZ. Since cloud droplets and drizzle have radar reflectivities less that 0 dBZ, the presence of 5 dBZ or greater typically indicates the presence of ice. Ice reduces liquid water and drizzle water content through depositional and accretional growth, thus limiting the build up of supercooled liquid water and drizzle (Geresdi et al. 2004). Since vertical motions in many of the icing clouds observed in previous icing programs are typically weak (< 10 cm/s) (Cober et al. 1996, Rasmussen et al. 1995, Murakami 1992), it does not take much ice to significantly deplete the water (freezing drizzle is typically not observed in regions in which ice crystal concentrations are greater than 0.1 L^{-1}, Rasmussen et al. 1995, Cober et al. 1996, Geresdi et al. 2004).

Based on these results, icing diagnosis algorithms, such as the Current Icing Product (CIP; Bernstein et al. 2004) significantly reduce the probability of icing when the radar reflectivity is greater than 5 dBZ. However, a recent evaluation of the algorithm using Pilot Reports (PIREPS) of icing has shown a significant under-estimation of icing over the Pacific Northwest, especially over higher terrain regions. The recent IMPROVE II field program (Stoelinga et al 2003) provided an excellent opportunity to examine icing in this region, especially the presence of moderate or greater icing in regions of radar reflectivity greater than 5 dBZ. The IMPROVE II program involved two instrumented aircraft (University of Washington Convair and the NRL P-3), the S-Pol multi-parameter radar, a microwave radiometer, sounding sites, and other instruments (Stoelinga et al. 2003). Fig. 1 provides a schematic of the field program region and the location of the various facilities as well as the main aircraft tracks during the Nov. 28 storm. The goal of the IMPROVE II program was to improve bulk microphysical parameterizations over regions of mountainous terrain in order to better predict precipitation in these critical regions. In this paper we examine the post-frontal period of a winter storms during IMPROVE II in which freezing drizzle was observed. This post-frontal period had freezing drizzle in regions with high radar reflectivity (up to 20 dBZ) and moderate and greater icing and relatively warm cloud top temperatures (> -18 C).

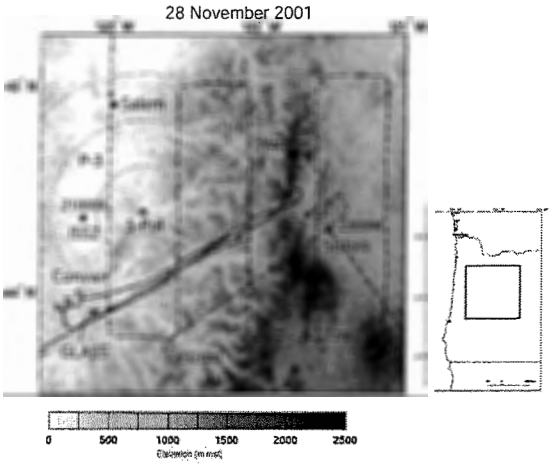

Figure 1: Topographic map of the study area. Convair (solid) and P-3's (dash-dot) flight tracks are overlaid. Crosses on the flight tracks are placed in a 10-minute inverval. Ground measurement sites are indicated by solid circles. Range rings are drawn every 25 km from the radar.

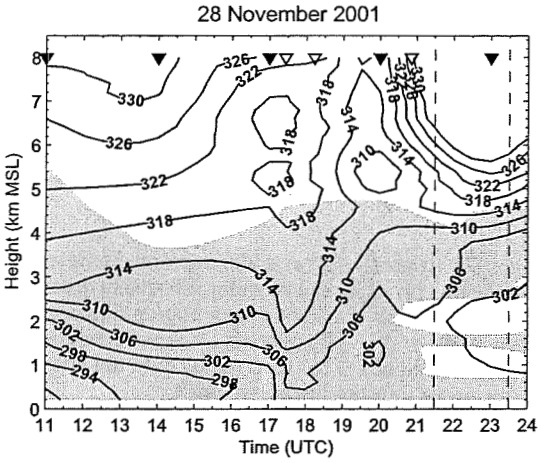

Figure 2: Time-height cross section of Θ_e (K) and relative humidity from the Salem and GLASS soundings on 28 November 2001. Dark (light) shaded is relative humidity above 80 % (between 70 and 80 %). Convair and P-3 were deployed between the times indicated by two vertical lines. Solid (open) triangles indicate the times of SLE (GLASS) soundings.

2. DESCRIPTION OF 28 NOVEMBER 2001 CASE

2.1 Synoptic and Mesoscale features

On 28 November a large synoptic low pressure system approached the northwest coast of the U.S. at 1200 UTC. With time the low pressure center took a northeastward track while the fronts swept across the coastal region from the southwest.

Warm frontal clouds enveloped the northern Oregon Cascades between 0300 and 1200 UTC. The S-Pol radar images started to indicate light rain at this location prior to 0700 UTC. Infrared satellite images reveal the leading edge of cold frontal clouds moving southeastward over ISS2 (Fig. 1) at 1800 UTC. In the next one hour, the cold frontal clouds advanced just past the radar site (S-Pol). The cloud top temperature of the cold frontal clouds is between –10 and –20°C, with a typical value of –15°C. The warm frontal cloud, in contrast, exhibited cloud top temperatures between –40 and –50°C.

The time-height cross-sections of equivalent potential temperature (Θ_e), relative humidity, wind direction, and wind speed (Fig. 2 from Salem) also indicate passage of warm frontal surface by 1300 UTC, suggested by the area of rapidly increasing Θ_e. Between 1400 and 1600 UTC, the lowest 1 km remains stable. Subsequently, the southwesterly winds intensify as the surface cold front approached and formed a barrier jet. The maximum speed of 45 m s^{-1} at 2 km MSL was recorded between 1700 and 1800 UTC at which time colder air associated with the front advanced. Behind the front (represented by the sloped surface of large Θ_e gradient), the lower atmosphere was nearly neutral. The top of the moist layer, which approximately indicates the cloud top height, at 1800 UTC was 5.3 km MSL and slowly descended to below 4 km. The 2300 UTC sounding showed a sub-saturated layer between 1.9 and 2.5 m MSL.

2.2. Aircraft data

The Convair flew from 2134 to 2255 UTC on a northeast-southwest flight track, oriented nearly parallel to the mean wind flow during post-frontal conditions (Fig. 1). Level flight track altitudes were at 5.4 km (cloud top), 5.1 km, and 4.6 km. It performed two sets of vertical flight stacks, each consisting of two level flight legs.

The P-3 flew parallel to and 25 km south of Convair at an altitude of 4.2 km between 2300 and 2318 UTC. This flight track was over a region where the solid orographic cloud still prevailed. P-3 also performed a "lawnmower" flight pattern (Fig. 1) between 2030 and 2300 UTC intersecting the Convair's northeast-southwest flight track at four locations at heights 2, 2.6, 3.5, and 5 km (Fig. 3).

3. Results

During the vertical aircraft stacks, the S-pol radar performed RHI scans over the eastern portion of the stack every 1 degree in azimuth between 81 and 141 degrees azimuth, repeating every 10 minutes. The advantage of this type of scan procedure is the high vertical resolution that can be achieved. In figure 3 we have re-constructed vertical cross sections of reflectivity along the Convair aircraft stack every 10 minutes using these data. Over 61 scans were used to produce this RHI, thus the features are resolved with 2 km resolution.

The first impression from these figures is the highly non-uniform nature of the radar echo along this vertical cross section. For example, there is a strong

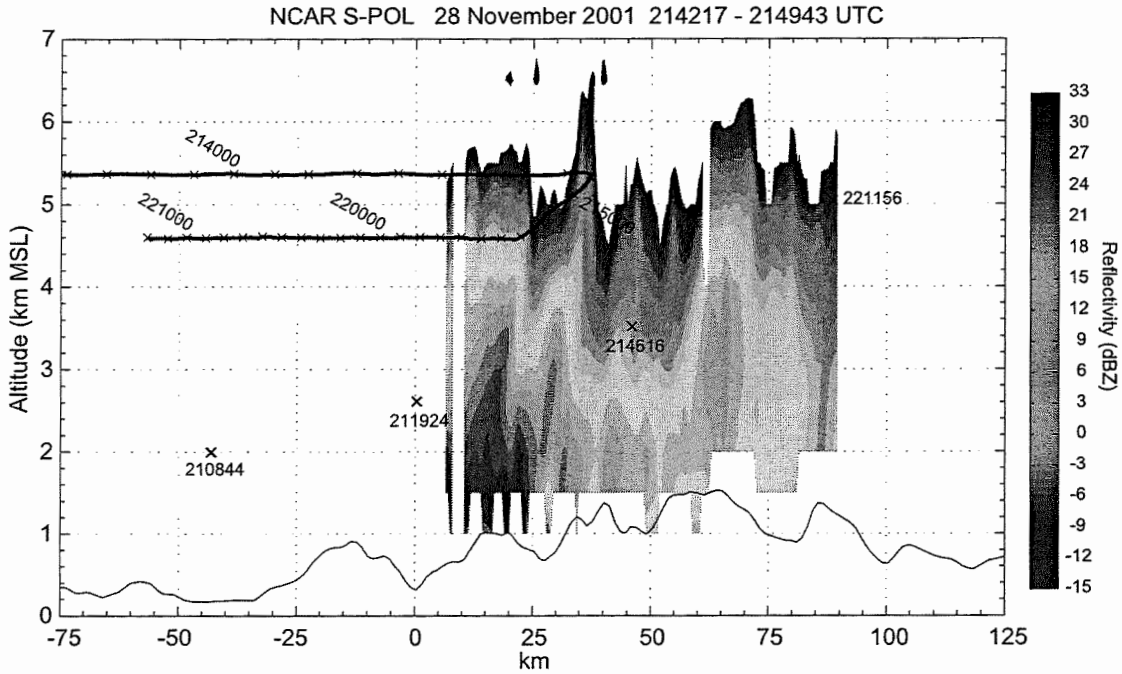

Figure 3: Reconstructed reflectivity RHI along Convair's Southwest-Northeast flight track between 213600 and 221200 UTC. The Convair flight track is indicated by a bold solid line. The crosses are placed every one minute. Four crosses at 2, 2.6, 3.5 and 5 km are locations that the P-3's north-south flight tracks intersected this vertical cross-section. Thin solid line is the topographic profile.

vertically coherent reflectivity maximum near 10 km horizontal distance, a second maximum near near 40, and a third near 75 km. Thus, there seems to be reflectivity maxima every 35 km or so. Examination of the cross sections every 10 minutes reveals that these maxima are moving with the mean winds in the layer at approximately 30 – 40 m/s (the lower level winds below 2.5 km height are , 30 m/s. The aircraft observer on the Convair aircraft noted that a convective cloud turrent was penetrated along the upper aircraft leg at 2146 UTC consisting of significant amounts of liquid water and ice corresponding to the first cloud penetration indicated in figure 3. Thus, the reflectivity maxima are most likely associated with embedded convection that is moving with the mean flow and generated by local ridges based on the fact that: 1) the lowest portion of the upstream sounding was convectively unstable, 2) the feature moved with the mean flow, and 3) the lifetime of each feature was on the order of 30 – 60 minutes or so.

Freezing drizzle is observed to occur near or within these reflectivity maxima. For instance, freezing drizzle is observed to occur during the cloud top penetrations shown in figure 3, and also at the two lower P-3 intersection points (211924 UTC and 214616 UTC). Each of these locations indicate the presence of freezing drizzle as indicated by spherical images between 100 and 300 microns diameter. In addition, the regions with radar reflectivity greater than 5 dBZ typically have snowflake aggregates present at sizes larger than 300 micons. Also note that drizzle is observed from – 3 to -18 C (other data not shown in this paper indicate the same result).

Since the air mass is maritime with a very low concentration of cloud droplets (< 30 cm^{-3} from the FSSP and the CCN counter), the cloud water value required to exceed before the onset of autoconversion is close to the observed value of 0.20 g/kg (Rasmussen et al. 2002). Drizzle formation typically occurs within 20 minutes for cumulus clouds with low concentrations of droplets (< 50 cm^{-3}), for example the shallow cumulus clouds upstream of Hawaii. Thus, the presence of drizzle in association with the embedded convection is entirely reasonable, especially when the ice crystal concentration is low and/or the updraft is over 0.5 m/s.

4. Conclusions

Microphysical conditions within a post-frontal cloud system during IMPROVE II are described based on aircraft, radar, and sounding data. The analysis showed that embedded convection was the main mechanism producing significant vertical motion, cloud

water, ice and drizzle. The embedded convection is most likely initiated by the deep vertical motion associated with flow over local ridges. Further model simulations will be required to verify this suggestion. Vertical motions were estimated to be between 0.5 to 1.5 m/s in the regions of cloud water maxima, significantly higher than 0.1 m/s values observed in the flat terrain storms. Thus, the higher condensate supply rate was able to maintain cloud water contents sufficiently high and for long enough periods to form drizzle in this maritime environment (typically cells lasted at least 30 minutes, drizzle onset was estimated to be 15-20 minutes). . A maritime environment allows drizzle to form for lower liquid water contents than for continental conditions (Rasmussen et al. 2002), allowing drizzle to form for the typically low water contents (< 0.2 gm^{-3}) observed in these storms.

Freezing drizzle was observed near cloud top in regions of low concentrations of ice crystals (< -5 dBZ), but also in the middle of the cloud in regions of actively growing convection. The reflectivity values in this case are on the order of 12 – 16 dBZ, significantly higher than typically observed with freezing drizzle. In this case, drizzle is able to survive the presence of ice crystal depletion due to the relatively strong vertical motions associated with the embedded convection and the updrafts generated by local ridges. Freezing drizzle was also observed to form in the updraft associated with flow over the highest portion of the terrain. Thus, freezing drizzle and super-cooled liquid water can occur over complex terrain when the CCN concentration is low and the updrafts relatively high.

5. Acknowledgements

This research is in response to requirements and funding of the Federal Aviation Administration (FAA). The views expressed are those of the authors and do not necessarily represent the official policy of the FAA.

6. References

Bernstein, B., T.A. Omeron, F. McDonough, and M.K. Politovich, 1997: The Relationship between Aircraft Icing and Synoptic-Scale Weather Conditions. *Wea. Forecasting*, **12**, 742 – 762.

Bernstein, B., T.A. Omeron, M.K. Politovich, and F. McDonough, 1998: Surface weather features associated with freezing precipitation and severe in -flight icing. *Atmos. Res.*, **46**, 57 – 73.

Bernstein, B. ,Frank McDonough, Marcia K. Politovich, Barbara G. Brown, Thomas P. Ratvasky, Dean R. Miller, Cory A. Wolff and Gary Cunning, 2004: Current Icing Potential (CIP): Algorithm Description and Comparison with Aircraft Observations. *J. Appl. Met.* (submitted).

Bernstein, B. C., 2000: Regional and local influences on freezing drizzle, freezing rain and ice pellet events, *Wea. Forecasting,* **15**, 485 – 508.

Cober, S. G., Strapp, and Isaac, G. A., 1996: An example of supercooled drizzle drops formed through a collision – coalescence process. *J. Appl. Met.*, **35**, 2250-2260

Geresdi, I, R.M. Rasmussen, Woitek Grabowski, and Ben Bernstein, 2004: Sensitivity of Freezing Drizzle Formation in Stably Stratified Clouds to Ice Processes. *Meteorology and Atmospheric Physics*). (In Press)

Isaac, G.A., S.G. Cober, A.V. Korolev, J.W. Strapp, and A. Tremblay, 1999: Canadian Freezing Drizzle Experiment. 37th AIAA Aerospace Science Meeting and Exhibit, American Institute of Aeronautics and Astronautics, Paper AIAA-99-0492, 10 pp.

Miller, D., T. Ratvasky, B. Bernstein, F. McDonough, and J.W. Strapp, 1998:NASA/FAA/NCAR supercooled large droplet icing flight research: Summary of 96-97 flight operations. *36th Aerospace Science Meeting and Exhibit,* Reno, NV, American Institute of Aeronautics and Astronautics Paper AIAA 98-0557, 20 pp.

Murakami, M. Y. Yamada, T. Matsuo, H. Mizuno, and K. Morikawa, 1992: Microphysical structures of warm-frontal clouds. The 20 June 1987 case study. *J. Meteor. Soc. Japan*, **70**, 877 – 895.

Pruppacher, H. R. and Klett, J. D., 1997: Microphysics of clouds and precipitation. Kluwer Academic Publishers, 945

Rasmussen, R. M., Bernstein, B., Murakami, M., Stossmeister, G. and Stankov, B., 1995: The 1990 Valentine's Day Arctic Outbreak. Part I: Mesoscale and microscale structure and evolution of a Colorado Front Range shallow upslope cloud. *J. Appl. Met.*, **34**, 1481-1511

Rasmussen, R, M., Geresdi, I., Thompson, G., Manning, K., and Karplus, E., 2002: Freezing drizzle formation in stably stratified layer clouds: The role of radiative cooling of cloud droplets and cloud condensation and ice initiation. *J. Atmos. Sci.*, **59**, 837 – 860.

Rasmussen, R.M., M. Politovich, J. Marwitz, W. Sand, J. McGinley, J. Smart, R. Pielke, S. Rutledge, D. Wesley, G. Stossmeister, B. Bernstein, K. Elmore, N. Powell, E. Westwater, B. Stankov, and D. Burrows. 1992: Winter Icing and Storms Project (WISP). *Bull. Am. Meteorol. Soc.*, **73**, 951 – 974.

Rauber, R.M., 1992: Microphysical structure and evolution of a central Sierra Nevada orographic cloud system. *J. Appl. Met.*, **31**, 3 – 24.

Rauber, R.M., L.S. Olthoff, M.K. Ramamurthy, and K.E. Kunkel, 2000: The relative importance of warm rain and melting processes in freezing precipitation events. *J. Appl. Meteor.*, **39**, 1185 – 1195.

Stoelinga, M.T., P.V. Hobbs, C.F. Mass, J.D. Locatelli, B.A. Colle, R.A. Houze, Jr., A.L. Rangno, N. A. Bond, B.F. Smull, R. M. Rasmussen, G. Thompson, B.R. Colman, 2003: Improvement of Microphysical Parameterization through Observational Verification Experiment. *Bull. Amer. Meteor. Soc.,* **84**, 1807 –1826.

Stuart, R.A. and G.A. Isaac, 1999: Freezing Precipitation in Canada. Atmosphere-Ocean, 37, 87 – 102.

Vivekanandan, J., D. S. Zrnić, S. M. Ellis, R. Oye, A.V. Ryzhkov, and J. Straka, 1999: Cloud microphysics retrieval using S-band dual-polarization radar measurements. *Bull. Amer. Meteor. Soc.*, 80, 381-388.

FALL ATTITUDES OF PRISTINE DENDRITIC SNOW CRYSTALS ESTIMATED FROM RADAR DEPOLARIZATION MEASUREMENTS

Roger F. Reinking[1] and Sergey Y. Matrosov[2]

[1]NOAA Environmental Technology Laboratory / Science & Technology Corporation
Boulder, Colorado, USA
[2]Cooperative Institute for Research in the Environmental Sciences (CIRES),
University of Colorado, and NOAA/ETL, Boulder, Colorado, USA

1. INTRODUCTION

Without electric field forces, perfectly symmetrical planar ice crystals with Reynolds numbers of $1<N_{Re}<100$ tend to fall with their major dimensions oriented horizontally. Eddies are shed and secondary motions including glide-pitch oscillations and spiral motions ("flutter") are introduced at $N_{Re} \geq 100$ (Pruppacher and Klett 1997). Many natural planar crystals have some asymmetry and begin to exhibit secondary motions if $N_{Re} \geq 40$ (Kajikawa 1992). The angular deviation from the horizontal orientation of these crystals is Gaussian (Sassen 1980).

Two depolarization-based approaches have been developed for estimating the standard deviation of the planar crystal axes of rotation from the vertical, which quantitatively describes particle flutter. With NOAA/ETL's polarization agile K_a -band radar, parameters to estimate the predominant flutter in populations of pristine dendritic crystals were measured in snowfall observed during the Mount Washington Icing Sensors Project (MWISP; Ryerson et al. 2000). The radar was set to measure linear depolarization ratios in two bases, standard horizontal-vertical (HLDR) and slant 45°-135° (SLDR), by rotating a phase-retarding plate, or PRP (Matrosov and Kropfli 1993). Both HLDR and SLDR depend on crystal shape. HLDR exhibits a strong dependence while SLDR depends only weakly on crystal orientation. The differences in these sensitivities of SLDR and HLDR provide a means to estimate the angular flutter. Assuming perfect radar system characteristics, a simple analytical expression is derived for the standard deviation of angular flutter as a function of the ratio, HLDR:SLDR. The flutter is also assessed by matching theoretical and observed depolarization patterns as a function of the elevation of the radar's beam, which accounts for radar imperfections.

2. ANALYTICAL EXPRESSION FOR FLUTTER

The depolarization ratios can be expressed in the decibel scale (i.e., SLDR and HLDR) and in linear units (S_{LDR} and H_{LDR}):

$$\mathrm{HLDR(dB)}=10\cdot \log_{10}(H_{LDR}),$$
$$\mathrm{SLDR(dB)}=10\cdot \log_{10}(S_{LDR}). \qquad (1)$$

Corresponding author: Dr. R. F. Reinking, NOAA/ETL, ET1, 325 Broadway, Boulder, CO 80301, USA; E-mail: roger.reinking@noaa.gov.

Matrosov (1991) derived the depolarization ratios S_{LDR} and H_{LDR} in terms of S_{hh} and S_{vv}, the backscattering amplitudes in the particle projection onto the radar polarization plane, and α, the canting angle between the projection of the particle axis of rotation onto the radar polarization plane and the vector of the vertical polarization. Orientation dependence of H_{LDR} and S_{LDR} is introduced primarily through α. For $\alpha = 0$, theoretically $H_{LDR} = 0$. In practice, H_{LDR} never reaches 0 due to "cross-talk" between the two polarimetric components. For small α (small flutter), and $S_{hh} \approx 1.8\ S_{vv}$, which is true for 500 μm to 2 mm dendrites viewed at low radar elevation angles, one can show that:

$$H_{LDR} / S_{LDR} \approx 2.6\ \alpha^2 \qquad (2)$$

(all angular quantities are in radians unless degrees are specifically mentioned).

The dendrite orientation in space is defined by two polar angles: the zenith angle θ and the azimuth angle ϕ of the dendrite axis of rotation. The distribution of θ is assumed normal (Gaussian), and the distribution of the dendrite axis of rotation with respect to the azimuth angle ϕ is random. From the general equations relating radar elevation angle χ, canting angle α, zenith angle θ, and azimuth angle ϕ (Holt 1984), for small values of χ and small flutter such that $\tan(\alpha)\approx\sin(\alpha)\approx\alpha$, and $\cos(\alpha)\approx 1$,

$$\alpha \approx \theta \sin\phi. \qquad (3)$$

The standard deviation σ_θ describes the magnitude of crystal flutter, although the radar polarimetric parameters depend primarily on α and not directly on θ. Full derivations by Matrosov and Reinking (2004) show that:

$$\sigma_\theta \approx 0.9\ (H_{LDR}/S_{LDR})^{0.5}. \qquad (4)$$

Most dendritic crystals grow rapidly to sizes that introduce some secondary motions. This rapid growth allows the assumption that flutter does not depend on crystal diameters, so (4) can be used for estimating σ_θ for particle populations. Note that approximations in (4) are for small radar elevation angles ($\chi \leq 5°$) and are referred to a perfect radar hardware (negligible polarization "cross-talk" and perfect horizontal-vertical and slant-45° linear polarization bases). The approximations become progressively less valid when α and θ increase beyond about 10°, and (4) is expected to become biased to higher values under these

conditions.

3. ESTIMATES FROM ANALYTICAL APPROACH

Polarization imperfections are usually ignored, but special calibration procedures during measurements in drizzle (Matrosov et al. 2001; Reinking et al. 2002) were used to establish real polarizations employed by the radar. A pair of over-the-top (vertical plane) range-height indicator (RHI) radar scans from the 87° azimuth provided HLDR and SLDR measurements closely separated in time (not shown). Simultaneous crystal samples at the radar and the Mt. Washington Observatory (at $\chi \approx 18°$, 1.2 km above the radar) indicated pristine, 2-mm dendrites with typical sizes of about 2 mm. The elevation angle dependencies of both HLDR and SLDR in Fig. 1 characterize the layer of dendrites at a fixed altitude of 1.4 km above the radar site. A distinct difference between HLDR and SLDR patterns with changing elevation angle is evident in Fig. 2. This difference is attributed to the preferential orientation effects, because if the crystals were randomly oriented, SLDR and HLDR would be identical. SLDR values are larger than HLDR values, and the dynamic range of SLDR is significantly larger than that of HLDR. A stronger cross-polar component allows less

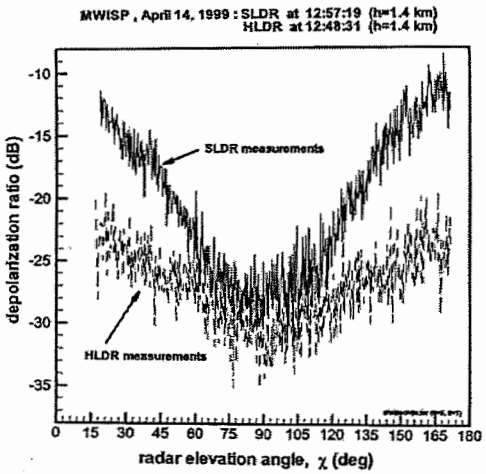

noise in the radar returns in SLDR. Homogeneity of the dendrite layer is indicated by the symmetry of depolarization values relative to χ=90°.

Figure 1. SLDR (a) at 12:57 UTC and HLDR (b) at 12:49 UTC as a function of the radar elevation angle as measured in the layer of single pristine dendrites at 1.4 km above radar site.

Observations of the magnitude of the co-polar return as a function of the PRP rotation angle for measurements taken at a fixed elevation angle allow one to determine the mean value of α (Matrosov et al. 2001). Measurements with a rotating PRP at several fixed values of χ (not shown) indicated that the mean value of α and hence that of θ were essentially zero, so the value of σ_θ was a proper sole parameter characterizing crystal orientation. The lowest radar elevation where reliable estimates of both HLDR and SLDR were possible was near χ = 15° and 165° (Fig.1). Using H_{LDR} and S_{LDR} values observed between χ = 15° and 165° in (4) results in an σ_θ estimate of ~ 12°.

4. ESTIMATES FROM MATCHING THEORETICAL AND EXPERIMENTAL DATA

Assumptions dictate that Equation (4) is applicable to the depolarization ratios in the perfect horizontal-vertical (for HLDR) and slant-45° linear (for SLDR) bases. This equation, although convenient, does not provide a direct estimate of the uncertainties involved in defining a flutter estimator. Another approach to estimate σ_θ is to calculate theoretically the ratios as a function of the radar elevation angle, χ, and to compare the results of calculations and measurements for different σ_θ values. Then there is no need to make assumptions that flutter is small, the ratio of backscattering amplitudes S_h and S_v is fixed, or the radar "cross-talk" is negligible. The actual polarization states can be considered by accounting for the parameters of the particular PRP (Matrosov et al. 2001). The depolarization dependence on χ can also be used to judge how well the flutter estimates fit a particular crystal type.

The calculations of HLDR and SLDR for the particular PRP characteristics (i.e., for the actual polarization bases used in MWISP) and the radar's polarization "cross-talk" of −35 dB were performed for a distribution of pristine dendrites modeled by the first-order gamma function with a modal diameter D_o = 2 mm (Mazin and Khrgian 1989). The computational algorithm for depolarization ratios is presented by Matrosov (1991) and Matrosov et al.(2001). Figure 2 shows the results of the depolarization calculations for σ_θ = 3°, 9°,

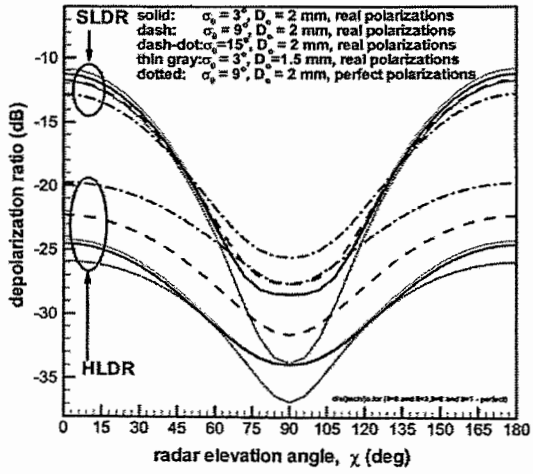

and 15°. Results for D_o=1.5 mm and σ_θ = 3° in this figure show the insensitivity of depolarization ratios to the choice of D_o; the variability of HLDR and

Figure 2. Results of modeling of SLDR and HLDR as a

function of radar elevation angle for pristine dendrites for several values of σ_θ and the characteristic dendrite diameter D_o.

SLDR with D_o in this range is rather small. Increasing D_o causes the particle to be more oblate, which increases depolarization. On the other hand, larger particles have smaller refractive indices (are optically "softer") than smaller particles, and hence, cause less depolarization compared to scatterers of the same oblateness but with a larger refractive index. This mechanism partially balances the increase in depolarization caused by the increase of the average oblateness. For D_o=2 mm and σ_θ=9°, HLDR calculated for the perfect horizontal-vertical polarization basis and SLDR calculated for the perfect slant-45° polarization basis are also shown in Fig. 2 for reference.

Also from Fig. 2, variability of SLDR due to variation in σ_θ is significantly less than that of HLDR, especially for χ < 60° and χ >120° and is almost nonexistent at $\chi \approx 45°$ and $\chi \approx 135°$. Measurements of SLDR at these radar elevation angles can be used to determine particle shapes since orientation effects here are minimal, and effects of the "imperfections" of the used polarizations are also small near these values of χ (Matrosov et al. (2001).

Figure 3 superimposes depolarization measurements on modeled data for σ_θ = 9°±3°. The calculations effectively bracket the measurements, especially for HLDR, which is significantly more sensitive to crystal flutter than SLDR. The results presented in Fig. 3 can be considered as an estimate of σ_θ *with its uncertainties.* The theoretical estimate of $\sigma_\theta \approx 12°$ obtained from (4) using experimental HLDR and SLDR data is on the high end of the estimate from matching the measurements with model calculations. This encouraging fact indicates that the magnitude of flutter and "imperfections" in the polarizations used in the radar configuration during MWISP are not very significant. Therefore, the estimate from the approximate analytical equation (4) using observed depolarizations is not much different from the careful estimate using the matching procedure. Also, if the calculated values of HLDR (~ -26 dB) and SLDR (~-11.7 dB) in perfect polarization bases for σ_θ = 9°, and χ=0° (Fig. 3), rather than observed HLDR and SLDR, are substituted in (4), they provide an estimate of $\sigma_\theta \approx 10°$ which is quite close to the matching result of σ_θ = 9°± 3°. Given the arguments expressed above, the matching estimate, σ_θ = 9°± 3°, should be considered meaningful and in general agreement with the estimate from the approximate analytical equation (4).

5. CONCLUSIONS

Analytical and matching approaches that compare radar paired depolarization ratios HLDR and SLDR were developed to deduce the magnitude of secondary motion, or "flutter," of falling planar ice crystals around their preferred horizontal orientation. The observed falling pristine dendrites were characterized by $N_{Re} \approx$ 40-100. Using the matching approach, the estimated flutter was about 9°±3° as expressed by σ_θ,

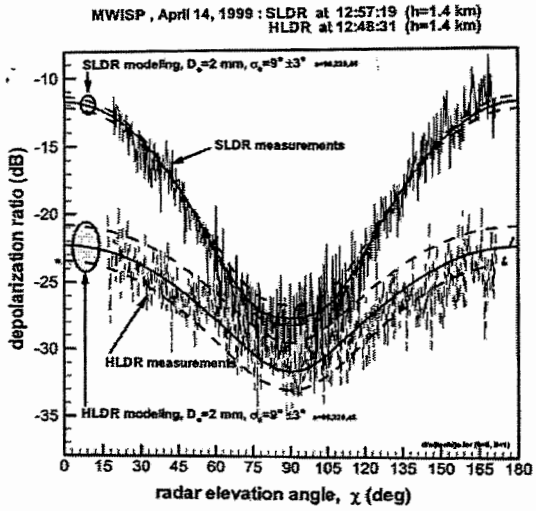

the standard deviation of the crystal rotation axes from the vertical. Such matching does not require crystal flutter to be small, is not limited to low radar elevation angles, and considers real polarization states and

Figure 3. Measurements of SLDR and HLDR from Fig.1 with superimposed results of calculations from Fig. 2 with σ_θ = 9°±3° and D_o = 2 mm.

"cross-talk" rather than perfect ones that are rarely achievable. For the analyzed case, the analytical expression provided a value of flutter of about 12°, which defined an upper bound to the more robust result from matching. This general agreement indicates that the magnitude of crystal flutter and "imperfections" in the polarization bases actually used were small enough for the analytical expression to provide a meaningful result. The value of the analytical derivation is that it displays the physical mechanisms responsible for unraveling the crystal shape and orientation effects. The noted values of flutter are comparable to estimates for planar crystals obtained in laboratory models and by individual crystal sampling (Zikmunda and Vali 1972; Kajikawa 1976; Mallman et al. 1980), but the radar can provide better estimates for whole in-cloud crystal populations. This approach can also be applied to the combination of HLDR and circular depolarization ratio (CDR) measurements, since SLDR and CDR are essentially identical for horizontally oriented planar crystals (Matrosov et al. 2001).

Acknowledgments. Irina Djalalova processed the data. MWISP was funded by the Aviation Weather Research Program of the Federal Aviation Administration (FAA) and NOAA/ETL. The views expressed are those of the authors and do not necessarily represent the official policy of the FAA.

REFERENCES

Holt, A.R., 1984: Some factors affecting the remote sensing of rain by polarization diversity radar in

3- to 35 GHz frequency range. *Radio Sci.,* **47**, 1399-1421.

Kajikawa, M., 1976: Observation of falling motion of columnar snow crystals. *J. Meteor. Soc. Japan,* **54**, 276-283.

Kajikawa, M., 1992: Observations of the falling motion of plate-like snow crystals, Part I: The free-fall patterns and velocity variations of unrimed crystals. *J. Meteor. Soc. Japan,* **70**, 1-9.

Mallman, A. J., J. L. Hock, and R. G. Greenler, 1980: Comparison of sun pillar with light pillars from nearby light sources. *Appl. Opt.,* **37**, 1441-1449.

Matrosov, S.Y., 1991: Theoretical study of radar polarization parameters obtained from cirrus clouds. *J. Atmos. Sci.,* **48**, 1062-1970.

Matrosov, S.Y., and R.A. Kropfli, 1993: Cirrus cloud studies with elliptically polarized Ka-band radar signals: A suggested approach. *J. Atmos. Oceanic Technol.,* **10**, 684-692.

Matrosov, S.Y., R.F. Reinking, R.A. Kropfli, B.E. Martner, and B.W. Bartram, 2001: On the use of radar depolarization ratios for estimating shapes of ice hydrometeors in winter clouds. *J. Appl. Meteor.,* **40**, 479-490.

Matrosov, S.Y. and R.F. Reinking, 2004: Inferring fall attitudes of pristine dendritic crystals. (Submitted to J. Atmos. Sci.)

Mazin,I.P., and A.K. Khrgian, editors, 1980: *Clouds and Cloudy Atmosphere*. Gidrometeoizdat. 648 pp.

Pruppacher, H.R., and J.D. Klett, 1997: *Microphysics of Clouds and Precipitation.* Kluwer Academic Publishers, 954 pp.

Reinking, R.F. S.Y. Matrosov, R.A. Kropfli, and B.W. Bartram, 2002: Evaluation of a 45° slant quasi-linear radar polarization state for distinguishing drizzle droplets, pristine ice crystals, and less regular ice particles. *J. Atmos. Oceanic Technol.,* **19**, 296-321.

Ryerson, C.C., et al., 2000: MWISP:: Conduct and preliminary results. *Proc. 38th AAIA Aerospace Science Meeting and Exhibit.* Paper No AAIA-2000-0488, Reno, NV, AIAA, 10 pp.

Sassen, K., 1980: Remote sensing of planar ice crystal fall attitudes. *J. Meteor. Soc. Japan,* **58**, 422-429.

Zikmunda, J., and G. Vali, 1972: Fall patterns and fall velocities of rimed ice crystals. *J. Atmos. Sci.,* **29**, 1334-1347.

SENSITIVITY OF CLOUD MICROPHYSICS AND SURFACE PRECIPITATION TO CCN AND GCCN CONCENTRATIONS IN A WINTER STRATIFORM EVENT

Stephen M. Saleeby* and William R. Cotton

Colorado State University, Ft. Collins, Colorado

1. INTRODUCTION

The microphysics model of the Regional Atmospheric Modeling System @ Colorado State University (RAMS@CSU) has extended the two-moment approach of prognosis of mixing ratio and number concentration of each hydrometeor species to the cloud droplet distribution via a parameterization for the formation of cloud droplets from activation of CCN and GCCN within a lifted parcel (Saleeby and Cotton 2004a). The Lagrangian parcel model of Heymsfield and Sabin (1989), based upon the Köhler equations for aerosol activation and the supersaturation equation for a lifted parcel, was utilized to determine the percent of CCN/GCCN that deliquesce, activate, and grow by condensation into cloud droplets.

The lookup table approach of Walko et al. (1995) was implemented to circumvent the need to couple the parcel model to the mesoscale model. These multi-dimensional data tables contain the percent of CCN that result in the formation of cloud droplets in an environment that varies with temperature, vertical velocity, and CCN concentration and median radius. The cloud droplet spectrum is a bi-modal distribution with small cloud droplets (cloud1) with diameters from 2-40μm and large cloud droplets (cloud2) from 40-80μm. Activation of CCN (GCCN) results in formation of cloud1 (cloud2) droplets.

This paper presents a series of tests of the new parameterization of cloud droplet formation in a winter-time, weakly-forced, near-freezing, strato-cumulus case which occurred from 29-30 January, 1998. This event provided rain and snow to Ohio, upstate New York, the Appalachians of West Virginia and Pennslyvania, and the eastern Great Lakes. The sensitivity of the module is examined with respect to varying concentrations of CCN and GCCN. Details concerning the synoptic conditions, sensitivity to the cloud2 mode, and model comparisons to aircraft data are given by Saleeby and Cotton (2004b).

2. MODEL FORMULATION

Simulations involving this winter icing event were run from 1200 UTC 1/29 to 1800 UTC 1/30 of 1998. The model configuration resembles the RAMS real-time forecast version with grids 1 and 2 having grid spacings of 48km and 12km, respectively (http://rams.atmos.colostate.edu). The model was initialized and nudged on the lateral boundaries with NCEP reanalysis, rawinsonde, and surface data. Further detais of the model configuration are given in Saleeby and Cotton (2004b). Simulations were run with single moment microphysics prognosing hydrometeor mixing ratio for snow, aggregates, graupel, and hail. Two-moment prediction of mixing ratio and number concentration was implemented for pristine ice and for the two cloud droplet modes. Initial aerosol concentrations and median radii of the aerosol log normal distribution are user-specified and vary among simulations. The sensitivity experiments are initialized with the following variations in CCN (GCCN) concentrations (cm^{-3}): EXP1 = 500 (10^{-1}), EXP2 = 50 (10^{-1}), EXP3 = 500 (10^{-5}), and EXP4 = 50 (10^{-5}). The respective CCN and GCCN median radii of the aerosol distribution are 0.04 and 3.0μm. Aerosol concentrations were initialized vertically and horizontally homogeneous without sources or sinks.

3. ICING EVENT SIMULATIONS: 29-30 JAN 1998

This wintertime, stratiform, icing case was chosen for simulation to assess the model response in the microphysics in weakly forced conditions dominated by cold cloud processes. The following discussion and figures examine differences among the simulations with respect to accumulated precipitation, domain-averaged vertical variations of cloud1, cloud2, and pristine ice mixing ratio and number concentration.

3.1 Accumulated precipitation

The fields of accumulated rainfall and snowfall for EXP1 and EXP3 reveal precipitation differences for constant, high CCN and varying GCCN concentrations (Fig. 1). Plots for EXP2 and EXP4 are not shown since differences are minor. When the GCCN number is increased, the rainfall is increased in New York and West Virginia. The greatest difference in rainfall due to CCN occurs when few GCCN are present, since development of rain relies upon activation of CCN and nucleation of cloud1 droplets. Fewer activated CCN take up more vapor per droplet and readily grow to raindrop sizes. A larger number of GCCN accelerates raindrop growth and reduces the dependence upon CCN for rain formation. In the case of ice and snow production, the greatest contrast in snow and ice accumulation occurs for the change in GCCN number,

Corresponding author address: Stephen M. Saleeby, Atmospheric Sci Dept., Colorado State Univ, Fort Collins, CO 80523; e-mail: smsaleeb@atmos.colostate.edu

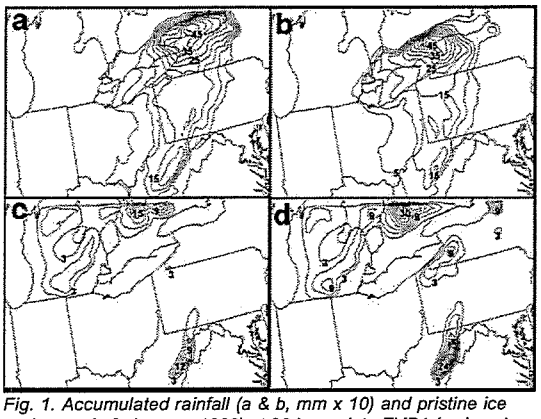

Fig. 1. Accumulated rainfall (a & b, mm x 10) and pristine ice and snow (c & d, mm x 1000) at 30 hours into EXP1 (a,c) and EXP3 (b,d).

irrespective of the CCN number. The larger number of GCCN results in nearly one-half the snowfall. This complements the relationship between GCCN and rainfall, such that the droplet growth due to GCCN nucleation reduces the amount of vapor that is allocated to cloud1 and ice nucleation. With cloud2 droplets forming from GCCN, collisions quickly produce rain size drops. These drops compete for vapor and are unlikely to freeze instantaneously since temperatures are above -10°C. Ice formation relies on vapor deposition onto IFN, contact freezing of cloud droplets on IFN, or ice splintering from ice crystal collisions with supercooled droplets. With much of the vapor allocated to cloud2 and rain, much less remains for cloud1 and pristine ice. Despite the vapor competition, there is an abundance of small ice crystals that are suspended in-cloud. When mixed-phase clouds are present in this stratiform environment, the GCCN enhance the cloud's colloidal stability with respect to ice crystals and its instability with respect to liquid drops. There are only small variations in snowfall when GCCN number is constant and CCN number is varied. The impact of CCN is largest when the number of GCCN is minimized. With few GCCN in the field, a greater number of CCN will produce more cloud droplets, which can aid in ice formation, and contribute to surface accumulation.

3.2 Vertical distribution of cloud1

Domain-averaged cloud1 mixing ratio distributions vary vertically and temporally with the initial aerosol distributions (Fig. 2). At each time, the simulation with the greatest cloud1 mixing ratio contains a maximum in CCN and minimum in GCCN. The typical maximum mixing ratio at each displayed time progresses from greatest to least in the following order: EXP3, EXP4, EXP1, EXP2. This trend in diminishing maximum cloud1 water reveals that LWC depends strongly upon both CCN and GCCN. The liquid water contribution to cloud1 is maximized when GCCN are few since these nuclei condense vapor more effectively than the smaller CCN due to larger radii and lower vapor pressure at their surfaces. The case with few CCN cannot deplete the vapor supply as effectively. The resulting larger cloud1 droplets readily grow to cloud2 sizes, thereby, removing water from the cloud1 mode.

The average number concentration profiles (Fig. 3) vary differently compared to the mixing ratio. Generally, the maximum cloud1 number concentration among the simulations progresses from greatest to least in the following order: EXP3, EXP1, EXP4, EXP2. The cloud1 concentration has the greatest dependence on the CCN number, such that EXP1 and EXP3 produce more cloud1 droplets. Throughout EXP1 and EXP3, there were reversals as to which simulation produced the maximum concentration of cloud1 droplets, suggesting that the influence of GCCN on cloud1 concentration is weak compared to mixing ratio. Even with many GCCN, there is enough vapor contributing to CCN nucleation so that cloud1 droplets are produced, though, they are smaller than in the cases with few GCCN. In response, the cloud1 droplets remain suspended higher in the cloud, and their collision efficiencies are also smaller, which delays and suppresses rain and ice growth.

The domain-maximum cloud1 LWC for each test occurs at 1634m at 2000UTC 1/29 in (g kg^{-1}) as: EXP1 (0.72), EXP2 (0.78), EXP3 (0.82), EXP4 (0.87).

3.3 Vertical distribution of cloud2

Though not shown here, the response of the cloud2 mixing ratio is opposite to that of the cloud1 mode. At most of the analysis times shown, the maximum mixing ratio among the simulations progresses from greatest to least in the following order: EXP1, EXP2, EXP3, EXP4. Cloud2 mixing ratio is almost completely dependent on the number concentration of GCCN. When GCCN number is at a minimum there is a negligible amount of liquid water in the cloud2 mode. At the time of maximum mixing ratio in EXP3 and EXP4, there is a slight dependence of mixing ratio on concentration of CCN. Magnitudes are higher when CCN are numerous; more CCN compete for vapor, more cloud1 droplets form, and more cloud2 droplets form and grow via self-collection of cloud1 or collection of cloud1 with cloud2. The dependence of cloud2 water on CCN number, for a large number of GCCN (EXP1 and EXP2), varies among the times shown. At the earliest displayed time, cloud2 mixing ratio is greater for EXP2, and the latter times reveal greater maximum values for EXP1. There is not a consistent dependence of cloud2 mixing ratio on the CCN number for numerous GCCN. Processes other than nucleation can cause the observed differences. When fewer CCN are present, more vapor diffuses to each activated nuclei; this can produce enhanced vapor growth with resulting larger droplets that have larger collection efficiencies, which would allow droplet growth to cloud2 size. On the other hand, a large number of CCN will divide up the excess vapor, resulting in numerous, small droplets; though vapor growth will be limited, there will be more small droplets

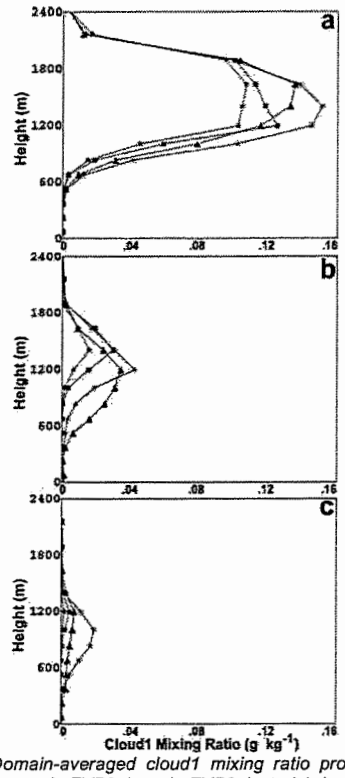

Fig. 2. Domain-averaged cloud1 mixing ratio profiles from EXP1 (squares), EXP2 (stars), EXP3 (asterisks), and EXP4 (triangles). Plots are for the following times: (a) 2300UTC 29th, (b)0700UTC 30th, and (c)1500UTC 30th.

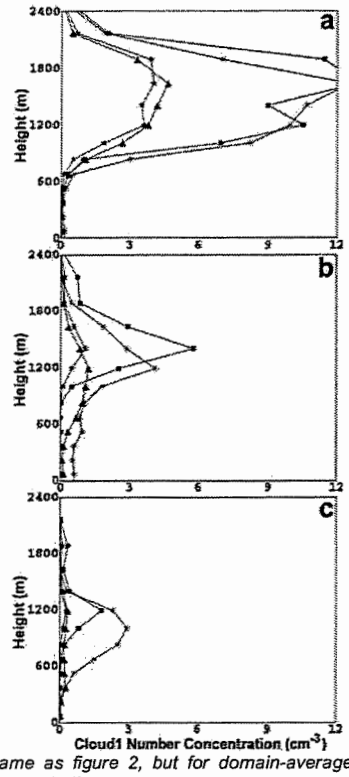

Fig. 3. Same as figure 2, but for domain-averaged cloud1 number concentration.

present for collisional growth. These processes are dominant at different times in the simulations. The domain-maximum cloud2 LWC for each test occurs at 1403m 2000 UTC 1/29 in (g kg^{-1}) as: EXP1 (0.040), EXP2 (0.050), EXP3 (0.010), EXP4 (0.005). This layer of cloud2 water is nearly an order of magnitude less than than of cloud1 and is at a lower altitude due to sedimentation.

3.4 Vertical distribution of pristine ice

In this winter icing event, temperatures up to 5000 meters were warmer than -20°C. For temperatures below -2°C, RAMS will initiate contact freezing of cloud droplets with IFN. If the temperature is less than -5°C and the air is saturated with respect to ice, there can be nucleation via deposition-condensation freezing with IFN, and from -3 to -8°C, ice splintering can occur from collisions between pristine ice and cloud droplets.

By 11 hours (Fig. 4a), ice forms into a distinct layer near cloud top and differences in the ice profiles among the simulations are evident. A basic ranking of max imum mixing ratio at a given time in terms of greatest to least occurs in the following order: EXP1, EXP2, EXP4, EXP3. The ice content dependence on aerosol is greatest for variations in number of GCCN. Despite the CCN number, a greater number of GCCN results in greater ice mass and number. For a constant GCCN concentration, the variation of CCN has less impact. There is no consistent relationship between ice crystal mixing ratio and CCN number that holds true for all given times. At most times, though, a lower CCN concentration results in a slightly greater ice mixing ratio. When GCCN concentrations are large, contact freezing of droplets with IFN and ice multiplication involving cloud2 droplets and pristine ice are significant sources for ice production. These processes depend upon droplet size, and are more effective when larger droplets are available. When few GCCN are present, more ice develops when the CCN number is small; fewer CCN will take up less vapor as a whole and will allow rapid droplet growth to large cloud1 or cloud2 droplets. This can enhance contact freezing and ice multiplication and provide high ice supersaturations for IFN nucleation.

4. CONCLUSIONS

The following points summarize the sensitivities of the RAMS@CSU model to CCN and GCCN:

1. The initial number concentrations of CCN and GCCN influence the amount of model precipitation,

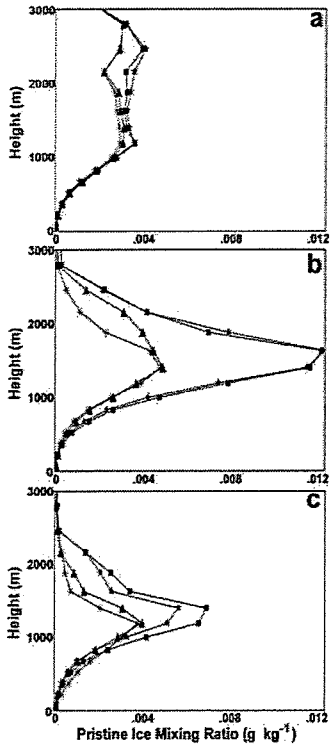

Fig. 4. Same as figure 2, but for domain-averaged pristine ice mixing ratio.

such that, the greatest difference in both the rainfall and snowfall patterns and magnitudes occurs for a change in GCCN number from 10^{-5} to 10^{-1} (cm^{-3}). (CCN number was varied from 50 to 500 (cm^{-3}), and resulting changes in precipitation are present to a lesser degree.)

2. The greatest production of cloud1 mixing ratio and number concentration occurs for a maximum in CCN and minimum in GCCN; the presence of GCCN reduces the amount of vapor allotted to CCN and the cloud1 category. The greatest production of cloud2 mixing ratio and number concentration occurs when the number of GCCN is large, regardless of the number of CCN.

3. The greatest production of pristine ice mixing ratio and number concentration occurs when GCCN are numerous. The number of CCN is influential to a lesser degree. This is attributed to increased efficiency in ice formation by contact freezing and ice multiplication involving the cloud2 droplets.

Acknowledgments. This research was supported by a grant from the National Center for Atmospheric Research under grant S00-19852 and by the National Science Foundation under grant ATM-9900929.

5. REFERENCES

Heymsfield, A.J., and R.M. Sabin, 1989: Cirrus crystal nucleation by homogeneous freezing of solution droplets. *J. Atmos. Sci.*, **46**, 2252-2264.

Meyers, M.P., P.J. DeMott, and W.R. Cotton, 1992: New primary ice-nucleation parameterizations in an explicit cloud model. *J. Appl. Meteor.* **31**, 708-721.

Saleeby, S.M., and W.R. Cotton, 2004a: A large droplet mode and prognostic number concentration of cloud droplets in the RAMS@CSU model. Part I: Module descriptions and supercell test simulations. *J. Appl. Meteor.*, **43**, 182-195.

Saleeby, S.M., and W.R. Cotton, 2004b: A large droplet mode and prognostic number concentration of cloud droplets in the RAMS@CSU model. Part II: Model sensitivity to a winter stratiform event *J. Appl. Meteor.*, (Submitted).

Walko, R.L., W.R. Cotton, M.P. Meyers, and J.Y. Harrington, 1995: New RAMS cloud microphysics parameterization: Part I. The single-moment scheme. *Atmos. Res.*, **38**, 29-62.

COMBINED MEASUREMENTS OF SNOWFLAKE CHARACTERISTICS IN THE MELTING LAYER

Raphael Schefold[1], Björn Baschek[1], Aaron Bansemer[2] and Eszter Barthazy[1]

[1]Institute for Atmospheric and Climate Science, ETH Zürich, Switzerland
[2]Mesoscale and Microscale Meteorology Division, NCAR, Boulder, USA

1. INTRODUCTION

Aggregates of crystals are the type of hydrometeors whose fall velocities and other properties are the least investigated. In radar studies, however, the larger aggregates play an important role as the energy backscattered by a particle depends on the sixth power of its diameter. Within the melting layer, melting, aggregation and break up of the ice crystals and snowflakes are important processes which influence the fall velocity and other properties of snowflakes. However, accurate experimental observations of size distributions, fall velocities, shape descriptions and masses, with description of the true spread of each property are scarce due to either the limited number of observed snowflakes, or to the limitations of the observations.

In situ experiments were carried out during several field campaigns for the measurement and description of these properties of snowflakes. The experiments included measurements of snowflakes with optical instruments, measurements of the water equivalent of snowflakes and the documentation of the different crystal types and riming degrees of the particles with the Formvar technique (Schaefer, 1941).

2. INSTRUMENTATION

2.1 Hydrometeor Velocity and Shape Detector

Except for some in situ techniques, where snowflakes are captured and examined, optical techniques are the best choice when velocities and side views of snowflakes are to be investigated. The Institute for Atmospheric and Climate Science at ETH has developed the Hydrometeor Velocity and Size Detector (HVSD) for this purpose. Its optical system consists of two vertically offset measuring planes with an area of 77 cm^2 and measures the side projection and velocity of each particle falling through the measuring area (Fig. 1). Sizes, shapes, and fall velocities of individual and number fluxes of ensembles of precipitation particles are thus measured and examined (Barthazy et al., 2003).

Corresponding author's address: Raphael Schefold, Institute for Atmospheric and Climate Science (IAC***ETH***), HPP L10, CH-8093 Zürich.
Email: raphael.schefold@env.ethz.ch

2.2 Snow Video Spectrometer

To measure the size, shape and water equivalent and therefore the mass of snowflakes, a Snow Video Spectrometer (SVS) (Fig. 2) was used (Borys, 2001). This instrument uses a direct imaging technique, where snowflakes and their melted drop equivalents are recorded. In the first step, snowflakes fall on a transparent Teflon tape for a defined measuring interval, where they were imaged from beneath while being illuminated from above. These images yield information about the size and the shape of snowflakes. In the second step, a heater melts the gathered snowflakes to produce drop equivalents of them. Images taken from the drop equivalents lead to information about the masses of snowflakes, because a relation between the diameter and the mass of the drops is experimentally known. The SVS yields information about relations between the mass, the size and the shape of snowflakes in a range of 0.2 mm to 4 mm for measured maximum diameters, 0.1 mm^2 to 1 mm^2 for measured particle areas and 3 µg to 1 mg for measured particle masses.

3. HYDRODYNAMIC THEORY

3.1 Description

A theory (Böhm, 1992) leads to a general relation between the Reynolds number $Re = (v_t\, d)/\nu$ and the Best number X which can be expressed as $X=(2mgd^2)/(\rho\nu^2 A)$. The relation is valid for all types of ice crystals and can be approximated (Fig. 3a) with $Re=aX^b$ for discrete intervals and where a and b are defined coefficients of the relation (Mitchell, 1996). In the given formulae, v_t is the terminal velocity of the particle; d a characteristic dimension of it; ν the kinematic viscosity of the air; ρ the density of the air; m the mass of the particle; g the gravitational acceleration, and A an effective bottom area of the particle. This general relation between Re and X has been experimentally verified for many types of crystals. Aggregates larger than 5 mm and with X larger than 10^5 have smaller values of Re than shown in Fig. 3a (Mitchell and Heymsfield, 2003). The approximated X-Re relation reveals a general relation between the particle describing variables m, v_t, d, and A:

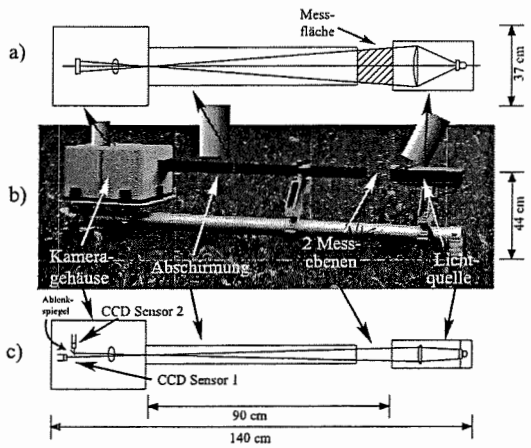

Figure 1: *Sensor of the HVSD. a) Top view drawing, b) photo, c) side view drawing.*

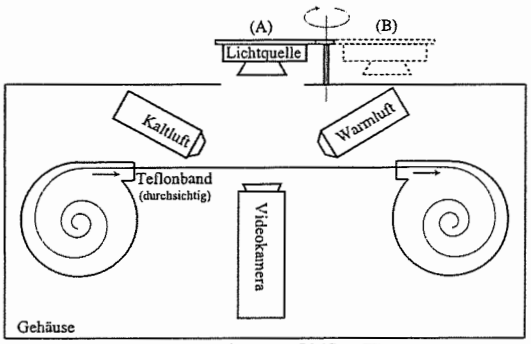

Figure 2: *Principle of the SVS. The light source serves also as shutter. To record snowflakes, cold air is used. To melt snowflakes and to produce the drop equivalents, warm air is used. Before the shutter is opened for further acquisition, the Teflon tape is moved to a clean spot.*

$$v_t = a\frac{\nu}{d}\left(\frac{2mgd^2}{\rho\nu A}\right)^b, \qquad (1)$$

where a and b are the coefficients of the defined approximation $Re=aX^b$. It is seen that the quotient m/A in equation 1 is important for the determination of v_t.

3.2 Experimental test

Fig. 3b shows the measured values of the X-Re relation. The values were measured with both instruments: Values of Re were determined with measurements from the HVSD and values of X were determined with measurements from the SVS. The instruments were run parallel and measured therefore the same type of crystals at the same time. By taking and examining Formvar samples, there were several time periods found with a primary crystal type. The observed crystal types were rimed dendrites, clumpy

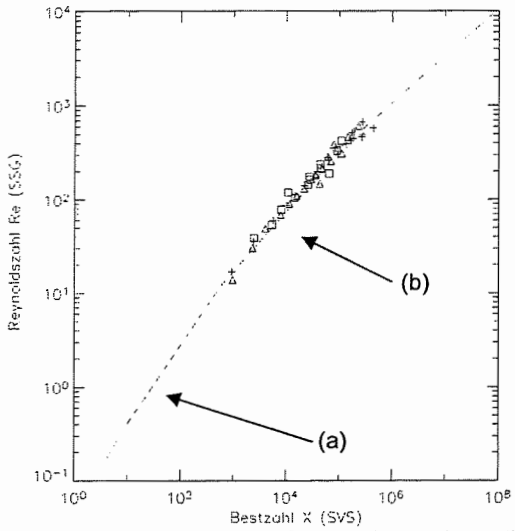

Figure 3: *(a) The four different lines show the piecewise approximation of the general X-Re-relation in four regions. Different line styles depict different regions of the approximation. (b) The symbols depict measurements of different particle types at different times and different sizes. The values of X were gained from SVS data and values of Re were gained from HVSD data.*

graupels, sector crystals, hexagonal plates and aggregates of different unrimed ice crystals with a size range of 0.1 to 4 mm. Different symbols in Fig. 3b depict different crystal types. The agreement of the values measured with the HVSD and the SVS and given through the approximation of the X-Re relation is very good (Figs. 3a, 3b). Parallel measurements with the HVSD and the SVS are therefore suited to study hydrodynamic aspects of ice crystals and snowflakes.

4. MASS ESTIMATION

In this work, we describe a method of combining the hydrodynamic theory with the measurements of the HVSD, yielding a full description of the characteristics of particles in or above the melting layer. For example, mass fluxes of snowflakes in or above the melting layer can be estimated and compared with mass fluxes of raindrops under the melting layer, as measured with disdrometers.

Equation (1) describes a relation between the particle describing variables m, v_t, d, and A, where v_t and d can be measured with the HVSD easily. Also, an estimation of A can be given, based on characteristics of snowflakes of similar type and size. By observing precipitation it is often seen that the observed primary particle type is conserved over a certain time period. For an ensemble of particles with similar type and size:

$$\bar{t} = \bar{b}, \qquad (2)$$

where t and b are defined in Fig. 4, and the $\bar{}$ denotes an average value within the particle ensemble, because no preferred orientation of the particle in the xy-plane exists. Similarly, it can be written:

$$\overline{\left(\frac{A}{tb}\right)} \approx \overline{\left(\frac{A_S}{hb}\right)}, \tag{3}$$

Note, that equation 3 is not as accurate as equation 2, because the left side of equation 3 is e.g. for merely horizontal aligned particles bigger than the right side. Equations 2 and 3 solve for A to:

$$A = \overline{\left(\frac{A_S}{hb}\right)}\bar{b}b \tag{4}$$

This expression can thus be determined for each particle ensemble. It follows, that the particle describing variables v_t, d, and A are known for each particle measured with the HVSD and the mass m can be determined from equation 1.

Fig. 5 shows a comparison of derived masses from the HVSD and the SVS for small aggregates of irregular particles. Note the different number of measured particles with the two instruments due to the differing measuring techniques. The $m(A)$-relations, which are important for the determination of v_t show good agreement between the SVS and the HVSD. The $m(d)$-relation and the $A(d)$-relation are overestimated by the HVSD compared to the SVS by up to 30%. A reason for this overestimation can be given through the inaccuracy of equation 3.

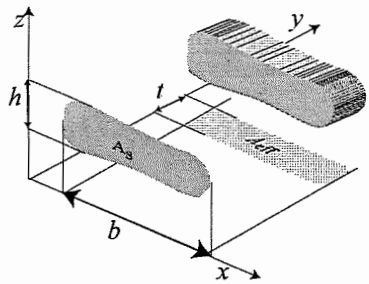

Figure 4: *Illustration for the estimation of A (here with A_{eff} depicted). Each member of the ensemble has outer dimensions h, b and t, where h, A_S and b are measured with the HVSD, but not A. t and A are then estimated based on common ensemble characteristics.*

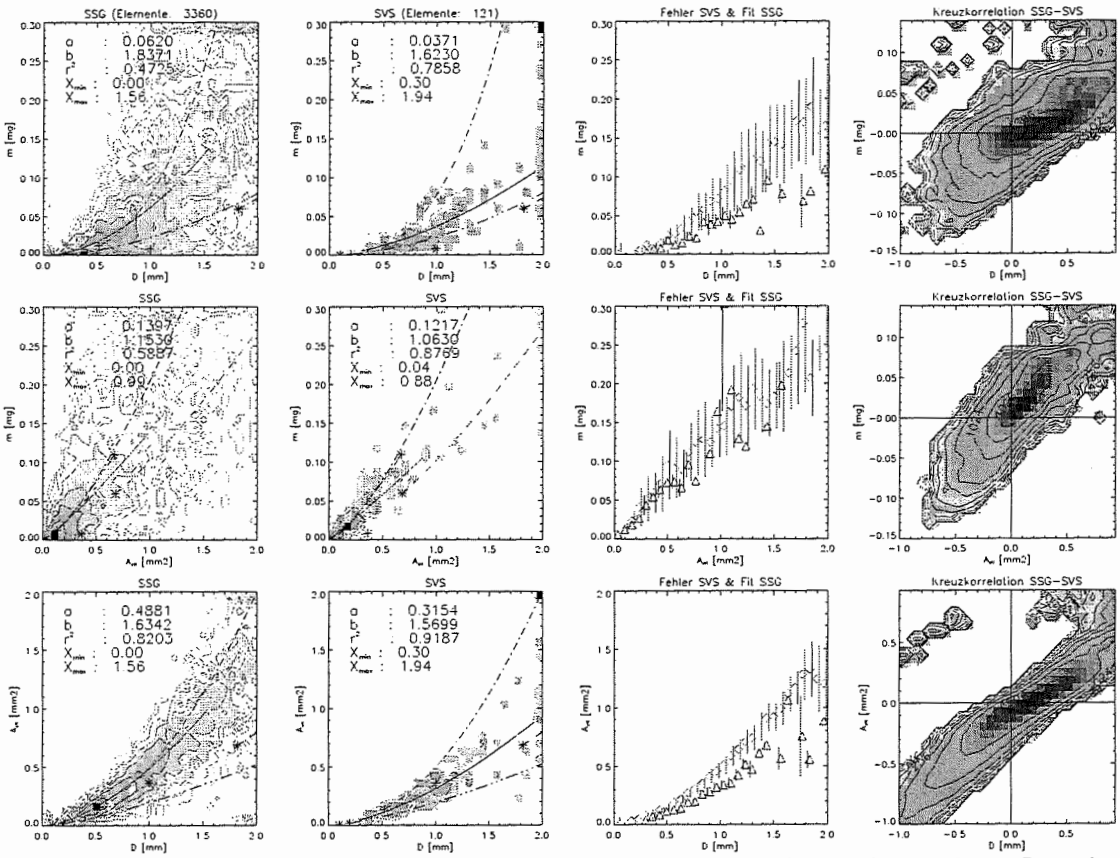

Figure 5: *Relations of $m(d)$ in the first row, $m(A)$ in the second row and $A(d)$ in the third row, in the first column derived from HVSD, in the second column derived from the SVS. The grayscales and the isolines depict the number of measurements. Given with solid lines are fit relations. Dotted lines are reference lines. The third column shows average values and standard deviations in bins for both instruments. The fourth row shows cross correlations between the instruments. The measured particles were small aggregates of irregular crystals.*

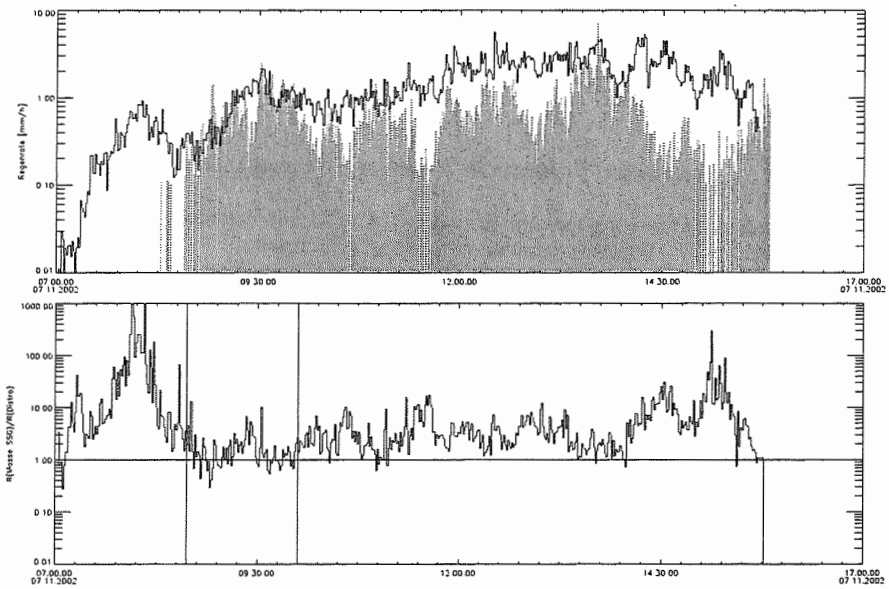

Figure 6: *The first row shows the integral mass flux computed with data from the HVSD above the melting layer (solid line) and the mass flux measured with a disdrometer under the melting layer (gray). The second row shows the quotient of the two mass fluxes. For the time between 8.40 and 10.00 and between the vertical lines no orographically effects or evaporation were assumed. The average quotient of the two mass fluxes is 1.5 between 8.40 and 10.00.*

5. MASS FLUX

The mass flux is defined as mv_t /V, where V describes a volume unit, and can be calculated from the estimated mass, as shown in section 4, and from the measured velocity. The calculation of the mass flux can be done for each particle individually, for mass- or size bins or integral. In Fig. 6 a mass flux series is shown, where the mass flux is integrated over all measured particles within a minute. The HVSD was situated 400 m above the top of the melting layer of a stratiform precipitation, where mostly small aggregates of irregular ice crystals were measured. The position of the melting layer was found using a vertically pointing X-band radar. As mass flux reference, a disdrometer positioned under the melting layer was used. The vertical distance between the distrometer and the HVSD was 1.2 km. Fig. 6 shows, that orographically induced effects or evaporation play a role (see e.g. time between 07.00 and 08.40). But for the time between 8.40 and 10.00 only small orographically induced effects or evaporation were assumed. The average quotient of the mass flux computed with data from the HVSD and the mass flux from the distrometer has between 08.40 and 10.00 a value of 1.5. In section 4 was shown, that the overestimation of the $m(d)$-relation by the HVSD compared to the SVS is 30%. Orographic effects or evaporation have therefore in this case between 08.40 and 10.00 an influence of 20% on the mass flux.

5. CONCLUSION

In this paper, tests of the hydrodynamic theory, comparisons of data of the HVSD, the SVS and a disdrometer are shown, which serve to study size-, mass- and shape distributions of ice crystals and snowflakes of different type and riming degree.

The introduced method of the combination of the hydrodynamic theory and measurements with the HVSD allows the estimation of individual snowflake masses. The masses are overestimated by the HVSD compared to the SVS by 30%, but a modification of equation 3 could solve this.

An application of this work is the construction of mass bins based on data of the HVSD, which can serve as control values for modeling purposes, e.g. of aggregation.

6. REFERENCES

Barthazy, E. S. Göke, D. Högl, and R. Schefold, 2003: An optical spectrometer for size, shape and fall velocity measurements of precipitation size hydrometeors, J. Atmos. Ocean. Tech., submitted.

Böhm, J.P., 1992: A general hydrodynamic theory for mixed-phase microphysics. Part I: Drag and fall speed of hydrometeors. Atmos. Res., 27: 253-274.

Borys, R., .2001: Private communication.

Mitchell, D.L., 1995: Use of mass-area-dimensional power laws for determining precipitation particle terminal velocities, J. Atmos. Sci., 53:171-1723.

Mitchell, D.L., and A.J. Heymsfield, 2003: Refinements in the treatment of ice particle terminal velocities, highlighting aggregates and graupel, J. Atmos. Sci., submitted.

Schaefer, V.J, 1941: A method of making snowflake replicas. Science 7:239-240.

EFFECTS OF COLLISIONAL BREAKUP ON MIXED-PHASE DEEP CONVECTION SIMULATED BY A SPECTRAL (BIN) CLOUD MODEL AND COMPARISON TO DROP SIZE SPECTRA MEASURED AT THE GROUND

Axel Seifert[1,3], Alexander Khain[2] and Ulrich Blahak[1]

[1]Institut für Meteorologie und Klimaforschung, Universität Karlsruhe / Forschungszentrum Karlsruhe, Germany
[2]Institute of the Earth Sciences, The Hebrew University of Jerusalem, Jerusalem, Israel
[3]Present Af?liation: National Center for Atmospheric Research, Boulder, Colorado, USA

1 INTRODUCTION

Coagulation and breakup of raindrops are key processes in shaping the raindrop size distribution (DSD) along the way down from the melting level to the ground. It is well known that, from a theoretical point of view, the DSD in homogeneous rain converges to a steady state or equilibrium distribution, whose shape is independent from the initial spectrum or the speci?c pathway of precipitation formation (e.g. warm rain vs. melted ice). When neglecting breakup, no equilibrium DSD is approached.

Recently a formulation of collisional breakup of raindrops was implemented in the spectral (bin) Hebrew University Cloud Model (HUCM). It is based on the parameterizations of the breakup kernel and fragment size distribution function of Low and List (1982), Beard and Ochs (1995) as well as Brown (1997).

The relative importance of the breakup process in the development of deep convective systems is investigated by various twodimensional cloud resolving simulations using HUCM with collisional breakup turned on and off. The terminal fall velocity difference of larger and smaller drops provides the key mechanism by which breakup in?uences the development of deep convective systems. Large drops break up into smaller ones, conserving the overall water mass but reducing the size and therefore the sedimentation velocity against possible vertical air motions and, therefore, the rainrate at the ground. In addition, evaporation below cloud base is enhanced when breakup is taken into account.

Nevertheless, the question arises if the used parameterization of collisional breakup is adequate to describe real precipitation. To this end, modeled spectra and raindrop spectra which where measured at ground level are carefully compared. In interpreting such a comparison, one has to keep in mind that raindrop spectra at the ground are the overall outcome of various microphysical processes operating in a cloud, partially involving the ice phase, whose description is still a source of uncertainty in all cloud models. Differences to observed spectra even in the model runs with active breakup have to be expected because the used breakup parameterization is almost entirely based on a few (but nevertheless very carefully conducted) laboratory measurements. In addition, it is only possible to investigate if the entire microphysical formulation in HUCM is "adequate" enough or not. For a more de?nite investigation, detailed measurements also inside cloud as well as below cloud base, or below the melting level, would be needed.

Corresponding author's address: Ulrich Blahak, Institut für Meteorologie und Klimaforschung, Universität Karlsruhe / Forschungszentrum Karlsruhe, Postfach 3640, D-76021 Karlsruhe, Germany;
E-mail: ulrich.blahak@imk.fzk.de.

2 DESCRIPTION OF THE MODEL SIMULATIONS USING HUCM

The basic hydro-/ thermodynamical equations solved in HUCM have been extensively described in Khain and Sednev (1996), Khain et al. (2000) and Khain et al. (2001). Detailed informations on the newly implemented breakup parameterization can be found in Seifert et al. (2004). In short, the microphysics scheme of HUCM comprises size distributions of 7 different hydrometeor types: water drops, three types of ice crystals (columnar, plate like and dendrites), snow?akes (aggregates), graupel and hail/frozen drops. Each size distribution is resolved by 33 mass doubling size classes (bins), leading to a total number of 231 microphysical prognostic variables. Further, the effects of the atmospheric aerosol are taken into account by a budget equation for the size distribution of these particles as well, which serve as cloud condensation nuclei. All microphysical processes and interactions which are currently considered to be important are resolved explicitly. Further, a height dependence of the collision ef?ciency and an enhancement of the collision rate by atmospheric turbulence are taken into account.

In the stochastic description of raindrop breakup as well as coagulation, all relevant probability distribution functions (collection kernel, collision ef?cency, breakup kernel, etc.) strongly depend on the sizes of the two colliding drops. Since HUCM uses a rather coarse resolution with 33 mass doubling bins, effects of numerical discretization cannot be ruled out a priori. To investigate this point, an idealized box model solving for the stochastic coagulation-breakup equation (only the raindrop breakup and coagulation part of the HUCM-microphysics scheme) is used to ?nd the equilibrium DSD for spatially homogeneous rain, using the same and higher bin resolutions as HUCM. The resolution parameter α is used herein to adjust a logarithmic mass

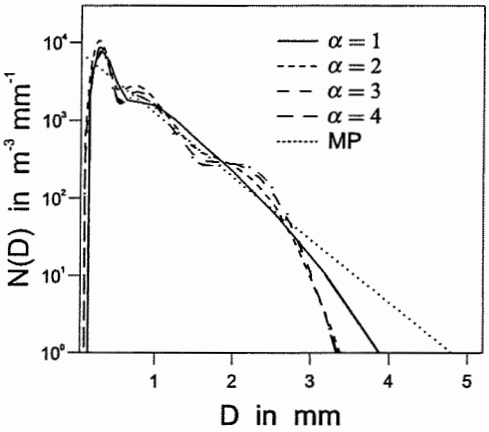

Fig. 1: Equilibrium DSDs in $m^{-3}\,mm^{-1}$ as a function of drop diameter in mm for parameters $\alpha = 1$, 2, 3 and 4 (see equation 1) and a rainrate R of 42 mm h^{-1}. HUCM uses $\alpha = 1$. Dotted line: Marshall-Palmer distribution (MP) with $R = 42$ mm h^{-1}.

coordinate x by

$$x_{i+1} = 2^{1/\alpha} x_i \,, \qquad (1)$$

where x_i denotes the ith mass value. Increasing α leads to a higher resolution and to different equilibrium distributions (?gure 1). A very similar result can be found in Hu and Srivastava (1995). To keep the computation time within manageable limits, HUCM uses $\alpha = 1$ (mass doubling), whereas stable convergence to the well known three-peak equilibrium distribution — the "true" reference — is reached only for larger values. With $\alpha = 1$, the equilibrium DSD is a unimodal distribution which contains more large drops than at higher resolutions. This indicates that HUCM numerically will slightly underestimate the breakup intensity which would be predicted by the used parameterizations at higher resolutions. This fact has to be kept in mind.

3 A CASE STUDY FROM THE GATE FIELD EXPERIMENT

Twodimensional simulations with HUCM are performed in an idealized way by triggering a single convective system through differential heating in the boundary layer over a ?at terrain. In that way, the in?uence of considering collisional raindrop breakup on some qualitative features like the timing, intensity and horizontal distribution of the precipitation event is investigated.

The semi-idealized case presented here is a maritime convective system initialized using pro?les from day 261 of the GATE ?eld experiment. The atmospheric conditions can be described as typical maritime with a rather moist boundary layer and a weak westerly background ?ow. For all simulations the model resolution was chosen to 250 m in the horizontal and 125 m in the vertical direction. Cloud condensation nuclei typical for a maritime regime are assumed.

Figure 2 (upper part) shows the time evolution of the surface rainrate R for the simulation without collisional breakup. The major precipitation event occurs about 30 min after the initialization and reaches a maximum instantaneous rainrate of $R_{max} = 178$ mm h^{-1}. Soon after this main event the precipitation rate decreases while the region of weak precipitation expands in up- and down-wind direction. Weak secondary convective precipitation events occur after about 90 min reaching a surface rainrate of about 10 mm/h. The surface precipitation resulting from the simulation with collisional breakup taken into account is shown in in the lower part of ?gure 2. With collisional breakup included, the major precipitation event occurs also after approximately 30 min nearly at the same spatial position as in the simulation without breakup, but with a much lower maximum rainrate of only $R_{max} = 90$ mm h^{-1}. The reason for the much weaker precipitation rate is the reduction of the number of very large raindrops, which are disrupted by collisional breakup. The second conspicuous difference compared to the ?rst simulation is the much stronger secondary precipitation event occurring in down-wind direction about 60 min after the primary convective event. Since collisional breakup leads

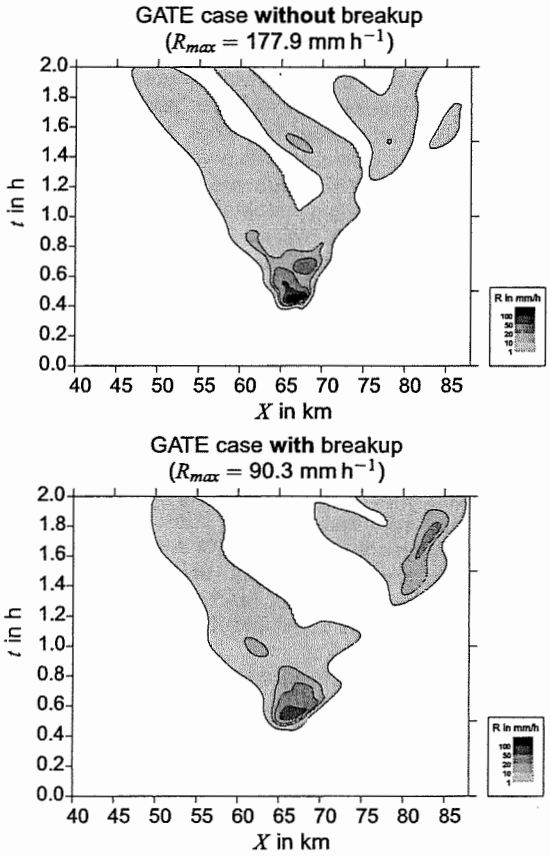

Fig. 2: Hovmöller-diagrams of the surface precipitation rate R in mm h^{-1} for the GATE simulation without breakup (upper plate) and with breakup (lower plate). The time in h refers to the start of the model run.

to the production of many small raindrops (breakup fragments), the evaporation of rain is increased leading to a stronger gust front and more intense secondary convection. This shows clearly that, due to the strong non-linear coupling between cloud microphysics and cloud dynamics, a single microphysical process like collisional breakup is able to affect the evolution of a mesoscale cloud system. Nevertheless, the effect of the breakup process on the overall accumulated precipitation is quite small in this case (not shown here). But there are other cases where the in?uence on the timing and the overall precipitation amount is much stronger (see Seifert, Khain and Blahak, 2004).

The modeled spectra without breakup for the GATE case (?gure 3, upper plate) are dominated by a rather high number concentration of large raindrops ($D > 3$ mm), which are very effectively destroyed by breakup when it is turned on (?gure 3, middle plate).

4 COMPARISON WITH OBSERVATIONS

Unfortunately, there are no direct observations of drop size spectra for the GATE-case. But under the assumption that breakup and coagulation are the main processes in forming the big drop end of the size distribution on the way down from the melting level to the ground, the drop spectrum at the ground should be more or less independent from the geographic location in heavy convective rain. Therefore, it might be allowed to compare the instantaneous shape of modeled spectra at ground with measurements from another location. Here the word "shape" denotes the relative contributions of the small and big raindrops to the spectrum.

We use a large data set of measured drop size spectra from Karlsruhe, South Germany, which were recorded during the summer months May to October during the time period 1996 to July 2003. During summer, heavy rain with rainrates of more than about 10 mm/h in that area are usually due to deep convective systems. The measuring device is a Joss-Waldvogel-Disdrometer with the standard aquisition system ADA-90 from Distromet, Ltd. It records drop counts on a measuring area of 50 cm^2 during a time interval of 1 min, and from that, the drop size distribution is calculated under the assumption of a certain fall speed law. A correction for the dead time of the instrument is applied. Available is a nearly continuous time series, which contains about 34000 1-minute-spectra with $R > 0.5$ mm h^{-1}.

When comparing instantaneous shapes of modeled DSDs with measured spectra, one has to consider the question of representativity. Modeled spectra resemble an average over a grid cell (in our case several million m^3) and a few seconds in time, whereas the equivalent sampling volume of the measured 1-minute-spectra is of the order of 1 m^3. One way to increase this sampling volume is to increase the measuring time, but on the cost of possibly averaging the DSD over different patches of rain, and therefore, over different microphysical regimes which corroborates the comparison with instantaneous modeled spectra. On the other hand, a longer measuring time increases the statistical signi?cance of the number concentration of the rarely found large raindrops. Here one has to ?nd a compromise. The stronger the rain, the shorter the measuring time can be chosen.

Since spectra with a higher rainrate presumably reach an equilibrium state earlier, it makes sense to stratify the data set into rainrate classes. We de?ne R-classes of 0.5 – 4.0 mm h^{-1}, 4.0 – 10.0 mm h^{-1}, 10.0 – 40 mm h^{-1} and $R > 40.0$ mm h^{-1}. The measuring times for comparison are chosen to 10 min, 5 min, 2 min and 1 min, respectively. Before classifying the measured spectra according to their rainrate, the whole data set is averaged to the corresponding measuring time. The same R-classi?cation is applied to the grid values of the modeled DSDs at the ground.

It is well known that the equilibrium distribution scales linearily with the rainrate. To compare the shapes of modeled and measured spectra, it therefore makes sense to normalize all DSDs to the same rainrate, which is chosen to be 10 mm h^{-1}. In that way, the rela-

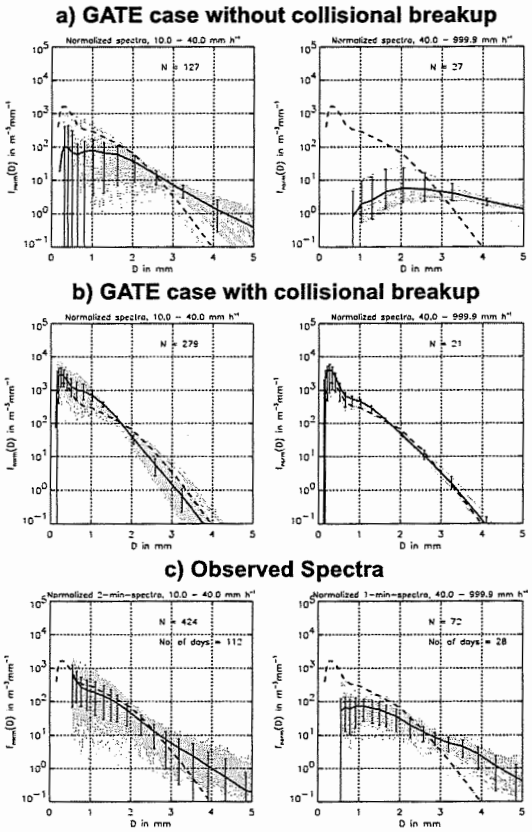

Fig. 3: DSDs at ground in m^{-3} mm^{-1} as function of raindrop diameter D in mm. **a)** GATE case without breakup taken into account, **b)** GATE case with breakup, and **c)** observations at Karlsruhe, Germany. **Left column:** rainrate class 10.0 – 40.0 mm h^{-1}, **right column:** rainrate class > 40 mm h^{-1}. **Black line:** average DSD in every diameter bin, error bars represent the corresponding 10-%- and 90-%-percentiles.

tive proportions of the numbers of small and big drops clearly can be identi?ed.

Figure 3 shows normalized DSDs as a function of drop diameter D for the upper two rainrate classes, where the effects of breakup can systematically be observed. Grey lines represent individual spectra, the black line is the average spectrum within the corresponding diameter bin, and the error bars show the upper and lower 10-%-percentiles. The measured DSDs (lower panel) for $R > 40$ mm h^{-1} (right side) seem to approach a "nearly equilibrial" gamma distribution with a maximum at approximately $D = 1$ mm. But no agreement to the theoretical equilibrium distribution is found, since the mean measured DSD contains much more large drops. In the range 10 – 40 mm h^{-1} the DSDs simulated without breakup are similar to the observed DSDs for $D > 2$ mm, but the observed spectra contain much more smaller drops. This is an indicator that breakup is needed to explain the observed number concentrations of smaller raindrops. Taking breakup into account in the simulation increases the number of small drops, but seems to overestimate the effect of breakup, especially for the large raindrops. For heavy precipitation the model without collisional breakup produces unrealistic DSDs with too many large and not enough small drops. But on the other hand, the model with breakup is also not in agreement with the observations, since the model approaches the theoretical equilibrium DSD, which differs signi?cantly from the observed mean DSD.

From the above-mentioned differences of the observed and modeled DSDs without collisional breakup taken into account it is obvious that collisional breakup plays an important role in shaping the DSD in natural rain. It is important to consider the process in spectral bin models since otherwise the number of small drops will be under- and the number of large drops overestimated, and ultimately, the rate and total amount of surface precipitation is overestimated.

To summarize, it is found that in heavy rain, a state-of-the-art breakup scheme results in DSDs containing too few large raindrops compared to the observations. Thus, the breakup parameterization seems to overestimate the breakup probability or the collision rate of the large drops, even more because the model HUCM itself numerically underestimates the breakup process as it is really described by the parameterized kernel functions.

5 CONCLUSIONS

It has been shown that collisional breakup is an important process of the precipitation formation in mixed-phase deep convective clouds, although the simulation shown here suffers from the coarse spectral resolution currently used in HUCM. With collisional breakup taken into accout, the raindrops remain much smaller in the initial phase of the cloud development. In principle, only large raindrops are able to fall against typical updraft velocities on the order of 10 m s^{-1} in convective clouds, therefore collisional breakup, which destroys such large drops, has a strong nonlinear effect on the surface precipitation. In addition, collisional breakup can have an intensifying effect on the formation of secondary convective cells by altering the DSD (more small drops), increasing raindrop evaporation and therefore the formation of gust fronts.

The statistical comparison of the modeled DSDs of the GATE case with longterm measurements (only summer seasons) at Karlsruhe, Germany, reveals discrepancies, especially at high rainrates. The model without breakup produces more large and less small raindrops compared to the observations, whereas the model with breakup does the opposite. Although such a comparison has its problems and de?ciencies (as mentioned in section 4), the results might be interpreted in a way that especially the Low and List (1982) parameterization of collisional breakup overestimates the effect systematically, which is in accordance with the results of Hu and Srivastava (1995). A reinvestigation of the breakup phenomena of intermediate and large raindrops and the formulation of improved parameterizations seems to be necessary to achieve an accurate description of rain formation by spectral bin models.

REFERENCES

Beard, K. V. and H. T. Ochs, 1995: Collisions between small precipitation drops. Part II: formulas for coalescence, temporary coalescence, and sattelites, *J. Atmos. Sci.*, **52**, 3977–3996.

Brown, P. S., 1997: Mass conservation considerations in analytic representation of raindrop fragment distributions, *J. Atmos. Sci.*, **54**, 1675–1687.

Hu, Z. and R. C. Srivastava, 1995: Evolution of raindrop size distribution by coalescence, breakup and evaporation: Theory and observations, *J. Atmos. Sci.*, **52**(10), 1761–1783.

Khain, A. P., M. Ovtchinnikov, M. Pinsky and H. Krugliak, 2000: Notes on the state-of-the-art numerical modeling of cloud microphysics, *Atmos. Res.*, **55**, 159–224.

Khain, A. P., D. Rosenfeld and A. Pokrovsky, 2001: Simulating convective clouds with sustained supercooled liquid water down to -37.5°C using a spectral microphysics model, *Geophys. Res. Lett.*, **28**, 3887–3890.

Khain, A. P. and I. L. Sednev, 1996: Simulation of precipitation formation in the eastern mediterranean coastal zone using a spectral microphysics cloud ensemble model, *Atmos. Res.*, **43**, 77–110.

Low, T. B. and R. List, 1982: Collision, coalescence and breakup of raindrops. Part II: Parameterization of fragment size distributions, *J. Atmos. Sci.*, **39**, 1607–1619.

Seifert, A., A. Khain and U. Blahak, 2004: Effects of collisional breakup on mixed-phase deep convection simulated by a spectral (bin) cloud model, *J. Atmos. Sci.*, accepted for publication.

STATISTICAL PROPERTIES OF VOLUMES SWEPT BY NON-SPHERICAL ICE PARTICLES IN A 3-D TURBULENT FLOW

M. Shapiro[1], H. Wirzberger[1], M. Pinsky[2], B. Grits[2] and A. Khain[2]

[1]Faculty of Mechanical Engineering, Technion, Haifa, Israel
[2]Department of Atmospheric Sciences, Institute of Earth Sciences, Jerusalem, Israel

1. INTRODUCTION

The problem of motion of non-spherical particles in a turbulent shear flow is very important in many fields of Aerosol Sciences and in particular in the context of Cloud Physics. Precipitation formation in clouds involves ice crystals, which collide with small cloud droplets as well as with other ice crystals to form graupel and snowflakes. Evaluation of the collision rates of non-spherical crystals is an important problem, attracting attention of cloud physicists. At the same time little is known about these processes due to complexity of the problem of motion and collision of non-spherical particles in shear flows. Random (both in space and time) shear turbulent flows force a non-spherical particle to move (often with tumbling) along a complicated trajectory. This causes significant difficulties in evaluating the volume swept by ice crystals, which is a key parameter required for calculation of collision rates. In view of the above, the swept volume of ice crystals in turbulent shear flow is a random quantity, and its statistical parameters (e.g., the mean value and variance) govern the droplets' collection rate and cloud spectrum size evaluation. The goal of the study is to evaluate the statistics of swept volumes of ice crystals in typical atmospheric conditions. For this aim we perform computer simulations of the motion of prolate and oblate spheroids (modeling needle-like and plate-like ice crystals) in 3D turbulent flow with the dissipation rate characteristic to cloudy air.

Corresponding author's address: M. Shapiro, Faculty of Mechanical Engineering, Technion, Haifa, Israel; E-Mail: mersm01@tx.technion.ac.il

2. STATISTICAL MODEL OF TURBULENT VELOCITY SHEARS

Our approach is based on the evaluation of the relaxation times and relaxation lengths of particles (with sizes from several microns up to 50 μm) moving in a turbulent flow. These times and lengths are of order 10^{-3} s and 10^{-4} m correspondingly, that are much smaller than the values of correlation times and lengths of wind shears (0.15 s and 0.01 m). This allows to model the particle motion in a turbulent field as a sequence of motions in volumes of size 0.01 m during 0.15 s. The flow in each such volume is a general shear flow with constant in space and time shear components. The set of strain tensors are produced by a statistical model generating strain tensor in a homogeneous and isotropic turbulent flow, Pinsky et al. (2004). The model generates nine strain components $[s_{ik}]$ having non-normal (with a given dispersion, skewness, S, and flatness, F) distribution. The PDF of shear components is described by 4-parametric Pearson distribution. The dispersion depends on the mean dissipation rate, $\langle\varepsilon\rangle$. Skewness and flatness can be evaluated as a function of Taylor scale based Reynolds number Re_λ using parameterization formula, Antonia et al. (1981). The model is possible to reproduce the intermittent nature of fully developed turbulence (nonzero S and F). $[s_{ik}]$ obey the continuity equation and correlations imposed by the Kolmogorov theory of homogeneous isotropic turbulent flows, Monin and Yaglom (1975), Pinsky et al. (2004).

Verification tests show that the generator reproduces successfully PDF of strains reported in literature, Pinsky et al. (2004). For example, **fig. 1** shows the PDF of s_{xx} component in a series of turbulent strains, generated for $\langle\varepsilon\rangle = 400 cm^2 s^{-3}$, S = -0.45 and F = 12 (solid line). For comparison, the Pearson approximating distribution (dashed

line) and the distribution of component s_{xx} measured in a turbulent flow (asterisks) with Re_λ = 1500, Belin et al. (1997), are presented as well.

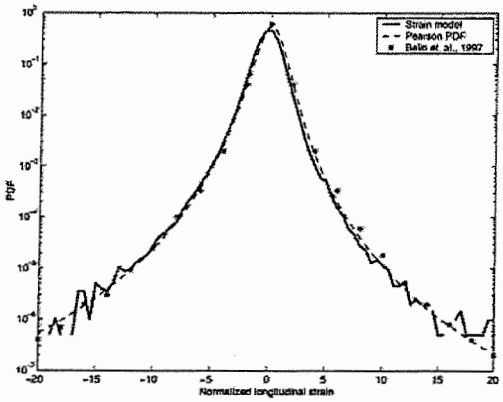

Fig. 1 PDF of s_{xx} component. S = -0.45, $\langle\varepsilon\rangle = 400cm^2s^{-3}$, and F = 12.

The character of fluid motion in each realization of strain tensor is defined by the eigenvalues of this tensor. It was found that four types of stagnation points are realized: stable and unstable saddle-node (strain dominated regions) and stable and unstable saddle-focus (vorticity dominated regions) points. The node (stable/unstable) and the focus (stable/unstable) stagnation points are not allowed because of air incompressibility.

3. SIMULATION OF ICE CRYSTALS MOTION

We investigate the statistics of motion of needle-like and plate-like ice crystals in this study. These particles are modeled by means of prolate and oblate spheroids respectively. For the ice crystals under consideration (with characteristic sizes less then 50 μm) and typical atmospheric conditions (velocity shears of order 30 s^{-1}) air motion near ice crystals may be regarded as a stationary creeping flow. The contribution of unsteady components (e.g., the Basset and added mass forces) to the total drag force for particles under consideration vanish afetr about 10^{-4} s, Broday et al. (1997). In this situation one may use the modified form of Faxen law for the hydrodynamic force and torque acting on spheroid placed in arbitrary creeping flow, Happel and Brenner (1973). In our case, when only the first spatial derivatives of fluid velocity are non zero, the equations for translational and rotational motion of spheroid in dimensionless form take the form :

$$\tau\frac{d\bar{v}}{dt} = \bar{\bar{K}}(\bar{u}-\bar{v}) + N(1-\frac{\rho_{air}}{\rho_{part}})\bar{e}_z \qquad (1)$$

$$\tau\left(\bar{\bar{I}}'\frac{d\bar{w}'}{dt} + [\bar{w}'\times\bar{\bar{I}}'\bar{w}']\right) = \bar{\bar{Q}}'(\bar{R}'\times\bar{u}') - \bar{\bar{\Omega}}'\bar{w}' \qquad (2)$$

Here $\bar{u}$ is the undisturbed fluid velocity at the location of particle center of mass, τ is the dimensionless particle relaxation time and N is the gravity parameter. $\bar{\bar{K}}$, $\bar{\bar{Q}}'$ and $\bar{\bar{\Omega}}'$ are resistance tensors for translational ($\bar{\bar{K}}$) and rotational ($\bar{\bar{Q}}', \bar{\bar{\Omega}}'$) motion, and $\bar{\bar{I}}'$ is the particle inertia tensor. The tensors $\bar{\bar{K}}$, $\bar{\bar{Q}}'$ and $\bar{\bar{\Omega}}'$ depend on particle shape only. $\bar{R}'$ is a rotor-like operator, dependent on particle shape. The equation (1) is written in inertial coordinate system, while the equation (2) is written in the particle-fixed coordinate system.

The numerical code for motion of prolate and oblate spheroids in 3D space was developed, basing on these equations. The modified midpoint method was chosen in order to integrate equations of motion, Press et al. (1992). The character of particles trajectory depends on the type of the strain tensor realization. **Fig. 2** and **3** present examples of prolate spheroid motion during 0.15 s for two realizations of strain tensor: unstable saddle-node (fig. 2) and unstable saddle-focus (fig. 3). In both the cases the minor axis is equal 5 μm and major axis is equal 15 μm and the motion begins from the point where air is at rest. Positive x axis direction is the direction of gravity.

4. STATISTICS OF VOLUMES SWEPT BY ICE PARTICLES

Spatially and temporary random turbulent shear fields force a non-spherical particle to move along a complicated trajectory and to constantly tumble, thereby changing its spatial orientation. This causes significant difficulties in evaluating the volume swept by non-spherical ice crystals, which is a key parameter required for evaluating the collision rates with cloud droplets. In view of the

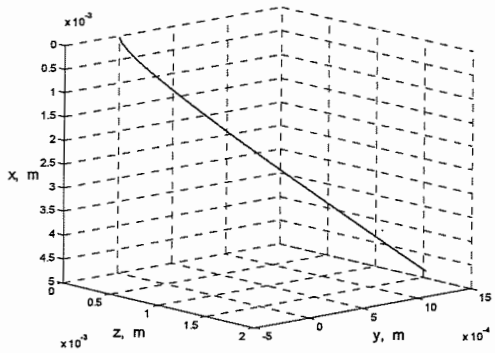

Fig. 2 Prolate spheroid motion near unstable saddle-node stagnation point.

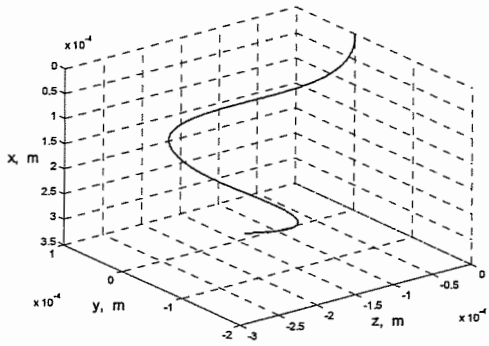

Fig. 3 Prolate spheroid motion near unstable saddle-focus stagnation point.

above, the swept volume of ice crystals in turbulent shear flow is a random quantity, and its statistical parameters (e.g., the mean value and variance) govern the droplets' collection rate and cloud spectrum evolution. In our approach the statistical ensemble is formed by swept volumes calculated for different realizations of strain tensor.

Frequency of collisions are determined by velocity fluxes of particles *A* of one size (and type) on particles *B* of another size (and type). Thus we have to calculate the volume swept by particle *A* with respect to particle *B*. This mutual swept volume of particles *A* and *B* may be calculated by integration of the rate of swept volume change

$$\dot{V}_S^{AB} = \left(\sqrt{S_A} + \sqrt{S_B}\right)^2 |\,\Delta\overline{\mathbf{v}_{AB}}\,| \qquad (3)$$

over the time during which the flow prevails (0.15 s). Here S_A and S_B are projection areas of spheroids *A* and *B* respectively on the direction of their relative velocity $\Delta\overline{\mathbf{v}_{AB}} = \overline{\mathbf{v}_A} - \overline{\mathbf{v}_B}$. The expression (3) is a generalization of expression for the rate of change of swept volume of spherical particles, settling under gravity, Pruppaher and Klett (1978) :

$$\dot{V}_S^{AB} = \pi\left(r_A + r_B\right)^2 |\,\Delta\overline{\mathbf{v}_{AB}}\,| \,.$$

For calculation of swept volumes only trajcetories of particles experienced collisions during 0.15 s are taken into account. For determination of statistics of swept volumes, the probability distribution functions of particle orientations are taken into account. These distribution functions are calculated independently from analysis of simulations of single particles' trajectories.

Fig. 4 and **5** show examples of evolution of $\dot{V}_S^{AB}$ with time for a spheroid with minor axis 10 μm and major axis 30 μm with respect to spheroids with minor axis 5 μm and major axis 15 μm. The calculation is performed during 0.15 s or while both spheroids stay within the volume of size 0.015 m. In case of fig. 4 the larger spheroid is oriented initially vertically and the smaller one – horizontally, and the stagnation point is unstable saddle-node. Fig. 5 presents realization with both the spheroids oriented initially horizontally, moving near unstable saddle-focus stagnation point. In both the cases spheroids in the beginning are in contact with each other and are situated at the center of volume (air velocity at the center is zero). The swept volume rate of change at the fig. 4 and 5 is normalized by the swept volume rate of change due to gravity.

The data on the statistics of volumes swept by prolate and oblate spheroids of different sizes and aspect ratios will be presented at the conference. This data will be calculated for different Re_λ and $\langle\varepsilon\rangle$. Besides that there will be also calculated the statistics of spatial orientation of spheroids.

5. CONCLUSIONS

Collision of non-spherical particles in a turbulent flow is an important, but still not well understood topic. In this study we introduce the concept of mutual swept volumes of two particles (or populations of particles of different types). Using a statistical model of turbulent strains, different realizations of sheared flow were generated. Trajectories and mutual swept volumes of particles of different mass and

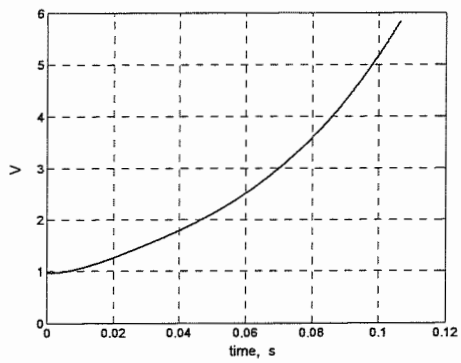

Fig. 4 Evolution of $\dot{V}_S^{AB}$. Stagnation point is unstable saddle-node.

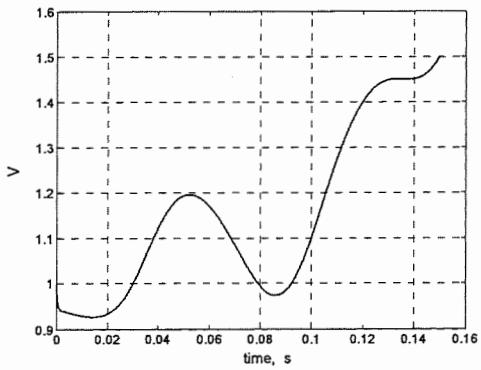

Fig. 5 Evolution of $\dot{V}_S^{AB}$. Stagnation point is unstable saddle-focus.

shapes are calculated. This study is the first important step to calculation of non-spherical particles' collisions in turbulent flows with high Reynolds numbers.

6. ACKNOWLEDGEMENTS

The study was performed under support of the Israel Science Foundation (grant 173/03) and the Israel Ministry of Science (grant WT 0403).

7. REFERENCES

Antonia, R.A., Chambers, A.J., and Satyaprakash, B.R., 1981: Reynolds number dependence of high-order moments of the streamwise turbulent velocity derivative. Boundary-layer Met., 21, 159-171.

Belin, F., Maurer, J., Tabeling, P. and Willaime, H., 1997: Velocity gradient distributions in fully developed turbulence: An experimental study. Phys. Fluids, 9, 3843-3850.

Broday, D., Fichman, M., Shapiro, M. and Gutfinger, C., 1998: Motion of spheroidal particles in vertical shear flows. Phys. Fluids, 10 (1), 86-100.

Happel, J. and Brenner, H., 1983: Low Reynolds Number Hydrodynamics. Martinus Nijhoff, The Hague.

Monin, A.S. and Yaglom, A.M., 1975: Statistical Fluid Mechanics: Mechanics of Turbulence. Vol. 2 MIT Press.

Pinsky, M., Shapiro, M., Khain, A. and Wirzberger, H., 2004: A statistical model of strains in homogeneous and isotropic turbulence. Physica D, In Press.

Pruppacher H. R. and Klett J. D. (1997) Microphysics of Clouds and Precipitation. Oxford Press, Oxford.

GROWTH OF SNOW CRYSTALS FROM FROZEN WATER DROPLETS

Chuji Takahashi

Department of Earth Science, Saitama University, Saitama City, 338-8570, Japan

1. INTRODUCTION

Nakaya(1954) has already found that many natural dendritic crystals had small hexagonal plate at the center. He also observed the growth process of such a crystal in the study of artificial snow crystals. At first a short column was formed and one of the basal face developed to a dendritic crystal. The other basal face grew only to a small hexagonal plate because of competition for the available moisture. Snow crystals with such double hexagonal plates are now called double plate crystals and thought to develop from single-crystalline frozen water droplets.

In order to study of the growth process of snow crystals, frozen water droplets of cloud droplet size were grown in free fall in a supercooled cloud and their shapes were observed. The preliminary results were described in Yamashita and Takahashi(1972). They observed twenty circular crystal faces(2 basal, 6 prism and 12 pyramidal faces) appeared on a spherical surface at the initial growth stage. Gonda and Yamazaki(1978) made in-site observation of the growth of frozen water droplets and showed the diagram of the growth mode. Since their experiments were made by using the diffusion cloud chamber, the growth of frozen droplets was lack of symmetry. The present study was carried out to observe the growth of frozen water droplets in the state close to natural clouds by falling water droplets freely in a supercooled cloud, following to Yamashita and Takahashi.

2. EXPERIMENTAL APPARATUS AND PROCEDURES

Experiments were carried out in a large cloud chamber as shown in Fig.1. It consisted of stainless steel pipe of about 6.5m in height and 28cm in diameter. It was cooled down to -33℃ by circulating cold air around it and its temperature was kept uniform within ±1℃ from the level of 50cm below the top to the bottom. Supercooled cloud was produced by semipermeable cellulose bag containing about

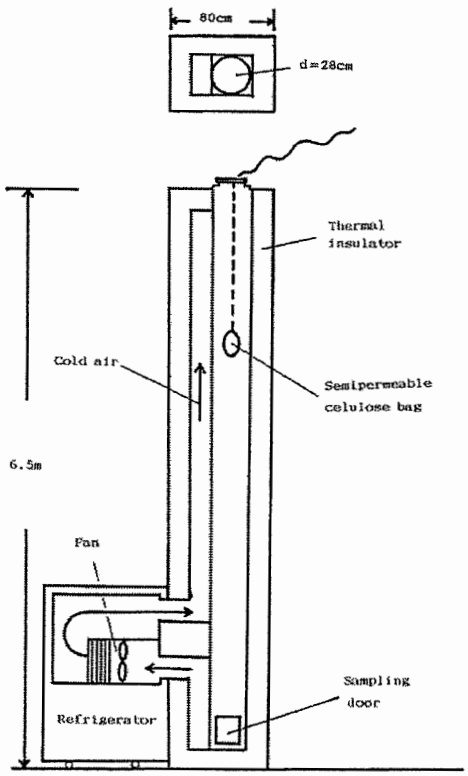

Fig.1 Large cloud chamber

400ml of hot water of about 70℃. The bag was introduced from the top and was removed from the top after hang down to the bottom. Supercooled cloud remained for about 10 minutes in the chamber after this operation. Water droplets were produced from silver iodide solution by mixing potassium iodide and silver nitrate solution whose concentration was 10^{-2}g/l. They were dropped from the top of the chamber by using a spray. They were nucleated by silver iodide in suspension at about -5℃. After freezing completely they grew to ice crystals and were collected in silicon oil at the bottom of the chamber. They were covered with a coverglass to prevent evaporation and were observed under polarizing microscope. The size of frozen water droplets ranged between 20 and 100μm in diameter.

3. RESULT

Frozen water droplets grew to various shapes when they were collected at the bottom of the chamber. Two growth modes were observed. In one mode, twenty circular crystal faces appeared on the surface of frozen water droplets. In the other mode, steps or irregular patterns are appeared in place of circular crystal faces.

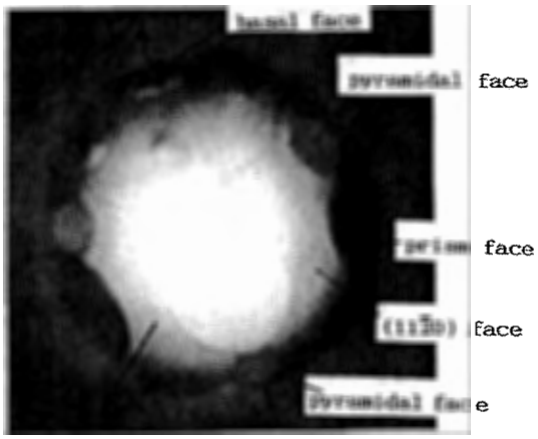

Fig.2 Circular crystal faces appeared on the growth of frozen water droplets

3.1 FORMATION OF CIRCULAR CRYSTAL FACES

It is possible to follow the growth process by observing ice particles classified into this mode. Fig.2 shows an example of these ice particles and Fig.3 shows the diagram of this growth process.

First stage Twenty circular crystal faces appeared. They were 2 basal, 6 prism and 12 pyramidal faces. The pyramidal faces corresponded to $\{10\bar{1}1\}$ faces. Another crystal faces were observed between two prism faces.

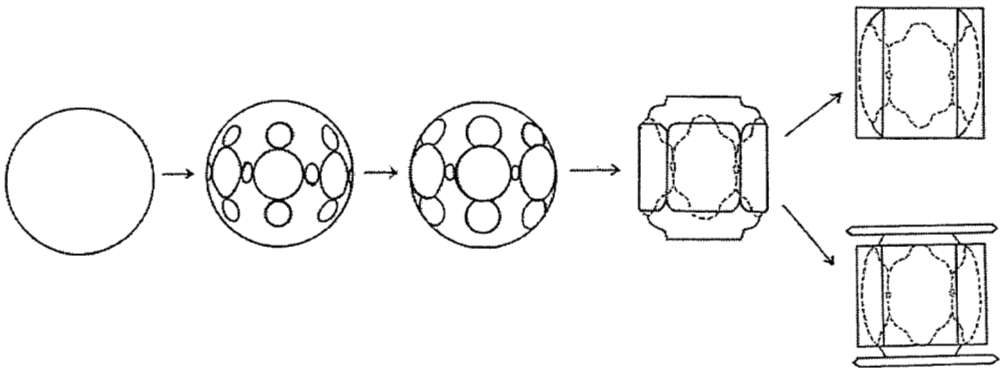

Fig.3 Diagram of the growth of frozen water droplets

They corresponded to $\{11\bar{2}0\}$ faces. The size of $\{11\bar{2}0\}$ faces was about 1/4 of the size of prism faces.

Second stage A prism face connected with two pyramidal faces after further growth. The size of a pyramidal face, which was nearly equal to that of a prism face at the initial stage, was apparently smaller than that of a prism face. The pyramidal face hollowed at the center. A step was usually formed between a basal face and pyramidal faces.

Third stage Adjacent prism faces connected. $\{11\bar{2}0\}$ faces disappeared and small cavities were observed between two prism faces as their traces. Pyramidal faces also disappeared and a hollow remained there.

Forth stage Frozen water droplets grew to short column-like crystals. Afterward they grew to snow crystals of well-known habit corresponding to the temperature and supersaturation.

3.2 FORMATION OF STEPS

In place of circular prism and pyramidal faces, several steps were frequently formed. These steps disappeared with further growth and frozen water droplets grew to column-like crystals finally. In several cases steps and circular prism and pyramidal faces appeared on the same frozen droplets. Such non-symmetric growth was more or less observed for every frozen water droplets, and seemed to be caused with the different vapor supply to each part of a frozen water droplet.

4. DISCUSSIONS

The existence of $\{10\bar{1}1\}$ and $\{11\bar{2}0\}$ crystal faces are suggested from the γ-plot of ice crystals by Higuchi(1961). He indicated these crystal faces are metastable and disappear during the growth process. $\{10\bar{1}1\}$ crystal faces were observed in the previous works, but were not observed $\{11\bar{2}0\}$ crystal faces. Two conditions were favorite for the appearance of $\{11\bar{2}0\}$ crystal faces in this experiment. One is that the size of frozen water droplets was large. Since the size of $\{11\bar{2}0\}$ crystal faces was small(about 1/8 of the diameter of frozen water droplets), it would be missed in the case of the growth of small frozen water droplets. The other is that the air temperature was low. $\{11\bar{2}0\}$ crystal faces were observed when the frozen droplets grew at temperatures about -30℃. It seems that low temperatures are favorite for the appearance of metastable crystal faces.

After pyramidal faces enlarged to observable size, they changed into flat faces with a hollow at the center. As prism faces enlarged and connected with pyramidal faces, the growth of pyramidal faces stopped. Finally pyramidal faces disappeared and cavities were left frequently as a trace of pyramidal faces. In the experiment by Gonda and Yamazaki, these hollows or cavities were not observed. In their experiment, the growth of frozen water droplets was slower than that in the present experiment because water vapor supply was small compared with the growth in a supercooled cloud in free fall. The condition of vapor diffusion around the frozen water droplets causes the difference of the growth mode.

5. CONCLUSIONS

Frozen water droplets grew in free fall in a large cloud chamber about 6.5m in height. It is possible to follow the growth process by observing ice particles of various shape collected at the bottom of the chamber. There are two

growth modes. In one mode, twenty circular crystal faces appeared. They are 2 basal, 6 prism and 12 pyramidal faces. $\{11\bar{2}0\}$ crystal faces are observed in several cases when the size of frozen water droplets was large and the air temperature was about -30℃. Pyramidal faces and $\{11\bar{2}0\}$ crystal faces disappear during the growth. Cavities are left as a trace of these metastable crystal faces frequently. In the other mode, steps or irregular patterns are formed in place of circular prism and pyramidal faces. After further growth, frozen water droplets grow to short column-like crystals in both growth modes.

Acknowledgements The author wishes to express his thanks to Masaru Mori who carried out this experiment with the author and also thanks to Emeritus Professor A. Yamashita for his helpful suggestions and discussions.

References

Gonda,T and T.Yamazaki, 1978: Morphology of ice droxtals grown from supercooled water droplets. J. Crystal Growth, 45, 66-69.

Higuchi, K., 1961: On the shape of ice crystals. J. Meteor. Soc. Japan, 39, 237-248.(in Japanese)

Nakaya,U., 1954: Snow Crystals. Harvard Univ. Press, Cambridge, 510 pp.

Yamashita, A. and C. Takahashi, 1975: Initial growth process of snow crystals from frozen water droplets. Proc. Intern. Cloud Physics Conf., London, 50-51.

EXPERIMENTAL STUDIES ON THE SUBLIMATION OF A SNOW CRYSTAL

Tsuneya Takahashi[1] and Tatsuo Endoh[2]

[1] Hokkaido Univ. of Education, Sapporo, 002-8501, Japan
[2] Tottori Univ. of Environ. Studies, Tottori, 689-1111, Japan

1. INTRODUCTION

The sublimation of a snow crystal is one of the fundamental precipitation processes. The sublimation process has important effects on the evolution of a cloud. The survival of snow crystals through sublimation process is important for discussing a seeder-feeder mechanism. The sublimation of a cloud, especially a cirrus, is inferred to be affected by radiation.

Young (1993) wrote in his textbook that long columns had apparently resulted from sublimation from the prism faces by the ventilation effect during falling with their long axis horizontal. On the other hand, Nelson (1998) showed that the crystals evolved completely rounded shapes with a constant aspect ratio by experiments on sublimation of ice crystals without ventilation. In this paper, we report the results of the experiments on the sublimation after growth of snow crystals and their regrowth in our vertical tunnel.

2. EXPERIMENTS

The present study was carried out using a supercooled cloud tunnel, in which a snow crystal can be suspended freely by adjusting without delay to the terminal fall velocity of a floating snow crystal, described in detail by Fukuta et al. (1982) and Takahashi et al. (1991).

After the growth of 7-15 minutes, fog droplets stopped supplying from an ultrasonic atomizer in the tunnel, a snow crystal was allowed to be sublimed. Also, sublimed crystals were regrown by resupplying fog droplets in the tunnel. The updraft velocity, the air temperature and the dew point of air were continuously monitored by a hot-wire anemometer, a thermistor thermometer and a quartz dew point hygrometer, respectively. The undersaturation was calculated from the air temperature and the dew point of air.

3. RESULTS

Figure 1 shows examples of sublimed snow crystals. The crystals were grown and sublimed at -6, -6.5, -10.5, -11.5 and -14°C, where needles, columns, thick plates, plates and dendrites are grown, respectively, as described in Takahashi et al. (1991). The shapes roughly remained unchanged, although crystal corners and edges were rounded. Even if the crystal mass was reduced to less than 10 percent of the mass at the end of growth, which was estimated using empirical relationship by Takahashi et al. (1991), the crystals remained faceted. For columnar crystals, three adjacent prism faces were sublimed. It is most likely due to the effects of ventilation, which seemed to accelerate the sublimation from the windward side of the crystals. Since columns and needles tend to fall with c-axis horizontal, as pointed out by Takahashi and Fukuta (1988), the sublimation would be accentuated from the windward prism faces. While planar crystals shrank, a rib at the center line of a branch was left.

Figure 2 describes the variation of the crystal axial ratio (a/c; a and c are the crystal dimensions along a- and c-axes) with temperature;

Corresponding author address:
Tsuneya Takahashi, Hokkaido Univ. of Education, Integrated Center for Educ. Res. & Training, Sapporo 002-8501, JAPAN; e-mail: takahasi@sap. hokkyodai.ac.jp

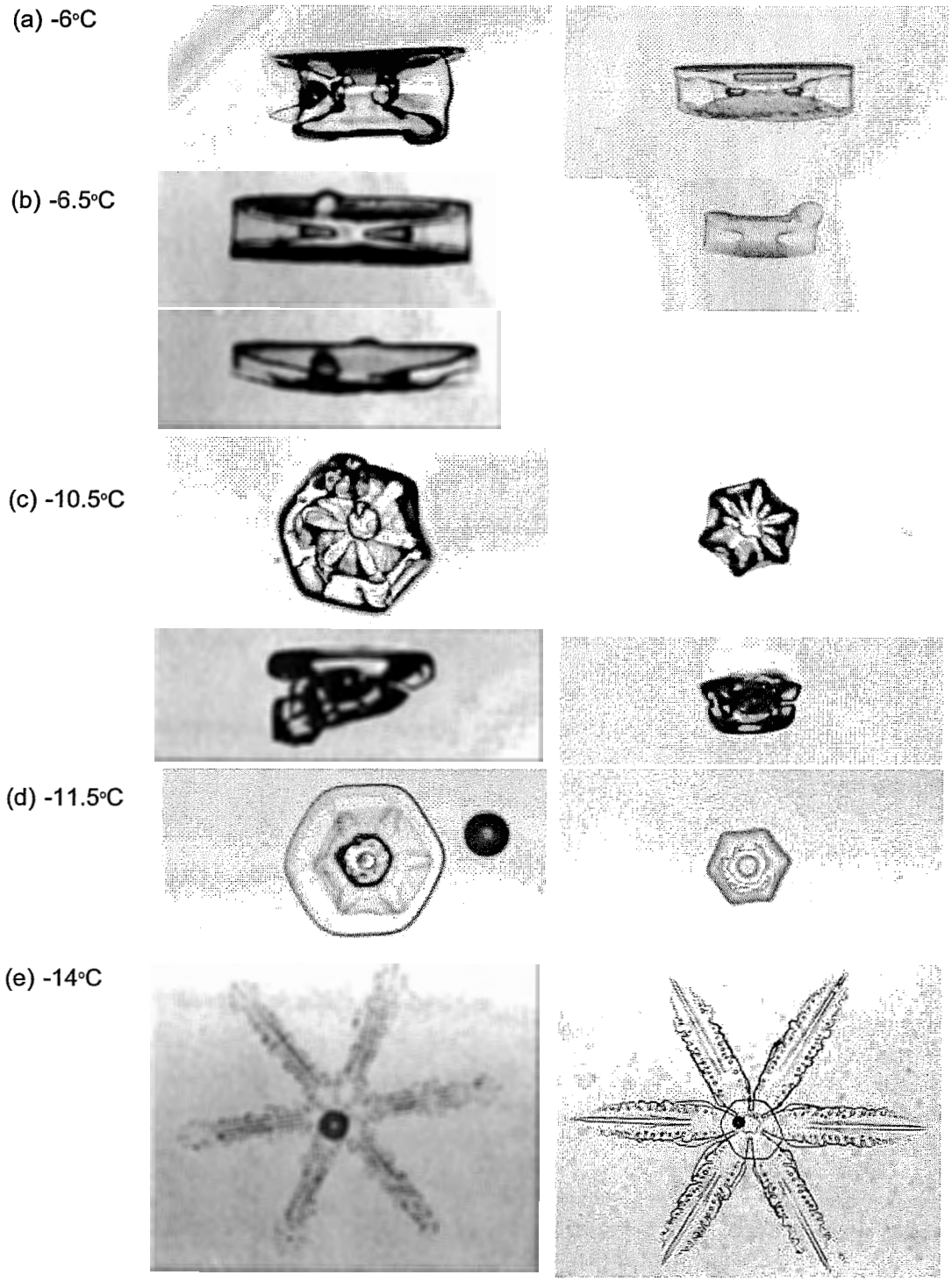

Fig. 1. Snow crystals obtained during sublimation after 10 min (the left of b, d) and 15 min (a, the right of b, c, e) of growth. The crystal mass was reduced to 20-70 percent (left row) and less than 10 percent (right row) of the mass at the end of growth, which was estimated using empirical relationship by Takahashi et al. (1991).

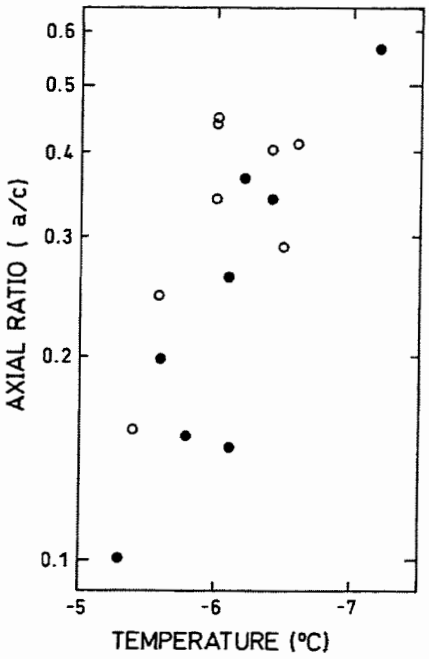

Fig. 2. Variation of crystal axial ratio (a/c) with temperature: snow crystals were grown for 15 min (black circles) and subsequently were sublimed (outlined circles). The data for crystals whose fall velocities were reduced to less than two-third of the maximum velocity at the end of growth were selected.

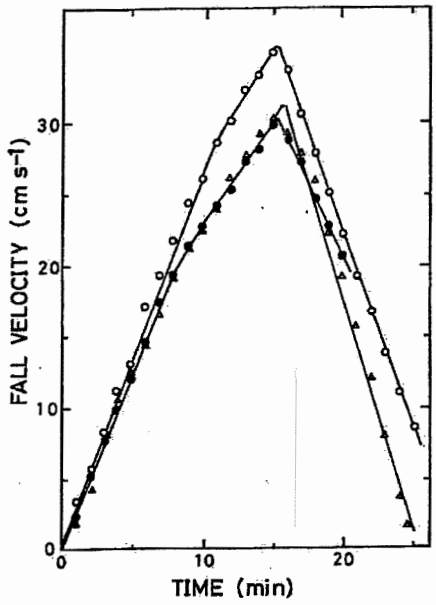

Fig. 3. Variation of fall velocities of snow crystals during growth and evaporation at -10°C. After a growth time of 15 min at water saturation, snow crystals were made to sublimate.

snow crystals were grown for 15 min and subsequently sublimed. There is no remarkable change in the axial ratio through sublimation process, as pointed out by Nelson (1998). Within the limits of the present experiments, sublimation brought no long columns.

The variation of the fall velocities of snow crystals during growth and evaporation at around -10°C are shown in Fig. 3: snow crystals were evaporated after growth of 15 min. The variation of the fall velocities of snow crystals relation was represented by two straight lines for the growth stage within 15 min; the relation on the sublimation stage was represented by a straight line. The slope varied with the undersaturation.

Figure 4 shows the example of a snow crystal through the regrowth process at water saturation. The corners and edges that had been rounded during the sublimation process were resharpened.

4. SUMMARY

Sublimation properties of snow crystals were studied under free suspension in a supercooled cloud tunnel. Even if the crystal mass was re-

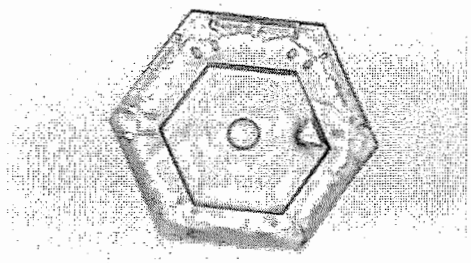

Fig. 4. A snow crystal that was grown at -12°C for 10 min under water saturation, sublimed for 10 min at 2.5% undersaturation, and regrown for 10 min.

duced to less than 10 percent of the mass at the end of growth, the crystals remained faceted. During the sublimation stage, three adjacent prism faces were sublimed for columnar crystals, and a rib at the center line of a branch of a planar crystal was left. There is no remarkable change in the axial ratio through sublimation process. The variation of the fall velocities of snow crystals on the sublimation stage was represented by a straight line. The corners and edges that had been rounded during the sublimation process became sharp again during the regrowth process.

REFERENCES

Fukuta, N., M. H. Kowa and N. H. Gong, 1982: Determination of ice crystal growth parameters in a new supercooled cloud tunnel. *Preprints Conf. on Cloud Phys.*, Chicago 15-17 Nov. 19 82, 325-328.

Nelson, J., 1998: Sublimation of ice crystals. *J. Atmos. Sci.*, 55, 910-919.

Takahashi, T., T. Endoh, G. Wakahama and N. Fukuta, 1991: Vapor diffusional growth of free-falling snow crystals. *J. Meteor. Soc. Japan*, 69, 15-30.

Takahashi, T. and N. Fukuta, 1988: Supercooled cloud tunnel studies on the growth of snow crystals between -4°C and -20°C. *J. Meteor. Soc. Japan*, 66, 841-855.

Young, K. C., 1993: *Microphysical Processes in Cloud.* Oxford University Press, 427 pp.

Comparing ice-cloud microphysical properties using CloudNET and ARM data

G.-J. van Zadelhoff and D.P. Donovan
Royal Netherlands Meteorological Institute, De Bilt, the Netherlands

1. INTRODUCTION

The importance of ice clouds in the Earth's radiation budget is well recognized (Arking 1991). Depending on their optical thickness, altitude and microphysical properties, ice clouds can either cause warming (greenhouse effect) or cooling (albedo effect) at the Earth's surface. Cirrus clouds cover more than 20% of the globe (Wylie and Menzel 1999) making it an important issue to know what the balance between these two processes turns out to be.

Because of uncertainties concerning the properties of ice clouds and the complex interactions between microphysics and radiation in these clouds, as well as the dynamics of the environment (Quante and Starr 2002), ice clouds are not well treated in climate and forecasting models.

An important parameter for determining the radiative characteristics of a cloud is the effective radius (R_{eff}) of its particles. For a given cloud volume, R_{eff} determines the relationship between the total mass and optical depth and influences the associated phase function and single-scattering albedo. For ice particles we may define

$$R_{\mathrm{eff}} = \frac{3}{4}\frac{\langle M(D)/\rho_i\rangle}{\langle A_c(D)\rangle}, \qquad (1)$$

where the braces denote averaging over a particle size distribution, D is the particle maximum dimension, M the mass, A_c the cross-section area and, ρ_i the density of solid ice.

Since the explicit treatment of ice cloud microphysics is beyond the capabilities of large scale atmospheric models, it is necessary to parameterize their microphysical properties. Previous parameterizations of ice cloud R_{eff} have been formulated using in sit observations using aircraft mounted instrumentation. In situ approaches more-or-less directly measure the particle size distribution. However, it is difficult to obtain large in situ data sets. In contrast, lidars and radars sample entire cloud profiles instantaneously and may operate continuously for long periods of time.

In this paper, we compare long time-series of ice cloud effective radii and ice water content (IWC) derived from combined lidar and radar observations. The measurements were made at the Atmospheric Radiation Measurement Program's Southern Great Plains (ARM-SGP) site and the Cabauw site (the Netherlands, part of CloudNET).

In this work, the differences seen at the two sites are discussed. In addition, the possibility that particle size may be parameterized according to geometrical depth into the cloud seen from cloud-top is presented. A more detailed comparison can be found in van Zadelhoff and Donovan (2004).

2. ALGORITHM FOR LIDAR/RADAR REMOTE SENSING

The cloud microphysical properties used in this work have been derived using both lidar and radar signals. The procedure used to calculate the microphysical properties has been extensively described in Donovan et al. (2001) and Donovan and van Lammeren (2002). In this section a short summary on the procedure is given.

The lidar/radar effective radius is defined as

$$R'^4_{\mathrm{eff}} = \frac{9}{16\pi\rho_i^2}\frac{\langle M^2(D)\rangle}{\langle A_c(D)\rangle} = R_{\mathrm{eff}}\frac{3}{4\pi\rho_i}\frac{\langle M^2(D)\rangle}{\langle M(D)\rangle}, \qquad (2)$$

which can be directly linked to the radar reflectivity ($Z_e \propto N_o\langle M^2(D)\rangle$) and optical extinction ($\alpha_{\mathrm{lid}} \propto N_o\langle A_c(D)\rangle$). The last term is obtained when inserting Equation 1 in Equation 2.

For lidar cloud measurements, multiple scattering can significantly contribute to the observed signal. A treatment of the multiple-scattering effects has been incorporated into the inversion process. The procedure has been found to be stable with respect to variations in the cloud backscatter-to-extinction ratio profile as well as measurement errors.

R'_{eff} can be looked at as the second moment of R_{eff} (Equation 1). The advantage of using R'_{eff} is its direct link to the observations, however it lacks

Corresponding author address: G.J. van Zadelhoff, KNMI PO Box 201, 3730 AE, De Bilt, The Netherlands; E-Mail: zadelhof@knmi.nl

a direct link to the calculation of the radiative influence due to ice particles. For this, a suitable particle habit (shape, orientation) and particle size distribution has to be adopted in order to estimate R_{eff} based on R'_{eff}.

In this paper all the particle sizes are given as the lidar/radar radius (R'_{eff}) and lidar/radar effective ice water content ($IWC' = IWC \times R'_{eff}/R_{eff}$).

3. USING THE ARM AND CLOUDNET DATA

In this comparison we make use of data from two facilities. The first is the U.S. Southern Great Plains Site established by the Atmospheric Radiation Measurement (ARM) Program, from here on referred to as the ARM site.

The second site is Cabauw (the Netherlands), which participates in the EU funded CloudNET research project. In all cases presented below the results for Cabauw and Chilbolton (another site within the CloudNET project) are the same within the error-bars.

In order to give a fair comparison of all the data, the similarities and differences in instruments at each of the sites have to be recognized and taken into account. The two instruments used for this comparison are a lidar and radar. In the case of the radar both the sites have a 35 GHz doppler-radar with similar sensitivities. In comparison, the lidars have different performance characteristics, where a CT-75K Ceilometer is placed at Cabauw, the ARM site uses the Multi-Pulse Lidar (MPL). The latter has a higher sensitivity compared to the CT-75K.

To make it possible to compare the data-sets a subset is defined for the sites. The subset is limited to those clouds which are fully visible in both the lidar and radar simultaneously, e.g. the cloud-top height seen by both the radar and lidar should be similar. The clouds fulfilling the criteria can reach optical depths up to $\tau \sim 4$.

4. COMPARING ARM AND CLOUDNET DATA

In the literature there has been much emphasize on finding particle size to temperature relationships (e.g. Boudala et al. 2002, Garrett et al. 2003) or a combination of temperature and IWC (e.g. McFarquhar et al. 2003, Donovan 2003). It is therefore of interest to see if these two different sites can be described by a same parameterization. First, however the effective particle sizes are correlated to their measured Doppler velocity (Figure 1). For ice particles, with a single habit and particle size distribution, it is expected that the

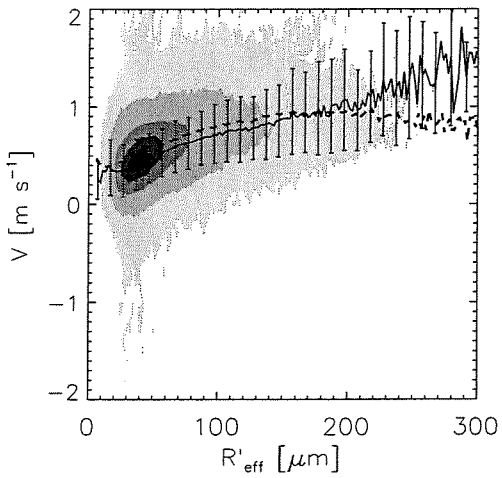

Figure 1: *Cumulative probability density plot of the occurrence of the Doppler velocity as measured by the radar to the calculated R'_{eff}. The greyscales, from dark to light, show the 10, 30, 60, 90 and 99 % probability of occurrence. The solid line shows the mean particle size at each temperature with the error-bars indicating the 1 σ level of the distribution. The dashed line shows the mean particle size as deduced from the ARM data.*

fall velocity depends on its size only (e.g. Heymsfield and Iaquinta 2000, Khvorostyanov and Curry 2002).

The distributions plotted in Figure 1 are wide but the mean doppler velocities for each effective particle size found at both the ARM site and the Cabauw site show a remarkable similarity. The same relation is observed at the Chilbolton site (not shown). As this is based solely on the observed quantities and no habit information or particle size distribution has been adopted, this suggests that a common mean ice particle habit, or habit combination, and size distribution at these sites dominates the statistics. More importantly the observed similarity implies that no large technical problems (such as radar calibration errors) are present that would prevent a meaningful comparison between each other.

In Figure 2 a correlation of the particle sizes and temperatures is made. The sizes of the distributions are comparable for the two sites, where it is clearly seen that the mean particle size at each temperature is higher at the ARM site. Secondly, it becomes clear that there are particles observed at lower temperatures at the latter site. This is due to the observed height of the cloud-tops within

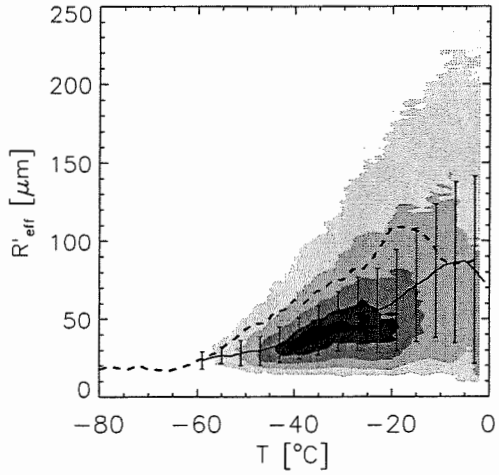

Figure 2: *Cumulative probability of occurrence of R'_{eff} as a function of temperature for optically thin ($\tau_{vis} \leq 4$) clouds at Cabauw. The contours and annotations follow the same scheme as in Figure 1.*

the sample; the ARM site has clouds reaching up to heights of 16 km, whereas the maximum cloud heights observed at the Cabauw site is 12 km. This comparison implies that the particle size-temperature relationships exist locally but that it is not possible to construct a simple global parameterization based on temperature only.

For a parameterization based on combination of IWC′ and T, the temperature versus IWC′ correlation should be different for the two sites to compensate for the differences seen in Figure 2. In Figure 3, the IWC′ is related to temperature for the Cabauw and ARM site. The two means overlap each other with a similar width of the distributions. The slope of the two means is slightly different, with hardly any temperature dependence at Cabauw and a small slope at the ARM site. Combining this with the previous results, the $R'_{eff}(T)$ differences observed do not seem to be related to IWC′ differences.

When plotting R'_{eff} versus temperature (Figure 2), effectively one compares R'_{eff} to the height of the clouds at the different sites and not directly to the influence of the temperature on the microphysics, e.g. coagulation of particles or freezing onto particle seeds. Therefore the R'_{eff} is related to the depth into the cloud seen from cloud-top ($Z_t - Z = \Delta Z_t$) in order to use a cloud related criteria (Figure 4), for all observed cloud thicknesses.

Even though the distribution is wide, the mean values for the two sites are very similar for depths up to 3 km. The two curves diverge for clouds with a depth greater than 3 km, which has to do with the differences in observed clouds statistics, especially total cloud thicknesses. Also here the results obtained at the Cabauw, ARM and

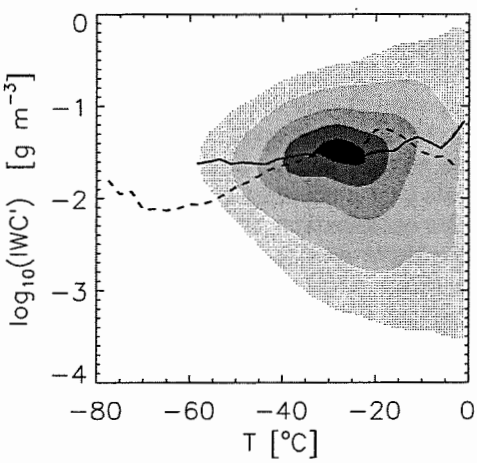

Figure 3: *Cumulative probability of occurrences of the ice water content (IWC′) as a function of temperature (T). The contours and annotations follow the same scheme as in Figure 1.*

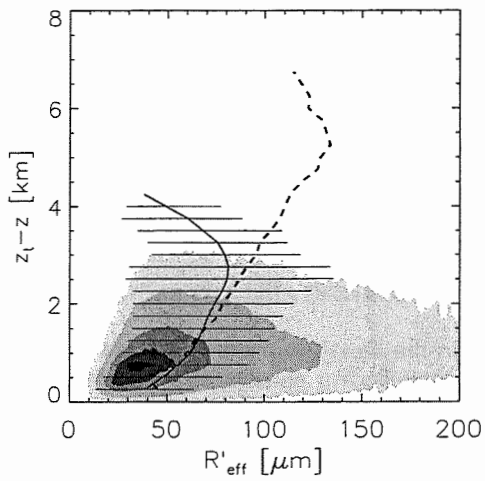

Figure 4: *Cumulative probability of occurrence of the particle size (R'_{eff}) to the depth in the cloud seen from cloud-top is made, where 0.0 stands for cloud-top. The contours and annotations follow the same scheme as in Figure 1.*

Chilbolton sites are the same, within the error bars (for more information, see van Zadelhoff and Donovan 2004).

If this feature can be observed on more points on Earth, using the CloudSAT and Calipso combination, a parameterization of particle sizes may be constructed depending on the depth into the cloud(ΔZ_t) and total thickness(H) of the cloud.

5. CONCLUSION

In this work a comparison on the microphysical properties of ice is presented for the ARM-SGP site and the Cabauw site. The main conclusions can be summarized as follows:

- The mean Doppler velocity at each of the mean derived particle sizes (R'_{eff}) is the same for all three sites. This suggests that the statistics at each of the sites is dominated by a common ice-habit and particle size distribution. For individual clouds, the habits may be quit different.
- The ice water content (IWC′)-temperature relation is similar at the two sites. The IWC′ seems not to depend on temperature at the Cabauw site and has a small slope at the ARM-site.
- It does not seem possible to construct a global $R'_{eff}(T)$ or $R'_{eff}(T,IWC)$ parameterization.
- The particle size (R'_{eff}) versus depth into cloud from cloud top (Z_t-Z=ΔZ_t) shows very similar results for the three sites. The $R'_{eff}(\Delta Z_t)$ profiles show increasing particle sizes for thicker(H) clouds. This can lead to a global parameterization of ice microphysical properties to include in GCMs.

The Cloudsat/Calipso combination should be able to confirm these results and make a global effective radius parameterization possible.

REFERENCES

Arking, A., 1991: The Radiative Effects of Clouds and their Impact on Climate., *Bull. Amer. Met. Soc., vol. 72, Issue 6, pp.795-953, 72*, 795–953.

Boudala, F. S., G. A. Isaac, Q. Fu, and S. G. Cober, 2002: Parameterization of effective ice particle size for high latitude clouds., *Int. J. of Climatol., 22*, 1267–1284.

Donovan, D. P., Ice-cloud effective particle size parameterization based on combined lidar, radar reflectivity, and mean Doppler velocity measurements, *J. Geophys. Res*, 108, 18, 4573, 2003.

Donovan, D. P., and A. C. A. P. van Lammeren, 2001: Cloud effective particle size and water content profile retrievals using combined lidar and radar observations, 1, Theory and examples, *J. Geophys. Res, 106*, 27,425–27,448.

Donovan, D. P., et al., 2001: Cloud effective particle size and water content profile retrievals using combined lidar and radar observations, 2, Comparison with IR radiometer and in situ measurements of ice clouds, *J. Geophys. Res, 106*, 27,449–27,464.

Garrett, T. J., H. Gerber, D. G. Baumgardner, C. H. Twohy, and E. M. Weinstock, 2003: Small, highly reflective ice crystals in low-latitude cirrus, *Geophys. Res. Lett., 30*, A12+.

Heymsfield, A. J., and J. Iaquinta, 2000: Cirrus Crystal Terminal Velocities., *J. Atmos. Sci., 57*, 916–938.

Khvorostyanov, V. I., and J. A. Curry, 2002: Terminal Velocities of Droplets and Crystals: Power Laws with Continuous Parameters over the Size Spectrum., *J. Atmos. Sci., 59*, 1872–1884.

McFarquhar, G. M., S. Iacobellis, and R. C. J. Somerville, 2003, SCM Simulations of Tropical Ice Clouds Using Observationally Based Parameterizations of Microphysics., *Journal of Climate, 16*, 1643–1664.

Quante, M., and D. O. C. Starr, 2002: Dynamical processes in cirrus clouds., *Cirrus, Lynch, D.K., Sassen, K., Starr, D.O C., Stevens, G. (Eds.), Oxford Univ. Press, New York*, pp. 346–374.

van Zadelhoff, G.-J., and Donovan, D. P., 2004: Comparing ice cloud microphysical properties using CloudNET and ARM data., *J. Geophys. Res*, submitted.

Wylie, D. P., and W. P. Menzel, 1999: Eight Years of High Cloud Statistics Using HIRS., *Journal of Climate, 12*, 170–184.

ICE CRYSTAL BREAKUP ON IMPACT

German Vidaurre[1] and John Hallett

Desert Research Institute
2215 Raggio Parkway, Reno, NV 89512

1. INTRODUCTION

Knowledge regarding the ice break up during aircraft encounter provides basic scientific underpinning for prediction of the icing process itself, having implications for aircraft icing and instrumentation for collection and characterization of ice in the atmosphere. It also has application to ice crystal electrification following collision and bounce and resulting in cloud electrification.

2. METHODOLOGY AND INSTRUMENTATION

Samples of ice crystals from convective clouds in Kwajex (Central Pacific), Camex (Florida) with air speed about 200 m/s, and continental clouds in Oklahoma at 120 m/s air speed, in the size range from 20 μm to 320 μm were collected in formvar solution by continuous replicator and also in the range from 0.3 mm to 2.5 mm were video-recorded following impact on optical flat of a cloudscope.

The replicator measures the collected particles and fragments directly, Hallett (1976) and Turner (1996). This process is very precise, being only affected by the cushioning effect followed by the slightly deformation of the crystal during the evaporation of the formvar after the collection process. With the replicator, several hundreds of broken ice particles were identified and the number of their corresponding fragments was established by direct counting. The summation of the surface area of all the fragments determined the total surface area of the ice particle after fracture.

The analysis of cloudscope data is relatively fast, Meyers (1999). In average, two or three segments of 40 seconds can be processed per day. The technique used digitalizes a segment of the movie, and later the different frames are processed and the surface area, in square pixels, is estimated. As a result of this process, the edges of the ice particle become smoother, and even the size and shape of the ice particle changes from the original movie frame to the final processed image. Due to the lack of resolution, the number of groups coming out of the impact on optical flat of a cloudscope is counted instead of the number of fragments.

3. ANALYSIS OF RESULTS

Figure 1 shows particle size classified in bins, and the expected number of fragments being given by an exponential function for the ice particles with diameters between 20 μm to 320 μm, assuming a circular shape.

Not broken ice particles were also measured in order to get the ratio of broken to non-broken particles. Most of these non-broken particles are small. As the size of the particles increases, the ratio increases, for example, the broken to non-broken ratio increased from 0.2 to 0.95 for particles smaller than 80 μm. However there is no an absolute dependency on the particle size.

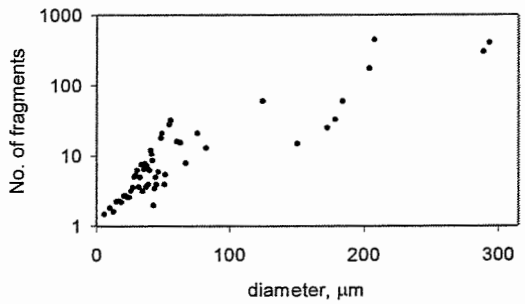

Figure 1. Average number of fragments vs. particle size for ice particles collected in formvar solution by continuous replicator from convective clouds in Kwajex (Central Pacific), Camex (Florida), and continental clouds in Oklahoma in the size range from 20 μm to 320 μm.

The variability of the number of fragments was large; for many bins the standard deviation corresponded to 67% of the average number. This variability was qualitatively related to the ice crystal shape. The shape of the ice particles varies from columns, plates, and 3-D poly-crystals, and the number of fragments observed will also depend in many cases on the way they impact the film.

Several thousands of broken ice particle were identified from the cloudscope data. The number of their corresponding fragments was established by counting them in a digitalized image. The total surface area of the ice particle corresponds to the summation of the surface area of all the fragments. Figure 2 shows the average number of groups observed as a function of the surface area of the ice particle.

Similarly to the replicator observations, the expected number of fragments given by an exponential function for the ice particles with diameters between 0.3 mm to 2.5 mm, assuming a circular shape.

Corresponding author's address: German Vidaurre, Desert Research Institute, 2215 Raggio Parkway, Reno, NV 89512. E-mail: gvidaurr@dri.edu

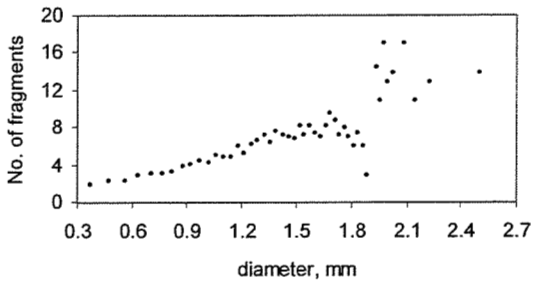

Figure 2. Average number of fragments vs. particle size for ice particles video-recorded following impact on optical flat of a cloudscope from convective clouds in Kwajex (Central Pacific), Camex (Florida), and continental clouds in Oklahoma in the range from 0.3 mm to 2.5 mm.

For small ice particles the broken to non-broken ratio is lower than 1. However, as the size of the particles increases, the ratio becomes very close to 1, indicating that almost 100% of the particles larger than 1.4 mm diameter are broken when they impact on the optical flat of the cloudscope.

The conversion of kinetic energy to surface energy as result of the impact was estimated by measurements of the crystal visible fracture area, Figure 3 and Figure 4. On average over the whole crystal, about 0.1 % of the kinetic energy is converted to surface energy. However, the observed range is significantly wider; some parts of the crystals showed many small fragments (more than 1% of energy conversion), meanwhile other parts showed few or no fragments at all.

Energy may also be absorbed internally in generating high-density dislocations. A problem remains in estimating internal defects not readily visible, and the viscous energy losses on impact into the formvar and in displacing air on impact.

4. CONCLUSIONS

Insights of the origin of small ice particles observed during collection by aircraft instruments, show that they may not only be a product of nucleation but also originate from the impacts on the instrument surface. Further, these conclusions can be also applied to ice-ice interactions, with smaller range of impact velocity during precipitation.

These conclusions are of major operational importance for the characterization of ice particle habits, instrument efficiency, and impact mechanism of ice particles on aircraft and other surfaces at different velocities. The detail of the fracture process may also be of importance in relation to charge separation between the particles after break up.

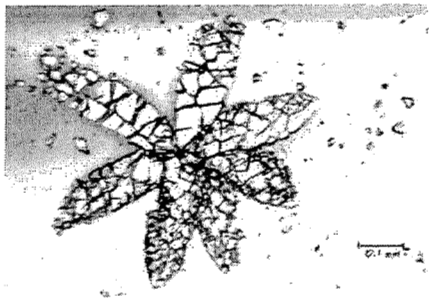

Figure 3. Broken ice crystal collected in formvar solution by continuous replicator, showing multiple fractures. The fracture density is not homogeneous, being the lower section the one most affected by the impact with the film.

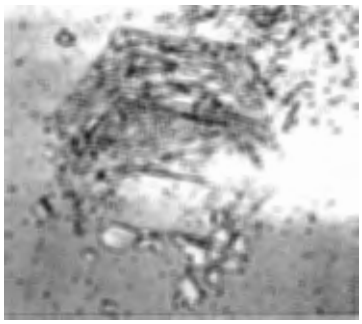

Figure 4. Broken plates, collected in formvar solution by continuous replicator, showing multiple fractures. Note ice fractures are parallel to crystal axis in many areas.

5. ACKNOWLEDGEMENTS

This work was partially supported by the Physical Meteorological Program of the National Science Foundation and data from TRMM program, NASA, and ARM, DOE.

6. REFERENCES

Hallett, J., 1976: Measurements of size, concentration, and structure of atmospheric particulates by the airborne continuous replicator, final report, Cloud Particle replicator for use on a pressurized aircraft. Air Force Geophysics. Laboratory.

Meyers, M., 1999: An assessment of Aircraft Mounted Cloud Probes and their Measurement Characteristics in a highly Variable Atmosphere. Thesis; University of Nevada, Reno.

Turner, M., 1996: Digital Image Analysis of Replicator Ice Crystal Data for Detection of Small Particles in Cirrus Clouds. Thesis; University of Nevada, Reno.

LABORATORY STUDIES ON THE ICE NUCLEATING ABILITY OF POLLEN PARTICLES IN IMMERSION FREEZING AND CONTACT FREEZING MODES

Nadine von Blohn[1], Subir K. Mitra[1], Stephan Borrmann[1,2]

[1]Institute for Atmospheric Physics, Johannes Gutenberg-University, Mainz, Germany;
[2]Cloud Physics and Chemistry Department, Max-Planck-Institute for Chemistry, Mainz, Germany

1. INTRODUCTION

Field measurements have shown that biological aerosol particles are an essential part of the total atmospheric aerosol.

Primary biological aerosol particles are for instance viruses, algae, plant fragments, spores, pollen and protozoa with diameters between 10 and 100µm.

The contribution of biological aerosol particles to the total atmospheric aerosol is about 25% by concentration or by volume in urban or rural air masses (Matthias-Maser and Jaenicke, 1995; Matthias-Maser, 1998) and 10% to 20% in remote marine air masses (Gruber et al., 1998).

Pollen are large biological particles with diameters ranging from 10 up to 100µm. Those with low sink velocities can be lifted to altitudes up to 3000m and higher in the atmosphere and stay there for long durations (Rempe, 1937; Gregory, 1978). Balloon ascents to and above an inversion layer show accumulations of pollen (Linkens and Jorge, 1986) which means that pollen may temporarily be present in the atmosphere in concentrations comparable to those of ice nuclei (Pruppacher and Klett, 1997).

On the surface of pollen grains one can find pores leading to its interior and surface imperfections which can possibly function as active freezing sites (Erdtman, 1954). Earlier studies have shown (Diehl et al., 2001) that pollen are able to take up significant amounts of water from a humid environment at their surface and transport the same into their interior by capillary effects.

The ice nucleating ability of some biological aerosol particles at relatively warm temperatures has already been demonstrated. Small leaf litters with diameters between 45nm and 100µm were shown to be able to act as immersion and contact freezing nuclei at temperatures up to -4°C depending on their state of decay due to the presence of ice-initiating particles that are byproducts of bacterial decomposition (Schnell and Vali, 1972, 1973, 1976; Yankofski et al., 1981; Schnell and Tan-Schnell, 1982). Some types of bacteria with diameters between 0.2 to 1µm have shown the ability to act as ice nuclei starting from -2°C (Vali et al., 1976; Maki and Willoughby, 1978; Levin and Yankofsky, 1983). A natural conjecture is that larger biological particles - among them pollen - might also act as ice nuclei.

Studies (Diehl et al., 2001) have already shown that pollen are able to act as ice nuclei in the condensation freezing mode at temperatures around -8°C. Earlier studies have also shown that pollen from anemophile plants are able to reach high altitudes and under favorable atmospheric conditions can be found at these altitudes with substantial concentrations.

In an earlier paper (Diehl et al., 2002) it was also shown that some types of pollen are able to act as ice nuclei in the immersion and contact freezing modes at temperatures as high as -5°C and lower.

The investigations described in the present paper were carried out in a similar fashion. The ice nucleating ability of some new pollen types was studied in the immersion and contact freezing modes by using the facilities of the vertical wind tunnel, which allows to freely float supercooled droplets in a vertical air stream. Pollen with diameters between 26 and 28µm, possessing low sink velocities and thereby having longer atmospheric residence times were chosen for this study.

2. EXPERIMENTAL METHODOLOGY

In the present study two sets of laboratory experiments were carried out to determine the ice nucleating ability of four new types of pollen particles namely Alder (alnus incana; deciduous tree pollen), Lombardy poplar (populus nigra; deciduous tree pollen), Redtop Grass (agrostis alba; grass pollen) and Kentucky blue (poa pratensis; grass pollen) in the immersion and the contact freezing modes. These pollen types were chosen because of their diameters were small, lying between 26 and 28µm and their corresponding low sink velocities around 2.5cm s^{-1} (Straka, 1975; Gregory, 1978). The pollen grains were commercially available in a standardized dried form which is free from impurities and especially free from bacteria.

The vertical wind tunnel in Mainz allows one to float drops with radii between 20µm and 4mm in the vertical air stream of the tunnel. Reference experiments with particle-free water droplets with radii between 200µm and 400µm in particle-free air showed no freezing of the drops above -28°C.

The observation volume of the wind tunnel was thermally insulated to improve the floating conditions at low temperatures and for small droplets so that the drops did not keep drifting towards the walls of the tunnel.

Corresponding author's address: Subir K. Mitra, Institute for Atmospheric Physics, Johannes Gutenberg-University, Becherweg 21, 55099 Mainz, Germany; Tel. 0049 6131 3923396; E-Mail:. subirmitra@gmx.net.

The insulation also reduced the vertical temperature gradient in the observation section thereby reducing the uncertainity in the temperature measurement.

In all experiments the air temperature in the observation section has been varied and the temperature whether the drop froze or not was recorded and classified in 2℃ intervals. From the observed number of droplets the fraction of the frozen drops was determined. For each pollen type the median freezing temperature (temperature at which 50% of the observed drops froze) was estimated from the fraction of frozen drops in both the freezing modes.

The drop radius was calculated from the recorded wind velocity since in order to keep the drop floating in the observation section the terminal velocity must be equal to the wind tunnel velocity. For both freezing modes the radii of the observed droplets varied between 315 and 380µm. This variation in drop size has little influence on its freezing behavior.

In the first set of experiments the immersion freezing ability of all four kinds of pollen was studied. Drops, generated from purified distilled water to which a defined amount of pollen, 35mg to 100ml water, was added, were injected into the observation area of the wind tunnel by means of a syringe and needle. The droplets were freely suspended in the air stream at various temperatures down to -28℃ and it was observed whether they froze. For each pollen type the number of drops observed was between 600 and 750. In this way a total number of about 3500 individual droplets were floated and investigated during the course of the study.

During the run of the experiments a few difficulities occured: the pollen grains quickly sedimented in the syringe; because of the low temperatures the needle often froze and also the amounts of pollen varied from drop to drop. In addition some droplets froze at once while others after a short time. Drops which did not freeze within a given time period (about 2min) were recorded as "not frozen".

A freezing drop could be identified because the droplet became opaque at once and changed its falling mode abruptly. A sudden reduction of the terminal velocity can be observed because of the phase change of the droplet. Some droplets drifted horizontally and described a spiral track, in a random fashion, some others became unstable while some others spinned around. About 10% of the droplets exploded during freezing.

In the second set of experiments the contact freezing mode of the different pollen types was investigated. Pure water drops were freely suspended in the observation area of the vertical wind tunnel in temperature equilibrium with the ambient air at various temperatures down to -28℃. A small cloud of pollen was manually generated upstream of the droplet by blowing a short burst of air through a tube containing the pollen grains. While the particles passed the drop it was observed whether the drop froze after a collision with a pollen grain. The temperature intervals were also distributed in 2℃ intervals. The number of studied droplets was approximately 200 per investigated pollen kind. Because of the higher level of difficulty encountered in this set of experiments, there could not be so many drops investigated like in the other freezing mode. It was harder to see whether the drop froze or not, because with the burst of air the drop became unstable and drifted towards the walls of the observation section. It could not also be determined how many pollen grains collided with the floating droplet.

3. RESULTS AND CONCLUSIONS

The new results strongly indicate the importance of biological aerosol particles as potential ice nuclei. It has been shown that pollen are able to act as ice nuclei in the immersion and even more efficiently in the contact freezing mode.

In this set of experiments the freezing temperatures were classified in 2℃ intervals. From the distribu tion of the freezing temperatures into intervals the freezing initiation temperatures and the median freezing temperature were determined.

The freezing initiation temperatures in the immersion freezing mode lay within -9 to -11℃ for Alder, -17 to -19℃ for Lombardy poplar, -15 to -17 ℃ for Redtop Grass and -13 to -15℃ for Kentucky blue pollen.

For the contact mode the freezing initiation temperatures lay within the intervals -9 to -11℃ for Alder, -13 to -15℃ for Lombardy poplar, -15 to -17 ℃ for Redtop Grass and -9 to -11℃ for Kentucky blue.

The median freezing temperatures in the immersion freezing mode were found to be -13,5 ± 0,2℃ for Alder, -21,5 ± 0,4℃ for Lombardy poplar, -21,0 ± 0,6℃ Redtop Grass and -19,8 ± 0,7℃ for Kentucky blue.

The mean freezing temperatures in the contact freezing modes were -12,6 ± 0,4℃ for Alder, -17,9 ± 1,2℃ for Lombardy poplar, -18,7 ± 0,7℃ for Redtop Grass and -16,1 ± 1,4℃ for Kentucky blue.

The results of the experiments are shown as two examples in figures 1 and 2 as a fraction of frozen drops in percent at given temperatures of the two decidous tree pollen.

Alder pollen showed the warmest median freezing temperatures.

For nearly every pollen kind the median freezing temperature in the contact freezing mode was a bit higher than that in the immersion freezing mode.

The new results together with earlier results on the ice nucleating ability of pollen particles, bacteria, leaf litter and marine plankton demand a detailed investigation of the climatic relevance of these biological particles specially regarding the influence on cloud and precipitation processes. It is also unclear why and how these pollen particles act as ice nuclei. In other words the dependence of ice nucleating ability on morphology, cell surface structure, membrane properties, protein composition and also on

intercellular space has to be studied. This, though, is a more basic question as a similar question regarding the particles formed of inorganic compounds acting as ice nuclei remains still incompletely answered.

Also more types of pollen have to be investigated to complete a sort of ice nucleating ability table which in conjunction with the seasonal and geographical

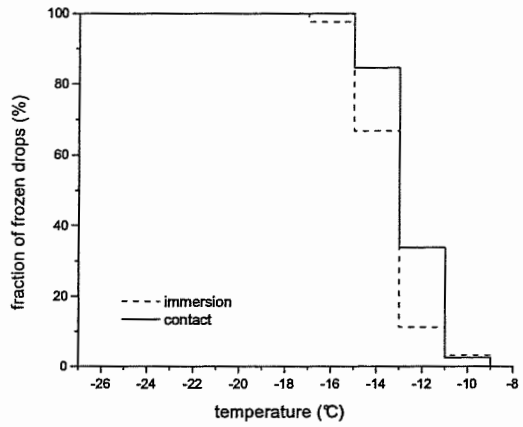

Fig.1 Variation of the fraction of drops frozen due to immersion (dashed lines) and contact (solid lines) freezing with temperature for Alder pollen.

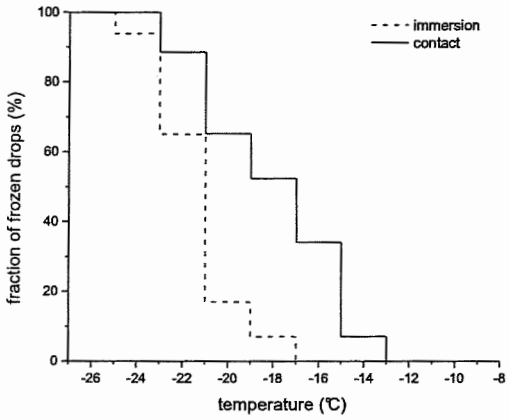

Fig.2 Variation of the fraction of drops frozen due to immersion (dashed lines) and contact (solid lines) freezing with temperature for Lombardy poplar pollen.

variation of sources for these pollen types will make it possible to include their effects in cloud models. In addition the altitudinal variation of pollen concentrations needs further measurements inside and outside clouds in order to assess the likelihoods of pollen being incorporated in or colliding with cloud droplets.

4. ACKNOWLEDGEMENTS

These studies were supported in part by the Ministry of Education and Research of the Federal Republic of Germany under project 07AF219/3. One of the authors, Nadine von Blohn, wants to thank the Institute of Atmospheric Physics at the University of Mainz for providing her with a stipend to carry out the research work. The extensive modifications of the Mainz Vertical Wind Tunnel Facility (MAVERT) necessary for this experiment was made possible by a grant (125-6006/550 HBFG) from the German federal Government for the development of Universities.

5. REFERENCES

Diehl, K., Quick, C., Matthias-Maser, S., Mitra, S. K., Jaenicke, R., 2001: The ice nucleating ability of pollen Part I: Laboratory studies in deposition and condensation modes. Atmospheric Research 58, pp. 75-87.

Diehl, K., Matthias-Maser, S., Jaenicke, R., Mitra, S. K., 2002: The ice nucleating ability of pollen Part II: Laboratory studies in immersion and contact freezing modes. Atmospheric Reseasch 61, pp. 125-133.

Erdtman,G., 1954: Pollen morphology and plant taxonomy. Bot. Not. 107, 65-81.

Gregory, P. H., 1978: Distribution of airborne pollen and spores and their long distance transport. Pageoph, Vol. 116, pp. 309-315.

Gruber, S., Matthias-Maser, S., Brinkmann, J., Jaenicke, R., 1998: Vertical distribution of biological aerosol particles above the North Sea. J. Aerosol Sci. 29 (Suppl. 1), 771-772.

Levin, Z. and Yankofsky, S. A., 1983: Contact versus immersion freezing of freely suspended droplets by bacterial ice nuclei. Journal of climate and applied meteorology, 22, pp. 1964-1966.

Linkens, H. F. and Jorge, W., 1986: Pollentransport in großen Höhe. Beobachtungen während der Fahrt mit einem Gasballon. Allergologie, 9, Nr.2, pp. 55-58.

Maki, L. R. and Willoughby, K. J., 1978: Bacteria as biogenic sources of freezing nuclei. Journal of applied meteorology, 17, pp. 1049-1053.

Matthias-Maser, S. and Jaenicke, R., 1995: The size distribution of biological aerosol particles with radii >0,2µm in an urban/rural influenced region. Atmospheric research, Vol. 39, pp. 279-286.

Matthias-Maser, S., 1998: Primary biological aerosol particles: their significance, sources, sampling methods and size distribution in the atmosphere. Harrison, R. M., von Grieken, R. E. (Eds.), Atmospheric particles. Wiley, pp. 349-369.

Pruppacher, H. R. and Klett, J. D., 1997: Microphysics of clouds and precipitation. Kluwer Academic Publishers, Vol. 18.

Rempe, H., 1937: Untersuchungen über die Verbreitung des Blütenstaubes durch die Luftströmungen. Planta, 27, pp. 93-147.

Schnell, R. C. and Tan-Schnell, S. N., 1982: Kenyan tea litter: A source of ice nuclei. Tellus 34, pp. 92-95.

Schnell, R. C. and Vali, G., 1972: Atmospheric ice nucleifrom decomposing vegetation. Nature 236, 163-165.
Schnell, R. C. and Vali, G., 1973: Worldwide source of leaf-derived freezing nuclei. Nature 246, 212-213.
Schnell, R. C. and Vali, G., 1976: Biogenic ice nuclei: Part I. Terrestrial and marine sources. Journal of atmospheric sciences 33, pp. 1554-1564.
Straka, H., 1975: Pollen- und Sporenkunde. Gustav Fischer Verlag, Stuttgart.
Vali, G., Christensen, M., Fresh, R. W., Galyan, E. L., Maki, L. R. und Schnell, R. C., 1976: Biogenic ice nuclei: Part II. Bacterial sources. Journal of atmospheric sciences 33, pp. 1565-1570.
Yankofski, S. A., Levin, Z., Berthold, T., Sandlerman, N., 1981: Some basic characteristics of bacterial freezing nuclei. J. Appl. Meteorol. 20, 1013-1019.

DISCUSSION ON ARTIFICIAL PRECIPITATION ENHANCEMENT CONDITIONS IN CYCLONE

Wang Yilin

Meteorological Institute of Shandong Province, Jinan, Shandong Province, 250031, P.R.China

1. INTRODUCTION

It is difficult to select the cloud seeding area during precipitation enhancement operation. Usually, because there is less supercooled water in stratiform clouds, the study of water vapour and saturated with respect to an ice surface is very important. According to the study of one dimension cloud model (Hu et al.,2001), the supersaturated water vapour with respect to ice could convert to precipitation by inducing artificial crystals. The purpose of this paper is to analyze the area of ice-saturation and the growth conditions of ice crystals in cyclone.

2. WEATHER PROCESS ON 13-16 MAY, 2002

There was an initial cyclone in the east of Hubei Province at 1200 UTC on 13 May 2002. It located in front of positive vorticity at 500hPa. The developing period of the cyclone was at 1200 UTC on 14 May. The dynamical and thermodynamic factors made the cyclone to be mature. Because of the strong cold air behind the cold front, the cyclone was in the occlusion period at 1200 UTC on 15 May. The cyclone was in dissipative stage at 1200 UTC on 16 May.

2.1 _ 13 May

Corresponding author's address: Wang Yilin, Meteorological Institute of Shandong Province, Jinan, 250031, P.R.China; E-mail: qxwyl@sohu.com.

Fig.1 gives the infrared imagery at 1230 UTC on 13 May. The initial cyclone located on 31°30'N and 115°E. The brightness temperature of convective cloud cluster in front of the cold front was about -63℃.

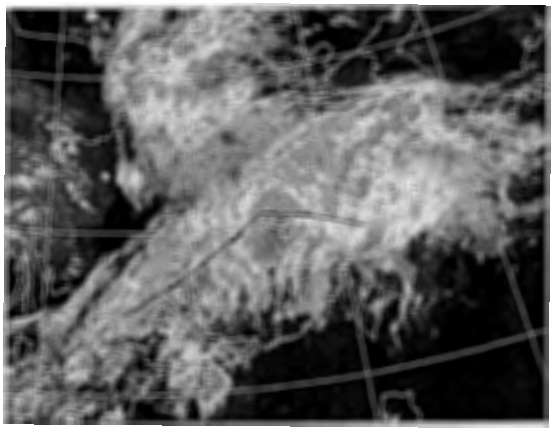

Fig.1 Infrared imagery at 1230 UTC on 13 May.

From Fig.2 it is can be seen that there were two warm tongues of θ_e=330°K that extend to 31°N from South China Sea and the east of Taiwan to northward. The cyclonic circulation was in the top of warm tongues. It provided warm wet air and unstable energy to cyclone. The gray area in Fig.2 is the distribution of cloud liquid water greater than 0.02cm (calculated from MM5) at 1500 UTC on 13 May. The cloud water and rainwater mainly concentrated in front of the cold front and near the warm front. Because the path of warm wet air was from southeast, there was less cloud water behind the cold front.

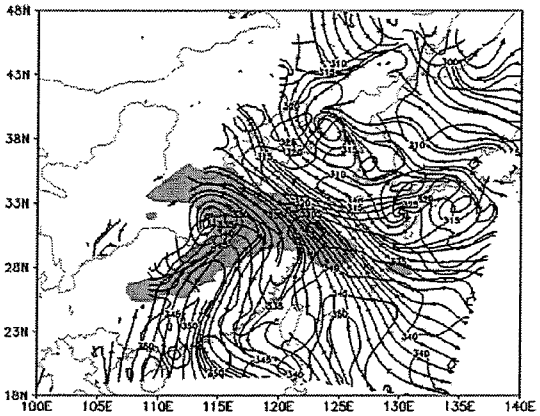

Fig.2 Distribution of streamline and θ_e at 925hPa at 1200 UTC on 13 May (gray area represents cloud liquid water content greater than 0.02cm from cloud top to bottom at 1500 UTC).

Fig.3 shows the distribution of integral vapor value (from MM5) below 0℃ at 1200 on 13 May. The gray areas represent the vapor integral value greater than 9mm. The shape agrees well with the distribution of cyclone wave. This indicates that the water vapor in cold cloud mainly concentrated in the clouds around the cold front and warm front of the cyclone. The water vapor below 0℃ was 1/6 of the whole water vapor of the cloud.

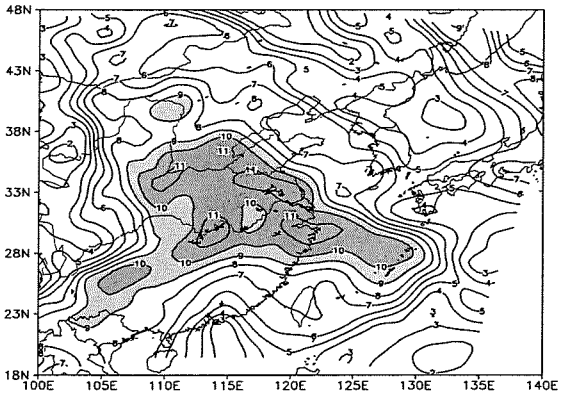

Fig.3 Distribution of integral vapor value below 0℃.

In order to determine the ice-saturation areas, the contours of e-E_{ice} (e expresses water vapor pressure, E_{ice} expresses saturation vapor pressure with respect to ice) are drawn from 0℃ to -30℃ at an interval of 5℃. Fig.4 shows the distribution of e-E_{ice} at -15℃ level. The gray

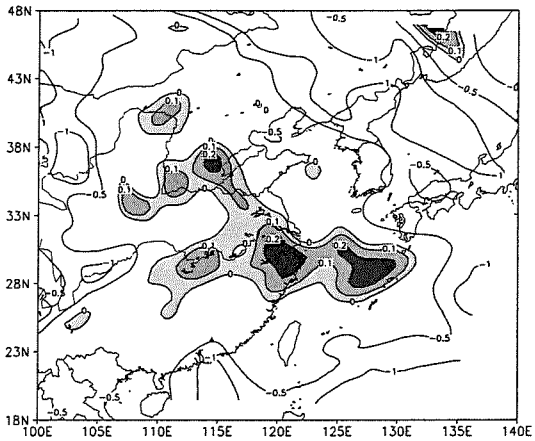

Fig.4 Distribution of e-E_{ice} at -15℃ level. (Grey areas represent e-E_{ice}>0).

areas represent the regions where e-E_{ice}>0. This is just the ice-saturation areas. In these areas, water vapor would sublimate on the surface of ice crystal, and the cloud droplet water would transfer to ice crystal by evaporation and condensation. According to the statistical result, the surface precipitation would occur when the integral vapor value is greater than 9mm. Then the area with e-E_{ice}>0 and the integral vapor value more than 9mm would be the best seeding areas. e-E_{ice}>0 and integral vapor value more than 9mm are the main criteria for cloud seeding.

Fig.5 is the zonal cross-section through the center (31.5°N) of the cyclone at 1200 UTC on 13 May. There were two upward air motions areas in 113°E-118°E and 120°E-126°E respectively. One was in the center of the cyclone with updraft of 0.1 m s^{-1} and maximum height at 200hPa. Another one was in the middle of the warm front. The downdraft played a dominant role above the cold front. Most of the liquid water in cloud existed around warm front (omitted). The areas of quasi-saturation with respect to water, T-Td≥2℃, were mainly between the cold and warm front and extended

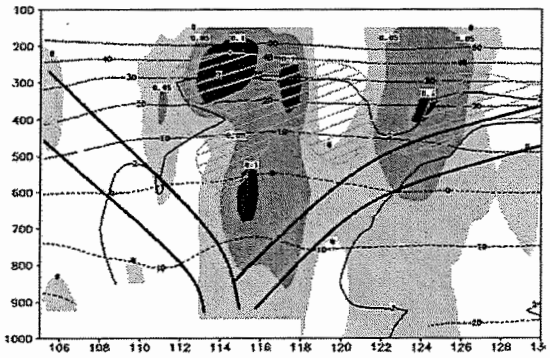

Fig.5 Zonal cross-section through the center (31.5°N) of the cyclone at 1200 UTC on 13 May. (Thick solid lines are the cold front and the warm front. Gray areas are updraft areas. Oblique lines are the ice-saturation areas. Fine solid line is T-Td=2°C. Dashed lines is isotherm.)

to 300hPa (-30℃). These areas are considered for cloud areas. In the areas, the cloud particles are not easy to evaporate during their descending. T-Td≤2℃ is also an important criterion for cloud seeding.

As seen from Fig.5, There were two ice-saturation areas (the areas of oblique lines) within updraft area in the center of the cyclone and above the warm front respectively. In the cross-section, overlap area of ice-saturation area, updraft area and quasi-saturation area is selected as cloud seeding area.

Fig.6 is the zonal cross-section through the south (30°N) of the cyclone at 1200 UTC on 13

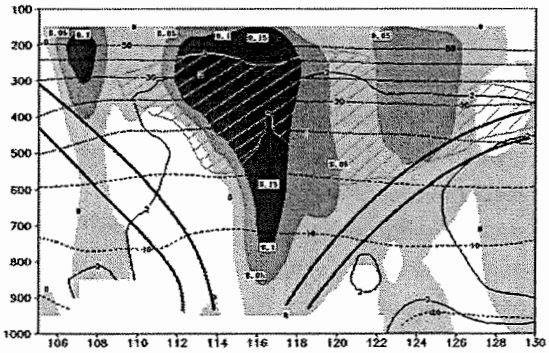

Fig.6 As in Fig.5, but for the south (30°N) of the cyclone.

May. There existed downward air motions along the cold front. The updraft area was mainly in 112°E-120°E with a maximum vertical velocity of 0.15 m s^{-1}. It is clearly seen the overlap area of ice-saturation area, updraft area and quasi-saturation area. This area should be selected for cloud seeding. Fig.7 is the zonal cross-section through the north (34°N) of the cyclone at 1200 UTC on 13 May. It is obviously seen the existence of the overlap area as in Fig.6.

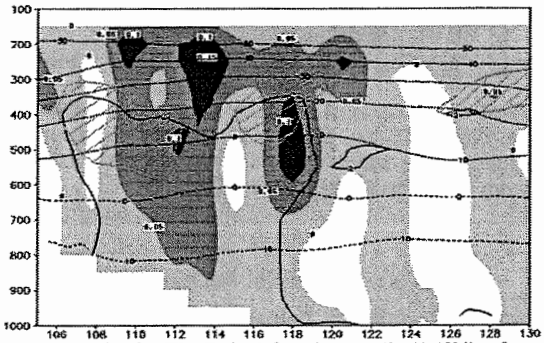

Fig.7 As in Fig.5, but for the north (34°N) of the cyclone.

2.2 14 May

Fig.8 shows distributions of streamline and θ_e at 925 hPa at 1200 UTC on 14 May. The grey areas represent the regions with liquid water more than 0.02cm in cloud at 15 UTC. Most of

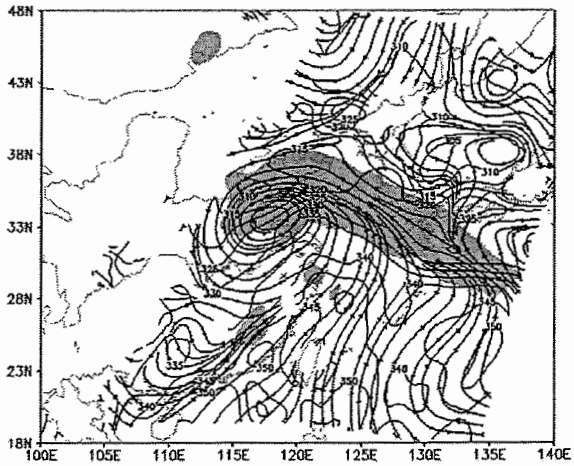

Fig.8 Distribution of streamline and θ_e at 925 hPa at 1200 UTC on 14 May. (Gray areas represent LWC greater than 0.02cm from cloud top to bottom at 1500 UTC).

the cloud water and rainwater distributed in the center of the cyclone and the front of the warm front. The center of integral vapor value below 0℃ occurred over Shandong Province. The value was greater than 14mm. The dry cold area behind the cold front and the warm wet area in front of the cold front formed the vapour front.

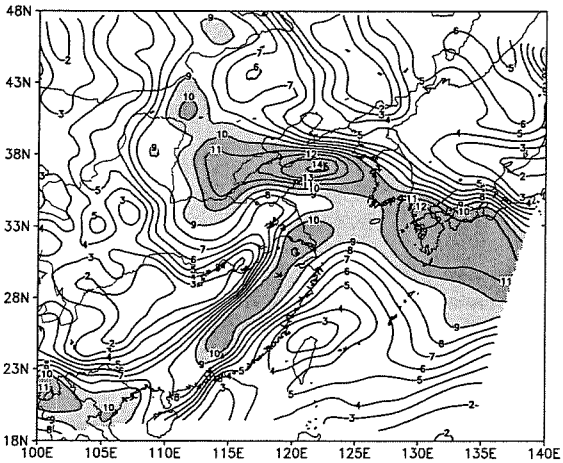

Fig.9 Distribution of integral vapor value below 0℃ at 1200 UTC on 14 May.

The integral vapor value below 0℃ was 10mm in front of the vapour front and 3mm behind the vapour front. There existed ice-saturation areas existed in front of the cold front and the north of the cyclone(omitted). The ice-saturation areas and the area with integral vapor value more than 9mm (Fig.9) formed the conditions for cloud seeding.

2.3 15-16 May

The cyclone was in the occlusion period at 12 UTC on 15 May (omitted), and it dissipated at 12 UTC on 16 May (omitted).

3 SUMMARY AND DISCUSSION

The ice-saturation area, integral vapour value more than 9 mm, vertical water vapour transportation and the existence of quasi-water-saturation area are the four important factors for selecting seeding area.

Before could seeding operation, the figures of e-E_{ice} at different temperature levels, vertical air motions and integral vapour value below 0℃ should be made. The zonal cross-section through different portions of weather system also should be made.

(1) The overlap area of ice-saturation area, updraft area and integral vapour value more than 9mm is used for selecting horizontal seeding area.

(2) The overlap area of ice-saturation area, updraft area and quasi-saturation (T-Td≤2℃) area is used for selecting seeding height.

4 REFERENCES

Hu Zhijin, 2001: Discussion on mechanisms, conditions and methods of precipitation enhancement in stratiform clouds. Q. J. Applied Meteorology, 12, Suppl., 10-13.

A SIMPLE MODEL OF SNOWFLAKE AGGREGATION

C. D. Westbrook[1], R. C. Ball[1], P. R. Field[2] and A. J. Heymsfield[3]

[1]Department of Physics, University of Warwick, UK.
[2] The Met Office, UK.
[3]National Centre for Atmospheric Research, USA.

1. INTRODUCTION

An understanding of aggregation of ice crystals is an important step towards modelling the evolution of ice clouds. Although pristine particles are present in large numbers, particularly at the top of the cloud, larger particles lower in the cloud are usually aggregates, and since many properties of the cloud are sensitive to the larger particles (eg. ice water content, radar reflectivity, etc.), understanding the geometry of aggregates is important. Aggregation also has a significant effect on the particle size distribution, broadening the range of sizes, and reducing the number of smaller particles, as larger ones aggregate with them.

We focus on the case of Cirrus, where the dominant physical mechanism governing the aggregation is believed to be differential sedimentation. A simple theoretical model of this process has been recently proposed by the authors [Westbrook *et al* (2004) – from now on W04], and appears to capture the essential features of the observed particle geometry and size distribution.

2. MODEL

The model is based on the rate at which the centres of two aggregates with fall speeds v_i , v_j and radii r_i , r_j come within a distance $(r_i + r_j)$ of one another (a close approach). This rate is given by:

$$K_{ij} = \pi(r_i + r_j)^2 \, | v_i - v_j | \qquad (1)$$

In our computer simulations we define the radii to entirely enclose the particles. Pairs of particles are picked at random, and an attempted collision is made with probability proportional to the rate K_{ij}. Once a pair of particles has been chosen, they are tracked along a randomly sampled path from all the possible close approach trajectories that the area $\pi\ (r_i + r_j)^2$ in equation 1 encompasses.

To calculate K_{ij} we use an explicit form form for the fall speeds. We assume that the drag force on the aggregate will be proportional to that on a sphere with the same mass and linear size. If this is correct then the drag force takes the form:

$$F_d \propto \rho\, \nu_\kappa\, f(\mathrm{Re}) \qquad (2)$$

where ρ is the density of the air, and ν_κ is the kinematic viscosity. The function f depends on the Reynolds number $\mathrm{Re} = rv/\nu_\kappa$ alone, and takes the forms:

$f \propto (\mathrm{Re})$ in viscous flow
$f \propto (\mathrm{Re})^2$ in inertial flow

Here we focus on the latter regime, however in W04 we consider a more general form $f \propto (\mathrm{Re})^{1/\alpha}$ where α is an adjustable parameter. The drag force (2) may then be equated with the weight of the particle to calculate its fall speed.

We have also persued a theoretical analysis based on the equations of Smoluchowski (1917), where we assume that a fixed fraction of close approach events result in a collision. Details are given in W04, and the results of this analysis match our computer simulations well.

3. GEOMETRY

The aggregates produced by our simulations have a fractal geometry: this is chacterised by the mass – diameter scaling:

$$m = a\, D^b \qquad (3)$$

where we find b≈2.05±0.1 in our simulations, while our theoretical arguments lead to b=2. This scaling may also be characterised in terms of effective density ρ_e (the mass of the particle divided by volume of a circumscribed sphere) – for our aggregates then we have $\rho_e \propto D^{-1}$. This is in good agreement with experimental studies, many of which have found exponents of around -1; for example Heymsfield *et al* (2002) quote an exponent of -0.96 in table 1 of their paper for aggregates of bullet rosettes.

The prefactor 'a' in equation (3) is a function of the geometry and size of the pristine particles from which the aggregate is composed, and is approximately the average mass of the pristine particles divided by the square of their length.

The aspect ratio of our simulated aggregates has been calculated. The maximum span of the particle D_m is measured, along with the longest span perpendicular to that longest axis, D_w. We find the ratio D_w/D_m quickly

Corresponding author's address: Chris Westbrook, Department of Physics, University of Warwick, Coventry, CV4 7AL, United Kingdom;
email c.d.westbrook@warwick.ac.uk

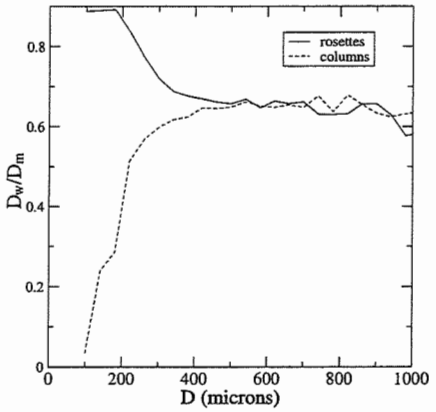

Figure 1 : Aspect ratio of simulated aggregates of 100μm column and bullet rosette crystal types. After only a few aggregations, the ratio approaches a constant value of approximately 0.65.

asymptotes with increasing aggregate size (after about four or five aggregations) to a value of ≈0.65±0.05. This is illustrated in figure 1. Korolev and Isaac (2003) observed a similar asymptotic behaviour for ice particles in cirrus approaching a ratio of approximately 0.6 – 0.7.

Crucially, both the aspect ratio and the mass diameter scaling $m \propto D^2$ are approached asymptotically irrespective of the pristine particle geometry.

Example images of ice aggregates sampled during a flight through a Cirrus cloud are shown in figure 2, alongside some of our simulation aggregates.

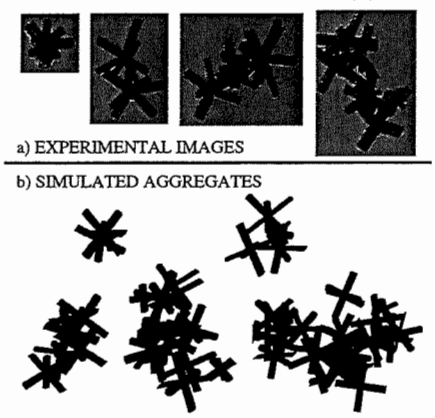

Figure 2 : Projected images of a) ice aggregates from a cloud particle imager (CPI, SPEC Inc., USA) during a flight through a Cirrus cloud, and b) sample aggregates from our simulations. The pristine particles composing the aggregates are bullet rosette crystal types.

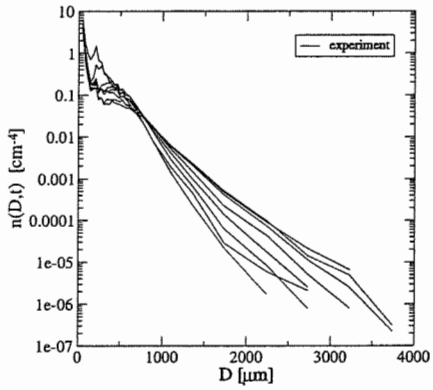

Figure 3 : measured particle size distribution averaged over 15km flight tracks, at altitudes between 9500m and 6600m.

4. SIZE DISTRIBUTION

It has been shown by Van Dongen and Ernst (1985) that Smoluchowski's equations for aggregation admits 'dynamical scaling' solutions:

$$n(m,t) = m_{av}(t)^{-\xi}\ \phi\ [\ m/m_{av}(t)\ ] \qquad (4)$$

where $n(m,t)$ is the concentration of clusters with mass m at time t . Equation (4) shows that the evolution of the particle size distribution may be described by a universal function ϕ which describes the underlying shape of the distribution, depending on the dimensionless variable m/m_{av} . This function is scaled by the evolution of the average mass $m_{av}(t)$; ξ is a positive constant. The shape of ϕ is independant of the initial particle shape, geometry or distribution, once the system has 'settled' into scaling.

In experimental observations, such as aircraft flights through cloud with imaging probes, measurement of particle mass is often not directly possible – only particle diameter. Sample distributions measured at various altitudes through a Cirrus cloud [as presented by Field and Heymsfield (2003)] are shown in figure 3. In the appendix of W04 we show that using equations (2) and (4) a scaling form may be found for the bin-width normalised cluster span distribution:

$$[M(2)]^{-1}\, D_{av}^{3}\ n(D,t) = \psi\ [\ D/D_{av}(t)\ ] \qquad (5)$$

where D_{av} is the average cluster span, and ψ is a universal function of D/D_{av} alone. To normalise the distribution we have used the second moment $M(2) = \Sigma D^2$. The form (5) allows a direct comparison between our simulation data and experiment. Figure 4 shows the experimental distributions of figure 3 rescaled according to equation (5), with simulation data rescaled in the same way overlaid. The correspondance is good, particularly given the simplicity of the model, but not perfect: in particular,

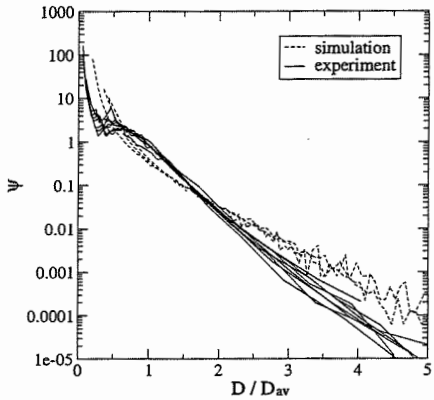

Figure 4 : rescaled experimental size distribution with simulation results overlaid (dashed lines).

we note the experimental data has a 'kink' at small sizes – this may be due to some hydrodynamic effect that our simple kernel in equation (1) does not capture. Never the less, the quality of the experimental data collapse in figure 4 suggests that there is one single dominant aggregation mechanism, although it is clear we have not captured it's form exactly.

5. DISCUSSION

A simple model of aggregation through differential sedimentation has been constructed, and applied to the problem of ice crystal aggregation in Cirrus. The geometry of the snowflakes produced by this process has been found to be fractal with a well defined mass – diameter scaling exponent (fractal dimension) of two. The aspect ratio of the particles has also been studied and found to quickly approach a value of about 0.65. These results are independant of the initial geometry or distribution of the pristine particles from which they are composed. Comparison with experimental data indicates that the essential features of the aggregate geometry have been captured.

The aggregate size distribution has also been studied, and we have successfully rescaled experimental and simulation distributions. The correspondance between the two rescaled distributions is good, but also indicates that further work is necessary to capture the exact form of the experimental data. We hypothesise that this may be due to hydrodynamic effects that our collision kernel does not capture, such as wake capture or small particles being swept around larger ones.

6. ACKNOWLEDGEMENTS

This work was supported financially by the Engineering and Physical Sciences Research Council, and The Met Office.

7. REFERENCES

Field P.R. and Heymsfield A.J., 2003: Aggregation and scaling of ice crystal size distributions. J. Atmos. Sci. **60** 544

Heymsfield A.J., Lewis S., Bansemer A., Iaquinta J. and Miloshevich L.M., 2002: A general approach for deriving the properties of Cirrus and Stratiform ice cloud particles. J. Atmos. Sci. **59** 3

Korolev A. and Isaac G., 2003: Roundness and aspect ratio of particles in ice clouds. J. Atmos. Sci. **60** 1795

Smoluchowski M., 1917: Z. Phys. Chem. **92** 129

Van Dongen P.G.V. and Ernst M.H., 1985: Dynamical scaling in the kinetics of clustering. Phys. Rev. Lett. **54** 1396

Westbrook C.D., Ball R.C., Field P.R. and Heymsfield A.J., 2004: A theory of growth by differential sedimentation with application to snowflake formation. Submitted to Phys. Rev. E – preprint available from http://arxiv.org/pdf/physics/0312057

THE MICROPHYSICAL AND ELECTRICAL STRUCTURE OF CONVECTIVE ANVILS

[1]P. T. Willis, J. E. Dye[2], S Lewis[2], W. D. Hall[2]

[1]NOAA/AOML/CIMAS, Miami, FL , 33149, USA
[2]National Center for Atmospheric Research, Boulder, CO, 80307, USA

1. INTRODUCTION

The airborne field mill project (ABFM) was carried out over central Florida during the early summers of 2000 and 2001 with an overall objective of improving, and quantifying, the basis for triggered lightning safety rules for spacecraft launches from Cape Kennedy. Numerous convective anvils were sampled with the University of North Dakota Citation aircraft. Detailed electric field measurements and rather complete concomitant cloud and hydrometeor microphysical measurements were obtained from the single airborne platform. Most of the sampling was done at anvil levels, nominally 10 km altitude and -35 deg C. The aim was to document the conditions as the fields decayed in anvils. But, in many cases the sampling was done as the anvils were being fed by flux of hydrometeors from active convective cells and updrafts. In this study we examine the microphysics in the vicinity of locations where the fields change significantly, but perhaps more generally, these measurements serve to characterize the microphysical characteristics of Florida convective anvil clouds. In this brief summary we use one case to illustrate the typical cloud microphysics.

2. CONCEPTUAL CONVECTIVE ANVIL MODEL

A conceptual model of the morphology of these convective anvils can provide a framework for interpretation of the myriad of complex varied observations. The framework outlined here is very preliminary. Anvils over East Central Florida typically are the result of convective cells (updrafts) initiated on the sea breeze front. At stochastically favored locations these smaller cells organize into a significant cloud system with strong updrafts (20 – 40 m/s). These updrafts shed non-buoyant elements and then detrain at their level of zero buoyancy, which is often near the tropopause. The divergence as the updrafts detrain, will build the anvil slightly upwind, but transport the bulk of the volume down the environmental flow, sometimes accelerated slightly. Some of the updraft flux is also incorporated into developing downdrafts. These cloud systems typically are multi-cellular, with new updraft cells developing on the upshear side of the cloud system. Decaying cells move mostly downshear, and develop into stratiform precipitation cloud regions, characterized by bright band and a melting layer, and rain extending to, or near, the surface. The cloud system evolves towards varying degrees of mesoscale organization, and these mesocale circulations may then control the movement of decaying cells, the anvil transport, and the location of new growth. In the convective cells below the 0 C isotherm, warm rain processes play an active role, and in fact influence the ice development at higher levels in the cloud. The bulk of the microphysical charge separation probably occurs in the active convective elements (updrafts). The subsequent spatial separation of charge, i.e. the evolution of charge centers, is driven by the differing cloud particle and hydrometeor trajectories. The trajectories of graupel remain in close proximity to the active convective cells, and fairly large, but less dense ice hydrometeors are lofted into the anvils. The observed anvils are characterized by a very broad range of particle sizes, including particles of quite large dimension, but of fairly low density and terminal velocities. These large hydrometeors coexist with high concentrations of small near spherical frozen cloud droplets.

Corresponding Author: Paul Willis, NOAA/AOML, Miami, FL 33149, E-mail: paul.willis@noaa.gov

The case of 13 June 2000 illustrates the aspects of the conceptual model, as well as the microphysical characteristics of the anvil clouds. The sounding taken at the Cape (XMR) at 2200 UTC. , and the shows environmental flow at anvil levels is from the SW, and upshear is to the S thru West. A series of high resolution visible satellite images clearly illustrate the system, but only one at 2115 UTC can be shown here (Fig. 1). The Melbourne WSR-88D Cappi's for 4km, 7 km and 10 km show that CG lightning is occurring in the main convective cell to the SSW of the flight track, that the anvil is building to the NE. New cells are developing to the SW, W, and NW of the primary cell, and the system has not yet built a stratiform precipitation area.

Fig. 1 Visible image and flight track 61300 2115 UTC

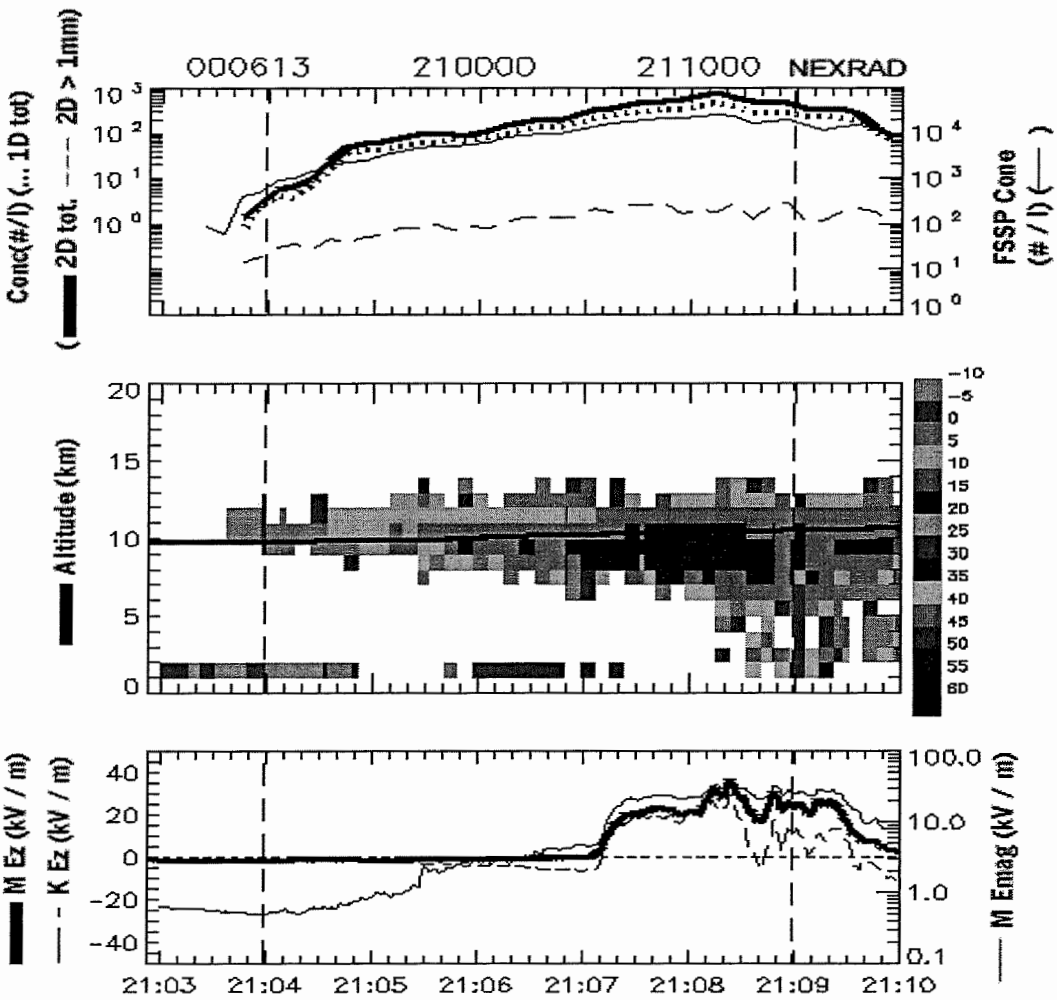

Fig. 2 Merged Summary Plot – track 3 Top Panel: Time history of particle concentrations; Center Panel: vertical MLB WSR-88D curtain of reflectivity columns along flight track; Bottom Panel: two retrievals of vertical electric field–linear, left; and resultant vector field Emag–log, right

3. CONVECTIVE ANVIL MICROPHYSICS

The microphysical measurements were made using multiple instruments spanning the size range from about 3 um (cloud droplets), to about 5 cm (ice hydrometeors), with adequate sample volume in each size range. The instruments are described in Dye, et al. (2004). The Rosemount icing detector did not find any evidence of supercooled liquid water in any of the anvils sampled during the project. Fig. 2 presents data along a typical flight track. The top panel summarizes the particle concentrations in several size ranges. The second a vertical curtain of reflectivity along the aircraft flight track. The bottom panel shows the electric field measured by the aircraft. Note that the field increases gradually from anvil entry to 210710, where there is a significant, almost step increase, to 20 kV/m.

As noted in Dye, et al. (2004) the particle concentrations of small ice, and medium to large size ice hydrometeors nearly always increase in concert. Regions of high concentrations of 2mm ice particles are also regions of high concentrations of small ice (3 – 60 um). Fig. 3 displays a series of 30s composite size spectra along the anvil flight track of fig. 2. In general as shown for this case the concentrations of all sizes increases along the track from the anvil edge into the dense portions of the anvil. Where there are fields significantly elevated above ambient, high concentrations over the full range of sizes appears to

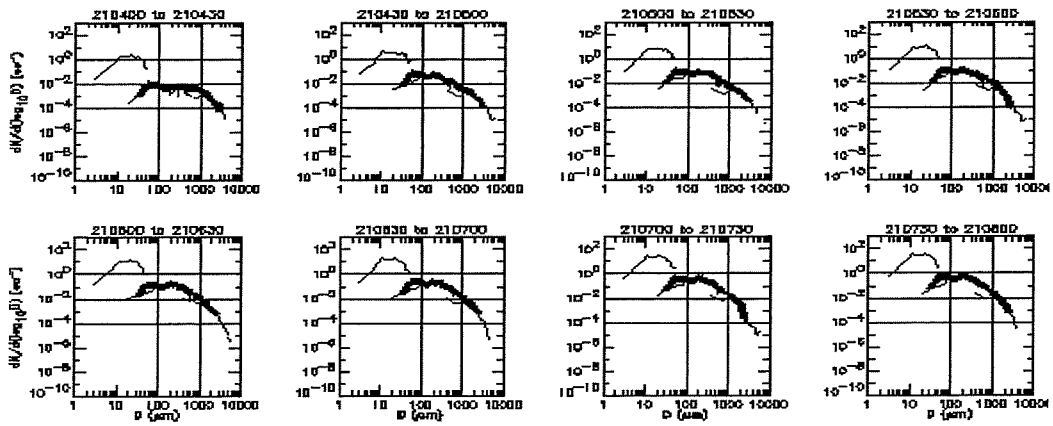

Fig. 3 Number size distributions–30s averages; FSSP light line, 2DC bold line, med line HVPS

be a necessary condition, but, there is no outstanding concentration inflection at the location of the immediate strong increase in field strength near 2107/10. There are often regions of significantly high concentrations of particles over a broad range of sizes, where the fields are not particularly elevated.

Fig. 4 shows detailed typical composite size distribution in two formats. Illustrated is the transition from a small size, low concentration distribution (2056), to a distribution with high concentrations at all sizes (dense anvil) (2059). In the second panel the same data are shown in a semi-log plot. It appears that a two exponential function fit may be appropriate for these distributions. This small sample series of distributions shown here is often repeated throughout this rather large sample of anvil microphysics.

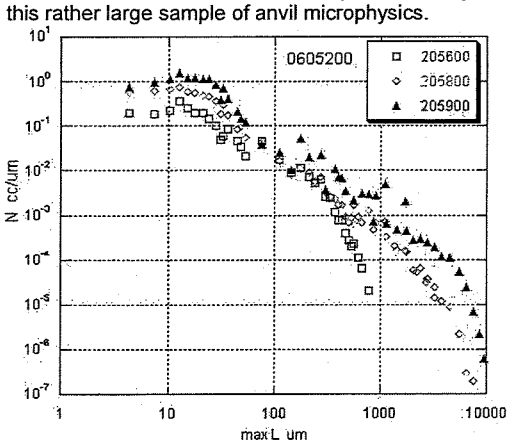

Fig. 4 Composite number size distribution – log log

The CPI images, with 3 um resolution, provide a detailed look at the characteristics (form and structure) of a wide range of particle sizes The sample volume is not adequate for obtaining concentrations of large hydrometeors, but concentrations can be derived for small particles of dimension < 100 um. The morphology of the particles, as with the size distributions, repeats throughout entire sample of

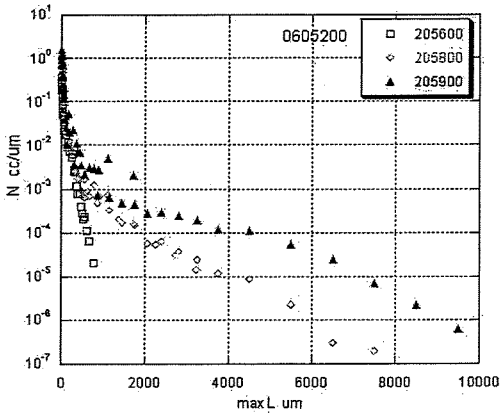

Fig. 5 Composite number size distribution – semi log

convective anvils. There are subtle differences, but the similarities are quite astounding. Only a very small sample of images can be shown here, but, even this very small sample illustrates the salient recurring features of the images. In Fig. 6 two half frames are shown that have been sorted by particle size, but not edited otherwise. The large particles shown here are ~ 1mm, but the data from the HVPS instrument show that hydrometeors to cm size do exist in these anvils, and probably have a very similar morphology to the images shown in Fig. 6a. Although some riming is present, these large hydrometeors do not appear to be heavily rimed. This is consistent with graupel being formed in the strong updrafts and having particle trajectories that fall out before these anvil samples. Aggregation was probably involved, to some degree, in the evolution of these particles, but for the most part they do not look like strictly like aggregates. Instead they appear to have a polycrystaline structure indicative of their tortuous growth history, as they were formed, and grown, in strong updrafts before being detrained at anvil levels. Along their trajectory the growth history in strong updrafts undoubtedly spanned a wide range of temperature and supersaturation conditions, and growth was probably forced at multiple sites and at multiple habits on each particle. It is surprising how

the same general structure of large hydrometeors recurs through the sample. These particles are microphysically very different from cirrus formed in the same geographical area by large scale gentle uplift. The formers convoluted particle morphology is in stark contrast to elegant bullet rosettes found in the latter.

In Fig. 7b an unedited sample of particles < 100um is shown. The very striking feature is that every thing smaller than about 40 um is an almost perfectly spherical frozen droplet. This is typical of nearly all of the anvils observed throughout the course of the project. This is consistent with the observation that regions of high concentrations of medium to large particles almost universally coexist with regions of high concentration small particles. These small particles are ubiquitous even in quite aged anvil parcels. They undoubtedly do collide with the larger hydrometeors of higher terminal fall velocities, but do not aggregate, so they can coexist. These small spherical ice particles are probably formed at some level in the strong updrafts through a condensation freezing nucleation mechanism. Also, the near sphericity of these small ice particles augers well for the trustworthiness of the FSSP data sample.

The fairly abrupt increase in Ez field strength, i.e. inflection in the field data in Fig. 4, occurs quite often. At these inflections along sampling flight tracks, the observed field strengths quickly increase from near a kV/m to tens of kV/m, often in an area where the bulk microphysical conditions (concentrations) appear to be either constant, or slowly monotonically increasing. We examine the relative concentrations in each of four size intervals from the CPI images for three field inflection points. The CPI sample area and actual sampling time was assumed to be constant for 30s periods. Microphysically the only difference from the low field side of the field increase to the high field side of the inflection. appears to be an increase in the concentration of small size cloud particles (<80 um). The situation is complex and this is a very small preliminary sample, but this may indicate that in the charge center responsible for the high fields, the charge may reside on the small particles (approx < 80 um). Of course, much more needs to be done to substantiate, or refute, this very preliminary result.

This result is consistent with the anvil charge decay model of Willett and Dye (2003), where the decay of anvil charge is due to a reduction of the bulk conductivity in parcels with significant particle area. These particles are smaller than the particles that contribute to the bulk of summed particle area cross section (> 100 um).

The microphysical conditions, size distributions and particle morphology, are generally quite repeatable throughout this anvil cloud sample. Surprisingly, there are more similarities than differences. Small near spherical frozen cloud droplets (< 60 um) are ubiquitous in this large sample of convective anvils. These small particles may be important keys to aspects of cloud and anvil electrification, and warrant further examination

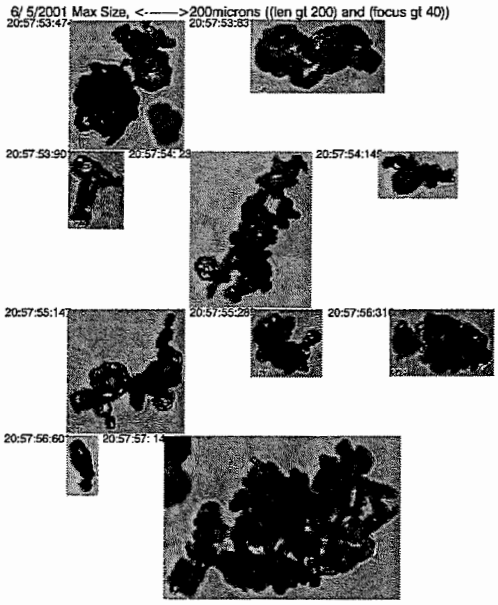

Fig. 6A typical large CPI images L > 400 um

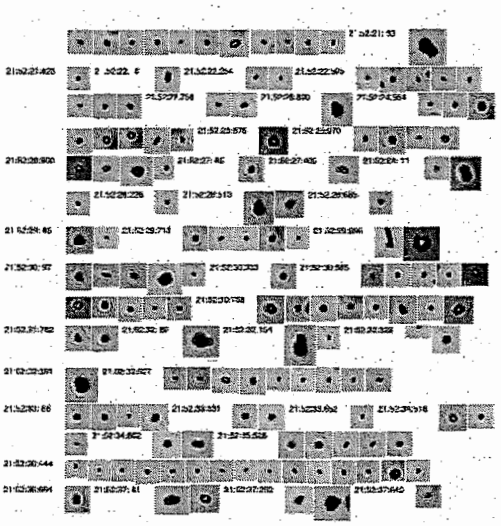

Fig. 6B typical small CPI images L< 100 um

Acknowledgement: The ABFM Project was funded by NASA KSC and the National Reconnaissance Office

References

Dye, J. E., et al, 2004: Airborne observations of microphysics and electric fields in anvils of Florida thunderstorms. This volume

Willett, J. C. and J. E. Dye, 2003: A simple model to estimate electrical decay times in anvil clouds. Proc. Internat Conf. on Atmospheric Electricity, Versailles, France, June 2003

HORIZONTAL AND VERTICAL CLOUD STRUCTURE OBTAINED USING W-BAND AIRBORNE RADAR

M. Wolde[1], S. Haimov[2], D. Marcotte[1], W. Strapp[3], G. Vali[2] and G. Isaac[3]

[1] National Research Council, Ottawa, Ontario, K1A 0R6, Canada
[2] University of Wyoming, Laramie, Wyoming, 82071, USA
[3] Meteorological Service of Canada, Toronto, Ontario, M3H 5T4, Canada

1. INTRODUCTION

The Flight Research Laboratory of the National Research Council (NRC), in collaboration with the Meteorological Service of Canada (MSC), uses the NRC Convair 580 (CV580) aircraft for atmospheric research. This aircraft is equipped with state-of-the-art instruments and has been used for various atmospheric research projects in Canada and abroad (Isaac et al., 2001). Research aircraft that are similarly equipped are routinely used to obtain detailed information of cloud microphysics and dynamics from in-situ probes installed on them. However, in-situ probes sample only small portions of clouds and provide data along a flight path. Therefore, documenting cloud properties at various cloud segments requires multiple sampling at various altitudes and locations. In a rapidly evolving system more than one aircraft is needed to capture changes in cloud properties. Combining in-situ measurements with airborne millimeter-wavelength (mm-wave) radars has been shown to be a promising technique to deduce or retrieve cloud microphysics and cloud dynamics information up to few kilometers away from the aircraft (e.g., Vali et al., 1998, Wolde and Vali, 2001).

To characterize winter clouds that lead to aircraft icing, the University of Wyoming polarimetric Doppler cloud radar (WCR) was installed on the NRC 580 during the first Intensive Operational Period of the 2003/04 second Alliance Icing Research Study (AIRS II) project, which was a collaborative effort between MSC, NRC and other research groups. In addition to the WCR, the CV580 was equipped with an array of cloud probes and a Ka-band radar, which are part of the standard instrumentation packages of the aircraft. The WCR was first tested in the NRC CV580 during the Canadian Surface Ocean–Lower Atmosphere Study (C-SOLAS), which preceded the AIRS II flights. The C-SOLAS project was conducted in October 2003 over Atlantic Canada, while the AIRS II project was conducted between November 2003 and February 2004 over the Mirabel airport near Montreal, Canada and the surrounding regions of Ontario and Quebec.

This paper presents examples from the WCR data obtained in different environments depicting horizontal and vertical structure of clouds sampled during these two experiments. While the data presented is still at an early stage of analysis, it is hoped to show the potential of using airborne radar to study horizontal and vertical cloud structures extending a few kilometers from the aircraft location.

Corresponding author's address: Mengistu Wolde, National Research Council, Ottawa, Ontario, K1A 0R6, Canada; E-Mail: Mengistu.wolde@nrc.gc.ca.

2. W-BAND DOPPLER RADAR

The WCR specifications and capabilities are well documented (e.g., Vali et al., 1998) so only a brief description of the radar installation on the NRC CV580 is given. The WCR was installed in the NRC CV580 cabin on a single shock-mounted adjustable rack in order to minimize the impact of vibration on the radar subunits (Figure 1). The WCR installation included a side-looking dual-polarized 12" Gaussian optics lens antenna (GOA) transmitting/receiving through a rexolite window and a down-looking single polarization 12" GOA pointing through a rexolite port on the belly of the aircraft. Both antennas were installed close to the RF source to minimize the loss from the waveguides. The space between the antennas and the rexolite windows was shielded with 14" tubes. For the side-looking antenna, the regular aircraft window frame was replaced with a machined frame that holds the rexolite window perpendicular to the beam.

The radar transmits sequences of either single polarized pulses using one or two antennas or dual polarized pulses using one antenna. During C-SOLAS the radar was

Figure 1 WCR installation on the NRC Convair-580

operated in a single polarization mode using the down-looking antenna, while during AIRS II, the radar was operated either in dual-polarization mode using the side-looking antenna or single polarization mode using both antennas. In the data that are presented in this paper, the aircraft motion is removed from the measured Doppler data by filtering out the aircraft motion using data obtained from an Inertial Reference System that was installed at the location of the down-looking antenna.

3. SOLAS Case: Stratocumulus (SCu) deck

The radar data discussed in this section were collected in a 1-2 km deep SCu cloud deck that was sampled in eastern Canada on October 18, 2003 using only the downward pointing antenna. A radar reflectivity image taken while the aircraft was descending towards the top of the cloud layer is shown in Figure 2a. The clouds were organized into small-scale 100-1000 m wide cells extending approximately 500 m from the top of the cloud. As the aircraft descended from 300 m above the cloud into the cloud top, the temperature decreased from –10°C to –18°C while the dew point increased from –50°C to –18°C. This strong temperature and moisture inversion explains the uniform cloud-top height seen in the radar image. Figure 2b shows time series of the radar reflectivity and Doppler velocity at the nearest usable range gate and temperature, dew point temperature and the Rosemount Icing Detector (RID) voltage at the cloud top. As indicated by the RID trace, the cloud contained suppercooled water. The LWC probes also measured (not shown) high liquid water content (> 0.5 g m^{-3}). The relative maxima in the reflectivity fields correspond to near 0 or slightly positive Doppler velocity, while the minima in the reflectivity corresponds to regions

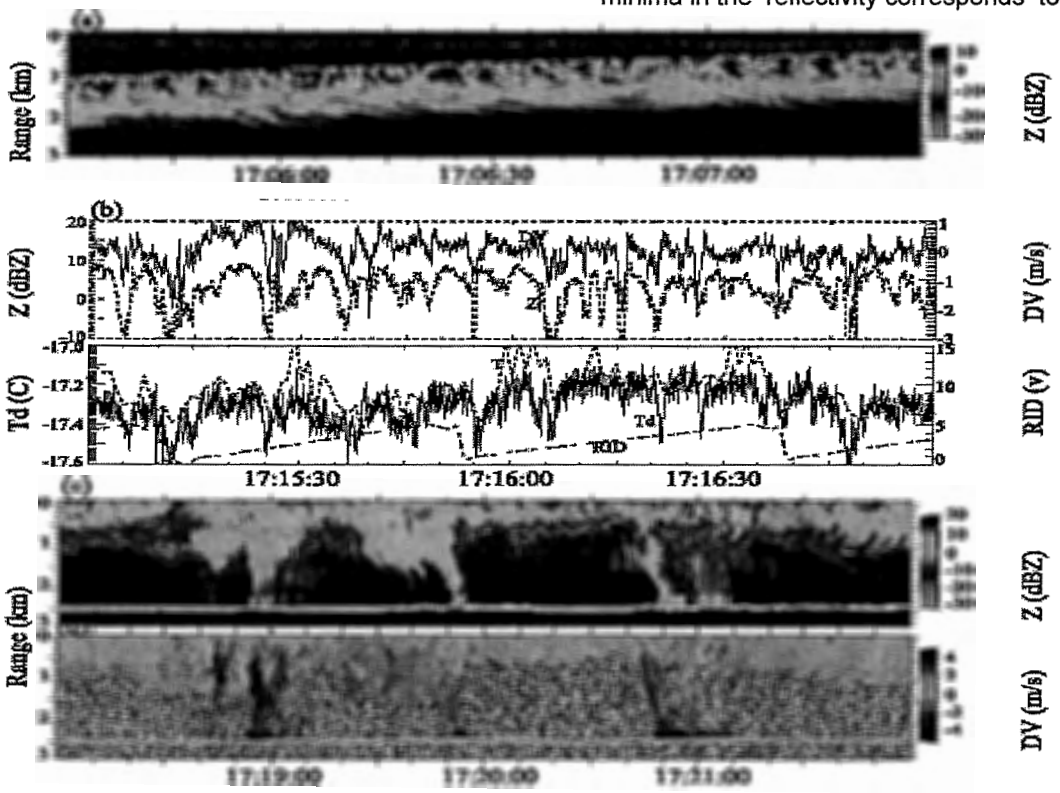

Figure 2. Radar and in-situ data obtained on October 18, 2003. a) Radar reflectivity (Z), b) traces of Z and Doppler velocity (DV), Temperature (T), Dew Point (Td) and RID voltage and c-d) vertical profiles of Z and DV.

of lower temperature and dew point and minima in Doppler velocity (stronger downward velocity). This suggests dry air intruding into the cloud layer in between the high reflectivity cells. The Radar reflectivity and the corresponding Doppler data obtained while the aircraft was inside the SCu cloud deck is shown in Figure 2c-d. For this segment, both the reflectivity and Doppler data show that 100-1000 m wide bands remain distinct in the vertical direction with some of them reaching the ground, with melting band signature a few hundred meters above the surface.

4. AIRS II Cases

In this section, radar reflectivity and Doppler structure of two different AIRS cases are presented. The first example is from the first AIRSII flight over the AIRS ground site at Mirabel, Quebec sampled on November 11, 2003. The vertical radar reflectivity obtained from the down-looking antenna at an altitude of 5.8 km and temperature of -21°C shows two cloud layers (Figure 3a). A low cloud layer with defined melting layer extending from the surface to 3.5 km and an upper cloud layer above an altitude of 3.6 km. The upper cloud layer at the flight level was fully glaciated (not shown).

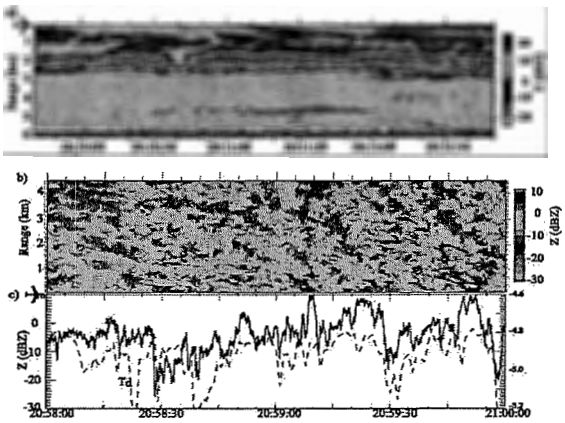

Figure 3. Radar and in-situ data from November 11, 2003 flight over Mirabel. Vertical (a) and horizontal (b) profiles of radar reflectivity and c) traces of radar.

The Horizontal cross-section of radar reflectivity obtained at the top of the lower cloud deck at a later time is shown in Figure 3b. During this segment clouds were mixed phase with LWC of up to 0.5 gm^{-3} at a temperature of -5°C. The cloud top of this lower layer exhibited a fine-scale cellular structure similar to the Oct 18 SCu deck shown in Figure 2. In this case, the reflectivity peaks are organized into 100-500 m wide cells. This horizontal structure resembles the marine stratus clouds studied by Vali et al. (2001). Traces of radar reflectivity from the nearest usable range gate and dew point temperature are shown in Figure 3c. It can be seen that the sharp decrease in radar reflectivity in between the high reflectivity cells also show a decrease in dew point temperature.

The 2nd example is from a November 19, 2004 icing flight over Mirabel in mixed phase cloud. In this case, the dual-antenna mode was chosen and simultaneous observations of the horizontal and vertical structures of the cloud were collected. The radar data shown in Figure 4 was taken at an altitude of 4.5 km and temperature of –7°C. At this flight level, the in-situ probes indicates clouds were mixed phase with a LWC of 0.2-0.4 g m^{-3} (not shown). The horizontal radar cross-section from the side-looking antenna shows a homogenous reflectivity field with Z of –20 dBZ extending 2 km from the aircraft. The absence of a radar signal beyond 2 km is due to the sensitivity limitation of the radar. Figures 4b-e show the radar data obtained from the down-looking antenna. It can be seen that the weak Z shown in the horizontal cross-section extends only to about 500 m below the aircraft level and the reflectivity sharply increased to 10 dBZ at 1 km range from the aircraft.

The vertical Doppler velocity on the other hand shows wave-like fluctuations near the flight level that extended to 2 km (Figure 4 c-d). This is more likely due to the roll angle change affecting the beam orientation (Figure 4d) and thus introducing a component of the horizontal wind to the vertical Doppler velocity. It is worth noting that this wave-like fluctuation is not seen the Doppler velocity from the ground, which confirms that the aircraft motion is removed from the Doppler data. Figure 4e highlights the vertical profiles of reflectivity and Doppler velocity taken at two different sections of the cloud segment. Both profiles show a peak in reflectivity and Doppler velocity at 2 km range. The first profile is taken at the beginning of image. This profile exhibits a number of peaks both in reflectivity and Doppler velocity, which represents cloud particles with different history in a given vertical cross-section. In contrast, the profile taken at the end of the image shows a decrease in reflectivity below the melting layer down to the

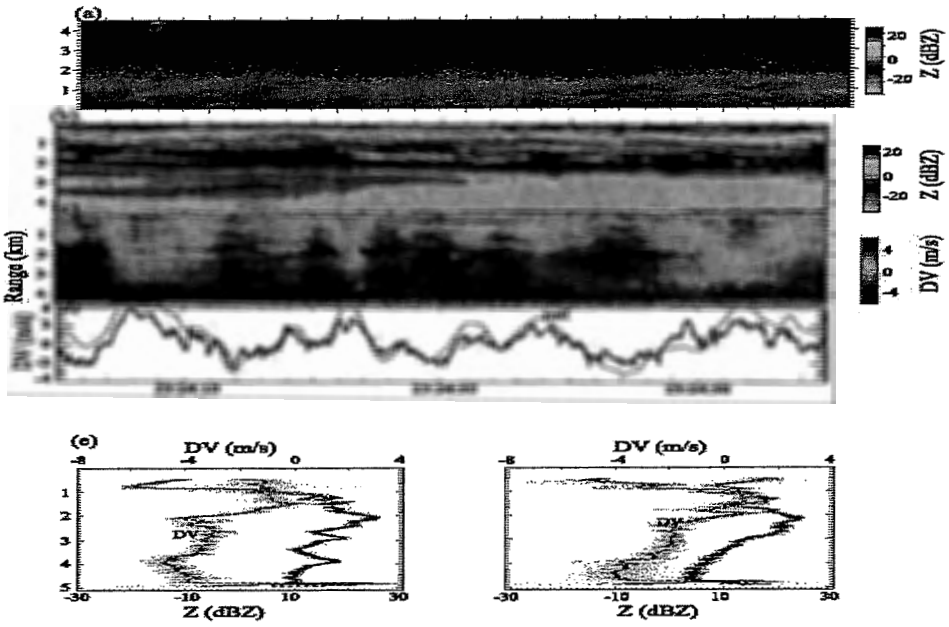

Figure 4. a) Horizontal profile of radar reflectivity (Z), b) vertical profiles of Z, c) Doppler velocity (DV), d) Traces of DV at the nearest useable range gate and aircraft roll angle (same as DV scale) and e) average vertical profile of Z and DV for a segment of the AIRS II flight on November 19, 2003.

surface. This decrease is due to the radar signal being attenuated by the rain, which is one of the limitations of using mm-radar in moist and/or high LWC and rainy conditions.

5. SUMMARY AND FUTURE WORK

This paper presents a limited number of cases of vertical and horizontal structure of clouds obtained using a W-band radar that was installed on the NRC CV580 aircraft for the first time. The cases presented show fine-scale cloud organization and layering that would be difficult to determine just from the in-situ measurements alone and clearly highlight the added value of airborne mm-wave radars in providing detailed cloud structure beyond the aircraft flight level and complementing the in-situ measurements for cloud studies. We will analyze this excellent radar and in-situ data to characterize the spatial variability of icing clouds and will also use the polarimetric dataset to classify cloud particle types and phase of winter clouds sampled during AIRSII.

6. ACKNOWLEDGMENTS

Funding for the W-band radar was provided by the NRC Institute for Aerospace Research New Initiative Fund. The AIRS II project was funded by MSC, NRC, Transport Canada and the Federal Aviation Administration, NASA-Glenn and others. The C-SOLAS flights were funded by the MSC. We are grateful to the NRC Design and Fabrication Service and the Flight Research Laboratory Engineering and instrumentation support personnel for a successful Installation and operation of the WCR on the CV580. We would like to acknowledge the Department of Atmospheric Science of the University of Wyoming for providing the WCR during AIRS II.

7. REFERENCES

Isaac, G.A. S.G. Cober, J.W. Strapp. A.V. Korolev, A. Tremblay, and D.L. Marcotte, 2001: Recent Canadian research on aircraft in-flight icing. Canadian Aeronautics and Space Journal, **47**, 213-221.

Vali, G., R.D. Kelly, J. French, S. Haimov, S. Leon, R.E McIntosh and A. Pazmany, 1998: Finescale structure and microphysics of coastal stratus. J. Atmos. Sci, **55**, 3540-3564.

Wolde, M. and G. Vali, 2001: Polarimetric signature from ice crystals observed at 95 GHz in winter clouds: Part I. Dependence on crystal type. J. Atmos. Sci, **58**, 828-841.

THE MOLECULAR DIFFUSION OF ICE CRYSTALS OF VARIOUS SHAPES

Hyun Youk, Roland List, and Theophilus Ola

Department of Physics, University of Toronto, Toronto, Ontario, M5S 1A7, Canada

1. INTRODUCTION

Two main controlling factors of ice crystal growth are the heat and (gaseous) mass transfers, H&MT, as characterized by the Nusselt number (Nu) for heat and the Sherwood (Sh) number for mass. Nu and Sh express the increase of the molecular diffusions by the relative motions of the particles in air as characterized by the Reynolds number (Re). Traditionally Nu is assumed to be identical to Sh. Past laboratory measurements with various ice crystal shapes by the Toronto Cloud Physics Group involved Sh, thus this study will deal with Sh. The growth of a crystal depends on its size and shape, its fall speed (through Re) and the flux of water vapour from the surrounding air. It is controlled by the diffusion of heat which carries away the energy released on the crystal surface by deposition. Sh is a function of Re and was established by Schemenauer and List (1978)[S&L78] for snow crystals and graupel. Their study, however, did not address the case of pure diffusion (i.e. Re=0). Such values based on approximations have been available in the literature (McDonald, 1963[Mc63], Jayaweera (1971)) only for a very limited number of shapes of crystals. Thus, it was decided to take a general approach to numerically calculate $Sh_{Re=0}$ for any ice crystal with a rectilinear shape. New values of $Sh_{Re=0}$ for additional shapes of crystals are addressed in this study along with the method developed for the computations.

The steady state diffusion is controlled by the Laplace equation. It was solved numerically with Dirichlet boundary conditions on a rectilinear 3 dimensional lattice system with variable lattice separation distances for hexagonal plates, hexagonal cylinders, stellar crystals, capped columns, and broad-branched crystals.

Corresponding author's address: Hyun Youk,
McLennan Physical Laboratories,
Department of Physics, University of Toronto,
Toronto, Ontario, M5S 1A7, Canada;
E-mail: hyun@atmosp.physics.utoronto.ca

2. ELECTROSTATIC ANALOGY

The water vapour density field (ρ) around a stationary ice crystal growing under steady state diffusion obeys the Laplace equation

$$\nabla^2 \rho = 0 \tag{1}$$

The initial growth of an ice crystal by the net deposition of water vapour in steady state diffusion, is controlled by the rate at which vapour diffuses to and from the crystal's surface. The rate at which heat is released by the crystal is exactly the same as the rate at which heat is diffused from the surface. This balance leads to quasi constant value of crystal's surface temperature, and this in turn leads to a constant local vapour density ρ_0 around the crystal. For a perfect capacitor that is geometrically similar to the crystal, the electrostatic potential V in vacuum also obeys the Laplace equation, with the surface electrostatic potential V_0 constant as is the case for perfect capacitors. Identifying V with ρ, the direct analogy between steady state diffusion and electrostatics is established. A capacitor that is geometrically similar to the crystal is then set in a rectangular box, a Faraday cage, sufficiently afar from its edges. The capacitor is then surrounded by the electrostatic potential obeying Laplace equation. The sides of the cage are set at potential zero to simulate "boundaries at infinity". Since the water vapour tapers off to a constant value sufficiently far away from the crystal, imposing this Dirichlet boundary condition preserves the similarity. In this analogy, one uses Gauss' flux law and Fick's law of diffusion to establish that $Sh_{Re=0}$ is given by

$$Sh_{Re=0} = \frac{4\pi CL}{A} \tag{2}$$

where A, L, and C are the surface area, characteristic length, and the crystal's capacitance, respectively. The units are in cgs for ease of comparison with S&L78 and Jayaweera(1971). Thus the problem of diffusion is reduced to finding capacitances of crystals with the Dirichlet boundary conditions mentioned above.

3. FINITE LATTICES AND JACOBI'S METHOD

To compute (2), a numerical scheme for finding the capacitances for crystals of rectilinear shapes was developed. "Rectilinear shapes" are those that can be constructed with a finite number of straight edges.

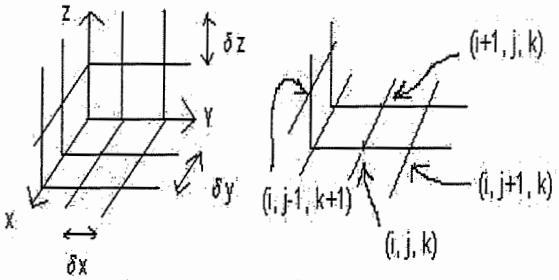

Figure 1: Discrete irregular Cartesian lattice

A Cartesian grid system is established with a finite number of lattice points within the Faraday cage, the outer most points representing the edges of the cage (box). Each side of the box is at least 20 times larger than the respective sides of the crystal. The separation between adjacent lattice points can be different along different axis directions. Each of the lattice points are labelled in terms of positive integer indices (i, j, k); where i, j, and k run along the x-axis, y-axis, and z-axis respectively (Fig. 1). For simplicity, μ is introduced, which can be either x, y, or z. Then $\hat{\mu}$ represents the unit vector along μ-axis. Assuming that the grid points are sufficiently close to one another, the partial derivatives of potential V can be approximated by the following set of finite difference equations

$$\frac{\partial V(i,j,k)}{\partial \mu} \equiv \frac{V((i,j,k)+\hat{\mu}) - V(i,j,k)}{\delta \mu} \tag{3}$$

where

$$A(\mu) \equiv V((i,j,k)+\hat{\mu}) + V((i,j,k)-\hat{\mu}) \tag{4}$$

then the finite difference approximation of 2nd order partial derivatives of V can be written as

$$\frac{\partial^2 V(i,j,k)}{\partial \mu^2} = \frac{A(\mu) - 2V(i,j,k)}{2(\delta\mu)^2} \tag{5}$$

For convenience, following proportionality constants are introduced:

$$\alpha \equiv (\frac{\delta y}{\delta x})^2 \qquad \beta \equiv (\frac{\delta z}{\delta x})^2 \tag{6}$$

Then the Laplace's equation in our discrete rectilinear grid system becomes

$$0 \approx \frac{B(x)}{2(\delta x)^2} + \frac{B(y)}{2\alpha(\delta x)^2} + \frac{B(z)}{2\beta(\delta x)^2} \tag{7}$$

where B(μ)≡ A(μ) - 2V(i,j,k). From (7), one can solve for potential $V(i,j,k)$ at any lattice point (i,j,k) in our Faraday cage. By rearranging the terms in (7), the following is obtained:

$$V(i,j,k) = \frac{\alpha\beta A(x) + \beta A(y) + \alpha A(z)}{2(\alpha\beta + \alpha + \beta)} \tag{8}$$

This is the expression used by the "Jacobi's" iterative scheme for solving Laplace equation. An algorithm is constructed that runs with (8). First, the values of V are assigned to the sides of the Faraday cage and the surface of the crystal, which is sitting in the middle of this Faraday cage. V is then set to zero on all other lattice points, followed by the running of a computational scheme for V(i,j,k) iteratively for each lattice point in the box at each iteration. The computation is started out from the crystal surface, then "branches out towards the edges of the box". This procedure is iterated until convergence by computing the difference $\delta V(i,j,k) = |V_n(i,j,k) - V_{n-1}(i,j,k)|$, where $V_n(i,j,k)$ denotes the value V(i,j,k) at n-th iteration. The scheme is halted when a desired "tolerance bound" is reached. This occurs when following criterion is met

$$\sum_{(i,j,k)} \delta V(i,j,k) < \epsilon \tag{9}$$

where the sum in (9) is carried out for all grid points in the box. It is well known from literatures in computational physics that the number of iterations 'r' required to reduce the error given by the sum (9) by a factor of 10^{-p} is

$$r \sim O(pN^3) \tag{10}$$

where N is the number of grid points in a NxNxN cubic regular Cartesian grid system. At the end of a run of this algorithm, values of all the V's would have been computed for each lattice point up to the desired precision ϵ.

Some comments are in order at this stage. Although no regular Cartesian grid system is used for many of the crystal models studied here, the order of convergence will be the same as (10). There are other computational methods to solve Laplace's equation numerically, such as Gauss-Seidel and the "simultaneous over-relaxation" (SOR) methods. The SOR method has a convergence rate of $O(N^2)$ for 3 dimensional Cartesian grid system. The classical Jacobi method, however, is one of the simplest algorithms that can be used for our study and is relatively free of the complications in implementation compared to the SOR method. It was thus selected for this study.

4. EXAMPLE: HEXAGONAL PLATE

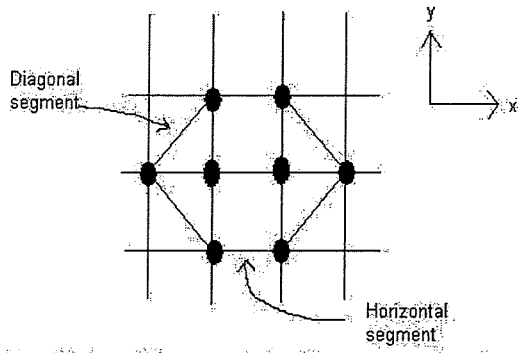

Figure 2: A possible representation of hexagon on a discrete lattice. Note that all the vertices of the hexagon lie on grid points with α=3. Also, note that "diagonal segments" and "horizontal segments" cannot be represented in our algorithm (they're drawn here for visual aid). Only the dots on lattice points can be "seen" in our algorithm, and are the only means to represent any geometric shape.

The hexagonal plate was modelled using a non-regular rectangular grid system, with the proportionality factors α and β not being equal. Only a finite number of grid points is available for "drawing" a hexagon to encapsulate the important features of the crystal, namely its vertices. Not all the vertices of the hexagon lie on lattice points if a regular ($\alpha = \beta$) Cartesian grid system is used. Hence a regular Cartesian coordinate system is not used for an optimal design of the crystal on our finite grid. α=3 allows for construction of a hexagon in which all its vertices lie on grid points. β can be chosen to be any positive value since the plate is assumed to be thinner than the lattice separation along the z-axis. Thus β=1 was selected, meaning that our plate lies on a single xy-planar layer of lattice points, in the middle of the box. This "optimal" representation of the hexagonal plate results in the relationship: $N_d = \frac{N_x}{2}$ where N_d and N_x represent the number of points used to represent a diagonal segment, and horizontal segment respectively. In a similar manner, "optimal" representation was achieved for other crystal shapes as investigated experimentally by S&L78 in a "liquid tunnel" (Schuepp and List, 1969).

5. DISCRETE VERSION OF GAUSS' FLUX LAW AND SCALING RULES

A simple method of numerically computing Sh_0 using the potential V for lattice points around the crystal involves computation of the capacitance C. This is done by applying Gauss' law to compute the "surface charge" of the crystal, via C=$\frac{Q}{V_0}$, where V_0 is the surface potential assigned to the crystal at the onset of Jacobi's method mentioned previously. The total electric flux of the crystal is obtained by first enclosing the crystal in a "rectangular cage". The sides of this cage are just one lattice point away from the closest side of the crystal. Each side of this enclosure consists of its grid elements, which are called "area element grids". These grids have the same respective lattice spacing as the grid for the Faraday box.

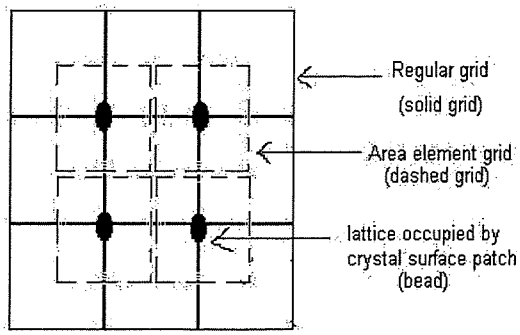

Figure 3: The area element grids are defined by the same α and β as the regular grid. An area element (dashed rectangle) is placed one lattice point away from a "bead". Flux through this area element due to this single bead is computed. This is done for all the "beads", and the net flux is computed by summing over all these individual fluxes.

Each of the "area element" is associated with a set of integers *I*. Then the discrete approximation of Gauss' flux law can be written as

$$\oint_S \vec{E} \cdot dA \approx \sum_I -\frac{\partial V(i,j,k)}{\delta\mu} \cdot A_i \qquad (11)$$

which is just a sum of flux through each of the area elements. Note that in (11), the fact that on the surface of a perfect conductor, the electric field is always perpendicular to its surface, was utilized. The flux through an area element whose outward unit normal is in $\pm\hat{\mu}$ direction is approximated discretely by

$$F_{\pm\mu} = -\frac{V((i,j,k) \pm \hat{\mu}) - V(i,j,k)}{\delta\mu}(\delta\nu)(\delta\gamma) \qquad (12)$$

where ν and γ are the other two coordinates not equal to μ. The main reason for placing our rectangular prism enclosure at most one lattice point away from sides of the crystal is that such a construction allows dealing only with $\frac{\partial V}{\partial \mu}$ rather than with the more complicated ∇V, when computing the flux. It is worth discussing the consequence of (12) for a specific direction μ. For the flux through a face with its unit normal in $\pm\hat{z}$ direction, the flux through this area element (12) reduces to

$$F_{\pm z} = \delta x \frac{\alpha}{\beta}[-V(i,j,k \pm 1) + V(i,j,k)] \qquad (13)$$

The main feature of (13) is that the only unknown value is δx. The flux through a face in any of the other directions reduce to expressions of the form (13). In all of these expressions, the only term with unknown value and dimension is δx. For solving (8), it is not necessary to know the physical value of δx since all the quantities, except for V, are in dimensionless form as proportionality constants α and β. Thus, the numerical evaluation of potential V does not depend on the choice of length unit; V can be in whatever unit one desires. But (13) draws attention to the actual physical value that δx represents in the grid system. But note that $Q \sim \delta x$, and so $C \sim \delta x$. Thus, when computing Sh via (2), it is seen that $Sh \sim \frac{(\delta x)^2}{(\delta x)^2} = 1$. In other words, although δx is unknown throughout our calculations, all δx's cancel out at the end because similarity numbers are involved in our modelling. Only the relative proportions of shapes and boundary conditions are of importance. The actual physical length scales are irrelevant in computation of dimensionless numbers, Sh and Nu, and this is well demonstrated in our model.

The total electric flux through the rectangular prism enclosure is calculated by summing the flux (12) through each of its area elements. From the net flux, the "surface charge" of crystal is computed, and thus its capacitance. The Sherwood number Sh at Re=0 is computed using (2), with δx carried throughout all these calculations but cancelling out at this last stage.

6. RESULTS AND DISCUSSION

The Sherwood number (Sh) for crystal shapes of interest in a cloud physics environment have been computed for zero convection (Re=0) using the methods outlined above. The results are listed in Table 1.

Crystal Shape	Approximate Sh	Numerical Sh	Difference
HP	2.74	2.84	+3.64%
HC	2.48	2.36	-4.83%
BB	4.02	3.88	-3.48%
SC	5.50	5.70	-3.51%
CC	N/A	5.67	N/A

Table 1: Present numerical calculations of dimensionless mass transfers (Sherwood numbers) of hexagonal plates HP, hexagonal columns HC, broad branched dendrites BB, stellar crystals SC, and capped columns CC; comparisons with previous values of Sh approximated by Mc63("Approximate Sh") and extrapolations by S&L78, with differences.

The "approximate capacitances" which lead to the corresponding approximate Sh were given by Mc63. Using the analytical calculations of capacitances of spheres and thin circular disks of radius r to approximate the capacitances, Mc63, S&L78, and Jayaweera have given expressions for capacitance for the shapes listed in Table 1 (with the exception of CC).

Crystal	Approximate capacitance	Dimensions used
HP	0.567r	r=8(δx)
HC	$\frac{a}{ln(\frac{2a}{b})}$	a=12.5(δx) b=8(δx)
BB	0.554r	r=24(δx)
SC	0.439r	r=6(δx)

Table 2.: Approximate crystal capacitances (Mc63, S&L78) [cgs units] and dimensions used for the calculations in Table 1. Note that no analytical or approximate expression of the capacitance of CC were given in either Mc63 or S&L78.

In summary, the numerical methods developed and applied here provide convincing values of the molecular diffusion of water vapour to ice crystals of various shapes when compared with the values obtained by approximations and extrapolations (Mc63). It is also of interest to see that the Sherwood number for capped columns is not much different from the value for columns and that the ordering of the values for Re=0 is consistent with the measurements of S&L78 at higher Reynolds numbers.

ACKNOWLEDGEMENTS

The authors wish to thank the Natural Sciences and Engineering Research Council (NSERC) of Canada for its support.

REFERENCES

K.O.L.F. Jayaweera, 1971: Calculations of ice crystal growth. J. Atmos. Sci. **28**, 728-736.

J.E. McDonald, 1963: Use of electrostatic analogy in studies of ice crystal growth. Z. angew. Math. Phys., **14**, 610-620.

P.H. Schuepp and R. List, "Mass transfer of rough hailstone models in flows of various turbulence levels", J. Appl. Meteor., **8**, No. 2, 254-263, 1969.

R.S. Schemenauer and R. List, "Measurements of the convective mass transfer of planar and columnar ice crystals", Borovikov Memorial Issue, Academy of Sciences of the USSR, Leningrad, 217-232, 1978.

SIMULATION AND OBSERVATION ON SUPERCOOLED LIQUID WATER AND ICE CRYSTALS OF PRECIPITATING STRATIFORM CLOUDS IN HENAN PROVINCE

Shi Yueqin[1,2] Liu Qijun[2] Liu Weiguo[2]

[1] School of Physics, Peking University, Beijing, 100871, China
[2] Chinese Academy of Meteorological Sciences, Beijing, 100081, China

1 INTRODUCTION

Stable stratiform precipitation of large region is the main precipitation in spring and autumn in Henan Province, and also the main operation object of weather modification. There are many studies about the synoptic situation, macroscale changes and the characteristics of Radar echoes of the regional stratiform precipitation. However there are few numerical simulation studies on the microphysical processes accompanied with the precipitation. Except the dynamic frame of mesoscale model and initiation data, cloud precipitation scheme is the key factor on whether the cloud microphysical processes and cloud parameters are rational. In the paper, using CAMS simple mixed-phase cloud scheme coupled in MM5v3.5 and Reisner cloud scheme, precipitation case on Oct. 19, 2002 and snowfall case on Dec. 22, 2002 of stratiform clouds in Henan Province were simulated. Supercooled cloud water and ice crystals were mainly studied. And compared with the cloud microphysical data acquired with microwave radiometer and Particle Measurement System (PMS) to indicate the simulation ability of models about the precipitation processes and main cloud parameters, and indicate the regional cloud resources condition of artificial rainfall enhancement.

[1] Corresponding author's address: Chinese Academy of Meteorological Sciences, 46 Zhongguancun South Street, Haidian District, Beijing, 100081, China; E-mail: shiyq@cams.cma.gov.cn

2 INTRODUCTION OF MODEL

In the paper, using mesoscale model MM5v3.5 (Penn State /NCAR), the large domain scale was 30 Km, vertical layers were 26, and time-step was 60 sec. In the wet physical process convective parameterization and explicit cloud scheme were simultaneously used. Sub-grid scale precipitation used Betts-Miller convective parameterization, and grid scale precipitation used CAMS simple mixed-phase cloud scheme or Reisner cloud scheme. Initiation data used T213 prediction data revised by radiosonde data.

Based on the scheme (Hu, 1998), in CAMS simple mixed-phase cloud scheme, fall speed and their collision process of ice particles were revised, and added the frozen process of supercooled cloud water (Liu, 2001). In the scheme, Qv was still mass content of vapor, the prognostic variables of hydrometers were Qc and Qp. In the warmer region (T>0°C) Qc was the mass content of cloud water, and Qp was raindrops; otherwise, in the colder region (T≤0°C) Qc was supercooled cloud water, and Qp was ice or snow crystals. In the scheme, seven microphysical processes were considered. In MM5 Reisner scheme (1998), water vapor, mass content of cloud water, raindrops, ice crystals, snow and graupels were the prognostic variables, and the number concentration of ice crystals was also being predicted. In the scheme 35 microphysical processes were considered.

3 RESULTS OF SIMULATION

3.1 Precipitation case of Oct. 19, 2002

3.1.1 Synoptic Situation

Influenced by upper trough, shear line and surface cold air, there began to precipitate at night on Oct. 18 from west to east in Henan Province, and lasted to the morning on Oct. 20. The max rainfall reached 20 mm, appeared in the west region of Henan Province, and the precipitation in the east region were smaller.

3.1.2 Simulation of rainfall

The simulation began at 0800 Oct. 18, 2002(LST), lasted 36 hours, and ended on 2000 Oct.19. The simulations of the two schemes appeared max rainfall region in the west region of Henan Province, which were bigger than 20 mm, and agreed well with the observation. From the observation, there was a heavy rainfall bigger than 60 mm in the south region of Sichuan basin, and the two schemes also simulated the heavy rainfall region bigger than 60 mm, only the region slightly south to the observation, which showed that the two schemes could simulate cold front precipitation. Because of no data over the sea, the rainfall simulated over the sea cannot be verified.

3.1.3 Simulation of supercooled cloud water and ice crystals

Fig. 1 was west-east cross section of cloud water and number concentration of ice crystals along 34°N, the dash lines were 0°C and -10°C. From the simulation of CAMS scheme, between 0°C and -10°C, mass content of supercooled cloud water was between 0.01 g kg^{-1} and 0.2gkg^{-1}, the maximum was 0.2 g kg^{-1}, and spatial range was thicker and deeper. The region of colder than -10°C, supercooled cloud water content was almost between 0.01 g kg^{-1} and 0.1 g kg^{-1}, and at the top of model there were a little supercooled cloud water. From the simulation of Reisner scheme, between 0°C and -10°C, content of supercooled cloud water was between 0.01 g kg^{-1} and 0.1 g kg^{-1}, and colder than -10°C, there were no supercooled cloud water. In general, supersooled cloud water content simulated by Reisner scheme was less than that simulated by CAMS scheme, and especially over the region colder than -10°C, the simulation content by Reisner scheme was slightly lower. Between 0°C and -10°C, the number concentration of ice crystals was about 10~100 m^{-3}, and colder than -10°C, the number concentration of ice crystals was more than 10^3 m^{-3}. However, in the precipitation stratiform cloud the number concentration of ice crystals was observed about 10^3~10^4 m^{-3} (Hu, 2001).

From the observation of Integrated Cloud Water (ICW) with microwave radiometer at Xinxiang City, its maximum was about 1.4 mm, most ICW was among 0.4 ~0.8 mm, and fluctuated with time. From the simulation of CAMS scheme, its maximum was about 1.3 mm, most ICW was between 0.4~0.8 mm, and also fluctuated with time and decreased with the development of precipitation. The simulation was better agreement with the observation. From the simulation of Reisner scheme, its maximum was about 0.6 mm, developed with the precipitation, and the simulation was less than the observation. Thus, the simulation by CAMS scheme took advantage over Reisner scheme on ICW.

3.2 Snowfall case of 22 Dec. 2002

3.2.1 Simulation of snowfall

The simulation began at 0800 Dec.21, 2002(LST), lasted 36 hours, and ended at 2000 Dec. 22. From the observation, snowfall was slightly heavy in the east region in Henan Province, was greater than 10 mm, and its maximum was 13 mm. However, snowfall was lower than 10 mm in the southwest region in Henan

Province, mainly about 3~5 mm, and there were no snowfall in the northeast region. CAMS scheme can simulate the snowfall, its maximum was bigger than 10 mm, and the snowfall region well agreed with the observation. However, the snowfall in the southeast was slightly simulated. The max snowfall simulated by Reisner scheme was about 13 mm, located in the southwest of Henan Province, and the snowfall in southeast cannot be simulated. In general, the region and intensity of snowfall simulated by Reisner scheme were greater than those simulated by CAMS scheme. But the total snowfall region was similar, the snowfall was almost equal, and was better agreement with the observation, which showed that CAMS scheme and Reisner scheme can simulate the stratiform snowfall.

3.2.2 Simulations of supercooled water and ice crystals

The supercooled cloud water simulated by CAMS scheme was almost between 0.01 and 0.1 g kg^{-1}, the region was bigger and deeper, and near 600 hPa there was a little region where cloud water was about 0.2gkg^{-1}. From the results of Reisner scheme, between 0°C and -10°C, only a little region appeared supercooled cloud water, about 0.01 g kg^{-1}, and the simulation was smaller than that of CAMS scheme. There were no ice crystals in the region which temperature was between 0°C and -10°C, colder than -10°C, the number concentration of ice crystals was greater 100 m^{-3}, which is smaller than the observation. From the simulation of Reisner scheme, between -3°C and -8°C where is the ice crystals multiplication region, because of little supercooled cloud water, the ice-phased precipitating particles were mainly snowflakes, and no graupels. Thus showed that the process of ice crystals multiplication was not manifest, and the number concentration of ice crystals was smaller.

In summary, though Reisner scheme finely classified ice-phased particles, over warmer than -20°C region there were only snowflakes. Ice-phased mass content simulated by CAMS scheme was nearly equal to that simulated by Reisner scheme. Thus, though the physical processes and categories of water substance in simple mixed-phase cloud scheme were simple, which can show some basic microphysical situation of cloud.

Fig. 2a and 2b were the mass content of cloud water and the number concentration of ice crystals in the middle of cloud (3900 m, -10°C) obtained by airborne-PMS on Dec. 22. From the observation, the mass content of cloud water was about between 0.02gm^{-3} and 0.08 g m^{-3}, and its average value was about 0.06 g m^{-3}. The number concentration of ice crystals fluctuated between 2000 and 2600 m^{-3}. The mass content of cloud water simulated by CAMS scheme at the height was about 0.02 g kg^{-1}. Reisner scheme did not simulate supercooled cloud water, and the number concentration of ice crystals was about 100 m^{-3}, which showed that Reisner scheme did not well simulate the number concentration, which was the common aspect of most cloud models. Fig. 2c and 2d were the mass content of cloud water and the number concentration of ice crystals at the top of cloud (6900m, -24°C) obtained by airborne-PMS on Dec. 22. From the observation, the mass content of cloud water was smaller than 0.02 g m^{-3}, its average value was 0.01gm^{-3}, and the number concentration of ice crystals was about 30 ~ 80 m^{-3}. The mass content of cloud water simulated by CAMS scheme was about 0.07gkg^{-1}. Reisner scheme did not simulate cloud water at the height, and the number concentration of ice crystals was about 10^5 m^{-3}.

4 SUMMARY

The simulations on the rainfall and snowfall of stratiform cloud in Henan Province showed that CAMS scheme and Reisner scheme can well simulate the stratiform precipitation, and the simulation were better agreement with the observation. Integrated cloud

water simulated by CAMS scheme were better agreement with the observation than that simulated by Reisner scheme.

The simulations on supercooled cloud water and ice crystals of stratiform cloud showed that using MM5 can simulate microphysical structure of cloud, and using MM5 can analyze cloud structure and guide artificial rainfall enhancement experiment.

From the simulations on the typical autumn precipitation and winter snowfall cases, in the autumn precipitating stratiform the supercooled cloud water was slightly abundant and the number concentration of ice crystals was lower. In the winter stratiform the supercooled cloud water was short and the number concentration of ice crystals was higher. And the potential of rainfall enhancement on the autumn stratiform was greater than that of the winter stratiform.

5 REFERENCE

Omitted.

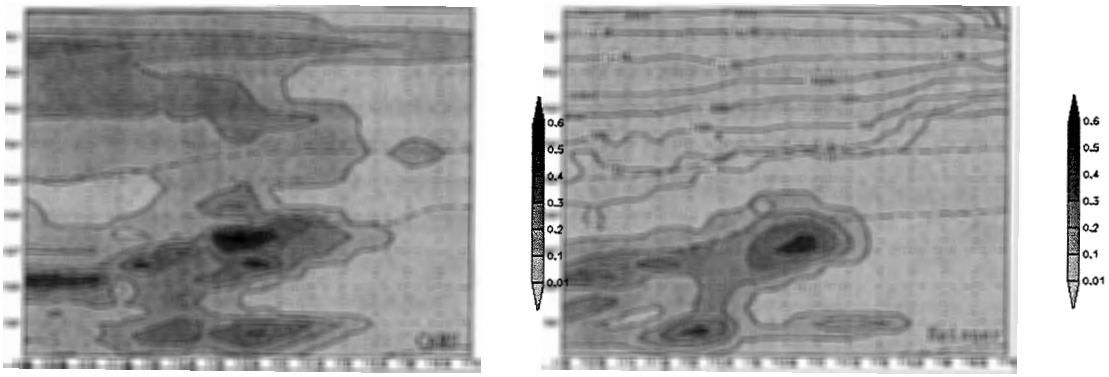

Fig. 1. West-east cross section of cloud water and number concentration of ice crystals along 34°N, the dash lines are 0°C and -10°C. (Units: g kg^{-1}, 1 m^{-3})

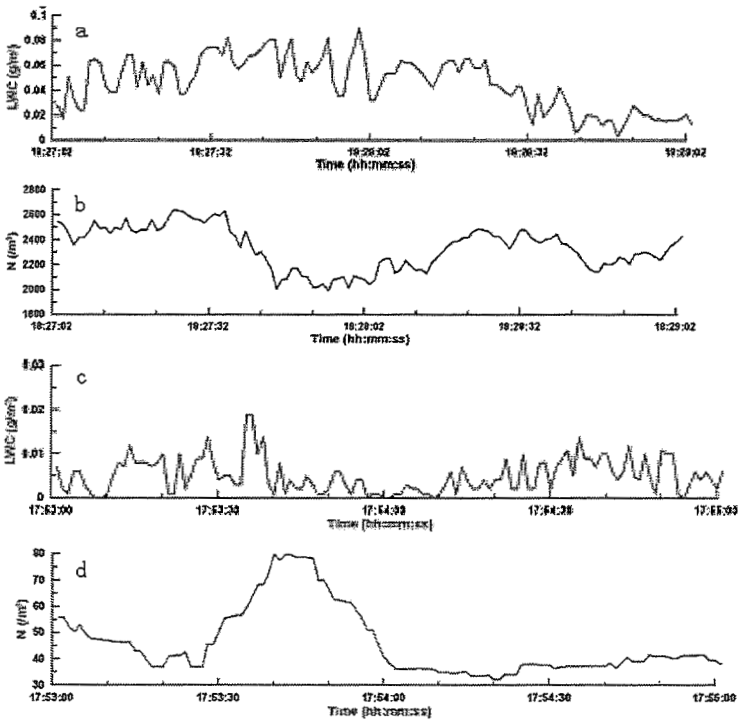

Fig. 2. The mass content of cloud water (g m^{-3}) and the number concentration of ice crystals (1 m^{-3}) obtained by airborne-PMS on Dec. 22, 2002.

THE STUDY OF HAIL IDENTIFICATION CRITERIA

Sun Yuwen[1], Duan Ying[1], Wu Zhihui[1] and Zhi Hai[2]

[1] Weather Modification Office of Hebei Province, Shijiazhuang, Hebei, 050021, P.R.China
[2]Ba Meng Meteorological Bureau of Inner Mongolia, Linhe, Inner Mongolia, 015000, P.R.China

1. INTRODUCTION

Hail is one of the main disasters in Zhangjiakou area. There are averaged 43 hail days in every year, hail caused great losses on agricultural production. For example, on 4 July 1987, hail occurred in four counties in the area and about 130 km^2 area crops were damaged. Hail is formed by strong convective weather system, with short time and difficultly predictable area of hailfall. In order to predict hail and suppress hail, the weather methods and radar (wavelength=3cm) are used in hail study. According to statistical data, from April to September, the hail days account for 94% in every year. In this paper, the weather characteristics and radar echoes of hail cloud from April to September in 1987 are analyzed.

2. RADAR ECHO OF HAIL CLOUD

2.1 Data

Hail cloud belongs to mesoscale or microscale system, and its horizontal scale is about a few to hundreds of kilometers (Jean 1960; Huang et al. 1980). In this study, because a hail cloud usually affected less area, if hail didn't fall down to the meteorological station, there would cause error in statistical results. So the rules for selecting hail cloud is (1) If hail fell to a meteorological station, the cloud echo over the station was used; when there was no strong echo over the station, the neighboring cloud strong echo was selected as hail echo according to its moving direction and velocity. Generally, the hail cloud moved from the northwest to the southeast, thus most of the clouds from northwest of meteorological station were selected. (2) If there were multiple strong echo centers occurred at different time over a hailfall point, the convective cloud echo suitable for hailfall was selected. (3) When there existed multiple strong echo centers simultaneously around the meteorological station, the hail cloud echo was selected according to the hail pad records around the station. Based on these rules, 56 hail echo samples were selected for this study.

Corresponding author's address: Sun Yuwen, Weather Modification Office of Hebei Province, Shijiazhuang, Hebei, 050021, P.R.China; E-Mail: syw0000000@sina.com.

2.2 Hail identification criteria

2.2.1 Echo top height

Table 1 gives the statistical results of echo top height H. 50 samples (89%) show that the echo top height is more than 11 km. Thus echo top height more than 11 km is chosen as one of the hail identification criteria.

2.2.2 Strong echo top height

Although some convective clouds have much more depth and height, hail doesn't occur. One of the reasons is that there is weak updraft in the upper level of the cloud. The height of strong echo top is important to the occurrence of hail. The 20 dB attenuation height of radar in echo intensity, H_{max}, is used in the analysis.

Table 1 Echo top height H of hail cloud

H (km)	H<10	10≤H<11	11≤H<12	12≤H<13	13≤H<14	14≤H<15	H≥15	Total
Case	2	4	13	17	14	4	2	56
Percent	4%	7%	23%	30%	25%	7%	4%	100%

Table 2 Strong echo top height H_{max} of hail cloud

H_{max} (km)	H_{max}<8	8≤H_{max}<9	9≤H_{max}<10	10≤H_{max}<11	11≤H_{max}<12	12≤H_{max}<13	13≤H_{max}<14	14≤H_{max}	Total
Case	1	7	9	8	11	6	4	3	49
Percent	2%	14.3%	18.4%	16.3%	22.5%	12.2%	8.2%	6.1%	100%

According to the statistics (table 2), 84% of samples have the strong echo top height of more than 9km. 9 km is a criterion for identifying hail.

2.2.3 Equivalent reflectivity factor

Equivalent reflectivity factor Z_e is an important factor in hail study. $Z_e=CR^2\times10^{N/10}$, where $C=4.1\times0^{-27}m$, R is the distance between radar site and hail cloud, N is the attenuation decibels. If Z_e is expressed in decibels, 87% hail clouds have the value of more than 35 dBz. The result is given in table 3. Thus 35dBz is also as a criterion.

2.2.4 Cloud depth

Table 3 Equivalent reflectivity factor Z_e

ΔH (km)	ΔH<9	9≤ΔH<10	10≤ΔH<11	11≤ΔH<12	12≤ΔH<13	13≤ΔH<14	ΔH≤14	Total
Case	2	4	8	10	17	11	4	56
Percent	4%	7%	14%	18%	30%	19%	7%	100%

Table 4 Cloud depth ΔH

Z_e (dBz)	$10< Z_e <30$	$30\leq Z_e <35$	$35\leq Z_e <40$	$40\leq Z_e <50$	$Z_e \geq 50$	Total
Case	1	6	15	30	4	56
Percent	2%	11%	27%	53%	7%	100%

From table 4, statistics show that 89% of cloud depth is more than 10 km. This is the other criterion.

2.2.5 Test

According to above 4 criteria, among 56 samples, 42 passed. Another 113 echoes from 1986 to 1988 were used to test. Of 59 echoes passed hail criteria, 42 were hail cloud, 17 occurred thunder shower or heavy rain (see table 5).

Table 5 Test for echo criteria

	Haillfall	Precipitation	Total
Case	42	17	59
Percent	71%	29%	100%

3. WEATHER SYSTEM

In order to improve the accuracy of hail prediction, synoptic situation is important to form hail. In Zhangjiakou area, there are 3 weather systems that easily form hails (1) Mongolian cold vortex, (2) Mongolian cold trough, and (3) Northwestern airflow. There are 20 hail weather systems during June-August 1987. Of 20 systems, 6 belong to Mongolian cold vortex, 5 belong to Mongolian cold trough, and 4 belong to Northwestern airflow.

4. CONCLUSION

Radar echo associated weather analysis could identify hail better. However, much more research should be done in the future.

5. ACKONWLEDGEMENTS

The authors express many thanks to Zhangjiakou Meteorological Bureau for providing radar data.

6. REFERENCES

Huang Meiyuan and Wang Angsheng, 1980:The outline on Hail Suppression. Science Press, Beijing.

Jean Dessens, 1960: Hail in Southwestern France I: Hailfall characteristics and Hailstorm Environment. J. Clima. Appl. Meteoro., 25(1).

CLOUD MICROSTRUCTURE DETECTION AND ANALYSIS IN BEIJING AND ITS NEIGHBORING AREA

Qiang Zhang, Hongyu Li and Lei Zhang

Beijing Weather Modification Office, Beijing, 100089, China

1. INTRODUCTION

Since traditional water sources and supplies of ground water and reservoirs in Beijing region are either inadequate or under threat from ever-increasing demands from growing populations, to alleviate water resources deficiency in such area are very urged. Cloud seeding by influencing and modifying cloud microstructure in regional precipitable cloud systems has become widely used as a potential way to enhance precipitation and consequently help to mitigate the dwindling water resources.

Based on advantageous synoptic situation for precipitation enhancement, detection of cloud microstructure in natural clouds by using airborne PMS (You 1994, Ma 2002, Liu et al. 2003) over the two crucial freshwater feeding reservoirs in Beijing (i.e. Miyun reservoir and Guanting reservoir), has been conducted. In this paper, the distribution of liquid water content and cloud particles spectrum detected within a humilis cumulus that occurred on August 28 2003 and another extensive stratus which occurred on September 4 2003 are presented respectively to display some features of cloud microstructure over Beijing and its neighboring area. It is to some extent hoped to provide some scientific basis for regional water resources amount evaluation and rainfall enhancement techniques as well as the evaluation of seeding effects.

2. OBJECTS

In the dusk of August 28 2003, the aircraft penetrated horizontally into a weak cumulus twice over Yanqing area, northwest of Beijing City. The cloud top is observed near 4.0km. The first in-cloud and out-cloud times are recorded about at 16:55:55 (Beijing time, and the same below) and 16:56:12 respectively. The flight is between 3557 and 3595 meters. The temperature along the penetration height is observed between minus 2.1 and minus 3.7 centigrade. The horizontal width of the small cumulus is only 2.0km. The second in–cloud and out-cloud times is recorded at 16:59:17 and 16:59:39 respectively with a lower penetration height between 3411 and 3435 meters. The temperature along this flight is between minus 0.7 and minus 2.4 centigrade. The penetration distance spans about 4.0km wide.

A wide-range stable precipitation fell throughout Beijing area on September 4 2003, and the area is seen to be full covered by radar echoes with an intensity 20 to 30 dBZ. After 9 am, the detecting aircraft took off and soon flied into the stratus part over Yanqing area. Observation showed that the stratus top is about 7500 meters high and its cloud base is below 1000 meters. First, the aircraft penetrated and detected horizontally near 4800 meters, then it continued to climb and detect aslant until to the cloud top. At the top of the stratus a horizontal detection was conducted too.

3. CLOUD MICROSTRUTURE

3.1 Liquid water content

Liquid water content (LWC) interior the weak cumulus differs distinctly from that exterior. Generally it is always detected less than 0.05 g/m^3 exterior, while it jumps from 0.5 to 2.0 g/m^3 interior (see Fig.1). With the flight descending the

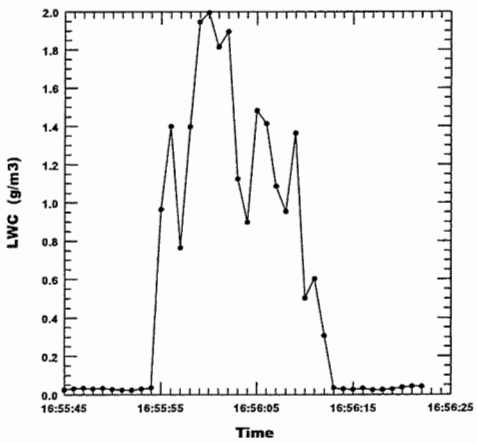

FIG.1. Liquid water content between 3557 and 3595 meters in the cumulus

Corresponding author's address: Qiang Zhang, Beijing Weather Modification Office, No.44, Zizhuyuan Road, Haidian District, China; E-Mail: BJRYB_zq@sina.com.

liquid water content exterior the cloud increases a little and that interior decreases. The undulation of liquid water content interior the cumulus also indicates very asymmetry microstructure the cumulus has.

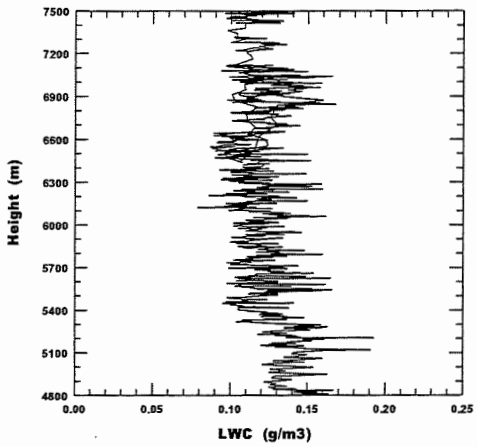

FIG.2. Liquid water content within the stratus

Within the stratus (see Fig.2), the liquid water content is about 0.1 g/m^3 and not more than 0.2 g/m^3. It tends to decrease with the increasing elevation. The asymmetry microstructure can also be seen within the stratus.

3.2 PCASP probing

The probe mainly detects aerosols with size between 0.1 and 3.0 microns. Detection shows that aerosol size interior the small cumulus is much larger than that exterior. The mean diameter of aerosols interior is between 0.4 and 1.0 microns, while it is less than 0.4 microns exterior the cumulus. With the height descending the mean diameter of aerosols exterior increases, but that interior decreases.

Distribution of aerosols size with elevation within the stratus displays a broader spectrum width. Aerosols in different size are found on top of the stratus. The mean diameter of aerosols mostly centers in a range between 0.1 and 0.2 microns and another range between 1.5 and 2.75 microns there. At the level between 3700 and 5500 meters, the mean diameter of aerosols mainly centers in 0.1 or 0.2 microns. At those levels below 4000 meters the aerosols also has a larger spectrum width. Aerosols with mean diameter between 0.1 and 2.75 microns are often detected.

3.3 FSSP-100 probing

Cloud droplets with diameters between 2 and 47 microns can exactly be detected by using this probe. Within the small cumulus, the mean diameter of cloud droplets is in size between 5 and 30 microns. Interior the small cumulus, the mean diameter of cloud droplets centers between 10 and 30 microns, while it is less than 10 microns exterior.

In the stratus, size distribution of cloud droplets diameter in the high level shows it is mainly in the range between 5 and 20 microns and just centers between 5 and 10 microns. Cloud droplets detected at levels below 5300 meters is much smaller. Entirely they center in 3.5 microns.

3.4 2D-C probing

The probe mainly detects those larger particles with size between 17.75 and 1562.5 microns. They may come from cloud droplets, raindrops, or other ice particles. Within the small cumulus, some cloud droplets with a mean diameter between 30 and 60 microns are detected. Its number concentration is about 1.0×10^6 per cube and its spectrum width enlarges with the height descending.

At the level near the stratus top, the mean diameter of large particles is seen between 200 and 400 microns. Their number concentration is between 10^1 and 10^2 per litre. The horizontal penetration along the level between 4770 and 4780 meters within the stratus shows most of the large particles are in mean diameter between 30 and 300 microns. The number concentration of particles with a mean diameter near 100 microns is between 1.0×10^6 and 3.0×10^6 per litre. The number concentration of those particles with a mean diameter larger than 200 microns is between 10^1 and 10^2 per litre.

3.5 Particle imaging

Particle imaging from 2D-C probe within the stratus displays that there are so many supercooled cloud droplets with a mean diameter about 30 microns at the level of minus 6.0 centigrade (see Fig.3 and Fig.4). Its number concentration is near 470 per litre. There are many small ice crystals with a mean diameter near 55 microns and the number concentration about 30 per litre. Also, some larger ice crystals, supercooled raindrops and snowflakes with a mean diameter between 100 and 300 microns are detected at the same level. Their number concentration is only 5 per litre.

At the level of minus 8.0 centigrade, many supercooled cloud droplets with a mean diameter near 30 microns and a number concentration about 280 per litre are seen. There are more than 50 ice crystals with a mean diameter near 55 microns. Large snowflakes are also displayed.

Supercooled cloud droplets with a mean diameter near 30 microns and a high number

concentration of 462 per litre are detected at the level of minus 12 centigrade. The number concentration of those Ice crystals in 55 microns is about 40 per litre. At this level, large supercooled raindrops, ice crystals or snowflakes with a maximum mean diameter 500 microns are not more than 3 per litre.

Near the stratus top (about minus 20.0 centi-grade), there are 2 per litre of supercooled raindrops or ice crystals with a mean diameter 129 microns. Some large snowflakes with a maximum diameter 800 microns are remarkably identified. But there are only 2 or 3 per litre.

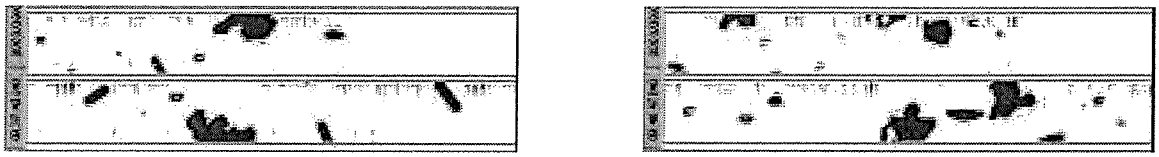

(a) –6.0 ℃ (b) –12.0 ℃

FIG.3. Particle imaging at (a) –6.0℃ and (b) –12.0℃ within the stratus

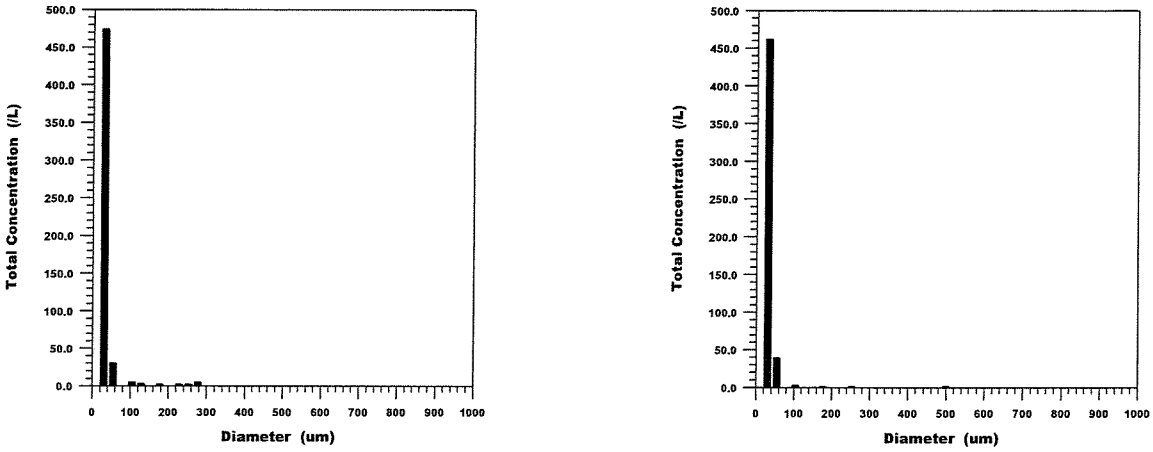

(a) –6.0 ℃ (b) –12.0 ℃

FIG.4. Particles spectrum at (a) –6.0℃ and (b) –12.0℃ within the stratus

4. CONCLUSION

Horizontal detection at two levels within a weak cumulus displays quite difference of the distribution of liquid water content and the spectrum of diversified particles such as aerosols, cloud droplets, raindrops and other ice particles. Microstructure interior the small cumulus differs distinctly from that exterior. Also, asymmetry and aforesaid difference at varied heights or temperature levels are found within the thick stratus.

At the middle-level of the stratus, the number concentration of ice crystals in a mean diameter smaller than 100 microns are between 30 and 50 per litre. It gets higher than what was detected before (Li et al. 2002) in several north areas of China. The number concentration of those larger ice particles with a mean diameter between 100 and 300 microns is less than 5 per litre.

REFERRENCE

Li D. S., et al., 2002: The Current Status and Prospect of Weather Modification. China Meteorological Press.

Liu W. G., Su Z. J., and Wang G. H., 2003: The new generation of airborne PMS and its application. Chinese J.Appl.Meteor.Sci. **14**(Supl.), 11-18.

Ma P. M., 2002: Detection of clouds and precipitation physics. The Current Status and Prospect of Weather Modification (China Meteorological Press), 207-222.

You L. G., 1994: Study on cloud microphysical process and rainfall enhancement qualification using PMS. Research on clouds and precipitation physics and rainfall enhancement techniques (China Meteorological Press), 236–249.

WIND TUNNEL MEASUREMENTS OF DRAG COFFICIENTS OF SPHERICAL AND SPHEROIDAL HAILSTONES

Guoguang ZHENG[1] Roland LIST[2]

[1] Chinese Academy of Meteorological Sciences, Beijing, CHINA 100081
[2] Department of Physics, University of Toronto, Toronto, Ontario, CANADA M5S 1A7

1. INTRODUCTION

Knowledge of drag coefficients of hailstones is necessary to understand their formation, aerodynamic behavior and hence, damage potential. The value of the drag coefficient of a hailstone has been a subject of controversy, since it depends on shape, surface roughness and Reynolds number. List (1959) measured the drag coefficients of real hailstones suspended in a horizontal wind tunnel. He obtained drag coefficients of 0.6 and 0.7 for spherical and oblate spheroidal hailstones, respectively. Subsequently, a number of experiments (Macklin *et al.*1961, Willis *et al.* 1964, Young *et al.* 1967, Matson *et al.* 1980, Knight *et al.* 1983) have been performed to determine drag coefficients of hailstones in a range of 0.24-0.90. Obviously, the experimental results of different authors show significant deviations from one another. However, the existing theories and numerical modeling of hailstone growth have been based on the drag coefficient of smooth spheres, C_D=0.45±0.03, given by Goldstein (1938).

Measurements on natural hailstones suggest *Re* in the range of $10^3 < e < 10^5$, with the majority between 5×10^3–5×10^4. Hailstones exhibit a wide diversity in shape including spherical, spheroidal, conical, ellipsoidal, and irregular. The most commonly observed shapes, for hailstones with major diameters ≥2cm, can be approximated by tri-axial ellipsoidal form (List 1958; Macklin 1963; Barge *et al.* 1973). These hailstones typically have a flattening on surface and smoothly rounded edges (Morgan *et al.* 1982). Since different shapes may result in different flow fields around them, the problem of the drag force becomes particularly complicated with hailstones. List *et al.* (1973) measured the drag coefficients of oblate spheroids with aspect ratios of 0.5–0.79 and $Re=4\times10^4$–4×10^5 for various inclinations relative to the airflow, and presented the inclination-dependent drag coefficients for oblate spheroids. Based on the data of List *et al.*, McDonald (1983) yielded an average C_D value of 0.29±0.02 for an oblate spheroids, with an aspect ratio of 0.67, gyrating in an airflow. This is much less than that for a smooth sphere. However, proper drag coefficients for the right shapes and in the required *Re* range are not well known. The present study will experimentally examine the drag coefficients for spherical and oblate spheroidal hailstones models with various aspect ratios, and possible effect of the deformed shape on the drag coefficient, over a range $8\times10^3 \le Re \le 7.3\times10^4$.

Corresponding author address: Dr. Guoguang, ZHENG
Chinese Academy of Meteorological Sciences
46, Zhongguancun Nandajie, Beijing, China 100081
E-mail: zgg@cma.gov.cn

2. DRAG COEFFICIENT

The drag force on an object is caused by the shear stresses and pressure gradient at the surface. The drag is usually evaluated using the expression

$$\frac{F_D}{A_c} = C_D \frac{\rho_a V_a^2}{2} \qquad (1)$$

where F_D is the drag force, A_c the cross-sectional area of the surface normal to the airflow, ρ_a the air density, V_a the air velocity, and C_D the drag coefficient. By convention, A_c is assumed to be the maximum cross-sectional area and the effect of the motion (such as tumbling) is reflected in the drag coefficient. Obviously, F_D can be determined as a function of V_a. However, the results are normally presented in the non-dimensional form as C_D which depends on V_a and the geometry of the particle. Therefore, C_D for a given particle at a fixed position in a known environment is only determined by F_D. Commonly, C_D is expressed as a function of Reynolds number, *Re*. As expected, C_D is also a function of angle of inclination of the minor axis to the airflow for non-spherical particles.

3. EXPERIMENTAL APPROACH

a. The wind tunnel system

The measurements were made in the University of Toronto Cloud Physics Wind Tunnel, which is a vertical closed circuit and its temperature, velocity, pressure, liquid water content and particle motion can be controlled (List *et al.* 1987). The velocity was varied between 6.3 and 43.0ms^{-1} within ±0.2ms^{-1}. The velocity profile across the tunnel varies by <2% from the velocity at the center, while the turbulence (the root-mean-square deviation) is <0.5%.

b. The test particles

Smooth test models were made of Delrin (Acetal Homopolymers) and ice. Five holes were bored into the particles at 22.5° intervals along the plane of the major axis. The test particles were smooth spheres and spheroids with major axis diameters (*D*) of 2cm, and axis ratios (α) of 0.5, 0.67, 0.74, 0.84, and 1.0. The shapes chosen were representative of natural hailstones. In order to investigate the effect of shape deformation on the drag coefficient of hailstones, two deformed oblate spheroids (α=0.67) and one rounded cylinder with *h*/*D*=0.67 (where *h* is the height of the cylinder) were also made. They represent the commonly and extremely deformed spheroidal

hailstones, respectively. A diagram of the cross-sections through the minor axes of the test particles used is shown in Figure 1.

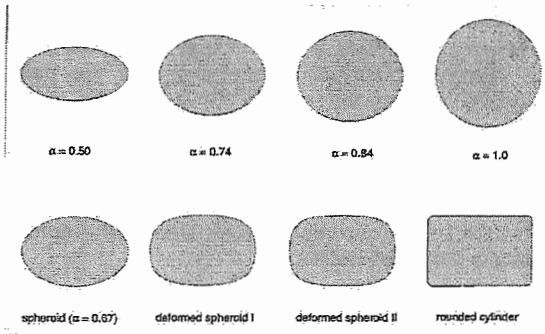

Fig.1: Configuration of the cross-sections through the minor axis of the test particles used in the drag force measurements. (α : axis ratio of the particles)

c. The drag measurement balance

Drag forces were measured using a specially designed balance, mounted on the outer wall of the tunnel. The test particle was suspended from the downstream side by a piano wire attached to a joint on one end of the balance arm. The wire was parallel to the airflow. A balance pan was suspended via a freely flexible joint on the other end of the balance arm. The balance was operated by loading it with weights, giving a measuring resolution of ±0.005g. With the tunnel velocity at zero, weight was added to the pan until it balanced the weight of the test particle. The tunnel velocity was then increased to a known value and weights were added to the balance pan to account for the drag force. The total drag force exerted on the test particle was obtained by multiplying by the ratio (=0.31) of the distance from the weight joint to the fulcrum to the distance from the support joint to the fulcrum. The diameter of the support wire was only 0.05*D* (where *D* is the major axis diameter of the particle), and the distance from the particle to the support joint with the balance arm was 7*D* (=14cm). Thus, the effect of the balance on the flow field around the particle would be very small. Further, the drag force on the support wire alone was measured and the net drag force exerted on the test particle was determined by subtracting the drag on the wire from the total drag force. A shield was built to prevent any drag on the part of the balance arm in the tunnel. An independent calibration of the balance alone was made by exerting a known force on the support.

The drag force was determined as a function of α, *Re*, and the angle of inclination of the major axis to the airflow (angle of attack ϕ). ϕ was varied between 0° and 90° because of the spin about the minor axis in the airflow. Measurements were made for all combinations of these variables, at intervals in air speed (V_a) of about $2ms^{-1}$ over a range of 6.3 to $43.0ms^{-1}$, corresponding to $8\times10^3 \leq Re \leq 7.3\times10^4$. Unfortunately, velocity limitations of the wind tunnel precluded the possibility of reaching critical *Re*.

4. RESULTS AND DISCUSSION

a. The drag coefficients of spheroids

The curves in Fig.2 describe the permissible relationships of the parameters related to C_D and *Re* for spherical and spheroidal particles with various axis ratios α at ϕ=0°, 45° and 90°. It can be seen that C_D is largely independent of *Re* up to $Re=7\times10^4$ although there is a slight increase of C_D with increasing *Re*. At ϕ=90° (the minor axis parallel to the airflow), the values of C_D for spheroids are larger than that for a sphere, and increase with decreasing α (Fig.2*c*). The C_D value of a spheroid with α = 0.50 is about 60% larger than that of a sphere. However, there are inverse results at ϕ=0° (the major axis parallel to the airflow) (Fig.2*a*), which show that C_D for spheroids are smaller than for a sphere, and decreases with decreasing α. C_D of a spheroid with α=0.50 is only 40–50% of a sphere. This is a result of the combined influence of the improved streamlining and diminishing cross-sectional area of the spheroid as ϕ decreases. In the case of ϕ=45° (Fig.2*b*) the results show a combination of the effects at ϕ=0° and 90°. There is few variation of C_D with α although the C_D values of spheroids are slightly larger than that of a sphere.

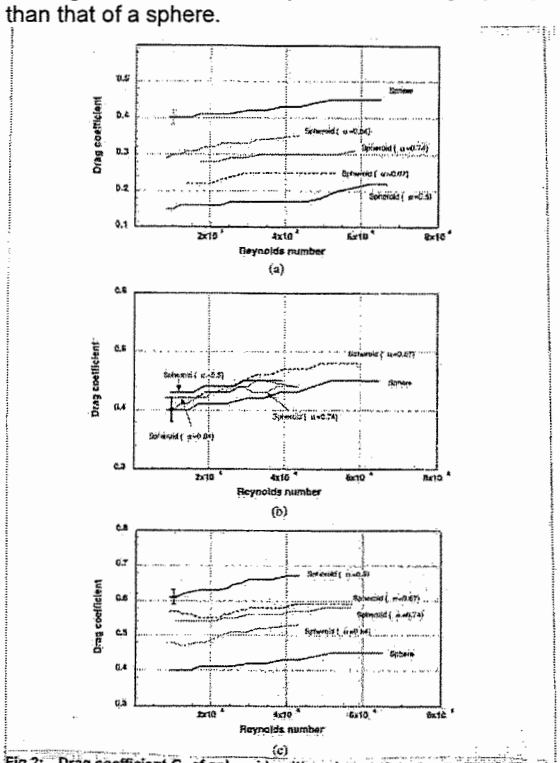

Fig.2: Drag coefficient C_D of spheroids with various axis ratios (α) as a function of Reynolds number at angles of attack (*a*) ϕ = 0°, (*b*) 45°, and (*c*) 90°.

Due to a small variation of C_D with *Re* at a given ϕ in most cases, C_D is assumed a constant over the *Re* range of the present work. Thus, C_D at any ϕ can simply be expressed by averaging the values over the *Re* range concerned. Fig.3 presents the results of the ϕ-dependent C_D for spheres and spheroids with various

α. It indicates that C_D depends strongly on ϕ and α, and increases with increasing ϕ. The C_D vs. ϕ curves in Fig.3 can be fitted by linear relationships which are listed in Table 1. It can be seen that as α increases (i.e., the particle becomes more spherical), the slope of the fitting curve becomes small and, thus, the curve becomes more flat. Therefore, the more spheroidal the particle is, the more significantly C_D depends on ϕ. Fig.3 also shows that the variation of C_D with ϕ for a spheroid with α=0.67 is smaller in the present study than that by List (1970) who used the experimental data of List *et al.* (1969). Here, C_D is only twice as large for ϕ=0° compared to ϕ=90°, whereas List found C_D to be five times larger. The possible reasons are the different experimental schemes and the *Re* ranges concerned.

Table 1. C_D vs. ϕ relation for hailstones with α

Axis ratio α	C_D vs. ϕ relation
0.50	$C_D = 0.180 + 0.00529\,\phi$
0.67	$C_D = 0.249 + 0.00396\,\phi$
0.74	$C_D = 0.293 + 0.00295\,\phi$
0.84	$C_D = 0.326 + 0.00196\,\phi$
1.0	$C_D = 0.423$
0.67 (Deformed I)	$C_D = 0.516 + 0.00628\,\phi$
0.67 (Deformed II)	$C_D = 0.267 + 0.00405\,\phi$
0.67 (Cylinder)	$C_D = 0.319 + 0.00388\,\phi$
0.67 (List *et al.* 1973)	$C_D = 0.142 + 0.00747\,\phi$

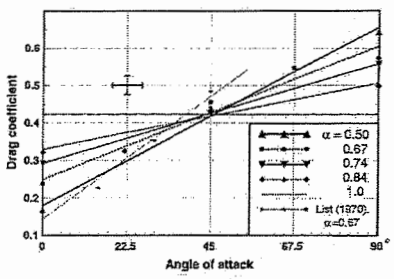

Fig.3: Drag coefficient C_D, averaged over $8\times10^3 \le Re \le 7.3\times10^4$, of smooth spheres and spheroids with various axis ratios (α) as a function of angle of attack; thin dashed dot line: List (1970) for a spheroid with α=0.67 over $4\times10^3 \le Re \le 8\times10^4$.

b. The influence of the particle deformation on drag coefficient

A possible effect of the deformation of the test particle on C_D is also investigated in the present study. The C_D as a function of *Re* at various ϕ for an oblate spheroid of α=0.67, its deformed bodies (I and II), and a rounded cylinder (*h*/*D*=0.67) are given in Fig.4*a-d*, respectively. It shows that the deformed spheroids and cylinder have the characteristics of C_D similar to the spheroids (Fig.2 and Fig.3*a*), indicating that C_D changes slightly with *Re*, and increases with increasing ϕ. Another noticeable characteristcs in Fig.4 is that the variation of C_D with ϕ is larger for 0°≤ϕ≤45° than for 45° ≤ϕ≤90°, which is consistent with the variation of the cross-sectional area of the particles to the airflow as ϕ changes. Fig.4 also shows that the rounded cylinder has larger C_D than the deformed spheroids at any ϕ. It is interesting because the C_D value of the cylinder is close to that of a plate (C_D~1.15) at ϕ=90°, and of a sphere (C_D~0.42) at ϕ=0°. It indicates implicitly that C_D is heavily dependent on the shape of the particle surface against the airflow. Obviously, the cylinder gives the maximum effect of the deformation of the spheroid with the same α at any given ϕ. It is expected since the cylinder has the maximum cross-sectional area to the airflow and more flat curvature of the forward part to the airflow compared to the spheroid and its deformed bodies.

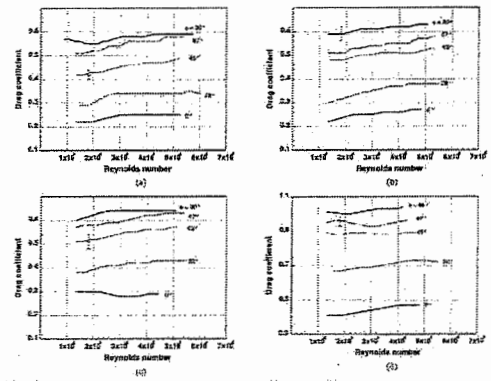

Fig.4: Drag coefficient C_D for (a) an oblate spheroid (α=0.67), (b) and (c) its deformed bodies (I and II), and (d) a rounded cylinder (*h*/*D*=0.67) as a function of Re at various angles of attack ϕ.

In order to illustrate clearly the effect of the particle deformation on C_D, Fig.5*a-c* present C_D as a function of *Re* at ϕ=0°, 45° and 90°, respectively. It is apparent that the deformed spheroids have the C_D values larger than that of a spheroid with the same α (0.67). The more the spheroid is deformed, the larger the C_D value is at any given ϕ. The deformed spheroid II, for example, has the C_D value of 15-30% larger than that of the spheroid at ϕ=0° whereas 10-15% larger at ϕ=90° over the *Re* range concerned. This is not surprising because the deformed spheroids have the improved streamlining and increasing cross-sectional area to the airflow as ϕ increases compared to the spheroid with the same α.

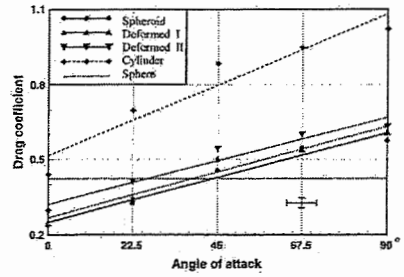

Fig.5: Drag coefficient C_D of an oblate spheroid (α=0.67), its deformed bodies (I and II), and a rounded cylinder (*h*/*D*=0.67) as a function of Re at angles of attack (a) ϕ=0°, (b) 45°, and (c) 90°.

Fig.5 also shows that the C_D value of the cylinder is much larger than those of the spheroid and its deformed bodies with the same α. There is an

interesting comparison that the deformed spheroid II has the C_D value close to that of a spheroid with α=0.74 at ϕ=0° and of a spheroid with α=0.50 at ϕ=90°. By comparing their curvatures of the forward part to the airflow, it is found that they have the similar curvatures of the surface to the airflow. Thus, C_D is also associated with the curvature of the particle surface to the airflow.

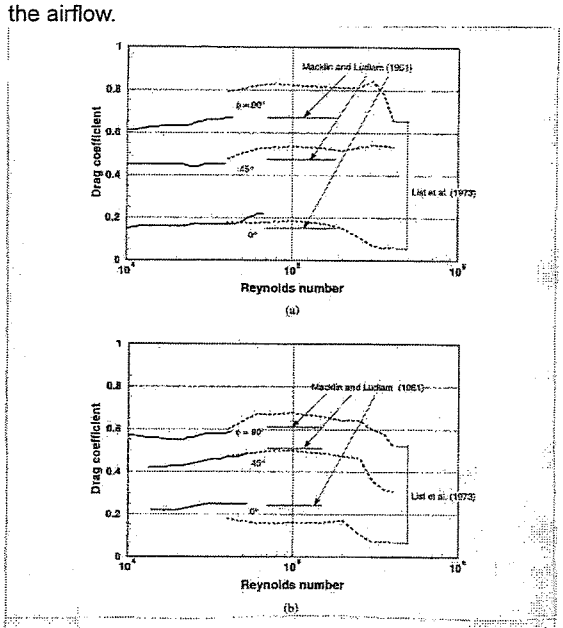

Fig.6: Comparison of C_D of smooth spheroids with axis ratios of (a) α =0.50 and (b) 0.67 at ϕ=0°, 45°, and 90°, with the results by List *et al.*(1973) (dashed lines), and Macklin (1961) (dotted lines). The data of Macklin in (a) is for spheroids with α =0.46.

Fig.6 gives a comparison of C_D–Re relationships for spheroidal particles with (*a*) α=0.50 and (*b*) α=0.67 at different ϕ. It shows that the C_D values of the present investigation over the "lower" Re range are close to those of Macklin *et al.* (1961) and List *et al.*(1973) over the higher Re range.

5. SUMMARY AND CONCLUSIONS

Drag coefficients of spherical and oblate spheroidal hailstone models with various axis ratios have been experimentally investigated in a wind tunnel over a Reynolds number range $8\times10^3 \leq Re \leq 7.3\times10^4$ at various inclination angles of the models to the airflow. The following conclusions were drawn from the experimental data:

(1) C_D was found to have a small variation with Re. It depends strongly on ϕ. The variation of C_D with ϕ for spheroids is good agreement with those of Macklin *et al.* (1961) and List *et al.* (1973) who made the measurements of C_D over the higher Re range. The C_D vs. ϕ data can be fitted by a linear relationship.

(2) The shape is one of the important factors to influence the C_D value. At any given ϕ, C_D of a spheroid depends on its axis ratio α. The C_D value increases at ϕ=0° and decreases at ϕ=90° as decreasing α. However, the variation of C_D with α becomes a small at ϕ=45°.

(3) The deformation of the spheroidal hailstones has a noticeable influence on C_D. The deformed spheroids were found to have C_D larger than that a spheroid with the same axis ratio, depending on the inclination angle to the airflow. The cylinder with h/D=0.67 gives the extreme C_D values for the deformation effect, with C_D=1.1 (close to that of a plate) at ϕ=90° and C_D=0.42 (close to that of a sphere) at ϕ=0°.

(4) It was demonstrated that the improved streamlining around the particle largely influences the C_D value, which is reflected by the curvature of the forward part of the particle to the airflow. The deformed spheroid II (α=0.67) has C_D close to that of the spheroid with α=0.74 largely because of their similar curvatures of the forward part to the airflow.

The present investigation will help to better understand the aerodynamic behavior of natural hailstones and improve the parameterization of computer models of hail study. It should be pointed out that further investigation is needed to address the effect of surface roughness on C_D in order to understand completely the aerodynamics of natural hailstones.

6. ACKNOWLEDGEMENTS

This work was sponsored by the Natural Sciences and Engineering Research Council of Canada (NSERC), and by the National Natural Science Fundation of China (NSFC) (40275001).

7. REFERENCES

Barge, B.L., and G. A. Isaac, 1973: The shape of Alberta hailstones. *J. Rech. Atoms.*, **7**, 11-20.

Goldstein, S., 1938: *Modern Developments in Fluid Dynamics.* Oxford Clarendon Press, 420pp.

Knight, N.C., and A.J. Heymsfield, 1983: Measurements and interpretation of hailstone density and terminal velocity. *J. Atmos. Sci.*, **40**, 1510-1516.

Kry, P.R., and R. List, 1974: Aerodynamic torques on rotating oblate spheroids. *Phys. Fluids*, **17**, 1087-1092.

List, R., 1958: Kennzeichen atmosphärischer Eispartikeln, 2. Teil. *Z. angew. Math. Phys.*, **9a**, No. 3, 217-234.

List, R., 1959: Zur Aerodynamik von Hagelkornen. *Z. angew. Math. Phys.*, **10**, 143-159.

List, R., U.W. Rentsch, and A.C. Byram, 1973: On the aerodynamics of spheroidal hailstone models. *J. Atmos. Sci.*, **30**, 653-661.

List, R., G.B. Lesins, F. García-García, and D.B. McDonald, 1987: Pressurized icing tunnel for graupel, hail and secondary raindrop production. *J. Atmos. Oceanic Technol.*, **4**, 454-463.

Lozowski, E.P., and A.G. Beattie, 1979: Measurements of the kinematics of natural hailstones near the ground. *Quart. J. Roy. Meteorol. Soc.*, **105**, 453-459.

Macklin, W.C., and F.H. Ludlam, 1961: The fallspeeds of hailstones. *Quart. J. Roy. Meteorol. Soc.*, **87**, 72-81.

Matson, R.J., and A.W. Huggins, 1980: The direct measurement of the sizes, shapes, and kinematics of falling hailstones. *J. Atmos. Sci.*, **37**, 1107-1125.

McDonald, D.B., 1983: *Heat transfer for melting spheroidal hailstones.* M.Sc. thesis, Department of Physics, University of Toronto, 55pp.

Morgan, G.M., and P.W. Summers, 1982: Hailfall and hailstorm characteristics. Thunderstorms: A Social, Scientific and Technological Documentary, Vol. 2, Chapter 11, 237-257.

Willis, J.T., K.A. Browning, and D. Atlas, 1964: Radar observations of ice spheres in free fall. *J. Atmos. Sci.*, **21**, 103-108.

Young, R.G.E., and K.A. Browning, 1967: Wind tunnel tests of simulated spherical hailstones with variable roughness. *J. Atmos. Sci.*, **24**, 58-62.

SIMULATION OF THE DEVELOPMENT OF ELECTRIC FIELD IN A 3-DIMENSIONAL WINTER THUNDERCLOUDS FIELD USING THE RAMS MODEL

Orit Altaratz[1], Tamir Reisin[2], Zev Levin[1]
[1]Department of Geophysics and Planetary Sciences, Tel Aviv University, Israel.
[2]Soreq Nuclear Research Center, Yavne, Israel.

1. INTRODUCTION

Previous studies made on the electrical activity of thunderstorms over Israel and the adjacent Mediterranean Sea showed that there are larger frequencies of lightning flashes over sea than over land and over the Carmel Mountain than over other parts of the coast (Altaratz et al. 2003). Hence, it is desirable to develop a capability to simulate electrified storms on a regional scale in order to study the influence of different geographical and meteorological factors on the dynamical and microphysical behavior of thunderstorms. Previous numerical studies (e.g. Takahashi, 1984; Helsdon and Farley, 1987; Ziegler et al., 1991; among others) of the electrification of thunderstorms described the development in single thunderclouds without any topography. This work describes the pre-lightning electrification of mid-winter thunderclouds over the coastal area of Israel: around Haifa and the Carmel Mountain (a mountain ridge, 500 m height, see fig. 1) in the northern coast. For brevity the simulations around Tel Aviv in the central coast will not be presented here. The goal was to study the influence of geographical factors on thunderclouds electrical evolution. For this purpose the RAMS, 3D mesoscale model, was modified to include the electrical development in a realistic cloud field. The model calculates charge separation, charge buildup and the development of charge centers, which is subsequently used to calculate the electrical field in the clouds. The results demonstrate the differences between the clouds that develop over the sea and those over land.

2. THE NUMERICAL MODEL

The Regional Atmospheric Modeling System (RAMS) is a 3-D multipurpose, numerical prediction model that simulates atmospheric circulations ranging in scale from an entire hemisphere down to eddies in the planetary boundary layer. A comprehensive review of the RAMS model can be found in Pielke et al., (1992) and Cotton et al., (2003).

Corresponding author's address: Zev Levin, Department of Geophysics and Planetary Sciences, Tel Aviv University, Ramat Aviv, 69978, Israel. E-mail: zev@hail.tau.ac.il

2.1 The microphysical scheme

The RAMS version 4.3 includes a bulk cloud microphysical scheme (with few exceptional processes, which are described by bin microphysics). The water class is divided into eight different categories: vapor, cloud droplets, rain, pristine ice, snow, aggregates, graupel and hail. Cloud droplets and rain are liquid water, pristine ice, snow and aggregates are completely frozen, and graupel and hail are mixed phase particles. A generalized gamma function is assumed for the size spectrum. A two-moment hydrometeor prediction scheme predicts the mixing ratio and the number concentration of all the water species. A full description of the microphysical model can be found in Walko et al. (1995, 2000) and Meyers et al. (1997).

2.2 Electrification scheme

In the present work the noninductive charging mechanism is the only charging process to be simulated. Two parameterizations of this mechanism were implemented into the model; one is based on the experimental studies of Saunders et al. (1991) and the other on the experimental results of Takahashi (1978). The parameterization of the noninductive charge separation mechanism requires the determination of charge transfer per separation event (collision and rebound) and the calculation of the number of these events (out of the collisions events) for the particular hydrometeor class at a grid point during a time step of the model. The charge transferred per separation event was calculated according to the two different schemes.

Saunders et al. (1991):

The charge δq, transferred to a graupel particle via collision and rebound with pristine ice, snow or aggregate is:

$$\delta q(D_i, D_g, T) = \left|\frac{\Delta V}{k}\right|^3 G(D_i) \qquad (1)$$

Where ΔV (m/s) is the difference between the large and small particle fall velocities, k is a constant equal to 3m/s, and $G(D_i)$ is a polynomial fit to the experimental data from Keith and Saunders (1989) in units of fC.

The polarity of the charge, which is transferred to the graupel, is a function of the temperature and of the effective liquid water content. Saunders et al. (1991) determined the effective liquid content as the accreted fraction of liquid water content in the path of the graupel, given by the ambient liquid water content multiplied by the collection efficiency ($EW=LWC*E_{coll}$). They gave the following expression for EW_{crit} (gr/m^3), valid for temperatures between -10.7°C>T>-23.9°C:

$$EW_{crit} = -0.49 - 6.64 \times 10^{-2} T \qquad (2)$$

If the effective liquid water content is above the value calculated in equation (2) the graupel is charged positively, otherwise negatively.

The Takahashi's scheme

The results of Takahashi's experiments, for the charge transferred per collision, have been stored in a lookup table in the model code (Takahashi, personal communication). A value of the charge transfer per collision event is retrieved from the lookup table, depending on the temperature and liquid water content in the interaction location. It should be pointed out that in contrast to Saunders who used charge per separation event, Takahashi describes his results in terms of charge per collision. Therefore, the charge per collision has to be multiplied by an efficiency factor α (Marshall et al., 1978, Takahashi 1984) that converts it to charge per separation event to yield:

$$\alpha = 5\left(\frac{D_i}{D_0}\right)^2 \left|V_g - V_i\right| / V_0 \qquad (3)$$

Where D_i is the ice (or snow or aggregates) diameter (m) and V_g and V_i are the terminal fall velocities of the graupel and ice (m s^{-1}). The values of D_0 and V_0 are 100 μm and 8 m s^{-1} respectively (Takahashi, 1978). α is restricted to a value of 10, which is the apparent saturation value for large snow crystals (Marshall et al., 1978). This factor determines the dependence of the riming charge magnitude on the ice crystal size and terminal velocities.

After the calculation of the charge transfer per separation event, the determination of the total charge transferred per time interval, is done by multiplying the calculated charge transferred per separation event by the number of these events.

The rate of change of the charge density ρ on the graupel category is given by:

$$\frac{\partial \rho}{\partial t} = \frac{\pi}{4} \int\int (D_g + D_i)^2 \left|V_g - V_i\right| E_{gi} n_i(D_i) n_g(D_g) \delta q dD_i dD_g \qquad (4)$$

Where D_g and D_i are the graupel and the ice diameters, respectively; V_g and V_i are the terminal fall velocities of the graupel and the ice, respectively; n(D) is the size distribution of the particular type of hydrometeor and E_{gi} is the collision-separation efficiency for graupel and ice.

The electric field is calculated offline after the RAMS model simulation is completed. It is done by the use of a standard numerical algorithm to solve for the electrical potential φ at all grid points by inverting the Poisson's equation. Finally, the electric field is computed from the value of this electrical potential. The electric field is computed until its value reaches a pre-assigned threshold value for the electric breakdown.

In order to use the numerical Poisson solver, boundary conditions for φ were specified. Since, the ground is an equipotential plane, the potential of the bottom layer of the grid was set to a constant. The lateral boundary conditions were set according to the fair weather potential (Gish, 1944) since they are far enough from the charge distribution in the clouds.

The upper boundary condition of the potential is set to the fair weather potential at the corresponding height.

3. RESULTS

The 5-6 January 2000 storm was a "Cyprus Low" event, which caused heavy rain and intense electrical activity along the coast of Israel. We chose to study the postfrontal electrical activity in order to be able to track the electrical evolution of a field of single clouds. Two different kinds of simulations will be presented, both of them focused on the Haifa region, the first one with real topography and the second one with a flat topography. The model was run for 8 hours, starting at 18:00 UTC (20:00 local time) on January 5th 2000. Initial and boundary data for the simulations were obtained from the European Center for Medium Range Weather Forecast (ECMWF) objective analysis for 18:00, 24:00 UTC of January 5th 2000. The resolution of these three-dimensional data sets was 50 km. The simulation utilized a two-way interacting nested grid configuration. Five grids were used to zoom down to the region of interest. The two finest grids had dimensions of 94X94X27 points, with 312 m horizontal resolution and 100 m grid spacing in the lowest layer and grid stretching of 1.11 times of this value in the upper levels. The two finest grids were centered at the latitude of Haifa, with one centered over the sea and the second over the land (both of them contained land and sea regions). The time steps for finest grids were 3 sec.

3.1 The Haifa real topography simulation

Eight clouds were analyzed (until their first lightning event), four of them over the sea west or northwest of the Carmel Mountain, and the other four over the mountain and its surroundings. The clouds moved with southwesterly to westerly winds. The cells are marked in figure 1, which shows the liquid water content in the clouds at 2266 m, at 19:22 UTC at the sea grid and 19:24 and 20:24 UTC at the land grid. The locations of the formation of the clouds over the land were not identical for all four cells. One of them formed over the slopes of the Carmel Mountain and it was followed until its first lightning occurrence over the top of the mountain (land1). Two other clouds were formed over the Carmel Mountain and their first electrical breakdown took place east of the northeastern slopes of the Carmel Mountain, over the plane (land2, 3). The last one formed over the sea in the Haifa bay and shortly afterwards moved over land (north of the Carmel) and its first lightning occurred over the slopes of the Galilee Mountains (land 4).

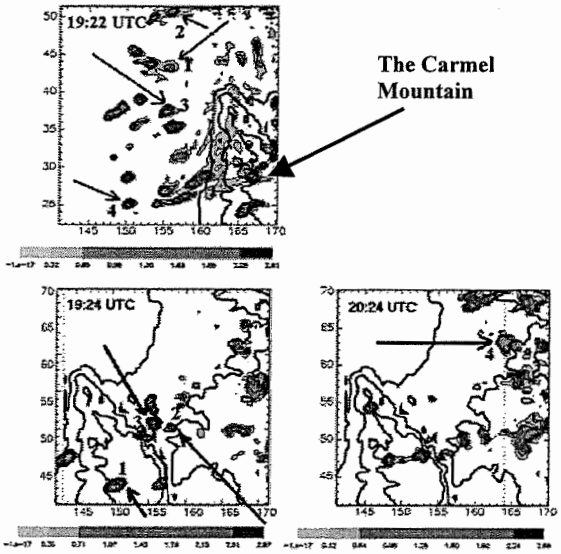

Figure 1: Contours of liquid water content (g Kg^{-1}) at 2266 m, at 19:22 UTC (sea grid), and 19:24, 20:24 UTC (land grid).

Based on Saunders' scheme, the total charge density in the middle of the clouds, shortly before the first lightning, had several possible structures: (a) a dipole (b) an inverted dipole (c) an inverted tripole (d) a tripole with another upper negative charge center. Examples can be seen in figure 2. In contrast to Saunders' scheme, the total charge density based on Takahashi's scheme produced a uniform dipole structure. Table 1 presents the general characteristics of the simulated clouds. The maximal updrafts in the sea clouds were between 15.5 and 18.1 m s^{-1}. The first two clouds (sea1, 2) with the strongest updrafts velocities had the shortest time interval to the first lightning (11 and 10 minutes). The time interval between the appearance of liquid water content of 1 g Kg^{-1} in the cloud and the first lightning was 10-13 minutes for the sea clouds and 12-26 minutes for the land clouds (figure 3). It was similar using both schemes (Saunders and Takahashi).

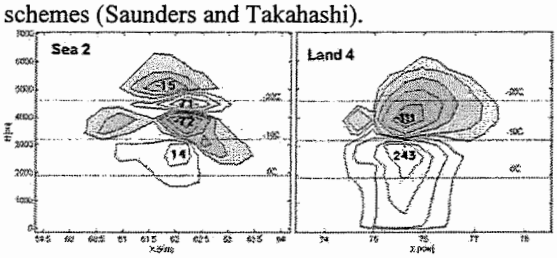

Figure 2: The total charge density for the clouds Sea 2 and Land 4.

The land clouds formed over different sites and as a result, the variance in their characteristics was large. The updraft velocities were between 10 and 18.2 m s^{-1}. Land 4, which was formed over the sea and moved to the land, had the lowest updraft and the longest time to the first lightning. The forcing of the topography didn't influence it.

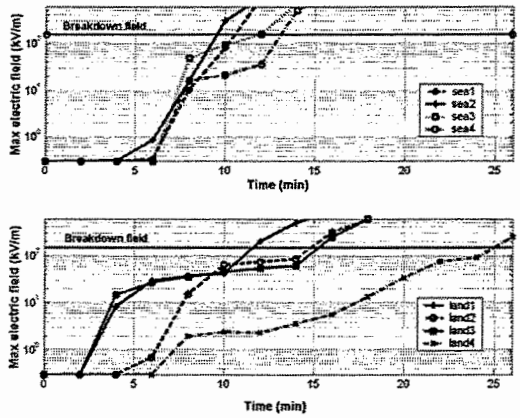

Figure 3: The maximal electric field in the clouds in the real topography simulation as a function of time (kV m^{-1}). The upper panel is for the sea clouds and the lower panel for the land clouds.

3.2 The Haifa flat topography simulation

In order to evaluate the role of the topography in the clouds' microphysical and electrical evolution, a simulation of the Haifa region with a flat topography was conducted, using only the Saunders' scheme. The electrical development of the clouds was compared with the development of similar clouds in the simulation of the Haifa region with real topography.

The model was run for 2 hours, starting at 18:00 UTC (20:00 local time) on January 5th 2000. The electrical

evolution of four clouds were tracked, three of them while moving over the sea (marked as Notopo_sea1, 2, 3) north west or west of the Carmel Mountain and one while moving over the land (Notopo_land1). The cloud that was tracked over the land was formed over the location of the Carmel Mountain (which was a plane in this simulation) and its first electrical breakdown took place east of the location of the northeastern slopes of the Carmel Mountain. A comparison between the characteristics of these clouds and the ones formed over the sea in the Haifa real topography simulation reveals that the microphysical and electrical characteristics of the clouds that developed in similar locations in both simulations were similar (table 1). However, the electrification rate of the cloud, which developed over the land in this simulation, was slower than of the similar clouds in the real topography simulation.

	W_{max} (ms^{-1})	RGP_{max} (gKg^{-1})	Time to the first light (min)	Charge structure (before the 1st lightning)	The charge centers levels
Sea1	18.1	0.59	11	Inverted tripole	-23°C, -19°C, -16°C
Sea2	19.7	0.25	10	Tripole+upper negative	-23°C,-19°C, -16°C, -5°C
Sea3	15.5	0.65	12	Tripole+upper negative	-27°C, -19°C, -12°C, -5°C
Sea4	16.0	0.34	13	Inverted tripole	-23°C, -19°C, -16°C
Average	**17.3**	**0.45**	**11.5**		
Land1	18.2	0.16	12	Tripole+upper negative	-22°C,-19°C, -16°C,-3°C
Land2	15.7	0.43	13	Tripole+upper negative	-27°C, -19°C, -8°C, 2°C
Land3	12.5	0.7	16	Inverted dipole	-16°C, -8°C
Land4	10	0.12	26	Dipole	-16°C, -8°C
Average	**14.1**	**0.35**	**16.7**		
Notopo sea1	17.9	0.21	11	Tripole+upper negative	-23°C, -19°C, -16°C, 0°C
Notopo sea2	17.5	0.2	11	Tripole+upper negative	-23°C, -19°C, -8°C, 2°C
Notopo sea3	17.5	0.17	11	Tripole+upper negative	-23°C, -19°C, -16°C, 1°C
Average	**17.6**	**0.19**	**11**		
Notopo land1	14	0.58	20	Tripole	-19°C, -16°C, -8°C

Table 1: Results for the clouds in the two simulations. W=maximal updraft velocity, RGP=graupel mass content.

To summarize these simulations, the results showed that most of the clouds that developed over the sea had higher tops and larger graupel mass contents (in the time prior to the first lighting) than the ones over land. The relative part of thunderclouds that can produce lightning (clouds with electric field high enough to generate lightning) that were found over the sea was larger than over the land. This can be explained by the heat and humidity fluxes from the sea surface. Comparison of the two charge separation schemes showed that in spite of the fact that both parameterizations produced similar charging rate, the charge build up using Takahashi's parameterization led to a simple dipole charge distribution while the parameterization of Saunders' produced more complicated charge distributions composed of multi charge centers. The flat topography simulation demonstrated that the effect of the topography on the electrical development of clouds was dominant for the clouds which formed over the topographic element itself, but it was not significant for clouds which formed over the sea less than 5 kilometers from the topographical obstacle.

4. REFERENCES

Altaratz, O., Z. Levin, Y. Yair, and B. Ziv, 2003: Lightning activity over land and sea on the eastern coast of the Mediterranean. Mon. Wea. Rev., **131**, 2060-2070.

Cotton, W. R., R. A. Pielke, Sr., R. Walko, G. E. Liston, C. J. Tremback, H. Jiang, R. L. McAnelly, J. Y. Harrington, and M. E. Nicholls, 2003: RAMS 2001: Current status and future directions. Meteor. Atmos. Phys, **82**, 1-4, 5-29.

Gish, O. H., 1944: Evaluation and interpretation of the columnar resistance of the atmosphere. Terr. Magn. Atmos. Elec., **49**, 159-68.

Helsdon, J. H., and R. D. Farley, 1987: A numerical modeling study of a Montana thunderstorm .1. model results versus observations involving electrical aspects. J. Geophys. Res. **92**, D5: 5661-5675

Keith, W.D. and C. P. R. Saunders, 1989: Charge transfer during multiple large ice crystal interactions with a riming target. J. Geophys. Res., **94**, 13,103-13,106.

Marshall, B. J. P., J. Latham and C. P. R. Saunders, 1978: A laboratory study of charge transfer accompanying collision of ice crystals with a simulated hailstone. Quart. J. Roy. Meteor. Soc., **104**, 163–178.

Meyers, M. P., R. L. Walko, J. Y. Harrington and W. R. Cotton, 1997: New RAMS cloud microphysics parameterization Part 2: the two moment scheme. Atmos. Res., **45**, 3-39.

Pielke, R. A., W. R. Cotton, R. L. Walko, C. J. Tremback, W. A. Lyons, L. D. Grassoo, M. E. Nicholls, M. D. Moran, D. A. Wesley, T. J. Lee and J. H. Copeland, 1992: A comprehensive meteorological modeling system – RAMS. Meteor. Atmos. Phys., **49**, 69-91.

Saunders, C. P. R., W. D. Keith and R. P. Mitzeva, 1991: The effect of liquid water on thunderstorm charging. J. Geophys. Res., **96**, 11007-17.

Takahashi, T., 1978: Riming Electrification as a Charge Generation Mechanism in Thunderstorms. J. Atmos. Sci., 35, 8, 1536-1548.

Takahashi, T., 1984: Thunderstorm electrification-a numerical study. J. Atmos. Sci., **41**, 2541-2558.

Walko, R.L., W. R. Cotton, M. P. Meyers and J.Y. Harrington, 1995: New RAMS cloud microphysics parameterization Part 1: the single moment scheme. Atmos. Res., **38**, 29-62.

Walko, R. L., W. R. Cotton, G. Feingold and B. Stevens, 2000: Efficient computation of vapor and heat diffusion between hydrometeors in a numerical model. Atmos. Res., **53**, 171-183.

Ziegler, C. L., D. R. MacGorman, P. S. Ray and J. E. Dye, 1991: A model evaluation of noninductive graupel-ice charging in the early electrification of a mountain thunderstorm. J. Geophys. Res., **96**, 12,833-55.

LABORATORY INVESTIGATION OF POSITIVE DISCHARGES FROM ICE CRYSTALS: POSSIBLE RELEVANCE TO LIGHTNING INITIATION AND ICE MULTIPLICATION

Matt Bailey[1] and John Hallett[1]
Danyal Petersen[2] and William Beasley[2]

[1]Desert Research Institute, Reno Nevada, 89512 USA
School of Meteorology, University of Oklahoma, Norman OK 73019 USA

1. INTRODUCTION

Observations of thunderstorms have revealed that intra cloud and even cloud-to-ground lightning can begin at altitudes in clouds where temperatures are well below -18 °C. Latham (2003) points out that models indicate the existence of a simple relationship between lightning frequency and the upwards flux of ice crystals in thunderstorm anvils, and ice crystal concentrations in thunderstorms are known to increase with each subsequent lightning discharge. While the main charging mechanism in thunderstorms appears to be related to interactions between ice crystals and graupel in addition to riming processes, positive corona emission from ice crystals may also play a roll. In laboratory experiments addressing electric corona from hydrometeors, Griffiths and Latham (1974) concluded that corona discharges from ice crystals were probably not significant below -18 °C. However, these results may have been limited by poor control of humidity during the discharge measurements.

A new laboratory investigation of corona emissions from laboratory grown ice crystals has been performed with improved control of relative humidity conditions. Positive streamer discharges were observed to continue down to temperatures of -36 °C where the discharges were then observed to become bipolar, involving both negative and positive streamers. During this investigation, a previously unreported phenomenon was observed consisting of extremely rapid growth of highly charged ice crystals following corona discharge when relative humidity conditions were near water saturation, conditions which are likely to exist in thunderclouds. This process could lead to rapid ice multiplication in electrified clouds.

2. POSITIVE STREAMERS FROM ICE CRYSTALS

For corona discharge measurements, a diffusion chamber was modified by placing a pair of parallel plate electrodes inside which were used to apply an electric field to ice crystals grown on a glass substrate as depicted in figure 1. Crystals of various habits were grown at temperatures ranging from - 4 °C to -38 °C, at ice supersaturations ranging from 10% with respect to ice up to water saturation, and pressures commensurate with those in the atmosphere for the particular growth temperature, approximately 700 mb to 300 mb, respectively. Crystals were grown to sizes ranging from 300 micrometers up to 2 millimeters on a drawn glass fiber. The fiber was attached to a polystyrene support which could be warmed at its base near the chamber wall in order to keep it ice free to ensure electrical isolation of the ice crystals on the glass substrate. The two parallel plate electrodes were separated by a distance of 14 millimeters and were swung away from the crystals during the growth phase to prevent them from perturbing the vapor diffusion field in the chamber. A heating element attached to each plate was powered at a very low level in order to keep them ice free until discharge measurements were performed. This prevented discharges from originating from ice growing on the plates rather than from the crystals on the substrate. Voltage was supplied to one of the plates with a 20 kV dc power supply in series with a high voltage low pass filter and was controlled with a variac.

Once crystals had been grown to a desired size and shape, the field plates were swung into position over a crystal and a an electric field was applied, quickly rising to a sub-threshold value in about 5 seconds and then increased to threshold values at a slower and more uniform rate over the course of 10-20 seconds, before any ice growth could occur on the plates themselves. With the lab totally dark, discharges were observed with a Generation II image intensifier, basically a military surplus night vision scope. An example of a discharge is shown in figure 2. The discharges were generally impossible to view directly, even with dark adapted eyes. Once discharge at threshold was observed, the field was increased until a subsequent discharge was observed. This process was repeated until the crystal went into constant discharge or until the crystal had substantially eroded due to the field. Threshold field values are shown in figure 3. The open symbols generally in the upper part of the figure are results observed at 850 mb while the lower solid symbols represent measurements at the pressures indicated. The symbols stacked up at -12 °C are the high and low values measured by Griffiths and Latham which were all performed at this temperature.

One drawback of the experimental setup was the fact that the parallel plates blocked the vapor field during the discharge measurement. It is likely that this resulted in vapor conditions just saturated with respect to ice or slightly higher. However, this approach still

Corresponding author's address: Matt Bailey, Desert Research Institute, 2215 Raggio Parkway, Reno, Nevada 89512 e-mail matt.bailey@dri.edu

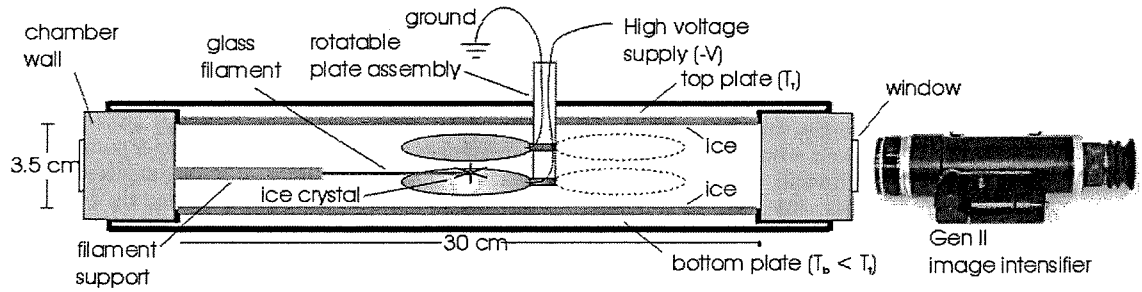

Figure 1. Schematic of the diffusion chamber with field electrodes (parallel plates) and image intensifier.

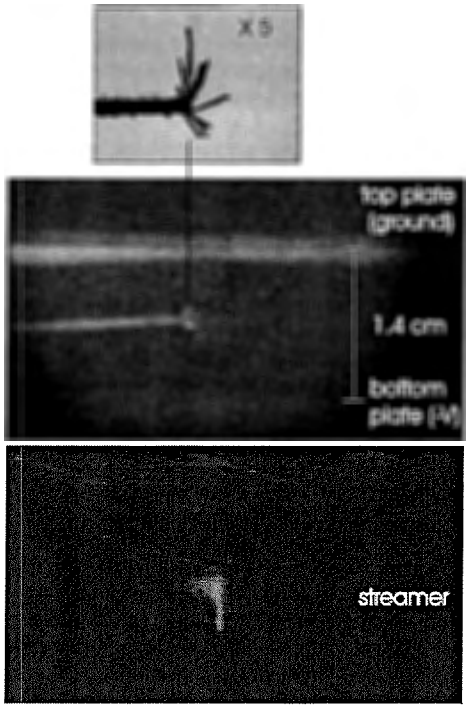

Figure 2. View of positive streamer through the image intensifier with a video camera.

represents an improvement over that of Griffiths and Latham where crystals, previously grown in a diffusion chamber, were transferred to a discharge chamber which was then placed in a freezer. Though a piece of ice was added to the chamber in an attempt to maintain some sort of ice supersaturation, this does not create an effective diffusion chamber, hence the environment was likely subsaturated with respect to ice. Between transferring the crystal and then placing it in a subsaturated environment, many of the sharp corners and features of crystals were probably rounded due to sublimation. This is likely one reason for the large variation in their results as seen in figure 3. However it is interesting to note that sharply pointed or faceted crystals did not appear to be the critical feature of crystals which exhibited the lowest threshold values in our experiments. It was instead crystal thickness. Thin crystals, whether thin plates or

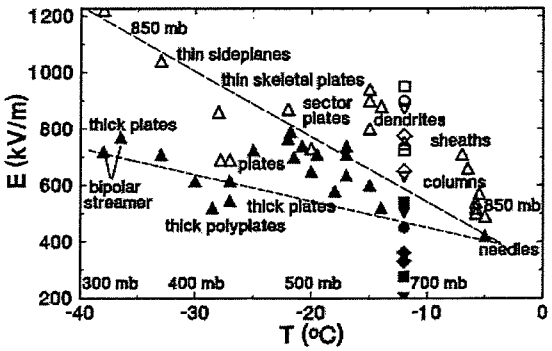

Figure 3. Threshold field values for corona emission from ice crystals grown in a diffusion chamber.

dendrites, were observed to rapidly erode under the application of the electric field and exhibited moderate to high threshold values. Thick robust habit forms such as thick plates, solid columns and needles, and thick sideplane or spearhead crystals such as those described in Bailey and Hallett (2004) exhibited the lowest threshold values and experienced a much smaller degree of sublimation than thin crystals.

3. POSSIBLE ICE MULTIPLICATION MECHANISM

The enhanced growth of needle-like ice crystals in electric fields is a well established phenomenon which occurs approximately above a threshold field value of 50 kV/m and results in maximum growth rates of approximately 20 micrometers per second, an example of which is shown in figure 4. It is believed that a strong electric field creates a sort of ventilation or "electric wind" which accelerates the incorporation

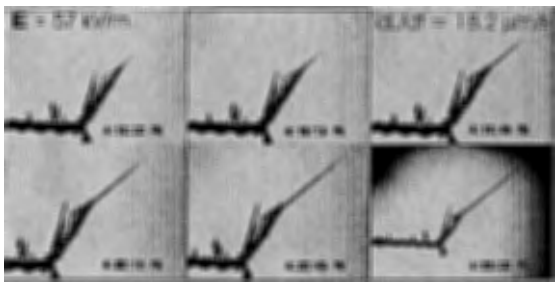

Figure 4. Example of normal electric needle growth which occurs above a threshold field value of 50 kV/m.

of water vapor molecules onto the surface of a growing crystal which takes a characteristic "electric needle" form which is quite different from the usual needle habit observed over the narrow temperature range from approximately -4°C to -5.5 °C.

An unexpected phenomenon was often observed during threshold measurements whenever the relative humidity was near water saturation. Following corona discharge from thick crystals, the field was quickly reduced to zero (plates grounded) and the plates were swung away to the side of the chamber which reestablished the vapor field. Under these conditions, electric needle crystals were observed to grow with extremely large growth rates but with no externally applied field! Examples of these are shown in figure 5.

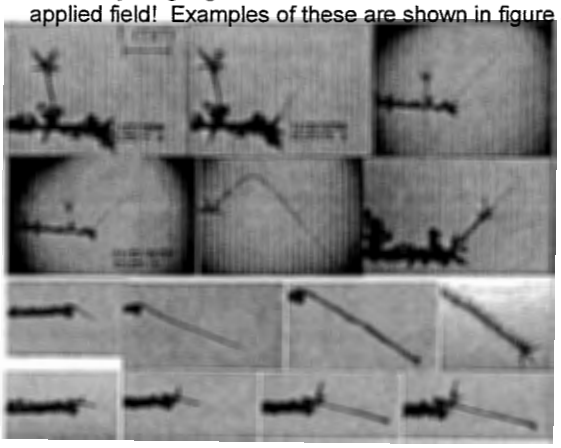

Figure 5. Sequences of post corona discharge needle growth with no externally applied field..

The crystals would sometimes grow to a millimeter or more in size in 20-30 seconds, a growth rate almost 4 times that of the normal electric needle growth. The crystals were extremely fragile and easily broke away from the parent crystal, typically after reaching lengths of several millimeters and sagging under their own weight. However, a light tap on the side of the chamber would also easily dislodge them at smaller sizes. Often after breaking off, another crystal would shortly begin to grow from the original growth site and the process would repeat itself, often lasting for several minutes. The observed growth rates of both the normal electric needles and the "anomalous" or zero external field electric needles are shown in figure 6.

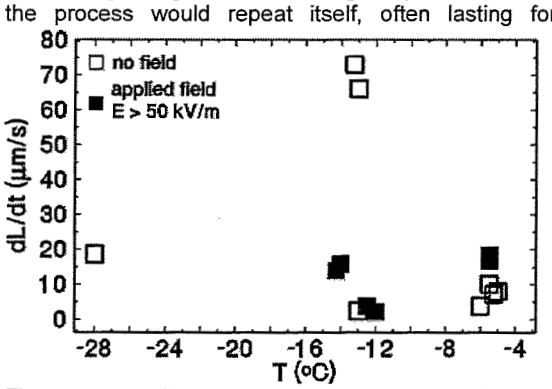

Figure 6. Growth rates of electric needle crystals both with and without an applied electric field.

It is likely that the post-corona discharge crystals were left so highly charged, that they generated their own intense fields at some point on their surface which resulted in the emergence of a needle-like structure with a sharp tip where the field would be even more intense due to the reduced radius of curvature. These needles were observed to maintain a very sharp tip throughout their growth and typically exhibited no side branching, except near the dendritic crystal regime as shown in the bottom of figure 5. Crystals were observed to grow, break off, and grow again until the charge had somehow leaked off and dropped below a critical level, at which point the remaining crystal would resume growth with a habit commensurate with the ambient temperature.

This phenomenon also appears to have been observed in the study of Mandal and Kumar (2002) where the effects of corona discharge on nucleation were explored. In that experiment, highly saturated water vapor in a flask cooled to temperatures between - 9 °C and -12 °C was subjected to a corona discharge. While they did not observe any significant increase in the nucleation of ice crystals, they often

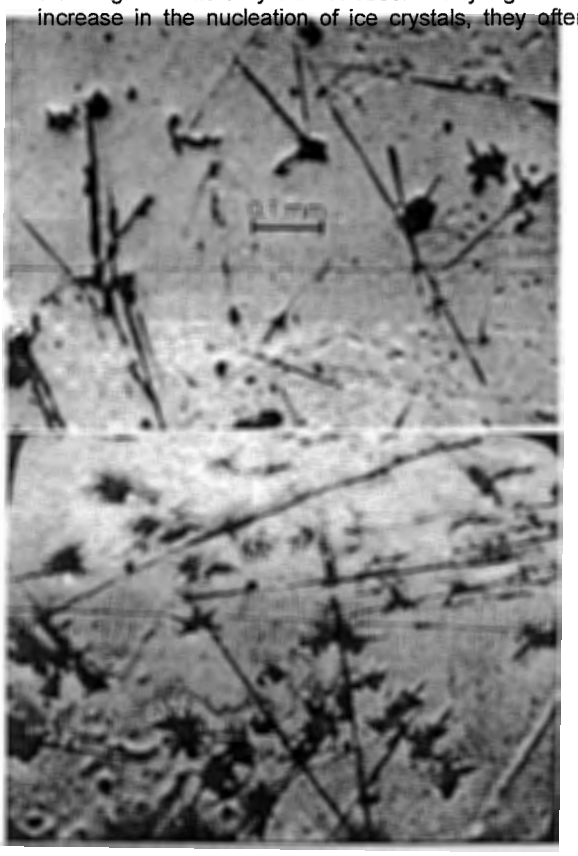

Figure 7. Post corona discharge needles observed by Mandal and Kumar (2002).

collected large numbers of long needle-like crystals growing from compact spatial crystals on microscope slides after short growth periods, examples of which are shown in figure 7. Some of the needles have clearly broken off from a parent crystal.

Field values of 50 kV/m are common in thunderstorm clouds and higher field values may be present under conditions of localized corona emission in addition to lightning discharges. Hence it seems plausible that large numbers of fragile electric needles would be produced under these cloud conditions where water saturation or near water saturation conditions exist. This would be the case for the normal electric needle growth previously reviewed in addition to the extreme growth of anomalous electric needles from post-corona discharge crystals or highly charged crystals in the vicinity of a lightning discharge. In the turbulent environments of thundercloud updrafts where crystal collisions are common, it is likely that these needles would be easily detached from the parent crystal, resulting in an increase of ice crystal concentrations. This multiplication process may continue for some time as observed in the laboratory until crystal charge drops below a critical value.

4. RELEVANCE TO LIGHTNING INITIATION

Currently, two processes are theoretically proposed for lightning initiation, positive streamer corona discharges emanating from ice hydrometeors (graupel and crystals) in strong electric fields and runaway electron avalanches initiated by secondary electrons from cosmic rays which are accelerated by thundercloud electric fields. Positive streamers undergo stable propagation in electric fields that are much weaker than the dielectric strength of air and can intensify and branch in stronger fields. Runaway avalanches or "runaway breakdown' can occur in fields of sufficient strength, though in both of these cases, the required field strengths are larger than those typically observed from hundreds of balloon-borne soundings which seldom exceed 150 kV/m and often don't even reach 100 kV/m. While the observed field strengths do not appear sufficiently strong for either corona discharge or runaway breakdown to initiate lightning discharges, this may be a reflection of the limited resolution of balloon-borne field mills with local field intensification occurring on a spatial scale too small to be detected. It may be that the two processes work in tandem to cause field intensification that results in the formation of a negative stepped leader, resulting in a lightning discharge. A future paper considering this possibility is currently in preparation.

The laboratory results demonstrate that corona emission can occur at temperatures colder than those inferred from previous experiments. They also suggest that highly charged crystals may play an important roll in ice multiplication in thunderstorm environments. One drawback of the current experiment previously mentioned was the interruption of the vapor field during corona discharge measurements. A larger diffusion chamber of improved design is currently being constructed which will eliminate this problem such that discharges can be observed under realistic conditions of relative humidity. These experiments will be complimentary to a series of real magnitude lightning simulations currently being performed at the University of Nevada, Nevada Terawatt Facility (NTF) in Reno Nevada.

ACKNOWLEDGEMENT

This work was supported by NSF-EPSCoR grant EPS-0082725.

REFERENCES

Bailey, M. and J. Hallett 2004: Growth Rates and Habits of Ice Crystals Between -20 °C and -70 °C. *J. Atmos. Sci.* **61**, 514-54.

Griffiths, R.R., and J. Latham, 1974: *Quart. J. Roy. Met. Soc.*, **100**, 163.

Latham, J., 2000: Legacies fund report. *13th International Conference on Clouds & Precipitation.* Reno, Nevada August 14-18, 2000.

Mandal, G. and P. Pradeep Kumar, 2002: A laboratory study of ice nucleation due to electric discharge. *Atmos. Res.*, **61**, 115-123.

AN EXPLICIT ELECTRICAL SCHEME FOR USE IN A CLOUD RESOLVING MODEL

C. Barthe*and J.-P. Pinty

Laboratoire d'Aérologie (CNRS-Université Paul Sabatier), Toulouse, France

1. INTRODUCTION

Electrification of clouds and lightning flash triggering are often related to severe thunderstorms. Lightning flashes are a natural phenomenon that are detectable by spaceborne sensors (LIS, OTD, FORTE) and by several surface networks. Interestingly, lightning flashes are implied as sources of NO_x, although there is a large uncertainty to quantify the amount of NO_x produced by intra-cloud and by cloud-to-ground flashes with different properties. For these reasons at least, it is worthwhile to study many electrical aspects of the storms and for this purpose to develop and evaluate an electrical scheme in a cloud resolving model.

The process of cloud electrification is strongly linked to the microphysics of ice particles and to the dynamics of the flow and of hydrometeors inside a storm. Consequently, it is convenient to consider a complete numerical model and its mixed-phase microphysical scheme. The french mesoscale model MésoNH gives the framework to implement the present cloud electrification parameterization.

There are three distinctive features in a standard electrical scheme. First, the generation and dissemination of electric charges are related to the microphysical description of the cloud. Then, the electric field is computed from the total charge density. Finally, the triggering and the propagation of the lightning channels and the partial neutralization of the electric charges, remains difficult task. A key aspect of cloud electricity is that both local and storm scales are needed to explain the electrical nature of the storms.

In the following, we describe the electrical scheme and we present some results obtained for a 3D idealized thunderstorm.

2. ELECTRIFICATION SCHEME

*Corresponding author's adress : Christelle Barthe, Laboratoire d'Aérologie, OMP, 14 av. E. Belin, 31400 Toulouse, France; E-mail barc@aero.obs-mip.fr.

The scheme (Barthe et al., 2004) is made up with several parts which are summarized in diagram 1. The complete cloud charging process is embedded in the microphysical scheme and the transport of the charges go along with that of the hydrometeors. The electric field is diagnosed at each time step. The occurence of lightning flashes and the charge neutralization is treated by a two step algorithm.

Five categories of hydrometeors (cloud water, rain, pristine ice, snow/aggregates and graupel/hail) and the vapor are considered in the bulk mixed-phase microphysical scheme. The charges are prognostic variables associated to each type of hydrometeor. The ions are also considered.

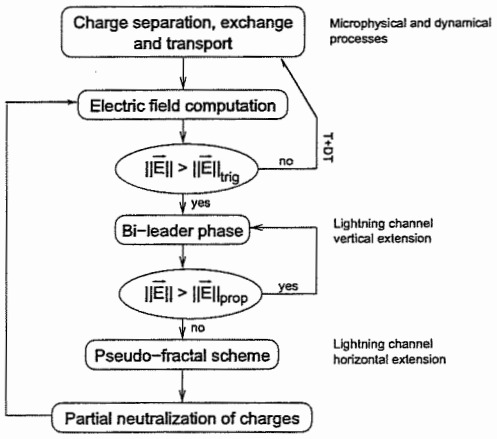

Figure 1: Flow chart of the electrification scheme.

2.1 Charge transfers

Numerous laboratory studies have shown that the non-inductive (NI) mechanism is the most efficient mean to explain the charge structure usually encountered in electrified storms. This involves elastic collisions between two ice particles of different nature (e.g. graupel-pristine ice) during which a variable quantity of charge is separated. Four different parameterizations are available, but in the

following we only present results with two of them (Takahashi, 1978; Helsdon and Farley, 1987).

The simplest parameterization comes from Helsdon and Farley (1987) where the amount of separated charge is fixed, but with a rough dependence of the polarity with temperature.

$$\delta q_{NI}^{HF} = \begin{cases} A & \text{if } T > TCR \\ -A & \text{if } T \leq TCR \end{cases} \quad (1)$$

δq is the charge captured by the biggest particle. TCR is the temperature charge reversal fixed at -10°C for which the sign of the exchanged charge A is reversed. A varies with the type of colliding particles. In case of graupel-ice collisions, the value of the constant is 2×10^{-15} C; it is 2×10^{-13} C and 2×10^{-14} C for graupel-snow and for snow-ice collisions, respectively.

In the parameterization of Takahashi (1978), the sign and the amplitude of the charge exchanged depend on the temperature, the liquid water content, the relative velocity of the two interacting particles and the size of the smallest one.

$$\delta q_{NI}^{T} = f_T(T, LWC) Min \left[10,5 \left(\frac{D_{i,s}}{D_0} \right)^2 \frac{|v_g - v_{i,s}|}{v_0} \right] \quad (2)$$

where f_T(T,LWC) results from an interpolation of the Takahashi's lookup table (Mansell, 2000). v_g is the fall speed of the graupel, and $v_{i,s}$ is that of the small particle (pristine ice or snow). The values of D_0 and v_0 are 10^{-4} m and 8 m.s^{-1}, respectively.

Once the charges have been locally separated by NI processes, the sedimentation of the particles leads to a macroscopic redistribution of the charges. The result is the formation of an intense electric field. In addition, charges are transfered between particles for each microphysical process. The charge transfer rates are computed by integrating the mass transfer rates multiplied by a charge-diameter relationship.

2.2 Electric field computation

The electric field **E** is solution of the Gauss's equation which source is the total charge density ρ :

$$\nabla \cdot \mathbf{E} = \frac{\rho}{\epsilon} \quad (3)$$

ϵ is the electrical permittivity of the air. The elliptic pressure solver of MésoNH is used to solve this equation with appropriate boundary conditions. The upper limit of the computational domain is assumed to be in the ionosphere while the lower limit is the ground level. The upper and lower limits are perfect conductors, and consequently, the electric field vector is orthogonal to these surfaces. Fair weather conditions are applied at the lateral boundaries of the domain.

2.3 Lightning parameterization

When the electric field goes beyond a threshold value, a lightning flash is triggered. There are two stages in the treatment of the lightning. The first one comes from the bidirectionnal leader theory (Kasemir, 1960). A positive leader develops toward the negatively charged region while the negative leader goes through the positively charged region. The bidirectionnal leader follows the line of maximum **E**: the positive (negative) channel of the leader propagates anti-parallel (parallel) to the electric field. As long as the electric field at the end of the positive and negative leaders is large enough to allow for propagation, a new segment is added at the tips of the channel. As soon as the ambiant electric field falls below a threshold value, the bidirectionnal leader stops propagating.

The most original part of the lightning scheme comes from the branching algorithm. Branches are added in regions where the charge density is higher than an prescribed value of the charges and where the local electric potential is higher than the potential of the channel. The maximum number of branches added at a given distance d from the triggering point obeys the fractal law (Niemeyer et al., 1984) $N(d) \sim d^{\chi-1}$. The branching algorithm allows the lightning channel to extend horizontally and to reach highly charged regions but with low electric field that would'nt be attained by the bidirectionnal leader alone.

2.4 Charge redistribution

The amount of charge neutralized along the lightning channel is computed following Ziegler and MacGorman (1994), and MacGorman et al. (2001). Charges are neutralized where the absolute charge density is higher than q_{excess}. If the flash is an intra-cloud flash, a global electrical neutrality is enforced. The quantity of charge to be neutralized is computed for each class of hydrometeor in proportion to their cross section. A cloud-to-ground flash is defined when the downward propagating lightning channel go through the cloud at a height of 1000 m at least. In this case, a connection is drawn perpendical to the ground and no check is performed to ensure the conservation of the total

charges neutralized.

3. NUMERICAL EXPERIMENTS

3.1 High resolution simulation

We choose to simulate an idealized 3D supercellular thunderstorm. The initial sounding is adapted from Klemp and Wilhemson (1978). It is characterized by a strong instability, a sheared environment with veering, and a very dry atmosphere aloft. Convection is initiated by a warm bubble (1.5 K) located in the planetary boundary layer at the south-west of the domain.

The domain is 128 × 128 × 60 points, with a resolution of 500 m in the horizontal and of 250 m in the vertical. The time step is 1s. The parameterization of Helsdon and Farley (1987) is used to initiate the NI charging process with $TCR = -10°C$.

Figure 2 shows the vertical cross section of the snow and the graupel mixing ratios alongwind of the most vigorous cell at 40 min. The coexistence of snow and graupel particles in the upper level of the storm is a favorable condition for cloud electrification as explained above. As shown in Fig. 3,

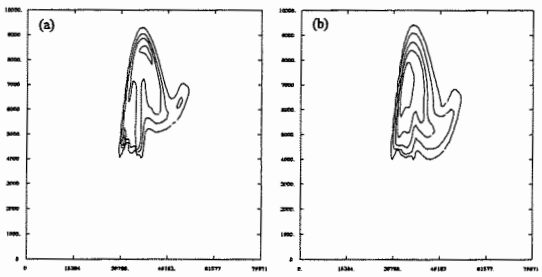

Figure 2: Vertical cross sections along the moving axis of the most vigorous cell of (a) snow (0.1, 0.3, 0.5 and 0.7 g kg^{-1}) and (b) graupel (0.2, 1, 3, 5 and 7 g kg^{-1}) mixing ratios at 40 min.

the snow and graupel charge density reverses polarity at a level corresponding to the -10°C isotherm. It is consistent with the representation of the NI process by Helsdon and Farley (1987). In place where the temperature is lower than TCR, the biggest particle (graupel) gains a negative charge, while the smallest particle (snow) gets a positive charge after rebounding. It is the opposite in the lower levels where the temperature is higher than TCR. The resulting structure of the total charge density is a tripole. This configuration reveals a predominance of the charge carried by graupels and by the pristine ice crystals aloft. This charge

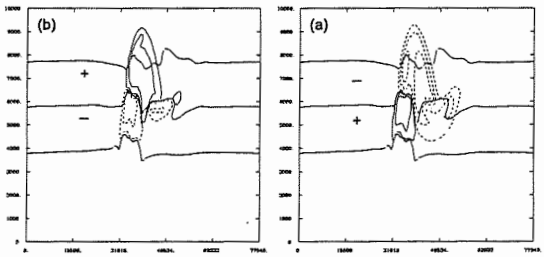

Figure 3: Vertical cross sections of (a) snow and (b) graupel volumic charge densities (-2, -1, -0.5, -0.1, 0.1, 0.5, 1 and 2 nC m^{-3}). Horizontal dashed lines represent temperature (0°C, -10°C and -20°C).

stratification leads to an intense electric field.

The temporal evolution of the maximum electric field module is given in figure 4, with a sampling rate of one point per minute. The figure shows that the maximum electric field remains well below the value of 200 kV m^{-1} all along the simulation. The plot also shows the effectiveness of the lightning scheme that limits the growth of the electric field and the total charge density.

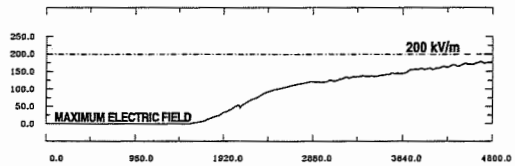

Figure 4: Temporal evolution of the maximum electric field module during the whole simulation. The horizontal line represents a constant electric field of 200 kV m^{-1}.

The temporal evolution of the lightning flash frequency is plotted in Fig. 5. The first lightning flash, an intra-cloud flash, is triggered after 40 min of simulation, this corresponds to the steep increase of the electric field module above 100 kV m^{-1}. Cloud-to-gound flashes occur 17 min later. The total flash frequency peaks around 1.2 flash/s roughly after one hour of simulation.

3.2 Sensitivity tests

In order to test different parameterizations of the NI process, we choose to run the model for the same sounding but with a coarser resolution. The domain is now 40 × 40 × 30 points with a grid spacing of 1000 m horizontally, and 500 m vertically.

Figure 6 presents the vertical cross sections of

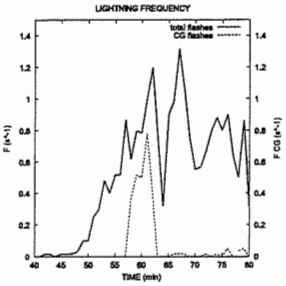

Figure 5: Temporal evolution of the total lightning frequency (bold solid line) and of the cloud-to-ground lightning frequency (dashed line).

the total charge density for different representations of the NI mechanism after 40 min.

The comparison of the results using the parameterization of Helsdon and Farley (1987) with $TCR = -10°C$ (Fig 6a) and with $TCR = -20°C$ (Fig 6b), shows a modification of the total charge structure. In the case of $TCR = -20°C$, the positive charge region of the graupel is increased because more graupels are positively charged under the TCR level.

With the parameterization of Takahashi (1978) depicted in Fig. 6c, more charges are produced in presence of supercooled water, and a tripolar structure clearly shows up.

4. CONCLUSION

An explicit electrical scheme is developed and tested in the cloud resolving model MésoNH. The scheme describes the complex nature of the electrical state of convective clouds including the origin and the spatial distribution of the electric charges, the computation of the electric field and the simulation of the lightning flashes. The study is made for an ideal case of thunderstorm and encouraging results are obtained. The global electrified structure of the storm is consistent with the tripolar picture which evolves along the life cyle of the storm. The maximum values of the mixing ratios and charge densities of each hydrometeor category, as well as the electric field and the lightning flash frequency are in the range of observed values. Further improvements are undertaken in the scheme before testing the model for a real meteorological situation.

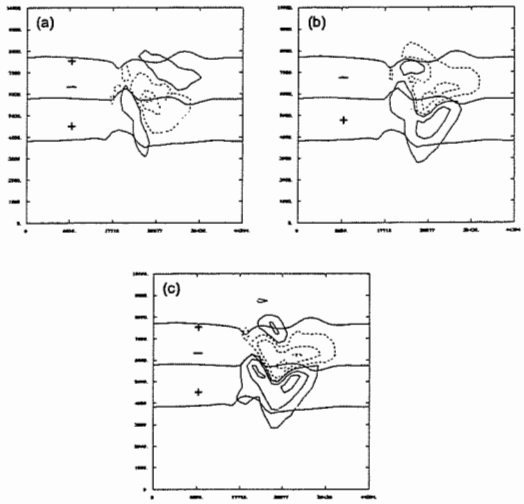

Figure 6: Vertical cross sections of the total charge density for different parameterizations of the NI mechanism : Helsdon and Farley (1987) parameterization with (a) TCR=-10°C and (b) TCR=-20°C, and (c) Takahashi parameterization. Positive charge densities are shown with solid lines (0.1, 0.5, 1 and 2 nC m^{-3}), and negative charge densities with dashed lines (-0.1, -0.5, -1 and -2 nC m^{-3}). Horizontal lines represent temperature (0°C, -10°C and -20°C).

5. REFERENCES

Barthe, C., G. Molinié, and J.-P. Pinty, 2004: Description and first results of n explicit electrical scheme in a 3D Cloud Resolving Model. Atmos. Res., in revision.

Helsdon Jr., J. H., and R. D. Farley, 1987: A numerical modeling study of a Montana thunderstorm : Part 2 : Model results versus observations involving electrical aspects. J. Geophys. Res., 92, 5661-5675.

Kasemir, H. W., 1960: A contribution to the electrostatic theory of a lightning discharge. J. Geophys. Res., 65, 1863-1878.

Klemp, J. B., and R. B. Wilhelmson, 1978: The simulation of three-dimensional convective storm dynamics. J. Atmos. Sci., 35, 1070-1096.

Mc Gorman, D. R., J. M. Straka, and C. L. Ziegler, 2001: A lightning parameterization for numerical cloud models. J. Appl. Meteor., 40, 459-478.

Mansell, E. R., 2000: *Electrification and Lightning in Simulated Supercell and Non-supercell Thunderstorms.* Ph. D. diss., Univ. Oklahoma, 211 pp.

Niemeyer, L., L. Pietronero, H. J. Wiesmann, 1984: Fractal dimension of dielectric breakdown. Phys. Rev. Let., 52, n. 12, 1033-1036.

Takahashi, T., 1978: Riming electrification as a charge generation mechanism in thunderstorms. J. Atmos. Sci., 35, 1536-1548.

Ziegler, C. L., and D. R. MacGorman, 1994: Observed lightning morphology relative to modeled space charge and electric field distributions in a tornadic storm. J. Atmos. Sci., 51, 833-851.

PRECIPITATION AND LIGHTNING ACTIVITY OVER THE MEDITERRANEAN SEA

E. Defer, K. Lagouvardos, D. Katsanos, and V. Kotroni

National Observatory of Athens, Institute for Environmental Research, Athens, Greece

1. INTRODUCTION

Ground based VLF long-range lightning sensors can monitor cloud-to-ground (CG) lightning activity on large scale and during long periods. Because lightning flashes can be instantaneously recorded and located from their electromagnetic radiation, it seems pertinent to use lightning reports for nowcasting applications.

New algorithms are currently under development in order to quantify the rain based on observations from low orbit and geosynchronous satellites. A recent product developed at NASA and labeled 3B42RT, is available (Huffman et al., 2003). It determines precipitation rate based on geosynchronous IR observations and low-orbit microwave measurements.

Several investigations have been published relating CG lightning activity to precipitation. We present here some preliminary results of a comparison of CG lightning activity as sensed by a long range VLF Sferics system and the NASA 3B42RT precipitation rate recorded over the Mediterranean Sea.

2. INSTRUMENTS AND METHOD

The UK Met Office VLF long range Sferics ATD system is designed to record the CG lightning activity (Lee, 1986; Holt et al., 2001). Each of the 8 stations of the ATD system senses the VLF signal radiated during the connection to the ground of the flashes. Each station records accurately the time of the lightning events. After identifying the same events from its waveform, the location of the strike, called ATD fix, is computed from equations dependent on the difference of time arrival of the VLF signal at the ATD stations. The ATD system covers all the Mediterranean Sea. Because a CG flash can be composed of many connections to the ground, and consequently many ATD fixes, algorithms must be developed in order to combine the ATD fixes in flashes based on time and space criteria. Those algorithms have been developed but for the present study, we only use the ATD fixes.

The NASA 3B42RT product provides precipitation rate estimated from infrared satellite observations coupled with microwave low orbit measurements (Huffman et al., 2003). A product dataset is available every three hours near real time. Rain rate is provided within 0.25 x 0.25 degrees grid boxes for latitudes ranging from 50N to 50S, and longitudes ranging from 0 to 360W.

We present here preliminary results of the analysis of CG flash density and rain estimate for 20 different days during the winter 2002-2003 over the Mediterranean Sea. CG flash density was computed per 3-hour period on a same grid as the one used for the estimate of the rain rate. For each grid point, rain rate and CG flash density were compared. Spatial distribution of the lightning activity was also compared to the precipitation field.

3. CASE OF THE 7th NOVEMBER 2002

Figure 1 shows the locations of the CG activity per 3-hour period for the 7th November 2002. During the first hours lightning activity was recorded East of Spain as well as over Greece and Tunisia. The system east of Spain moved southeast to die on the Algerian coastline and stopped producing CG flashes at about 0900 UT. In central Mediterranean Sea the lightning activity was distributed along a very well defined line. This line rotated slowly to the East about a pivot located over the Aegean Sea. Later the southern part of the line started moving faster while the line was still electrical activity at its pivot. After 2100 UT the electrical line started moving toward the Turkish western coastline to finally die along the southwestern Turkish coastline.

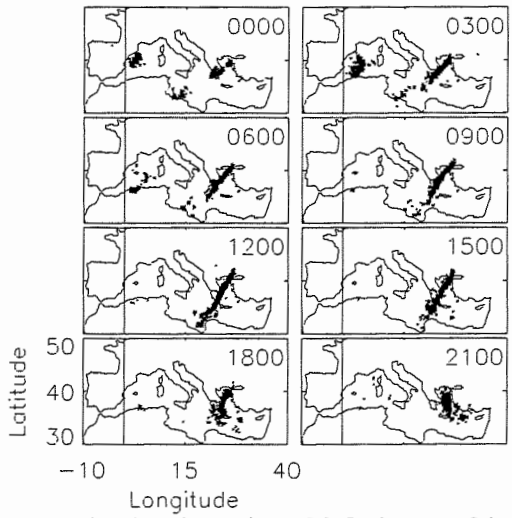

Figure 1. Geo-locations of the CG flashes per 3-hour period recorded on the 7th November 2002.

Corresponding author's address: Eric Defer, National Observatory of Athens, Institute for Environment Research, Lofos Koufou, 15236 Penteli, Greece; E-mail: defer@meteo.noa.gr.

Figure 2 presents the NASA 3B42RT precipitation product as retrieved at 15 UTC on the 7th November 2002 in the Mediterranean region. High precipitation rates were retrieved over Bulgaria, the Aegean Sea and over the southeastern part of Peloponese. Precipitation was also retrieved over Central Mediterranean Sea, the Algerian coastline, the North of Egypt. Precipitation rate was The estimated precipitation rate ranged from 0.1 to 13 m/h.

Figure 3 shows the CG flash density as recorded during the period 1330-1630 UT. As already mentioned CG flashes were distributed in Eastern Mediterranean Sea along a very well defined line. The flash density exceeded 450 flashes per 0.25 x 0.25 degrees for 3 hours.

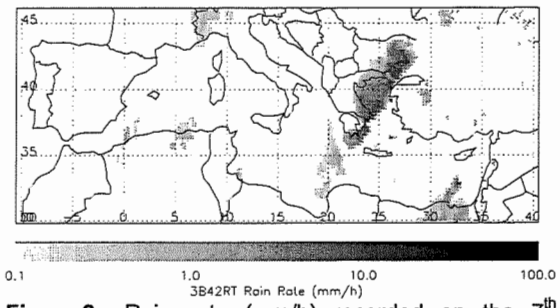

Figure 2. Rain rate (mm/h) recorded on the 7th November 2002 from 13:30 to 16:30 UT.

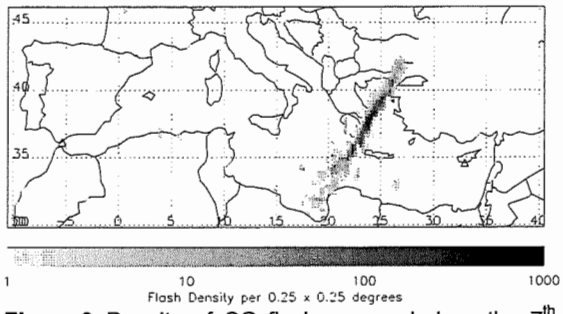

Figure 3. Density of CG flashes recorded on the 7th November 2002 from 13:30 to 16:30 UT per 0.25 x 0.25 degrees (max=476 flashes per pixel).

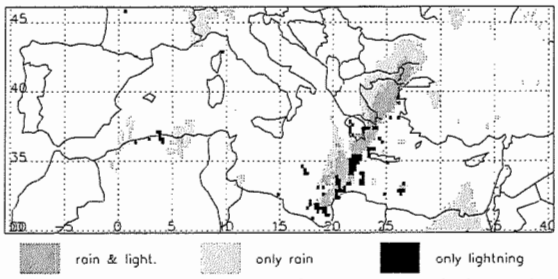

Figure 4. Precipitation and flashes recorded on the 7th November 2002 from 13:30 to 16:30 UTC. Dark, gray and light gray pixels correspond respectively to rain and lightning observed simultaneously (248 pixels), only rain measured (953 pixels) and only lightning recorded in the pixel (133 pixels).

Figure 4 shows an overlay of the precipitation and lightning activity. For the main line, the CG flashes seem to be located in the front of the precipitation field. Over the Aegean Sea, there are relatively few pixels with only lightning flashes, while in the southern part of the line there are more pixels only with lightning flash. This feature may be explained by the fact that the northern part of the line is well organized, while the southern part is composed of isolated and growing electrical cells not yet precipitating.

As expected some rain systems did not exhibit lightning activity. It can be seen in Figure 4 as well as in Figure 5, where for each pixel the precipitation rate is plotted as a function of the 3-hour CG density. Precipitating pixels with no lightning activity are shown with a CG flash density set arbitrary at 0.2. Inversely pixels with only lightning flashes are plotted with a rain rate set arbitrary at 0.002 mm/h. Figure 5 shows that for a given rain rate, the lightning activity can range over many orders of magnitude.

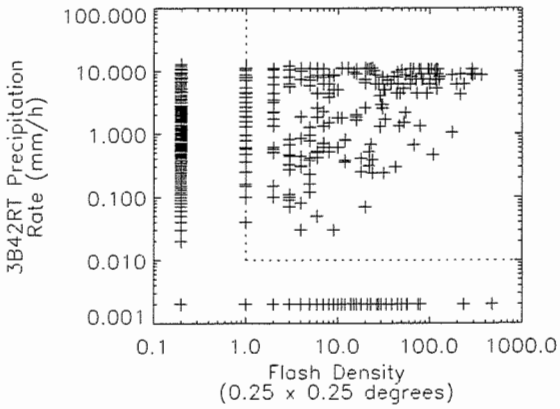

Figure 5. Rain rate (mm/h) as a function of the flash density recorded on the 7th November 2002 from 13:30 to 16:30 UT.

4. OVERVIEW FOR THE 20 DAYS OF THE STUDY

For 20 different days recorded during the winter 2002-2003, we analyzed both 3B42RT rain rate and density of the CG flashes. We noted consistent locations between lightning activity and precipitation field for well-organized systems. However for isolated storms, the 3B42RT algorithm often does not retrieve precipitation while CG lightning activity was recorded. The NASA algorithms might be not sensitive enough to retrieve precipitation for isolated storms.

Figure 6 shows 3B42RT rain rate as function of CG flash density for the 20 days of the analysis. For a given bin of CG flash density, we counted the number of pixels within a given bin of rain rate. Pixels with only one flash exhibited a distribution of the rain rate almost uniform and spanning over a large range. For higher CG flash density, rain rate reached higher values while for a given rain rate, CG flash density can vary over more than 3 orders of magnitude as it was shown in Figure 5. This feature implies that the relationship CG flash density and 3B42RT rain rate is highly variable.

However it appears from Figure 6 that an upper limit of rain rate can be inferred from the CG flash density.

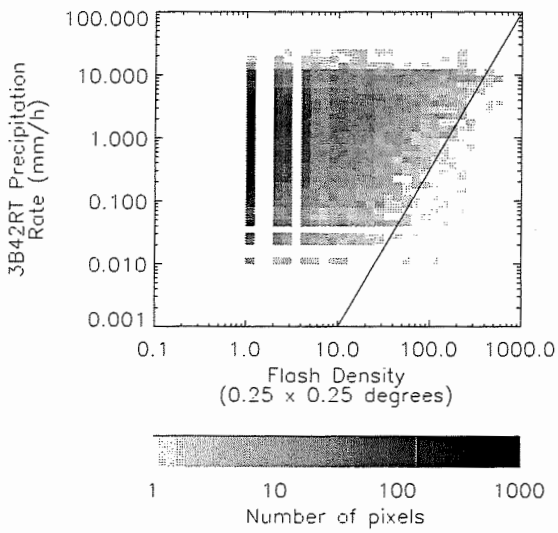

Figure 6. 3B42RT rain rate versus CG flash density for the 20 days for 16255 pixels with lightning and precipitation. Maximum is 334.

5. PROSPECTS

Investigations are underway in order to identify and quantify the different uncertainties in the comparison of the 3B42RT rain rate to the lightning activity. This work will include assessment of errors in the rain rate estimation and in the lightning locations as well as assessment of the impact of the 3-hour time period used in the computation of the lightning flash density.

6. ACKNOWLEDGMENTS

The Greek General Secretariat for Research and Technology (Excellence in Research Centers – MIS64563) supported this work.

7. REFERENCES

Holt, M. A., P. J. Hardaker, and G. P. McLelland, 2001: A lightning climatology for Europe and the UK, 1990-99, Weather, 56, 290-296.

Huffman, G.J, R.F. Adler, E.F Stocker, D.T. Bolvin and E.J. Nelkin, 2003: Analysis of TRMM 3-hourly multi-satellite precipitation estimates computed in both real and post-real time. *Proceedings of the 12th Conference on Satellite Meteorology and Oceanography*, AMS, Long Beach California, 10-13 February 2003

Lee, A. C. L., 1986: An experimental study of the remote location of lightning flashes using VLF arrival time difference technique, Q. J. R. Meteorol. Soc., 112, 203-229.

DERIVATION OF THUNDERSTORM ICE HYDROMETEOR CHARACTERISTICS FROM LIGHTNING MEASUREMENTS

Wiebke Deierling[1], Walter A. Petersen[2], John Latham[3#], Scott M. Ellis[3] and Hugh J. Christian Jr[4]

[1]University of Alabama, Huntsville, Alabama, USA
[2]Earth System Science Center, University of Alabama, Huntsville, Alabama, USA
[3]National Center for Atmospheric Research*, Boulder, Colorado, USA
[#]Also at: Physics Dept, UMIST, Manchester, UK
[4]Global Hydrology & Climate Center, NSSTC, Huntsville, Alabama, USA

1. INTRODUCTION

Thunderstorm electrification resulting in lightning activity is very complex and not yet fully understood. To produce lightning, in general, a strong updraft in the mixed phase region is required. This is the region where non-inductive charging mechanisms are thought to generate most of the storm electrification. Non-inductive charging mechanisms include graupel and smaller ice interactions and depend on liquid water content, temperature, size, and collision velocity of the particles. It is thought that the extent of the zone where effective charging takes place is limited (Latham et al., 2003). The upper limit of the charging zone is thought to be a diffuse level above which graupel can no longer be supported by the updraft and supercooled liquid water is absent. The lower boundary of the charging zone is also diffuse and depends on the prevailing glaciation mechanism, but might characteristically be taken to be a few degrees colder than 0°C.

Analytic calculations by Blyth et al. (2001), Latham et al. (2003) and Petersen and Rutledge (2001) yielded the prediction that the lightning frequency f was roughly proportional to the product of the downward mass-flux p of solid precipitation (graupel) and the upward mass-flux I of small ice crystals, the values of p and I being those at the top of the charging zone. Hereafter this relationship will be referred to as the flux hypothesis. The predicted equation, valid in the charging zone, that describes the flux hypothesis is:

$$f = C \cdot p \cdot I,$$

where C is a constant.

To investigate this hypothesis further, this study compares trends of precipitable ice as well as small ice with total lightning activity of the Radiation, Aerosols and Ozone (STERAO) 10 July storm. Precipitable ice as well as small ice were determined using Colorado State University (CSU) CHILL S-band polarimetric radar data and the National Center for Atmospheric Research (NCARs) hydrometeor classification algorithm (Vivekanandan et al. 1999, Straka et al. 2000,) that relates the radar data to bulk microphysical hydrometeor types. It should be kept in mind that radar reflectivity, which is weighted heavily in hydrometeor classifications, depends on the 6th power of the particle diameter. Thus the radar measurements are dominated by the largest particles in the resolution volume and will not detect smaller ice crystals or droplets mixed with graupel. However, results of this study show that bulk microphysical trends categorized as precipitable ice (graupel, hail) and smaller ice are related to lightning activity.

2. DATA

The data presented in this study were collected during the Stratospheric-Tropospheric Experiment: Radiation, Aerosols and Ozone (STERAO) experiment that took place in Northern Colorado in the summer of 1996. For the 10 July storm, polarimetric radar data was collected from the CSU-CHILL radar and total lightning activity was recorded by the Office Nationale d'Etudes et de Recherches Aerospatiales (ONERA) 3-D lightning interferometer as well as cloud-to-ground lightning by the National Lightning Detection Network (NLDN).

Corresponding author's address: Wiebke Deierling, Univ. Ala. Huntsville, Dept. Atmos. Science, 320 Sparkman Dr., Huntsville Al., 35805; email: deierling@nsstc.uah.edu

*NCAR is sponsored by the National Science Foundation

3. METHOD

The NCAR Particle Identification Algorithm (PID) (Vivekanandan et al., 1999) was used to determine hydrometeor types and it distinguishes between 14 hydrometeor types. The hydrometeor types relevant to this study include graupel, graupe/rain, hail, hail/rain, dry snow, irregular ice crystals, and oriented ice crystals. Due to similarities and ambiguities among some of the hydrometeor classifications, two or more particle classifications were in some cases added together. For example the PID categories of hail, hail/rain, small hail/graupel and small hail/graupel/rain above the 0°C level are added together to form the precipitable ice category. In this study, radar fractions of those hydrometeor types identified in the PID algorithm that are most likely to contribute to the verification of the flux hypothesis were computed. The volumes of the individual radar gates were computed in radar coordinates and summed over the entire radar volume scan. The particle volumes were then normalized by the total storm volume defined as the region containing hydrometeor classifications from the PID and in the following addressed as fractions. The scanning strategy used resulted in beam overlaps in elevation angle, which were accounted for in computing the bulk hydrometeor volumes. Beam overlaps present in the radar volume scans were removed by splitting the overlapped region into two equal parts and assigning particle types identified in the lower (upper) beam to the bottom (upper) half of the overlapping region. The volume time was defined to be the center time of the volume scan.

4. STERAO 10 JULY STORM

The STERAO 10 July storm developed northwest of Kimball, Nebraska. It exhibited lightning activity for approximately 4.5 hours between 21:52 UTC and 02:32 UTC 11 July. For the first 3 hours, the storm had a multicellular character with several cells elongated along a confluence line. In its later stage - around 01:15 UTC – it evolved into a low precipitation supercell storm with rotation at lower levels as well as a bounded weak echo, but not having a well defined precipitation shaft. The total lightning frequency peaked at over 50 flashes per minute in both the multicellular and supercellular stages, at around 23:15 UTC and 01:30 UTC respectively. Several smaller peaks in lightning frequency occurred during the transition period between multicell and supercell stages. A comparison with the radar data shows that these peaks in lightning activity occurred during new cell development and subsequent merges. Note, that this storm exhibited little cloud-to-ground lightning and over most of its lifecycle the ratio of intra-cloud to total lightning was larger than 95% (Dye et al, 2000; Lang et al., 2000; Defer et al., 2001).

5. RESULTS

The flux hypothesis proposes that total lightning flash rate, f, is correlated to the product of the upward ice mass flux, I, and the downward precipitable ice mass flux, p. In the following, trends of precipitable ice fractions and small ice fractions are presented.

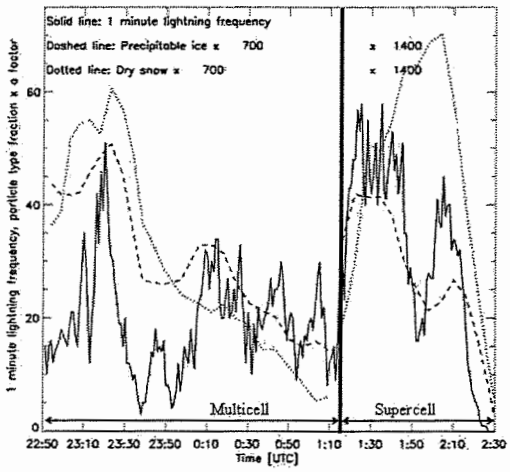

Figure 1. *Time series of total lightning flash rate (flashes per minute), dry snow fractions above the -45°C level, precipitable ice fractions above the 0°C level. The vertical black line at 1:15 UTC marks the separation between the multicellular and supercellular character of the storm. Dry snow fractions and precipitable ice fractions were multiplied by a factor of 700 for the multicellular part of the storm and by a factor of 1400 for the supercellular part of the storm.*

Figure 1 shows a time series of total lightning frequency, f, per minute and the values of hydrometeor fractions for precipitable ice above 0°C and dry snow above -45°C. Note, that scaling actors were applied to the lighting data to facilitate interpretation of the graphs. The supercell stage was scaled by a factor twice that of the multicell stage due to the significantly

smaller total storm volume for the supercell stage.

In Figure 1 the two major peaks in f at around 23:15 and 1:30 UTC are seen to be well correlated with the relative trends of both precipitable ice fractions and dry snow fractions. The precipitable ice fractions are also well correlated with a smaller peak in f near 02:10 UTC, and the dominant peaks occurring in the transition between multicell and supercell stages.

The dry snow category is presented in Figure 1 rather than the sum of the non-precipitating ice particles (dry snow, irregular ice, oriented ice categories) because the correlation with lightning was not visible for total ice fractions located above the 0°C level. It turns out that the calculated radar fractions of total non-precipitating ice are quite large and are dominated by small ice residing in the anvil. This suggests that changes in the small ice volume fraction due to the upward flux are overwhelmed by the long-lived anvil and are difficult to detect. Also the non-precipitable ice-mass we are concerned with is located in the charging region (mixed phase zone) where radar parameters are dominated by larger rimed hydrometeors, which effectively mask the presence of smaller ice particles. Thus as a working proxy, we assume that the small ice and snow particles generated in the charging zone, and involved in the charging process, have small terminal velocity and are eventually transported upward and detrained into the anvil region above the -45°C level. For example, Rutledge and MacGorman (1988) and Schuur and Rutledge (2000) suggest that snow advected rearward into the anvil and growing in an ice-saturated environment (through aggregation), is a dominant carrier of positive charge in stratiform regions of mesoscale convective systems. This suggests that temporal trends in radar returns categorized by the PID as dry snow in the upper regions (Temperature ≤ -45°C) of convection may capture fluctuations in smaller crystal ice (mass) fractions related to charging.

While the correlations between precipitation-ice, dry snow fractions, and lightning are not totally unexpected, the flux hypothesis actually concerns the product of the upward ice crystal and downward precipitation ice fluxes. Figure 2 presents a time series of f and the product of the trend for precipitable ice fractions (sum of hail, small hail/graupel, hail/rain mix, small hail/graupel/rain mix categories above the 0°C level) and non - precipitating ice (dry snow

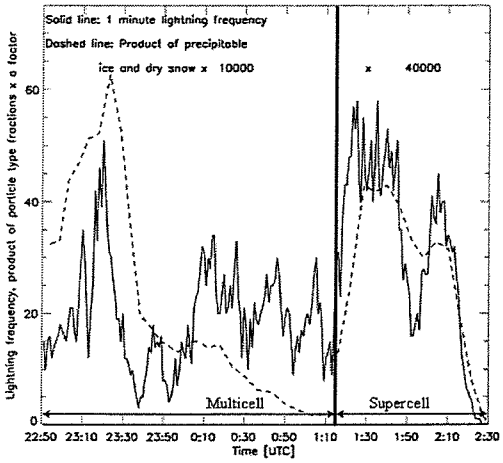

Figure 2. *As in Fig. 1 but trend of the product of the dry snow fraction above the -45°C level and precipitable ice fraction above the 0°C level.*

fractions above the -45°C level). As expected level) and non-precipitating ice (dry snow figure 2 shows that this product has its most significant peaks at times close to those of the primary peaks in lightning activity. However, no significant correlation is found between these two parameters for smaller-scale features.

As mentioned above, the flux hypothesis involves the upward mass-fluxes, not only trends of the volume/fraction displayed or utilized in figures 1 and 2. Therefore these trends have to be multiplied by the updraft speed and by calculated particle type masses in order to obtain the flux of dry snow as well as precipitable ice.

Very preliminary results using divergence fields computed from radial velocities indicate that increases in upper level divergence consistent with stronger updrafts coincide with increased lightning activity. As mentioned before, the peaks of precipitable ice and dry snow trends are larger for the multicellular peaks than for the supercell stage. In the multicellular stages, two or more cells contribute differently to hydrometeor fractions as they grow, decay or merge, as opposed to just one cell in the supercellular stage. The supercellular stage, with its single core, does not produce the large ice fractions noted for the multicellular stages. Nevertheless, it seems to be more efficient in producing lightning. This may be compensated for in part due to the presence of larger updraft speeds in comparison to the cells in the multicellular stage. This is consistent with the flux hypothesis because the higher updraft

speeds would increase the mass flux and thus increase the lightning frequency f, accounting for similar lightning frequencies but different volumes of the multi and supercell stages.

6. CONCLUSIONS AND OUTLOOK

In this study some provisional support exists for the flux hypothesis. Bulk microphysical trends of dry snow fractions above -45°C and precipitable ice fractions above 0°C show reasonably good correlation to the lightning activity of the 10 July storm.

Future plans include calculating the mass of hydrometeor types and the updraft speeds. Calculating the mass and vertical velocity to estimate the mass fluxes might equalize differences in trends between the multicellular stage and supercellular stage, e.g. the supercellular stage may exhibit stronger updrafts, thus compensating a reduction in the product of p and I but maintaining or increasing f. Furthermore, for the multicellular stage of the storm a cell analysis will be performed to take into account different contributions of growing, decaying and merging cells.

7. ACKNOWLEDGEMENTS

JL wishes to acknowledge the support of USRA/NASA. WAP and WD acknowledge funding from NASA ESE Lightning Imaging Sensor Project. WD would like to thank Dr. Jim Dye for helpful discussions. The authors gratefully acknowledge Mr. David Brunkow and Mr. Patrick Kennedy for providing the CHILL radar data and Dr. Eric Defer for providing total lightning data for the STERAO 10 July storm.

REFERENCES

Blyth, A.M., Christian H.J., Driscoll, K., Gadian, A.M. and J. Latham, 2001: Determination of ice precipitation rates and thunderstorm anvil ice contents from satellite observations of lightning. *Atmos. Res.*, **59-60**, 217-229.

Defer, E. P. Blanchet, C. Thery, P. Laroche, J.E. Dye, M. Venticinque, K.L. Cummins, 2001: Lightning activity for the 10 July, 1996, storm during the Stratosphere-Troposphere Experiment: Radiation, Aerosol, and Ozone-A (STERAO-A) experiment. *J. Geophys. Res.*, **106**, 10,151-10,172.

Dye, J.E., Ridley, BA, Skamarock W., Barth, M., Venticinque, M., Defer, E, Blanchet, P., Thery, Laroche, P., Baumann, K., Hubler, G., Parrish, D.D., Ryerson, T., Trainer, M., Frost, G., Halloway, J.S., Matejka, T., Bartels, D., Fehsenfeld, F.C. Tuck, A., Rutledge, S.A., Lang, T., Stith, J., Zerr, R., 2000. An overview of the Stratospheric-Tropospheric Experiment: Radiation, Aerosols, and Ozone (STERAO)-Deep Convection experiment with results for the July 10, 1996 storm. *J. Geophys Res.*, **105**, 10,023-10,045.

Lang, T.J., S.A. Rutledge, J.E. Dye, M. Venticinque, P. Laroche and E. Defer, 2000: Anomalously low negative cloud-to-ground lightning flash rates in intense convective storms observed during STERAO-A. *Mon. Wea. Rev.*, **128**, 160-173.

Latham, J., Blyth, A.M., Christian, H. J. Jr., Determination of Precipitation Rates and Yields from Lightning Measurements, *J. Hydrol.*, accepted.

Rutledge, S. A., and D. R. MacGorman, 1988: Cloud-to-ground lightning activity in the 10-11 June 1985 mesoscale convective system observed during OK PRE-STORM. *Mon. Wea. Rev.*, **116**, 1393-1408.

Schuur, T.J., and S.A. Rutledge, 2000: Electrification of stratiform regions in mesoscale convective systems. Part I: An observational comparison of symmetric and asymmetric MCSs. *J.* Atmos. Sci., **57**, 1961-1982.

Straka J.M., D.S. Zrnic, A.V. Ryshkov, 2000: Bulk hydrometeor classification and quantification using polarimetric radar data: synthesis of relations. *J. Appl. Meteor.*, **39**, 1341-1372.

Petersen, W.A. and S.A. Rutledge, 2001: Regional Variability in Tropical Convection: Observations from TRMM. *J. Climate*, **14**, 3566-3586.

Vivekanandan, J., D.S. Zrnic, S. M. Ellis, R. Oye, A. V. Ryzhkov, and J. Straka, 1999: Cloud microphysics retrieval using S-band dual-polarization radar measurements. *Bull. Amer. Meteor. Soc.*, **80**, 381-388.

AIRBORNE OBSERVATIONS OF MICROPHYSICS AND ELECTRIC FIELDS IN ANVILS OF FLORIDA THUNDERSTORMS

J. E. Dye[1], S. Lewis[1], W. D. Hall[1], J. C. Willett[2], P. Willis[3], A. C. Grainger[4], D. Mach[5], M. Bateman[5] and H. J. Christian[5]

[1]National Center for Atmospheric Research, Boulder, Colorado, USA
[2]Garrett Park, Maryland, USA
[3]NOAA/Hurricane Research Division, Miami, Florida, USA
[4]Univ. of North Dakota, Grand Forks, North Dakota, USA
[5]NASA Marshall Space Flight Center; Huntsville, Alabama, USA

1. INTRODUCTION

Numerous studies have been conducted to examine the microphysical conditions that are present in convective clouds when charge separation is occurring and electric fields are intensifying. There also have been some studies that use multi-parameter radar to examine particle types in relationship to lightning frequency and storm type. But few studies have been conducted to examine the changes in microphysics when electric fields are decaying after lightning has ceased. At NASA Kennedy Space Center (KSC) Florida triggered lightning is a significant hazard to the launch of the shuttle and other space vehicles. In the case of anvils, an important question is: "How much time must elapse after the last lightning before a vehicle can be launched safely through different locations in an anvil." During June 2000 and 2001 the Airborne Field Mill (ABFM) project was conducted at KSC to investigate the relationships in anvils between microphysics, radar reflectivity and the decay of electric fields spatially and temporally. In-situ observations of electric field, particle concentrations, types and sizes and standard thermodynamic and flight measurements were made from the Citation II jet aircraft of the Univ. of North Dakota. The aircraft measurements were coordinated with radar measurements from the Patrick Air Force Base WSR74C, 5 cm, radar and the Melbourne, Florida NEXRAD, 10 cm radar. Measurements of total lightning (IC and CG) were made using the KSC Lightning Detection and Ranging (LDAR) and the Cloud to Ground Lightning Sensing systems. In this paper we present an example of observations for one anvil case and some results from the project.

Corresponding Author: James E. Dye, NCAR, Boulder, CO, 80307, E-mail: dye@ucar.edu

2. THE ANVIL OF JUNE 4, 2001

The storm of June 4, 2001, one of our best anvil cases, first formed NE of Lake Okechobee around 1900 with first anvil formation around 1915. The anvil tip moved towards 110 degrees at about 18 m/s. The Citation investigated this anvil for over 3 hours, first with a NS pass very near the storm core at 2010. An example of measurements for one E to W pass almost 2 hrs after anvil formation is shown in Fig. 1. In this figure the eastern edge of this anvil is roughly 150 km from the convective core and the Citation is 100 to 125 km downwind of the core. Lightning was still occurring in the core and sporadically extended out as much as 75 km into the anvil.

The radar structure shown in Fig. 1 is the curtain of reflectivity along the Citation track. Until ~2108 the aircraft was flying north across the eastern part of the anvil but after 2108 was heading ~290 degrees along the center of the anvil at a temperature of –36C. From 2108 to 2116 there is a gradual increase of particle concentration in all size ranges, but the increase is slightly larger for the smaller particles. The electric field is weak (<2 kV/m) until after 2110 but rapidly increases to >10 kV/m by 2111 with lots of variability. Note that the abrupt increase in electric field occurs as the aircraft flies into reflectivities of 10 to 15 dBZ. We often, but not always, found that electric field rapidly increased when the aircraft entered reflectivities ~>10 dBZ.

The microphysical observations were made with the PMS FSSP, 1D-C, 2D-C and the SPEC Cloud Particle Imager and High Volume Particle Spectrometer, thus spanning particle sizes from a few microns to about five centimeters, i.e. frozen cloud droplets to very large aggregates. A Rosemont icing detector showed no evidence of supercooled water in any of the anvils investigated. All particles discussed herein are

ice. The 3-dimensional vector electric fields were measured using a set of 6 field mills as described in Mach and Koshak, 2003 and had a range from <0.1 to >100 kV/m.

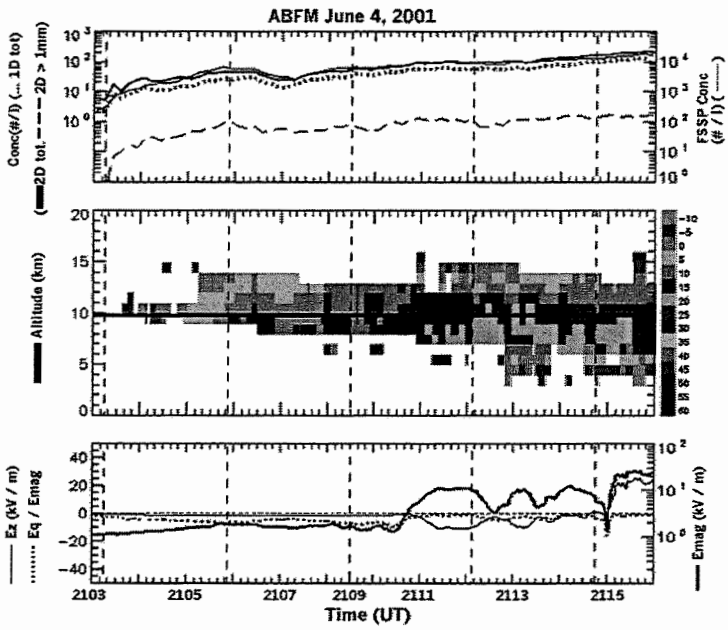

Figure 1

Top Panel: Time history of Particle concentrations:
FSSP: light, solid line = total conc. On right
2D-C: bold line = total conc., dashed line = conc. >1 mm on left
1D-C: dotted line = total conc. on left

Middle Panel: Radar reflectivity curtain above and below the aircraft from WSR74C radar at Patrick AFB FL, bold line = aircraft altitude

Bottom Panel: Vertical electric field, Ez, light line on left, linear scale, and the resultant vector field, Emag, bold line on right, log scale.

The measurements in this and other anvils show that when electric fields are strong (> 10 kV/m) the concentration of particles in all sizes is significantly greater than when electric fields are weak (< 1 kV/m). In regions with strong electric fields the microphysical observations showed a surprising consistency of concentrations of all sizes from one storm to another. As the aircraft flew from downwind edges of anvils towards the convective cores, concentrations in all size ranges gradually increased. Normally, the electric fields increased more abruptly and showed much greater variability.

Figure 2 shows number and particle area size distributions for 4 separate 30 s averages along the flight track. The first three are for selected times from Figure 1 to illustrate changes in distribution as the aircraft flies towards the storm core. Images from the CPI show the smaller particles to be frozen cloud droplets, particles from ~0.1 to roughly 0.4mm were mostly irregular or small aggregates, but those larger than ~0.4 mm and the larger ones are aggregates some of which were nearly 1 cm. We want to emphasize that even at this eastern extent of the anvil ~125 km downwind of the core there are aggregates >1 mm size. Either the aggregates have not fallen out, or more likely, aggregation is continuing to occur. Given the strength of the electric fields in some parts of this anvil, it is probable that they enhanced aggregation. There was normally little evidence of riming except close to the convective cores.

3. THE ROLE OF MICROPHYSICS IN THE DECAY OF THE ELECTRIC FIELD IN ANVILS

An estimate of the decay of electric field with time has been calculated using a simple model (Willett and Dye, 2003). The mechanism for field decay in the model is that ions produced by incoming cosmic rays attach to cloud hydrometeors by electrical drift and diffusion, thereby decreasing the bulk conductivity inside the cloud. Bulk current flow to the surfaces of the anvil reduces the charge contained in its interior. The model assumes no turbulent mixing, no sedimentation of particles and the absence of active charge separation in the anvil. The model calculates electric-field decay times based on observed particle size distributions and assumes that a given size distribution is uniform and constant everywhere in the model anvil during the decay of electric field. The assumptions provide lower bounds on the rate of decay of electric field and upper bounds on the time to decay. A "high-field limit" is identified, for ambient field intensities greater than about 1 kV/m, in which the model field decays linearly with time; and a decay time scale, τ_E, is defined

as the time required for the cloud field to decay to zero from an arbitrary initial value of 50 kV/m. τ_E is found to be proportional to the particle effective electrical cross section (area), integrated over the size distribution. See Willett and Dye for more details.

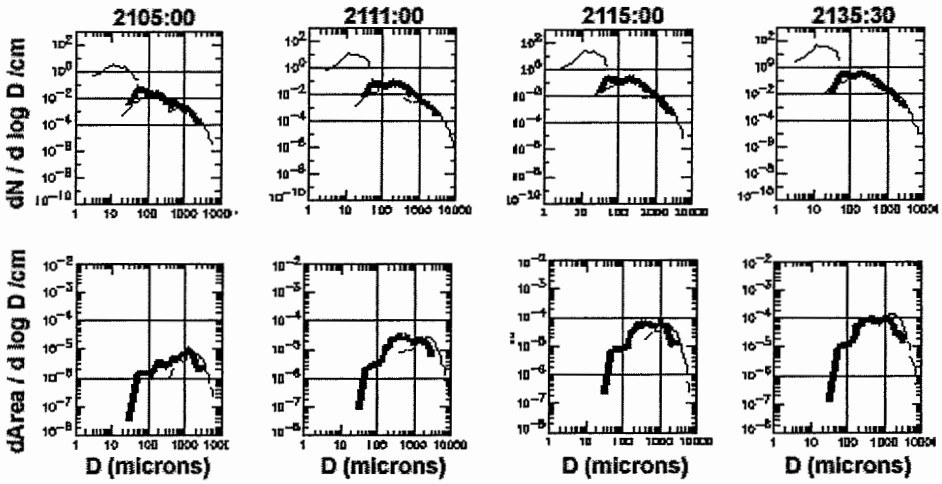

Figure 2. Top: Number size distributions (30 sec averages) for times as indicated. Bottom: Particle area size distribution for the same periods. Light line on the left of each plot – FSSP (off scale for area); Bold line – 2D-C; light line on right – SPEC High Volume Particle Spectrometer.

Particle area distributions in Figure 2 show a peak near 1 mm in the edge of the anvil, but as the aircraft moves more centrally into the anvil, the area distributions have a broad mode from 0.2 to 2 mm and show the dramatic increase of almost two orders of magnitude in integrated area. This dramatic change in area from 0.2 to 2 mm was found for all anvils that contained strong fields. The observations coupled with model results show that this part of the size distribution largely controls the rate of field decay in these anvils. τ_E for the first 3 time periods of Figure 2 is 351, 2105, 3037 s, respectively. τ_E increases by a factor of 10 from the edge to the central part of the anvil. Thus on the edge of the anvil the decay of electric field is very rapid (<10 min) while in regions with greater concentrations, particularly in the range of 0.2 – 2mm the decay will be much, much slower.

4. SECONDARY DEVELOPMENT OF A STRATIFORM-LIKE AREA

During the first 1 ½ hr of the growth of this anvil, it had the structure of a classic anvil with blow-off and translation down wind of material ejected from the core of the storm. But beginning around 2045 an area of reflectivity >20 dBZ began to appear, particularly at 7 - 8 km. This was not sedimentation alone because a N-S penetration at 2040 to 2045 in the same drifted locale as Fig. 1 shows reflectivity at all altitudes to be <20 dBZ. The radar curtain in Fig. 1 is during the early stage of this "secondary development". By 2130 the area of reflectivity >20 dBZ at 7 km had grown considerably both horizontally and somewhat vertically. Fig. 3 shows the vertical curtain of reflectivity, particle and electric field measurements along the Citation track for 2130 to 2140 in this secondary development.

This pass, just as that in Fig. 1, was toward the WNW and along the main axis of the anvil. Compared to Fig. 1 the increase in reflectivity is readily apparent as is the relatively uniform structure. Similarly, the particle concentrations were relatively uniform and the electric field was uncharacteristically uniform, unlike those in Fig. 1, with strong electric fields of 25 to 30 kV/m. At the 120 m/s flight speed of the Citation this is a distance of ~70 km. At its largest extent near ~2200 this feature had a length of 50 to 75 km and was 40 to 50 km across. Even though the vertical structure such as that in Fig. 3 looks like an anvil, this anvil has evolved into a stratiform-like area. This stratiform area persisted until at least ~2245. By this time it was at the limit of the radar range.

Between 2045 to 2200 reflectivity has grown in area and magnitude. Electric fields have

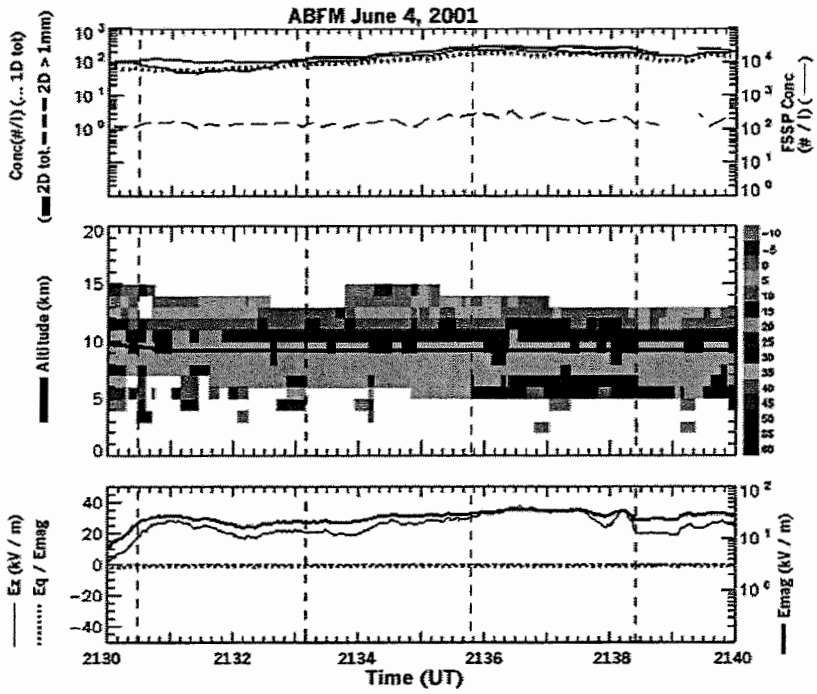

Figure 3. As in Figure 1 except for time period 2130 to 2140

maintained themselves and grown in area and uniformity. Similarly particle concentrations and sizes of the largest particles have grown (Fig. 2, 2115 compared to 2135:30). The cross sectional area size distribution has also increased causing the electrical decay time, τ_E, to increase from 3037 to 5662 s (46 to 94 min) between 2115 and 2135:30.

There were probably several reasons for this development. First, the base of the anvil started to drop below the melting level near 2100. Charge separation in melting zones has been well documented by others (Shephard et al., 1996). Electric fields grew strong enough to enhance the aggregation process, leading to larger particles and reflectivity. But if reflectivity growth was due to aggregation alone we would expect a decrease in the concentration of the small and intermediate particles. But Fig. 2 clearly shows increases rather than decreases in this range. The area of this anvil and secondary development was ~100 km east of the coast and probably over the gulf stream, a source of moisture and warmer temperatures, possibly inducing additional dynamical circulation. This seems to be fairly common off the coast east of KSC, and warrants further investigation. We observed at least 3 cases for which stratiform-like development occurred from an anvil.

ACKNOWLEDGEMENTS

The ABFM project was funded primarily by NASA Kennedy Space Center with a significant contribution from the National Reconnaissance Office. NCAR is sponsored by the National Science Foundation.

REFERENCES

Dye, J.E. et al., 2003: The Decay of Electric Field in Anvils: Observations and Comparison with Model Calculations, Proc. Internat. Conf. on Atmospheric Electricity, Versailles, France, June 2003.

Mach, D. M. and W. J. Koshak, 2003: General Matrix Inversion Technique For The Calibration Of Electric Field Sensor Arrays On Aircraft Platforms, Proc. Internat. Conf. on Atmospheric Electricity, Versailles, France, June 2003.

Willett, J.C. and J.E. Dye, 2003: A Simple Model to Estimate Electrical Decay Times in Anvil Clouds, Proc. Internat. Conf. on Atmospheric Electricity, Versailles, France, June 2003.

Shephard et al., 1996: Electric Fields and Charges near 0C in Stratiform Clouds, Mon. Wea. Rev., **124**, 919-938.

THE ELECTRICAL FIELD BENEATH THE THUNDERSTORMS AND ITS RELATIONSHIP WITH THE METEOROLOGICAL VARIABLES

Valter Gennaro*, Dario B. Giaiotti†, and Fulvio Stel†

† OSMER - ARPA FVG Regional Meteorological Observatory Italy
* FENICS Work Group - Unione Meteorologica del Friuli Venezia Giulia

1 INTRODUCTION

It is well known that deep atmospheric convection is related to lightning strikes and that they occur as the result of an high electrical potential difference between two areas in a thundercloud or between the cloud and the ground. Lightning strikes are just the visible and the most violent manifestation of clouds electrification, Rakov and Uman (2003); generally the electrical field belonging to a cloud is the physical variable suitable for investigating electrification effects produced by convection. In each point of the space, the atmospheric electric field is a function of the charge density distribution which is related to the charge separation processes. In this work measurements produced by a field mill placed at the ground are compared in various meteorological situations such as thunderstorms, non convective rains and non convective snowfalls; preliminary results on the measurements beneath thunderstorms are shortly discussed.

2 MEASUREMENTS

The Earth electric field has been measured by means of an electric field meter (MacMorgan and Rust 1998). The instrument has been made according to a well known principle (Winn 1993) and it has been placed in the northeastern Italy. The measurement site is in the open country, close to a village (Ziracco) located in the plane, and the field meter is quite far from the influence of artificial or natural vertical structures, like buildings or trees; the surrounding terrain is flat. Calibration of the field meter has been done every three months; records are almost continuos time series of the Earth electrical field with a time resolution of 1 second.

Corresponding author's address: Dario B. Giaiotti, OSMER-ARPA FVG, Via Oberdan 18/A, I-33040 Visco (UD) ITALY, E-Mail dario.giaiotti@osmer.fvg.it

The precision of the measurements are about 20 Vm^{-1}. Northeastern Italian plane is a very interesting meteorological region because it experiences a variety of weather situations: quite cold winters with snowfalls, heavy precipitation events caused by the Alpine ridge orographic effects on the Mediterranean moist fluxes and stormy events. The daily climatological probability for thunderstorms is close to 0.6 in the summer period, that is from April to September (Prodi 1976, Giaiotti and Stel 2001). These weather characteristics give the opportunity to measure the Earth electrical field, in the same geographical place, during the occurrence of very different meteorological phenomena.

3 NON CONVECTIVE RAINS

During non convective rain events, the electric field presents variations.

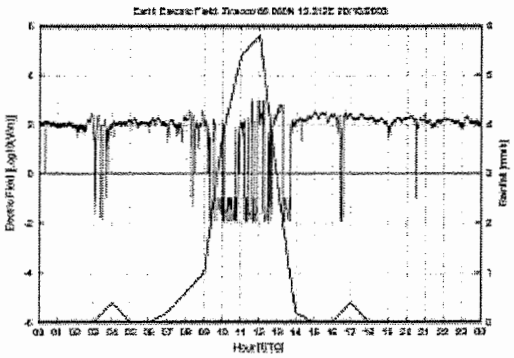

Figure 1: time series of Earth electric field and hourly rainfall measurements recorded on October 20, 2003. Field intensity [V m^{-1}] is plotted in logarithmic scale (left) and rainfall in [mm h^{-1}] in liner scale (right). The jagged curve refers to the electric field while the hourly broken line is that of precipitation.

Usually the amplitude of variations seems to be slightly correlated with the rainfall intensity.

A general behaviour of the electric field during this kind of precipitation is it inversion, in fact from the fair weather downward direction, it suddenly points upwards when rainfall is measured, as in the case of an excess of negative charges present at the ground. The amplitude of the upward field is comparable with that downward measured before and after the rainfall. Figure 1 shows the field intensity time series recorded in a rain day superimposed to the hourly rainfall measurement. Positive values represent field pointing downward. In that episode the upward field intensity was non larger than 100 V m^{-1}.

4 THUNDERSTORMS

Thunderstorms produce large changes in the Earth electrical field. During the storm onset, the field is strengthening of about two orders of magnitude from the typical fair weather value. In the mature phase of the thunderstorm the electrical field reaches values greater than 10 kV m^{-1} and the effect of lightning discharges are recorded as sharp and sudden inversions of the field. A careful look at the discharge parts of the records suggest that there should be a recovery mechanism that works to restore the vertical potential gradient after the discharging action of the lightning strike. The recovery curves resemble to a typical capacitor load curve. The end of the storm is characterised by one or a few long, about one hour, smooth oscillations before the field completely relax over the usual fair weather value.

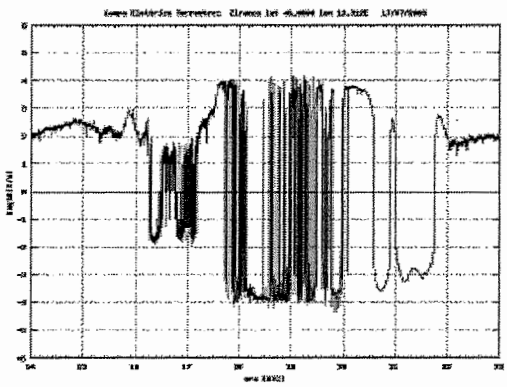

Figure 2: time series of Earth electric field recorded on July 17, 2003, during a stormy event. Field intensity è [V m^{-1}] is plotted in logarithmic scale.

Comparison between electrical field records and the Vertical Maximum Intensity of radar echoes aloft the field mill suggests that a single cell thunderstorm extends its electrical influence over an area that is close to the storm less than some kilometres. At larger distances the Earth electric field is just slightly affected. In figure 2 a typical time series of the field in a stormy day is reported. The central part of the record is mainly populated by lightning discharge signals and their consequent recovery curves. In this part the field experiences inversions from upward and downward direction with an intensity of about 10 kV m^{-1}. That value is reached during the storm on set. In figure 2, the onset is the region between 17:15UTC and 17:40UTC. The end of storm oscillation (MacMorgan and Rust 1998) is clearly recognisable after 20:00 UTC. The small increase in the record just before 16:00 UTC is produced by a storm that developed about 20 km far from the instrument.

5 SNOWFALLS

In case of non convective snow falls the Earth electric field presents inversions similar to those observed during non convective rainfalls. Furthermore the average of the field intensity out of the precipitation episode is close to zero instead of significant non null upward values.

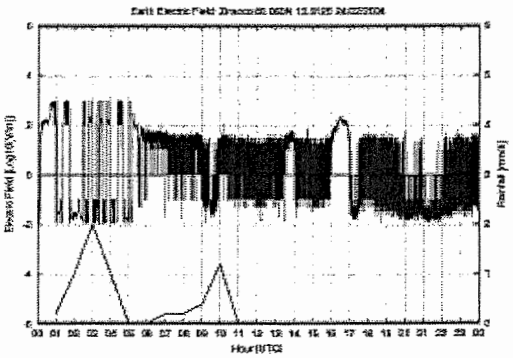

Figure 3: time series of Earth electric field and hourly precipitation measurements recorded on February 24, 2004. Field intensity è [V m^{-1}] is plotted in logarithmic scale (left) and precipitation in [mm h^{-1}] in liner scale (right). The jagged curve refers to the electric field while the lower hourly broken line is that of snowfall. Snow has been immediately converted in water and measured in mm h^{-1} when it was caught by the heated tilting bucket pluviometer.

In figure 3, the time series of a day with slight snowfalls is reported. During the main episode of snow, before 06:00 UTC the Earth electric field had a response similar to those observed during non convective rainfalls. In a second snow episode, around 10:00 UTC it showed a weaker response. There is also an interesting long period oscillation, from 16:00 UTC lasted about one hour that it is not associated with precipitation events apart from the cloudiness present all over the day. It is also interesting to note that the average intensity of the field out of the precipitation areas is close to zero.

6 CONCLUSIONS

Measurements of the Earth electric field made by a field meter, at the ground, in the same place and in different meteorological situations show the variety of field variations. Time scales of these variations range from a few seconds during the lightning phase of the thunderstorm, to some hours in the relaxation occurring at the end of the storm. Snowfall episodes and non convective rainfall ones have some similarities but they are not completely comparable. Radar reflectivity suggests that the influence of a normal, single cell, thunderstorm on the electric field at the ground is limited to some kilometres of distance from the storm.

After this general survey on the response of the Earth electrical field to the different weather situations, further studies are going to focus on the field recovery curves following a lightning discharge, a finer exploration of the radar reflectivity and differential reflectivity correlation with the field variations and the effects of the low level winds on the field.

7 REFERENCES

Giaiotti B. Dario and Stel Fulvio, 2001, A comparison between subjective and objective thunderstorm forecasts, Atmos. Res., 56, 111-126

MacMorgan Donald R. and Rust David W., 1998, The electrical nature of storms, Oxford University Press - Oxford, pp. 422

Prodi Franco, 1976, Hailstorms in the Po valley., Riv. Ital. Geofis. III (1/2), 21-31

Rakov Vladimir A.and Uman Martin A., 2003, Lightning: physics and effects, Cambridge University Press - Cambridge, pp 688.

Winn W. P., 1993, Aircraft measurements of electric field: Self Calibration, J. Geophys Res., 98, 7351-7365.

CHARACTERISTICS OF THE PRECIPITATING SYSTEMS DURING THE 2002 DRY-TO-WET FIELD CAMPAIGN IN THE AMAZON REGION

Carlos Augusto Morales[1], Luiz Augusto Toledo Machado[2], Maria Assunção Faus Silva Dias[1,2], Wando Amorim[1], Maria Eugenia Baruzzi Frediani[1]

[1]Department of Atmospheric Science, University of São Paulo, São Paulo, São Paulo, Brazil
[2]Weather and Climate Prediction Center – CPTEC, INPE, Cachoeira Paulista, São Paulo, Brazil

1. INTRODUCTION

The Amazon region presents unique spatial and temporal rainfall variability along the year, and as one of the main sources of convection, and as a consequence, it has a major contribution in the global circulation through the release of latent heat. Several efforts, through several field campaigns, tried to understand and characterize the precipitating system. Nevertheless, most of the measurements concentrated in the wet raining season. In this paper, we present preliminary results observed during the 2002 Dry-to-Wet field campaign in the Amazon region, as a part of Radiation, Cloud, and Climate Interactions (RACCI) of LBA.

This experiment was set during the pre-wet season in order to understand the transition between the dry to wet raining season and the impact of the aerosols produced by forest burning in the development of clouds.

This paper gathers weather radar, rain gauges, and lightning measurements to depict the main precipitation characteristics observed during this field campaign in order to understand the transition of dry to wet raining season.

In the following sections, this paper will present the characteristics of the instruments used and their quality control, and it will present the preliminary results found until the present moment.

2. DATA SET

In order to characterize the precipitating systems, we used measurements of: a) one weather radar, b) a rain gauge network, and c) a cloud-to-ground lightning network. As an auxiliary data, we have used the number of forest fires.

2.1 Weather Radar

Brazilian weather radar manufactured by the TECTELCOM was used in this campaign. This radar is a Doppler S-Band (2.7-3 GHz), with 2 degrees antenna aperture, with a maximum power of 750 kW, running on GAMIC operating software. The radar was installed at the central part of Rondonia State (Figure 1), in the southwestern part of the Amazon basin, with longitude of 62.4171 W, latitude of 10.9005 S at an a altitude of 433 meter.

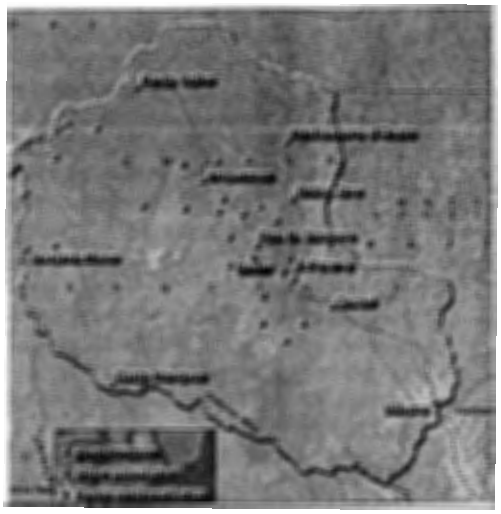

Figure 1. Map of Rondonia State in the Southwestern Amazon basin, and the location of the instruments used in the RACCI/LBA field campaign.

During the experiment, 10 minutes interval volume scans with 24 elevations were realized to better describe the horizontal and vertical distribution of the precipitating systems. The period of measurements concentrated during September 16th through November 7th of 2002.

Since this is the first time that this radar is been used in research, we performed several electronic calibrations to detect the stability of the measurements. Additionally, we performed an intercomparison with the Tropical Rainfall Measuring Mission (TRMM) Precipitation Radar (PR) [Kummerow et al. 1998] to depict an existence of a bias offset.

The retrieval of the bias offset followed the methodology developed by Anagnostou et al. (2001) that makes an intercomparison between ground weather radars and the TRMM-PR. The methodology can be summarized as follow:

a) Common 3-D grid Boxes, with 5 x 5 km horizontal resolution and 1(2) km vertical resolution;

Corresponding author's address: Carlos A. Morales, Universidade de São Paulo, IAG, Departamento de Ciências Atmosféricas, Rua do Matão 1226, CEP 05508-900, Cidade Universitária, São Paulo, São Paulo, Brasil.; E-Mail: morales@mode.iag.usp.br.

b) Intercomparison between 7 and 12 km height only, and only in grid boxes classified as stratiform rain;

c) Grid-boxes with 15 and 35 dBZ; and up to 100 km from the radar;

d) Finally, compute the radar reflectivity histogram difference of matched grid-boxes, mainly, Z(TECTELCOM)– Z(TRMM).

Following the above methodology, we were able to find a + 6.47 dBZ bias offset, mainly the TECTELCOM overestimated the measurements, Figure 2a and 2b. Figure 2a displays the matched radar reflectivity factor distribution for both radars observing at the same time in 5 TRMM orbits. It is clear that the TECTELCOM ground radar presents a shift towards high reflectivity values. In Figure 2b, we present the radar reflectivity difference for the cases of Figure 2a, and we can see that this radar showed a bias offset. Possible causes for this type of error are still been investigated, but one possible problem is the antenna gain, that has not been computed since the first time this radar is in operation.

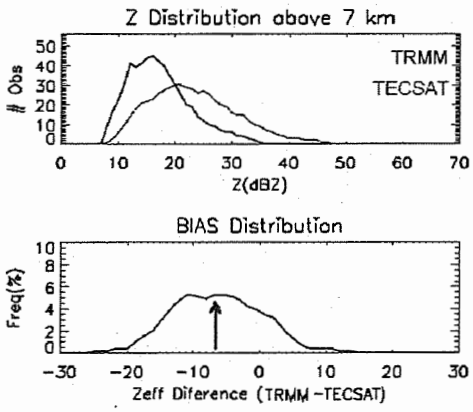

Figure 2. a) Radar reflectivity factor distribution observed by TRMM (black) and TECTELCOM (gray) on coincident grid-boxes (top); b) Histogram difference between TRMM-PR and TECTELCOM (bottom).

After this bias offset correction, Constant Altitude Plan Position Indicator (CAPPI) were retrieved at 5x5 km horizontal and 1km height resolution, from 2 to 19 km altitude, for all the experiment based on weighted volume beams, Anagnostou et al. (1999).

2.2 Rain Gauge Network

A rain gauge network consisting of 29 tipping buckets have been installed around the State of Rondonia, Figure 1. The rain gauges have a temporal resolution of 10 seconds, and 0.254 mm of precipitation. Each tipping bucket have been calibrated before the installation according to the manual owners, in order to obtain 0.254 mm for each bucket.

2.3 Cloud-to-Ground Lightning Network

A lightning network consisting of 4 Advanced Lightning Direction Finder (ALDF) sensors were installed by Marshall Space Flight Center (MSFC) of NASA in 1999 during the TRMM/LBA field campaign, in Guajara Mirim, Ouro Preto, Machadinho do Oeste and Vilhena, Figure 1. These sensors measure the magnectic field emitted by a lightning and detect only lightning strokes that go to ground. By measuring the magnetic field, it is possible to record the direction, strength and time of each strike. The location of a strike is found by combining the measurements from at least two sensors in the network.

2.4 Number of Fires

The number of fires used in this study was retrieved by CPTEC, and can be access at: http://www.cptec.inpe.br/queimadas. The number of fire is calculated using the thermal emission channel (3.7 μm) of NOAA/AVHRR satellite.

2.5 Data Access

All the dataset used in this study and other datasets measured during the Wet-to-Dry 2002 Field campaign can be accessed at: http://master.iag.usp.br

3. Methodology and Results

3.1 Daily Means

Daily mean time series of 35 dBZ mean height, number of fires and lightning strikes are used to seek an indication of correlation between convection in the impact of forest burning.

The 35 dBZ mean height are computed from 3D CAPPIs at 5x5 km resolution in order to find the strength of the storms. It is well known that 35 dBZ between the freezing level and –15°C, where it is a region of negative charge, is associated with the presence of lightning strokes, Toricinta et al. (1996). Therefore, the higher the level is, more vigorous the storms become.

Lightning measurements can be associated with the strength of the thunderstorms, mainly because they develop the ice phase, and consequently more rain volume.

Finally, number of fires are used to check how polluted the area is, and if large concentration of aerosols can be responsible for the development of giant storms, or the suppression of rain.

Figure 3 displays the daily mean time series of 35 dBZ height, daily lightning strikes, and daily number of fires over an area described by 150 km far from the radar.

The vertical development observed by the 35 dBZ height is very well correlated with the high incidence of lightning strikes. Nevertheless no unique relation between both parameters can be performed on a daily basis. In another hand, it is important to note that

whenever we have forest burning (high values of number of fires), the 35 dBZ height levels was very low or absent, except at Julian day 267. Inspecting the meteorological maps during the days of large amount of fires, the region was over an influence of subsidence, and at the present moment no conclusions can be postulated to the effect of aerosols in the clouds.

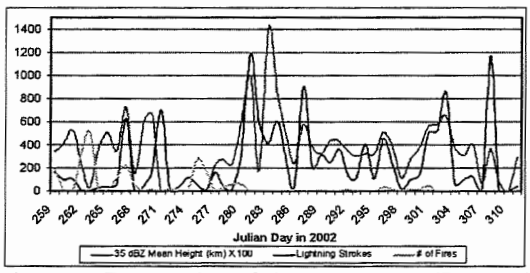

Figure 3. Time series of daily mean 35 dBz Height, daily lightning strikes, and number of fires over the radar area.

3.2 Daily Cycle

The daily cycle of precipitation is first inspected by analyzing the vertical distribution of 30, 35 and 40 dBZ height as function of time, Figure 4a,b, and c. These 3 plots shows that most of the convection is concentrated around 17-19 UTC, where local convection is more intense. In addition, these convections present most of the vertical development, reaching in average 10, 8,7 km for 30, 35 and 40 dBZ respectively. Nevertheless, there are development through all day, later night and early day, but no vertical strength is found.

Figure 4d presents de mean diurnal cycle of negative and positive lightning strikes and the convective fraction. Most of convective fraction is observed between 15 and 22 UTC, and note that the maximum convective fraction anticipates the maximum of lightning discharges by ~ 1 hour at least. This time lag can be explained that the maximum lightning frequency occurs during the mature stage of the thunderstorms. Finally, by comparing the negative and positive lightning discharges, we observe that most of the electrical discharges are negative, and there is a delay in the maximum frequency of positive discharges. A possible explanation for this delay could be that in general, positive lightning discharges are observed during the dissipating stage of the thunderstorms, which is confirmed by the decrease of convective fraction.

4. CONCLUSION

This paper presented an overview of the data measured during the Wet-to-Dry 2002 field campaign as part of the RACCI/LBA project.

The preliminary results presented here show a strong correlation between lightning strikes and the vertical development of the 35 dBZ height. The role of the aerosols produced by biomass burning in the enhancement or the suppression of precipitation could not be achieved. Nevertheless most of the time we have fires, the area was under subsidence influence and no or little rain development was observed.

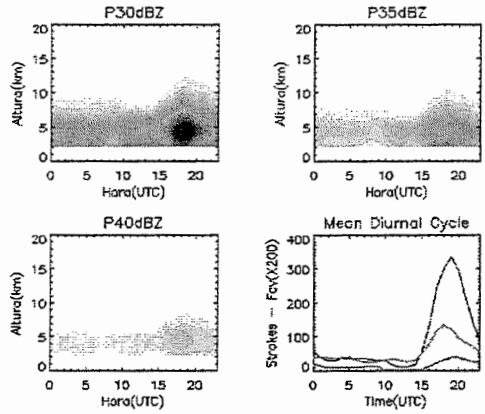

Figure 4. a)top-left, mean 30 dBZ height distribution over the day; b)top-right, same as (a) but for 35 dBZ; c) bottom-left, same as (a) but for 40 dBZ; d) bottom-right, diurnal cycle of convective fraction (middle line), negative lightning strikes (top line) and positive lightning strikes.

Finally, the diurnal cycle analyses showed that most of the convection shows a strong component of local convection with vigorous vertical development. Afterwards, the maximum convective fraction led the maximum negative discharges that also led the positive lightning strikes. These delays are a response of the thunderstorm stage, mainly: during mature stage it is observed the maximum lightning discharges, and during the dissipating stage we observe a maximum frequency of positive strikes.

5. REFERENCES

-Anagnostou, E., C.A. Morales, T. Dinku, 2001, J.A.O.Tech., 18, 4, pp. 616-628.

-Anagnostou, E., V. Krajewski, Witold, 1999, J.A.O.Tech., 16, 2, 189-197.

-Kummerow, C., W. Barnes, T. Kozu, J. Shiu and J. Simpson, 1998: The tropical rainfall measuring mission (TRMM) sensor package, *J. Atmos. Oceanic Technol.*, **15**, 809-817.

-Toracinta, E.R., K.I. Mohr, E.J. Zipser, and R.E. Orville, 1996: A comparison of WSR-88D reflectivities, SSM/I brightness temperatures, and lightning for mesoscale convective systems in Texas. Part I: radar reflectivity and lightning. *J. Appl. Meteor.*, **35**, 902-918.

6. ACKNOWLEDGEMENTS

We would like to thanks FAPESP for funding the Wet-to-Dry 2002 field campaign as a part of RACCI/LBA project, grant # 01/06901-7, and CAPES, grant #0379/2002-2004, for the financial support.

LIGHTNING BY CAVITY QUANTUM ELECTRODYNAMICS?

T.V. Prevenslik

Consultant, 14 B, Brilliance Court, Discovery Bay, Hong Kong

1. INTRODUCTION

Atmospheric electricity is generally thought caused by the loss of charge neutrality in the collisions of rising ice crystals and falling hail pellets. *Iribarne and Cho* [1980]. Electrons are assumed knocked-off the rising crystals that carry positive charge to the top of the cloud while the newly knocked-off electrons gather at the bottom of the cloud. But the electrons in water molecules are tightly bound to the hydrogen and oxygen atoms, and therefore ice crystal and hail pellet collisions are unlikely to free electrons.

The notion that electrons are loss in collision of particles in atmospheric electricity is similar to that proposed by *Adams* [1987] to explain static electricity by rubbing of solids. Unless the solids are already charged, rubbing only produces particles of atoms that are neutral because the binding energy of the electron to the atom is greater than the energy binding the atoms to each other. *Prevenslik* [2002a,2003]

2. ELECTRIFICATION MECHANISM

Since Einstein's explanation of the photoelectric effect, electromagnetic (EM) energy at vacuum ultraviolet (VUV) frequencies is required to free electrons from atoms in molecules while only infrared (IR) radiation is available at ambient temperature. But EM energy at VUV levels may be produced in bubbles by cavity quantum electrodynamics (QED). For cavity QED theory, see e.g., *Harouche and Raimond* [1993].

The cavity QED mechanism has explained atmospheric electricity including sprites. *Prevenslik* [2002b, 2002c]. By this theory, water dissociates into hydronium H_3O^+ and hydroxyl OH^- ions as bubbles in graupel nucleate in the supercooled volume expansion at freezing altitudes. Cavity QED induced EM radiation is described in Appendix A.

3. THEORETICAL BACKGROUND

The electrification of the atmosphere by graupel in the thundercloud is depicted in Fig. 1.

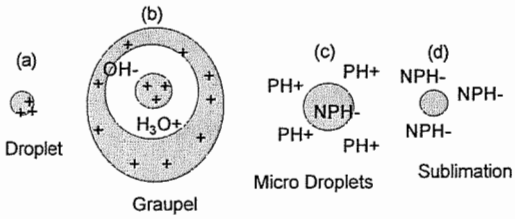

Fig. 1 Thundercloud Electrification

A water droplet having an acid pH about to undergo supercooling at freezing altitude is illustrated in Fig. 1(a). The increase in the volume of water in supercooling places the droplet in a state of hydrostatic tension, thereby nucleating numerous bubbles. Each bubble contains a water particle formed by surface tension while leaving an annular gap with the bubble wall. For clarity, only a single bubble in an enlarged droplet is shown in Fig. 1(b). Cavity QED induced VUV radiation at the instant of nucleation is depicted to dissociate water molecules on the gap surfaces into hydronium and hydroxyl ions.

Charge separation of hydronium and hydroxyl ions within the bubble follows a proposal by *Loeb* [1958] that ionic charge may be separated if the charge of one sign collects in the vapor-state while the charge of the opposite sign collects in the liquid-state. In a bubble, this condition is nicely satisfied. The drop has an acid pH, and therefore the particle and bubble wall carry a positive background charge. Fig. 1(b) shows a hydronium ion repulsed to the bubble vapor in the annular gap while the hydroxyl ion is adsorbed on the wall of the bubble.

Supercooling drives dissolved air out of the liquid water into the annular gap to mix with the hydronium ions. The hydronium ions combine with water vapour and air to form positive charged $H_3O^+ \cdot (H_2O)_n$ proton hydrate (PH) clusters, while the highly reactive hydroxyls combine with nitrogen oxides in the air to form nitric acid which reacts with water to produce negative charged $NO_3^- (HNO_3)_m (H_2O)_n$ non-proton hydrate (NPH) clusters. *Swider* [1985].

Freezing begins with a layer of ice on the graupel surface. Fig.1(c) depicts the surface solidification placing the interior supercooled water under high-pressure. *Cheng* [1973] showed air and PH clusters are expulsed through the ice layer to produce buoyant positive charged micro-droplets that form PH clouds that rise to the stratosphere. Fig. 1(d) shows the NPH clusters to remain with the falling graupel to sublime in the troposphere as negative charged NPH clouds.

In this paper, lightning is the electron avalanche that follows the path of least electrical resistance through the troposphere between the PH/NPH cloud interface and the earth, the conductivity of the troposphere depending on the dispersion of NPH clusters from the thundercloud. The electrons that initiate and supply the avalanches are produced by the breakdown of air in the cloud-to-cloud lightning between PH and NPH clouds. Only the electrons and not the NPH clusters undergo the avalanche, although once initiated the electron collisions with atmospheric gases produces additional electrons.

4. ANALYSIS

The path of the pilot streamer, stepped leader, and lightning stroke in an electronegative gas (e.g. NPH clusters) is generally thought caused by the random process of local breakdown of space charge close to the leader tip, the leader tip acting as a continuous pulse of positive voltage. See e.g., *Niemeyer* [1986]. On this basis, stepped leader simulations have found analogy with switching surge breakdown in long air gaps. *Farouk* [1989]. Indeed, the electric field associated with the space charge of positive surge pulse has been confirmed for the breakdown of air in about 10-meter lengths. Given that stepped leaders are observed to follow the pilot streamer in comparable steps, *Kumar and Nagabhushana* [2000] make the argument that the surge pulse experiment extended by continuous inception and breakdown is applicable to the propagation of stepped leaders over thousands of meters in the troposphere.

But lightning cannot propagate at all unless the thundercloud first produces the NPH clusters to increase the conductivity of the troposphere.

If so, a surge pulse is not necessary. Electrons are continually being produced by the breakdown of air in cloud-to-cloud lightning at the PH/NPH cloud interface. Thus, the pilot streamer, stepped leader, and lightning stroke propagate thousands of meters only because the NPH clusters have increased the conductivity of the troposphere to the level necessary to sustain the respective avalanche currents along the path of least resistance.

Consider the thundercloud as a dipole of positive PH and negative NPH clouds having charge $\pm Q_o$ shown in Fig. 2.

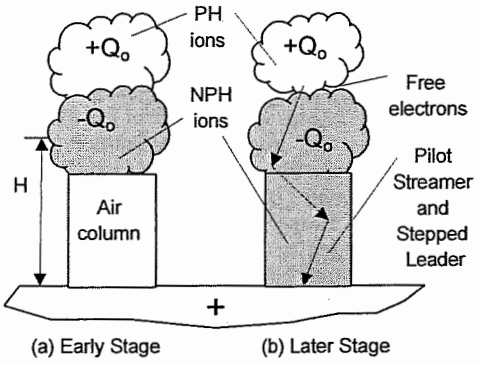

Fig. 2 Storm Condition -Thundercloud Stages

Under fair conditions, the earth is charged negative. But at the time of a storm, the earth carries a positive charge.

4.1 Early Stage of Thundercloud

The thundercloud in the early stage comprises the NPH cloud separated from the ground by height H including an otherwise neutral column of air as shown in Fig. 2(a). Treating the NPH clouds and ground as the plates of an air capacitor, the capacitance C_o is,

$$C_o = \frac{\varepsilon_o A}{H} \qquad (1)$$

where, ε_o is the permittivity of free space and A is the area of the air column. The potential V_o of the ground above the NPH cloud is, $V_o = Q_o / C_o$.

The thundercloud is treated as a dipole having charge Q_o of about ±30 C located about 2500 m above the earth following *Kumar and Nagabhushana* [2000]. For a thundercloud having total volume of about 40 cubic kilometers, the PH and NPH clouds each have a volume V_c of 20 cubic million kilometers. Taking an air column area $A = V_c^{2/3} \sim 7.35\text{x}10^6$ m^2 gives $C_o \sim 2.6\text{x}10^{-8}$ F and $V_o \sim 1.15\text{x}10^9$ V.

Even though under high voltage V_o, electrical breakdown of the air column does not occur because the average electric field $E = V_o / H \sim 4.6\text{x}10^5$ V·m^{-1} is less than the breakdown strength of air $E_{BD} \sim 2.6\text{x}10^6$ V·m^{-1}, i.e., $E < E_{BD}$. Nevertheless, a small current I_o leaks to ground. The resistance R of the air as a column of area A and length H is given in terms of the conductivity σ,

$$R = \frac{H}{\sigma A} = \frac{V_o}{I_o} \qquad (2)$$

where, I_o is the leakage current. For air in the initial stage of the storm, the conductivity $\sigma \sim 10^{-14}$ $(\Omega\cdot m)^{-1}$. *Swider* [1985]. Thus, $R \sim 3.4\text{x}10^{10}$ Ω and current $I_o \sim$ 34 mA.

4.2 Later Stage of Thundercloud

In the later stage of the thunderstorm, the NPH clusters have migrated under the electric field of the earth to increase the conductivity of the air column as depicted in Fig. 2(b). Electrons are continuously being produced in the breakdown of air in cloud-to-cloud lightning to initiate and supply the avalanche. Indeed, microscopic breakdown of air between a single PH and NPH cluster produces electrons. Breakdown of air occurs when a PH ion comes within a distance x of a NPH ion,

$$x = \sqrt{\frac{e}{4\pi\varepsilon_0 E_{BD}}} \qquad (3)$$

where, e is the electron charge. For $E_{BD} \sim 2.6\text{x}10^6$ V·m^{-1}, x ~ 24 nm. Similarity is found with St. Elmo's fire and ball lightning, as NPH clusters fall on positive charged protrusions on the earth's surface.

The NPH clusters move in the average electric field E at velocity V_{NPH},

$$V_{NPH} = \mu E \qquad (4)$$

where, μ is the mobility of the NPH ion in air. *Swider* [1985] cites $\mu \sim 1.6\text{x}10^{-4}$ m^2·(V·s)$^{-1}$ giving $V_{NPH} \sim 74$ m·s^{-1}. Since the time $H / V_{NPH} \sim 33$ s, any potential

build-up in the NPH cloud is promptly compensated by an increase in the conductivity of the air column while the PH cloud mixing with the NPH cloud continually produces electrons.

Stepped leaders are brought down at currents from 600 to 2600 A. See e.g., *Kumar and Nagabhushana* [2000]. For the stepped leader having an electron avalanche current $I_o \sim 860$ A, Eqn. 2 gives the air column resistance $R \sim 1.33\times10^6\ \Omega$ and conductivity $\sigma \sim 2.5\times10^{-10}\ (\Omega\cdot m)^{-1}$. Thus, the NPH clusterss increase the air conductivity of the troposphere by a factor of 25,000. The stepped leader resistance $R/H \sim 532\ \Omega\cdot m^{-1}$ is less, but consistent with *Kumar and Nagabhushana* [2000] that cite a resistance of $1000\ \Omega\cdot m^{-1}$ for the preliminary leader. Absent the NPH clusters from the thundercloud, the stepped leader as an electron avalanche cannot propagate thousands of meters to the ground.

The number density N_{NPH} of NPH clusters to sustain the stepped leader avalanche current,

$$N_{NPH} = \frac{\sigma}{e\mu} \tag{5}$$

Numerically, $N_{NPH} \sim 9.7\times10^{12}\ m^{-3}$. That the NPH cloud can provide the number density N_{NPH} is established in the following.

In the thunderstorm, moisture is converted to graupel. Typical 1-mm diameter graupel pellets are known to produce at least 10,000 micro-droplets. *Cheng* [1973] Appendix A shows each bubble to produce 5.2×10^5 hydroxyl ions. If every micro-droplet is produced by a bubble, the number $n_{NPH} \sim 5.2\times10^9$ of NPH clusters, or about 1 nC of negative charge per graupel pellet. The mass m_p of the graupel pellet is,

$$m_p = \frac{4}{3}\rho\pi r^3 \tag{6}$$

where, ρ is the density of water and r is the pellet radius. For r = 500 μm and ρ = 1000 $kg\cdot m^{-3}$, $m_p \sim 5.24\times10^{-7}$ kg. The mass M_c of water in the cloud is,

$$M_c = \rho_c V_c \tag{7}$$

where, ρ_c is the density of water in the thundercloud. For cumulonimbus clouds, ρ_c varies from 0.005 to 0.015 $kg\cdot m^{-3}$. See e.g., *Wahlin* [1989]. Taking an average of $\rho_c \sim 0.010\ kg\cdot m^{-3}$, the water mass of the thundercloud is, $M_c \sim 2\times10^8$ kg. The upper bound number density N_{UB} of NPH clusters in the air column,

$$N_{UB} < \frac{M_c}{m_p} n_{NPH} \Big/ AH \tag{8}$$

Numerically, $N_{UB} \sim 1\times10^{14}\ m^{-3}$, and therefore even with 50% recombination, $N_{NPH} < N_{UB}$. Thus, only 1 in 10 graupel pellets need to supercool to provide the number density N_{NPH} necessary to sustain stepped leader propagation.

5. DISCUSSION

The stepped leader charge Q brought down from the electron charge Q_o at the PH/NPH cloud interface may be expressed in terms of the time t by,

$$Q = Q_o\left[1-\exp\left(\frac{-t}{\tau}\right)\right] \tag{9}$$

where, τ is the relaxation time constant for the simple RC_o circuit,

$$\tau = RC_o = \frac{\varepsilon_o}{\sigma} \tag{10}$$

and the time constant τ is, $\tau \sim 14$ ms. The avalanche I_o current is,

$$I_o = \frac{dQ}{dt} = \frac{Q_o}{\tau}\exp\left(\frac{-t}{\tau}\right) \tag{11}$$

For charge $Q_o \sim 30$ C, the currents I_o vary from 600 to 2600 A. *Kumar and Nagabhushana* [2000]. Stepped leader response for relaxation times τ of 11, 35, and 50 ms that correspond to conductivity $\sigma \sim 8$, 2.5, and $1.75\times10^{-10}\ (\Omega\cdot m)^{-1}$ are shown in Fig. 3.

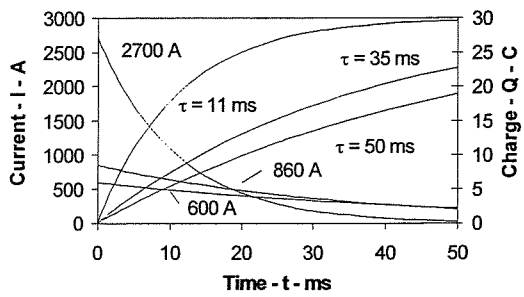

Fig. 3 Stepped leader current and charge

The stepped leader relaxation time ($\tau \sim 11$ ms) corresponds to the full charge $Q_o \sim 30$ C brought down in time $t \sim 50$ ms while giving the highest current $I_o \sim 2700$ A. The lowest avalanche current $I_o \sim 600$ A ($\tau \sim 50$ ms) brings down about 20 C at time $t \sim 50$ ms. The response for a relaxation time ($\tau \sim 35$ ms) is shown because it coincides with (Fig. 4 of *Kumar and Nagabhushana* [2000]) that shows about 1.5 C of charge brought down at time $t \sim 1.8$ ms.

Electron avalanche currents in the lightning stroke average 25 kA and may even reach 400 kA. *Wahlin* [1989]. Higher electrical conductivity is required to sustain the stroke than for the stepped leader, but after the stepped leader is brought down, the atmospheric gases are ionized and the path no longer needs to rely on NPH clusters for the conductivity necessary to propagate the stroke.

APPENDIX A

The cavity QED mechanism is illustrated in Fig. A-1

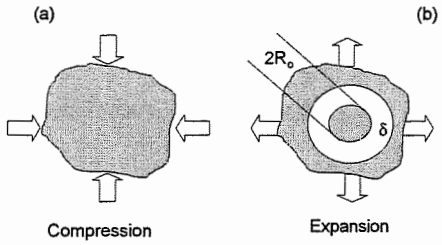

Fig. A-1 Frequency Up-conversion Mechanism

- Prior to bubble nucleation, the liquid water in the graupel is in hydrostatic compression as shown in Fig. A-1(a). The water molecules at 300 K freely emit IR radiation given by the harmonic oscillator (See e.g., *Christy and Pytte* [1965]) shown in Fig. A-2.

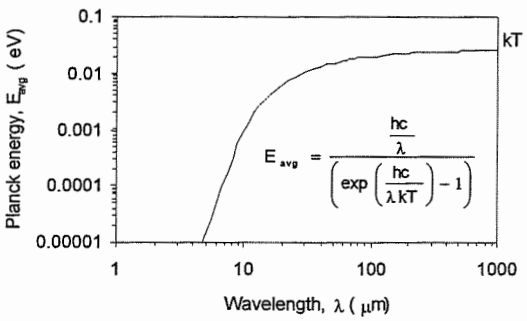

Fig. A-2 Planck energy of harmonic oscillator at 300K

- Graupel on the abrupt volume expansion causes the bubble wall to separate from the particle of radius R_o leaving an annular gap δ as depicted in Fig. A-1(b). The spherical particle radius $R_o = 2\ S/\ P_{atm}$, where S is the surface tension and P_{atm} is ambient pressure. For water, $R_o \sim 1.44$ μm.
- The bubble is a QED cavity having a resonant wavelength $4R_o \sim 5.76$ μm. All longer wavelength EM radiation is suppressed by cavity QED. The IR energy suppressed in the particle is,

$$U_{IR} = 4\pi kT\left(\frac{R_o}{\Delta}\right)^3 \qquad \text{(A1)}$$

where, Δ is the cubical spacing between water molecules at liquid density, Δ ~ 0.31 nm. Thus, $U_{IR} \sim$ 5.2 nJ.

- To conserve EM energy within cavity QED constraints, the suppressed IR energy by the particle is compensated by an equivalent gain in the gap.
- But the gap is resonant in the VUV and beyond, and therefore at least VUV radiation is promptly produced, the process called frequency up-conversion of far IR radiation to the VUV.
- The number N_{VUV} of VUV photons produced is,

$$N_{VUV} = \frac{U_{IR}}{E_{VUV}} = U_{IR}\left(\frac{2\delta}{hc}\right) \qquad \text{(A2)}$$

where, E_{VUV} is the Planck energy of the VUV photon standing in the gap δ, h is Planck's constant, and c is the velocity of light. For δ ~ 0.1 micron, E_{VUV} = 6.21 eV giving $N_{VUV} \sim 5.2\text{x}10^9$ photons.

- The yield Y of hydronium and hydroxyl ions is not known but should exceed 10^{-4} giving $YN_{VUV} > 5.2\text{x}10^5$ dissociated molecules, or 83 fC of positive and negative charge per bubble.

REFERENCES

Adams, C. K., 1987: *Nature's Electricity*, Blue Ridge Summit, PA, USA Tab Books Inc.

Cheng, R. J., 1973: Photomicroscopical Investigation of the Fragmentation of Hydrometeors in the Laboratory, Microscope, pp. 149-160.

Christy, R. W. and A. Pytte, 1965: *The Structure of Matter Introduction to Modern Physics*, New York, Benjamin.

Farouk, F. A. M., 1989: A model for switching impulse leader inception and breakdown of long air-gaps, IEEE Trans. Power Del., 4, pp. 596-606.

Harouche S. and J-M Raimond, 1993: Cavity Quantum Electrodynamics, Scientific American, pp.54-62, April.

Iribarne, J. V. and H. R, Cho, 1980: *Atmospheric Physics*, .D. Reidal Publishing Company, Boston.

Kumar, U. and G.R. Nagabhushana, 2000: Novel model for the simulation of lightning stepped leader, IEE Proc.-Sci. Meas. Technol., 147, pp. 56-63.

Loeb, L. B., 1958: *Static Electrification*, Springer, Berlin.

Niemeyer, L., 1986: A stepped leader random walk model, Appl. Phys. 20, pp. 897-906.

Prevenslik, T. V., 2002a: Cavity QED Induced Photoelectric Effect, Proceedings ESA-IEJ Meeting, Northwestern University, 25-28 June, pp. 230-240.

Prevenslik, T., 2002b: Sprites and bubbles, International Union of Radio Science, XXVII General Assembly, Maastricht, 17-24 August.

Prevenslik, T. V., 2002c: Bubble and sprites, Proceedings ESA-IEJ Meeting, Northwestern University, 25-28 June, pp. 230-240.

Prevenslik, T. V., 2003: Flow electrification and quantum electrodynamics? IEEE Conference on Electrical Insulation and Dielectric Phenomena, Albuquerque, October 19-22.

Swider, W., 1985: Ionic mobility, mean mass, and conductivity in the middle atmosphere from near ground level to 70 km, Radio Science *23*, pp. 389-399.

Wahlin, L., 1989: *Atmospheric Electrostatics*, J. Wiley & Sons, New York.

Author's Email: esaconf2003@yahoo.com

CHARACTERISTICS OF WINTER THUNDERCLOUDS IDENTIFIED WITH DUAL POLARIZATION RADAR IN HOKURIKU, JAPAN

K. Sakashita[1], H. Uyada[1], T. Maesaka[1], T. Shinoda[1], K. Kontani[2], and K. Shinjo[2]

[1]Hydrospheric Atmospheric Research Center, Nagoya University, Nagoya, 464-8601, Japan

[2] Lightning Research and Consulting Center, Hokuriku Electric Power Company, Toyama, Japan

1. INTRODUCTION

Thunderclouds often occur and cause great damages to human lives in winter in Hokuriku District, Japan. Winter thunderclouds in this region attract worldwide attention because of occurrence of positive ground flash at high rates. Recently, dual polarization radar, which can identify the precipitation particles in thunderclouds, was installed in this area.

On this occasion, we investigated the distribution of precipitation particles, especially graupel, in thunderclouds using dataset of dual polarization radar. We analyzed the relative position between graupel area in thunderclouds and positive ground flash (hereinafter called PGF) or negative ground flash (hereinafter called NGF). We showed characteristics of winter thunderclouds in Hokuriku district.

2. DATA AND ANALYSIS

2.1 Data

Figure 1 shows observation range of data used in this study. Dual polarization C-band radar of Hokuriku Electric Power Company (hereinafter called HEPC) is positioned at Goishigamine. Reflectivity of horizontal polarized wave (Z_h) and differential reflectivity (Z_{DR}) are used for analyses.

Radio sonde observation station is positioned at Wajima, about 60km north of the radar site. We utilized vertical profile of temperature and relative humidity at this station.

Lightning Location System (hereinafter called LLS) of HEPC provided data of lightning location and time. The detection area of lightning by LLS is in Fig.1 except north west and south east corner. LLS data in dashed rectangle in Fig.1 are used for analysis.

Radar, radio sonde and LLS data, observed during 2 seasons, December 2000 to February 2001 and December 2001 to February 2002, are used for detailed analyses.

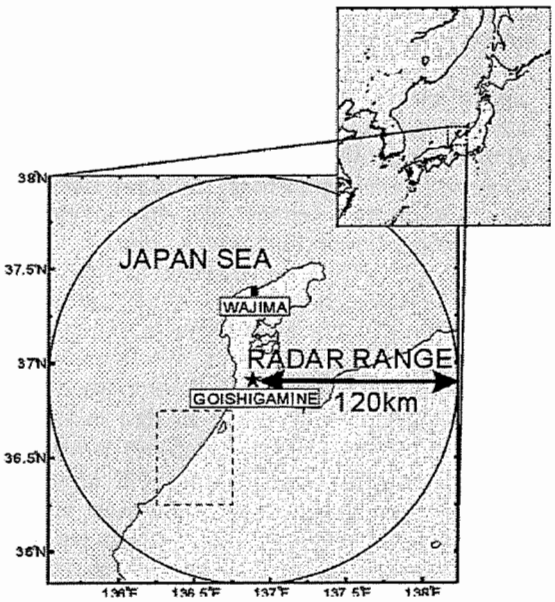

Fig.1. Map of observation network. The radar is located at Goishigamine and the radio sonde observation point is located at Wajima.

2.2 Analysis method

We chose the thunderclouds in the following manner to analyze in detail. At first, the days of winter pressure pattern are selected. Second, cloud-to-ground discharges (hereinafter called CGDs) occurred on the days in the dashed rectangle in Fig.1 are picked up. At the last, the thunderclouds with the CGDs are chosen. We classify the chosen thunderclouds into three types by polarity of CGDs occurred from. They are types with PGF only, NGF only and both of PGF and NGF. We show the

Corresponding author's address: Keiichiro SAKASHITA, Hydrospheric Atmospheric Research Center, Nagoya University, Nagoya, Aichi, 464-8601, Japan;
E-Mail: sakasita@rain.hyarc.nagoya-u.ac.jp

analysis result of one case each for three types.

Thunderclouds are analyzed from the viewpoint of cell and graupel area. The cell was defined as interior of Z_h over 28 dBZ_e. The graupel area was defined as the area of Z_{DR} less than 0.25 dB in thundercloud cell. The graupel area on the ground is defined as the area projected the graupel area into the ground. The position of CGD is corrected using moving speed of the thundercloud at 1.0 km altitude.

3. RESULTS

3.1 Thundercloud with positive ground flash

On 26 December 2000, a thundercloud with PGF occurred in the dashed rectangle. It moved eastward from ocean and reached the coastline at 0836 JST (JST=UTC+9h). CGD occurred in 0847 JST in the mature stage of the cloud. After that it declined. Figure 2 shows vertical profile of temperature and relative dew-point temperature at 09JST on this day at Wajima. The altitude of –10℃ layer was 1.4 km altitude. The air was almost saturated below 700 hPa. Humidity profiles of the other two thunderclouds were the same as this.

Thundercloud on coastline at 0836 JST is shown in Fig.3. Zonal vertical section along A-B line in Fig.3 at the same time is shown Fig.4. The height of the cell in this thundercloud reached 1.5 km altitude; The temperature was around -10℃. The graupel existed in leeward side of it. These facts suggest that the graupel generated above the altitude of -10℃ layer.

Thundercloud moving to inland at 0846 JST is shown in Fig.5. Figure 6 shows zonal vertical section along C-D line in Fig.5 at the same time. The graupel reached to the ground.

PGF occurred at 0847 JST. The position of the PGF is plotted at the exterior of graupel area on the ground (Fig. 6).

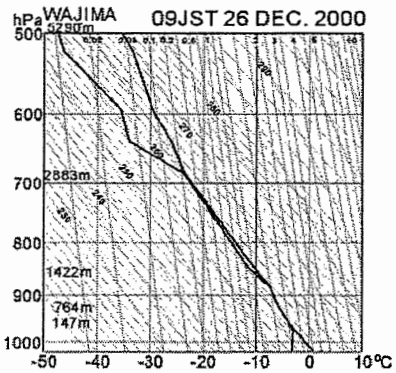

Fig.2. Vertical profile of air and dew-point temperature in Wajima at 09JST.

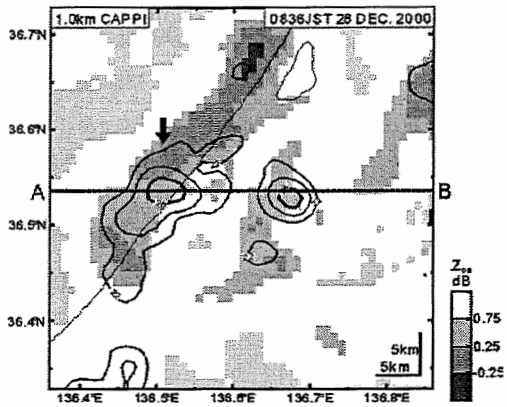

Fig.3. CAPPI at 1.0 km near the thundercloud at 0836 JST. Horizontal Reflectivity (Z_h) is displayed in gray colors and Differential Reflectivity (Z_{DR}) is displayed in contours every 3 dBZ_e from 22 dBZ_e. The thundercloud is shown by broad arrow.

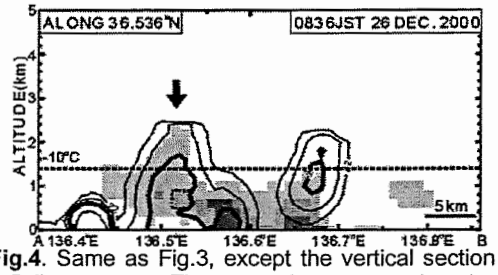

Fig.4. Same as Fig.3, except the vertical section of A-B line in Fig.3. The graupel area is enclosed with dash line.

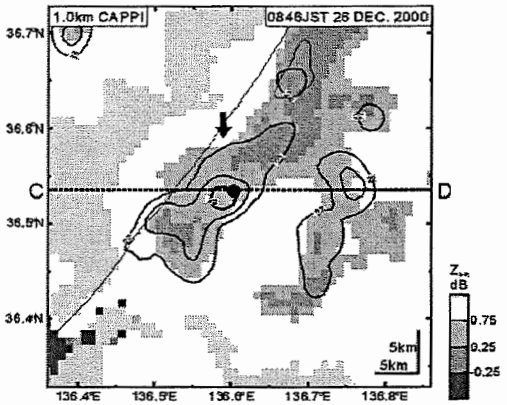

Fig.5. Same as Fig.3, except at 0846 JST. Position of PGF is shown by filled circle.

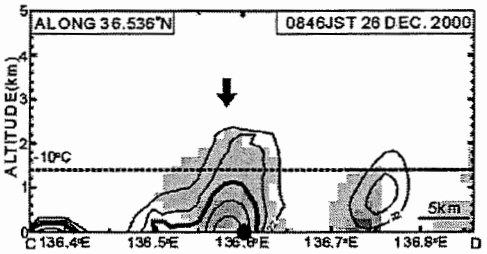

Fig.6. Same as Fig.3, except the vertical section of C-D line in Fig.5 at 0846 JST. Position of PGF is shown by filled circle.

3.2 Thundercloud with negative ground flash

On 15 December 2001, thundercloud with NGF occurred. The height of the cell in this thundercloud reached 3.5 km altitude; The altitude was above -10℃ layer. The graupel existed in leeward side of it (not shown).

In the thundercloud, NGF occurred three times at 1123-1127 JST. The all positions of the NGFs were plotted at the interior of graupel zone on the ground.

3.3 Thundercloud with positive and negative ground flash

On 24 December 2000, thundercloud with PGF and NGF occurred. The height of the cell in this thundercloud reached 4.5 km altitude; The altitude was above -10℃ layer.

Figure 7 shows thunderclouds close to coastline at 2236 JST. Figure 8 shows zonal vertical section of it (E-F line in Fig.7) at the same time. The height of the cell in this thundercloud reached above the altitude of -10℃ layer. The graupel existed in leeward side of it. These facts suggest that the graupel generated at higher layer than the altitude of –10℃ layer.

Figure 9 shows thunderclouds moving to inland at 2256 JST. Figure 10 shows zonal vertical section of it (G-H line in Fig.9) at the same time. The graupel descended to the ground.

There were five CGDs from this thundercloud. The first and last PGF occurred at 2247 JST and 2257 JST. The positions of them are plotted at the exterior of graupel zone on the ground. The positions of other three CGDs, which consists of two NGF and one PGF, were plotted the interior of graupel area on the ground.

3.4 Overview of three types of thundercloud

Table 1 shows characteristics of three types of thunderclouds. The common factors of them are as follows. The graupel generated at higher layer than the altitude of -10℃ layer. The graupel existed in leeward side of the thunderclouds. CGD occurred in the mature stage and at the beginning of declination of the thunderclouds.

The difference of them is as follows. In the thunderclouds with the taller cell over 3 km altitude, NGFs occurred, but in the thunderclouds with shorter cell, PGF only occurred.

We show the relation between the position of graupel area on the ground and GCDs. NGFs occurred at the interior area of graupel area and PGFs occurred in the exterior of the area.

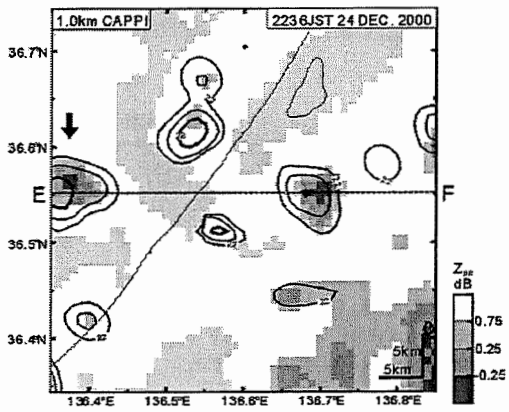

Fig.7. Same as Fig.3, except at 2236JST on 24 December 2000.

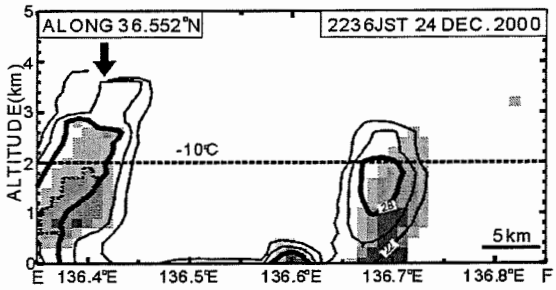

Fig.8. Same as Fig.3, except the vertical section of E-F line in Fig.7 at 2236JST on 24 December 2000. The graupel area is enclosed with dash line.

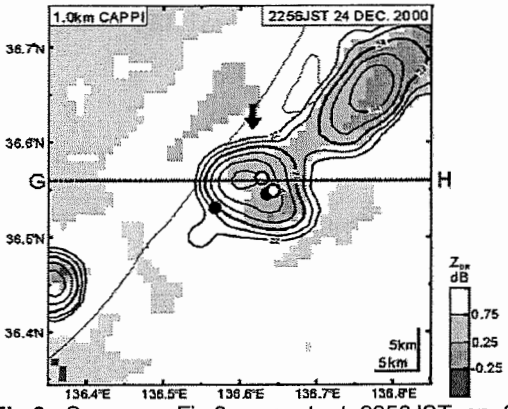

Fig.9. Same as Fig.3, except at 2256JST on 24 December 2000. Position of PGF is shown by filled circle. Position of NGF is shown by open circle.

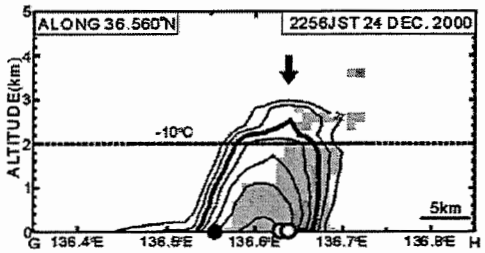

Fig.10. Same as Fig.3, except the vertical section of G-H line in Fig.9 at 2256JST on 24 December 2000. Position of PGF is shown by filled circle. Position of NGF is shown by open circle.

4. DISCUSSIONS

The graupel generated above -10℃ layer. According to Takahashi (1978), the graupel in thunderclouds was negatively charged.

Figure 9 shows that the positions of PGF were not only leeward side of thundercloud but also windward side of it. According to this fact, the reason why PGFs occurs more frequently in winter than in summer, is not explained by horizontal sparation of negatively charged graupel and positively charged upper layer snow particles explained by Brook et al (1982).

Thunderclouds with only PGF as shown in Table 1 are expected to be short. In the thundercloud, the negatively charged graupels in thunderclouds fell quickly because of shortness of clouds. The positive charge only stays in thunderclouds, as Kitagawa (1996) mentions.

5. CONCLUSIONS

We investigated the relative position between graupel in thunderclouds and positive ground flash or negative ground flash by using dual polarization radar and Lightning Location System. The positive ground flashes of winter thunderclouds are explained as follows. Thunderclouds developed rapidly to form graupel particles near the coast. The negatively charged graupel in thunderclouds fell quickly to reach the ground before the positive lightning from the positively charged snow layer starts.

Acknowledgements

We could use radar and LLS data by the courtesy of Hokuriku Electric Power Company. We thank Koichiro Kami to cooperate to use the data.

References

Brook, M., Nakano, M., Krehbiel, P., and Takeuti, T., 1982: The electrical structure of the Hokuriku winter thunderstorms. *J. Geophys. Res.*, **87**, 1207-1215.

Kitagawa, S., 1996: Meteorological characteristics of winter thunderclouds in the coast of the sea of Japan. *Tenki*, **43**, 89-99. (in Japanese)

Takahashi, T., 1978: Riming electrification as a charge generation mechanism in thunderstorms. *J. Atmos. Sci.*, **35**, 1536-1548.

Table 1. Comparison of 3 types of thunderclouds.

Thundercloud types	PGF only	NGF only	PGF and NGF both
Height of -10℃	1.4km	1.6km	2.0km
Achievement height of graupel	Over 1.2km	Over 1.8km	Over 1.4km
Horizontal position of graupel	Leeward side of the thundercloud cell		
Cell top height (Z_h over 28dBZ)	1.5km	3.5km	4.5km
Occurrence time of CGDs	Mature stage and beginning of declination of thundercloud		
Positions and Timings of CGDs	1 Exterior	3 Interior	PGF: 2 Exterior 1 Interior (after NGF occurred) NGF: 2 Interior

"Interior" means interior of graupel zone on the ground and "Exterior" does exterior of that.

C-G LIGHTNING ACTIVITIES AND RAINDROP ELECTRIC CHARGE DISTRIBUTIONS OBSERVED DURING BAIU MONSOON SEASON

K. Suzuki[1], T. Kawano[2] and M. Yoshizaki[3]

[1]Yamaguchi University, Yamaguchi, Yamaguchi, 753-8515, Japan
[2]Kyushu University, Fukuoka, Fukuoka, 812-8581, Japan
[3]Meterological Research Institute, Tsukuba, Ibaraki, 305-0052, Japan

1. INTRODUCTION

It is known that lightnings are often active in Baiu monsoon season. It is classified into the frontal thunderstorm, which has different features from winter thunderstorms. It is important for the understandings of the precipitation mechanisms in clouds to reveal their distributions and evolutions. In this study, cloud-to-ground (C-G) lightning activities and raindrop electric charge distributions were investigated as a part of the field program for the X-BAIU-02 Project conducted in June-July 2002, which targeted mesoscale convective systems (MCSs) during Baiu monsoon season over the East China Sea and Kyushu, Japan (Yoshizaki et. al., 2002).

2. OBSERVATION

Simultaneous measurements of raindrop charge, atmospheric electric field and rainfall intensity were made at Sendai, the southwestern region of Kyushu, Japan (Figure 1), from 20 June through 7 July 2002. The induction ring method was used for the measurement of raindrop electric charges at the ground. C-G lightning data obtained from JLDN (Japan Lightning Detection Network) was also examined. During the observation period, the enhancement of Baiu monsoon and the outer band of Typhoon 0205 (Rammansun) brought heavy precipitation, and landslide disasters were reported.

3. C-G LIGHTNING ACTIVITIES DURING BAIU MONSOON SEASON

Lightning activities by the typical monsoon rain and the outer band of Typhoon 0205 were investigated. Lightning frequencies and pattern of

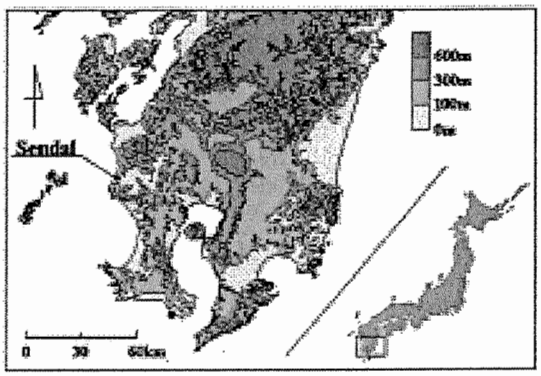

Figure 1: Map of Southern Kyushu, Japan.

C-G lightning locations were related to observed precipitation structures and life stages.

On June 30, Baiu front was located on the northern Kyushu. Rainbands with solid high radar reflectivities in the broad precipitation region were observed over the East China Sea, and it moved eastward. Figure 2(a) shows the number of C-G lightning for 10 minutes observed 120km around the observation site. Negative C-G lightning was dominant (92.4%), and four peaks were defined. Figure 3 shows the weather radar echoes of 2km-CAPPI with the locations of C-G lightning. The locations of negative C-G lightning were limited in the narrow area. Maximum flash rate was 10.3/min at 0840 JST. Negative C-G lightnings were located in the areas with high reflectivites more than 12mm/hr, while positive C-G in the 4mm/hr. After the landing of rainband, the number of C-G decreased and very few of positive C-G observed. The number of C-G lightning corresponded to the area of strong radar reflectivity (Figure not shown). Rutledge and MacGorman (1988) found that positive C-Gs were often located in stratiform region and that negative C-Gs in deep convection in Oklahoma. Shafer et. al. (1999) found that most of C-Gs in the developing rainbands were negative. C-G lightnings observed in this study were similar to

Corresponding author address: Kenji Suzuki, Yamaguchi University, Yamaguchi 753-8515, Japan; E-mail: kenjis@yamaguchi-u.ac.jp

the lightning activities in Oklahoma in the period of the developing stage.

On July 6, the outer band of Typhoon 0205 was observed. Typhoon 0205 moved northwestward over the East China Sea, and landed on Korean Peninsula in the morning on July 6. Most C-G lightnings were negative, which ratio was 72.7%. C-G lightning distributions were similar to the case of June 30, negative C-Gs were located in the area with strong reflectivities, and positive C-Gs were occasional (Figure 4). Positive C-Gs was confined to the inland region after the landfall of the Typhoon outer band. This was similar to the findings by Samsury and Orville (1994), which was that most of C-G was located in the outer convective rainbands in the right front and right rear quadrants of the hurricanes. However, the relationship between the number of C-G and the 2km-CAPPI echo area was not distinct, and the peak of C-Gs occurred about I hour behind the peak of the strong reflectivity area. The vertical reflectivity distribution (Figure not shown) indicated that the main C-G activity did not occur in the early developing stage, which had the maximum reflectivity area on 2km-CAPPI, and ice formation process might not be active at the higher level. This suggested that the C-G activity of typhoon might be different from the monsoon cloud systems, related to the precipitation particle formation processes.

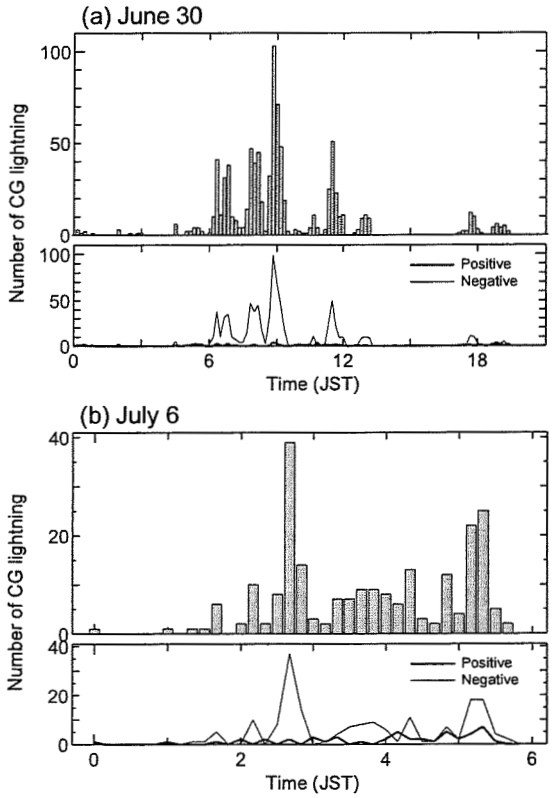

Figure 2: The number of C-G lightning for 10 minutes observed within 120km around on (a) June 30, and (b) July 6.

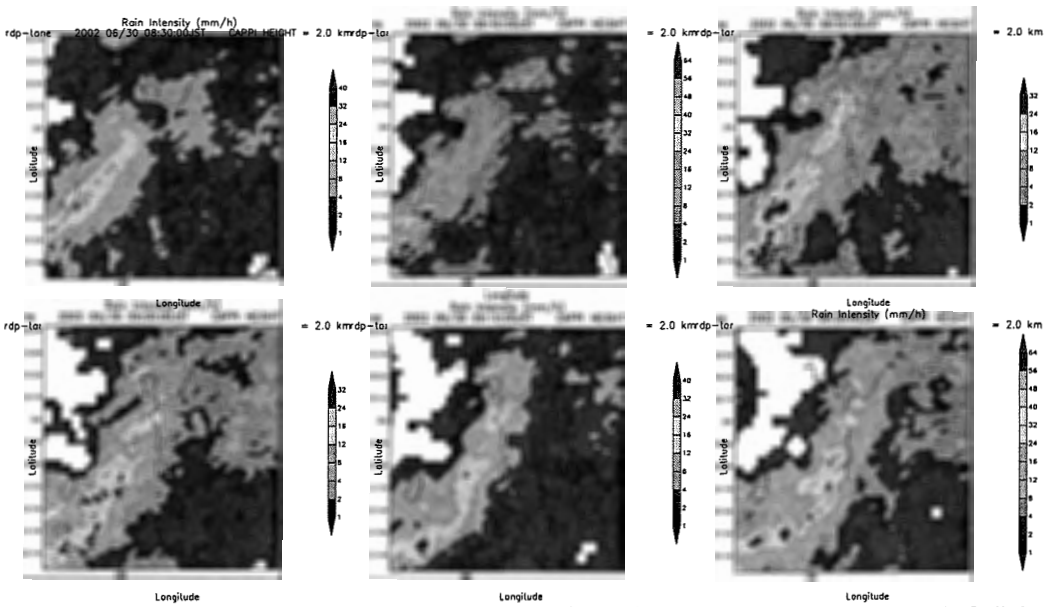

Figure 3: JMA Kagoshima radar echoes (2km-CAPPI) on June 30 with locations of C-G lightning. Symbols of plus and square indicate positive and negative, respectively.

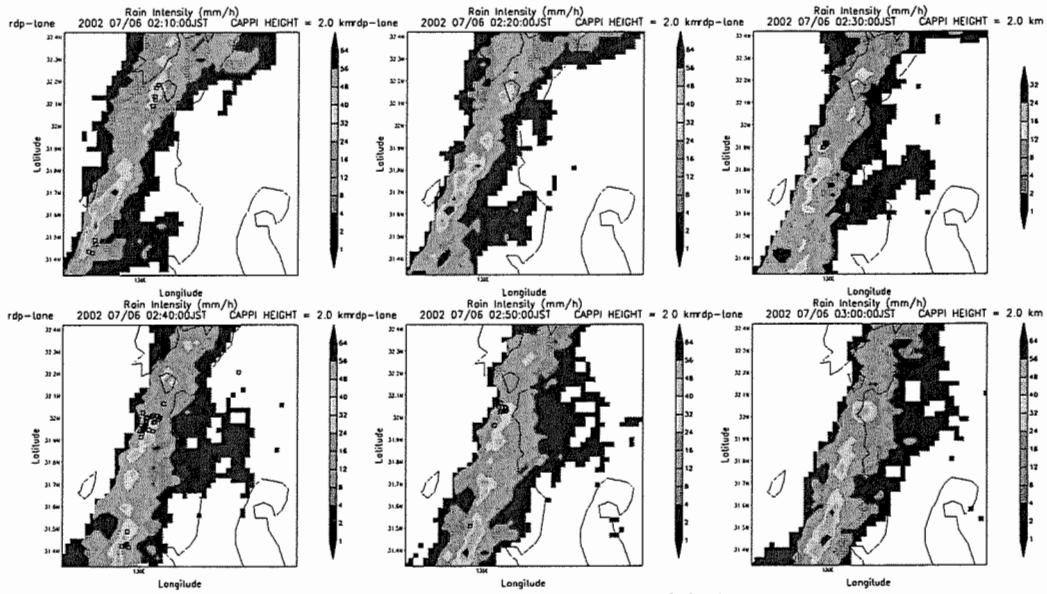

Figure 4: Same as Figure 3 on July 6.

4. RAINDROP CHARGE DISTRIBUTIONS

Raindrop electric charge distributions were obtained from four different types of precipitation, which was measured using the induction ring method. The raindrop charge distributions were related to the rain patterns. Figure 5 shows the raindrop electric charge accumulated for 10 minutes on June 28-29, June 30, and July 6. On June 28-29, the electric potential gradient at the ground showed the warm rain pattern, and the maximum positive charge for 10 minutes was 3000-5000pC. On June 30, two rain systems were passed over the site with more than 6000pC positive charges. The negative charge was larger than the case of June 28-29. On July 6, the electric potential gradient showed the thunderstorm pattern as well as the case of June 30. The maximum positive charge reached 10000pC. The maximum positive charges accumulated for 10 minutes appeared with the maximum rainfall intensities in the all cases, while the maximum negative charges after the heavy precipitations were observed. The net charge is positive except in the beginning and ending of precipitations with the weak precipitations. 10-minute averaged positive charge shows an increase with rainfall intensity for all the rain. 10-minute negative charge, however, does not depend on the rainfall intensity in the case of typical monsoon rain and typhoon outer band, which produced heavy precipitations (Figure 6). This was similar to the raindrop electric charge distributions of Indian Monsoon rain observed by Selvam et. al. (1977). The raindrop charges measured at the surface may not be exactly representative of in-cloud electrification mechanisms due to the mirror image effects (Takahashi, 1984; Asuma et. al., 1987). Raindrop charge distributions, however, suggests the different mechanisms in the different rain types.

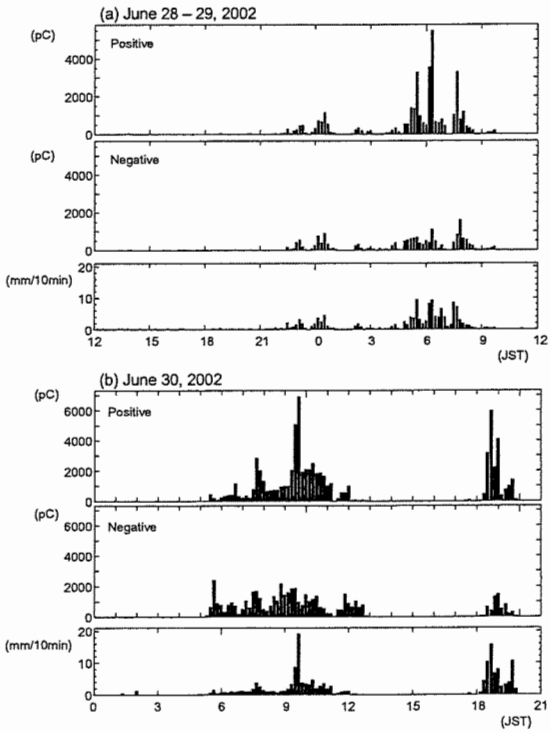

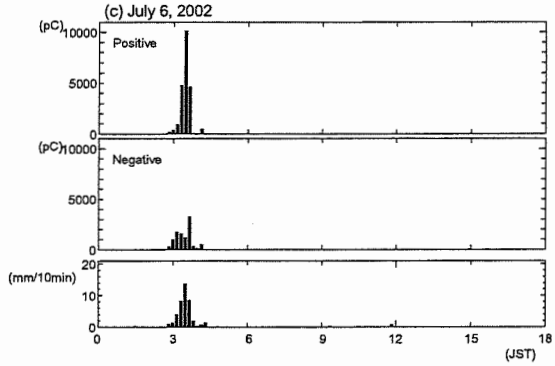

Figure 5: 10 minutes accumulated raindrop electric charge and 10 minutes precipitation on (a) June 28-29, (b) June 30, and (c) July 6, 2002.

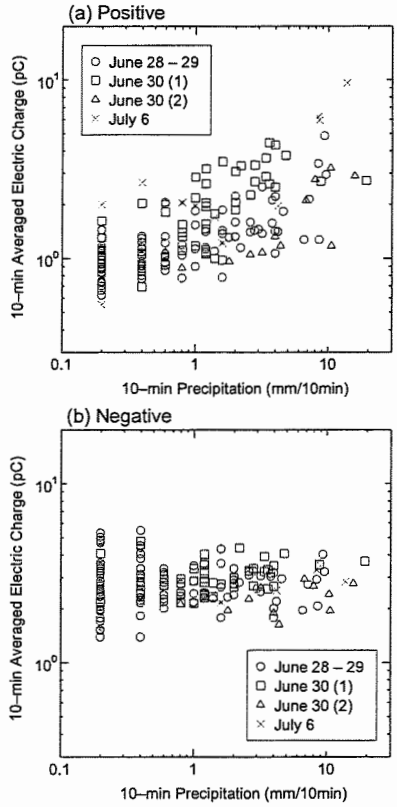

Figure 6: Relationship between 10-min averaged electric charge and precipitation. (a) positive (b) negative.

REFERENCES

Asuma, Y., K. Kikuchi, and T. Taniguchi, 1987: A simultaneous observation system of the electric potential gradient and the precipitation charge in the lower atmospheric layer. J. Meteor. Soc. Japan, 65, 991-998.

Chauzy, S. and S. Despiau, 1980: Rainfall rate and electric charge and size of raindrops of six spring showers. J. Atmos. Sci., 37, 1619-1627.

Rutledge, S. A. and D. R. MacGorman, 1988: Cloud-to-ground lightning activity in the 10-11 June 1985 Mesoscale Convective System observed during the Oklahoma-Kansas PRE-STORM project. Mon. Wea. Rev., 116, 1393-1408.

Samsury, C. E. and R. Orville, 1994: Cloud-to-ground lightning in Tropical Cyclones: A study of Hurricanes Hugo (1989) and Jerry (1989). Mon. Wea. Rev., 122, 1887-1896.

Shafer, M. A., D. R. MacGorman, and F. H. Carr, 2000: Cloud-to-ground lightning throughout the lifetime of a severe storm system in Oklahoma. Mon. Wea. Rev., 128, 1798-1816.

Selvam, A. M., G. K. Manohar, L. T. Khemani, and B. V. Ramana Murty, 1977: Characteristics of raindrop charge and associated electric field in different types of rain. J. Atmos. Sci., 34, 1791-1796.

Takahashi, T., 1984: Thunderstorm electrification – A numerical study. J. Atmos. Sci., 41, 2541-2558.

Yoshizaki, M., T. Kato, C. Muroi, H. Eito, S. Hayashi, and CREST Observation Group, 2002: Recent activities of field observations on mesoscale convective systems (MCSs) over East China Sea and Kyushu in Baiu season and over the Japan Sea in winter, Proc. Int. Conf. Mesosocale Convective Systems and Heavy Rainfall/Snowfall in East Asia, Tokyo, Japan, 80-85.

THE IMPACT OF LIGHTNING ON A LIFE CYCLE OF CONVECTIVE CLOUDS: A NUMERICAL STUDY

Zlatko R. Vukovic[1] and Bosko T.Telenta[2]

[1]Meteorological Service of Canada, Toronto, Ontario, M3H 5T4, Canada
[2]SENES Consultants Limited, Ontario, L4B 3N4, Canada

1. INTRODUCTION

As observations show us, lightning could cause a sudden redistribution of mass among cloud hydrometeors (Moore, Vonnegut, and Vrablik, 1964; Curic and Vukovic, 1991; Carey and Rutledge, 1994; Vukovic and Curic, 1996, 1998, 2000). The main goals of this study are to parameterize lightning within 3D numerical cloud models with complex microphysics, and to analyze the possible impact of lightning on the life cycle of deep convective clouds. A parameterization scheme is designed to treat this redistribution, which is always irregular in time and space.

2. PARAMETERIZATION SCHEME

The Advanced Regional Prediction System (ARPS) model is used for numerical simulation of the life cycle of convective clouds (Xue et al., 2001). Since the model's microphysics does not include electrification and related processes, it is necessary to parameterize spatial and temporal occurrences of lightning, and the proposed mass redistribution.

2.1 Lightning parameterization

The most suitable lightning parameterizations for our purpose, without electrification, have been developed and described by Price and Rind (1994). The parameterization is based on observations that show that thunderstorm electrification is closely linked to the updraft intensity in the cloud, which in turn is linked to the vertical development of convective clouds. For continental thunderstorms the relationship is:

$$F_c = 3.44 \times 10^{-5} H^{4.90}, \qquad (1)$$

Where F_c is the lightning frequency (flashes per minute) and H is the cloud-top height above ground (km).

The parameterization of the lightning position in the cloud is based on the results of location relations of lightning centers and radar-echoes studies (Chagnon, 1991). They found that flashes tended to cluster away from main reflectivity areas and occurred in regions of high gradients.

Corresponding author's address: Zlatko R. Vukovic, Meteorological Service of Canada, Toronto, Ontario, M3H 5T4, Canada; E-Mail: zlatko.vukovic@ec.gc.ca.

According to this idea, the lightning channel is parameterized as a set of model points that belongs to the vertical line that passes through one of the randomly chosen surrounding points from the point of maximum radar reflectivity in the layer between the $-10\,^{\circ}C$ and $-25^{\circ}C$ isotherms.

2.2 Mass redistribution parameterization

For the purpose of this study, the ice microphysics scheme in the ARPS that has two liquid phases (cloud droplets and rain) and three ice categories (ice cloud, snow, and hail or graupel) after Lin et al. (1983) was chosen. The transformation of cloud categories due to lightning is assumed to occur only between four categories: cloud droplets (q_c), rain (q_r), ice particles (q_i), and hail (q_h). The mass redistribution parameterization is derived from the following physical examination.

The total mass change in the lightning grid point satisfies mass conservation:

$$\Delta q_c + \Delta q_r + \Delta q_i + \Delta q_h = 0. \qquad (2)$$

The change in the mass of cloud droplets is always negative (loss of cloud droplets mass) and is equal to a fraction (f_c) of the original cloud mass: $\Delta q_c = -f_c q_c$.

The change in rain mass could be positive or negative, depending on the amount of cloud droplets that comes in the rain category and the amount of rain that is transformed into hail: $\Delta q_r = = -f_r q_r + \varepsilon_{cr} f_c q_c$, where f is a fraction of the rain that is transformed into hail, and ε_{cr} is a parameter that determines what fraction of lost cloud droplets successfully collides and increases the rain mass.

In general, the ice particles could gain mass in collision with cloud droplets, and also lose mass in collision with rain, when they are transformed into hail: $\Delta q_i = -f_i q_i + \varepsilon_{ci} f_c q_c$. The parameter ε_{ci} has the same meaning as ε_{cr}; it determines what fraction of lost cloud droplets successfully collides and increases the ice particle mass.

Opposite to cloud droplets, hail could only increase the mass from all three categories: $\Delta q_h = \varepsilon_{ch} f_c q_c + f_r q_r + f_i q_i$. The parameter ε_{ch} has the same meaning as ε_{ci} and ε_{cr}, but for cloud droplet–hail collision.

Substitution of all the parameterized category mass changes in (2) gives:

$$\varepsilon_{cr} + \varepsilon_{ci} + \varepsilon_{ch} = 1. \qquad (3)$$

From the proposed category-mass redistribution parameterization, we need three parameters (f_c, f_r, and f_i must all be ≤ 1) to describe what fraction of cloud, rain, and ice categories is lost due to the simulated lightning influence. Also, we need two parameters to describe the redistributed cloud-droplet loss among the rest of the three categories. The chosen values must be ≤ 1 and satisfy equation (3).

2.3 Released heat energy

Released heat energy due to phase transformations of cloud elements is also included in the adjustment to the potential temperature θ.

$$\delta\theta = -L_v / (\Pi C_p), \quad (4)$$

where L_v is the latent heat of evaporation, defined by:

$$L_v = 2500780\ (273.15 / T)^{(0.167 + 3.67E\text{-}4\ T)}. \quad (5)$$

The temperature is in ^oK, and L_v in Jkg^{-1}. Π is the Exner function, given by:

$$\Pi = (p/p_o)^{Rd/Cp}, \quad (6)$$

where R_d is the gas constant for dry air, and C_p is the specific heat for dry air. p_o = 1000mb, which is a constant reference pressure.

3. MODEL SIMULATIONS

3.1 ARPS initialization

The model is initialized using the same sounding as the well-documented and extensively studied storm of 20 May 1977 in Del City, Oklahoma (Ray et al., 1981; Lin et al., 1993).

For all experiments, the horizontal grid spacing is 500m and the vertical grid is 250m. The domain is $40x40x15km^3$ in size. The storm was initiated by a 3.2^oC ellipsoidal thermal bubble centered at x = 48km, y = 16km and z = 1.5km, and wth radii of 10km in x and y directions and 1.5km in the vertical direction. The large and small time step sizes are 3s and 1s, respectively.

3.2 Lightning initialization

The model is integrated for 60 minutes. During that time, in every big time step, the cloud-top height as a predictor for lightning was calculated (eq. [1]). If the rounded flash rate was equal or greater than 1, in the next minute of simulation, in each big time step, the parameterized mass redistribution was activated until the number of calculated flashes was reached. The new rounded flash rate was calculated after a predicted number of flashes occurred, and at least one minute past.

The location of the vertical set of grid points, where mass redistribution had occurred, was randomly chosen around the area with the maximum radar reflectivity. The procedure was followed. After the point with maximum reflectivity was determined, one of eight surrounding grid points in the horizontal plain was randomly chosen. The horizontal coordinate of that grid point was the x, y coordinates of the simulated lightning influence.

3.3 Experiments

As a referent simulation, a run without lightning parameterization was used (case0). The next three runs were with lightning parameterization and different combinations of the mass redistribution parameters, Table 1. In all three runs with lightning parameterization, cloud-drops redistribution parameters ε_{cr}, ε_{ci}, and ε_{ch} were the same, while the fractions of transformed cloud, rain, and ice mass were increased by 5%.

Table 1. The ARPS model sensitivity test, involving lightning mass redistribution parameters. The parameters f_c, f_r, and f_i are the fractions of cloud, rain, and ice mass-category redistribution, respectively. The parameters ε_{cr}, ε_{ci}, and ε_{ch} are the mass of cloud droplets redistribution between the cloud, rain, and ice mass categories, respectively.

case	f_c	f_r	f_i	ε_{cr}	ε_{ci}	ε_{ch}
0	0	0	0	0	0	0
1	0.05	0.05	0.05	0.50	0.25	0.25
2	0.10	0.10	0.10	0.50	0.25	0.25
3	0.15	0.15	0.15	0.50	0.25	0.25

4. RESULTS AND DISCUSSION

For the same initial conditions the ARPS model was run for a case without (case0) and with lightning parameterization (case1, case2, and case3). The total surface precipitation is shown in Fig. 1. The vertical cross-sections of the cloud (case0), with velocity field, through 35.957N line, are shown in Fig. 2.

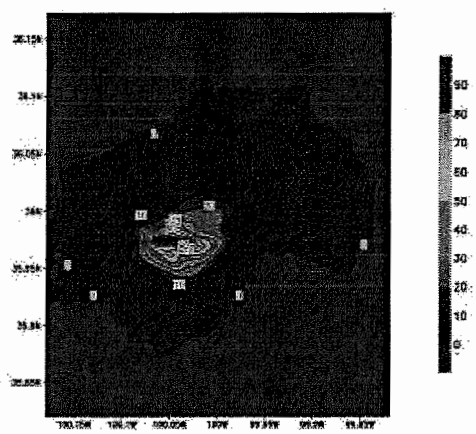

Fig. 1. Horizontal surface cross-section of the total rain for case0, t = 45 min. The shaded legend is in mm.

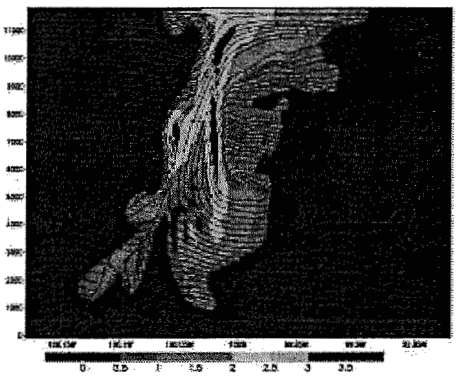

Fig. 2. Vertical cross-section, x-z plane, of cloud water and ice with wind field; for case0 in t = 45 min, y = 8.5km (35.957N). The shaded legend is in g/kg.

The surface difference of case1–case0 for the total amount of rain is shown in Fig. 3, while the difference of rain rate, is shown in Fig. 4. It is obvious that lightning simulation, even for case1, gives a measurable difference in surface precipitation.

From the vertical cross-sections for vertical velocity (Fig. 5), we can see noticeable change in cloud dynamics structure, which is closely related to the hail field (Fig. 6).

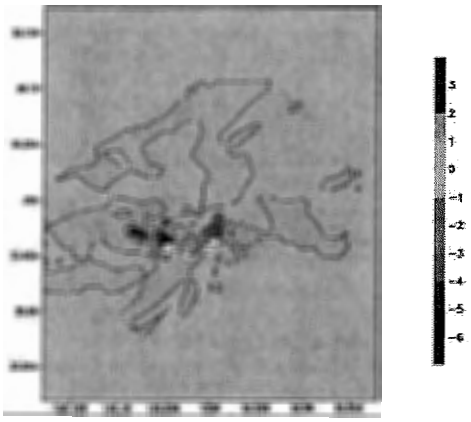

Fig. 3. The surface difference of total rain (case1–case0) in t = 45 min. The shaded legend is in mm.

The general differences of three lightning simulations could be measured by the time series of differences in the maximum vertical velocity (Fig. 7a) and radar reflectivity (Fig. 7b).

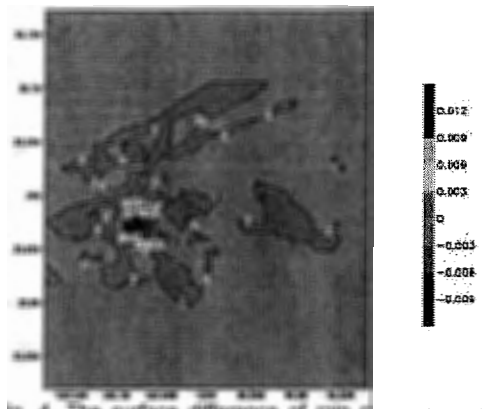

Fig. 4. The surface difference of rain rates (case1–case0), t = 45 min. The shaded legend is in mm/min

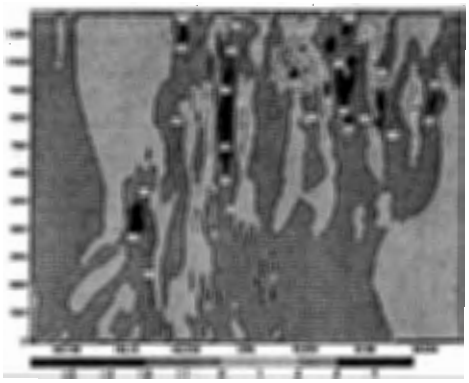

Fig. 5. Vertical cross-section, x-z plane, of difference of vertical velocity fields; case1 – case0, t = 45 min. y = 18.5km (35.957N). The shaded legend is in m/s.

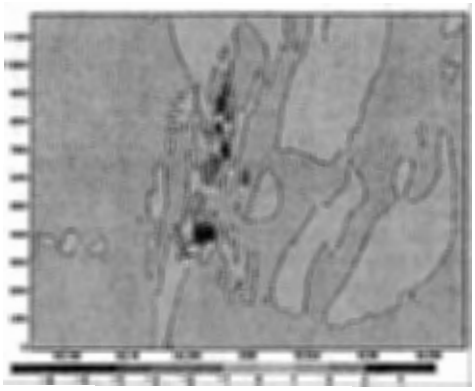

Fig. 6. Vertical cross-section, x-z plane, of difference of hail fields; case1 – case0, t = 45 min. y = 18.5km (35.957N). The shaded legend is in g/kg.

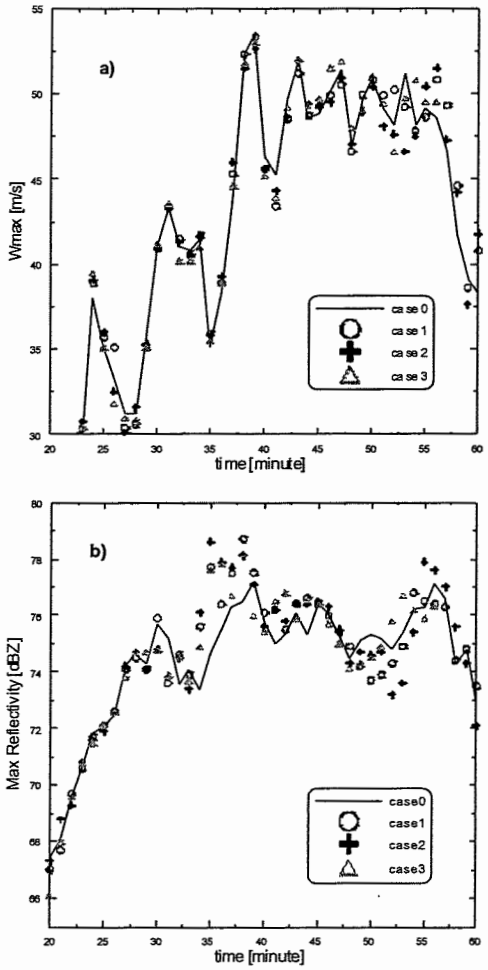

Fig. 7. The time series of (a) the maximum vertical velocity and (b) the maximum radar reflexivity in the four simulations of the storm in Del City, Oklahoma, May 20, 1977

From the presented results, it is clear that, with suggested lightning parameterization, relatively small changes in mass redistribution (5%) in the very restricted area of cloud (lightning channel grid points), could make a noticeable change in the precipitation field and the dynamics of cloud.

The results also show that, with purposed or improved parameterization, we could successfully use a 3D numerical cloud model as a tool for further study of the importance of different processes that cause sudden changes in the distribution of cloud mass.

3.8 References

Carey, Lawrence D., and Rutledge, Steven A. 2000: The Relationship between Precipitation and Lightning in Tropical Island Convection: A GBand Polarimetric Radar Study. *Monthly Weather Review*: Vol. 128, No. 8, pp. 2687–2710.

Chagnon, S. A. 1991: Temporal and Spatial Relations between Hail and Lightning. *Journal of Applied Meteorology*: Vol. 31, pp. 587–604.

Curic, M. and Vukovic, R. Z. 1991: The Intfluence of Thunderstorm Genereted Acoustic Waves on Coagulation. Part One: Mathematical Formulation. *Z.Meteor.* Vo. 41, pp.164-169.

Lin, Yuh-Lang, Farley, Richard D., and Orville, Harold D. 1983: Bulk Parameterization of the Snow Field in a Cloud Model. *Journal of Applied Meteorology*: Vol. 22, No. 6, pp. 1065–1092.

Lin, Ying, Ray, Peter S., and Johnson, Kenneth W. 1993: Initialization of a Modeled Convective Storm Using Doppler Radar–Derived Fields. *Monthly Weather Review*: Vol. 121, No. 10, pp. 2757–2775.

Moore, C. B., Vonnegut, B. , and Vrablik, E. A. 1964: Gushes of Rain and Hail After Lightning. *Jour. of Atm.* and McCaig, A.D. *Sci.* Vol. 21, pp.646-665.

Price, Colin, and Rind, David. 1994: Modeling Global Lightning Distributions in a General Circulation Model. *Monthly Weather Review*: Vol. 122, No. 8, pp. 1930–1939.

Ray, P.S., Johnson, B.C., Johnson, K.W., Bradberry, J.S., Stephens, J.J., Wagner, K.K., Wilhelmson, R.B., and Klemp, J.B. 1981: The Morphology of Several Tornadic Storms on 20 May 1977. *Journal of the Atmospheric Sciences*: Vol. 38, No. 8, pp. 1643–1663.

Vukovic, R.Z., and Curic, M. 1996: A Possible Relationship between Lightning Discharge in Cloud and Gushes of Rain. *Pro 12. ICCP*, Zurich, Switzerland.

Vukovic, R.Z., and Curic, M. 1998: The Acoustic-Electric Coalescence and the intesification of Precipitation Radar Echoes in Clouds. *Atm.Res*: Vol. 47-48, pp. 113-125.

Vukovic, R.Z. and Curic M. 2000: The ice initialisation by the acoustic-electrostatic coalescence. *Pro 13. ICCP*, Reno, Nevada, USA.

Xue M, K.K. Droegemeier, V. Wong, A. Shapiro, K. Brewster, F.Carr, D. Weber, Y. Liu, and D. Wang, 2001: The Advanced Regional Prediction System (ARPS) – A Multi-scale Nonhydrostatic Atmospheric Simulation and Prediction Tool. Part II: Model Physics and Applications. *Met. Atmos. Phys*: Vol. 76, pp. 143-165.

THE RESEARCH ON PRECIPITATION AND LIGHTNING MAP

Wan Xia[1] Zhang Qiang[1] and Cai Xiaoyun[2]

[1] Beijing Weather Modification Office, Beijing, 100089,China
[2] Beijing Meteorological Bureau ,Beijing, 100089, China

1. INTRODUCTION

In order to see the changes of cloud, some equipments that are used to observe are recorded in this paper. We pay attention to the situation on satellite ,radar and lightning map. The lighting map is conducted recently. It can describe the change of lightning on time. We could tell from some different cloud by experiment about many years in radar. Weather modification was very important to agriculture in China. It would avoid reducing the loss of property and the hurt of body. So more and more people were engaged in this field.

The different process to precipitation will be applied to vary with weather. Some instruments are chosen in different weather. There are some instructions such as airplane, rocket and so on. When it is stable, airplane is often used to seed. Rocket and others should be applied if it were convectional rain.

2. SEVERAL TYPES OF CLOUD WITH THE DISTRIBUTING OF LIGHTNING

The lightning data was earlier than the observation in radar. It was a qualitative index to judge. Convectional rain and non-convectional rain were large dissimilar distribution in lightning mapping.

There were lightning mass when it was convectional precipitation. They got together several to some dozens of kilometers. And the frequency of CG lightning flashes would decrease sharply after the first frequent top of CG flashes. There were no large frequency in the remainder hours in hail cloud. While there were the second frequent top of CG lightning flash. In any case, airplanes would not be apply to precipitation enhancement in this kind of weather situation. On the contrary, there were dispersed to hundreds kilometers in non-convectional rain. Even if few CG lightning flash were detected when it was Nimbostratus (Ns). Under these situations, airplane was used to operation.

3. THE CASES

3.1 General description

The lightning map is not only lightning location but also three-dimensional (3-D) map, which will help us to find the situation of microphysics of cloud. It will show many actions of atmosphere, and it will present the phenomena of discharge. That was the basic of our studies. The apparatus of lightning location could be benefit for research the development of convective activity in cloud since it can reflect electrification process of cloud. Several cases to precipitation are introduced in this paper.

3.2 The analysis of some cases

To compare the different characters between hail cloud and others, some data of plan position indicator (PPI) or range-height indicator (RHI) in Radar were paid attention to analyze. There were all cases in Beijing in this paper.

The cell storm was recorded to show the development of physical changes in cloud on May 31, 2000 . In this event, the cloud-to-ground (CG) lightning flash were detected. From lightning map, CG were near the center of strong echo. Almost CG flashes matched very well with RHI in Radar, but they were about 30 minutes earlier than the data from Radar. The result had an advantage to hail suppression because there would be more time to operation.

The band-shape of radar echo often occurred for the typical character of hail cloud in Beijing. It was in accord with the shape of radar echo, which showed the electric activities in cloud. The precipitation particles were in collision with each other, which formed hail. The more angry electric field was, the more there was a violent storm.

To detect the character of hail cloud, many cases were analyzed. Therefore, Nimbostratus (Ns) and thundercloud cases were analyzed, too.

The structure of thunderstorm was relative in CG lightning flashes. While the strong echo occurred, there were +CG lightning flash together (Figure 1).

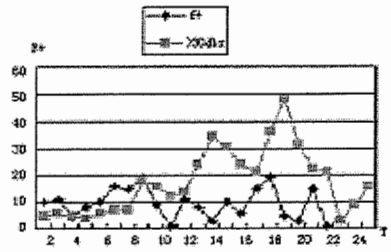

Figure 1. the relationship between +CG lightning frequency and the strong echo area on July 4,2000.

Corresponding author's address: 44 Zizhuyuan Road, Haidian District, Beijing, 100089,the People's Republic of China; E-Mail: lucywan@sina.com

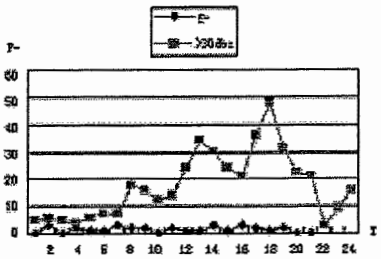

Figure 2. the relationship between –CG lightning frequency and strong echo area on the same time.

From figure 2, it could be seen that, –CG lightning frequency and strong echo, they did not match well. Their changes had no relativity.

The intra-cloud discharges (IC) could be detected by 2003. These lightning discharges take place inside thunderstorm cloud. This is the most important part of electrical activity, since they can represent up to 99.5% of total electrical activity in severe thunderstorms. Moreover, thunderstorms always begin with IC discharges, which can occur up to 1 hour before the first cloud-to-ground discharges (SAFIR system).

4. 3-D LIGHTNING MAPPING

The three-dimensional (3-D) lightning mapping was applied to research the physical changes in cloud. The height of discharges in cloud could be detected, which provided the range of cloud to research in some extent.

5. CONCLUSION

To choice safe operational manner, CG lighting flashes and IC lightning flash were applied to be early-warning. The lightning mapping provided the trend of developing storm to short-time forecast.

According to the distribution of lightning flashes, activities in cloud was known. Convectional rain and non-convectional rain were large dissimilar distribution in lightning mapping. Therefore, some different instruments are chosen in strong weather to precipitation enhancement.

6. ACKNOWLEDGEMENTS

Thank our colleagues in our office for helping in this paper. The illustrative contents of Intra-cloud discharges (IC) was from SAFIR user manual.

REFERENCES

B. J. Mason, 1971: The Physics of Clouds. Oxford University Press.

Cai Xiaoyun, Wan Xia, Guo Hu, 2001: Analysis of Lightning Activities in Beijing Area. 3rd National Scientific Conference on Lightning Physics, Lightning Detection and Protection, 73 -75.

Goodman, S. J., 1990: Predicting thunderstorm evolution using ground based lightning detecting networks. NASA Tech. Memo. 103521,117-120.

Solomon,R.,and M.Baker,1994:Electrification of New Mexico Thunderstorms, MONTHLY WEATHER REVIEW,122,1878-1886.

Thomas,R.J.,et al,2000:Comparison of ground -based 3-dimensional lightning mapping observations with satellite-based LIS observations in Oklahoma. Geophy. Res. Letters, Vol.27, No.12,1703~1706.

Wan Xia, 2000: The Research of the Effect to Detected Lightning data, 13th Physics Research to precipitation of cloud and weather Modification, 218-219.

IMPROVED RETRIEVAL OF STRATUS CLOUD MICROPHYSICAL PROPERTIES USING MILLIMETER-WAVE RADAR AND VISIBLE OPTICAL DEPTH

Richard T. Austin and Graeme L. Stephens

Department of Atmospheric Science, Colorado State University, Fort Collins, Colorado, 80523, USA

1. INTRODUCTION

A retrieval of stratus cloud microphysics using either millimeter-wave radar and visible optical depth (RVOD) or radar only (RO) and an estimation theory approach was reported by the authors in 2001 (Austin and Stephens 2001, hereinafter AS2001). The retrieval algorithm assumed a lognormal distribution of cloud droplets, with a droplet number concentration and distribution width parameter that were constant through the cloud column. Furthermore, the width parameter was assigned a fixed value (based on climatology); in the RO case, the number concentration value was also assigned a fixed value. These assumptions allowed the retrieval of a profile of values of the geometric mean radius (and, in the RVOD case, the column droplet number concentration). From these quantities, derived products such as effective radius r_e and liquid water content (LWC) are easily obtained, together with their uncertainties.

An improved retrieval has recently been developed (Austin and Stephens, in preparation) in which the width parameter and (in the RO case) number concentration values are retrieved, rather than being assigned to climatological values with large uncertainties. The poster describes this improved retrieval and discusses the advantages it provides compared to the AS2001 retrieval. These include (1) a better estimate of uncertainty in the width parameter and in derived products; (2) direct calculation of covariances between the retrieved width parameter, number concentration, and radius values; (3) a better fit of retrieved microphysical parameters to the measurements; and (4) a more complete utilization of all the information provided by the measurements.

2. IMPROVED ALGORITHM FORMULATION

2.1 Motivation for Improved Algorithm

The AS2001 algorithm assumed an assigned, fixed value and uncertainty for the distribution width parameter over the entire vertical extent of the cloud column in both the RVOD and RO versions of the retrieval. While the retrieval seemed to perform well, this assumption of a fixed width parameter had several disadvantages. Because the fractional uncertainty of the width parameter was much larger than the fractional uncertainty of the measured reflectivities and visible optical depth, the width parameter dominated the retrieval uncertainty. Consequently, reductions in the uncertainty of the retrieval could be obtained only by reducing the uncertainty of the width parameter, which seemed unlikely.

The use of an assigned width parameter made determination of the retrieval uncertainties difficult. Initial uncertainty estimates for derived quantities retrieved using the AS2001 algorithm assumed that all covariance terms were zero; that is, the retrieved values of geometric mean radius r_g and droplet number concentration N_T were assumed independent of each other and independent of the (fixed) width parameter σ_{log}. These values were considered to be overestimates, because the three distribution parameters were almost certainly (negatively) correlated to some degree. Determination of the needed covariance terms was problematic with the AS2001 retrieval structure, however. Covariances involving the width parameter σ_{log} were not part of the retrieved covariance matrix $\mathbf{S_x}$ because σ_{log} was not part of the retrieved state vector $\mathbf{x}$. Alternative analytical and numerical techniques were investigated, but no satisfactory method of determining values of these covariance terms was found.

A third disadvantage of the fixed width parameter was reflected in two aspects of retrieval performance. In an early application of the AS2001 retrieval to field data, the algorithm was unable to find a state vector $\mathbf{x}$ that fit the measurements more closely than 5-6 dBZ in some cases while using the prescribed fixed value of σ_{log}. Comparisons of retrieved LWC values and in situ measurements also indicated a slight bias, although the source of this bias was unclear.

The difficulty in determining covariance terms involving σ_{log} and further review of Rodgers (2000) led to the question: "What if σ_{log} were retrieved, rather than being assigned at some poorly known value?" A principal assumption in developing the AS2001 algorithm had been that σ_{log} must be assigned as a forward model parameter in order to avoid having too many unknowns in the state vector, but Rodgers (2000) shows many cases where a priori data allow retrievals in which the number of unknowns is greater than the number of available measurements.

Corresponding author's address: Richard T. Austin, Department of Atmospheric Science, Colorado State University, 1371 Campus Delivery, Fort Collins, CO 80523, USA; E-Mail: austin@atmos.colostate.edu.

2.2 Simplest RVOD Retrieval Case

The implications of adding σ_{log} to the state vector are best illustrated by a simple example. Consider the simplest RVOD retrieval case: a single-bin cloud column, where the cloud is described by two measurement values: a radar reflectivity Z_1 and a visible optical depth τ. Writing equations for the measured values, we have

$$Z_1 = 64 N_T r_{g1}^6 \exp(18\sigma_{log}^2) 10^{-12},$$
$$\tau = 2\pi N_T r_{g1}^2 \exp(2\sigma_{log}^2) 10^{-6} \Delta_z.$$

Combining these equations by eliminating N_T gives

$$\frac{\pi \Delta_z 10^{-6} Z_1}{32 \quad \tau} = r_{g1}^4 \exp(16\sigma_{log}^2).$$

For a given pair of measured values (Z_1, τ), any (r_{g1}, σ_{log}) pair satisfying the above equation will fit the measurements exactly.

The illustration clearly shows that the two measurements do not give sufficient information to obtain a unique retrieval of three distribution parameters. Rodgers (2000) shows how a priori data can be utilized as an additional source of information, allowing the selection of a unique solution in this situation. Instead of directly solving n forward model equations for n unknown state variables (impossible here—too few equations), the solution is obtained by minimizing a cost function Φ that represents a weighted sum of the state vector-a priori difference and the measurement vector-forward model difference:

$$\Phi = (\hat{\mathbf{x}} - \mathbf{x_a})^T \mathbf{S_a}^{-1} (\hat{\mathbf{x}} - \mathbf{x_a}) + [\mathbf{y} - \mathbf{F}(\hat{\mathbf{x}})]^T \mathbf{S_y}^{-1} [\mathbf{y} - \mathbf{F}(\hat{\mathbf{x}})].$$

The algorithm seeks a point in the three-dimensional state space that lies between the a priori point and the curve representing an exact fit to the measurements such that the sum of the weighted distances is minimized. The weighting of the two terms determines the location of the solution point between the a priori value and the exact fit curve. For example, if the measurement uncertainty is small (small values in $\mathbf{S_y}$) and the a priori uncertainty is large (large values in $\mathbf{S_a}$), the retrieval will place the solution point close to the exact fit line. (This is the usual case.) Note that the solution is unique; the cost function has a unique minimum because the a priori data constrain the solution to a region near a particular segment of the exact measurements curve. Thus, we are selecting the most likely state vector (point in state space) that is consistent with both the measured data and with a priori information about a particular type of cloud.

The AS2001 algorithm retrieved r_g and N_T but used a fixed value of the width parameter σ_{log}. In terms of the state space, the AS2001 solution was restricted to a fixed σ_{log} plane containing the a priori point. Depending on the shape and location of the exact measurement fit curve and the a priori data value, the true minimum of the cost function may not lie in that plane—a better solution is obtained by allowing σ_{log} to vary, that is, to *retrieve* the value of σ_{log} that minimizes the cost function. The improved algorithm described in the next section implements this change.

2.3 Structure of Improved Algorithm

The improved algorithm has a structure very similar to the AS2001 algorithm. The retrieval assumes a lognormal size distribution of cloud droplets:

$$N(r) = \frac{N_T}{\sqrt{2\pi}\sigma_{log} r} \exp\left[\frac{-\ln^2(r/r_g)}{2\sigma_{log}^2}\right],$$

where N_T is the droplet number concentration, r is the droplet radius, r_g is the geometric mean radius, and σ_{log} is the geometric standard deviation, commonly referred to as the width parameter of the distribution. The distribution is fully specified by three parameters: N_T, σ_{log}, and r_g. All measured quantities (Z, τ) and derived retrieval quantities (r_e, LWC, liquid water path [LWP]) may be expressed in terms of these three parameters.

The state vector $\mathbf{x}$ is the vector of unknown cloud parameters to be retrieved. In the improved RVOD algorithm, for a cloud profile consisting of p bins, the state vector will have $n = p + 2$ elements:

$$\mathbf{x} = \begin{bmatrix} r_g(z_1) \\ \vdots \\ r_g(z_p) \\ N_T \\ \sigma_{log} \end{bmatrix},$$

where N_T and σ_{log} are the droplet number density and width parameter for the entire profile. The height of the radar resolution bin at cloud base is z_1; z_p is the height at the top of the cloud profile. The state vector has one additional element in the improved algorithm as compared to the AS2001 algorithm. The a priori vector $\mathbf{x_a}$ has an additional element as well, but the measurements vector $\mathbf{y}$ is unchanged from AS2001. The $\mathbf{K}$ matrix (the sensitivity of the forward model to various elements in $\mathbf{x}$) gains an additional column and is no longer square. Similar changes occur in the RO retrieval, where the state vector $\mathbf{x}$ gains two elements to take the same form as the RVOD version above.

2.4 Advantages of Improved Algorithm

The improved RVOD and RO algorithms differ from those described in AS2001 in that the distribution width parameter σ_{log} (RVOD case) is retrieved, rather than being pegged to a fixed value based on climatology or other pre-existing information. By allowing the retrieval this additional degree of freedom, one obtains an uncertainty in σ_{log} that is proportional to the measurement uncertainties and considerably smaller than the uncertainty in the fixed climatological value. As a result, the uncertainties of derived quantities are also significantly reduced. Furthermore, the uncertainties may be evaluated in full

because all the covariance terms are now given explicitly in $\mathbf{S}_x$.

The decrease in retrieval uncertainty is accompanied by an increase in retrieval performance in terms of accuracy. First, the retrieval is able to find a solution that fits the measurements more closely when σ_{log} is allowed to vary. While fitting the measurements vector is a necessary but not sufficient condition for a "good" retrieval, the new algorithm can also be shown to have a smaller bias.

The improved algorithm is appealing because it treats the three drop size distribution parameters more consistently. Rather than saying that σ_{log} is known exactly and the other parameters (N_T and r_g) with some uncertainty (AS2001) or saying σ_{log} and N_T are known exactly and r_g not at all (traditional power-law Z-LWC relationships), the new algorithm says that all three parameters have a priori values and uncertainties.

3. TESTS ON SYNTHETIC DATA

Synthetic data sets were constructed for use in testing aspects of the improved algorithm and comparing its performance to the AS2001 and traditional algorithms, where appropriate.

3.1 Dependence on A Priori Data

A priori data are a necessary component of the improved algorithm; they make a unique retrieval solution possible. In most cases, the uncertainties associated with the a priori data will be much larger than those associated with the measurements. The first test of the algorithm examines the influence of the a priori values and uncertainties on the accuracy and uncertainty of the retrieval solution.

The test utilized the simplest retrieval case: a single-bin cloud. A set of cloud properties was generated for a hypothetical cloud filling a radar bin with a vertical dimension of 60 meters: r_g = 8.2 μm, N_T = 62.4 cm^{-3}, and σ_{log} = 0.342. These distribution parameters were converted into synthetic measurement data: Z = -20 dBZ, τ = 2.0. RVOD retrievals were performed using a four-dimensional grid of a priori values in which r_g varied from 4.4 to 12.4 μm, N_T from 66 to 126 cm^{-3}, σ_{log} from 0.2 to 0.4, and uncertainty ratio from 0.5 to 2.0. (Uncertainty ratio is the ratio of a priori uncertainty for a given retrieval run to the uncertainty of typical a priori values for a marine stratus cloud. Thus an uncertainty ratio of 0.5 implies a priori uncertainties equal to half the typical values; a ratio of 2.0 implies double.)

A partial set of results for the series of RVOD retrievals is shown in Figure 1. In each component plot, each symbol in the 5x5 grid represents a single a priori value. The arrow emanating from the symbol points to the corresponding retrieval solution. The shape of the symbol represents the normalized χ^2 value for the retrieval, with circles and diamonds denoting $\chi^2/m \leq 2.0$, indicating that a solution was found consistent with the a priori value and the measurements. (These points fall closer to the exact fit line as a priori uncertainty decreases.) The symbol shading indicates the fractional error in the retrieved LWC for each retrieval, with a hollow black symbol denoting those a priori values with errors between -5 and 5% (a large swath of values are in this range). The a priori value N_{TAP} is given above each plot. The solid curve in each plot represents the projection of the exact measurements fit line onto the (σ_{log}, r_g) plane. Note that the retrieved values converge to this line as a priori uncertainty increases.

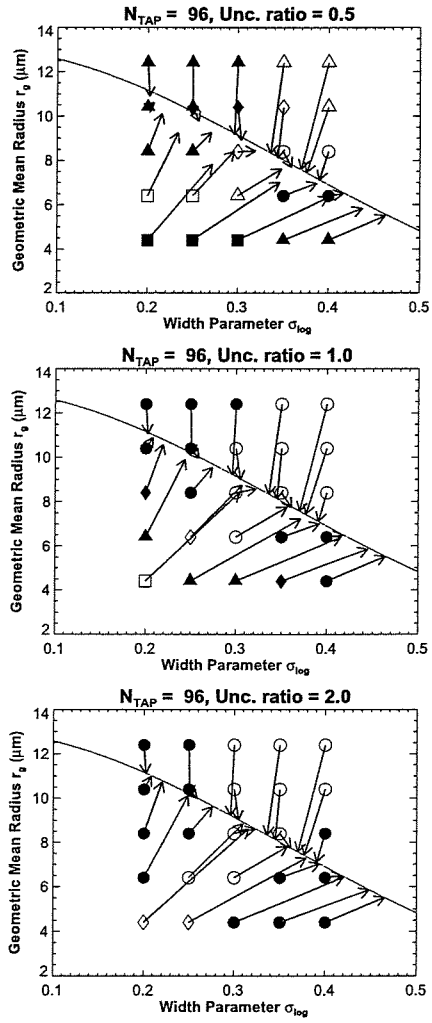

Figure 1: Sensitivity of improved RVOD retrieval to a priori data values and uncertainties. Arrows indicate the retrieval values corresponding to each a priori value. The solid curve in each plot represents the projection of the exact measurements fit line onto the (σ_{log}, r_g) plane.

The RO retrieval may be analyzed in a similar way. As expected, errors tend to be larger in the RO case, because the retrieval is based on less information. Results from the RO case are given on the poster.

3.2 Retrieval Performance

An ensemble of synthetic cloud profiles were prepared to test the performance of the improved retrieval algorithm. Nine sets of 100 5-bin-thick cloud profiles were generated; each set used a pair of (N_T, σ_{log}) values from the following range of values: N_T = 66, 96, 126 cm^{-3}; σ_{log} = 0.25, 0.3, 0.35. The radius values were random with a Gaussian distribution and mean and standard deviation 6.4 ± 2.04 μm. These distribution parameters were converted into synthetic measurement data and corrupted by the addition of random noise (Z_{noise} = 0 ± 1 dBZ; τ_{noise} = 0 ± 8%).

RVOD retrievals were calculated for each synthetic profile using a single set of a priori data. Each set of 100 retrievals were then summarized using histograms; a subset of these histograms are shown in Figure 2. While the retrieved distribution parameters (r_g, N_T, σ_{log}) showed some bias, the derived quantities (r_e, LWC, LWP) had very small bias, with mean fractional errors less than 3%. More extensive results on the improved RVOD and RO algorithms are given in the poster; they are also compared with the corresponding AS2001 versions.

4. APPLICATION TO EXPERIMENTAL DATA

Results from applications of the improved retrieval algorithms to measurements from a field campaign and from regular observations at an Atmospheric Radiation Measurement Program site will be summarized in the poster. Comparisons to in situ measurements and correlative observations will be described.

ACKNOWLEDGEMENTS

This research was supported by NASA Research Grants NAS5-99237 (CloudSat) and NAG5-11109 (AMSR-E).

REFERENCES

Austin, R. T., and G. L. Stephens, 2001: Retrieval of stratus cloud microphysical parameters using millimeter-wave radar and visible optical depth in preparation for CloudSat, 1. Algorithm formulation, *J. Geophys. Res.*, **106**, 28233-28242.

Rodgers, C. D., 2000: *Inverse Methods for Atmospheric Sounding: Theory and Practice*, World Sci., River Edge, New Jersey, USA, 238 pp.

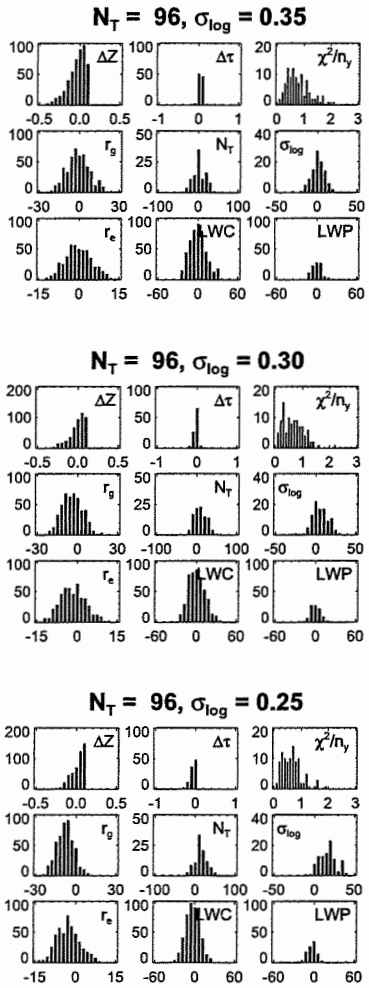

Figure 2: Histogram summaries of RVOD retrieval performance for synthetic data sets, all retrieved with a common set of a priori data (r_g = 6.4 ± 2.04 μm; N_T = 96 ± 47 cm^{-3}; σ_{log} = 0.3 ± 0.072). The top three histograms in each set show the difference between measured and modeled Z and τ and the distribution of the goodness-of-fit parameter. The lower six plots in each set show distributions of fractional error in the three retrieved and the three derived quantities.

A NEW LOOK AT THE BRIGHT BAND

K. M. Baker and J. Verlinde
Department of Meteorology, Pennsylvania State University, PA 16803

1. INTRODUCTION

The melting layer of precipitation has been the object of numerous studies, including numerical (see summary of previous work in Szyrmer and Zawadski 1999), experimental (summary of previous work in Mitra et al. 1990 and Fujiyoshi and Muramoto 1996), and observational (i.e.: in situ/surface: Ohtake 1969, 1970; Steward et al. 1984; Yokoyama et al. 1985; Willis and Heymsfield 1989; Raga et al. 1991; and radar: Takeda and Fujiyoshi 1978; Yokoyama et al. 1984; Zrnic et al. 1993; Fabry and Zawadski 1995). Fairly consistent pictures of the melting process of snow crystals (aggregates) and the complex physical phenomena of the melting layer processes emerged from these studies.

Aggregation forms larger hydrometeors in the few 100 meters above the zero degree isotherm. As these snowflakes fall through the zero degree isotherm, melting commences (the exact moment when melting starts depends on the relative humidity of the environment), with an associated increase in reflectivity. The melting of snowflakes is considered to be a four stage process, summarized by Mitra et al. (1990) as: 1) intense melting on the periphery of flakes produces small drops of tens of microns on the tips of branches, 2) the melt water flows to linkages of branches where water accumulates, 3) the small branches in the flake interior melt, while the flake density increases as it changes from one "with many small openings to one with a few large openings," and 4) the ice frame collapses suddenly and the hydrometeor pulls itself together into a drop shape.

With melting the effective dielectric constant of the hydrometeors increases, resulting in an increased slope in the reflectivity profile. There still is a debate on whether aggregation and breakup play a significant role in the hydrometeor size distribution during the melting process, although evidence derived from observations mostly points in that direction. When the snowflakes collapse and accelerate, there is a net divergence of particles, and the reflectivity slope reverses sign. Polarimetric measurements through the melting layer reveal a distinct maximum in reflectivity above maxima in differential reflectivity and linear depolarization. The relative location of these maxima depends on the details of the precipitation processes in the cloud (Russchenberg and Ligthart, 1993).

In this paper, we combine a simple microphysical model with a cluster-of-spheres model to examine the electromagnetic scattering from melting aggregates.

Corresponding author's address: Hans Verlinde, Department of Meteorology, Penn State University, PA 16803 E-mail: verlinde@ems.psu.edu.

Hassiotis et al. (2002) and Verlinde et al. (2002) described measurements of spectral differential reflectivity taken by the 3.3 GHz Transportable Atmospheric Radar (TARA), operated by the University of Delft, during uniform, continuous rain on 19 September 2001. High-resolution co- and cross-polar Doppler power spectra were used to produce hydrometeor polarimetric characteristics as a function of fall velocity, the relationship of which may be exploited to characterize the state of melting as a function of hydrometeor size as particles fall through the melting layer.

2. THE OBSERVATIONS

The analysis of Hassiotis et al. (2002) documented the changes in the spectral reflectivity and differential reflectivity (sZDR) through the melting band (see Fig. 6). Above the melting layer the sZDR has a positive slope through the core of the spectrum. Once melting starts the sZDR slope flattens somewhat, but remains positive. As melting continues and more low density aggregates compact into higher density, faster falling aggregates, there is a net divergence of scatters, and the integrated reflectivity drops. The value of the sZDR at the right edge of the spectrum (slower falling) increases and advances towards the peak of the spectrum. This results in a rapid increase in the slope of the sZDR spectrum. The final stage of melting identified by Mitra et al. is the complete collapse of the ice structure to produce a spherical particle. The contribution of these collapsed particles will act to reduce the sZDR, and the slope of sZDR spectrum changes sign to that characteristic of rain.

3. THE HYPOTHESIS

Verlinde et al. (2002) presented a hypothesis based on the laboratory results of Mitra et al. (1990) to explain the observed sZDR slope changes. In the first stage of melting identified by Mitra et al. (1990), small drops of tens of microns in diameter appear at the tips of crystal branches, while the larger crystal structure remains intact. For aggregates with sizes in the millimeter to centimeter range, it can be expected that these drops are well separated. Since the hydrometeor retains the larger aggregate structure, it maintains the aggregate fall characteristics: however, because of the large difference in the dielectric constants for liquid and solid water, the individual drops forming at the tips will scatter as non-interacting scatterers caught in a coherent structure.

This hypothesis is an alternative to effective permittivity models, which assume that the water inclusions are uniformly distributed in the ice matrix,

and thus, that the particle can be treated as homogeneous with effective dielectric properties. According to the hypothesis presented here, the scattering properties of the low-density aggregates are mostly derived from individual, high dielectric constant, spherical droplets which affect the "electromagnetic" shape of the particle by not being uniformly distributed.

The sZDR values of the low-density aggregates tend, therefore, towards that of the drops themselves (that is, towards 0 db) as the melting progress and the water contribution increases, with a resulting flattening of the sZDR slope in the fall velocity range representing these hydrometeors. As the various small drops of liquid migrate inward from the branch tips and accumulate at the linkages (Mitra et al. 1990), the droplets come into closer proximity, and begin to scatter interactively. The differential reflectivity from this melting aggregate will then be determined by the relative orientation of the droplets to the incoming electromagnetic wave.

The particles begin to collapse into more compact forms even while the melt water holds the component crystals together; thus hydrometeors can be expected largely to retain their oblate shapes during the melting process. Finally, the frame collapses, the aggregate looses its oblate shape, and scatters the like a liquid drop.

4. THE MODEL

Building on the laboratory work by Mitra et al. (1990), we modeled the electromagnetic scattering properties of a melting aggregate at S-band (10 cm wavelength) frequency using a cluster of spheres model (Mackowski 1991; 1994). In this first attempt, we ignore the contribution of the low bulk density ice, and treat the scattering of the melting aggregate as being derived entirely from the liquid drops on its outer perimeter. With the size of the aggregate small relative to the wavelength, the aggregate is modeled (for scattering purposes) as a two-dimensional oblate with spherical liquid drops distributed randomly on the perimeter.

A simple microphysical model for the melting of an aggregate was constructed following Szyrmer and Zawadski (1999). It is assumed that the aspect ratio and the bulk density of the ice structure remains constant during the melting process (to determine its instantaneous size) even as the bulk density of the melting aggregate (water and ice) increases due to its decreasing volume. It is assumed that the melted water is added to a set number of liquid drops, the centers of which remain on the perimeter of the aggregate by moving radially towards its center. When two drops touch they are merged.

5. THE RESULTS

Each test consisted of a 1000 simulations of different realizations of melting of the same aggregate, each with drops distributed randomly on the perimeter. Figure 1 present the mean ZDR and its variance for an aggregate with major axis (radius) 500 μm and aspect ratio of 1:2, with 80% of the drops on the lower hemisphere of the aggregate. In the initial melting stages the ZDR signal fluctuates around a value close to 0 db; when the melt fraction approaches 60% ZDR rapidly increases to a value of 1.2 db, similar, though a bit lower, than the observed maximum ZDR. The variance has a distinct peak in the final melting stages as the last few drops interact prior to merging, again in qualitative agreement with the observations.

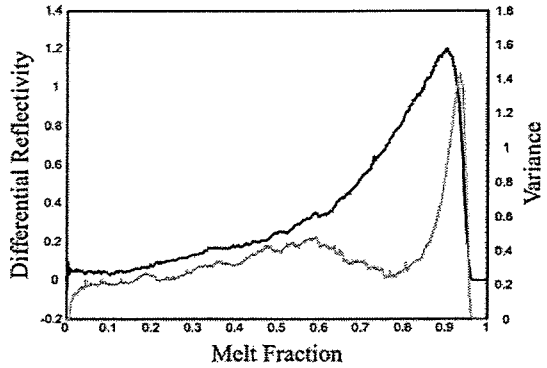

Figure 1 Mean differential reflectivity (dark line) and its variance (lighter line) for 1000 realizations of the model. Each simulation was initialized with 15 drops distributed randomly on the aggregate perimeter, with 80% of the drops on the lower hemisphere.

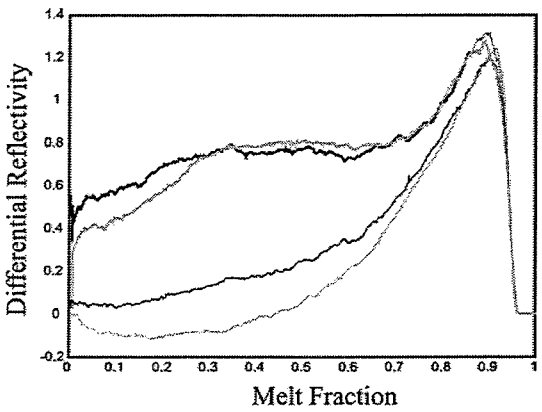

Figure 2 Mean differential reflectivity for simulations with aspect ratio of melting aggregate 1:2 (dark lines) and 1:5 (lighter lines). The two dark lines are results where 80% of the 15 drops are on the lower hemisphere of the aggregate, the two lighter lines results where the 15 drops are randomly distributed.

Next we performed a series of tests to determine the sensitivity of the model to various input parameters Figure 2 present the results from a series of test where the aspect ratios was varied from 1:2 to 1:5, and the

15 drops either concentrated (80%) on the lower hemisphere or distributed randomly along the perimeter. The ZDR is quite sensitive to the assumed aspect ratio. Higher aspect ratios result in a more horizontally relative orientation of the drops, with a resultant higher positive ZDR. When drops are distributed randomly along the perimeter of the aggregate and the aspect ratio is lower, the mean relative orientation is vertical during the intial stages of melting, and the ZDR is negative. The impact of the oblate shape of the aggregate is only felt in the later stages of melting, when the ZDR rapidly shoot up to maximum values similar to the other simulations.

Figure 3 presents results from simulations where the sizes and aspect ratios of the melting aggregates were varied. As before, it can be seen that the aspect ratio is the dominant effect.

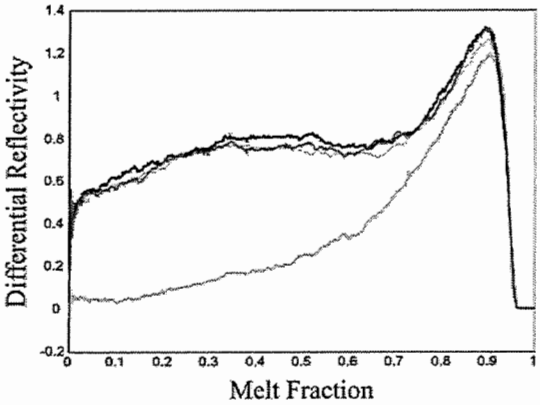

Figure 3 Mean different reflectivity for simulations with aspect ratio of melting aggregate 1:2 (thick light line) and 1:5 (top three lines). Three simulations with 1:5 aspect ratios were aggregates with different initial sizes, 500 μm, 994 μm, and 1250 μm.

Finally, Figure 4 presents results from the sensitivity test to the number of droplets we assume. The test revealed almost no sensitivity.

At the conference we will present results from the combined microphysical/scattering model. A realistic distribution of aggregates will be allowed to fall through the melting layer. A spectrograph of ZDR contours on a velocity-height plot, similar to how radar measurements are presented, will be constructed from these simulations.

6 CONCLUSIONS

Model simulations from a cluster of spheres simulation were performed of melting aggregates. These simulations produced spectral differential reflectivity profiles similar to what is observed in the melting layer. Sensitivity test with the model revealed that the results are quite sensitive to the assumed aspect ratio of melting aggregates, but not to the

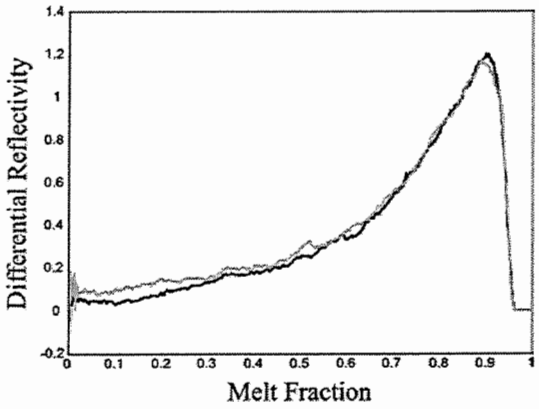

Figure 4 Mean differential reflectivity for simulations with 15 (dark line) and 30 (lighter line) drops on the melting sphere.

number of assumed drops, the distribution of drops around the perimeter, or the size of the aggregate. These results provide an alternative and physically more intuitive method to the melting aggregate problem. Future work will include comparisons with effective permittivity results.

Acknowledgements:
We thank Daniel Mackowski for the help he provided in getting his model adapted for this problem. This research has been supported in part by the National Science Foundation under grant ATM 9873643.

References:

Fabry, F. and I. Zawadski, 1995: Long-term radar observations of the melting layer of precipitation and their interpretation. *J. Atmos. Sci.*, **52**, 838-851.

Fujiyoshi, Y. and Muramoto, K, 1996: The effect of breakup melting on the resulting size distribution of raindrops. *J. Meteor. Soc. Japan*, **75**, 343-353.

Hassiotis, A.D., N.C. Skaropoulos, H.W.J. Russchenberg, 2002, Quantitative analysis of spectral differential reflectivity in the radar bright band, Proc. Of ERAD 2002, 122-125 [http://www.copernicus.org/erad/proceeding.htm]

Macowski, D.W., 1991: Analysis of radiative scattering for multiple sphere configurations. Proc. Royal Soc. Of London A **433**, 599-614.

Macowski, D.W., 1994 Calculation of total cross sections of multiple sphere clusters. J. Optical Soc. Of America A, **11**, 2851-2861.

Mitra, S.K., O. Vohl, M. Ahr and H.R. Pruppacher, 1990: A wind tunnel and theoretical study of the melting behavior of atmospheric ice particles. Part IV: Experiment and theory for snow flakes. *J. Atmos. Sci.*, **47**, 584-591.

Ohtake, T., 1969: Observations of size distributions of hydrometeors through the melting layer. *J. Atmos. Sci.*, **26**, 545-557.

Ohtake, T., 1970: Factors affecting the size distributions of hydrometeors through the melting layer. *J. Atmos. Sci.*, **27**, 804-813.
Raga, G.B., R.E. Steward, and N.R. Donaldson, 1991: Microphysical characteristics through the melting region of a midlatitude winter storm. *J. Atmos. Sci.*, **48**, 843-855.
Russchenberg, H. W. J. and Ligthart, L. P., 1996: Backscattering by and propagation through the melting layer of precipitation: a new polarimetric model. *IEEE Trans. Geosci. Remote. Sensing*, **34**, 3-14.
Straka, J.M., D.S. Zrnic, and A.V. Ryzhkov, 2000: Bulk hydrometeor classification and quantification using polarimetric radar data: Synthesis of relations. *J. Appl. Meteor.*, **39**, 1341-1372.
Stewart, R.E., J.D. Marwitz, J.C. Pace and R.E. Carbone, 1984: Characteristics through the melting layer of stratiform clouds. *J. Atmos. Sci.*, **41**, 3227-3237.
Szyrmer, W., and I. Zawadski, 1999: Modeling of the melting layer. Part I: Dynamics and microphysics. *J. Atmos. Sci.*, **56**, 3573-3592.
Takeda, T. and Y. Fujiyoshi, 1978: Micro-physical processes around the melting layer in precipitating clouds as observed by vertical pointing radar. *J. Meteor. Soc. Japan*, **56**, 293-303.
Verlinde, J. D. Moisseev, Skaropoulos, N., W.F. v.d. Zwan, S.H. Heijnen and H.W.J. Russchenberg, 2002: Spectral polarimetric measurements in the radar bright band. Open Symposium on Propagation and Remote Sensing, URSI Commission F, Garmisch-Partenkirchen, Germany.
Willis, P.T. and A.J. Heymsfield, 1989: Structure of the melting layer in mesoscale convective system stratiform precipitation. *J. Atmos. Sci.*, **46**, 2008-2025.
Yokoyama, T., H. Tanaka, K. Nakamura, and J. Awaka, 1984: Microphysical processes of melting snowflakes detected by two-wavelength radar. Part II. Application of two-wavelength radar technique. *J. Meteor. Soc. Japan*, **62**, 668-678.
Yokoyama, T., and Coauthors, 1985: Observations on microphysical processes in the stratiform precipitation including melting layers at Mt. Fuji. *J. Meteor. Soc. Japan*, **63**, 100-111.
Zrnic, D.S., N. Balakrisnan, C.L. Ziegler, V.N. Bringi, K. Aydin and T. Matejka, 1993: Polarimetric signatures in the stratiform region of a mesoscale convective system. J. Appl. Meteor., 32, 678-693.

CUMULUS CLOUD PROCESSING OF AEROSOL PARTICLES IN THE MEXICAN EAST PACIFIC

Darrel Baumgardner*, Jose Carlos Jiménez and G. B. Raga

Universidad Nacional Autónoma de México,Ciudad Universitaria Mexico City, 04150, MEXICO

1. INTRODUCTION

Maritime clouds are an important component of the earth's climate system because of the large fraction of the surface that they cover during any season of the year. There are many environmental variables that are involved in the development of clouds. In particular, aerosols have a dominant role in cloud formation and lifetime. The process by which a cloud droplet forms on an aerosol particle, i.e. a cloud condensation nucleus (CCN), is well understood and can be described theoretically (e.g. *Pruppacher and Klett*, 1997) and validated with observations, if the composition of the particles is known (e.g. *Twomey*, 1991). Less well understood, however, are aerosol interactions with clouds, in which the physical and chemical properties of particles are changed after one or more cycles through clouds. Aircraft measurements have shown increases of aerosol average size in regions of high relative humidity (RH) near clouds (*Baumgardner et al.*, 1996; *Baumgardner and Clarke*, 1998). Other studies (e.g. *Saxena et al.*, 1970), found that CCN concentrations are often higher in outflow from evaporating clouds than in the environment further from the clouds.

Aerosol composition can change as a result of aqueous chemistry (*Hegg et al.*, 1980) and nucleation scavenging of aerosols increases the subsequent size of the aerosol after the droplet evaporates (*Hobbs*, 1993). Theoretical studies (*Flossmann*, 1998) show the importance of clouds in the redistribution/transport of aerosols from the boundary layer to the free troposphere.

When the properties of a particle are changed by cloud processing, the subsequent interaction with the environment may be modified, i.e. droplets can activate at lower supersaturations if the particle mass has increased or the chemistry has changed (*Pruppacher and Klett*, 1997).

The present study reports an analysis of airborne measurements of aerosols and clouds from the Inter Tropical Convergence Zone (ITCZ) of the Mexican East Pacific. The objective is to evaluate the primary cloud processing mechanisms and to assess the relative importance of each one in changing the ambient aerosol properties .

*Corresponding author's address: D. Baumgardner, Centro de Ciencias de la Atmosfera, UNAM, Ciudad Universitaria, 04510 Mexico DF, MEXICO; E-Mail: darrel@ servidor.unam.mx.

2.MEASUREMENTS AND METHODOLOGY

The data used in this study were obtained during flights of the NCAR C-130 research aircraft during the 2001 East Pacific Investigation of Climate (EPIC) project. Nine of the nineteen flights between 1 September and 15 October 2001 were dedicated to aerosol and cloud studies. These flights were within the region 8° - 12° N, 93° - 97° W, approximately 800-1000 km from Mexico and Central America in the ITCZ region. Measurements near and in cloud were made at constant levels of 30 m, 300 m, 1000 m, 2500 m and 4200 m ASL. The 30 m and 300 m measurements were made to characterize aerosol properties near the sea surface and at average cloud base, respectively. The clouds in the research area consisted of shallow cumulus and deep convection. The investigation concentrated on these latter clouds that had developed along lines that formed from SW to NE. The flight patterns sampled across and along the cloud lines at each level. The across-the-line patterns normally sampled in the regions of newer growth and the along-the-line flight legs sampled cells in both developing and decaying stages. In the across-the-line flight tracks the aircraft sampled cloud-free air for at least 20 Km on each side of the cloud.

The physical and optical properties of aerosol particles are derived directly from the measured particle size distributions (PSD). A composite PSD was synthesized from the measurements of three optical particle spectrometers: the PMS Passive Cavity Aerosol Spectrometer Probe (PCASP), the Forward Scattering Spectrometer Probe Model 100 (FSSP-100) and model 300 (FSSP-300). The concentrations in overlapping size ranges were averaged prior to creating the composite.

The concentration of condensation nuclei (CN) was measured with a TSI Model 3760, measurements of Cloud Condensation Nuclei (CCN) were made with a University of Wyoming Static Diffusion Cloud Chamber, and the coefficients of light scattering and absorption were measured with a nephelometer and particle soot absorption photometer (PSAP), respectively (both manufactured by Radiance

Research). All measurements were averaged into one second intervals except the CCN that requires 60 seconds to make one measurement.

The three optical size spectrometers were mounted on the wing pods of the C-130. A heater on the inlet to the PCASP reduces the RH of the sampled air stream to less than 30%, hence the PCASP measures aerosol particles whose water content have been removed. The FSSP-100 and FSSP-300 measure particles at the ambient RH. In order to combine the measurements from the FSSP 100 and 300 with those of the PCASP, the spectra were adjusted to a dry equivalent. This adjustment assumes that the measured particles are deliquesced NaCl with the amount of water mass on the particle determined by the ambient RH (*Tang,* 1980). The resulting sizes are calculated by removing the predicted water mass.

The CN, CCN, PSAP and nephelometer were mounted in the cabin and sampled from inlets mounted on the aircraft exterior. The CN's inlet was mounted on the bottom of the fuselage with a special housing to minimize spurious counting caused by drop breakup on the inlet lips. Examination of the CN measurements when in rain indicated that this housing was ineffective and CN during these periods are not included in the current analysis. The CCN, PSAP and nephelometer shared a common, backward facing inlet, to minimize droplet shattering and to allow measurements of interstitial aerosols in cloud. The largest size that can enter this inlet is approximately one micrometer, a threshold estimated by comparing the nephelometer measurements with scattering coefficients derived from the optical particle counters.

3. ANALYSIS AND RESULTS

3.1 Air mass characteristics

Out of the nine flights available, we have selected five flights for the analysis, which include 10 cloud groups. An early inspection of the data had indicated that the air mass characteristics varied significantly among some of them. The flights were classified by aerosol type, i.e. "polluted" or "clean". Figure 1 shows frequency distributions of the CN and PCASP measured concentrations at ? 300 m for the five days. Flights 7 and 17 have average concentrations significantly higher than the other three flights indicating the influence of easterly winds that brings anthropogenic particles from southern Mexico and northern Central America. Flights 9, 12 and 13 were made on days with maritime or "clean" aerosol background and when winds were from the southwest.

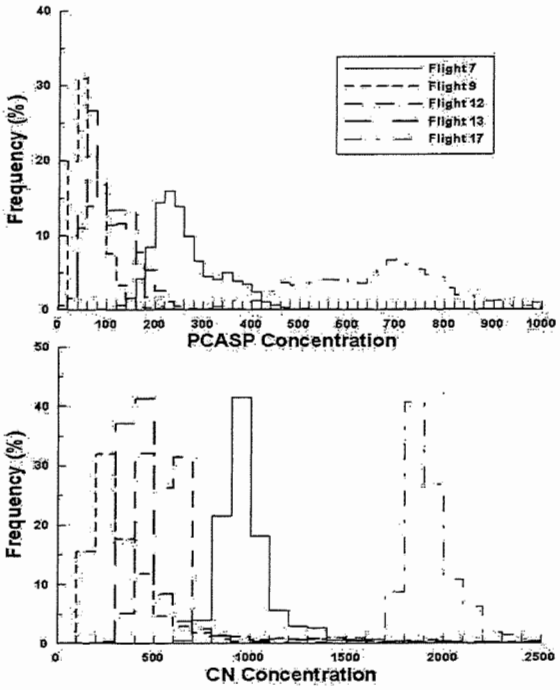

Figure 1: The frequency of occurrence of 300 m concentrations measured by the PCASP (top panel) and CN (bottom) are shown here for the five days used in the case studies.

3.2 Analysis of Cloud Processing Signatures

Cloud processing of aerosol particles may modify their size, concentration and/or composition. The changes can be observed by comparing the near-cloud and far-cloud PSDs, at different heights above cloud base, with the PSD at cloud base. The cloud base PSD is used as a reference with the assumption that the majority of cloud droplets during cloud evolution are formed from CCN that enter at cloud base. In the present study, near-cloud is defined as within 500 m from cloud edge and far-cloud from 500-1500 m. The choice of 500 m as the near-cloud region is based on an evaluation of changes in aerosol properties with distance from cloud edge.

The cloud boundaries are defined by the FSSP-100 measurements whose lower size threshold is approximately 2 μm . When the droplet concentration exceeds 1 cm^{-3} the measurements are defined as "in-cloud". This criterion is based on measurements at 30 m, where there are no visual signs of clouds and only super-micron sea salt particles will be measured by the FSSP-100. Based upon a visual inspection of the

PSDs at four levels, four patterns have been identified that are associated with cloud processed particles:

A: vertical transport with mixing and dilution
B: aqueous phase oxidation of aerosol precursors
C: droplet coalescence
D: removal by precipitation

Results indicate that the most frequent cloud processing mechanism is transport and redistribution of boundary layer aerosols into the free troposphere, (Figure 2). There is also circumstantial evidence of changes of composition by aqueous phase chemistry, and mass changes through droplet coalescence. The category NM (No Match) in the figure corresponds to the cases that could not be classified in the aforementioned 4 categories. The are no significant differences in the results, when the data are classified in clean and polluted clouds. The differences in height are also minimal.

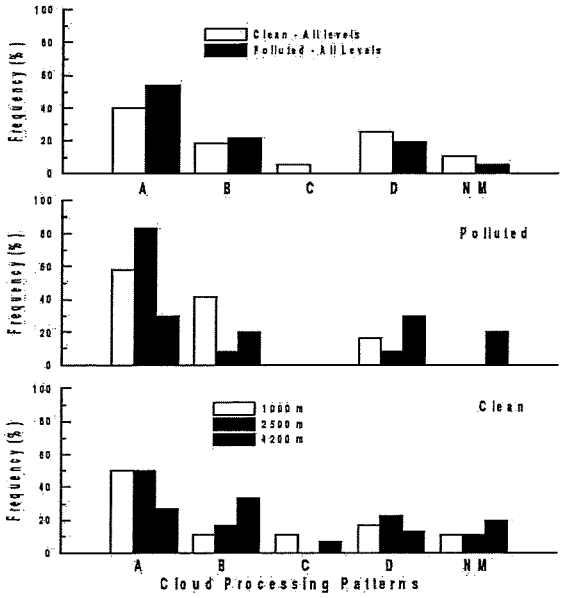

Figure 2: The cloud processing signatures, derived from the vertical profiles of particle properties and evaluation of particle size distributions are summarized for the clean cases (bottom panel), contaminated cases (middle), and combined cases. The diagrams identify the percentage of cases that are represented by each type of pattern (see text).

A comparison of CCN (at 0.4% supersaturation) and PCASP concentrations shows moderately good agreement, as shown in Figure 3. The best-fit lines through the points for polluted and clean days (solid and dashed lines) show that almost all particles larger than 0.1 μm, the lower threshold of the PCASP, would be activated as cloud drops at 0.4% supersaturation. On clean days, 80% of the particles would be activated at this level of supersaturation. The PCASP measures at a much higher rate than the CCN, i.e. 1 Hz vs. 1 sample each 60 seconds; hence, the PCASP measurement is used as a proxy for CCN in the following analysis.

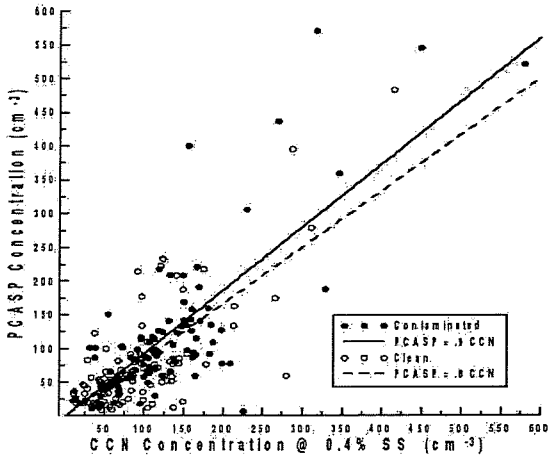

Figure 3: The PCASP and CCN are correlated for measurements in cloud-free air ≤ 300 m. The regression lines are forced through the origin.

The correlation between cloud base aerosol, measured with the PCASP, and the maximum cloud droplet concentration between 1000 and 2500 m was also examined. The cloud base aerosol and droplet concentrations are highly correlated and clearly indicate that the polluted clouds have larger concentrations of cloud droplets, evidence of the aerosol indirect effect. On average, the maximum droplet concentration is approximately 20% higher than the average PCASP cloud base concentrations. This indicates that in most cases, particles smaller than 0.1 μm are being activated as clouds droplets.

Even though there is a clear separation between "clean" and "polluted" clouds, and that this may affect how particles are processed by clouds, Figure 2 suggests that this is not the case.

3.2 Derivation of Refractive Index and Scattering Coefficient

Since there were no measurements of aerosol chemical composition during this project, an indirect method to assess changes in particle composition

was derived by comparing the light scattering coefficient, σ_m that was directly measured by the nephelometer, with the scattering coefficient, σ_c, calculated from the composite size distribution.

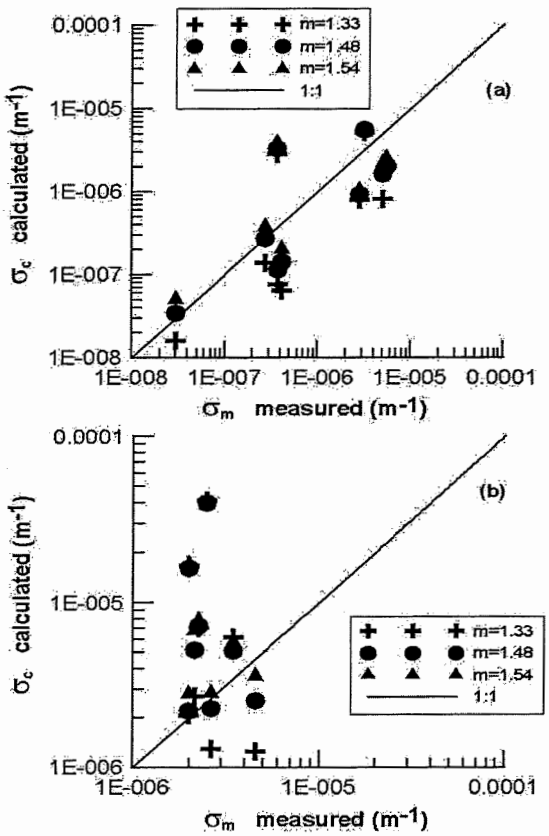

Figure 4: The scattering coefficients calculated from the optical particle counters and measured with the nephelometer for three refractive indices, 1.33, 1.48 and 1.54, for (a) clean and (b) polluted days .

A scattering coefficient was derived from every PSD and 28 values of ?the refractive index (*m*) from 1.33 to 1.60. The?*m* that produced the minimum difference between the derived ?σ_c?and measured σ_m is assumed to represent the average refractive index of the ensemble of particles in the size range of the PSD, which was truncated at 0.8 μm to account for the losses in the nephelometer inlet. The choice of m? values was made to cover the expected range in composition, e.g. the refractive indices of water, ammonium sulfate and sodium chloride are 1.33, 1.48 and 1.54, respectively.

The derived refractive indices provide a means of assessing changes in the composition of the aerosols, e.g. by aqueous phase chemistry. Figure 4a compares derived and measured scattering coefficients for all passes at 2500m in the clean cases, showing general agreement. The agreement is much poorer for the polluted cases as seen in Figure 4b. Often the derived coefficients are much higher than measured values, regardless of the refractive index, a possible result of light-absorbing anthropogenic particles. In such cases, the measured coefficients would be lower than those derived with no absorption taken into account.

In summary, the results from measurements of aerosols and clouds in EPIC suggest that clean and polluted air masses were present, and the cloud droplet populations reflected this fact. Regardless of the aerosol concentration, the dominant mechamism for the processing of aerosols by clouds was transport and redistribution of boundary layer aerosols into the free troposphere. A technique to estimate the index of refraction was developed and was found to be successful only in the clean cases.

Processed aerosols near the cloud edges in the clean cases showed larger scattering coefficients than those further away from the clouds. Vertical profiles of the refractive index were derived for the clean cases, near and away form clouds. The vertical integral of the scattering coefficients provides an estimate of the optical depth of the aerosols near and away form the clouds. The results indicate that in most of the cases the optical depth near the cloud is ten times larger than further away. This could be related to a cooling at the ocean surface, due to the direct effect of the cloud-processed aerosols.

Acknowledgements

The authors are grateful to David Raymond for enabling UNAM's participation in EPIC2001. Thanks to the technical staff and crew of the NCAR C-130. The study was funded through CONACYT grant # 33319 and UNAM-DGAPA.

References

Baumgardner D., Cooper, W.A., Radke, L.F., 1996, 12th Int. Conf. on Clouds and Precipitation. Zurich, 308-311.

Baumgardner, D., Clarke, A., 1998, *J. Geophys. Res.*, **103**, No. D13, 16,525-16,534.

DeFelice, T.P., Cheng, R. J., 1998, , *Atmos. Res.*, 47-48.

Flossmann, A.I., 1998, *J. Atmos. Sci.*, **55**,879-887.

Hobbs, P., 1993: Aerosols-Cloud Interactions "Aerosol-Clouds-Climate Interactions", Academic Press. Cap **I**, pp. 33-73

Pruppacher H. R. and Klett J. D., 1997: Microphysics of Clouds and Precipitation, Kluwer Academic Publisher., 954 pp.

Saxena, V.K., Burford, J.N., And Kassner, J.L. J.R., 1970, *J. Atmos.Sci.*, **27**, 73-80.

Tang, I. N., 1980, Chapter 7, in Generation of Aerosols, de. Science Publishers, 153-167.

Twomey, S. 1991, Aerosols Clouds and Radiation, *Atmos. Environ.*, **25A**, 2435-2442.

RAINFALL ESTIMATES OF CONVECTIVE CLOUDS USING METEOSAT-6 RAPID SCAN DATA IN CENTRAL EUROPE

Franz H.Berger

Technische Universität Dresden, IHM – Meteorology, D-01062 Dresden, Germany

1. INTRODUCTION

In August 2002 (from August 8 until August 13, 2002) heavy rainfalls led to huge damages in Central Europe, especially in Austria, Czech Republic, and Germany. A typical Vb cyclone, which can be often observed during spring and fall, moved from the North Atlantic (August 8) via the Mediterranean Sea (August 10, August 11) to Eastern Europe (August 12 and August 13). During this movement heavy rainfalls occurred first in Austria and led to floods of various rivers, like Salzach, Inn, Enns and Danube. A few days later, the Vb cyclone moved slowly northward with heavy floods in Czech Republic (Moldau). In Saxony, in the Eastern Part of Germany, two flood occurred during this period. The first is timely close related to the Vb cyclone and to a northerly wind flow and therefore an enhanced precipitation (August 12, 2002) in this area. During a 24 hours period from August 12, 07:00 UTC to August 13, 07:00 UTC rain rates up to 312 mm/24 hours (Zinnwald-Georgenfeld) are observed in the Eastern Ore Mountain region, which led to different floods of small rivers and a following heavy flood (river Weißerritz) with various damages in Dresden. A few days later the second flood could be observed at the river Elbe with a maximum river level of 9.42 m in Dresden. This flood occurred due to the heavy precipitation in Czech Republic and the flood wave from the river Elbe coming from Czech Republic.

This flood event gives now a good opportunity to study the precipitation with Meteosat-6 Rapid Scan data. The main difference to conventional Meteosat data is the better time resolution of 10 minutes instead of 30 minutes. The spectral bands (VIS, WV and IR) are the same. This allows the study of cloud life cycle and the study of Vb cyclone move. It gives further the opportunity to demonstrate the use of Meteosat imagery for future flood predictions together with precipitation/run-off modelling. So within this study, several techniques are adapted and applied to this specific event. Furthermore a technique could be developed especially considering the high temporal resolution of Meteosat-6 Rapid Scan data. A comparison with modeled rainrates (DWD LM model) with surface radar observations closes is given.

Corresponding author's address: Franz H. Berger, Technische Universität Dresden, Institute of Hydrology and Meteorology, Department of Meteorology, 01062 Dresden; E-Mail: berger@forst.tu-dresden.de

2. ANALYSIS OF REMOTELY SENSED DATA

To infer rain rates from meteorological satellite data several techniques were applied. These techniques can be grouped into four categories:

- IR methods, using the IR cloud top temperature as an indicator for rainrates of convective clouds,
- IR / WV methods, which take furthermore into account the temperature of the water vapour band,
- IR / SMM/I method, using a IR cloud top temperature / rainrate method together with rain rates inferred from microwave measurements, and
- IR / WV - cloud life cycle method, using additionally the information about changes in horizontal and temporal cloud top temperatures.

Thus, three different IR methods could be adapted and applied for all Meteosat-6 Rapid Scan scenes: a power law regression developed for the use of GOES 10.7 μm channel (Vicente et al, 1998), the GOES Multispectral Rainfall Algorithm (GMSRA) after Ba and Gruber (2001) and a probability matching method after Grose et al (2002).

The first of two IR/WV methods is a statistically based technique, which uses the brightness temperature in the 11 μm and the temperature difference between 11 μm and 6.7 μm (Kurino, 1997). Another IR/WV technique – Enhanced Convective-Stratiform Technique (ECTS) uses IR and IR/WV temperature differences including numerical simulations (climatological analyis; Reudenbach et al., 2001). This technique could only be applied in a very simplified version to the Meteosat-6 rapid scan data due to missing numerical simulations.

The combination of measurements from different satellite instruments (IR / SSM/I method) is realised with the Eumetsat Multi-Sensor Precipitation estimate (MPE, Heinemann et al., 2003).

The last technique (Berger, 2003) uses the advantages of previous described methods (Grose et al., 2002, Tjemkes et al., 1997, Kurino, 1997) but considers additionally the cloud life cycle. For this method the spatial variability is determined with changes in cloud top temperature and related changes of standard deviation of an 3x3 pixel element. Coupled

with the temporal changes in cloud top temperatures and related temperatures based on the information of three consecutive images, the rainrate estimates after Grose et al (as standard assumption) are modified.

Additionally to satellite inferred products, all available radar data from the Dresden DWD weather radar with a 10 minute time resolution could be taken into account. The rainrates were inferred with the operationally applied DWD technique (Seltmann, 2003).

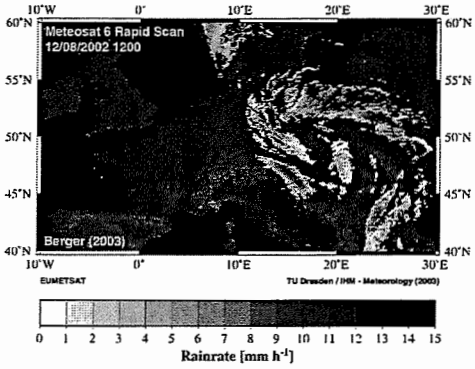

Figure 1: Rain rates inferred from Meteosat-6 Rapid Scan data (after Berger, 2003)

Figure 1 shows one example of inferred rain rates from Meteosat-6 rapid scan data for the huge flood event in August 2002. In this figure a large spatial variability and different small scaled structures can be seen. Comparing the inferred rain rates with surface measurements, a good agreement for the rain event (temporal scale) could be found, where the intensity is largely underestimated. A comparison with radar observation indicates also that both the radar and the satellite inferred rain rates underestimate the observed heavy rain rates. This can partly be explained by using conventional robust techniques for all remotely sensed data.

3. MODELLED RAIN RATES

Another significant attempt to characterize the temporal rainfall pattern was the use of the German Lokalmodell (DWD LM model), which is initialised by the global model of the german weater service DWD. A detailed description of the model can be found on the COSMO model websites. In Figure 2 a corresponding result for August 12, 2002 is plotted for a limited area in Central Europe. And it can be seen that the model overestimates low rain rates (perhaps drizzle) and underestimates significantly the heavy rain rates during the flood event. Comparing the whole flood event, there is always a significant underestimation of heavy rainfall.

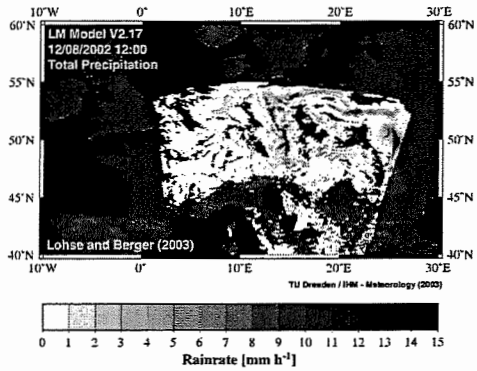

Figure 2: Rain rates modelled with the DWD LM model (Version 2.17)

4. OUTLOOK

Considering the weather conditions on August 12, 2002 the Vb cyclone was located at 12:00 UTC over Czech republic. This situation was dominated by a transport of humid air masses from the Mediterranean Sea, which was modified by cold, polar air masses due to the high pressure system over France. This leads to stratiform scaled precipitation (fraction larger than 65 percent) and convective scaled precipitation (fraction less than 35 percent; Rudolf and Rapp, 2002). Comparing various techniques for meteorological satellite applications it has to be noticed that with all techniques it was not possible to infer the observed huge rain rates for this specific flood event in Central Europe. Nevertheless, the temporal rainfall patterns could be observed without any time shift. And the development of a modified IR/WV technique considering explicitly the cloud life cycle leads to better representation of specific, short-term rainfall events and structures. Another diffiiculty is the determination of stratiform rainfall, which was the dominating rainfall for this specific period. Thus, more intentions will be made to improve also this weakness in remote sensing analysis.

The additional use of radar data together with modeled precipitation fields show that there also exist urgent needs to improve either the parameterisation schemes in numerical modelling or the techniques to convert radar signals to rain rates. Both aspects will be covered in near future and will lead to a better understanding of extreme precipitation events. Finally the use of recently available Meteosat-8 SEVIRI data with enlarged spectral information will lead to further improvements in the determination of spatial rainfall patterns together with their intensities.

References

Ba, M.B. and A. Gruber, 2001: GOES Multispectral Rainfall Algorithm (GMSRA).*J. Appl. Meteor.*, **40**, 1500-1514.

Berger, F.H., 2003: *Quantification of the Flood 2002 Precipitation using Meteosat-6 Rapid Scan Data.* Report prepared as Visiting Scientist.

Grose, A.M.E., E.A. Smith, H.-Y. Chung, M.-L. Ou, B.-J. Sohn, and F.J. Turk, 2002: Possibilities and Limitations for Quantitative Precipitation Forecasts Using Nowcasting Methods with Infrared Geosynchronous Satellite Imagery. *J. Appl. Meteor.*, **41**, 763-785.

Heinemann, T., A. Lattanzio and F. Riveda, 2003: The Eumetsat Multi-Sensor Precipitation Estimate (MPE). Internal Eumetsat Report.

Kurino, T., 1997: A Satellite Infrared Technique for Estimating "Deep/Shallow" Precipitation. *Adv. Space Res.*, **19(3)**, 511-514.

Reudenbach, C., G. Heinemann, E. Heuel, J. Bendix and M. Wininger, 2001: Investigation of summertime convective rainfall in Western Europe based on a synergy of remote sensing and numerical models. *Meteor. Atmos. Phys.*, **76**, 23-41.

Rudolf, B., and G. Rapp (2003): The Century Flood of the River Elbe in August 2002: Synoptic Weather Development and Climatological Aspects. Quarterly Report of the Operational NWP-Models of the Deutscher Wetterdienst, Special Topic July 2003

Seltmann, J., 2003: personal communication.

Tjemkes, S., L. van den Berg and J. Schmetz, 1997: Warm Water Vapour Pixels over High Clouds as Observed by Meteosat. *Beitr. Phys. Atmosph.*, **70(1)**, 15-21.

Vicente, G.A., R.A. Scofield and W.P. Menzel, 1998: The Operational GOES Infrared Rainfall Estimation Technique. *Bull. Amer. Met. Soc.*, **79(9)**, 1183-1898.

THOR - Cloud Thickness from Offbeam Lidar Returns

Robert F. Cahalan[a,*], Matthew McGill[a], John Kolasinski[a], Tamás Várnai[b], and Ken Yetzer[c]

[a]Laboratory for Atmospheres, NASA/Goddard Space Flight Center, Greenbelt, Maryland
[b] Joint Center for Earth Systems Technology, University of Maryland Baltimore County, Baltimore, Maryland
[c] *Raytheon, SSAI, Lanham, Maryland*

1. INTRODUCTION

Conventional wisdom is that lidar pulses quickly fade away after penetrating clouds to an optical thickness of about 2. Beyond this limit, multiple scattering by cloud particles increasingly spreads the distinct pulse into a diffuse halo. Since this halo lies outside the narrow field-of-view of most lidars, they are able to probe only thin clouds and the edges of thick clouds. As a result, much of the Earth's cloud cover remained outside the reach of lidar remote sensing.

However, theoretical studies reveal that a lidar pulse entering a cloud spreads by multiple scattering, creating a bright halo that can be mined for cloud information (e.g., Davis et al. 1999). The studies show that in homogeneous clouds the size of the bright halo is proportional to the geometrical cloud thickness: Photons, undergoing random walks by scattering from cloud droplets, create wider halos in thicker clouds because they travel farther without escaping through cloud base. Such results raise the possibility of using halo observations for retrieval of cloud geometrical thickness, and internal properties.

The theoretical advances (confirmed by laboratory experiments) spurred the simultaneous development of three wide field-of-view lidar systems. The up-looking WAIL (Wide-Angle Imaging Lidar) was developed at Los Alamos National Laboratory for ground-based observations, and, having a wider field-of-view, can image halos in lower clouds than a ground-based THOR (Love et al. 2001). Another system, an *in situ* cloud lidar, was built in Colorado for aircraft flights inside clouds (Evans et al. 2003). The THOR instrument described here took its first ground-based measurements of mid- and high-level clouds at NASA GSFC in April 2001, and THOR's first airborne measurements of boundary layer clouds were collected over Oklahoma in March 2002.

THOR reveals the structure of diffuse halos by collecting time-dependent return signals not only from the immediate vicinity of the spot illuminated by its laser, as most lidars do, but also from seven additional rings around this spot (Figure 1). These observations are used for retrieving the geometrical and optical thickness of optically thick stratiform clouds, as well as the vertical profile of cloud volume extinction coefficient.

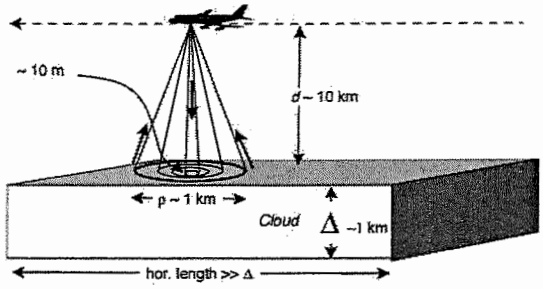

Figure 1. Schematic view of THOR observations.

2. THE INSTRUMENT

2.1 System description

The THOR system's basic structure is illustrated in Figure 2, and its main parameters are listed in Table 1.

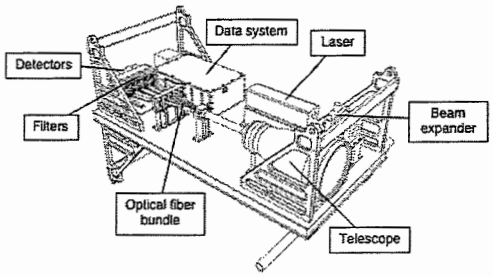

Figure 2. Layout of THOR.

This section discusses THOR's components by following the path of a laser pulse through the system.

When the laser power supply and control unit determines that it is time to emit the next laser pulse, it sends out two simultaneous signals. One signal goes to the data system computer, which then records the pulse's timing and starts archiving the photon counts reported by THOR's detectors. The other signal goes to the laser unit, and causes the solid-state, fiber-coupled Nd:YALO laser to emit a single pulse of green light. The pulse passes through an energy monitor, which determines the pulse energy and reports it to the data system. Next, the pulse is collimated by a 4X beam expander, reducing its divergence to 325 μrad (full angle). The pulse then leaves the system and travels until scattered by atmospheric particles.

Table 1. Main parameters of the THOR system

Laser	
Pulse rate	1 kHz
Wavelength	540 nm
Pulse duration	8 ns
Pulse energy	max. 225 μJ
Beam divergence	325 μrad
Receiver	
Telescope lens diameter	19.05 cm
Telescope focal length	23.80 cm
Spectral filter bandwidth	7 nm
Maximum view angle of outermost channels	106.7 mrad (full angle)

Photons returning from the atmosphere are collected by THOR's custom-designed telescope, which creates a 2.5 cm diameter image at its focal plane.

The light forming this image is then collected by THOR's most unique component, a custom-made optical fiber bundle. The bundle consists of approximately 250,000 optical fibers, each 66 cm long, that guide photons from the focal plane to the appropriate detectors. Each fiber has a diameter of about 50 μm, except for a single 200 μm fiber that originates at the center of the focal plane. This central fiber captures photons coming from THOR's central field of view—that is, the direct backscatter signal. The remaining fibers are organized into seven concentric annular rings, each collecting photons from a corresponding ring in the focal plane image. Each fiber in a given ring then leads to an associated detector, except for the outermost ring, whose ~150,000 fibers are approximately equally divided among three detectors, that each "see" one of three 120° azimuthal sectors of the outermost annular ring.

This arrangement is necessary, because THOR compensates for the outward weakening of halo signal by doubling the width of each successive fiber ring. This results in each ring collecting light from a four times larger area than its inner neighbor.

Upon leaving the optical fiber bundle, photons pass through spectral filters, each with about 7 nm bandwidth. The filters pass nearly all the returning lidar signal, but block most background illumination. This is crucial, because strong background illumination implies poor signal-to-noise ratio. The current filters are sufficient for nighttime observations, but would pass too much sunlight for effective daytime measurements. As a result, THOR is currently operated only at night.

Photons that pass through the filters are counted by single-photon-counting photo-multiplier-tubes. To keep the data volume manageable, the data system sums up 23 subsequent (0/1) photon detection results in 500 subsequent laser pulses. This reduces THOR's range-resolution to 30.8 m, and its time-resolution to 0.5 s. Considering the NASA P-3B aircraft's cruising speed, this time-resolution corresponds to a spatial resolution of about 77 m.

2.2 Calibration

THOR's calibration involves three separate stages.

First, laboratory experiments establish the relative calibration of the 10 THOR channels. A calibration sphere is attached to THOR's telescope that illuminates the front lens uniformly and isotropically. Since we know how the fields-of-view increase from one channel to the next (successively doubling in radius), we can predict how the photon counts of successive uniformly illuminated channels would increase in an ideal instrument (for most channels, by a factor of 4). The increases observed for the actual instrument are somewhat different from the ideal values. Observing the deviations from ideal increase values allows a relative calibration of THOR channels.

The second stage of calibration is an in-flight check of whether the instrument behavior changed substantially since the last relative calibration. The idea is the same as in the laboratory, but this time the uniform illumination is provided not by a spherical calibration lamp, but by the moonlight reflected from extended cloud fields.

The final, third stage of calibration provides absolute calibration for Channel 1, using the Rayleigh scattering signal returning from clear air. Since relative calibration anchors all channels to Channel 1, Rayleigh scattering can provide an absolute calibration for all THOR channels. Unfortunately, this absolute calibration can be performed only when THOR flies over a thick layer of cloud-free and aerosol-free air.

3. DATA PROCESSING METHODOLOGY

The analysis of THOR data starts with an initial processing that prepares the data for scientific interpretation. This initial processing includes radiometric calibration, removal of background illumination, merger with navigational data coming from the P-3B aircraft, and flagging of data as unsuitable for cloud retrievals whenever the aircraft pitch and roll angle is larger than 3°.

The second step of THOR data analysis estimates the cloud properties by comparing the observations to look-up tables that contain simulated THOR data for a wide variety of clouds—and by selecting the case whose simulated data are most similar to the observations.

3.1 Look-up table generation

The simulated THOR data were generated using a suitably modified version of the UMBC5 Monte Carlo model that participated in the International Intercomparison of 3-dimensional Radiative Codes (I3RC) (http://i3rc.gsfc.nasa.gov/).

The main challenge in creating the look-up tables is to keep the computational time manageable while performing low-noise simulations for a wide range of clouds. The Monte Carlo model uses the method of local estimates, and it reduces the simulation noise by smoothing out the forward peak of scattering phase

function for photons that have already been scattered many times (Barker et al. 2003). In addition, we further reduce the required simulation time by several orders of magnitude by using the same photon paths in simulations of many clouds. The scattering angles are identical for all clouds, while the pathlengths between subsequent scattering events are resized according to each cloud's extinction coefficient profile.

Unfortunately, Monte Carlo simulations are quite slow even with these efficiency enhancement methods. Therefore we perform Monte Carlo simulations for only three values of each independent cloud parameter other than geometrical thickness, and we use multidimensional cubic interpolation to fill the entire high-resolution look-up-tables.

Our current computational resources allow us to vary up to seven cloud parameters. Our strategy has been to start by generating look-up tables for simple idealized clouds that can be described by only a few parameters, and then to proceed to more and more complex cloud structures. Our current cloud models have vertical extinction coefficient profiles consisting of linear segments (Figure 3). The cloud retrievals consider all available look-up tables.

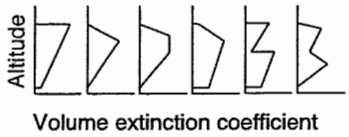

Figure 3. Illustration of some cloud models used in creating THOR look-up tables.

3.4 Estimation of cloud properties

A sample THOR observation used for cloud retrievals is illustrated in Figure 4. The figure shows that THOR's central channel observes intense direct backscatter from near the cloud top, while the outer channels observe a fainter halo formed by multiple scattering deep inside the cloud. The signal of outer channels is delayed because photons need time to reach the halo's outer portions, and it is stretched because some photons meander more while others follow more straight paths.

To maintain maximum flexibility, the retrievals treat the spatial aspect and time-dependence of THOR observations separately. The spatial aspect is characterized through each channel's contribution to the overall detected photon count. The time-dependence is characterized through the width of time (i.e., range) intervals that contain certain percentiles of the time-integrated return signal of each channel.

In practice, retrievals focus on the time-dependence of signals, because this does not require accurate calibration, and on the outer channels and on the tails of time distributions, where cloud thickness has the largest influence.

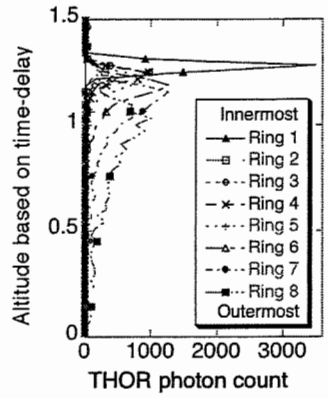

Figure 4. A sample THOR observation collected during the THOR validation campaign described in Section 4.

This has the added benefit of reducing the errors arising from uncertainties in cloud droplet size, as multiple scattering washes out the influence of details in the scattering phase function by the time photons reach the outer rings. On the other hand, focusing on the outer channels and on the tails can create difficulties if the observational noise is large or if the surface reflection can be mixed up with reflection from the lower portions of a cloud. Thus retrieval parameters (e.g., the weight of each channel and percentile bin) must be selected by considering several factors such as the spot size observed by each channel (determined by THOR's altitude above the cloud top), calibration accuracy, noise level (governed by the intensity of background illumination), and surface reflection (influenced by cloud altitude and surface albedo).

4. THOR VALIDATION CAMPAIGN

THOR's first airborne cloud observations took place during the March 2002 THOR validation campaign. During this campaign the NASA P-3B aircraft made repeated passes over the Department of Energy (DOE) Atmospheric Radiation Measurement (ARM) program's Southern Great Plain (SGP) site in central Oklahoma. This site was chosen because of its rich collection of ground-based instruments that provided a wealth of information for validating THOR's cloud thickness retrievals. (See http://www.arm.gov/) The idea was to compare THOR's halo-based cloud thickness estimates with thickness values that were obtained as the difference between the cloud top altitude measured by THOR and the cloud base altitude obtained by use of ground based instruments.

The campaign's first three flights took place on the nights of March 19 20, and 24, respectively. These flights were dedicated to testing the instrument behavior during THOR's first airborne operations and to collecting clear-sky data. The campaign's main science flight took place on March 25, 2002. During the 5 hour long flight, the vicinity of the ARM SGP site was covered by two distinctive cloud layers.

First, a low-level stratus cloud covered the sky completely, thus providing an excellent target for THOR's halo-based retrievals. The cloud base varied from 200 to 500 m above the ground (see below), and the cloud thickness ranged from 500 to 1000 m. Figure 6 shows that the ARM Micropulse Lidar (MPL) clearly detected the cloud base, though it could not provide information on the clouds' inside and top, as cloud droplets quickly scattered the MPL's laser pulses outside its field-of-view.

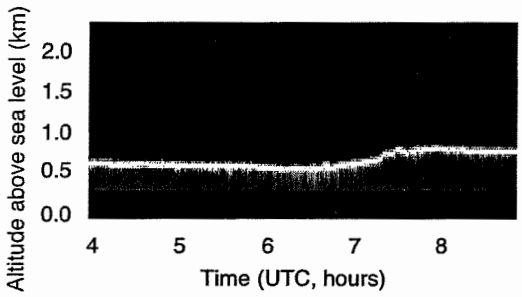

Figure 6. ARM MPL data during THOR's flight.

The second cloud layer was a Cirrus approximately 5.5 km above the ground. Although this cloud was optically too thin to produce a significant halo, it complicated the retrievals for the low-level stratus cloud: It scattered parts of the well-focused downwelling laser pulses into a wider cone, and this widened the halo observed at the low cloud. Thus in order to correctly interpret the halo observations, cloud retrievals need to properly account for the Cirrus spreading effect. Although flying below the Cirrus can certainly help, low-altitude observations pose different challenges: THOR's fixed viewing angles imply that if it flies at lower altitudes, THOR observes smaller areas of a given cloud top, and even its outermost channels see only the relatively inner portions of the bright halo. In order to provide observations from a variety of conditions, THOR made passes over the ARM site at several altitudes.

In addition to the ARM data, we also made use of near-surface temperatures and dew point temperatures at five Oklahoma Mesonet sites that were closest to our flight track. This data was used to estimate the cloud base height via the calculated lifting condensation level. The data revealed significant cloud base variations along the flight track, with a maximum change of up to 350 m from East to West. Thus the cloud base values obtained for the central facility and for these five locations were supplied to a 2D interpolation scheme, which estimated the cloud base at THOR's constantly changing location.

Naturally, the estimated cloud bases are most accurate when THOR flew near the central facility: the uncertainties range from about 20 m within 4 km of the central facility to about 50 m at 30-40 km away. Initial retrievals for a few flight segments (where the Cirrus cloud was thin) showed that THOR cloud thickness retrievals were within the range of uncertainties. Detailed retrieval results are presented at the conference and in Cahalan et al. (2004).

4. CONCLUSIONS

This paper described the new airborne lidar instrument called THOR, outlined the methodology of its cloud retrievals, and briefly discussed the March 2002 THOR Validation Campaign.

THOR was built to probe clouds that have optical thicknesses larger than 2. The inside of these clouds is beyond the reach of conventional lidar, because cloud particles scatter the distinct laser pulses into a diffuse halo that lies outside the narrow field of view of conventional lidar. THOR's multiple wide fields-of-view allow detailed observations of the reflected halo from aircraft flying several kilometers above clouds. Currently, the primary use of halo observations is retrieving the geometrical thickness of optically thick stratiform cloud layers, although the retrievals simultaneously estimate cloud optical thickness and vertical cloud extinction profile.

Future developments are expected in several areas, including further testing and development of cloud retrievals, exploring the possibility of microphysical retrievals, and an expansion of THOR's capabilities to daytime operations and to measurements of the thickness of snow and sea ice. For more information on THOR, see Cahalan et al. (2004).

5. ACKNOWLEDGMENTS

THOR has been funded by the Goddard Director's Discretionary Fund and the NASA Radiation Sciences Program. We are grateful to Anthony Davis for fruitful discussions, to Luis Ramos-Izquierdo for designing THOR's telescope, to all engineers who helped building THOR, and to all who contributed to the success of the 2002 THOR validation campaign.

REFERENCES

Cahalan, R. F., M. McGill, J. Kolasinski, T. Várnai, and K. Yetzer, 2004: THOR—cloud thickness from offbeam lidar returns. *Manuscript in preparation.*

Davis, A. B., R. F. Cahalan, J. D. Spinhirne, M. J. McGill, and S. P. Love, 1999: Off-beam lidar: An emerging technique in cloud remote sensing based on radiative Green-function theory in the diffusion domain. *Phys. Chem. Earth (B)*, **24**, 757-765.

Evans, K. F., R. P. Lawson, P. Zmarzly, and D. O'Connor, 2003: In situ cloud sensing with multiple scattering cloud lidar: Simulations and demonstration. *J. Atmos. Ocean. Tech.*, **20**,1505-1522.

Love, S. P., A. B. Davis, C. Ho, and C. A. Rohde, 2001: Remote sensing of cloud thickness and liquid water content with Wide-Angle Imaging Lidar. *Atmos. Res.*, **59-60**, 295-312.

ON THE SENSITIVITY OF MODIS VISIBLE/1.6 μM CHANNELS TO RADAR-MEASURED GROUND PRECIPITATION

Davide Capacci[1], Alessandro Battaglia[1] , Simone Mantovani[2], Federico Porcù[1], Bryan Conway[3] and Franco Prodi[1,2]

[1]Dept of Physics, University of Ferrara, Ferrara, 44100, Italy
[2]ISAC-CNR, Bologna, Italy
[3]Met Office, Fitzroy Road, Exeter, Devon, EX1 3PB, UK

1. INTRODUCTION

The operational Meteosat-7 is going soon to be replaced by Meteosat Second Generation (MSG) or Meteosat-8, and means of exploiting the larger range of spectral information from MSG to improve the rainfall analyses are needed. Particular interest is focused on the near infrared band (NIR) measurements that will be possible thanks to the 1.6μm and 3.9μm SEVIRI (Spinning Enhanced Visible and InfraRed Imager) channels. MSG data were not available at the time of this work; therefore the investigations were carried out by considering SEVIRI-like measurements from the MODIS (Moderate Resolution Imaging Spectro-radiometer) on board the Terra polar-orbiting satellite [see the web site http://modis.gsfc.nasa.gov/ for sensor characteristics].

The relevance of those measurements rises from the following considerations: the 3.9μm scattered radiation is mainly determined by the cloud-top particles size (Nakajima and King, 1990, Rosenfeld and Gutman, 1994), whereas the 1.6μm scattered radiation depends upon both the optical thickness and the cloud-top particles size (King et al., 1997). A parameter related to the mean distribution of clod-top particles size is the effective radius. Pending the availability of the optical cloud thickness this quantity is retrievable. The latter can be obtained from visible measurements and for this reason the proper use of the 1.6μm channel is in combination with the visible channel. Previous work (Rosenfeld and Lensky, 1998) shown that the 3.9μm effective radius is correlated to the precipitation in case of deep convective cloud. On the other hand the investigations onto the correlation between 1.6μm effective radius and precipitation belong to a very new research area. Recent works (Chang and Li, 2002, Rosenfeld et al., 2004) show that this parameter is related to deeper cloud layer and thus in combination with the 3.9μm effective radius offers the possibility to estimate vertical variation of cloud droplet effective radius.

In this work we investigate the correlation between VIS/1.6μm channels and the ground precipitation by a statistical approach.

Corresponding author's address: Davide Capacci, University of Ferrara, Dept. Of Physics, Ferrara, I-44100, Italy; E-Mail: capacci@fe.infn.it.

We adopt an elementary physical retrieval scheme in order to estimate the 1.6μm and 3.9μm effective radii. As preliminary study, their sensitivity to rainfall rate at the ground for some convective and stratiform precipitation cases is analysed .

2. DATA AND STATISTICAL ANALYSIS

The data set collected consists of 60 cases in and around the UK from November and December 2000, January 2001, December 2002 and January 2003. Due to the timing of the satellite overpasses, the data are concentrated between 10.30 and 11.30 UTC. The MODIS channel considered were: 0.65μm, 0.85μm, 1.64μm, 3.96μm, 6.71μm, 7.32μm, 8.55μm, 11.03μm, 12.02μm; similar to SEVIRI channels. The precipitation data used to train the statistical algorithm and test its performance were archived analyses from Nimrod based on observations from the UK weather radar network (Fair et al, 1990).

The grid on to which the radar and satellite data are remapped is the Nimrod grid where the spatial resolution is 5 km.

The statistical analysis of that data set has been developed at the Met. Office (U.K.) in collaboration with the University of Ferrara (Italy) (Capacci and Conway, 2004). The statistical method used is the Artificial Neural Network (ANN) technique (Rosenblatt, 1962). Its role is determining a correlation function between inputs parameters (as satellite measurements) and output parameters (as classes of precipitation). Only two classes of precipitation are here considered: rain and no-rain classes. In this case the ANN output directly gives the Probability of Precipitation (PoP).

The correlation function is determined in the training phase by calculating (by means of a proper learning procedure) the ANN parameters called weights. The data set used is called training data set. To assess the ANN obtained (testing phase) a second independent data set is needed: the testing data set. The two sub-data sets are randomly selected from the total of 60 cases given. They are constituted of around 350.000 cloudy pixels each. The cloudy pixel were selected by considering the MODIS cloud mask product.

The performance in the testing phase is evaluated by calculating the Equitable Threat Score (ETS). This statistical parameter is required to be as great as possible and gives the performance evaluation with respect to a random performance.

All the combinations of pair of channels were considered as ANN inputs. The table 1 shows the first five best results obtained in term of ETS.

INPUTS	ETS
0.65μm and 1.6μm	0.276
0.85μm and 1.6μm	0.274
0.65μm and 8.55μm	0.220
0.65μm and 11.03μm	0.219
0.65μm and 12.02μm	0.217

Table 1. Five best results for two-inputs ANN classifier.

The VIS/1.6μm ANN classifier assigns cloudy pixels to rain or no-rain classes with ETS around 27% that is largely the best among all the possible pair of channel. It is worth to highlight that the ANN classifier built with only one channel and tested on the same data sets has performances around 14% for visible channel and around 3% for 1.64μm channel alone.

3. EFFECTIVE RADIUS RETRIEVAL PROCEDURE

The retrieval procedure to get 1.64μm and 3.92μm effective radii is based on the look-up tables method. The tables consists of a series of reflectance values simulated for several 1-dimensional clouds scenes. By comparing and interpolating the measured reflectance values with those simulated the cloud scene can be inferred. The simulation are computed by considering a Monte Carlo forward radiative transfer (RT) model.

It is worth to put in evidence the approximation onto which the simulation are based:

- Atmosphere is non-scattering and non-absorbing (perfect "window");
- Cloud-top particles are ice spheres;

Varying the effective radius of the 1-dimensional cloud it is possible to obtain the look-up table for the 3.9μm case. Varying the cloud optical thickness it is possible to obtain the look-up table for the visible case. Varying the cloud optical thickness and the effective radius the 1.6μm look-up table is obtained.

In the 3.9μm case the reflected part of measured radiation has to be separated from the emitted part. From the reflected part the reflectance is calculated and interpolated with the look-up table reflectances so as to estimate the effective radius. In this procedure the cloud transmissivity is assumed to be zero. In case of 1.6μm the reflectance is directly measured from satellite. The effective radius retrieval is in this case based onto two steps. In first step the cloud optical thickness has to be retrieved from VIS measurement and this is possible by interpolating visible reflectance value with the visible look-up table. Once that value is fixed the 1.6μm effective radius retrieval can be done in the same way as for the 3.9μm case.

Both the procedure take in account the sun-cloud-satellite geometry.

For a fixed geometry figure 1 shows the simulated reflectance values versus cloud optical thickness and for several effective radius values.

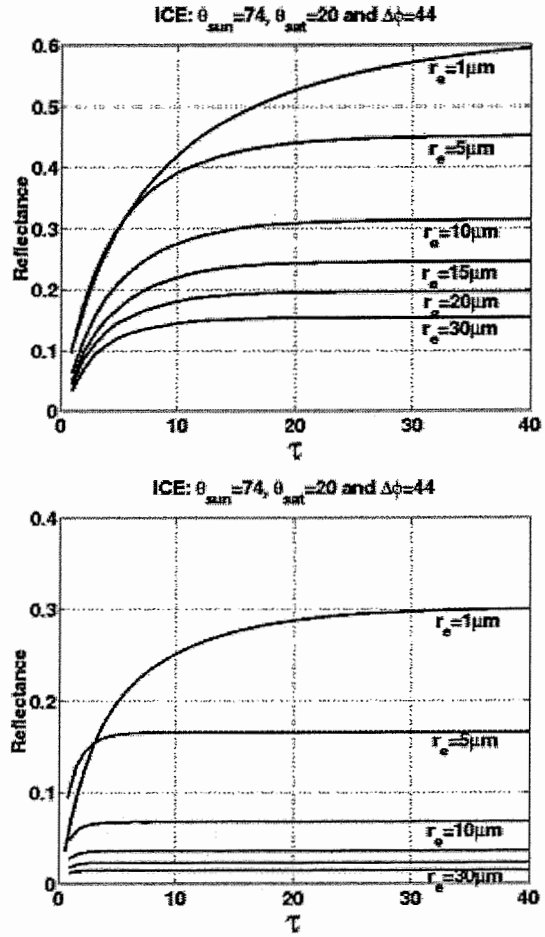

Figure 1. Reflectance as function of cloud optical thickness for different effective radius, for 1.6 μm (a) and 3.9 μm (b).

4. CONVECTIVE AND STRATIFORM PRECIPITATION: CASE STUDIES

As a preliminary study we apply the retrieval scheme to convective and stratiform cases, to verify the different behaviour of those two parameters for different kind of clouds. By visual inspection eight cases of evident convective precipitation and eight cases of evident stratiform precipitation were selected

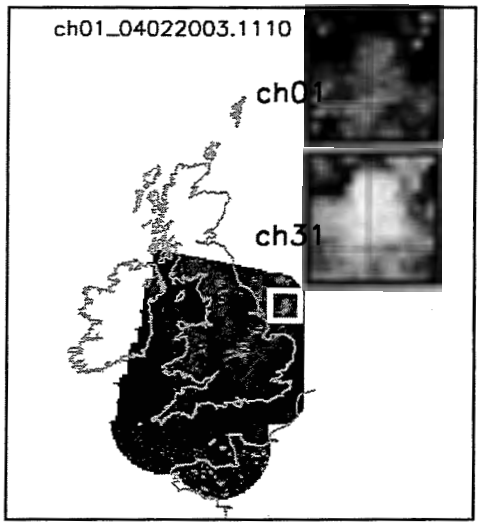

Figure 2. Visible image from which the convective area is selected.

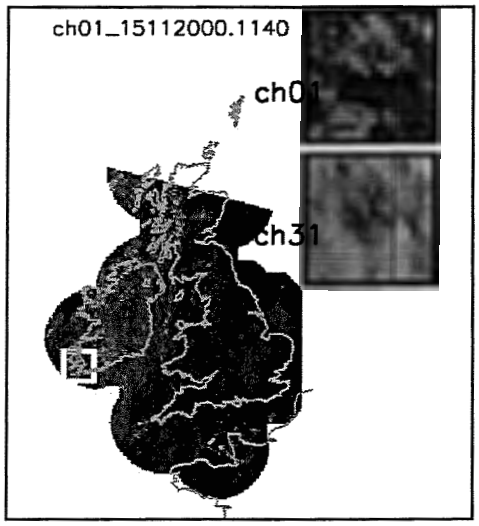

Figure 4. Visible image from which the stratiform area is selected.

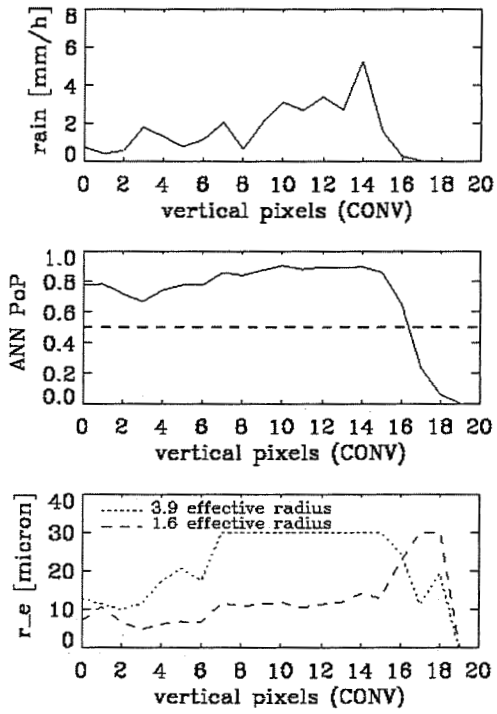

Figure 3. Rainfall rate, VIS/1.6μm ANN PoP, 1.6μm and 3.9μm effective radii along the vertical cross-section of selected convective area

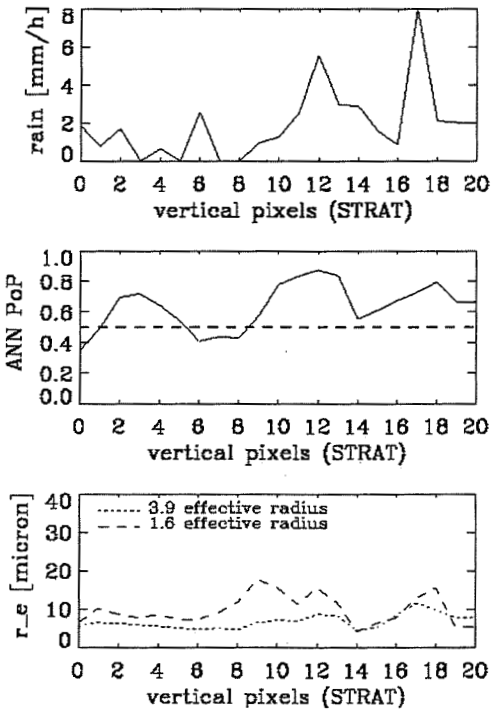

Figure 5. Rainfall rate, VIS/1.6μm ANN PoP, 1.6μm and 3.9μm effective radii along the vertical cross-section of selected stratiform area

from the total data set available. For each case (consisting in a square of 20x20 pixels) a vertical and horizontal cross-section lines are considered. Along those cross-section lines the following parameters are considered: radar rainfall measurement, VIS/1.6μm ANN PoP, retrieved 1.6μm and 3.9μm effective radii. Figure 2 show a case of convective precipitation and figure 4 show a case of stratiform precipitation. The first is well representative of all the other convective cases. The 3.9μm effective radius along the vertical cross-section (figure 3) is greater than the 1.64μm effective radius coherently with what found by Chang and Li (2002). The second one is representative of stratiform cases where the 1.64μm effective radius is slight greater or comparable with the 3.9μm effective radius (as in figure 5). However other stratiform cases are more similar to convective cases.

5. DISCUSSION AND CONCLUSIONS

The statistical approach shows an high correlation between the VIS/1.6μm combination and the radar-measured ground precipitation. This is a new and interesting result that deserve to be analysed and explained. By an elementary physical procedure the 1.6μm and 3.9μm effective radii were inferred. By analysing some convective and stratiform precipitation cases what emerged is that the statistical PoP function describes the precipitation better than the physical retrieved parameters. However the two cases analysed show an interesting characteristic: the combined use of the two retrieved effective radius can have different behaviour for different kind of clouds. In fact in all the convective cases analysed the 3.9μm effective radius is clearly greater than the 1.6μm effective radius. This does not happen in several stratiform case where the two effective radii are comparable. This results, supported also by previous works (Chang and Li, 2002, Rosenfeld et al., 2004), indicate this area of research as a very promising area about the estimation of precipitation from satellite measurements

REFERENCES

Capacci Davide and Bryan Conway, 2004: Estimation of Probability of Precipitation from MODIS visible and infrared imagery with artificial neural networks. *Met. Appl.*, submitted.

Chang Fu-Lung and Zhanqing Li, 2002: Estimating the vertical variation of cloud droplet effective radius using multispectral near-infrared satellite measurements. *J. of Geophys. Res.*, **107**, no D15,4257.

Fair, C. A., P. K. James and P. Larke. 1990: The United Kingdom weather radar network. Pp. 147-154 in: Weather Radar Networking, seminar on COST Project73. Ed. C. G. Collier and M. Chapuis, Kluwer Academic Publishers, Dordrecht. EUR12414 EN-FR.

King, M.D., S. Tsay, S. E. Platnick, M. Wang and K. Liou, 1997: Cloud Retrieval Algorithms for MODIS: Optical Thickness, Effective Particle Radius, and Thermodynamic Phase. MODIS Algorithm Theoretical Basis Document No. ATBD-MOD-05 MOD06, 79 pp.

Lensky, M. and D. Rosenfeld, 1997: Estimations of precipitation area and rain intensity based on the microphysical proprerties retrieved from NOAA AVHRR data. *J. Atmos. Res.*, **36**, 234-242.

Nakajima, T. and M. D. King, 1990: Determination of the optical thickness and effective particle radius of clouds from reflected solar radiation measurements. Part I: Theory. *J. Atmos. Sci.*, **47**,1878-1893.

Rosenblatt, F., 1962:. Principles of Neurodynamics: Perceptrons and Theory of Brain Mechanisms. Washington DC: Spartan.

Rosenfeld, Daniel and Itamar M.Lensky, 1998: Satellite-based insights into precipitation formation processes in continental and maritime convective clouds. *Bull. Am. Met. Soc.*, **79**, 2457-2476.

Rosenfeld, D., E. Cattani, S. Melani, and V. Levizzani, 2004: Considerations on daylight operation of 1.6 micron vs 3.9 micron channel on NOAA and METOP satellites. *Bull. Am. Meteor. Soc.*, in press.

AKNOWLEDGEMENTS

This work has been jointly funded by the Met Office U.K. and EURAINSAT a shared-cost project (contract EVG1-2000-00030) co-funded by the Research DG of the European Commission within the RTD activities (5th Framework Program).

ANALYSIS OF PLUDIX DISDROMETER PERFORMANCE DURING THE BBC-2 CAMPAIGN

Clelia Caracciolo[1], Franco Prodi[1,2], Remko Uijlenhoet[3] and Stefano Natali[4]

[1]University of Ferrara, Dept. of Physics, Ferrara, I-44100, Italy
[2]ISAC-CNR, Bologna, I-40129, Italy
[3]Wageningen University, Wageningen, PA-6709, The Netherlands
[4]Nubila s.a.s, Bologna, I-40128, Italy

1. INTRODUCTION

The observed variability in the drop size distribution (DSD) or its integrated parameters is attributable to two main sources: instrumental effects and natural (spatial or temporal) variability. It is therefore important to compare different kinds of instruments in order to understand whether the DSD variability is due to nature or to differences among the instruments. The object of this work is to compare the performances of different disdrometers, which measure the DSD using different principles. In particular, it aims to test a recent device, called the Pludix. All the instruments analysed here are collocated: although in the past numerous DSD studies have used various types of disdrometers, only a few have compared the simultaneous DSD measurements by collocated disdrometers (Tokay et al., 2001).

The X-band rain-gauge disdrometer Pludix (Prodi, 1994) was employed over three months, from May 13 to August 13, 2003 in the BBC-2 (Baltex Bridge Cloud Campaign 2) at CESAR (Cabauw Experimental Site for Atmospheric Research) in The Netherlands, near Utrecht. The campaign was a large cloud measurement campaign, organized by the Royal Netherlands Meteorological Institute (KNMI), involving different kinds of instruments. One of the aims of the ground precipitation analysis was to compare different kinds of disdrometers in order to measure and parameterise the rainfall microstructure. Also used in the experiment were a two-dimensional video disdrometer (2DVD), two optical (infrared) disdrometers and different tipping-bucket rain-gauges (TB-RG). For the first time, Pludix was used alongside optical disdrometers. The aim of the present study is to compare the performances of these instruments, based on different measuring principles in the rainfall-rate (R) and DSD estimates.

Moreover, several events are analysed at the Ferrara (Italy) site (Dept. of Physics-University of Ferrara), where the Pludix has been collocated since November 2001 alongside a Joss-Waldvogel (hereinafter JW) (Joss and Waldvogel, 1967) impact disdrometer. Many more samples of simultaneous Pludix and JW measurements than in previous studies (Prodi et al., 2000a; b) were collected, in order to provide a more robust DSD parameterization and to study the instrument dependency on the relationships between R integral parameters and precipitation types for different R regimes. Much of this part of the work is based on the first author's PhD thesis (Caracciolo, 2004).

Corresponding author's address: Clelia Caracciolo, University of Ferrara, Dept. of Physics, Ferrara, I-44100, Italy; E-Mail: caracciolo@fe.infn.it.

2. INSTRUMENTS SET-UP AND METHODOLOGY

The Pludix is a rain-gauge/disdrometer based on the analysis of an X-band (9.5 GHz) continuous wave radar signal backscattered by hydrometeors. It provides more detailed information than a classical TB-RG and to disdrometers, giving data on the precipitation type. The JW data in Ferrara consist of number of raindrops n_i of diameter D_i in 20 categories, ranging in size from 0.35 to 5.25 mm, in variable steps. No correction is applied to the DSD to account for the dead time problem of the instrument. The Pludix data in Ferrara and Cabauw consist of number of raindrops n_i of diameter D_i in 21 categories, ranging in size from 0.8 to 7.0 mm, with a constant step of 0.3 mm. The Pludix data collected in Ferrara are contaminated by ground physical noise signals (due to an anemometer presents at the site) at the smallest frequencies (<50 Hz), which are removed from each measurement.

The Pludix and JW were operated during the period November 2001 – May 2002 at the Physics Department of the University of Ferrara with a time resolution of 60 s. A TB-RG is used to validate the rain measurements. From the overall database, four light and nine moderate R events are selected and analysed. The performances of the two instruments in both R and DSD measurements are tested. An average DSD in each time period of each event is considered. The N_0 [1/mm/m^3] and Λ [1/mm] parameters of the exponential DSD are computed using the Waldvogel (1974) method. The m, N_0 [1/mm^{1+m}/m^3] and Λ [1/mm] values of a gamma DSD are computed following the Tokay and Short (1996) method of moments. The R [mm/h] and the reflectivity Z [dBZ] are computed by the observed N(D) and compared. The Z-R relationships are computed by a linear regression method for each instrument.

In addition, a 2DVD and Pludix, installed at the Cabauw site (The Netherlands), with a time resolution of 60 s, are compared. The 2DVD is an optical disdrometer

recording characteristics (size, velocity, shape) of each single hydrometeor falling through its sensing area. The instrument therefore works on an optical basis. To obtain a front and side view of each hydrometeor, two optical systems are used. They consist of a high-speed line scan camera and a background illumination device, and are orthogonally aligned against each other with a height offset of some 6 mm. Any particle falling through the beam of light will appear to the cameras as a dark silhouette against the bright background. Only particles seen in both cameras are counted. A detailed description of the instrument is given in Urban (1996) and Kruger et al. (2002). The 2DVD data in Cabauw consist of number of raindrops n_i of diameter D_i in 22 categories, ranging in size from 0.2 to 4.4 mm, with a constant step of 0.2 mm. Several rain-gauges are used to validate the rain measurements. The two instruments were operated during the period May 13, 2003 – August 13, 2003. From the overall database, fifteen events are selected, most of which very intense (R> 20 mm/h) and occurring in July. The performances of the two instruments in both R and DSD measurements are tested. Different rainfall integral and DSD parameters are computed and compared for the analysed events.

3. RESULTS

3.1 Comparison of the Pludix and JW in Ferrara: rainfall-rate and DSD analyses

The R analysis over the entire seven month database shows that the Pludix generally tends to underestimate the less intense precipitation events and to overestimate the most intense precipitation events with respect to the TB-RG and JW (see fig. 1 for April 11, 2002). The light-moderate R events are characterized by more small drops (between 0.3 and 0.8 mm), which the Pludix does not consider; this is probably the reason for the underestimation. In the most intense events, large drops are present and the Pludix gives R values higher with respect to JW and more similar to the TB-RG (often higher than the TB-RG). In this case, it is supposed that the Pludix values are more realistic, because JW counts drops only until D=5.3 mm, and during heavy events the TB-RG is a less reliable instrument because of the bucket mechanism. Considering the thirteen light/moderate selected events, it is found that the Pludix records 9.5% less rain amount, while the JW records 3% less rain amount than the TB-RG. The frequency distributions of JW and Pludix rain occurrence show that the Pludix records a higher percentage of light rain than the JW, for the coincident measurements. In any case, the correlation between the two disdrometers is good.

The Pludix tends also to underestimate Z compared to the JW. It is expected that the situation will invert for heavy events, because of the maximum Pludix detected diameter equal to 7 mm. Another important aspect is that, the Pludix tends to count a lot of drops especially in the 0.8-1.5 mm diameter interval for almost all the events. This interval contributes most to R, while there is a presence of more and very large drops in the JW except in the very first size range. The underestimation of small drops by the JW has also a limited effect on Z, because this parameter is related to the higher moments of the DSD.

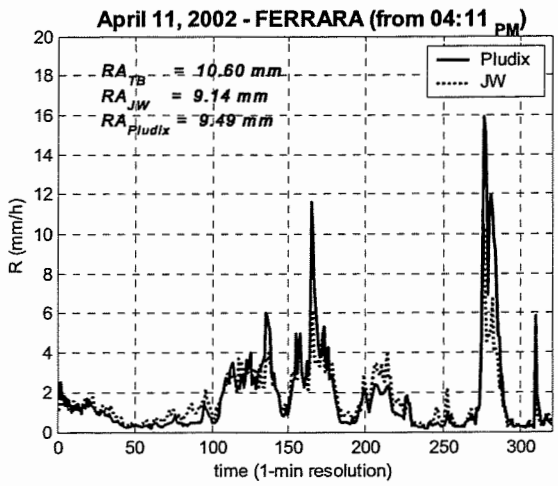

Fig. 1: 1-minute time rainfall-rate evolution for April 11, 2002 in Ferrara (dashed line JW; solid line Pludix).

To show the instrumental dependence on the coefficients of the Z-R relationship, Z-R relations obtained from DSD measurements by the two disdrometers are examined. If one considers two DSDs, at the same R, the spectrum that has more large drops turns out to have a lower coefficient A than the spectrum with less large drops, assuming a constant exponent b. In this comparison, the Pludix A coefficient is generally lower than the JW A coefficient, while the Pludix b coefficient is nearly always lower than the JW b coefficient. This is due to the R and Z underestimation of the Pludix as compared to the JW.

Simultaneous measurements of DSDs by the JW and Pludix are performed for the thirteen selected events. The composite DSDs derived for all these observations show a good agreement among the two instruments. The DSDs for the two instruments are similar for the same D classes. Qualitatively, the measurements in the mid-diameter range (1<D<3 mm) of DSD behave similarly, with a concentration relatively lower in the Pludix than in the JW. The Pludix is able to detect large drops not measured by the JW, although the concentration of large drops is very small, because of light rains. There are also differences in drop concentrations at D<1 mm, mainly due to the underestimation of small drops by the JW (dead time

problem), and to the large concentration of drops in the first Pludix diameter class of 0.95 mm. The coincident DSDs of the two instruments for three different rain intervals (R<2, 2<R<5, 5<R<10 mm/h) and for the total rain range (see fig. 2) are also averaged. A good agreement is found between the two disdrometers at all three scales, especially for R<2 mm/h, with less concentration of medium size drops in the Pludix. To parameterise the DSD, the exponential and gamma functions are applied to each average DSD. The parameters of the exponential and gamma DSD derived from the Pludix spectra are often higher than those derived from the JW spectra (the DSD is narrow). Moreover, the Pludix DSD is better parameterised by an exponential DSD, while the JW DSD is better parameterised by a gamma DSD. For D<0.5 mm, JW shows N(D) in defect of the exponential model. As R increases, the DSDs show increasing curvature relative to the exponential model: the number concentrations of both small and large drops are lower. A gamma DSD fits the data better. For the Pludix, the shape of all the curves represents an exponential DSD quite well, except for large D and for high rains. Otherwise, for 2<D<5 mm the Pludix generally shows N(D) in defect of the exponential model.

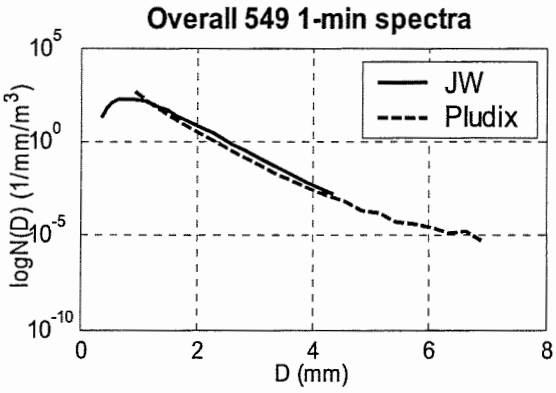

Fig. 2: Average coincident measurements of the two instruments (dashed line Pludix; solid line JW) for all the coincident observations in Ferrara.

3.2 First results of the comparison between the Pludix and 2DVD in CABAUW

Fig. 3 shows the Pludix and the 2DVD rainfall-rate 1-minute time evolution for the May 19, 2003 event occurred in Cabauw. In general, it is found that for the less intense events, the Pludix tends to underestimate R with respect to the 2DVD. Otherwise, for the heavy events (R>10 mm/h) the Pludix tends generally to overestimate R (not shown here). This behaviour is attributable to the different size classes of the two instruments and to the minimum detected diameter (0.8 mm for the Pludix and 0.2 mm for the 2DVD). The maximum Pludix detected diameter of 7.0 mm can also influence the final result for the heavy rain events.

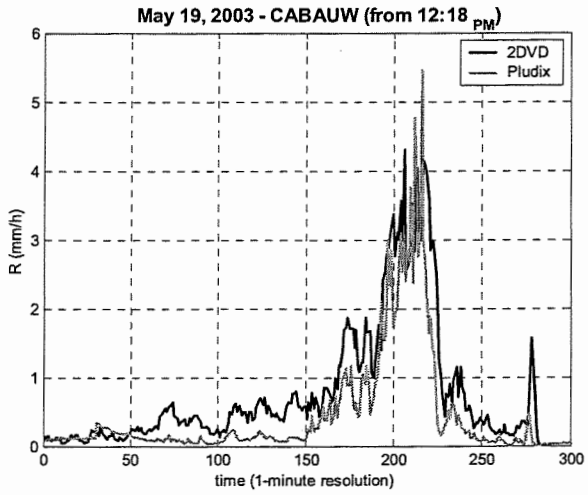

Fig. 3: 1-minute time rainfall-rate evolution for May 19, 2003 in Cabauw (grey line Pludix; black line 2DVD).

4. CONCLUSIONS AND FURTHER WORK

Two disdrometers based on different measuring principles installed in Ferrara (Italy) were compared: a classical JW disdrometer and a recent device, called the Pludix. The performances of the two disdrometers were analysed by comparing their rain amounts with the nearby TB-RG and by comparing their DSDs. The most important rainfall integral parameters (like R and Z) and DSD parameters were analysed and compared.

Regarding the R comparison, both types of disdrometers underestimate total rain, but, for the light/moderate R events analysed here, the agreement is better between JW and the TB-RG. The Z values of the two instruments are quite close, with the Pludix reflectivity always quite less that the JW reflectivity. The Z-R relationships were derived; the A and b values of the two instruments are quite close, with the Pludix A and b values generally lower than the JW values. These results are probably due to the fact that the light-moderate R events analysed here are characterized by many small drops (between 0.3 and 0.8 mm), that the Pludix does not consider, because its minimum detected diameter is 0.8 mm.

Comparing the DSDs, it was found that for the same D classes the two instruments have similar DSDs. The long-time-period averaged DSDs were parameterised by an exponential and a gamma DSD. It was found that Pludix DSD is better parameterised by an exponential DSD, while the JW DSD by a gamma DSD. This

behaviour also reflects on the average exponential and gamma DSD parameters, which are nearly always greater in the Pludix with respect to the JW. To better compare the two instruments, the coincident measurements of DSDs performed by the two instruments were averaged for three R classes. A good agreement was found between the two measurements at all three scales, especially for R<2 mm/h. A good agreement was also found when all the coincident DSD measurements of the JW and Pludix were averaged, with less concentration of medium size drops in Pludix.

The comparison between the Pludix and a 2DVD installed at Cabauw site (The Netherlands) has also shown that for the less intense events the Pludix tends generally to underestimate R with respect to the 2DVD. Otherwise, for the heavy events (R>10 mm/h) the Pludix tends generally to overestimate R. This behaviour is attributable to the different size classes of the two instruments and to the minimum detected diameter (0.8 mm for the Pludix and 0.2 mm for the 2DVD). The maximum Pludix detected diameter of 7.0 mm can also influence the final result for the heavy rain events.

Considering the different natures of the instruments and the fact that the Pludix is still in a calibration and testing phase, the results found here are encouraging. The analysis has also demonstrated the good capability of the Pludix in evidencing R and the DSD with high accuracy. In the future, a new signal inversion algorithm will be tested, which will allow the counting of drops in the whole diameter interval 0.3-7.0 mm. It is expected that this will lead to more accurate results. The results found here also suggest that the Pludix can be used together with other disdrometers to investigate the differences in DSD in different R regimes and to exploit their inherent strengths. The ability to measure very large drops with the Pludix should also be considered a substantial improvement in DSD research. Moreover, the Pludix can easily discriminate between any type of hydrometeor (e.g. hail, snow, ...) while other classical disdrometers or rain-gauges do not do. It can therefore be considered as a Present Weather Sensor (PWS). In the future the instrument will be used in local networks for the simultaneous control of large remote areas, investigating time and space variability of the rainfall events.

5. REFERENCES

Caracciolo C., 2004: Reconsideration of the analysis methods and measuring instruments for the raindrops size distributions investigation. PhD thesis. Ferrara University, Italy, 265 pp. (available from the author).

Joss J. and A. Waldvogel, 1967: Ein spectrograph für niederschlagstropfen mit automatischer auswertung. Pure and Appl. Geophys., 68, 240-246.

Kruger A. and W. Krajewski, 2002: Two-dimensional video disdrometer: a description. J. Atmos. Ocean. Technol., 19, 602-617.

Prodi F., 1994: Pluviometro-disdrometro in banda X. Proposta nell'ambito della legge 29 nov. 1990 n. 366: "Completamento ed adeguamento delle strutture del Laboratorio di Fisica Nucleare del Gran Sasso".

Prodi, F., A. Tagliavini and F. Pasqualucci, 2000a: Pludix: an X–band sensor for measuring hydrometeors size distributions and fall rate, Proc. of the 13th ICCP, 338-339.

Prodi F., Tagliavini A. and R. Medini, 2000b: Time variability in rainfall events observed by Pludix. Phy Chem Earth(B), 25, n. 10-12, 959-963.

Tokay A. and D. Short, 1996: Evidence from tropical raindrop spectra of the origin of rain from stratiform versus convective. J. Appl. Meteor., 35, 355-371.

Tokay A., A. Kruger and W.F. Krajewski, 2001: Comparison of drop size distribution measurements by impact and optical disdrometers. J. Appl. Met., 40, 2083-2097.

Urban H.E., 1996: 2D video disdrometer users manual. Under ESTEC Contract No. 9949/92/NL/PB(SC). Joanneum Research, Graz (Austria).

Waldvogel A., 1974: The N_0 jump of raindrop spectra. J. Atmos. Sci., 31, 1067-1078.

PHASE-DOPPLER INTERFEROMETRY FOR IMPROVED CLOUD MICROPHYSICAL MEASUREMENTS

P. Y. Chuang[1] and W. A. Bachalo[2]

[1]Department of Earth Sciences, University of California Santa Cruz, Santa Cruz, CA 95064, USA
[2]Artium Technologies Inc., Sunnyvale, CA 94086, USA

1. INTRODUCTION

The measurement of the cloud droplet size distribution is important for the study of a wide range of fundamental cloud microphysical processes. The subsequent implications for precipitation formation and cloud radiative properties are critical to improving our understanding of the role of clouds in weather and climate. We describe here an instrument based on the phase-Doppler interferometry (PDI) technique. PDI was initially developed more than two decades ago, and subsequent refinement has yielded a technique whose uncertainties are well-documented. PDI has been demonstrated to have several advantages over light scattering intensity devices (such as the FSSP) for cloud microphysical measurements. PDI is extensively used in the spray sciences community (for studies in areas ranging from fuel injectors to drug delivery), but its application to cloud microphysics has been much more limited. A new instrument (dubbed PICS, or Phase-Doppler Interferometry Cloud Spectrometer) has been developed that is optimized for cloud studies, with a special emphasis on high quality measurement of larger (>30 μm diameter) drop, and which incorporates the most recent technology available along with new methods for signal processing. This presentation will outline the basic ideas behind PDI, and discuss some of the specific features of PICS.

2. PHASE-DOPPLER INTERFEROMETRY

The measurement principle is based on light scattering interferometry, which utilizes the ***wavelength*** of light as the measurement scale. In contrast, almost all existing optical probes utilize the ***intensity*** of scattered light to make the measurement. This confers PDI with many advantages, primarily significantly improved performance under conditions of contaminated optics and/or electronic drift and noise, and a significantly reduced need for calibration. Therefore PICS exhibits tremendous improvements in data quality and robustness, very desirable characteristics for use with aircraft platforms.

Corresponding author's address: Patrick Y. Chuang, Department of Earth Sciences, University of California Santa Cruz, Santa Cruz, CA, USA, 95064; E-mail: pchuang@es.ucsc.edu.

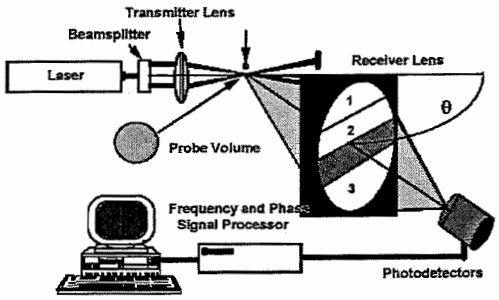

Figure 1: Typical PDI setup

The optical system for PDI is similar to that of laser Doppler velocimetry (LDV), and is shown in Figure 1. The measurement volume is defined by the intersection of two identical beams separated from a single polarized laser. Interference of these two beams in the measurement volume leads to a sinusoidal pattern of constructive and destructive interference fringes. As a particle passes through the beam intersection volume, it scatters light into the surrounding space. The receiver is situated to collect this scattered light and images it onto a series of detectors; for simplicity we will assume that only two detectors are used. Each detector will record a time-varying signal that resembles the sinusoidal pattern of interference fringes (see example in Figure 2), called "Doppler bursts," which are characterized by two important parameters. The first is the ***frequency***, which is a measure of the ***velocity*** of the droplet, and which is the same for both signals. The second is the ***phase shift*** between these two signals (denoted by the Δ in Figure 2), which is directly proportional to the droplet ***diameter***. The origin of this phase shift can be understood by thinking of the particle as a small lens that is refracting light as it falls through the interference fringes. If one were to freeze the motion of the particle "lens" as it passes through the measurement region, one would find that the lens projects an image of the fringes into surrounding space. The smaller the particle, the more expanded the projected fringes will be in the surrounding space. It is this spatial frequency of the projected fringe pattern that is measured by the phase shift between two detectors. The analogy of a particle as a lens suggests two important properties that particles must satisfy in order that PDI be a successful technique: they must be optically homogenous with known

refractive index, and they must be spherical. In the case of liquid cloud droplets, this will be satisfied under most realistic atmospheric conditions for the size range of 2 to 250 μm diameter that PICS focuses on.

The phase difference between any two detector signals can be shown to bear a nearly monotonic, linear relationship with droplet diameter. Therefore, the phase can be measured and used to infer the diameter of the spherical particle. There are oscillations in the phase-diameter relationship at the smallest drop sizes due to resonances, and this sets the measurement uncertainty of drop diameter at about ±0.5 μm for this technique.

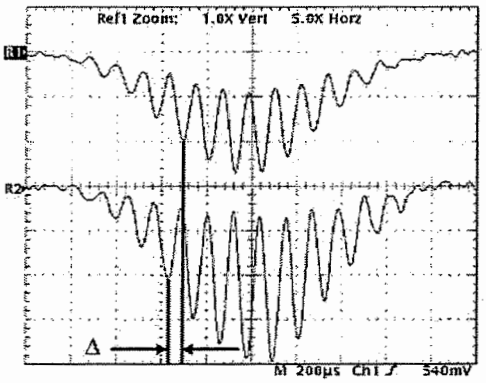

Figure 2: Example of a PDI measurement using two detectors. Note that each detector measures a Gaussian-shape signal on which a sinusoidal oscillation is superimposed. Δ denotes the phase shift between the signal of two detectors, and is a measure of drop size. The signal frequency (the same for both detectors) is a measure of droplet velocity.

3. PICS DESIGN FEATURES

There are a number of features of PDI that cause PICS to be significantly different from other single cloud droplet instruments. The underlying reason for all of these novel features is that the scattering volume has a very specific and well-understood structure (i.e. a Gaussian distribution of intensity superimposed by constructive and destructive interference bands), which then causes the scattering signal also to be very specific.

3.1 Design Features

a. Droplet Sizing

- Droplet sizing uncertainty: ±0.5 μm
- Dynamic range: 125:1
- Minimum droplet size: 2 μm
- Maximum droplet size: 250 μm

Droplet sizing fundamentally depends on the phase difference between signals from proximate detectors, which in turn depends on only three parameters: (1) the wavelength of the laser; (2) the intersection angle of the two beams; (3) the refractive index of the spherical drop. For warm clouds, none of these is expected to change significantly. Note that fluctuations in light intensity do not affect the measured drop size. This is a great advantage for aircraft operations, since contamination of optics or fluctuations in laser or detector performance will not affect the drop size measurement.

b. Droplet concentration

- Droplet concentration uncertainty: 5% per size bin.

Accurate measurement of drop concentration requires accurate knowledge of the collection area in the plane perpendicular to the direction of aircraft motion, which for PICS (and all previous single droplet instruments) is drop size dependent. The two dimensions of this area (Figure 3) that need to be defined, then, are (i) x, the length in the direction of the laser, (termed depth-of-field for FSSPs) and (ii) y, height of the beam. Because PICS does not utilize near-forward scattering, x can be defined using a physical aperture that limits the view volume of the detector. PICS will further incorporate a motorized aperture selector that will permit in-flight switching among a small number of aperture sizes, performed either automatically or by an operator. In the other dimension, y is drop size dependent. This occurs because the cross-sectional intensity of a laser is Gaussian (although it can be conditioned to other profiles), and the detection limit for the detectors is at a fixed intensity. This means that larger drops, which scatter more light, can be present in weaker parts of the beam than can smaller drops, which would need to be closer to the beam center to generate the same intensity of scattered light. This means that y increases as drop size increases.

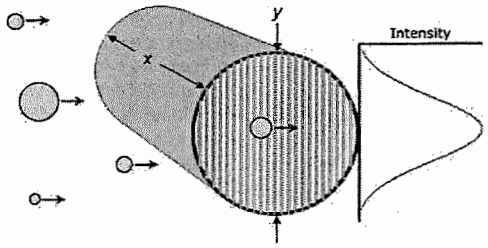

Figure 3: Idealized picture of a PDI view volume. Droplets that pass through the view volume further from the center in the y-direction scatter less light and fewer fringes. This permits accurate near real-time determination of the size-dependent view volume. The x-dimension of the view volume can be altered during flight, permitting control of coincidence rates in order to account for varying conditions.

PDI has an inherent method to measure this dependence, as shown in Figure 3. As drops penetrate the view volume at increasing *y*, they are not only passing through regions of lower light intensity, they will also scatter fewer fringes. Therefore, determining the minimum number of fringes scattered by drops of a given size leads to a near-real time measurement of *y* as a function of size. If conditions change during flight (for example, optics become contaminated) and therefore incident light intensity changes, this can be accounted for on the time scales for which a statistically significant sample can be obtained, say every 100 drops per size bin. The overall uncertainty in concentration, then, is dependent on our ability to accurately determine *x* and *y*, which we estimate to be ~5% for any given size bin.

c. Coincidence

One important feature of PICS is that the signal obtained when two (or more) droplets are present in the view volume is very different from that of any single droplet. As a result, coincidence will not lead to distortions of the cloud drop spectrum. However, the unique nature of PDI permits an improved method to analyze coincident events. If two droplets enter the view volume at different times, droplet size can be estimated even if for some duration the drops are indeed coincident in the view volume. The measurement is achieved by examining those parts of the signal when only one of the droplets was present. This allows measurement of droplets separated by distances O(10 μm), which is much smaller than the overall length of the view volume, about 100 μm. This is therefore an important feature of this probe. The sizing precision in these cases is reduced, since the phase difference in the signals is not as accurately computed. Tests to establish the precision under these conditions remain to be performed.

With the ability to make measurements when two drops are coincident in the view volume, the probe view volume is specified in such a way as to minimize the probability that *three* droplets are coincident. This depends on the expected cloud droplet concentration. The range of cloud droplet concentrations that can be encountered in nature span roughly two orders of magnitude. Fixing the view volume dimensions would lead to a situation where we would need to choose the smallest volume possible in order to make reasonable measurements at the highest concentrations. However, this leads to poor sampling statistics at low droplet concentrations. Instead, PICS will possess the capability to dynamically change the view volume using a combination of hardware and software techniques in response to changes in ambient droplet concentration. View volume length (*x* in Figure 3) is adjusted using apertures of different sizes. Since the probability that three drops are present in the view volume depends approximately on (view volume)^3, an ability to use apertures which are different in size by a factor of 4 (say 0.5 to 2 mm) will permit control of the coincidence rate to within a factor of $4^3 = 64$, which is likely to be sufficient dynamic range to adjust for changes in cloud drop concentration even among clouds with very different characteristics. This feature therefore permits optimization of the view volume size to maximize droplet sample rate, while maintaining reasonable coincidence rates.

d. Droplet velocity measurements

- Maximum velocity uncertainty: 0.1% of full scale
- Velocity range: ± 1 m/s nominal (user selectable between ±0.1 and ±5 m/s).

Although not the primary function of PICS, there exists the capability to measure droplet velocity. This is a well-documented feature of PDI.

e. Droplet spacing

- 1-D spacing uncertainty: estimated to be O(10 μm)

Droplet spacing can also be measured by PICS. Again, this is not a primary goal of the instrument, and therefore it is not optimized for such purposes, but the achieveable 1-D spacing uncertainty is estimated to be O(10 μm), which is the characteristic length scale of the fringe spacing.

f. Calibration

PDI instruments need to be calibrated only once during their lifetimes. This calibration is needed in order to establish the relationship among the laser wavelength, laser intersection angle, and detector positions. The first is constant, while the latter two are fixed as long as the optical components are not purposely modified and therefore no subsequent calibrations are required. Tests on past PDI instruments have shown that the original factory calibration can be maintained to better than 1% even after 20 years of continuous operation under harsh industrial conditions. This is a tremendous advantage for during aircraft field operations, where calibration is (at best) difficult to do well.

4. SUMMARY

PICS will incorporate a number of novel features in order to maximize the potential of PDI for warm cloud microphysical measurements, particularly for use onboard aircraft platforms. It is expected that these measurements will be significantly improved over previous ones, and thereby lead to new insights and understanding of warm cloud processes and evolution.

MEASUREMENTS OF THE DROPLET SPECTRA WITH THE FSSP-100: A STOCHASTIC MODEL OF PROBE FUNCTIONING

A. A. Coelho[1], J. L. Brenguier[2] and T. Perrin[2]

[1]Federal University of Ceará, Physics Department, Fortaleza, Ceará, 60455-760, Brazil
Visiting Scientist at Meteo-France/CNRS, CNRM/GAME
[2]Meteo-France/CNRS, CNRM/GAME, Toulouse, 31057, France

1. INTRODUCTION

After more than 30 years of operation, the Forward Scattering Spectrometer Probe (FSSP-100) still remains the most commonly used airborne instrument for measurements of the droplet size distribution in clouds. This instrument is counting and sizing cloud droplets into 15 size classes, from 2 to 47 µm in diameter. The probe limitations have been extensively studied and probabilistic procedures have been developed for correcting both the total droplet concentration and the droplet spectral shape. These procedures are evaluated in this paper by using a stochastic model of probe functioning that demonstrates the efficiency of total droplet concentration corrections, while large discrepancies in the spectral shape remain unsolved. New methods are described to address this issue.

2. DESCRIPTION OF PROBE FUNCTIONING

In the FSSP-100, droplets are crossing a laser beam in the sampling tube. At the exit of the tube, the beam is masked by a dump spot and the light scattered by the droplets between 3 to 13° solid angles is collected by the optics. An optical setup refered to as the depth of field (DOF) is used to select droplets crossing the central section of the beam in the middle of the sampling tube. Among the DOF selected droplets, those crossing the beam edge are rejected by comparing their pulse duration to the mean pulse duration. This second selection procedure is refered to as the velocity acceptance (VAC). The droplet size distribution is derived as:.

$$c_i = n_i / (S_{DOF}\ VAC\ v_a)\ ,$$

where c_i is the concentration in the i class, n_i is the counting rate in this class, S_{DOF} is the probe DOF sampling section, VAC is the ratio of VAC selected to DOF selected droplets, and v_a is the air speed.

3. ERRORS AND CORRECTION PROCEDURES

Errors affect the counting rate, the droplet sizing and the sampling section. The counting rate is smaller than the actual rate of droplets crossing the beam because of coincidence and dead-time events. When two droplets are simultaneously present in the beam, only one pulse is detected (coincidence). If a second droplet crosses the beam during the electronic dead-time of the probe, the pulse is not detected. Coincidence and dead-time losses are significant at a droplet concentration larger than 200 cm^{-3}. Losses can be corrected using probablistic formulae, based on the counting rate, the probe activity (sum of pulse durations and dead times) or the measured frequency distribution of interarrival times between detections (Brenguier et al., 1994).

Errors in droplet sizing and the probe sampling section are more difficult to correct. First, the intensity of light scattered forward is not a monotonic function of the droplet size. Droplets of different sizes may scatter the same intensity, hence may be counted in the same size class. This is refered to as Mie ambiguities. Second, the laser beam intensity is not uniform. The intensity of scattered light thus depends on the location of the droplet in the beam, hence producing spectral broadening. This is refered to as beam heterogeneities. Third, the pulse duration depends on the pulse amplitude. If the spectrum is monodispersed, only droplets crossing the 62 % central section of the beam are selected. Droplets crossing the beam edge (the remaining 38 %) produce a pulse shorter than the mean and they are rejected by the VAC. However, if the spectrum is broad, the bigger droplets are producing pulses that are statistically greater than the small ones, hence they have a higher probability to be selected. Fourth, coincidences of droplets that can be either in the VAC, in the DOF or outside, statistically affect both DOF and VAC acceptance ratios.

Cooper (1988) developed a general probabilistic framework for solving these uncertainties. Let n_a be the droplet spectrum as it should be measured by an ideal probe, and n_m the actually measured one. The transfer matrix of the instrument $[P(i,j)]$ is defined as the probability for a droplet that should be counted in class i to be measured in the class j, that is

$$n_m = [P(i,j)]\ n_a\ .$$

Inversion of the transfer matrix then allows to estimate the ideal spectrum from the measured one.

There are two severe limitations to this approach. First the transfer matrix is not unique because the VAC depends on the mean pulse duration, that itself depends on the droplet spectrum. Second, the transfer matrix does not address spectral distortion due to coincidences. When accounting for coincidence effects, the above formula becomes non-linear. Even

Corresponding author's address: A. A. Coelho, Centre National de Recherches Météorologiques, CNRM/GMEI, 42 av. Coriolis, 31057 Toulouse Cedex 01, France. E-Mail: coelho@cnrm.meteo.fr.

for coincidences of only two droplets (second order), the coincidence matrix can hardly be inversed.

4. THE STOCHASTIC PROBE SIMULATOR

4.1 Description of the simulator

To go beyond the limitations of the probabilitic approach, a simulator of probe functioning has been developed. It is based on the same probe model as for the probabilistic approach, comprising a detailed mapping of the beam intensity, and a comprehensive description of the probe optics and electronics. Droplets are then randomly distributed along a virtual tube of air to be sampled by the probe, and their sizes are randomly choosen according to a prescribed spectrum. The measurements are then simulated by progressively moving the droplets through the probe sampling tube, by calculating for each time step the scattered power on the detection diodes, and the response of the electronics, thus composing detection pulses, and finally by simulating the probe logics for selection of the pulses and the sizing of the selected ones.

4.2 Spectral distortion at low concentration

Figure 1 shows the probe sensitive (DET), DOF and VAC sampling sections. Below 2 µm, droplets are detected in a very narrow section of the beam. Above 2 µm, the sensitive section progressively increases from 2 mm^2 to about 3.5 mm^2 for the biggest droplets. In contrast, both the DOF and VAC sections remain constant. As a result the DOF acceptance ratio decreases from 30 % for the smallest to about 10 % for the biggest droplets, a feature of the real probe that has been documented by Burnet and Brenguier (2002) with actual data collected in flight.

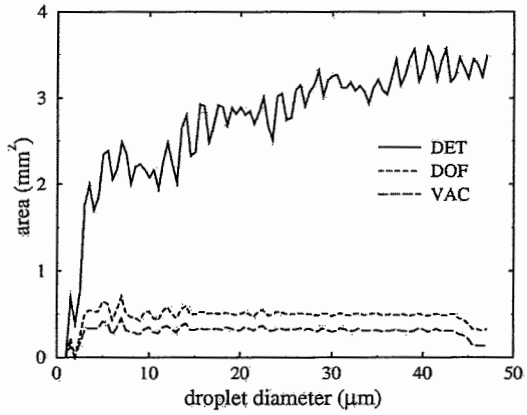

Figure 1: DET, DOF and VAC sampling sections

Another important feature of the probe is the variation of the mean pulse duration, *<TTG>*, with the droplet diameter. It is illustrated in Figure 2. Simulations are performed with monodispersed spectra, with a diameter varying from 1 to 47 µm. According to the probe electronics, the mean pulse duration is calculated only for droplets accepted in DOF. The predicted variation is derived by assuming the pulses have a gaussian shape, whose amplitude is a function of the droplet diameter, and the pulse duration is measured with respect to a fixed detection threshold.

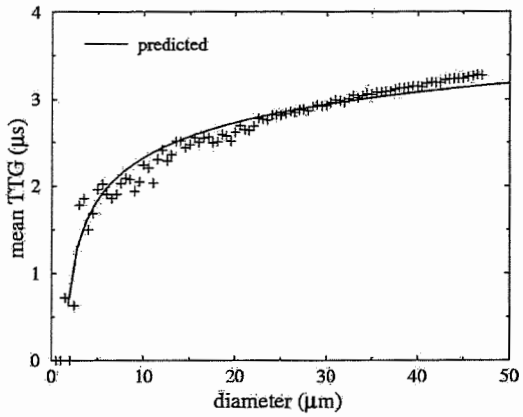

Figure 2: <TTG> as a function of the droplet diameter

This *<TTG>* variation is a significant source of distortion when the spectrum is broad. Figure 3 shows the difference between spectra of 10 µm and 30 µm droplets, depending if they are sampled separately or homogeneously mixed in the same sample. When sampled separately, 10 µm droplets are counted in the size classes 3 and 4, while 30 µm droplets are counted in class 9 to 11, as indicated by the solid line. When they are sampled simultaneously, the *<TTG>* is an average of the 10 µm and 30 µm *<TTG>* values. It is too large for 10 µm droplets that are underestimated, and too small for 30 µm droplets that are accepted even when they cross the beam edge and therefore are undersized. The resulting spectrum distortion is represented by the dashed line.

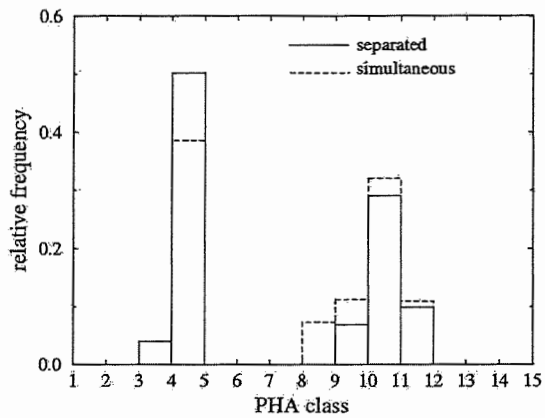

Figure 3: Effects of <TTG> on a measured spectrum.

4.3 Correction of the spectral distortion at low concentration

The impact of the mean pulse duration on droplet sizing can be accounted for by using different transfer matrices for each value of *<TTG>*. Two examples are shown in Figure 4, for *<TTG>=1 µs* (Fig. 4a) and *<TTG>=3 µs* (Fig. 4b). The probability for a droplet

with a diameter as indicated on the Y axis, to be counted in the size class indicated in the X axis is represented by a grey scale. In figure 4a, all droplets are counted, but the big ones are accepted even when they cross the beam edge and therefore they are undersized (the grey area in the upper left). In contrast, with a longer *<TTG> of 3 µs*, droplets smaller than 14 µm are all rejected, and bigger droplets are better sized.

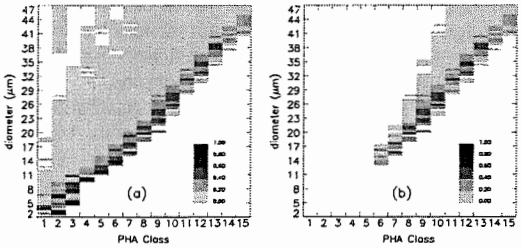

Figure 4: Transfer matrices for different <TTG> values.

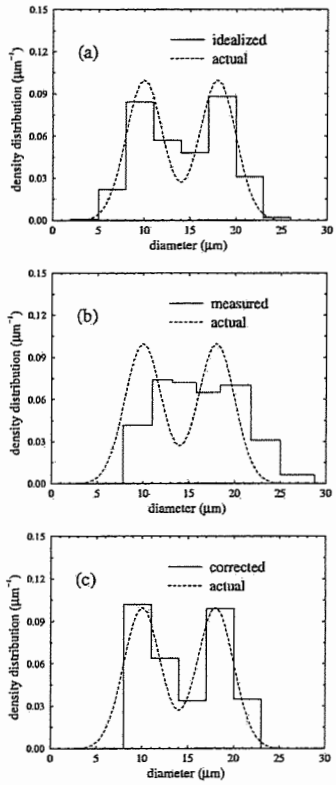

Figure 5: Measurements of a bimodal spectrum with the FSSP-100: (a) Ideal instrument, (b) measured spectrum, (c) corrected spectrum.

For correcting the spectral distortion, it is therefore necessary to first calculate a guess of the *<TTG>*, that is then used to select the most appropriate transfer matrix to be applied to the measured spectrum for inversion.

The efficiency of the correction procedure is illustrated in Figure 5. Fig. 5a shows the original spectrum and how it would be measured with an ideal probe. Fig. 5b shows the spectrum actually measured with the FSSP-100, and Fig. 5c represents the spectrum derived from the measured one after correction by the transfer matrix.

4.4 Correction of coincidence effects

The stochastic simulator, unlike the probabilistic model, can simulate any value of droplet concentration. Figure 6 shows the evaluation of three correction procedures. (*m-coeff*) refers to the empirical formula proposed by Dye et al. (1984) for deriving the actual rate from the counted rate and probe activity. (*jlb89*) corresponds to the system of equations derived in Brenguier (1989), and (*slope*) corresponds to the procedure described by Baumgardner (1986) and based on the measured frequency distribution of interarrival times between detected pulses.

The figure shows that, at an actual concentration of 1500 cm^{-3}, the empirical method underestimates the actual rate by 25 %, the system of equations underestimates it by 8 %, while the interarrival time method provides the most accurate estimation of the actual droplet rate.

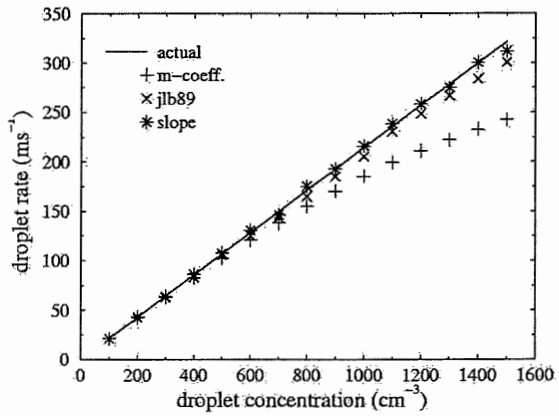

Figure 6: Evaluation of coincidence and dead-time losses correction procedures for the droplet rate.

Coincidences however also impact the spectral shape. When coincident droplets enter the beam simultaneously, their pulse amplitudes are cumulated and the resulting detection is oversized. In contrast, when droplets enter the beam successively, their pulse durations are added and the resulting *<TTG>* is increased. The impact on droplet sizing is similar as for the bimodal spectrum illustrated in Figure 3.

Figure 7 shows how a bimodal spectrum is measured by the FSSP-100 when the concentration is equal to 50, 300 and 1500 cm^{-3}, respectively. As the concentration increases, the proportion of small droplets is underestimated, while artefacts of big droplets are produced.

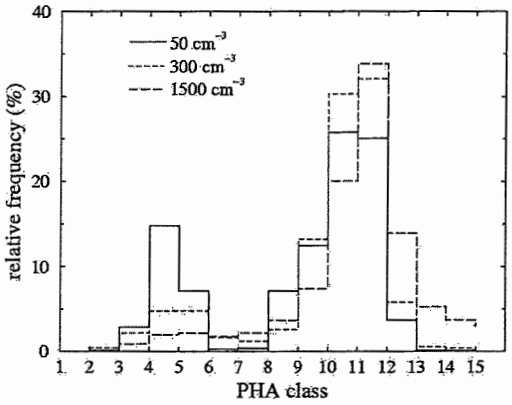

Figure 7: comparison between a bimodal spectrum measured with an ideal probe and the spectrum actually measured with the FSSP-100, for a total concentration of 50, 300 and 1500 cm^{-3}, respectively.

Consequently, when cloud samples are processed, if only the droplet rate is corrected for coincidence and dead-time losses, the derived liquid water content (LWC) may be significantly overestimated because of spectral distortion. This is illustrated in Figure 8 showing LWC as a function of droplet concentration, its actual value, the measured one, and the value derived after correction of concidence and dead-time losses, while keeping the measured spectrum unchanged. The mean volume diameter (MVD) of the measured spectrum is also reported, with a scale on the right hand side.

The measured LWC is slightly underestimated, which implies that coincidence and dead-time losses compensate the MVD overestimation. However, if the concentration is corrected, the LWC is overestimated by a factor of two at a concentration of 1500 cm^{-3}.

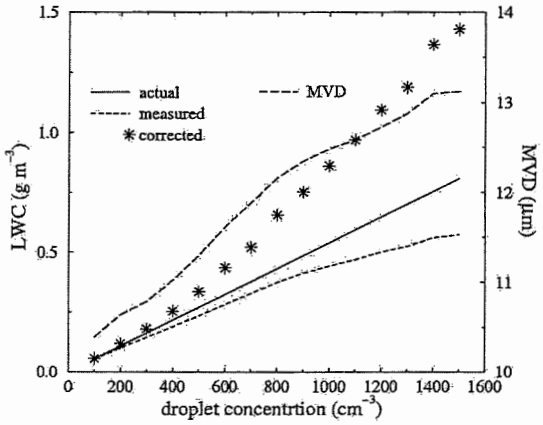

Figure 8: Effect of coincidences on LWC measurements: Actual LWC (thick solid line), measured LWC (dashed line), LWC estimate after correction of coincidence losses (stars) and MVD (long dashed line).

5. CONCLUSIONS

The stochastic simulator of probe functioning is a robust technique, that precisely simulates the main features of the actual probe at both low and high concentrations.

It reveals that the distortion of the spectral shape at low droplet concentration, can be significant when spectra are broad or bimodal. The transfer matrix procedure can easily account for this effect, by storing a set of matrices corresponding to diffrent values of the mean pulse duration. The guess of the mean pulse duration derived from the measured spectrum is in fact sufficient for selection of the most appropriate matrix and the retrieval of the droplet spectrum.

At high droplet concentration, corrections of the coincidence and dead-time losses with either the complete system of equations derived in Brenguier (1989) or the slope of the measured frequency distribution of interarrival times described in Baumgardner (1986) provide accurate estimate of the actual rate. However, the inversion of the transfer matrix is no longer feasible for correction of the spectral distortion. Since the simulator is not deterministic, it cannot be inversed for deriving an estimate of the actual spectrum from the measured one. Empirical solutions only can be used, especially for avoiding strong overestimation of the LWC, when only the concentration is corrected.

Acknowledgements

A. A. Coelho acknowledges the support of Meteo-France visiting scientist programme. This work is supported by Meteo-France and CNRS/INSU.

References

Baumgardner, D., 1986: A new technique for the study of cloud microstructure. *J. Atmos. Oceanic Technol.*, **3**, 340-343.

Brenguier, J.-L., 1989: Coincidence and dead-time corrections for particle counters. Part II: High concentration measurements with an FSSP. *J. Atmos. Oceanic Technol.*, **6**, 585-598.

Brenguier, J.-L., Baumgardner, and B. Baker, 1994: A review and discussionof processing algorithms for FSSP concentration measurements. *J. Atmos. Oceanic. Technol.*, **11**, 1409-1414.

Burnet, F. and J. L. Brenguier, 2002: Comparison between Standard and Modified Forward Scattering Spectrometer Probes during the Small Cumulus Microphysics Study. *J. Atmos. Oceanic Technol.*, **19**, 1516-1531.

Cooper, W. A., 1988: Effects of coincidence on measurements with a Forward Scattering Spectrometer Probe. *J. Atmos. Oceanic Technol.*, **5**, 823-832.

Dye, J. E. and Baumgardner, D., 1984: Evaluation of the Forward Scattering Spectrometer Probe. Part I: Electronic and optical studies. *J. Atmos. Oceanic. Technol.*, **1**, 329-344.

EVALUATING CLOUD LIQUID WATER IN NWP AND CLIMATE MODELS USING MEASUREMENTS FROM THE BALTEX CLOUD LIQUID WATER NETWORK: CLIWA-NET

Susanne Crewell[1], Ulrich Löhnert[2] and Erik van Meijgaard[3]

[1]Meteorological Institute, University of Munich, Theresienstr. 37, 80333 München, Germany
[1]Meteorological Institute, University of Bonn, Auf dem Hügel 20, 53121 Bonn, Germany
[2]Royal Netherlands Meteorological Institute, PO Box 201, 3730 AE De Bilt, The Netherlands

1. INTRODUCTION

The main objectives of the BALTEX Cloud Liquid Water Network project (CLIWA-NET; 2000-2003) were i) to implement a prototype of a European cloud observational network (ECON), ii) to contribute to the program of the continental–scale experiment BALTEX, and iii) to objectively evaluate cloud related output of atmospheric models for weather and climate prediction.

ECON comprised ground-based and satellite-borne observations, thus combining high temporal resolution measurements at single stations with high-spatial resolution satellite observations. Within the ground-based network microwave radiometers were chosen as key instruments since this technique is by far the most direct and accurate method to determine the liquid water path (LWP). The network was established during three campaigns by co-ordinating the use of existing passive microwave radiometers, infrared radiometers, lidar ceilometers and, at a limited number of sites, cloud radar. The first two campaigns (CNNI: Aug/Sep 2000, and CNNII: Apr/May 2001) were conducted on the continental scale covering the Baltic catchment, while BBC (Aug/Sep 2001) focused on the regional scale.

For a future long-term implementation of ECON a low-cost microwave radiometer has been designed. Owing to external funding the first systems were already built (Fig. 1). Four European NWP/climate models were involved in an objective evaluation of cloud related output produced by short-term forecasts. In this contribution we focus on the evaluation of liquid water path and the vertical distribution of cloud liquid water based on observations from ground-based measurements.

2. LIQUID WATER PATH

Time series of observed LWP have been inferred from continuous microwave radiometer (MRAD) measurements on the basis of harmonized retrieval algorithms for the different radiometers involved

Corresponding author's address: Susanne Crewell, Meteorological Institute, Munich, Germany; E-Mail: crewell@meteo.physik.uni-muenchen.de.

Precise knowledge of rain events turned out to be critical for the validation of observations. Due to rainfall, MRAD-measurements are meaningless as long as the water on the instrument has not completely evaporated. Rain detection, preferably with in-situ instruments, was used to filter out all MRAD measurements synchronous with rain events. Based on this experiences the low-cost radiometer includes a rain sensor which controls a shutter system protecting the antenna in case of precipitation (Fig. 1).

Information on cloud base parameters inferred from synchronous and collocating measurements with lidar ceilometer and IR radiometer was found very useful in classifying the cloud component of the atmospheric conditions. It has been used to identify the presence and altitude of clouds, allowing the distinction of ice and water clouds.

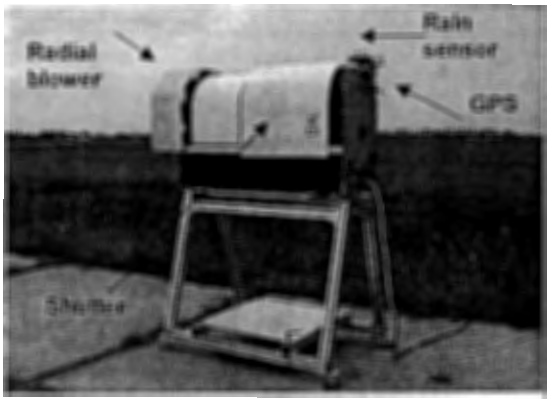

Figure 1. Photo of the low cost radiometer

Isolated periods with conditions free of water clouds have been used to assess MRAD inferred LWP biases. For the purpose of model evaluation a procedure has been developed to quantify the bias correction. Provided such conditions occurred with sufficient regularity this correction method is considered to significantly reduce the systematic bias in observed LWP that originates from instrumental drifts and uncertainties in the retrieval assumptions (mainlywater vapor absorption).

Four European institutes participated in the evaluation of model predicted cloud parameters. ECMWF with the global forecast model operated at an effective horizontal resolution of 45 km and with 60 layers in the

vertical, DWD with the Lokal Modell (LM) operated in non-hydrostatic mode at a resolution of 7 km and with 35 layers in the vertical, the Rossby Center with a climate version of HIRLAM, here referred to as RCA, and KNMI with RACMO carrying the physics of the ECHAM4 model. The latter two models have been operated with a horizontal grid spacing of 18 km and with 24 model layers, and are forced from the lateral boundaries by ECMWF analyses. The output from all models refers to a 12 to 36 hour window taken from each daily forecast initiated at 12 UTC.

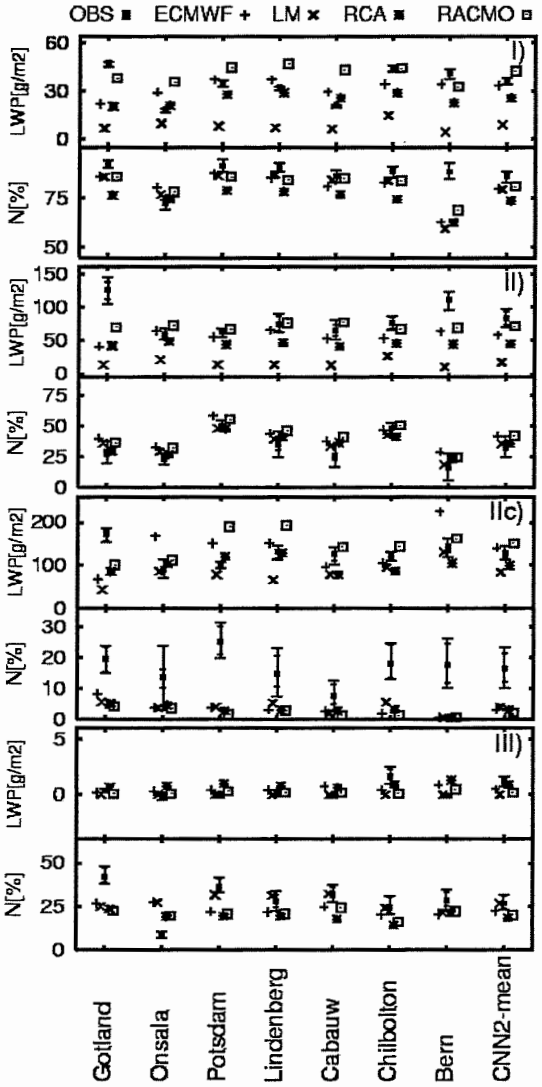

Figure 2. Model predicted and observed LWP and relative occurrence (N) for the CNN2 campaign. The classes I), II), IIc) and III) are described in the text. The central values in the observations refer to an aggregation time of 30 minutes. The uncertainty bars combine the sensitivity to variations in the employed cloud base thresholds and variations in aggregation times in the range from 10 to 60 minutes.

Results of a comparison of statistical properties derived from the observations and model predictions are shown in Figure 2. (*van Meijgaard and Crewell*, 2004). With the help of cloud base observations and rain detection various atmospheric conditions have been sampled. The model output has been processed in an equivalent way. In Figure2, the conditions are defined as follows from top to bottom: I) non-precipitating periods, II) non-precipitating water clouds with cloud base below 3000 m and warmer than 0°C (e.g. pure water clouds), IIc) overcast conditions, being a subset of II) that is found fully cloudy during a time interval, and III) periods free of water clouds with cloud base above 5000 m and colder than -30°C. Class II) and III) are exclusive and fall in class I). For each class the frequency rate of occurrence (N) and the mean LWP amount are shown.

In general, the model predictions are found very consistent in mutual respect, although exceptions can be noticed. Compared to the observations, all models tend to overpredict precipitation, in particular the RCA-model. The models tend to slightly overpredict the amount of non-precipitating water clouds. On average, three models predict LWP in the right order of magnitude, whereas the LM significantly underpredicts LWP. Concerning overcast conditions, model predicted LWP values are found in the same range as observed, but the spread among the stations is large. The occurrence of these conditions is greatly underestimated. During CNN2, models fairly well predicted the amount of (water) cloud free situations with the exception of Gotland and Onsala. It is nicely confirmed that observed mean LWP in this condition is indeed very close to zero.

3. CLOUD LIQUID WATER VERTICAL DISTRIBUTION

During the BBC-campaign centered at Cabauw in the Netherlands, the multitude of instruments including cloud radar revealed the complex vertical structure of clouds (Fig. 3).

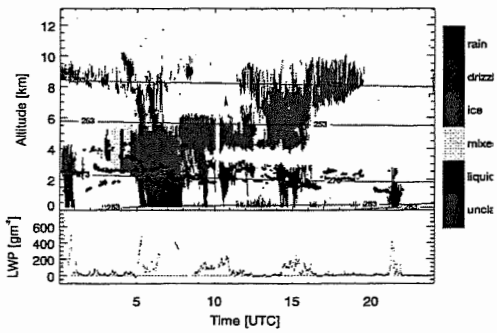

Figure 3. Cloud classification based on the synergy of different sensors and corresponding LWP time series.

In case only one liquid water cloud is present a new synergetic retrieval algorithm could be applied, which simultaneously derives cloud liquid water content (LWC), temperature and humidity profiles during non-precipitating conditions. This integrated profiling technique (IPT) combines brightness temperatures measured at 19 frequencies, cloud radar reflectivity profiles, cloud base height, and operational radiosonde data within an optimal estimation framework (*Löhnert et al.,* 2001 and 2004).

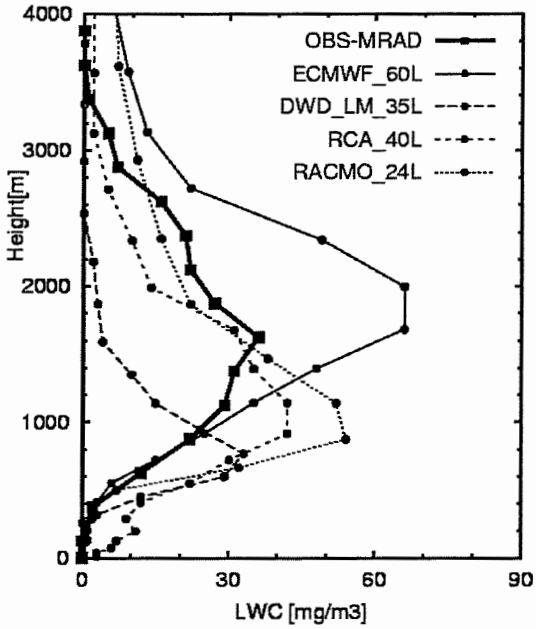

Figure 4. Mean retrieved and model predicted liquid water profiles at Cabauw during about 7% of the BBC campaign time. Model profiles are synchronous with the IPT retrieved profiles.

The model predicted vertical structure of cloud liquid water has been evaluated on the basis of the IPT retrievals at Cabauw. Results are shown in Figure 4. The model predictions are confined to time slots for which profile information was successfully retrieved from the measurements. Model predicted profiles are furthermore restricted to cases without (model) precipitation reaching the surface. Significant differences are found between the various model predictions both in total LWC-amounts as in the altitude where the LWC is largest on average. RCA and RACMO predict this height to occur at 1000 m, which is significantly below the observed height of about 1600 m. The LWC amounts found by these models are in the same order of magnitude as observed. The ECMWF model, on the other hand, puts the level with largest LWC at almost 2000 m, which is beyond the observed height. LWC-amounts in the ECMWF-model are considerably larger than observed. Contrary to this result, the LM predicts the level of the maximum below 1000 m and its profile exhibits much smaller amounts of LWC than is observed.

4. CONCLUSIONS

The recent CLIWA-NET observational campaigns have provided a wealth of cloud parameters, including liquid water path and vertical profiles of cloud liquid water. In analyzing the observations precise knowledge of rainfall occurrence turned out to be critical. In general, all models overpredict the occurrence of precipitation. On average, models predict LWP values in the right order of magnitude as observed, but the spread among the models is considerable. The ability of models to represent certain cloud scenes varies from reasonable to poor. In particular, the occurrence of overcast conditions is greatly underestimated by all models. With respect to the vertical distribution of liquid water the models show huge differences among themselves and no model is capable of matching the retrieved LWC profiles. Numerous possible reasons can be thought of to explain the found shortcomings of these state-of-the-art atmospheric models in representing cloud liquid water parameters. The challenge in future will be to go beyond an evaluation of the model performance and to exploit the observational datasets for testing and improving the actual cloud parametric assumptions.

Acknowledgements

Part of this work was done within the CLIWA-NET project sponsored by the EU under contract number EVK2CT-1999-00007.

References

Crewell, S,. M. Drusch, E. Van Meijgaard und A. Van Lammeren, 2002: Cloud Observations and Modelling within the European BALTEX Cloud Liquid Water Network, Bor. Env. Res., 7, 235-245.

Löhnert, U., S. Crewell, A. Macke and C.Simmer, Profiling cloud liquid water by combining active and passive microwave measurements with cloud model statistics, J. Atmos. Oceanic Technol., 18, 1354-1366, 2001.

Löhnert, U., S. Crewell, C. Simmer, 2004: An integrated approach towards retrieving physically consistent profiles of temperature, humidity, and cloud liquid water, J. Appl. Met., accepted.

Meijgaard, E. van, and S. Crewell, 2004: Comparison of model predicted liquid water path with ground-based measurements during CLIWA-NET, submitted to *Atmos Res.*

POLARIZATION-LIDAR PROBING OF CLEAR AND CLOUDY ATMOSPHERE OVER GADANKI, A REMOTE CONTINENTAL STATION IN INDIA

P.C.S. Devara[1], Y. Jaya Rao[1], Atul Kumar Srivastava[1], Y. Bhavani Kumar[2] and D. Narayana Rao[2]

[1] Indian Institute of Tropical Meteorology, Dr. Homi Bhabha Road, Pune 411 008, India
[2] National MST Radar Facility, P O Box:123, Tirupati 517 502, India

1. INTRODUCTION

In recent years, the ability of lidars to quantify the properties of sub-visual targets such as elevated aerosol and thin cirrus cloud layers has focused attention on the possible radiative effects of these weakly scattering atmospheric layers (Sassen et al., 1989). The polarization-lidar is recognized to be a versatile remote sensing technique for the study of composition and structure of different cloud types for understanding the cloud-climate feedback processes (Sassen, 1991). Besides providing anisotropy property of scattering particles in both the clear- and cloudy-atmosphere, this technique has potential to discriminate ice from water in atmospheric clouds. Because the cross-polarized component can arise only from the multiple scattering, it can provide direct measure of multiple scattering in clouds, as opposed to the clear-air scattering. The horizontal inhomogeneity in cirrus clouds, often appears as thin continuous haze layer (Del Gousta et al., 1994). Very limited research programs employing polarization-lidar technique have been conducted in the past for climate-related cloud studies. In this communication we report some interesting results of clear- and cloud-air scattering, polarization properties of clouds associated with different composition that have been studied using an Nd:YAG polarization-lidar at Gadanki (13.5°N, 79.2°E, 390 m AMSL), India.

2. LIDAR SYSTEM AND OBSERVATIONS

The basic lidar system used in the present study has been described previously (Bhavani Kumar et al., 2000; Parameswaran et al., 2000). It is essentially a pulsed, mono-static, Nd:YAG dual-polarization lidar, established in collaboration with Communication Research Laboratory (CRL), Japan, at the National MST Radar Facility (NMRF), Gadanki, India. It has been in operation since 1998, twice a week for about 3 hours during early night period on each day. The observations carried out during the year 2000 have been utilized in the present study to characterize the lidar backscatter signatures recorded during cloudy- and clear-sky conditions. From the data recorded in P (co-polarized) and S (cross-polarized) channels of the lidar, the altitude profiles of backscatter (R_S) and linear depolarization (δ) ratios have been computed for each experimental day. The monthly mean profiles and height-time cross-sections, deduced from special data sets containing series of profiles within a night also have been studied.

Corresponding author's address: Dr. P.C.S. Devara, P. M. & A. Division, Dr. Homi Bhabha Road, N.C.L. Post Office, Pune – 411 008, India; E-Mail: devara@tropmet.res.in

3. ESTIMATION OF LIDAR BACKSCATTER AND POLARIZATION PARAMETERS

The two basic parameters that were considered in this paper to synthesize the lidar returns from clear- and cloud-air are (i) the backscatter ratio (R_S) and (ii) linear depolarization ratio (δ). The backscattering ratio, which is the ratio of molecular plus aerosol / backscatter coefficients to the molecular component alone and which is indicative in an integral sense of particle size and number. The linear depolarization ratio, which is the calibrated ratio of signals in the perpendicular polarization plane to that in the parallel plane and which provides a semi-quantitative indicator of particle morphology. From the lidar signals recorded in P and S channels, these ratios at different altitudes (z) were computed by assuming a reasonable value for molecular depolarization correction for dry air and also by neglecting the aerosol contributions in the upper troposphere and stratosphere during non-volcanic conditions. The backscatter ratio (R_S) is computed as

$$R_S(z) = \beta_t(z) / \beta_m(z)$$

where $\beta_t(z)$ is total column backscatter coefficient containing contributions from both aerosols and

air molecules. The backscatter coefficient is generally deduced from the measurements of backscatter light intensity (lidar), temperature and pressure (radiosonde). The linear depolarization ratio (δ) is evaluated as

$$\delta(z) = \beta_t(z)\perp / [\beta_t(z)\| - \beta_m(z)\|]$$

where the subscripts (⊥) and (‖) denote the scatter coefficients estimated at perpendicular polarized plane to the polarization plane of emitted laser pulse and at parallel plane, respectively. In order to determine the cloud optical depth, the backscatter coefficients are vertically integrated over different cloud height range cells.

4. RESULTS AND DISCUSSION

4.1 Clear Air and Dust Haze

Figure 1 shows a sample of the vertical profiles of R_S, δ and R_S for P and S channels separately obtained on 12 January 2000. It is evident that R_S value is well below 1.5, which

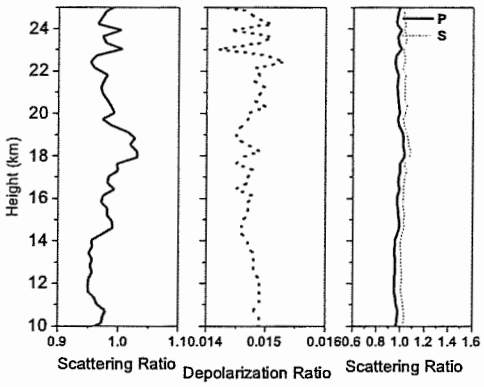

Figure 1: Typical profiles of scattering and depolarization ratios obtained during clear-sky conditions on 12 January 2000.

is considered to be the upper limit for clear-air scattering (Sassen et al., 1989; Sassen, 1991). A series of profiles obtained at different timings of the day on 13 December 2000 is shown plotted in Figure 2. It is clear that R_S values are smaller. The peak value of R_S observed around 18 km in each profile denotes the tropical tropopause height. The smaller values of δ indicate the isotropic nature of the targets in the experimental region. The monthly mean profiles of R_S and δ for the year 2000 are shown in Figure 3. Besides signatures from the tropopause, anisotropic nature of particles can be seen in the upper troposphere almost in all the months considered in the study except January. It is possible that a weak inversion

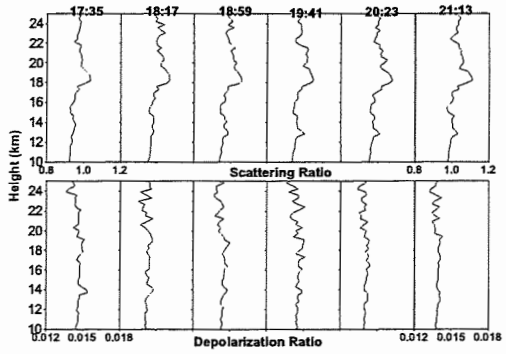

Figure 2: Time-height evolution of scattering and polarization ratios of lidar clear-air profiles observed on 13 December 2000.

exists around this altitude, and as a result the dust-like aerosol, transported from neighboring regions is trapped below this inversion.

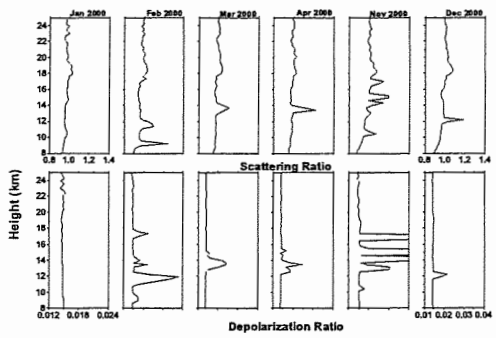

Figure 3: Monthly mean profiles of lidar scattering and depolarization ratios observed during 2000.

4.2 Cloud Air

The lidar data recorded during the cloudy-sky conditions have been classified into three categories: (i) water cloud, (ii) ice cloud and (iii) mixed-phase cloud, and the features observed for these three different types of clouds are discussed here. Figure 4 depicts the vertical profiles of R_S, δ and R_S for P and S channels separately. On cloudy days, it is observed that, most of the time, R_S for S channel dominates (almost four times in the present case) the P channel and increases initially with altitude in the cloud region. These features are seen in this figure except that $\delta \leq 0.1$, which is normally be considered as cloud with water content (Sassen, 1991).

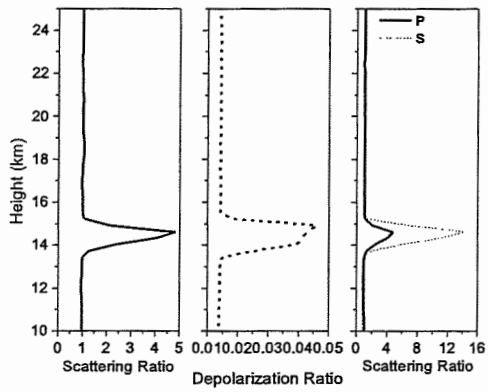

Figure 4: Same as Figure 1 but during cloudy-sky conditions on 29 March 2000. Cloud (around 14-15 km altitude) with water content may be noted.

The lidar-return profiles from an ice cloud are shown plotted in Figure 5. Besides the dominance of scattering ratio in S channel as compared to P channel, as opposed to the case of water cloud, values are much larger and above 0.1, which is normally considered as cloud with ice crystals. The vertical thickness and hence the scattering ratio of this cloud is found to be higher than that of water cloud shown in Figure 4.

The lidar signatures captured from a mixed–phase cloud are shown in Figure 6. Unlike the case of water and ice clouds, two distinct features are observed. They are (i) scattering ratio for P channel dominates that of the S

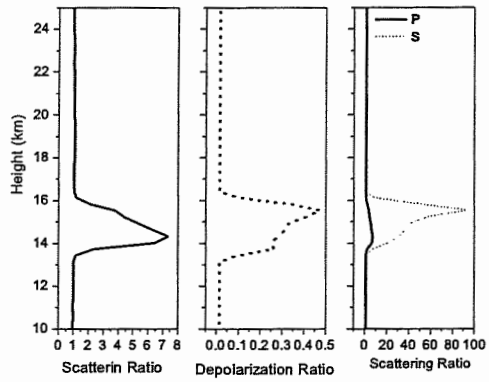

Figure 5: Same as Figure 4 but obtained on 23 December 2000. Cloud (13.5-15.5 km) embedded with ice crystals may be noted.

channel and (ii) depolarization ratio initially decreases, reaches near-zero and thereafter increases with increase in altitude within the cloud region. The time-height evolution of

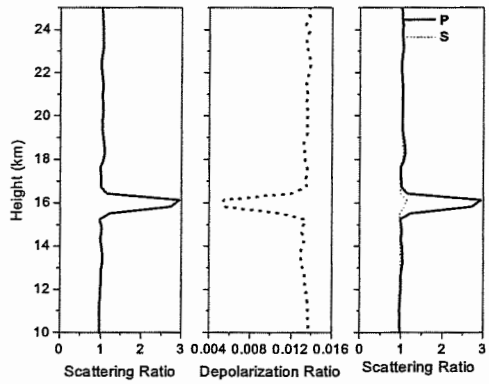

Figure 6: Same as Figure 1 but during cloudy conditions on 19 January 2004.

cloud layer around 10-12 km altitude region on 20 December 2004 is shown in Figure 7. The splitting and merging of clouds during the course of observations can be seen from the figure. From the depolarization ratio value, it can be inferred that these clouds are basically of cirrus clouds containing ice crystals. The variation in the structure and concentration of ice crystals within the cloud can also be noticed from the time sequence profiles.

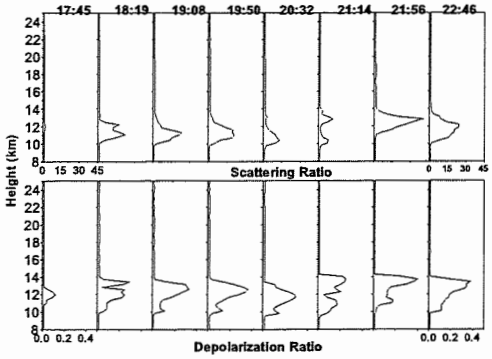

Figure 7: Same as figure 2 but for cloudy conditions.

The monthly mean lidar profiles of R_S and δ for the year 2000 are depicted in Figure 8. The time evolution of cirrus cloud formation and

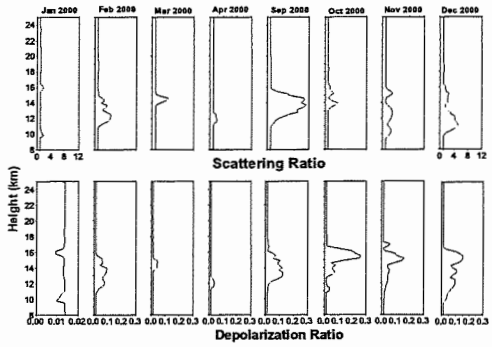

Figure 8: Same as Figure 3 but for cloudy-atmospheric conditions.

development in the 10-16 km height region can be seen from the figure clearly. Conversion of water clouds into ice clouds and vice-versa is an interesting feature observed in these time-sequence profiles. The integrated backscatter coefficients (IBC) for sub-cloud and cloud regions for the data recorded on each experimental day has been evaluated to examine their association. In general, the coefficients estimated for the cloud region are found to be much larger (one to two orders of magnitude or even more depending on the vertical thickness of cloud) than those in the sub-cloud layer. This is considered to be due to multiple scattering effect (Pal and Carswell, 1985). However, the association between the IBCs of the sub-cloud and the cloud air layers is also found to be different for different types of clouds.

5. ACKNOWLEDGEMENTS

We would like to thank the Director, IITM, Pune for encouragement and support. The lidar facility at NMRF, Gadanki was established in collaboration with the CRL, Japan and is operated under Department of Space (DOS). We acknowledge the support of the ISRO-RESPOND project by the DOS under Grant No. 10/2/271. One of the authors (AKS) is grateful to ISRO-RESPOND for financial support.

REFERENCES

Bhavani Kumar, Y., Raghunath, K., Siva Kumar, V., Rao, P.B., Jain, A.R., Mizutani, K., Aoki, T., Yasui, M. and Itabi, T., 1999, NMRF-CRL Lidar system and data processing, Proc. IRSI'99, Bangalore, India, 560-570.

Del Gousta, M., Morandi, M., Stefanutti, L., Stein, B., Kolenda, J., Rairoux, P., Wolf, J.P., Matthey, R. and Kyro, E., 1994: Multiwavelength lidar observation of thin cirrus at the base of the Pinatubo stratospheric layer during the EASOE campaign. Geophys. Res. Letts., 21, 1339-1342.

Pal, S.R. and Carswell, A.I., 1985: Polarization anisotropy in lidar multiple scattering from atmospheric clouds. Appl. Opt., 24, 3464-3471.

Parameswaran, K., Sasi, M.N., Geetha, R., Nair, P.R., Deepa, V., Krishna Murthy, B.V., Raghunath, K., Rajendraprasad, T., Krishaniah, M., 2000: Altitude profile of temperature from 4 to 80 km over the tropics from MST and lidar. J. Atmos. Sol. Terr. Phys., 62, 1327-1337.

Sassen, K., Griffin, M.K. and Dodd, G.C., 1989: Optical scattering and microphysical properties of subvisual cirrus clouds, and climatic implications. J. Appl. Meteorol., 28, 91-98.

Sassen, K., 1991: The polarization lidar technique for cloud research: A review and current assessment. Bull. Amer. Meteor. Soc., 72, 1848-1866.

IN SITU CLOUD SENSING WITH MULTIPLE SCATTERING LIDAR

K. Franklin Evans[1]*, R. Paul Lawson[2], Pat Zmarzly[2], Darren O'Connor[2], and Warren J. Wiscombe[3]

[1]University of Colorado, Boulder, Colorado, USA
[2]SPEC, Inc., Boulder, Colorado, USA
[3]NASA Goddard Space Flight Center, Greenbelt, Maryland, USA

1. INTRODUCTION

In situ probes are the most direct means of measuring cloud properties. For liquid clouds, optical particle counting probes, such as the Particle Measuring Systems FSSP, provide accurate physical and optical properties of the volume sampled. A major source of error, often not considered, is that the sampling volume of traditional cloud probes is tiny compared to the volumes of clouds (e.g. an FSSP measures less than a liter of air in crossing a 1 km cumulus cloud which might contain 10^{12} liters). The large variability in cloud density inside a turbulent cloud makes it extremely unlikely that a traditional probe can measure the mean properties with useful accuracy. Applications which require mean cloud properties over large volumes, such as validation of remote sensing measurements, would bene?t from an accurate in situ method capable of sampling volumes of millions of cubic meters.

This report describes a new cloud measurement technique we call in situ lidar. The in situ lidar differs from a regular lidar in that it uses wide ?eld of view detectors pointed away from the laser beam direction (see Fig. 1 for a depiction of the instrument con?guration). Inside an optically thick cloud, the laser pulse is multiply scattered by cloud droplets and a small portion of the light returns to be measured by the detectors. The signal measured by the instrument is the number of photons returned as a function of time. The amplitude and shape of the returned pulse contain information about the distance to the cloud boundaries and the volume average extinction (units of km^{-1}) in water clouds at different spatial scales around the instrument. At visible wavelengths extinction is proportional to the water droplet surface area, and thus the in situ lidar could be valuable for cloud physics and chemistry research, as well as for measuring the optical properties of clouds. The theory of the in situ cloud lidar and simulations of the retrieval accuracy for optical properties are detailed in Evans et al. (2003).

*Corresponding author's address: Frank Evans, PAOS, University of Colorado, 311 UCB, Boulder, CO 80309; email: evans@nit.colorado.edu

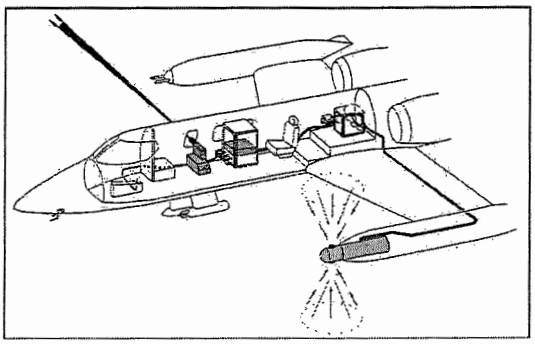

Figure 1: An artist's rendition of the in situ cloud lidar, showing the laser beam exiting the Learjet cabin window to the right, while upward and downward viewing detectors on the left wingtip record a time series of the multiply scattered light.

2. THEORY AND SIMULATIONS

2.1 Diffusion Theory

A diffusion solution to the radiative transfer equation can approximate the in situ lidar situation. Diffusion theory is appropriate after the lidar pulse photons have scattered enough times that all knowledge of their initial direction is lost. The time to reach the diffusion regime (t_d) is roughly twice the time to cover a transport mean free path (l_t):

$$t_d \approx \frac{2l_t}{c} = \frac{2}{c(1-\omega_0 g)\beta}$$

where $l_t = 1/[(1-\omega_0 g)\beta]$, c is the speed of light, β is the volume extinction coef?cient, ω_0 is the single

scattering albedo, and g is the asymmetry parameter. For visible wavelengths there is no absorption by cloud droplets, so $\omega_0 = 1$. For typical liquid cloud droplet distributions $g = 0.84 - 0.87$ is derived from Mie theory.

A directed laser beam becomes effectively isotropic after traveling one transport mean free path. When an isotropic, instantaneous pulse of light is emitted from a point source in an in?nite uniform medium, the solution to the diffusion equation for the photon energy density is a Gaussian with an rms radius of $\sqrt{2ctl_t/3}$. An extinction of 60 km^{-1} and $g = 0.86$ results in a diffusion time scale of 0.8 μs, at which time the rms radius is about 140 meters. The in situ lidar returned photon signal can be approximated by the radiance at the center of this Gaussian. The detected energy is expressed by the fraction of emitted photons per detector area per detector solid angle per time,

$$f_p = \frac{E_d}{E_p A_d \Omega_d \Delta t},$$

where E_d is the energy at a detector, E_p is the energy in the emitted pulse, A_d is the detector area, Ω_d is the detector solid angle, and Δt is the detector time bin size. The diffusion solution for the photon fraction in a uniform in?nite cloud is

$$f_p = \frac{c}{(4\pi)^{5/2}} \left(\frac{3(1-\omega_0 g)\beta}{ct} \right)^{3/2} e^{-c(1-\omega_0)\beta t}.$$

For a homogeneous in?nite cloud, diffusion theory predicts that the in situ lidar signal is a power law in time multiplied by an exponential if there is absorption ($\omega_0 < 1$). The photon fraction is proportional to the 3/2 power of the scaled extinction, $(1 - \omega_0 g)\beta$. In liquid clouds, for which the asymmetry parameter g is well known, the extinction can be readily determined from f_p.

As the Gaussian bubble of diffusing photons reaches the cloud boundaries, the loss of photons from the cloud causes the in situ lidar time series to decay more rapidly than the original power law. The diffusion equation also can be solved for a homogeneous medium with boundaries in the vertical. Let the in situ lidar be at the center of a cloud of thickness H, and de?ne $H_e = H + \frac{4}{3} l_t$ ($H_e \approx H$ for high optical depth clouds). For times $t > t_b/2$, where $t_b = 3H_e^2/(\pi^2 c\ l_t)$, the diffusion equation solution for the photon fraction is approximately

$$f_p = \frac{3}{8\pi^2 H_e l_t t} e^{-c(1-\omega_0)\beta t} e^{-t/t_b}.$$

The photon fraction for times $t < t_b/2$ is well approximated by the in?nite medium solution. For a nonabsorbing uniform medium, diffusion theory predicts that the time series behavior at times after $t_b/2$ is a power law (t^{-1}) multiplied by an exponential (e^{-t/t_b}) with the time scale depending on the square of the cloud thickness. For a 1000 m thick cloud with extinction of 60 km^{-1}, $t_b = 11.4\ \mu$s, and the non-power-law behavior become apparent after about 6 μs. Thus the time of transition from a power law to exponential behavior contains information about the distance to the cloud boundaries.

2.2 Retrieval Simulations

Retrieval simulations were performed to determine how accurately the in situ lidar can measure extinction, optical depth, and cloud thickness in realistic warm stratocumulus clouds. Three-dimensional inhomogeneous fractal clouds were simulated with a Fourier noise ?ltering algorithm that generates partially correlated liquid water content and droplet number concentration ?elds. The 100 cloud ?elds generated, with 25 m pixels and 3200 m domain size, had a wide range of thickness, mean liquid water path, variability, smoothness, and mean droplet concentration. A Monte Carlo model simulated the 532 nm wavelength in situ lidar time series signal for upward and downward pointing detectors at four positions along a randomly chosen ?ight altitude in each cloud. The lidar time series, $p(t)$, are reasonably well ?t by the function $\ln[p(t)] = a - b\ln(t) - ct$ (inspired by the diffusion theory solution). A retrieval algorithm is developed by training a neural network to predict the volume average extinction (gaussian weighted average at four scales) from the a, b, and c parameters for each detector. Half of the 400 cases are used to train the neural net, and half are used to test the retrieval accuracy. The rms fractional error in extinction ranged from 6% to 8% depending on the volume scale. The in situ lidar was able to retrieve the cloud thickness with about 60 m rms accuracy (thicknesses ranged from 200 to 1000 m). Using only those airplane altitudes near the center of the cloud gave an the optical depth retrieval accuracy of under 10%. The in situ lidar technique is only weakly dependent on the calibration accuracy with a 50% calibration error giving an extinction error of 25% and causing very little increase in cloud thickness error. These retrieval accuracies are applicable to overcast warm (liquid) stratocumulus clouds with well de?ned top and base altitudes. The extinction retrieval accuracy should

be comparable for any liquid cloud, as the extinction in this simulation ranged from 5 to 250 km^{-1} and the cloud mean droplet concentration ranged from 50 to 300 cm^{-3}.

Simulations were also performed for a potential dual wavelength in situ lidar with wavelengths at 532 nm and 1550 nm. The absorption at 1550 nm is proportional to the cloud droplet radius, which allows the accurate retrieval of liquid water content (LWC) and effective radius. The simulated rms accuracy of LWC ranges from 10% to 12% depending on scale, while the effective radius accuracy is about 0.5 μm.

3. PROTOTYPE IN SITU LIDAR TESTING

An airborne prototype in situ lidar is being built at SPEC, Inc. under a NASA contract. The 532 nm wavelength YAG laser ?res 180 mJ pulses at 10 Hz horizontally out of a cabin window in the Learjet. The laser beam passes through 0.5° diverging optics to achieve the level of no visual interference to pilots at a distance of 300 m. The upwards and downward pointing detectors are mounted in a PMS canister on the Learjet tiptank on the opposite wing. There are two sets of optics for each detector, each with 50 mm diameter apertures. For nighttime, a compound parabolic collector (Winston cone) collects the laser light over a ±30° ?eld of view (FOV). A 77 nm full width half-maximum (FWHM) interference ?lter blocks non-laser background light. For daytime use, the strong solar background light is blocked more aggressively with a temperature controlled 0.37 nm FWHM interference ?lter, which only passes the laser light over a FOV of about ±3°. The optics blocks scattered sunlight beyond 3° with a ?eld stop. The returned laser light is measured with Hamamatsu H7680 high-speed gated photomultiplier tube (PMT) units. A dedicated electronics board controls the PMT gain, converts the PMT output current to voltage, ampli?es the signal, digitizes the signal, and transmits the results to a computer in the aircraft via a high speed serial interface. Due to the limited dynamic range of high speed analog-to-digital converters, the electronics uses multiple gain stages.

The components of the airborne in situ cloud lidar were tested on March 6, 2004 in a "breadboard" con?guration at the Storm Peak Laboratory (Borys and Wetzel, 1997) on the top of Mt. Werner above Steamboat Springs, Colorado. The laser beam pointed vertically, while the detector viewed nearly horizontally to the west. From the early afternoon through the evening on March 6 there was blowing snow and episodes of cloud enveloping the laboratory.

Fig. 2 shows an example lidar signal from one of the higher density cloud events occurring at night. The narrow FOV (daytime) optics happened to be on at that time. The manufacturers PMT gain curve and quantum ef?ciency are used to convert the measured PMT output current to the rate of photons incident on the PMT. The signal ?rst rises as the PMT gain ramps up. Then the signal decreases in a fairly power law manner as expected from theory. The power law slope from 0.4 to 2.0 μs is -1.51. The change in slope around 5 μs may be related to the extinction changing further away in the cloud or due to the laser light interacting with the surface (snow and trees). The downward spike seen around 20 μs is due to the gain changing from the second to the third stage. The multiple stages allow this lidar signal to be recorded over four orders of magnitude. Even with the narrow FOV optics, which collect only about 1% of the light of the wide FOV optics, the signal is above the noise out to the end at 40 μs. (The noise is shot noise due to the small number of photocathode electrons during each 50 ns interval). The noise at the end of the signal is reduced dramatically by averaging over logarithmically spaced time bins.

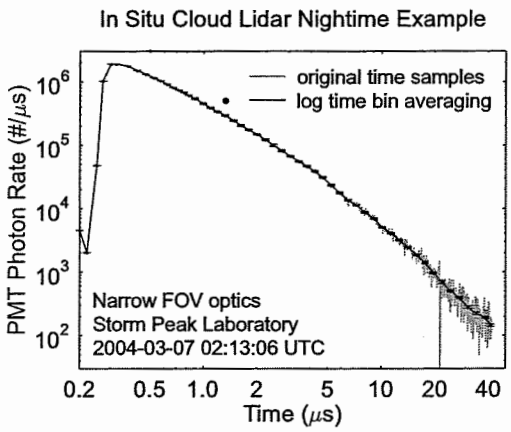

Figure 2: Example in situ lidar signal at night. The time averaged signal is shown with error bars.

Fig. 3 shows an example lidar signal measured during the daytime. The beginning of the lidar return signal is about one order of magnitude above the solar background level. The background is constant over tens of μs and can be sub-

tracted from the time series to estimate the true lidar signal. This procedure works quite well, resulting in useful signal out to 10 μs and over 2.5 orders of magnitude.

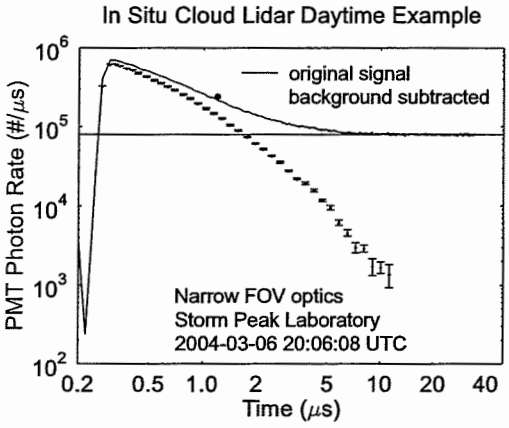

Figure 3: Example daytime in situ lidar signal, showing solar background subtraction. The time averaged and background subtracted signal is shown with error bars.

Since this ground-based experiment was an engineering test of the in situ lidar components, retrievals and validation of extinction and cloud thickness are not warranted. However, the physical units of photon fraction can be estimated using an optical throughput calculated from ?lter measurements and the size and FOV of the optics. With the 180 mJ laser pulse and the narrow FOV optics, the PMT photon rate is multiplied by 4.5×10^{-17} cm^{-2} ster^{-1} to get the photon fraction in (μs cm^2 ster)$^{-1}$. For example, the photon fraction at 1.2 μs in Fig. 2 is 1.52×10^{-11} μs^{-1} cm^{-2} ster^{-1}. For comparison, the photon fraction time series was computed by the Monte Carlo model for uniform 1000 m thick liquid clouds (effective radius of 8 μm) with the lidar at the center. A ?t to the simulated time series from 0.4 to 8 μs gives the photon fraction as a function of time and extinction:

$$f_p = 1.9 \times 10^{-14}\, t^{-1.23}\, \beta^{1.74}\,,$$

where f_p has units of (μs cm^2 ster)$^{-1}$, t is in μs, and β is in km^{-1}. Using this formula on the photon fraction at 1.2 μs, results in an estimate of 53 km^{-1} for the extinction.

4. CONCLUSIONS

The in situ cloud lidar technique is a new method for measuring extinction averaged over regions hundreds of meters in diameter in optically thick water clouds. Retrieval simulations in fractal stratocumulus clouds indicate that the technique will accurately measure volume averaged extinction and area averaged cloud thickness and optical depth. Simulations of a dual wavelength in situ lidar suggest that accurate measurements of liquid water content and effective radius would be possible.

SPEC, Inc. in Boulder, Colorado is building an airborne prototype in situ lidar operating at a wavelength of 532 nm. Recently an engineering test of the components was made on a mountain top enveloped in cloud. The in situ lidar time series from this test agree with those expected from diffusion theory. The lidar signal was measured over 4 orders of magnitude, and at least 100 times more dynamic range is expected to be possible. Although Evans et al. (2003) indicated that daytime operation would not be possible, the ground-based test showed that using a very narrow interference ?lter and a narrow ?eld of view detector can give a surprisely wide range of useable signal in daylight.

For the poster we plan to report on tests of the in situ lidar on the Learjet aircraft in a variety of cloud types. The performance of the airborne in situ lidar will be evaluated by comparing extinction retrievals in relatively homogeneous clouds with averages of local extinction determined from an FSSP and the SPEC cloud extinctometer.

ACKNOWLEDGEMENTS

We thank Dr. Randy Borys, Director of the DRI Storm Peak Laboratory (http://stormpeak.dri.edu/), for providing valuable technical and logistical support. Financial support was provided by NASA SBIR phase 1 contract NAS5-01193 and phase 2 contract NAS5-02111 to SPEC, Inc.

REFERENCES

Borys, R. D., and M. A. Wetzel, 1997: Storm Peak Laboratory: A research, teaching, and service facility for the atmospheric sciences. *Bull. Amer. Meteor. Soc.*, **78,** 2115-2123.

Evans, K. F., R. P. Lawson, P. Zmarzly, D. O'Connor, and W. J. Wiscombe, 2003: In situ cloud sensing with multiple scattering lidar: Simulations and demonstration. *J. Atmos. Ocean Tech.*, **20,** 1505–1522.

A COMPARISON BETWEEN THE ROSEMOUNT ICING DETECTOR AND THE SMALL ICE DETECTOR

P. R. Field[1], P. R. A. Brown[1], G. A. Isaac[2], J. W. Strapp2, A. V. Korolev[3], S. Cober[2], E. Hirst[4], R. S. Greenaway[4], P. H. Kaye[4]

1. Met Office, Exeter, UK. 2. Meteorological Service of Canada, Toronto, Canada. 3. Sky Tech Research Inc.Canada. 4. University of Hertfordshire, UK.

1. INTRODUCTION

The BF Goodrich Aerospace Rosemount Icing Detector (RICE) is commonly used on civilian aircraft. They are used to either directly activate anti-icing systems or notify the pilot of icing conditions so that appropriate action can be taken. Here, we compare the response of the RICE to supercooled liquid water with a Small Ice Detector (Hirst et al. 2001) that uses particle sphericity to infer the dominant phase encountered.

2. INSTRUMENT DESCRIPTION

The Rosemount icing detector probe is an oscillating cylinder 6.35 mm in diameter and 25.4 mm long. Ice buildup on the sensing cylinder through the accretion of supercooled liquid water droplets changes the frequency of oscillation. The voltage signal that this generates can be used to estimate the amount of ice accreted and hence determine the supercooled liquid water content (LWC). When approximately 0.5mm of ice has built up on the cylinder a heater cycle is started that lasts for 5s and requires a further ~10s for the cylinder to return to ambient temperature. The response of the Rosemount icing detector varies from probe to probe and airspeed. For the NRC Convair-580 ~90% of the 1-s noise on the RICE signal is within ± 4 mV s^{-1} for true air speeds around 100 m s^{-1} (Cober et al. 2001).

The hypothesis that liquid droplets are spherical and ice crystals are not spherical is the basis of the phase determination method used by the SID probe. SID is a laser scattering device that can count and size spherical particles between 1 and 35 μm (diameter) and count non-spherical particles. The probe uses six detectors arranged azimuthally at a forward scattering angle of 30°, with a seventh detector mounted at the forward scattering angle. One of the six 30° detectors has an iris fitted to allow it to define a 400x800μm ellipse on the scattering laser. When light is detected by this detector and one other detector, a particle is known to be in the sample volume and the detector responses are recorded. By comparing the responses of the azimuthally arranged detectors an 'asphericity factor' (Af) is obtained for each particle measured that ranges from 0 for spherical particles to 100 for very non-spherical particles (see Hirst et al. 2001 for more details). The five 30° detectors that are not stopped down with the iris are used to compute Af using:

$$Af = k\frac{\sqrt{\sum_{i=1}^{5}(< E > - E_i)^2}}{< E >}, \qquad (1)$$

where k is a constant set to place Af in the range 0-100, E_i are the detector values and $< E >$ is the mean of E_i. In practice, noise and differences between the detectors mean that the spherical droplets that should give $Af = 0$ will in general produce non-zero values.

3. AIRS-1.5 DATA

The Alliance Icing Research Study (AIRS) is a collaborative effort involving several research agencies and Universities, principally in Canada and the USA. AIRS is a project supported by the Aircraft Icing Research Alliance (AIRA), and also by the World Meteorological Organisation World Weather Research Program project on Aircraft In-Flight Icing. The AIRS-1.5 field campaign took place between Dec 2002 and Feb 2003 as a trial project for the larger campaign (AIRS-2) the following year. The aims of these campaigns include the validation of remotely-sensed observations and forecasts of supercooled liquid water in cloud and precipitation. During AIRS-1.5, in-situ measurements were made using the Convair 580 aircraft of the National Research Council of Canada. Data presented here were used from flights on 4th, 6th, 7th, 13th, 18th February 2003.

4. DATA

In the data comparison we will consider 1-s data that were collected with true airspeeds 91$\pm$10 m s^{-1} in the temperature range -8 to -33C. For the SID probe the number weighted phase of the particles measured in each second is obtained using the method described in Field et al. 2004. This method determines the dominant phase detected by the SID for a 1-s period and uses the distribution of Af values (Af bins 1-unit wide) obtained in each 1-s period. A cumulative frequency histogram is computed (using a minimum of 5 particles : 0.2 cm^{-3}) and then compared with the two reference cumulative frequency curves for assumed ice only (cirrus T<-40C) and liquid only conditions (stratocumulus T>0C) using a Kolmogorov-Smirnov test . The Kolmogorov-Smirnov test statistic is found by examining the difference between the reference curve and the measured curve in each Af bin. The largest difference is the test result. The test determines whether the observed distribution is closest to the ice or liquid reference curve

[1] Corresponding author: Paul Field, Met Office, FitzRoy Road, Exeter, Devon, EX1 3PB, UK.

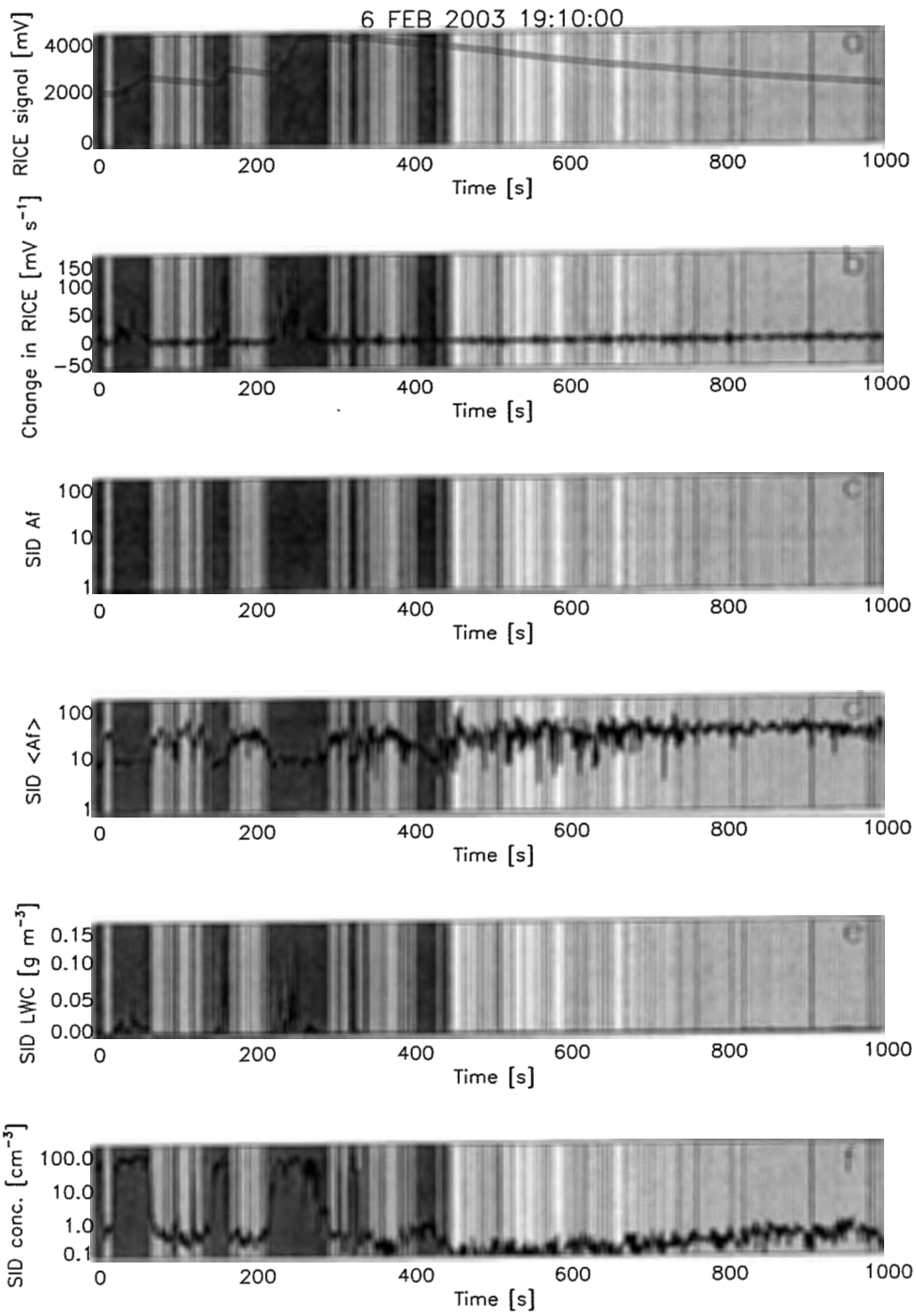

Figure 1: Data from 6th February 2003. a) RICE output signal. b) Backward differenced change in the 1-s RICE signal. c) Individual particle Af values obtained from SID. d) 1-s averaged Af values from SID. e) SID LWC. f) SID concentration. For all of the panels the dark-grey background indicates regions determined by SID to contain super-cooled liquid water (larger ICE particles may also exist, the light-grey background represents ice cloud and the white regions indicate that the measured concentration was smaller than 0.2 cm^{-3}.

and hence defines the phase for that 1-s (~100 m) period.

Using this method provides an estimate of the number weighted dominant phase in the sub ~50 μm size range for every ~100 m of horizontal flight.

The RICE probe provides a series of voltage measurements to represent the oscillation frequency of the collection cylinder. To analyse the RICE data we have generated a time series of voltage jumps by backwards differencing the RICE measured voltage. We have ignored 30s following a deice cycle to allow the probe to return to ambient conditions and eliminated any points that exceed the Ludlam limit

We have also ignored points where large amounts of ice were coincident with the super cooled liquid water for the Nevzorov-RICE comparison eliminated points where |NLW/NTW-1|>0.3.

5. DATA COMPARISON

Figure 1 is a section of flight data to show the response of the RICE and SID. This section taken from the 6th February 2003 flight shows several regions where the RICE signal rises indicating the presence of supercooled liquid water and regions where the RICE signal slowly tails off as the rimed ice sublimates and is lost from the RICE probe. In all of the panels the colour background indicates the phase determined from the SID probe from the statistical comparison of measured Af distributions with reference curves. In panel b the 1-s difference in the RICE signal clearly shows good correlation with the dark-grey regions indicated to contain super cooled liquid. Some regions indicated by SID to contain liquid water appear to be missed by the RICE (e.g. 400-450s) but also have low LWC (panel e) and particle concentration (panel f). Panel c shows the individual Af values from the particles measured by the SID. When concentrations are high (e.g. 200-300s) it is difficult to clearly see what Af values are, but in lower concentration regions (e.g. 600-1000s) it is can be seen that the Af values are high. We know from test cases that 90% of Af values from ice particles will be >12 which can be seen in the second half of the data section presented. In panel d the 1-s average Af value is given and is generally below 10 in the liquid regions.

It is known that the change in RICE signal is directly proportional to the LWC accreted (Mazin et al. 2001, Cober et al. 2001). We confirm this in figure 2 [left] where we show the 1-s change in RICE signal against LW mass accreted per second, $\Delta M/\Delta t$

$$\frac{\Delta M}{\Delta t} = DLUW = k\frac{\Delta V}{\Delta t} \qquad (2)$$

where D is the RICE cylinder diameter, L is the RICE cylinder length, U is the aircraft true air speed, W is the measured LWC from the SID or Nevzorov probe, k is the RICE probe calibration constant, and V is the RICE signal. A correlation between the change in RICE signal and the water accreted inferred from the SID (circles) and Nevzorov (+) is evident. Previous best fits from Mazin et al. and Cober et al. with other data using this probe are shown for comparison. Here we have fitted a straight line by minimizing Chi squared for the Nevzorov (dashed) and SID (solid). Assumed errors in the RICE signal of 3 mV s^{-1} and the standard deviation of the SID and Nevzorov liquid water were esimated by computing the standard deviations of these data in 50 mV s^{-1} bins. The resulting best fit lines are:

$$\frac{\Delta M_{Nev}}{\Delta t} = (1.39\pm0.04)\times10^{-5}\frac{\Delta V}{\Delta t}+(2.62\pm0.14)\times10^{-7} \qquad (3)$$

$$\frac{\Delta M_{SID}}{\Delta t} = (1.46\pm0.05)\times10^{-5}\frac{\Delta V}{\Delta t}+(0.53\pm0.06)\times10^{-7} \qquad (4)$$

Ignoring the small intercept, the gradients given in eq. 3,4 are similar to those found by Cober et al. (1.23×10^{-5}) and Mazin et al. ($(1.35\pm0.42)\times10^{-5}, (1.40\pm0.15)\times10^{-5}$). The intercept represents the RICE threshold for detecting supercooled LWC but may also be affected by the baseline correction of the Nevzorov probe. The minimum detectable LWC is given as 0.003 g m^{-3} from the SID data.

Assuming that the SID is more sensitive than the RICE probe at detecting supercooled liquid water then we can compare the hit rate and false alarm rate of the RICE probe against SID. For periods in cloud (SID concentration >0.2 cm^{-3}) where the RICE probe was not in a deice cycle we generated a binary time series, r, of with 0 representing the presence of supercooled LWC in a 1-s period and 1 representing no LWC (i.e. ice). Several time series for the RICE were made by using different thresholds for the change in RICE signal. Changes exceeding this threshold indicated the presence of supercooled LWC. A binary time series was generated for the SID probe, s, to represent the phase determined using the Kolmogorov-Smirnov test and compared with the RICE series to obtain a Brier score, b:

$$b = \frac{\sum_{i=0}^{n}(s-r)^2}{n}. \qquad (5)$$

Figure 3 shows the Brier score as a function of RICE threshold (solid line). The lowest (best) score is obtained when a threshold of 6 mV s^{-1} is used. The hit rate (number of coincident LWC events seen by SID and RICE/ number of events seen by SID) is 72% (dashed line) and the false alarm rate (number of LWC events seen by RICE but not SID/ number of non LWC points) is less than 0.5% (dot-dash line). A threshold of 6 mV s^{-1} is equivalent to a LWC of 0.008 g m^{-3} using the fit to SID data or 0.021 g m^{-3} using the Nevzorov fit.

6. CONCLUSIONS

Two probes that make use of different detection methods, the Small Ice detector and Rosemount icing probe, have been compared using in-situ mixed-phase cloud data and show good agreement.

Using a RICE threshold of 6mV s^{-1} (LWC threshold in the range 0.008-0.021 g m^{-3} to indicate the presence of supercooled liquid water results in a 72% hit rate and less than 0.5% false alarm rate relative to the SID probe.

The good agreement between the RICE and SID probe confirms that using particle sphericity to determine phase

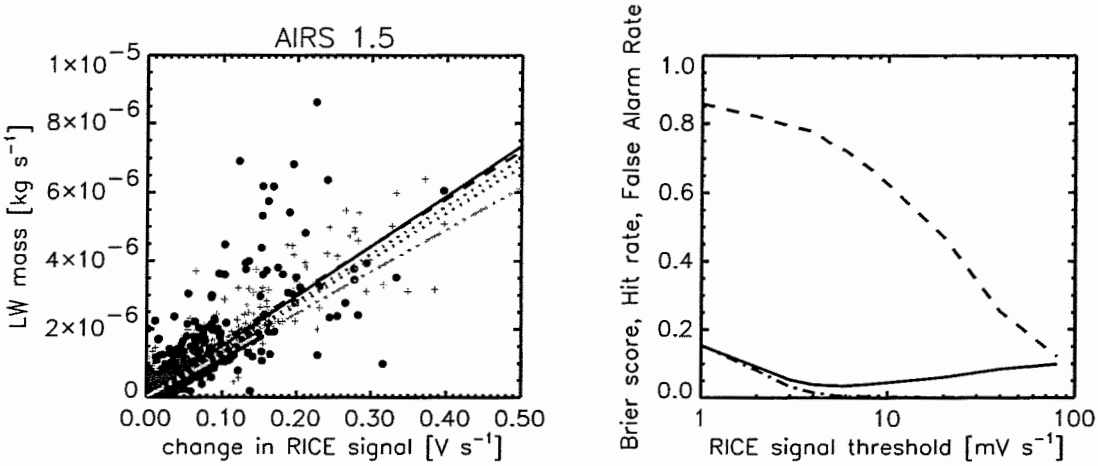

Figure 2: [left] Plot of accreted supercooled liquid water estimated from SID (circles, 2833 points) and the Nevzorov total water probe (+, 1235 points) against 1-s change in RICE signal. Results from previous work are also shown: dash-dotted is from Cober et al., grey dotted are from Mazin et al. The solid line is the fit to the SID data and the dashed line is the fit to the Nevzorov data.[right] The Brier score from comparing the RICE indication of supercooled LWC with the SID using different RICE thresholds

is a useful method.

7. REFERENCES

Cober S. G., Isaac G. A. and Korolev A. V.,2001. Assessing the Rosemount Icing Detector with in situ measurements. *J. Atmos. Ocean Technol.*, 18(4), 515-528.

Field P. R., R. J. Hogan, P.R.A Brown, A.J. Illingworth, T.W. Choularton, P. H. Kaye, E. Hirst and R. Greenaway, 2004. Simultaneous radar and aircraft observations of mixed-phase cloud at the 100-m-scale Q. J. Royal. Met. Soc., In Press.

Hirst E., Kaye P. H., Greenaway R. S., Field P. and Johnson D. W., 2001. Discrimination of micrometre-sized ice and super-ccoled droplets in mixed-phase cloud. *Atmos. Environ.*, 35(1),33-47.

Mazin I. P., Korolev A. V, Heymsfield A., Isaac G. A. and Cober S. G.,2001. Thermodynamics of icing cylinder for measurements of liquid water content in supercooled clouds. *J. Atmos. Ocean Technol.*, 18(4), 543-558.

A FIELD INTERCOMPARISON OF A PHASE DOPPLER PARTICLE ANALYSER AND FSSP AT THE SPHINX MOUNTAIN LABORATORY.

M. J Flynn, M. W. Gallagher, K. N. Bower

Department of Physics, University of Manchester Institute of Science and Technology (UMIST), PO Box 88, Manchester, M60 1QD, United Kingdom.

1. INTRODUCTION

Obtaining reliable insitu measurements of cloud microphysical properties is an essential part of understanding cloud processes and how these are affected by anthropogenic emissions. This is important in assessing and predicting how the radiative forcing of clouds will respond to anthropogenic activities and climate change.

In this work results from a Forward Scattering Spectrometer Probe (FSSP) are compared with an Airborne Droplet Analyser (ADA). The FSSP and other similar probes have been widely used over almost the last thirty years to make insitu measurements of cloud droplet size distribution and number concentration. The ADA is a recently developed instrument, using a different measurement technique which promises to overcome many of the traditional uncertainties associated with FSSP measurements.

2. INSTRUMENTATION

The FSSP measures the intensity of light scattered as single particles pass through a laser beam. The design of the probe limits the sample region to a small well defined portion of the total beam length, allowing particle size to be determined from Mie scattering theory, and number concentration to be determined from the number of counts, the area of the beam and the air speed. There have been many publications analysing the performance of the FSSP under a variety of conditions. These have highlighted problems such as dead time, coincidence errors (Baumgardner et al. 1985) and uncertainty in sizing (Dye et al. 1984, Jaenickle and Hanusch 1993) due to the ambiguities in Mie scattering theory at certain particle size in FSSP measurements. Much effort has focussed on better calibration techniques (Hovenac and Lock 1993), and correction algorithms and modelling (Brenguier et al. 1994) to improve the quality of FSSP measurements. While recent advances in electronics have improved the performance of the FSSP some significant issues remain under certain conditions.

The FSSP used for this project was a PMS FSSP-100, with a nominal size range of 1-47 microns, which has had the DMP SPP-100 electronics upgrade. This upgrade removes the problems of electronic deadtime by using modern digital signal processor technology, and buffering. Additionally it allows flexibility in the number of size channels used, and how the Mie scatting intensity vs particle size curve is represented.

The ADA uses phase doppler particle analyser (PDPA) technology which is an extension of the laser doppler velocimetry (LDV) technique, which allows for simultaneous measurement of size and velocity (up to three components) of individual particles. This technology is widely used in laboratory applications, eg. characterisation of jets and sprays (Wigley et al. 1999) and for precise measurement of fluid flow (Brenn et al. 2003) in pipes and wind tunnels.

This technique uses properties of the interference pattern generated in the light scattered when a particle passes through the intersection point of two laser beams having nearly, but not exactly the same frequency (40MHz difference in frequency). The doppler frequency of the pattern is used to determine particle velocity, while phase difference between pairs of detectors places a slightly different detection angles is used to deduce particle size. Scattering intensity and transit time are also measured, but are used to ensure data quality rather than as the primary measurement.

Recently a 1-D PDPA system has been developed which is suitable for airborne and ground based measurement of cloud droplets and large deliquesced aerosol. The probe used for this study, the TSI Airborne Droplet Analyser (ADA) has a total size range of about 0.5 – 200 microns, with a dynamic range of 1:50, is capable of measuring droplet concentrations up to thousands per cc, and can measure at any air speed without the need for aspiration. Additional information such as particle interarrival time (useful for probing fine cloud structure), and some information on particle sphericity (useful for rejecting ice particles) is also available from the data.

The PDPA technique eliminates the problems associated with FSSP measurements, but does have additional problems of it's own. In particular the Gaussian nature of the beam means that the effective sample area is reduced at smaller sizes, requiring a complicated correction algorithm to produce a representative distribution across all sizes. Additionally probe performance is partially determined by how well the two beams are matched, and the total laser power available. Also under certain conditions, ambient sunlight can interfere with the measurements. These issues combine with the complexity of the instrument set up, to make the ADA a rather more difficult instrument to operate in the field than the FSSP, but when operated well, capable of producing much high resolution, and possibly better quality data.

3. THE CLACE-2 EXPERIMENT

The CLACE2 project at the Jungfraujoch High Alpine Research Station Sphinx Laboratory during June and July 2002. This project, to examine cloud – aerosol interactions in the lower free troposphere involved an extensive range of aerosol and cloud microphysical instrumentation, part of which included an ADA and FSSP mounted in close proximity on the roof of the lab. During the project a wide variety of cloud conditions were experienced, and a considerable amount of in cloud data was obtained. This provided an ideal dataset for the intercomparison and evaluation of the performance of the ADA and FSSP under a wide range of conditions, and in the light of additional information from other instrumentation employed at the site.

4. RESULTS

A very comprehensive dataset was obtained with both instruments operating well. During the campaign there were several periods of continuous cloud lasting a number of days, with a wide variety of spectral shapes and mode diameters observed. In general droplet number concentration was observed to be in good agreement between the two probes typically agreement was within 20%.

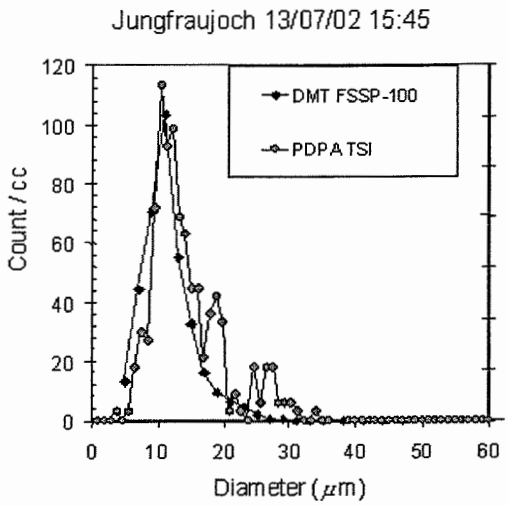

FIGURE 4-1. Mono-modal droplet distribution observed at the Jungfraujoch, showing good agreement between ADA and FSSP. Note the additional detail observed on the ADA spectra.

Particle size distributions show good agreement under certain conditions and poor agreement under others. Figures 4-1 and 4-2 illustrate these cases. Figure 4-1 shows that under conditions with a mono-modal distribution there is good agreement in both spectral shape and peak positions. It can also be seen that the greater size resolution available with the ADA allows the measurement of smaller features which are entirely missed by the FSSP. Figure 4-2 shows that with a bi-modal distribution, although both probes agree on the general shape of the distribution, the ADA measures the position of the second peak to be between 5 and 7 microns larger than that reported by the FSSP. This has significant implications for the calculated liquid water content reported by the probe.

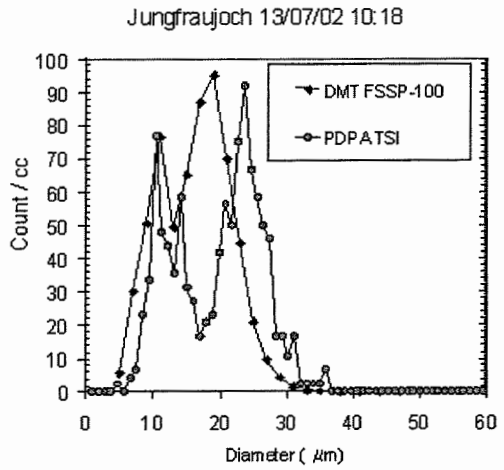

FIGURE 4-2. Bi-modal droplet distribution observed at the Jungfraujoch, showing poor agreement between the ADA and FSSP, particularly in relation to the position of the large mode. The size reported by ADA is about 7 microns larger than that reported by the FSSP.

5. CONCLUSION

Interesting differences have been observed between the size distributions reported by the ADA and FSSP, which require some further investigation in light of the known issues with FSSP measurements which are reported in the literature. There are a number of possible explanations for the differences in size, including problems with FSSP sizing due to Mie Scattering Theory ambiguities, and errors in ADA size measurements due to possible saturation of the photomultipliers when measuring larger particles. Further tests are needed, particularly on the response of the ADA under atmospheric conditions, before this issue can be completely resolved.

In general these results show that if operated correctly for the conditions being measured ADA has the potential to be a powerful new addition in the field of microphysical measurements. ADA's higher resolution size data, immunity from Mie Scattering problems and coincidence errors, as well as the additional information which can be obtained from the data represent significant advantages over existing technology. However ADA has it's own problems which need to be fully investigated and characterised.

6. REFERENCES

Baumgardner, D., Strapp, W. and Dye, J. E. 1985. Evaluation of the forward scattering spectrometer probe. Part 2: Corrections for coincidence and dead time losses. *J. Atmos. Ocean. Tech.* **2**, 626-632.

Brenguier, J. L., Baumgardner, D. and Baker, B. 1994. A review and discussion of processing algorithms for FSSP concentration measurements. *J. Atmos. Ocean. Tech.* **11**, 1409-1414

Brenn, G., Braeske, H., Zivkovic, G. and Durst, F. 2003. Experimental and numerical investigation of liquid channel flows with dispersed gas and solid particles. *Int, J Multiphase Flow*. **29**, 219-247.

Dye, J. E. and Baumgardner, D. 1984. Evaluation of the Forward Scattering Spectrometer Probe. Part 1: Electronic and Optical Studies. *J. of Atmos. and Oceanic Tech.* **1**, 329-344.

Hovenac, E. A. and Lock, J. A. 1993. Calibration of the Forward Scattering Spectrometer Probe – modelling scattering from a multimode laser beam. *J. Atmos. Ocean. Tech.* **10**, 518-525.

Jaenicke, R. and Hanusch, T. 1993. Simulation of the optical-particle counter Forward Scattering Spectrometer Probe-100 (FSSP-100) – consequences for size distribution measurements. *J. Aerosol Sci. Tech.* **18**, 309-322.

Wigley, G., Hargrave, G. H. and Heath, J. 1999. A high power, high resolution LDA PDA system applied to gasoline direct injection sprays. *Part. & Part Systems Characterization*. **16**, 11-19.

Airborne Digital In-Line Holographic Detector for Cloud Particle Studies

Jacob P. Fugal, Ewe Wei Saw, Alex V. Sergeyev and Raymond A. Shaw*

Department of Physics,
Michigan Technological University. Houghton, MI 49931, USA

1. INTRODUCTION

An assumption made, often implicitly, in models for precipitation formation, remote sensing of clouds, and radiative transfer through clouds, is that cloud droplets are Poisson-distributed through space at small scales. However, recent research has suggested that cloud droplets are correlated at sub-mm to cm scales (e.g. Kostinski and Shaw 2001, Pinsky and Khain 2001). The data on which this research is based were obtained in a one-dimensional geometry. Although Holtzer and Collins (2002) have demonstrated how to generalize such data to three dimensions, this generalization requires restrictive assumptions and is not robust on the smallest scales which happen to be of greatest interest.

One way to measure the three-dimensional distributions of particles is holography. Recent technological advances in digital cameras and digital data storage has made digital holography practicable. Digital holography bypasses the processing of holographic film and the tedious optical reconstruction which makes up most of the data-analysis time. While digital holography cannot match the resolution of photographic film, it turns out that it is adequate given that we use inline holography, low cloud droplet densities (<1 droplet per mm^3), and are willing to accept a depth uncertainty of order 10 droplet diameters (Hinsch 2002). Note that there are some methods of reducing this depth uncertainty to just a few droplet diameters, (see Pan and Meng 2003).

We designed and built an instrument called Holographic Detector for Clouds (HOLODEC) with the purpose to establish proof of concept of an airborne digital holographic detector for cloud droplets. We tested the instrument during nine flights in August to September 2003 on the National Center for Atmospheric Research's C-130 aircraft in Colorado, USA as part of the IDEAS III project. We obtained holograms containing cloud droplets of diameter 10 to 20 μm. We also obtained holograms of ice crystals of characteristic length 10 to 1000 μm.

In this extended abstract we briefly describe the holographic method, our digital hologram reconstruction method, and then we show holograms and reconstructed pictures of cloud droplets and ice crystals.

2. THE HOLOGRAPHIC METHOD

In our instrument, a laser beam is expanded and propagated past the droplets. The droplets and ice crystals emit a scattered wave which interferes with the incident beam and the resultant interference pattern is measured by a CCD camera. The resultant intensity for a single scatterer is

$$I = E_R E_R^* + E_R E_S^* + E_R^* E_S + E_S E_S^* \qquad (1)$$

where E_R is the incident plane wave which serves as the reference beam, and E_S is the scattered wave from the particle. Note we have assumed an uninterrupted plane wave which is not valid for large ice crystals. This explains part of the difficulty of reconstructing such crystals. The first term is a constant background which may be subtracted. The second and third terms are the real and virtual images respectively, and the last term is negligible because the scattered wave is much weaker than the reference wave. Only the real or virtual image is appreciable at any particular depth $z \gg D^2/\lambda$, so we may arbitrarily neglect the virtual image for small enough particles.

3. RECONSTRUCTION METHOD

Our holographic reconstruction method is done using a Huygens-Fresnel kernel. In reconstruction,

*Corresponding author's address: Raymond A. Shaw; MTU Physics Department; 1400 Townsend Dr; Houghton, MI 49931; E-Mail: rashaw@mtu.edu

the relevant diameter is the size of the CCD aperture which is 3.6 x 4.8 mm (1024 x 768 pixels; 4.65 μm square pixels). Since we are interested in the reconstructed field at less than a few aperture widths away, we cannot use the Fraunhofer approximation or, it turns out, even the Fresnel approximation.

The Huygens-Fresnel kernel is

$$U(f_x, f_y; z = d) = U(f_x, f_y; z = 0)H(f_x, f_y; d) \quad (2)$$

where $U(f_x, f_y; z = d)$ is the Fourier transform of the field at distance d from the CCD surface, $U(f_x, f_y; z = 0)$ is the Fourier transform of the field at the CCD camera and

$$H(f_x, f_y; d) = \exp\left(jkd\sqrt{1 - \lambda^2(f_x^2 + f_y^2)}\right) \quad (3)$$

and $k = 2\pi/\lambda$. The algorithm to reconstruct the intensity at some depth d for small particles (e.g. cloud droplets) is: (1) Take the negative of the intensity measured at the CCD surface (i.e. subtract each measured pixel intensity from the maximum measured pixel intensity) which emulates what photographic film measures. Then treat this negative as an intensity filter through which we propagate a unit-amplitude zero-phase plane wave. Thus the field takes on the values of the negative of the measured intensity. (2) Take the field's Fourier transform. (3) Multiply by $H(f_x, f_y; d)$. (4) Take the inverse Fourier transform. (5) Take the modulus squared to get intensity.

In this abstract, the algorithm for larger particles (e.g. large ice crystals) omits the first and fifth steps because it makes clearer reconstructed images. So cloud droplets and small ice crystals will appear bright while the larger ice crystals will appear as silhouettes.

4. CALIBRATION

To test the accuracy of the depth perception we took advantage of dirty optics. We found that by reconstructing nearly any frame, we could find the dust on the optical surfaces of the instrument from a filter just 10 mm from the CCD surface clear to the nearest lens on the beam expander 160 mm away. Thus we have confidence in our ability to reconstruct objects with a characteristic length down to about 10 μm within the sample range of our probe (about 34 to 80 mm from the CCD surface).

We tested the lateral accuracy of the instrument by using drops of known size. Figure 1 shows a reconstruction of both a 50μm droplet and a 25μm droplet. We see that we are accurate within a pixel (4.65 μm).

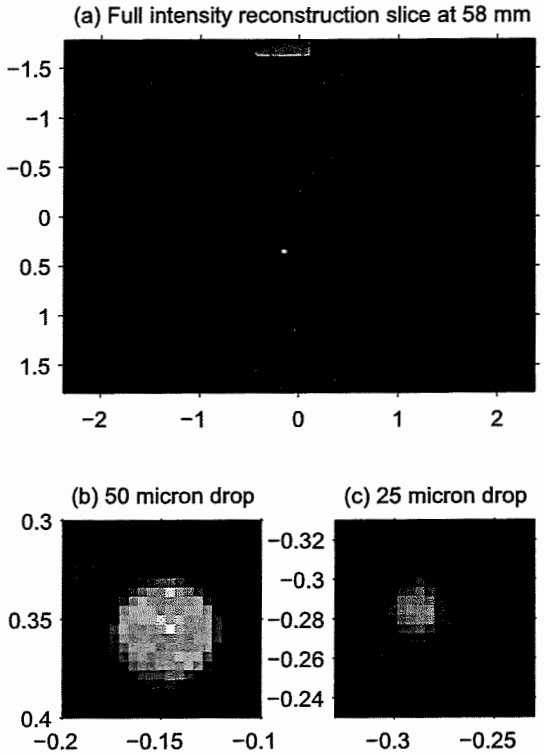

FIG. 1: Frame (a) shows a reconstruction slice at 58 mm from the CCD. The droplet generator tip is shown at the top of the frame and a 50 μm diameter droplet is also visible. Frame (b) shows a closeup of the 50 μm diameter drop while (c) shows a 25 μm diameter drop. Note that the reconstructed images of the droplets are within a pixel (4.65 μm) of the known diameter. We thank Uwe Maixner and Dagmar Nagel (GKSS) for providing these calibrated droplets.

5. WATER DROPLETS AND ICE CRYSTALS

Figure 2 shows several reconstruction slices of 10 to 20 μm diameter droplets. It also shows how the droplets appear when they are not in the reconstruction plane. Visually, we can pick out perhaps within 0.1 mm (order 10 particle diameters) where the drops appear to be the smallest and the most intense. We note that several methods exist for obtaining particle depth positions more accurately (e.g. Pan and Meng 2003).

Figure 3 shows several reconstructions of large ice crystals. Note that can reconstruct surprisingly large ice crystals. However for larger ice crystals, the reconstructions are less clear. Figure 4 shows reconstructions of small ice crystals. Note that for

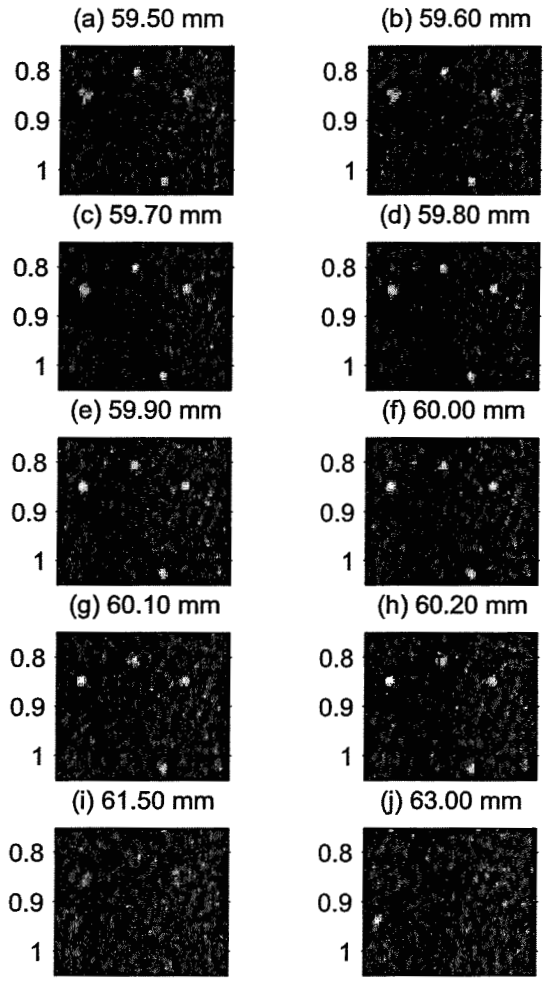

FIG. 2: Frames (a) through (h) show four cloud droplets (10 to 20 μm in diameter) shown in different reconstruction slices at the distances indicated above each frame. Units on each axis are in mm and the aspect ratio is square. Note in frame (i) how each drop has an interference pattern that is larger the further the drop is from its object plane. Frame (j) shows that the interference pattern of the four droplets is nearly lost in the noise just a couple millimeters out of the respective object's plane.

smaller ice crystals, although nonspherical, appear to have nearly circular interference fringes where the larger ice crystals' interference fringes can be very noncircular.

Figure 5 shows the hologram and a reconstruction slice of a field of very small ice crystals in a concentrated volume. Perhaps these crystals are shards leftover from the impact of a larger ice crystal on a probe tip.

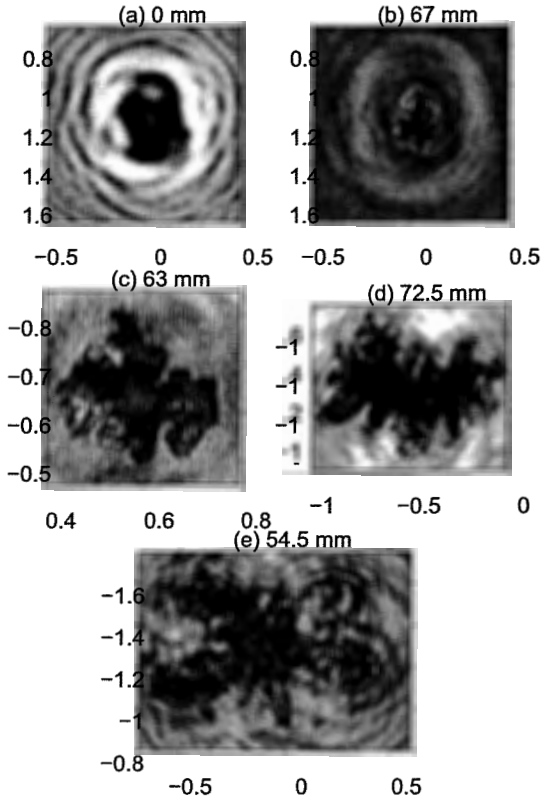

FIG. 3: Various reconstructions of large ice crystals and one of their original holograms. The distance from the CCD is indicated above each frame and the units on each axis is in mm. Frame (a) shows the section of the hologram from which the ice crystal in frame (b) was reconstructed. Frames (c), (d), and (e) are other reconstructions of large ice crystals.

6. CONCLUSION

We see that indeed this probe is proof of concept that an airborne digital holography is practicable. Not only can it measure the three-dimensional spatial distribution of cloud droplets, but it can also yield clear reconstructions of small ice crystals and some large ice crystals.

Further instrument development is needed eliminate or minimize the problems we faced in building and testing this probe, such as condensation on the windows. A much larger (more pixels) and a higher frame rate camera would allow us to find many more droplets per frame (sample volume) and more frames taken in the same area of the cloud. This will greatly enhance the scientific value of each sample volume.

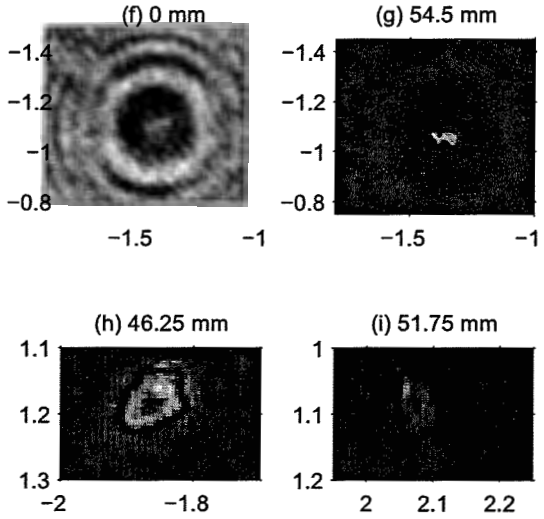

FIG. 4: Various reconstructions of small ice crystals and one of their original holograms. The distance from the CCD is indicated above each frame and the units on each axis is in mm. Frame (a) shows the section of the hologram from which the ice crystal in frame (b) was reconstructed. Frames (c), and (d) are other reconstructions of small ice crystals.

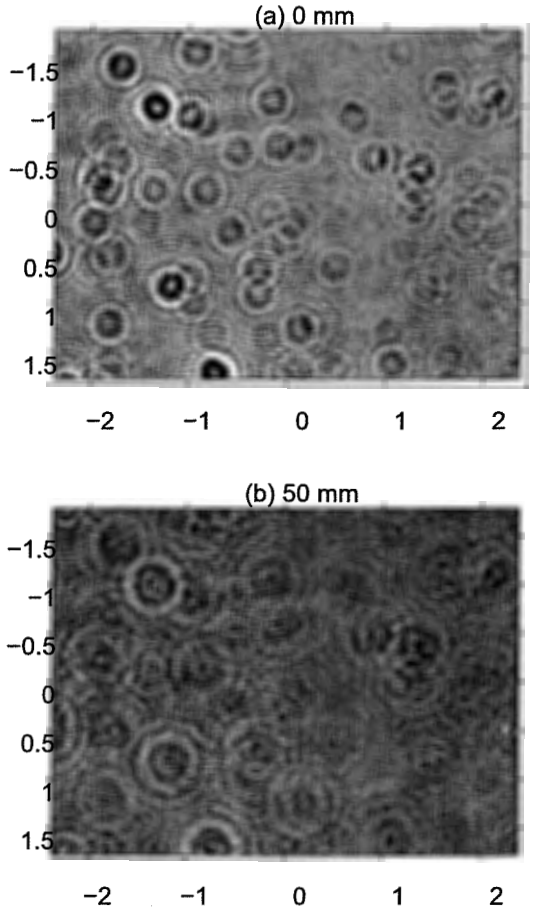

FIG. 5: Frame (a) shows the hologram of the many ice crystals shown in frame (b). All the ice crystals in this frame are concentrated between 46 and 51 mm. Perhaps the localization of these ice crystals is due to a shattered ice crystal on a probe tip.

ACKNOWLEDGEMENTS

We thank D. Cook and J. Howe for help with mechanical design and construction, and the NCAR Research Aviation Facility staff for their help with integrating the probe with the C-130 instrument system. We are especially grateful to J. Stith, RAF Director, for his invitation to participate in IDEAS III and his encouragement on the probe development. We are grateful to Uwe Maixner, and Dagmar Nagel for giving us time with their calibrated droplet generator. This research was supported by NASA (NAG-10568) and NSF (ATM-9984294) (RAS), and an NSF Graduate Research Fellowship (JPF).

REFERENCES

Hinsch, K. D., 2002: Holographic particle image velocimetry. *Measurement Science and Technology*, **13**, R61-R72.

Holtzer, G. L., and Collins, L. R., 2002: Relationship between the intrinsic radial distribution function for an isotropic field of particles and lower-dimensional measurements, *Journal of Fluid Mechanics*, **459**, 93-102.

Kostinski, A. B., and Shaw, R. A., 2001: Scale-dependent droplet clustering in turbulent clouds. *Journal of Fluid Mechanics*, **434**, 389-398.

Pan, G. and Meng, H., 2003: Digital holography of particle fields: reconstruction by use of complex amplitude. *Applied Optics*, **42**, 827-833.

Pinsky, A. and Khain, A. P., 2001: Fine structure of cloud droplet concentration as seen from the Fast-FSSP measurements. I. Method of analysis and preliminary results, *Journal of Applied Meteorology*, **40**, 1515-1537.

ON THE MEASUREMENT OF RAINDROPS FALL SPEEDS AT THE GROUND USING OPTICAL ARRAY PROBES

F. García-García and G. Montero-Martínez

Centro de Ciencias de la Atmósfera, Universidad Nacional Autónoma de México

1. INTRODUCTION

An accurate knowledge of the terminal velocity of cloud and precipitation particles is needed for performing computations in numerical models and for interpreting radar data. Although several investigators have measured fall speeds of drops in laboratory conditions, most of them at sea level (Lenard 1904, Laws 1941, Gunn and Kinzer 1949, Beard and Pruppacher 1969), direct field data are relatively scarce [for a summary of early field measurements, see Best (1950)]. These field and laboratory data have been used to develop terminal speeds parameterizations that, due to the wide range of values involved for sizes from cloud to rain drops, have to take into account several flow regimes (Beard 1976).

On the other hand, measurements of raindrop size distributions are of importance because they contain basic information regarding the mechanisms responsible for cloud and precipitation development and other related to interactions between dynamical and microphysical aspects of precipitation processes. Various instruments have been developed over the years for measuring raindrop sizes and number concentration both at the ground and aloft. These include electromechanical impactation devices, such as the Joss and Waldvogel (1967) disdrometer, and those that use shadowgraph imaging techniques (Knollenberg 1970, Illingworth and Stevens 1987, Baumgardner *et al.* 2002). Most of them depend on an accurate knowledge of the sampling speed to determine the sampling volume, which is in turn used to obtain the particle spectra.

*Corresponding author's address:
Fernando García-García.
Centro de Ciencias de la Atmósfera.
Universidad Nacional Autónoma de México.
Circuito de la Investigación Científica,
Ciudad Universitaria. Del. Coyoacán.
04510 México, D.F. México.
e-mail: ffgg@atmosfera.unam.mx

Furthermore, many of these instruments have been designed for use on the ground at a fixed location, in which case the sampling speed is a variable function of the fall velocity of each drop. To overcome this problem, most investigators have chosen semiempirical parameterizations for determining fall speeds. For the case of optical array probes, some have opted for trying other probing modes which require constant, non-dependent of particle size sampling speeds, either by using aspirators or mobile platforms (Holroyd 1986, Montañez and García 1992, to mention a few).

Over several years, the Cloud Physics Group of the National University of Mexico has carried out raindrop spectra determinations on the ground at a fixed location in Mexico City (García and Montañez 1992, García and Montero 2004). For this purpose, two Optical Array Spectrometer Probes (OAP's by Particle Measuring Systems - PMS, Knollenberg 1981) have been used. The aim of the present report is to describe the capabilities of these instruments to measure fall speeds of individual raindrops, given a proper handling of the data they provide, and to discuss their limitations.

2. INSTRUMENTATION APPRAISEMENT

Briefly, an OAP uses a photodiode array and associated photodetection electronics to achieve two-dimensional information from particles passing through a laser beam at the sampling region. Each probe employs 32 active photodiode elements in the array and takes image slices of a particle as it progresses through the sampling volume at a rate given by a clock (Figure 1). The clock also serves to keep track of both the time a particle takes to cross the array (particle transit time) and of particles inter-arrival times. Thus, the size of the particle is determined from the maximum width across the array; and its velocity is determined by dividing its size by the transit time. It should be remembered that PMS two-

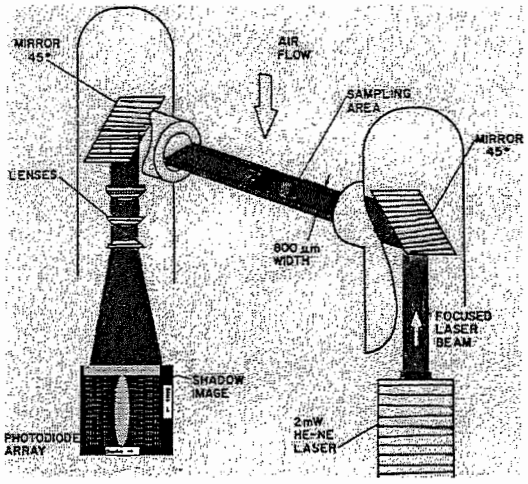

Figure 1. Schematics depicting the optical system of an OAP-2D-C.

dimensional optical array probes were originally designed for airborne use, so the clock frequency (4 MHz) was chosen such that, for a sampling speed of 100 m s^{-1}, shadow images would have circular shapes. In order to operate the probes at other, constant sampling speeds without loosing the "roundness" of the images, the frequency of oscillation can be varied at will via electronic circuitry for one of the probes, with the second probe frequency "slaved" to the first one by a factor of 8. Thus, for 2D-probes operating in a stationary mode, the resulting images will always appear elongated in either direction, exception made of those corresponding to the particle size whose fall speed matches the constant sampling frequency used.

The probes theoretical response is shown in Figure 2, which was obtained by calculating the number of slices that the system, operating at a given sampling clock rate, would detect for drops of given sizes falling at their terminal speeds. The particle size was assumed from the expected number of shadowed diodes based on the probes calibrations, and corrections due to raindrop shape deformation were introduced as proposed by Green (1975). The terminal velocities were calculated from the parametric equations given by Beard (1976) using typical atmospheric conditions in Mexico City. An analysis of Figure 2 illustrates that the selection of the sampling frequency will be a compromise between the expected particle-size range and the corresponding drops fall-speeds. For example, if the clock rate were too slow, the accuracy for the measured falling speeds of the larger particles would be lost. On the other hand, a very fast frequency prevents the system from detecting the smaller particles. It should also be noticed that the system has a 100-slice cut-off value to prevent noise introduced by possible drop splashing and undesirable long particle transit times. This latter feature is also controlled by the sampling frequency and limits the threshold particle size detection for the 2D-C.

3. FIELD DATA AND RESULTS

The expected behavior of the instrumentation described in the previous section was tested with field data obtained with two OAP's: a 2D-C and a 2D-P (20 to 640 µm and 200 to 6400 µm nominal drop diameter ranges; 25 and 200 µm resolution; respectively). The probes were operated fixed at the surface in a vertical orientation, without aspiration. Measurements were performed on the roofs of and at the garden next to the Center of Atmospheric Sciences buildings of the university campus in Mexico City (2,200 masl). It should be noted that the electronics of the two particular OAP's used here were updated in the year 2001. This included the changing of the original laser light-source, from a lamp tube to a photodiode system, and a new data acquisition system with its corresponding software (PACS by Droplet Measurement Technologies, from Boulder, Co.). However, the optical systems remained unchanged.

The particle image data were reduced by means of an objective software routine specifically developed for the particular sampling conditions, with a reconstruction algorithm based on a center-in technique (Álvarez and Torreblanca 1992). Laboratory performance tests and calibrations were conducted on the OAP's prior to each field data collection. Details on the peripheral equipment, its operation and on data reduction can be found in Montañez and García (1992).

Determinations of fall speeds for individual raindrops were made for several rain events under calm wind conditions. Data were classified in terms of precipitation type, and averaged according to drop size and sampling frequency. (Figure 3). For rain of stratiform origin, data from both probes follow extremely well previous theoretical and laboratory predictions within the expected sampling capabilities as discussed above. For the case of convective rain, 2D-C data depart considerably from those values for practically all sizes (below 400 µm) for otherwise identical sampling conditions.

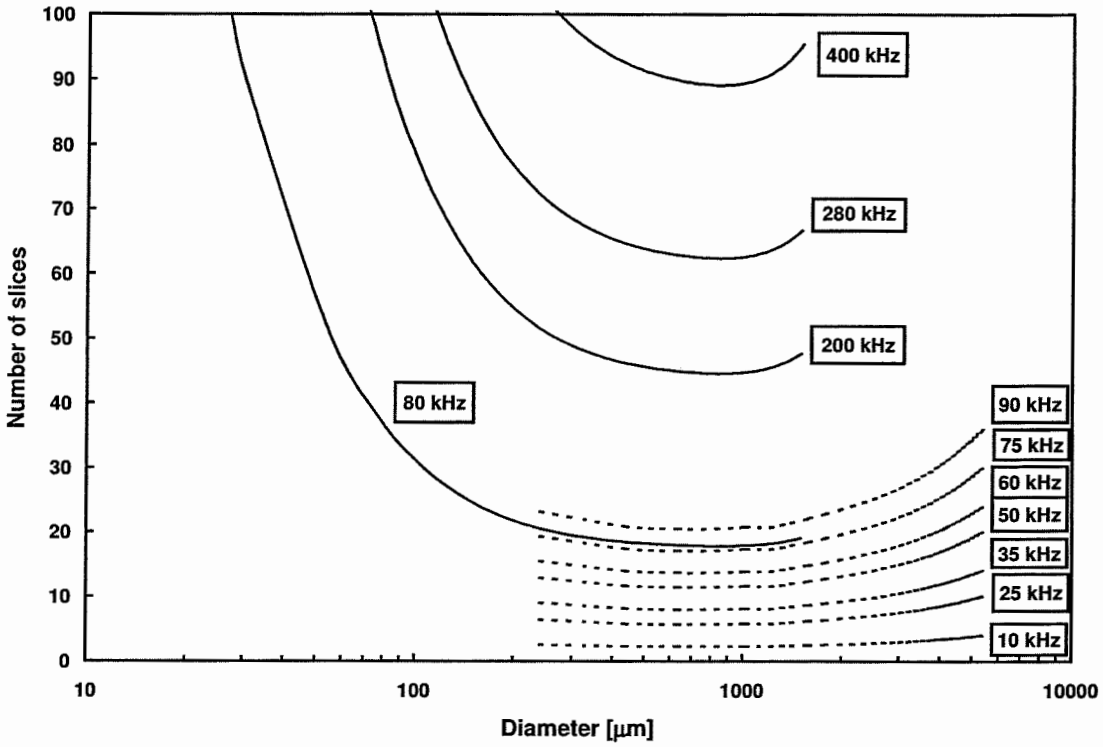

Figure 2. Expected response of the 2D-C (solid lines) and the 2D-P (slashed lines) probes, given a sampling frequency and a drop size. Note that the clock rates of the probes are "slaved" to each other by a factor of eight.

A comparison of the two cases presented in Figure 3 leads to the conclusion that the anomalous increase in fall-speed values for drops less than about 400 μm diameter, as determined with the 2D-C probe, is not due to an instrument malfunction. Instead, this may represent an indication of the presence of satellite droplets produced by the breakup of larger raindrops. In addition, it is possible that the smaller drops are being accelerated because of a "wake effect" due to the presence of relatively larger concentrations of large drops. These microphysical aspects, including uniformity of precipitation events, may be further studied making use of the instruments capabilities shown here to determine drop inter-arrival times.

4. SUMMARY AND CONCLUSIONS

Measurements of shadow images and transit and arrival times of individual raindrops were performed with two OAP's fixed at the surface for operation in a vertical orientation. The particle reconstruction technique includes shape corrections to consider the oblate-like geometry of larger raindrops. These sampling and analyzing procedures allow one to determine the terminal fall-speed of individual drops. It is shown here that the selection of the proper sampling frequency depends on the expected drop-size range The results compare well with previous experimental investigations. Effects on fall velocities of drops due to rainfall origin, in particular for convective events, include possible wake effects due to the presence of relatively larger concentrations of large drops. The use of optical array probes with this technique may prove to be a valuable tool to better understand several precipitation features, including studies on homogeneity and steadiness of rain.

Acknowledgments.

The authors appreciate the continuous technical support provided by Messrs. J. Escalante, W. Gutiérrez, A. Rodríguez and V. Zarraluqui. This research was partially sponsored by DGAPA-UNAM, under grant PAPIIT IN109102-2.

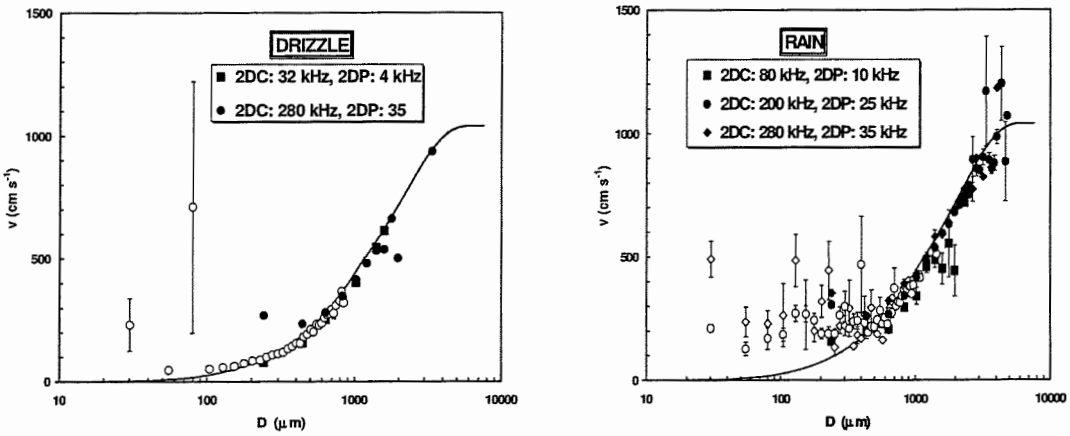

Figure 3. Raindrop fall-speed as a function of drop size, as measured with the 2D-C (○ and ◇) and the 2D-P (●, ■ and ◆) probes, for various sampling frequencies. The left panel includes cases of precipitation of stratiform origin ("drizzle"), and the right panel to convective rain cases. The continuous line shows calculated values based on the parametric equations developed by Beard (1976). Error bars indicate one standard deviation from the average.

REFERENCES

Álvarez P., J.M., and J. Torreblanca B., 1992: *Desarrollo de un Sistema de Software para Interpretación y Análisis de Datos de Espectrómetros de Gotas.* Tesis de Licenciatura. Departamento de Computación, Facultad de Ingeniería, Universidad Nacional Autónoma de México. 150 pp.

Baumgardner, D., G. Kok, W. Dawson, D. O'Connor and R. Newton, 2002: A new groundbased precipitation spectrometer: the Meteorological Particle Sensor (MPS). *Proc. 11th Conf. Cloud Phys.* Amer. Meteor. Soc. [Boston, Mass., USA]. CD-ROM, Paper P8.6, 4 pp.

Beard, K.V., 1976: Terminal velocity and shape of cloud and precipitation drops aloft. *J. Atmos. Sci.*, **33**, 851-864.

Beard, K.V., and H.R. Pruppacher, 1969: A determination of the terminal velocity and drag of small water drops by means of a wind tunnel. *J. Atmos. Sci.*, **26**, 1066-1072.

Best, A.C., 1950: The size distribution of raindrops. *Quart. J. Roy. Meteor. Soc.*, **76**, 16-36.

García-García, F., and R.A. Montañez, 1992: Ground-based raindrop spectra observations for the analysis of summer convective showers in Mexico City. *Proc. 11th Int. Conf. Clouds Precip.* IAMAP/ICCP, **1**, 151-153.

Green, A.W., 1975: An approximation for the shapes of large raindrops. *J. Appl. Meteor.*, **14**, 1578-1583.

Gunn, R., and G.D. Kinzer, 1949: The terminal velocity of fall for water droplets in stagnant air. *J. Meteor.*, **6**, 243-248.

Holroyd, III, E.W., 1986: Surface sampling of a snowstorm by a 2D-C probe with and without aspiration. *J. Atmos. Oceanic Technol.*, **3**, 757-758.

Illingworth, A.J., and C.J. Stevens, 1987: An optical disdrometer for the measurement of raindrop size spectra in windy conditions. *J. Atmos. Oceanic Technol.*, **4**, 411-421.

Joss, J., and A. Waldvogel, 1967: Ein Spektograph für Niederschlagstopfen mit automatische Auswertung. *Pure Appl. Geophys.*, **68**, 240-246.

Knollenberg, R.G., 1970: The optical array: an alternative to scattering and extinction for airborne particle size determination. *J. Appl. Meteor.*, **9**, 86-103.

Knollenberg, R.G., 1981: Techniques for probing cloud microstructure. *Clouds: Their Formation, Optical Properties, and Effects*, P.V. Hobbs and A. Deepak (Eds.), Academic Press, 15-91.

Laws, J.O., 1941: Measurements of the fall-velocity of water-drops and raindrops. *Trans. Amer. Geophys. Union*, **22 (3)**, 709-721.

Lenard, P., 1904: Über Regen. *Meteor. Z.*, **21**, 248-262.

Montañez, R.A., and F. García-García, 1992: Instrumented vehicle for ground-based microphysical observations. *Proc. 11th Int. Conf. Clouds Precip.* IAMAP/ICCP, **2**, 972-974.

Montero, G., and F. García-García, 2004: Multipeak raindrop spectra observations from convective showers in Mexico. *Proc. 14th Int. Conf. Cloud Precip.* IAMAP/ICCP (this volume).

ASSESSING CLOUD SPATIAL AND VERTICAL DISTRIBUTION WITH INFRARED CLOUD ANALYZER

Iliana Genkova[1], Chuck Long[1], Thierry Besnard[2], Didier Gillotay[3]

[1]PNNL, Richland, WA
[2]ATMOS SARL, Le Mans, France
[3]Institut d'Aeronomie Spatiale de Belgique, Brussels, Belgium

1. INTRODUCTION

In the effort to resolve uncertainties about global climate change, the Atmospheric Radiation Measurement (ARM) Program (www.arm.gov) is improving the treatment of cloud radiative forcing and feedbacks in General Circulation Models (GCM). Understanding cloud properties and how to predict them is critical in that cloud properties may very well change as climate changes. The cloud amount at any given time, and cloud horizontal and vertical distribution, are needed for improving the performance of GCMs.

This study is dedicated to assessing cloud spatial and vertical distribution with a recently developed infrared cloud analyzer, named CIR (Cloud Infrared Radiometer). The experiment took place at the ARM Central Facility, located in Oklahoma, USA (36° 37 ' N, 97° 30 ' W). The CIR was deployed and run for approximately three months from February 20, 2003 until June 3rd, 2003. One of the primary purposes of the experiment was to assess the performance and capabilities of the CIR, thus the instrument was located within about 10 meters distance from other ARM instruments used operationally for estimating cloud amount and cloud height.

2. INFRARED CLOUD ANALYZER

The CIR is a commercial instrument produced by ATMOS, France. It operates 7 infrared sensors for the prototype version, each with a 6-degree field of view, and spectral range 8-14 μm. The sensors are mounted at angles 0, 12, 24, 36, 48, 60 and 72 on a semi-circular azimuthally rotating curved band (Fig.1).

They are based on OMEGA OS 65–V-R2-4-BB model pyrometers. The original sensors were modified in order to reduce the total weight from 0.3 to 0.1 kg per sensor, and to prevent the accumulation of liquid water at the optics entrance. The main technical characteristics of the sensor are given in Table 1.

Corresponding author address:Iliana Genkova, Pacific Northwest National Laboratory, P.O. Box 999, MSIN K9-24, Richland, WA 99352, iliana.genkova@pnl.gov

Table 1. Technical characteristics of the pyrometer

Spectral Range	8-14 μm
Temperature range	216K ÷398 K
Temperature accuracy	±1°K
Repeatability	±1°K
Response time	300 ms
Full FOV	11.9
Emissivity	0.1 to 0.99

A "hemispherical" mosaic of 181 brightness temperature measurements centered on the zenith is obtained by the rotation of the semi-circular band around the vertical axis (azimuthally), performing 30 scans, every 12° from 0° (North) to 348 °.

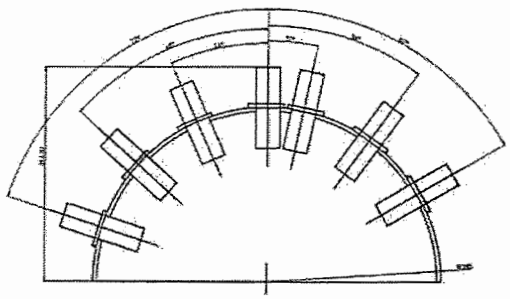

Figure 1. Schematic view of the instrument design

3. MEASUREMENTS

The downward thermal emission from the clouds and the air column between the clouds and the instrument is measured by infrared pyrometers. The temperature of the clouds is derived from a combination of Planck's and Stephan-Boltzmann's laws, resulting in an equation of the general form

$$F = \varepsilon f(T),$$

where F is the downward IR flux integrated for the band pass of the detector (Wm^{-2}), ε is the hemispheric emissivity and f(T) is a 4th-order relationship between temperature and infrared emittance in the spectral range of the detector.

The estimation of the hemispheric emissivity value is of great importance and can significantly affect the quality of the infrared temperature measurement. For practical reasons and in agreement with the values published in the literature, a mean value of $\varepsilon = 0.90$ has been selected for the whole-sky dome in presence or absence of cloud cover. The consequence of this choice is that emissivity variations are not taken into account, inducing some error in the brightness temperature determination. However, temperature differences between cloudy and clear sky conditions are for most cases large enough for discrimination.
As mentioned above, the variability of the hemispherical emissivity is not taken into account. The mean value ($\varepsilon = 0.90$) seems to be reasonable to describe practically all type of clouds. However, cirrus clouds with very variable emmissivity factors (0.7-1.0) will likely be poorly identified by this method.
A second source of error could be induced by the composition of the lower layer of the troposphere (0-2 km). An atmosphere rich in greenhouse effect constituents like ozone, carbon dioxide, water vapor can affect significantly the downward IR flux, and consequently the measured temperature. This contribution will depend of course on the zenith angle (minimum influence at the zenith and maximum for the observations close to the horizon).
Finally, under clear sky or broken clouds conditions, the presence of direct sun radiation will disturb the temperature determination, but only in one solid angle element. This disturbance can be useful to determine the presence or absence of direct sun radiations.

To account for the uncertainty in the emissivity, we suggest and apply an algorithm that utilizes the brightness temperatures from the CIR and given the precipitable water vapor amounts and vertical profiles of the thermodynamic state of the atmosphere from independent measurements, derives *clear sky brightness temperature thresholds* as a function of the precipitable water vapor. Line-by-Line Radiative Transfer Model is used to calculate the thresholds. The brightness temperatures measured by the CIR are then compared to these thresholds to classify a scene as clear or cloudy

4. RESULTS

The results presented below are for March, 2003. Figure 2 compares the day-time cloud amount (CA) frequency distributions as retrieved by a Whole Sky Imager (WSI) (dark blue bars) (Slater, 2002), Total Sky Imager (TSI) (blue bars) (Long, 2000), SW Flux Analysis (SWFA) (cyan bars) (Long, 1999), Nephelo (yellow bars), effective fractional sky cover *Ne* from spectral interferometer data (AERI Ne)(orange bars) (Takara, 2003) and the opaque portion of the TSI measured sky cover (TSI Opaque) (brown bars).
We note a difference between the CIR cloudiness histogram and the other retrievals. However, one must

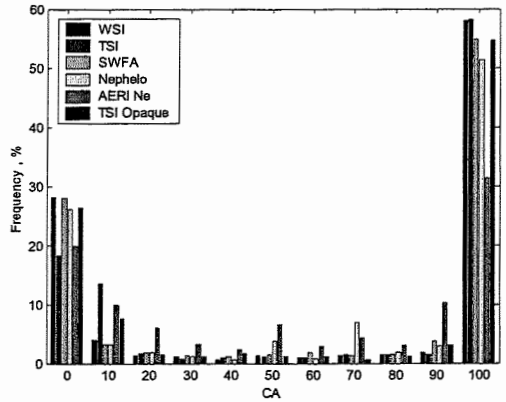

Figure 2. Frequency distribution of cloud amounts retrieved with various techniques during day-time

keep in mind that these techniques are based on differences in physical phenomena, spectral ranges, fields-of-view, and time resolution. The correlation coefficients between the CIR cloud amounts and the cloudiness from other retrievals are: 0.73 with WSI, 0.73 with TSI, 0.77 with TSI Opaque, 0.75 with SWFA, 0.51 with AERI's *Ne*.
The best agreement is observed with TSI opaque cloud amounts. This result confirms our expectation that the CIR more easily detects opaque clouds.
One of the CIR advantages is its ability to assess night-time cloud distributions. We study the CIR performance by comparing it to the WSI (the whole sky imager is the only hemispherical night time imager available at the ARM Central Facility). Figure 3 illustrates the cloud amount (CA) frequency distribution for WSI and the CIR. The correlation coefficient is 0.69.

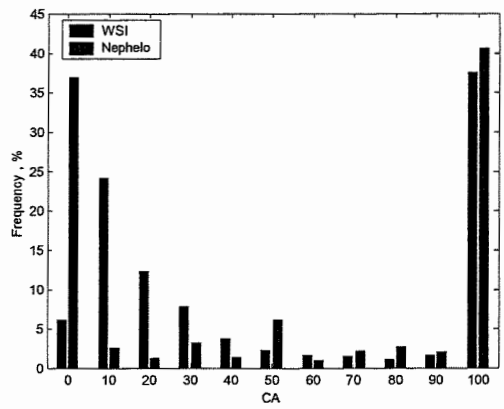

Figure 3. Frequency distribution of cloud amounts retrieved with two techniques during night-time

Figure 4 shows an example of a 24-hour record of CIR cloud amounts along with the other available techniques. During the night, the difference between the WSI and CIR CA varies from 5% to 50%. Some of

this disagreement is a manifestation of the uncertainty in the cloud emissivity, as explained above. We also speculate that another possible reason for the difference is the fact that the WSI has not been compared to any other instrument to date. Hence, the WSI CA uncertainty is unknown, and thus could be somewhat suspect.

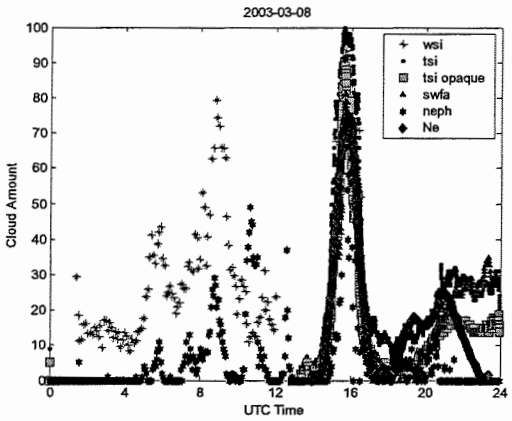

Figure 4. Cloud amounts for March 8, 2003

Once measured, the brightness temperature of the cloud can be easily converted to cloud height, given a vertical profile of the atmospheric state. This approach was applied to the Nephelo's data to assess the vertical distribution of clouds as depicted in Figure 5. The estimated cloud base height is first retrieved using all 7 CIR sensors (CIR), and then using only the top 3 sensors, thus allowing for a smaller FOV of 40 deg. These two time series are compared to an independant cloud base retrieval (ARSCL) (Clothiaux, 2000), and to a Vaisala ceilometer measurement (VCEIL). Our study shows that the CIR cloud base heights agree with the other retrievals under two conditions - warm low clouds and high cloud amounts.

5. CONCLUSIONS

We have investigated the possibility of estimation horizontal and vertical cloud distribution with a recently developed infrared cloud imager. We suggest an algorithm that utilizes the brightness temperatures from the CIR, given precipitable water vapor amounts and vertical profiles of the thermodynamic state of the atmosphere from independent measurements. The algorithm estimates the cloud amount and determines the vertical distribution of the clouds. We have tested the algorithm and the instrument performance through inter-comparison with well-studied ground-based retrieval techniques developed within the ARM Program.

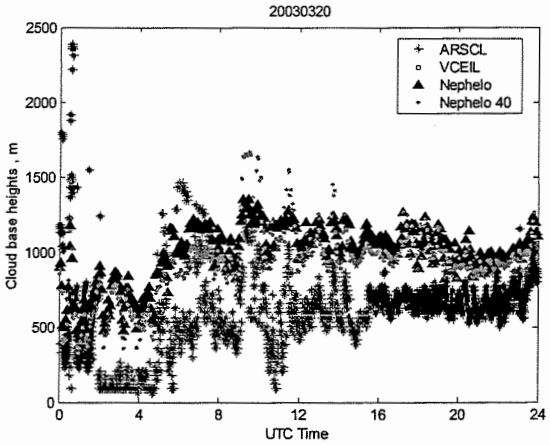

Figure 5. Cloud base heights for March 20, 2003

Initial analyses show good cloud amount assessment and spatial mapping abilities. The vertical distribution retrieval is currently limited, however the amounts of low, middle and high clouds could be determined and studied further.

Acknowledgement: Authors would like to thank Dave Turner from PNNL for his helpful comments and the Line-By-Line radiative transfer model runs.

6. REFERENCE

Clothiaux, E.E., T.P. Ackerman, G.G. Mace, K.P. Moran, R.T. Marchand, M.A. Miller, and B.E. Martner, 2000: Objective determination of cloud heights and radar reflectivities using a combination of active remote sensors at the ARM CART sites. J. Appl. Meteor., 39, 645-665

Long, C., T. Ackerman, J. J. DeLuisi, and J. Augustine, 1999: Estimation of Fractional Sky Cover from Broadband SW Radiometer Measurements, Proc. 10th Conf. on Atmos. Rad., June 28-July 2, 1999, Madison, Wisconsin.

Long, C., D. Slater, and T. Tooman, 2000: Total Sky Imager (TSI) Model 880 Status and Testing Results. ARM Report, Proc. 11th ARM STM, April 8-12, 2002, St. Petersburg, Florida

Slater, D. W., Long, C. N., and Tooman, T. P., 2002: Comparison of the TSI/WSI Cloud Fraction Estimates at the SGP, Proc. 12th ARM STM, April 8-12, 2002, St. Petersburg, Florida

Takara, E. E. and R. G. Ellingson,2003: Using Narrow and Wide Field of View Instruments to Evaluate Longwave Parameterizations for Fair Weather Cumulus Cloud Fields. Proc. 13th ARM STM, March 31-April 4, 2003, Broomfield, Colorado

NEPHELOMETER MEASUREMENTS IN FLORIDA THUNDERSTORMS

H. Gerber[1], T. Garrett[2], A. Heymsfield[3], M. Poellot[4], C. Twohy[5]

[1]Gerber Scientific Inc., Reston, VA 20190
[2]University of Utah, Salt Lake City, UT 84112
[3]National Center for Atmospheric Research, Boulder, CO 80307
[4]University of North Dakota, Grand Forks, ND 58202
[5]Oregon State University, Corvallis, OR 97331

1. INTRODUCTION

The CRYSTAL-FACE study was held in southern Florida in the summer of the 2002 for the purpose of measuring and modeling thunderstorms and their anvils. This study provided an opportunity of deploy two cloud integrating nephelometers (CIN; Gerber et al, 2000; Garrett et al, 2001), one on the NASA WB-57 aircraft and the other on the U. of North Dakota Citation aircraft. The CIN measures in situ the optical extinction coefficient and asymmetry parameter of cloud particles, and in combination with the counter-flow virtual impactor (CVI, Twohy et al, 1997) also measures the effective radius of the particles. A brief description of the CIN is given here, and some of the experimental results are presented.

2. CIN

The CIN mounted to an aircraft is shown in Fig. 1. It

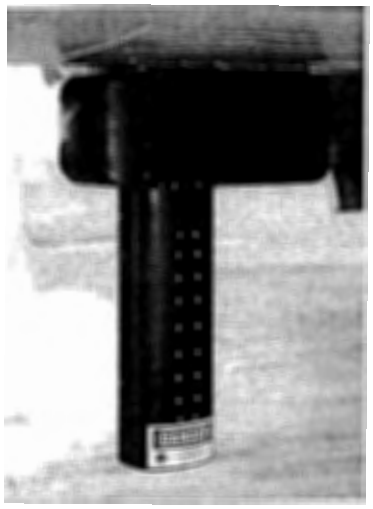

Fig. 1 - Cloud Integrating Nephelometer

consists of an electronic box on which is mounted a split elliptical strut that is separated to permit airflow and the passage of a 635-nm laser beam. The long dimension of the strut faces into the direction of flight. Four detectors with Lambertian response are mounted on the inner surfaces of the strut, two detectors have in addition cosine-response masks. The arrangement of laser beam and detectors in the CIN is illustrated in Fig. 2. Light scattered by cloud particles passing

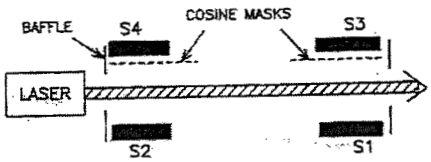

Fig. 2 - Schematic of CIN optics, S denotes sensors with Lambertian response.

through the laser beam is measured by the detectors whose output is combined with a simple analytical function to yield the extinction coefficient and the asymmetry parameter, g. The detectors integrate the scattered-light phase function over an angular range that permits measurement of primarily the diffracted portion of the scattered light which is nearly half of the total scattered light.

The CIN is about 50-cm long, has a sample volume of 30 cm^3, and weighs about 25 lbs. It provides seamless integrated measurements for particle sizes from about 5-um to 2,500-um diameter.

3. MEASUREMENTS

The following provides a few examples of measurements made with the CIN, CVI, and the CPI (cloud-particle imager; SPEC) on the the U.N.D. Citation aircraft in flights through the Florida thunderstorms and their anvils. Figure 3 shows CIN extinction measurements made on 16 July, 2002 while the Citation spiraled upward through an aged anvil near the CRYSTAL-FACE western-coast ground site (1), and flew transects at ever lower altitudes through a new anvil (3). The maximum extinction (2) corresponds to about a visual range of 20m, and is caused by a large density of small ice crystals formed near the anvil's source. The spiral through the aged anvil is unusual in that extinction decreases with

Corresponding author's address. H. Gerber, Gerber Scientific Inc., 1643 Bentana Way, Reston, VA 20190, USA, E-Mail: hgerber6@comcast.net

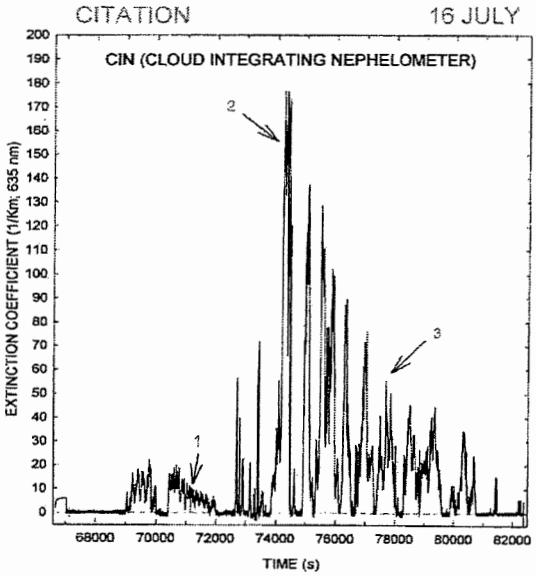

Fig. 3 - Extinction coefficient measured in two anvil clouds (1) and (3).

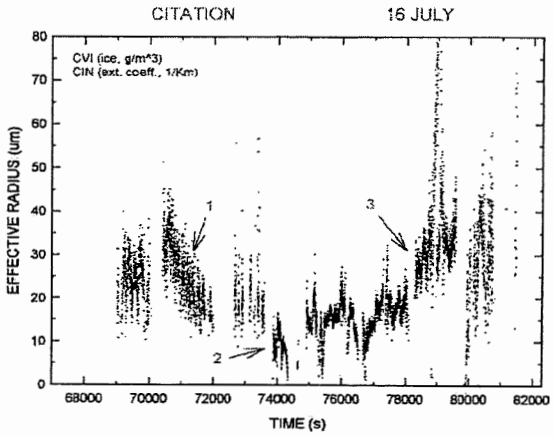

Fig. 4 - Effective radius of the anvil ice crystal for the same flight segment as shown in Fig. 3.

height in the anvil, rather than increasing which is the norm in the less aged anvils.

The effective radius, Re, derived from the CIN and CVI data for the same Citation flight interval as shown in Fig. 3 is shown in Fig. 4. Re is calculated (Gerber et al, 1995) using

$$\mathrm{Re} = \frac{3}{\rho_i} \frac{\sum IWC}{\sum PSA}$$

where ρ_i is the bulk density of ice, *IWC* is the ice water content measured by the CVI, and *PSA* is the total particle surface area which is directly porportional to the particles' extinction coefficient measured by the CIN.

Figure 4 shows that Re decreases with height in the two anvils, which is also the norm for other anvils. The smallest values of Re ~ 10-um radius, (2) in Fig. 4, is found for the largest extinctions shown in Fig. 3 and coincides with the small ice crystals found at that location.

Figure 5 gives the composite of all g values measured during the Citation flights that were made almost exclusively in clouds containing only ice crystals. The overall average g value is 0.73 +/- .015, and the approximately Gaussian curve about this average is not broad. An attempt was made to relate ice-crystal shapes as observed with the CPI with the values of g. This proved to be difficult, given the relatively small variation in the g composite. However, some generalizations can be attempted:

The smallest values of g, some smaller than 0.7, often correlate with densely-packed ice crystal aggregates. See the left-most CPI image in Fig. 5, and also see Table 1 which summarizes the given images.

#	g	T(°C)	H(m)
1	.681 +/- .013	-38	10,000
2	.737 +/- .006	-49	12,000
3	.767 +/- .007	-46	10,400
4	.860 +/- .024	-5	5,500

Table 1 - g value, temperature T, and Citation aircraft altitude H, corresponding to the CPI images (# left to right) shown in Fig. 5.

The second image corresponds to the anvil location (2) indicated in Figs. 3 and 4. Here we see small ice crystals that are often loosely coagulated into a form resembling chain aggregates. The third image shows single ice crystals in the form of bullet rosettes. Single crystals were a rarity in all the Citation flights. The fourth image shows supercooled water droplets during a flight not far from the base of a cumulus cloud. The liquid water and ice phases are readily discernable with the CIN, because separation between g values for ice and water is significant.

The relatively small values of g in the Fig. 5 composite are consistent with the general complexity of the ice crystals observed during CRYSTAL-FACE. It is suggested that ice clouds with less vigorous turbulence and mixing than the thunderstorms would produce more single crystals and larger values of g.

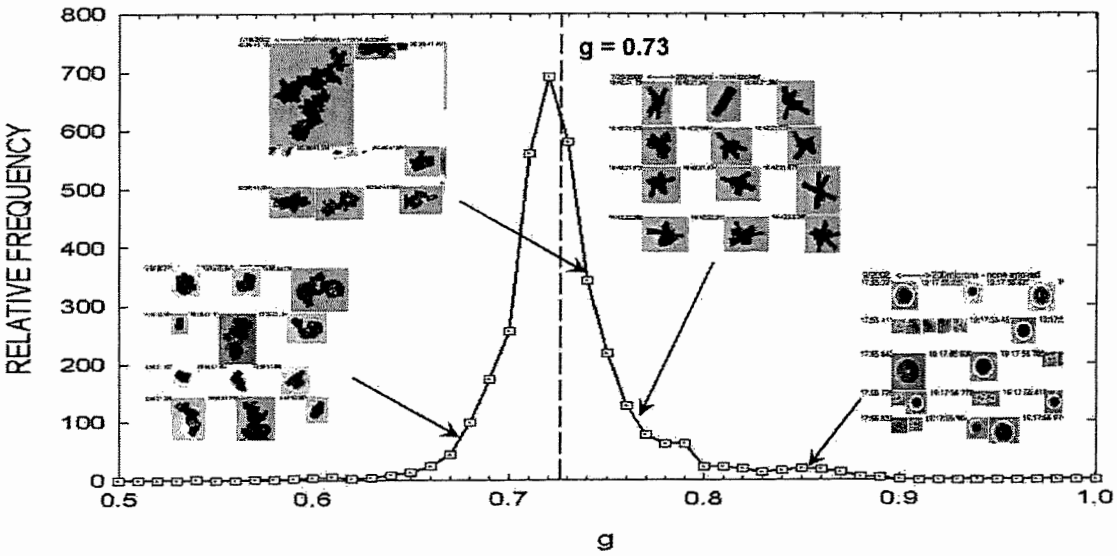

Fig. 5 - Composite frequency distribution of the asymmetry parameter, g, measured on all flights of the U. of North Dakota Citation aircraft during the CRYSTAL-FACE study. The ice-crystal and water droplet images were collected with the NCAR CPI

5. ACKNOWLEDGMENT

The crew of the University of North Dakota Citation aircraft is thanked for their expert and dedicated effort during CRYSTAL FACE, for deploying the CIN on their aircraft, and for logging the data. H.G. was supported by NASA Grant NAG5-11618.

6. REFERENCES

Garrett, T.J., P.V. Hobbs, and H. Gerber, 2001: Shortwave, single-scattering properties of arctic ice clouds. *J. Geophys, Res.*, **106**, 15,155-15,172.

Gerber, H., P.J. DeMott, and D.C. Rogers, 1995: Laboratory investigation of direct measurement of ice water content, ice surface area, and effective radius using a laser-diffraction instrument. *Final Report, Grant NAS2-14261*. NASA Ames Research Center, pp. 142.

Gerber, H., Y. Takano, T.J. Garrett, and P.V. Hobbs, 2000: Nephelometer measurements of the asymmetry parameter, volume extinction coefficient, and backscatter ratio in Arctic clouds. *J. Atmos. Sci.*, **57**, 3021-3034.

Twohy, C.H., A.J. Schanot, and W.A. Cooper, 1997: Measurement of condensed water content in liquid abd ice clouds using an airborne counterflow virtual impactor. *J. Atmos. Oceanic Technol.*, **14**, 197-202.

FLOW FIELD AND PARTICLE TRAJECTORY SIMULATIONS OF A STRATOSPHERIC COUNTERFLOW VIRTUAL IMPACTOR

Måns Håkansson[1], Kevin J. Noone[1], Johan Ström[2]

[1]Department of Meteorology, Stockholm University, S-10691 Stockholm, Sweden
[2] Institute of Applied Environmental Research, Stockholm University, S-10691 Stockholm, Sweden

1. INTRODUCTION

Direct measurements of the chemical composition of polar stratospheric clouds (PSCs) and the properties of cirrus clouds in the tropical tropopause region have proven to be very difficult to obtain. Despite the importance of PSCs to the Antarctic and Arctic "ozone hole" phenomenon, and of tropical cirrus clouds to climate and the transport of water into the stratosphere, the difficulties associated with making direct, *in situ* measurements in these clouds have limited our ability to fully understand their properties.

To this end, a Counterflow Virtual Impactor (CVI) payload was designed and developed for use on the Russian M-55 *Geophysika* stratospheric research aircraft.

The CVI system was deployed for the first time on the M-55 *Geophysika* during a test campaign in Forlí, Italy, and in the APE-THESEO field campaign in the Seychelles in 1999 [*Stefanutti et al.*, 2004]. Instrumentation to measure the condensed water content, nitric acid concentration in the condensed phase, and crystal number concentration was attached to the probe. While some success was achieved with the payload in these campaigns, there were instances where the behavior of the sampling system was difficult to interpret. The purpose of our modeling activities discussed here is to better determine the sampling characteristics of the CVI system so that it may be used in future deployments, and to enable us to more fully interpret and exploit the past data produced by the instruments associated with the CVI.

In this paper, we present flow field and particle trajectory simulations for this CVI system. The simulations were carried out for typical conditions encountered in the tropical lower stratosphere during the APE-THESEO experiment. We examine the flow field and particle trajectories inside and outside the probe for different particle sizes and different attack angles of the CVI inlet.

Corresponding author's address: Kevin J. Noone, Department of Meteorology, Stockholm University, S-10691 Stockholm SWEDEN; E-Mail: zippy@misu.su.se.

2. PROBE AND MODEL GEOMETRY

Figure 1 shows an image of the actual CVI probe flown on the *Geophysika* taken during the APE-THESEO field campaign for comparison with the model geometry shown in Fig. 2. The probe was mounted on the starboard side of the aircraft, below the cockpit and ahead of the engine inlet. The probe was pitched downward to compensate for the average upward pitch of the aircraft during measurement legs.

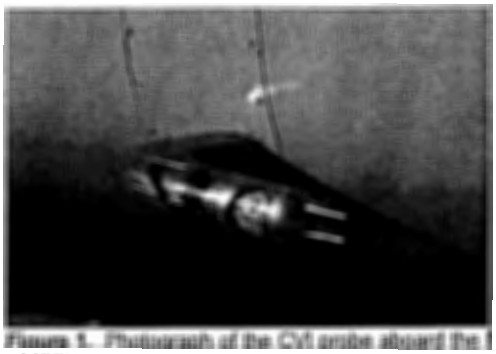

Figure 1. Photograph of the CVI probe aboard the M-55 *Geophysika* during the APE-THESEO campaign.

Figure 2 shows the model geometry for the external parts of the probe, and the grid on which the flow, pressure, etc. fields are calculated.

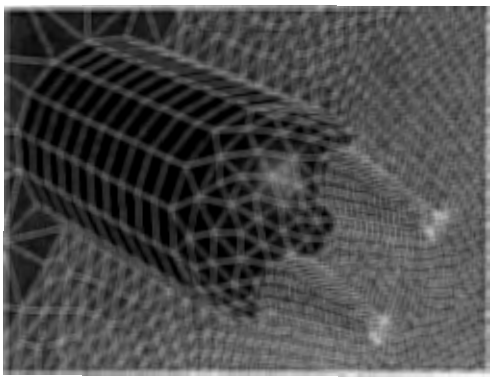

Figure 2. Modeled probe external geometry and solver grid.

3. MODEL DESCRIPTION

We are using the state-of-the-art Computational Fluid Dynamics (CFD) software package FLUENT®. The code is specifically derived for modeling fluid flow and heat transfer in complex geometries by solving the Reynolds-averaged Navier-Stokes (RANS) equations with a finite elements method (FEM). A multitude of flow situations and parameterization strategies are covered by the package which also features a separate program, GAMBIT, made for the implementation of the model geometry and generation of the grid to be used in the numerical simulations.

The model domain is divided into grid cells of varying sizes, with the highest resolution in the vicinity of the twin tips at the probe head (shown in Figure 2). Because of the geometrical shape of the problem at hand, a grid consisting mainly of tetrahedrons was chosen. The gridded volume is then imported into FLUENT where it is slightly adjusted for improved numerical consistency.

Once the probe geometry was created and a computational grid developed, calculations were performed to simulate the flow field around the probe for the conditions "typical" for the APE-THESEO flights. State variables were set to a temperature of 200K and a pressure of 50mb. Calculations were performed for two angles of attack – 0 and 5 degrees. The purpose of these calculations was to see whether changing the angle of attack of the probe could cause any serious changes in the flow field near the probe inlets, which may themselves influence the sampling characteristics of the probe.

4. EXAMPLE RESULTS

4.1 External Flow Field

Figure 3 shows the external flow streamlines for the CVI calculated for a zero degree angle of attack.

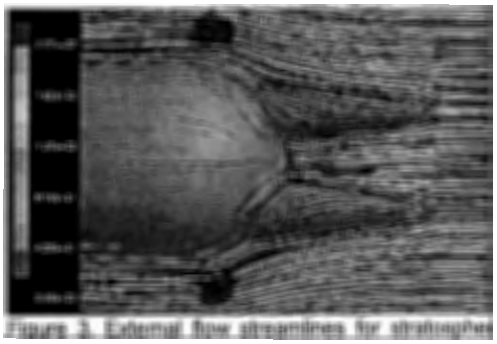

Figure 3. External flow streamlines for stratospheric conditions.

The disturbance in the flow field due to the presence of the probe does not propagate upstream more than roughly the diameter of the probe tip. Closer examination of the flow near the probe tips shows that separation can occur aft of the edge of the probe tip, but that this separation does not influence the flow field upstream of the probe or at the probe inlets.

4.2 Internal Flow Field

Figure 5 depicts a cross-section of the probe, and shows both the internal and external probe geometry and flow fields for one of the two CVI inlets, calculated for a zero angle of attack.

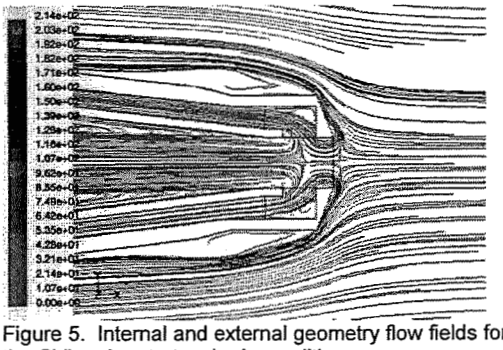

Figure 5. Internal and external geometry flow fields for the CVI under stratospheric conditions.

Carrier gas flows in the annular region between the external probe tip and an internal solid tube. The carrier gas is forced through a short length of porous stainless steel that connects the external and internal parts.

Two stagnation planes can be seen in the flow field. The first, located just ahead of the probe inlet, separates the external air from the carrier gas inside the probe. The calculations show that no external air is aspirated into the CVI. The second stagnation plane is located just aft of the inlet, roughly half way down the length of the porous tube inside the probe tip. This stagnation plane separates the carrier gas that is forced out the tip of the probe from the gas flows to the instrumentation in the CVI payload. In order to be sampled, cloud droplets or crystals must have sufficient inertia that they can deviate from the flow streamlines around the CVI inlet, and proceed through the two stagnation planes.

4.3 Particle Trajectories

Figures 6, 7 and 8 show trajectories for particles of 2, 2.5 and 3 μm diameter for a zero angle of attack. Particles (assumed to be sulfuric acid droplets) are imbedded at evenly-spaced intervals in the free-stream flow ahead of the CVI probe. Figure 6 shows that none of the 2μm particles has sufficient inertia to enter the probe and be sampled. Figure 7 shows that all the 2.5μm particles within the area swept out by the probe inlet are sampled by the CVI. Particles on grazing trajectories are assumed to bounce off the wall of the probe.

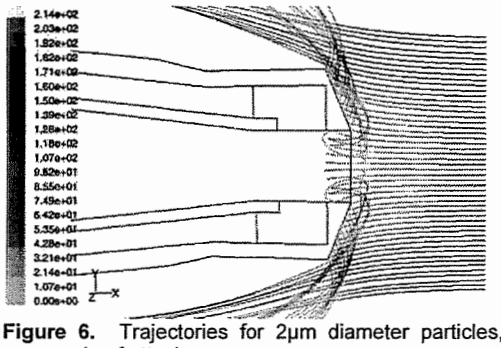

Figure 6. Trajectories for 2μm diameter particles, zero angle of attack.

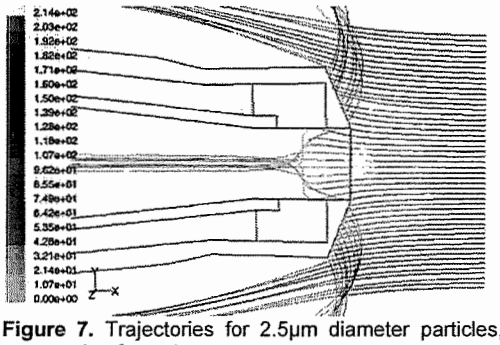

Figure 7. Trajectories for 2.5μm diameter particles, zero angle of attack.

The internal flow field concentrates the 2.5μm particles near the centerline of the probe, minimizing any contact with the interior walls of the CVI near the probe tip.

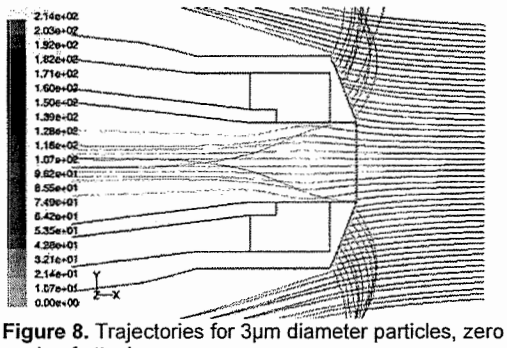

Figure 8. Trajectories for 3μm diameter particles, zero angle of attack.

Figure 8 shows that all of the 3μm particles are sampled by the CVI, and that they are less concentrated at the probe centerline than the smaller 2.5μm particles.

The calculated sampling efficiency for this particular CVI geometry under stratospheric conditions is rather sharp – going from zero at 2μm to unity at 2.5μm.

4.4 Non-zero Angle of Attack

Figure 9 shows trajectories calculated for 3μm particles when the probe is at a five degree angle of attack.

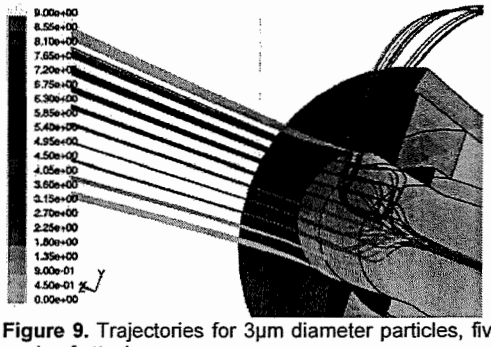

Figure 9. Trajectories for 3μm diameter particles, five angle of attack.

At a zero degree angle of attack (as shown in Fig. 8), all of the 3μm particles are sampled. At a five degree angle of attack, some of the particles are rejected. The interior flow field and trajectories of the sampled particles are not substantially altered. The calculated effect of a non-zero angle attack does not lead to any contamination by outside air, but it will broaden the sampling efficiency vs. particle size relationship.

5. DISCUSSION

Experimental calibrations of land-based CVIs [*Anderson et al.*, 1993; *Noone et al.*, 1988] have shown that the general sampling characteristics of the CVI can be predicted using Stokes' theory. Previous model calculations using an idealized potential flow approach [*Lin and Heintzenberg*, 1995; *Lin and Noone*, 1996] were consistent with experimental calibration results, and showed rather sharp sampling efficiency vs. size curves, with high sampling efficiencies for droplets larger then the 50% cut size for the modeled probe. A modeling study of an airborne CVI probe using a different computational fluid dynamics program [*Laucks and Twohy*, 1998] indicated that the sampling efficiency for large droplets for this particular probe were well below unity. Comparisons between land-based [*Hallberg et al.*, 1994] and airborne [*Glantz et al.*, 2003] CVIs and Forward Scattering Spectrometer Probes (FSSPs) showed good agreement between the two independent measurement systems, indicating a relatively high sampling efficiency. The lower efficiencies calculated in the [*Laucks and Twohy*, 1998] study may be due to the particular geometry of their probe.

The calculations presented here are the first carried out for a stratospheric CVI system. The results of the

calculations suggest that, under stratospheric conditions

- The sampling efficiency vs. size for this CVI geometry goes from zero for 2μm particles to near unity for 2.5μm particles;
- A five degree angle of attack will broaden the sampling efficiency vs. size behavior of the CVI, but does not lead to contamination of the CVI sample stream by ambient air.

Further calculations will be carried out for different particle compositions and shapes. In addition, we plan to examine the energy of the collisions between particles on grazing trajectories with the interior walls of the inlet to see whether droplet/crystal shattering or etching of the interior surface of the CVI can be possible.

7. ACKNOWLEDGEMENTS

This research has been supported by the European Commission APE-INFRA project.

7. REFERENCES

Anderson, T.L., R.J. Charlson, and D.S. Covert, Calibration of a counterflow virtual impactor at aerodynamic diameters from 1 to 15 μm, *Aerosol Sci. Tech.*, *19*, 317-329, 1993.

Glantz, P., K.J. Noone, and S.R. Osborne, Comparisons of airborne CVI and FSSP measurements of cloud droplet number concentrations in marine stratocumulus clouds, *J. Atmos. Ocean Technol.*, *20* (1), 133-142, 2003.

Hallberg, A., K.J. Noone, J.A. Ogren, I.B. Svenningsson, A. Flossmann, A. Wiedensohler, H.-C. Hansson, J. Heintzenberg, T. Anderson, B. Arends, and R. Maser, Phase partitioning of aerosol particles in clouds at Kleiner Feldberg, *J. Atmos. Chem.*, *19*, 107-127, 1994.

Laucks, M.L., and C.H. Twohy, Size Dependent Collection Efficiency of an Airborne Counterflow Virtual Impactor, *Aerosol Sci. Technol.*, *28* (1), 40-61, 1998.

Lin, H., and J. Heintzenberg, A Theoretical Study of the Counterflow Virtual Impactor, *J. Aerosol Sci.*, *26* (6), 903-914, 1995.

Lin, H., and K.J. Noone, A Simulation of Cloud Formation and Sampling using the Counterflow Virtual Impactor, *Beitr. Phys. Atmosph.*, *69* (2), 321-332, 1996.

Noone, K.J., J.A. Ogren, J. Heintzenberg, R.J. Charlson, and D.S. Covert, Design and calibration of a counterflow virtual impactor for sampling of atmospheric fog and cloud droplets, *Aerosol Sci. Tech.*, *8*, 235-244, 1988.

Stefanutti, L., A.R. MacKenzie, V. Santacesaria, A. Adriani, S. Balestri, S. Borrmann, V. Khattatov, P. Mazzinghi, V. Mitev, V. Rudakov, C. Schiller, G. Toci, M. Volk, V. Yushkov, H. Flentje, C. Kiemle, G. Redaelli, K.S. Carslaw, K. Noone, and T. Peter, The APE-THESEO tropical campaign: An overview, *J. Atmos. Chem.*, in press, 2004.

MEASUREMENTS OF "LARGE" CCN

James G.Hudson[1] and Seong Soo Yum[2]

[1]Division of Atmospheric Sciences, Desert Research Institute, Reno, Nevada, 89512-1095, USA
[2]Department of Atmospheric Sciences, Yonsei University, Seoul 120-749, South Korea

1. INTRODUCTION

Traditional cloud condensation nuclei (CCN) instruments can discriminate particles according to critical supersaturation (S_c) only over the Aitken nuclei range (diameter < ~ 0.1 μm) because they cannot successfully operate at supersaturations (S) below 0.1%. This is mainly due to the difficulty of distinguishing unactivated haze droplets from activated cloud droplets at the lower growth rates available at lower S. However, since a large proportion, often a majority, of CCN have S_c below 0.1% it is highly desirable to extend the S range lower so that discrimination according to S_c can be accomplished in the Large nuclei range (diameter ~ 0.1-1 μm). There are numerous significant reasons for this extension of CCN range:

1) S can be less than 0.1% especially in stratiform type clouds with lower updrafts or clouds with higher droplet concentrations due to continental or especially polluted air masses.

2) Static (first) CCN closure-- comparisons of measured aerosol size and composition with measured CCN--requires accurate and **complete** spectra. Otherwise unique solutions are not possible.

3) Dynamic (second) CCN closure--comparisons of predictions of cloud droplet concentrations (or even spectra) based upon measured CCN spectra and measured updraft velocities with measured cloud droplet concentrations (or even spectra)--requires **complete** CCN spectra. This is because the amount of water that is condensed depends strongly on the inverse of S_c.

4) Large nuclei may be drizzle embryos.

5) Cloud droplet spectral width, which is so important for precipitation initiation, depends on complete CCN spectra (e.g., Takeda and Kuba 1982; Miles et al. 2000).

6) Very difficult and as yet controversial Giant nuclei (diameter > 1 μm) measurements would be more credible if consistent with Large nuclei measurements, especially if those are consistent with traditional CCN measurements (Aitken range), which already have a climatology.

Corresponding author's address: James G. Hudson, Division of Atmospheric Sciences, Desert Research Institute, 2215 Raggio Pkwy., Reno, NV 89512-1095, USA: E-mail: hudson@dri.edu.

7) Wider CCN spectral measurements are needed in order to obtain accurate measurements of the sizes of ambient CCN (Hudson and Da 1996). This is because variations in particle composition cause greater variations in S_c.

The Desert Research Institute (DRI) CCN spectrometers (Hudson 1989) are able to estimate below 0.1% because they deduce particle S_c by comparing droplet sizes grown on ambient particles with those grown on particles of known Sc under identical conditions. This means that the S range is only limited by the size range of the calibration particles. The correctness and accuracy of the DRI instruments can be tested by operating the two DRI instruments at different S ranges. These tests are especially important to test the extension of the measurements into the Large nuclei range. There is less controversy about the accuracy of these instruments at the upper ends of their ranges where they are operating essentially almost at the maximum S as determined by the maximum delta temperature (T) of the parallel plates. It is at the lower end of the S ranges that CCN spectrometry is more challenging. Therefore, concentrations at the upper end of the S range of the instrument that is operating over a more limited range of S (lower S range) can be considered as an accurate standard to judge the performance of the larger S range instrument. Agreement between the two instruments over the S range of overlap may be considered as evidence of the accuracy of the spectra of the higher range instrument. Agreement (accuracy) at the overlap would also suggest accuracy at higher S where the instrument is less spectrally challenged.

The DRI CCN spectrometers are distinguished by their age--old and new. The newer cloud chamber is slightly smaller and has fewer temperature-controlled sections--6 instead of 8. That is, it is essentially 6 thermal gradient diffusion chambers in series instead of 8 for the older instrument. Both are calibrated with the same series of variously sized monodisperse salt aerosols.

2. RESULTS

Figure 1 shows examples of agreement of differential spectra in the overlapping S range of 0.1-0.4%. Disagreement below 0.1% S is mainly caused by spectral broadening and coincidence events in the higher S range instrument. Usually coincidence seems to more likely be the problem because there is usually greater lower S disagreement when concentrations are higher.

Figure 1. Differential CCN spectra measured at the surface at the ARM-CART site in Oklahoma, USA on May 23, 2003. The first panel shows data obtained between 0915 and 1030 and the second panel shows data obtained between 1246 and 1310. The solid lines show data from the newer spectrometer that was operating with maximum plate delta T of 8.0C, while the symbols ((triangles) show data from the older spectrometer operating with a maximum plate delta T of 6.3C.

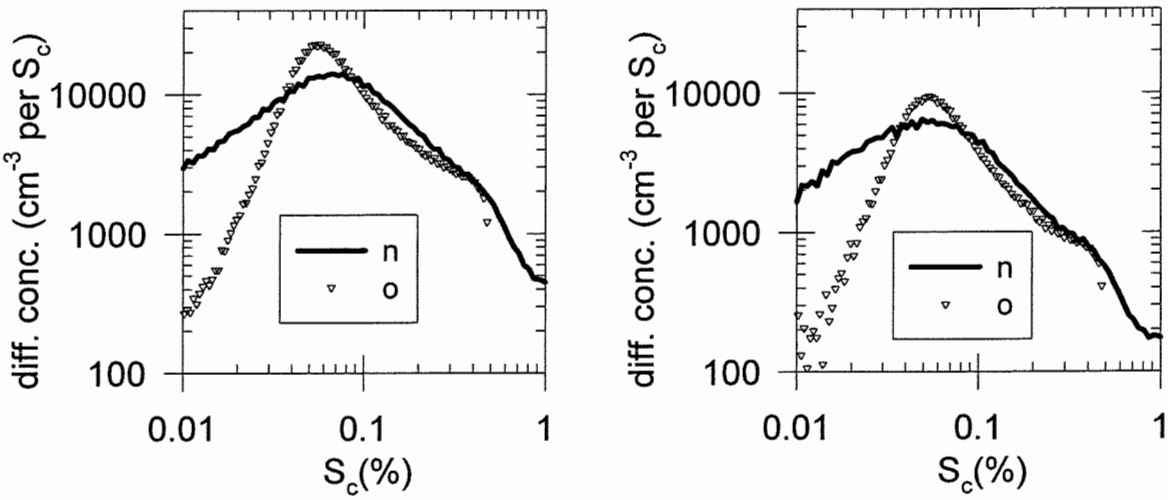

Figure 2. Data as Fig. 1 but a time plot of differential concentrations within the S range of 0.4-0.1%. New spec. data is solid line and old spectrometer is symbols.

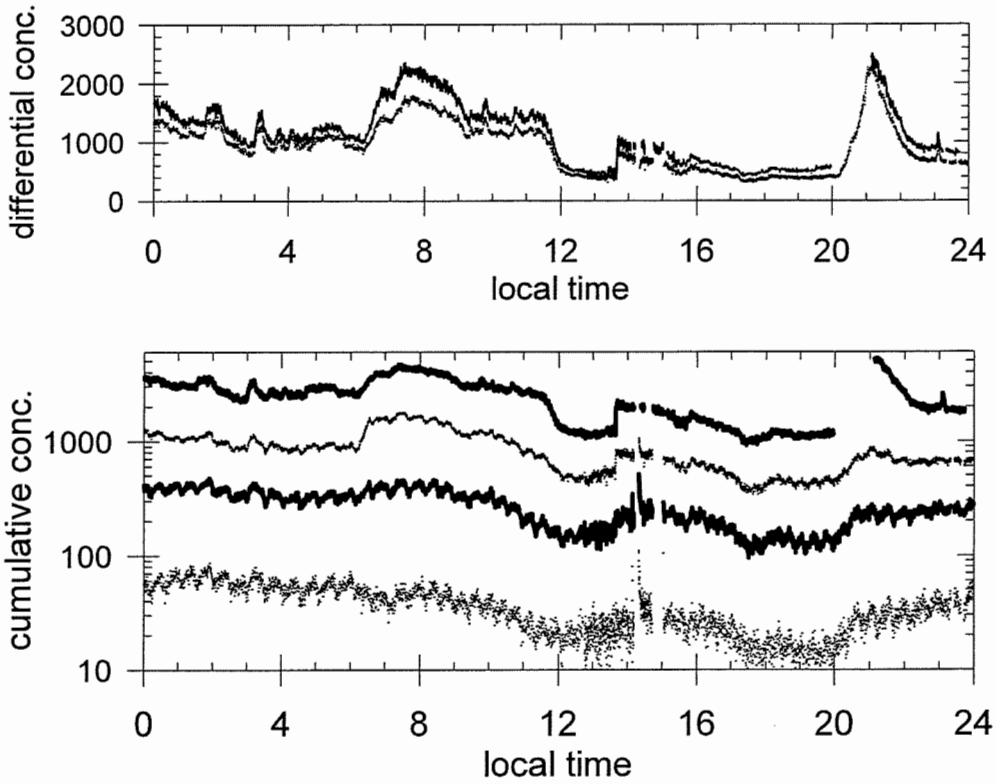

Figure 3. As Fig. 2 but cumulative number concentrations at S of 1.0% (new spec.) and 0.1%, 0.05%, and 0.03% (old spec.).

Figure 4. As Fig. 1 but at Reno, Nevada, USA on September 30, 2003. The first panel shows data obtained between 1756 and 1815 on inside (room) air and the second panel shows data obtained between 2135 and 2146 from a duct to outside air. The solid lines show data from the older spectrometer that was operating with maximum plate delta T of 9.49C, while the symbols ((triangles) show data from the newer spectrometer operating with a maximum plate delta T of 3.0C. The instruments are thus reversed with respect to Figs. 1-3.

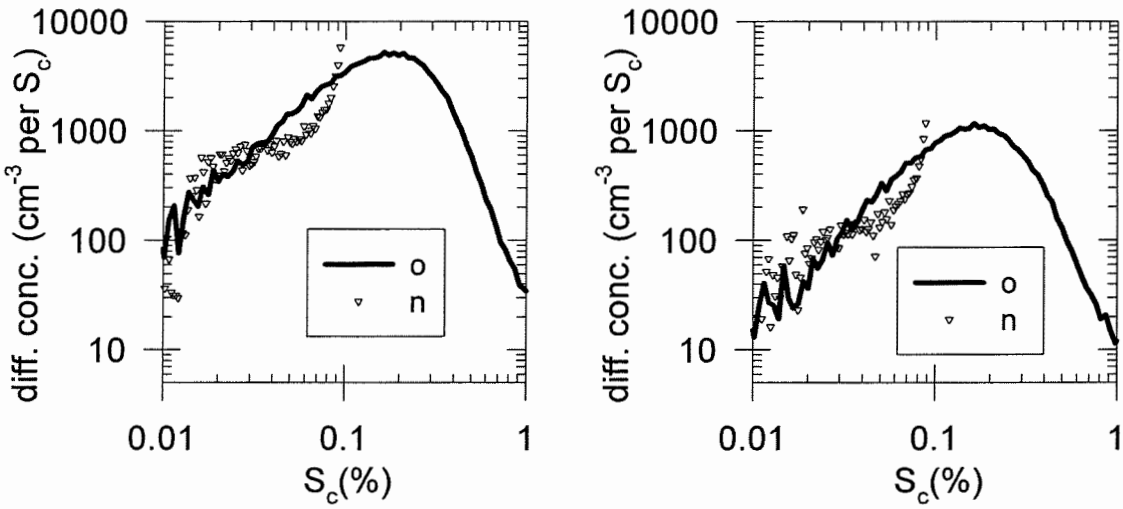

Figure 5. As Fig. 2 but for the data noted in Fig. 4. But here the S range is 0.03-0.01%. Older spec. data is solid line and newer spectrometer is symbols. At 1845 the sample inlet was changed from room air to outside air.

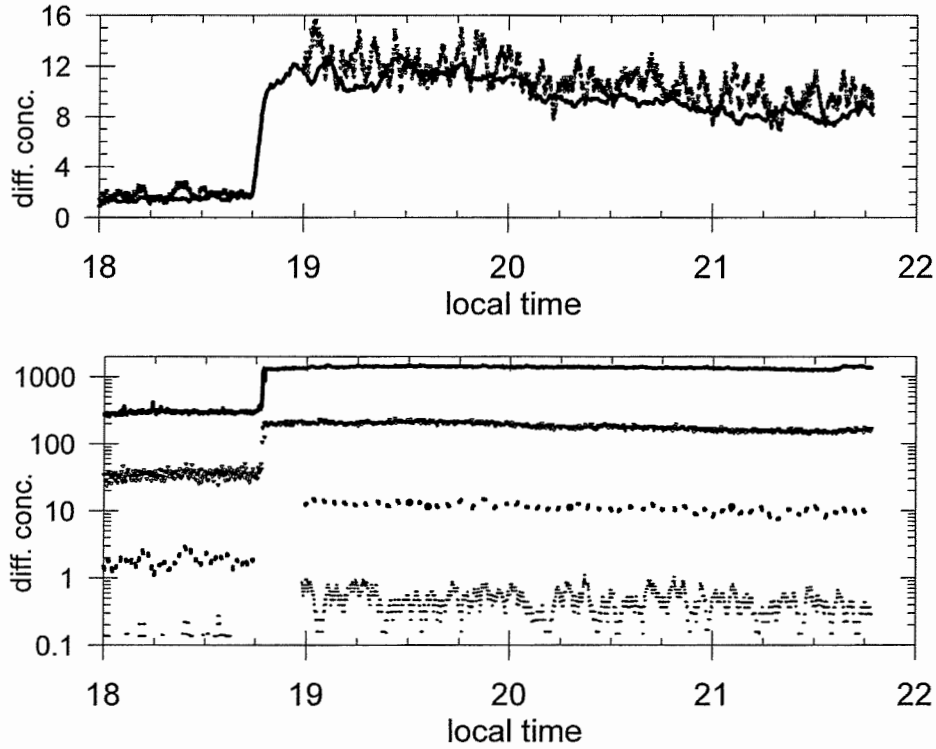

Figure 6. As Fig. 3 but for data noted in Figs. 4 and 5. Cumulative number concentrations at S of 1.0% and 0.1% (old spec.) and 0.03% and 0.01% (new spec.).

Higher overall concentrations result in more coincidence events. Coincidence causes slight underestimates of the more numerous higher S_c particles and significant overestimates of lower S_c particles. Figure 2 shows agreement over most of a day of the differential concentrations measured by the two instruments in the overlapping S range of 0.4-0.3% that is apparent in Fig. 2. Figure 3 shows a continuous record of cumulative concentrations of total CCN (at 1% S) from the new spectrometer and large nuclei cumulative concentrations from the old spectrometer at 0.1, 0.05, and 0.03% S.

Figures 3 and 4 show more examples of both differential and cumulative concentration agreement. Here the instruments both operated at lower ranges of S. In opposition to Figs. 1 and 2, here the newer instrument is at a lower S range than the older instrument.

3. DISCUSSION

There has been extensive agreement between the two instruments in various combinations of S ranges. These up and down the ladder comparisons yield confidence in the ability of the instruments to obtain accurate CCN spectra over a substantial range of S. However, there are limits to the range of S that can be obtained with one instrument. The major limiting factor seems to be coincidence pulses, which cause greater inaccuracies at lower S when there are higher total CCN concentrations. This can be overcome by using a lower sample flow rate to reduce the rate of coincidences even for high concentrations. However, small sample flow rates can result in diffusion losses especially for the smaller (higher S_c) particles. Although a dump flow has always been used to limit diffusion losses, the need to directly measure the sample flow necessities 30 cm of sample tube beyond the dump flow. Recently the dump flow has been put downstream of the cloud chamber to reduce diffusion losses. But this means that the sample flow rate cannot be directly measured. However, sample flow rate can be inferred by calibration comparisons with the other instrument directly measuring sample flow rate with large monodisperse particles that are not subject to diffusion losses.

Figure 7 shows cumulative spectra from the data that is displayed in Figs. 1 and 4. Here the lower S instrument data is used for the lower S range and then the differential spectra from the higher S range instrument are added incrementally to the cumulative data from the lower S range instrument. Thus, the data at higher S is compiled from both instruments. These measurements can be considered to be somewhat typical of extended-range CCN spectra.

Agreement between the DRI CCN spectrometers for wide ranges of ambient conditions (various different spectra and various total concentrations) and with a variety of operating conditions (mainly various plate delta T's and especially maximum delta T's) suggests that the problems noted by Chuang et al. (2001) and Nenes et al. (2002) may have been exaggerated.

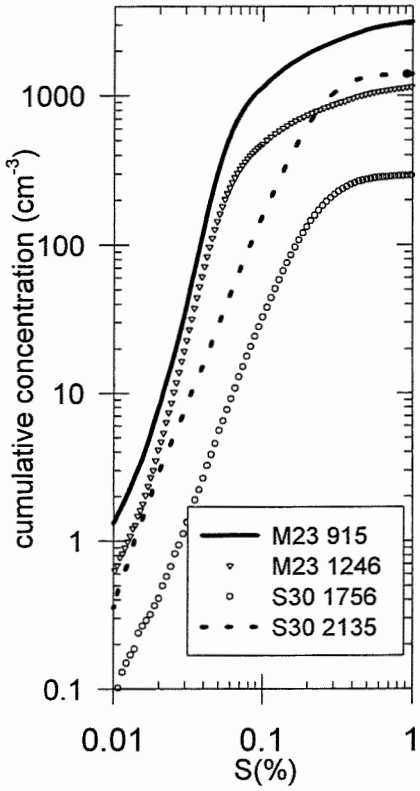

4. ACKNOWLEDGEMENTS

This work was supported by the US National Science Foundation and the US Department of Energy through Battelle Northwest Labs.

5. REFERENCES

Chuang, P.Y., R.J. Charlson, and J.H. Seinfeld, 1997: Kinetic limitations on droplet formation in clouds. *Nature*, **390**, 594-596.

Hudson, J.G., 1989: An instantaneous CCN spectrometer. *J. Atmos. & Ocean. Tech.*, **6**, 1055-1065.

Hudson, J.G. and X. Da, 1996: Volatility and size of cloud condensation nuclei. *J. Geophys. Res.*, **101**, 4435-4442.

Miles, N.L., J. Verlinde, and E.E. Clothiaux, 2000: Cloud droplet size distributions in low-level stratiform clouds. *J. Atmos. Sci.*, **57**, 295-311.

Nenes, A., C.Y. Chuang, R.C. Flagan, and J.H. Seinfeld, 2001: A theoretical analysis of cloud condensation nucleus (CCN) instruments. *J. Geophys. Res.*, **106**, 3449-3474.

Takeda, T., and N. Kuba, 1982: Numerical study of the effect of CCN on the size distribution of cloud droplets. Part I Cloud droplets in the stage of condensation growth. *J. Meteor. Soc. Japan*, **60** 978-992.

AN AUTOMATED SYSTEM FOR IDENTIFYING TYPES OF SOLID PRECIPITATION BY IMAGE PROCESSING

M. Ishizaka[1], T. Shiina[2], K. Muramoto[3], S. Nakai[1] and A. Sato[1]

[1]Snow and Ice Research Group, National Research Institute for Earth Science and Disaster Prevention, Nagaoka, 940-0821, Japan

[2]The dept. of Electrical Engineering, Toyama National College of Technology, Toyama, 939-8630, Japan

[3]The dept. of Information and Systems Engineering, Kanazawa University, Kanazawa, 920-8667, Japan

1. Introduction

For precise interpretation of radar power returned from hydrometeors and for modeling precipitation processes, it is important to know both the amounts and types of precipitation particles. However, it is generally not possible to record and analyze all particles precisely. In practice, many solid precipitations are falling, and although they are sometimes the same kind of particle, at other times many kinds of solid precipitation are falling simultaneously. To determine their complex characters, it is preferable to observe each particle carefully with a microscope, but the large number of particles makes this impractical. Therefore an automatic apparatus or system to observe them both quantitatively and qualitatively is desired. The instrument developed by the Institute of Atmospheric and Climate Science at the ETH (Barthazy and Schefold, 2001) is one of such a system.

This paper also describes a system for automatically identifying the types of solid precipitation by image processing. The system is an improvement of the existing computer-based measurement system developed from 1984 (Muramoto K. and K. Matsuura, 1993). With this system we can automatically obtain not only quantitative data of precipitation particles, i.e. the size distribution and number of particles per unit volume, but also information that distinguishes them into several types of snow, i.e. aggregates of snow crystals with different riming stages and different types of graupels.

Crresponding author*s address: Masaaki Ishizaka, Nagaoka Institute of Snow and Ice Studies, Suyoshi, Nagaoka, 940-0821, Japan; E-Mail: ishi@bosai.go.jp.

2. System

2.1 Configuration

For detecting the natural falling speed of hydrometeors, the measuring part of the system was placed in a space enclosed by double-net fences (Fig. 1). The measuring system is shown in Fig. 2. Precipitation particles falling into the narrow space (0.2

Fig. 1 Snapshot of the observation site.

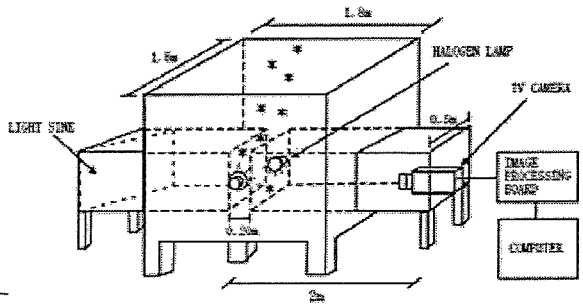

Fig. 2 Configuration of the measuring system

m in width) under no wind condition are illuminated by halogen lamps and photographed through the zoom lens of a CCD video camera set at a distance of 2 m. The shutter speed of the camera was set at 1/4000 second. At this high shutter speed, the displacement of particles due to falling motion was negligibly small. The size of captured image was 0.12 m (H) x 0.16 m (W) which corresponds to 240 pixels x 640 pixels.

2.2 Data Recording

Particles were recorded continuously for two-thirds of a second, which corresponded to 480 frames, at every 5 seconds, and images were stored in an image processor (resolution: 240 x 640 dots, 256 levels). The recording interval depends on the performance of the computer's CPU, because the time when not capturing must be used for image processing. In the image processing, binarization of all captured images with an appropriate threshold level was carried out to detect precipitation particles. Then, for each detected particle, data concerning the position of the highest dot, maximum horizontal width, lowest position, peripheral dots and so on were calculated and stored in the computer's hard disk.

2.3 Detection of fall speed

The falling speed of precipitation particles was obtained by processing the numerical data with the following algorithm. Figure 3 shows two images captured consecutively. The right image was captured 1/60 second later than the left one. The falling speed of the particles can be calculated from the displacement of the same particle recorded in the two images. To identify the same particle in corresponding images, we introduce the following function that evaluates the similarity of each pair of images:

$$X_{ij}=\exp(-C_x|X_i-X_j|/X_i)$$

Where X_i is any element of i-th image and C_x is constant.

In this study we selected five elements of the particle image: the horizontal (W) and vertical widths

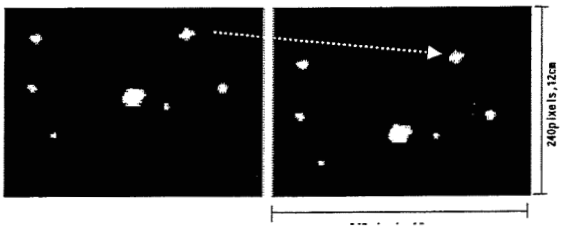

Fig. 3 the continuous two images after binarization.

(H), cross-sectional area (A) and coordinates of the highest position (X, Y), and then calculated the product:

$$Z_{ij}=W_{ij}\,H_{ij}\,A_{ij}\,X_{ij}\,Y_{ij}.$$

A higher value of Z_{ij} indicates that the i-th image was more similar to the j-th image. Comparing all images in the left-hand side with the right-hand ones, we chose the pair of images of the same particle that had the highest value of Z_{ij}, by setting an appropriate cut-off value.

After identifying two images, we calculated the falling speed from the vertical displacement of the same particle in the two images.

3. Observations

We installed the system at the Nagaoka Institute of Snow and Ice Studies, Nagaoka City in Japan, and have carried out observations in winter since 2002. The system worked throughout the winter seasons. To verify the performance of the system, we carried out manned observations with a microscope for several snowfall events every winter. For the observations, we used a low-temperature room (–5°C) into which snow fell through a window in the roof. We caught particles

Fig.4 Recording system of close-up photos of precipitation particles falling into the low temperature room.

in the room and took microscopic photographs of particles. From these photographs, we observed the constituent crystals and extent of riming of snowflakes, and differences in types of graupel. However, the duration of manned observations was limited, so close-up photographs of the particles, which were automatically carried by a conveyor from the deposited position (Fig. 4), also were taken by CCD video camera at 10-second intervals. The images were continuously stored on hard disk. The photographs taken by close-up lens could not reveal the details of the constituent snow crystals but were useful for roughly classifying the precipitation particles into several categories: graupel, snowflakes and graupel-like snow.

4. Results

In the winters of 2002 and 2003, we observed various types of snow, i.e. various kinds of aggregates with different riming stages and different types of graupel. A comparison of the detail manned observations and numerical data obtained by the automated system showed that the relationship between the maximum diameter and the falling speed of snow particles deduced from numerical data accurately represented the types of precipitation particle.

Figure 5 shows this relationship and microscopic photographs of precipitation particles during a period of about 10 minutes. Each spot in the graph corresponds to one particle. The falling speeds are obtained by the algorithm mentioned previously. In this analysis, the particles which had cross-sectional areas of smaller than 5 pixels (corresponding to around 0.75 mm in diameter) were eliminated from the plotting data, because the lack of characteristics of small particles made it difficult to identify the correct pairs of corresponding images in the falling-speed algorithm. Curves a and b in the figure indicate the best-fit curves of the cone-shaped graupel and the heavy rimed snowflake obtained by other authors (Locattelli and Hobbs, 1974). The microscopic photographs of typical precipitation particles were taken at the same times shown in the graphs. Case 1 and case 2 in the figure show that typical precipitation particles are cone-shaped graupel and heavily rimed snowflakes, respectively, and that the spots are distributed around each best-fit curve. In case 3, many spots are distributed between these curves and the corresponding photograph indicates that the typical particles in this case were graupel-like snows. The results are reasonable because this type of particle has an intermediate falling speed between that of graupel and that of heavy rimed snowflake based on

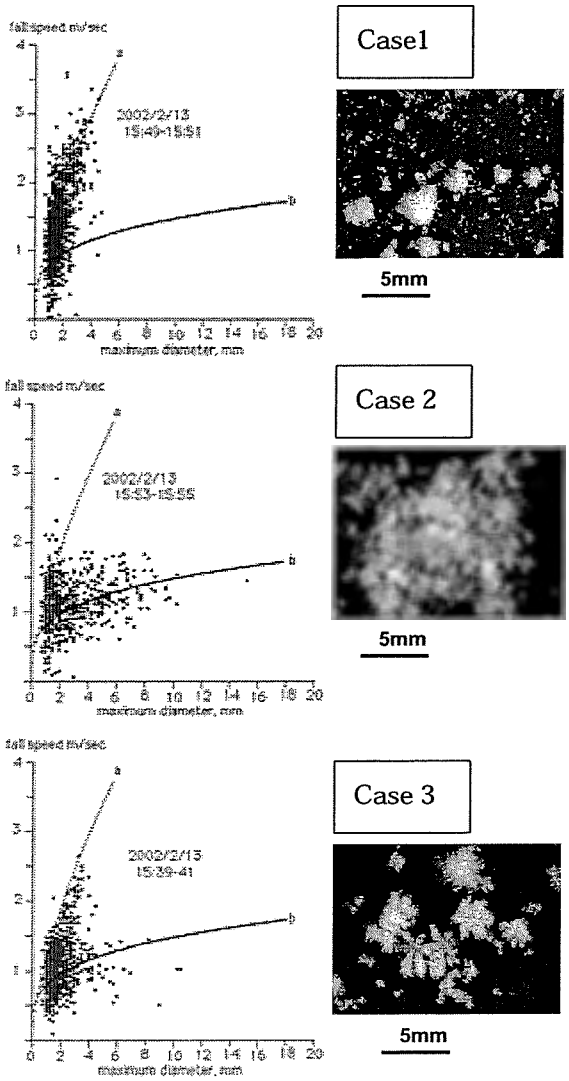

Fig. 5 The relationship between the dimension and fall speed calculated from the recorded data and the microscopic photos of typical particles taken at the same periods.

its aerodynamics. Also, this graupel-like snow fell in the period between case 1 and case 2. In fact, when relatively large snowflakes are falling, many such small particles are falling simultaneously, in larger numbers than conspicuously large precipitation particles. Figure 6 shows two more results of different kinds of solid precipitation, i.e. an aggregate of unrimed dendritic snow crystals and irregular-type graupels. The falling speeds of these are smaller than those of rimed snowflake and the cone-shaped graupel respectively, as shown in the graph.

These results indicate that the system can identify variations in the type of solid precipitation even during several minutes (in the case of Fig. 5).

5. Conclusion

We described a system for automatically identifying the types of solid precipitation particle. In this computer-based system, solid precipitation particles are captured as they fall and data of their images are stored numerically after image processing. By using the system in the condition that precipitation particles fall at their terminal velocity, we can determine the types of hydrometeor from the relationship between their dimensions and falling speed, and so can obtain continuously both quantitative and qualitative data of falling particles through snowfall events with a fine time resolution. This information is useful for analyzing problems relating to snowfall, such as interpretation of radar power returned from hydrometeors, snow accretion, poor visibility induced by heavy snowfall, and modeling of precipitation processes.

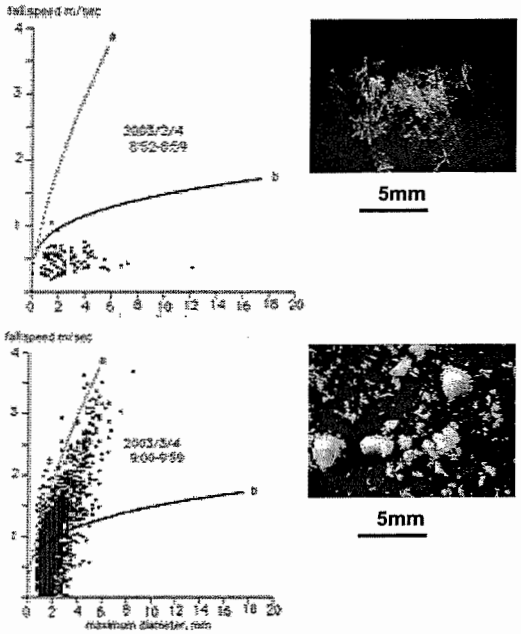

Fig. 6 The relationship between the dimension and fall speed of the aggregates of unrimed dendritic snow crystals and the irregular type graupels.

6. References

Eszter B. and R. Schefold, 2001; A new ground-based optical instrument to measure snowflakes. Proc.of the 30th Int. Conference on Radar Meteorology, 545-547.

Locattelli, J. D. and P. V. Hobbs, 1974: Fall speeds and masses of solid precipitation particles. J. Geophys. Res., 79, 2185-2197.

Muramoto K. and K. Matsuura, 1993; A computer database for falling snowflakes. Ann. Glaciol., 18, 11-16.

Analysis of Millimeter-wave Measurements of Frozen Hydrometeors

[1]Min-Jeong Kim , [1]J. A. Weinman, [2]D.-E. Chang, [3]J. R. Wang, [4]S. Tanelli, [5]J. Roman, and [5]S. Sekelsky

1. Department of Atmospheric Sciences
University of Washington, Seattle, WA 98195, USA
Phone: 1-206-685-1851, Email: mjkim@atmos.washington.edu

2. Forecast Research Laboratory,
Meteorological Research Institute, Seoul, 156-720, Korea

3. NASA Goddard Space Flight Center, Code 975, Greenbelt, MD 20771, USA

4. Atmospheric Radar Science and Engineering group
Jet Propulsion Laboratory, California Institute of Technology, Pasadena, CA 91109, USA

5. Department of Electrical and Computer Engineering
University of Massachusetts, Amherst, MA 01003, USA

Abstracts

Snowfall is an important part of the Earth's precipitation and hydrological cycle. Understanding the behavior of frozen hydrometeors has been limited because it is hard to measure microphysical and electromagnetic properties of snowfall due to its various habits, density, and size distributions.

Ground-based radars have been widely used to monitor snowfall intensity, but even those measurements are difficult to relate to water equivalent of snow because of the vast diversity of snow habits. Moreover, the spatial coverage of radar networks is limited over most regions other than the U.S.A., southern Canada, Europe, and Japan. Snowfall measurement from space has been suggested as a solution to overcome this limitation. Interest has focused on frozen hydrometeor measurements at millimeter-wavelengths that are short enough to react with frozen hydrometeors and for which water vapor obscures the variable emission from the underlying surface.

This study analyzes the millimeter-wave measurements of frozen hydrometeors during the Wakasa bay field experiment that was held in Wakasa bay of Japan in January/February, 2003. Observations provided by Microwave Imaging Radiometer (MIR) covering from 90 to 340 GHz, the dual frequency Airborne Precipitation Radar (APR-2) operating at 14 and 35 GHz, and the Airborne Cloud Radar (ACR) operating at 94 GHz during January 29th 2003 are investigated in this study The MM5 cloud simulation is employed to provide temperature and humidity profiles for the radiative transfer calculations.

Parameterizations to represent the electromagnetic scattering properties of snow at millimeter-wave frequencies are applied to the hydrometeor profiles derived by airborne radar measurements. Calculated brightness temperatures, radar reflectivities are compared with the millimeter-wave measurements.

THE COMPACT CLOUD SPECTROMETER AND IMPACTOR

Greg L. Kok[1], C. Twohy[2] and D. Baumgardner[3]

[1] Droplet Measurement Technologies, Boulder, CO, 80301, USA
[2] Oregon State University, Corvallis, OR, USA
[3] Universidad Nacional Autónoma de México, Mexico City, Mexico, 04510

1. INTRODUCTION

The counterflow virtual impactor (CVI; Ogren et al., 1985, Noone et al., 1988, Twohy et al., 1997) is a versatile technique for measuring total condensed water content over a broad range of cloud particle sizes and water contents. Almost all versions of airborne CVIs require a trained operator and the inlet must be fuselage-mounted to be near to the pumps and sensors that are installed in the aircraft cabin. This conventional system has now been streamlined for cloud physics measurements and new features have been added to expand the CVI capabilities, i.e. 1) a new inlet design, 2) measurement of water vapor with a TDL, 3) measurement of TAS, 4) size distributions from 2 – 60 μm diameter and 5) completely automated control system. Additionally, the ability to mount the new instrument on an aircraft wing allows more accurate measurement of large drops and ice crystals, which may be distorted by flow around the aircraft fuselage itself (King, 1984, Twohy and Rogers, 1993).

2. INSTRUMENT DESCRIPTION

The new condensed water measurement system, the compact cloud spectrometer and impactor (CSI), shown schematically in Fig. 1, consists of three components: 1) a CVI 2) a miniature optical particle spectrometer (CDP) and 3) a pitot tube to measure air speed. The counterflow for the CVI is provided by compressed air from a cylinder inside the CSI canister. Particles enter through a shrouded inlet and the water vapor from particles evaporated in the heating section is measured with a tunable diode laser (TDL) hygrometer (mfg. by Spectra Sensors, Inc). The water vapor pressure is converted to total water content at the temperature and pressure of the measurement. The particle size distribution, from 2 – 60 μm diameter, is measured with the CDP whose sensing head is mounted on the canister. The canister footprint matches that of a standard PMS canister, although the total size is larger.

A number of aerosol inlets use a shroud around the tip to straighten the airflow when the angle of attack is not zero. Usually these have been attached between the inside of the shroud and the inlet itself. This causes two problems in that the struts block part of the airflow and the attachment to the tip requires significant additional structure. A new shroud attachment has been designed that relies on external fins to mount the shroud. In addition to minimizing the problems of airflow and structure, the external fin design is much easier to fabricate and assemble than previous designs. The inlet design itself is based on the "mini-CVI" design of Anderson et al. (1993).

Locations for the CVI and CDP were selected based on computational fluid dynamical calculations at typical aircraft speeds. For example, Fig. 2 displays calculated trajectories of 40 micron droplets around the canister (upstream flow speed 100 m s^{-1}), showing which locations would not be suitable for sampling these droplet sizes. Prior to manufacturing the inlet, calculations were run to assess the flow field around the complete inlet system and the attached CDP. These simulations verified that the velocity should be near isokinetic at the entrance of the inlet and at the sample volume of the CDP.

In previous installations of the CVI, the sample inlet was located between 1 and 3 meters from the water vapor measuring instrumentation. This meant that droplet transit times were on the order of several seconds. This had the advantage of allowing time for the droplets to evaporate, but increased response time and smeared out the water vapor signal as there was considerable surface for adsorption. The new design of the CSI has a path length of only 30 cm from the tip of the inlet to the sample volume of the TDL hygrometer. Water droplets are efficiently vaporized with an innovative, miniaturized heating system. In this system, a ceramic tube, 1 cm x 3 cm, has been machined with a series of holes on the perimeter. Nichrome wire is woven through these holes and forms an internal "screen" in the bore of the cylinder. The wire is resistively heated to form a low surface area droplet vaporizer.

The CSI is controlled by a PC-104 computer system that manages all of the temperature and flow controls. The instrument is designed to operate autonomously or to have the data displayed in real time on an operator's computer in the aircraft cabin. The operating software uses the commercially available DAQFactory.

Figure 3 is a photograph showing the front portion of the CSI. Figure 4 is a photograph of the CSI

Corresponding author's address: Greg Kok, Droplet Measurement Technologies, Boulder, CO 80301, E-Mail: glkok@dropletmeasurement.com

mounted on the NCAR C-130 during the Alliance Icing Research Study-II (AIRS-II) project, discussed in the following section.

3. RESULTS

The CSI was installed on the NCAR C-130 as part of the AIRS-II deployment. The aircraft was stationed in Cleveland, Ohio during November and December, 2003. In addition to the CSI, a number of cloud particle spectrometers and hot wire water sensors were mounted on the aircraft for this project, including the PMS FSSP, 2D-C and 2D-P and a Nevzorov liquid and total water sensor.

The data set from this project is still in the preliminary stages of processing and analysis, and all results reported here are to be viewed with caution as quality control was still on-going at the time of this submission. The measurements from a single flight are presented here in order to demonstrate that the new design provides results consistent with other independent measures of total condensed water content.

Figure 5 shows comparisons between the CSI TWC and the combined water contents measured with the FSSP and 2Ds (right panel) and with the Nevzorov LWC and TWC (left panel). The water contents from the optical probes and Nevzorov sensors represent averages in equal intervals of 0.05 gm^{-3} as measured with the CSI. The vertical bars are the standard deviation of the average in each interval. These results indicate that in this case, the TWC measured by the CSI is generally higher in relation to that measured with the other instruments, possibly due to more efficient measurement of large drops and ice crystals. For very small TWC the CSI and other instruments agree very well. Also, time series plots (not shown) reveal that the baseline value of water content as measured by the CSI and TDL is very stable throughout a six-hour flight.

4. ACKNOWLEDGEMENTS

The CSI was funded by the National Science Foundation as part of the Small Business Transfer of Technology and Research Program, NSF award # DMI-0110358. AIRS-II data were acquired through NSF award ATM-0312036. We also acknowledge the originators of the CVI concept, John Ogren, Jost Heintzenberg, and Bob Charlson.

4. REFERENCES

Anderson, T. L., R. J. Charlson, et al. (1993). Calibration of a counterflow virtual impactor at aerodynamic diameters from 1 to 15 µm. Aerosol Sci. Tech. **19**: 317-329.

King, W.D. (1984). Air flow and particle trajectories around aircraft fuselages. 1: Theory, J. Atmos. Ocean. Tech, **1:** 5-13.

Ogren, J. A., J. Heintzenberg, et al. (1985). "In situ sampling of clouds with a droplet to aerosol converter." Geophys. Res. Lett. **12**(3), 121-124.

Noone, K. J., R. J. Charlson, et al. (1988). "Design and calibration of a counterflow virtual impactor for sampling of atmospheric fog and cloud droplets." Aer. Sci. Technol **8**: 235-244.

Twohy, C.H. and D. Rogers (1993). Airflow and water drop trajectories at instrument sampling points around the Beechcraft King Air and Lockheed Electra. J. Atmos. Oceanic Technol., **10**, 566-578.

Twohy, C. H., A. J. Schanot, et al. (1997). "Measurement of condensed water content in liquid and ice clouds using an airborne counterflow virtual impactor." J. Atmos. Oceanic Tech. **14**(1): 197-202.

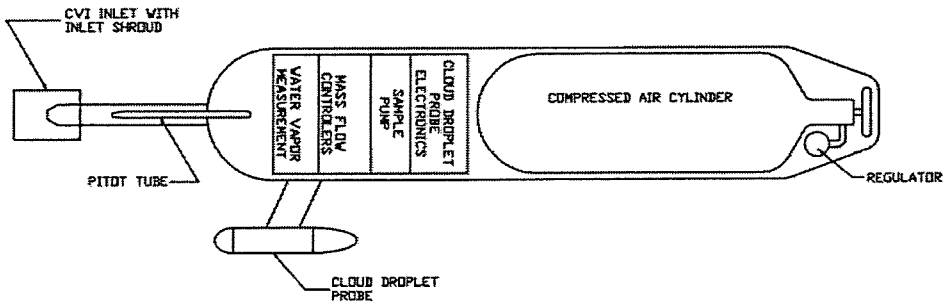

Figure 1

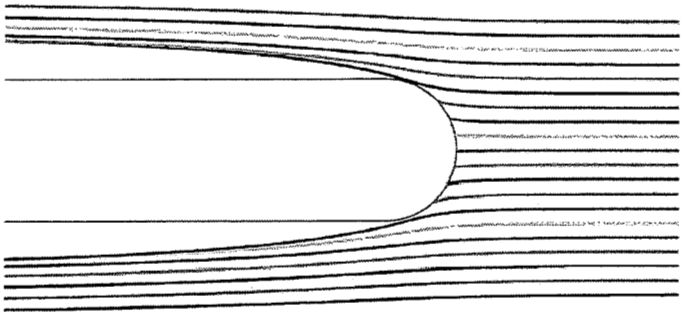

Figure 2

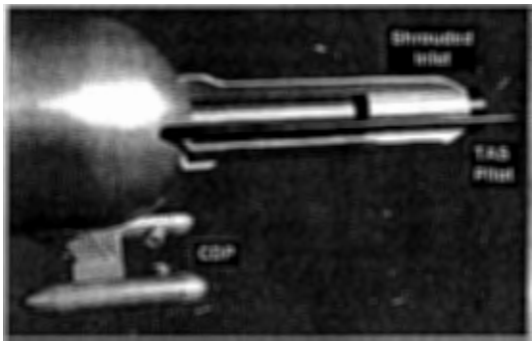

Figure 3

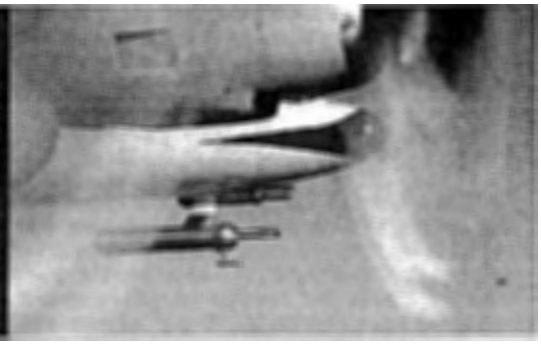

Figure 4

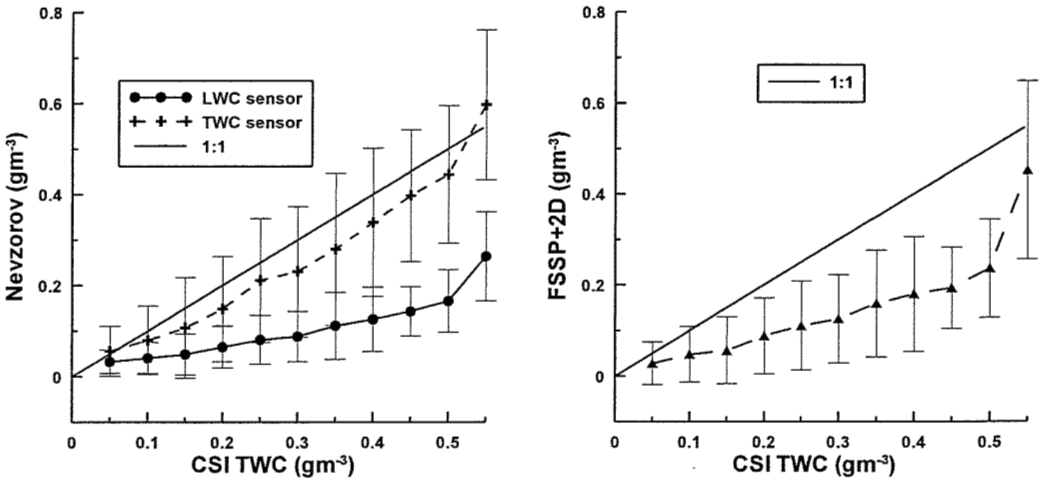

Figure 5

Shattering during sampling by OAPs and HVPS

Alexei Korolev[1] and George A. Isaac[2]
[1] *Sky Tech Research Inc., Richmond Hill, ON, Canada*
[2] *Cloud Physics Research Division, Meteorological Service of Canada, Toronto, ON, Canada*

1. Introduction

The data on cloud particle sizes and their concentrations, collected with the help of aircraft imaging probes PMS OAP-2DC, OAP-2DP and SPEC HVPS, are widely used for cloud parameterization and validation of remote sensing. The goal of the present work is to study shattering of ice particles during sampling. The shattering of cloud particles may affect the concentration, water content and radar reflectivity calculated from 2D data.

Figure 1. HVPS (1), OAP-2DP (2), OAP-2DC (3), and OAP-2DC with modified tips (4). The probes are mounted on a pylon underneath the wing of the NRC Convair 580.

2. Instrumentation and data processing

The OAP-2DC, OAP-2DP and HVPS instruments belong to the so-called "imaging array probes" and have the same principle of operation (Knollenberg 1981; Lawson et al. 1998). The outputs of these probes are binary (black-and-white) images of cloud particle shadows at a resolution of 25μm for the OAP-2DC, 200μm for the OAP-2DP and 200x400μm for the HVPS. These instruments were installed on the same pylon underneath the wing of the National Research Council (NRC) Convair 580 (Fig. 1). Such a location removes the possibility of measuring ice particles broken up due to their impact with the fuselage or propeller. The data were collected during the AIRS 1.5 and AIRS2 projects in frontal clouds over the Southern Ontario and Quebec area during two winter seasons 2003 and 2004.

The study of shattering is based on the analysis of an amount of isolated images in different frames.

Corresponding author's address: Sky Tech Research Inc., 28 Don Head Village Blvd., Richmond Hill, ON, L4C 7M6, Canada, E-mail: Alexei.Korolev@rogers.com

The term "isolated image" refers to a group of 8-connected pixels. Two pixels are considered 8-connected if their edges or corners touch each other. In this case, the pixels are parts of the same image, otherwise they belong to different isolated images. The term "frame" will be applied to a single registration act resulting in a binary image matrix *NxM*, where *N* is the number of active photodiodes in the probes array (e.g. *N*=32 for OAP-2DC/P) and *M* is the number of pixels along the air speed direction.

The images of fragments may overlap forming one isolated image instead of several ones. Some of the fragments may go outside of the view of the probe's optics, so that only some fraction of the fragments will be seen by the probe. Thus, the number of isolated images in the shadowgraphs of a shattered particle will be less or equal to the actual number of fragments. Therefore, a number of isolated images may be used as a lower estimate of the number of fragments resulted from shattering.

The data were analyzed with the help of a 2D-software package developed by Sky Tech Research. The 2D-software provides particle image size, habit recognition, analysis of multiple images, interarrival time, size distributions, and concentration. The analysis presented below was based on 2D data averaged over 10 second time intervals.

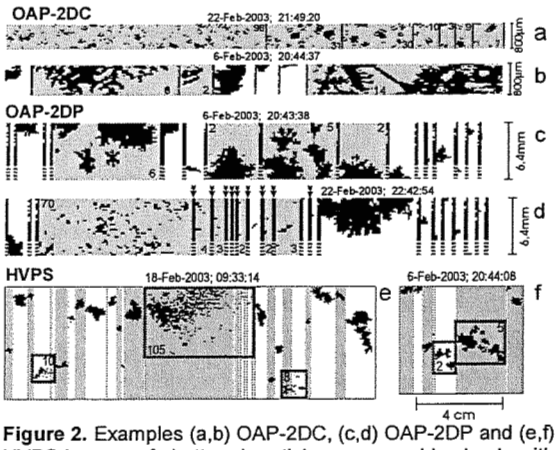

Figure 2. Examples (a,b) OAP-2DC, (c,d) OAP-2DP and (e,f) HVPS images of shattered particles measured in clouds with aggregates of dendrites. The numbers indicate the amount of isolated images (or fragments) associated with the shattered images.

3. Results

a. Examples of ice particle shattering during sampling

Figure 2 shows images of the cloud particles measured by the OAP-2DC (a,b), OAP-2DP (c,d) and HVPS (e,f). In Figs 2(a-d) the gray color highlights the frames containing multiple isolated images, and the

numbers in the corners indicate the amount of isolated images in those frames. The images in the rectangle frames in Figs. 2a,c,d were identified as being fragments from shattering. In Figs. 2e,f the shattered images are outlined by rectangles.

There are two distinct patterns of particle shattering in the OAP-2DP and HVPS imagery. In the first case, the images of shattered particles consist of multiple isolated small images (Fig.2a,d,e). The number of images in such frames may exceed 200. The characteristic size of the fragments in such images is about 25 μm for the OAP-2DC and 200μm for the OAP-2DP/HVPS, which is close to the probe's pixel resolution. In the second case, the images of the shattered particles consist of a fewer number of large isolated images, and their sizes vary from 1mm to 10mm (Fig.2c,f).

In case of the OAP-2DC, the multiple isolated images may result from transparent plate-like crystals and dendrites with developed branches (Fig.2b). The number of isolated images may reach 30-40 per frame. Since the OAP-2DC shattering events are masked by many events of multiple isolated images not related to fragmentation, the main attention will be focused on examining the OAP-2DP and HVPS.

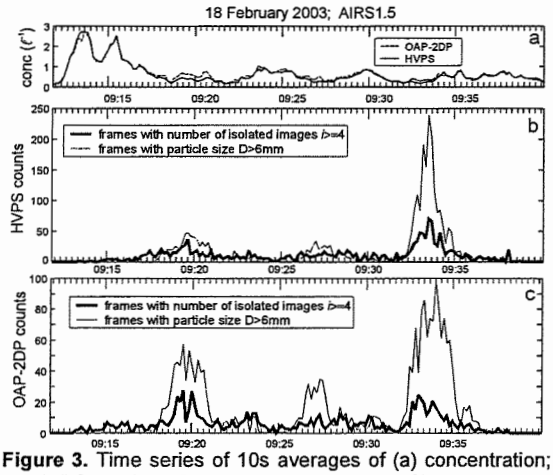

Figure 3. Time series of 10s averages of (a) concentration; (b) HVPS number of frames having number of isolated image $i \geq 4$ and that with particles D>6mm; (c) same as in (b) but for OAP-2DP. Montreal area, Ns, H=1800-3600m; T=-5 -15°C.

b. Correlation between shattering and particle size

In the case of shattering, the number of multiple isolated images is anticipated to correlate with the sizes and concentration of large particles. Figure 3 shows time series of particle concentration (n), the number of frames with non-fragmented particles having sizes larger than 6mm ($N_{D>6}$) and number of frames with $i \geq 4$ isolated images ($N_{i \geq 4}$) measured by the HVPS and OAP-2DP. The comparisons of the diagrams in Fig. 3a, 3b and 3c suggest that $N_{i \geq 4}$ correlates better with $N_{D>6}$, rather than with the total concentration n.

Figure 4 shows the dependence of the correlation coefficient between N_i and N_D ($K(N_i,N_D)$) versus D for different i for the OAP-2DP and HVPS for one flight, part of which is shown in Fig. 3. The maximum of the curve $K(N_i,N_D)$ moves towards large sizes with an increase of i. Thus, the diagram in Fig. 4a suggests, for the OAP-2DP, particles with D~2mm will most likely result in two fragments, but particles with D~8mm will most likely generate 10 fragments. Similar behavior can be seen in Fig. 4b for the HVPS. The quantitative differences between Figs 4a and 4b are related to the difference in the sample areas and housings of the probes. Figure 4 demonstrates that the number of fragments is related to the particle size.

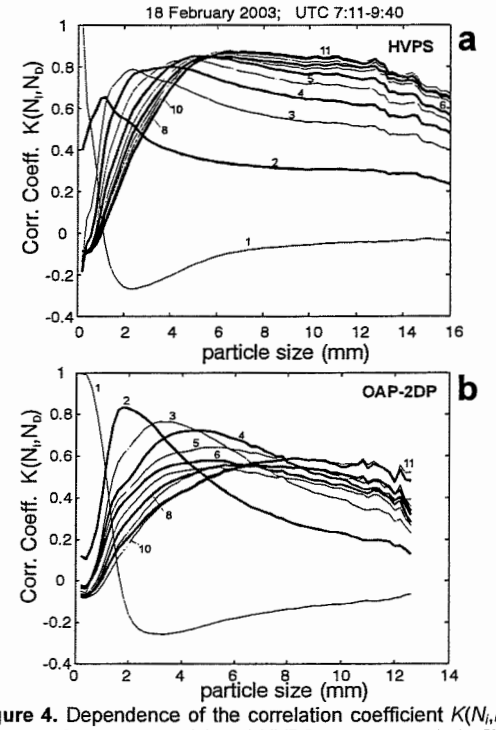

Figure 4. Dependence of the correlation coefficient $K(N_i,N_D)$ versus D for OAP-2DP (a) and HVPS (b) for the whole flight on 18 February 2003. Numbers indicate the value of i.

Besides shattering, the multiple isolated images may result from coincidences in sample volumes of the probes. To estimate the probability of such coincidences, assume that the particles are distributed in space randomly, and the probability of the coincidences are described by the Poisson statistics:

$$P(m) = \frac{(nV)^m}{m!} \exp(-nV) \qquad (1)$$

here m is the number of particles in the volume V, and n is the number concentration of particles.

The sample volume can be estimated as $V=LWd$, where L is the length, W is the width, and d is the depth of the sample volume. For simplicity, assume that: (1) L, W and d are constant and do not depend on the particle size, (2) d=2mm, (3) L is equal to the distance between the probe arms, and (4) $W=k\Delta x$, where k is the number of active photodiodes in the photodiode array, Δx is the pixel resolution; (5) the

particle concentration is equal to its maximum $n=3l^{-1}$ for the considered time period in Fig. 3a. Under these assumptions the sample volume of the OAP-2DP is equal to 5.2cm^3 and for HVPS is 24.4 cm^3.

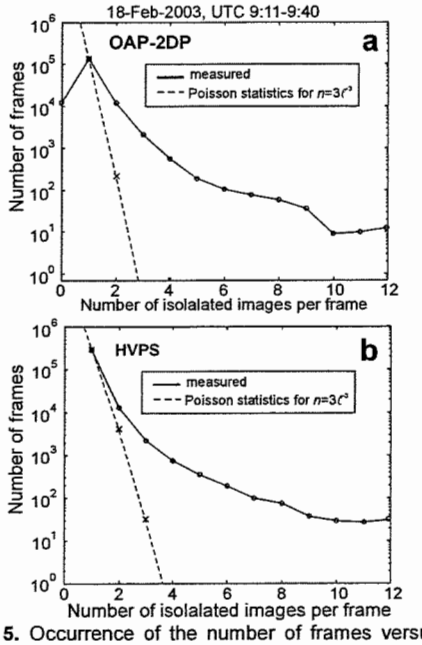

Figure 5. Occurrence of the number of frames versus the number of isolated images in it (solid line). Occurrence of coincidences of particles in the sample volume assuming Poisson statistics for $n=3l^{-1}$ normalized on the number of particles (dashed line). OAP-2DP (a); HVPS (b).

Figure 5 shows occurrence of m coincidences in the sample volume calculated from Eq.1 and normalized to the number of frames (dashed line) and the measured occurrence of frames versus the number of isolated images. The probability of coincidences gives an upper estimate, since the average concentration in Fig. 3 is lower than $3l^{-1}$ and the length and depth of the sample volume for small particles are smaller. Even for such rigorous assumptions, Figs. 8 indicates that the observed number of multiple isolated images is much higher than that calculated from Poisson statistics and, therefore, it cannot be explained by random coincidences. For clouds with a higher concentration ($n>10l^{-1}$) the number of frames with two isolated images can be well explained by coincidences. In most cases the occurrence of triple isolated images exceeds the Poisson statistics of coincidences. Therefore, the frames with $i\geq3$ isolated images can be considered as a result of shattering, and $N_{i\geq3}$ can be used as an estimate of the number of shattering events.

c. Shattering efficiency.

As discussed in section 3b, the value of $N_{i\geq3}$ can be used as a surrogate of the number of all shattering events, and therefore the ratio $N_{i\geq3}/N_{tot}$ will give an estimate of the integral shattering efficiency

Figure 6 shows scatter diagrams of $N_{i\geq3}/N_{tot}$ and $N_{i\geq10}/N_{tot}$ versus D_{max} measured by the OAP-2DP and HVPS. As seen from Fig.6 the ratios of $N_{i\geq3}/N_{tot}$ and $N_{i\geq10}/N_{tot}$ have a tendency to increase with an increase in the maximum particle size. The area under the straight lines contains 97% of all events. Figures 9a,b show that in some cases the shattering efficiency may reach 10%.

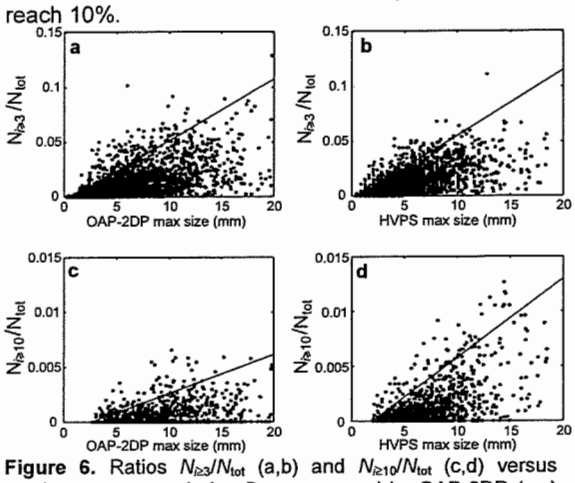

Figure 6. Ratios $N_{i\geq3}/N_{tot}$ (a,b) and $N_{i\geq10}/N_{tot}$ (c,d) versus maximum measured size D_{max} measured by OAP-2DP (a,c) and HVPS (b,d), calculated for seven flights during AIRS1.5.

Figures 6c,d indicate that particles smaller than approximately 3mm for the OAP-2DP and 2mm for the HVPS do not generate more than 10 fragments. Processing of the diagrams similar to that in Fig.6 for different values of i resulted in Fig.7 which shows the maximum number of fragments that particles with size D can generate in the field of view of the OAP-2DP or HVPS. The difference in the curves reflects the differences in the housings and sizes of the sample areas of the OAP-2DP and HVPS.

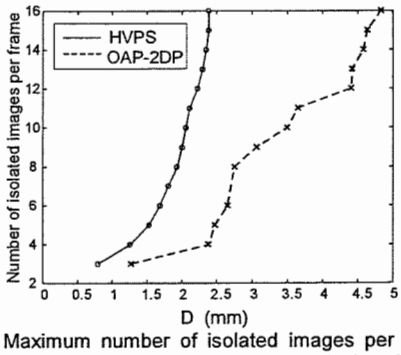

Figure 7. Maximum number of isolated images per frame versus particle size measured by HVPS (solid line) and OAP-2DP (dashed line) calculated based on 17 flights during AIRS1.5 and AIRS2.

d. Maximum measured size.

The effect of the probe's housing becomes even more pronounced after comparisons of maximum size D_{max} measured by the HVPS, OAP-2DP and OAP-2DC shown in Fig. 8. For the HVPS D_{max} was calculated for complete images, whereas for the OAP-

2DP and OAP-2DC D_{max} was calculated for both complete and partial images. The size of the partial images was retrieved using the assumption that particle images are circles (Heymsfield and Parrish 1979; Korolev and Sussman 2000). As seen from Fig. 8a, D_{max} measured by the HVPS agrees well with that measured by the OAP-2DP. However, D_{max} measured by the OAP-2DC becomes significantly different from that measured by the OAP-2DP for particles larger 3mm. Theoretically, the OAP-2DC with a 25μm pixel resolution is capable of measuring 25mm particles, i.e. when the particle occults all 1024 slices in a 2D buffer. However, Fig. 8b indicates that D_{max} measured by OAP-2DC does not exceed 8mm. This finding suggests that large particles are disintegrated by turbulence and wind shear generated by the probe's housing before entering the sample volume of the OAP-2DC. The distance between the arms of the OAP-2DC is 6.1cm, which becomes comparable with 2-3cm snowflakes.

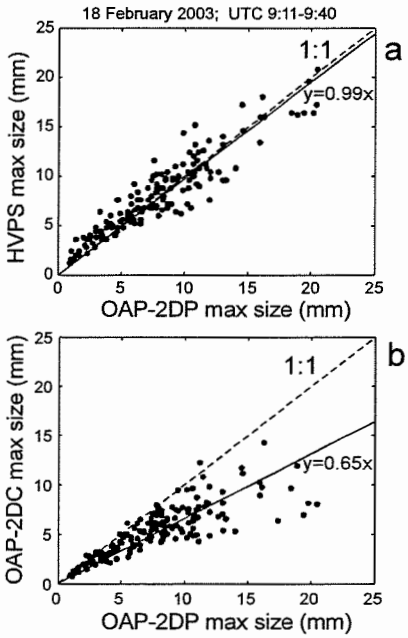

Figure 8. Maximum particle size measured by HVPS versus that measured by OAP-2DP (a); maximum particle size measured by OAP-2DP versus that measured by OAP-2DC (b). Each data point is averaged over 10s time interval.

The maximum size of the snowflakes that can be sampled by the OAP-2DP and HVPS without fragmentation is not known. There are a number of ground-based observations of snowflakes with sizes 6 to 10 cm and in some cases even reaching 38cm (Abbe 1915). However, airborne observations using the HVPS have never documented snowflakes larger 5cm (Lawson et al. 1998). During the AIRS1.5 and AIRS2 flight campaigns, the maximum measured snowflake size did not exceed 4cm. It is possible that the maximum snowflake size that can be measured without fragmentation by the OAP-2DP and HVPS is limited by 5cm.

4. Discussion and conclusions

Shattering may result in the following: (1) overcounting of small particles, due to multiple small fragments generated during shattering; (2) undercounting of large particles due to their fragmentation.

Shattering of particles during sampling depends on: (1) ice particle habits; (2) particle size; (3) probes housing; (4) airspeed.

Ice particles with different habits have different shattering capabilities. For example aggregates of dendrites, having weak bonds between particles, can be relatively easily disintegrate in the air flow disturbance generated by the probe's housing. Hailstones and graupel, which can be considered as solid particles, will resist tearing apart by aerodynamic forces and they will not shatter unless they mechanical impact with the probe's housing.

The following conclusions have been obtained:

1. The shattering of ice particles during sampling occurs due to: (a) the mechanical impact of particles with probe parts upstream of the sample area; and (b) due to interaction with the aerodynamic field around the probe's housing.
2. For aggregates of dendrites, it was found that the fraction of shattered particles, may reach 10% of total number of sampled particles.
3. The threshold particle size, resulting in shattering, is estimated as 0.6mm for the HVPS and 1.2mm for the OAP-2DP. The minimum size of shattered fragments registered by the OAP-2DC is 25μm, which is equal to the probe's resolution. The actual size of the fragments can be even smaller.
4. Future designs of aircraft microphysical instrumentation should consider the shattering potential of the probe's housing.

Acknowledgements

The aircraft data were obtained using the NRC Convair-580 and the scientific and technical efforts of many NRC and MSC staff. Alexei Korolev has performed this work under the contract KM175-012030/001/TOR to the Meteorological Service of Canada, which was partially supported by Canadian Climate Action Fund. Financial support for the NRC Convair flights was partially given by Transport Canada, the National Search and Rescue Secretariat, and FAA.

References

Abbe, C. Jr. 1915: Gigantic snowflakes. *Monthly Weather Rev.*, **43**, 73

Heymsfield, A J. and Parrish, J. 1979: A computational technique for increasing the effective sampling volume of the PMS two-dimensional particle size spectrometer. *J. Appl. Meteor.*, **17**, 1566-1572

Knollenberg, R. G. 1981 Techniques for probing cloud microstructure. In: *Clouds, their formation, Optical properties, and Effects*, P. V Hobbs, A. Deepak, Eds. Academic Press, 495 pp.

Korolev, A., Sussman, B. 2000: A Technique for Habit Classification of Cloud Particles. *J. Atmos. Oceanic Technol.*, **17**, 1048–1057.

Lawson, R. P., R. E. Stewart and L. J. Angus, 1998: Observations and numerical simulations of the origin and development of very large snowflakes. *J. Atmos. Sci.*, **55**, 3209-3229

WARM RAIN PROCESSES OVER THE TROPICAL OCEANS AND IMPLICATIONS FOR CLIMATE

William K. M. Lau[1] and Huey-Tzu Jenny Wu[2]

[1]Laboratory for Atmospheres, NASA/GSFC, Greenbelt, Maryland, 20771, USA
[2]Science and Systems Application Inc., Lanham, Maryland, 20706, USA

1. INTRODUCTION

"Warm rain" refers to rain derived from non ice-phase processes in clouds. Warm rain processes are not restricted to low-to-middle level clouds, but may also occur in deep convection clouds (Schumacher and Houze, 2003). As such, warm rain is an integral component of the tropical precipitation system. It contributes to heating and moistening of the lower troposphere, modifies the stability and heating profiles, and possibly alters the recycling time scales of original convection and large scale circulation systems in the tropics (Johnson et al., 1999; Mapes, 2000).

Launched in November 1997, the Tropical Rainfall Measurement Mission (TRMM) has provided unique multi-year rainfall products (Kummerow et al., 1998) that can be exploited for studies of the basic *modus operandi* of the tropical precipitation system. In this study, we will show results from TRMM regarding the characteristics of warm rains over the tropical oceans, and the dependence of the rate of warm rain production on sea surface temperature (SST). The results lead to the hypothesis that warm rain production efficiency may be heightened in a warmer climate. We explore the climate implications associated with warm rain and the sensitivity of dynamical processes with respect to changes induced by precipitation efficiency with the Goddard Earth Observing System (GEOS) II GCM.

2. CHARACTERSTICS OF WARM RAIN

Using TRMM data, Lau and Wu (2003) find that warm rain is more abundant than previously known. Warm rain accounts for 31% of the total rain amount and 72% of the total rain area in the tropics, and plays an important role in regulating the moisture content of the tropical atmosphere.

Lau and Wu further apply the TRMM observations to estimate the bulk autoconversion rate in an empirical cloud liquid water-rainrate relationship commonly used in state-of-the-art weather and climate models with prognostic clouds (Sundqvist *et al.*, 1989; Tiedtke, 1993; Sud and Walker, 1999). In such a scheme, the rate of release of precipitation P is given by

$$P = C_o m\left[1-\exp\left(-\frac{m^2}{m_r^2}\right)\right], \quad (1)$$

where m is the cloud water content, C_o indicates the efficiency of production of precipitation, with $1/C_o$ representing a characteristic time scale for conversion of cloud droplets to raindrops, i.e. the autoconversion time scale. The critical value m_r gives the typical value of cloud water content beyond which the collision-coalescence growth of cloud-drops to raindrops becomes substantial.

Application of TRMM data on equation (1) yields a bulk autoconversion time scale of approximately 400-800 seconds, and critical cloud water content of 0.6-0.8 mm, with a possible range of 200-1000 seconds, and 0.5-1.1 mm respectively. State-of-the-art climate models considerably underestimate the precipitation efficiency of warm rain compared to observations, constituting an important source of model error.

TRMM observations also show a substantial increase in precipitation efficiency of light warm rain with higher SST, but the precipitation efficiency of deep convection is independent of SST. This feature is illustrated in Figure 1, which shows the dependence of the fractional change in precipitation efficiency in warm rain on SST.

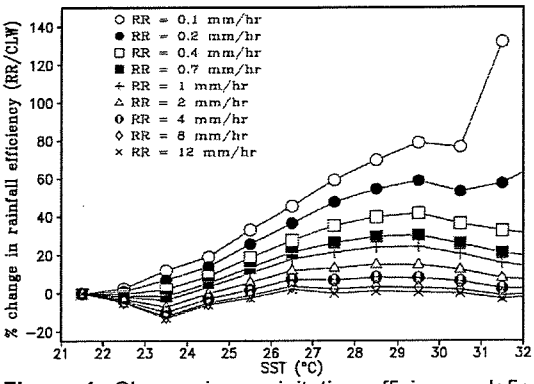

Figure 1. Change in precipitation efficiency, defined as the ratio of surface rainrate (RR) to cloud liquid water (CLW) as a function of sea surface temperature (SST) and RR from collocated daily values from the eastern Pacific region (20-20N, 140-85N) for 12/8/1997-8/31/2000.

For each degree change in SST, the rate at which cloud water rains out increases by 8 to 10 % for drizzle

Corresponding author's address: William K. M. Lau, Laboratory for Atmospheres, NASA/GSFC, Greenbelt, MD 20771, USA; E-mail: William.K.Lau@nasa.gov

and light rains, defined to be there with instantaneous rainrate of less than 0.2 mm/hr. The results imply that in a warmer climate, more warm rain amount will be squeezed out from middle and low-level clouds.

3. GCM EXPERIMENTS

3.1 Model description and experiment design

The GEOS II GCM (Sud and Walter, 1999) used in this study has a resolution of 4-degree latitude by 5-degree longitude and 20 sigma-layers. The radiation scheme is by thermal infrared parameterization by Chou and Suarez (1994). A prognostic cloud scheme named McRAS (Microphysics of Clouds with Relaxed Arakawa-Schubert Scheme) is used to treat the cloud processes. The cloud water and rainrate relationship is defined in equation (1) with critical water content of 0.3 mm for large-scale clouds and 1.0 mm for convective and boundary-layer clouds. The autoconversion time scale is 1000 seconds for control run (E0), 200 seconds for fast run (E1), and 5000 seconds for slow run (E2). For all three experiments, the basic autoconversion time and the critical water content are further modified by three additional parameters to account for factors such as temperature, pressure and cloud water phase. Details can be found in the study of Sud and Walker (1999).

All three experiments were integrated for 65 months. The integration was initialized with the European Centre for Medium-Range Weather Forecasts analysis of observations for 1 January 1987 and was forced with the observed SST and sea-ice distribution.

The resulting joint probability distribution functions (JPDF) of rainrate versus cloud liquid water (CLW) from the three experiments are illustrated and compared to the observed in Figure 2. The slope of JPDF gives an approximate estimate of the residence time of 6 minutes for E1, (9, 24) minutes for the two branches in E0, and 20 minutes to infinity time for E2.

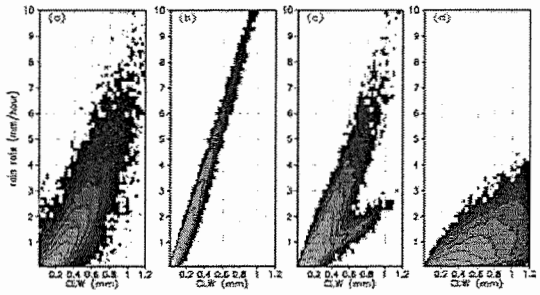

Figure 2. JPDF of daily CLW and rainrate values for (20S-20N, 100E-60W) of (a) TRMM observation (1997-1998) (b) model simulations (1987-1988) of E1 (c) E0 and (d) E2.

The five year (1987-1992) averaged precipitation and outgoing longwave radiation (OLR) from the control run (E0) agree reasonably well with the observed in both horizontal patterns and magnitudes (not shown).

3.2 Cloud-radiation feedback

The results show that fast autoconversion (E1) leads to heavier rain in deep convective region. The area of low OLR (less than 240-250 watt per meter square), usually associated with upper level cloudiness, is much reduced compared to the slow autoconversion (E2). The climate in low latitudes is most sensitive to the changes in autoconversion time (not shown).

Figure 3 shows the vertical profile of diabatic heating terms for E1 and E2 for the western Pacific region. Increasing precipitation efficiency destabilizes the atmosphere in this main convective region, with more low-to-middle level condensational heating and less shortwave heating near the cloud top.

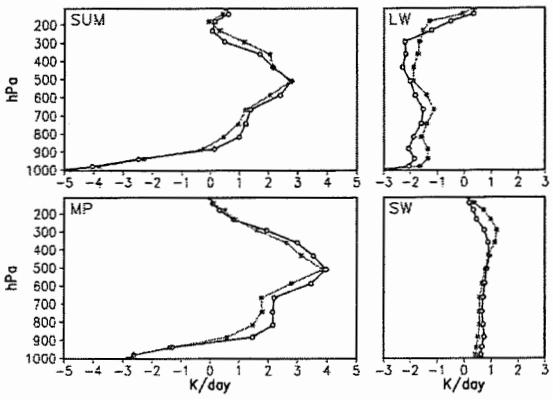

Figure 3. Averaged heating profiles from different components (MP: moisture processes; LW: longwave radiation; SW: shortwave radiation) and their sums for E1 (open circle) and E2 (solid square) for the western Pacific region (100-160E, 12S-12N, 1987-1990)

Further delineation of the vertical profiles of vertical velocity and temperature with respect to the corresponding rainrate indicates that the cloud-radiation feedback to the change in precipitation efficiency has strong dependence on cloud type/ rainrate. For temperature and vertical velocity fields, the response is most sensitive in the upper troposphere (peak around 200-hPa). For low-latitudes (20S-20N), the averaged difference between E1 and E2 is up to 4 degrees with E1 (E2) having a colder temperature and less upward motion for lighter (heavier) rain.

Figure 4 shows that for light warm rain (RR< 2 mm/day) increase in precipitation efficiency (E1-E2) leads to cloud reduction mainly in low-level atmosphere (peak at 800-hPa with 7% reduction). For heavy cold rain (RR > 15 mm/day), on the other hand, the main reduction in cloudiness is at middle level (peak at 600-hPa with 16% reduction), and there is an increase in upper level cloudiness (peaked at 200-hPa with 8% more).

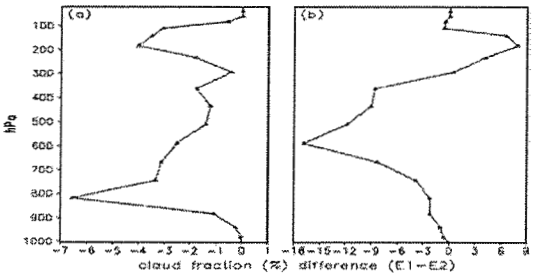

Figure 4. The difference (E1-E2) in the vertical profiles of cloud fraction averaged for (20S-20N, 1987-1990) for (a) RR < 2 mm/day, and (b) RR > 15 mm/day.

3.3 Intraseasonal variation

All three experiments simulate organized eastward propagation of Madden Julian Oscillation (MJO)-like signals in their precipitation, OLR, and velocity potential fields especially in the northern winter and spring. E2 has much lower OLR values compared to E1. For the northern summer E2 features predominantly westward propagating high frequency disturbances as illustrated in figure 5 that shows the equatorial averaged daily OLR of E1 and E2.

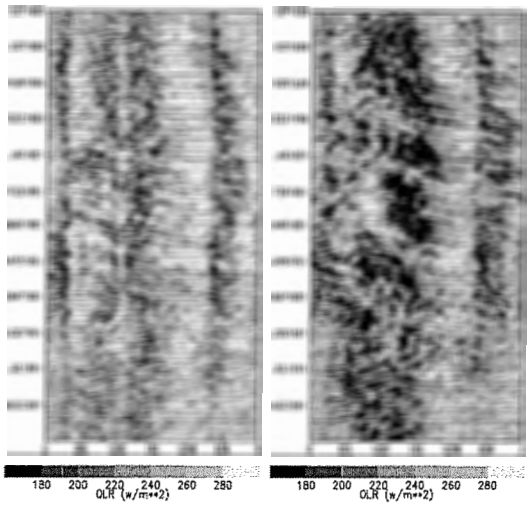

Figure 5. Time-longitude sections (8S-8N averaged) of daily OLR from (a) E1 and (b) E2 for September 1, 1990 to August 31, 1991.

The 20-70 day band-pass filtered velocity potential fields shown in Figure 6 illustrate that increasing precipitation efficiency tends to organize MJO with a shorter time period especially during the northern spring. Application of the spectral analysis on the filtered velocity fields in the equatorial region (8S-8N averaged) results in two dominant periods (at 24 and 40 days) for E1, as opposed to a single dominant period (at 40 days) for E2.

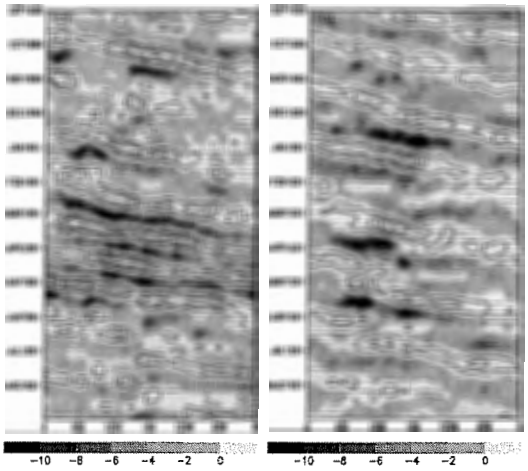

Figure 6. Time-longitude sections (8S-8N averaged) of band (20-70 day) pass filtered 200-hPa velocity potential fields for (a) E1 and (b) E2 for September 1, 1990 to August 31, 1991.

Also noted is that increasing precipitation efficiency leads to shorter recycling time of deep convection. Figure 7 shows the maps of the averaged time of deep convection events for E1 and E2. In all three most active convection regions (central Africa, maritime continent, and central America), the recycling time of the deep convection for E1 is about 2 to 5 days shorter than that of E2.

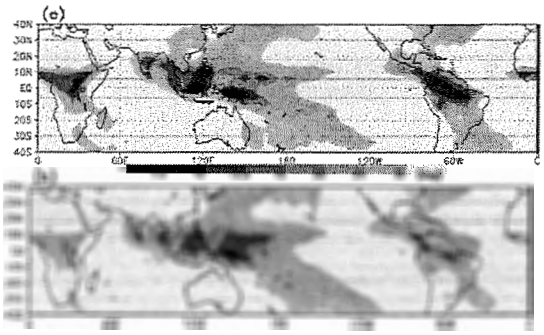

Figure 7. Maps of recycling time of deep convection events, defined as the averaged time interval between occurrences of deep convection whose heating due to moisture processes around 450 mb must be greater than 8 K/day, for (a) E1 and (b) E2.

4. CLIMATE IMPLICATIONS

Our results imply that in a warmer climate, there will be a partial spinning up of the tropical water cycle with increased warm rains, by virtue of the collision-coalescence processes. The increased efficiency in warm rain leads to a reduction of low clouds and less water transport to the upper troposphere and hence less upper level cloudiness. However the increased

warm rain and reduced upper level cloudiness cause more low level heating and more radiative cooling of the upper troposphere, hence may destabilize the atmosphere, invigorating a shallow secondary circulation capped by the freezing level (see Figure 8). This may lead to an increase in the middle level cumulus congestus clouds.

Some of the convection induced by warm-rain may also acquire enough buoyancy to break through the mid-troposphere detrainment layer at the melting level, and develop into deep, penetrative convection with strong updraft. Nevertheless, because of increased rain-out at low to middle levels, deep penetrative convection will actually occur less frequently in a warmer climate, provided the mean water mass flux at cloud base remains constant. This will be so when the warming is weak. As the global warming intensifies, the total cloud mass flux may increase, which will lead to the occurrence of more deep convections.

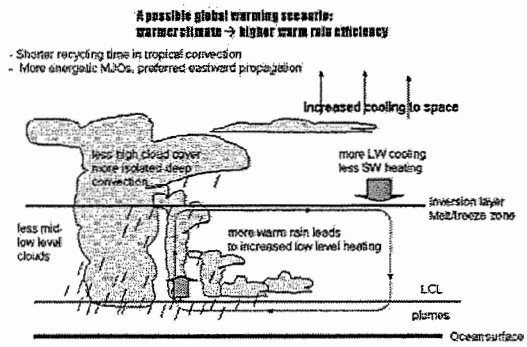

Figure 8. Schematic representation of the atmospheric responses to a warmer climate.

5. ACKNOWLEDGEMENTS

This work is supported by the Tropical Rainfall Measuring Mission (TRMM) Project of the NASA Earth Science Enterprise.

6. REFERENCES

Johnson, R. H., T. M. Rickenbach, S. A. Rutledge, P. E. Ciesielski, and W. H. Schubert, 1999: Trimodal characteristics of tropical convection. *J. Climate*, ***12***, 2397-2418.

Kummerow, C., W. Barnes, W. T. Kozu, J. Shiue, and J. Simpson, 1998: The Tropical Rainfall Measuring Mission (TRMM) Sensor Package. *J. Atmos. Oceanic Tech.*, *15*, 808-816.

Lau, K.-M., and H.-T. Wu, 2003: Warm rain processes over tropical oceans and climate implications. Geophy. Res. Lett., **30**, 2290-2294.

Mapes, B. E., 2000: Convective inhibition, subgrid scale triggering energy, and stratiform instability in a toy tropical wave model. *J. Atmos. Sci.,* ***57,*** 1515-1535.

Schumacher, C., and R. A. Houze, 2003: The TRMM precipitation radar view of shallow, isolated rain. *J. Applied Meteorology*, 42, 1519-1524.

Sud, Y. and G. K. Walker, 1999: Mircophysics of clouds with the relaxed Arakawa-Schubert cumulus scheme (McRAS), Part II: Implementation and performance in GEOS II GCM. *J. Atmos. Sci.*, 56, 3221-3240.

Sundqvist, H., E. Berge, and J. E. Kristjansson, 1989: Condensation and cloud parameterization studies with a mesoscale numerical weather prediction model. *Mon. Wea. Rev.,* 117, 1641-1657.

Tiedtke, M., 1993: Representation of clouds in large scale models, *Mon. Wea. Rev.*, 121, 3040-3061.

AN IMPROVED ALGORITHM FOR IN SITU ICE WATER CONTENT MEASUREMENTS WITH APPLICATIONS TO CIRRUS AND OTHER ICE CLOUDS

R. Paul Lawson and Brad Baker

SPEC Incorporated, Boulder, CO 80301 USA

1. Introduction

The ice water content (IWC) of natural clouds is a quantity that is fundamental to several disciplines in the atmospheric sciences, including studies of the formation of the ice phase and precipitation, radiative transfer, cloud chemistry and all numerical models that include cold cloud processes. Several investigators have collected data sets of ice crystal images on the ground and photographed the crystals and their equivalent melted drops under a microscope (e.g., Davis 1974; Locatelli and Hobbs; 1974; Mitchell et al. 1990). The ice crystals are sorted into habit categories and size-to-mass relationships of the form $M = \alpha L^{\beta}$ are determined, where M is particle mass, L is particle maximum dimension and α and β are constants determined by curve fitting to a population of ice particles.

The relationships are often applied to two-dimensional (2D) cloud particle images, for example, the 2D-C probe described by Knollenberg (1970), which has been a standard in the research community for the past 30 years. In this paper, we show results of a re-analysis of the data set collected by Mitchell et al. (1990), hereafter M90. In addition to L, the new analysis incorporates the particle width (W), area (A) and perimeter (P). Significant improvement in the determination of particle mass, about a 50% reduction in RMS error, is achieved using the new algorithm. In addition, the new technique does not require that the 2D images be segregated by habit, which is often impossible with 2D image data. The new algorithm can be applied to large existing data sets of 2D particle images.

2. The New Algorithm

Figure 1a shows an example from M90 of ice particle images and equivalent melted drops data collected during their 1986-87 field study. A set of fifty-one 35-mm photographic slides of ice particle and associated melted drop data that were collected during the 1986-87 field season was obtained from Dr. Mitchell. The 35-mm photographic slides were digitally scanned and software was used to derive several parameters, such as maximum particle dimension, width, area, perimeter, degree of roundness and radial harmonics (Lawson et al. 2001).

Figure 1b shows examples of three of the ice crystals (circled in **Figure 1a**) that were digitally scanned and then ingested by software that automatically finds the perimeter of the particle, which is shown drawn around each particle in **Figure 1b**, and computes the particle dimensions used in this study. **Figure 1c** shows a schematic comparison of the single parameter, maximum particle length (L) used in the M90 analysis, and the four parameters, L, W, A and P, used in the present analysis. The comparison can be explained by considering the relationship $M = \alpha X^{\beta}$, where $X = L$ in the M90 analysis, and $X = A \times W \times 2(L + W) / P$ in the reanalysis. The new relationship, illustrated in **Figure 1c** and called the "new algorithm", improves on the M90 analysis by measuring parameters that describe the shape of the ice particle. In the new algorithm, A represents the solid part of the particle on the 2D image, W represents its extension out of the 2D plane and $2 \times (L + W)/P$ reflects its decreased average density when its perimeter is convoluted. The new algorithm will over predict the mass of spherically shaped particles with diameters less than 100 μm. Since this is physically unrealistic, the algorithm is applied with the condition that, if the computed mass exceeds that of a sphere with diameter equal to L, then the mass of the equivalent sphere is used.

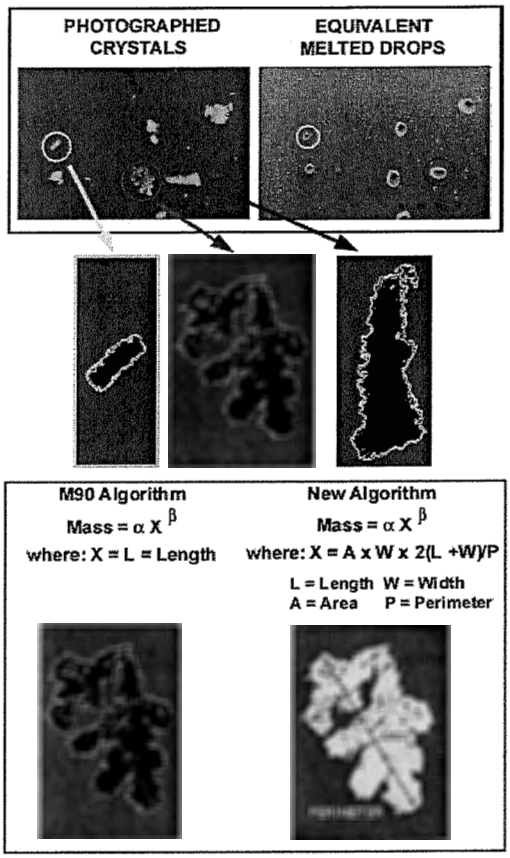

Figure 1. Photographs of (top) M90 ice crystals, (middle) digital images and schematic of M90 and the new algorithm used in the re-analysis.

Corresponding Author's Address: Dr. R. Paul Lawson
SPEC Incorporated, 3022 Sterling Circle, Suite 200,
Boulder, CO. 80301 USA plawson@specinc.com

In M90, the shapes of the particles are considered by classifying each particle as a certain type, and then using a size-to-mass relationship determined for that type of crystal. In the current technique, the particle shape information is included in the single parameter $X = A \times W \times 2 \times (L + W)/P$. In addition to including more parameters, the new technique eliminates the need to initially (manually or algorithmically) classify the images by particle type. Ice particle images in data sets collected by 2D-C probes can rarely be automatically (or manually) classified into the habit categories used by M90, so the shape information supplied by M90 is seldom of practical value.

As shown in Table 1 in M90, 643 ice crystals were classified in the original study. In our reanalysis, we selected 549 of these ice particle and equivalent melted drop images that we could unambiguously identify. Next, we added an analysis of 315 images that were collected by M90 but not analyzed, bringing the total to 864 particle images. We verified our analysis technique by re-analyzing 21 of the particle images in the original data set. Excellent agreement was found between M90 and our computation of maximum particle dimensions and equivalent melted drop diameters.

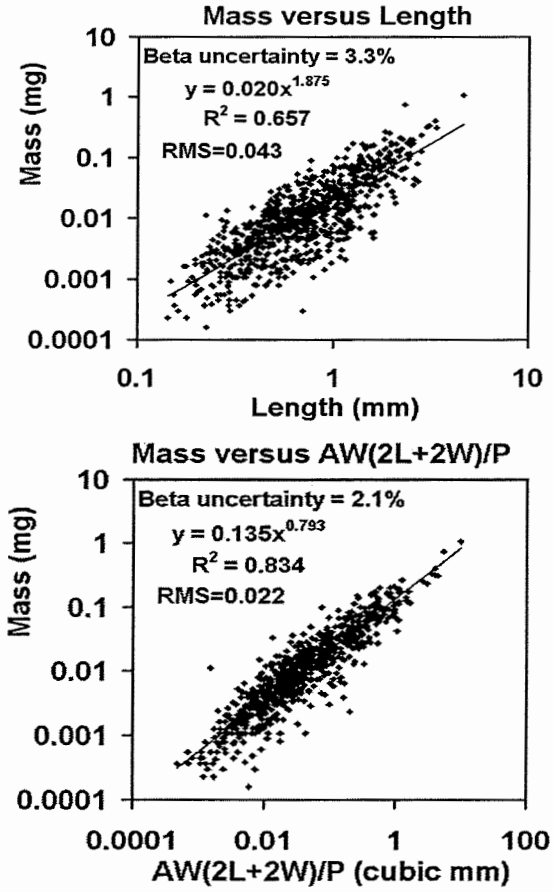

Figure 2. Scatter plots of (top) Mass vs Length and (bottom) the new parameter with statistical parameters explained in the text.

2. The New Parameter versus Length Alone

Two measures were chosen to quantify the improvement achieved using the new parameter. These relate to two basic types of error. One type of error is simply the differences between the actual particle masses and their estimated masses using the mass-size relationship. This we call error type I and represent it with the RMS differences and the correlation coefficient. The other is the robustness of the mass-size relationships, which is an estimate of how accurately β was determined from the limited data set. This we call error type II and explore it with a bootstrap analysis that yields an uncertainty in β, which is calculated as the standard deviation divided by the mean of the bootstrapped βs. Type I error influences how many particles must be averaged together to obtain an acceptable estimate of ice water content assuming the relationship is correct on average. Type II error deals with whether the mass size relationship is correct on average when extended to other similar data.

Figure 2 shows results from a comparison of the new parameter versus Length alone. Using Length, which is substantially the same analysis conducted by M90 but using 849 instead of 643 images, the RMS error in the predicted mass is 0.049 mg and the uncertainty in β is 3.3%. If each of the images is first classified by habit and a separate mass-to-length relationship used for each habit type (not shown), the RMS error reduces slightly (by ~16%) to 0.041 mg, and the uncertainties in β for each habit-conditioned relationship increase (9% to 34% depending on habit type). Using the new parameter, the RMS error in predicted mass (Type 1 error) is reduced (by about 50%) to 0.022 mg and the uncertainty in β (Type 2 error) is reduced to 2.1%. Thus, the new parameter, $X = A \times W \times [2 \times (L + W)/P]$ is a much better predictor than length alone, or even length alone but with a in different relationship for each crystal type.

3. Application to Data Collected in Natural Clouds

As mentioned in the Introduction, there are a number of empirical fits to experimental data using the relationship $M \ \alpha \ L^{\beta}$, which results in estimates for α and β. Two of the most common algorithms currently in use are reported by M90 and Brown and Francis (1995), hereafter BF95. The coefficients α and β are determined from least squares fits to the experimental data, either after sorting the particles by habit or using the entire data set. As mentioned previously, it is rarely possible using 2D-C and 2D-P imagery to effectively sort particles by habit, so the best-fit equation to the entire experimental data set is generally used.

Next, we discuss the results of applying the M90 and new IWC algorithms to data sets collected in natural clouds. The first data set we discuss was collected by a cloud particle imager (CPI) (Lawson et al. 2001) on the ground at the South Pole. The crystals fell a very short distance from clouds that were within 1 km of the ground, and the crystals were formed at the cold temperatures typically observed in

cirrus and wave clouds. Also, the crystals are often pristine and unrimed, so that comparisons of the algorithms can be performed on a controlled data set. An added advantag is that the geometry of South Pole ice crystals is very similar to those found in cirrus clouds, so that the crystals observed at the South Pole may be used as a surrogate for cirrus crystals. A disadvantage of the South Pole data set is that the crystal size rarely exceeded 300 μm in length, so analysis of these data only applied to crystals < ~ 300 μm. The second data set we discuss was collected by the SPEC Learjet research aircraft in cirrus, wave, anvil and deep convective clouds, and by a C-130 research aircraft operated by the National Center for Atmospheric Research (NCAR) in a deep Arctic stratus cloud. This data set contains ice particles measured by FSSP, CPI and 2D probes that are combined into a composite particle size distribution. The sizes of crystals in this data set ranged from about 20 μm to in excess of 1 cm. The discussion of this data set is especially useful for evaluation of IWC errors using M90 and BF95 algorithms compared with the new algorithm in various cloud types.

Figure 3 shows examples of ice crystals imaged by a CPI at the South Pole and IWC calculations using M90, BF95 and the new algorithm. The images have been automatically sorted into particle habit categories so that the comparisons can be evaluated under controlled conditions. The results from **Figure 3** show that the IWCs computed using average M90 and BF95 algorithms are generally close in value. The new algorithm gives IWCs that are close in value to M90 and BF95 when the aspect ratios of the particles are close to one, such as for plates, budding rosettes and rosettes. In contrast, the average M90 and BF95 algorithms both significantly overestimate IWC for crystals up to 300 μm that have high aspect ratios. For example, **Figure 3** shows that both the average M90 and BF95 algorithms overestimate IWC by a factor of 5 for South Pole columns, compared with the new algorithm.

Figure 4 shows examples from several natural cloud types of particle images collected by 2D-C and CPI probes and IWC computed using M90, BF95 and the new algorithm. 2D-P images are also used in the data set collected by the NCAR C-130 in Arctic stratus clouds. The 2D-P is similar to the 2D-C except that it has 200 μm pixels; we used 2D-P data for L > 1 mm in this study. In the upper parts of cirrus and wave clouds at temperatures < - 50 ° C, where the particle types are mostly small spheroidal particles and budding rosettes < 200 μm, IWC from the average M90 and BF95 algorithms (which reduce to the formula for a sphere) are nearly identical to the new algorithm. However, in clouds with particles > ~300 μm and aspect ratios < 2:1, the average M90 and BF95 algorithms tend to underestimate IWC by about a factor of 2. If the particle size distribution contains high concentrations of small (~50 μm) particles and/or particles with high (> 4:1) aspect ratios, the average M90 and BF95 algorithms tend to slightly overestimate IWC compared with the new algorithm.

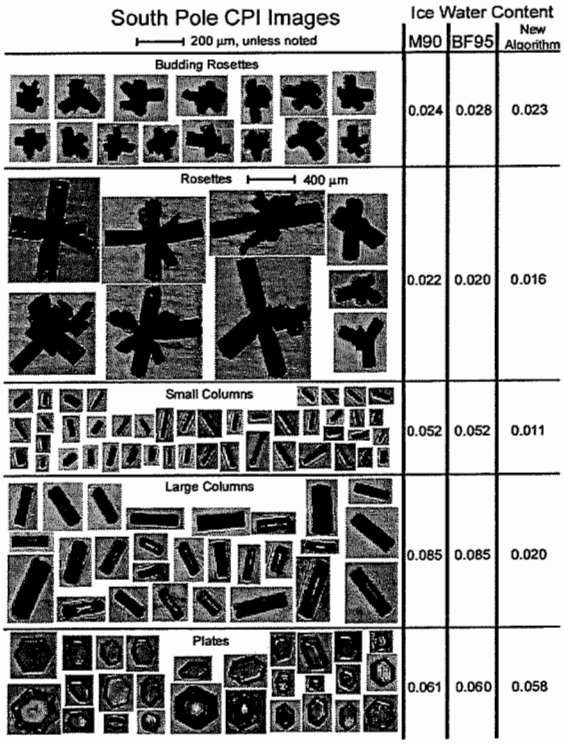

Figure 3. Example of CPI images of ice crystals collected at the South Pole and IWC values computed using the new algorithm compared with M90 and BF95.

Acknowledgements

This research was funded under NSF Grant No. ATM-9904710. We are very appreciative of the cooperation and guidance offered by Dr. David Mitchell of the Desert Research Institute.

References

Brown, P.R.A. and P.N. Francis, 1995: Improved measurements of the ice water content in cirrus using a total-water probe. *J. Atmos. Oceanic Technol.*, **12**, 410-414.

Davis, C.I., 1974: The ice-nucleating characteristics of various AgI aerosols. *University of Wyoming, Department of Mechanical Engineering*, Ph.D. dissertation.

Knollenberg, R.G., 1970: The optical array: An alternative to scattering or extinction for airborne particle size determination. *J. Appl. Meteor.*, **9**, 86-103.

Lawson, R.P., B.A. Baker, C.G. Schmitt and T.L. Jensen, 2001: An overview of microphysical properties of Arctic clouds observed in May and July during FIRE.ACE. *J. Geophys. Res.*, **106**, 14,989-15,014.

Locatelli, J.D. and P.V. Hobbs, 1974: Fall speeds and masses of solid precipitation particles. *J. Geophys. Res.*, **79**, 2185-2197.

Mitchell, D.L., R. Zhang and R.L. Pitter, 1990: Mass-dimensional relationships for ice particles and the influence of riming on snowfall rates. *J. Applied Meteor.*, **29**, 153-163.

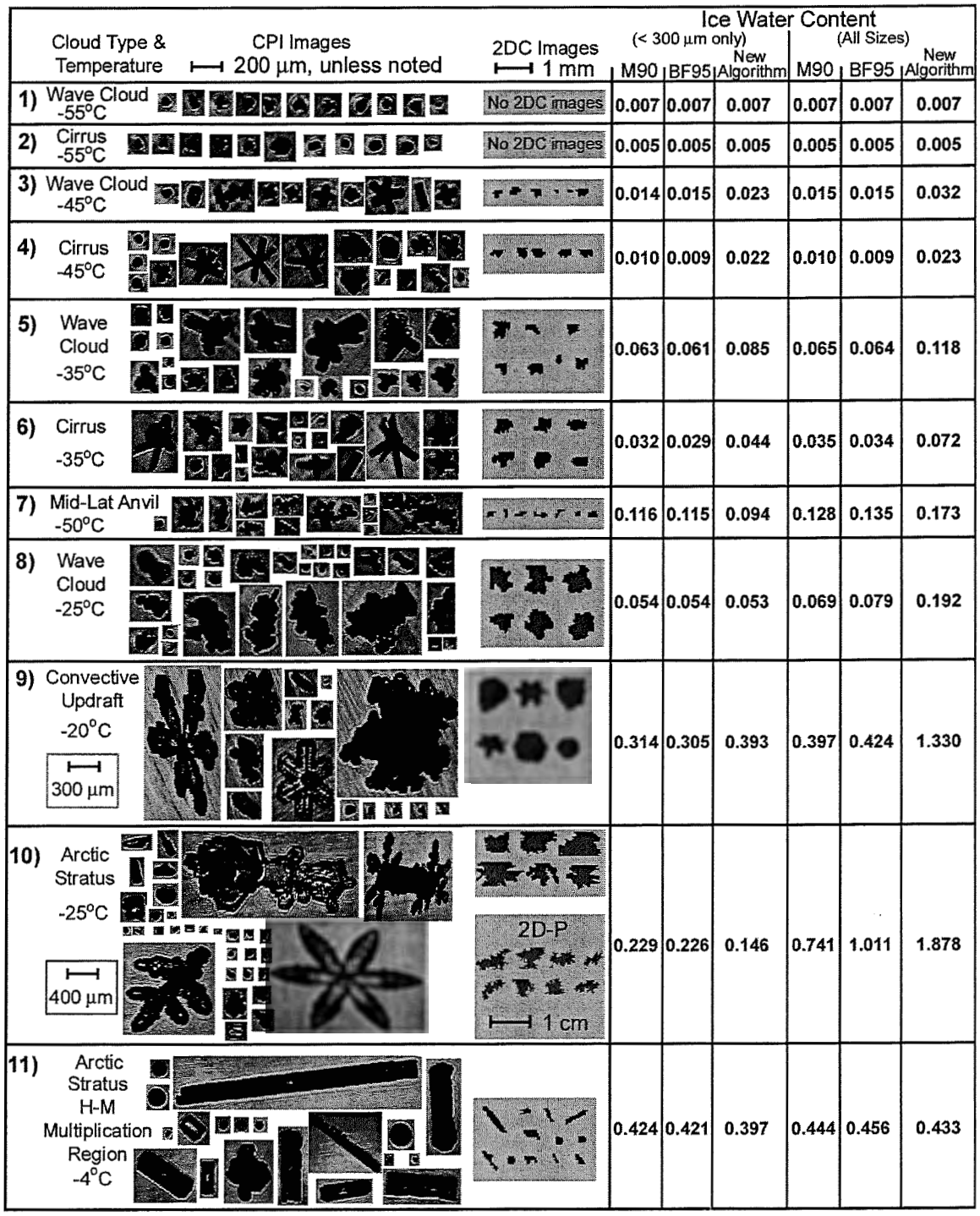

Figure 4. Examples using the new algorithm with M90 and BF95 of IWC computations in various types of clouds. The cloud type and temperature are shown in the column at the left, examples of CPI and 2D images are shown in the middle and values of IWC (separated for particles < 300 µm and all particles) are shown in columns at the right.

RAINFALL MEASUREMENTS FROM SPACE: WHERE ARE WE?

Vincenzo Levizzani, and Alberto Mugnai

CNR-Institute of Atmospheric Sciences and Climate, Bologna and Roma, Italy

1. INTRODUCTION

Measuring precipitation from space is a long standing need of operational meteorology, hydrology and climate. Since the launch of the first meteorological satellites in the 60s methods for "inferring", rather than "measuring" rainfall intensity from space were conceived and calibrated from time to time. Since then the products have greatly evolved in time and always offered a sufficient quality when averaged over suitable time and space scales, but generally suffered from contradictory performances when coming down to instantaneous rainrates. New methods try to incorporate the physical basics of precipitation formation and evolution: the cloud physics content of the algorithms is re-examined and better observational and modeling tools are now available.

International efforts in the field of precipitation measurements from space focus on:

- Cloud microphysics and cloud modeling for advanced rain retrieval algorithms;
- Cooperative missions including the Global Precipitation Measurement (GPM), the European contribution to GPM (EGPM), the Earth Clouds Aerosol and Radiation Explorer (EarthCARE), CloudSat, Calypso, Megha-Tropiques;
- International teams such as the International Precipitation Working Group (IPWG) and the Global Precipitation Climatology Project (GPCP).

Currently open problems are, among others:

- Quantitative measurements for all kinds of applications;
- Measurement of solid precipitation at high latitudes;
- Improvements required to measure light rain and sustained low rainrates during stratiform events;
- Synergy between active and passive sensors;
- Validation strategies that need to be upgraded to match the modified sensor performances and the enhanced physical content of the algorithms.

Synergies between satellite meteorology, cloud physics, cloud modeling, numerical weather prediction (NWP), hydrology, and climate change studies are necessary to advance performances of algorithms at all scales, regional to global (Levizzani et al. 2004).

2. THE PRECIPITATION PROBLEM

Knowledge of precipitation amount and precipitation processes is directly related to the understanding of the global energy and water cycle through climate diagnostics and modeling, NWP, nowcasting, hydrological applications, oceanography, flood forecasting, transportation, agro-meteorology, and water resource management (ESA 2004).

Precipitation is a major source of energy for driving the atmospheric circulation through the storage, transport and release of latent heat associated to the precipitation formation processes. It constitutes about 75% of the heat energy of the atmosphere. The energy equivalent of precipitation at the surface is estimated to be of the order of 85 W m^{-2}: this is about one third of the solar radiative energy available to the Earth's system, and 80% of the net radiative energy at the surface. Therefore, accurate knowledge of precipitation is crucial for understanding weather and climate at all scales. Cloud-aerosol interactions are also crucial in precipitation formation and play a key role in global climate changes.

Clouds are the source of all precipitation, but details of precipitation formation processes are poorly understood. Understanding them is crucial for quantitative precipitation forecasting (QPF). The societal benefits in providing warning of flash flooding would be immense. Global observations of the probability distribution function of vertical motions within the grid box to constrain convective parameterization schemes are also needed. Measurements of precipitation amount from space are therefore very much needed for local as well for global weather and climate applications considering the necessarily sparse distribution and scarce amount of raingauges, which are obviously limited to the continents. Science and technology are advancing fast and considerable efforts are being devoted to the task.

3. MEASURING PRECIPITATION FROM SPACE: HOW?

It is difficult to look at satellite precipitation estimates from a unified perspective encompassing all possible applications and considering all instrument-related aspects (e.g. Levizzani et al. 2002). Rainfall estimation methods have been conceived using data from sensors in the visible/infrared (VIS/IR) and passive microwave (PMW), and from precipitation radar (PR). It has been clearly demonstrated that PMW and PR data are more linked to the physical structure of the cloud and therefore more responsive to precipitation formation processes.

Technical limitations presently limit the launch of PMW sensors to Low Earth Orbits (LEO) though advancements are in view leading to the first PMW

sensor at the geostationary level (Bizzarri et al. 2003). Technological developments of PMW instruments and radar on board LEO orbiters at the end of the 90s culminated in the launch of the Tropical Rainfall Measuring Mission (TRMM) (Kummerow et al. 2000), which marked a breakthrough in our observational capabilities of the atmosphere-ocean system.

However, the use of VIS, IR and water vapor (WV) channels of geostationary satellites is by no means over considering the need for truly global and instantaneous coverage. Rainfall estimation methods that work in this spectral range attribute precipitation levels based on cloud top brightness temperature. Ancillary quantities such as water vapor vertical content, wind field, cloud classification, and radar rainfall data sets may play a role from time to time, but the assignment of rainrates is in general very indirect and regardless of the actual cloud structure.

"Blended" methods that combine rainrates as retrieved by PMW sensors at LEO orbits with brightness temperatures in the IR from GEO sensors have recently come out (e.g. Turk et al. 2000; Kidd et al. 2003). The idea is to dwell upon the superior performances of PMW sensors that overpass scarcely a given area and "calibrate" the IR temperatures of the GEO imagery that is available at 15-30 min intervals. Frequently upgraded rain maps are thus produced with the necessary space-time coverage for a number of different applications that range from assimilation into NWP models to hydrology and climate change.

The specific application of satellite-retrieved rainrates obviously determines the space-time accuracy and the monitoring strategy. From very frequent instantaneous measurements for hydrology and water management to 6-hourly data for NWP assimilation up to daily and monthly values for climatological applications, a wide range of algorithms is available. In particular, satellite retrievals (e.g. Huffman et al. 2001) have revealed instrumental to an increased understanding of global change trends as the GPCP group has demonstrated.

4. CHALLENGES POSED BY GPM AND APPLICATIONS

The GPM mission will further advance the current capabilities of measuring precipitation from space widening the scope to global measurements with its advanced radar and radiometer systems and constellation concept (Shepherd et al. 2002). The GPM, while trying to fill in a gap of global data and space-time coverage, poses clear problems and challenges that were already hidden between the lines of past missions and algorithms.

Kummerow et al. (2004) point out that it is "of utmost importance the need for a transparent, parametric algorithm that insures uniform rainfall products across all sensors". The key requirements for the new algorithm(s) are:

1. Based on an open architecture that will allow the international community to participate in the algorithm development, its refinement, and its error characterization.
2. Parametric structure given the fact that GPM is a cooperative mission between many agencies and algorithms cannot be designed for specific radiometers with defined frequencies, viewing geometry, spatial resolutions or noise characteristics.
3. Robustness in such a way that differences between sensors can be confidently interpreted as physical differences between observed scenes rather than artifacts of the algorithm.

One of the top challenges is represented by the full characterization of uncertainties at any space-time scale from instantaneous estimates needed for hydrologic and weather forecasting applications (e.g. Ebert 2003) to large space and time averages required for climate model verification and climate trend monitoring (e.g. Gebremichael et al. 2003). Such a complete error characterization does not currently exist and is undoubtedly the greatest challenge facing the community. Ongoing efforts are being sponsored by the IPWG (http://www.isac.cnr.it/~ipwg/) and the GPCP (http://cics.umd.edu/~yin/GPCP/) as part of their institutional activities.

5. UPFRONT RESEARCH TOPICS

In order to meet the operational GPM requirements and, more generally, to improve the quantitative standard of rainfall measurements, several key research topics are identified. We will briefly examine a few of them that are directly related to cloud physics:

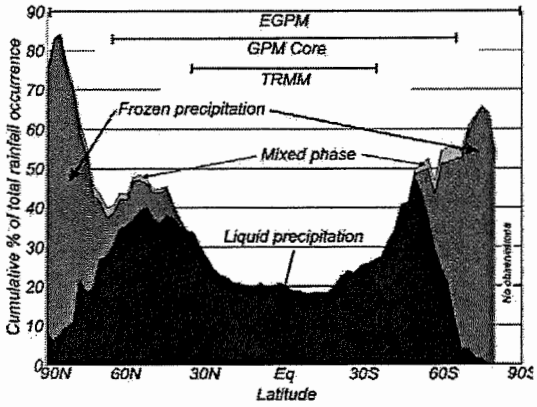

Figure 1. Mean zonal occurrence of oceanic light precipitation (% of total rainfall occurrence) derived from the Comprehensive Ocean-Atmosphere Data Set using ship-borne meteorological observations (1958-1991). The bars indicate the latitudinal coverage of TRMM and those foreseen for GPM and EGPM. (courtesy of C. Kidd, Univ. of Birmingham, and European Space Agency, ESA 2004)

- Snowfall and light rain measurement.
- Cloud-aerosol interactions and physics of precipitation formation.
- Verification of model output.

When referring to precipitation measurements it is rarely considered that in reality we are dealing with liquid precipitation. However, at latitudes above about 60 N-S frozen precipitation becomes predominant for large part of the year as is clear from Fig. 1 where data from the Comprehensive Ocean-Atmosphere Data Set (COADS) are shown. For instance, while the typical annual average precipitation total in Canada is 535 mm, with 36% falling as snow, in northern Canada the proportion of snowfall to total precipitation ramps up to approximately 90%, almost all of which is produced in the form light snowfall (Mugnai et al. 2004). The latitudinal dependence of the snow to total precipitation ratio is shown in Fig. 2 for three locations from south to north Canada. Therefore, light snowfall, and a smaller component of light rainfall, are key drivers to the water cycle in mid to northern latitudes. This issue is manifest in seeking to understand how snow accumulation is changing in the context of the current global warming trends, for example the presumed growth of the Greenland ice sheet, which seems very small to represent a real response to a warmer polar climate (Davis et al. 1998).

The EGPM mission is specifically designed to detect and measure snowfall, light rain, and warm rain – both over land and ocean – particularly in mid and northern latitude climates (Mugnai et al. 2004). The payload consists of: (1) an innovative conically scanning PMW radiometer combining the conventional rain-measuring window channels at 18, 23, 37, and 85 GHz, a high-frequency window channel at 150 GHz, and four cross-paired temperature-sounding channels near 52 and 118 GHz (four channels in each O_2 absorption region); and (2) a Ka-band (35.6 GHz) 3-beam nadir-pointing precipitation radar having a sensitivity of ~5 dBZ.

The sounding channels respond to scattering by snow and are less sensitive to surface emission than the window channels. Additionally, coupled radiometric observations within the strong oxygen absorption band between 50-54 GHz and near the strong O_2 absorption line at 118.75 GHz, permit the accurate retrieval of precipitation information by exploiting differential atmospheric absorption within each band and differential hydrometeor scattering between the two bands. Choosing pairs of frequencies in the two O_2 absorption regions that have similar weighting functions for clear skies over precipitating clouds, enables vertical partitioning (slicing) of the frozen cloud constituents.

Cloud physics research aspects are key to another important area of rainfall measurements from space, the aerosol-cloud interactions. Satellite observations have shown direct evidence that aerosols from forest

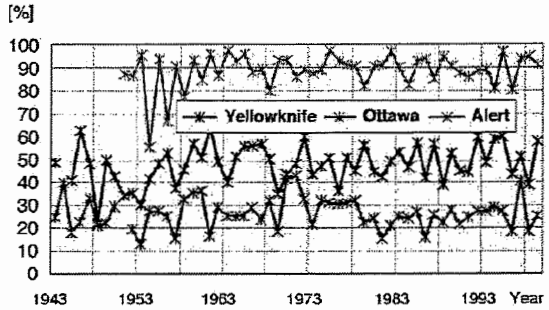

Figure 2. Snow to total precipitation ratio for selected latitudinal locations in Canada. Bottom to top curves: Ottawa (~48°N), Yellowknife (~63°N), and Alert (~84°N). (courtesy of P. Joe, Meteorological Service Canada, and European Space Agency, ESA 2004)

fires (Rosenfeld 1999) and urban and industrial pollution (Rosenfeld 2000) inhibit precipitation formation. Ramanathan et al. (2001) argue that aerosols can lead to an increase in solar heating of the atmosphere, changes in the atmospheric temperature structure, suppression of rainfall, and less efficient removal of pollutants. These effects can contribute to weaken the hydrological cycle.

In particular, recent studies were carried out in the Amazon rainforest area to find out more about the aerosol influence on cumulus cloud formation and the net climate forcing actions. Koren et al. (2004) have used satellite data over the Amazon region during the biomass burning season to show that scattered cumulus cloud cover was reduced from 38% in clean conditions to 0% for heavy smoke (optical depth of 1.3). At the same time Andreae et al. (2004) have demonstrated that heavy smoke from forest fires in the Amazon reduces cloud droplet size insofar delaying the onset of precipitation from 1.5 kilometers above cloud base in pristine clouds to more than 5 kilometers in polluted clouds and more than 7 kilometers in pyro-clouds. Suppression of low-level rainout and aerosol washout allows transport of water and smoke to upper levels. Elevating the onset of precipitation allows invigoration of the updrafts, causing intense thunderstorms, large hail, and greater likelihood for overshooting cloud tops into the stratosphere. There, detrained pollutants and water vapor would have profound radiative impacts on the climate system.

Finally, let us mention the issue of cloud structure and model verification that will see clouds and precipitation physics from space play a crucial role for the improvement of precipitation measurements. Three major points need to be addressed first:

- It has been demonstrated that radar and lidar can distinguish liquid and ice phases in clouds (e.g. Hogan et al. 2003) thus helping rainfall measurements based on physical algorithms.

- Calculations show the presence of supercooled liquid water to be fundamental to for the radiative properties of cloud.
- Yet, cloud representation in models is very crude and unevaluated.

An adequate synergy of ground based and satellite borne instruments is required to address open cloud structure issues. Missions such as EarthCARE and CloudSat, in synergy with GPM and EGPM, offer the appropriate suite of instruments and observing strategies that are needed to link together the cloud physics and the precipitation communities in a combined effort. This will also be the target of international projects that are now being conceived and will be launched in the next future.

Model verification is a compelling issue at all scales and it is clear that precipitation measurements from space must attain a higher quality level to be effective in this direction. This will proceed in parallel with the improvement of clouds and precipitation parameterization in the models.

Acknowledgements

This research was sponsored by the EURAINSAT project, a shared-cost project (contract EVG1-2000-00030), co-funded by the Research DG of the European Commission within the RTD Activities of a Generic Nature of the Environment and Sustainable Development sub-programme (5th Framework Programme). Partial support was provided by the Italian Space Agency (ASI). Collaboration from the International Precipitation Working Group (IPWG) and the Global Precipitation Climatology Project (GPCP) is gratefully recognized.

REFERENCES

Andreae, M. O., D. Rosenfeld, P. Artaxo, A. A. Costa, G. P. Frank, K. M. Longo, and M. A. F. Silva-Dias, 2004: Smoking rain clouds over the Amazon. *Science*, **303**, 1337-1342.

Bizzarri, B., A. Gasiewski, and D. Staelin, 2003: Frequent rain observation from geostationary satellite by millimeter sub-millimeter- wave sounding. *Proc. 1st IPWG Workshop*, ISBN 92-9110-045-5, 101-112. [http://www.isac.cnr.it/~ipwg/]

Davis, C. H., C. A. Kluever, and B. J. Haines, 1998: Elevation change of the southern Greenland ice sheet. *Science*, **279**, 2086-2089.

Ebert, E. E., 2003: Verifying satellite precipitation estimates for weather and hydrological applications. *Proc. 1st IPWG Workshop*, ISBN 92-9110-045-5, 215-224. [http://www.isac.cnr.it/~ipwg/meetings/madrid/madrid2002-proc.html]

ESA, 2004: EGPM–European Contribution to Global Precipitation Measurement. *Rep. for Mission Selection: The six candidate Earth Explorer Missions.*, ESA SP-1279(5), 69 pp. [http://www.esa.int/export/esaLP/SEMF2KYV1SD_index_0.html]

Gebremichael, M., W. F. Krajewski, M. M. Morrissey, D. Langerud, G. J. Huffman, and R. F. Adler, 2003: Error uncertainty analysis of GPCP monthly rainfall products: a data-based simulation study. *J. Appl. Meteor.*, **42**, 1837-1848.

Hogan, R. J., P. N. Francis, H. Flentje, A. J. Illingworth, M. Quante, and J. Pelon, 2003: Characteristics of mixed-phase clouds. I: Lidar, radar and aircraft observations from CLARE'98. *Quart. J. Roy. Meteor. Soc.*, **129**, 2089-2116.

Huffman, G. J., R. F. Adler, M. M. Morrissey, D. T. Bolvin, S. Curtis, R. Joyce, B. McGavock, and J. Susskind, 2001: Global precipitation at one-degree daily resolution from multisatellite observations. *J. Hydrometeor.*, **2**, 36-50.

Kidd, C., D. R. Kniveton, M. C. Todd, and T. J. Bellerby, 2003: Satellite rainfall estimation using combined passive microwave and infrared algorithms. *J. Hydrometeor.*, **4**, 1088-1104.

Koren, I., Y. J. Kaufman, L. A. Remer, and J. V. Martins, 2004: Measurement of the effect of Amazon smoke on inhibition of cloud formation. *Science*, **303**, 1342-1345.

Kummerow, C., H. Masunaga, and P. Bauer, 2004: A next-generation microwave rainfall retrieval algorithm for use by TRMM and GPM. In: *Measuring precipitation from space*, V. Levizzani, P. Bauer, and F. J. Turk, Eds., Kluwer Acad. Publ. Dordrecht, in press.

Kummerow, C., J. Simpson, O. Thiele, W. Barnes, A. T. C. Chang, E. Stocker, R. F. Adler, A. Hou, R. Kakar, F. Wentz, P. Ashcroft, T. Kozu, Y. Hong, K. Okamoto, T. Iguchi, H. Kuroiwa, E. Im, Z. Haddad, G. Huffman, B. Ferrier, W. S. Olson, E. Zipser, E. A. Smith, T. T. Wilheit, G. North, T. Krishnamurti, and K. Nakamura, 2000: The status of the Tropical Rainfall Measuring Mission (TRMM) after two years in orbit. *J. Appl. Meteor.*, **39**, 1965-1982.

Levizzani, V., R. Amorati, and F. Meneguzzo, 2002: *A review of satellite-based rainfall estimation methods.* European Commission Project MUSIC Report (EVK1-CT-2000-00058), 66 pp. [http://www.isac.cnr.it/~meteosat/pub.shtml]

Levizzani, V., P. Bauer, and F. J. Turk (Eds.), 2004: *Measuring precipitation from space.* Kluwer Acad. Publ., Dordrecht, in press.

Mugnai, A., S. Di Michele, E. A. Smith, F. Baordo, P. Bauer, B. Bizzarri, P. Joe, C. Kidd, F. S. Marzano, A. Tassa, J. Testud, and G. J. Tripoli, 2004: Snowfall measurements by proposed European GPM mission. In: *Measuring precipitation from space*, V. Levizzani, P. Bauer, and F. J. Turk, Eds., Kluwer Acad. Publ. Dordrecht, in press.

Ramanathan, V., P. J. Crutzen, J. T. Kiehl, and D. Rosenfeld, 2001: Aerosols, climate, and the hydrological cycle. *Science*, **294**, 2119-2124.

Rosenfeld, D., 1999: TRMM observed first direct evidence of smoke from forest fires inhibiting rainfall. *Geophys. Res. Lett.*, **26**, 3105–3108.

Rosenfeld, D., 2000: Suppression of rain and snow by urban and industrial air pollution. *Science*, **287**, 1793-1796.

Shepherd, J. M., E. A. Smith, and W. J. Adams, 2002: *Bridging from TRMM to GPM to 3-hourly precipitation estimates.* GPM Rep., 7, 12 pp. [http://gpm.gsfc.nasa.gov/library.html]

Turk, J. F., G. Rohaly, J. Hawkins, E. A. Smith, F. S. Marzano, A. Mugnai, and V. Levizzani, 2000: Meteorological applications of precipitation estimation from combined SSM/I, TRMM and geostationary satellite data. In: *Microwave Radiometry and Remote Sensing of the Earth's Surface and Atmosphere*, P. Pampaloni and S. Paloscia Eds., VSP Int. Sci. Publisher, Utrecht (The Netherlands), 353-363.

All-sky Visible and Infrared Images for Cloud Macro Characteristics Observation

Daren Lu Juan Huo Wenxing Zhang

Institute of Atmospheric Physics, Chinese Academy of Science

1. INTRODUCTION

Cloud and cloud system are highly inhomogeneous both in its spatial structure and temporal variation, with very different effects on the cloud-radiation interaction, precipitation producing, as well as atmospheric chemistry. Observation of clouds have been conducted with satellite remote sensing, air-borne measurements, and ground-based remote sensing such as meteorological radar and other optical and infrared observation. Each of these techniques has its own function. Although satellite remote sensing of cloud has many advantages, ground-based remote sensing of cloud is still important. For monitoring the sky cloud distribution and its variation, we developed an all-sky imaging system that is consisted of two subsystems. One is the digital camera with all sky fish-eye lenses for daylight images of sky and cloud. Based on observation experience and radiative transfer model simulation, the criteria for identify cloud pixel is established and used to estimate cloudiness and distribution. The other is a scanning infrared thermometer that is used to observe all sky brightness temperature distribution. Based on radiative transfer model simulation, we establish the relationship between IR brightness temperature T_B and cloud base height, surface temperature T_S and humidity H_S, as well as surface visibility V, and aerosol type. Thus from T_B, T_S, H_S, we may estimate cloud base height and their distribution. Long-term observations with this system have been made to reveal cloud macro characteristics. In this paper, we will briefly introduce the systems, retrieval schemes, field observation and preliminary results.

2. OBSERVATION SYSTEMS

For quantitative observation of cloud/clear sky distribution, two systems are developed.

2.1 All-sky visible image system (ASIS)

The first system is an all-sky visible imager, which is consisted of a calibrated digital camera with fish-eye lens and a platform with attitude-controlled direct sunlight protector/attenuator. The digital camera we used in the field observation is a Nikon Colpix4500 digital camera with adapted fish-eye lens. Its field of view is over 180^0. For obtaining quantitative directional sky radiance in broad bands of red, green, and blue, (RGB), calibrations for its geometry, limb darkening, and broad band radiance were conducted in the laboratory. After these calibrations, the sky image can be converted to sky radiance distribution for RGB band, respectively. Then these observation data can be compared with radiative transfer modeling for future applications. The observation can be remote controlled

As the first object of ASIS is to detect cloud pixel and estimate cloud fraction in the daytime, a criteria is established based on color ratio, i.e., the ratio between the radiance in blue band and total radiance (the sum of RGB). This kind of criteria is very similar to those criteria by other scientists[1]. The advantage of this method is that the principle is similar to human eye's function to identify cloud/clear sky. The disadvantage is that for situation of near-horizon, near sun sky, the detection accuracy will be low. In heavy hazy sky of low visibility, the difficulty will be more serious. But all these problems are same for human eye observation. Fig.1 shows the ASIS.

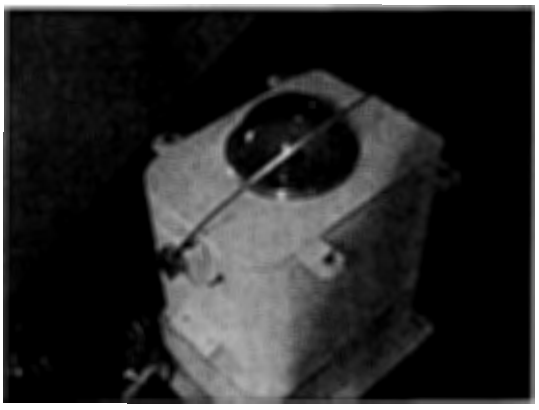

Fig 1. All-sky visible image system

2.2 Scanning Infrared Observation System (SIRS)

As mentioned above, ASIS may obtain the daylight sky image and cloud distribution. Cloud observation in the right time is still a problem. Although there has been high sensitivity sky imager for dark sky observation [2], it is not easy to use routinely in meteorological stations and many other applications. For solving this problem, sky thermal infrared (THIR) observation is a good candidate. For ground-based observation, thermal infrared emission from most clouds can be identified as blackbody with the temperature at cloud base height. In clear sky, water vapor is the major contributor to THIR emission and aerosols play minor role as its size much smaller than the wavelength of THIR (typically ~10 μ m). Therefore,

it is possible to identify cloud by using THIR brightness temperature observation. The other obvious advantage of THIR observation is that this kind of observation and can be made all day and night.

A scanning THIR brightness temperature (T_B) observation system (SIRS) is made by us, which is consisted of a THIR thermometer and a platform. The platform can be scanned in all directions (from zenith to nadir and all azimuths) as all sky/ground THIR T_B can be obtained with this system. The thermometer we used is the Model RangerMX4. Its dynamic range is -50^0C-500^0C. Obviously the lower limit (-50^0C) of this thermometer is not small enough to cover cold clear sky as well as cold thin cirrus clouds. Fig.2 shows the SIRS in the field(lower right of the figure).

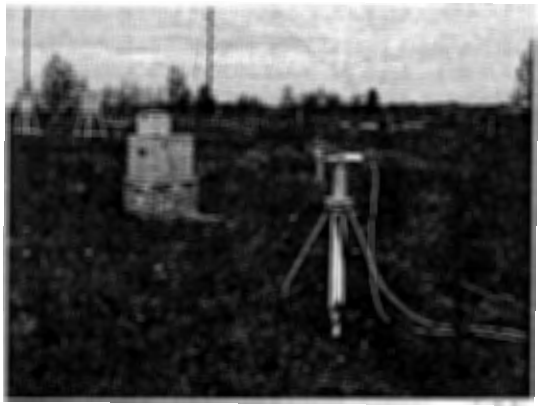

Fig.2 Scanning Infrared Observation System (SIRS)

To identify in certain direction the sky is clear or cloud and determine the cloud base height from THIR brightness temperature observation T_B (θ , Φ), a series of radiative transfer computation of T_B (θ , Φ) are made for different atmospheric profiles (i.e., temperature and humidity profiles) and different cloud layers. In the computation, cloud layer is assumed optically thick and downward thermal infrared emission is same as air temperature at cloud base height. Since in most cases the real time atmospheric profile is not available, we need to make computation with real time surface temperature T_S and humidity H_S, and the average profiles which are adapted to surface parameters. Thus, a series of empirical formula are established to derive clear/cloud and cloud base height by observation of T_B (θ) and T_S, H_S. In fact, this kind of identification of clear/cloudy is statistically valid, because the clear sky brightness temperature will vary for different temperature and humidity profiles in same T_S, H_S. Also clouds are not all optically thick. For thin cirrus clouds, the ability of present method is limited. But for middle and low clouds, the present method is very useful even in low visibility situation.

The ASIS and SIRS have been used for field observation in Beijing and Inner Mongolia grassland. Some examples are introduced in this section.

ASIS observation.

statistics of cloud fraction with different zenith angle

Cloud distribution over Beijing generally tends to two limits, i.e., clear sky and overcast; 2) For same cloud fraction bin, cloud fraction in high zenith angle zone tends higher than that in near zenith zone. It means the vertical extents of cloud play different roles in deferent zenith angles.

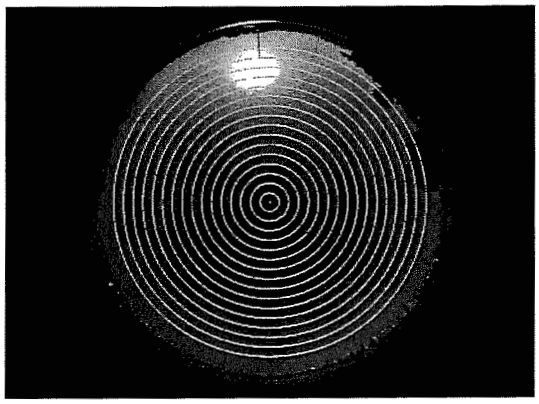

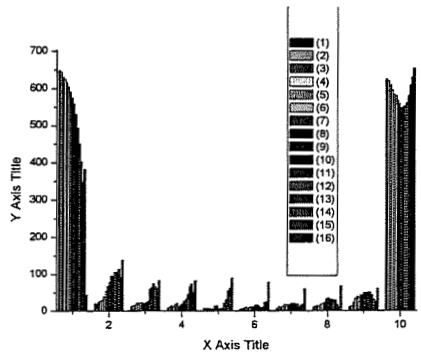

Shoot term observation of SIRS has been conducted in Beijing and Inner Mongolia. A case is shown here. Fig.4 shows a case of SIRS observation at IAP'S field observatory (about 50 km southeast of Beijing). It is a north-south cross section of T_B (θ), from nadir-north-horizon-zenith-south horizon-nadir. Those thin lines mask clear sky, cloud with different cloud base heights, respectively. The cloud and clear sky can be easily identified in this figure. And the approximate

cloud based height can be determined by comparing $T_B(\theta)$ and those lines of iso-cloud base height.

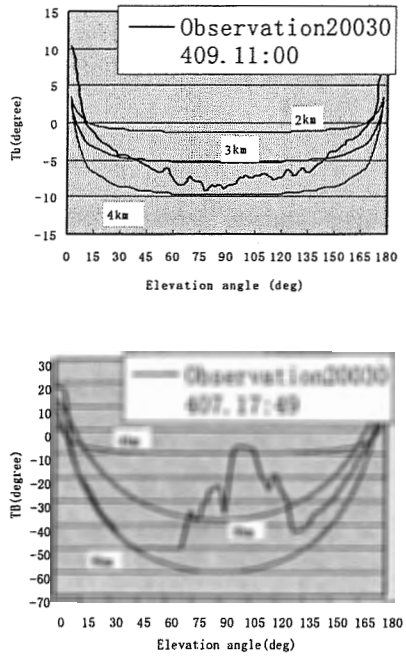

Fig.4 Observation of T_B distribution and corresponding $T_B(\theta)$ of iso-cloud base height at two time intervals.

In this paper, we have introduced two systems, i.e., all sky visible imager (ASIS) and scanning thermal infrared imager (SIRS) for ground-based observation of clear and cloudy sky. Algorithms are developed for identification of clear/cloud sky with ASIS and identification of clear/cloud sky and cloud base height with SIRS. Field observations with these two systems have been conducted at Beijing and Inner Mongolia. Preliminary results show that these systems are useful for operational observation and further research applications.

This work is supported by NSFC

sky imaging and its impact on surface solar irradiance.

sky imager for field assessment of cloud cover distribution and radiance distributions. Thenth Symp. On Meteorological Observations and Instrumentation.

MICROPHYSICALLY-BASED RETRIEVAL OF RAINING CLOUDS BY GROUND-BASED MULTISPECTRAL MICROWAVE RADIOMETRY

Frank S. Marzano[1], Domenico Cimini[1] and Randolph Ware[2]

[1] Centro di Eccellenza CETEMPS, Università dell'Aquila
[2] Radiometric Corporation, Boulder, Colorado

1. INTRODUCTION

Ground-based microwave radiometry has been mainly investigated for estimating temperature, water vapor and cloud liquid profiles in the absence of precipitation (Westwater, 1993). However, the increasing use of multi-frequency radiometers in ground-based stations has raised the question of their potential for retrieving also rainfall rate from ground (Liu et al., 2001; Marzano et al., 2001). From an experimental point of view, one of the main problems of ground-based radiometry for rainfall retrieval is the possible impact of water layers on the receiving antenna whose measurements can be heavily contaminated (Jacobson et al., 1994). From a modeling point of view, the approach to rainfall signature characterization requests a thorough insight into the electromagnetic interaction between the microwave radiation and the scattering medium. The radiative transfer theory has been so far the most used approach to take into account multiple scattering and vertical inhomogeneity of the atmosphere in the presence of hydrometeor scattering (Smith et al., 2002).
Following previous works (Marzano et al., 1999, 2002), the objective of this paper is to investigate about the rainfall signature on multispectral microwave measurements from ground. We develop inversion algorithms for ground-based retrieval of surface rainrate, adopting a model-based approach.

2. RADIOMETRIC MODELING OF RAIN

A general theoretical framework to model the down-welling brightness temperature, measured by a microwave radiometer and due to clouds and precipitation, is given by the radiative transfer theory. For a plane-parallel geometry, the unpolarized down-welling brightness temperature T_b, observed from ground at a frequency ν, can be formally expressed by means of the integral form of radiative transfer equation (RTE). The discrete-ordinate numerical method has been chosen to numerically solve RTE in this work (Tsang et al., 1985). The atmosphere is assumed to consist of L adjacent homogeneous layers in which volumetric albedo w, extinction coefficient ke and phase function p are taken to be constant within layers.

2.1 Rain models

In previous works we described a technique to use cloud-resolving model outputs to physically constrain the vertical correlation of hydrometeor contents within cloud layers. The gross vertical distribution of four species of hydrometeors is described: cloud droplets, raindrops, graupel particles, and snow particles. Cloud structures have been vertically resolved in seven homogeneous layers with a variable vertical resolution of about 1.5 km. The cloud data set, classified into stratiform and convective clouds, has been then extended by means of a Monte Carlo statistical procedure, based on the use of a truncated Gaussian multivariate generator defined by mean and covariance matrix of the hydrometeor contents of each class. Meteorological variables have been supposed to be uniformly variable around their mean values within a given percentage. In this work we have considered both stratiform rainfall (i.e., nimbostratus) and convective rainfall (i.e., cumulonimbus). Consistently with the RTE adopted scheme, within each cloud layer the temperature has been assumed linearly dependent on the height. Microwave gaseous absorption has been computed by means of the Liebe model.

Corresponding author's address: Frank S. Marzano, monteluco di Roio, 67040, L'Aquila. E-mail: marzano@ing.univaq.it

The land-surface emission has been characterized by a Lambertian emissivity model, depending on surface humidity. The humidity value has been supposed randomly variable in order to cover a large variety of surface conditions. The hydrometeor shapes have been assumed all spherical and characterized by inverse-exponential particle size distributions (PSD's). In the logarithmic plane the intercept of a PSD has been derived from the assigned EWC within each layer, while the slope has been parameterized to surface rain-rate using a Marshall-Palmer, a Sekhon-Srivastava and a Gunn-Marshall PSD for raindrops, ice graupel and snow, respectively. Cloud droplets have been assumed to follow a modified Gamma PSD.

2.2 Simulations

By using the coupled rainfall and radiative transfer model illustrated before, a large data set, consisting of 5000 cloud structures together with related brightness temperatures at given frequencies and observation angles, has been simulated. The analysis has included the frequency bands of the operational multi-channel radiometer MWRP. The observation angle has been chosen in accordance to the application, in principle between 0 and 90 degrees elevation. We will show results only for zenith observations in order to be able to compare simulations with radiometric and rain gauge measurements.

3. COMPARISON WITH MEASUREMENTS

In order to interpret and test the rainfall model simulations, we have used measurements from the Microwave Radiometer Profiler (MWRP), manufactured by Radiometrics Corp. The MWRP can provide, by using neural network inversion algorithms, temperature and humidity soundings up to 10 km height and low resolution cloud liquid soundings (Ware et al., 2003). The radiometer observes radiation intensity at 12 frequencies in a region of the microwave spectrum that is dominated by atmospheric water vapor, cloud liquid water, and molecular oxygen emissions. The observation frequencies (i.e., 22.035, 22.235, 23.835, 26.235, 30.00, 51.250, 52.280, 53.850, 54.940, 56.660, 57.290, 58.800 GHz) were chosen by eigenvalue analysis to optimise profile retrieval accuracy. The radiometric profiler includes a vertical infrared sensor and surface temperature, humidity, pressure and rain sensors.

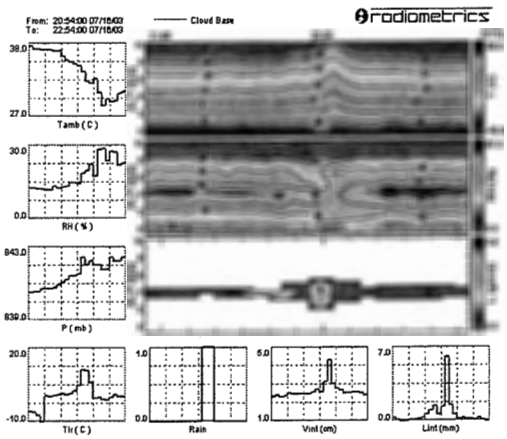

Figure 1 An example of MWRP operational screen output. Plots refer to data collected during 16 July 2003, in Boulder, Colorado, USA. A rain shower happened roughly at 22:00 UTC. Surface temperature, relative humidity, and pressure are shown on the left. Infrared cloud temperature, rain detection, integrated content of vapour and liquid are shown in the bottom. Contour plots show time-height cross sections of atmospheric temperature (top), relative humidity (middle) and liquid water (bottom).

Figure 1 shows the operational real-time output printed on the screen by the proprietary MWRP data acquisition and processing software (VizMet). Time series of temperature, relative humidity, and pressure at the instrument level are shown on the left. Time series of infrared cloud temperature, rain detection, integrated content of vapour and liquid are shown in the bottom. Contour plots show time-height cross sections of atmospheric temperature (top), relative humidity (middle) and liquid water (bottom) retrievals. Thus, the operational output allows the user to monitor in real-time ten fields of meteorological interest simultaneously.

Figure 2 shows the time series of radiometric observation during a rain event occurred on 17 July 2003 in Boulder, Colorado. Rain occurrence is strongly related to the decrease of temperature, the increase of humidity and the increase of measured Tb's in the window region and saturation/depression in the absorbed band. This behaviour is due to the predominance of either emission or scattering in the Tb signature from ground with respect to the clear-air value.

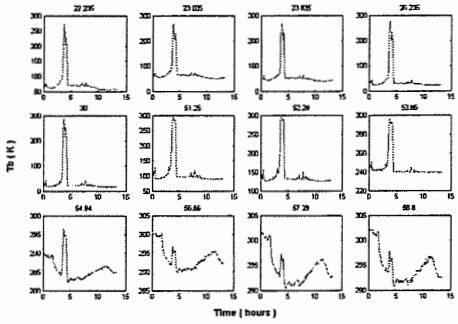

Figure 2 Time series of Tb observed by the MWRP twelve channels during 17 July 2003 in Boulder, Colorado. A rain shower occurred at 04:00 (elapsed time). For each channel, the corresponding frequency is shown on top (GHz).

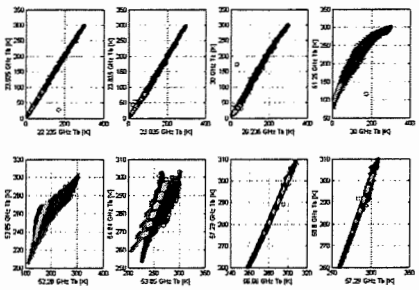

Figure 3 Rainfall spectral signature in terms of scatterplots between Tb at different frequencies. About one year of measurements are shown.

Figure 3 shows rainfall spectral signature in terms of scatterplots between Tb at different frequencies. About one year of radiometric observations at ARM SGP site are involved in this plot. Tb from the simulated dataset are shown in blue, while measurements are shown in red. Non-raining cases from the simulated database are evidenced in green, thus illustrating the emission and scattering signature mechanisms. Figure 3 demonstrates that simulations are able to represent the dynamics of measured Tb's, both for weak absorption (20-30 GHz) and strong absorption (56-60 GHz) frequencies. In the 50-55 GHz range there are some differences, which might be related to water film on the antenna or to modelling assumptions. Radiometric simulations have been in a way tuned to the ambient conditions of the observed event. This means that the surface temperature, pressure and humidity have been used to constrain the random meteorological vertical profiles based on standard vertical gradients.

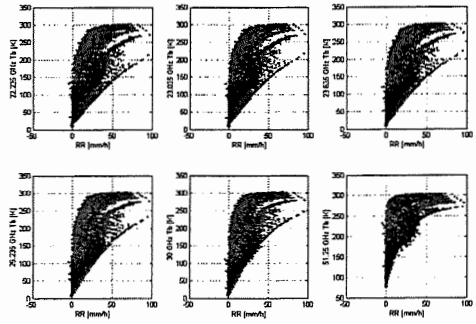

Figure 4 Scatterplots between Tb and rain rate. Simulations are shown together with radiometric observations and respective rain rate estimates.

Figure 4 shows the relationship between rain rate and Tb in the weak absorption region (20-50 GHz). Blue dots represent Tb and rain rate extracted from the simulated database, while red dots correspond to Tb measured by the MWRP and rain rate estimates obtained from radiometric measurements applying a non-linear regression technique. Therefore, Figure 3 verifies the consistency between measurements and simulations, while Figure 4 between measurements, simulations and estimates.

In the top panel of Figure 5, a time series of rain rate as derived from MWRP observations is plotted in blue. The red line represents the rain sensor detection, which can only be 0 (no rain detected) or 1 (rain detected),

although we multiply values by 10 for enhancing the comparison. It is evident that the estimate based on radiometric observations senses rain for a shorter period than does the rain detector. This is due to a residual water film laying on top of the MWRP, which is misinterpreted by the rain detector. Indeed, the retrieval algorithm we have developed is able to interpret this water as a residual film and distinguish it by rainfall.

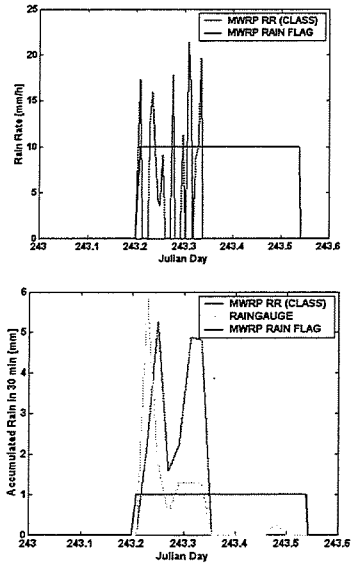

Figure 5 Top: Time series of MWRP estimated rain rate with a line, representing rain sensor detection (0/1), has been multiplied by 10 for convenience. Bottom: Time series of 30-minute accumulated rain for the same case with rain sensor detection (0/1), measurements from a rain gauge, and radiometric estimates.

Bottom box of Figure 5 validates this explanation, by comparing measurements from a collocated rain gauge. MWRP rain rates have been averaged into 30-min accumulated rain (blue line) in order to match the rain gauge (cyan line) time resolution, while rain detector measurements are shown in red with their original values (0/1). Rain gauge measurements clearly confirm the duration of the rain shower sensed by radiometric observations.

4. CONCLUSIONS

A large set of ground-based multi-frequency radiometric measurements and simulations for different precipitation regimes has been analysed. The modelled frequencies have been selected in order to match the set of channels currently available on an operational ground-based radiometric system. Rain events occurred in Boulder, Colorado and at the ARM SGP site have been analysed in terms of comparisons between measurements and model data.

ACKNOWLEDGMENTS. This work has been funded by the EU Fifth-Framework EURAINSAT project (EVG2-2000-00522). Support by the ASI, MIUR and by the GNDCI-CNR project is also acknowledged.

REFERENCES

Jacobson M. D., D. C. Hogg, and J. B. Snider: 1986: Wet reflectors in millimeter-wave radiometry-Experiment and theory, *Trans. Geosci. Remote Sensing,* GE-24, pp. 784-791.

Liu, G.R., Liu C.C., and Kuo, T.H. (2001), "Rainfall intensity estimation by ground-based dual-frequency microwave radiometers", *J. Appl. Meteor.*, vol. 40, pp. 1035-1041

Marzano F.S., E. Fionda, P. Ciotti and A. Martellucci, 2002: Ground-based multi-frequency microwave radiometry for rainfall remote sensing", *Trans. Geosci. Rem. Sens.,* 40, 742-759.

Marzano, F.S. , Fionda, E., and Ciotti, P.: 1999, "Simulation of radiometric and attenuation measurements along earth-satellite links in the 10 to 50 GHz band through horizontally-finite convective raincells", *Radio Sci.*, 34, 841-858.

Smith E. A., P. Bauer, F. S. Marzano, C. D. Kummerow, D. McKague, A. Mugnai and G. Panegrossi, 2002: Intercomparison of microwave radiative transfer models for precipitating clouds, *Trans. Geosci. Remote Sens.*, 40, 197-203.

Tsang L., J. A. Kong, and R. T. Shin, 1985: Theory of Microwave Remote Sensing, New York: Wiley.

Ware R., F. Solheim, R. Carpenter, J. Gueldner, J. Liljegren, T. Nehrkorn, and F. Vandenberghe, 2003: A multi-channel radiometric profiler of temperature, humidity and cloud liquid, *Radio Sci.*, 38(4), 8079, 1-13.

Westwater E. R., 1993: Ground-based microwave remote sensing of meteorological variables in: Janssen, M. A. (ed) *Atmospheric Remote Sensing by Microwave Radiometry*, Wiley, New York

FIRST AIRBORNE CLOUD MEASUREMENTS WITH A COUNTERFLOW VIRTUAL IMPACTOR EQUIPPED WITH A PASSIVE WIND TUNNEL FOR OPERATION ON SLOWLY FLYING AIRCRAFT

S. Mertes[1] and A. Schwarzenböck[2]

[1]Institute for Tropospheric Research, D-04318 Leipzig, Germany
[2]Laboratoire de Météorologie Physique (LaMP), Université Blaise Pascal, F-63177 Aubière, France

1. INTRODUCTION

The counterflow virtual impactor (CVI) technique has been successfully used in airborne cloud studies to sample and separate hydrometeors (cirrus ice particles or cloud droplets) from interstitial particles (e.g. Heintzenberg et al., 1996; Twohy et al., 1997). Upon sampling, the hydrometeors remain airborne in the CVI system and are evaporated in a particle free and dry carrier air without wall contamination. The liquid water and volatile compounds within the droplets are transferred into the gas phase whereas the non-volatile components remain as residual particles, sometimes called cloud droplet nuclei (CDN). Gaseous and particulate constituents can be measured by dedicated sensors located downstream of the CVI inlet.

The segregation of the interstitial phase is achieved by a counterflow pressed out of the CVI inlet tip, which can only be overcome by cloud elements of sufficient inertia provided that the cloud air is accelerated towards the inlet. The higher the air velocity at the CVI inlet, which is attained by the flight velocity of the research aircraft, the lower the minimum droplet diameter that can be sampled. Above 150 m s^{-1}, the lower cut off diameter of the operating CVI systems is about 5 µm, allowing to sample the whole droplet size distribution. Unfortunately, the high flight velocity leads to a poor spatial resolution of the sensing system, which is a drawback for measurements in inhomogeneous and small-scale clouds. Therefore a CVI system with the same cut-off characteristic was developed for aircrafts flying at air speeds of only about 70 m s^{-1}.

2. METHODOLOGY

The CVI itself is identical to the development successfully used for ground-based operation with a lower cut size of 5 µm (Schwarzenböck et al., 2000). The new system was operated for the first time onboard a Partenavia P68B (enviscope GmbH, Frankfurt, Germany) at maximum flight speeds of 80 m s^{-1}. In order to maintain the sampling of small droplets at lower flight velocities, the CVI tip is installed inside a passive wind tunnel, which is unique for airborne CVI systems. The wind tunnel has a length of 814 mm and an opening of Φ140 mm (Fig. 1).

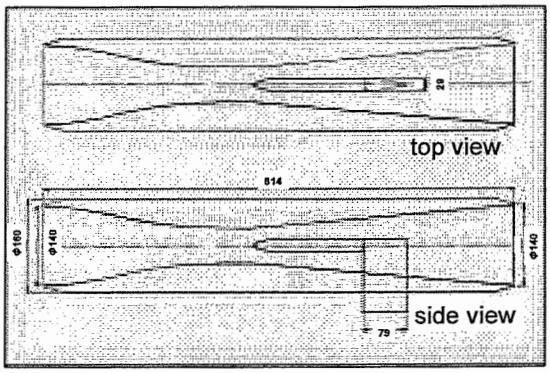

Fig.1. Top and side view of the wind tunnel including the CVI inlet. Dimensions are given in mm.

The conically tapered shape (Φ61 mm at the CVI inlet tip) is designed to accelerate the air speed at the CVI inlet tip compared to the aircraft velocity by a factor of two. Onboard the Partenavia the wind tunnel was mounted on top of the fuselage outside the aircraft´s boundary layer.

Fig. 2 shows a comparison of the Partenavia true air speed and the air velocity at the CVI tip, which is derived from a pressure difference measurement inside and outside the wind tunnel.

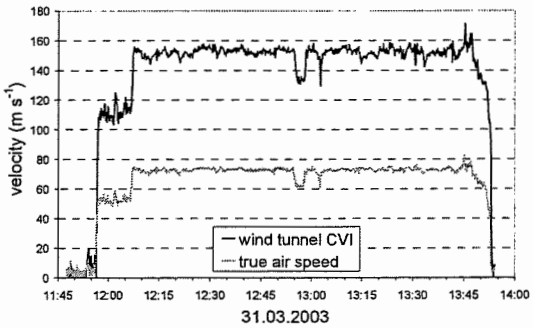

Fig.2. Comparison of the Partenavia true air speed and the air velocity at the CVI tip inside the passive wind tunnel

It confirms that the required air speed of 150 m s^{-1} is achieved inside the wind tunnel at a much lower aircraft velocity.

Corresponding author's address: Stephan Mertes, Institute for Tropospheric Research, Permoserstr. 15, 04318 Leipzig, Germany; E-Mail: mertes@tropos.de.

3. INSTRUMENTATION

Downstream the inlet three sensors were employed. The number concentration and the absorption coefficient of the CDN are determined by a Condensation Particle Counter (CPC, TSI-3760A) and a Particle Soot Absorption Photometer (PSAP), respectively. The mass concentration of graphitic carbon (GC) is derived from PSAP measurements using an instrument dependent conversion factor of 15 m^2 g^{-1} (Mertes et al., 2004). The liquid water content (LWC) sampled and evaporated by the CVI system was measured by two Lyman-α hygrometers. One hygrometer was connected to the sample flow and the second to the so-called waste flow. Hydrometeors larger 50 µm are entering the waste flow, i.e. the occurrence of very large cloud drops or rain is detected by an increase of the LWC signal compared to the sample flow. In order to assess the sampling characteristic of the new CVI inlet, the LWC measurements are compared to results obtained by an airborne Particle Volume Monitor (PVM-A) mounted under the wings. Furthermore a droplet segregating interstitial inlet, a round jet impactor (RJI) with an upper cut size of 5 µm (Maser et al., 1994) was installed close to the CVI wind tunnel to measure number concentration and particle absorption of non-activated particles by a second CPC and PSAP. Ambient aerosol particles were sampled by the RJI whenever the aircraft was flying outside cloud. The data was recorded all 4 sec and the PSAPs were operated with a 30 sec time resolution.

4. RESULTS

Flights were conducted in March 2003 above a low mountain range in Germany (Eifel), west of Cologne. The measurements reported here stem from a flight carried out on March 29 between 11:56 and 13:54 local time. After ascent a broken stratocumulus cloud field was penetrated during two rectangular horizontal flight legs (side length about 100 and 20 km) in an altitude of 1850 and 2170 m, respectively. Ambient temperatures were about 277 and 274 K during the two flight legs.

4.1 Sampling characteristic of the new CVI system

In order to test the sampling characteristic of the passive wind tunnel CVI system long durations in stratus clouds would have been favourable. Unfortunately the actual transects through the available stratocumulus clouds was only in the range of maximal 3 minutes. Fig. 3 shows a time series of parameters measured by the CVI along with LWC results from the PVM through cumulus clouds during leg 1. The effective droplet diameter R_{eff} was 6 µm. The transit times of the droplet constituents from the sampling point at the CVI tip to the different sensors cause a time shift of the CVI data, which is already accounted for with respect to the PVM. It can be noticed that both LWC measurements within the CVI are equal but did not reach the in-situ values obtained by the PVM. This is due to the diffusional broadening of the water vapour in the sampling lines towards the hygrometers. This is a principal feature of all CVIs and is even more striking when the cloud passage is short (cf. Fig. 3, 12:49:15). Integrating the total amount of condensed water sampled by the CVI and measured by the PVM yields a LWC sampling efficiency of 84 % for the CVI prototype.

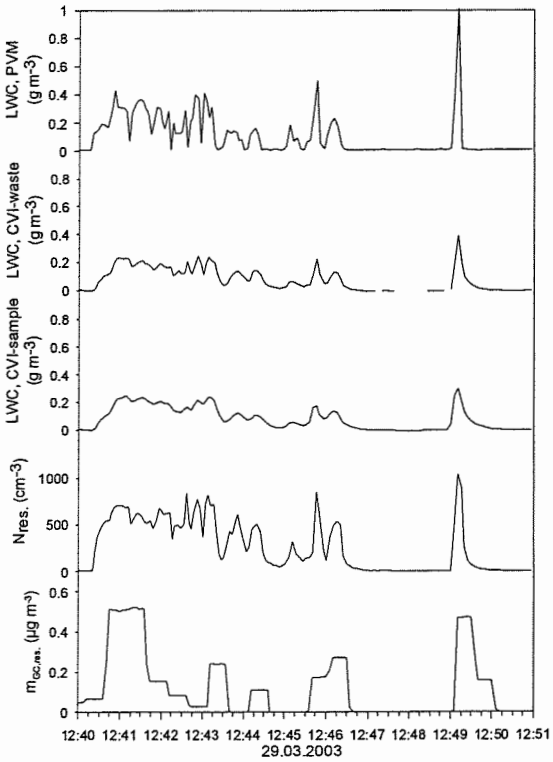

Fig.3. Time series of LWC measured by PVM and CVI along with residual particle concentration N_{res} and residual mass concentration of GC $m_{GC,res}$ sampled by the CVI in cumulus clouds of leg 1.

Assuming that one sampled droplet releases one residual particle, the CVI results suggest a droplet concentration between 600 and 900 cm^{-3}. The existence and missing of droplets smaller than the lower cut of the CVI is unlikely at a R_{eff} of 6 µm, but it exists no direct measurement of the droplet concentration and size distribution for justification.

$$R_{MVD} = \frac{1}{2}\sqrt[3]{\frac{3LWC_{PVM}}{4\pi N_{res}}} \qquad (1)$$

The satisfactory comparison of the droplet mean volume radius R_{mvd} (eq. 1) with R_{eff} presented in Fig. 4 is anyway an indirect confirmation that neither droplets are missed nor droplet shattering occurred in the wind tunnel, which would produce more than one residual

particle per droplet. In Fig. 3 it is furthermore obvious that the PSAP was able to measure GC mass concentrations (m_{GC}) clearly attributed to the sampling of CDN despite the short residence times inside cloud.

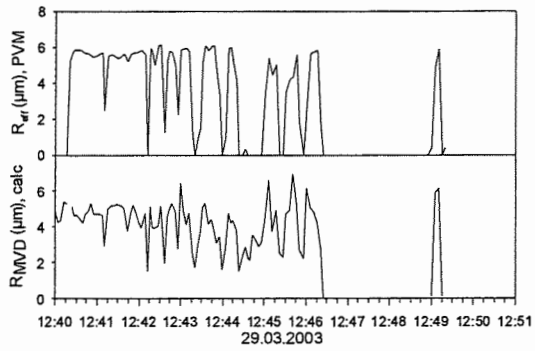

Fig.4. Comparison of the effective droplet radius measured with the PVM and the mean volume radius calculated partly from the residual particle concentration.

The only occasion the Partenavia entered a more stratiform cloud occurred at the end of the second leg. After a short transect of a small cumulus cloud, the aircraft flew along the cloud base of a higher situated large stratocumulus for 3 minutes (Fig. 5).

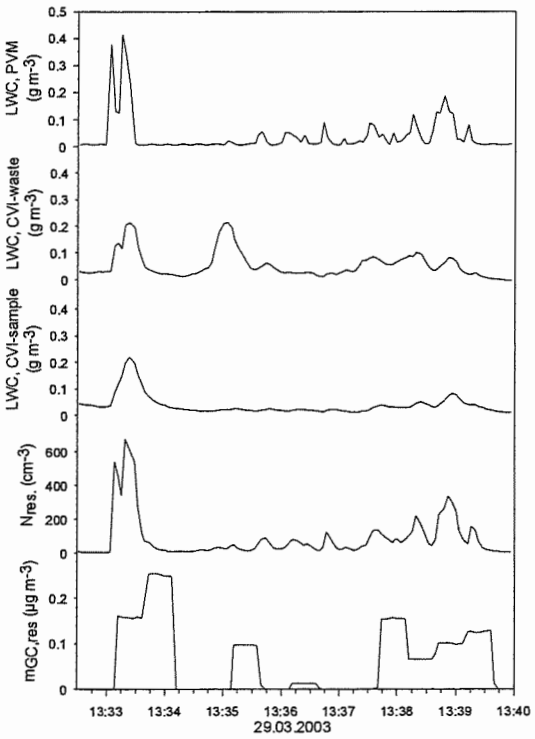

Fig.5. Same parameters as in Fig.3 measured during leg 2 crossing a small cumulus and the cloud base of a stratocumulus cloud.

It can be noticed that the Lyman-α hygrometer in the waste flow identifies rain drops around 13:35 consistent with the notes of the flight protocol. Thus the simultaneous GC peak and small particle counts could be attributed to rain drops. At the cloud base of the stratocumulus cloud, LWC and droplet concentration were much lower compared to the preceding cumulus. At a liquid water content below 0.1 g m^{-3}, the determination of the CVI LWC sampling efficiency is affected by the accuracy of the hygrometer itself and ranges between 60 and 78 %. However, the residual particle concentration is again consistent with the effective droplet radius and the measurement of the residual GC mass concentration is still significant.

4.2 CVI results combined with RJI measurements

Results of the whole flight from March 29 are presented in Fig. 6. It includes the cruising altitude and LWC to indicate ascent, both flight legs, descent and transition of clouds.

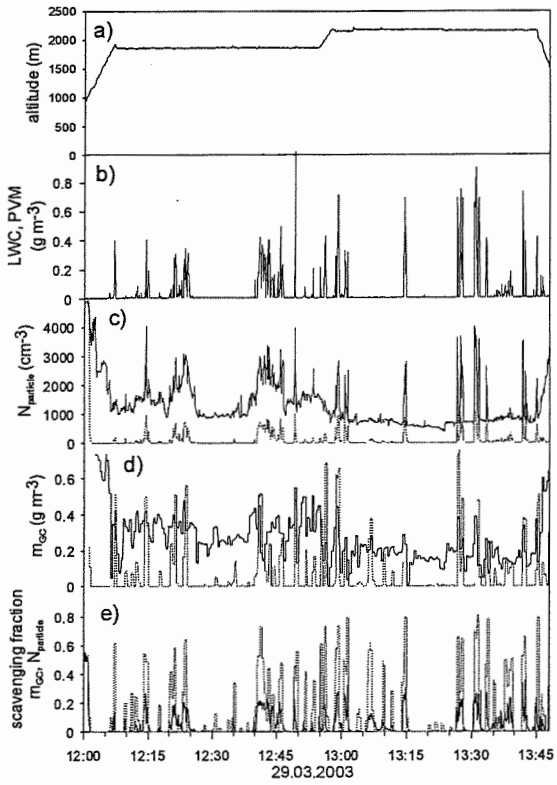

Fig.6. Time series of aerosol parameters measured by the CVI and RJI along with a) cruising altitude and b) LWC. In c), d) light curves denote CVI and dark curves RJI results. In e) the light curve refers to m_{GC} and the dark curve to $N_{particle}$.

In general the liquid water content and the concentration of residual particles representing cloud droplet concentration increased with height, resulting in a constant effective droplet radius for both cloud legs (not shown here). The particle concentration and m_{GC} out of cloud decreased with altitude. Inside the cumulus clouds the number of interstitial particles is up to three times higher than in cloud free regions. These

particles are most likely transported from lower levels by vertical motion below and inside the cumuli. This interpretation is supported by higher particle concentrations measured during ascent and descent (Fig. 6). The similar pattern compared to the LWC suggests that the particles follow the up and downdrafts inside cloud. Often the particle concentration was observed to rise 300 to 600 m apart from the cloud edges. An enhancement inside cloud is also seen for the interstitial mass concentration of GC, but much less significant probably due to the poorer time resolution of the measurements. Fig. 6 also includes the scavenging fraction *sf* of the particle concentration and GC mass fraction calculated by eq. 2,

$$sf_X = \frac{X_{CVI}}{X_{CVI} + X_{RJI}} \qquad (2)$$

where X_{CVI} and X_{RJI} denote the corresponding parameter sampled by the CVI or RJI, respectively. The scavenging fractions of both parameters slightly increase within the higher flight leg with the exception of the stratocumulus cloud base (13:36 – 13:40), where the *sf* values are significantly lower than for the surrounding cumulus clouds. The scavenging fraction of m_{GC} is rather high with peak values between 0.5 and 0.8 at total concentrations of about 0.8 µg m^{-3} inside cloud. The high abundance of graphitic carbon in the droplets might affect the radiative properties of these clouds due to the strong absorption efficiency of GC.

5. CONCLUSION

At the Institute for Tropospheric Research Leipzig an airborne CVI equipped with a passive wind tunnel was developed for operation on slow aircrafts. It could be demonstrated that the passive wind tunnel accelerates the sample air sufficiently to collect droplets down to 5 µm and is thus suitable for operation in slow flying aircraft. The sampling efficiency for LWC is higher than 80 % and concerning droplet concentration close to one (droplet sizes larger 5µm). A remarkable droplet shattering in the passive wind tunnel was not observed during sampling. In cumulus clouds concentrations from 600 to 900 cm^{-3} were determined for residual particles, which include graphitic mass concentrations of about 600 ng m^{-3}. In combination with a droplet segregating interstitial aerosol inlet (round jet impactor) an enhancement of particles in cumulus clouds was observed, which is attributed to vertical transport from below. Scavenging fractions higher than 50 % were determined for graphitic carbon in cumulus clouds, which might affect their radiative properties and evaporation. The new CVI system was verified to operate properly and to be ready for use in further cloud microphysical and chemical investigations.

6. ACKNOWLEDGEMENT

The authors like to acknowledge the assistance received from enviscope GmbH Frankfurt during the preparation and realisation of the aircraft measurements.

7. REFERENCES

Heintzenberg, J., Okada, K., and Ström, J., 1996: On the composition of non-volatile material in upper tropospheric aerosols and cirrus crystals. Atmos. Res., **41**, 81-88.

Maser, R., Franke, H., Preiss, M., and Jaeschke, W., 1994: Methods provided and applied in a research aircraft for the study of cloud physics and chemistry, Contr. Phys. Atmos., **67** (4), 321-334.

Mertes, S., Dippel, B., and Schwarzenböck, A., 2004: Quantification of graphitic carbon in atmospheric aerosol particles by Raman spectroscopy and first application for the determination of mass absorption efficiencies. J. Aerosol Sci., **35** (3), 347-361.

Schwarzenböck, A., Heintzenberg, J., and Mertes, S., 2000: Incorporation of aerosol particles between 25 and 850 nanometers into cloud elements: Measurement with a new complementary sampling system. Atmos. Res., **52** (4), 241-260.

Twohy, C.H., Schanot, A.J., Cooper, W.A., 1997: Measurement of condensed water content in liquid and ice clouds using an airborne counterflow virtual impactor. J. Atmos. Oceanic Technol., **14**, 197-202.

LINK BETWEEN SIZE-RESOLVED HYGROSCOPIC GROWTH MEASUREMENTS OF AEROSOL PARTICLES ENTERING A HILL CLOUD AND NUMBER SIZE DISTRIBUTIONS OF INTERSTITIAL AND CLOUD DROP RESIDUAL PARTICLES MEASURED IN-CLOUD

S. Mertes[1], K. Lehmann[1], D. Galgon[1], A. Nowak[1], A. Massling[1] and W. Wieprecht[2]

[1]Institute for Tropospheric Research, D-04318 Leipzig, Germany
[2] Air Chemistry Department, Brandenburg Technical University Cottbus, D-12489 Berlin, Germany

1. INTRODUCTION

Within the joint research project FEBUKO (field investigations of budgets and conversions of particle phase organics in tropospheric cloud processes, part of the German atmospheric research program AFO2000) two ground-based field campaigns were conducted in 2001 and 2002. One aim of the project was to obtain a better understanding of aerosol-cloud interactions by a detailed physico-chemical characterization of the aerosol phase upwind, inside and downwind a hill cap cloud under connected-flow conditions. The field experiments were carried out in a forested region in Germany (Thuringian forest) where a mountain ridge extends from south-east to north-west direction so that at south-westerly winds the air masses need to traverse the mountain ridge.

2. METHODOLOGY

Fig. 1 shows a cross section of the mountain ridge including the luff (Goldlauter, GL, 600 m asl), lee (Gehlberg, GB, 738 m asl) and cloud (Schmücke, SM, 960 m asl) station.

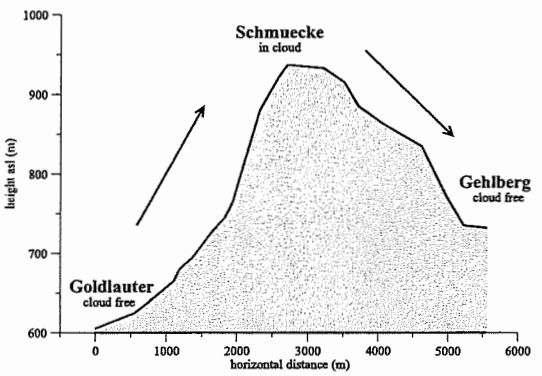

Fig.1. Cross section of the mountain ridge of the Thuringian forest including the horizontal and vertical distances between the three stations.

Measurements were carried out at south-westerly winds when the liquid water content (LWC) at SM was above 0.1 g m^{-3} and the valley stations remained underneath the cloud. All cloud events were analyzed using the LM model of the German Weather Service in combination with a detailed synoptical and hydrodynamical examination to assure a connected air flow between all three stations. Whenever this condition was confirmed, the hygroscopic properties of aerosol particles measured in GL are compared to the particle activation determined inside cloud.

Corresponding author's address: Stephan Mertes, Institute for Tropospheric Research, Permoserstr. 15, 04318 Leipzig, Germany; E-Mail: mertes@tropos.de.

3. MEASUREMENTS

At GL the hygroscopic growth of aerosol particles with dry sizes of 50, 150 and 250 nm at 90 % rel. humidity was measured by a Hygroscopicity Tandem Differential Mobility Analyzer (HTDMA, Svenningsson et al., 1992) with a time resolution of 40 min. The growth factor (gf) of a particle is defined as the ratio of the wet to the dry diameter. Thus, a number distribution as a function of the observed gf can be derived for a fixed dry particle diameter (Fig. 2). Using the hygroscopic growth of ammonium sulfate as a reference, the measured growth factors are transferred to solubility mass fractions ε by means of eq. 1 (Pitchford and McMurry, 1994).

$$\varepsilon = \frac{gf^3_{measured} - 1}{gf^3_{(NH_4)_2SO_4} - 1} \qquad (1)$$

Finally, the distribution of the soluble mass fraction is divided in a discrete number of solubility classes, as shown exemplarily in Fig. 2.

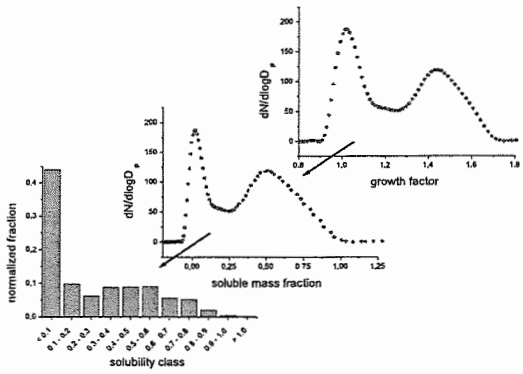

Fig.2. Conversion of a measured growth factor distribution to a normalized fraction of solubility classes as explained in the text.

Assuming ammonium sulfate to be the only soluble particle constituent introduces an error in the determination of ε. Nevertheless, the good agreement between the mean solubility mass fractions derived from hygroscopic growth measurements and the ε values obtained independently from the chemical analysis of size corresponding impactor stages justifies this method (Fig. 3).

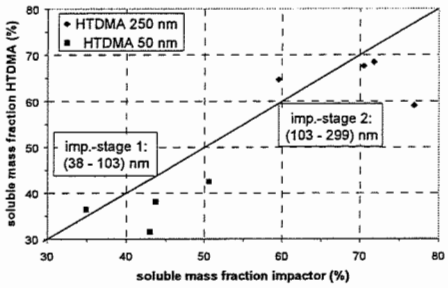

Fig.3. Comparison of the aerosol soluble mass fraction determined from simultaneous HTDMA and impactor measurements.

AT GL and GB the particle number concentration and dry size distribution was determined by condensation nucleus counters (CPC,TSI-3010) and differential mobility particle sizers (DMPS).
Inside cloud on the mountain ridge station non-activated particles and cloud droplets were separately collected by an interstitial (INT) and a counterflow virtual impactor (CVI) inlet (Schwarzenböck et al., 2000). Both inlets were designed for a separation diameter of 5 µm (Schwarzenböck and Heintzenberg, 2000). Inside the CVI system the collected droplets remain airborne and are evaporated in a dry and particle free carrier air releasing dry residual particles. Likewise drying the interstitial particles allowed to measure dry number size distributions and concentrations of residual and interstitial particles with two CPC and DMPS at the same time. The aerosol activation fraction *af* as a function of particle size is derived from the two size distributions using eq. 2.

$$af = \frac{\frac{dN_{CVI}}{d\log d_P}}{\frac{dN_{CVI}}{d\log d_P} + \frac{dN_{INT}}{d\log d_P}} \qquad (2)$$

A Particle Volume Monitor (PVM) and a Forward Scattering Spectrometer Probe (FSSP-100) were used to determine LWC and droplet concentration in the cloud.

4. RESULTS

The meteorological evaluation confirmed clear connected flow conditions in only 3 of 14 cloud events. Two of them were analyzed in detail and the results are presented in the following. The first cloud event (event A) occurred from October 26 - 27, 2001 (22:00-13:00) and the second (event B) prevailed from October 16 – 17, 2002 (21:00-04:00). Using back-trajectories and synoptical weather maps, the air masses were characterized to be marine sub-polar (event A) and marine mid- latitude origin (event B).

4.1 Particle number concentration

Fig. 4 show different time series of particles concentration for both case studies. In the lower part of the figures it becomes obvious that the residual particle concentration resulting from evaporated droplets (SM, residual) is consistent with the droplet concentration (about 400 cm^{-3}) measured in situ with the FSSP for the same lower size cut (FSSP > 6 µm). The total particle concentration upwind (GL,total) and downwind (GB,total) the cloud as well as the interstitial particle concentration (SM, interstitial) show the same temporal behavior. Moreover, the sum of interstitial particle and droplet concentration (SM, interstitial + FSSP) is found in both events equal to the downwind concentration GB,total. Only the upwind concentration was slightly higher most likely due to local pollution.

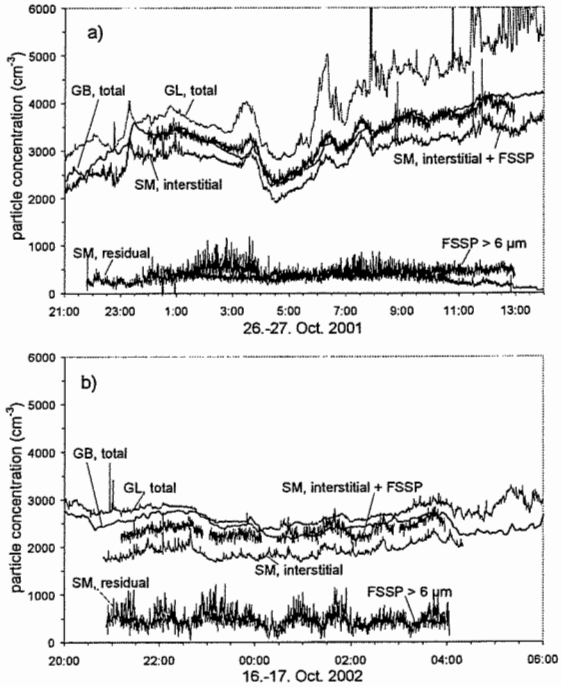

Fig.4. Time series of different particle concentrations measured upwind (GL), downwind (GB) and inside cloud (SM, FSSP) as explained in the text for a) event A and b) event B.

4.2 Particle number size distribution

The dry particle size distributions averaged over the entire cloud event duration are shown in Fig. 5. The total particle distributions outside (GL, GB) and inside cloud (adding residual and interstitial particles, $SM_{CVI+INT}$) look very similar in the measured size range between 25 and 900 nm. This implies that the small

enhancement observed for the upwind particle concentration can be attributed to a particle size range below 25 nm, which do not play a role in droplet formation.

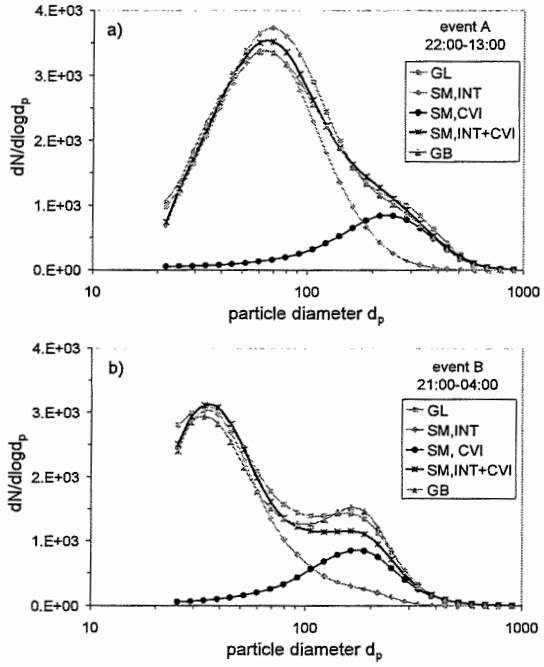

Fig.5. dry particle size distributions measured upwind (GL), downwind (GB) and inside cloud (SM) for a) event A and b) event B. SM_{INT} and SM_{ICVI} denote interstitial and residual particles, respectively.

The size distributions of both events contain an Aitken and accumulation mode, but the mode diameters in event A (70 and 250 nm) are larger than in event B (30 and 160 nm). Small particles mainly remain in the interstitial (SM_{INT}) phase, whereas the larger ones appear in the residual (SM_{CVI}) size distributions. The overlap region is due to a different ability of equal sized particles to act as cloud condensation nuclei (CCN).

4.3 Particle hygroscopic growth upwind cloud

The solubility mass fractions of particles entering the cloud determined by means of hygroscopic growth measurements at 90 % rel. humidity in GL are plotted as event averages in Fig. 6. It can be noticed that the 50 nm particles possess much less soluble material and show a different ε distribution compared to particles with larger diameters. This might be an indication that the 50 nm particles are rather of local origin than the larger ones. During event B the 150 and 250 nm particles contain nearly the same fraction of soluble material whereas in event A the ε distribution of the 250 nm particles is shifted to larger solubility fractions. The non-zero values for the solubility class > 100 % reveal the slight existence of aerosol components growing stronger than ammonium sulfate.

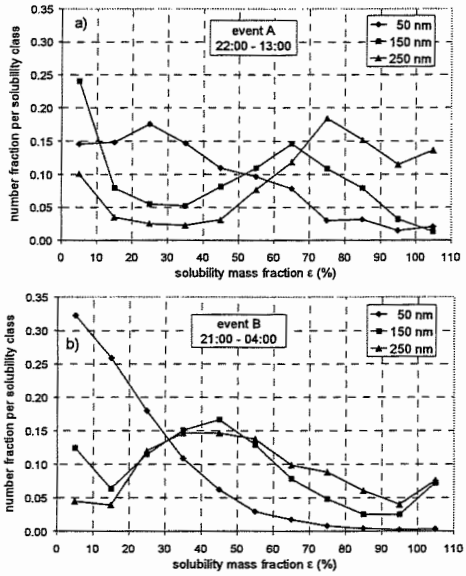

Fig.6. solubility mass fraction distributions derived from HTDMA measurements for three dry particle sizes carried out upwind cloud (GL). a) event A and b) event B.

4.4 Hygroscopic growth and droplet formation

The fraction of particles activated to cloud droplets as a function of dry particle diameter calculated according to eq. 2 is presented in Fig. 7 for both events. The activation function for event B is much steeper compared to event A yielding a 50 % activation diameter d_{50} of 110 nm. The d_{50} is reached at 180 nm during event A. Additionally, particle number fractions of solubilities above a certain ε limit are indicated on the same scale as a function of particle size. These values are calculated by adding up the number fractions of solubility classes for each dry diameter (Fig. 6) from high to low solubility mass fractions. The resulting data points for the three diameters are interpolated by straight lines for a better visibility, even if the behavior in between is unknown. However, a distinction between event A and B is clearly noticed by the different curvature of the curves (Fig. 7). In both case studies the number fractions of the different upper ε limits increase with particle size but less steep than the activation fraction. This indicates that larger particles need less soluble material to grow into droplets, which is in agreement to Köhler theory. Moreover, the comparison also quantitatively elucidates which minimum soluble mass fraction at a certain dry particle size was required to act as CCN. The curves in Fig. 7 also imply that the strong gain of the solubility classes from 50 to 150 nm impacts the steepness of the activation fraction in this size range for event B. The same influence is found for event A, but the strong increase happens between 150

and 250 nm leading to a significant higher 50% activation diameter.

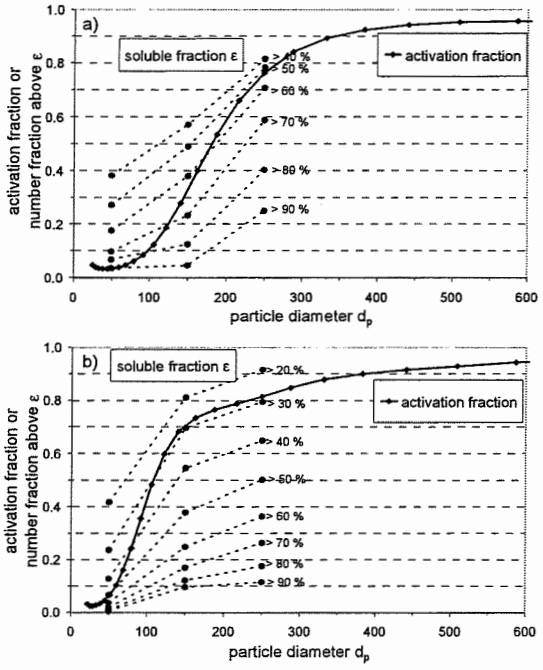

Fig.7. particle activation fraction inside cloud (solid line) calculated from eq. 2. and number fraction of particles above the given ε limit upwind cloud (dotted lines) as a function of dry particle size. a) event A and b) event B.

The activation of smaller and less hygroscopic particles during event B leads to the formation of smaller droplets in relation to event A (Fig. 8) at comparable droplet concentration above 5 µm (Fig. 4).

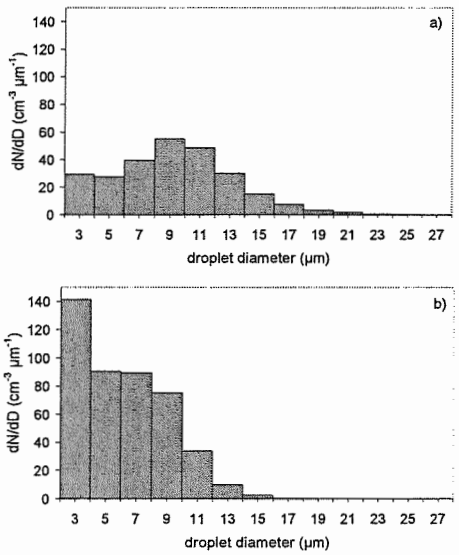

Fig.8. mean droplet size distribution measured with the FSSP. a) event A and b) event B.

5. CONCLUSION

Within the German AFO2000 cloud project FEBUKO meteorologically verified connected flow events between the upwind, in-cloud and downwind station were confirmed by the analysis of particle concentration and size distribution. Thus, the solubility of the cloud input aerosol derived by hygroscopicity measurements upwind cloud could be related to particle activation measured in-cloud. The soluble mass fraction derived from hygroscopicity results correlated well with the chemical analysis of impactor measurements. It was found that the increase of the soluble mass fraction with size influences the steepness of the activation curve and thus the 50 % activation diameter d_{50}. Moreover, the minimum solubility fraction of particles that took part in droplet formation could be determined for different dry particle sizes. These findings imply consequences for the droplet size distribution, which was in fact experimentally observed.

6. ACKNOWLEDGEMENTS

This work was funded by the Ministry for Education and Research of the Federal Republic of Germany (BMBF) within the AFO2000 research program under grant 07ATF01 (FEBUKO).

7. REFERENCES

Pitchford, M.L., McMurry, P.H., 1994: Relationship between measured water vapor growth and chemistry of atmospheric aerosol for Grand Canyon, Arizona, in winter 1990. Atmos. Environ., **28** (5), 827-829.

Schwarzenböck, A., and Heintzenberg, J., 1999: Cut size minimization and cloud element break-up in a ground-based CVI. J. Aerosol Sci., **31**, 477-489.

Schwarzenböck, A., Heintzenberg, J., and Mertes, S., 2000: Incorporation of aerosol particles between 25 and 850 nanometers into cloud elements: Measurement with a new complementary sampling system. Atmos. Res., **52** (4), 241-260.

Svenningsson, B., Hansson, H.C, Wiedensohler, A., Ogren, J.A., Noone, K.J., Hallberg, A., 1992: Hygroscopic growth of aerosol particles in the Po Valley. Tellus, **44B**, 556-569.

"Meteorological surveillance techniques based on Unmanned Aerial Vehicle system"

Slobodan ***Petkovic***[1], *Goran* ***Memon***[4],
[1, 2] EDePro, Belgrade, Kralja Milutina 33, Serbia and Montenegro, Tel/fax: 381 11 8064 380
E-mail: [1]spzika@ptt.yu [2]memon@net.yu

1. Introduction

Purpose of this paper is presentation of meteorology surveillance technique based on unmanned aerial vehicle (UAV) as platform. There is also presented elements of study for project of meteorologically UAV system named STORM EYE and their meteorological applications, especially such as meteorological surveillance platform. In surveillance mission STORM EYE work as aerosonde UAV and participate in several meteorological missions such as:

- Hail suppression, rain enhancement, fog dispersion and snow pack enhancement.
- Automatic climate monitoring
- Air-sea exchange of momentum, heat, moisture and CO_2
- Research platform for development of meteorological instruments
- Storm monitoring and tracking platform
- Cirrus cloud research vehicle platform
- Water and climate change study
- Atmospheric chemistry study

2. Surveillance problems in meteorology

Climate monitoring is a matter of great importance. To reach the right policy every society must be aware of possible climate changes and know whether they are statistically significant. The presence meteorological surveillance basically networks has limited coverage for example over the oceans.

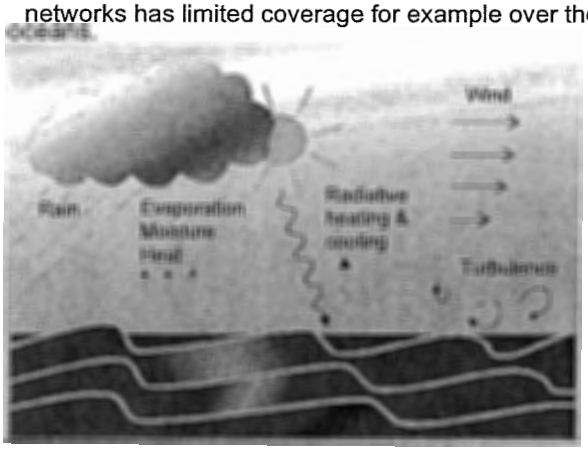

Fig.1 Meteorology dynamic processes interference

Weather surveillance is crucial phase of storm prediction, process analysis, choosing of proper method and handling of meteorological situation. Generally, meteorological surveillance is in the global plane solved with satellite or radar measuring and detecting, but tactically surveillance is still a problem. Meteorological processes are marked with high dynamic intensity and depend of many factors. One of these factors is terrain configuration, which is full of many varieties. In specific terrain configuration with enlarged climb, radar surveillance and tracking system isn't efficiency enough. There is better solution local meteorological measuring and detecting techniques. For local measuring on tactical level UAV as a surveillance platform is very practical and economical. First of all, UAV is full mobile and modular system, which provides great affordability and maintainability. Second, UAV system is much more reliable and economically reason based solution because meteorological radar is still very expensive. Third, UAV system is highly compatible with present meteorological radar and tracking systems. And at the end on UAVs can be boarded variety of different surveillance equipment. This practical means that UAV can be optimized for every different mission tasks and requirements. In practice, tactical reconnaissance mission are provided with piloted aircraft because the pilot has a much better view and orientation in space, but in this case is recommended bigger piloted twin engine turboprop aircraft (needed flight altitude is up to 10,000 m) which is expensive and complex for maintenance and handling. Also aircrafts always required prepared runways and logistic support. For this purpose unmanned aerial vehicle (UAV) is more acceptable then piloted aircraft because first of all there is not human pilot limitation. Also the ability of UAVs to operate at moderate subsonic speeds and varied levels of flight make them uniquely suited to perform cloud seeding mission. Second, UAV can fly near cloud zone in more turbulence conditions then piloted aircraft and finally UAV is more secure and cheaper in long time exploitation. So for this reasons we start to create multipurpose meteorological system based on UAV vehicle called STORM EYE, equipped with payload cargo bay for carrying different types of meteorological and surveillance equipment.

3. STORM EYE vehicles

STORM EYE UAV is basically intended to carry on varied types of meteorologically payload up to 20 kg. Also STORM EYE changeable flight profile and

range radically increased flight zone. With improved aerodynamically capabilities, flight performances, and modular cargo bay section STORM EYE vehicle is capable to lift different meteorological payload up to 6000m heights and cruise at 150km range. Cruising velocity is 0.5 Mach number. It is a high dynamic vehicle with upgraded performance flight characteristics provided by optimised wing design and a thrust of two turbojet engines.

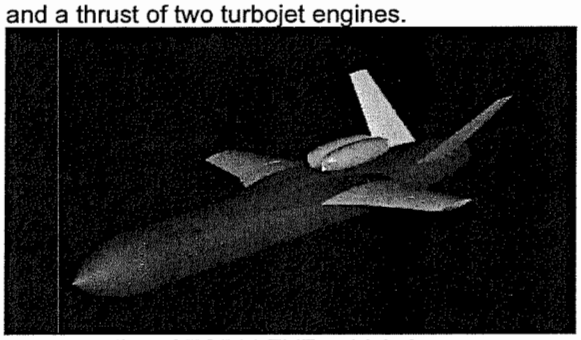

Fig.2 STORM EYE vehicle layout

The STORM EYE vehicle has been designed in classical form with cranked leading edge wing and elliptical body cross-section. Empennages formed as V shaped tail sections and two fins positioned below rear fuselage section. This constructive composition allows rapid assembly and disassembly for easier maintenance and for changing payloads. The nose and tail sections are easily removed for accessing the electronic equipment. The complete wiring harness is easily removed for repair or replacement. The airframe is mainly fabricated from a light alloy and composite. Power section is considered of two TMM-25 turbojet engines, with 25daN thrust each, positioned above fuselage in common pylon. Main role in STORM EYE mission has flight control system. The flight control system comprises:

- A flight control system based on a microcomputer including an input/output unit.
- An emergency flight control system, similar to the main flight control system.
- A processor unit based upon a microcomputer.
- An emergency processor unit similar to the main processor unit.
- Management control subsystem for flare ejection (there is possibility to change firing time schedule)
- Vehicle self destruction capabilities

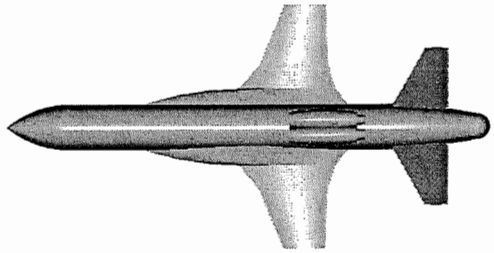

Fig. 3 STORM EYE basic dimensions

It is important that all avionics and electrical subsystems are realised from commercial components according commercial PC\104 Standard. The STORM EYE vehicle can be ground launched from launching ramp with the aid of booster (jet assisted take-off), or, it can be air launched from a fixed wing aircraft or helicopter. Mobile launchers are also available for rapid deployment ground launch. Recovery of the STORM EYE is accomplished by means of a parachute for ground recovery. When the vehicle contacts the ground or water the deployed parachute (which is positioned in fuselage rear section) automatically released and for smooth landing airbag automatically activated and extended. STORM EYE basic dimensions are presented in Fig.3 and summary of technical data are listed in table 1.

Table 1 The STORM EYE technical data

Specifications	
Country of Origin	Serbia and Montenegro
Role	Commercial purpose
Wing Span	2.000 m
Length	3.600 m
Height	0.500 m
Weight	130 kg
Engine	Two turbojet TMM-25
Maximum speed	Mach number 0.6
Cruising speed	Mach number 0.5
Range	150 km
Service Ceiling	6,000 m
Crew	Two man ground crew
Cost	Estimated. 50,000 $
Program status	Development

4. STORM EYE reconnaissance mission

STORM EYE vehicle operate in an automatic navigation mode performing in on-board computer with GPS correction flight path. Flight attitude is stabilised by an autopilot that controls roll, pitch and

heading. In the automatic navigation mode the STORM EYE is capable of flying beyond the radio horizon of ground control increasing the range of the mission up to 150 km. In this configuration the STORM EYE fly autonomously a pre-programmed flight path changing heading, altitude and speed and turning sensors on and off at selected way points. Finally, in any time during the flight, mission can be cancelled vehicle can be recovered in launch area and safety landed. On the ground, STORM EYE vehicle subsystem co-operated with ground control station (GCS). The GCS team consists of 2 people. In preprogrammed flight mode the GCS Operator just sends a command to go in this mode, and from they're the UAV flies autonomously according to the preprogrammed parameters. Depend on mode; the operator can watch the telemetry data on the screens. Also, the operator can switch the system to predefined flight mode. For navigation purposes the location of the UAV is taken from the on board system. This location is also transmitted with the downlink message to the GCS for presentation. In case the GPS is inoperative because of lack of coverage or malfunction in the equipment, the tracking system find the UAV azimuth to the station, and by measuring the time between transmitting a signal and receiving it back the computer calculate the range to the UAV. The airborne altitude sensor gives the UAV altitude. With those inputs the station determines the UAV location

5. Conclusion

In conclusion of this paper presented some of STORM EYE advantages. Also STORM EYE compiled the desired capabilities for a range of applications, many of which were in the meteorological domain as the meteorological surveillance sector and weather modification purpose for example as hail suppression, rain enhancement, fog dispersion and snow pack enhancement, etc.
The unique features of the STORM EYE system would be:

- Reliability:

1. Return-home feature in case of the command link failure.
2. Back-up power battery.
3. Emergency parachute and airbag recovery
4. GPS location system.

- Communality - using digitally techniques, enable easy modifications in parameters and adapting various payloads to the air vehicles.
- Friendly use - as the STORM EYE platform has inherent stability, and the UAV can fly very easily. The unique human engineering of the stations contributes to the ease-of-operation features of the system.
- Maintainability - having microcomputer technology in the UAV and the stations, simplifies the maintenance requirements, and provides ease-of-maintenance characteristics to the system.
- And last but no list, low cost - unique price/performance ratio (because STORM EYE system will be manufactured almost from commercial components.

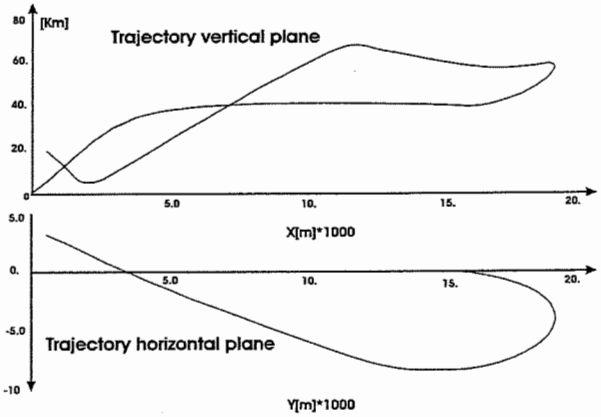

Fig. 4 STORM EYE trajectory in vertical and horizontal plane

The STORM EYE system offers a break-through in cost and ease-of operation and maintenance, and can effectively be used for the many applications: The variety of the possible payloads facilitates the use of one system for a wide range of missions. This feature greatly increases the cost-effectiveness of the STORM EYE and ensures that end-users, will find that the system delivers an impressive cost-benefit yield, in areas of considerable importance. As conclusion there are main advantages of presented STORM EYE UAV system compared to analyzed agricultural anti-hail rocket:

- Flight plan of UAV dictated from the ground;
- Flight plan can be changed during flight;
- Full off-line and on-line mission simulation;
- Telemetric tracking;
- Possibilities to after flight full mission profile analysis;
- Quick-launch capability;
- Transportable to field in a pickup-size vehicle;
- Multimission capabilities
- Changeable payload for specified type of missions;
- Possibilities to multimission activities during single flight (cloud seeding, monitoring, etc.).

Also there are several problems and activities which must be solved in near future. Future unmanned

aerial vehicles (UAVs) are designed to fly at long range and high endurance, and to perform complex and demanding tasks such as surveillance and reconnaissance. The current preprogrammed ground control strategy will not be able to meet the task complexity, long range and high endurance requirements. There are few challenging issues in controlling future UAVs, including:

- Sensor payload management in support of a wide variety of mission types (e.g. coordinating use of camera images, terrain maps, and data from meteorological, radioactivity, chemical agent sensors and detectors).
- Collaborative planning and coordinated control of multiple UAVs by an engaging unit in achieving a common mission goal.
- Real-time responsiveness given perturbations to connectivity between the air vehicle and ground control station.

Fig. 5 STORM EYE flying trough clouds (computer animation)

Currently STORM EYE program is in development phase and this is first time in our country that one unmanned system will be used in meteorological purpose. We also estimate that STORM EYE system is just a beginning of generally purpose UAV participations in commercial role. Also European integrations are involving in meteorological services so future larger meteorological space (for example on Balkan peninsula) required more capable systems (vehicles).

For this long endurance missions STORM EYE vehicle is equipped with multirole payload section.

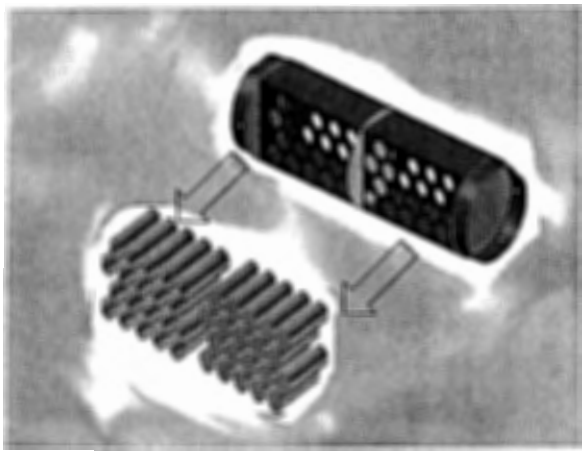

Fig. 6 STORM EYE payload section with ejectable flares housing

For STORM EYE UAV system is specially developed payload section for ejectable flares storage (Fig.6). Modular storage bay is maddened from light alloy and provide storage possibility separate from main vehicle. This is important because chemically agent and explosive fuzzes required specially storage conditions.

Specially designed payload storage bay is intended for storage of maximum 40 ejectable flares. These ejectable flares are intended for chemically agent delivery in required cloud zone. Also ejectable flares provide wider zone of agent dispersion then classical anti-hail rocket because flares are separately launched on both sides of UAV during flight. Also chemically content of each flare can be different for different type of mission. There is possibility for using different type of flares during same flight. On that way we have two different missions during same flight. This is possible because time delay between two firings is easy to moderate on the ground before flight or during same flight, as it is required. This is explanation why is UAV system like this more efficient then classical anti hail rocket platform. At the same time UAV became multirole meteorological platform for different meteorological missions. Also all subsystem-excluded flares are fully recoverable and easy to prepare for second mission, which rapidly decrease costs and increase efficiency of complete meteorological campaign.

USE OF DIGITAL HOLOGRAPHY FOR SIZE ESTIMATION OF AEROSOL PARTICLES FROM THEIR BROWNIAN MOTION

[1,2] F.Prodi, [1]G.Santachiara, [1]S.Travaini, [3]F.Belosi
[4]A.Vedernikov, [4]F.Dubois, [4]J.C.Legros

[1] Institute ISAC-CNR, Clouds and Precipitations Group, Bologna, Italy
[2]Department of Physics, University of Ferrara, Ferrara, Italy
[3] Institute ISAC-CNR, Lecce, Italy
[3] Microgravity Research Center, Chimie-Physique EP-MRC, Université Libre de Bruxelles , Belgium

1. INTRODUCTION

Aerosol particles in the atmosphere have a wide range of sizes, ranging from 0.01 μm as a lower limit to approximately 100 μm as the upper limit. The lower limit approximates roughly the point where the transition from molecule to particle takes place.

Generally a particle is imagined to be spherical or nearly, then its diameter can be used to describe particle size. For a monodisperse aerosol a single measurement describes the diameter of all particles, but with polydisperse aerosols certain presumptions must be made as to size distribution.

Microscopic observation of aerosol particles permits direct measurements of particle size. The optical microscope is suitable for sizing solid particles with diameters higher than about 1 μm, (resolving power is about 0.2 μm), while SEM and TEM have a resolution limit of about 10^{-2} and 10^{-4} μm, respectively.

Most atmospheric processes are related to the aerodynamic diameter of the aerosol. It is the key particle property for characterizing filtration, respiratory deposition, and performances in many types of air cleaner. In many situations is not necessary to know the true size, shape factor and density of a particle, if its aerodynamic diameter is known.

Knowledge of the real size of particles is essential in the treatment of the results of most aerosol experiments, particularly, those dealing with phoretic forces. Suffice it to mention that even in a so-called monodisperse aerosol, there are particles of different sizes but also aggregates. In cases where aerosol particles are observed individually, the information on the true size of the observed particle removes statistical uncertainty and increases accuracy of the results. Recent developments in digital holography have made it possible to obtain valuable information on an aerosol sample in a much shorter time and with less effort. A digital holographic velocimeter (DHV) has proved to be an essential tool in the reconstruction of particles trajectories inside the observation volume during experiments in microgravity.

Corresponding author address: F.Prodi ISAC-CNR, Bologna, Italy.
E-mail: f.prodi@isac.cnr.it

Since the particle trajectories developing under the effect of temperature and vapour concentration fields are influenced by Brownian motion, we analysed whether the size of a specific particle could be defined from its Brownian motion characteristics. By inspecting the mean spread in the particle trajectories due to Brownian behaviour, it should be possible to infer mean dimension of the particles. This procedure is confirmed by comparing the measurements of the size of particles, obtained by SEM observation, to the size obtained from their trajectories reconstructed by the DHV.

2. EXPERIMENTAL

External forces producing aerosol movement include gravity, electrostatic, thermo- and diffusio-phoretic forces. Phoretic forces, due to temperature or vapour pressure gradient, are of central interest in the scavenging of aerosol particles in clouds, when droplets and/or ice crystals grow or evaporate, and below cloud, during fall of hydrometeors.

In normal gravity, the gas flow of natural convection induced by temperature gradient has an influence on particle behaviour. The difficulty can be avoided if experiments are performed in microgravity, where the effect of natural convection becomes negligible.

The microgravity environment was obtained in two ways. The first was in Parabolic Flights on a zero-g Airbus (Bordeaux, 2000-2001 campaigns). A reduced gravity environment was achieved by flying through a series of parabolic manoeuvres, which results in about twenty-two second periods of 0-g acceleration (actually around 10^{-2} g). In the second case, the experiments were performed in the Bremen Drop Tower (2003). There is a residual acceleration of 10^{-6} g during the free fall (t= 4.7 s).

In the experiments related to thermophoretic velocity and Brownian motion measurements, the internal dimensions of the cell were 18.5x18.5x7 mm (LxWxH). The cell perimeter consisted of a mono-block glass vessel. The top and the bottom were made of metal plates overstepping the glass vessel. The temperature of the top plate was regulated to obtain a constant gradient.

As aerosol we used carnauba wax, paraffin and sodium chloride. The carnauba wax was produced by the MAGE, a condensation aerosol generator for solid particles designed by V.Prodi (1972), while paraffin aerosol was obtained with a new model modified for microgravity experiments (MINIMAGE).

The sodium chloride aerosol came from the vaporization of a thin film of sodium chloride deposited on a heated ceramic tube. The aerosol was injected into the cell after the desired temperature gradient was reached.

Three-dimensional particles velocities of the aerosol subjected to the temperature or concentration gradient were obtained by a digital holographic velocimeter (Dubois et al., 1999), having the observation volume of about 0.5x0.5x0.5 mm^3. The recent development of digital holography yields a complete set of information on a sample, through the interference pattern, which is recorded on a charge-coupled device (CCD) camera, between a beam reflected by a sample and a reference beam. The interference fringes are recorded by the CCD camera every 1/30 s. This holographic record codes both the phase and amplitude of the object containing the 3-D shape information on the sample. Classical optical reconstruction is replaced by a computer reconstruction.

Based on digital image processing, the experimental volume is reconstructed slice by slice in order to achieve a full focused volume.

For aerosol applications, three dimensional co-ordinates of the particles are retrieved by such procedures and particles trajectories are reconstructed by analysing the sequence of the particle position.

Because the thermophoretic forces in our experimental device act only along the vertical axis (named y), we can record and afterwards measure the displacement of aerosol particles along a perpendicular axis (e.g. z), where the only motion is Brownian.

3. THEORETICAL APPROACH

Brownian motion is an irregular motion of an aerosol particle, which is caused by random variations in the incessant bombardment of gas molecules against the particle. It plays a key role in many processes involving submicron aerosol particles.

When a particle moves in a Brownian motion the chance that it will ever return to its initial position is negligibly small. Thus, there is a net displacement with time of any single particle, even though the average displacement for all particles is zero. So, if we consider at t=0 a large number of particles at z=0, where there are no external forces present, Brownian motion will cause the particles to spread out with time, and the distribution of particles at the left and right of the origin will be a normal distribution, with a mean value of zero and a standard deviation

$$\sigma = \langle z \rangle = (2Dt)^{0.5} \qquad 1)$$

$$D = KTB \qquad 2)$$

where: $\langle z \rangle$ is the root mean square displacement, D the diffusion coefficient of the particles, B the particle mobility, t the time, k the Boltzmann's constant and T the gas temperature.

Mobility represents the velocity given to a particle by a constant unit driving force, and it is given by

$$B = \frac{C_c}{3\pi\eta d}$$

where C_c is the Cunningham correction factor, d the particle diameter, η the dynamic viscosity.

The diffusion coefficient increases with temperature. For small particles with large slip correction factors, D is proportional to d^{-2}, while for larger particles where slip correction can be neglected, D is inversely proportional to particle size (W.C. Hinds, 1982). The variance σ^2 of the distribution of particle positions increases with time. The percentage of 68.3, 95.5 and 99.7 of the considered particles should be in the range $\pm\sigma$, $\pm 2\sigma$, $\pm 3\sigma$, respectively, at a fixed time.

Two main aims drove our interest in Brownian motion. Firstly (Case A), we compared the observed mean square displacement of particles suspended in the nitrogen gas with the theoretical values, in order to test the validity of the Gaussian distribution hypothesis. Subsequently (Case B), in the presence of a polydisperse aerosol, we tried to deduce the range of particle diameter from the displacement.

4. EXPERIMENTAL RESULTS

We examined the two different cases.

A) We first considered an experiment carried out during the 2001 parabolic flight campaign. The aerosol used in thermophoretic experiments was carnauba wax , with mean radius r = 0.28 μm and standard deviation σ = 0.10 μm. The size distribution was measured by sampling aerosol on a Nuclepore filter and examining under SEM. The Brownian motion is considered along the z axis, perpendicularly to the temperature gradient between the plates (y-axis).

Fig. 1 shows the trajectories of 20 particles obtained using the procedure indicated in the experimental part. In this figure, the origin of all trajectories was set to z=0 for time equal to zero. The position of each particle was reported every 0.05 s, during the time interval t = 1.08 s.

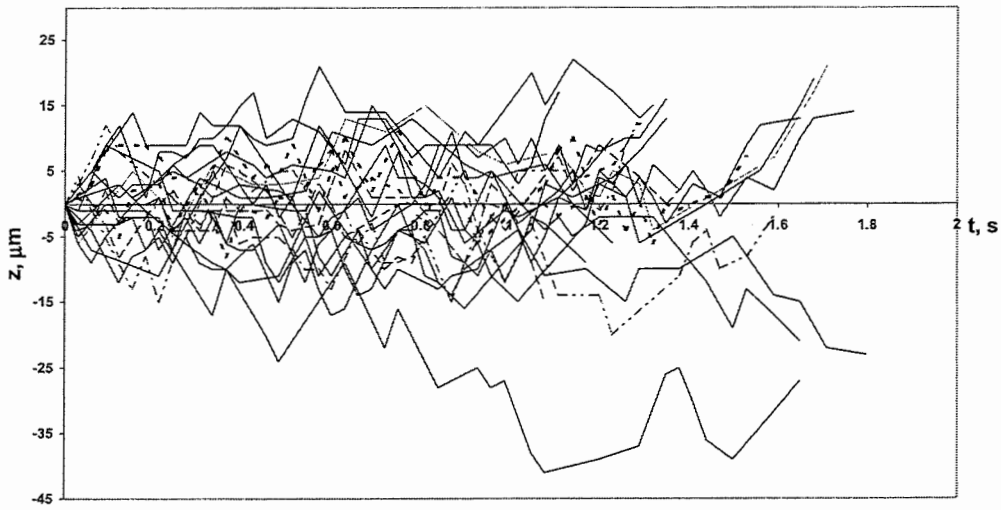

Fig.1. Trajectories of aerosol particles undergoing Brownian motion

The diffusion coefficient, calculated from 2), at T= 319° K, mean temperature of the gas inside the cell, turns out to be D=61 $\mu m^2 s^{-1}$. The root mean square displacement along z-axis is : $\langle z \rangle = \sigma = 11.5$ µm. The theoretical number of particles in the range $\pm\sigma, \pm 2\sigma, \pm 3\sigma$, was 14, 19, 20, respectively, while the experimental number was 14, 19 and 19, respectively. There is a good agreement between experimental and expected data. We note one trajectory which differs from general trend. Here, we suppose that the size of the particle differs significantly from the considered mean radius.

This procedure was extended to additional experiments made during the 2000 and 2001 parabolic flights campaign, and the results were similar. We therefore deduced that the displacement of particles in microgravity, due to Brownian motion, follows a Gaussian distribution.

B) The conclusion of case A) allows us to compare the aerosol diameter experimentally measured with the one deduced from Brownian displacement. Measurements were made during the Drop Tower campaign (2003). No temperature gradient was applied to the plates of the cell, so the movement of the particles was due to Brownian motion only.

Fig. 2 shows one of the trajectories recorded from the digital holographic microscope. The mean aerosol diameter, measured with SEM, is 1.2 µm, and geometric standard deviation 1.3. We considered the displacements σ of the trajectories during a time t=3.06 s. We obtained that 68% , 95.5% and 99.7 % of the displacements are in the range ± 11µm, ± 25µm and ±35 µm, respectively, while the mean square root displacement turns out to be 11.7 µm. With this value, from eq.1, we obtained d= (1.06±0.1) µm, which is in agreement with the measured diameter.

As the next step, we considered one experiment performed with sodium chloride aerosol (r = 0.16 µm; σ =0.13µm) during the D.T. campaign. We obtained that 68% of the displacements (t=1.02 s) are in the range ± 24 µm, 95.5% in the range ± 29 µm, and 99.7 between ± 32 µm.

We obtained the following values of the mean square root displacement: 24 µm, 14.5 µm, and 10.8 µm, respectively. The minimum value was 10.8 µm and the maximum 24 µm.

From the formula of mean square displacement, $\sigma^2 = 2\,D\,t$, we computed the diffusion coefficient and then the corresponding radius.

We obtained r_{min} = 0.045 µm and r_{max} = 0.22 µm. This conclusion is in satisfactory agreement with the measured sizes.

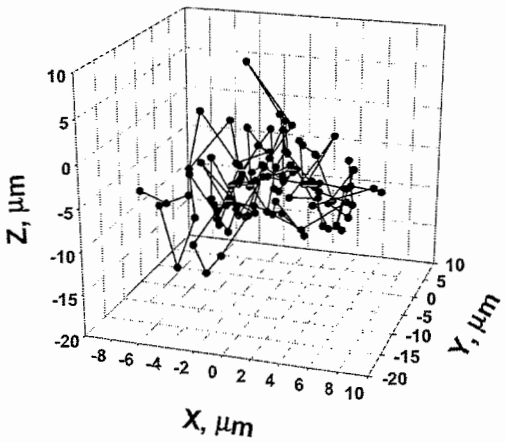

Fig.2.Example of a three-dimensional trajectory of a Brownian particle in microgravity conditions

4. CONCLUSIONS

Thermophoretic experiments in aerosol carried out in microgravity conditions during parabolic flights and in the Bremen drop tower, allowed us to extract useful additional information from the Brownian motion of particles, i.e. estimation of the particles size. We achieved a good agreement between particle radii obtained from SEM measurements, and those calculated from the three-dimensional trajectories provided by the holographic microscope.

Following this approach, it is possible to find the particle radius related to each observed trajectory and, as a consequence, to a particular estimation of a required parameter (velocity, external force). Not only does it increases the reliability and accuracy of aerosol experiment results, but it should also make the evaluations easier and less time-consuming.

5. ACKNOWLEDGEMENTS

ESA/ESTEC, OSTC (Belgium), Novespace (France) and Bremen Drop Tower Operation and Service Company ZARM FABmbH (Germany) are gratefully acknowledged.

6. REFERENCES

Dubois, F., Joannes,L., Legros, J-C., 1999: Improved three dimensional imaging with digital holography microscope using a partial spatial coherent source, *Appl.Opt.* **38**, 7085-7094.

Hinds, W.C., 1982: Aerosol Technology, John Wiley and Sons, Inc., pg.136 .

Prodi, V. 1972: A condensation aerosol generator for solid monodisperse particles. In: *Assessment of airborne particles*. Edited by T.T.Mercer, P.E.Morrow and W.Stober, 169-181.

COMPUTATIONAL FLUID DYNAMICS STUDIES OF AN ICE NUCLEUS CHAMBER

David C. Rogers[1], Derek Straub[2], and Paul J. DeMott[3]

[1]National Center for Atmospheric Research, Boulder, Colorado, USA
[2]Department of Geological and Environmental Science, Susquehanna University, Selinsgrove, PA, USA
[3]Department of Atmospheric Science, Colorado State University, Fort Collins, Colorado, USA

1. INTRODUCTION

The CSU continuous flow ice nucleus chamber describes a pair of devices used in laboratory and airborne measurements of ice nuclei over the past eight years (Chen et al. 2000; Rogers et al. 2001; DeMott et al. 2003). Ice nuclei are the special subset of atmospheric particles that catalyze the transition from liquid or vapor to ice. Their abundance and characteristics are important in determining the concentration of ice particles in supercooled clouds, hence they effect the amount and distribution of precipitation, radiative properties of clouds, and other aspects of weather and climate.

This chamber is the annular space between two concentric cylinders; the cylinder axis is vertical and air flows downward. The chamber walls are ice-coated and held at two different temperatures, for example -30 and –18°C, in order to create a supersaturation in the space between the walls. It is a thermal-gradient diffusion chamber. The design and operation of the chamber were guided by earlier experience, by exploratory lab studies, and by a variety of quantitative estimates of heat transfer and flow velocity profiles.

Earlier mathematical studies of this chamber were based on simplified assumptions about the geometry, such as treating the sample air as a non-mixing ribbon injected between flat parallel plates. The studies used analytical solutions for steady-state and time-dependent problems. In the study reported here, computational fluid dynamics methods were used to simulate numerically the flow of air and the development of temperature and water vapor fields between the walls. The true geometry was modeled with a high resolution mesh, and the flow and thermodynamics were found using a computational fluid dynamics (CFD) solver (FLUENT, Inc.). This approach was not possible until recently, with the advent of complex flow solvers running on high-end PC's. FLUENT has been used successfully for the analysis of internal flow fields and particle trajectories in a variety of cloud and aerosol instruments (Straub and Collett, 2002; 2001; Middha and Wexler, 2003).

In this paper, some FLUENT results are compared with the earlier simplified analytical solutions for conditions typically used in atmospheric sampling. Particle trajectories of cloud droplets were calculated to assess the likelihood of impaction losses. Questions of particular interest include:

(a) time and distance for developing steady thermodynamic fields; these determine the nominal operational sampling set points;
(b) location of the sample air lamina and associated uncertainties in sampling temperature and supersaturation;
(c) recirculation of flow and particles, driven by buoyancy from temperature gradients >20°C cm^{-1};
(d) inertial motions and wall losses of ice crystals that form on activated ice nuclei; and
(e) turbulent mixing in the sample injection region and the outflow cone.

This paper is a preliminary report of the modeling studies; it compares some of the new results with earlier analyses. Some important aspects are not included in this paper, such as particle microphysics, and diffusio-phoretic transport mechanisms.

2. DESCRIPTION OF CHAMBER

Figure 1 shows the basic shape of the chamber. Ice is on the walls, starting ~11 cm from the top. Sample and sheath air are injected at the top. Sheath air enters as circular jets; sample air is a thin continuous ribbon. All flow converges to a single hole in the exit cone leading to an optical particle counter.

3. COMPUTATIONAL MODEL

A computational mesh of the chamber was built using Gambit. Figure 2 shows section views of the mesh, as seen from the top. Since the chamber is circularly symmetric, the model needs only a 5° sec tor to represent the structure. The mesh is a mix of ~80,000 triangular and quadrilateral cells, dense in transition regions and uniform in the chamber center section where gradients are smaller.

Flow dynamics, thermodynamics, and particle trajectories within the chamber were solved using FLUENT, a finite volume based CFD software package. FLUENT applies the Navier-Stokes equations to individual control volumes within the computational domain. Integration of mass and momentum conservation equations produces a set of algebraic equations that are linearized and solved through an iterative process. Model output includes fluid velocities, profiles of pressure and temperature, turbulence characteristics, and other fields of interest. For this study, solutions were generated for two descriptions of the chamber: 2D axisymmetric and 3D. The 2D model domain extends from the inlet to

[1]. Corresponding author's address: David C. Rogers, NCAR/RAF, 10802 Airport Ct., Broomfield, CO, 80021; E-Mail: dcrogers@ucar.edu

44 cm, about half-way to the bottom of the chamber, while the 3D case extends only 18 cm below the inlet.

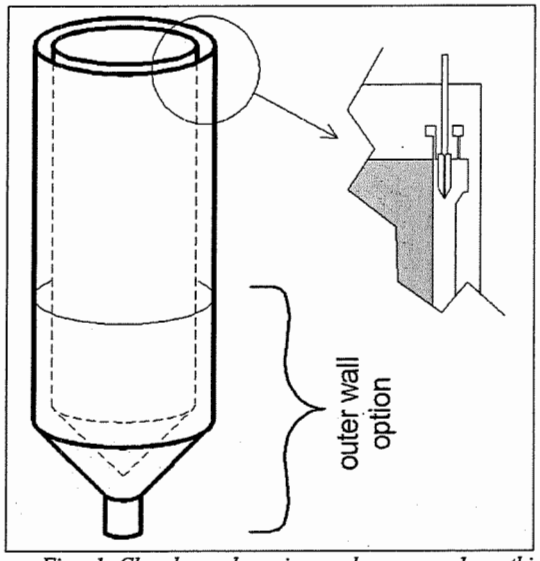

Fig. 1. Chamber volume is annular space ~1 cm thick between two cylinders (7.94 cm o.d., 10.16cm i.d.), length 90 cm (airborne version) and 150 cm (lab version). Flow is down. Inset shows details at top. Wall separation 1.12 cm. Bottom of outer wall is dry or ice-covered.

For the 2D and 3D cases, a second order interpolation method, the QUICK scheme, was used to reduce the effects of numerical diffusion. Turbulence was parameterized with a Reynolds Stress Model, and flow properties in control volumes adjacent to the chamber walls were explicitly calculated. To reduce model run time for the 3D case, a 5° sector of the chamber was modeled at steady state, with rotationally periodic boundary conditions to simulate the existence of the full annular region. Air density was calculated with the ideal gas law; gravity was included in order to capture buoyant effects.

After generating a solution to the air flow through the chamber, the trajectories of spherical particles were simulated using FLUENT's Lagrangian particle model. It uses a force balance to relate particle acceleration to the forces acting on it and is solved for individual particles as they pass through the computational domain. Included in the particle force balance are the drag, gravitational, and virtual mass forces, and a force that results from pressure gradients. Thermophoresis, diffusiophoresis, and Brownian motion are neglected here, though future modeling studies will include them. The effects of turbulence in the air flow were not included in the particle trajectory calculations.

Sample air contains aerosol particles and is 1 LPM. It is sandwiched between two equal particle-free sheath flows at the chamber inlet region. Both cylinders are coated with a thin layer of ice (~0.1 mm thick) that starts 11 cm from the inlet. Ice on the inner cylinder extends to the bottom, but the outer cylinder has ice only on the upper two-thirds. There are two options for ice length of the outer cylinder; in the laboratory version, ice extends to the exit cone. In the airborne version, ice is only on the upper two-thirds; the lower one-third is dry and is not a heat conductor (Fig. 1).

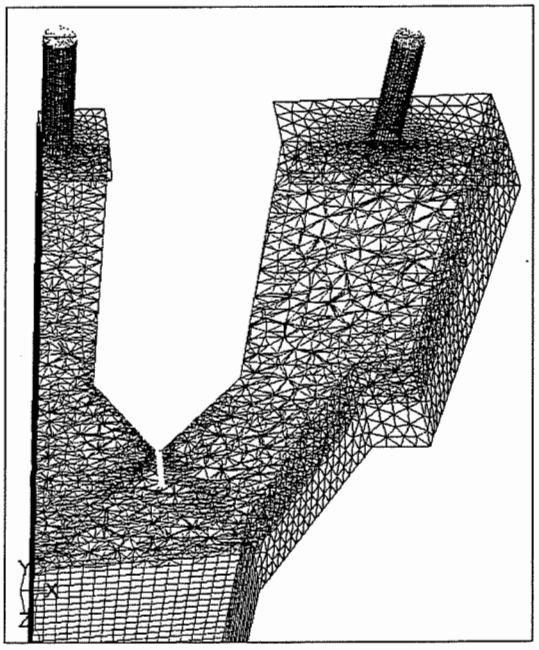

Fig. 2 Sections of computational mesh at chamber top. Cold wall left, warm wall right, flow downward. Sheath flow (90%) enters through round holes. Sample air (10%) enters through slit.

*The inner cylinder is the cold wall at a constant temperature, **Tc**, and the outer cylinder is the warm wall at **Tw**. Wall temperatures can be set over a wide range, from –5 to –65℃, but in practice, the temperature difference is limited in order to avoid reverse flow (Rogers 1988). For the simulation described here, the walls were –18 and –30℃; this sets the steady-state conditions for the sample air at –25.5℃ and 91.4% RH. The 2D axisymmetric model uses FLUENT's multi-component mixture (air and water vapor) and mass transfer capabilities; ice-saturated conditions were specified for all ice coated walls in the chamber. Presently the ability to model an air-water vapor mixture and associated mass transfer has not yet been incorporated into the 3D simulation but is planned in future studies.*

4. RESULTS & DISCUSSION

Several crucial aspects of chamber performance are being examined in this study:

- Development of thermodynamic fields, because particle nucleation and growth depend on sufficient time (distance) and thermodynamic forcing;
- Location of the aerosol sample lamina;
- Reverse (upward) flow must be avoided because it may lead to recirculation of particles and

confuse calculating the sampling conditions. A reverse flow component is driven by the air density difference between the walls, with the cold side tending to sink and the warm side tending to rise. Upward flows are suppressed by increasing the total downward flow. The minimum total to prevent any upward flow is defined as *critical*.

Figure 3 shows the velocity field for the 3D simulation. The sheath air enters as two high speed jets that quickly relax toward viscosity-controlled profiles. Maximum velocities occur where sheath and sample air enters chamber.

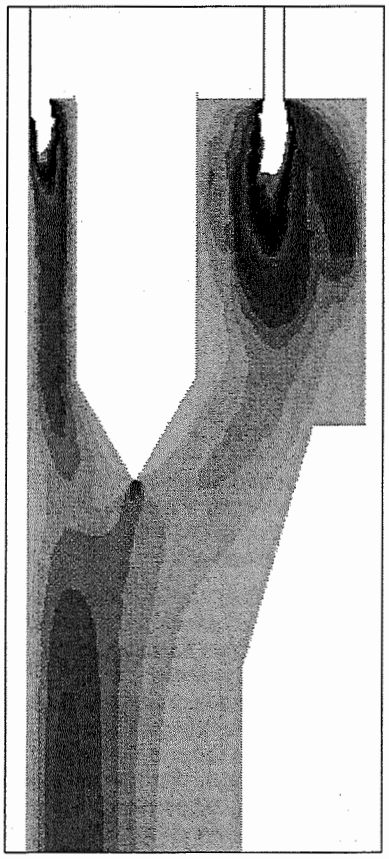

Fig. 3. Velocity field at inlet region, 3D simulation. Twenty evenly-spaced contours 0 to 45 cm s^{-1} (max at sheath jets near top). Width 1.12 cm at bottom.

Flow path lines at the inlet region for this case are shown in Figure 4. Notice that recirculation is evident where both of the particle-free sheath air inlets enter. The sample air merges smoothly between sheath flows and is deflected toward the cold wall in response to the buoyant circulation. Recirculation at these locations is not a problem since the sheath air is particle-free, low humidity, and does not lead to transient supersaturations.

Development of the temperature profile is shown in Figure 5, along with differences from the steady-state profile (–18 to –30℃) for the 2D and 3D simulations. For the 2D case, the profile is within ~0.05℃ of linear at 42 cm from the inlet (approximately half-way to the outlet). Closer to the inlet, the temperature profile has not yet reached equilibrium.

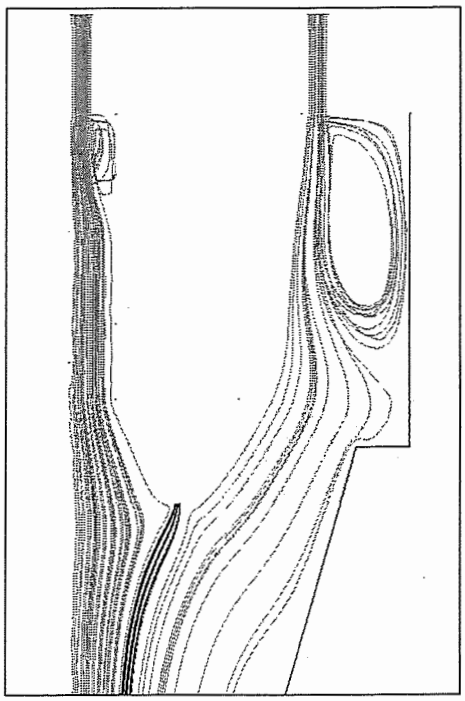

Fig. 4 Path lines show recirculation of sheath air (grey). Density difference deflects sample air (black) to cold side. Overall width of chamber 1.74 cm at top.

Notice that the temperature profile is slower to develop in the 3D case than the 2D case (cf., thick vs dash lines). This difference likely arises due to the ways that sheath air injection is portrayed in the 2D and 3D cases. In the axisymmetric 2D representation, the sheath air inlets are continuous low velocity annuli; in the 3D case, they are discrete jets with high inlet velocity. These jets affect the flow field further downstream than the 2D approximation. The location of the sample lamina is indicated by the shaded band, as predicted by the steady-state solution for flat parallel walls. Comparisons of the model-predicted lamina locations will be addressed in a future paper.

Development of the relative humidity profile is shown in Figure 6 for the 2D FLUENT case and the flat parallel wall steady-state approximation. RH increases with distance down the chamber and at 42 cm is within 1% of the steady-state value in the sample lamina.

Trajectories of 1 and 15 μm particles are shown in Figure 7 through the exit cone, where they have reached maximum size. We treat the particles as passive spherical tracers of fixed size. The results suggest that impaction losses may occur > 15 μm. Calculations and experiments indicate ice particles

reach ~5 μm or smaller in the chamber (Rogers, 1988).

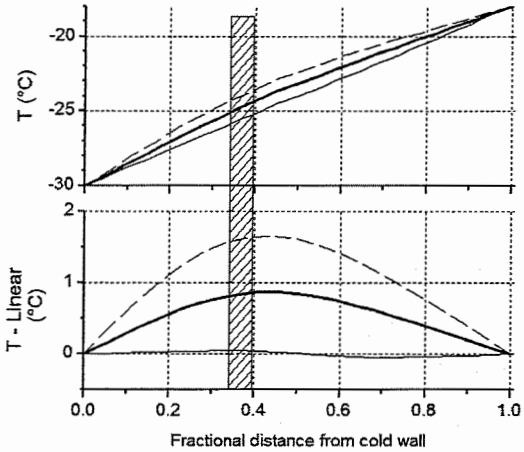

Fig. 5. Development of temperature profiles (top) and difference from linear gradient (bottom). Solid lines are 2D simulations at 17.5 cm (thick) and 42 cm (thin) from inlet. 3D simulation (dash) at 17.5 cm. Shaded band shows location of sample air.

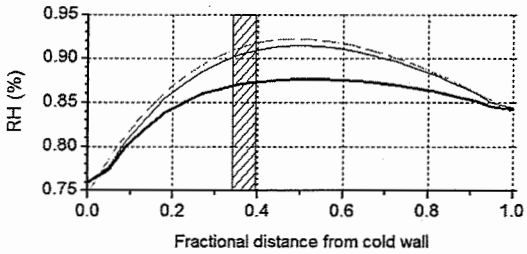

Fig. 6 Development of relative humidity profile. Solid lines are 2D simulations at 17.5 cm (thick) and 42 cm (thin) from inlet. Dash line is steady-state solution for flat, parallel walls.

5. CONCLUSIONS

This is a preliminary report of on-going CFD studies. Because 3D features show significant differences from the 2D approximation, future studies will focus on 3D and extend the computational domain to the full length of chamber. Additional aspects will include: heat transfer through the walls, particle nucleation and growth, ice evaporation on warm wall and frost growth on cold wall, comparisons with real-time operations.

6. ACKNOWLEDGEMENTS

This research was supported by NSF grant ATM97-14177 and NASA grant NAG1 2063. The National Center for Atmospheric Research is operated by the University Corporation for Atmospheric Research under sponsorship of the National Science Foundation. Any opinions, findings, conclusions, or recommendations expressed in this publication are those of the author(s) and do not necessarily reflect the views of the National Science Foundation.

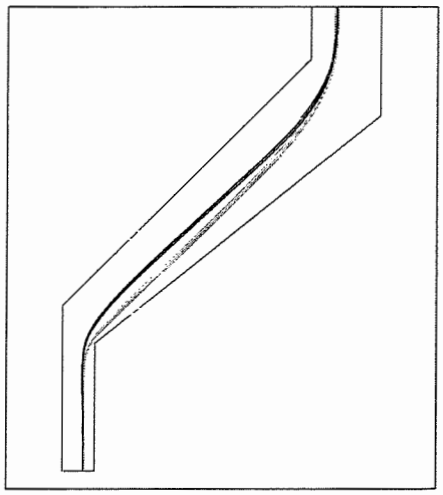

Fig. 7. Trajectories in the exit cone region for unit-density particles 1 μm diameter (black) and 15 μm (grey) spherical particles. Chamber 1.12 cm at top.

7. REFERENCES

Chen, Y, P.J. DeMott, S.M. Kreidenweis, D.C. Rogers and D. Eli Sherman, 2000: Ice formation by sulfate and sulfuric acid aerosol particles under upper tropospheric conditions, *J. Atmos. Sci., 57, 3752-3766.*

DeMott, P.J., Sassen, K., Poellot, M., Baumgardner, D.,Rogers, D.C., Brooks, S., Prenni, A.J. and S.M. Kreidenweis, 2003: African dust aerosols as atmospheric ice nuclei, *Geophys. Res. Lett.*, **30** (14)

Middha, P. and A.S. Wexler, 2003: Particle focusing characteristics of sonic jets, *Aer. Sci. Technol.*, **37**, 907-915.

Rogers, D.C., 1988: Development of a continuous flow thermal gradient diffusion chamber for ice nucleation studies. *Atmos. Res.*, **22**, 149-181.

Rogers, D.C., P.J. DeMott, S.M. Kreidenweis, and Y. Chen, 2001: A continuous-flow diffusion chamber for airborne measurements of ice nuclei. *J. Atmos. Ocean. Technol.*, **18**, 725-741.

Rogers, D.C., P.J. DeMott, and S.M. Kreidenweis, 2001: Airborne measurements of tropospheric ice nucleating aerosol particles in the Arctic Spring, *J. Geophys. Res.*, **106**, 15,053-15,063.

Straub, D.J., and J.L. Collett, Jr., 2002: Development of a multi-stage cloud water collector: Part 2 - Numerical and experimental calibration. *Atmos Environ.*, **36**, 45-56.

Straub, D.J., and J.L. Collett, Jr., 2001: Numerical and experimental performance evaluation of the 3 Stage FROSTY Supercooled Cloud Collector. *Aerosol Sci. Technol.*, **34**, 247-261.

OXYGEN A-BAND MEASUREMENTS FOR SOLAR PHOTON PATH LENGTH DISTRIBUTION STUDIES

T.Scholl and K.Pfeilsticker

Institut für Umweltphysik, Im Neuenheimer Feld 229, 69120 Heidelberg, Germany

1. INTRODUCTION

Radiative transfer (RT) of cloudy skies is one of the most challenging tasks in climate modelling, primarily because cloud covers tend to be inhomogenous, broken in places and frequently occur in mulit-layers (*IPCC-2001*). In the past, numerous attempts have been undertaken either by theoretical or experimental methods to improve the understanding of cloudy sky RT. Among them photon path length studies using oxygen A-band spectroscopy emerged into a powerful technique in recent years (*Pfeilsticker et al.*, 1998 and 1999; *Veitel et al.,* 1998; *Min et al*, 1999 and 2004; *Davis et al.*, 2002). For example, the novel oxygen A-band technique revealed that, for optically thick clouds, the photon transport only obeys classical diffusion laws for single layered coverage, whereas for more complicated cloud covers (multi-layered or broken in places) the physical laws for anomalous diffusion (c.f. trunctated Lévy-distributed) may provide in general a more appropriate description for cloudy sky RT (*Davis and Marshak,* 1998; *Pfeilsticker et al.*, 1999; *Min et al.,* 2001). Here we provide further evidence for the different (normal vs anomalous) photon transport regimes in cloudy sky RT.
The photon path length data we are reporting on were collected during two dedicated European cloud research campaigns (BBC1 and BBC2) held at the KNMI experimental site in Cabauw/Netherlands in September 2001 and May 2003.

2. METHOLOGY

2.1 Inferring Path Length Information

The method to infer photon path length is based on high resolution spectroscopy of the oxygen A-band (760 - 780 nm) in zenith scattered skylight. The multitude of different line strengths offered by the oxygen A-band implicitly provide direct information on the path length distribution of the photons transmitted to the ground. This is since photons with wavelength of strong/weak atmospheric absorption intrinsically probe smaller/large regions of the cloudy sky. This characteristic of cloudy sky RT can be expressed by eqn. (1)

$$\frac{I(\lambda_i)}{I_0'(\lambda_i)} = \int_0^\infty p(l)e^{-\alpha(\lambda_i)l}dl = \tilde{p}(\alpha(\lambda_i)) \qquad (1)$$

where $p(l)$ is the wanted photon PDF, $\alpha(\lambda_i)$ is the wavelength dependent extinction, and $I(\lambda_i)/I_0'(\lambda_i)$ is the wavelength dependent intensity ratio (transmission) of the atmosphere. Eqn. (1) constitutes a Laplace transformation of $p(l)$ to $\tilde{p}(\alpha)$ with $\tilde{p}(\alpha)$ being measured for different absorptions $\alpha(\lambda_i)$ for the oxygen absorption lines $[i]$. The back transformation of eqn. (1), however, is mathematically ill-conditioned, and thus eqn. 1 can only be solved by constraining $p(l)$, c.f. by assuming a Γ-type PDF as is indicated by theoretical RT studies for many cloudy skies. Fortunately, the Laplace transform of the Γ-distributions is known ($\kappa =< L > /var(l)$)

$$p(l) = \frac{1}{\Gamma(\kappa)\left(\frac{\langle l\rangle}{\kappa}\right)^\kappa} l^{\kappa-1} \exp\left(-\frac{\kappa l}{\langle l\rangle}\right) \qquad (2)$$

rendering the constraint inversion to become mathematically possible (*van de Hulst,* 1980).

2.2 Instrumentation

The instrument used for the present study basically consists of three major components (Fig. 1): (1) a light intake telescope optic with a field of view of 1° pointed to the zenith to which transfer optics are attached, (2) a Fastie Ebert grating spectrometer (Sopra UHRS F1500, f/13.5, focal length 1500 mm, slit width 70 μm, a 316 groove/mm Echelle grating) and (3) a CCD detector (Marconi EE42-

[0]Corresponding author address: Thomas Scholl, Institute for environmental physics, Im Neuenheimer Feld 229, 69120 Heidelberg, Germany. Email: thomas.scholl@iup.uni-heidelberg.de

10, 2038x512 pixel). The CCD array is cooled to -50C in order to reduce the dark noise. The spectrometer provides a full width half maximum (FWHM) resolution of 0.0135 nm with a signal to noise ratio of S/N < 1000 for zenith sky spectra recorded in less than 20 seconds. A high optical stability of the whole instrument is achieved by careful temperature stabilization to 30°C.

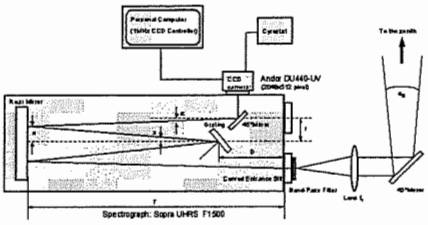

Figure 1. Set-up of the high resolution oxygen A-band spectrometer

Compared to our instrument used previously - for which the monitoring of a single oxygen A-band spectrum with a spectral resolution 0.019 nm and a S/N ratio > 1000 took 900 seconds - the improved technical features allowed us for the first time to infer photon PDFs within spatial scales smaller than the so called radiative smoothing scale.

2.3 Spectral Retrieval

The major problem in inferring photon path length from oxygen A-band spectra is drawing a compromise between full-width half maximum (FWHM) spectral resolution, out of band rejection (OBB), and pixel coverage per FWHM and information content of the measured spectra (e.g., *Min et al.*, 2001). In our study, the chosen values for the compromise are: FWHM = 13.5 pm, OBB < 0.001, pixel coverage 6 pixel per FWHM, which ensure an information content of 4 independent pieces of information that can be drawn from our spectra. The spectral retrieval is solved by (1) forward modelling, at high spectral resolution ($0.5 \cdot 10^{-4}$ nm), the measured spectra with a prescribed photon PDF (usually a Γ- function, see above) and (2) its convolution with the instrument's slit function to resolution of the measured spectrum. (3) The free parameters of the Γ-function are then iteratively calculated by minimizing the mean square distance between the measured and modelled spectrum. The forward RT model divides the atmosphere into 40 layers and uses the oxygen A-band absorption line data from the HITRAN2000 database (*Rothmann et al.*, 2003) the solar line data from Kurucz et al., (1984), actual radio sonde atmospheric pressure and temperature profiles, and assumes Voigt line profiles.

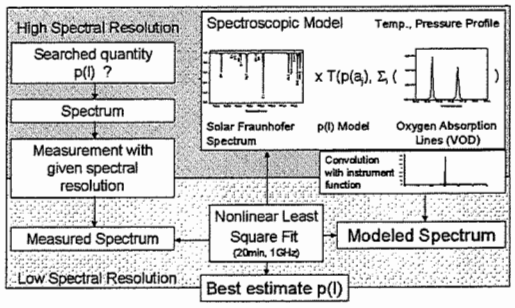

Figure 2. Scheme of the evaluation process

3. RESULTS

Exemplary for the large amount of data taken during the BBC2 campaign, we discuss here the results obtained for May 22, 2003, 09:00 - 17:00 UTC. Figure 3 shows the inferred first and second moments ($< L >$ and $< L^2 >^{0.5}$) of the photon PDF (left vertical axis in units of optical depth of a vertical atmospheres, VOD) binned together into one-minute steps (x-axis). For comparison, the right vertical axis shows the measured liquid water paths (LWP) obtained from the University of Bonn microwave instruments Miccy and the Hat-Pro instrument are shown (right vertical axis).

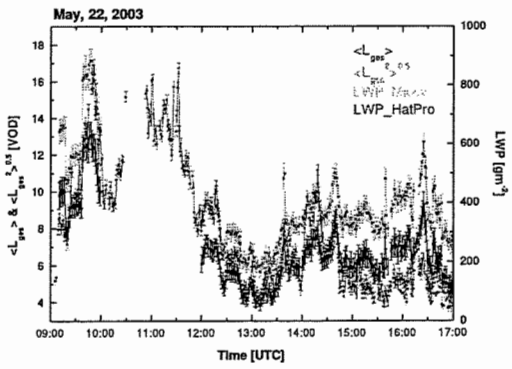

Figure 3. Time series inferred first and second moment (in unit of vertical optical depth (VOD) the atmosphere, left vertical axis) of the photon PDF and of measured LWPs /right vertical axis) over Cabauw/NL on May 22, 2003.

Clearly, for the May 22, 2003 data the mean and variance of the photon path lengths correlate well with the measured LWP. In fact, for a given effective cloud droplet radius (R_{eff}), the liquid water path is proportional to cloud optical thickness (τ, see eqn 3), and hence to number of Mie scattering events within the cloud and thus path length, i.e.

$$\tau = (\Delta H/\lambda_{Mie}) = (3 \cdot LWP \cdot \Delta H)/(2 \cdot R_{eff}) \quad (3)$$

with λ_{Mie} being the Mie scattering length, ΔH the cloud vertical extension, and LWP = LWC $\cdot \Delta H$. Here we explore our data to test the hypothesis of normal versus anomalous diffusion of solar photons suggest by Davis and Marshak, (1998), which the authors refined in 2002. It states that the mean photon path length $< L >$ for photons being transmitted through a cloud or cloud system of vertical extension (ΔH) should follow the relation

$$< L >= 1/2 \cdot [1 + C(\epsilon)] \cdot (1-g)^{\alpha-1} \cdot \tau^{\alpha-1} \cdot \Delta H$$
$$= 1/2 \cdot [1 + C(\epsilon)] \cdot \tau^{*\alpha-1} \cdot \Delta H \quad (4)$$

and

$$C(\epsilon) = (\epsilon/2)(4 + 3\epsilon)/(1 + \epsilon) \quad (5)$$

with g the asymmetry parameter, $\tau^* = \tau \cdot (1-g)$ the rescaled cloud optical thickness after accounting for the efficiency of Mie scattering to randomize the light, $\epsilon = 0.7017/\tau^*$, and the so called Lévy index α which is a number that ranges between 1 to 2.

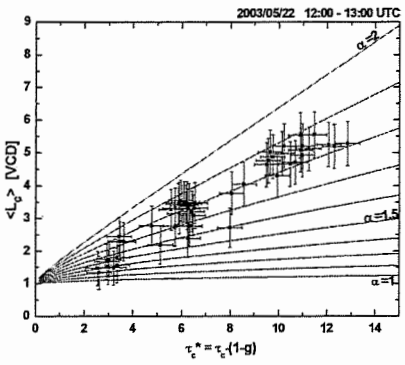

Figure 4. Scatter plot of inferred mean $< L >$ photon path length as function of rescaled optical thickness (τ^*) for the May 22, 2003 observation from 12:00 to 13:00 UTC.

In transport physics, the Lévy index determines the shape of the underlying Lévy PDF. In particular, equation (4) indicates the average path length for photons diffusing through a slab of thickness ΔH, where the value $\alpha = 2$ is attained for a homogenous slab and for $\alpha < 2$ for inhomogeneous slab. The latter should thus support photon transport for inhomogeneous cloud with support on an increased probability for very short and very long jumps between individual Mie scattering events.

In Figure 4, the enhancement of the mean photon path length in and under the cloud (actual ΔH is here counted from cloud top to the ground) as a function of rescaled cloud optical depth $\tau^* = \tau \cdot (1-g)$ is shown. Remarkably, and in reasonably good agreement with the prediction of eqn. 5, Lévy-indices $\alpha \leq 2$ are inferred. This finding confirms earlier claims of Pfeilsticker et al. (1999) and Min et al. (2001) that for single layered clouds the photon transport is well described by classical (homogenous) diffusion physics, whereas for complicated cloud covers (multi-layered or broken in place clouds)ï anomalous diffusion provides a more appropriate description.

4. CONCLUSIONS

The determination of photon path lengths PDFs by high resolution oxygen A-Band spectroscopy is a powerful tool to study cloudy skies the radiative transport (RT). In particular, the method's strengths evolve when combined with simultaneous measurements of the cloud structure and liquid water content. Photon PDF thus serves as a new observable to test cloudy sky RT modelling. Our observations provide further evidence for the anomalous diffusion transport of solar photon being transmitted by complicated cloud covers, i.e., multi-layer and broken clouds.

Acknowledgments. This work is funded through the AFO-2000 4D clouds project (07ATF24) funded by the BundesMinisterium für Bildung und Forschung (BMBF), Germany. We are grateful to M.Quante/GKSS for the Radar data and S.Crewell/Munich for the LWP data. We also thanks KNMI for the excellent working conditions in Cabauw.

References

Davis, A. and A. Marshak: *Lévy kinetics in slab geometry: Scaling of transmission probability,* In M. M. Novak and T. G. Dewey (Eds.), Fractal Frontiers, pp. 63-72. World Sci., River Edge, N.J., 1998.

Davis, A. and A.Marshak, *Space-time characteristics of light transmitted by dense clouds: A Green function analysis*, J. Atmos. Sci., 59, 2713-2727, 2002.

Gamache, R. R., Goldman, A., Rothman, L. S., *Improved Spectral Parameters for the Three Most*

Abundant Isotopomers of the Oxygen Molecule, J. Quant. Spectr. Rad. Trans., Vol. 59, No 3-5, pp. 495-509, 1998.

Holten et al., *IPCC Third Assessment Report - Climate Change 2001,* WMO 2001.

Kurucz, Furenlid, Brault, and Testerman, *Solar Flux Atlas from 296 to 1300 nm*, NSO, Tucson, Atlas no. 1, 1984.

Min, Q.-L., and L. C. Harrison, *Joint statistics of photon path length and cloud optical depth,* Geophys. Res. Lett., 26, 1425-1428, 1999.

Min, Q.-L., and L. C. Harrison, and E. Clothiaux, *Joint statistics of photon pathlength and cloud optical depth: case studies,* J. Geophys. Res., 106, 7375-7386, 2001.

Pfeilsticker, K., F. Erle, O. Funk, H. Veitel, and U. Platt, *First geometrical path lengths probability density function derivation of the skylight from spectroscopically highly resolving oxygen Aband observations. 1. Measurement technique, atmospheric observations, and model calculations,* J. Geophys. Res., Vol. 103, No. D10, 11,483-11,504, 1998, and *2. Derivation of the Lévyindex for the sky light transmitted by midlatitude clouds*, . Geophys. Res., Vol. 104, No. D4, 4101-4116, 1999.

Rothman, L., et al., *The HITRAN Molecular Spectroscopic Database: The HITRAN molecular spectroscopic database: edition of 2000 including updates through 2001,* J. Quant. Spec. and Rad.Trans., 82 (2003) 544,2003.

Van de Hulst, H. C., *Multiple Light Scattering, Tables, Formulas and Applications, Volume 1 and 2. London: Academic Press,* 1980.

Veitel, H., O. Funk, C. Kurz, U. Platt, and K.Pfeilsticker, *Geometrical pathlength probability density functions of the skylight transmitted by midlatitude cloudy skies: Some case studies*, Geophys. Res. Lett., 25, 3355-3358, 1998.

THE STUDY OF CLOUD WATER RESOURCES BY DOPPLER RADAR

Shi Lixin[1], Duan Ying[1], Wu Zhihui[1] and Tang Dazhang[2]

[1]Weather Modification Office of Hebei Province, Shijiazhuang, Hebei, 050021, P.R.China
[2]Nanjing Institute of Meteorology, Nanjing, Jiangsu, 210044, P. R. China

1. INTRODUCTION

In recent years, water resources become more and more important to the world. Precipitation enhancement activity is a significant attempt to develop water resources in the atmosphere. Precipitation efficiency is one of the key factors in the study of cloud water resources. Some different methods have been used in estimating precipitation efficiency (e.g. Braham 1952; Hobbs et al. 1980; You et al. 1994).

Lhermitte and Atlas (1961) developed the velocity-azimuth display (VAD) technique by Doppler radar observation. By the assumption of a wind field linearly varying in space, Browning and Wexler (1968) made a thorough analysis of the VAD technique. They obtained the divergence and deformation of the wind field via Fourier harmonic analysis. Wilson et al. (1981) studied the precipitation efficiencies of three cases by VAD technique; they estimated vertical air motions from vertical upward integration of the mass continuity equation. However, the derived mean divergence is based on a linear wind field. In fact, for nonlinear wind fields, the mean horizontal divergence still can be obtained by VAD technique (Caya et al., 1992). Shi et al. (2003) studied the precipitation efficiency during two stratiform cloud precipitation processes. Based on Doppler radar VAD technique, the purpose of this paper is to preliminarily analyse cloud water resources.

2. METHOD

The radial velocity V_r can be expressed as

$$V_r = V_h \cos\alpha \cos(\theta_0 - \theta) + V_f \sin\alpha \qquad (2.1)$$

where V_h is the horizontal wind speed, V_f the fall velocity of the particles, θ the azimuth angle measured from the north, θ_0 the direction, and α the antenna elevation angle.

According to Fourier harmonic analysis, the average horizontal divergence

$$Div(V_h) = \frac{a_0}{r\cos\alpha} - \frac{2V_f}{r} tg\alpha \qquad (2.2)$$

where a_0 is a Fourier coefficient, and r is the radius of the VAD circle.

If the circle is full of echo data, and the radial velocities are measured at 1° azimuth angle interval, a_0 can be calculated by

$$a_0 = \frac{1}{180}\sum_{i=1}^{360} V_r \qquad (2.3)$$

V_f means the fall velocity of particles in effective scanned volume, involving w_0, the mean fall velocity of particles with various sizes in still air, and w, the vertical air speed.

In stratiform clouds, vertical air motions have speeds of only a few or a few tens centimeters per second. Compared with w_0, the vertical air velocities whose magnitudes are small are neglected, and then in (2.2) w_0 can be substituted for V_f approximately.

w_0 can be estimated by w_0-z relation (Joss and Waldvogel, 1970)

$$w_0 = 2.6z^{0.107} \qquad (2.4)$$

where z is the radar reflectivity factor. After the correction of air density, it is given by

$$w_0 = 2.6z^{0.107}\left(\frac{\rho_0}{\rho_H}\right)^{0.5} \qquad (2.5)$$

where ρ_0 is the air density in standard status, and ρ_H the air density at H height. ρ_H is determined from the equation of state

$$\frac{\rho_0}{\rho_H} = \frac{p_0 T_H}{p_H T_0} \qquad (2.6)$$

where p_0 is 1013.25 hPa, T_0 is 273.15 K. p_H and T_H are the pressure and temperature at H height respectively, which can be obtained from radiosonde.

Vertical velocities can be derived by upward vertical integration of the mass continuity equation

$$Div(V_h) + \frac{1}{\rho(z)}\frac{\partial(\rho w)}{\partial z} = 0 \qquad (2.7)$$

where ρ is air density in kg m^{-3}, w is vertical speed in m s^{-1}, and z is height in m. Thus the theoretical precipitation rate (R) can be estimated. The condensation rate in vertical column of air above the radar is assumed to be equal to the precipitation rate (R)

$$R = -\int_{cloud\ base}^{cloud\ top} \rho(z) w(z) \frac{dq_s}{dH} dz \qquad (2.8)$$

where q_s is the saturation specific humidity which can be taken from radiosonde at the beginning of the period. R is in kg m^{-2} s^{-1}. R' is the precipitation rate whose unit is mm cm^{-2} hr^{-1}

$$R' = 3600R \qquad (2.9)$$

The actual precipitation rate (I) is measured by the automated raingauge. The precipitation efficiency (E) can be estimated by

$$E = \frac{I}{R'} \qquad (2.10)$$

Corresponding author's address: Shi Lixin, Weather Modification Office of Hebei Province, Shijiazhuang, Hebei, 050021, P.R.China; E-Mail:shilixin@sina.com.

3. CASE STUDY

The data of 20 June 1999 were analyzed. A cold front precipitation process was observed by a C-band single Doppler radar in Beijing. The volume scan data of 20 km range are used in the study.

Fig.1 shows the Doppler velocities of a PPI scan (elevation angle α=1.5°) at 1300 BST. As seen from Fig.1, there exists convergence within a radius of 20 km.

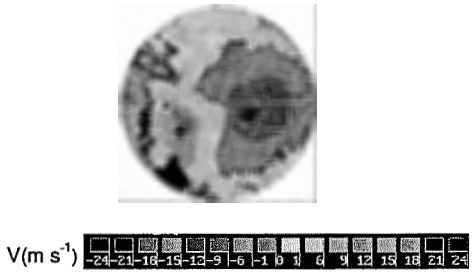

Fig.1 Doppler velocities of a PPI scan (elevation angle α=1.5°) at 1300 BST on 20 June 1999. Maximum range 40 km. "+" positive velocity, and "-" negative velocity.

Fig.2 shows the time series of the calculated precipitation rate and the actual gauge-measured precipitation rate. It is clearly seen that, the calculated precipitation rate agrees well with the gauge-measured precipitation rate. The average estimated precipitation efficiency is 37%.

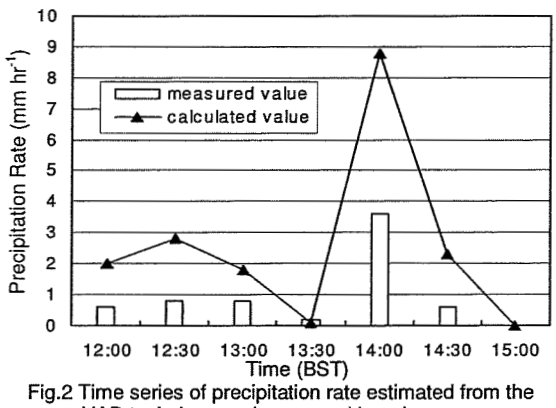

Fig.2 Time series of precipitation rate estimated from the VAD technique and measured by raingauge.

From the surface precipitation, the total precipitation amount is 2.6×10^6 m^3. According to the efficiency of precipitation, the estimated amount of cloud water that didn't convert to precipitation is about 4.4×10^6 m^3.

4. DISCUSSION

4.1 As one of the methods, this is a useful attempt for analysis of water resources in the atmosphere. It should be pointed out that w_0 is substituted for V_f when we calculate average horizontal divergence. Usually this is suitable for widespread precipitation, but not for convective clouds because of the great variation of vertical air motions.

4.2 In the adjacent area, based on a ground-based dual-channel microwave radiometer, Duan (1999) studied the precipitation efficiencies of stratiform clouds He found the liquid water, which convert to precipitation by natural precipitation process only accounts for a small part of the total liquid water. In most of the precipitating stratiform clouds, the precipitation efficiencies were less than 50%. This study has the similar result.

5. ACKNOWLEDGEMENTS

The authors express appreciation to Beijing Meteorological Bureau for providing Doppler radar data.

6. REFERENCES

Braham, R. R., 1952: The water and energy budgets of the thunderstorm and their relation to thunderstorm development. J. Meteor., 9, 227-242.

Browning, K. A., and R. Wexler 1968: The determination of kinematic properties of a wind field using Doppler radar. J. Appl. Meteor., 7, 105-113.

Cava, D., and I. Zawadzki, 1992: VAD analysis of nonlinear wind fields. J. Atmos. Oceanic Tech., 9, 575-587.

Duan Ying, 1999: Estimation of artificial precipitation resource condition and cloud seeding potential by ground-based remote sensing data. Acta Meteor. Sinaca, 13, 103-114.

Hobbs, P. V., T. J. Matejka, P. H. Herzegh, J. D. Locatelli, and R. A. Houze Jr., 1980: The mesoscale and microscale structure and organization of clouds and precipitation in midlatitude cyclones. I: A case study of a cold front. J. Atmos. Sci., 37, 568-596.

Joss, J., and Waldvogel, 1970: A., Raindrop size distributions and Doppler velocities. Preprints 14th Radar Meteor. Conf., Boston, AMS, 153-156.

Lhermitte, R. M., and D. Atlas, 1961: Precipitation motion by pulse Doppler radar. Proc. Preprints 9th Weather Radar Conf., Boston, AMS, 218-223.

Shi Lixin, Tang Dazhang, Wan Rong and Zhang Peng, 2003: The study of precipitation efficiency by Doppler radar. Preprints 8th WMO Scientific Conference on Weather Modification, Casablanca, Morocco, WMO/TD1146, 405-408.

Wilson, J., R. Carbone, and B. Ramsay, 1981: Precipitation and precipitation efficiencies derived from single Doppler radar. Preprints 20th Conf. On Radar Meteor., Boston, AMS, 461-468.

You Laiguang, Wang Xiaobin, Cai Huaqing, and Zheng Xinjiang, 1994: Study of cloud water content with a dual band microwave radiometer in Beijing. 6th WMO Scientific Conf. on Weather Modification, Peastum, Italy, WMO/TD596, 383-386.

AIRBORNE DATA ACQUISITION SYSTEMS

Sergey N. Skuratov, Victor V. Petrov, Victor P. Korneev[1],
Vladimir A. Glushykhin, Vasily V. Volkov[2]

[1]Agency of Atmospheric Technologies
[2]Center for implementation of methods and means of weather modification "AQUA"

In weather modification activities, in accordance with the objectives, the various types of planes equipped with different technical and measuring instruments are used.

A new series of devices of the data acquisition systems (DAS) was developed as the universal tool for maintenance not only the works on weather change, but also airplane investigation of atmospheric processes, in particular the processes of clouds physics. The basic features of the new series of DAS are:

- an opportunity of easy installation aboard the airplane of any type;
- an opportunity of connection of measuring devices and gauges with various output interfaces;
- an opportunity of adjustment of a measuring network, namely connection of various number of measuring devices to measuring channels in the any order;
- an opportunity to make a choice of a measurements synchronization methods;
- internal uninterruptible power supply source;
- reserve storage of the measurements data;
- preliminary processing of the measurements results, to obtain the real physical meanings of the atmospheric parameters;
- an opportunity of the program adjustment, to display the measurements results accordanly with the onboard aerologist (operator) requirements;

The DAS systems are executed as two blocks. First block is specialized one-crystalline computer (controller), which carries out digital transformation of the measured parameters, provides synchronization of measurements and their archiving and prepared set of obtained data for net account. The second block provides display of the information, its reserve storage and preliminary processing. As the second block, the PC compatible notebook under OS Windows is used. Such configuration of DAS systems provides on the one hand the real-time mode of data gathering, and with another, allows to use the powerful Windows graphic interface and advanced user opportunities of this OS.

The developed DAS systems differ, basically, by hardware realization of the first block. In a present, the series of devices contains three controllers.

The systems with the minimal opportunities are based on the controller DAS-VG-001. It is intended for transformation, operative processing and registration in a digital form of the following signals and parameters:

- values of pressure in outside air inlets of the airplane (static and dynamic pressure);
- values of the airplane outside air temperature sensor resistance, with different standards of nominal (both 50 and 100 Ohm);
- values of frequencies of electrical pulses sequences for three digital channels (airplane Doppler speed and a bearing corner measuring system);
- the information from the GPS receiver (offer NMEA-083 sentences $GPRMC and $GPGGA).

For systems with the extended opportunities the controller DAS-VG-002m is intended. It is used for transformation, operative processing and registration in a digital form of the following signals and parameters:

- the total input set of DAS-VG-001;
- values of a voltage of an electrical current 0 - 10 Volts on two analog channels, which are used, mainly, for Nevzorov LWC/TWC probe;

Corresponding author's address: Sergey N. Skuratov, Agency of Atmospheric Technologies, Novovagankovsky 8, Moscow, Russia; E-mail: attech@attech.ru

- the information from airborne condensation hygrometer ACH - temperature of a mirror, photocurrent of water and ice;
- the information from additional port of the interface RS232.

For cloud physics and weather modification research activities we are using a complete set of airplane adopted instruments for microstructure and thermodynamic parameters measurements, connected to Data Acquisition System - VGSS-005.

The hardware of DAS-VGSS-005 has the following characteristics:

- 32 input channel for analog signals (+/- 5V,) with 12 bit analog to digit conversion;
- the possibility of analog signals gathering up to 10 times per second;
- 32 input channel for frequency modulated signals;
- an opportunity to use the frequency channels both in a mode of the account of pulses, and for measurement of signals frequencies;
- data gathering of GPS signals (offer NMEA-083 sentences $GPRMC, $GPRMB and $PGRMZ);
- 4 channels of data gathering in a digital consecutive code (interface RS-232);
- synchronization of measurements by the internal timer;
- an opportunity to use one of the input channels as a source of synchronization;
- an opportunity to use an external input for the synchronization;
- an opportunity of time intervals choice for data gathering of each of measuring channels;
- a reserve storage of all gathering information by using internal memory EPPROM;
- formation of uniform data packages for net account;
- an opportunity to change the controller managing program;
- set of obtained data;
- internal uninterruptible power supply source.

The software used by computer for preliminary processing, archiving and displaying the measured data are practically identical for the each type of DAS controller. The user software interface is identical for the all systems, that is essentially for the training facilitates and the scientific activity of the onboard aerologists. The differences are contained only in the block of reception of the data and in the scheme of internal communications (connections) of the software.

The software is constructed by using the multithreads technology. Reception of the data, their preliminary processing, displaying the results of measurements, archiving of the primary data and archiving the results of processing occur in parallel, by using possibility of OS Windows multitask

One of computer communication ports is used to receive the total set of data obtained. Number of the accepted channel, position of measured data in a storage file, type of the data coding, method of preliminary processing, factors of calibration, etc. are put in conformity each other in many dimensional massive, which is used as the software cross field. The tuning of cross field is possible directly by the user interface.

There are the internal protections against failure in a flow of the data measured in the program code. Absence the single parameter of the data measured, occurrence of sizes leaving for an allowable range and, even, complete breakage of communication (connection) with the controller are fixed and do not result in the software failures.

All collected data are processed to the physical values of parameters. Thus, the opportunity of display both, the initial signals (voltage, frequency, digital code), and physical values, appropriate to them is realized.

The user interface of the program represents a set of easily switched windows, containing the necessary information. The set of displayed parameters in each of windows can be operatively adjusted according to the requirements of the user.

The software uses various manners of data displaying. For convenience of the user the data are represented in style of analog devices, which are simulating the airplane equipment, digital

indicators, diagrams and as the graphical dependencies. The registration of visual information by the onboard aerologist is also presented by software. This registration is considerably facilitated by using a type-setting field, containing the basic types of clouds and atmospheric phenomena. The data, typed (collected) by the user in the electronic diary, are supplemented by time stamp and data of air temperature, humidity and wind automatically.

The set of windows provides:

- display of an initial data flow (the terminal mode) and parameters of work of all equipment;
- display of navigating parameters;
- display of meteorological parameters;
- graphic display of horizontal stratification of any four chosen parameters;
- graphic display of vertical stratification of any three chosen parameters;
- display of records in electronic onboard diary;

Simultaneously with the specified windows the user interface allows to display a route of flight and modification zones on a geographical map. There is also the possibility to display the table of data collected during any interval of flight. The program provides preservation of a map with the flight route in a separate file.

The requirements of the program to hardware are not excessive. So, during tests with the computer configuration Pentium 4 1,4 GHz, RAM 512 Mb, at the preliminary operative memory reservation for data collection of value 45 Mb, the loading of the processor was 4 %, and usage of physical memory has not exceeded 30 %.

The DAS systems were tested and successfully used in a series of works on weather modification in 2003. In particular there were the works on meteodefense of cities of Tashkent, Moscow, St.-Petersburg per days of nation holidays and public festive, as soon as the works on artificial precipitation enhancement in Yakutia.

ASSESSMENT OF SUPERSATURATION IN DIFFUSION CHAMBERS

Jefferson R. Snider and Markus D. Petters

University of Wyoming Department of Atmospheric Science, Laramie, WY, 82071, jsnider@uwyo.edu

1 - INTROCUCTION

Progress toward obtaining improved characterizations of the cloud condensation nuclei (CCN) is limited by the vexing problem of obtaining accurate assessments of the applied water supersaturation in CCN instruments. In the 1970's this issue was addressed by several investigators (e.g., Fitzgerald (1972) and Katz and Mirabel (1975)). The latter concluded that expressions for the maximum applied supersaturation in a thermal diffusion chamber can be approximated in terms water saturation vapor pressures evaluated at the top and bottom chamber boundaries. Their recommendation was based on modeling work which included the Soret and Dufour effects as well as terms describing Fickian diffusion. This approach was adopted by Gerber et al. (1977) who showed that measurements of the critical supersaturations and dry sizes of laboratory test particles were consistent with Köhler theory.

The past several years has witnessed a renaissance of CCN studies with some investigators using field CCN measurements to constrain predictions of the 1st and 2nd indirect effects of aerosols on climate and others conducting laboratory studies of CCN instrument performance. Here we focus on the latter problem. Our approach is to utilize two different techniques to prepare quasi-monodisperse aerosols and to use these to evaluate threshold particle sizes which activate to form cloud droplets in two University of Wyoming (UWyo) thermal diffusion CCN instruments. From this size we infer a critical supersaturation, via Köhler theory[1], and thus the maximum steady-state chamber supersaturation. Henceforth we will refer to the latter derived quantity as the effective chamber supersaturation. A companion paper (Petters et al., 2004) utilizes activation efficiency versus particle dry size relationships developed here and data obtained from two UWyo CCN instruments operated in the field during the 2001 DYCOMS-II field campaign. Petters et al. report a successful comparison of predicted and measured CCN in an aerosol-to-CCN closure study.

[1] Our Köhler theory model is described in Snider et al. (2003). The model can be run on line at http://www-das.uwyo.edu/ccp/web.

2 - THE D_{me} -to- D_{se} ABIGUITY

Several investigators have probed the problem of relating mobility equivalent dry particle diameters (D_{me}), defined by selection in a differential mobility analyzer (DMA), to spherical equivalent diameters (D_{se}) (e.g., Kelly and McMurry, 1992; Hämeri et al., 2001). By D_{se} we imply the diameter that would result if a test particle, characterized by D_{me}, was compacted to its bulk density and shaped into a sphere. A connection between D_{me} and D_{se} is desired for achieving our objective of inferring critical supersaturations and thus the effective chamber supersaturation. The main problems in relating laboratory-generated values of D_{me} to D_{se} result from: 1) the tendency for NaCl, and other test materials, to form particles which are aspherical, 2) inhibited efflorescence during particle drying, and 3) the occurrence of voids within the generated particles. Each of these effects can lead to overestimation of the dry salt mass, an overestimation of D_{se}, an underestimation of critical supersaturation (obtained via Köhler theory) and thus an underestimation of the effective supersaturation (Snider et al., 2003).

Figure 1 illustrates the technique we used to resolve the D_{me} -to- D_{se} ambiguity and thus resolve the effective supersaturation without recourse to the assumption that D_{se} is equivalent to D_{me}. On the left is a laboratory-generated test particle, characterized by an assumed complex shape. In the middle of the figure is the particle after deliquescence and growth to its equilibrium size at RH=90%, and on the right the particle is constrained to a smaller wet size prescribed by RH=70%. Observe that RH and D_{wet}, plus Köhler theory, provide a path to three properties: 1) particle mass (m), 2) sphere equivalent dry diameter[2] (D_{se}), and 3) particle critical supersaturation (S_c).

[2] From our definition of D_{se}, and the inferred value of m, we infer the former as $D_{se} = \sqrt[3]{6m/(\pi\rho)}$, where ρ is the bulk density of the salt

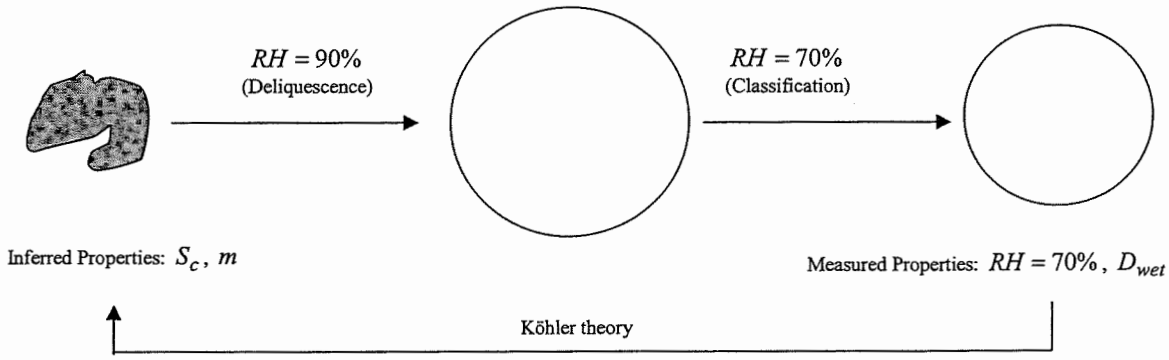

Figure 1 - The wet particle classification technique

3 – EXPERIMENTAL

Figure 2 illustrates one of the two approaches we used for generating quasi-monodisperse test aerosol. Aqueous solutions of either ammonium sulfate or NaCl were atomized, diffusion dried, charge equilibrated, rehumidified at RH=90% (humidifier #1) and mobility classified in a DMA. The humidity of the sheath air entering the DMA was controlled at RH=70% using a Sable Systems DG-1 dew point generator (humidifier #2). The RH of the polydisperse aerosol, the sheath air, the excess air and the test aerosol streams were monitored using capacitance RH sensors. On the assumption that the polydisperse aerosol, upon entering the DMA, equilibrated with the sheath air humidity on a time scale much shorter than the particle residence times in the DMA, the selected value of D_{wet} and the measured RH can be used to infer m, D_{se} and S_c (Figure 1). Particle residence times in the DMA are 2 s while ~0.05 s is required for the 90% to 70% RH adjustment for the sizes of interest (i.e., dry sizes smaller than ~0.2 μm), so the assumption appears valid. This approach is referred to as the "wet test particle classification technique."

Past investigators of effective supersaturations in the UWyo CCN instruments (Leaitch et al., 1999; Snider et al., 2003) utilized test particles of known composition and mobility equivalent size. In both studies the test particles were classified dry (RH~10%), and known differences between D_{me} and D_{se} were assumed negligible (i.e., the test particles were assumed to be spherical, compact and composed of a single component (dry salt)). This approach is referred to as the "dry test particle classification technique."

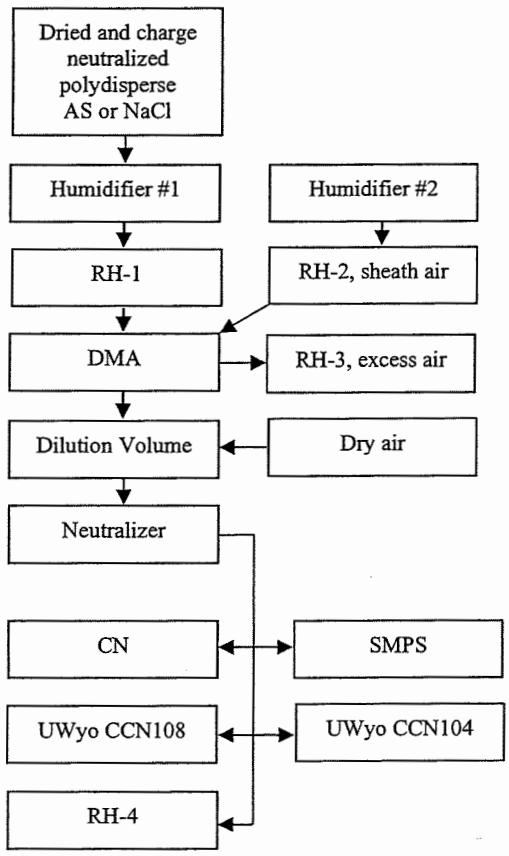

Figure 2 – Setup used to generate quasi-monodisperse particles via the wet test particle classification technique

4 – RESULTS

In Figure 3 we show time series data from the four RH sensors indicated in Figure 2. RH values range from ~90% at the exit of humidifier #1, a value sufficient for deliquescing either ammonium sulfate (AS) or NaCl, to RH~10% at the exit of the mixing chamber (i.e,, immediately upstream of the CCN and aerosol instrumentation). We did demonstrate that values of D_{se} inferred from D_{wet} and RH measurements (RH-3) agreed with dry mode sizes evaluated by the Scanning Mobility Particle Sizer (SMPS). RH measurement accuracies are $\pm 5\%$ and this introduces a $\pm 3\%$ uncertainty in the inferred dry sizes when the sheath air is introduced into the DMA at RH = 70%. Temperatures were measured at the same locations as the RH measurements and these deviated by less than 0.5 °C from the temperature of our air conditioned laboratory.

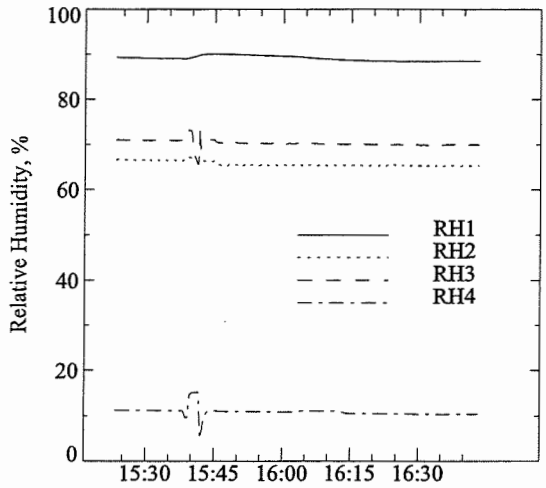

Figure 3 – Time series of RH measurements at the sensor locations indicated in Figure 2. Air flow was interrupted at ~15:40.

Results obtained with NaCl prepared via the wet test particle classification technique are indicated by the data points in Figure 4. These represent means of several (20 to 30) CCN-to-CN ratio measurements made at the indicated sizes. It is apparent that particles characterized by D_{se} values larger than ~0.10 μm are efficiently activated in both UWyo CCN instruments, which for this particular experiment were operated at a nominal chamber supersaturation of S = 0.2%. By the nominal chamber supersaturation we mean the value calculated using measured top and bottom plate temperatures (T_1 and T_2) and the corresponding saturation vapor pressures ($e_w(T_1)$ and $e_w(T_2)$) (Katz and Mirabel, 1975).

$$S = 100 \cdot \left(\frac{1}{2} \cdot \frac{e_w(T_1) + e_w(T_2)}{e_w((T_1 + T_2)/2)} - 1\right) \qquad (1)$$

The solid line is a fitted activation efficiency curve, from which a 50% activation size, a critical supersaturation (via Köhler theory) and the effective chamber supersaturation were inferred. The dotted line is a fit of data obtained via the dry test particle classification technique but here we omit the CCN-to-CN averages. A comparison of the activation efficiency function obtained from the wet test particle classification technique (solid line) and dry test particle classification technique (dashed line) indicates only a very small and experimentally insignificant differences between the 50% activation sizes obtained via these two techniques.

The long dashed vertical line shown in Figure 4 represents D_{se} anticipated using the nominal chamber supersaturation (S=0.2%) and Köhler theory. Based on results of the dry test particle selection technique, we have reported correction factors which allow users of the UWyo CCN instruments to convert from nominal supersaturation (Equation 1) to the effective supersaturation (Snider et al., 2003). This correction is based on the mobility equivalent dry size corresponding to 50% activation efficiency, the assumption that $D_{me} = D_{se}$ and Köhler theory. Since the wet test particle selection technique yields the same 50% activation dry size as the dry particle selection technique (Figure 4) that result corroborates the Snider et al. correction.

5 – CONCLUSIONS

Considerable debate has focused on the problems of either predicting or determining effective supersaturations within a thermal diffusion CCN instrument. We have utilized two techniques, neither of which is novel, with the goal of obtaining independent estimations of the dry particle sizes which characterize the onset of cloud droplet nucleation in the UWyo CCN instrument. The experimental 50% activation sizes were also compared to theoretical predictions based on a parameterized description of the maximum steady state supersaturation in a thermal diffusion chamber (Equation 1). We report that the former two techniques, referred to as the dry and wet particle classification techniques, yield consistent estimates of the threshold activation size and thus consistent estimates of the effective chamber supersaturation. Furthermore, we show that the experimentally-determined threshold dry sizes are substantially larger than the prediction of Equation 1 and Köhler theory.

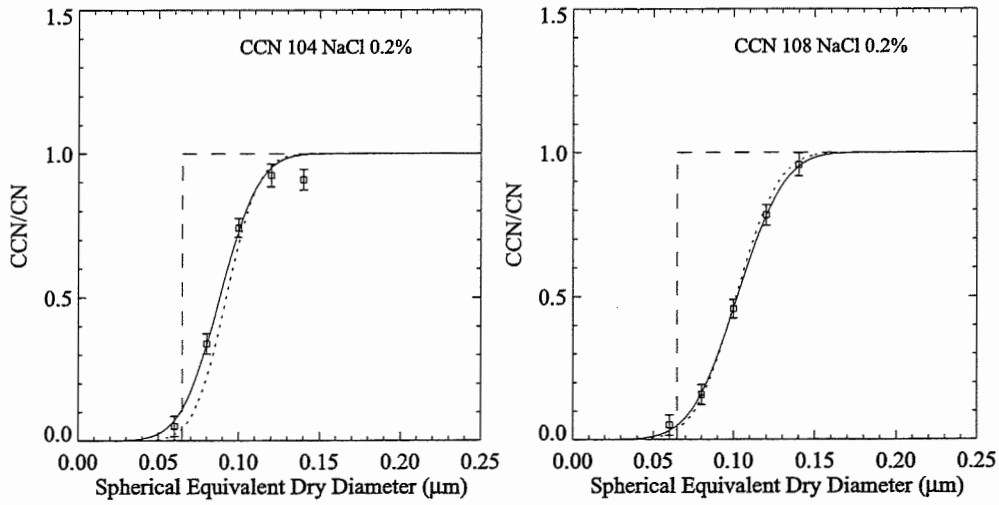

Figure 4 - Measured CCN-to-CN ratios versus spherical equivalent dry diameter corresponding to DMA-classified NaCl aerosols at 0.2% nominal supersaturation. Data points correspond to results of a wet test particle selection experiment (D_{se} inferred from values of RH and D_{wet}) and the corresponding fitting function (normalized Gaussian) are shown as a solid line. The dotted line corresponds to results of a dry test particle selection experiment and are contingent on the assumption that $D_{me} = D_{se}$. The vertical long dashed line corresponds to the critical sphere equivalent dry diameter anticipated by the nominal supersaturation (0.2%) and Köhler theory (Equation 1).

6 - REFERENCES

Fitzgerald, J.W., On the computation of steady-state supersaturation in thermal diffusion chambers, *J. Atmos. Sci.*, 29, 779-781, 1972

Gerber, H.E., W.A.Hoppel and T.A.Wojciechowski, Experimental verification of the theoretical relationship between size and critical supersaturation of salt nuclei, *J. Atmos. Sci.*, 34, 1836-1841, 1977

Hämeri, K., A.Laaksonen, M.Väkavä and T.Suni, Hygroscopic growth of ultrafine sodium chloride particles, *J. Geophys. Res.*, 106, 20749-20757, 2001

Katz, J.L., and P. Mirabel, Calculation of supersaturation profiles in thermal diffusion cloud chambers, *J. Atmos. Sci.*, 32, 646-652, 1975

Kelly, W.P., and P.H.McMurry, Measurement of particle density by inertial classification of differential mobility-generated monodisperse aerosols, *Aerosol Sci. Technol.*, 17, 199-212, 1992

Leaitch, W.R., J.W.Bottenheim, T.A.Biesenthal, S.-M.Li, P.S.K.Liu, K.Asalian, H.Dryfhout-Clark, F.Hopper, and F.Brechtel, A case study of gas-to-particle conversion in an eastern Canadian forest, *J. Geophys. Res.*, 104, 8095-8111, 1999

Petters, M.D., J.R.Snider, C.Twohy, and J.R.Anderson, Prediction of cloud condensation nuclei from physicochemical data, this issue, 2004

Snider, J.R., and, S.Guibert, J.-L. Brenguier, and J.-P.Putaud, Aerosol activation in marine stratocumulus clouds: Part – II Köhler and parcel theory closure studies, *J. Geophy. Res.*, 108, 8629, *doi:*10.1029/2002JD002692, 2003

DEVELOPMENT OF A LOW POWER AND HIGH SENSITIVITY CLOUD PROFILING FM-CW RADAR AT 95 GHz

Toshiaki TAKANO[1,2,3], Hiroshi KUMAGAI[4], Tamio TAKAMURA[3,5], and Teruyuki NAKAJIMA[6]

[1]Graduate School of Science and Technology, Chiba University, Inage, Chiba 263-8522, JAPAN
[2]Department of Electronic and Mechanical Engineering, Faculty of Engineering, Chiba University
[3]Center for Frontier Electronics and Photonics, Chiba University
[4]Communications Research Laboratory, Koganei 184-8795, JAPAN
[5]Center for Environmental Remote Sensing, Chiba University
[6]Center for Climate System Research, The Univ. of Tokyo, Komaba, Meguro 153-8904, JAPAN

1. INTRODUCTION

It is getting more important to know the global environment and the global change of climate for the human beings. It is necessary to know balance of solar energy coming to the Earth and cycle of water for the comprehension. One of the most significant features to know them is cloud. Information on 3-dimensional structures of clouds, sizes and distribution of cloud particles, and so on are desirable to solve role of clouds. Conventional radars operated at 5GHz can detect precipitation particles but are not able to detect particles in clouds because their sizes, less than a few tens microns, are much smaller that the wavelengths and, therefore, their cross sections are quite small. The cross sections of particles increase rapidly with frequency in Rayleigh scattering region. Rader observations of cloud particles at millimeter waves, which have been realized recently, have much more sensitive [1]. Observations of clouds with radars in millimeter waves would be most powerful method to derive the information rather than other wavelengths. Several groups have reported the development and observational results that demonstrate powerful performances to investigate cloud particles [2,3,4]. We, therefore, have designed and developed a cloud profiling radar at 95GHz.

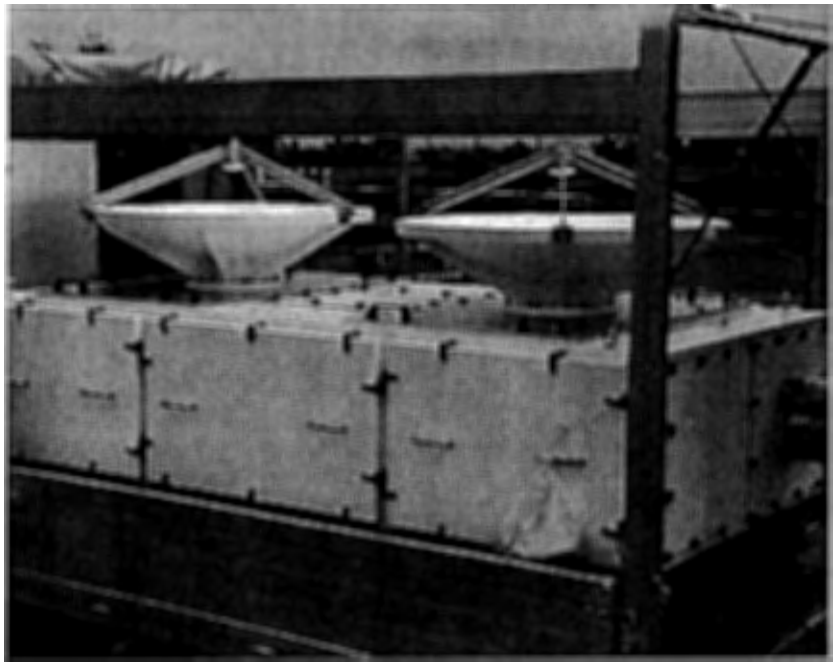

Fig.1. The developed cloud profiling FM-CW radar at 94GHz.

Corresponding author's address: Toshiaki TAKANO, Graduate School of Science and Technology, Chiba University, Inage, Chiba 263-8522, JAPAN; E-Mail: takano@faculty.chiba-u.jp.

2. DESIGN CONCEPTS AND CONSTRUCTION

Fig.1 shows the developed radar [5]. The radar consists of two antennas of 1m diameters.

2.1 FM-CW radar

We adopt a frequency-modulated continuous wave (FM-CW) radar rather than a pulse radar because the former can achieve more sensitive system than the latter if comparing with same instantaneous output power of transmitted millimeter wave. The principle of an FM-CW radar is shown in Fig.2. The signal frequency is modulated in the range of f_0+/-F. Transmitted signal from one of the antennas is reflected by cloud particles, returns, and is received by the other antenna with a delay time of t relative to the original transmitted signal. Mixing the transmitted and received frequencies, beat frequencies f_b are observed in the spectra, which are caused by ensemble of clouds particles:

$$f_b = 4 F r / (c T_m) \qquad (1),$$

where r is the height of the clouds, T_m is the modulation interval, and c is the light velocity. When the objects move in the line of sight, the frequencies of reflected signals change by f_d :

$$f_d = -2 (f_0 / c) (dr / dt) \qquad (2).$$

2.2 Design concept and requirement

Because one of the purposes of the facility is evaluation and verification of an FM-CW radar at 94 GHz, we design it to be a simple system so as to develop with commercially available components and to make maintenance and upgrade by ourselves.
We designed the facility to observe clouds between 0.3 and 15 km in height with a resolution of 15 m. The velocities measured as Doppler shift should be less than 1 m/sec. The facility should be mobile for measurement at variety of places.

2.3 Radar Hardware

According with the requirements described above, we decided parameters of antenna listed in Table 1 [6]. The block diagram of the transmitter and receiver section is shown in Fig.3 and parameters are summarized in Fig. 2. All signals including the transmitted FM-CW signal at 95GHz and local frequencies are generated from and referred to two signal generators in 140 MHz range, which are synchronized each other.

Table 1. Designed parameters of antennas.

Antenna Diameter	1 m
f/D ration of Antenna	0.35
Antenna Optics	Cassegrain
Gain of Antennas	57 dBi
Beam Width	0.18 degree
Antenna Separation	1.4 m
Direction of Antennas	Zenith
Polarization	1 Linear

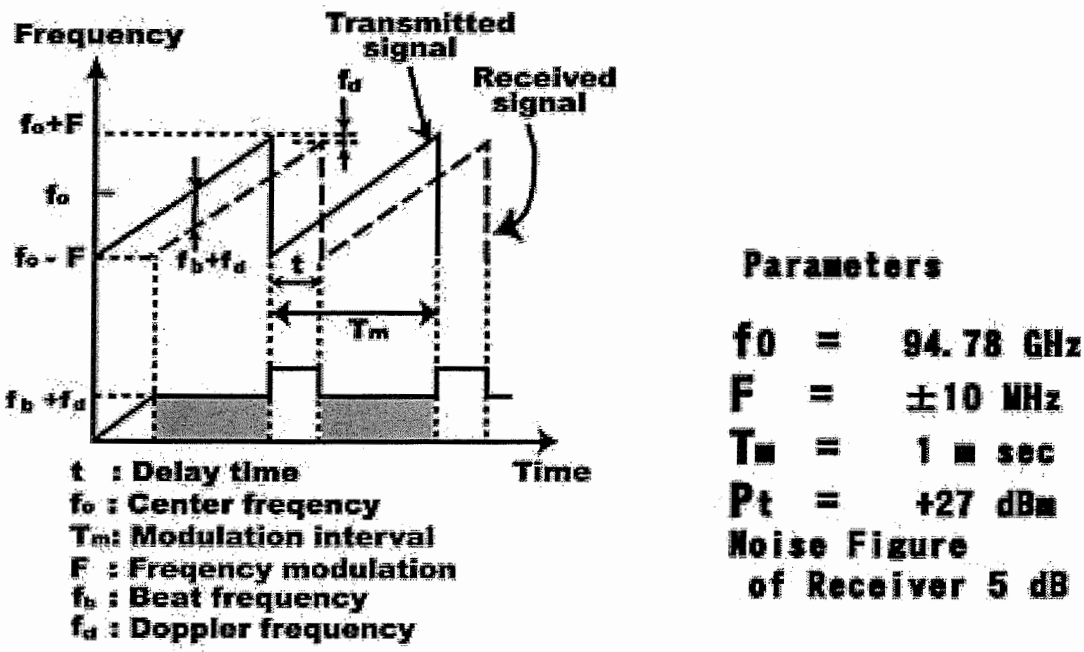

Fig.2. Principle of an FM-CW radar.

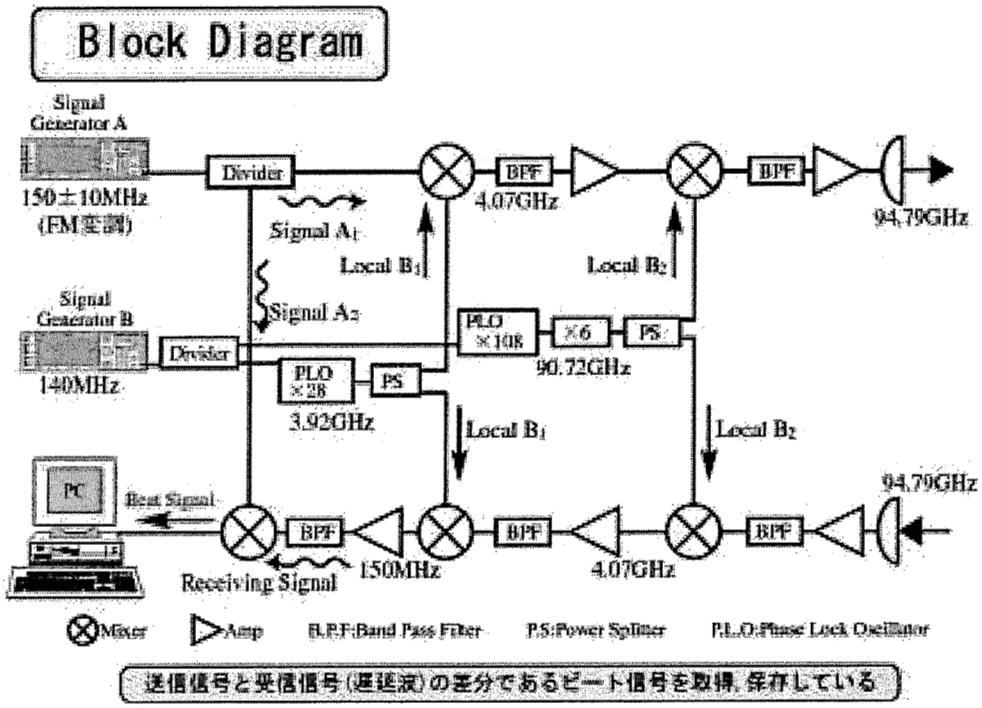

Fig.3. Block diagram of the transmitter and receiver section.

3. OBSERVATIONAL RESULTS

3.1 Simultaneous Observations with SPIDER

After measurements of long-term stabilities, we made simultaneous observations with a pulse radar named SPIDER [2] shown in Fig.4 of Communications Research Laboratory, Japan. Comparison between the developed FM-CW radar and SPIDER is summarized in Table 2. We have to stress that the output power at 95 GHz of SPIDER is 3000 times higher than that of our FM-CW radar. An example of results is shown in Fig.5.

Table 2. Comparison between the developed FM-CW radar and SPIDER.

FM-CW Radar and SPIDER

	FM-CW Radar	SPIDER (CRL)
Purpose	Ground based obs.	Airborn obs.
Obs direction	at Zenith	Downward to horizon
Type of radar	FM-CW	Pulse
Antenna	[illegible]	[illegible]
Frequency	94.79 GHz	95.04 GHz
Output Power	0.5 W	1600 W
Duty Rate	Continuous	100-1000
Sensitivity (at 5km)	-32 dBZ	-35 dBZ

We can recognize that same clouds were detected in both data. There results show that the radar has good performance to detect thin clouds. We estimate the sensitivity of the developed FM-CW radar is about -32 dBZ for clouds at 5 km range [7,8].

Fig.4. SPIDER: a pulse radar of the Communications Research Laboratory, Japan.

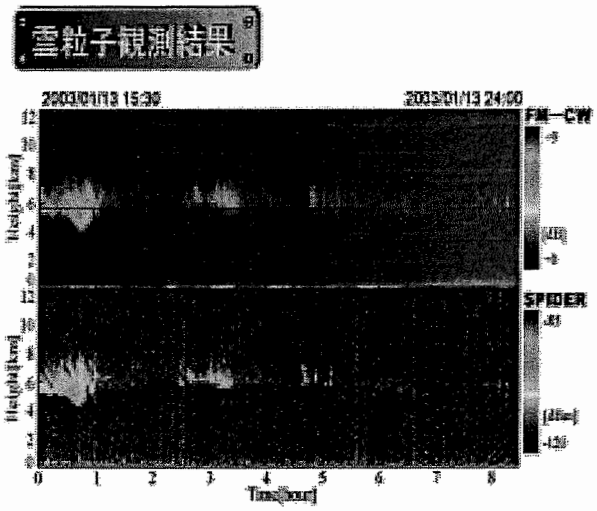

Fig.5 First results of test measurements of clouds. Measurement started 11:30 JST on 2002 June 26th and continued for 7 hours. The gap between 5 and 6 hours is caused by putting an absorber of millimeter wave in front of the feed horn of the transmitting antenna. We can recognize the bottom of the clouds in several hundred meters high and clouds spread up to around 3 km high.

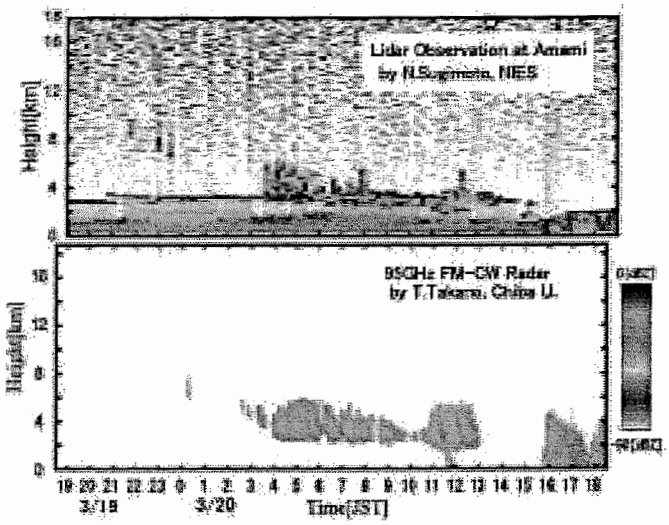

Fig.6 Example of simultaneous observations of clouds with developed FM-CW radar and lider obtained by Dr. Nobuo SUGIMOTO, NIES at March 19-20th 2003 during the APEX-E3 campaign at Amami Island. Similar structures of clouds are seen around 4 km high.

3.2 Long-term Observations

We made observations with the developed FM-CW cloud profiling radar during the APEX-E3 campaign at Amami Island in March to April 2003. The facility ran well and we obtained cloud profiles in almost whole period of the month [9]. Comparison of the data to lidar observations of NIES (National Institute for Environmental Studies, obtained by Dr. Nobuo SUGIMOTO) shows that the FM-CW radar is useful to observe inner structure of clouds as shown in Fig.6.

Acknowledgements

This work is supported with the project APEX (Asian Atmospheric Particle Environment Change Studies) in CREST (Core Research for Evolutional Science and Technology) of Japan Science and Technology Corporation and is in part supported with the Grant-in-Aid for Scientific Research by the Japanese Ministry of Education, Culture, Sports Science and Technology (14380241) and with an open use program in the Center for Environmental Remote Sensing, Chiba University (#14-12, #15-12). Dr. Nobuo SUGIMOTO, National Institute for Environmental Studies, Japan kindly provided their data of lider observations at Amami Island.

References

[1] Clothiaux, E.E., M.A.Miller, B.A.Albrecht, T.P. Ackerman, J.Verlinde, D.M.Babb, R.M.Peters, and W.J.Syrett, "An evaluation of a 94-GHz radar for remote sensing of cloud properties", Journal of Atmospheric and Oceanic Technology, Vol.12, No.2, p.201, 1995.

[2] Horie, H., T.Iguchi, H.Hanado, H.Kuroiwa, H.Okamoto, and H.Kumagai, "Development of a 95-GHz cloud profiling radar (SPIDER) – Technical aspects", The Transactions of the Institute of Electronics, Information and Communication Engineers, Vol.E83-B, No.9, p.2010, 2000.

[3] Kumagai, H., H.Okamoto, H.Horie, H.Kuroiwa, and S.Iwasaki, "Vertical profiling of liquid cloud properties retrieved from 95-GHz cloud radar and microwave radiometer", Asia-Pacific Radio Science Conference (Tokyo), PF-27 (p.333), 2001.

[4] Matkin, N., J.Nash, T.Oakley, B.Ellison, M.Oldfield, and J.Bradford, "A trial of the Rutherford Appleton Laboratory 78.2GHz cloud radar", Fifth International Symposium on Troposphere Profiling, Adelaide, Australia, p.113, 2000.

[5] Suga, Y., S.Hoshi T.Takano, S.Shimakura, H.Kumagai, T.Takamura, and T.Nakajima, "Design and development of an FM-CW radar at 94GHz for observations of cloud particles", 2001 Asia-Pacific Radio Science Conference (Tokyo), PF-28 (p.333), 2001.

[6] Hoshi, S., Y.Suga, Y.Kawamura, T.Takano, and S.Shimakura, "Development of an FM-CW radar at 94GHz for observations of cloud particles – Antenna section", Proceedings of the Society of Atmospheric Electricity of Japan, No.58, p.116, 2001 (in japanese).

[7] Takano, T., Y.Suga, K.Takei, Y.Kawamura, T.Takamura, H.Kumagai, and T.Nakajima, "Development of a Cloud Profiling FM-CW Radar at 94GHz", Proceedings of the 27th General Assembly of the International Union of Radio Science (URSI) (Maastricht, The Netherlands), FP-11, p1789, 2002.

[8] Takano, T., Y.Suga, K.Akita, Y.Kawamura, K.Sakai, H.Kumagai, T.Takamura, Y.Nakanishi, and T.Nakajima, "Development of a Cloud Profiling FM-CW Radar at 94GHz and Its Observation Results", Proceedings of IUGG2003 General Assembly (Sapporo, Japan), MI02, July 2003.

[9] Takano, T., Y.Suga, K.Akita, Y.Kawamura, H.Kumagai, T.Takamura, Y.Nakanishi, and T.Nakajima, "First Observational Results with the Newly Developed Cloud Profiling FM-CW Radar at 95GHz", Proceedings of SPIE Symposium on Remote Sensing (Barcelona, Spain), 5235-67, Sept. 2003.

APPLICATIONS OF PMW RAINFALL ALGORITHMS TO MEDITERRANEAN AREA EVENTS

F. Torricella[1], V.Levizzani[1], and V. Poli[1]

[1]Institute of Atmospheric Sciences and Climate, ISAC-CNR, Bologna, I-40121, Italy

1. INTRODUCTION

The application of passive microwave (PMW) and blended PMW-IR algorithms for satellite rainfall measurement is well established, especially if averaged or cumulated precipitation intensities are at stake. The application of operational global algorithms (GPROF, NESDIS, NRL) to specific case studies in complex orography regions as the Mediterranean demonstrates that regional applications are not viable without adapting the algorithms to the specific geographical area and season of the year. Often, in the *land* part of the algorithms, the initial screening that is supposed to discriminate the various surface types (ice, snow, desert, arid land) and precipitation seems to work only to a certain extent, being based on empirical global thresholds that hardly fit all specific local conditions. Cloudy and precipitating pixels can be erroneously classified as snow or ice contaminated and thereby discarded from the rain retrieval procedure altogether. Hereafter the analysis of two precipitation events occurred in the Mediterranean basin is presented, namely the storm on 4-5 December 2002 in the Antalya region (Turkey), and the November 2001 Algeria flood. Heavy rainfall events often occur during autumn and winter over the Central and Eastern Mediterranean, producing significant rain amounts and eventually leading to floods.

The present analysis demonstrates that in certain cases paying attention to the coastal environment and to pixel classification the overall performance of the methods can significantly improve. The rain maps are compared to nearly coincident time-space measurements taken from the precipitation radar (PR) onboard the Tropical Rainfall Measurement Mission (TRMM).

2. DATA AND ALGORITHMS

SSM/I measurements (brightness temperatures in 7 polarized channels from 19.2 to 85.5 GHz) available from the operational platforms F13, F14, and F15 were collected over the area. Data from the 1B11 operational algorithm of the TRMM Microwave Imager (TMI) were used. From these data, rain rates were derived by means of the NOAA-NESDIS operational algorithm (Ferraro and Marks 1995; Ferraro 1997) and the Goddard Profiling Algorithm (GPROF) (Kummerow et al. 2001; McCollum and Ferraro 2003, and references therein). The NESDIS algorithm derives rainrates at the A-scan resolution of the SSM/I (~25 km) by means of non-linear relationships among the instrument channels (vertical and horizontal polarization) that have been calibrated using large sets of ground reference data collected by radar networks in different countries.

The latest GPROF algorithm (version 6) calculates instantaneous rainfall rate estimates from the weighted average of rainfall rates from different vertical hydrometeor profiles created from numerical cloud models, primarily the Goddard Cumulus Ensemble (GCE) model. Radiative transfer calculations using the frequencies and resolutions of a particular satellite are carried out to produce a library of vertical profiles with the associated brightness temperatures. The profiles used for estimation are chosen and given weights based on the proximity of the observed MW radiances to those of the library of profiles. An additional application of the profiles is in estimating latent heating profiles for model assimilation. The physical basis of the GPROF algorithm is most useful over oceans, where the low and predictable oceanic emissivity results in information about ice and liquid hydrometeors over the range of MW frequencies. The high and variable emissivity of the land surface makes the information from lower frequency channels more ambiguous, so that the ice scattering at higher frequencies is currently the most useful way to estimate rainfall over land.

The PR reference data were taken from the 2A25 official rain product (near surface rain variable).

3. CASE STUDIES

3.1 The 2001 Algeria Flood

In early November 2001 a widespread frontal system and upper air trough from northeast Scandinavia to southwest Spain led to an extreme precipitation event in Algiers, causing severe flooding and huge mudslides. More than 120 mm of rain fell in 12 h during the night between 9 and 10 November and more than 130 mm during the next 6 hours on the mountains behind Algiers. The unusually high rain rates were fed by the cold maritime arctic air that picked up moisture crossing the warm Mediterranean waters and met maritime subtropical air. An intense orographic enhancement was caused by strong surface winds oriented towards the high mountains of the African coast (> 2300 m a.s.l.).

Corresponding author's address: Francesca Torricella, Institute of Atmospheric Sciences and Climate ISAC-CNR, Bologna, I-40129, Italy; E-Mail: f.torricella@isac.cnr.it.

Due to the short duration of the event (about 20 h), the area was imaged only a few times by PMW instruments. The event was extensively studied in the past, with the disappointing result that, due to the particular combination of unfavorable conditions (precipitation in coastal environment, rapid onset of the event, no availability of ground reference data), no rain retrieval method based on satellite-based passive observations was able to detect rain over Algiers and its surroundings. The characteristics of the clouds and precipitation fields were definitely different over land (warm rain) with respect to the convective cells embedded in the storm system, which developed over the sea very immediately offshore. Very likely the orography played a major role, especially the relief south of Algiers, shaping a precipitating system that, although embedded in a larger field, was neither detected by PMW algorithms nor by blended PMW-IR techniques.

3.2 The 2002 Antalya Flood

On 4 and 5 December 2002 an intense storm swept the Antalya coastal region in Turkey leading to floods in the area. The 24-h accumulated rainfall ending at 1800 UTC on 5 December exceeded 72 mm and reached 153 mm at two stations in the area around the city of Antalya. The electric activity during this event was quite important.

On 0000 UTC, 4 December 2002, a surface low of 998 hPa was centered over southern Italy with a cold front spanning north to south over the Adriatic Sea. At 500 hPa a cut-off low of 5400 m was located slightly to the west of the surface low with the axis of the trough being oriented northwest-southeast. The Aegean Sea and the eastern – southeastern part of Turkey were under the influence of the diffluent trough. During the following 48 h the cut-off low stayed almost stationary without any deepening while only the axis of the trough slowly turned cyclonically dislocating the area of maximum diffluence over the southwestern part of Turkey. At the same time at surface levels the low pressure center was also stationary with a central pressure of 1000 hPa over southern Italy, while the associated cold front had progressed northeastwards also turning cyclonically and turned to an occluded front at 0000 UTC on 6 December.

4. RESULTS

In Fig. 1 the pixel-by-pixel classification for the Algeria case is presented for the TRMM orbit imaging the area around 0209 UTC on day 10, i.e. during the peak of the event. These results are taken from the GPROF classification, largely based on the work of Groody (1991) and Adler et al. (1994). It is apparent that in this case, the majority of land and coastal pixels is discarded prior the rain retrieval procedure, being classified as contaminated by the presence at the surface of ice or desert, or flagged as certainly non-raining. The comparison with the coincident IR image

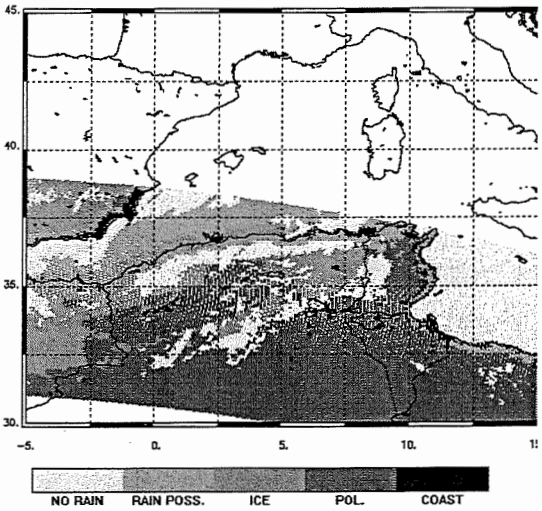

Figure 1. Pixel classification for the TRMM orbit #22742 (overpass time 0209 UTC, November 10) from GPROF6 applied to TMI brightness temperatures.

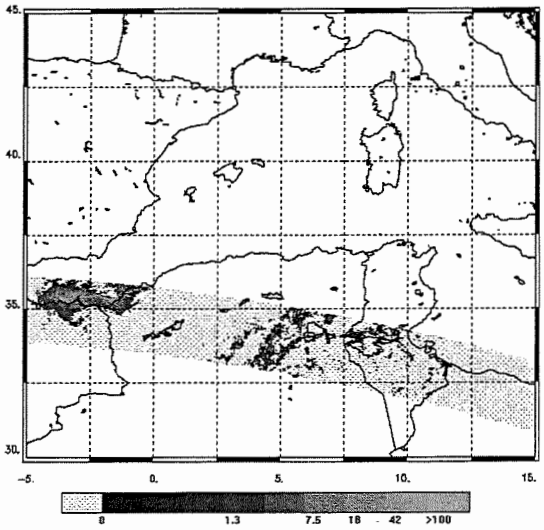

Figure 2. Rain map (in mm h^{-1}) for the same orbit of Fig. 1 derived from the 2A25 PR operational product.

of the VIRS spectrometer (not show) reveals that the non-realistic ice detection is in reality connected with precipitating clouds, as confirmed by the PR (Fig. 2).

In Fig. 3 the results of GPROF upon application of the pixel analysis in Fig. 1 are shown, revealing that precipitation over land and the coastal area detected by the PR is missed altogether by the algorithm, as well as the very intense precipitation cells off the Morocco-Algeria coast. In Fig. 4 the TMI measurements are re-processed with GPROF after a correction of the screening procedure aimed at eliminating the ice flagging. It is evident that the new screening corrects the wrong attitude of the retrieval,

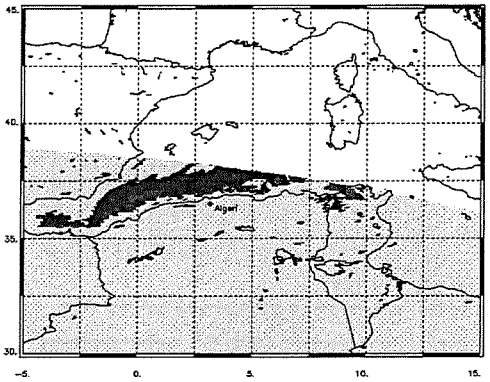

Figure 3. Rain map (in mm h^{-1}) for the same orbit of Fig. 1 derived from the from GPROF6 applied to TMI brightness temperature. Color palette as in Fig. 2.

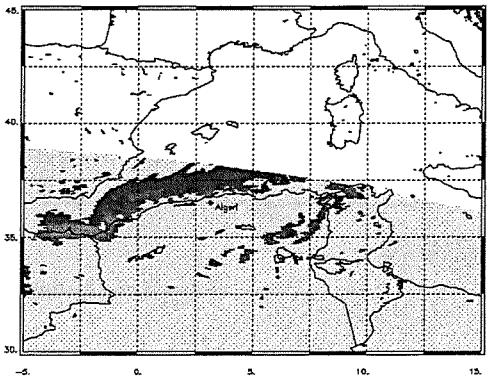

Figure 4. Same as in Fig. 3 but after correcting the pixel classification.

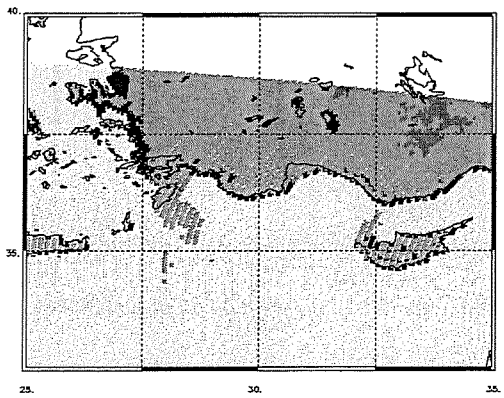

Fig. 5 Pixel classification for the TRMM orbit #28831 (overpass time 1808 UTC, December 5) from GPROF6 applied to TMI brightness temperatures.

and the convective precipitation off coast is detected. SSM/I overpasses (1919 and 1958 on day 9) processed by means of NESDIS algorithm (not shown) reveal very similar features in the precipitation field and do not add relevant information for the analysis of the event.

The effect of the screening procedure for the Antalya case is shown in Fig. 5. Non-realistic features did not arise over this area, and the pixels classified as "rain-possible" fairly correlate with cloud features in the VIRS IR pictures (not shown). Nevertheless, the intrinsic weakness of PMW rain algorithms in locating and gauging rain in coastal zones shows up in comparing results with the PR data (see Fig. 6, unfortunately only marginal overpasses are available, due to the small PR swath). In PMW rain maps (Fig 6, left: TMI; Fig. 7 and 8: from SSM/I) the rain field shows unphysical discontinuities across the coastline, perhaps more evident in TMI data with respect to SSM/I's.

5. REFERENCES

Adler, R. F., G. J. Huffman, and P. R. Keehn, 1994: Global tropical rain estimate from microwave adjusted geosynchronous IR data. *Remote Sens. Rev.*, **11**, 125-152.

Ferraro, R. R., 1997: Special sensor microwave imager derived global rainfall estimates for climatological applications. *J. Geophys. Res.*, **102** (D14), 16715-16735.

Ferraro, R. R., and G. F. Marks, 1995: The development of SSM/I rain-rate retrieval algorithms using ground-based radar measurements. *J. Atmos. Oceanic Technol.*, **12**, 755–770.

Grody, N. C., 1991: Classification of snow cover and precipitation using the Special Sensor Microwave Imager. *J. Geophys. Res.*, **96**, 7423-7435.

McCollum, J. R., and R. Ferraro, 2003: Next generation of NOAA/NESDIS TMI, SSM/I, and AMSR-E microwave land rainfall algorithms. *J. Geophys. Res.*, **108** (D8), 8382, doi:10.1029/2001JD001512.

Kummerow, C., Y. Hong, W. S. Olson, S. Yang, R. F. Adler, J. McCollum, R. Ferraro, G. Petty, and T. T. Wilheit, 2001: The evolution of the Goddard Profiling Algorithm (GPROF) for rainfall estimation from passive microwave sensors. *J. Appl. Meteor.*, **40**, 1801-1820.

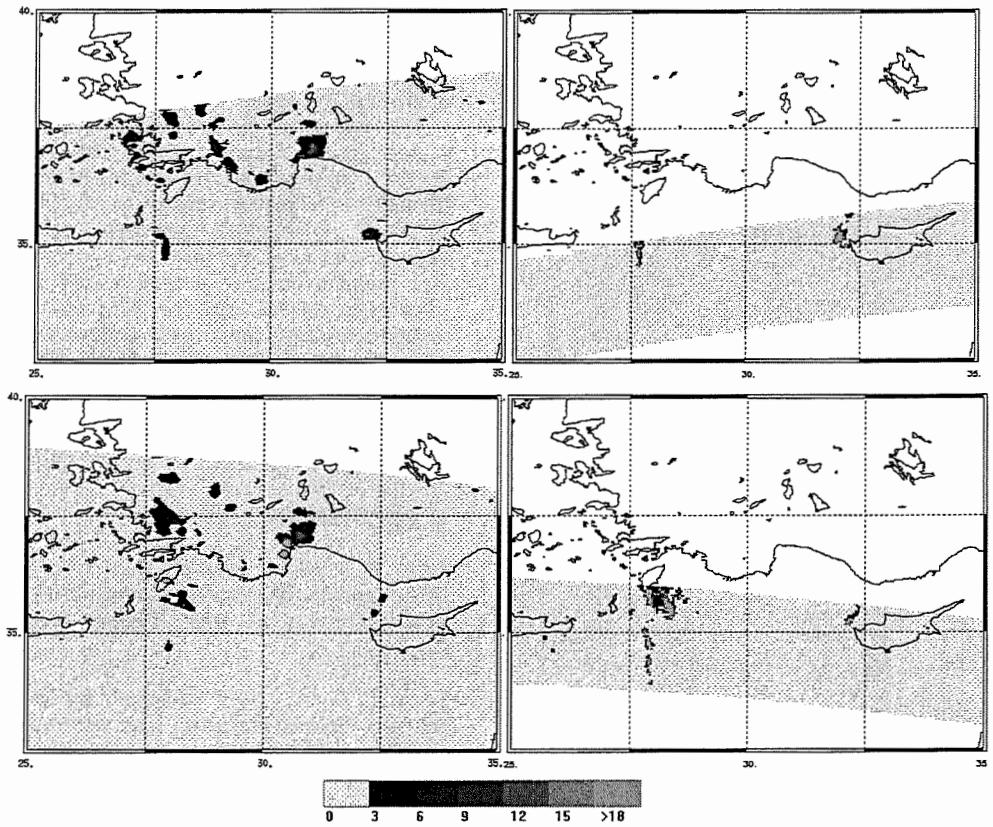

Fig. 6 Rain maps (in mm h^{-1}) derived by means of GPROF from TMI data (left), and from PR operational product 2A25 (right) for the TRMM orbit #28830 (top) and #28831 (bottom), on December 5.

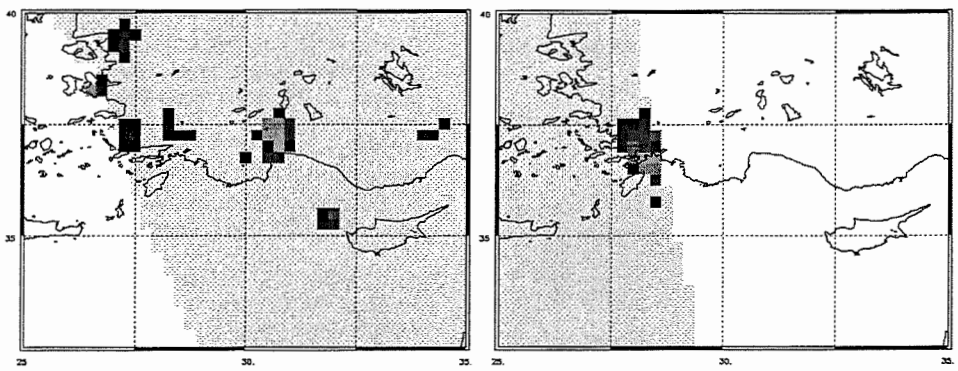

Fig. 7 Rain maps (in mm h^{-1}) derived by means of GPROF from SSM/I data. Left: orbit 1452-1538. Right: orbit 1858-1947. Color palette as in Fig. 6.

USING ICE CRYSTAL ANALOGUES TO VALIDATE CLOUD ICE PARAMETER RETRIEVALS FROM THE CPI ICE SPECTROMETER DATA

Z. Ulanowski[1], P. Connolly[2], M. Flynn[2], M. Gallagher[2], A.J.M. Clarke[1] and E. Hesse[1]

[1]Science & Technology Research Centre, University of Hertfordshire, Hatfield, Herts AL10 9AB, United Kingdom
[2]Physics Department, UMIST, Manchester M60 1QD, United Kingdom

1. INTRODUCTION

The most important microphysical quantities that must be accurately predicted from environmental variables to determine ice and mixed-phase cloud radiative forcing are the equivalent ice particle radius (r_{equ}), ice particle number density (N_i), ice water content (IWC) and ice water path (IWP). For example, a 50% uncertainty in r_{equ} can cause a change in the net cloud radiative forcing by up to 10 Wm^{-2} (Gultepe *et al.* 1998), and smaller crystals have been shown to lead to net cooling whilst larger ones to net warming (Zhang *et al.* 1999). Many studies using global and regional models have also highlighted the importance of N_i. Quoted uncertainties in N_i measured in clouds by aircraft instruments are often of the order of a magnitude or more and this can lead to changes of up to 70% in net regional cloud forcing (Ghan *et al.* 1997). Most GCMs and mesoscale regional climate models use prognostic equations for N_i and assume it to be a simple function of temperature (T) or supersaturation ratio with respect to ice (Meyers *et al.* 1992). This predicts an exponential increase in N_i for decreasing T. This sensitivity and consequences for the associated ice water path together with other uncertainties can lead to significant changes in cloud forcing results.

One likely but little studied source of errors associated with measurements using airborne ice spectrometers is the application of spherical particles for calibration purposes. Lack of more suitable test materials forces the use of such particles, but they are a poor representation of highly nonspherical, faceted ice crystals. One way to improve the accuracy of observations of r_{equ}, N_i, IWC and IWP obtained from ice spectrometers is to use precisely dimensioned ice crystal analogues for laboratory calibrations. Such analogues should cover the most important ice crystal habits observed in clouds, have correct refractive index and be stable enough so that their dimensions can be accurately characterised. Here we report on such analogues and show preliminary findings from experiments to calibrate common ice spectrometers. The objective is to test the accuracy of particle size, IWC and surface area retrieval algorithms that are commonly used with such instruments. The first spectrometer tested is the SPEC Cloud Particle Imager (CPI). Accuracies of retrieval algorithms for representative crystal habit types are presented.

Corresponding author: Z. Ulanowski, STRC, University of Hertfordshire, College Lane, Hatfield, Herts AL10 9AB, United Kingdom; e-mail: Z.ulanowski@herts.ac.uk

2. METHODS AND MATERIALS

The ice analogues were crystalline particles of sodium fluorosilicate Na_2SiF_6 grown from solution on glass substrates. The crystals can be produced in a variety of habits characteristic of atmospheric ice and have a refractive index very close to that of ice (Ulanowski *et al.* 2003). Single crystals were selected using a micromanipulator and transferred onto microscope coverslips. The shape and dimensions of the crystals were then determined using low-vacuum scanning electron microscopy (without coating with a conducting layer, Fig. 1) and optical microscopy (Fig. 2). Further examples can be found at http://strc.herts.ac.uk/ls/ise.html. In the case of complex crystals, the shape was determined by constructing a 3-dimensional geometric model on the basis of images taken at different crystal orientations.

The crystal-containing coverslips were attached to a 3-axis translation stage and inserted into the imaging path of the CPI, with their surface perpendicular to the optical axis. The stage permitted varying the distance of the coverslips from the object plane of the imaging system. The CPI was triggered continuously to allow measurements on stationary samples. Since position-sensitive triggering was not used, image acceptance for further analysis was based on the sharpness of the crystal image – the "*focus*" measure given by the CPI.

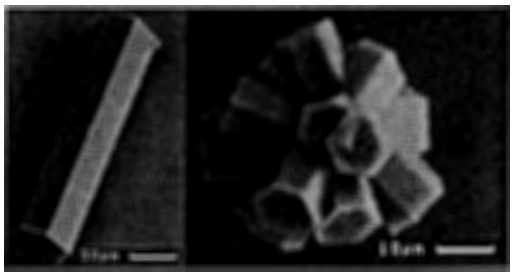

Fig. 1. Electron microscopy image of the ice-analogue column *col166* (left) and "germ rosette" *gros48* (right).

The single scattering properties of ice crystals were calculated using geometric optics enhanced by the inclusion of diffraction on facets. The model is a 3-dimensional extension of a method previously applied to long hexagonal columns (Hesse *et al.* 2003).

3. RESULTS

Fig. 3 shows typical images obtained by the CPI

spectrometer. Table 1 gives a summary of results from size measurements based on microscopy, compared to results obtained from the CPI. CPI-derived values were selected for two different image sharpness conditions: good focus (*focus*>50) and medium to good focus (*focus*>20). To ensure uniform weighting against the object plane distance, mean and standard deviation values were obtained from medians calculated with respect to the distance. Figs. 4 to 8 display example measurement results as a function of distance from the object (optimum imaging) plane.

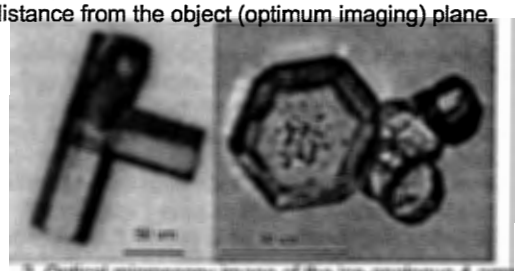

Fig 2. Optical microscopy image of the ice-analogue 4-arm rosette *ros172* and plate aggregate *plag102*.

Fig. 3. CPI images of the ice-analogue rosettes *gros48* (left) and *ros172* (right).

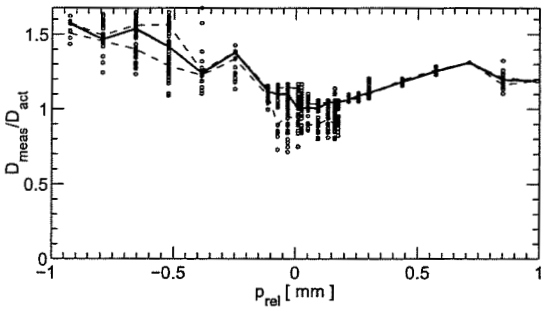

Fig. 4. Ratio of measured to actual (determined from microscopy) maximum dimension *D* for the rosette *gros48* as a function of the distance from the CPI object plane. In Figs. 4 to 8 quartiles (broken line) and medians (solid line) are shown for *D* and *A*, and medians for *V*. Volume relations in Figs. 6 to 8 are as in Table 1: BF95 (Δ, dot-dash), H04 (+, broken line), M95 or CYL (o, cont. line).

4. DISCUSSION AND CONCLUSIONS

Ice-crystal analogues, previously developed for light scattering experiments have been used for the first time for the calibration of an imaging cloud probe.

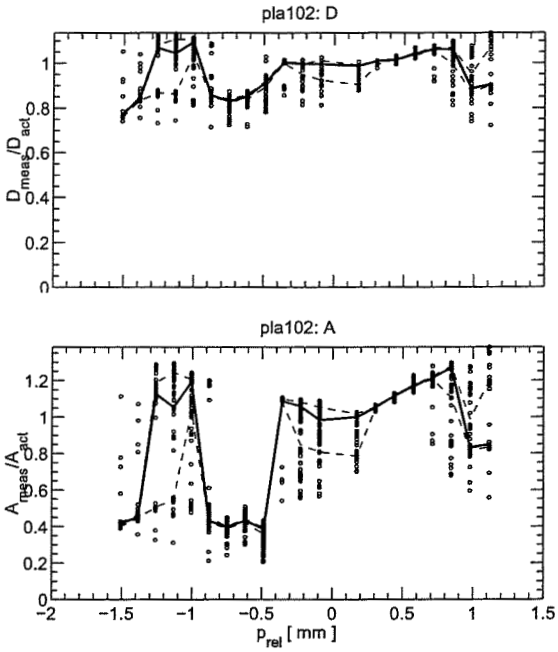

Fig. 5. As Fig. 4, but *D*, *A* and *V* for plate *pla102*.

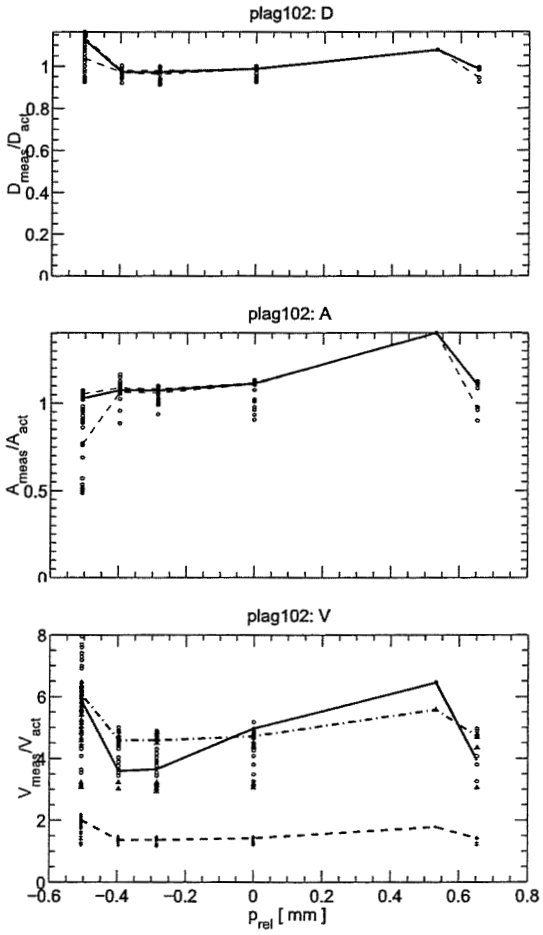

Fig. 6. As Fig. 4, but *D*, *A* and *V* for aggregate *plag102*.

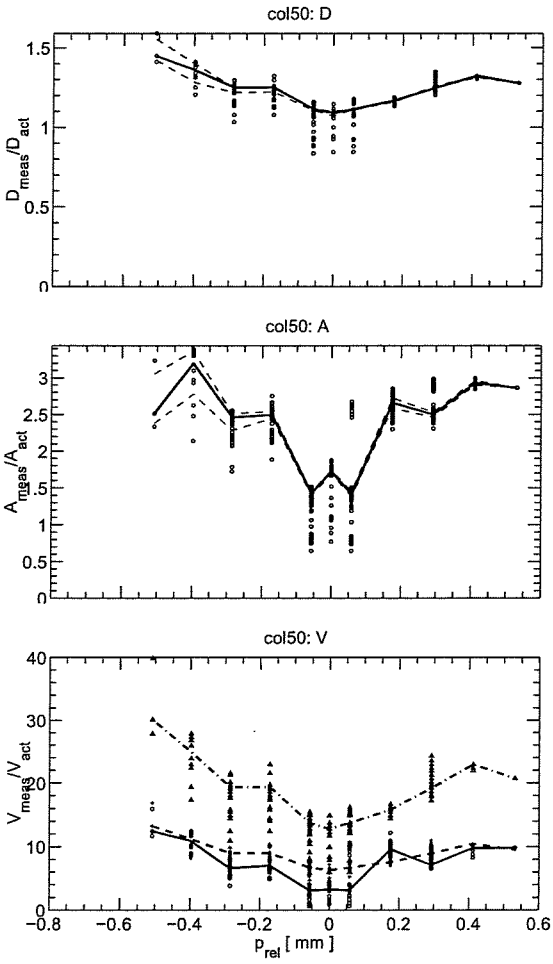

Fig. 7. As Fig. 4, but *D*, *A* and *V* for column *col50*.

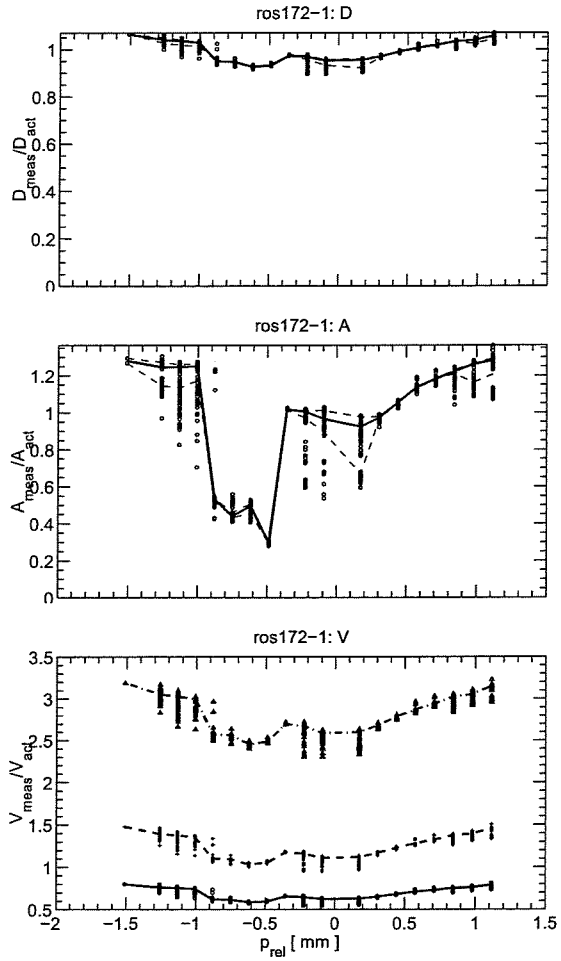

Fig. 8. As Fig. 4, but *D*, *A* and *V* for rosette *ros172*

The analogues are stable at room temperature, so their shape and size can be determined with high precision using optical and/or electron microscopy. They can be transported between laboratories and stored for long periods, permitting additional measurements or re-analysis.

Precisely known dimensions of the analogues allow accurate calibration of ice spectrometers. Our results show that the particle size inferred from CPI probe images depends on the position of the particle with respect to the object plane of the imaging system. The size in general increased with distance from the

Table 1. Ice crystal analogues used in this work. Shown are the actual (determined from microscopy) maximum dimension *D*, width *W* (normal to *D*), projected area *A* and volume *V*, and ratios of measured to actual parameters for two focus conditions: good focus (upper value) and medium to good focus (lower value). Mean ± standard deviation is given; ND = not determined. For the columns the actual length and diameter are given in brackets. The relations for obtaining V_{meas} were from: H04 - Heymsfield *et al.* (2004), M96 - Mitchell (1996), BF95 - Brown and Francis (1995), CYL – solid circular cylinder (see text).

shape	name	D_{act} (μm)	W (μm)	A_{act} (μm^2)	V_{act} (μm^3)	D_{meas}/D_{act}	A_{meas}/A_{act}	V_{meas}/V_{act} BF95	H04	M95	CYL
column	*col50*	51.7	24.1	623	5000	1.15 ±0.09	1.98 ±0.62	15 ±3.8	7.7 ±1.6	ND	5.4 ±3.0
		(50.2)	(12.4)			1.24 ±0.11	2.38±0.60	19 ±5.3	9.0 ±2.1	ND	7.5 ±3.3
column	*col166*	173	83	7210	201000	1.02 ±0.04	0.92 ±0.31	7.2 ±0.5	3.1 ±0.3	ND	1.9 ±0.5
		(168)	(42.9)			1.02 ±0.04	0.92 ±0.31	7.2 ±0.5	3.1 ±0.3	ND	1.9 ±0.5
plate	*pla102*	108	89	7240	200000	0.95 ±0.08	0.88 ±0.28	ND	ND	ND	ND
						0.96 ±0.10	0.88 ±0.32	ND	ND	ND	ND
compact rosette	*gros48*	46.8	41.7	ND	ND	1.06 ±0.10	ND	ND	ND	ND	ND
						1.19 ±0.17	ND	ND	ND	ND	ND
4-arm rosette	*ros172*	178	135	12700	540000	0.98 ±0.17	0.94 ±0.29	2.7 ±0.20	1.19 ±0.12	0.66 ±0.06	ND
						0.99 ±0.04	0.99 ±0.31	2.8 ±0.23	1.25 ±0.14	0.69 ±0.07	ND
plate aggr.	*plag102*	104	75.2	4650	114000	0.98 ±0.05	1.02 ±0.29	4.3 ±1.0	1.4 ±0.21	ND	ND
						1.01 ±0.07	1.13 ±0.14	5.0 ±0.6	1.6 ±0.27	ND	ND

object plane, leading to maximum overestimates for smaller crystals of up to 40%, and for crystals >100 μm of up to ≈10%. Typical mean overestimates were near 20% for the smaller crystals but became much lower for the larger ones. Particles "in focus" were typically sized within a few percent of the actual value and were often slightly undersized (see Table 1).

While the accuracy of volume retrievals followed a general trend similar to that of D, it was very strongly affected by the choice of the size to volume relationship, as Table 1 and Figs. 6 to 8 demonstrate. Particularly large overestimates were present for the columns. For this reason we included a simple approximation for column volume, assuming the column to be a solid circular cylinder: $V=\pi D(W/2)^2$. It can be expected to overestimate the volume, especially for small aspect ratio columns, as both D and W are larger then true column length and diameter, respectively. However, it gives better results than the other two relations.

Furthermore, we found that when image acceptance was based on image quality (sharpness), as was the case for the test results presented here, the sampling volume within which crystals were counted increased with crystal size. This situation is relevant to *in situ* cloud observations where crystal number density is so high that more than one crystal is, on average, present in the CPI sampling volume. Such conditions render ineffective the discrimination on the basis of crystal position (i.e. proximity to the object plane of the imaging system, where focusing is good). Preliminary estimates indicated that the sampling volume varied approximately as D^3 for crystals up to about 100 μm in size, and became nearly size-independent above that value. This relationship was different for spheres.

Of special importance is the case of small, compact crystals, represented here by the "germ rosette" *gros48* (Fig. 1 and 3). These particles may be very abundant under some conditions, especially in upper portions of cirrus (Yang *et al.* 2003, Gayet *et al.* 2002, Hirst *et al.* 2001). Such crystals are normally classified as spheres or spheroids on the basis of CPI (or other probe) images, even if they are strongly non-spherical, as a comparison of Figs. 1 and 3 reveals. The precise identity of these objects will remain unclear until better cloud probes are deployed, and we must meanwhile allow the possibility that they may be faceted, as demonstrated here. One consequence of assuming spherical shape is overestimating crystal mass even at good focus, as the true effective density will be lower than for a sphere (which has effective density of bulk ice). At poor focus, the mass ($\sim D^3$) was in our tests overestimated by an additional factor of up to about three – see Fig.4.

However, lack of discrimination between spherical particles and faceted crystals influences not only crystal mass retrievals but leads also to incorrect inferences concerning single scattering properties. For example, an ice sphere equal in size to the compact rosette shown in Fig. 1 and 3, has the asymmetry parameter g=0.881 at visible wavelengths. In contrast, calculations using the diffraction on facets model show that a 20-facet droxtal (Yang *et al.* 2003) of the same size has g=0.805 and a compact 8-arm rosette g=0.776 – Fig. 9. Such reduction in g can significantly lower the value of shortwave cloud forcing. For illustration purposes, geometric optics calculations predict that replacing spheres of similar size with polycrystals can reduce net (shortwave and longwave) cloud forcing by nearly 30 W/m^2 (Zhang *et al.* 1999).

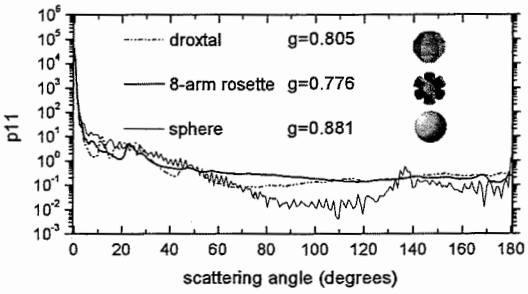

Fig. 9. Phase functions for a sphere, droxtal and 8-arm compact rosette, representing the crystal *gros48*.

Acknowledgements

This research was supported by a NERC grant NER/T/S/2001/00203. We are indebted to Bill Liley for the electron microscopy images.

References

Brown, P.R.A., and P.N. Francis, 1995: Improved measurements of the ice water content in cirrus using a total-water probe. J. Atm. Sci., 12, 410-414.

Gayet, J-F. *et al.*, 2002: Quantitative measurement of microphysical and optical properties of cirrus clouds. Geophys. Res. Lett. 29, 2230.

Ghan, S.J., L.R. Leung, and Q. Hu, 1997: Application of cloud microphysics to NCAR community climate model. J. Geophys. Res. - Atm. 102, 16507-16527.

Gultepe I, *et al.*, 1998: Effects of ice crystal shape on the radiative characteristics of low level ice clouds. *Conf. on Cloud Physics*, AMS, Everett; 372–375.

Hesse, E., and Z. Ulanowski, 2003: Scattering from long prisms using ray tracing combined with diffraction on facets. J. Quantit. Spectr. Rad. Transf. 79-80, 721-732.

Heymsfield, A.J. *et al.*, 2004: Effective ice particle densities for cold anvil cirrus. Geophys. Res. Lett., 31, L02101.

Hirst, E., P.H. Kaye, R.S. Greenaway, P. Field, *et al.*, 2001: Discrimination of micrometre-sized ice and super-cooled droplets in mixed-phase cloud. Atm. Env. 35, 33-47.

Meyers M.P., P.J. DeMott, and W.R. Cotton, 1992: New primary ice-nucleation parametrizations in an explicit cloud model. J. Appl. Meteor. 31, 708-721.

Mitchell, D.L., 1996: Use of mass- and area-dimensional power laws for determining preciptitation particle terminal velocities. J. Atmos. Sci., 53, 1710-1723.

Ulanowski, Z., E. Hesse, P.H. Kaye, A.J. Baran, and R. Chandrasekhar, 2003: Scattering of light from atmospheric ice analogues. J. Quantit. Spectr. Rad. Transf., 79-80, 1091-1102.

Yang P., B.A. Baum, A.J. Heymsfield *et al.*, 2003: Single-scattering properties of droxtals. J. Quantit. Spectr. Rad. Transf. 79–80 1159–1169.

Zhang, Y. *et al.*, 1999: Effect of crystal size spectrum and crystal shape on stratiform cirrus radiative forcing. Atmos. Res. 52, 59–75.

RADIATIVE TRANSFER IN SHALLOW CUMULUS CLOUD FIELDS: OBSERVATIONS AND FIRST ANALYSIS WITH THE DIRAM INSTRUMENT DURING THE BBC-2 FIELD CAMPAIGN IN MAY 2003 *

Han van Dop and Keith M. Wilson

IMAU, Utrecht University, 3508 TA The Netherlands

1. INTRODUCTION

Atmospheric radiation plays a major role in greenhouse studies. Virtually all energy on Earth originates from solar radiation which is scattered, reflected and partially absorbed at the surface and in the atmosphere (primarily by clouds and aerosols). This energy flux is balanced by the upwelling infrared radiation from Earths surface and the atmosphere. Small disturbances of this balance (e.g., enhanced absorption of infrared radiation by increasing concentrations of green-house gases, or enhanced reflection of solar radiation by increasing aerosol concentrations) are major topics in climate studies. Clouds are major actors in this process and their role is complex since their abundance and optical properties are influenced by climate parameters (aerosol content, evaporation, temperature). The Earth albedo is greatly determined by the mean cloud cover, which reflects $\sim 20\%$ of the solar radiation, corresponding with approximately 250 Watt/m2. If we realize that detectable climate effects amount to a few Watt/m2 only, it is obvious that the way in which radiation interacts with clouds, is an important element in climate studies. Satellite and surface observations assist in determining the radiation budget (and its changes). Up to now it has not yet been possible to balance it: a few Watts are still missing. The uncertainty is of the same order as the present estimated climate effect !

In atmospheric modelling of radiation transfer, clouds are often represented as extended homogeneous layers of constant thickness. Homogeneity is assumed in e.g. droplet size, liquid water content and droplet number concentration. In reality these quantities may strongly vary on all scales, even in stratiform cloud types. This variance in cloud properties has a distinct influence on the radiation transfer process (Los and Duynkerke (2001)). One of the consequences is that the horizontal divergence of radiative fluxes cannot always be neglected. Also, in regions with scattered clouds, a full 3-D analysis of radiation transfer is required. The albedo of a broken cloud field can be quite different from a similar, but homogeneous cloud layer (albedo bias) (Barker (1992), Barker et al. (1996), Cahalan et al. (1994)). This is a matter of concern since in all numerical climate studies the horizontal resolution is (and will be) much larger than the scale of the cloud inhomogeneity which, as a consequence, has to be parameterized.

Figure 1: The upper dome of the Perspex DIRAM instrument.

What apparently is required, is an insight in cloud-radiative properties, based on experimental evidence as a function of azimuthal and zenith angle (radiances) under conditions where simplifications like the plane parallel approximation are likely to be invalid. Measurements of the angular distribution of scattered radiation (relative to the solar incidence) yield bidirectional reflectance distribution functions (BRDFs) which provide the required information on radiative scattering processes in clouds.

In this presentation we shall report the design and properties of an instrument (DIRAM, directional radiance distribution measurement device) which determines the (anisotropy in the) scattering of solar radiation by clouds. We shall first give a brief description of the instrument and its properties and then present some results from a flight campaign in the Netherlands which was held in May 2003, the BBC-2

*Corresponding author's address: Han van Dop, IMAU, Utrecht University, p.o. box 80.005, 3508 TA Utrecht, The Netherlands; e-mail: h.vandop@phys.uu.nl

(second Baltex Bridge) campaign.

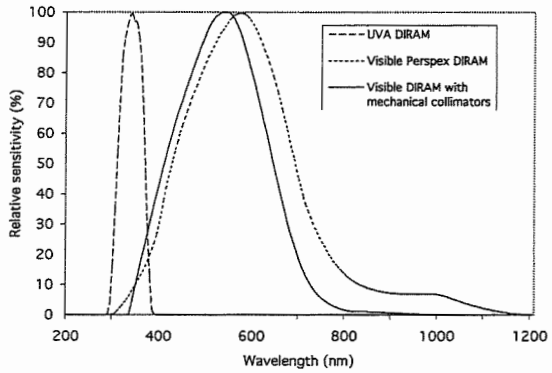

Figure 2: The relative spectral response of the three DIRAM instruments.

2. INSTRUMENT

The DIRAM instrument is described in van der Hage et al. (2001). There are three versions of the DIRAM instrument, each consisting of a pair of domes; the original prototype Perspex DIRAM (visible), a new visible DIRAM with mechanical collimators and the UVA DIRAM. The domes can be placed at ground level, or on top and below a research aircraft. The construction contains 42 sensors, consisting of a collimation system and a detector, which are mounted in two domes (21 in each). The collimators collect broadband visible radiation in 42 regularly distributed viewing angles. The 42 signals are continuously stored by a data logger with variable frequency up to 25 Hz.

2.1 Spectral characteristics

The Perspex DIRAM instrument dome is shown in Figure 1. The collimators are made of solid Perspex cylinders, 8 mm in diameter and 24 mm long, which are fully transparent in the visible range. Three diaphragms are carved in each cylinder to reduce the field of view to 7 and to reduce the stray light. The detector is a commercially available silicon photodiode for the visible spectral range with a response close to the human eye, due to a built in filter (Figure 2). A duplicate instrument has now been developed which employs filtered silicon detectors sensitive in the UVA region (Figure 2), and solid quartz collimators. An improved visible light DIRAM has also been constructed which employs quartz windows and mechanical collimators for measurements between 350 and 750 nm (Figure 2), with increased sensitivity. This instrument is still at the testing and calibration stage.

2.2 Calibration

For the calibration of the instruments, a spectrally calibrated 1000 W halogen lamp at the Laboratory for Radiation Research, RIVM, Bilthoven was employed as a reference. Not all sensors were individually calibrated, as the lamp has a limited time period in which it is calibrated. 1 - 3 sensors in each dome, were selected for this purpose in order to get an impression of the mutual variability. The measured calibration factor was 8.71 to 11.68 $Wm^{-2}V^{-1}$ (average = 9.41 $Wm^{-2}V^{-1}$) for 6 of the visible Perspex dome sensors, and 1.57 and 1.70 $Wm^{-2}V^{-1}$ for 2 of the UV sensors. The remaining sensors were calibrated relative to these sensors. The estimated errors amount to 1.5 % for the visible and 3 % for the UV sensors, respectively. To determine this relative sensitivity of each sensor, a dual fibre optic (microscope) light source (or UV light source with dual liquid light guides) is used to illuminate each one of the sensors on the domes, while the light source is monitored by an identical reference sensor fixed to the end of the second fibre optic. The 1m long flexible fibre optic arm allows a cylinder fixed to the end to locate the light source over each sensor in the same position by means of a groove cut in the dome. The (42) relative sensitivity factors had a measured range of 0.76 to 1.44 for the Perspex DIRAM (measurement error of 1.1 %), and 0.67 to 1.12 for the UVA DIRAM (measurement error of 0.7 %).

3. RESULTS

3.1 The BBC-2 campaign

From May 3rd till May 24th 2003, the BBC-2 intensive (cloud) measurement campaign was held at Cabauw, the Netherlands. The BBC2 campaign was jointly organized by the University of Bonn and KNMI. Beside these two research groups a number of other institutes participated, in total some 100 scientists from 20 institutes. Although the focus of the campaign is on clouds and radiation, other subjects of research are of interest like turbulence in the atmospheric boundary layer and small scale structure of rainfall.

Instrumentation deployed covers a wide range of important parameters. A number of advanced active and passive remote sensing systems were operated in Cabauw. In-situ particle probes were operated on

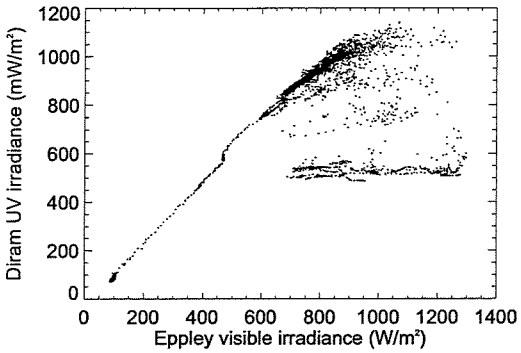

Figure 3: Irradiance comparison between to instruments

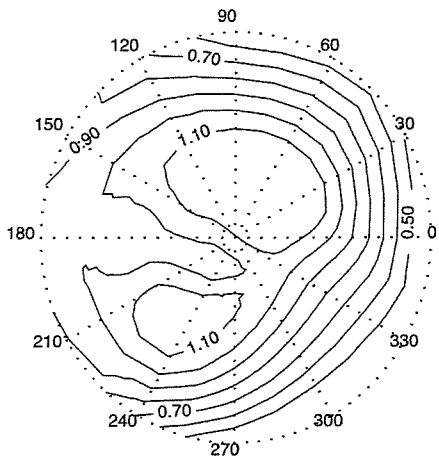

Figure 4: Bidirectional transmittance in dimensionless form. The radius is the viewing angle (from 0 (zenith) to 90°) and the polar angle is the azimuth with the sun at 0°.

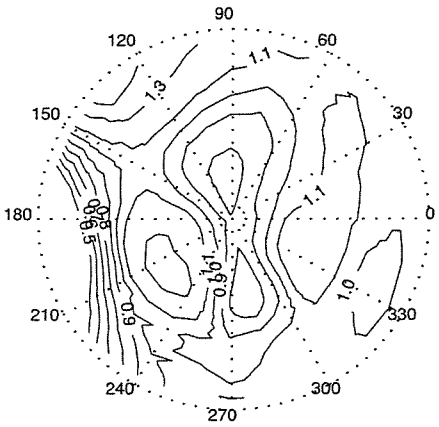

Figure 5: The same as Figure 4 but now for the reflectance. The nadir is at the centre.

aircraft and from a tethered balloon. Radiation sensors for long and short wave range were mounted on aircraft and operated on the ground. Turbulence measurements were performed on the different platforms, including the 213 m high meteorological tower. Radiosondes were launched regularly during the campaign.

Thirteen flights were undertaken with the Merlin-IV aircraft in the period 5-22 May 2003. On 5 and 8 May the broad-band visible DIRAM was mounted and for the remaining flights the UV-DIRAM was mounted on the aircraft. The aircraft was based at Rotterdam airport and most flights were over the Netherlands in easterly directions, often overflying Cabauw.

Different weather conditions were encountered during the campaign with a dominant presence of Cumulus and Stratocumulus clouds at altitudes varying from 400 to 4500 m. During most flights it was dry and partly sunny.

Apart from standard set of flight parameters the Merlin aircraft measured up and downward irradiation (visible and IR), liquid water content (lwc) (Lyman-α, King-Probe and Gerber PVM-100) and Refractive index. The Gerber PVM-100 provides also the droplet integrated surface (a) (in m^2/m^2) which can be related to the average droplet radius (r_e) by

$$r_e = \frac{q_L}{\rho\, a},$$

where q_L is the lwc ($kg\ m^{-3}$) and ρ the air density.

3.1 Analysis of 22nd of May flight

In a first analysis we focussed on the data of the 22nd of May during a flight near Cabauw from 10 to 11 UTC. It was partly cloudy (stratocumulus) to overcast with cloud layers between 400-1000 m and 1600-2000 m. The maximum flight level was 3700 m. First we compared in 1s intervals the results from the Eppley (visible) irradiance with the UV DIRAM irradiance (see Figure 3). Data points fall into two categories: one set is well-correlated and another, smaller set does not show a correlation. It marks the difference between measurements in situations with and without direct solar radiation. The Eppley instrument measures the sum of direct and diffuse radiation, whereas the DIRAM measures diffuse radiation only (DIRAM measurements where the solar

radiation was incidentally trapped by one of the sensors were excluded because of over saturation of the detector amplifier). So the horizontal band in the Figure refers to a predominantly clear sky situation which indicates that the UV diffuse radiation is approximately 50 % of the UV irradiance at flight levels ranging from $\sim$ 2000-3700 m. We have made a similar analysis of the corresponding downward looking instruments. These signals appear to be very well correlated.

Next we have looked to the angular distribution of up and downward radiation. For this purpose we have selected an in-cloud situation at an altitude of $\sim$ 750 m in a cloud-layer extending from 400-1200 m altitude. The lwc was 0.4 g/m^3. The angular distribution is shown is Figures 4 and 5. We have shown the bidirectional reflection (transmission) functions (B) defined by

$$B \equiv \pi \frac{R(\theta, \varphi)}{I_{r,t}},$$

where $R(\theta, \varphi)$ is the radiance and $I_{r,t}$ the integrated radiance of the reflected (0.376 W/m^2) and transmitted (0.533 W/m^2) radiation, respectively.

Finally we have plotted the azimuthally averaged reflectance (transmittance) in Figure 6. The transmittance curve shows a forward maximum at the solar zenith angle (38°) and limb darkening in line with the findings of Bréon (1992). The upwelling profile becomes brighter towards the limb. (Note that the profiles shown can be plotted as one continuous profile from 0-180° if properly dimensionalized).

The numerical study of Bréon (1992) and the observations of Brenguier et al. (2003) relate radiative properties of homogeneous and broken clouds to solar zenith angle and to optical thickness. The data assembled during this campaign offers a good opportunity to pursue these relations further, which was one of the major objectives in the design of the DIRAM.

ACKNOWLEDGMENT

The authors are grateful to the Météo-France Merlin IV for their support and their efficient provision of the data collected during the campaign. We are also indebted to the European Commission's support through the CAATER programme and we want to thank the BBC-2 management team for over-all coordination. One of the authors (KMW) is indebted to the Technology Foundation (STW) for financial support.

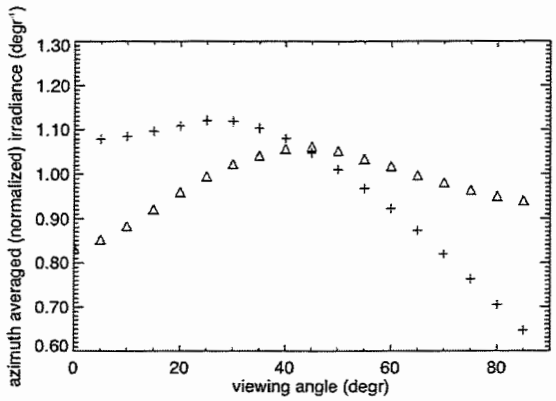

Figure 6: Azimuth-averaged transmittance(+) and reflectance(△) in mid-cloud.

References

Barker, H., 1992: Radiative transfer through clouds possessing isotropic variable extinction coefficient. *Quart.J.Roy.Meteorol.Soc.*, **49**, 1145–1162.

Barker, H., B. Wielicki, and L. Parker, 1996: A parameterization for computing grid-averaged solar fluxes for inhomogeneous marine boundary layer clouds part ii: validation using satellite data. *J.Atmos.Sci.*, **53**, 2304–2316.

Brenguier, J.-L., H. Pawlowska, L. Schller, R. Preusker, J. Fischer, and Y. Fouquart, 2003: Radiative properties of boundary layer clouds: Droplet effective radius versus number concentration. *J.Atmos.Sci.*, **57**, 803–821.

Bréon, F.-M., 1992: Reflectance of broken cloud fields: simulation and parameterization. *J.Atmos.Sci.*, **49**, 1221–1232.

Cahalan, R., W. Ridgeway, W. Wiscombe, T. Belland, and J. Snider, 1994: The albedo of fractal stratocumulus clouds. *J.Atmos.Sci.*, **51**, 2434–2455.

Los, A. and P. G. Duynkerke, 2001: Parametrization of solar radiation in inhomogeneous stratocumulus: albedo bias. *Quart.J.Roy.Meteorol.Soc.*, **127**, 1593–1614.

van der Hage, J., H. van Dop, A. Los, W. Boot, and D. van As, 2001: A multiple direction radiation sensor, diram. *J.Atmos. Ocean Technol.*, **18**, 2013–2020.

FIRST MEASUREMENTS WITH AN EXPANSION TYPE CCN COUNTER

J.S. van Ekeren[1,2], M. Fierz[2], U. Baltensperger[1], H. Burtscher[2] and E. Weingartner[1]

[1] Paul Scherrer Institut, Laboratory for Atmospheric Chemistry, CH-5232 Villigen, Switzerland
[2] Fachhochschule Aargau, Institut for Sensors and Signals, CH-5210 Windisch, Switzerland

1. INTRODUCTION

Clouds play a very important role in the climate system. Cloud droplets are formed in the atmosphere by the presence of low supersaturation and aerosol particles. Human activity changes the aerosol population in the atmosphere, which is believed to change cloud properties. This is the so-called indirect effect of aerosols. Long-term measurements on CCN are lacking in order to quantify this effect. Cloud droplets are formed in the atmosphere by the presence of low supersaturation and aerosol particles. We have developed a new cloud condensation nuclei (CCN) counter to measure CCN concentrations at the Global Atmosphere Watch (GAW) station Jungfraujoch. The new counter determines the CCN concentration by comparing directly the light scattering signal and extinction signal from the growing droplets with Mie theory (Holländer et al., 2002).

2. EXPERIMENTAL

2.1 Instrumentation

Existing CCN counters create a supersaturation with a thermal gradient (Nenes et al., 2001). This has as disadvantage that the supersaturation is achieved rather slowly. Easily activating particles will start growing earlier. They remove water vapour, so that other potential CCN are not able to activate anymore. Another difficulty is the non-uniform supersaturation in the cloud chamber. Our new instrument creates a well defined supersaturation by fast expansion of the cloud chamber (volume 4.2l), where the expansion time is 50ms. The supersaturation is therefore uniform in the chamber and is exposed to all particles at the same time. The volume of the chamber can be expanded up to 0.3% in 63 steps. This corresponds to a maximum supersaturation of 1.8%. At SS=0.45% for NaCl all particles larger than Dp=50nm will grow into droplets according to Köhler theory. Great care is taken that the initial relative humidity of the sampled air is very close to 100%. This is achieved by a prehumidifier (see Fig 1a) consisting of Gore-Tex tubes surrounded by water. In order to make sure that prior to the expansion the sampled air has a relative humidity of 100%, we have wetted walls and water reservoirs in the lower and upper part of the chamber. A laser (λ=670nm) illuminates the particles and the scattered light is measured at a constant angle of 30°±1.61° with a photomultiplier (Fig 1b). The signal of scattered light and the extinction gives the information to determine the number concentration of the activated nuclei. During the expansion we monitor the pressure, light scattering and aerosol optical depth. The last two parameters give us the knowledge of the growth of the particles into droplets. From this we can also determine the CCN concentration under noisy conditions. The CCN concentration is then calculated as follows:

$$N_{CCN} = F \frac{E_{s,exp}}{E_{s,theory}},$$

where $E_{s,exp}$ is the experimental scattering signal, $E_{s,theory}$ is the theoretical scattering signal and F is an experimentally determined factor which depends on the amplification factor of the PM, the path length of the laser and the PM solid angle (Holländer et al., 2002). We can monitor how long it takes to get a certain size of a droplet.

The CCNC has a lower detection limit of around N_{CCN}= 50cm^{-3} and an upper limit around N_{CCN}=10000cm^{-3}. The upper limit is caused by limited water vapour availability. The CCN concentration at the Jungfraujoch is usually between these detection limits. The accuracy of the CCN number concentration is of the order of 20%. Diffusion losses caused by the laminators have been determined and are around 10% for initially dry NaCl particles greater than $D_{p,dry}$=80nm (van Ekeren, 2004).

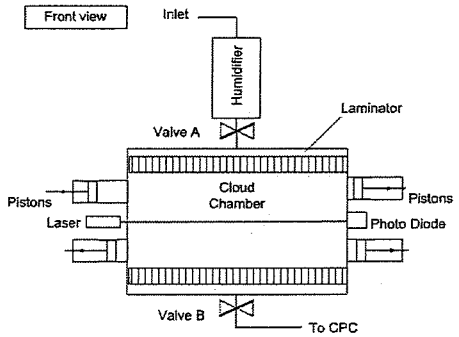

Fig. 1a: Schematic picture of the expansion CCN counter. The sampled air passes the humidifier before it enters the expansion chamber. 8 pistons are used to create a supersaturation by fast expansion.

Corresponding author's address: Stefan van Ekeren, Paul Scherrer Institut, Laboratory of Atmospheric Chemistry, CH-5232 Villigen, Switzerland, E-Mail: stefan.vanekeren@psi.ch

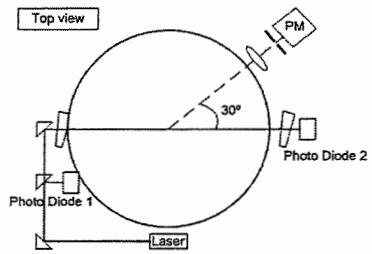

Fig. 1b: Top view of the CCN counter. The light scattering measured with the photomultiplier is at a constant angle of 30°.

2.2 Measurement setup

During the CLACE III campaign (Cloud and Aerosol Characterization Experiment) the CCNC was in operation in the field for the first time. The campaign was held in March 2004 at the high alpine measurement station Jungfraujoch, central Switzerland. Clouds are at the station rather frequently, about 40% of the time (Baltensperger et al., 1998). For our measurements we used a heated inlet, which was designed to evaporate cloud droplets before entering the sampling tube. In this way the CCN concentration of the total aerosol is measured. A TSI 3010 CPC was used on the same inlet to measure the total particle concentration. This instrument is part of the permanent aerosol measurement within the GAW program.

The CCN counter was operated in two different modes. In the first mode we kept the supersaturation constant. In the second mode the supersaturation was changed after a fixed time interval to another supersaturation. When the system was operating in this mode, we shifted the supersaturation in 5 steps between 0.484% and 0.76%. In general, we measured with a constant supersaturation over one hour, whereafter the supersaturation was changed to another level.

3. RESULTS

The temporal evolution of the light scattering signal for a calibration experiment with monodisperse D_p=40nm NaCl particles is shown in Fig 2. The bold curve is the theoretical light scattering according the Mie theory. For these laboratory measurements the CCN number concentration was determined in combination with a CPC parallel to the CCNC. After this calibration where we determine factor F (see section 2.1) we are able to calculate the CCN concentration directly from the light scattering and extinction signal.

Dividing the extinction signal by the light scattering signal gives a clear signal peak at α^2=270, which corresponds to a droplet diameter of 3.5μm. The Mie size parameter α, is a function of particle diameter and wavelength of the light source:

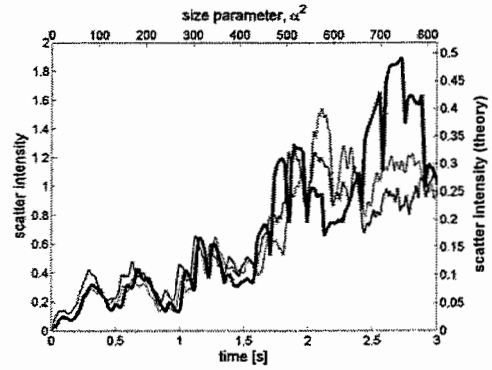

Fig. 2: Light scattering signal from two laboratory measurements with NaCl particles ($D_{p,dry}$=40nm) at a SS=0.51%, N_{CCN}=470 cm^{-3}.

$$\alpha = \frac{\pi D_p}{\lambda}$$

In Fig 2 the droplet diameter of 3.5μm is reached after 0.8 sec.

The aerosol at the Jungfraujoch is polydisperse with lower total number concentration, so the light scattering data is more scattered and the data is noisier compared to the laboratory experiments. Fig 3 shows light scattering data from the Jungfraujoch aerosol at a supersaturation of 0.86%.

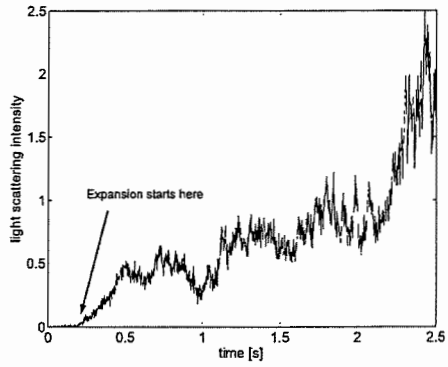

Fig. 3: Light scattering from the Jungfraujoch aerosol at March 6 2004, SS=0.86%, N_{CCN}=158cm^{-3}. The expansion is started at t=0.25s. The dip in the curve at t=1s marks the moment where the droplet size is 3.5μm.

When we compare the data from Fig 2 and 3, we see that a droplet size of 3.5μm is reached in the same time, despite the difference in supersaturation. This gives a first indication that we can observe different particle chemistry by looking at the time of growth of the droplet. The Jungfraujoch aerosol grows more slowly than the NaCl particles in the laboratory experiment.

Preliminary results show the time for a particle to reach the size of a 3.5μm droplet as a function of the supersaturation in Fig 4. At a higher supersaturation the growth of the droplet is faster than for lower supersaturations. Also, the time to reach this particular

size is more spread out for the lower supersaturations. In the figure only data over two days of the beginning of the campaign are shown. The chemical composition is thought to have a great influence on the growth velocity.

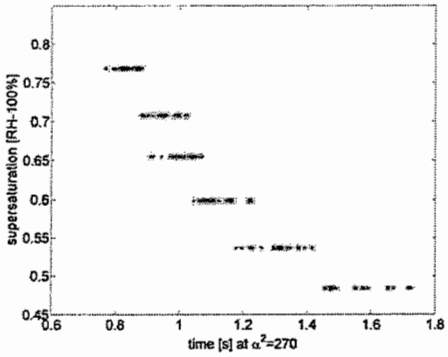

Fig. 4: The time to reach α^2=270 is plotted against supersaturation. A higher supersaturation causes a faster growth of the droplets. Chemical properties of the aerosol might influence this time strongly.

An example of the CCN concentration during a day is shown in Fig. 5. The CCN concentration was measured at *SS*=0.51%. The Jungfraujoch aerosol is an aged aerosol and is assumed to be internally mixed (Weingartner, E. et al., 2002). The activation to a cloud droplet therefore mainly depends on particle size. The light grey line is the aerosol number concentration for particle sizes between 44nm and 720nm. The CCN concentration is lower than this line. According to earlier studies at the Jungfraujoch, the aerosol behaves like slightly less hygroscopic than sulphate particles. Pure sulphate particles of 44nm would grow into droplets at a supersaturation of 0.51%. The present experiment does confirm that the Jungfraujoch

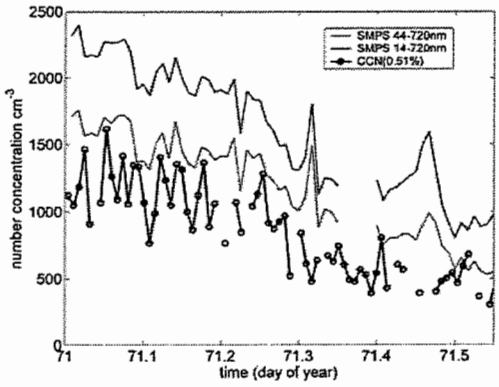

Fig. 5: Aerosol number concentration and CCN concentration at the Jungfraujoch for 11 March, 2004. The CCN concentration was measured at *SS*=0.51% and is close to the aerosol particle concentration for D_p>60nm.

aerosol is slightly less hygroscopic than sulphate particles, because the aerosol is not activated as easily as the sulphate particles at the same supersaturation.

4. CONCLUSIONS

The new expansion-type CCNC was successfully operated at the high alpine site Jungfraujoch, Switzerland and the CCN concentration was determined. The measurements were conducted during the CLACE III campaign in March 2004. The measurements were made at supersaturations between 0.48% and 0.77%. Our preliminary conclusion is that the CCN concentration during a normal day was between 40% and 60% of the total aerosol particle concentration.

5. ACKNOWLEDGEMENTS

Leo Scherrer (ETH Zürich) is greatly acknowledged for his help in building the instrument. We also acknowledge that the International Foundation High Altitude Research Stations Jungfraujoch and Gornergrat (HFSJG), 3012 Bern, Switzerland, made it possible for us to carry out our experiments at the High Altitude Research Station Jungfraujoch. In addition we would like to thank the custodians Mr and Ms Fischer for their additional support at the Jungfraujoch.

Bart Verheggen and Julie Cozic (PSI) are acknowledged for providing SMPS data from the CLACE III campaign.

6. REFERENCES

Baltensperger, U., M. Schwikowski, D. T. Jost, S. Nyeki, H. W. Gaggeler, and O. Poulida, 1998: Scavenging of atmospheric constituents in mixed phase clouds at the high-alpine site Jungfraujoch part I: Basic concept and aerosol scavenging by clouds. *Atmos. Env.*, **32,** 3975-3983.

Holländer, W., W. Dunkhort, H. Lödding, and H. Windt, 2002: Theoretical simulation and experimental characterization of an expansion-type Kelvin spectrometer with intrinsic calibration. *J. Atmos. and Oceanic Techn.*, **19,** 1811-1825.

Nenes, A., P. Y. Chuang, R. C. Flagan, and J. H. Seinfeld, 2001: A theoretical analysis of cloud condensation nucleus (CCN) instruments. *J. Geophys. Res.-Atmos.*, **106,** 3449-3474.

Van Ekeren, J.S., et al, 2004: Development and calibration of an expansion-type CCN counter. *In preperation.*

Weingartner, E., M. Gysel, and U. Baltensperger, 2002: Hygroscopicity of aerosol particles at low temperatures. 1. New low-temperature H-TDMA instrument: Setup and first applications. *Env. Sc. & Techn.*, **36,** 55-62.

SATELLITE RAINFALL ESTIMATION OVER SOUTH AMERICA: THE HYDROESTIMATOR TECHNIQUE

Daniel A. Vila [1] and Alexandra A. Lima [2]

[1] Sistema de Alerta Hidrológico, Instituto Nacional del Agua, Buenos Aires, Argentina
[2] Divisao de Satelites e Sistemas Ambientais, CPTEC, Cachoeira Paulista, SP, Brasil

1. INTRODUCTION

Rainfall is the most important atmospheric variable. However, due to high temporal and spatial variability of this variable, the use of the conventional methods (rain gauge measurements) makes your monitoring very difficult.. The solution of this issue is the use of remote sensing like geostationary satellites. Particularly over regions like South American, where the scarcity of real time rain gauge data and the existence of large unpopulated regions, make satellite based approaches an excellent tool to investigate the spatial distribution of precipitation (Vila, 2003). Vicente et al. (1998) develop a fully automated method (called "autoestimator", hereafter AE) using an empirically power-law function that generates rainfall rates (mm/h) based on a relationship between precipitation (radar estimation) and the cloud top brightness temperature on GOES–8 (10.7 mm – channel 4). Numerous improvements have been made to the first version to arrive at the currently operative version, called "Hydro-Estimator" (Vila, 2003). In the next section will be described briefly some of these improvements to the "autoestimator"-method for the South American region, and a small description of data used. The statistical validation will be shown in the third section. We conclude and discuss our results in the last section.

2. DATA AND METHODOLOGY

2.1 Data

Two summer months (January – February 2003) over Del Plata basin (40° S – 20° S, 60° W – 35° W) were chosen to assess the performance of the technique (Figure 1). Due to limited availability of southern hemisphere GOES-8 images (with gaps of up to 180 minutes between images) only 27 days with more than 28 images in 24 hours could be selected to evaluate the algorithm. Rain gauge measurements mainly from the World Weather Watch Network and other regional agencies provide ground truth data. Numerical Weather Products was obtained from CPTEC-ETA model, which has been used to estimate precipitable water (PW) and relative humidity (RH).

Corresponding author's address: Daniel A. Vila, Instituto Nacional del Agua, (1804) Buenos Aires, Argentina; E-Mail: dvila@ina.gov.ar.

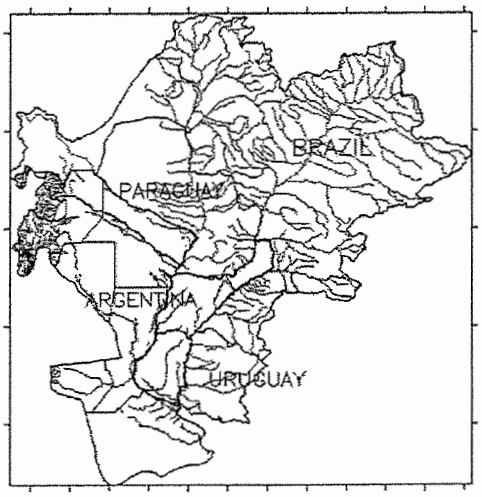

Figure 1: Del Plata Basin limits

2.1 Methodology

Main features of the algorithm applied in this paper should be outlined as follows:

- *Rain rate estimation*: fully automated method using an empirical power-law function that generates rainfall rates (mm/h) based on GOES-8 channel 4 brightness temperature (Vicente et al, 1998). Two types of precipitation are defined: 'core' precipitation: computed essentially by the empirical power-law function; and 'non core' precipitation: whose maximum value cannot exceed 12mmh^{-1} and must be less than the fifth part of the convective rainfall for a given pixel. For more details; see Vila (2003)
- *Moisture correction*: a moisture correction was developed by applying the PW and RH corrections separately. The precipitable water has become a moisture availability factor, and the rainfall rate curve is now adjusted upward or downward based on the PW value (ETA model), while the RH factor has been modified, such that a fixed amount of precipitation is evaporated prior to reaching the ground, rather than removing a fraction of the falling precipitation (Kuligowski, personal communication).
- *Orographic correction*: a Digital Elevation Model of South America at the GOES scale combined

with low-level winds produce an orographic correction to the satellite rainfall rate distribution producing enhanced precipitation upstream and less rainfall downstream (Vicente et al, 2001).

- *Screening method*: This technique assumes that raining pixels are colder than the mean of the surrounding pixels. (Vila, 2003).
- *Cloud threshold segmentation*: only the pixels that belong to a given cloud (T< 241 K) enter in the statistics (screening method). This approach allows a closer delineation of rainy region edge and produce adjustments resulting in more realistic patterns of rain, especially for small-scale convection.

Another important improvement over the original A-E that was used in this particular work is the method of rainfall accumulation. In the A-E and H-E, if no images are available for more than an hour, the estimate during this period is zero; this assumption was eliminated for this work over South America. At many times during the day, the gap between images is greater than one hour and the dry bias obtained for some cases suggests that the rain continues during the period without available images. Two time integration is carried out between successive images (3 hours maximum) to avoid no-rainfall outputs during these periods. Constant rate integration assumes constant rain rate for a given pixel between $(t_1+t_2)/2$ and $(t_2+t_3)/2$ where t_1, t_2 and t_3 are the time of available images. A second one integration is carried out using cubic splines interpolation to 24 hours series. A physical criterion is applied to avoid spurious data: if estimation is below zero, it's set to zero and rain rate must be less than 80 mm h-1 during 1 hour period.

3. STATISTICAL VALIDATION

3.1 Intercomparison of Satellite and Gauge Rainfall

Verification methods may be carried out using different approaches. The first one, called the best adjusted value (MVE) (Vila, 2003), assumes that each rainfall data pixel is matched with the most similar satellite estimate within a 16-pixel kernel centered in the rain gauge location, instead of using the satellite pixel corresponding directly to the rain gauge due to the fact that there are uncertainties regarding the precise gauge location and in satellite resampling methods.

The other one, based on spatial averages, will take into account those regions (0.5° X 0.5°) whose raingauge network exceed four stations. This limit is imposed to ensure that the spatial average is representative of that region. In this case, both averages (observed mean rainfall and mean satellite estimation) are compared.

3.2 Statistical Definitions

The statistical measures and definitions used to compare the satellite estimates with the gauges were taken from the results of the 3rd Algorithm Intercomparison Project of the Global Precipitation Climatology Project (GPCP) (see Ebert 1996). The first set of parameters is related with the difference in the amount of observed and estimated rainfall: bias, correlation coefficient and root mean squared error (RMSE). Parameter based on Rain / No Rain Contingency table are calculated in order to measure the skill of the rainfall estimates in pinpointing rain where there is rain observed: probability of detection (POD) and false alarm ratio (FAR). A detailed definition of these parameter can be found in Vila (2003).

4. RESULTS AND CONCLUSIONS

Considering the first validation technique (MVE) and using cubic splines interpolation, satellite estimation underestimates the average rainfall by an amount of 4.0 mm. The averaged RMSE is 12.7 mm and the correlation coefficient is 0.79 for all cases. Figure 2 shows that most of the days have a dry bias (only two cases exhibit positive values)

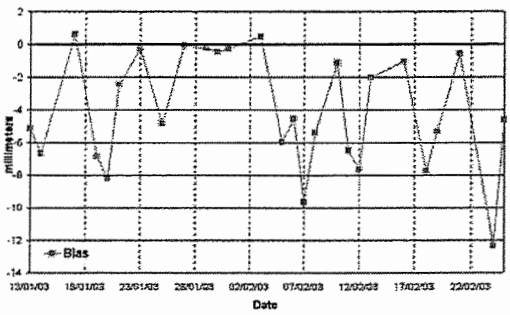

Figure 2: Mean bias for all cases presented in this paper

On the other hand, the probability of detection remains always above 0.67 (1.00 is perfect detection) and the mean value is 0.82. The false alarm ratio exhibits a similar behavior. This statistic has a mean value of 0.05 for all cases. This kind of result shows that the algorithm is delineating the rainy regions with reasonable accuracy.

The comparison based on spatial averages shows different results, due to the fact that only ten boxes (on average) are available each day for comparison. However, this methodology exhibits higher values: 12.0 mm for bias and 50.0 mm for the averaged RMSE. This apparent disagreement between both intercomparison methods may be caused by two reasons: the high variability of rainfall, particularly with small scale convection and the spatial representativeness of the rain gauge average.

In order to evaluate the algorithm performance, a case study will be presented. This case corresponds to a storm over northeast of Argentina, Paraguay and south of Brazil, whose maximum observed value was

147 mm registered in Posadas Airport (55.97° W; 27.37° S) on 20 January 2003. The observed values and the estimation can be seen in Figure 3 and 4.

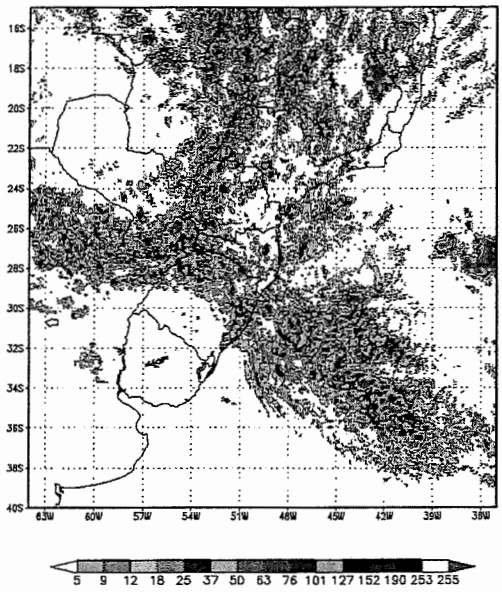

Figure 3: Hydroestimator rainfall estimation

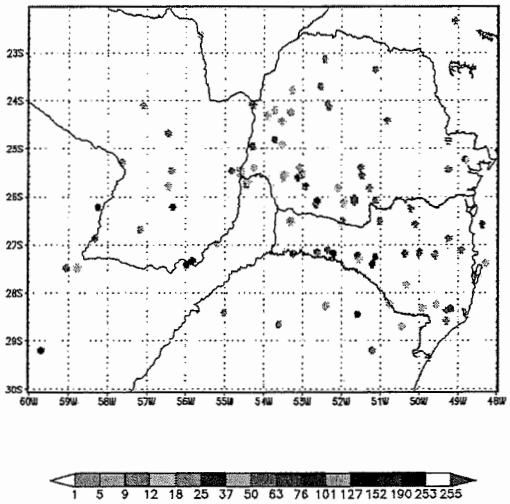

Figure 4: 24-hour rainfall observed values for 20 January 2003

Table 1 shows the statistical information for different rainfall thresholds. In all cases the bias is negative: the satellite underestimates the average rainfall by an amount ranging from 0.5 mm to 12.0 mm for different thresholds. The weighted averaged RMSE is 7.9 mm and the averaged correlation coefficient is 0.95. The probability of detection is higher for the lower intervals (92 – 96 % for the first classes) and decreases to 74% for higher amounts of observed rainfall. The false alarm ratio is low (less than 3%) for all classes.

THRESH (mm)	NUM	BIAS	CORR	RMSE	POD	FAR
0 7	5575	-0.54	0.98	4.62	0.92	0.01
7 26	3300	-0.92	0.97	5.95	0.96	0.03
26 52	1267	-2.72	0.94	9.26	0.93	0.03
52 +	256	-11.87	0.89	19.57	0.74	0.01
WTAVG	19291	-2.45	0.95	7.88	0.92	0.02

Table 1: Statistics for the storm of 20 January 2003 in the Del Plata basin region. THRES is the interval of observed amounts in mm; WTAVG is the weighted average. NUM is the number of pixels in each interval, BIAS the additive bias, CORR the correlation coefficient, RMSE the root-mean-squared error, POD the probability of detection and FAR the false alarm ratio.

Using the spatial average method, only colored boxes were chosen to perform statistics. In this case, bias is around 10.0 mm and RMSE is 50.0 mm. Performing the mean difference between the maximum and minimum value registered by rain gauge network inside each box is around 21 mm (twice the mean bias approximately). In other words, dispersion is very high inside each box, so the average would not be able to be representative of the observed rainfall in the corresponding box. This fact may be caused, at least, by two reasons: there is not enough ground truth points in each box; or small scale convection is playing an important role in the rainfall process, so that the spatial average is not a good estimator of the observed rainfall.

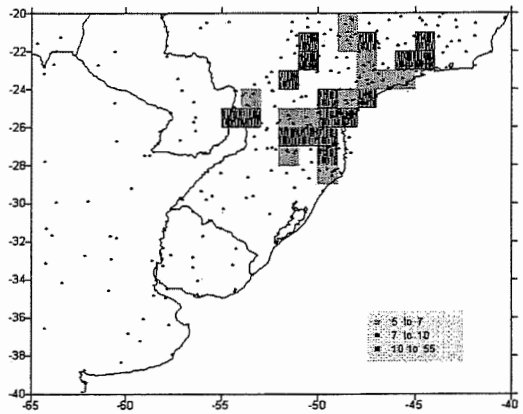

Figure 5: Number of rain gauges in each 0.5 x 0.5° box. Only colored boxes where chosen to perform all statistics

5. ACKNOWLEDGMENTS

The authors would like to recognize the NOAA/NESDIS Hydrology Team and Mr. Juan Ceballos from DSA/CPTEC for their important contributions to this research. Special thanks are conveyed to Till Neff for his critical review. The first author is supported by Instituto Nacional del Agua - Argentina and partially financed by UBACyT – grant X149 and CPTEC.

6. REFERENCES

Ebert, E. E.,1996: Result of the 3rd Algorithm Intercomparison Project (AIP-3) of the Global Precipitation Climatology Project (GPCP). Bureau of Meteorology Center, Report N° 55, Melbourne, Australia, 199 pp.

Scofield, R.A., and R.J. Kuligowski, 2003: Status and outlook of operational satellite precipitation algorithms for extreme precipitation events. Wea. Forecasting, in press.

Vicente, G. A., J. C. Davenport, and R. A. Scofield, 2001: The role of orographic and parallax corrections on real time high resolution satellite rainfall distribution. Int. J. Remote Sens., 23, 221 - 230.

Vila D., Scofield R., Kuligowski R., Davenport C., 2003, Satellite Rainfall Estimation Over South America: Evaluation of Two Major Events. NOAA Technical Report N° 114, US Department of Commerce, Washington, D.C., June 2003.

SMALL-SCALE RAIN NONUNIFORMITY AND ITS EFFECT ON CORRECTION OF NONUNIFORM BEAM FILLING IN SPACEBORNE RADAR RAIN MEASUREMENT

Ling Zhang, Daren Lu, Shu Duan, and Jinli Liu

LAGEO, Institute of Atmospheric Physics, Chinese Academy of Sciences, Beijing 100029, China

1. INTRODUCTION

It is well known that, nonuniform beam filling (NUBF) causes a spatial smoothing error for quantitative spaceborne radar rainfall measurement because of nonlinear relationships between radar observables and rainrate, and especially, such error becomes more significant for a radar whose resolution size is comparable to or larger than a convective rain cell size. Analyses of the NUBF error have found biases in retrieved rainrate for a spaceborne radar. These biases have been analyzed by a number of authors using nonuniform rain cell model, or raingage data, or ground-based radar data (Nakamura 1991; Testud et al. 1992, 1996; Amayenc et al. 1993, 1996; Durden et al. 1998; Kozu and Iguchi 1999). In order to enhance radar resolution, Zhang et al. (1998) proposed a deconvolution method for retrieving nonuniform reflectivities in the radar beam and tested the method using the artificial sinusoidal variation reflectivities and ground-based radar observation data.

In the above mentioned works, the resolution of radar data they used to investigate the NUBF was primarily around or more than 1 km, so this might smooth out variations within small scales less than 1 km and result in the error in the smoothing error analysis. In order to know how much the nonuniformity of rainfall field within less than 1 km spatial scale and its influence on the radar rainfall measurement smoothing are, Zhang et al. (2003) implemented rain observations with a high range resolution of 125 m using a 3-cm-wavelength meteorological radar in the summer of 2000 at a site (39° 45′ N, 116° 58′ E) near Beijing, and then used this high resolution radar dataset to simulate the spatial smoothing error of Z - R relationship based radar rainfall measurement. The possible connections between the smoothing error and other parameters, such as average reflectivity, strength of nonuniformity, true rainrate, size of radar resolution volume, etc., were also analyzed in that paper. Using this high resolution dataset, Zhang et al. (2004) investigated the statistical nature of spatial smoothing error due to NUBF in the k - R relationship based spaceborne radar rain measurement.

Corresponding author's address: Ling Zhang, LAGEO, Institute of Atmospheric Physics, Chinese Academy of Sciences, Beijing 100029, China; E-Mail: lzhang@mail.iap.ac.cn.

In this work, following the works of Zhang et al. (2003, 2004) we investigate the correction method of the NUBF error in the spaceborne radar rain measurement based on surface reference technique (SRT) using the high resolution radar data.

2. DATA AND SIMULATION ALGORITHM

The deployed radar for our rain observations is an X-band meteorological radar. To realize the high resolution observation, the radar scanned in a specially designed mode that, the antenna scans vertically within a range of elevation at several adjacent azimuths with an identical interval in an azimuth sector, at a speed lower than that in the regular operation. During the three rainfall processes occurred on 22 August, 4, and 20 September 2000 respectively near Beijing, we obtained a large quantity of rain echo data with a range resolution of 125 m from the X-band radar working in this special scan mode.

In rainrate retrieval from spaceborne radar, the path-integrated attenuation (PIA) which can be obtained by the SRT is a very important parameter, since it provides a constraint to stabilize the rain attenuation correction procedure for retrieving heavy rainrate, and in addition, it can be directly converted to path-integrated rain rate (Amayenc et al. 1993; Testud et al. 1996; Durden et al. 1998). Therefore, only the PIA is chosen for studying in this work. Since the resolution of the radar data is high along beam with the fixed value of 125 m but across beam is lower, variable and gets worse as the range increases, only one dimensional integration is considered in our NUBF simulations.

According to the above reasons, we used a relative simple rain model and a simple NUBF error simulation algorithm which should reveal the primary characteristics of the NUBF error. A rain cell model illuminated in an instantaneous field of view (IFOV) by a spaceborne radar is assumed and illustrated in Fig. 1. This model is vertically uniform, horizontally nonuniform, with a depth of 5 km. In horizontal plane the cell is assumed to be nonuniform in only one dimension corresponding to the along range variation of radar reflectivities but uniform in the other dimension. The IFOV is assumed to be square-shaped for simplicity and with a side length of Δr_m, i.e. the resolution of the spaceborne radar. If the reflectivity factor, the rainrate, and the specific attenuation of rain for the i th rain element in the IFOV are represented

by Z_{hi}, R_{hi}, and k_{hi} respectively, the power law Z-R and k-R relationship can be written:

$$Z_{hi} = aR_{hi}^{b}, \quad k_{hi} = cR_{hi}^{d}, \qquad (1)$$

where Z_{hi} is in mm^6m^{-3}, R is in mm h^{-1}, k is in dB km^{-1}, a and c are the constant coefficient, b and d are the exponent. We choose the values of a and b for Beijing district at 3 cm wavelength (The microwave remote sensing group 1982, p. 127). For the spaceborne radar, we use the values of c and d derived from Marshall-Palmer DSD (Marshall and Palmer 1948) at the 13.8 GHz of the TRMM PR by Marecal et al. (1997).

The radar measured two-way PIA from the SRT, A_{sm}, in decibels, can be computed by averaging over the IFOV:

$$A_{sm} = -10\lg\left[\frac{1}{N}\sum_{i=1}^{N}\exp\left(-\frac{\ln 10}{10}k_{hi}\bullet 2H\right)\right], N = \frac{\Delta r_m}{\Delta r_h}, \qquad (2)$$

where the subscript s and m denote the "SRT" and the "measured" respectively, N is the number of rain elements within the IFOV, H is the rain cell depth and is 5 km, Δr_h is the range resolution of the high resolution radar data and equals 0.125 km. Here we make use of the uniform PIA, A_u, which is defined as the PIA converted from average rainrate with a k-R relationship when rain is assumed uniform in the IFOV:

$$A_u = 2Hc\left(\frac{1}{N}\sum_{i=1}^{N}R_{hi}\right)^{d}. \qquad (3)$$

The difference between the measured value A_{sm} and the uniform value A_u is the spatial smoothing error due to the NUBF. We define the absolute and the relative PIA error due to the NUBF which are denoted by ΔA and δA respectively

$$\Delta A = A_{sm} - A_u, \quad \delta A = \frac{\Delta A}{A_u}. \qquad (4)$$

Using the reflectivity factors of the high resolution radar data as the inputs of the Z_{hi} and performing computations of Eq. (1)-(4), the A_u, the error ΔA and δA, etc., can be all calculated.

The detailed account for the radar data and the simulation algorithm is given by Zhang et al. (2004).

3. RESULTS

3.1 Data Processing and Computation

Before the simulation was carried out, some constraints were set for the selection of the radar data that would be used in the NUBF error simulation. The extent of the radar ray elevation angles is chosen from 3° to 20° above the horizon, so that the chosen radar rays are high enough to avoid the touching of any noising surface targets and to meet only precipitating cloud particles, and also are not too high to represent

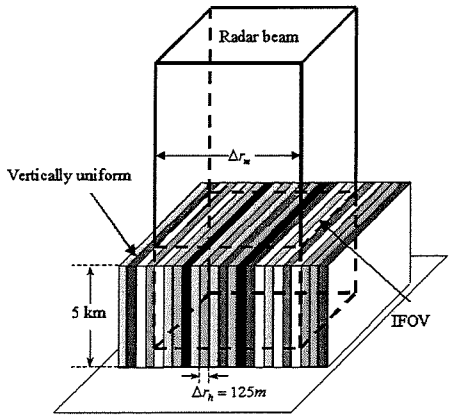

Fig. 1. Schematic diagram of rain cell sensing by a spaceborne radar.

horizontal nonuniformities of rainfall. The radar data was processed for attenuation correction using the H-B solution given by Hitschfeld and Bordan (1954). A k - R relationship for Beijing district at 3 cm wavelength (The microwave remote sensing group 1982, p. 127) is chosen and used in the H-B solution. Since the H-B solution can lead to unstable at high rainrates, we determined a quality control criterion based on experiences in the attenuation correction process. The criterion is that if the two-way PIA in a radar ray is greater than 30 dB, the corrected reflectivity data in this ray is suspected to be unreliable and is excluded in the simulation. For deleting suspected unreliable big values, if there is any

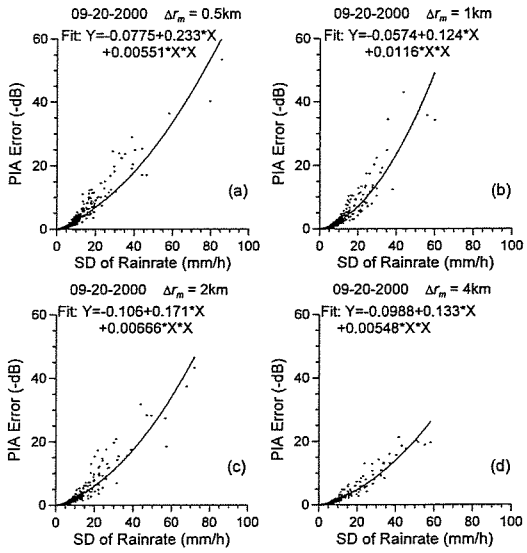

Fig. 2. Scatter plot of the PIA NUBF error versus the SD of rainrate obtained from the rain observations on 20 September 2000. The bend line is a polynomial fit with its equation given. The IFOV sizes are (a) 0.5 km, (b) 1 km, (c) 2 km, and (d) 4 km respectively.

attenuation-corrected reflectivity that is greater than 60 dBZ in an IFOV, this IFOV will be excluded in the simulation.

The reflectivity data in every radar ray that satisfies the above constraints are all taken for the simulation. In the simulation, the sizes of the IFOV were chosen as 0.5, 1, 2, 3, and 4 km. In addition to the NUBF error, several other parameters, such as the nonuniformity strength, the uniform PIA, the averaged reflectivity, etc, were computed.

3.2 Correlations between PIA NUBF Error and other Parameters

In order to look for possible correlations between the NUBF error and other parameters, we analyzed the correlations of the PIA error versus the reflectivity excursion (the difference between the maximum and the minimum of reflectivities in the IFOV), the relative error versus the reflectivity excursion, the PIA error versus the uniform PIA, the relative error versus the uniform PIA, the PIA error versus the standard deviation (SD) of rainrate, the relative error versus the SD of rainrate, the PIA error versus the normalized standard deviation (NSD, the SD divided by the mean) of rainrate, the relative error versus the NSD of rainrate. We found a relatively better correlation between the PIA error and the SD of rainrate. For the radar data of the rainfall process occurred on 20 September 2000, the scatter plot of the PIA error versus the SD of rainrate is given in Fig. 2.

It can be seen in Fig. 2 that, the PIA error and the SD of rainrate have a quite good correlation to some extent and exhibit a trinomial relationship. The calculations using the data observed for the other two rainfall processes on 22 August and 4 September 2000 also gave a trinomial relationship which reasonably agrees with that in Fig. 2. This trinomial relationship can be used in the rain retrieval algorithm for partially correcting the NUBF error.

3.3 Trinomial Relationship using High and Low Resolution Data

Kozu and Iguchi (1999) investigated the method for correcting the NUBF error. However, in their work, the resolutions of the radar data they utilized were 1 km. The using of these low resolution data would cause errors in the NUBF error simulation, because the real rain cell has nonuniformity within the small scales less than 1 km as indicated in Fig. 2. We made the comparisons between using the 125 m resolution data and using the 1 km resolution data. Before the NUBF simulation was done, the 1 km resolution data set was obtained by averaging the 125 m resolution data over every 8-range-bin segment. Then the simulation was made by using the 125 m resolution data and the 1 km resolution data respectively. An example of fit curves of the PIA NUBF error versus the SD of rainrate obtained in the same rainfall process as that of Fig. 2 is given in Fig. 3.

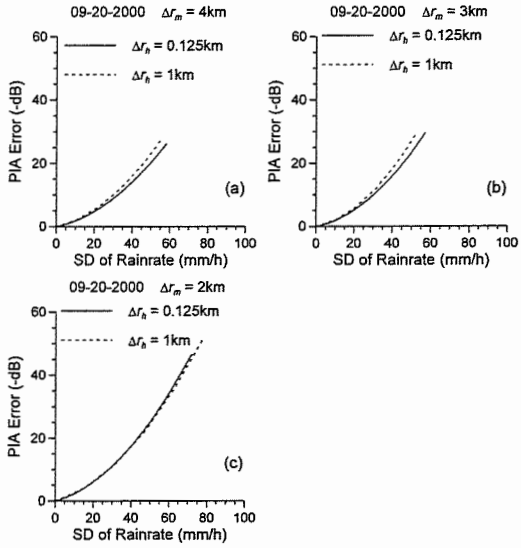

Fig. 3. Trinomial fit curve of the PIA NUBF error versus the SD of rainrate obtained from the same rain data as those in Fig. 2. The IFOV sizes are (a) 4 km, (b) 3 km, and (c) 2 km respectively. The resolutions of data used are 0.125 km (high, solid), and 1 km (low, dashed) respectively.

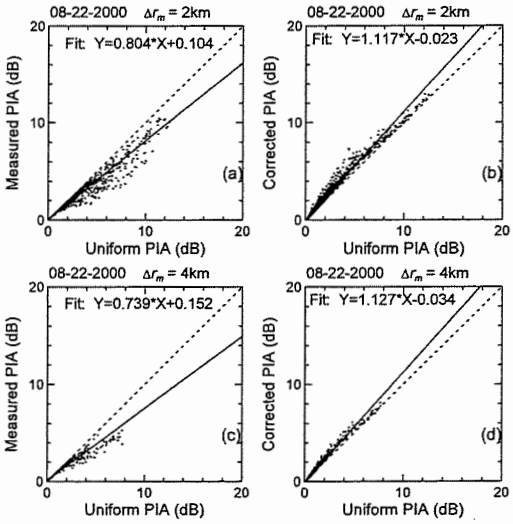

Fig. 4. Scatter plot of the measured PIA and the corrected PIA versus the uniform PIA obtained from the same rain data as those in Fig. 2. The straight line is a linear fit with its equation given. The IFOV sizes are (a) 2 km, (b) 2 km, (c) 4 km, and (d) 4 km respectively.

Fig. 3 shows that, the difference of the fit curves between using the 125 m resolution data and using the 1 km resolution data is evident and not neglectable, and also increases with the increasing of the SD of rainrate, except that the difference is small for 2 km IFOV. For the 4 km and 3 km IFOVs, the error

using low resolution data is greater than that using high resolution data in Fig. 3. The results from the data of the other two rainfall processes also showed that, the error using low resolution data is usually obviously greater than that using high resolution data, although the amount of the difference depends on different rainfall processes.

3.4 NUBF Correction Results

To test the validity of correction method, we used the trinomial fit equations in Fig. 2 to correct the measured PIA A_{sm} and got the corrected PIA. We made these correction simulations using the radar data in the mentioned three rainfall processes. One example of results is given in Fig. 4. It can be seen in Fig. 4 that, the biases of the corrected PIA ((b), (d)) from the uniform PIA are smaller than those of the measured PIA ((a), (c)), and the random errors of the corrected PIA are also smaller than those of the measured PIA. Simulations using the data of the other two rainfall processes also indicated the similar results.

4. CONCLUSIONS

We investigated the correction method of the NUBF error of the PIA by the surface reference technique in spaceborne radar using the reflectivity data with a high range resolution of 125 m in three rainfall processes occurred in the summer of 2000 near Beijing. We analyzed the possible correlations between the NUBF error and other parameters, such as the reflectivity excursion, the uniform PIA, and the SD and NSD of rainrate, etc., in the IFOV, and found that the PIA error and the SD of rainrate has a trinomial relationship with a quite good correlation, which can be used in the rain retrieval algorithm to correct this NUBF error partially. We compared these trinomial relationships computed from the 125 m range resolution radar data with those from the simulated 1 km resolution radar data, and found that the difference between them cannot be neglected and also increases with the increasing of the SD of rainrate. Therefore, it is very important to use the high resolution radar data in deriving the fitting relationships for the NUBF correction in sapceborne radar. Our simulations indicated that the correction method used in this work could effectively remove the NUBF error. The results presented here will provide valuable references for the system design and the rain retrieval algorithm development of the next generation spaceborne radar.

ACKNOWLEDGMENTS. This work was supported by the National Natural Science Foundation of China under the Contract No. 40075006, the Dept. of Science and technology of China under project No. 2001CCA02200 & 2001CB309402, and the innovation foundation of Institute of Atmospheric Physics.

REFERENCES

Amayenc, P., M. Marzoug, and J. Testud, 1993: Analysis of crossing-beam resolution effects in rainfall rate profile retrieval from a spaceborne radar. *IEEE Trans.*, **GE-31**, 417-425.

——, J. P. Diguet, M. Marzoug, and T. Tani, 1996: A class of single- and dual-frequency algorithms for rain rate profiling from a spaceborne radar, Part II: Tests from airborne radar measurements. *J. Atmos. Oceanic Technol.*, **13**, 142-164.

Durden, S. L., Z. S. Haddad, A. Kitiyakara, and F. K. Li, 1998: Effects of nonuniform beam filling on rainfall retrieval for the TRMM precipitation radar. *J. Atmos. Oceanic Technol.*, **15**, 635-646.

Hitschfeld, W., and J. Bordan, 1954: Errors inherent in the radar measurement of rainfall at attenuating wavelengths. *J. Meteor.*, **11**, 58-67.

Kozu, T., and T. Iguchi, 1999: Nonuniform beamfilling correction for spaceborne radar rainfall measurement: implications from TOGA COARE radar data analysis. *J. Atmos. Oceanic Technol.*, **16**, 1722-1735.

Marecal, V., T. Tani, P. Amayenc, C. Klapisz, E. Obligis, and N. Viltard, 1997: Rain relations inferred from microphysical data in TOGA COARE and their use to test a rain-profiling method from radar measurements at K_u-band. *J. Appl. Meteor.*, **36**, 1629-1646.

Marshall, J. S., and W. M. Palmer, 1948: The distribution of raindrops with size. *J. Meteor.*, **5**, 165-166.

Nakamura, K., 1991: Biases of rain retrieval algorithms for space-borne radar caused by nonuniformity of rain. *J. Atmos. Oceanic Technol.*, **8**, 363-373.

Testud, J., P. Amayenc, and M., Marzoug, 1992: Rainfall-rate Retrieval from a spaceborne radar: Comparison between single-frequency, dual-frequency, and dual-beam techniques. *J. Atmos. Oceanic Technol.*, **9**, 599-623.

——, P. Amayenc, X. Dou, and T. Tani, 1996: Tests of rain profiling algorithms for a spaceborne radar using raincell models and real data precipitation fields. *J. Atmos. Oceanic Technol.*, **13**, 426-453.

The microwave remote sensing group, the Institute of Atmospheric Physics, Chinese Academy of Sciences, 1982: *The Microwave Radiation and Propagation Characteristics of Chinese Clear, Cloudy, and Rainy Atmospheres*. National Defense Industry Press, 161 pp. (in Chinese)

Zhang, Ling, Shuowen Yang, Jinli Liu and Daren Lu, 1998: A method for retrieving inhomogeneous reflectivity fields within the radar beam. *J. of Remote Sensing*, **2**, 81-88. (in Chinese)

——, Ling, Daren Lu, Shu Duan, and Jinli Liu, 2003: Rain spatial nonuniformity and spatial smoothing error of radar rainfall measurement. *Remote Sensing Technology and Application,* **18**, 364-373. (in Chinese)

——, Ling, Daren Lu, Shu Duan, and Jinli Liu, 2004: Small-scale rain nonuniformity and Its effect on evaluation of nonuniform beam filling error for spaceborne radar rain measurement. *J. Atmos. Oceanic Technol.*, (Accepted).

ONE MEASUREMENT OF CLOUD LIQUID CONTENT BY AN AIRBORNE UP-LOOKING MICROWAVE RADIOMETER

Zhang Xiaoqing and Lei Hengchi

Institute of Atmospheric Physics, Chinese Academy of Sciences, Beijing 100029, China

1. INTRODUCTION

Cloud liquid water content is always one of the most important quantities in many subjects and operations, particularly in modification weather conditions of cloud liquid water and supercooled liquid water content are the predetermination conditions of seeding clouds. At present, the measuring methods are not enough and these known methods are in all kinds of shortages.

The airborne up-looking microwave radiometer was used to detect cloud liquid in the 80's of the last century. It isn't easy to make an instrument that must be good at measuring faint signal. With the developing of technology, producing microwave instruments is feasible. So the Institute of Atmospheric Physics, Chinese Academy of Sciences cooperate with Jilin Weather modification office, Changchun consigning the Institute of Geography , Changchun to develop the airborne up-looking microwave radiometer for the first time in China. The measuring results on the 18th April in Yan'an city are introduced in this paper.

2. MEASURING INSTRUMENTS AND CALIBRATION AND RETRIEVAL METHOD OF RADIOMETER

2.1 Measuring instruments

We used the plane of YUN-12 in increasing rain mission artificially in Shanbei region in China in 2003. Besides the microwave radiometer on the plane, particle measuring system(PMS) and GPS and resistance measuring temperature instrument are on it. The microwave radiometer is in wavelength 0.95cm and fixed on the top of the plane. Its antenna is pointed to the sky perpendicularly.

2.2 Calibration and retrieval of data

Calibration and retrieval methods are introduced in detail in some papers. We only introduce retrieval method in brief: Based on historic radiosonde data of Yan'an city, Shanxi Province and on the typical model of profiles of cloud liquid water content for strati, the coefficients of retrieval equation are obtained as the functions of height in July in the city.

3. WEATHER BACKGROUND AND FLIGHT COURSE

On the basis of numerical value forecast we can know precipitation would come on the 18th April. Compositive measuring of cloud liquid content was made that day. The cloud detected was stratus. The plane flew along the route designed.

4. ANALYSE OF CLOUD LIQUID WATER MEASURED

4.1 Vertical distribution of cloud liquid water content

We obtain cloud liquid water content vertical profile obtained by airborne up-looking microwave radiometer and by FSSP-100.Two profiles are approximately consistent and is in correlation to echo of radar. The analyzed result showed the average supercooled liquid water content was 0.0171g/m3 in strati.

4.2 Plane distribution of cloud liquid water content

In the process of plane flying horizontally, the curve of cloud liquid content obtained by the airborne microwave radiometer along the flight course shows existing a high value area of supercooled liquid water content. It was fit to have an increasing rain or snow's operation in the area by seeding cloud. The comparisons of radiometric measurements with 711 digital radar and PMS's measuring results show a good consistency .

5. CONCLUSION

Analysis of cloud liquid content data on the 18th April in Yan'an city measured by airborne instruments shows the following conclusions:

1) In the process of the plane going down, cloud liquid water content vertical profile obtained by airborne up-looking microwave radiometer is approximately consistent with the profile obtained by FSSP-100 and is in correlation to echo of radar. results show that the airborne microwave radiometer can detect the vertical distribution of cloud liquid content and supercooled liquid water content and is better than FSSP-100 in representative character of samples. In the process of plane flying horizontally, the curve of cloud liquid content obtained by the airborne microwave radiometer along the flight course shows existing a high value area of supercooled liquid water content. Because of the restriction of detecting principle and sampling volume, only the value obtained by FSSP-100 is difficult to make sure and find the high value area while the plane flying horizontally at a height. The analyses show that that the airborne up-looking microwave radiometer is a new measuring means in good foreground.

2) Cloud liquid water content data on the 18th April in Yan'an city measured by the airborne microwave radiometer can be used in practice. The vertical profile of cloud liquid content and the profile of temperature's analysis shows making seeding in the upside of strati being helpful for crystal of ice to increase.

6. REFERENCES

[1] Baumgardner, D., Empirical evaluation of airborne liquid water measuring devices, Journal de Recherches Atmosphiques, Clermont-Ferrand, France, 1979, 13(4): 316.

[2] Jiang Fang, Wei Chong, Measurement of Column Cloud Liquid Water Content by Airborne Upward-Looking Microwave Radiometer II:Retrieval Method, Tableland weather, 23(2),2004

[3] Lei Hengchi, Wei Chong, Measurement of Column Cloud Liquid Water Content by Airborne Upward-Looking Microwave Radiometer I:instrument and calibration, Tableland weather, 22(6),2003

[4] J. Warner and J. F. Drake, Field tests of an airborne remote sensing technique for measuring the distribution of liquid water in convective cloud, J. Atmos. Oceanic Tech., 1988, 5: 833-843.

PHYSICOSTATISTICAL MODEL FOR ROAD ICING FORECAST AND CONTROL

N.A.Bezrukova[1], E.A.Stulov[1], M.F.Khalili[2]

[1]Central Aerological Observatory, Dolgoprudny, Moscow Region, 141700 Russia
[2]Moscow State University, Moscow, 119992 Russia

1. INTRODUCTION

Current approaches to developing automated systems of prophylactic road de-icing maintenance imply the availability of an efficient model of slipperiness forecast optimized for a particular area. The effort to reduce de-icing agents consumption and thus to decrease the adverse effects on the environment induce the upgrading of the model employed.

This report presents a model for diagnosing and predicting road icing and packed snow formation based on measurements of automated road weather stations (RWS). The first version of the model BEST-98 by N. Bezrukova and E. Stulov was validated using RWS measurements obtained by the Swedish company TELUB in the winter seasons of 1996-97 and 1997-98 and upgraded in 1999 by Bezrukova and Stulov (2000). In 2002-2003, the model was modified and adjusted for the RWS of the German company Lufft used at some sections of Moscow Ring Road with critical longitudinal slope. This modification consisted in considerable improvement of the meteorological forecasting and diagnosing block and the development of a chemical block governing the dispensing of de-icing agents. Additional introduction of the chemical block extended the scope of application of the program complex ICE_2002 to include both conventional road maintenance and use in automated systems of road icing forecast and control. The model has been adjusted to the conditions of Moscow area.

2. ICE LOADING IN MOSCOW REGION

The cold season of the European part of Russia is characterized by atmospheric circulation processes leading to variable weather, frequent air mass changes accompanied by phase changes close to and below 0^0C. All this makes ice loading and rime formation formation typical of cold season's weather in the European part of Russia.

Moscow area is characterized by the following types of ice and rime phenomena: glazed frost, glaze ice, granular and crystalline rime, radiation rime frost, hoar-frost, packed snow and ice. For motor transport, such phenomena, as hoar-frost, packed snow and ice, glaze ice, and atmospheric glazed frost are the most dangerous ones. The authors have fulfilled climatic zoning for the road network of Moscow area and the neighboring ones in TASIS Report (1997). Based on the classification of glazed frost and rime phenomena, typical combinations of air temperature, humidity, dew-point temperature, form and amount of precipitation, all of them responsible for the above diversity of ice formations and slipperiness on the road, are formalized. Model graphs of the variation of parameters for basic types of ice/snow deposition are plotted using long-term observational data on atmospheric ice deposition presented in the Science Application Manual (1990) and Monthly Meteorological Tables (1966-1990).

3. FORECAST MODEL DESCRIPTION

Russia is lacking a regular network of road weather stations, although a certain progress has been made in its development: the ring motor road around Moscow has been equipped with seven automated road weather stations. However, there is still no regular data exchange between the stations of different subordination and prognostic divisions of the Weather Service. As a first step in developing the model, the authors had to solve the problem of road icing/slipperiness forecast by RWS measurements at a single point. This required forecast to be timely enough to take measures for road treatment with de-icing agents from motor vehicles. For the 1st-class road maintenance, forecast must be issued from 1 to1,5-2 hours in advance.

In many models, the instant at which ice forms on the road is predicted by the road temperature (T_r) approaching dew-point temperature (T_d) in a hazardous range of temperatures close to 0^0C. The critical temperature difference $\Delta T = T_r - T_d$ is commonly taken to be 0.25 – 0.5^0C. This method, straightforward, but crude enough, leads to numerous false alerts and misses of slipperiness events that are not associated with the above temperature difference as with snowfalls. Apart from ice, the traction coefficient on road slopes is reduced on snow compacted by motor vehicles at temperatures close to 0^0C. Note that the role of snow, as a reason for road slipperiness, is especially pronounced on the European territory of Russia.

Corresponding author's address: Natalia A.Bezrukova, Central Aerological Observatory, Pervomayskaya 3, Dolgoprudny, Moscow Region, 141700, Russia; E-Mail: nataly_bez@yahoo.com; Evgeni A. Stulov, stulov_e@yahoo.com; Marat F. Khalili, Physics Department of MSU, 119992 marat_khalili@bigfoot.com

The physicostatistical model ICE_2002 includes:

- a set of typical glaze frost events;
- a scheme of automated search and identification of such events in the course of analyzing measurement data and their prognostic values;
- a system of predicting the time of ice formation.

Slipperiness forecast is forecasted in two steps:

1st step: road surface temperature is predicted according to the developed prediction scheme.

The most important is the prediction of road temperature changing while approaching freezing temperature. The schemes of road temperature prediction developed using only data from RWS sensors, without any other information involved, are as follows:

1. Inertial forecast for a period of 30 min. to 1 hour provided there is a smooth parameter change resulting from heat / cold advection. Under an abrupt change in this process when the role of diurnal temperature variation increases, the probability of errors within ranges close to extremes rises sharply, and changes in the prognostic curve will then fall behind real measurements.

2. A forecast based on an approximate solution of the heat balance equation yielding rather good results under cloudless weather without precipitation.

3. A statistical forecast technique using known correlations between a number of predictors and subsequent temperature and humidity changes. Different combinations of weather parameters measured by RWS can serve here as predictors. In the simplest case, the difference between the temperatures of road surface and air can be such a predictor.

The model allows for diurnal temperature variation by distinguishing its three basic types such as: Advection where time variation of meteorological elements is due to the air mass changing; Air-mass where changes in meteorological elements occur due to diurnal temperature variation, and Mixed where changes in meteorological elements are due to both advection and diurnal temperature variation.

2nd step: Based on prognostic values of road temperature, an expected situation out of a set of typical ones is diagnosed.

To predict road icing 30 to 60 min. in advance, RWS must have sensors to measure road surface and air temperature, relative humidity, precipitation type and intensity, and road surface state. To make a prediction for a 60–120-min. period, additional sensors are required to measure wind speed and direction, temperature at depths of 5 and 30 cm, radiation balance in the range of 0.3 – 40 μ, and atmospheric pressure.

4. DIAGNOSING AND FORECASTING ROAD ICING

The algorithmic block-scheme includes: 1) a control block of RWS input parameters; 2) a block of road temperature forecast; 3) a block of situation diagnosis; 4) a block of decision-making on road treatment agent dosing, and 5) a visualization block, i.e., graphic interface. The block-scheme provides sampling with an interval from one minute to two hours.

In analyzing the current situation, the following parameters and their combinations are used: T_a , T_r and T_d which are temperatures of air, road, and dew point, respectively; relative humidity, f; road temperature change (^{0}C/hr) for the last 30 min, ΔT_r ; type and intensity (I) of current precipitation and their amount for the last 24 hours (R). The diagnostic scheme builds on a principle of a stepwise filter screening of situations with conditions typical of different types of icing phenomena. Depending on the extent of situation hazard, the time concerned is assigned a conventional index, ***ice*** (***0, 1, 2, 3...***). The current index value shows on the traffic dispatcher's computer display. When the index ***ice*** is equal to or more than ***2***, an "***alarm***" signal is given.

The scheme is run on condition that: $T_a < 5^oC$, $T_r < T_{kr}$°C. The critical T_{kr} value is selected taking into consideration the sensor's precision, possible temperature decrease for a period comparable with the measurement interval, and spatial variability of meteorological elements. At $T_{kr} > 1.5$ °C, ice formation on road surface is thought unlikely.

Consecutively, block by block, conditions for possible formation if one or another type of road icing are examined.

The block of diagnosing hoar-frost checks for the condition of direct water vapor sublimation on the road, i.e., a possibility of dew-point temperature exceeding road temperature.

The block of packed snow/ice diagnosing is run in the presence of solid precipitation at road temperature below 0^{0}C, in case of heavy precipitation at $I > 0.3$ mm/hr. or when the integral amount of precipitation for the last 24 hours $R > 5$ mm.

The block of glazed ice diagnosing distinguishing situations that may lead to freezing precipitation that fell out before or melt water at road temperature tending to decrease during the last measurement interval or coincidence of two conditions:

$-1.0 < T_r < 0.5$ ***and*** $\Delta T_r < -0.5$.

5. CHEMICAL BLOCK OF PROPORTIONING DE-ICING ACTIONS

In the model, apart from road surface temperature, the amount of water on the road surface is also predicted, which is necessary in case of heavy precipitation for launching preventive actions.

The algorithm of issuing recommendations for salt dispersal over the road surface is aimed at preventive anti-ice road treatment in the zone of the system's responsibility. Also, the algorithm is designed to minimize the agent consumption. The recommendations are given as surface density values (g/m^2) of the dispersed salt. In issuing recommendations, the algorithm

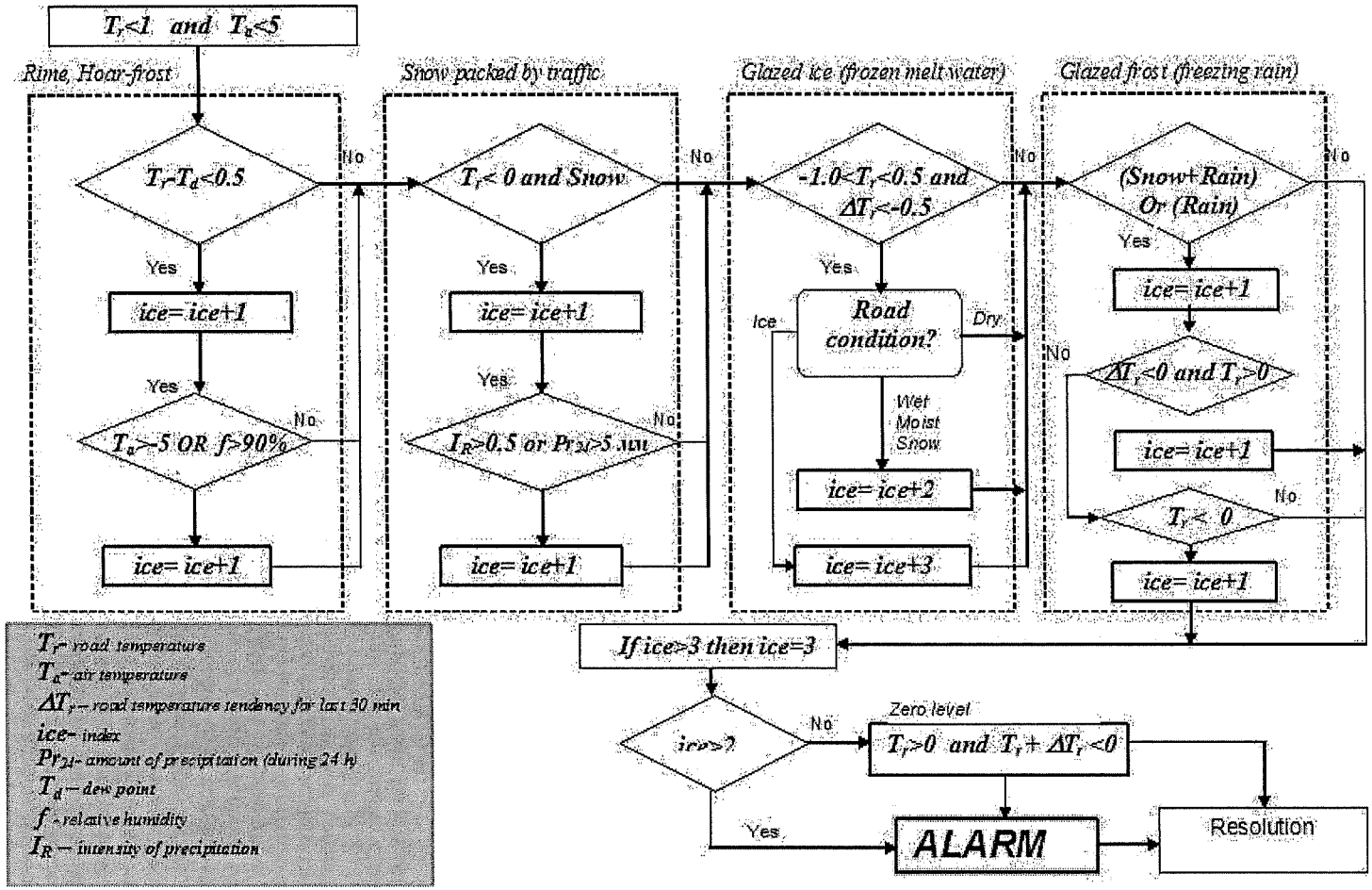
$T_r<1$ and $T_a<5$
Rime, Hoar-frost
$T_r-T_d<0.5$
Yes
No
ice= ice+1
Yes
$T_a>-5$ OR $f>90\%$
No
ice= ice+1
Snow packed by traffic
$T_r<0$ and Snow
Yes
No
ice= ice+1
Yes
$I_R>0.5$ or $Pr_{24}>5$ mm
No
ice= ice+1
Glazed ice (frozen melt water)
$-1.0<T_r<0.5$ and $\Delta T_r<-0.5$
Yes
No
Road condition?
Ice
Dry
Wet
Moist
Snow
ice= ice+2
ice= ice+3
Glazed frost (freezing rain)
(Snow+Rain) Or (Rain)
Yes
No
ice= ice+1
$\Delta T_r<0$ and $T_r>0$
No
ice= ice+1
$T_r<0$
No
ice= ice+1
T_r - road temperature
T_a - air temperature
ΔT_r – road temperature tendency for last 30 min
ice - index
Pr_{24} - amount of precipitation (during 24 h)
T_d – dew point
f - relative humidity
I_R – intensity of precipitation
If ice>3 then ice=3
ice>2
No
Zero level
$T_r>0$ and $T_r+\Delta T_r<0$
Yes
ALARM
Resolution

is guided by information about the state of road surface state at road sensor location. Accordingly, the position of this sensor must specifically suit the zone of responsibility concerned. Besides, the distribution of agent over the road surface is assumed to be uniform.

In some cities, in order to reduce ecological loading, legal limitations on the amount of agent to be dispersed are introduced. If the predicted amount of agent per unit area to be used exceeds the adopted norm a signal of emergency is applied and automated agent dispersal is stopped. This may be due to a very low temperature of the road surface, a large amount of water on the road, or a combination of these factors. The program continues running and issuing recommendations for road maintenance services to switch to another de-icing technique. In such a case, it is recommended that conventional means of road maintenance say motor snow-removers, be employed.

6. MODEL EVALUATION

During the winters of 1996/97 and 1997/98, the model was being evaluated using data from two weather stations – RWS-102 of Road Maintenance Office (RMO) No.14 in Oktiabrsky, Moscow Region, and RWS-104 in Tver Region. The obtainable model diagnosis and a test forecast for a 2-hr. period were compared with the regular records in the log of the RMO shift supervisor and hourly data from the nearest weather stations.

The verification of the model by the data of RWS-102 indicated that the relative skill score of slipperiness diagnosing was 79% (Fig.1) in the winter 1997/98 when no precipitation measurements were available at the station and 83% (Fig.2) in the winter 1996/97, with false alerts of 13 and 15% and missed events of 8 and 2%, respectively.

The model verification by the data of RWS-104 showed faultless diagnosing in the winter 1997/98 to be 89%, with false alerts of 10% and missed events of 1%. The results of verifying the scheme run in a diagnosing regime show its suitability for use in a prognostic regime.

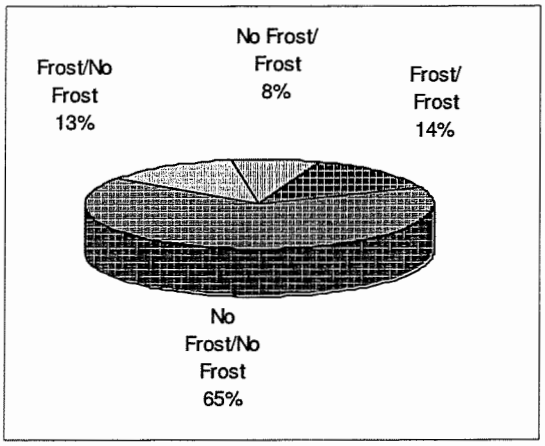

Fig. 1 Percentage of Correct Frost Diagnosis, 125 days of winter 1997/98, no data about precipitation.

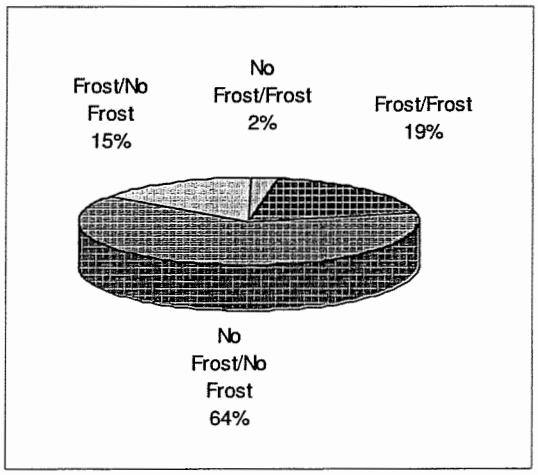

Fig. 2 Percentage of Correct Frost Diagnosis,135 days of winter 1996/97.

7. ACKNOWLEDGMENTS

The authors are thankful to the former Chief of RMCO No.14 V.Yu. Travkin , Director General of the National Chamber of Industry and Commerce S.Yu. Panov, and their staff for having enabled the authors' working with the on-line data of the automated road stations. The subsequent updating of the prognostic model has been made possible due to the authors' participation in the project for the development of an automated de-icing system at the flyover of the Yaroslavl road junction of Moscow Ring Road.

8. REFERENCES

1. Bezrukova, N. A., Stulov, E. A., 2000: Physics-statistical model BEST-98 for road ice formation control and forecast. International Seminar GURME, **WMO**, Moscow, November, 1999.

2. Implementation Plan for Road Weather Information System, 1997: **Tacis** Report 7.1 (Edition: Bezrukova, N.A., Dunkel, G.), Federal Highway Administration of Russia.

3. Monthly Meteorological Tables, 1971-1990: Part 1, Novosibirsk, Gidrometeoizdat, (in Russian).

4. Science Application Handbook on the USSR Climate, 1990: Ser. 3, part 1-6, vyp. 8, Leningrad, Gidrometeoizdat (in Russian).

APPLICATION OF A SEMI-SPECTRAL CLOUD WATER PARAMETERIZATION TO COOLING TOWER PLUMES

Emmanuel Bouzereau[+°], Luc Musson-Genon°, Bertrand Carissimo°, Éric Dupont°

° CEREA (joint lab. EDF R&D - ENPC), 6, quai Watier, BP 49 - 78401 Chatou Cedex, France
[+] University Pierre et Marie Curie Paris VI, LODYC-IPSL, France

I. INTRODUCTION

MERCURE, an anelastic and non-hydrostatic 3D meteorological model, developed at EDF (Carissimo *et al.*, 1997), has been modified to introduce a new parameterization of the cloud liquid water. This modification was necessary in order to better simulate cloudy atmospheres, especially the cooling tower plumes and its interactions with fogs or natural clouds. It will also permit to better describe the interactions of the cloudy atmosphere with the atmospheric pollutants, the radiation transfer ...

To do so, we developed a double-moment parameterization for the cloud liquid water. We have then used the model to simulate the plumes produced by the four natural draft cooling towers of the Bugey electrical power plant, which is located on the Rhone River in France. To validate our model outputs, we have used the data of the measurement campaign carried out at Bugey in 1980. These data are composed of meteorological radiosoundings, photographic records of the plumes, microphysical measurements inside one cooling tower and airborne microphysical and dynamical measurements inside the plume at various heights (Hodin, 1980 and Hodin *et al.*, 1981).

II. MICROPHYSICS

Microphysical processes inside the plume are parameterized by assuming that the main phenomenon governing droplet evolution is condensation and evaporation. This assumption is justified by the fact that the coalescence mechanism, fundamental in the further growth of droplet, starts to be efficient for droplets bigger than 10 to 20 µm in radius and that droplets bigger than 25 µm in diameter are almost never found in the measured droplets spectra (the mean diameters found lie between 4.8 and 16.2 µm). It is also important to take into account the nucleation, the only source of new droplets in the free atmosphere, as we will see in our results.

Hence, we have developed a semi-spectral cloud water parameterization based on the cloud water literature described below. This model is based on a sub-grid scale diagnosis of the liquid water content (LWC) and on a prognostic equation for the cloud droplet number concentration (N_c). The sub-grid scale LWC is diagnosed from: the prognostic variables liquid water potential temperature and total water specific humidity, following the work of Bougeault (1981).

While the condensation and evaporation processes are implicitly taken into account by the sub-grid scale diagnosis for the LWC, these processes are parameterized explicitly for the N_C, as in Cohard and Pinty (2000). The nucleation is also explicitly described according to the parameterization of Pruppacher and Klett (2000) and Chaumerliac *et al.* (1987).

Cloud droplets are assumed to be log-normally distributed; the parameters of the distribution are LWC, N_c and the width. The latter has to be fixed for all the simulation.

III. DATA

In this article, we will focus on the information collected on 13 March 1980. On this day, the radiosoundings were recorded at 1pm and 7pm at Satolas (15 km far from Bugey) and at 2:30pm at Loyettes (1 km far from Bugey). The in-cloud airborne measurements were carried out between 4:09pm and 4:42pm, whereas the photographic records of the plumes were taken at about 5:20pm. On the ground, the temperature and the humidity were recorded hourly, and the pressure every 3 hours. Furthermore, the temperature, the vertical velocity and the LWC at the top of the towers had been computed previously by a specific code. Finally, some information on the droplet spectra at the top of

Corresponding author's address: Emmanuel Bouzereau, CEREA (joint lab. EDF R&D - ENPC), 6, quai Watier, BP 49 - 78401 Chatou Cedex, France; E-Mail: emmanuel.bouzereau@edf.fr

the towers can be extrapolated from droplet spectra measurements inside one cooling tower.

We interpolate the meteorological soundings to simulate two cases: **case A**, the shape of the plume at 5:20pm, and **case B** the dynamic and the microphysics at about 4:30pm. In **case A**, we compare the simulated plume with in-situ photographs analysis at 5:20pm. In **case B**, we compare our results with those given by airborne measurements.

IV. COMPUTATION

In these simulations, the grid mesh is structured and Cartesian. The grid spacing is constant along the vertical axis (Δz=60m), but spatially variable on the horizontal axes: from 15m around the towers to 100m near the boundaries. Besides, each of the four towers is modeled by a bloc of 2 meshes high (120m almost as high as the real towers high of 128m) and with a section of 16 square meshes (60mx60m, close to the real section of 3.632 m²).

We impose meteorological profiles on the upstream: the front and the left lateral boundaries. At the ground, there are frictional surface conditions; on the other boundaries, there are free flow conditions with imposed pressure. At the top of the towers, vertical velocity, temperature, humidity, LWC and N_c are imposed from measurements and computations or extrapolations; kinetic turbulent energy and its dissipation are fixed from high-resolution tower simulations performed independently. The N_c value at the top of the towers is fixed at 5.000 cm^{-3} for the case B with nucleation and at 10.000 cm^{-3} for the case B without nucleation. These values lie within the range found for N_c inside the towers, from 5.000 to 25.000 cm^{-3}, and give the best fit with the first spectra met (FIG. 4a and 5a). Note that we perform a steady state simulation, all the boundary conditions being fixed as constant.

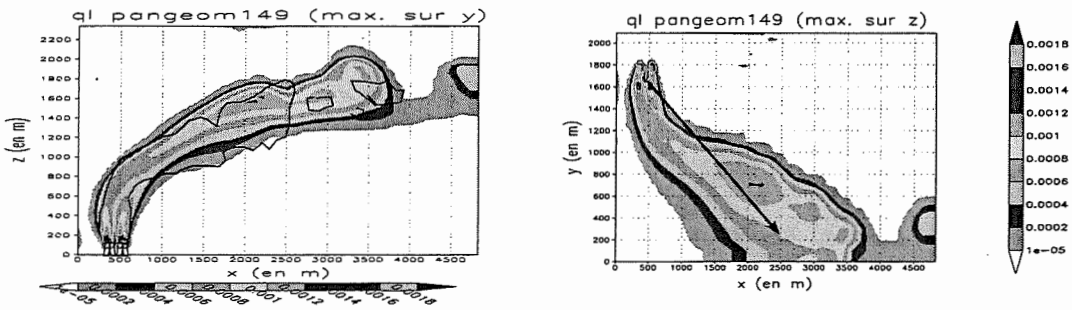

FIG. 1 **Case A**: Shaded plots of the maximum of the LWC (kg/kg). The black contour plot is the actual plume contour from photographic records [from side]. The black arrow is the actual plume main direction [from above].

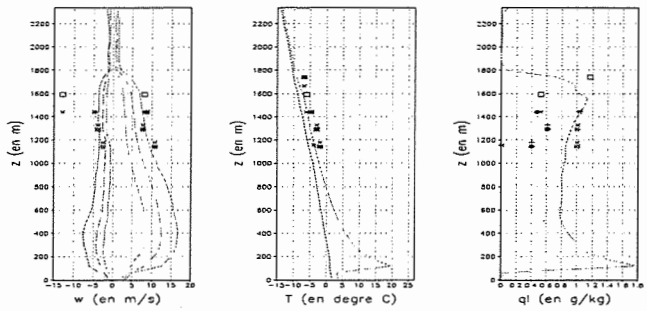

FIG. 2 **Case B**: Comparison simulation results vs. airborne measurements. On the left, extremum of the vertical velocity. Dotted line: W; dashed line: $W\pm(2k)^{1/2}$; solid line: $W\pm2(2k)^{1/2}$ (k is the TKE, and $(2k)^{1/2}$ an approximation of σ_w). Squares are airborne measurements of the extremum of the instant vertical velocity at one flight level. In the middle, solid lines: extremum of the temperature; squares: temperature average through the plume. On the right, solid lines: maximum of the LWC. Squares: from FSSP sensor; rounds: from Johnson-Williams sensor. + and x are raw data whereas •, ■, ○ and □ are obtained after re-computing the altitude from pressure and temperature profiles; ○ and □ have high uncertainties in altitude or in measurement.

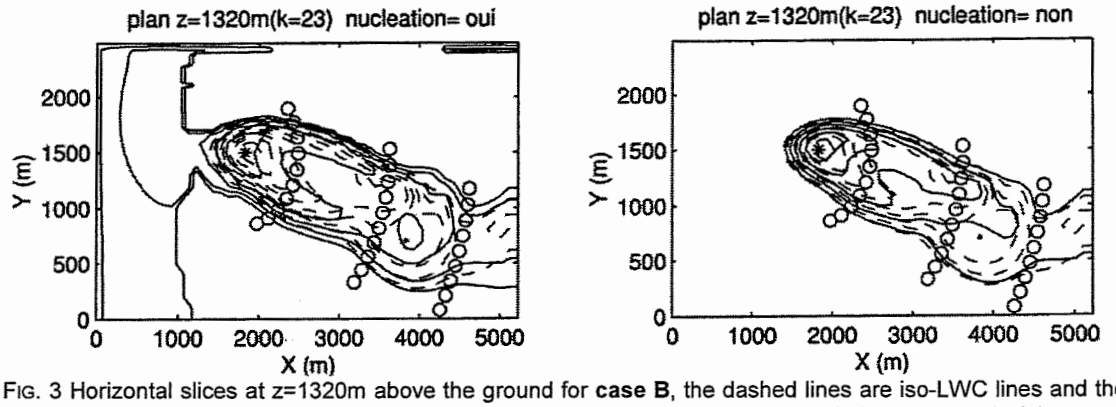

FIG. 3 Horizontal slices at z=1320m above the ground for **case B**, the dashed lines are iso-LWC lines and the solid lines are iso-N_c lines. The symbol * shows the maximum of LWC, and the circles **o** are part of the same arc whose center is *. The nucleation is activated on the left figure but not activated on the right.

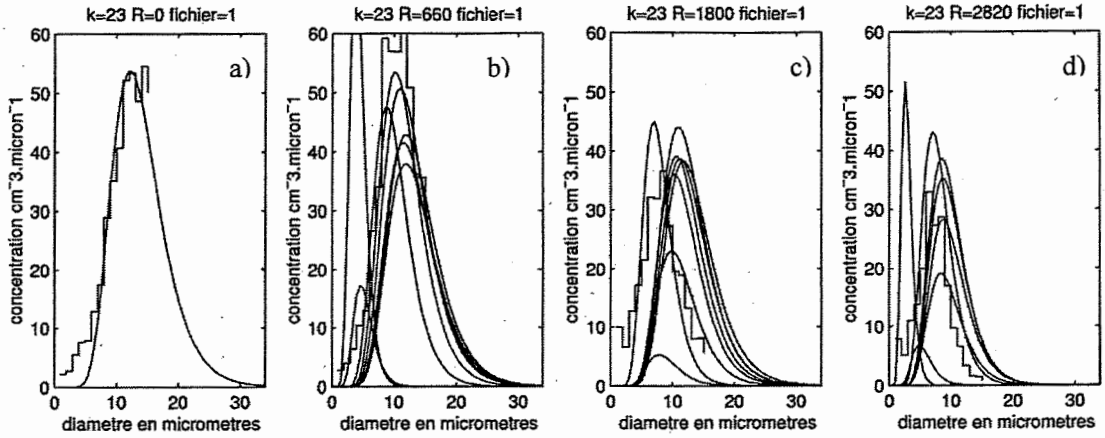

FIG. 4 Comparison of the in-situ spectra measured by the aircraft (step curves) with the simulated ones (log-normal curves) for increasing distance R. The nucleation is activated. The figure a) shows the first measured spectra and the log-normal curve obtained from the LWC and N_c values given by the code at the position marked by a * in FIG. 3. The figure b) shows the measured spectra 660m further and the log-normal curves; these latter are obtained from the LWC and N_c values given by the code at the **o** of the first arc located 660m far from the *. Idem for the figures c) and d) but at, respectively, 1800m and 2820m far from *.

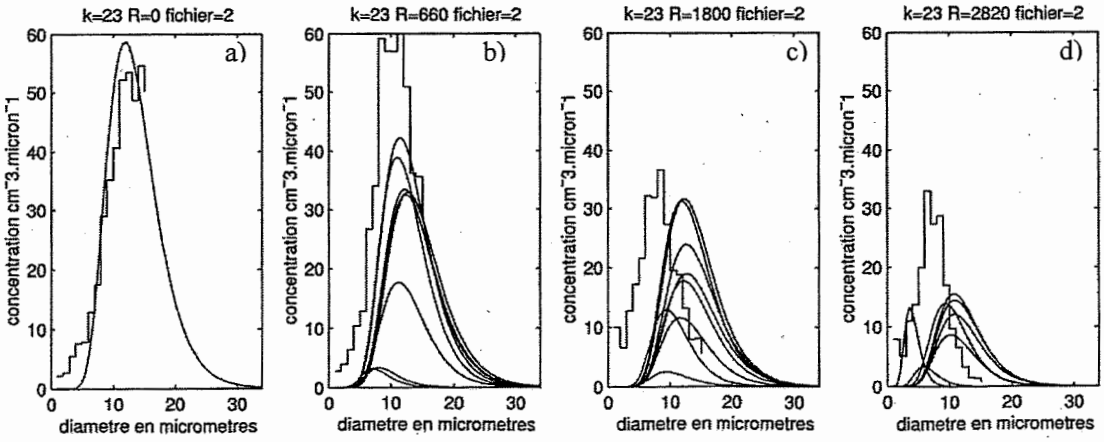

FIG. 5 As FIG. 4 but without nucleation.

V. RESULTS

From vertical and horizontal cross section of LWC in **case A** (Fig. 1), we can see that the shape as well as the direction of the plume are well simulated. From detailed aircraft measurements in **case B** (Fig. 2), we have a good agreement between measurements and simulations, even if the model temperature is a bit too cold and the model LWC values are slightly overestimated (although they lie between the observed values of the two types of sensors, they are two times bigger than the Johnson-Williams reference sensor). This can be due to the difference between the real temperature and humidity profiles at 4:30pm, and the interpolated profiles used for the simulation.

The figure 4, with nucleation activated, show a good agreement between the airborne spectra measurements and the simulated ones. From the figures 4 and 5, the process of nucleation appears necessary to reproduce well the in-situ data. Note that during the flight, whereas the altitude and cruise speed (60m/s) are well known, we do not know very accurately the direction of the airplane. Moreover, the position of the airplane, when the first spectrum is measured, cannot be very precisely known. This is the raison why we decided to compare the first measured spectrum with the simulated spectrum at the location of the maximum of LWC. For the followings measured spectra, we chose to compare each of them with a set of 10 simulated spectra located at the same distance R to the first spectrum.

It has to be noted that our numerical results are sensitive to the turbulence closure and the turbulent variables imposed at the boundaries (especially the forcing at the top of the cooling towers) because of the strong wind gradients. Other sensitivity tests have been carried out with a smaller influence on the results: buoyancy flux, sub-grid scale distributions ... Apart from turbulent variables, it is of course very important to know as well as possible the forcing due to the cooling towers and the meteorological profiles since it is responsible for the dynamical and physical framework of the simulated case.

VI. CONCLUSIONS

The results obtained show that, on a typical local scale of few kilometers, the two-moment cloud microphysics can reproduce well the main dynamical, physical and microphysical characteristics of the observed plumes. For a more complete validation, this encouraging simulation will be followed by the simulations of other plume cases. In our future works, we will study the interactions between the cooling tower plumes and natural clouds (including fogs) and we will investigate the effect of the precipitating cloud on the plume. The microphysical scheme of MERCURE has already been completed by a two-moment rainwater parameterization under validation.

REFERENCES

Bougeault Ph., 1981: Modeling the trade-wind cumulus boundary layer. Part I: Testing the ensemble cloud relations against numerical data *J. Atmos. Sci.*, 39, 2691-2700.

Carissimo B., E. Dupont, L. Musson-Genon and O. Marchand, 1997, Note de principe du code MERCURE. Version 3.2, EDF-DER, Technical Note HE-33/97/002A.

Chaumerliac N., E. Richard, J.-P. Pinty and E.C. Nickerson, 1987: Sulfur scavenging in a mesoscale model with quasi-spectral microphysics: Two-dimensional results for continental and maritime clouds. *J. Geophys. Res.*, 92, 3114-3126.

Cohard J.-M. and J.-P. Pinty, 2000: A comprehensive two-moment warm microphysics bulk scheme. I : Description and tests. *Quart. J. Roy. Meteor. Soc.*, 126, 1815-1842.

Hodin A., 1980: Etude expérimentale des panaches des réfrigérants atmosphériques du Bugey 4-5. Premier bilan des mesures physiques effectuées entre le 25 février et le 13 mars 1980, EDF, Technical Note HE/32-80.33.

Hodin A., C. Allet and J.-P. Pinty, 1981: Structure dynamique et microphysique des panaches des réfrigérants atmosphériques de la centrale du Bugey. Campagne expérimentale de février-mars 1980, EDF, Technical Note HE/32-81.36.

Pruppacher H.R. and J.D. Klett, 2000: Microphysics of Clouds and Precipitation. Atmospheric Science Library. Kluwer Academic Publishers, Boston, MA. Second Revised and Enlarged Edition with an Introduction to Cloud Chemistry and Cloud Electricity.

AN OVERVIEW OF THE RECENT NATIONAL RESEARCH COUNCIL OF THE NATIONAL ACADEMY OF SCIENCES REPORT ON: CRITICAL ISSUES IN WEATHER MODIFICATION RESEARCH

R. T Bruintjes[1] and M. Garstang[2]

[1]National Center for Atmospheric Research, P.O. Box 3000, Boulder, CO 80307, USA
[2]University of Virginia, Charlottesville, Virginia.

1. INTRODUCTION

The NRC report is the latest in a series of assessments of weather modification carried out by the National Academies, which produced reports in 1964, 1966, and 1973, aimed at guiding weather modification research and policy development. The last National Academies report is nearly three decades old and, despite more recent assessments by other bodies such as the American Meteorological Society and the World Meteorological Organization, a need was seen for an evaluation of weather modification research and operations in the United States.

In November 2000, the National Academies' Board on Atmospheric Sciences and Climate (BASC) organized a program development workshop to assess whether it would be useful to take a fresh look at the scientific underpinnings of weather modification. A year later, a study committee was convened, and four committee meetings were held over eight months. The Committee received input from individuals in federal and state agencies, scientists who have or are conducting relevant research, and professionals active in operational weather programs. The charge to the Committee explicitly excluded consideration of the complex social and legal issues associated with weather modification. This part of the question is of such importance in any weather modification effort that the Committee did go so far as to note, but not elaborate upon, the most critical questions in this area. Also in accordance with its charge, the Committee did not address inadvertent global-scale modification of climate and weather (e.g., global warming). However, the potential local and regional impacts of both intentional and inadvertent weather modification are considered.

2. MOTIVATION AND TASK

The weather on planet Earth is a vital and sometimes fatal actor in human affairs. Efforts to control or reduce the harmful impacts of weather go back far in time. In recent decades our ability to observe and predict various types of meteorological systems has increased tremendously.

Increasing demands for water require that the potential for enhancing the sources, storage, and recycling of freshwater be examined carefully. Destruction and loss of life due to severe weather, which is increasing with population growth and changing demographics, require that we examine ways to reduce these impacts. In addition, there is ample evidence that human activities worldwide, such as the emission of industrial air pollution, can alter atmospheric processes on scales ranging from local precipitation patterns to global climate. Documentation of anthropogenic effects on the weather strengthens the physical basis for deliberate attempts to alter the weather. These inadvertent impacts on weather and climate require a concerted research effort, yet the scientific community has largely failed to take advantage of the fact that many of the scientific underpinnings of intentional and unintentional weather modification are the same.

In this, the latest National Academies' assessment of weather modification, the Committee was charged to present an updated assessment of the ability of current and proposed weather modification capabilities to provide beneficial impacts on water resource management and weather hazard mitigation. It was asked to examine new technologies, such as ground-based, in situ, and satellite detection systems, and fast reacting seeding materials and dispensing methods. The Committee also was asked to review advances in numerical modeling on the cloud- and meso-scale and consider how improvements in computer capabilities might be applied to weather modification. This study was not designed to address policy implications of weather modification; rather it focused on the research and operational issues. Specifically, the Committee was asked to:

- review the current state of the science of weather modification and the role of weather prediction as it applies to weather modification, paying particular attention to the technological and methodological developments of the last decade;
- identify the critical uncertainties limiting advances in weather modification science and operation;
- identify future directions in weather modification research and operations for improving the management of water resources and the reduction in severe weather hazards; and
- suggest actions to identify the potential impacts of localized weather modification on large-scale weather and climate patterns.

3. CURRENT OPERATIONAL AND RESEARCH EFFORTS

Corresponding author's address: Roelof T. Bruintjes, National Center for Atmospheric Research, P.O. Box 3000, Boulder, CO 80307, USA; Email: roelof@ucar.edu

The growing evidence that human activities can affect the weather on scales ranging from local to global has added a new and important dimension to the place of weather modification in the field of atmospheric sciences. There is a need, more urgent than ever, to understand the fundamental processes related to intentional and unintentional changes in the atmosphere. The question of how well current technology, practice, and theory are equipped to meet these broader goals of weather modification is central to the report. The challenge to find the right balance between assured knowledge and the need for action is one which must guide the future actions of scientists, practitioners, and administrators concerned with weather modification.

By the late 1970's, difficulties in demonstrating repeatability of weather modification experiments, providing convincing scientific evidence of success, and overcoming serious social and legal problems led to the moderation of the early predictions of success in weather modification. The need to understand the fundamental physical and chemical processes underlying weather modification became obvious, and a dedicated research effort was repeatedly recommended by successive national panels. Failure to devote significant public and private resources to basic research polarized both the support agencies and scientific community, generating serious feelings of ambivalence within these communities toward weather modification.

Despite significant advances in computational capabilities to deal with complex processes in the atmosphere and remarkable advances in observing technology, little of this collective power has been applied in any coherent way to weather modification. The potential for progress in weather modification as seen by the Committee is dependent upon an improved fundamental understanding of crucial cloud, precipitation, and larger-scale atmospheric processes. The Committee believes that such progress is now within reach should the current advances be applied in a sustained manner to answer fundamental outstanding questions. While the Committee acknowledges the prospect of achieving significant advances in the ability of humans to exercise a degree of control over the weather, it cautions that such progress is not possible without a concerted and sustained effort at understanding basic processes in the atmosphere. Furthermore, such results are as likely to lead to viable weather modification methodologies as they are to indicate that intentional modification of a weather system is neither currently possible nor desirable.

Advances stemming from weather modification research will produce results well beyond the initial objective and will lead to applications in totally unexpected areas. For example, the ability to make useful precipitation forecasts, particularly from convective storms, may be a valuable by-product of weather modification research. The Committee is also acutely conscious of the fact that, particularly in modifying severe weather, researchers may be required to have, before attempting treatment, a reliable and proven ability to predict what would have taken place had the system not been treated. As a chaotic system, the atmosphere is inherently predictable only for a limited time, with the time limit shorter for smaller spatial scales. Thus, predictions must be couched in probabilistic terms that may not satisfy the user community that a reliable prediction has been made.

Operational weather modification programs, which primarily involve cloud-seeding activities aimed at enhancing precipitation or mitigating hail fall, exist in more than 24 countries (more than 100 projects), and there were at least 66 operational programs being conducted in 10 states across the United States in 2001. Despite the large number of operational activities, less than a handful of weather modification research programs are being conducted worldwide (eg. United Arab Emirates, Israel, Mexico, Japan, China and a few projects in the USA).

Several assessments of individual seeding projects, or groups of projects, have been made by individual scientists familiar with cloud physics and cloud seeding but not directly involved with the projects they assess. Generally speaking, these authors conclude that cloud-seeding experiments have not yet provided the evidence required to establish scientific validity, though the prospects are promising and worth pursuing.

The dilemma in weather modification is that while little funding is available for research and understanding others are willing to spend funds to apply technologies which are not scientifically accepted. We know that human activities can affect the weather, and we know that seeding will cause some changes to a cloud. However, we still are unable to translate these induced changes into verifiable changes in rainfall, hail fall, and snowfall on the ground, or to employ methods that produce credible, repeatable changes in precipitation. Among the factors that have contributed to an almost uniform failure to verify seeding effects are such uncertainties as the natural variability of precipitation, the inability to measure these variables with the required accuracy or resolution, the detection of a small induced effect under these conditions, and the need to randomize and replicate experiments.

The increase in operational programs over the past 10 years indicates a growing perceived need for enhancing water resources and mitigating severe weather in many parts of the world, including the United States. For users and operators of weather modification technologies, the decision of whether to implement or continue an operational program is a matter of cost-benefit risk management, which raises questions about what constitutes "successful" modification. Cloud-seeding experiments have shown mixed results, but many operational cloud-seeding programs continue, based on what is seen in some instances as strong probabilistic evidence of positive seeding-induced effects. The absence of adequate

understanding of critical atmospheric processes is seen as the primary reason for the lack of predictable, detectable and verifiable results.

4. PROMISING DEVELOPMENTS AND ADVANCES.

Despite the lack of scientific proof, our scientific understanding has progressed on many fronts in the last twenty years. For instance, there have been substantial improvements in the ice-nucleating capabilities of new seeding materials. Recent experiments using hygroscopic seeding particles in water and ice (mixed-phase) clouds have shown encouraging results, with precipitation increases attributed to increasing the lifetime of the rain-producing systems. There are strong suggestions of positive seeding effects in winter orographic glaciogenic systems (i.e., cloud systems occurring over mountainous terrain). Satellite imagery has underlined the role of high concentrations of aerosols in influencing clouds, rain, and lightning, thus drawing the issues of intentional and inadvertent weather modification closer together. Changing levels of background aerosols associated with inadvertent weather modification can influence the potential for deliberate weather modification. This and other recent work has highlighted critical questions about the microphysical processes leading to precipitation, the transport and dispersion of seeding material in the cloud volume, the effects of seeding on the dynamical growth of clouds, and the logistics of translating storm-scale effects into an area-wide precipitation effect. By isolating these critical questions, which currently hamper progress in weather modification, future research efforts can be focused and optimized.

Additional advances in observational, computational, and statistical technologies have been made over the past two to three decades. These include, respectively, the capabilities to (1) detect and quantify relevant variables on temporal and spatial scales not previously possible; (2) acquire, store, and process vast quantities of data; and (3) account for sources of uncertainty and incorporate complex spatial and temporal relationships. Computer power has enabled the development of models that range in scale from a single cloud to the global atmosphere. Numerical modeling simulations—validated by observations whenever possible—are useful for testing intentional weather modification and corresponding larger-scale effects. Few of these tools, however, have been applied in any collective and concerted fashion to weather modification.

5. CRITICAL UNCERTAINTIES

The report identifies areas of critical uncertainties where future research efforts should be focused. These are summarized below with statements in boldface type considered to have the highest priority.

1. *Cloud and precipitation microphysics issues*

- **Background concentration, sizes, and chemical composition of aerosols that participate in cloud processes**
- Nucleation processes as they relate to chemical composition, sizes, and concentrations of hygroscopic aerosol particles
- Ice nucleation (primary and secondary)
- Evolution of the droplet spectra in clouds and processes that contribute to spectra broadening and the onset of coalescence
- Relative importance of drizzle in precipitation processes

2. *Cloud dynamics issues*

- **Cloud-to-cloud and mesoscale interactions as they relate to updraft and downdraft structures and cloud evolution and lifetimes**
- Cloud and sub-cloud dynamical interactions as they relate to precipitation amounts and the size spectrum of hydrometeors
- Microphysical, thermodynamical, and dynamical interactions within clouds

3. *Cloud-modeling issues*

- **Combination of the best cloud models with advanced observing systems in carefully designed field tests and experiments**
- Extension of existing and development of new cloud-resolving models explicitly applied to weather modification
- Application of short-term predictive models including precipitation forecasts and data assimilation and adjoint methodology in treated and untreated situations
- Evaluation of predictive models for severe weather events and establishment of current predictive capabilities including probabilistic forecasts
- Advancement of the capabilities in cloud models to simulate dispersion trajectories of seeding material
- Use of cloud models to examine effects of cloud seeding outside of seeded areas
- Combination of cloud models with statistical analysis to establish seeding effects

4. *Seeding issues*

- **Targeting of seeding agents, diffusion and transport of seeding material, and spread of seeding effects throughout the cloud volume**
- Measurement capabilities and limitations of cell-tracking software, radar, and technologies to observe seeding effects
- Analysis of recent observations with new instruments of high concentrations of ice crystal
- Interactions between different hydrometeors in clouds and how to best model them
- Modeling and prediction of treated and untreated conditions for simulation
- Mechanisms of transferring the storm-scale effect into an area-wide precipitation effect and tracking possible downwind changes at the single cell, cloud cluster, and floating target scales

6. RECOMMENDATIONS AND CONCLUSIONS

Because weather modification could potentially contribute to alleviating water resource stresses and severe weather hazards, because weather modification is being attempted without clear scientific proof supporting or refuting its efficacy, because inadvertent atmospheric changes are a reality, and because an entire suite of new tools and techniques now exist that could be applied to this issue, it is recommended that there be a renewed commitment to advancing our knowledge of fundamental atmospheric processes that are central to the issues of intentional and inadvertent weather modification. Such an effort must be sustained, nationally coordinated and draw upon existing research programs and facilities.

In particular, a sustained research effort is called for in the areas of cloud and precipitation microphysics, cloud dynamics, cloud modeling, and cloud seeding for enhancement of atmospheric water resources, mitigation of weather hazards, and understanding of inadvertent atmospheric effects. Such an effort must be directed at answering fundamental scientific questions, which will yield results that go well beyond application to intentional modification. The emphasis must be on understanding processes and not on modification.

Weather modification should be viewed as a fundamental and legitimate part of atmospheric and environmental science. Due to the growing demand for freshwater, the increasing levels of damage and loss of life resulting from severe weather, and the reality of inadvertent atmospheric changes, there is an unprecedented responsibility on the scientific community to assess the potential efficacy and value of intentional weather modification technologies. Some specific recommendations for a coordinated research program should include: capitalizing on new remote and *in situ* observational tools (e.g., doppler/polarimetric lidars, radars and satellites, microwave radiometers, new cell-tracking software, and new airborne in-situ instrumentation, etc.) to carry out exploratory and confirmatory experiments in a variety of cloud and storm systems. Some especially promising possibilities where substantial further progress may occur include:

➢ *Hygroscopic seeding to enhance rainfall.* The small-scale experiments and larger-scale coordinated field efforts proposed by the wmo report on the workshop on hygroscopic seeding could form a starting point for such efforts.

➢ *Glaciogenic cloud seeding to enhance precipitation.* A randomized program that includes strong modeling and observational components, employing advanced computational and observational tools could substantially enhance our understanding of seeding effects and winter orographic precipitation.

➢ *Studies of specific seeding effects.* This may include studies such as those of the initial droplet broadening and subsequent formation of drizzle and rain associated with natural, hygroscopic seeding and anthropogenic sources of particles.

➢ *Improving cloud model treatment of cloud and precipitation physics.* Special focus is needed on modeling cloud microphysical processes.

Although there still is no convincing scientific proof of the efficacy of intentional weather modification efforts, probabilistic evidence for seeding-induced changes is strong in some instances. This lack of proof does not challenge the scientific basis of weather modification concepts. Rather it is the absence of adequate understanding of critical atmospheric processes that, in turn, lead to a failure in producing predictable, detectable, and verifiable results. Questions such as the transferability of seeding techniques or extra area effects can only be addressed through sustained research of the underlying science combined with carefully crafted hypotheses and physical and statistical experiments.

In closing, the committee felt strongly that the scientific community has an obligation to advance our understanding of issues related to weather modification. The basic science that will be learned in pursuing questions related to weather modification undoubtedly will lead to knowledge and capabilities in unexpected areas.

7. ACKNOWLEDGEMENTS

This paper is based on a recent report conducted by The National Academies' National Research Council. The report, entitled "Critical Issues in Weather Modification Research", was written by a committee of 10 people with expertise in weather modification, cloud physics and numerical modeling. The committee consisted of the following members: Michael Garstang (*chair*), University of Virginia, Charlottesville; Roscoe R. Braham, jr., North Carolina State University, Raleigh; Roelof T. Bruintjes, National Center for Atmospheric Research, Boulder, Colorado; Steven F. Clifford, University of Colorado, Boulder; Ross N. Hoffman, Atmospheric & Environmental Research, Inc., Lexington, Massachusetts; Douglas K. Lilly, University of Oklahoma, Norman; Roland List*, University of Toronto, Ontario, Canada; Robert J. Serafin, National Center for Atmospheric Research, Boulder, Colorado; Paul D. Try, Science & Technology Corporation, Silver Spring, Maryland; Johannes Verlinde, Pennsylvania State University, University Park

" Resigned 9/02

8. REFERENCES

National Research Council of the National Academy of Sciences, 2003, *Critical Issues in Weather Modification Research*, Board on Atmospheric Sciences and Climate, Division on Earth and Life Studies, National Research Council of the National Academy of Sciences, The National Academy Press, 123pp.

NUMERICAL SIMULATION OF AFFECTING RANGE FOR CLOUD SEEDING WITHIN SUPER-COOLED STRATIFORM CLOUD

Jin Dai[1], Xing Yu[1], Peng Fan[2] and Zhengqi Chen[2]

[1]Meteorological Institute of Shaanxi Province, Xi'an, 710015, China
[2]Center of Weather Modification of Shaanxi Province, Xi'an, 710015, China

1. INTRODUCTION

It is essential to learn whether the seeding material can reach the suitable positions and scope in precipitation enhancement within super-cooled stratiform cloud. Once the synoptic situation and the seeded cloud are determined in the process of cloud seeding, the seeding effect will depend on the seeding material concentration. The pertinent problem of seeding material concentration is transport and diffusion of seeding material in the clouds, which is more difficult to deal with. Bruintjes et al. (1999) pointed out that some critical problems remain in the precipitation enhancement, and one of fundamental impediments is the diffusion and transport of seeding material throughout the cloud. Combining a nonhydrostatic mesoscale model, Yu et al. (1998, 2000) formulated a three-dimensional numerical model of transport and diffusion of seeding material within stratiform cloud.

In this study, the spatial and temporal concentration distributions are simulated, the dispersing shape, scope, width, and length of the cloud seeding material are compared with the features of cloud trace revealed by the satellite data during the cloud seeding. And then the affecting ranges for different concentrations are analyzed. In the next section, the cloud seeding operation is described and the features of NOAA satellite image are analyzed. In the section 3, the model and the simulation method are introduced, and the comparison results at the receiving time of satellite data are given. In section 4, affecting ranges of different concentration are analyzed. A conclusion closes the study.

2. CLOUD SEEDING AND NOAA SATELLITE DATA

2.1 Cloud Seeding

At 0615 UTC 14 March 2000, a cloud seeding operation was carried out in this area and its western neighbor by Center of Weather Modification of Shaanxi Province. The operational aircraft was An-26 with an airborne silver iodide solution burner, and the average flight speed was 360kmh^{-1}. The seeding time was 94 minutes, and consumed AgI 1200 g. The seeding height was 4.35 km, where temperature was -10.0°C. The heights of the cloud bottom and top were 2.2 and 4.5 km, where temperatures were 2.0 and -13.0°C, respectively.

Corresponding author's address: Jin Dai, Meteorological Institute of Shaanxi Province, No. 36 Beiguanzhengjie, Xi'an 710015, P. R. China, E-mail: daijohn @msn.com

2.2 NOAA Satellite Data

During the process of cloud seeding, fortunately, NOAA-14 satellite flew over this area. At 0735 UTC, the satellite image was received. Due to there no high cloud above the seeded cloud, there appeared a clear cloud trace on the satellite image (Fig. 1). The image was synthesized from visible, near infrared and infrared channels, respectively. Cloud top except for F' was even and flat, which implied the cloud was stratiform. The turning points A', B', C', D', E', G' on the cloud trace were distinguishable and clear, they were corresponding to the turning points A, B, C, D, E and G of cloud seeding. The cloud trace was approximately zigzag, whose middle was wider and two ends were narrower. The maximum width was 11 km (near C'), and its average was 8.3 km. F' point corresponding to the turning point F of cloud seeding could not distinguished (instead of E" and F" on the image), this may be that the cloud feature around F' was different obviously from the one at its northwest, which caused the microphysical effects not to be discerned on the satellite image, or not to be reflected at that time.

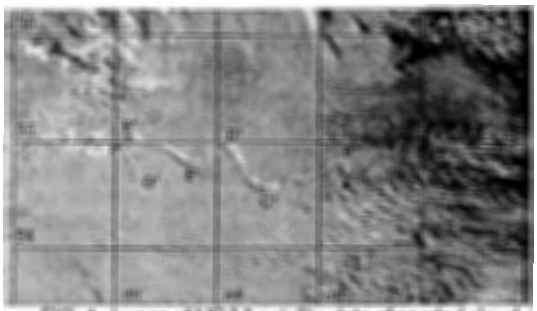

FIG. 1. Image of NOAA satellite data of seeded cloud

3. COMPARISON

3.1 Model Description

The model consists of the puff trajectory model and a three dimensional nonhydrostatic mesoscale model.

The puff trajectory model can deal with the tempo-spatial variation of source parameters with meteorological elements, and can be used to simulate the diffusion of all kinds of scales and sources (Ludwig et al. 1977, 1989). It is a practical and effective method to represent

the diffusion of pollutant source. So it is introduced to simulate diffusion of seeding material within stratiform cloud. In order to partly consider effect of vertical shear on diffusion, in vertical direction, each puff is divided equally into 7 smaller puffs (sub-puffs).

The accuracy and efficiency of the puff trajectory model depend on the accuracy of flow and turbulence fields. So the nonhydrostatic mesoscale model is formulated. The nonhydrostatic governing equations of the mesoscale model are composed of prognostic equations of velocity component, potential temperature and vapor, turbulent kinetic energy, dissipation rate and anelastic continuity equation, following the coordinate transformation (Pileke and Martin 1981). The diffusive coefficients are obtained by turbulent kinetic energy and dissipation rate prognostic equations (Huang and Raman, 1989).

3.2 Method Of Simulation

Because fine grid is needed to distinguish the features of transport and diffusion of the seeding material, considering the receiving time of NOAA data and scope of cloud trace, the simulation horizontal domain is 33.50°-35.70°N,106.83°-109.50°E (250 km×250 km). The horizontal and vertical grid intervals are 1 and 0.2 km. The time step is 20 s. Because the turning points on the image, relative to I and J points of cloud seeding, can not been seen on the satellite image, AB, BC, CD, DE, EF, FG and GH are chosen as 7 segments of seeding line. The operational time was 66 minutes, and consumed 880 g of AgI. Taking the nucleation rate as 5×10^{13} at temperature of -10°C, the line source strength is 1.11×10^{13} s^{-1}. One puff is introduced into the model every 20 s, and the total numbers of puff is 198.

Based on the meteorologically measured surface and sounding data at 0000 UTC, the predicted results of the mesoscale model were output every hour. Fields of wind and turbulence were input to the puff trajectory model to calculate the concentration distribution and variation of seeding material.

3.3 Comparison Results

At the receiving time of satellite data (0735 UTC), the position, shape, width and length of seeding material concentration are compared with that of the cloud trace.

Compared the cloud trace with seeding line, the scope and position of concentration projected on the surface coincides better with that of the cloud trace, the turning points of seeding line entering the cloud generally accord with that of the cloud trace, but decline southwards in the south-north direction. The main reason may be that the wind direction at 0000 UTC was just W on 500 hPa, the modeling u component is good and the v is smaller in the mesoscale model.

The shapes and the widths of concentration greater than $10L^{-1}$ or less than $1L^{-1}$ are greatly different from that of the cloud trace, the maximum widths corresponding to concentrations 1, 4, 5 L^{-1} are 18.3, 11.4, and 10.6 km, their average widths are 12.9, 8.6, and 7.9 km. The widths and the shapes of concentration 4 and $5L^{-1}$ are similar to that of the cloud trace, and the ones of concentration $4L^{-1}$ is more similar. All these show that only concentration reaches some magnitude, the obvious effect of seeding can be obtained. To different cloud the concentration magnitude may be different. For this operational seeding cloud, when the concentration projected on the surface is greater than or equal $4L^{-1}$, the effect of cloud seeding will obvious, if the concentration projected on the surface is less than $1L^{-1}$, the effect of cloud seeding will be fainter.

TABLE 1. Lengths of the actual seeding line, of the cloud trace and of the modeling line

Seeding line	AB	BC	CD	DE	EF	FG	GH	total
Actual line length(km)	22.8	48.8	62.4	41.1	67.2	67.0	81.7	391.0
Seeding time(min)	4	14	9	6	11	9	13	66
NOAA line length (km)	14.7	83.3	55.5	36.7	61.2	49.8		301.2
Modeling line length (km)	22.0	65.3	60.4	44.1	63.7	63.7	93.1	412.3

Table 1 displays the lengths of the actual seeding line, of the cloud trace and of the modeling line for concentration $4L^{-1}$.The actual line length is calculated by flight distance between two points, and the seeding time is the flight time between them., the lengths of seeding line segments CD, DE and EF are close to the length of the actual line and of the cloud trace. The modeling line lengths of CD and EF are shorter than the actual seeding line, but DE is longer, three all together are shorter than by 2.5 km (1.5 per cent). However, they are longer than the cloud trace, and three all together are longer than by 14.8 km (8.4 per cent). The length of the cloud trace is shorter by 17.3 km (10.1 per cent) than the actual seeding line.

However, the modeling line length of AB, BC and FG are different greatly from the ones of the actual line and of the cloud trace.

The modeling length of AB is 22.0 km. The length of the cloud trace A'B' is 14.7 km, shorter by 8.1 km (35.5 per cent) than its actual length. One of the reasons may be that physical effect acted on the cloud top caused by AB seeding line is decreasing.

The length of the cloud trace and the modeling length corresponding to the seeding line BC are longer by 34.5 km (70.7 per cent) and 16.5 km (33.8 per cent) than its actual length. Because there was no measurement of Globe Position System (GPS), the seeding parameter was based on the record of the flight. The recorded time of BC line was 14 minutes, the flight speed was 400 kmh^{-1}, but the actual length was only 48.8 km (should be 93.3 km), so there existed a great difference and had an uncertainty among them. Due to lack the factor enlarging the seeding line, the actual length of seeding line might reach to 80 km. The pos-

sible fact was that the aircraft flew westwards 30 km after arriving the point C. The simulation describes the seeding process according to the record and not to the baseless correction, which may leads to the simulating error.

There exists a broken part on the cloud image corresponding to the turning point F (see Fig. 1), which leads to a great length difference 17.2 km (25.7 per cent) between cloud trace F"G' and the actual seeding line FG. However, the modeling FG length is only shorter by 3.3 km (4.9 per cent) than its actual length.

Comparisons between the simulating results and the cloud trace show that the position, shape, width and length of seeding material concentration are rather agreed with that of the cloud trace. The cloud trace is caused by the cloud seeding, is physical effect reflected on the cloud top. The model can reveal the main characteristics of transport and diffusion of seeding material.

4. AFFECTING RANGE

The cloud trace on the satellite image is physical reflection of cloud seeding. The seeding material interacts with the cloud physical process, and causes the change of the cloud. This change is transmitted to the cloud top, and forms the cloud trace. Different levels of seeding material contribute to the cloud trace, comparison between the features of the cloud trace and concentration distribution on a given level leads to a limitation. On the other hand, the position and width of the cloud trace are reflection of transport and diffusion of seeding material at some extent, and are response of concentration distribution scope and position of seeding material. It is reasonable to use the concentration projected on the surface in the comparison. Actually, the concentration projected on the surface is the maximum concentration in the vertical direction.

The tracer experiment or airborne probing only shows information at different limited time and spatial points, can not display the full profile on a cross-section. The satellite image gives us manifest and complete panorama on the seeding cloud top at 0735 UTC. However, it can not picture concentration distribution at different time and space. With the numerical simulation, it is helpful and advantageous to analysis the spatial and temporal dispersing scope for different concentration of seeding material.

Theoretically, the obvious seeding effect can be obtained when the seeding concentration is greater than or equal to base concentration of the seeded cloud. From this point of view, the affecting range whose components include area and volume, depth and width for concentrations 1, 4, 5, and 10 L^{-1} is calculated. Table 2 gives the affecting area S (km^2) and volume at different time. The subscript denotes the concentration value. T is time interval from 0615 UTC.

TABLE 2. The affecting area S and volume V at different time

T(min)	S_{10}	S_5	S_4	S_1	V_{10}	V_5	V_4	V_1
10	185	204	206	229	53.6	66.6	72.4	101.4
40	1164	1438	1521	1905	658.8	1006.8	1122.4	1825.8
60	1804	2552	2759	3742	**1034.2**	1972.4	2332.2	4419.0
70	**1918**	2968	3285	4706	1006.8	2381.6	2882.8	6033.0
80	1448	**3130**	3534	5486	797.2	**2619.4**	3262.0	7704.6
90	1124	3123	**3639**	6072	629.2	2536.0	**3413.4**	9217.4
100	754	2775	3550	6488	379.4	2127.8	3238.4	10530.0
120	65	1409	2420	**7047**	16.2	1014.8	2009.6	**12570.0**
average	958.7	1916.1	2303.0	3916.6	518.1	1462.8	1973.0	5708.2

TABLE 3. The vertical distribution of effective area on different levels

H (km)	10	20	30	40	50	60	70	80	90	100	110	120
3.75	0	0	0	60	257	401	472	**478**	462	398	176	58
3.95	0	123	386	684	951	1240	1502	**1514**	1375	1162	894	566
4.15	81	368	752	1221	1746	2264	2622	**2773**	2643	2055	1552	1116
4.35	**206**	**470**	**974**	**1521**	**2098**	**2716**	**3191**	**3371**	**3379**	3108	2339	1560
4.55	75	358	742	1325	1877	2466	3035	3338	**3484**	**3366**	**2862**	**1958**
4.75	0	102	367	800	1328	1786	2233	2787	**3080**	3039	2597	1851
4.95	0	0	0	1	197	776	1163	1535	1898	**2005**	1802	1479
5.15	0	0	0	0	0	12	195	418	598	879	**1004**	917
5.35	0	0	0	0	0	0	1	96	148	180	394	**400**
5.55	0	0	0	0	0	0	0	0	0	0	0	**143**

At the same time, the high concentration covers small area, volume, depth and width, the relative low concentration, can covers large or affect rather larger range.

For concentration 10 L^{-1}, the extreme of affecting area, volume, width, and depth are 1918 km^2, 1034 km^3, 5.05 km, and 0.60 km, and their average are 958.7 km^2, 518.1 km^3, 4.18 km, and 0.49 km, respectively.

For concentration 5 L^{-1}, the extreme of affecting area, volume, width, and depth are 3130 km^2, 2619 km^3, 7.94 km, and 0.84 km, and their average are

1916 km^2, 1462 km^3, 6.17 km, and 0.70 km, respectively.

The comparison between the affecting area, width, scope of concentration distribution shows that the area, volume, width, and depth corresponding to concentration of 4 L^{-1} is the effective volume, width, and depth. Their extremes are 3639 Km^2, 3413.4 Km^3, 9.19 Km and 0.94 Km respectively, and their averages are 2303 Km^2, 1973 Km^3, 6.87 Km and 0.78 Km respectively. Table 3 shows the vertical distribution of effective area on different levels (H) beginning from 0615 UTC. The effective area on different levels is mainly concentrated from 3.95 to 4.75 km (Table 3), its extreme was located on 4.45 km before 80 minutes, and on 4.55km after 90 minutes. Its upward extension was greater than the downward.

5. COCLUSION

Although some measurements and airborne probing can supply information at limited time and spatial points, they could not display the full profile on a cross-section. The satellite data can give us manifest and complete panorama on the seeding cloud top at a given time. It is the evidence of cloud seeding although it is difficult to obtain it. Fortunately, the satellite data were received during the process of cloud seeding on 14 March 2000 in middle part of Shaanxi Province, China. The vivid cloud trace appeared on the satellite image, and its features were detailedly analyzed.

The transport and diffusion of every segment of seeding line is well corresponding to every segment of the cloud trace. The distributions of concentration, the turning points of seeding line entering the cloud, the movements of seeding material, the diffusive width all reveal that the cloud trace is resulted from the cloud seeding and physical respond of cloud on the cloud top. The feature comparisons between the simulating spatial and temporal distributions of concentrations and the cloud trace suggest that the three-dimensional model can simulate the transporting and diffusive characteristics of seeding material, and the model is reasonable and reliable.

The affecting area, volume, width, and depth depend on the concentration. There exist a concentration value can lead to the better seeding effect. For this simulation case, it is 4 L^{-1}.

The method used in this study should be paid attention or be done in the future. The particles of seeding material are assumed to be inert in the model and they have no interaction with the particles of the cloud or precipitation. Also, three points must be noted. First, the cloud trace is the reflection of cloud top, but not of obvious effect of cloud seeding within the cloud. Second, the satellite resolution determines the size of the cloud trace. Third, due to the complexity of cloud and its microphysics, there exist a lot of uncertainties. For those reasons, the effective range may be larger, and its concentration may range from 1 to 4 L^{-1}, for this cloud seeding.

Acknowledgments

We would first like to thank all those who participated in the preparation and filed phases of cloud seeding operation. The satellite data were supplied by Agricultural Remote Sensing Information Center of Xianyang City, Meteorological Bureau of Xianyang City. This work was supported by Chinese ministry of science and technology Grant 2001BA901A41.

References

Bruintjes, R. T., G. L. Kok, D. W. Breed and V. Salazar, 1999: Hygroscopic seeding: theory and practice. Seventh WMO scientific conference on weather modification. WMO/TD-No. 936, 65-68.

Huang, C. Y., and S. Raman, 1989: Application of the E-ε closure model to simulations of mesoscale topographic effects. Boundary-Layer Meteor., **49**, 169-195.

Ludwig F. L., L. S. Gasiorek and R. E. Ruff, 1977: Simplification of a Gaussian puff model for real-time minicomputer use. Atmos. Environ., **11**, 431-436

Ludwig F. L., R. Salvador and R. Bornstein, 1989: An adaptive volume plume model. Atmos. Environ., **23**, 127-138

Pielke, R. A., and C. L. Martin, 1981: The derivation of a terrain-following coordinate system for use in a hydrostatic model. J. Atmos. Sci., **38**, 1707-1713.

Yu Xing, Fan Peng, Wang Xiaoling, Dai Jin, and Li Zhaoyuan, 1998: Numerical simulation of multiple line source diffusion of seeding agent within stratus. Acta Meteorologica Sinica, **56**, 190-197.

Yu Xing, Dai Jin, Jiang Weimei and Fan Peng, 2000: A three-dimensional model of transport and diffusion of seeding material within stratus. Advances in Atmospheric Sciences, **4**, 617-635.

THE DEVELOPMENT OF A NEW EXPLICIT MICROPHYSICAL SCHEME USING IN MM5

ZHEN ZHAO, HENG-CHI LEI and YU-XIA WU

Institute of Atmospheric Physics, Chinese Academy of Sciences

1. INTRODUCTION

The production of realistic clouds and precipitation forecasts with detailed mesoscale models is a difficult task. Increasing the microphysics complexity implies the specification of a number of adjustable parameters and processes, which requires extensive research and numerical experimentation. Furthermore, a large number of predictive equations and microphysical processes significant increase computational time and thus limit the use of complex cloud microphysics schemes in operational applications.

A complex mixed-phase explicit microphysical parameterization scheme was developed for use in the NCAR/Penn State Mesoscale Model Version5 (MM5). The single-moment schemes, in which the mixing ratio of ice species are predicted and number concentration specified, performed reasonably well if a diagnostic equation for $N_{0,s}$, the Y-intercept of the assumed exponential snow distribution, is allowed to vary with snow mixing ratio. The scheme assumes a Marshall-Palmer distribution law for rain, snow and graupel. In its essence, the scheme predicts only the mixing ratios (third-order moments) of drops.

The research presented in this paper aims at developing a new double-moment microphysical scheme, in which both the mixing ratios and number concentrations of cloud water, rain water, cloud ice, snow and graupel were predicted. Besides its impact in the formation of the first raindrops by autoconversion, the prediction of cloud-droplet number concentration is especially important in cloud chemistry and radiative transfer. The results obtained by running the new scheme are not discussed in this paper.

2. THE LIQUID WATER IN THE SCHEME

The new scheme is based upon the drop size distributions are assumed to follow the gamma distribution form:

$$n_x = N_{0x} D^{\alpha_x} \exp(-\lambda_x D) \qquad (1)$$

where the index x∈[i, r, s, g] stands for ice, rain, snow and graupel, respectively. Our strategy is to predict only two of the most significant moments of Eq. (1) that posses a clear physical meaning, namely the zeroth, number concentration N_x

$$N_x = \int_0^\infty n_x dD$$

and third-order moments, mixing ratio q_x

$$\rho q_x = \int_0^\infty \frac{\pi}{6} \rho_x D^3 n_x(D) dD .$$

As these two moments are determined from Eq. (1), the variable slope parameter λ_x and the slope intercept N_{0x} can be deduced from

$$\lambda_x = \left[\frac{\pi \rho_x N_x \Gamma(4+\alpha_x)}{6 \rho q_x \Gamma(1+\alpha_x)} \right]^{1/3} \qquad (2)$$

$$N_{0x} = \frac{N_x \lambda_x^{1+\alpha_x}}{\Gamma(1+\alpha_x)}, \qquad (3)$$

whereas the remaining parameters α_x are mostly related to the spectral breadth of Eq. (1), are held fixed for the moment. The parameters α_x are setting

3. RESULTS

The flight started at 11:26, seeded at 11:46 with height of 2413m and temperature of 0℃. The seeding ended at 12:24 with height of 3300m. The amount of liquid CO_2 used in seeding was 20kg, the seeding rate was set to 9g/s, and the seeding thickness was 1000m. By 12:34, the flight height reached to 4830m and then started to descend. After passing the seeding layers, the airplane landed at 12:55.

Fig.2 (a) and Fig.2 (b) show the radar echoes in RHI at 12:26 and in PPI at 12:24, respectively. The RHI is echo for 2 minutes after seeding. The flight distance at 4500m is 34km, and with west wind speed of 13m/s. The relative echo top height in 3a is 6500m; the sea level height at radar station is 1170m. The height of 0℃ layer should be 2230m if calculated with the top height of 25dBz. Below the 0℃ layer, the 40dBz echo area was located at 20-30km from radar station. The interesting phenomenon is that there are two symmetrical high echoes with 15dBz above the 40dBz region. Based on the preliminary analysis, the high echo regions are related to the dynamical effect by liquid CO_2 seeding.

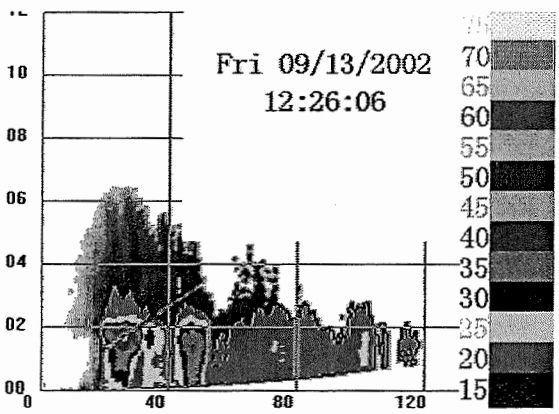

Fig. 2(a) Radar echo in RHI (12:26)

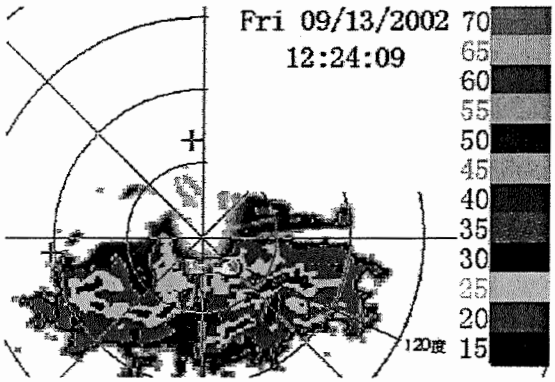

Fig. 2(b) Radar echo in PPI (12:24)

Table 1 shows that before seeding, there are less cloud droplet and ice crystal in clouds. The maximum precipitation rate was only 2.3mm/h. After liquid CO_2 seeding, the super-cooled water in seeded layer decreased and the particles with 2-5μm increased. The number concentration in 25μm sampled by 2D-C increased one order, and most of them is cloud ice formed by seeding.

Table 1 The number concentration at different seeding levels

H (m)	FSSP-100 (2-5μm) $N_1(m^{-1}\mu m)$		2D-C (25-5μm) $N_2(L^{-1}*25\mu m)$		FSSP-100 total water content (gm^{-3})	
	no seed (10^6)	seed (10^6)	no seed	seed	no seed (10^{-3})	seed (10^{-3})
3500	0.2098	0.3892	1.3	17.2	0.3	0.1
4000	0.2470	0.4348	3.8	27.3	2.7	1.2
4500	0.2559	0.2891	5.4	49.5	4.8	2.9

The rain intensity is shown in Fig 3. It indicates that the high rainfall time is from13:00 to 16:00, and rain intensity in seeded region in Yanan is two times of the unseeded region in Ansai, which was considered to be relevant to liquid CO_2 seeding. The Ansai station, 30km far from Yanan in NNW direction is located in the upwind of seeding region. The accumulated rainfall in

un-seeded region in Ansai is 3.4mm, which is much less than 12mm in seeded region in Yanan.

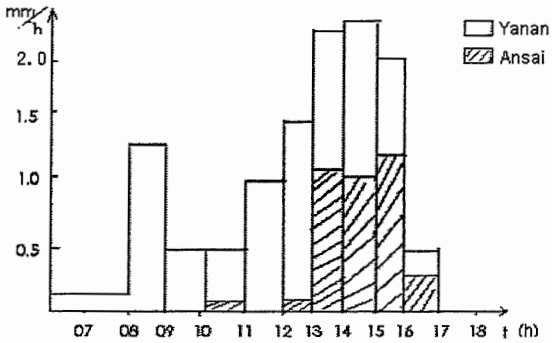

Fig. 3 Comparison of rain intensity in seeded region of Yanan and un-seeded region of Ansai

4. SUMMARY

The seeding experiment was conducted by using liquid CO_2 on September 13, 20032 in Shaaxi. The following results are obtained:

(a) The airborne liquid CO_2 seeding device was developed and used in airplane seeding.

(b) Liquid CO_2 is better than AgI in the low-level seeding based on this experiment.

(c) Two ice thermal bubbles were produced after liquid CO_2 seeding from radar echo analysis.

(d) Liquid CO_2 seeding enhanced the precipitation at the surface.

5. ACKNOWLEDGEMENTS

This work is supported by the Key Project of the Ministry of Science and Technology of China under Grant 2001BA901A41.

6. REFERENCES

Norihiko Fukuta, 13th Conf. on Planned and Inadvertent Weather Modification, January28–February 2, 1996, Atlanta, 164—171.

Takahashi, T., and N. Fukuta, 1988:Supercooled cloud tunnel studies on the growth of snow crystals between –4 and –20°C. J. Meteor. Soc. Japan, 66, 841-855.

Eamanucl, K.A, 1994: Atmospheric Convection. Oxford Univ. press, N.Y., 580.

FLYING CASE STUDY OF A PRECIPITATION SHEET CLOUDS ARTIFICIAL RAIN ENHANCEMENT MICRO DETECTION ON MAY 9TH, 1995, IN JILIN PROVINCE

Gu Shufang[1] Gao jianchun[2] Jin Dezhen[1] Zhang Jinghong[1] Wei qiang[2]
Hu Zhongming[3] Chen Zhixin[1] Li Zhanzhu[1] Wang Xiaomei[1] GuoJunmei[1]

[1] JiLin Weather Modification Office, ChangChun, 130062, China
[2]Beijing Application Meterorological Institute, Beijing 100081
[3]Jilin Meteorological observatory, Changchun 130062

1. WEATHER ANALYSIS AND SURVEY OF THE ARTIFICIAL RAIN ENHANCEMENT DETECTION

1.1 Weather Analysis

On the 500hpa upper-air chart of May 9th, 1995, the entire Euro-Asian area had two troughs and two ridges. A deep trough extended from western Siberia through the border between China and Mongolia till the He Tao area of our country. Behind the trough there was a strong cold air mass, at the center of which the temperature was –36℃. Its highest layer situated over the central area of Jilin Province, and the hinder high pressure lay in Mongolia. All the three layers of the front area lay in the Northeast-Southwest direction in "V" shape. All the SW torrents in front of the trough were quite good; the source of the vapor was from the Bay of Bengal. Influenced by this weather system, there was a general light to moderate rainfall across our province from west to east.

1.2 A Survey Of The Flying Detection

On the day, the artificial rain enhancement detection airplane made a flight along the route as showed in Diagram 1(a) to detect the precipitation sheet clouds over Jilin city. The vertical range of this etection was 1900-5200 meters. The top of the clouds was 5000 meters high; the bottom of the clouds untouched. The 0℃ layer was 400 meters thick, situating at the height of 1900-2200 meters. The airplane seeded twice, once at the top of the clouds, the other time in the clouds, with seeding temperature at –12.3℃ and –5.1℃ separately. After the seeding operation, the plane made three horizontal detection flights at the heights of 2930m, 2430m and 2140m—see Diagram 1(b), which illustrates the change curve of temperature, dew-point and height with time during the detection flights over Jilin city.

Corresponding author's address: No.653, HePing Street, ChangChun City, JiLin Province,130062,China; E-Mail: zhangjh8070@sina.com.cn

2. FACILITIES USED IN THE FLYING DETECTION

We took Y-12 airplane as the platform of seeding and detection operation. On the plane we installed: (1) GPS (the Global Positioning System); (2) drikold seeding instrument; (3) PMS airborne particle detection equipment; (4) senor for macroparameters in the clouds, i.e., temperature, dew point, height, airspeed, and LWC.

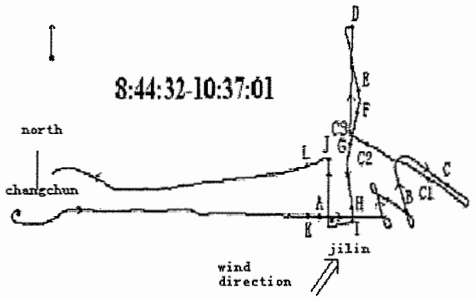

Diagram 1 (a) course of the airplane's artificial rain enhancement flight

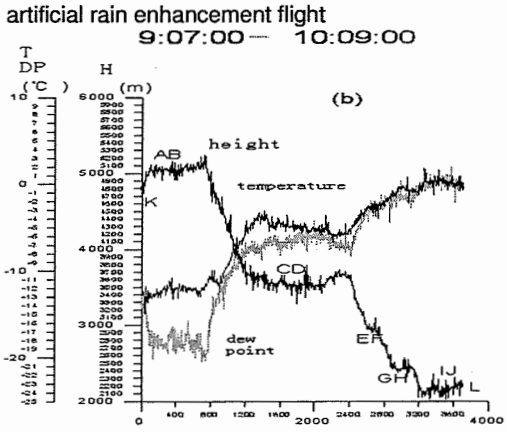

Diagram 1 (b) change curve of temperature, dew point, and height with time

3. MICROPHYSICAL CHARACTERISTICS OF THE CLOUDS OVER JILIN CITY

3.1 The Temporal-Spatial Variation Of Particle Density, Water Content, Liquid Water Content As Detected By The Three Probes

3.1.1 The Horizontal Variation of Particle Density, water Content and Liquid Water Content As Diagram 2(a) (omitted) and Diagram 2(b)(omitted) show:

(1)PCASP probe's particle density decreased in a whole with time (decrease of height); meanwhile its water content increased.

(2) FSSP probe's particle density and water content increased apparently with time (decrease of height).

(3) GA2 probe's particle density and water content increased apparently with the time at AB-GH trail, then decreased sharply at IJ trail.

(4) The value of LWC increased apparently with time (decrease of height), and the trend of its change curve is quite similar with the change curve of FSSP probe's water content value.

(5) Viewed as a whole, the time variation of particle density, water content and liquid water content is uneven.

3.1.2 The Vertical Variation of Particle Density, Water Content and Liquid Water Content

(!)PCASP probe's particle density generally followed a decreasing trend with the decreasing of height to 2500m, while increased a little at the height of 2200-2400m. The value of water content didn't manifest a single trend of variation, but it formed three peaks at the height of 2400m, 3400m and 4500m, the values were 1.29E-04gm^{-3}, 1.32E-04gm^{-3},and 2.32E-04gm^{-3}.

(2) The change trend of FSSP probe's particle density was exactly the opposite to that of PCASP: it showed an increasing trend with the decrease of height, and formed 4 peaks at 1900m, 2700m, 3500m, and 4900m. At the peaks of particle density, the water content value also formed peaks, which were 5.6E-03gm^{-3}, 4.7E-03gm^{-3}, 2.95E-03gm^{-3}, and 1.28E-03gm^{-3}.

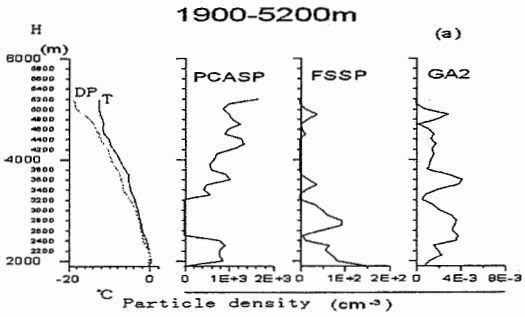

Diagram 3 (a) the variation of particle density, temperature, temperature and dew point with the variation of height

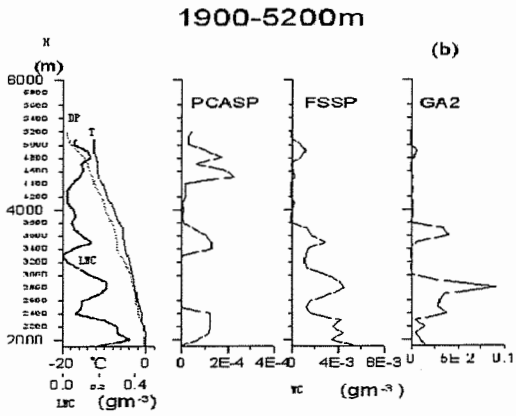

Diagram 3 (b) the variation of WC, LWC, temperature and dew point with the variation of heigh

(3) GA2 probe's particle density manifested a generally increasing trend with the decrease of height; at 2400m it reached a peak of 3.7E-03gm^{-3} and decreased again, then, at 2700m, 3600m and 4900m it reached another 3 peaks, the value of which were separately 3.5E-03gm^{-3}, 4.1E-03gm^{-3}, 2.9E-03gm^{-3}. The water content increased with the decrease of height, at 2800m it reached a peak of 9.7E-02gm^{-3}, then gradually turned to drop. At the height of 3600m, 4900m where particle density reached peaks, the water content value also formed peaks, they are 4.1E-02gm^{-3} and 6.7E-03gm^{-3}.

(4) Liquid water content basically followed an increasing trend with the decrease of height, completely in accord with the variation trend of FSSP probe's water content value. It reached peaks at 2000m, 2800m, 3500m and 4800m, the peak values were separately 0.366gm^{-3}, 0.246gm^{-3}, 0.162gm^{-3}, and 0.151gm^{-3}.

(5)PCASP probe's particle density was 0cm^{-3} at the height of 2500-3200m. At this level, FSSP and GA2 all manifested a high value region of particle density, also the high value regions of LWC and WC

4. DISCUSSIONS AND RESEARCH

Through analysis of the time-spatial data of the precipitation sheet clouds artificial rain enhancement detection flight on May 9th, 1995, we means to provide a method for studying the microstructure of sheet clouds. The result of our initial analysis shows that:

(!) The time variation of particle density, water content and liquid water content is uneven.

(2)The values of particle density and water content measured by PSS probe and GA2 probe are in good accord, i.e., when particle density value reaches a peak, the water content value also form a peak. On the other hand, the results of PCASP probe's detection are not so closely in accord with those of the other two probes.

(3)At the five flying phases, the particle spectrums measured by the three probes are not of different levels.

References

You Laiguang: Use Particle Measurement System to Study Cloud Physical Process and the Conditions for Artificial Rain Enhancement, Cloud Precipitation Physics and Artificial Rain Enhancement Technological Conditions Study, Beijing Meteorology Press, 1994, P236.

Gao Jianchun: An Introduction of Airborne Particle Measurement System, Data Processing Software and Processing System Results, Weather Modification, January 1996, Vol. 9, P64-68.

Woodley, Willian L.Rosenfeld, Daniel Evidence for changes in microphysical structure and cloud drafts following AgI seeding, MGA Number: 51110104 The Journal of Weather Modification, Fresno,CA, 32 (1): 53-67, April 2000.Refs.,figs.

PRECIPITATION CHARACTERISTICS OF CLOUDS OVER THE UNITED ARAB EMIRATES

Tara L. Jensen[1], Roelof T. Bruintjes[1], Daniel W. Breed[1], Vidal Salazar[1], Abdulla Al Mangoosh[2] and Abdulla Al Mandoos[2]

[1]National Center for Atmospheric Research, Boulder, Colorado, USA
[2]Department of Water Resources Studies, Office of His Highness the President, Abu Dhabi, UAE

1. INTRODUCTION

The United Arab Emirates (UAE) is located on the Arabian Peninsula at approximately 24 degrees north latitude and 55 degrees east longitude. The majority of the country is desert and is bounded to the north by the Arabian Gulf and to the east by the Oman Mountains. Precipitation is scarce despite hot and humid surface conditions near the coast. In response to decreasing fresh water supplies, the use of hygroscopic seeding as a possibility for increasing rainfall is being explored. The potential for such man-made increases in rainfall is strongly dependent on the natural microphysics and dynamics of the clouds to be seeded. To study these characteristics, four three-month field programs (two winter and two summer) were conducted in the UAE and surrounding area during 2001 and 2002. Summaries of aircraft observed precipitation measurements are included in this paper.

2. INSTRUMENTATION

A Piper Cheyenne II (in 2001) and a Beechcraft King Air 200 (in 2002) aircraft were used for the cloud physics investigations and hygroscopic seeding. Aerosol and atmospheric chemistry measurements were also made to help understand the environment in which the clouds were forming. Details of the project infrastructure may be found in RAP (2003). Observations from C-band (5-cm wavelength) radars, located near Abu Dhabi, Dubai, and Al Ain, provided critical information about the location and longevity of precipitation-bearing clouds. Aircraft observations include measurements from a modified Forward Scattering Spectrometer Probe (FSSP), a 2D-C and 2D-P Optical Array Imaging Probes, and a King Liquid Water Content (LWC) sensor.

3. SUMMARY OF CONVECTION

3.1 Winter

During winter (January through March), precipitation often occurs as drizzle and rain falling from pre-frontal stratiform clouds. These events occur approximately eight times per season with the highest frequency in February and March.

Corresponding author's address: Tara L. Jensen, NCAR/RAP, P.O. Box 3000, Boulder, Colorado, 80307, USA; Email: jensen@ucar.edu

As seen in Figure 1, the entire gulf and part of the country is covered with drizzle and light rain (20-30 dBZ) from altostratus clouds. Embedded convection with maximum reflectivities of 40 to 45 dBZ sometimes occurs closer to the mountains. However, rain from embedded convective elements is often subject to increased evaporation in the subcloud layer, resulting in only drizzle-size drops reaching the ground. Figure 2 shows locations of cloud penetrations in 2002, which were designed to sample convective cells. The locations of convective elements during the 2002 winter season (and the 2001 winter, not shown) were spread over the majority of the country.

The annual mean precipitation for Al Ain, a city near the mountains, peaks during February and March at approximately 30 mm (RAP, 2003). However, the standard deviation exceeds the mean, suggesting that precipitation is highly variable in this region. Post-frontal convection with maximum reflectivities of 45 to 60 dBZ occurs on occasion from late February through April. These episodes can add significantly to the recorded rainfall and thus explain a portion of the variability of the climatological rainfall pattern.

3.2 Summer

Summer precipitation (June through September) is generally more convective in nature. Figure 3 is a radar image from 19 July 2001 that shows a typical precipitation event during the summer. Improved radar coverage during 2002 showed that convection occurs regularly over the mountains just south and east of Al Ain. The frequency of convective days tends to peak near late July and early August. Figure 3 indicates there can be several uni- and multi-cellular storms occurring simultaneously. During their mature stage, these convective elements form heavy precipitation (indicated by maximum reflectivities of 45 to 60 dBZ) that can result in strong wadi flow. Many times when the storms dissipate, they leave a deck of altostratus cloud containing precipitation particles for an additional hour or so. One such cloud deck is indicated in Figure 3 by the dispersed area of weak echos (about 20 dBZ) at the northern end of the convective development. Figure 4 shows locations of cloud penetrations during summer 2002 and suggests that the majority of convective elements occur due to oragraphic lifting over the mountains. However, some convection occurred over the southern desert and east of Dubai. These convective events are driven by more complex mesoscale features such as colliding boundaries.

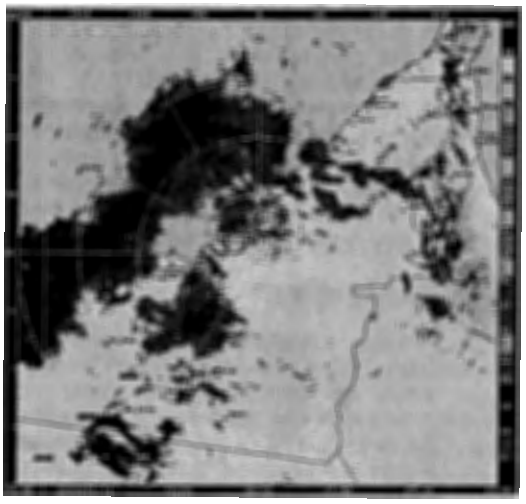

Figure 1. Composite Radar Image from 18 March 2001 at 05:19 UTC.

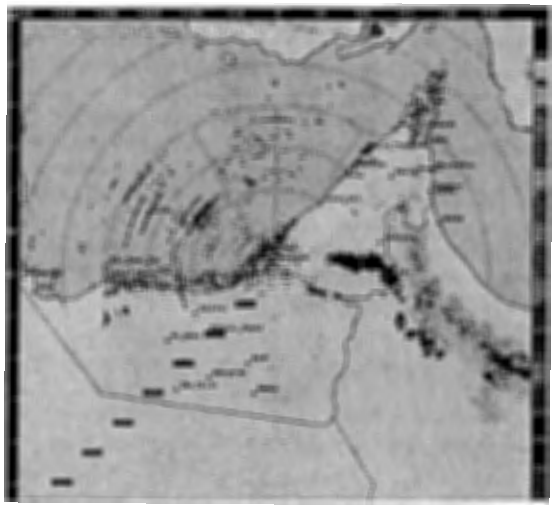

Figure 3. Composite Radar Image from 19 July 2001 at 12:01 UTC.

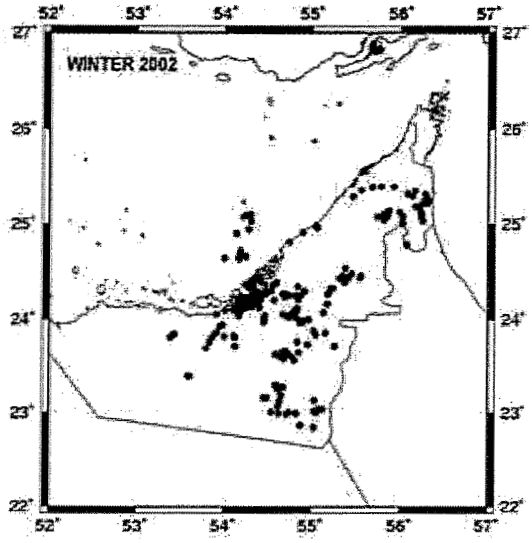

Figure 2. Geographical locations of cloud microphysical measurements during the 2002 Winter (January through April) field project.

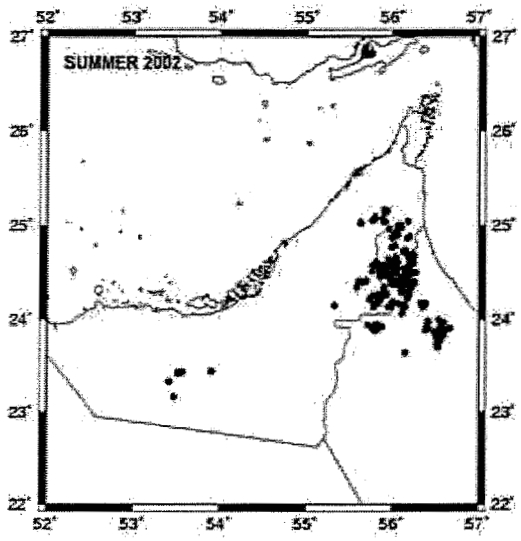

Figure 4. Geographical locations of cloud microphysical measurements during the 2002 Summer (June to September) field project.

4. AIRCRAFT OBSERVATIONS

The characteristics of the clouds differed between seasons due to both synoptic and mesoscale influences. Typically, the winter clouds were more stratified in nature. They had lower cloud droplet concentrations (200-600 cm^{-3}) and lower liquid water contents (0.1-0.4 g m^{-3}) near cloud base. Summer clouds were more convective, with continental cloud base droplet concentrations (400-1000 cm^{-3}) and high liquid water contents (0.3-1.2 g m^{-3}) near cloud base. Regardless of the season, measurements above and below the freezing level (0° C) indicate that riming played a role in precipitation formation. As an example, the results from two summer cases in 2002 (July 12 and 21) are presented in this section.

4.1 Above the Freezing Level

Measurements made at or above the freezing level contribute to the knowledge of supercooled liquid water and cold rain processes at this level. The region of the cloud between -3 to -8 °C is important for understanding precipitation development through: 1) ice multiplication via the Hallet-Mossop process; 2) freezing of large drops (if they exist); and 3) graupel

formation through initial riming on frozen drops (Rogers and Yau, 1989). Penetrations were performed at or above the freezing level on at least ten cloud days during the two summer seasons. Generally: 1) graupel was not apparent at temperatures warmer than -2 °C unless the cloud was in the dissipating stage, 2) there was an abundance of graupel and supercooled liquid water at -5 °C, and 3) there were pristine ice crystals present during the two penetrations made at -10 °C. Figure 5 shows a time-series of measurements taken on 21 July 2002 during a cloud penetration at approximately -5 °C.

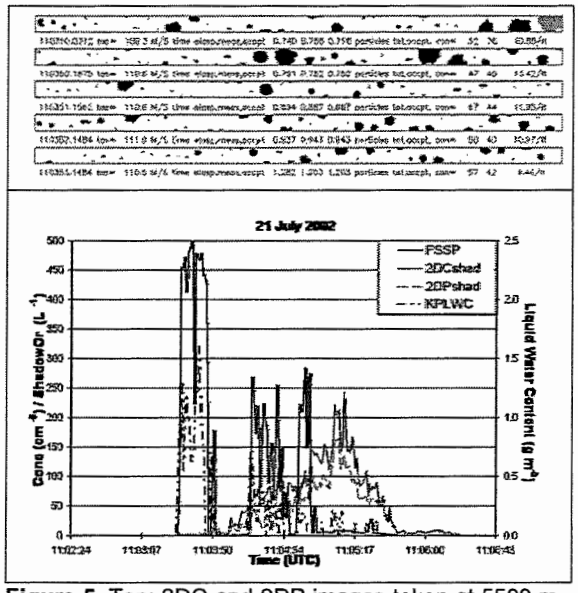

Figure 5. Top: 2DC and 2DP images taken at 5500 m (-5 °C) between 11:04:33-11:04:34 UTC on 21 July 2002. Bottom: ***[Left axis]*** FSSP concentration (thick solid), 2DC shadow-or (thin solid), and 2DP shadow-or (thin dashed); ***[Right axis]*** King LWC (thick dashed) measured from 11:02:24 to 11:06:43 UTC.

The leading edge of the storm (11:03:20-11:03:55) appears to be dominated by new growth with a peak cloud droplet (FSSP) concentration of 500 cm^{-3} and a maximum liquid water content of 1.6 g m^{-3}. Few precipitation-sized particles are evident.

The middle part of the penetration (11:03:55–11:04:55) appears to be through a mature portion of the cell. The 2DC images in Figure 5 were taken in this region. The combined 2D shadow-or concentrations were approximately 140 L^{-1} and FSSP concentrations had dropped to 200 cm^{-3} (Note: 2D shadow-or appears to be a reasonable estimate of concentration due to the high percentage of valid images). The irregular edges of many of the images suggest the particles are rimed (i.e. graupel). Smaller particles appear to be relatively smooth and spherical indicating that they may be super-cooled or recently frozen drizzle-size drops. The lack of needles and splinter-shaped particles suggests that the Hallet-Mossop mechanism may not be active in this region.

The last portion of the cloud (11:04:55–11:06:21) appears to be in the dissipating stage with little to no cloud droplet concentrations but with a sizable increase in 2D concentrations (to 250 L^{-1}). The 2D imagery in this region shows heavily rimed particles (that appear to have initiated on aggregated dendrites) and graupel. Time series plots (not shown here) indicate that there is an increased concentration from 2 to 100 L^{-1} of particles greater that 3 mm in diameter during this time (taken from 2DP data).

4.2 Near Cloud Base

Cloud base penetrations were performed at approximately 300 meters above cloud base on a regular basis to characterize the cloud droplet population and ascertain the absence or presence of large cloud droplets. Figure 6 provides observations of cloud droplet concentration, liquid water content and 2D shadow-or during a cloud base pass on 12 July 2002 from 11:35-11:38 UTC. These measurements were taken in an isolated cell similar to that penetrated on 21 July 2002 (shown in Figure 5).

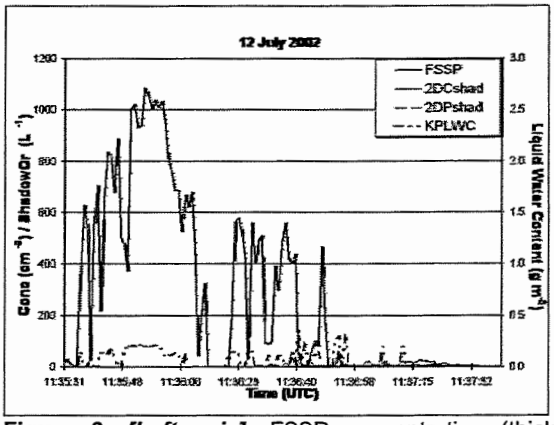

Figure 6. ***[Left axis]:*** FSSP concentration (thick solid), 2DC shadow-or (thin solid), and 2DP shadow-or (thin dashed); ***[Right axis]:*** King LWC (thick dashed) measured from 11:35:31 to 11:37:40 UTC at 3850 m (7.5 °C) on 12 July 2002.

Peak cloud droplet concentrations of 1000 cm^{-3} were measured near the beginning of the cloud penetration (11:35:35-11:36:10). These concentrations were accompanied by a liquid water content of 0.25 g m^{-3}. The high droplet concentration and lower liquid water content suggests the droplet distribution was made up of primarily small cloud droplets. Inspection of the cloud droplet size distribution (not shown here) shows a median diameter of 8.2 μm and no droplets greater than 20 μm. The cloud penetration continued through weaker clouds (11:36:20-:11:36:45) and into the beginnings of a rainshaft, as indicated by the sharp drop in cloud droplet concentrations and a small amount of precipitation-sized particles (2DC shadow-or). The raindrop size distribution was derived from

2DC and 2DP images and is very similar to that presented in Section 4.3 (Figure 7).

4.3 Below Cloud Base

Penetrations through precipitation shafts were obtained to characterize the raindrop size distributions of natural and seeded clouds. Figure 7 shows the instantaneous raindrop size distribution (5 second average) taken just below cloud base of an isolated cumulus cloud on 12 July 2002 (within 7 km of the one presented in Figure 6).

The presence of cloud droplets is caused by the penetration of cloud debris or scud clouds while obtaining this sample. This distribution was sampled at a time when 2DC and 2DP concentrations were at a maximum of 50 L^{-1}. As noted in the previous section, the distribution in Figure 7 is remarkably similar to the raindrop distribution measured near cloud base fifteen minutes later (Figure 7). The lack of variability in the raindrop distribution between the two clouds at different sampling heights deserves further investigation. One interpretation is that evaporation is not significant or not significantly changing the raindrop distribution between these two levels.

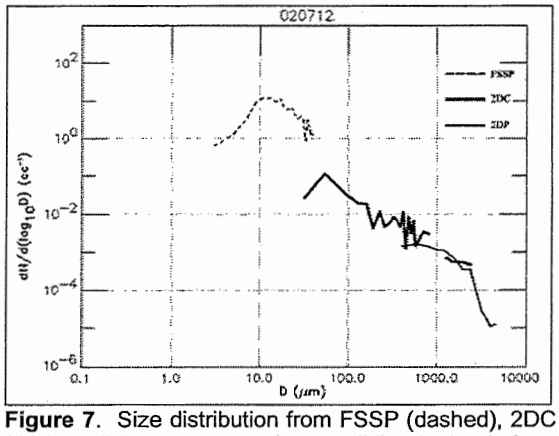

Figure 7. Size distribution from FSSP (dashed), 2DC (thick solid), and 2DP (thin solid) obtained from 11:20:50 to 11:20:55 UTC at 3500 m (13 °C) on 12 July 2002.

An exponential fit to the distribution in Figure 7, using the 2DC data for particles smaller 1 mm and the 2DP data for those larger than 1mm, is shown in Table 1. The slope of the fit, -2.77, is similar to that reported for thunderstorm rain in Switzerland by Joss and Gori (1978) but differs from the Marshall-Palmer fit reported for their observed rainrate (see Table 1). Differences in the multiplicative factor are most likely due to the UAE measurements being taken in a less intense rainfall (~ 25 dBZ) than those taken by the disdrometer in Joss and Gori. Large differences between instantaneous (sampling period less than one minute) and distributions averaged over hundreds of sampling periods were also reported by Joss and Gori. This suggests further investigation of the fits, both instantaneous and averaged, is required before implications to rainrate calculations and radar derived quantities are considered.

Table 1. Exponential raindrop size distribution fits.

UAE	$N = 122 \exp^{-2.72D}$
Joss-Gori *	$N = 14369 \exp^{-2.70D}$
Marshall-Palmer *	$N = 8000 \exp^{-2.53D}$

**N is normalized number concentration in m^{-3} mm^{-1} and D is diameter in mm. [* indicates values reported in Joss and Gori (1978)]*

5. SUMMARY

Results from four three-month field programs (two winter and two summer) conducted during 2001 and 2002 indicate that winter clouds are generally more stratiform, producing drizzle and light rain. However some convective events do occur. Summer precipitation is dominated by convective clouds formed by orographic lifting over the mountains and mesoscale interactions over the desert.

Based on the examples in Section 4, cloud droplet concentrations can reach a peak of 1000 cm^{-3} near cloud base and 500 cm^{-3} at -5 °C. Precipitation-sized particle concentrations tend to reach a maximum in the mature to dissipating stage of the cloud and may be as large as 250 L^{-1}. The high degree of riming evident in the 2D images suggest an active ice-phase process. The one example of raindrop size distributions from two clouds on the same day, but at different altitudes, showed a remarkable lack of variability but did show similarity to measurements reported by Joss and Gori (1978).

6. ACKNOWLEDGEMENTS

This research was funded through the Department of Water Resource Studies, Office of His Highness the President, United Arab Emirates. Aircraft and crew were provided by Weather Modification Incorporated. We are grateful to Dr. Stuart Piketh, Dr. Kristy Ross, Roelof Burger, Margaret Barenbrug, Dr. Tomoko Kojima, and Dr. Li Jia for their assistance in collecting the data. Special thanks goes to Dr. William Hall for his assistance in generating the size distributions from the 2D probes. NCAR is sponsored by the National Science Foundation.

7. REFERENCES

Joss, J. and E.G. Gori, 1978: Shapes of raindrop size distributions. *J Appl. Meteor.*, **17**, 1054-1061.

RAP (Research Applications Program), 2003: Rainfall enhancement and air chemistry studies, United Arab Emirates 2001-2002. *NCAR/RAP*, Boulder, CO, USA, 532 pp.

Rogers, R.R., and M.K. Yau, 1989: A short course in cloud physics. *Pergamon Press,* New York, 293 pp.

OBSERVATION EXPERIMENT OF AIRBORNE MICROWAVE RADIOMETER IN WEATHER MODIFICATION

Jin Dezhen[1], Gu Shufang[1], Zhen Jiaoheng[1], Zhang Jinghong[1], Li Maolun[1], Chen Xinzhi[1]
Lei Hengchi[2], Wei Zhong[2], Shen Zhilai[2]

[1]Jilin Weather Modification Office, Changchun, 130062
[2]Atmosphere Physics Research Institute of the Chinese Academy of Sciences, Beijing 10081

1. INTRODUCTION

In artificial precipitation modification operations, the liquid water content in the clouds is an extremely important cloud physical parameter, and the super-cooled water content in the clouds is a physical indicator that receives special attention in artificial precipitation modification. We made use of the airborne microwave radiometer developed by the Atmosphere Physics Research Institute of the Chinese Academy of Sciences and conducted some observation experiments of the artificial precipitation operations in Jilin Province between April and July from 2001 to 2002. Our findings show that instrument can do a good job in surveying the contents of liquid water and super-cooled water in vertical path integration clouds, and meanwhile, it can be used conveniently in scientific exploration in integration clouds so that operators can soon learn about the super-cooled water vertical content- rich distributions in the convective layer of the clouds, and they can get the liquid water vertical profile of the integration clouds. The flying below the clouds can acquire data about the whole liquid water content and its horizontal distribution in consecutive clouds. The flying in the 0 °C layer can obtain the super-cooled water content value in the clouds. It is an effective instrument in searching for the most potential area for artificial precipitation modification. So we can say that the airborne microwave radiometer is a new tool in measuring liquid water in clouds in weather modification activities. It is a blessing to the observations and experiments in weather modification.

2. PRE-OBSERVATION AND OUTLINES OF THE OBSERVATION

We installed the airborne microwave radiometer, developed by the Atmosphere Physics Research Institute of the Chinese Academy of Sciences, on the Y-12 plane used for artificial precipitation modification and conducted consecutive ground experiments for more than 200 hours in nearly 20 times near the Dafangshen Airport of Changchun, Jilin Province, between April and July from 2001 to 2002. The instrument could rather accurately measure the liquid water contents in the vertical paths above, and it could sensitively reflect their changes. Besides, in two years, we also conducted observation tests with the airborne microwave radiometer in 52 plane flights, aggregating to 122 flying hours, between April and July from 2001 to 2002.

Corresponding author's address: No.653, HePing Street, ChangChun City, JiLin Province,130062,China; E-Mail: jlwm@public.cc.jl.cn

3. PRELIMINARY FINDINGS OF THE OBSERVATIONS

In order to better illustrate the observed liquid water and super-cooled water with the help of the radiometer, we will make analyses of the observation findings obtained through the flights respectively on July 9, 2001 and April 22, 2002.

3.1 Survey of Liquid Water and Super-cooled Water Contents on July 9, 2001

3.1.1 Weather Conditions

The weather on that day showed obvious cold front system impacts. The system was quite thick with fairly good dynamic conditions.

3.1.2 Liquid Water and Super-cooled Water Observation Findings

On that day, there were heavy sheet clouds over the areas of our flying routes. There were two layers of sheet clouds in 1-3 km, and above 3.5-7 km were high sheet clouds and cirro-cumulus. That day's survey showed that the zero layer was at about 4.0 km.

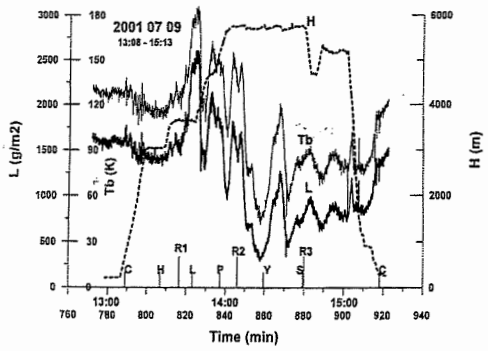

Chart 1: Height – time order of one flight survey on July 9, 2001.

Chart 1 shows the findings of one afternoon flight observation on July 9, 2001. the dotted line in the chart is the flight height reported by GPS (H); the thin line shows the Tb after the original records are determined; the thick line refers to the liquid water content (L) on the vertical path of the clouds; R1, R2 and R3 indicate the time of the three PPI scan by meteorological radar of 5 cm.

From the L curve in the chart we can see that the whole liquid water content could reach 2500g/m^2 and over 1000g/m^2 in places where the super-cooled water content was rich. The L curve in Chart 1, which appeared between Huaide and Liaoyuan, experienced 10-20-minute periodic changes (the corresponding spatial distance was 40-80 km). After that, though the surging ranges changed, the sub-periodic changes remained till the plane flow through Shuangyang ; there were periodic fluctuations of about 5 minutes between the various peak value sections on the L curve along Liaoyuan-Panshi-Yitong (spatial distance 20 km).

In order to understand the causes for these changes, we analyzed the radar echoes at three time periods. The radar echoes show that, on the L curve, the second half value level was obviously lower than that of the first half, which was exactly the reactions after quite strong wave subsided. It can be seen that there was plenty of super-cooled water in the convective rain zone in the sheet clouds.

3.2 Survey of Liquid Water and Super-cooled Water Contents on April 22, 2002

3.2.1 Weather Conditions

The weather conditions that impacted this precipitation was upper air cold eddy and its corresponding lower cold front zone, which were the major dynamics. The water vapor from the southwest quick currents was sufficient with good water vapor conditions, so the rain mainly occurred in the eastern part of our province where both the warm front and the cold front collided.

3.2.2 Observation Findings of Liquid Water and Super-cooled Water

On that day, along the flight route, there were As, whose bottom altitude was 3700-2800 m, and Sc, which was found between 1000 m and 2000 m. the radar observation told that that the top of the As was about 5500 m.

Chart 2 shows the time order of that days observations. The red line in the chart shows the liquid water content cLw (g/m^2); the blue line was the plane flying height, H (m) line obtained with the help of GPS. The horizontal coordinates indicate the time order.

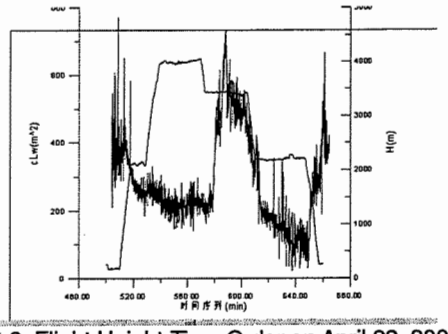

Chart 2: Flight Height-Time Order on April 22, 2002

In order to interpret the fluctuations of the liquid water contents, we analyzed that day's 250 km PPI radar echoes and learned that there was an east-west cloud belt to the south of Changchun. It was about 300 km long and about 50-100 km wide. It was moving up north. Besides, we say that, near Shuangliao, the radar echo was rather weak and its intensity was below 10 dbz; the echo close to Siping was becoming increasingly stronger, 15 dbz; and the echo in Panshi was further intensified to 20-25 dbz.

Chart 2 shows that the maximum value and the minimum value of the super-cooled water content in the whole layer of clouds were respectively 790.7 g/m^2 and 28.8 g/m^2. The average liquid water content was 286.7 g/m^2, and the average content of super-cooled water was 272.4 g/m^2. when the plane rose to 2000 m, the microwave radiometer detected that the liquid water content was the result of the joint impacts of As and Sc. The first peak value appeared, when the average liquid water content was 509.6 g/m^2, and the average super-cooled water content was 349.7 g/m^2. The plane started to fly horizontally when it rose from 2000m to 4000m. Now the detected super-cooled water content was comparatively low (refer to Chart 2), averaging at 233.9 g/m^2. Viewed from the macro section recorded by the flying operators, at this moment, the cloud was thin and bright (experience told that that it meant little water content). Now the radar echo was weak, below 10 dbz.

Between 09:38 and 10:12, the plane was at 3500m. Now the super-cooled water content was beginning to increase, which led to large peak value ranges. The changing ranges of the super-cooled water was 259.3-734.6 g/m^2. The biggest peak value appeared near Panshi, 734.6 g/m^2. Viewed from the macro section, now the cloud was dark, the plane exterior was beginning to freeze (experience told us that the water content was large), and the cloud was thick. The radar echo indicated that the echo intensity increased from 15 dbz to 25 dbz. Now the cloud conditions were good.

When the plane descended to 2000m, the contents of super-cooled water and the liquid water showed the tendency to increase. This agreed to the observation findings between the plane takeoff and its altitude at 2000m. It was the result of the joint work of

both layers of clouds.

From the above two instances, we have discovered that though the super-cooled water content of our detection was the same as the results of the radar echo and the macro observation, the findings of both surveys had 10^1 discrepancies. We probed into the cause and found out that, in the first instance, the plane observed as cloud, which contained many convective bubbles. In the second instance, the plane also observed as cloud, but the cloud was comparatively stable and without sandwich in between. The radar charts of these two days' flights tell that that, in the first instance, the maximum radar echo reached 35 dbz; and in the second instance, the maximum radar echo reached 25 dbz. From the two days' flight routes and the rain that corresponded to the ground in the leeward of the flights, we also discovered that, in the first instance, at the minimum rain spot (Yongji) in the leeward, the rain was 0.3mm in 6 hours at 20:00 hours, and the maximum rain spot (Huadian) witnessed 0.5mm; in the second instance, the rain was zero at various spots in the leeward in 6 hours at 14:00 hours. We hold that the above analyses reveal the causes of the discrepancies between the observations findings in these two days. It also demonstrates that our observation findings are authentic and reliable.

To sum up, we can see from these two instances that the findings about liquid water with the help of the microwave radiometer and the radar observation findings can be combined closely, which is enough to verify its operation.

4. BRIEF SUMMARY

This paper outlines and discusses the method of using airborne microwave radiometer to survey water and vapor contents in clouds. It offers a reliable way to make use of microwave radiometer to search for the zones with sufficient liquid water in the clouds in the sky so that we can raise the efficiency of artificial precipitation modification operations. The findings of ground observation experiments and the two flights reveal the principle of making use of airborne microwave radiometer to measure liquid water contents in the clouds. It verifies the practicality and the operational possibility of the airborne microwave radiometer, which has updated the new technology and new equipment for artificial precipitation modification operations by planes and further promoted the A&D in our country's artificial weather modification areas.

References

Zhu Yuanjing, Zhao Bailin, et al, Applications of Microwave Radiometer in Artificial Weather Modification, Beijing University Journal (Natural Science Edition) Volume 30, 5th issue, September 1994.

Robert J. Serafin, Gerard Szejwach, Byron B. Phillips, Applications of Airborne Remote Sensing In Atmospheric Sciences research J. G. R. 1986, 91 (C2), 2510-2516

Airborne Microwave Radiometer Measurements of Liquid Water content I: Instrument and Demarcation.

Airborne Microwave Radiometer Measurements of Liquid Water Content II: Inversion Method

THE COMPREHENSIVE OBSERVATION ANALYSIS OF A LC SEEDING MAN-MADE STEERING ICE CRYSTAL EXPERIMENT

Jin Dezhen[1] Lei Hengchi[2] ZhengJiaoheng[1] Xiao Hui[2] Cui Lian[1] Wu Yuxia[2] Liu Jian[1]

[1]JiLin Weather Modification Office, ChangChun, 130062, China
[2]Atmosphere physical research institute of Chinese Academy of Science, Beijing, 100871, China

1. INTRODUCTION

AgI is the widely used seeding agent in man-made rain-enhancement experiments and operation at home and abroad, it has a wonderful performs, the ice crystal nucleation rate is very high when the temperature is lower(below –10℃).But AgI has its limitation, in the cold clouds whose temperature is 0-4℃,AgI has no seeding function. Practical observation shows: super-cooled water content in this temperature range is remarkable higher than that in low temperature range (-5--20℃), it is advantageous to rain enhancement. If refrigerant (solid and liquid CO_2) is used as seeding agent, the limitation of temperature perhaps is broken. Using solid CO_2(SC), Schaefer had a man-made rain enhancement and fog dispersal, he achieved success. Fukuta.N provided "liquid CO_2 (LC)ice forming techniques", analyzed its effect fundamental, then had a wonderful result in wild field rain enhancement operation in Japan. Doctor Guo Xueliang developed three dimensional sheets model, had a model calculation to spreading LC, It shows that ten minutes later after spreading LC dynamic effect occurred in clouds, the development of the clouds is very fast, ice crystal and water content have a remarkable increased. Using the techniques, the workers from JIIIN Precipitation Modification and Hail Suppression Office made an experiment flying to research micro change of clouds before and after spreading LC and the effect to precipitation on July 11th,2002.This experiment flying mainly used airborne particle measure systems (PMS) to research, using three different sonde, measure particle that include clouds cloud droplet, ice snow crystal and rain droplet, the scale is 0.5μ-6400μ,the radar, satellite and microwave radiometer were used to research the change of super-cold water and clouds.

2. WEATHER CONDITION AND OBSERVATION SITUATION

IN 850hpa weather maps of 08h on July 11th,2002, low vortex center was near to Qiqihar city(123E,47N), ChangChun city was in southwest air-flow of vortex base; From 700hpa weather map(figure 1), there was a low vortex whose geopotential height was 296 in the same location, the back of the vortex was matched by cold air, ChangChun was in northwest air-flow. From 500hpa maps, East Asia was in long wave trough, the vortex center location is to the north. From 10h satellite clouds maps (figure 2), there was a vortex clouds system near Jilin province, the vortex center is on the boundary of inner Mongolia, from 11h to 13h, the vortex was steady, the tail of the vortex clouds systems move towards northeast slowly. The spreading operation area was in southeast quadrant of the vortex systems.

Corresponding author's address: No.653, HePing Street, ChangChun City, JiLin Province,130062,China; E-Mail: jlwm@public.cc.jl.cn

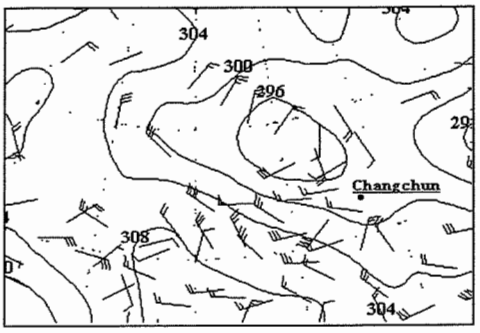

Figure 1. 700hpa weather map in 08h July 11th, 2002

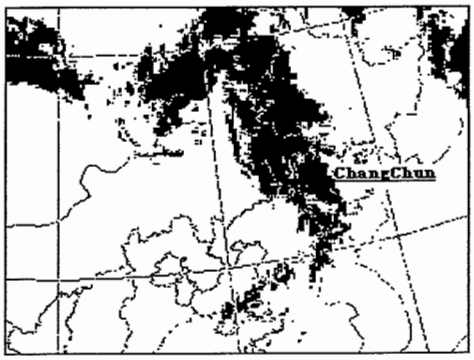

Figure 2. Infrared satellite cloud map in 10h, July 11th 2002

3. DETECTION AND SEEDING RESULT

3.1 The Effect of Operation to Cloud Mic Physical Characteristics

Table1 shows that the total concentration of the clouds droplet had no large change before and after

operation, but the water content increased two times, the average diameter and volume diameter of clouds droplet have increased, it means that the clouds droplets became bigger quickly after spreading LC, the precipitation element concentration in clouds increased.

Table1. Clouds droplet characteristic distribute before and after operation(F100 sonde)

	time	Tot con (N/m^3)	Tot water (g/m^3)	Ave Dia(μ)	Ave v-Dia (μ)
Before	11:24-11:34	$3.05*10^6$	2.09E-3	9.98	12.1
After	11:34-11:44	$2.08*10^6$	4.50E-3	14.3	16.6

Concentration of precipitation particle have a remarkable increase after operation, ice crystal concentration have a 33% increase, the concentration of the particle whose diameter is above 300μ decreased, it means that the increase of concentration of precipitation particle is caused by ice crystal. The water content of particle whose diameter is above 300μ had a large increase that means the average diameter of precipitation particle increased after operation. Professor Zhao BoLin thought that when the water content is 0.1g/m^3, only the concentration of the ice crystal is 125/L, precipitation efficiency can reach maximum. The water content in this experiment area is 0.2 g/m^3, but the concentration of ice crystal is lower, it means that the clouds systems in experimental area have a large seeding potential, much more spreading amount is needed. The precipitation particle concentration decreased after operation, water content increased. The super-cool water content from radiometer measure decreased after operation perhaps because the increase of ice crystal concentration and the growth process of precipitation particle expend a lot of super-cool water.

Figure 3 is the precipitation particle two dimension picture of 2D-C sonde probe before and after spreading, the above two is before spreading, the sampling heights 5130 meters and 5190 meters, the temperature is -2℃, the concentration of precipitation particle is 9443-10425/m^3, the biggest particle diameter is 400μ, the shape of particle are mainly snowflake and columnar ice crystal; the below three in figure 3a is the two dimension picture of precipitation particle after operation, the above two sampling height is 5100 meters, the temperature is about -2℃, the concentration of precipitation particle is 13278-25477/m^3, the biggest particle diameter is 350μ; the last one is gotten from the probe near 0℃ layer, the height is 4520 meters, the particle concentration is 8135/m^3, the biggest diameter is 600 μ, mainly smooth-edge rain droplet and irregular aggregation ice crystal.

Figure 4 is the precipitation particle two dimension picture of 2D-P observation, flying height is the same as 2D-C. the above two is before spreading, the particle concentration is 36-120/m^3, the average is78/m^3, the biggest particle diameter is 2000μ, the below three in figure 3b is the two dimension picture of precipitation particle after operation, the shape of particle is more complicated than that before spreading, there are columnar ice crystal, riming snowflake etc, the particle concentration is about 1785/m^3, the biggest particle diameter is 2400μ. the concentration change of precipitation particle after operation is not large, the biggest particle diameter is remarkably increase, smaller particle concentration decreased.

Figure 3. 2D-C precipitation particle picture before and after spreading

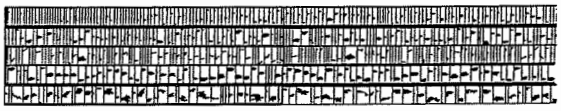

Figure 4. 2D-P precipitation particle picture before and after spreading

3.2 The change of precipitation echo intensity after operation

The radar data is from 5cm radar of JiLin province meteorological observation. Effect area is in the leeward of operation, the diffuse angle is 105 degree. The length is 100km, the operation line is 40km. Because the aircraft can not reach contract area to have a cloud micro physical observation, only use precipitation echo biggest intensity and 35Dbz,30Dbz and 25Dbz area change to discuss the effect of operation to clouds(table 3). On 11:16, the operation was not made, the precipitation echo of effect area and contract area stand for natural situation, the two area are all sheet precipitation echo, contract area was stronger than that in effect area, contract area echo intensity is 35dbz, that in effect area is 20dbz. From 11:30 to 12:00, echo intensity and area in contract area have no large change, biggest echo intensity in effect area enlarged from 20dbz to 35dbz, the area of 25dbz enlarged from 4500km^2 to 7000km^2, this had a match with precipitation particle enlargement after operation.

4. CONCLUSION

After spreading LC in sheet clouds, there are following changes in operation area:

(1) cloud droplet concentration has no large change, average diameter and volume diameter of cloud droplet have remarkable increased, so the concentration of precipitation element increased;

(2) ice crystal concentration is 11020/m^3 before spreading and 14615/m^3 after spreading, the increase rate is 33%;

(3) the super-cool water content in clouds reduced from 850.7g/m^3 to 579.7g/m^3, decrease rate is 32%;

(4) The water content of particle whose diameter is above 300μ had a large increase, the concentration reduced, it means that average diameter of precipitation particle have a remarkable enlarge;

(5) area of radar strong echo have a increase, the area of 25dbz enlarged from 4500km^2 to 7000km^2,have a 36% increase. In a word, after spreading LC, dynamic effect occurred, ice crystal intense, precipitation element intense and the average diameter of precipitation particle in clouds have remarkable increased, these made ground precipitation increase.

Reference

Wang XueLin, Gu ShuFang, 2001: Clouds and rain characteristic of twice Jianghuai cyclone and the comprehensive analysis of man-made seeding clouds. Applied meteorology vol. 12, Match.

Ye JiaDong , Fan PeiFen, 1992: The micro structure analysis of sheet precipitation area in a slowly moving meso-scale convection convergence body. Atmosphere science, Vol. 16, No.4 July,

PRECIPITATION OVER THE SEA IN THE COASTAL AREA OF ISRAEL; A POSSIBLE NEW SOURCE OF WATER

Zev Levin, Joseph Breitgand and David Shtivelman

Department of Geophysics and Planetary Science
Tel Aviv University, Ramat Aviv, 69978, Israel

1. BACKGROUND

The search for new water resources in arid and semi-arid regions like Israel is crucial (Margat at al. 2000, Gabbay 1998). Recent dry years in this region have demonstrated how critical these situations can become. One source of fresh water that has not been utilized is rainfall over the sea. Although precipitation in the eastern Mediterranean falls only in the late fall, winter, and early spring, the amount of water that falls over the sea, just a few kilometers to the west of the coast of Israel, for example, could potentially be used as a new and relatively inexpensive additional source of natural high quality fresh water. In this paper, we describe measurements that show the potential of this unexplored source and suggest a method for collecting rainwater over the sea.

2. RAIN OVER THE SEA VERSUS OVER LAND

Meteorological observations conducted in the area of Tel-Aviv during the rainy seasons in the last ten years, using the Tel Aviv University C-band meteorological radar show that the quantity of precipitation over the sea near the coast is sometimes similar, but often substantially greater than the quantity of precipitation over a similar area on the land just to the east of it. Moreover, even during dryer years over the land, the precipitation over the sea west of the coast of Israel is still substantial. The reasons for this stem from the fact that in the winter the Mediterranean Sea is warmer than the adjacent land, leading to land breeze from east to west in the lower elevations. This wind opposes the synoptic westerly winds, slowing the approaching storms and in some cases preventing the clouds from crossing the sea shores (Khain at al. 1993).

Corresponding author's address: Zev Levin, Department of Geophysics and Planetary Science, Tel Aviv University, Ramat Aviv, 69978, Israel; E-mail: zev@hail.tau.ac.il

In order to better quantify the difference between quantity of the rain falling over the sea versus that that is falling over land, we defined an area of a 60 km radius around the Tel Aviv University meteorological radar (northern Tel-Aviv). The analysis of the data indicates that in this area the ratio of the monthly average precipitation over the sea to that over the land ranges from 1:1 to 3:1 (Figure 1).

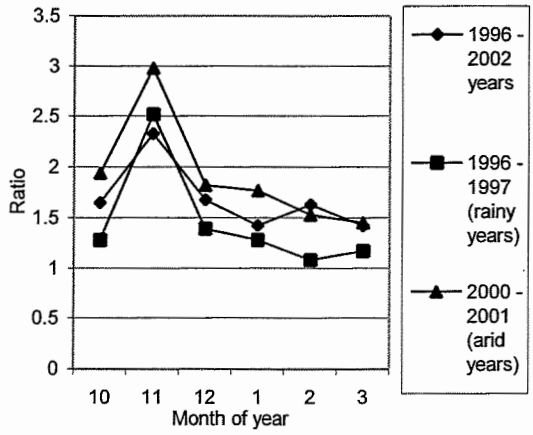

Figure 1. Sea / land precipitation ratio.

In other words, the amount of precipitation falling on the sea near the coast is as much as three times that falling over the adjacent land. In addition, the precipitation period in the costal sea area is often as much as two months longer then that over the adjacent land.

Figure 2 demonstrates the total precipitation amount in November 1996. In this month sea /land precipitation ratio was 2.5 and, as we can see, most of precipitation falls in the sea near the coastline of Israel.

In order to determinate the possible water harvesting time more qualitatively, we defined the effective precipitation region. That region is the compact region, were the precipitation rate exceeds a threshold value during fixed time. This is the time that we define as the potential water harvesting time. In our present evaluation we take into account only

water harvesting regions with water harvesting time of more than two hours. We suggest that such regions could fit well our water harvesting technology.

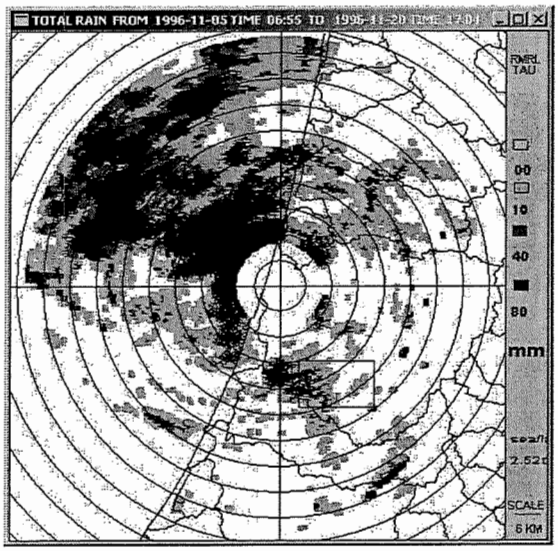

Figure 2. Radar integrated precipitation amount in November 1996.

Using archived radar data we calculate the harvesting time for effective precipitation regions having intensities of more than 35 mm / hour.

Taking into account that the data is not complete because of the radar technical problems, we have the following results.

Table 1 demonstrates the potential of harvesting time in effective regions with rain intensity threshold 35 mm / hour in the sea near the coastline of Israel in 60 km radius from the Tel Aviv University radar. It is about 400 hours for rainy and ordinary years and it exceeds 250 hours for dry years. Assuming that the characteristics of the rain is similar in adjacent areas of larger extend, the harvesting time may be enlarged accordingly. We estimate that the harvesting time could be enlarged by factor of 2 – 3 in 100 – 150 km region along the coastline of Israel.

Season (years)	Harvesting time (hours)	Type of season	Observation period (month)
1997 – 1998	396	Mean	1997:10,11,12 1998:1,2,3
2000 – 2001	248	Dry	2000:10,12 2001:1,2
2002 – 2003	387	Rainy	2002;10,11,12 2003:1,2,3

Table 1.Harvesting time in the sea near the coastline of Israel (60 km radius area) for different years.

Figure 3 demonstrates the monthly distribution of potential harvesting time in effective regions with rain intensity threshold 35 mm / hour in 60 km radius area from Tel Aviv University radar.

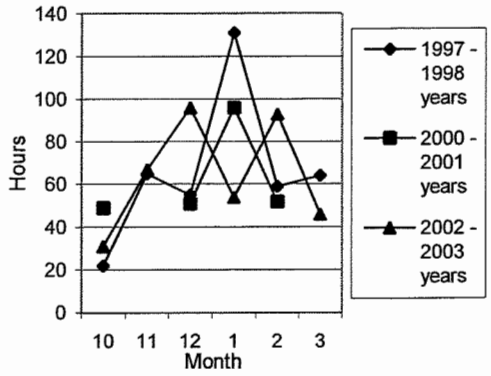

Figure 3. Distribution of potential water harvesting time.

Investigations conducted in Israel (Gabbay 1998, Mamane 1987, Singer 1994) also show that the quality of the rainwater falling over the sea near the coastline is higher (particularly with regard to PH) then that of rainwater over continental regions. This is primarily due to the degradation by pollution over the continent. This suggests that the rainwater over the sea might be of sufficiently high quality to make the proposed technology economically feasible not only due to the lower cost of water collection, but also due less expensive treatment to make it ready for human consumption.

3. THE PROPOSED METHOD FOR HARVESTING RAINWATER OVER THE SEA

The method consists of a ship or ships with relatively large rain collecting surfaces. Rainwater is collected by guiding the ship/s to the center of the rain shaft in the storm and by continuously remaining under it during the storm's lifetime.

Important elements of the rainwater harvesting technology involve the use of long and short-range weather forecasting tools. These tools can be composed of numerical forecasting models for the longer-range prediction (MM5 (Grell at al.1995) or RAMS (Walko at al. 2001)) and radar tracking and forecasting tools (e.g. TITAN -Thunderstorm Identification, Tracking and Analysis (Dixon at al. 1993)). The role of these tools is to identify in advance the place, time and characteristics of the rain in real time, to accurately forecast the rain process development and to direct the ships to the area where the maximum rainwater can be collected.

In order to maximize rainwater production while minimizing the overhead costs, the routes of the collecting vessels have to be optimized. The optimization algorithms need to take into account that at any time there can be a number of regions with similar rain potentials and rain intensities. If a number of vessels for water harvesting are used, it is important to take into account the relative mutual positions of the vessels with respect to the rainy regions, and the costs versus expected benefits of deploying a specific vessel to a specific region for the next time window.

Therefore, to perform this work effectively the following components are needed:

- Radar-based estimation of maximal precipitation potential and maximal rain intensity over the sea, west of the coast of Israel.
- Forecasting of precipitation development and storm movement using both radar and numerical-statistical models.
- Choosing optimal routes for ships on which the potential for water harvesting is maximal.
- Navigating, managing and controlling the vessels used for water harvesting.

4. THE MANAGEMENT OF THE OPERATIONS

Although the system seems rather simple, it does require number of components in order to manage the operations and optimize the harvesting process. The basic system components are the management center, the meteorological radar, ships and the port quay.

The management center contains hardware and software for the meteorological radar data control system; the meteorological forecasting system; the ship control system; the radio communication system.

The meteorological radar is equipped with the special purpose hardware and software for presenting the information about the current precipitation rate and ship's location in real time. This information is used by the management center to navigate the ship towards, and within the water collection region.

The ship is equipped with special means for water collection, radio communication system, GPS system and active reflector for facilitating the recognition of the ship's coordinates on the radar.

In the port we need a quay being equipped for unloading and transporting the water from the ship to the storage places or for disseminating it to the users.

5. COST ESTIMATION

Although the precise evaluation of this method and the best ways to utilize it are still under investigation, it is worthwhile to estimate the cost of the proposed method. Characteristics of the modern vessels such as tankers and ocean barges that can be used for water harvesting, suggest that an area of water harvesting on the top of such vessels can reach a size of 6000 - 15000 m^2 per vessel (Marcon International).

From the statistics of the Israeli Meteorological Service (Shacham 1992) and from our radar measurements (Table 1) we know that during the rainy season there are about 400 suitable hours per year within effective precipitation regions with rain intensity threshold 35 mm /hour in the sea near the coastline of Israel in 60 km radius area from Tel Aviv University radar.

Therefore, potentially, 84,000 - 300,000 cubic meters of fresh water can be harvested per season using a single vessel. Of course, a number of such ships could be used simultaneously and special facilities for increasing the rain harvesting area on the ships can be designed to improve the collection by a factor of 1.5 – 2.

The method is economically affordable and not harmful to the environment. Using this method one can harvest natural high quality fresh water at the price of less than about 0.45 USD per cubic meter. This price is equivalent or lower than the current best estimates for desalination, but it could be reduced considerably if more than one ship is used and larger area is covered. It should also be remembered that the quality of water from the rain is much better than the water obtained from desalination, so that subsequent treatment is much cheaper. In addition, the presented method has no additional costs such as removal of salt or other complicated maintenance issues.

6. CONCLUSION.

In this paper, we describe measurements that show the potential of one unexplored source of natural fresh water, namely rainfall over the sea, and suggest a method for collecting this water. The method is economically affordable and not harmful to the environment. Using this method one can harvest natural high quality fresh water at the price of less than about 0.45 USD per cubic meter.

Although the proposed system seems rather simple, it does require number of components in order to manage the operations and optimize the harvesting process. The basic system components are the management center, the meteorological radar, ships and the port quay.

The proposed technology could be used not only in Israel but also in many other regions suffering from water deficiency and lying near the coastline. Such a system could be very useful for small islands with very little rainfall and not many underground

resources. Examples of regions in which such a system could be effective include: Cyprus, Sicily, Crete, Crimea, Singapore, some of the Greek Islands and more. Investigation of the characteristics of these regions could provide information for optimal configuration of the proposed technology so that the local factors can be taken into account.

7. REFERENCES

Dixon, M., Wiener, G., 1993: TITAN: Thunderstorm Identification, Tracking, Analysis, and Nowcasting – A Radar-based Methodology, Journal of Atmospheric and Oceanic Technology, pp. 785 – 797.

Gabbay, S., 1998: The Environment in Israel, Jerusalem, pp. 17 - 57.

Grell, G. A., Dudhia, J., Stauffer, D. R., 1995: A Description of the Fifth-Generation Penn State/NCAR Mesoscale Model (MM5), NCAR/TN-398+STR, pp. 1 - 91.

Khain, A. P., Rosenfeld, D., Sednev, I., 1993: Coastal effects in the Eastern Mediterranean as seen from experiments using a cloud ensemble model with detailed description of warm and ice microphysical processes, Atmospheric Research, 30, pp. 295 - 319

Mamane, Y., 1987: Chemistry of precipitation in Israel, The Science of the Total Environment, 61, Elsevier Science Publishers, pp. 1- 13.

Marcon International, Inc., Ship Brokers and Marine Consultation, Internet site.

Margat, J., Vallee, D., 2000: Mediterranean vision on water, population and the environment for the 21st Century, Medtac Blue Plan report, pp. 5 - 29.

Shacham, Report of rain enhancement, 1992, (in Hebrew), pp. 1 – 41.

Singer, A., 1994: The Chemistry of Precipitation in Israel, Israel Journal of Chemistry, vol. 34, pp. 315 - 326.

Walko, R., Tremback, C. J., 2001: RAMS - Regional Atmospheric Modeling System, Introduction, Technical Report, pp. 1 –11.

DETECTION OF DIFFUSION ON MOUNTAINS OF BEIJING

Ruijie Li

Beijing Weather Modification Office, Beijing, 100089, China

1. INTRODUCTION

Beijing Is encircled mountains from 3-directions. Aim for this situation, for the demand that enhancing-rain (snow) in winter and spring, Beijing Weather Modification Office has empoldered Silver Iodide Generator of Ground Based, and studied its applied technology that using in Beijing.

In order to grasp diffusion law of catalyst In mountains, we be on experimentation to know atmospheric hierarchical stability and diffused parameter, these is impotant data.

In the article, detection in western mountain of Beijing as a example, to explain method of detect, data of experimentation, method of assay data, conclusion, and demonstrate to characteristic diffusion In mountains of Beijing.

2. AIM OF DETECTION

Now, most of modles be used to simulate diffusion of plain, don't suit mountain. There are some experimentation that research diffusion of mountain, have resumptively summarized its characteristic and experiential parameter. But surve a given area, there is must idiographic experimentation to know its trait.

3. INSTRUMENT OF DETECTION AND CONDITION OF GEOGRAPHY

We detect wind speed on 3-orientation, as main mothed. the automatic weather station (6-factor) is secondary, be used to collect meteorologic data on peak. Two instrument are mounted on top of mountain Jianzi. It stand on western of Beijing, geographical coordinate is north latitude 39°59.605′ and east longitude 116°08.737′, height above sea level is 760 meters.

4. ACADEMIC BASIS

The method of compute data is corresponding with method of detection. Compute veer of the wind every second. The horizontal and vertical respectively.

Corresponding author's address: Ruijie Li, Beijing Weather Modification Office, No.44, Zizhuyuan Road, Haidian District, China; E-Mail: leeruijie@sina.com.

Them are marked as σ_A and σ_E on standard deviation of angles is standard that classify stability of meteoric samdwich.

σ_A and σ_E reflect diffusivity of turbulence directly, their computing are used in the process that compute diffused parameter by Cramer mode.

5. CONDITION OF DATA

The examination that detect 3-direction wind speed from November 20,2002 to March 20,2003, over whole winter of Beijing. The examination got momentary a set of wind speed every second, their units are m/s. There is 3600 groups in a hour. the amount make compute be trusty.

The automatic weather station (6-factor) was used from November 20,2002 to today, has gained meteorologic data over whole year. The six factors are temperature, humidity, wind direction, wind speed, air pressure, and radicalization.

6. CLASSIFY STABILITY OF METEORIC SAMDWICH BY STANDARD DEVIATION OF ANGLES THAT WIND VEER

We adopt Pasquill's classified method to classify stability of meteoric samdwich. There are six levels—A, B, C, D, E, and F. they respectively denote exceeding instability, middling instability, slender instability, neutral, slender stability, and middling stability.

The standard deviation of angles that wind veer is standard that classify stability of meteoric samdwich. Final result needs to be corrected by wind speed.

The veer of wind direction is continual. We must reduce the effect that wind direction warp to the best of one's abilities. Cut a long period of time (a hour) as some shot period of time (ten minutes). The method can suffic amount (more than 360) of data as well as accord with aerographical familiar length of period of time.

7. COMPUTE DIFFUSED PARAMETER

According as nether formula (H.E.Cramer, 1957) , we compute the diffused parameter.

$$\sigma_y = \sigma_A \cdot x^p$$

$$\sigma_z = \sigma_E \cdot x^g$$

Thereinto, p and g are functions of stability as soon as leeward distance-x. Units of σ_A and σ_E are radian.

According to levels of stability, we class the standard deviation of angles that wind veer, compute diffused parameter. Then compute diffused coefficient by regression.

It is time-list data that be detected by examination on one space-point, the diffused parameter don't change along with change of distance, its characteristic curve show as a beeline.

8. RESULTS

Compare diffused parameter of western mountain with northern mountain, with plain area.

We get diffused character of Beijing mountain.

We can conclusion diffused condition by the character and meteorologic data that on peak, and use the parameter in diffused mode.

REFERENCE

Jiang W.M., Cao W.J., and Jiang R.B., 1993: Tutorial of air pollution meteorology. China Meteorological Press.

Shi X.C., Jiao D. J., and Wang W., 1982: Calibration method of surface wind data in mountainous pollution meteorology research. Proceeding of turbulence diffusion and pollution meteorology. 139-145.

Chen J.Y., 1987: Evaluation of atmospheric environment effects. environmental scientific center of Beijing university.

EFFECT EVALUATION OF SEEDING ROKETS OPERATION IN BEIJING REGION

Shuyan Li[1] and Wei Li[2]
[1]Beijing Weather Modification Office, Beijing, 100089, China, E-mail:lw1024@263.net
[2] Atmospheric Observing Experimental Base of CMA, 100089, China

1. introduction

The operational area are Yanqing district and changping district in Beijing, according to the cloud system's moving direction (northwest to southeast), we take Chicheng county and Chongli county as contrast area which lie to the upwind area of Beijing and will not be influenced by seeding. Both operational area and contrast area are mountain region. There is an isolated zone of 4-5km width between operational area and contrast area. There was totally 19 times seeding operations during flood season from 2001 to 2003. Because randomized experimental scheme is not suitable to anti-drought and outfield experiment and only suitable to scientific research. So in this paper what we utilized is non-randomization experimental scheme, non-randomization experimental scheme includes sequential analysis method, regression analysis method and regional comparison method.

2. Example analysis

We take September 26,2003 as an example to illustrate the process of seeding rocket operation. seeding rocket flares (10 grams AgI in one rocket flare) was seeded for every 100 square kilometers in our seeding operation. and rockets can reach to 6300m.

Shuyan Li: No.44, zizhuyuan road, haidian district Beijing weather modification office., Beijing, 100089, China.e-mail: lw1024@263.net

At that day warm and humid airflow which came from southwest met with cold weak airflow that came from northwest and then formed the stable precipitation that lasted for 2~3 days. At 08:00(Beijing time), On 700hPa level and 500hPa level the southwest airflow was dominant airflow and the wind velocity was 12m/s. Wind direction was 260 degree on 400hPa(7460m) while wind velocity was 21m/s. We launched 8 seeding rockets continuously at location A from 10:59 (Beijing time)to 11:03(Beijing time), the radar echo intensity was 25-30dbz at Yanqing (area B)before operation and then strengthen and reached to 30-35dbz half an hour later after operation, and area of intense radar echo obviously increased. Similar change could also be found from radar liquid content image that both liquid water content and liquid water area increased. Furthermore we could see from figure 3 that precipitation region extended to northeast along operational region and formed a heavy precipitation center at Yanqing(location B).

The real precipitation measurement value is 28.7mm/24hr , expectation value calculated with regression analysis method was 16.47mm/ 24hr , so relative precipitation enhancement ratio was 44.95%.

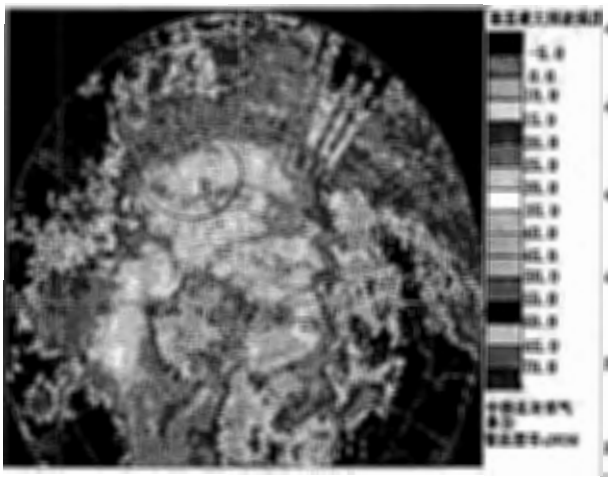

Fig.1 vertical maximal intensity of radar echo at 11:03(Beijing time), on September 26,2003

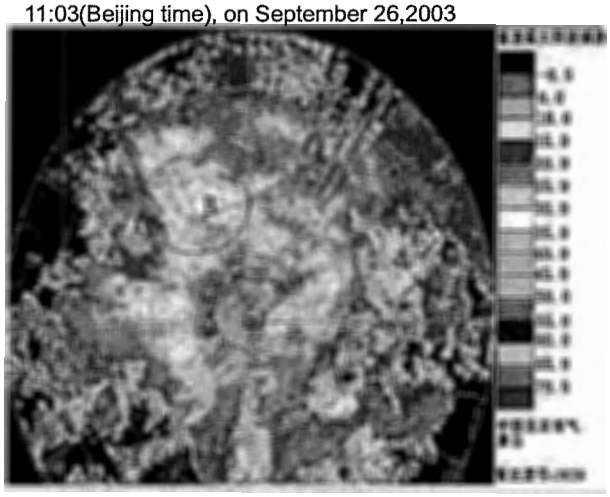

Fig.2 vertical maximal intensity of radar echo at 11:30(Beijing time), on September 26,2003

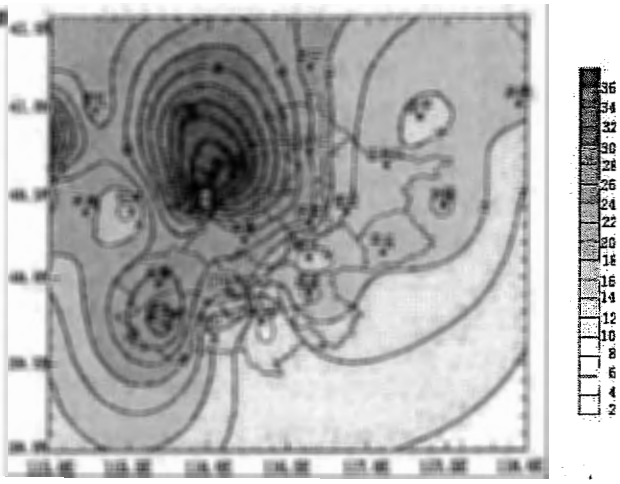

Fig.3 actual rainfall distribution(24h) at 08:00(Beijing time) from 26 to 27, September 26,2003. seeding rocket was launched at point A .

3. Evaluation of precipitation enhancement effect using three different statistical methods

3.1 Sequential analysis method to evaluate precipitation enhancement effect

Because of great difference of temporal and spatial precipitation distribution, there exists limitation in physical sense using sequential analysis method. False effect will be caused when we substitute historical average precipitation for natural precipitation in operational period, and the false effect changes with different length of historical data. Based on statistical theory, if we want to get obvious effect of artificial precipitation (a=0.05), the expecting rain amount increased by seeding must should be much more than the possible value increased by precipitation enhancement. So the sensitivity of sequential analysis method is low.

3.2 Regional comparison method to evaluate precipitation enhancement effect

Table 1. Evaluate precipitation enhancement effect using regional comparison method

	Total amount of rain in operational area from 2001 to 2003(mm)	Total amount of rain in contrast area from 2001 to 2003(mm)	Absolute rain enhancement(mm)	Relative rain enhancement(%)	Statistical power(a)
June	66.1	37.3	28.8	43.57	a≤0.05
August	67.8	47.8	20	29.5	a≤0.1
September	35.1	23.85	11.25	32.05	a≥0.1

Table 2. Evaluate precipitation enhancement effect using regression analysis method

	Total amount of rain in operational area from 2001 to 2003(mm)	Total amount of rain in contrast area from 2001 to 2003(mm)	Regression equation	Absolute rain enhancement(mm)	Relative rain enhancement(%)	Statistical power(a)
June	66.1	37.3	Y=2.857+0.532X	23.45	35.47	a≤0.005
August	67.8	47.8	Y=0.634+0.543X	20.69	30.52	a≤0.005
September	35.1	23.85	Y=1.957+0.571	10.239	29.17	a≤0.005

Table 3. Evaluate precipitation enhancement effect using sequential method

	Average amount of rain in operational area from 1991 to 2000(mm)	Average amount of rain in contrast area from 2001 to 2003(mm)	Absolute rain enhancement(mm)	Relative rain enhancement(%)	Statistical power(a)
June	5.745	8.263	2.518	30.47	a≥0.1
August	7.445	13.56	6.115	45.09	a≤0.05
September	5.885	5.85	-0.035	-0.59	

At different geographical region the precipitation distribution is very different, so it is hard to evaluate the effect of precipitation enhancement in scientific and objective way.

3.3 Regression analysis method to evaluate precipitation enhancement effect

This method doesn't suppose that precipitation change with time and region must be stable, so it's more applicable than sequential analysis method and regional comparison method. But it takes the hypothesis that the relativity between precipitation in operational area and precipitation in contrast area should be the same as precipitation relativity of the two area in the same seeding season. However the weather in experimental period and the weather in historical period when we built the regression formula are possibly asymmetric, the asymmetry would make the physical basis of the scheme not so sufficient.

4.Conclusion:

1 Number of historical sample, number of operational sample and precipitation correlative coefficient will directly affect the evaluation of precipitation enhancement. The more the historical sample, the better the precipitation correlative coefficient will be, in turn the more closer to real increased precipitation the evaluation result using statistical methods.

2 Although each method owns its advantage and disadvantage, evaluation results using the three statistic methods shows that seeding operation with rockets in June and August is sure to have increased rainfall. Although there is no obviously increased rainfall using regression analysis method to assess rain enhancement in September, positive results still can be obtained with the other two methods. So we can draw the conclusion that rocket method of precipitation enhancement is effective and can obviously increase precipitation. For stable cloud system if we operate several times in 24 hours the effect of precipitation enhancement is obvious.

Reference:

Guangping, Zeng 1991, analysis of rain enhancement at Gutian reservoir during 1975-1986, atmospheric science, 15(4),97-108.

Guang ping Zeng, feng Xiao,1983,influence of natural

VIL AS AN INDICATOR OF HAIL SIZE

Laura López, Eduardo García-Ortega, Jean Dessens and José Luis Sánchez

Laboratorio de Física de la Atmósfera, Instituto de Medio Ambiente, Universidad de León, Spain.

1. INTRODUCTION

The parameter known as *Vertically Integrated Liquid* (VIL), introduced by Greene and Clark (1972), is today one of the tools most widely used by forecasters when it comes to detecting hail cells in conventional meteorological radars. Numerous studies have been devoted to this parameter (Edwards and Thompson, 1998; Boudevillain and Andrieu, 2003).

Amburn and Wolf (1997), aware of some of the limitations of VIL, defined a new variable called *VIL Density* (DVIL) and showed its usefulness as a severe hail forecaster in northeastern Oklahoma and northwestern Arkansas. This same parameter has been subsequently tested at regional levels by various authors (Turner and Gonsowski, 1997; Roeseler and Word, 1997; Troutman and Rose, 1997 and Blaes et al., 1998).

The aim of both parameters, VIL and DVIL, is to develop a criterion that informs radar operators of the potential occurrence of severe hail events. Some previous studies have shown that an increase in VIL Density brings with it a parallel increase in the maximum hailstone size registered (Blaes et al., 1998; Amburn and Wolf, 1997; Belk and Wilson, 1998; Hart and Frantz, 1998). A similar process has been observed with the VIL parameter (Edwards and Thompson, 1998). This last fact will be of great use in this paper to forecast hailstone sizes registered on the ground in the study zone on the basis of the values of these parameters.

2. STUDY ZONE

The study zone is located in the Middle Ebro Valley, in the northeast of the Iberian Peninsula.

Corresponding author´s address: J. L. Sánchez Gómez, Lab. Física de la Atmósfera, Campus Universitario, Universidad de León, 24071 León, Spain; e-mail: dfqjsg@unileon.es

It has a land area of approximately 50,000 km^2 (Figure 1). Hail storms are very frequent in this area during the summer (Font, 1983). The mechanisms that explain the formation of these hailstorms have been analyzed by various authors (Ramis et al. 1999; Tudurí et al., 2003).

With respect to the intensity of hailfalls in the Iberian Peninsula, the results show that most of the storms do not lead to severe hail events (Fraile et al., 2001), following the same trend as in the rest of Europe (Giaiotti et al., 2001; Dessens and Fraile, 1994).

FIG. 1. Study zone and range of the meteorological radar.

3. METHODOLOGY

The Laboratory for Atmospheric Physics at the city of Zaragoza owns a meteorological C-band radar. Two types of data were employed to determine which storms had caused hailfalls:

1. Data provided by a network of 169 hailpads displayed in an area of 2,700 km^2.

2. Data provided by an dense network of observers. Thus, as soon as a storm was detected the local observer was called and informed of the likelihood of a hailfall. The observer would then be prepared to record any possible hail event and the approximate sizes of the hailstones.

This working procedure avoids what some authors (Blaes et al., 1998; Wyatt and Witt, 1997) consider the most important source of errors in this type of study: inaccuracies in locating and verifying hailfalls.

The database used for this paper is made up of 75 storms, of which 58 caused hailfalls (some severe and some not).

4. RESULTS AND DISCUSSION

The correlations found between hailstone size and both VIL and VIL Density are statistically significant at a level of 0.01. However, the correlation for VIL Density is slightly better.

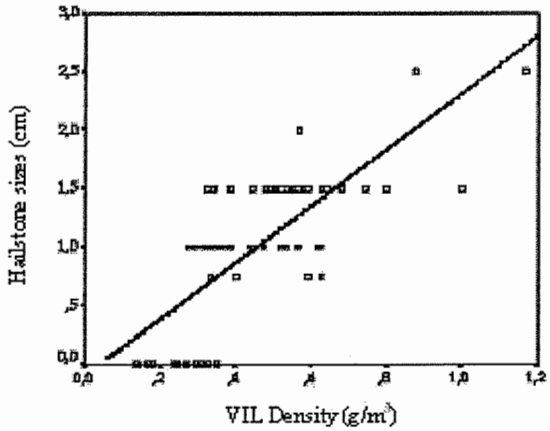

FIG. 2. Hailstone size versus VIL Density. The dots represent separate storm events.

Figure 2 shows that there is a wide range of variation for sizes larger than 1.5 cm. These low values make the relationship poorer. These results coincide with those found by other authors (Edward and Thompson, 1998), highlighting the small correlation between VIL and hailstone sizes smaller than 5 cm.

4.1 Case studies

The relationships found between the maximum estimated hailstone size and both VIL and VIL Density have shown satisfactory correlations. We then decided to apply these relationships to the study area where hailpads were available. The results would thus be applied to a particular case study to test its validity in forecasting hail events.

The hailpads affected by a storm on July 3rd 2001 in the area of Fraga-Lleida have been evaluated. Previous studies (López, 2003) have been devoted to estimating the likelihood of hailfalls taking into account a number of radar variables, including VIL. In this case, the likelihood of a hail event increases dramatically from 1650 UTC on and drops again at 1731 UTC, coinciding with the times provided by the observers.

Table 1 shows the data measured by the indented hailpads on the study day. Each hailpad provides the following information: maximum estimated diameter, number of indents per unit of area, total mass of ice corresponding to hail indents per square meter, and the energy measured in
J m^{-2}.

TABLE 1. Maximum diameter, number of indents, total mass of ice, and energy for each hailpad.

Hailpad (nº of plate)	Diameter (mm)	Number (stone m^{-2})	Mass (kg m^{-2})	Energy (J m^{-2})
1	12.4	529	0.089	5.585
2	15.7	2040	0.635	53.672
3	12.1	550	0.088	5.499
4	20.1	960	0.554	69.460
5	29.4	1330	0.862	118.520
6	6.9	100	0.009	0.437
7	9.9	420	0.058	3.331
8	9.3	180	0.023	1.248

The maximum diameter shown in Table 1 is the one measured directly on hailpads (Fraile et al., 1999). An additional theoretical parameter has also been calculated, namely the *maximum expected size* (López et al., 2003). This parameter attempts to reduce the variability underlying maximum hailstone sizes measured on hailpads due mainly to the type of sampling.

Table 2 shows the correlations reached by the maximum size calculated using VIL and the

maximum size calculated using VIL Density with the maximum size measured on hailpads as well as with the *maximum expected size.*

TABLE 2. Precision indices for the sample. All the correlations are significant at a level of 0.05.

Maximum size (hailpad data)	Estimated size	
	DVIL	VIL
measured	0.750	0.750
expected	0.786	0.792

It can be seen that in this case the values estimated using VIL and VIL Density are very similar (Edwards and Thompson, 1998). In the case of the *maximum expected size* both values increase.

The results show that the most promising methods are those that classify hail in terms of severe versus non-severe, without distinguishing intermediate sizes. In addition, the improvement in obtaining objective information about hailstone sizes recorded on the ground will contribute to reducing inaccuracies. It has already been illustrated that the calculation of the maximum hailstone size using VIL is improved if it is contrasted not with the size recorded on the ground by means of hailpads, but with the corrected size, known as *maximum expected size.*

Finally, the authors would like to point out that it is necessary to increase the number of storms analyzed as well as the hailpad network to come closer to more precise results.

5. REFERENCES

Amburn, S. and P. Wolf, 1997: VIL density as a Hail Indicator. *Wea. Forecasting*, **12,** 473-478.

Belk, N. M. and L. D. Wilson, 1998: Using Cell-Based VIL Density to Identify Severe-Hail Thunderstorms in the Central Appalachians and Middle Ohio Valley. Eastern Region Technical Attachment, **No 98-8,** National Weather Service, NOAA, Charleston, West Virginia.

Blaes, J. L., C. S. Cerniglia Jr, and M. A. Caropolo, 1998: VIL density as an indicator of hail across eastern New York and western New England. Eastern Region Technical Attachment, **No 98-8,** National Weather Service, NOAA, Deparment of Commerce,Bohemia, NY.

Boudevillain, B. and H. Andrieu, 2003: Assessment of Vertically Integrated Liquid (VIL) Water Content Radar Measurement. *J. Atmos. Oceanic Technol.*, **12,** 404-409.

Dessens, J. and R. Fraile, 1994: Hailstone size distributions in southwestern France.*Atmos.Res.,* **33,** 57-73.

Edwards, R. E., and Thompson, R. L., 1998: Nationwide Comparisons of Hail Size with WSR-88D Vertically Integrated Liquid Water and Derived Thermodynamic Sounding Data, *Wea. Forecasting*, **13,** 277-285.

Font, I., 1983: *Atlas Climático de España.* INM y Ministerio de Transportes, Turismo y Comunicaciones. Madrid, 296 pp.

Fraile, R., J.L. Sánchez, J.L. de la Madrid, A. Castro and J.L. Marcos, 1999: Some results from the hailpad network in León (Spain): Noteworthy correlations among hailfall parameters. *Theor. Appl. Climatol.,* **64,** 105-117.

Fraile, R., A. Castro, J.L. Sánchez, J.L. Marcos and L. López, 2001: Noteworthy C-band radar parameters of storms on hail days in northwestern Spain. *Atmos. Res.,* **59-60,** 41-61.

Giaiotti, D., E. Gianesini and F. Stel, 2001: Heuristic considerations pertaining to hailstone size distributions in the plain of Friuli-Venezia Giulia. *Atmos. Res.,* **57,** 269-288.

Greene, D. R., and R.A. Clark, 1972: Vertically integrated liquid-A new analysis tool. *Mon. Wea. Rev.*, **100,** 548-552.

Hart, P.A., and K. Frantz, 1998: A Comparison of VIL Density and Wet-Bulb-Zero Height Associated with Large Hail over North and Central Georgia. SR- Technical Attachment 98-30.

López, L., 2003: *Convección atmosféric severa : Pronóstico e identificación de tormentas con granizo.* Universidad de León, Tesis doctoral, 207 pp.

Ramis, C., López, J.M., Arús, J., 1999: Two cases of severe weather in Catalonia

(Spain) : a diagnostic study. *Meteorol. Appl.* **6**, 11-27.

Roeseler, C. A., and L. Wood, 1997: VIL density and associated hail size along the Northwest Gulf Coast. Preprints, *28th Conf. on Radar Meteorology*, Austin, Amer. Meteor. Soc., 434-435.

Tudurí, E., R. Romero, L. López, E. García, J.L. Sánchez, C.Ramis, 2003: The 14 July 2001 hailstorm in northeastern Spain: diagnosis of the meteorological situation. *Atmos. Res.*, **67-68,** 541-558.

Turner, R. J., and D. M. Gonsowski, 1997: A review of VIL density performance at NWSO Goodland, Kansas. Preprints, *28th Conf. on Radar Meteorology*, Austin, Amer. Meteor. Soc., 370-371.

Wyatt, A., and A. Witt, 1997: The effect of population density on ground-truth verification of reports used to score a hail detection algorithm. Preprints, *28th Conf. on Radar Meteorology*, Austin, TX, Amer. Meteor.

AN ALGORITHM FOR CONTINUOUS EVALUATION OF CLOUD BASE HEIGHT, CLOUD BASE TEMPERATURE, AND CLOUD COVERAGE AT LOCAL SCALE

Esmaiel Malek

Department of Plants, Soils and Biometeorology
Utah State University, Logan, Utah 84322-4820, U.S.A.

1. INTRODUCTION

Clouds are visible aggregations of minute droplets of water or tiny crystals of ice suspended in the air. They produce rain or snow, thunder or lightning, rainbows or halos. Clouds affect the radiation budget of our planet by the reflecting, absorbing and scattering of solar radiation, and the re-emission of terrestrial radiation. They affect the weather and climate by positive or negative feedback. Many researchers have worked on the parameterization of clouds and their effects on the radiation budget.

The Vaisala model CT-12K laser beam ceilometer is used at the Automated Surface Observing Systems (ASOS), at the U.S. airports, to measure the cloud base height and report sky conditions on an hourly basis or at shorter intervals. This laser ceilometer is a fixed-type whose transmitter and receiver point straight up at the cloud (if any) base. It is unable to measure clouds that are not above the sensor. To report cloudiness at the local scale, many of these types of ceilometers are needed. This is not a perfect method for cloud measurement. A single cloud hanging overhead the sensor will cause overcast readings, whereas, a hole in the clouds could cause a clear reading to be reported. To overcome this problem, we have set up a ventilated radiation station at the Logan-Cache airport, Utah, U.S.A., since 1995, along with an algorithm for the evaluation of the cloud base temperature, cloud base height, and percent of skies covered by cloud at the local scale.

2. INSTRUMENTATIONS

This research has been started in Logan (41° 47' N, 111° 51' W, 1349 m above MSL), Utah, U.S.A., since October, 1995. The experimental site is far away from any obstacle, about one mile from the ASOS, and is located in the middle of a field covered mostly by cheatgrass (*Bromus tectorum* L.) during the growing season. Two CM21 Kipp & Zonen pyranometers (one facing down) were used to measure the solar or shortwave radiation. The facing-up pyranometer measured the incoming (R_{si}) shortwave or solar radiation, and the inverted one measured the outgoing (R_{so}) or reflected shortwave radiation. located in the middle of a field covered mostly by cheatgrass (*Bromus tectorum* L.) during the growing season.

Esmaiel Malek, Department of Plants, Soils and Biometeorology, Utah State University, Logan, Utah 84322-4820, U.S.A; E-Mail: emalek@mendel.usu.edu.

Two CG1 Kipp & Zonen pyrgeometers (one facing down) were used to measure the longwave radiation. The facing-up measured the incoming longwave (R_{li}) or atmospheric radiation, and the inverted one measured the outgoing longwave (R_{lo}) or terrestrial radiation. Both pyrgeometers have a field of view of about 150°. The pyranometers and pyrgeometers were equipped with 4 CV2 Kipp & Zonen CVB1 ventilation systems.

The ventilation air was heated at the rate of 5 W (and occasionally to 10 W) to prevent precipitation of dew and frost, and evaporation of light to moderate rain and snow before reaching the upper pyranometer and pyrgeometer, which otherwise would disturb the measurement, and to suppress the infra-red offset, which is produced by cooling down of the glass domes under calm, clear sky conditions. An AC power source (110 Volts) has been provided to ventilate the Kipp & Zonen radiation system and for heating the rain and snow gage throughout the years. Other instruments used are reported by Malek (1997).

3. THEORETICAL CONSIDERATIONS

Considering the additional longwave radiation captured by the facing-up pyrgeometer during cloudy skies, coming from the cloud in a wave band which the gaseous emission lacks (from 8-13 μm), we developed an algorithm which provides the continuous 20-min cloud information (cloud base height, cloud base temperature, and percent of skies covered by cloud) over the Cache Valley during day and night throughout the year. The comparisons between the ASOS and the algorithm data during the period June through August 2002 are reported in this article.

3.1 Cloudless skies

Many researchers have attempted to formulate the cloudless sky effective atmospheric emissivity ($\varepsilon_{a(Cloudless)}$) based on theoretical and empirical concepts. A brief review of some of the past work is reported here. Among them are Brunt (1932), Brutsaert (1975), Idso (1981), and Monteith and Unsworth (1990), who applied either the 2-m actual vapor pressure (e_{a2}), the 2-m air temperature(T_{a2}), or both to compute cloudless sky emissivity.

The empirical constants *a* and *b* in their equations needed to be found. To do that, we selected the 20-min values of measured incoming longwave radiation (R_{lim}) during 12 cloudless days (24-h period) from 1999 through 2000 in Logan (based upon the ASOS and our measurements when high pressure existed over the region) and the 2-m moisture and

temperature data to find *a* and *b* in the related equation. Statistical analyses are shown in Table 1.

Despite having almost identical correlation coefficients and Standard Error of Y Estimates (the difference between the measured (R_{lim}) and computed R_{lic}) incoming longwave radiation among the above-mentioned approaches, we chose Idso's formula, which has the lowest Std Err of Y Est, for computation of (R_{li}) as:

$$R_{li(Cloudless)} = [0.793 + 4.99 * 10^{-5} * e_{a2} * \exp(1500/T_{a2})] * \sigma * (T_{a2})^4 \quad (1)$$

where e_{a2} is in mb, T_{a2} is in K, $\sigma = 5.76*10^{-8}$, and $R_{li(Cloudless)}$ in W m^{-2}.

3.2 Cloudy skies

Prediction of cloud amount (A_c) and cloud height (H_c) is of great importance to climate modeling. Clouds play a key role in the radiative energy budget of the earth and in transfer of energy between the surface and the atmosphere. They form when air becomes saturated. This results most commonly from adiabatic cooling when air ascends above its lifting condensation level (LCL). The effect of cloud amount enters into the climate model only via radiation. Thus, presence of cloud increases the flux of atmospheric radiation received at the surface because the radiation from water vapor and carbon dioxide in the lower atmosphere is supplemented by emission from clouds in the waveband (8 - 13 μm) which gaseous emission lacks.

Comparing the incoming atmospheric radiation measured by the pyrgeometer ($R_{li(meas)}$) for any sky conditions (cloudless or cloudy) with the one calculated by Idso's formula (Equation 1) for cloudless skies ($R_{li(cloudless)}$) yields:

$$R_{li(meas)} = R_{li(cloudless)} + A_c(1 - \varepsilon_{a(Cloudless)}) * \sigma * T_c^4 \quad (2)$$

where A_c (from zero for cloudless skies to one for overcast skies) and T_c are the cloud amount and the cloud base temperature, respectively. Whenever $R_{li(meas.)}$ is almost equal to $R_{li(cloudless)}$, this implies a cloudless sky. When $R_{li(meas)} > R_{li(cloudless)}$, the sky conditions could be from partly cloudy to overcast. Equation (2) can be rewritten as:

$$A_c = (R_{li(meas.)} - R_{li(cloudless)}) / ((1 - \varepsilon_{a(cloudless)}) * \sigma * T_c^4) \quad (3)$$

To solve Equation (3) with two unknowns (A_c and T_c), we start from Poisson's equation as:

$$\theta = (T_{a2} + 273.15)(1013.25 / P_{sur})^{0.286} \quad (4)$$

where θ is the potential temperature in K (dry adiabat), T_{sur} is the 2-m air temperature in °C, 1013.25 and P_{a2} are the standard and local surface atmospheric pressure in mb (hPa), respectively. This potential temperature remains constant during ascent or descent of the air parcel (a conserved quantity). Equation (4) can be used for determination of the lifting condensation level (LCL) as:

$$\theta = (T_c + 273.15)(1013.25 / P_c)^{0.286} \quad (5)$$

where T_c is the cloud base temperature in °C, and P_c is the cloud base pressure in mb. P_c is related to the elevation or cloud base height (H_c) as (assuming 10 °C km^{-1} dry adiabatic lapse rate, Wallance and Hobbs, 1977):

$$H_c = 100T_{sur} [1 - (P_c / P_{sur})^{0.293}] \quad (6)$$

where H_c is in m and T_{sur} in K.

Another conserved property of an air parcel is its mixing ratio (χ, kg of water vapor/kg of dry air) as:

$$\chi = 0.622e_{a2} / P_{sur} \quad (7)$$

where e_{a2} is the actual vapor pressure in mb can be computed as:

$$e_{a2} = (RH_2 / 100) * e_{s,Ta2} \quad (8)$$

where RH_2 is in % and $e_{s,Ta2}$ is the saturation vapor pressure at T_{a2} in mb. The following equation is applied for computation of the saturation vapor pressure ($e_{s,Ta2}$) in mb (Chow et al., 1988):

$$e_{s,Ta2} = 6.1121 \text{ EXP}[17.502T_{a2} / (240.97 + T_{a2})] \quad (9)$$

where T_{a2} is in °C. Equation (9) can be used for determination of the lifting condensation level as:

Table 1. Constants *a* and *b* for the Brunt, Brutsaert, Idso and Monteith and Unsworth formulas and the relationships between the measured (R_{lim}) and computed (R_{lic}) incoming longwave radiation during selected cloudless periods in Logan during 1999-2000.

Formula	*a*	*b*	R_{lic} v.s. R_{lim}	R[¶]	n[☆]	Std Err of Y Est
Brunt (1932)	0.732	.032	$R_{ic} = 1.002*R_{lim}$	0.96	864	13.71 W m^{-2}
Brutsaert (1975)	1.380	-----	$R_{lic} = 1.005*R_{lim}$	0.95	864	15.82 W m^{-2}
Idso (1981)	0.793	4.99^(-5)	$R_{lic} = 1.000*R_{lim}$	0.99	864	6.65 W m^{-2}
Monteith and Unsworth (1990)	13.30	0.825	$R_{lic} = 0.999*R_{lim}$	0.93	864	14.67 W m^{-2}

[¶] R = Correlation coefficient, [☆] n = number of observations.

$$\chi_s = \chi = 3.802EXP[17.502T_c / (240.97 + T_c)] / P_c \quad (10)$$

where χ_s is the saturation mixing ratio, T_c is in °C and P_c is in mb.

According to Normand's rule ((Wallance and Hobbs, 1977; McIlveen, 1992), on a pseudoadiabatic chart (thermodynamic diagram or tephigram), the lifting condensation level (LCL) of an air parcel is located at the intersection of the potential temperature line (Equation 6), which passes through a point located by the local temperature and pressure of the air parcel, and the mixing ratio line (Equation 10), which passes through a point determined by the local dew point and pressure of the air. In other words, Equations (6) and (10) can be rewritten as follows:

$$P_c = 1013.25\ [(T_c + 273.15) / \theta]^{3.496} \quad (11)$$

and

$$P_c = (3.802 / \chi) * EXP[17.502T_c / (240.97 + T_c)] \quad (12)$$

Equating Equations (11) and (12) yields:

$$EXP[17.502T_c / (240.97 + T_c)] = 266.5\ \chi[(T_c + 273.15) / \theta]^{3.496} \quad (13)$$

or

$$17.502T_c / (240.97 + T_c) = Ln(266.5\ \chi) + 3.496Ln[(T_c + 273.15)/\theta] \quad (14)$$

Finally

$$Ln[(T_c + 273.15) / \theta] - 5.01T_c / (240.97 + T_c) + 0.286Ln(266.5\chi) = 0.0 \quad (15)$$

After solving Equation (15) for T_c (using a first guess and iterating it by computer until the result comes to zero), either Equation (11) or Equation (12) can be used to compute the P_c. Then Equation (6) can be used to calculate the cloud base height (H_c), and thus the cloud type (i.e., low, middle or high clouds). To expand the network at regional scale, the satellite link (i.e., the NOAA GOES West satellite) will allow constant monitoring of the radiation systems' performance and maintenance scheduling on an "as needed" basis (Malek et al., 1990).

4. RESULTS AND DISCUSSIONS

Figure 1 shows the 20-min relation between the computed cloudless-skies incoming longwave (R_{lic}) (using Equation 1) and the measured R_{lim}, (by pyrgeometer) during cloudless skies in Logan during the period of 1999-2000 (1080 observations during 15 days of 24-h data, days and nights).

To test the performance of the proposed algorithms, first we chose the periods of June 12-13, 2003, at the Logan airport where these instruments and the ceilometer are located, then the period of June through August 2003 will be considered. The hourly values of measured (R_{lim}) and computed (R_{lic}) incoming longwave radiation in Logan during the period of June 12-13, 2003, are depicted in Figure 2. Whenever $R_{lim} > R_{lic}$, this is an indication of cloudy skies.

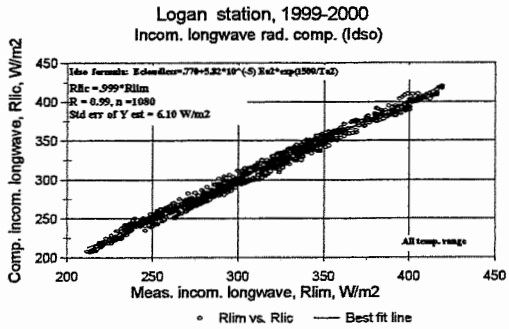

Figure 1. The relationship between R_{lic} and R_{lim}.

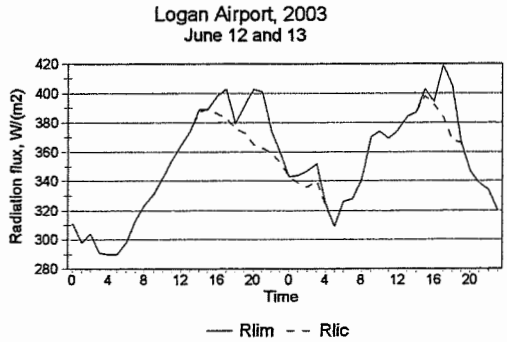

Figure 2. Measured (R_{lim}) and computed (R_{lic}) incoming longwave radiation in Logan during the period of June 12-13, 2003.

These clouds could be formed overhead or developed over the surrounding mountains in this valley. Those overhead are captured both by the ceilometer and the model. The surrounding clouds can be viewed only by the instruments. As a result, many

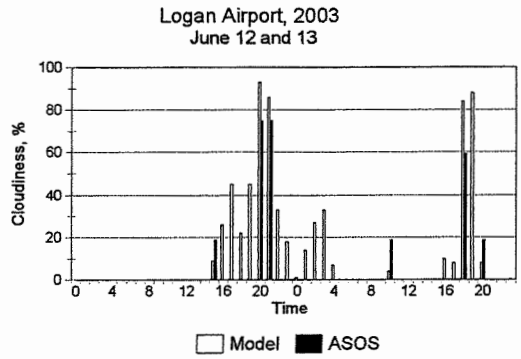

Figure 3. Cloudiness modeled and reported by ASOS in Logan during June 12 - 13, 2003.

hours of cloudiness not reported by ASOS is captured by the model. This is because of the 150° field of the instruments used in the model (ceilometer views vertically the sky above, only).

Figure 3 presents the percent of cloudiness evaluated by the model and ASOS (reported by National Center for Climatic Data (NCDC)) on these days. As shown in Figure 3, there were many hours of cloudiness not reported by ASOS during this period, but captured by the instruments.

The 24-h mean 2-m air temperature and humidity, and total precipitation in Logan during June-August 2003are shown in Figure 4. The occasional precipitation during this summer-time dry spell is the result of cumulonimbus activity (a convective phenomenon).

Figures 5 and 6 reveal the model hourly values of cloudiness and cloud base temperature; and cloud base height, respectively, in Logan during the period of June through August 2003 in Logan.

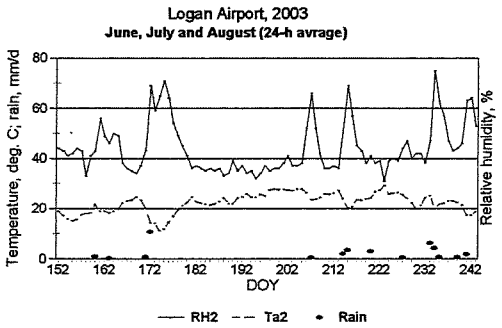

Figure 4. The 24-h mean 2-m air temperature and humidity, and total precipitation in Logan during June-August 2003.

Figures 5 and 6 reveal the model hourly values of cloudiness and cloud base temperature, and cloud base height, respectively, in Logan during the period of June through August 2003.

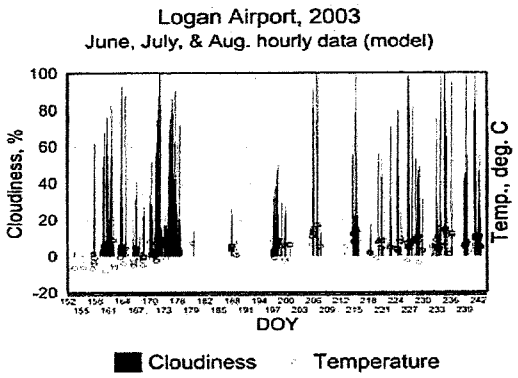

Figure 5. Model hourly cloudiness in Logan during June-August 2003.

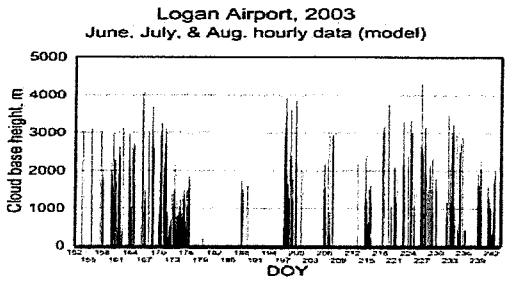

Figure 6. 24-h values of cloudiness in Logan during June-August 2003.

5- Concluding Remarks

Comparison between the hourly cloudiness reported by ASOS and the model showed that out of 22208 hours of cloudiness reported by ASOS were confirmed by the model, and the model showed 194 hours of cloudiness which was not reported by ASOS. As shown, the proposed algorithm is a promising approach for evaluation of cloud base temperature, cloud base height, and more importantly, the percent of skies covered by cloud during the experimental period. A cloud base height around zero is an indication of fog formation near the ground.

6- Acknowledgment

This research was supported by Utah State University and the Utah Agricultural Experiment Station. The author wishes to express his thanks to both.

7- References

Brunt, D., 1932: Notes on radiation from the atmosphere. Quart. J. Roy. Meteorol. Soc., 58, 389 - 418.

Brutsaert, W. H., 1975: On a derivable formula for longwave radiation from clear skies. Water Resour. Res., 11, 742-744.

Chow, V. T., Maidment, D.R., and Mays, L.W., 1988: Appl. Hydrol., McGraw Hill., 753 pp.

Idso, S. B., 1981: A set of equations for full spectrum and 8-14 μm and 10.5-12.5 μm thermal radiation from cloudless skies. Water Resour. Res., 17, 295-304.

Malek. E., 1997: Evaluation of effective atmospheric emissivity and parameterization of cloud at local scale. Atmos. Res., 45, 41-54.

Malek, E., Bingham, G. E., and McCurdy, G. D., 1990: Evapotranspiration from the margin and moist playa of a closed west desert valley., J. Hydrol. 120, 15-34.

McIlveen, R., 1992: Fundamentals of Weather and Climate. Chapman and Hall., 497 pp.

Monteith, J. L. and Unsworth, M. H., 1990: Principles of Environmental Physics., Edward Arnold, New York., 291pp.

Wallance, J. M., and Hobbs, P. V., 1977: Atmospheric Physics: An Introduction Survey., Acad. Press., 467 pp.

THE MACROSCOPIC AND MULTIPLE PARAMETER MEASURING SYSTEM OF AIRCRAFT PRECIPITATION ENHANCEMENT

Li maolun Jin Dezhen

Jilin Weather Modification Office, ChangChun 130062,P.R.China

1. INTRODUCTION

There are more than forties years histories for aircraft precipitation enhancement in our province, In this period, the main aircraft model which we used are Y12、Y7、double otters and An26 etc., its plane speed is normal 328~430km/h, the max voyage is 1440~2350km, it is more fit to aircraft precipitation enhancement from one province to another. We need some elementary equipments of the macroscopic and microcosmic research of cloud and rain in aircraft precipitation enhancement in order to making the cloud layer parameters of aircraft for the cloud layer altitude、temperature、humidity、ice-particle density、measure、liquid-water content 、 position etc. these main equipments are GPS、aircraft thermograph、aircraft humidity meter、the liquid water content indicator and PMS etc..

2. THE MACROSCOPIC AND MULTIPLE PARAMETER MEASURING SYSTEM OF AIRCRAFT PRECIPITATION ENHANCEMENT OF JILIN

Many macroscopic equipments are often used in aircraft precipitation enhancement of Jilin province, such as aircraft thermograph、aircraft humidity meter、altitude meter、velocity meter etc., the main questions existed is inferior linear of sensor、float of zero point、delayed of measuring、trouble of demarcate、record data by hand etc., So the questions of notes synchronism caused trustworthy problems of requiring data. We designed the system by computer technology、sensor technology、interface technology and data gathering technology in order to solve above problems. The system is made up of GPS receiver、temperature sensor、humidity sensor、multiple user interface of RS232C、software of computer control and computer data requiring etc.

Corresponding author's address: No.653, HePing Street, ChangChun City, JiLin Province,130062,China. E-Mail: jljyb@public.cc.jl.cn

2.1 the technology key of system

According to characteristic of aircraft precipitation and survey of scientific research, We should select a GPS with more width of velocity range、integrated sensor of temperature and humidity as good responding velocity、accuracy、quite good stability in order to survey meteorological essential factor, We should attention the influence for dynamic warming of aircraft、effect of aircraft boundary layer、complexity of background etc., and found the module of demarcating sensor with writing software of requiring data 、processing data、displaying data、saving data etc. In order to make corrections error of interference of various kinds, ensuring stability and reliability of data.

2.2 Culling of macroscopic synthetic parameter

On the basis of macroscopic parameter in carrying out aircraft precipitation enhancement are temperature of airline、humidity、altitude、longitude、latitude、ground velocity、wind velocity、wind direction etc., whether the aircraft is in the catalyzing layer of 0℃~-20℃ or in the catalyzing region of objective, and the essential factor of temperature、humidity、altitude、longitude is main judgment basis. But the parameter of wind direction、wind velocity is calculating basis of judging

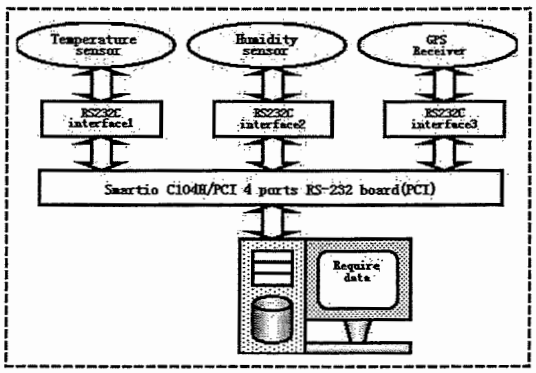

Fig.1: the flow chart of system measuring

spreading direction of catalyst and coverage. So the macroscopic parameter of temperature、humidity、altitude、longitude、latitude、ground velocity、wind velocity、wind direction etc. is our need of macroscopic surveying, and the parameter of wind direction、wind velocity must be base on TAS and course data of aircraft, the flow chart of system measuring is seeing the Fig 1.

2.3 Principle and temperature calculation of the DS1820 digit temperature sensor

Atmosphere temperature of airline is more important parameter that we must require, and the background or environment of aircraft precipitation enhancement is complicate and changeable, for this reason, temperature sensor of DS1820 (DALLS Crop. of America) is selected by us to survey atmosphere temperature, "faster respond、width range、high accuracy、good stability" is the characteristic of this element, and it conquered the shortcoming of A/D circuit debug of temperature examining system such as complex circuit、high cost、troublesome test、indirect error and a series of questions. By temperature measuring technology of slice, DS1820 counts pulse of oscillator of low temperature coefficient, oscillator of high temperature coefficient determines cycle of count pulse. Standard criterion of - 55℃ was set in advance by counter and temperature storage devices, if counter reaches before the end of pulse cycle, temperature storage devices will begin to increase, it indicates that temperature is over - 55℃, and it circulates to increase, The final number of temperature storage devices is our measuring data. Temperature data form of DS1820 is following table 1.

According to table 1., temperature counting method of 0.5℃ and 0.1℃ accuracy are giving the following:

①The temperature counting method of standard 0.5℃ accuracy :

positive temperature data : t=0.5×D negative temperature data : t=-0.5×D

②The temperature counting method of 0.1℃ high accuracy :

D1= (D AND FEH)

positive temperature data :

t= (0.5×D1-0.025+(A-B)/A)

negative temperature data :

t= (-0.5×D1-0.25-(A-B)/A)

Table 1. The data form of temperature

BYTE1	BYTE2	BYTE3	BYTE4
Temperature status byte	Temperature status byte	Counting constant B	Counting constant A
When BYTE2=00H , D=(+1)×BYTE1		B	A
When BYTE2=FFH , D=(256-BYTE1)			

Length is limited so that instructions table of DS1820temperature sensor etc. was leaved out.

2.4 Characteristic and calculation of the HS1101 digit temperature and humidity sensor

HS1101 digital integrated temperature and humidity sensor of France is new model sensor. Recuperative circuit and temperature sensor (temperature compensating and measuring) are integrated in the sensor. The advantage of HS1101 sensor is high measuring accuracy、good line、cycle using and good stability etc.. The data form is following the table 2.

Table 2. The data form of humidity

BYTE1	BYTE2	BYTE3	BYTE4
A	B	C	D
Data of temperature		Data of humidity	

Each data of temperature or humidity occupies four bytes(16) , Two bytes of A and B are temperature data , two bytes of C and D are humidity data. The max high status of B is status of sign. When S = 0 , temperature data is positive. When S=1, temperature data is negative. The low four status of A is reserved. The other status AND the seven status of B is temperature data, the temperature and humidity counting method is the following:

①when S=0 , t=(B×16+(A&0XF0)/16)×0.0625

②when S=1,

A1=255-B

B1=16-(A&0XF0)/16

t= (A1×16+B1) × (- 0.0625)

③h1=0X70+C, h2=0X150+D,

hum=(h1/h2-0.2354)/0.00474(%)

when C=FEH(or FFH) , humidity is illegal data ;

when D=FEH(or FFH) , the power supply voltage of temperature and humidity sensor is unusual.

2.5 Requiring of GPS parameter

Due to the SA policy was abolished by America, a normal fixed position accuracy of aviation GPS has been less than three meters, the 3D fixed position accuracy which it united and counted by more than 4 satellites was more improved, it can be satisfied the

need of aircraft precipitation enhancement.

"$GPGGA" of NMEA-0183 data form can offer the parameters of longitude、latitude、altitude、velocity、course etc., So long as GPS has I/O interface of RS232C, the data of our need will be required by computer and be processed.

2.6 Requiring software of data

We write the data requiring software of interface by VB6.0, the main technology line: the I/O interface buffer program of RS232C was compiled by MSCOMM of VB6.0, and the data required were classified、saved backstage and displayed immediately. (Length is limited so that the source program was leaved out.)

2.7 Item of attention

The sensor must be closed by aircraft flow cover so that the increasing temperature effect of condensing、rubbing or obstructing to sensor slow down because of high velocity airflow. And avoid lashing of rain or ice crystal to sensor. As installing, it must avoid the aircraft boundary layer and make correction of dynamics increasing temperature according to different model aircraft.

3. CONCLUSION

According to contrasting test of this system and traditional aircraft macroscopic measuring equipment, we believe that the system has many advantages such as auto data requiring、saving、processing、displaying、multiple parameters 、 simple demarcating and maintenance etc. Not only saving manual labor, but also providing ensure for the large data process later stage.

Along with the development of computer technology and new model digital sensor studying, the new model macroscopic multiple parameters measuring system of aircraft precipitation enhancement is going to the development direction in future.

DIAGNOSIS OF THERMODYNAMIC CONDITIONS REQUIRED FOR OCCURRENCE OF FREEZING RAIN

Hiroki Matsushita[1] and Fumihiko Nishio[2]

[1]Graduate School of Science and Technology, Chiba University, Chiba, 263-8522, Japan
[2]Center for Environmental Remote Sensing, Chiba University, Chiba, 263-8522, Japan

1. INTRODUCTION

Freezing rain with a supercooled state is frozen on the obstacles such as power lines and trees at the ground, and could cause the traffic accidents or power failure. In general, it is necessary for freezing rain to be occurred that a warm air layer to melt snowflakes exist above a cold air layer which acts to supercool descending raindrops near the ground (Fig. 1). When raindrops refreeze before reaching the ground, ice pellets are observed. This vertical atmospheric structure has been known for a long time, and it is called "melting ice process".

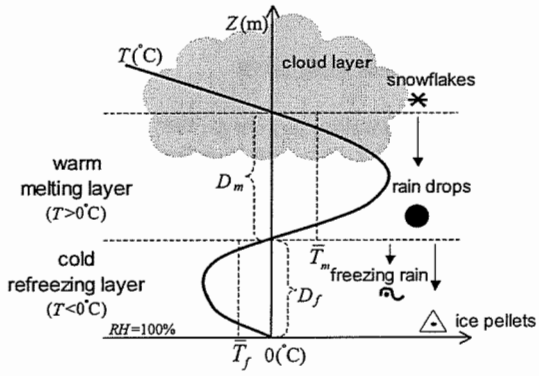

Fig. 1 Schematic atmospheric condition for occurrence of freezing rain.

In addition, although temperature in the atmosphere is everywhere colder than 0 °C, supercooled water drops grow through the warm rain process and/or the collision coalescence process. However, freezing drizzle forms most often through these processes (e.g., Bocchieri 1980; Huffman and Norman 1988; Rauber et al. 2000). In this paper, only melting ice process has been considered.

Atmospheric conditions necessary for the occurrence of freezing rain and ice pellets have been well studied on the vertical profile of air temperature, and depths, heights and thermal conditions of the warm and cold air layers (e.g., Zerr 1997; Rauber et al. 2000; Robbins and Cortinas 2002). Furthermore, diagnostic method to distinguish the freezing rain and ice pellet occurrences using these meteorological parameters were suggested (Ishihara and Tadokoro 1990; Stewart et al. 1990; Czys et al. 1996; Rauber et al. 2001) and forecasting of precipitation types including the freezing rain were proposed (Stewart and King 1987; Bourgouin 2000; Hux et al. 2001).

In this study, we have designed the simple thermodynamical parameters that expressed the atmospheric conditions for snowflake to be melted and raindrop to be frozen in the case of Tokyo on January 2003.

2. DATA

Surface meteorological data and mesoscale objective analysis data provided by Japan Meteorological Agency were used in this study. The surface meteorological data are including the records of hydrometeors, and the mesoscale objective analysis data consist of relative humidity, air temperature, wind speed and direction at grid points (10 km x 10 km) on the standard pressure levels.

Only observation of hydrometeors at Musashino-city was carried out by author. The time used in this paper is the Japan Standard Time (JST).

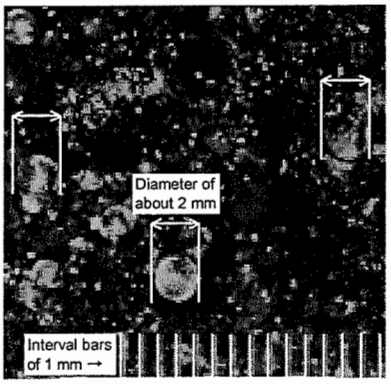

Fig. 2 Ice pellets observed at Musashino-city.

Corresponding author's address: Hiroki Matsushita, Graduate School of Science and Technology, Chiba University, 1-33 Yayoi, inage, Chiba, 263-8522, Japan; E-Mail: hmat @graduate.chiba-u.jp.

3. CASE OF FREEZING RAIN IN TOKYO

Freezing rain have been observed in Tokyo region at 18-24 JST 3 January 2003. At Musashino, ice pellets were fallen before freezing rain occurred. These ice pellets were composed of clear and bubble-free transparent spherical ice particles with a diameter of about 2mm (Fig. 2).

In this region, cold air drainage from inland peculiar to this plain formed cold air layer near the ground (Fig. 3), and warm air advection associated with synoptic low pressure existed above this cold air layer, so that the condition of melting ice process was produced (Fig. 4).

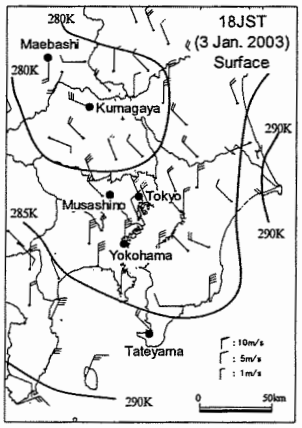

Fig. 3 Spatial distribution of equivalent potential temperature and wind.

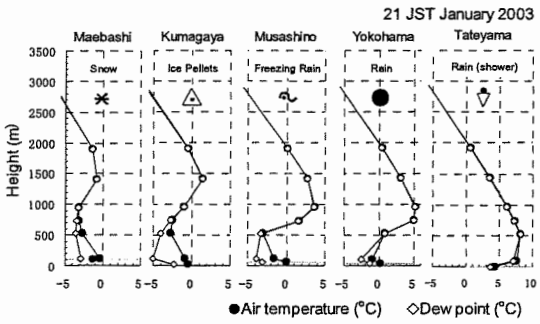

Fig. 4 Vertical air temperature profiles and precipitation types.

The cold air layer in which air temperature is below 0 °C near the ground developed in inland area, while warm air layer above 0 °C over the southern coastal area is thicker than the northern inland area. Precipitation types at the surface were observed in consequence of this vertical atmospheric structure. Therefore, thermal conditions in the warm and cold air layers were considered both states of melting snowflakes and freezing raindrops.

We considered theoretically the thermodynamical conditions required for the occurrence of freezing rain and ice pellets on the case of January 2003 in Tokyo.

4. MELTING OF SNOWFLAKES

4.1 Heat budget between snowflakes and air

Since melt water on the surface of snowflakes flows into the interior of flakes (Matsuo and Sasyo 1981; Mitra et al. 1990), we could consider the heat budget on ice surface with assuming of spherical sharps of snowflakes with radius r_i.

$$-\rho_i L_m r_i \frac{dr_i}{dt} = k_a \bar{f}_h \Delta T + L_s D_v \bar{f}_v \Delta\rho_v \qquad (1)$$

Were, ρ_i is density of ice-skeleton structure of snowflake, L_m latent heat of melting of ice, k_a thermal conductivity of air, $\bar{f}_h$ ventilation coefficient for heat diffusion, ΔT temperature difference between snowflake and air, L_s latent heat of sublimation, D_v coefficient of molecular diffusion of water vapor in air, $\bar{f}_v$ ventilation coefficient for water vapor diffusion, and $\Delta\rho_v$ difference between water vapor density of air and equilibrium water vapor density at snowflake surface.

The equation (1) means that the transfer rate of latent heat of melting equal to the rate of heat supplies by conduction and sublimation.

4.2 Melting time of snowflakes

According to Matsuo and Sasyo (1981), assuming that relative humidity of air is 100% and the latent heat of sublimation (second term in the right side of equation (1)) can be neglected, time for melting snowflakes t_m is given by

$$t_m = \frac{2L_m\rho_i}{\alpha^4 \varepsilon k_a \Delta T}\left(\frac{\alpha^3}{3}\left(r_{i0}^{3/2} - r_i^{3/2}\right) - \frac{\alpha^2}{2}\left(r_{i0} - r_i\right) + \alpha\left(r_{i0}^{1/2} - r_i^{1/2}\right) - \ln\frac{1+\alpha r_{i0}^{1/2}}{1+\alpha r_i^{1/2}}\right), \qquad (2)$$

where $\varepsilon = 1.75$, r_{i0} is initial snowflake radius, $\alpha = 0.24(2U_i/\nu)^{1/2}$, U_i is fall velocity of snowflakes, and ν is coefficient of kinematic viscosity of air.

4.3 Fall velocity of snowflakes

Fall velocity of snowflakes U_i expressed by Böhm (1989) was used in this study.

$$U_i = \frac{R_e \eta}{2\rho_a}\left(\frac{\pi}{A}\right)^{1/2} \qquad (3)$$

Where R_e is Reynolds number, η is air viscosity, ρ_a is air density, A is cross-sectional areas of snowflakes.

4.4 Depth of air layer for snowflakes to melt

We can obtain a depth of warm air layer required for complete melting of snowflakes (D_m) from equations of (2) and (3).

$$D_m = t_m U_i \tag{4}$$

4.5 Diagnosis for melting snowflakes

Fig. 5 shows that the relationship between the mean temperature $\overline{T}_m$ and depth D_m of warm air layer and precipitation types at 21 JST January 2003. Two lines in this figure indicate calculations for snowflakes with equivalent water radius r_w of 1.0 mm and 0.9 mm given from equations (2), (3) and (4). These lines discriminate between complete and partial melting or no melting of snowflakes. We defined melting index MI as

$$MI = \int T dz \approx \overline{T}_m D_m , \tag{5}$$

and obtained constant values of MI = 270 °C m for r_w = 1.0 mm and MI = 220 °C m for r_w = 0.9 mm, respectively.

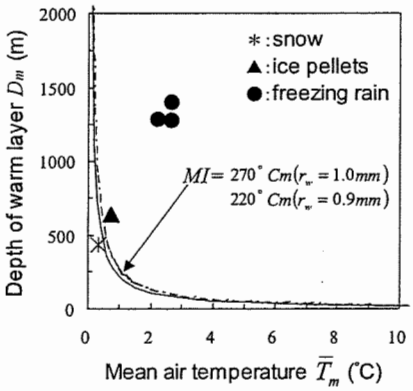

Fig. 5 Diagnosis for melting snowflakes.

5. FREEZING OF RAINDROPS

5.1 Heat budget between raindrops and air

Assuming that raindrops are spherical water drop with radius r_w and a spherical ice will form, heat balance between raindrop and air on the ice surface of drop is expressed as

$$\rho_w L_m r_w \frac{dr_w}{dt} = k_a \bar{f}_h \Delta T + L_s D_v \bar{f}_v \Delta \rho_v , \tag{6}$$

where ρ_w is density of water and ΔT is temperature difference between raindrop and air. The left hand side of equation (6) means the rate of release of latent heat due to freezing, and the right hand side is the rate of heat loss by conduction and sublimation to the environmental air.

5.2 Freezing time of raindrops

A fraction $(1 - c_w \Delta T / L_m)$ of water volume yet to freeze in initial nucleation which have a relatively short time is considered, and saturated environmental condition is assumed (Pruppacher and Klett 1997), so that freezing time of raindrops t_f is expressed as

$$t_f = \frac{\rho_w L_m r_w^2 (1 - c_w \Delta T / L_m)}{3 \bar{f} \Delta T \left(k_a + L_s D_v \left(\frac{d\overline{\rho}_v}{dT} \right)_{sat,i} \right)} , \tag{7}$$

where c_w is specific heat of water, $(d\overline{\rho}_v / dT)_{sat,i}$ is the mean slope of the ice saturation vapor density curve over the temperature difference of raindrop and air.

5.3 Fall velocity of raindrops

Fall velocity of raindrops U_w can be estimated by using of equation of Atlas et al. (1973).

$$U_w = 965 - 1030 \exp(-12 r_w) \tag{8}$$

5.4 Depth of air layer for raindrops to freeze

Depth of cold air layer D_f required for complete freezing of raindrops is given from the freezing time (7) and the terminal velocity (8) of raindrops.

$$D_f = t_f U_w \tag{9}$$

5.5 Diagnosis for freezing raindrops

The mean temperature $\overline{T}_f$ and depth D_f of cold air layer with respect to freezing of raindrop is illustrated in Fig. 6. Solid and broken lines in this figure indicate

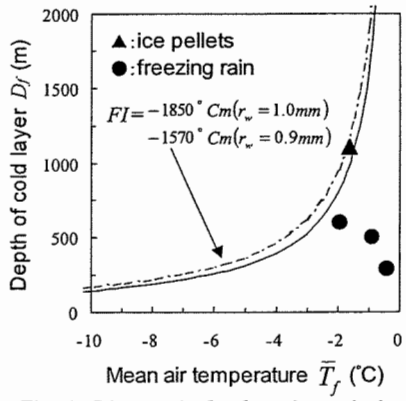

Fig. 6 Diagnosis for freezing raindrops.

calculations for r_w = 1.0 mm and 0.9 mm by using of equation (7), (8) and (9). These lines discriminate between complete and partial freezing or no freezing of raindrops. We defined freezing index FI as

$$FI = \int T dz \approx \overline{T}_f D_f \cdot \qquad (10)$$

On average over temperature range of 0 to -10 °C, FI = -1850 °C m for r_w = 1.0 mm and FI = -1570 °C m for r_w = 0.9 mm, respectively.

6. DIAGNOSIS METHOD

Fig. 7 shows the diagnosis diagram for occurrence of freezing rain and ice pellets using the melting index MI and the freezing index FI. Although precipitation type depend on air temperature near the ground, using of these simple parameters would make possible a determination of precipitation types including the freezing rain and ice pellets through the melting ice process.

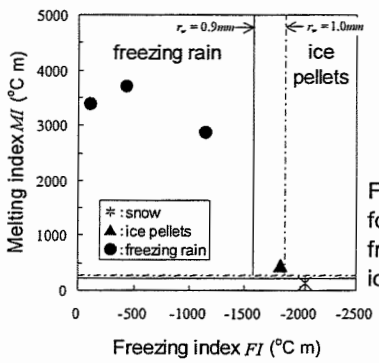

Fig. 7 Diagnosis for occurrence of freezing rain and ice pellets.

7. CONCLUDING REMARKS

A moisture condition of atmosphere could also affect both states of melting snowflakes and freezing raindrops. In addition to this study, other environmental condition (e.g., the concentration of suspended particulate matter in the atmosphere on contact freezing with supercooling raindrops) may have an influence on the hydrometeors. These atmospheric conditions should be considered in the further studies.

REFERENCES

Atlas, D., R. C. Srivastava and R. S. Sekon, 1973: Doppler radar characteristics of precipitation at vertical incidence. Rev. Geophys. Space Phys., **11**, 1-35.

Bocchieri, J. R., 1980: The objective use of upper air soundings to specify precipitation type. Mon. Wea. Rev., **108**, 596-603.

Böhm, H. P., 1989: A general equation for the terminal fall speed of solid hydrometeors. J. Atmos. Sci., **46**, 2419-2427.

Bourgouin, P., 2000: A method to determine precipitation types. Wea. Forecasting, **15**, 583-592.

Czys, R. R., R. W. Scott, K. C. Tang, R. W. Przybylinski and M. E. Sabones, 1996: A physically based, nondimensional parameter for discriminating between locations of freezing rain and ice pellets. Wea. Forecasting, **11**, 591-598.

Huffman, G. J., and G. A. Norman Jr., 1988: The supercooled warm rain process and the specification of freezing precipitation. Mon. Wea. Rev., **116**, 2172-2182.

Hux, J. D., P. C. Knappenberger, P. J. Michaels, P. J. Stenger, H. D. Cobb and M. P. Rusnak, 2001: Development of a discriminant analysis mixed precipitation (DAMP) forecast model for mid-Atlantic winter storms. Wea. Forecasting, **16**, 248–259.

Ishihara, K., and Y. Tadokoro, 1990: Meteorological analysis of glaze occurrence in Japan. Proceedings, 5th International Workshop on the Atmospheric Icing of Structures, Tokyo, Japan, A1-6-(1)- A1-6-(4).

Matsuo, T., and Y. Sasyo, 1981: Empirical formula for the melting rate of snowflakes. J. Meteor. Soc. Japan, **59**, 1-9.

Mitra, S. K., O. Vohl, M. Ahr and H. R. Pruppacher, 1990: A wind tunnel and theoretical study of the melting behavior of atmospheric ice particles. IV: Experiment and theory for snow flakes. J. Atmos. Sci., **47**, 584-591.

Pruppacher, H. R., and J. D. Klett, 1997: Microphysics of clouds and precipitation. Kluwer Academic Publishers, Dordrecht, Netherlands, 954pp.

Rauber, R. M., L. S. Olthoff, M. K. Ramamurthy and K. E. Kunkel, 2000: The relative importance of warm rain and melting processes in freezing precipitation events. J. Appl. Meteor., **39**, 1185-1195.

Rauber, R. M., L. S. Olthoff, M. K. Ramamurthy and K. E. Kunkel, 2001: Further investigation of a physically based, nondimensional parameter for discriminating between locations of freezing rain and ice pellets. Wea. Forecasting, **16**, 185-191.

Robbins, C. C., and J. V. Cortinas Jr., 2002: Local and synoptic environments associated with freezing rain in the contiguous United States. Wea. Forecasting, **17**, 47-65.

Stewart, R. E., and P. King, 1987: Freezing precipitation in winter storms. Mon. Wea. Rev., **115**, 1270-1279.

Stewart, R. E., R. W. Crawford, N. R. Donaldson, T. B. Low and B. E. Sheppard, 1990: Precipitation and environmental conditions during accretion in Canadian east coast winter storms. J. Appl. Meteor., **29**, 525-538.

Zerr, R. J., 1997: Freezing rain: An observational and theoretical study. J. Appl. Meteor., **36**, 1647-1661.

A REAL-TIME SATELLITE-BASED ICING DETECTION SYSTEM

Patrick Minnis[1], William L. Smith, Jr.[1], Louis Nguyen[1], Mandana M. Khaiyer[2], Douglas A. Spangenberg[2]
Patrick W. Heck[3], Rabindra Palikonda[2], Ben C. Bernstein[4], and Frank McDonough[4]

[1]Atmospheric Sciences, NASA Langley Research Center, Hampton, VA 23681 USA
[2] AS&M, Inc., Hampton, VA 23666 USA
[3]CIMSS, University of Wisconsin-Madison, Madison, WI 53706 USA
[4]National Center for atmospheric Research, Boulder, CO 80303 USA

1. INTRODUCTION

Aircraft icing is one of the most dangerous weather conditions for general aviation. Currently, model forecasts and pilot reports (PIREPS) constitute much of the database available to pilots for assessing the icing conditions in a particular area. Such data are often uncertain or sparsely available. Improvements in the temporal and areal coverage of icing diagnoses and prognoses would mark a substantial enhancement of aircraft safety in regions susceptible to heavy supercooled liquid water clouds. The use of 3.9-µm data from meteorological satellite imagers for diagnosing icing conditions has long been recognized (e.g., Ellrod and Nelson, 1996) but to date, no explicit physically based methods have been implemented. Recent advances in cloud detection and cloud property retrievals using operational satellite imagery open the door for real-time objective applications of those satellite datasets for a variety of weather phenomena. Because aircraft icing is related to cloud macro- and microphysical properties (e.g., Cober et al. 1995), it is logical that the cloud properties from satellite data would be useful for diagnosing icing conditions. This paper describes the a prototype real-time system for detecting aircraft icing from space.

2. DATA AND METHODOLOGY

The datasets used in the retrievals include half-hourly GOES-8, 10, and 12 4-km spectral radiances. The GOES-8 and 10 imagers measure radiances at 0.65, 3.9, 10.8, and 12 µm, while GOES-12 uses a 13.3-µm channel in place of the 12-µm channel. GOES-12 replaced GOES-8 at 75°W in April 2002, while GOES-10 remains at 135°W. Hourly Rapid Update Cycle (RUC) analyses (Benjamin et al., 2004) provide hourly profiles of temperature and humidity at a spatial resolution of 20 km. The profiles are used to assigning height from the retrieved cloud temperature *Tc* and to correct the radiances for atmospheric attenuation. Clear-sky visible (VIS; 0.65 µm) reflectance for each location is derived from the CERES clear-sky albedo map available on a 10' grid (Sun-Mack et al., 1999). Spectral surface emissivity derived from GOES (Smith et al. 1999) and CERES (Chen et al. 2002) data are used with the RUC data to specify the clear-sky radiating temperatures at 3.9, 10.8, and 12-µm. The data are ingested and analyzed within ~15 minutes of the GOES observation.

The visible infrared solar-infrared split-window technique (VISST; Minnis et al., 2001) is used during daytime, defined as the time when the solar zenith angle *SZA* is less than 82°. It matches the observed values with theoretical models of cloud reflectance and emittance (Minnis et al., 1998). At night, the solar-infrared infrared split-window technique (SIST) is used to retrieve all of the cloud properties. The SIST, an improved version of the 3-channel nighttime method (Minnis et al. 1995), uses thermal infrared data only. For each pixel, the methods retrieve *Tc*, cloud height *z* and thickness *h*, phase, optical depth τ, effective droplet radius *re* or effective ice crystal diameter *De*, and LWP or ice water path *IWP*. SLW clouds are those pixels with *Tc* < 273 K and a phase of liquid water. Other properties related to icing include *h*, τ and *LWP*. Recently, a new method was introduced to derive low-level cloud heights because of the difficulty in accurately representing boundary-layer inversions in numerical weather analyses. The new method (Heck et al., 2004) uses a fixed lapse rate that is anchored to the 24-hr running average surface temperature. This new approach minimizes the cloud-top altitude over-estimate that was common for low-level stratus clouds.

Aircraft icing potential depends on many factors, but generally requires supercooled liquid water (SLW), relatively large droplets, and relatively large concentrations of droplets or high liquid water content (LWC). Obviously, *Tc* can be used to discriminate SLW from warm clouds and the concentration of large droplets should be related to *re*. LWC ican be estimated as LWP/*h*. However, since both LWP and *h* depend on τ, only LWP is used here as a surrogate for LWC. Using matched VISST and in situ aircraft data, Smith et al. (2003) found some weak positive dependencies of icing intensity on LWP and *re*, and a weak negative dependency on *Tc*. Using those results as guidelines, a prototype icing classification system was developed to begin the refinement process to arrive at a reliable algorithm for converting real-time cloud properties to icing assessments. The preliminary algorithm is summarized in Table 1. When no clouds are present, no SLW is detectable, the cloud is relatively thin (LWP < 100 g m^{-2}), the retrieved cloud

Corresponding author's address: Patrick Minnis, MS 420, NASA Langley Research Center, Hampton, VA, 23681 USA; E-Mail: p.minnis@nasa.gov.

Table 1. Prototype icing classification criteria.

Value	criteria			icing intensity
0	clear or water cloud w/ Tc > 272 K or LWP < 100 gm^{-2} or ice cloud with $\tau < 8$)			none
1	ice cloud with $\tau > 8$			unknown
	re (μm)	LWP (gm^{-2})	Tc (K)	
2	> 11	> 100	< 272	low
3	> 11	> 200	< 272	mid
4	> 11	> 300	< 272	high
5	> 9	> 400	< 272	low
6	> 9	> 500	< 272	mid
7	> 11	> 300	< 253	high
8	> 9	> 400	< 253	high

is classified as optically thin ice, or the results do not satisfy any of the other criteria, then the algorithm returns a classification of no icing. If the cloud is determined to be an optically thick ice cloud, then it is assumed that the icing is unknown because the upper ice cloud may or may not hide a lower-level SLW cloud. The remaining classifications are various icing categories. These classes will be used until enough statistical data from PIREPS and field programs can be gathered to verify or to alter this classification system.

3. RESULTS

3.1 Continental United States (CONUS)

The cloud property and icing methodology is currently being applied in near-real time to GOES-10 data between 25°N and 50°N and 100°W and 130°W and to GOES-12 data between 25°N and 50°N from 65°W to 100°W. The results are derived separately and stitched together. Figure 1 shows an example of the CONUS results for GOES-10/12 imagery taken at 1915 UTC, 15 March 2004. The colder high clouds over the central and northwestern CONUS are classified as indeterminate or unknown because they are optically thick. The cirrus clouds over Arizona and New Mexico and Minnesota and Wisconsin are ignored and given the no icing classification. The low clouds over the southeastern CONUS are too warm to contain SLW. Icing is primarily diagnosed over western Washington, Nebraska, Missouri, Tennessee, North Carolina, North Dakota, Colorado, and eastern Canada. In the last area, the cloud deck is inhomogeneous so that the pixels diagnosed to contain icing conditions are scattered in space and in intensity. Some of the pixels, like those near the tail of

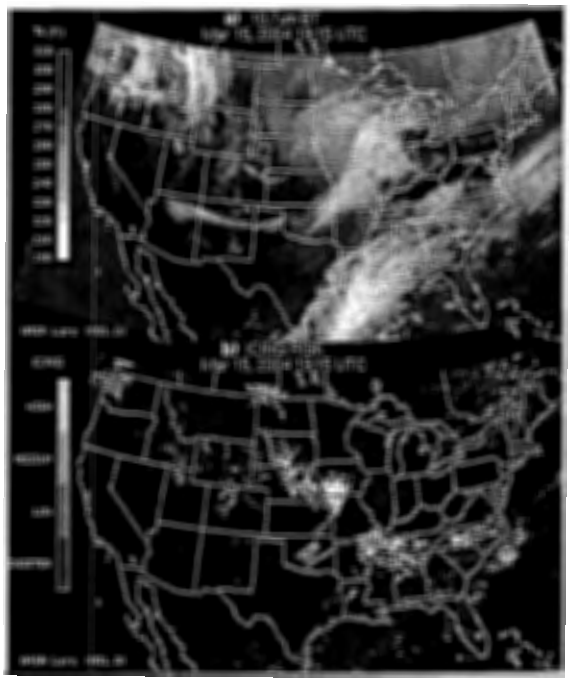

Fig. 1. Cloud and icing data for 1915 UTC, 15 March 2004. (a) Stitched GOES-10/12 infrared brightness temperature images. (b) Icing categories.

cirrus shield in Oklahoma, are probably misclassified because a thin cirrus over a low cloud can produce radiances similar to those from a SLW cloud. This confusion factor needs further scrutiny.

3.2 Field programs

The most important parameters for air safety are the horizontal locations of icing intensity and the range of altitudes where it is expected to occur. In these products, the cloud top and base altitudes are provided. The uncertainties in those altitudes are being determined through various validation studies. In early studies, Smith et al. (2000) verified that, when overlying cirrus clouds were absent, the VISST retrieved SLW in 98% of the PIREPS reports of positive icing.

Since then the VISST cloud products have been used to support both formal and informal field projects designed to study icing using in situ and ground-based instrumentation. In turn, the measurements yield valuable validation data for the remote sensing products. The VISST SLW identification was further validated with comparisons to cloud top penetrations by NASA Glenn Research Center's Twin Otter (hereafter, NGTO; see Smith et al., 2002). Later NGTO flights during 2003 successfully used the VISST results in real time to guide them to areas of icing confirming the general relationships used to establish the icing criteria. Microphysical data from NGTO flights have become available, facilitating objective assessment of the satellite observations.

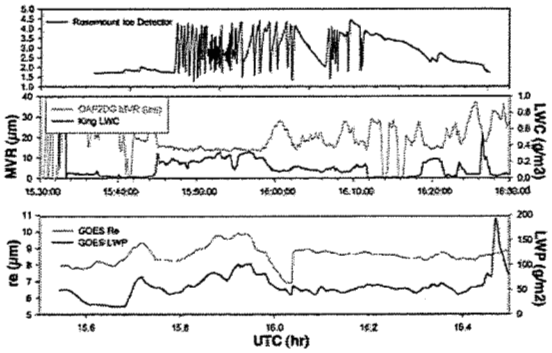

Fig. 3. Comparison of NGTO in situ and GOES-8 VISST data over Lake Erie, 5 March 1998, 1530 –1630 UTC.

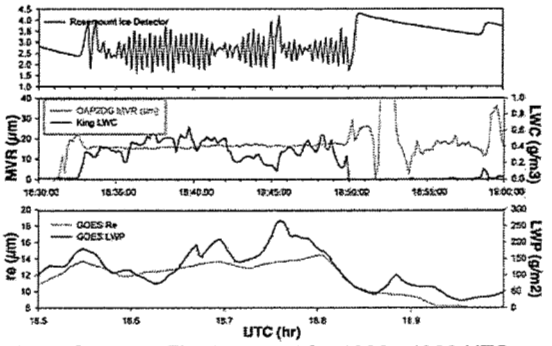

Fig. 4. Same as Fig. 3, except for 1830 –1900 UTC.

Figures 3 and 4 show closely matched NGTO and VISST parameters measured over northern Ohio and Lake Erie by NGTO flights during 5 March 1998. The top panel in each figure is a plot of the Rosemont ice detector signal. It indicates ice accumulation when the response varies rapidly. Thus, icing occurs between 1546 and 1602 UTC (Fig. 3) and between 1832 and 1850 UTC (Fig. 4). The mean volume droplet radius (MVR) ranges between 16 and 22 µm during the first episode while LWC varies from 0.2 to 0.3 gm^{-2}. The corresponding range in r_e is 8.5 – 10 µm and LWP rises from 50 to 100 gm^{-2}. The later flight (Fig. 4) produces much clearer correspondence between the satellite and NGTO data. During the icing event, the MVR is steady at 18 µm while r_e ranges from 12 to 14 µm. The LWP and LWC values are elevated above 100 gm^{-2} and 0.3 gm^{-3}, respectively. The largest values of LWP appear to be coincident with the lower amplitude variations during each icing episode. The satellite data during both events are at or just below the icing threshold levels in Table 1 suggesting that the LWP and r_e thresholds should be reduced.

More recently, data were taken at Montreal from the surface while aircraft flew over the site and over other areas in southern Canada as part of the second Alliance Icing Research Study (AIRS-II) and the Atlantic THORpex Regional Campaign (ATReC) during November and December 2003. The VISST products were generated throughout the experiment

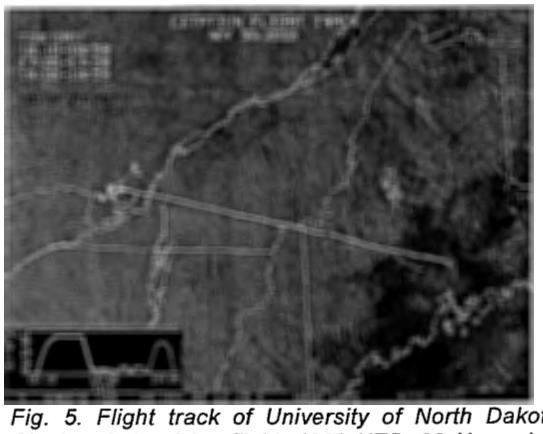

Fig. 5. Flight track of University of North Dakota Citation during icing flight, 1800 UTC, 30 November 2003.

using GOES-12, NOAA-16 Advanced Very High Resolution Radiometer (AVHRR), and *Terra* and *Aqua* Moderate Resolution Imaging Spectraradiometer (MODIS) data to provide a variety of views and resolutions to better understand the retrievals, provide support for the experiments, and validate the remote sensing methodologies. The various datasets are unprecedented for studying icing conditions.

An example of one of the icing flights is shown in Fig. 5 for 30 November 2003 when the University of North Dakota Citation flew from Bangor, Maine to the Montreal site. It performed several spirals through the clouds, reporting two decks with one top at 2.2 km and the other at 1.2 km. The 0.3-km-thick upper layer was producing light-to-moderate rime ice and had greater LWC and larger MVR than the lower cloud. The satellite retrievals from GOES-10 (Fig. 6) show clouds between 2 and 4 km in the vicinity of Montreal around 1800 UTC when the Citation was passing over the site. These altitudes are around 1 km higher than the reported cloud tops and are near the uncertainty limit of the VISST retrievals (Heck et al., 2004). Multiple inversions in many of these cases exacerbate estima-

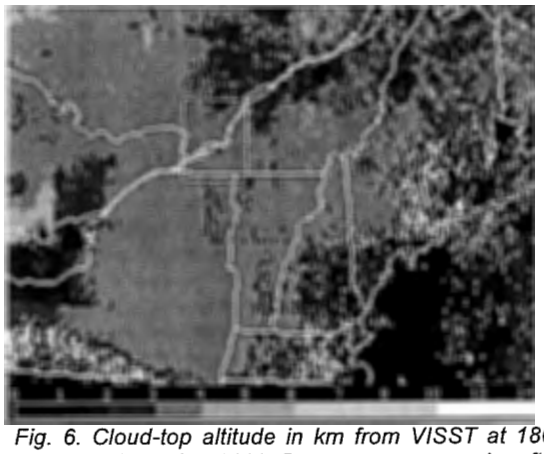

Fig. 6. Cloud-top altitude in km from VISST at 1800 UTC, 30 November 2003. Box encompasses aircraft in situ flight tracks.

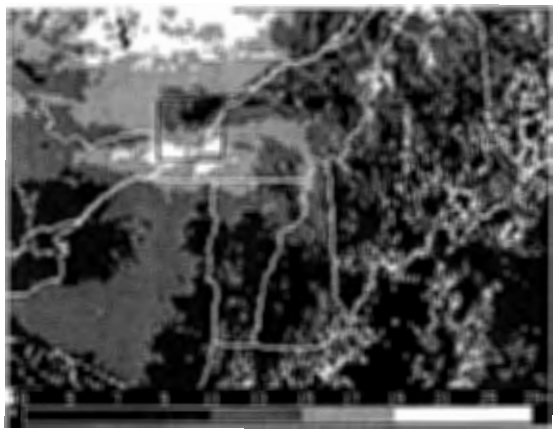

Fig. 7. Same as Fig. 6, except for r_e in μm.

tion of cloud height from *Tc*. Despite the height errors, the VISST retrieved larger droplets (Fig. 7) for the higher cloud compared to values of r_e < 11 μm for the lower cloud, a result consistent with the initial reports from the Citation. The classification algorithm yields moderate to heavy icing for the upper clouds and light to moderate icing for the lower clouds within the vicinity of the site. Most of the area within the domain in Fig. 7 was diagnosed with moderate to heavy icing mainly because of very high values of LWP.

4. CONCLUDING REMARKS

A prototype, physically based method for real time detection of icing conditions has been developed and implemented over the continental United States and southern Canada. The results, currently available on the World Wide Web at http://www-pm.larc.nasa.gov/icing/icing.html, are just one part of a comprehensive aircraft icing program being developed by NASA, NOAA, and the FAA. Ultimately, the results will be combined with PIREPS, model forecasts, and other data to provide a near-real time optimized characterization of icing conditions for pilots and flight controllers.

The methodology is promising, but more refinements are needed to address the uncertainties and outstanding issues. The most glaring problems include the determination of more reliable thresholds, more objective definitions of intensity, mulitlayer misclassifications, height errors, and nocturnal retrievals. Many of these will be addressed using the available in situ and surface datasets to define the "cloud truth" conditions objectively and adjusting the algorithms using the relevant sounding and satellite data. The results presented here are just the beginning of efforts to exploit the valuable datasets from field programs like ATReC and AIRS-II.

Acknowledgements

This research was funded by the NASA Earth Science Enterprise and the NASA Aviation Safety Program through the NASA Advanced Satellite Aviation-weather Products Initiative. Additional support was provided by the Environmental Sciences Division of U.S. Department of Energy Interagency Agreement DE-AI02-97ER62341 through the ARM Program.

References

Benjamin, S. G., et al., 2004: An hourly assimilation-forecast cycle - the RUC. *Mon. Wea. Rev.*, **132**, 495-518.

Chen, Y., S. Sun-Mack, P. Minnis, D. F. Young, and W. L. Smith, Jr., 2002: Surface spectral emissivity derived from MODIS data. *Proc. SPIE,* Vol. 4891, 361-369.

Cober, S. G., G. A. Isaac, and J. W. Strapp, 1995: Aircraft icing measurements in east coast winter storms. *J. Appl. Meteor.*, **34**, 88-100.

Ellrod, G. and J. P. Nelson, 1996: Remote Sensing of Aircraft Icing Regions Using GOES Multispectral Imager Data, *Proc. AMS 15th Conf. Weather Anal. & Forecasting*, 19-23 August, Norfolk, VA, 9-12.

Heck, P. W., P. Minnis, M. M. Khaiyer, S. Sun-Mack, and X. Dong, 2004: Improvements in cloud height determination in ARM satellite retrievals. *Proc. 14th ARM Sci. Team Mtg.*, Albuquerque, NM, Mar. 22-26. (http://www.arm.gov/docs/documents/technical /conf_0403/heck-pw.pdf)

Minnis, P., D. P. Garber, D. F. Young, R. F. Arduini, and Y. Takano, 1998: Parameterization of reflectance and effective emittance for satellite remote sensing of cloud properties. *J. Atmos. Sci.*, **55**, 3313-3339.

Minnis, P., et al., 1995: Cloud Optical Property Retrieval (Subsystem 4.3). "Clouds and the Earth's Radiant Energy System (CERES) Algorithm Theoretical Basis Document, Volume III: Cloud Analyses and Radiance Inversions (Subsystem 4)", *NASA RP 1376 Vol. 3*, pp. 135-176.

Minnis, P., et al., 2001: A near-real time method for deriving cloud and radiation properties from satellites for weather and climate studies. *Proc. AMS 11th Conf. Satellite Meteorology and Oceanography*, Madison, WI, Oct. 15-18, 477-480.

Smith, W. L., Jr., P. Minnis, B. C. Bernstein, A. D. Rapp, and P. W. Heck, 2002: Supercooled liquid water cloud properties derived from GOES: Comparisons with in situ aircraft measurements. *10th AMS Conf. Aviation, Range, and Aerospace Meteorol.*, Portland, OR, May 13-16, 89-92.

Smith, W. L., Jr., P. Minnis, and D. F. Young, 2000: An icing product derived from operational satellite data. *Proc. AMS 9th Conf. Aviation, Range, and Aerospace Meteorol.*, Orlando, FL, 11-15 Sept., 256-259.

Smith, W. L., Jr., P. Minnis, D. F. Young, and Y. Chen, 1999: Satellite-derived surface emissivity for ARM and CERES. *Proc. AMS 10th Conf. Atmos. Rad.*, Madison, WI, June 28 – July 2, 410-413.

Sun-Mack, S., Y. Chen, T. D. Murray, P. Minnis, and D. F. Young, 1999: Visible clear-sky and near-infrared surface albedos derived from VIRS for CERES. *Proc. AMS 10th Conf. Atmos. Rad.*, Madison, WI, June 28–July 2, 422-425.

COMPARATIVE STUDY OF NUCLEATION BY ALCOHOLIC SOLUTION OF BENZOIN, BENZOIN DUST, AND BENZIL DUST.

Sahana Paul[1], Anupam Hazra[1], U.K.De[1*], S. Bhar[2] and K. Goswami[3].

[1]Environmental Science Program, Jadavpur University, Kolkata 700032, India
[2]Chemistry Department, Jadavpur University, Kollkata 700032, India
[3]Physics Department, Jadavpur University, Kolkata 700032, India

1. INTRODUCTION

The ice nucleating ability of organic substance was first invented in 1957 (Baskirova & Krasikov). Since then, similar ability of large number of organic molecules, bacteria, marine plankton, leaf litters and fungi have been reported. One such material is Benzoin and its nucleating ability was first reported in 1963 (Langer et. al.). Incidentally, Benzoin is soluble in alcohol. So, in the present work, the nucleation properties of the Benzoin solution in Alcohol and Benzoin dust have been studied systematically both below and above 0°C in an aqueous environment of a Cloud Chamber. The two agents have vastly different nucleation abilities. Both of them can nucleate ice below 0°C, but the alcoholic solution has the greater ability. However, the most significant observation is the nucleation ability of the dust above 0°C. As ice cannot exist above 0°C, the question arises – what are there crystals? To answer this question, some supporting experiments have been carried out.

Firstly, crystals have been grown in an incubator keeping mixture of Benzoin and water at a fixed temperature above 0°C. Crystals are found to grow around a bead of a grain of Benzoin dust and the magnitude of growth is consistent with the number of crystal count for Benzoin dust seeding in the actual experiment. So these grown up crystals may be taken to be identical with the seeded crystals. Then NMR study of the grown crystals have been carried out in $CDCl_3$ solvent. One can conclude from NMR analysis that the grown up crystals are essentially hydrated form of Benzoin with water caging around Benzoin crystals.

Lastly, as Benzoin molecule has OH group in its structure, so both Benzoin dust as well as Benzoin solution in alcohol are expected to have growth of H_2O around it (Fig.1 & 2). However, Benzil has a similar structure like Benzoin , but it has no OH group in the molecule (Fig.3). To verify the role of OH group in the nucleation of H_2O, Benzil is seeded in a similar experiment. Only few crystals are found to be formed below 0°C and no nucleation occur above it.

Corresponding Author: Prof. U.K. De., Env. Sci. Prog., Jadavpur University, Kolkata-700032., India. E-Mail: deutpal@hotmail.com

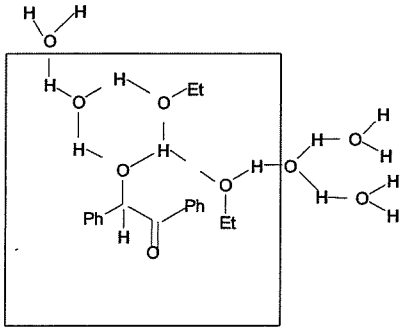

Fig 1: Ice Nucleation in Alcoholic Solution of Benzoin.

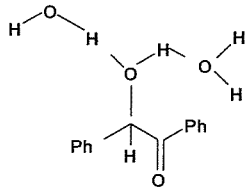

Fig 2: Ice Nucleation in Benzoin Dust.

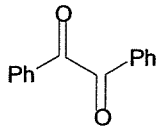

Fig 3: Benzil

2. EXPERIMENT

The nucleation experiment is performed inside a single door metallic chamber with refrigerant lining and its dimensions are 0.72 m, 0.72 m and 1.325 m as length, breadth and height respectively

(Diagram 1). One thermistor is kept just above the seeding port and the temperature by it, is mentioned as the cloud temperature. Another thermistor is kept near the floor to measure the temperature gradient inside the chamber. During the experiment the temperature difference between the two sensors does not exceed 0.5°C. The sensors are calibrated at ice and steam points, and the calibration error does not exceed 0.1°C.

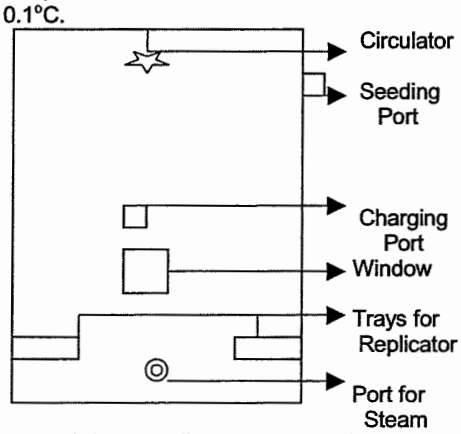

Diagram 1: Schematic diagram of cloud chamber

A cloud of supercooled droplets is produced by cooling the chamber and then passing steam through a hole near the floor of the chamber. One circulator is fixed at the roof of the chamber to circulate the supercooled droplets evenly in the chamber and also to equalize the temperature of the chamber. The amount of water content in the chamber is controlled by adjusting the flow of steam. The lowest temperature attainable in the chamber is –33.5°C.

At first , the temperature of the chamber is brought to a desired value of low temperature. Then, steam is passed until a steady temperature is attained. This steady temperature can be controlled in two ways i.e. by fixing the temperature at which steam is allowed to pass and by controlling the flow of steam. At that steady temperature, the seeding is done. The steady temperature of the chamber is being called the seeding temperature. Here, in case of seeding of alcoholic solution of Benzoin, 0.4 gm of Benzoin is dissolved in 40 C.C. of alcohol and the entire amount is seeded with the help of a sprayer. Benzoin being used here has 99% purity and rectified spirit with 95% alcohol content is used as the solvent. In case of Benzoin or Benzil dust seeding, only 0.4 gm of the dust is seeded with the help of a dust feeder.

A solution is prepared with 0.4 gm of Polyvinyl Formal Resin (Formvar) in 10 C.C. of Chloroform. A thin layer of this solution is coated in 4 slides at a time and these slides are kept in two separate trays near the floor of the chamber to collect the signature of the crystals falling there. When the slides are brought outside after the experiment, Chloroform quickly evaporates, leaving behind a plastic film of Formvar. On the other hand, the ice part of the crystal is converted into water. Details about Formvar coated slides is existing in the literature (Saunders and Wahab 1973, Hallet 1976). The slides are then kept inside a desiccator with sufficient silica gel, so that water will evaporate and be quickly absorbed by silica gel. By this process a replica of the arrested crystal is retained in the slide. One can observe this replica through a microscope.

The microscope being used here has a magnification of 400. In each slide 10 fields of view are considered for counting. There are 4 slides and at each temperature 4 separate observations are taken. So the number of crystals observed at any seeding temperature is actually mean of 160 observations.

In the first supplementary experiment , 5 gm of Benzoin dust is mixed with 25 C.C. of water. Incidentally, Benzoin hardly dissolves in water at room temperature and the solubility increases with temperature. A slide with a bead of a grain of Benzoin dust fixed on it, is placed inside the mixture and the entire system is placed inside an incubator. The temperature of the incubator is set at a particular value and it is left undisturbed for at least 48 hours.

In case of NMR study, at first 0.5 C.C.of $CDCl_3$ is taken and a blank operation is done keeping a fixed number of scan (fig.4). In the next, some amount of grown up crystal is placed in 0.5 C.C. of solvent and the same number of scan is drawn (fig.5). Then, some grown up crystal is taken and heating is started. When the temperature reaches 85°C, water starts to drain out of the crystal. The crystal itself starts to melt around 93-94°C. The heating is continued up to 100°C, so that all water may evaporate out. Then the whole thing is allowed to cool and a lumped up crystal is obtained. It is to be noted that anhydrous Benzoin has melting point of 133°C. The fall in melting point is due to Benzoin hydrate, which is formed due to binding of hydrogen with Benzoin. In the last, some amount of water drained and lumped up crystal is placed inside the same volume of solvent , and again the same number of NMR scan is carried out (fig.6).

3. RESULTS AND DISCUSSIONS

The variation of crystal count with temperature in both cases of seeding is presented in fig.7. Seeding is done up to –22.0°C on the negative side of 0°C. In case of seeding of alcoholic solution of Benzoin, the following conclusions may be drawn:

(i) At –22.0°C, the crystal count is very insignificant, but does not vanish altogether.

(ii) No nucleation occurs above 0°C.
(iii) Maximum nucleation occurs at –14.4°C.
(iv) Most of the crystals have rod shape. Crystals have common tendency to aggregate and present star like formation (photo 1).

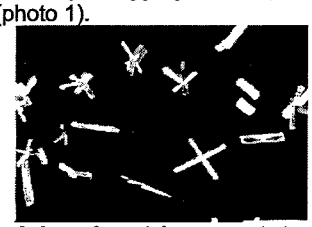

photo 1: Rod shaped crystals aggregate to give star-like formation at – 14.4 ° C for alcoholic solution of Benzoin

(v) Below –17.0°C, dendrite formations have been observed (photo 2).

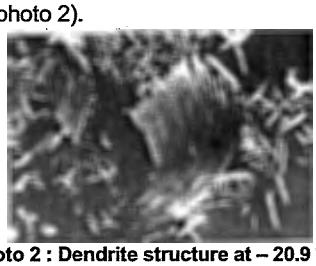

photo 2 : Dendrite structure at – 20.9 ° C for alcoholic solution of Benzoin

On the other hand, Benzoin dust has the following properties as nucleating agent:

(i) It can nucleate both below and above 0°C.
(ii) Below 0°C, crystal concentration is much lower compared to that of alcoholic solution of Benzoin, though there are some small peaks.
(iii) Crystal concentrations are significantly higher at temperatures above 0°C. Maximum nucleation occurs close to 4°C. Beyond, the crystal concentration gradually decreases and vanishes at 7°C. However, the maximum count around 4°C, is significantly less than the maximum count in case of alcoholic solution of Benzoin.
(iv) In this case, crystals have very clear edge. Below 0°C, crystals have dominantly rod and hexagonal shape . Above 0°C, cubic crystals are more dominant (photo 3). Around 0°C, needle like structures are also observed (photo 4).

In case of seeding of Benzil dust, there are some nucleation below 0°C, but the number is quite small. Above 0°C, no crystal is formed.

photo 3 : Cubic structure at 5°C for Benzoin dust

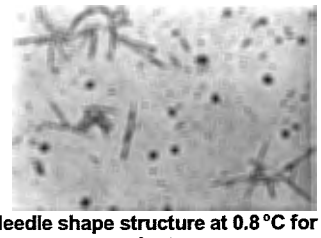

photo 4: Needle shape structure at 0.8 °C for Benzoin dust

It should be stressed that below 0°C, only ice is nucleated around the seeding agent. This is justified by the fact that, below 0°C whenever the slide is brought outside in room temperature, the ice part of the crystal melts. But, in case of Benzoin dust above 0°C, crystals do not give out water even if the slide is kept at room temperature.

In the incubator the maximum growth is found to occur close to 4.0°C (Photo 5). The growth vanishes altogether at 7°C and above.

Photo 5. Growth of Benzoin in incubator at 4 °C

In the blank NMR scan of solvent $CDCl_3$, three peaks occur at δ 7.26158, δ 1.55008 and δ 0.00000 (fig 4). All these response are due to the presence of $CDCl_3$. When grown up crystal of Benzoin is dissolved in $CDCl_3$ and NMR scan is taken, presence of water in the crystal is established through the peak at δ 4.6028 (fig.5). The other peaks are due to Benzoin and $CDCl_3$ only. Since water is present along with Benzoin only, one can conclude that the grown up crystal is essentially hydrated form of Benzoin. But the hydrated form may exist in two ways:

(i) H_2O may enter into the molecular structure of Benzoin,

or

(ii) H_2O may cage around Benzoin crystals and it will then act only as binder for Benzoin crystals.

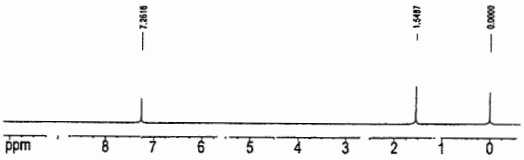

Fig. 4: Blank NMR for $CDCl_3$

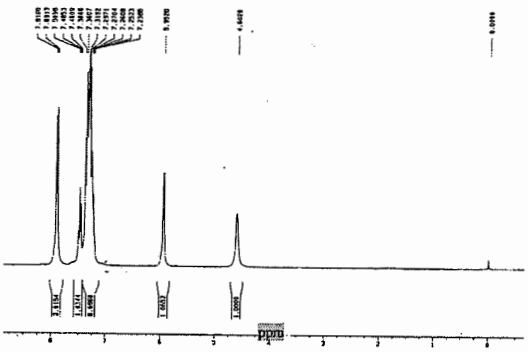

Fig.5: NMR for grown up Benzoin in $CDCl_3$

The fact that the grown up crystals start liberating water from 85°C, clearly indicates that the hydrated form of Benzoin is due to caging of water. After complete liberation of water, the lumped up form of Benzoin is obtained as it is Benzoin hydrate, unlike the dust like nature of anhydrous Benzoin. Absence of water is evident in fig.6. All dominant peaks are due to Benzoin only.

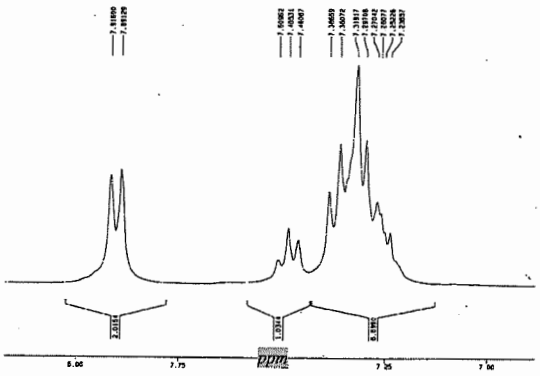

Fig. 6: NMR for lump up Benzoin in $CDCl_3$

4. CONCLUSION

Comparing the three seeding agents, alcoholic solution of Benzoin is found to be most effective ice nucleating agent below 0°C. This is due to the fact that Benzoin gets easily dissolved in alcohol and in combination, the molecule creates additional sites for attracting other water molecules through intermolecular hydrogen bonding. This leads to highly ordered, compact, energy minimized and quasi-planar framework.

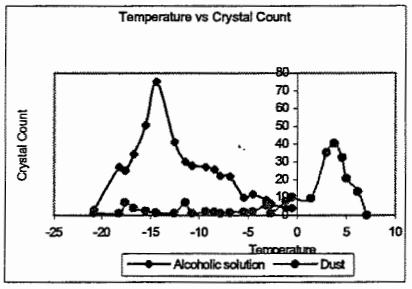

Fig. 7: Variation of crystal count with temperature

Benzoin dust has good ability to form hydrate crystal with water on the positive side of 0°C. The nucleation dominantly occurs around 4°C. Around 4°C, the water molecules are arranged in relatively ordered fashion as volume is minimized. Here water cages around Benzoin crystals and it acts only as binder.

The nucleation capability of both alcoholic solution of Benzoin and Benzoin dust is due to presence of OH group in the molecule.

5. ACKNOWLEDGEMENT

The authors' thanks are due to India Meteorological Department, Government of India, for the sanction of a research project. The present work is a part of that project.

6. REFERENCE

Baskirova, G. M. & Krasikov P. N., 1957 : Experiments in studying certain substances as reagents in crystallization of supercooled fog. Trudy Glavnoi Geofiz. Obs., 72, 118-126.

Hallet, J., 1976 : Cloud particle replicator for use on a pressurized aircraft: part 1 & 2. Operating Manual, Air Force Geophysics Laboratory, United States Air Force, Hanscom AFB, Mass.

Langer, G., Rosinski, J. & Bernsen, S., 1963 : Organic crystal as icing nuclei. Jour. Atmos. Sci., 20, 557-562

Saunders, C.P.R. & Wahab, N. A., 1973 : The replication of ice crystals. J. Appl. Meteorol., 12, 1035 – 1039.

THE SCREEN OF WEATHER MODIFICATION LN MEDIUM

Qi Ying[1] Wang Xuelin[1] Zhen Jiaoheng[1] He Feng[1] Chen Zhixin[1]
Wang Xiaomei[1] Guo Junmei[1] Yu Xiangren[2]

[1]JiLin Weather Modification Office, ChangChun, 130062, China
[2]Meteorological Sciences Institute, Beijing, 100081,China

1. SELECTION OF EXPERIMENTAL MATERIALS

The ideal liquid nitrogen carrier should have strong ability to absorb and maintain liquid nitrogen and strong low temperature insulation, proper specific gravity, maintain proper falling speed in clouds, be convenient for storage, transportation and utilization, be easy to get, inexpensive, and non-polluting to environment at the same time.

The above conditions met, we made a lot of survey and research for the experiment and finally narrowed down to 13 kinds of experimental materials: diatomite, #1 inside of plants, chemical-fiber cotton, molecule sieve, polyacrylamide, plaster, JK, puffing substances, aperture paper, volcano rock, slag bricks, and foam plastic.

Most of the above materials can be obtained locally from extensive sources. Meanwhile, we collected and made several kinds of small containers as carriers and tested them in the open air (experiment description omitted).

Now matter what kind of materials the carriers are made of, they must be in proper sizes. If they are too big, the carriers will fall rapidly out of the clouds once they have absorbed liquid nitrogen; if they are too small, the carriers will not fall down even with liquid nitrogen because of the rising air currents. In neither of the two situations will they will function as carriers in the real sense.

2. EXPERIMENTAL METHODS

First of all, we tested the size, weight and specific gravity of the various materials. After that, we conducted comparative experiments to them in terms of their ability to absorb liquid nitrogen and their abilities to control volatilization and maintain the temperature when they have absorbed sufficient liquid nitrogen in situations of constant temperature, low temperature, and in static and dynamic (with air currents) conditions. Finally, we took the selected carriers to the open air to measure their falling speed and the results of volatilization after they landed onto the ground.

2.1 Measurements of Major Physical Features

Corresponding author's address: No.653, HePing Street, ChangChun City, JiLin Province,130062,China; E-Mail: jlwm@public.cc.jl.cn

The carriers for our experiments are generally made into spheres, squares and cylinders. We sue precision electronic scales and vernier calipers to measure their volumes, weights, and specific gravities.

2.2 Comparative Experiments of Liquid Nitrogen Absorption Ability

First of all, we scaled the average weight of various carriers; then we soaked them in liquid nitrogen and weighed them every 10 seconds till their saturation with absorption, and that was their maximum absorption. In order to study their absorption ability in low temperatures, we lowered the temperature with the help of fridges, and measured their absorption ability at the same time.

2.3 Experiments of Liquid Nitrogen Volatilization and Temperature Retaining

First, we saturated the selected carriers with liquid nitrogen and weighed them with scales. We hung them with thin ribbons respectively in static and dynamic (air current) conditions. Now the absorbed liquid nitrogen was gradually evaporating. It was absorbing the heat in its surrounding air and was volatilized quickly, which resulted in the decrease of the carriers' weight and the increase of their temperature. We weighed them every 30 seconds and recorded the temperature shown by the temperature detector. It is repeated till all the absorbed liquid nitrogen was fully volatilized and the temperature of the carriers dropped to 0 ℃. In this way, we can gather the data about the liquid nitrogen volatilization characteristics in various carriers and the temperature changes as time passes by.

2.4 Falling Experiments on Top of the Television Tower

In order to simulate the real liquid nitrogen volatilization of the carriers when they are falling from the sky and measure their falling speed, we first conducted an experiment on the 6th floor (21.45 m) by dropping them to the ground so that we could measure their falling speed and the volatilization situations when they landed. After that, we made the same experiment on top of the Jilin Province TV Tower at the height of 146 m. in order to ensure the

accuracy of the measures, we used mobile phones to keep synchronous contact besides eyeballing. As the height is fixed, as long as we could determine the time it took to them to fall, we could obtain the average fall speed. After the carriers landed, we could perform investigations about the volatilization.

3. EXPERIMENT RESULTS

3.1 The Ability of Liquid Nitrogen Absorption of the Carriers

After soaking the carriers in liquid nitrogen for 30 seconds and 60 seconds, we measured their absorption abilities and found great differences among them. The maximum absorption ratio (suppose the original weight of the carrier is g, and the maximum weight of it is G after it has absorbed liquid nitrogen, and the absorption ratio is A, and then, A=(G-g)/g) was 28.8, and the minimum absorption ratio was only 0.1. JK had the maximum absorption ratio, followed by foam plastic (10.4) and diatomite (6.2).

When all these carriers were soaked in liquid nitrogen for 30 seconds, their absorption ability was greatly lowered; and they all reached saturation in 60 seconds. After that, no absorption increase was found.

3.2 Abilities of the Carriers to Maintain Liquid Nitrogen and Low Temperature

The abilities of the carriers to maintain liquid nitrogen and low temperature are related to many factors of the carriers such as nature, size, shape, etc. In order to compare these two abilities, we selected carriers with the same shape and volumes. First, we let them absorb liquid nitrogen till saturation, hung them in static environment (the room temperature was 24.0 ℃), and measured the time it took the liquid nitrogen to fully volatilize and the corresponding temperature changes. When the carriers were with liquid nitrogen in natural air, their temperature was rising rapidly. It took 227 seconds for the liquid nitrogen to fully volatilize from the JK carrier of 2.0 cm diameter, saturated with liquid nitrogen; it took about 590 seconds for the temperature to rise from –190 ℃ to –40 ℃, and about 900 seconds for the temperature to rise to 0 ℃. As for the foam plastic of the same volume, saturated with liquid nitrogen, it took 180 seconds for the liquid nitrogen to fully volatilize and it took about 350 seconds for the temperature to rise from –190 ℃ to –40 ℃, and about 730 seconds to rise to 0 ℃.

The carriers' ability to maintain low temperature is also related to wind speed. The more the wind speed is, the shorter time it maintains the temperature. When the wind speed was 2-4 m/s, generally, the temperature maintaining time was more than 30 seconds shorter. Volatilization was slower with fog, but the difference was not very big under foggy or non-foggy conditions.

3.3 Tests of the Falling Speed of Various Carriers

On the top of the Jilin Province TV tower, we made tests of carriers of various sizes saturated with liquid nitrogen and obtained their average falling speed. For the same carrier, with the increase of its weight, its average falling speed increased, too. The average falling speed of JK carrier of diameter 1.5-3.0 cm, saturated with liquid nitrogen, was between 9.9 and 19.5m/s, and that of foam plastic was between 7.5-10.0m/s.

4. DISCUSSION

4.1 Through the selection processes among the 13 types of short-listed materials, compared with foreign experiments, we think that JK is the best liquid nitrogen carrier. The reasons are as follows:

A. JK has very strong ability to absorb liquid nitrogen, and the liquid nitrogen it can absorb is 28 times as much as its own weight. Some people in China experimented with diatomite and found that it could 2.0 times as much liquid nitrogen as its own weight. The maximum absorption ability of other carriers in our experiments was no more than 10.4 times as much as its own weight.

B. Compared with other materials of the same volume and shape, when JK has fully absorbed liquid nitrogen, it keeps the liquid nitrogen the longest, 3-5 times longer than other materials. It also has the strongest low temperature maintaining ability. It takes about 590 seconds for the temperature to rise from – 196 °C to – 40 °C, while it takes other carriers only 150 – 350 seconds; it takes JK 900 seconds for its temperature to rise from –196 °C to 0 °C, but it takes other carriers only 300-700 seconds to do it.

C. JK is soft in nature, and will not hurt people or crops when it lands. It is erosion-free, non-poisonous and easy to decompose, so it will not cause pollution to the ecological environment.

D. JK is easy to get at low prices; it is easy to store and use.

4.2 The carrier's ability to keep low temperature is related to wind speed, water and vapor conditions in the environment.

The speedier the wind, and the drier the environment, the poorer the temperature keeping ability; the less speedy the wind, and the more humid, the stronger the temperature keeping ability. However, the discrepancies are not very big when the wind speed is low.

4.3 Owing to the fact that JK has strong ability to keep low temperature and liquid nitrogen, we should select JK of different sizes as carriers according to various purposes of weather modification and different cloud conditions.

On the whole, we should choose JK carriers of

diameter 1.0-3.0 cm. The JK carriers of diameter 1.5 cm can catalyze clouds of about 2000 m thick within 200 seconds. If they are too big, they will fall out of the cloud too soon and then fail to function as good carriers.

References

R. A. Bakhanova. B. N. Leskov. R. V. Oleinik., Field Experiments Porous Granules Saturated with Liquid Nitrogen As Reagent for Modification of Clouds, SIXTH WMO SCIENTIFIC CONFERENCE ON WEATHER MODIFICATION, 233-235, 30 May-4 June 1994.

Song Runtian, et al, Analysis of Precipitation Velocity When Liquid Nitrogen Is Applied and of Precipitation Modification with Liquid Nitrogen, 161-165, Meteorological Press, September 1997.

Li Lunge, et al, Technical Plans for Precipitation Modification in Qinghai Province, and Study on the Qingzhang Plateau Cloud and Weather Modification, 161-173, Meteorological Press, September 2000.

A. N. Zemshov, L. I. Krasnovskaya, L. M. Roschina and A. A. Chernikov, Development of the Method for Dispersal of Supercooled Clouds and Fogs Using Liquid Nitrogen, SIXTH WMO SCIENTIFIC CONFERENCE ON WEATHER MODIFICATION, 255-258, 30 May-4 June 1994.

Xu Xiaomao, et al, Liquid Nitrogen Carrier Experiment and Selection Analysis, and Precipitation Modification with the Help of Liquid Nitrogen, 147-154, Meteorological Press, September 1997

A THREE-DIMENSIONAL MODELING STUDY OF HAILSTORM SEEDING

Vlado Spiridonov and Lena Jovanovska
Hydrometeorological Institute of Macedonia, Skupi bb 1000 Skopje, Macedonia

1. INTRODUCTION

The principle of hail suppression is based on the conceptual models with all uncertainness, which this approach brings itself. Over the past two decades a number of papers have investigated the cloud seeding using numerical modeling. Results of the cloud seeding experiments (Hsie et al., 1980; Orville and Chen, 1992) have revealed that the seeded cloud exhibits the earlier initiation of precipitation which is crucial to the seeding effects, leading to increased precipitation, slight dynamics and microphysics interactions and difference in cloud life history. Farley (1987) found that hailfall decreased and rainfall could be increased in some situations, although some redistribution in hail spectrum can be expected. Aleksic et al., (1992) from their model simulation have found that only 2-3% of the target volume is actually being seeded. DeMott (1995) has quantified four ice nucleation mechanisms for the seeding aerosols. Cloud drops size spectra and its relation to cloud seeding effects of hailstorm are studied by Curic et al. (1997). In the last decades three-dimensional cloud models started to apply for cloud seeding simulations (e.g. Farley et al., 1994). This study has been focused on two aspects: a three-dimensional simulation of agent transport, diffusion and activation during supercell storm seeding case and the effects obtained from a number of sensitivity experiments by using different initial seeding parameters. Finally the results are summarized and the principal conclusion of the optimal seeding criteria is given.

2. MODEL

Only few basic characteristics of the model are summarized here. The present version of the model is a three-dimensional, compressible system which is based on the Klemp and Wilhelmson (1978) dynamics Lin et al. (1983) microphysics and Orville and Kopp (1977) thermodynamics. For the parame-
terization of the microphysical processes we use the integrated (bulk) water parameterization Lin et al.(1983). The equivalent radar reflectivity factors for hail and rain are computed on the equations given by Smith et al., (1975) and empirical equation for snow by Sekhon and Srivastava (1970). More detailed informations about the cloud model are discussed by Spiridonov and Curic (2003a,b).

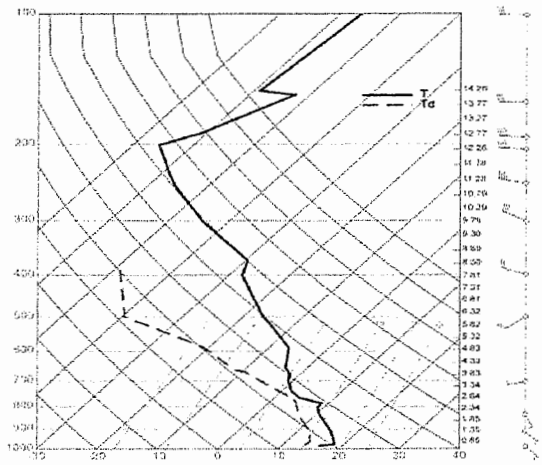

Fig. 1 A representative sounding taken at 01 UCT from Skopje on May 18, 2003

Since the model dispersion of the agent is in its initial phase on a sub-grid scale, the advection and diffusion should be parameterized. This problem is solved by considering the seeding line as the series of the individual spherical puffs by the radius of 10 m. The agent spread is than simulated by the movement and spread of the each individual puff. Its advection is calculated by the wind field bilinear interpolated from the four adjacent grid points. The trajectories of the puffs are computed in the model. The radius σ of these puffs has been calculated for each step as a function of the

___Corresponding author's address:
Hydrometeorological Institute of Macedonia
Skupi bb 1000 Skopje, R.Macedonia,
E-mail: vspiridonov@mol.net.mk

turbulent diffusion coefficient Georgopoulos and Seinfeld (1986) by the solution of the equation

where K is the diffusion coefficient. A three mechanisms of AgJ nucleation activation based on Hsie (1980) are considered in the model:

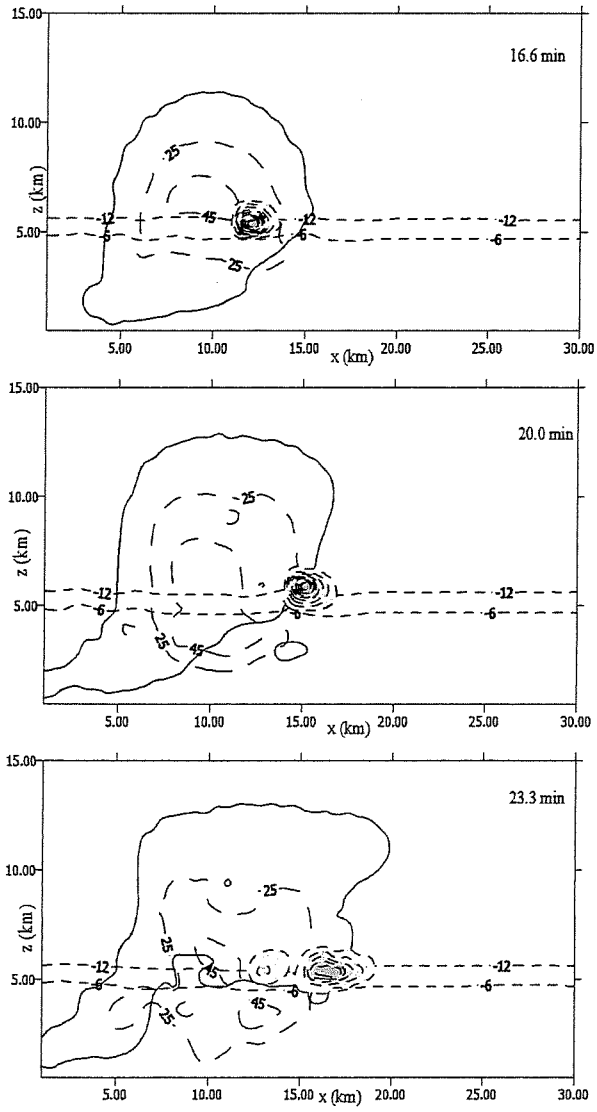

Fig. 2a) Time evolution of the AgJ field in the x-z plane at y=15 km at 16.6, 20.0 and 21.6 min. Cloudy areas are outlines by a solid line. Reflectivity contours are given by dashed lines.

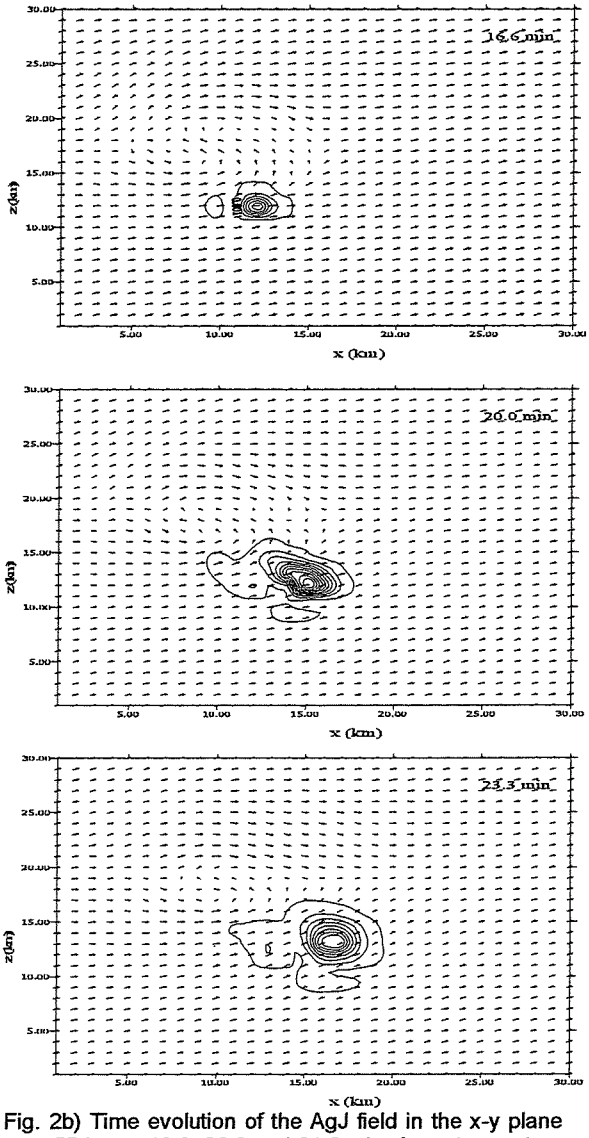

Fig. 2b) Time evolution of the AgJ field in the x-y plane at z=55 km at 16.6, 20.0 and 21.6 min. An outer contour of 0.05 μg kg^{-1} is taken for 16.6 and 20.0 min and 0.015μg kg^{-1} contour for 23.3 min, with contour interval of 0.01μg kg^{-1} The arrows show the two-dimensional representation of the wind field.

a) contact freezing nucleation-Brownian collection and inertial impact due to cloud drops; b) contact freezing nucleation-Brownian collection and inertial impact due to raindrops; c) deposition nucleation due to water vapor at ice supersaturation. Initial impulse for convection is an ellipsoidal warm bubble with the maximum temperature perturbation in the bubble center ($T_0 = 5.6°C$) with exponentail decrease towards zero on the bubble boundaries.The model is chosen to be 30x30x15 km for 3-d runs and 45x15 km for 2-d runs, respectively. The horizontal resolution of the model is 0.5 km; the vertical one is 0.2 km. The temporal resolution of the model is 10 s time step for integration of the dynamics, microphysics and chemistry and a smaller one is (2 s) for solving the sound waves. A representative sounding taken at 01 UTC from Petrovec on May 18, 2003 with the corresponding wind profile is presented in Fig.1. The sounding is dry and stable near the surface and unstable and moist with wind veering above the surface layer, so the cloud develops very quickly in response to the initiating perturbations.

3. RESULTS

The silver iodide agent is directly injected into the simulated cloud at a five- minute interval at 16.6 and 21.6 min, in the area between -8° C and -12°C isotherms and 25dBz-45dBz echo contours at 5.5 and 5km height, respectively. The time evolution of the AgJ field in the X-Z cross sections is depicted in Fig.2a. After seeding the agent is advected and diffused

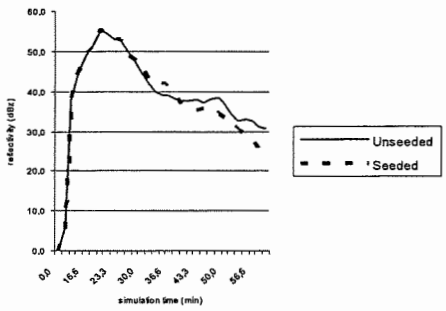

Fig. 3. The time evolution of reflectivity factors of seeded and unseeded case

within the cloud by the turbulent flow field. Some of the AgJ has been activated, small part tends to be drawn back into the cloud as it descends to the lower levels by the downdrafts, while the large portion is transported outside the target volume above -12°C isotherm. The limited time spread of agent is may be due to the strong air circulation within the cloud. Only 13% of the AgJ remains inactivated as a result of less than optimal placement of the seeding agent and the limited advection time of 2-3 min that limits the time available for agent diffusion. The maximum agent spread within the target area during simulation time is less than 60 m from the axis depending on the local turbulence. Fig. 2b shows the X-Y cross sections at z=5.5 km. It is seen from this figure that after the seed was introduced into the target area the AgJ is slowly diffused in response to the existing horizontal wind field at that level. The AgJ mixing ratio decreases from 0.28 μg kg^{-1} at 16.6 min to 0.065 μg kg^{-1} at 26.6 min. Most of the AgJ has been activated during the first five-minute interval. The inactivated AgJ is initially transported toward southeast and downward. After repeat seeding two separated AgJ fields are propagated and distributed toward eastern quadrant of the cloud model domain. In order to gain a qualitative understanding of

Table 1. A model sensitivity experiments

Experiment	Time repeat of seeding (min)	Total rainfall on the ground (kg/m^2)	Total hailfall on the ground (kg/m^2)
Base run	Unseeded	150.51	18.18
A0	0	152.90	18.42
A1	1	150.12	18.77
A2	2	157.85	18.98
A3	3	152.92	18.43
A4	4	149.60	18.36
A5	5	153.56	18.26
A6	6	152.29	18.28
A7	7	151.84	18.66
A8	8	149.60	18.36
A9	9	150.20	18.14
A10	10	152.20	18.78

seeding conditions of a hailstorm suiting seeding. Table 1 lists the parameters that distinguish the ten simulations performed here. The first run (B), is chosen as a standard non-seeded case which serves as a basis for comparison with other experiments. It is evident that the total rainfall and hailfall at the ground for all experiments increase relative to the base run One sees that the greatest increase of both rainfall and hailfall is observed for

a two-minute repeat seeding, for case A2, with percentage values of 4.65% and 4.40%, respectively. The optimal seeding effects are obtained by five-minute seeding interval for the simulation A5, when rainfall and hailfall increase by 2.02% and 0.44%, respectively. The effects of AgJ seeding in respect to their microphysics are apparent if we consider the time evolution of reflectivity factors of the unseeded and seeded cloud (Fig.3). There is a slight similarity between the reflectivity echo contours after the initial seeding. The difference in the reflectivity echo fields between these runs becomes more evident as the cloud enters its mature stage.

4. SUMMARY

According to hail suppression hypothesis it is logical to expect significant decrease of hail at the ground as in the other carefully setup hail suppression experiments. Despite positive statistical results from a number of numerical studies our sensitivity experiments indicate peak hailfall depth increased by about 0.44 to 4.40%. This inconsistency may be due to the bulk water parameterization used in our study, which does not recognize the size dimensions of ice particles. This is also a consequence of the limited spread of the seeding agent and the relatively low time of its diffusion and activation in the case of vigorous isolated cells. Finally, numerical models should be enabling to correctly simulate the agent dispersion, witch is in its initial phase on a sub-grid scale. However, it is not possible easy to say that the seeding does not have any effects considering the differences especially in respect to their microphysics.

REFERENCES

Aleksic, N., B. Telenta and S. Petkovic, 1992: Model simulation of seeding repeat rates for direct injection seeding rockets. J. Wea.Mod., 24, 84-88

DeMott, P. J., 1995: Quantitative description of ice formation mechanisms of silver iodide-type aerosols. Atmos. Res., 38, 63-99

Curic, M., D. Janc, and V. Vuckovic, 1997: The influence of cloud drop size distribution on simulated seeding effects of hail-bearing cloud. J. Wea. Mod., 29, 70-73.

Farley, R. D., 1987: Numerical modeling of hailstorms and hailstone growth. Part III: Simulation of Alberta hailstorm-natural and seeded cases. J. Appl. Meteor., 26, 789-812

Farley, R.D., P. Nguyen and H.D. Orville. 1994: Numerical simulation of cloud seeding using a three-dimensional cloud model. J. Wea.Mod.., 26, 113-124.

Georgopoulos, P.G. and J.H. Seinfeld, 1986: Mathematical modeling of turbulent reacting plumes-General theory and model formulation. Atmos. Envir., 20, 1791-1802

Hsie, E.-Y., R.D. Farley and R. D. Orville, 1980: Numerical simulation of ice-phase convective cloud seeding. J.Appl.Met. 19,950-977

Klemp, J.B. and R.B. Wilhelmson, 1978:The simulation of three-dimensional convective storm dynamics.J.Atm.Sci. 35,1070-1096

Lin, Y. L. Farley, R. D. and H.D. Orville, 1983: Bulk water parameterization in a cloud model. J.Climate Appl. Met.,22, 1065-1092, 1983.

Smith, P.L, G. G. Myers and H.D. Orville, 1975: Radar reflectivity calculations on numerical cloud model using bulk parameterization precipitation. J. Appl. Meteor., 14, 1156-1165

Orville, H. D. and F.J. Kopp, 1977: Numerical simulati-on of the history of a hailstorm. J.Atmos. Sci., 34, 1596-1618

Orville, H. D. and J-M.Chen, 1982: Effects of cloud seeding, latent heat of fusion and condensate loading on cloud dynamics and precipitation evolution: A numerical study. J. Atmos. Sci., 39, 2807-2827.

Sekhon, R.S. and R.C. Srivastava, 1970: Snow size spectra and radar reflectivity. J. Atmos. Sci., 27, 299-307

Smith, P.L., G.G. Myers and H.D. Orville, 1975: Radar reflectivity factor calculations on numerical cloud models using bulk parameterization of precipitation. J. Appl. Meteor.., 14, 1156-1165

Spiridonov, V, and M. Curic, 2003a: Application of a cloud model in simulation of atmospheric sulfate transport and redistribution. Part I. Model description. Idojaras, Quart.Vol. 107, No. 2, p. 85-115.

Spiridonov, V, and M. Curic, 2003b: A three-dimensional numerical simulation of sulfate transport and redistribution. Can. J. Phys. 81, 1067-109

Computation of Electromagnetic Characteristics of Frozen Hydrometeors and Comparisons with Millimeter-wave Measurements

James A. Weinman and Min-Jeong Kim

Department of Atmospheric Sciences
University of Washington, Seattle, Box 351640, WA 98195, USA
Phone: 1-206-685-1851, Fax: 1-206-543-0308
Email: weinman@atmos.washington.edu

1. Introduction

Remote sensing of frozen hydrometeors has been a topic of increasing interest to satellite and radar meteorologists because understanding the behaviors of frozen hydrometeors is crucial for several atmospheric science fields such as cloud microphysics, hydrology, and local and global climate research.

To develop a physical model to retrieve snowfall from millimeter-wave measurements, it is essential to calculate scattering and emission properties which can generate brightness temperatures (Tbs) and/or radar reflectivities that are consistent with observations. Frozen hydrometeors have various sizes, shapes, orientations, phase, and density so that it is difficult to parameterize their electromagnetic (EM) properties. For many physical approaches in remote sensing, non-spherical frozen hydrometeors are parameterized as spherical particles and Mie-theory is employed because it is faster than more rigorous analyses of scattering by aspherical particles.

This study seeks a parameterization to represent the EM properties of snow at millimeter-wave frequencies. This study presents results at millimeter-wave frequencies (94 GHz to 340 GHz) frequencies for scattering from ice crystal models. The finite difference time domain (FDTD) and the Discrete Dipole Approximation (DDA) methods are employed. Snow microphysical properties, such as density, dimension, and particle size distribution are assumed based on previously measured observations. Effects of snow crystal orientation on scattering properties are presented.

2. Snow crystal model

Ice crystals growing from the vapor phase can assume two basic type of habits, either platelike or prismlike (Pruppacher and Klett 1997). The basic habit of an ice crystal and its variation are determined by the temperature and humidity conditions at which the ice crystal grows (Magono and Lee, 1966).

The length of columnar crystals and the diameter of plate-like crystals typically is known to range from 20 μm and 3mm. Figure 1 shows the dimension relationships observed in previous studies (Hobbs et al. 1974, Auer and Veal 1970, Heymsfield 1972, Davis 1997). Results show that small dimensions for columnar crystals are generally thicker than the plate-like crystals. For example, the ranges of small dimensions are 0.3 mm ~ 0.7 mm for columnar crystals, 0.045 mm ~ 0.08 mm for plate-like crystals when large dimension is 3 mm.

It is known that the density of snow crystals is less than that of the pure ice, 0.91 g/cm^3. Figure 2 shows the observed bulk density of snow crystals in Heymsfield 1972. Hexagonal plates was Observed bulk density of hexagonal plates is 0.9-g/cm^3 regardless of size. Columnar crystals in warm region have the large bulk density greater than 0.8 g/cm^3. Dendrite and stellar crystals have much small bulk density, less than 0.6 g/cm^3 for large dimension greater than 1 mm.

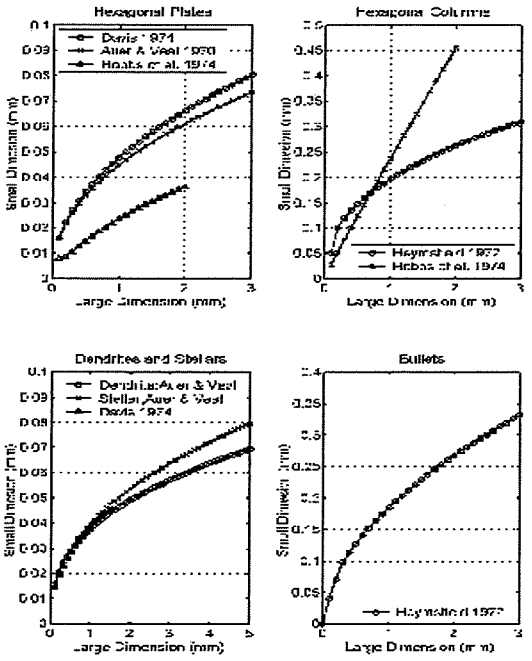

Figure 1. Dimensional relationships of snow crystals observed in previous studies

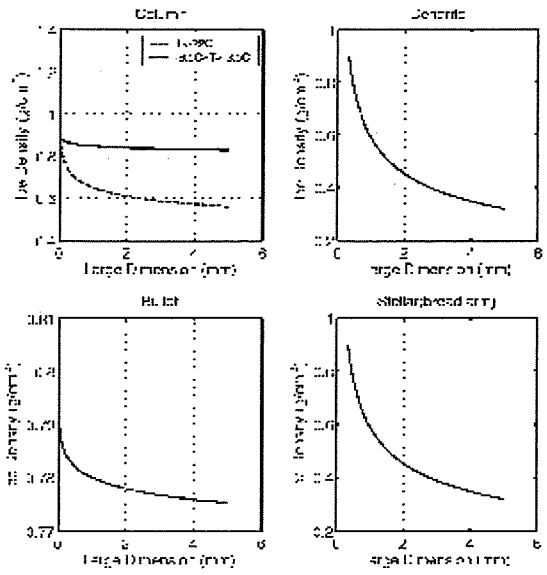

Figure 2 Bulk density of snow crystals observed in Heymsfield 1972.

3. Single Scattering Properties

The finite-difference time domain (FDTD) method is a numerical technique for the solution of the Maxwell equations using appropriate absorbing boundary condition. It is one of the most robust and accurate numerical methods. The descriptions for the FDTD method used in this study are given in Sun et al. (1999). The discrete dipole approximation (DDA) consists of approximating the actual target by an array of polarizable points (the "dipoles"). The DDA is a flexible technique for studying the scattering and absorption of electromagnetic radiation by targets with sizes comparable to the wavelength. While this technique is not particularly suitable for targets with very large complex refractive index m, it works well for materials with $|m-1| \leq 3$ and target dismension $D \leq 5\lambda$, where λ is the wavelength in the surrounding medium (Draine and Flatau 1994).

Since the DDA method is much faster than the FDTD method in the millimeter-wavelengths for realistic dimension relations with large aspect ratio, we employ the DDA method to calculate the single scattering properties of nonspherical snow crystals. The FDTD method's results are used as a benchmark to check the accuracy of the DDA results. The dipole size assumed in the DDA method was 3 μm, 6 μm, 12 μm, 20 μm, 30 μm, 30 μm and 30 μm when large dimension of snow crystals are 60 μm, 120 μm, 250 μm, 500 μm, 1000 μm, 2000 μm, and 3000-μm, respectively.

Figure 3 shows the percentage error of the DDA method in extinction efficiency, scattering efficiency, and asymmetry factor calculations. The Mie solution and the FDTD method's results are employed for spherical and cylindrical particles, respectively. The aspect ratios of the hexagonal particles used in this calculation follow the dimensional relationship observed by Hobbs et al. (1974). The result shows that the DDA results are accurate with errors less than 3 %.

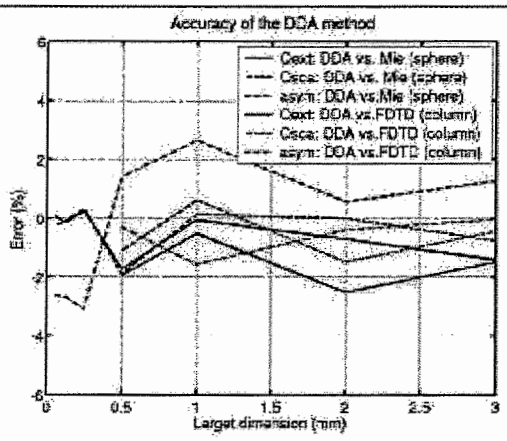

Figure 3. Errors of the DDA method in extinction efficiency, scattering efficiency, and asymmetry factor calculations

Figure 4 and 5 show the 94 GHz extinction cross section, backscattering cross-section, and asymmetry factors for hexagonal columns and hexagonal plates at incidence angles between 0° and 90°, respectively.

When snow crystals are assumed to fall with their long axis perpendicular to the vertical direction, cosine of incidence angle is 1 for incident radiation in nadir (side) for hexagonal plates (hexagonal columns).

The results show that the extinction and backscattering cross sections at incidence angle of 0° is larger than at incidence angle of 90° for most of snow crystal sizes regardless of shapes while the asymmetry factors at incidence angle of 0° are smaller than at incidence angle of 90°. In addition, it is shown that the extinction and backscattering cross sections for hexagonal columns are larger than the hexagonal plates by a factor of 2.

4. Discussion

The single scattering properties can be significantly different depending on orientation and shape of snow crystals. Erroneous assumptions for orientation and aspect ratios of snow crystals in scattering calculations may cause significant errors in radar attenuation and backscattering calculations and in brightness temperature calculations for passive microwave remote sensing studies.

Acknowledgements

This work has been supported by NASA Grant #NCC-5-584 and #S-69019-G. We thank Dr. Ramesh Kakar of Code Y at NASA Headquarters for his support and encouragement. We also thank Dr. Tao at NASA Goddard for sponsoring us to use the Goddard supercomputer. We thank Dr. Wenbo Sun and Dr. Bruce Draine for providing us with the FDTD and the DDA codes, respectively.

References

Pruppacher, H. R., and J. D. Klett, 1997: *Microphysics of Clouds and Precipitation* , 2nd Edition, Kluwer Academic Publishers, Dordrecht, The Netherlands, 954 pp.

Magono, C., and C. Lee, 1966: Meteorological classification of natural snow crystals. *Journal of the Faculty of Science, Hokkaido University*, Ser. VII, **2**, 321-335.

Hobbs, P. V, S. Chang, and J.D. Locatelli, 1974: The Dimensions and Aggregation of Ice Crystals in Natural Clouds, *J. Geoph. Res.*, **79**(15), 2199-2206.

Auer, A. H. and D. L. Veal, 1970: The dimension of ice crystals in natural clouds, *J. Atmos. Sci.*, **27**, 919-926

Heymsfield, A.J., 1972: Ice crystal terminal velocities, *J. Atmos. Sci.*, **29**, 1348-1357.

Sun, W., Q. Fu, and Z. Chen, 1999: Finite-difference time domain solution of light scattering by dielectric particles with a perfectly matched layer absorbing boundary condition. *Appl. Optics*, **38**, 3141.

Draine, B.T., and Flatau, P.J. 1994, "Discrete dipole approximation for scattering calculations", *J. Opt. Soc. Am.*, **A11**, 1491

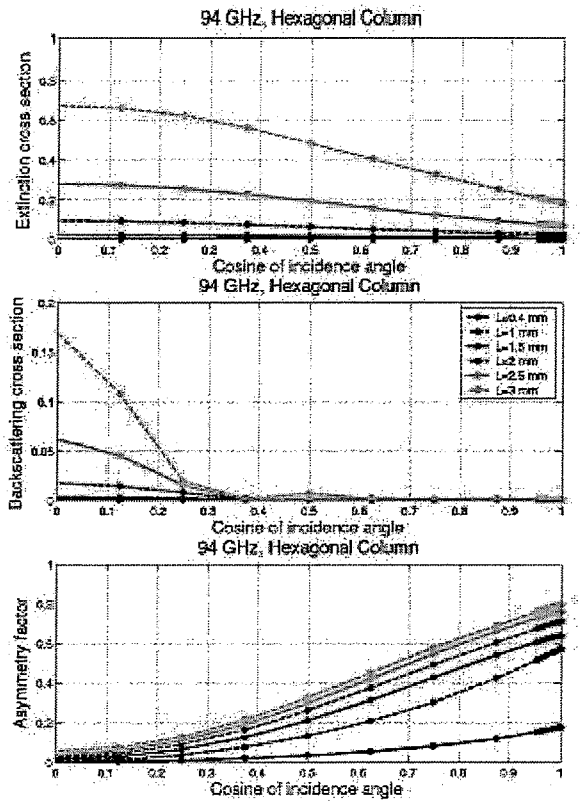

Figure 4. The extinction cross section, backscattering cross section, and asymmetry factor calculations at 94 GHz as a function of incidence angle with respect to the axis of symmetry for hexagonal columns..

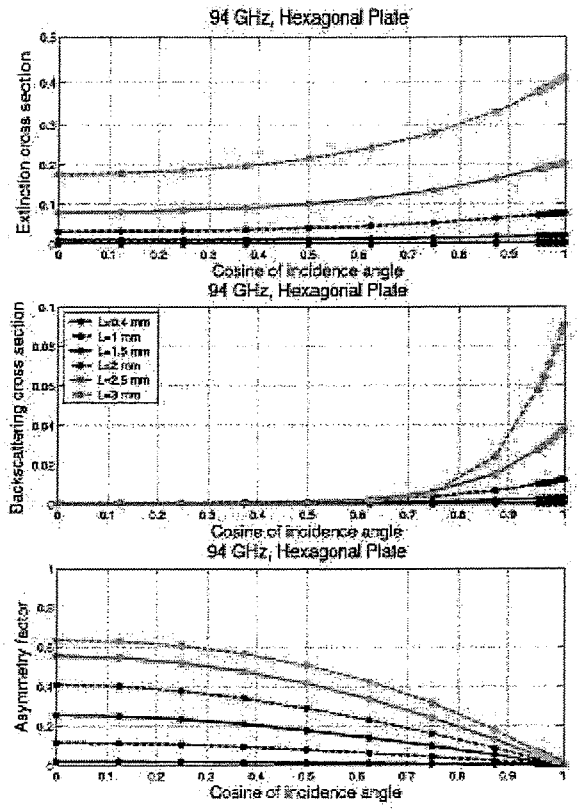

Figure 5. The extinction cross section, backscattering cross section, and asymmetry factor calculations at 94 GHz as a function of incidence angle with respect to the axis of symmetry for hexagonal plates.

THE DEVELOPMENT OF GROUND-BASE WEATHER MODIFICATION TOOLS IN CHINA

Wu yuzhong and Chen guangxue
Shaanxi Zhongtian Rocket Technology Co.,Ltd. ,Xi'an, Shaanxi,710025,China

1 INTRODUCTION

In China, the modern weather modification was started in 1958, to lighten the summer drought in Jilin province, aircraft was applied to seed dry-ice in the cloud. Through more than 40 years of development, a modern system under the guidance of real radar observing and seeding by aircraft and ground-base tools has been established. For its low cost and convenience, the ground-base tools are widely used to enhance rainfall and suppress hail in China

2 DEVELOPMENT OF GROUND-BASE TOOLS

2.1 37 gun

The traditional tool used is the 37 gun which can shoot shells carrying 1g silver iodide and reach a maximum height of 5km in most regions in China, it is too low to reach the target cloud. The ice nucleating effectiveness is only from 10^9 to 10^{13} for each gram of silver iodide. The shoot failure rate is 1/30 or so, it's not safe enough.

2.2 Simple rocket

Since 1960s to the later 1970s, the "simple rocket" made by paper, wood, black powder and silver iodide was developed by meteorological workers to substitute the 37 guns, but the maximum launch altitude was 600m-4000m, they were too dangerous to use and low efficiency.

Corresponding author's address: Wu yuzhong, Shaanxi Zhongtian Rocket Technology Co.,Ltd. ,Xi'an, Shaanxi,710025,China; E-mail: wyz421@yahoo.com.cn

2.3 Advanced new rocket

Since 1994, the WR-1B rocket came into use and extended widely in China. Through 10 years of application and development, the quality of the rocket progressed continuously and the operation method has been developed fully by the meteorological workers. WR-1A was developed according to the user's requirements.

Compared with the 37 gun shell, the WR rocket is more effective for the reasons below:

(1) The covering area is large, the effective range above 4km can be as far as 8km;

(2) The seeding agent used in the rocket is BR-91-Y pyrotechnics whose ice nucleating effectiveness is 10^{15} per gram silver iodide at temperature –7～-21℃, its nucleating rate is so quick that 90% of the silver iodide will be activated within 5min.

3 CHARACTERS OF THE WR ROCKET

3.1 Working process of the rocket

When the rocket is launched, the fire-delay mechanism within the rocket will activate the seeding unit at the preset time. The seeding material is then sprayed continuously along the rocket's trajectory, forming an arc of seeding area. Once the distribution is complete, the safety landing system of the rocket will open the parachute at the preset time to allow the rocket descend safely to the ground.

3.2 High performance pyrotechnics

The seeding agent used in the rocket is the BR-91-Y pyrotechnics developed by China's Meteorological Science Academy. Characteristics of the seeding agent are shown as below:

(1)The BR-91-Y seeding agent's ice nucleating effectiveness is high. It reaches as high as 10^{15}/g AgI at -8℃. That is 2 orders of magnitude higher than that of the TB-1 and 1 order of magnitude higher than the silver-spare agent's(Refer Fig1).Feng daxiong,(1995).

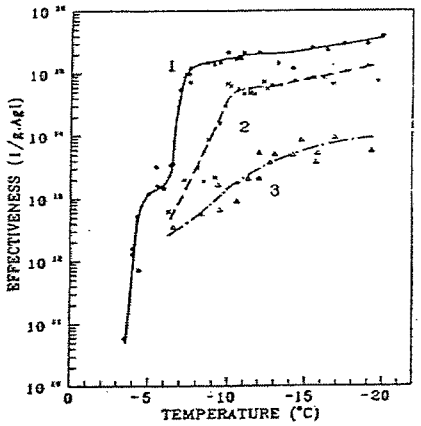

Fig. 1 Ice nucleating effectiveness of three pyrotechnics measured in $2m^3$ cloud chamber
1. BR-91-Y 2. Silverspare 3. TB-1

(2) The BR-91-Y's nucleating rate is so quick that 90% of the aerosol would be nucleated within 5 minutes after being absorbed into the cloud chamber. For other seeding agents only about 25% would have nucleated within this time period(Refer Fig2). Feng daxiong,(1995).

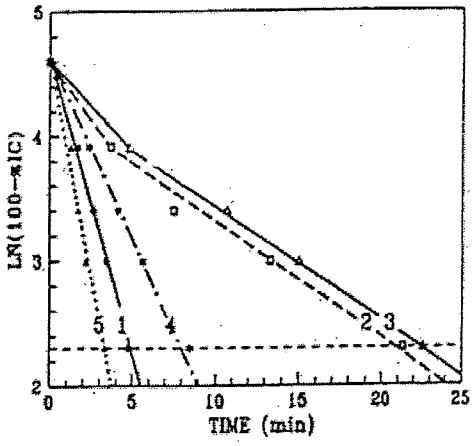

Fig. 2. The nucleating rate for three pyrotechnics
1. BR-91-Y 2. Silverspare 3. TB-1
4. BR-91-Y at temp. below -12℃
5. BR-91-Y at temp. above -12℃

3.3 High reliability and safety

The rocket is made by composite materials such as glass fiber, cloth and glues, no metal or explosive is in the rocket. The rocket remains lands at a speed lower than 8m/s with the aid of parachute, it avoids the threat and damage to the person, livestock and buildings. According to the static of 10 years using in the field, it's success rate is higher than 99.5%.

3.4 Various launchers

There are 3 types of launcher for each rocket model, the ground-base launcher, mobile launcher on a vehicle and ship. The user can choose according their requirement. In general, for hail-suppression the ground-base one is suitable, for rainfall-enhancement on land the mobile one on vehicle is good, but for rainfall-enhancement near the sea, the mobile launcher on a ship is the best choice. All these launchers are simple to operate and maintain.

3.5 Main parameters of the various model

Table-1 Main parameters of WR-1A rocket

Parameter		Index
Diameter	mm	Φ66
Length	mm	1250
Mass	kg	5.0
Launch altitude	km	6.5
Mass of pyrotechnics	g	400
Mass of AgI	g	20
Nucleating effectiveness of each gram of AgI		1.8×10^{15}

Table-2 Main parameters of WR-98 rocket

Parameter		Index
Diameter	mm	Φ82
Length	mm	1450
Mass	kg	8.2
Launch altitude	km	8.0
Mass of pyrotechnics	g	725
Mass of AgI	g	30
Nucleating effectiveness of each gram of AgI		1.8×10^{15}

4 APPLICATION IN CHINA

Till 2003, weather modification in China has reached the largest scale in the world. More than 300 million Yuan was expensed. The operation tools includes airplane, rocket and 37 gun. For ground base operation, the WR rocket is the main tools used.

In China, the Xinjiang autonomy region, Guangxi autonomy region, Hebei, Gansu, Shaanxi, Liaoning,Guangdong provinces are the biggest consumers of the rocket and have achieved great benefit in solving the water shortage and hail suppression.

Guangdong province suffered a steady draught and some region serious draught in 2002. The Guangdong government invested 6.7 million Yuan to purchase 30 launchers and 668 rockets in order to enhance precipitation. During the operation period, 486 rockets were launched and obtained a very good effect. According to the meteorological department's report, the total precipitation arrive at 9.66 billion cubic meters during the operation period, the increase amount reaches 28.98 billion cubic meters.

Hebei province adopted the WR rocket to enhance rainfall and suppress hail since 2000, till now 1.8 billion tons water was increased so the draught was released and the water reserves of reservoir was increased. Meanwhile, the hail-suppression during flood season have protect the 10 million acres field to be free from hail storm.

5 NEWEST TREND OF DEVELOPMENT

With the development of cloud physics and seeding agent, the ground-base tools are also being developed continuously.

5.1 Development of seeding agent

According to research by the Center of China Weather Modification, the nucleating effect of seeding agent relates to the flying speed of carrying vehicle, high AgI proportion is beneficial at high flying speed. So the new more effective seeding agent is under researching. Rate of AgI may be as high as 6～12%, it's more suitable for rocket seeding.

5.2 Seeding by ejecting flares

To compensate the loss of nucleating effectiveness due to high speed, seeding by ejecting flares is a good method. Because the drop speed is much lower than flying speed of the rocket, it's beneficial for nucleating. Together, the drop of many flares can form a volume of seeding area and penetrate the cloud perpendicularly. The new rocket under developing can carry 15 pyrotechnics flares and reach a altitude of 10km, each flare can drop in a perpendicular distance of 1km. It's more effective for hail-suppression.

5.3 Mobile short-range weather radar

The best effect of rainfall-increase should be obtained by precise radar observing and scientific operation method. To command the rocket launching real time, a mobile short-range weather radar TWR01 was developed to meet the requirement. Its main specifications was listed below:

⊙ Action range of radar

a. Alarm range ≥ 100km (displaying the target on PPI)
b. Operation rang≥50km (displaying the operation target on RHI)

⊙ Action scope of radar

a. Azimuth: ±180°
b. Elevation: 0° ～80°
c. Target: Thick cloud layer; Cumulonimbus; Hail cloud

⊙ Intensity identification: Color 16 grades (standard)

⊙ Azimuth error≤1° (RMS)

⊙ Range error≤60m(RMS)

⊙ Characteristic identification variety: All operation targets of WR series rockets

⊙ Characteristic identification method: Manual /Totally automatic

⊙ Radar image: Color display

⊙ Operation temperature: -30~50℃

6 PROSPECT

Weather modification is a science subject

not fully developed, but for China which is so short of water, it is of great significant. The China government pay more and more attention to weather modification in the recentt years. It is a great force to impulse the development of weather modification science and the tools equipped.

REFERENCE

Feng daxiong,1995: A High Efficient AgI Pyrotechnics and Its Ice Nucleating Properties, 6th WMO Scientific Conference on Weather Modification, 1995.

STATISTICAL EVALUATION FOR THE PRECIPITATION EFFECTIVENESS OF CLOUD SEEDING IN HENAN COUNTY OF CHINESE QINGHAI PROVINCE

Zhanyu Yao[1], Chenhai Xu[1], Hui Xiao[2], Lijun Wang[3], Anping Sun[3], and Jiangping Pu[4]

[1] Chinese Academy of Meteorological Sciences, Beijing 100081, P. R. China
[2] Institute of Atmospheric Physics, Chinese Academy of Science, Beijing 100029, P. R. China
[3] Qinghai Meteorological Bureau, Xining 810001, P. R. China
[4] Nanjing Institute of Meteorology, Nanjing 210044, P. R. China

1. INTRODUCTION

Cloud seeding techniques are often used to change microphysical structure of clouds and impel the transformation from cloud water to precipitation for the purpose to enhance or advance precipitation. The results of cloud seeding operation must be evaluated in order to know weather the amount of rain on the ground increased.

The effectiveness of precipitation enhancement after cloud seeding is not the real precipitation observed but the part increased or decreased apart from the original precipitation due to natural development of clouds without seeding. Therefore the local natural precipitation must be realized first in order to evaluate the precipitation effectiveness of cloud seeding.

In this study we estimate the effectiveness of precipitation enhancement in Henan county of Chinese Qinghai province based on the above thought. First the local natural precipitation without cloud seeding is simulated using suitable mathematic method. According to the real rain observed after cloud seeding and the natural precipitation simulated, the difference between them is confirmed to be the effectiveness of precipitation enhancement operation.

2. STUDY REGION AND DATA ANALYSIS

Cloud seeding operations have been carrying out at the upper part of Yellow River Basin in Qinghai Province since 1997 for the purpose of increasing the flow-off of upper part of Yellow River, and Henan County, our study region (34.73°N, 101.60°E), is one of the main bases of cloud seeding in Qinghai.

Corresponding author's address: Prof. & Dr. Zhanyu YAO, Chinese Academy of Meteorological Sciences, 46 ZhongGuanCun South Street, Beijing 100081, P. R. China; E-Mail: yaozy@cams.cma.gov.cn.

Yearly evaluations for the precipitation effectiveness of cloud seeding in Henan County have been made by means of statistical methods since 1997. The historical precipitation data for thirty years from normal weather stations as well as some other related data within a certain control area (31-38°N, 98-105°E) are used for natural precipitation simulation.

3. FITTING OF NATURAL PRECIPITATION IN HENAN COUNTY

The historical precipitation data for thirty years from normal weather stations as well as some other related data within the control area (31-38°N, 98-105°E) are interpolated into 0.5°×0.5° grid points. As factors, they are used to set up an experiential regression equation as below to calculate the natural precipitation and its variation in Henan County, the target area of our study (34.73°N, 101.60°E),

$$\hat{Y}_{(t)} = 226.14 + 0.69x_{1(t)} + 43.79x_{2(t)}, \quad (1)$$
$$-0.36x_{3(t)} - 71.54x_{4(t)} + 75.40x_{5(t)}$$

in which $\hat{Y}_{(t)}$ is the fitting natural precipitation and $X_{1(t)}$ – $X_{5(t)}$ are regression factors.

According to our experiential expression (1), the precipitation in target area is fitted quite well using these factors and data. Figure 1 offers an example of comparison between our fitted precipitation based on the experiential expression (1) and the real observation value from 1971 to 1997. The average deviation between our fitted precipitation and the real deviation of fitting for natural precipitation determines the accuracy of cloud seeding evaluation.

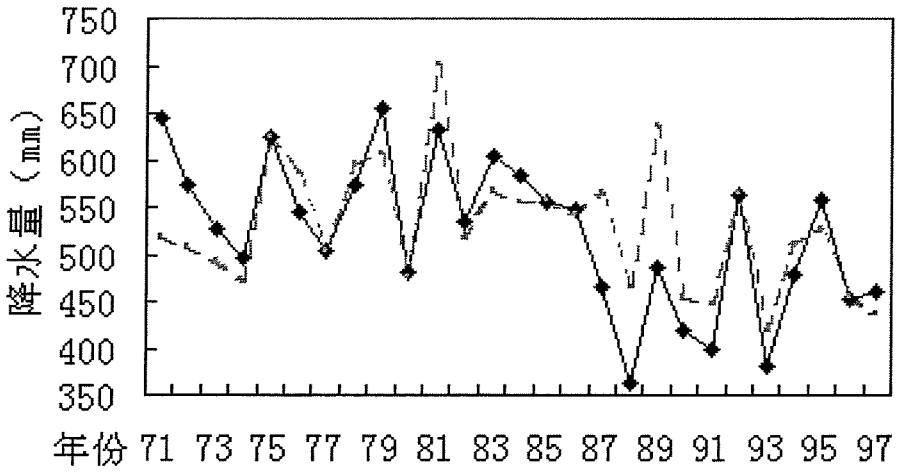

Fig. 1 Comparison of total precipitation amount from April to September between the fitted values (broken line) and the observation ones (real line) in Henan county from 1971 to 1997.

COUNTY

In the target area, the whole year's precipitation is mainly concentrated from April to September, therefore the operations of precipitation enhancement are basically performed during this period, and the characteristics and variations of total precipitation amount from April to September can represent the whole year's precipitation situation in this area.

Yearly evaluations for the effectiveness of precipitation enhancement operations in Henan County have been made by means of statistical methods. The yearly effectiveness of precipitation enhancement in Henan County in 1997 has been estimated as an example.

In 1997, the real observation value of total precipitation amount from April to September is 459.6 mm. Based on our experiential expression (1), the natural precipitation amount at the same period is fitted as 398.5mm. Because the

according to the comparison above, the reasonable estimation of natural precipitation amount should be 398.5×(1 ± ~ 411.7 mm, and the real observed precipitation is 47.9~74.3 mm more than the fitted natural one. Therefore the precipitation enhancement operations in Henan County brought about 47.9 ~ 74.3 mm (average 61.1 mm) more yearly precipitation on the basis of its natural precipitation in 1997, and the yearly effectiveness of precipitation enhancement in

~

according to our statistical evaluation.

Statistical methods are commonly used for effectiveness evaluation of precipitation enhancement operations. One of the key points is the fitting of natural precipitation, and the suitability of these kinds of evaluation methods relies on the accuracy of estimation of natural precipitation. The more precise for the fitting of natural precipitation, the more credible for the evaluation of effectiveness of precipitation enhancement.

The experiential method in this study for natural precipitation fitting is proved to be suitable in the area of Qinghai province and may be extended to the northwest part of China. It greatly supports the statistical evaluation of effectiveness of precipitation enhancement operations in these areas.

Program of Science and Technology of China (2001BA610A-06-05) and the National Natural Science Foundation of China (40375001).

COMPARISON BETWEEN SIMULATION OF TRANSPORT AND DIFFUSION OF SEEDING AGENT IN PRECIPITATION ENHANCEMENT BY AIRCRAFT WITH NOAA SATELLITE DATA

Xing Yu [1], Jin Dai [1], Peng Fan[2] and Zhengqi Chen[2]

[1]Meteorological Institute of Shaanxi Province, Xi'an, 710015, China
[2]Center of Weather Modification of Shaanxi Province, Xi'an, 710015, China

1. INTRODUCTION

Transport and diffusion of seeding material in the clouds is one of main concerns of precipitation enhancement. Bruintjes et al. (1999) pointed out that some critical problems remain in the precipitation enhancement, and one of fundamental impediments is the diffusion and transport of seeding material throughout the cloud. For the stratiform cloud, directly entered by an aircraft, it can be seeded. The capability of transport and diffusion of seeding material is more important.

The methodologies of transport and diffusion of seeding material in the clouds generally include gaseous tracer experiment (Holroyd et al., 1988, Warburton et al., 1995) and numerical simulation (Bruintjes et al., 1995, Levin et al., 1997). The model mostly used was Gaussian plume model.

However, there are some important factors affect transport and diffusion of the seeding material in the cloud such as synoptic condition, effects of topography, airflow, wind shear and thermodynamics and dynamics. Combining a three-dimensional fine-grid nonhydrostatic mesoscale model, Yu et al. (1998, 2000) formulated a three-dimensional numerical model of transport and diffusion of seeding material within stratiform cloud. Although case simulation and sensitive experiment were conducted, and relationship between concentration distribution and mass conservation was discussed, no measurement or indirect proof demonstrates the validity and reliability of the model.

In this study, we will try to use the evidence, the cloud trace revealed by the satellite data during the cloud seeding, to verify the model. In the next section, we introduce the model. In the section 3, the detailed cloud seeding operation is described and the features of NOAA satellite image are analyzed. In section 4, the simulating shape, scope, width, and line length of seeding line are compared with that of the cloud trace. A conclusion closes the study.

2. MODEL DESCRIPTION

The model consists of the puff trajectory model and a three dimensional nonhydrostatic mesoscale model.

Corresponding author's address: Ying Yu, Meteorological Institute of Shaanxi Province, No. 36 Beiguanzhengjie, Xi'an 710015, P. R. China, E-mail: yuxing23 @163.com

The puff trajectory model can deal with the tempo-spatial variation of source parameters with meteorological elements; it is a practical and effective method to represent the diffusion of pollutant source (Ludwig et al. 1977, 1989). So it is introduced to simulate diffusion of seeding material within stratiform cloud. The puff trajectory model describes the line sources with a series of discrete puffs moving along the seeding line. The puff is idealized as a large ellipsoid. In order to partly consider effect of vertical shear on diffusion, in vertical direction, each puff is divided equally into 7 smaller puffs (sub-puffs). The mass or concentration of 7 sub-puffs can be obtained by ellipsoidal integration.

The accuracy and efficiency of the puff trajectory model depend on the accuracy of flow and turbulence fields. So the nonhydrostatic mesoscale model is formulated. The nonhydrostatic governing equations of the mesoscale model are composed of prognostic equations of velocity component, potential temperature and vapor, turbulent kinetic energy, dissipation rate and anelastic continuity equation, following the coordinate transformation (Pileke and Martin 1981). The diffusive coefficients are obtained by turbulent kinetic energy and dissipation rate prognostic equations (Huang and Raman, 1989).

3. CLOUD SEEDING AND NOAA SATELLITE DATA

3.1 Cloud Seeding

On 14 March 2000, influenced by front system, the middle part of Shaanxi Province was dominated by altostratus (As) and altocumulus (Ac), there was spare rain on the surface. At 0615 UTC, a seeding operation of precipitation enhancement was carried out in this area and its western neighbor by Center of Weather Modification of Shaanxi Province. The operational aircraft was An-26 with an airborne silver iodide solution burner, and the average flight speed was 360kmh^{-1}. The seeding time was 94 minutes, and consumed AgI 1200 g. The seeding height was 4.35 km, where temperature was -10.0°C. The height of the cloud bottom was 2.2 km, where temperature was 2.0°C. The cloud top ranged from 4.5 to 5.0 km, where temperature was about -13.0°C.

3.2 NOAA Satellite Data

The tracer experiment or airborne probing only showed information at different limited time and spatial

points, could not displayed the full profile on a cross-section. However, the satellite image gives us manifest and complete panorama on the seeding cloud top at 0735 UTC. It is a pity that the magnitude of concentration at a given time and space can not be confirmed by the image. During the process of cloud seeding, fortunately, NOAA-14 satellite flew over this area. At 0735 UTC, the satellite image was received. Due to there no high cloud above the seeded cloud, there appeared a clear cloud trace on the satellite image (Fig. 1). The image was synthesized from visible, near infrared and infrared channels, respectively. Cloud top except for F' was even and flat, which implied the cloud was stratiform. The turning points A', B', C', D', E', G' on the cloud trace were distinguishable and clear, they were corresponding to the turning points A, B, C, D, E and G of cloud seeding. The cloud trace was approximately zigzag, whose middle was wider and two ends were narrower. The maximum width was 11 km (near C'), and its average was 8.3 km. F' point corresponding to the turning point F of cloud seeding could not distinguished (instead of E" and F" on the image), this may be that the cloud feature around F' was different obviously from the one at its northwest, which caused the microphysical effects not to be discerned on the satellite image, or not to be reflected at that time.

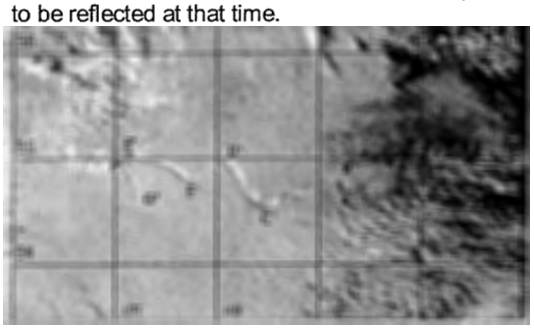

FIG. 1. Image of NOAA satellite data of seeded cloud

4. COMPARISON

4.1 Method Of Simulation

Because fine grid is needed to distinguish the features of transport and diffusion of the seeding material, considering the receiving time of NOAA data and scope of cloud trace, the simulation horizontal domain is 33.50°-35.70°N,106.83°-109.50°E (250 km×250 km). The horizontal and vertical grid intervals are 1 and 0.2 km. The time step is 20 s. Because the turning points on the image, relative to I and J points of cloud seeding, can not been seen on the satellite image, AB, BC, CD, DE, EF, FG and GH are chosen as 7 segments of seeding line. The operational time was 66 minutes, and consumed 880 g of AgI. Taking the nucleation rate as 5×10^{13} at temperature of -10°C, the line source strength is 1.11×10^{13} s^{-1}. One puff is introduced into the model every 20 s, and the total numbers of puff is 198.

After the position of every sub-puff is determined in simulated domain, temporal concentration in a grid point can be calculated by superposing the sub-puff concentration.

Based on the meteorologically measured surface and sounding data at 0000 UTC, the predicted results of the mesoscale model were output every hour. Fields of wind and turbulence were input to the puff trajectory model to calculate the concentration distribution and variation of seeding material.

4.2 Comparison Results

Due to different levels of seeding material contributing to the cloud trace, it is reasonable to use the concentration projected on the surface in the comparison. Actually, the concentration projected on the surface is the maximum concentration in the vertical direction.

Figure 2 displays the seeding material concentration projected on the surface, at the seeding altitude 4.35, 4.55 and 4.75 km at 0735UTC. The positions of the concentration distribution are consistent in horizontal cross section, but their scopes for a given concentration are different. The scope of a given concentration projected on the surface is maximum, and next in 4.35 km, the third in 4.55 km, and the last in 4.75 km. It is rather wider at the seeding altitude and becomes narrower on the levels of 4.55 and 4.75 km. The concentration distribution and magnitude for each segment of seeding line are various, the scope and positions of a given concentration projected on the surface is equivalent to that on seeding altitude.

Compared the cloud trace with seeding line, the scope and position of concentration projected on the surface coincides better with that of the cloud trace, the turning points of seeding line entering the cloud generally accord with that of the cloud trace, but decline southwards in the south-north direction. The main reason may be that the wind direction at 0000 UTC was just W on 500 hPa, the modeling u component is good and the v is smaller in the mesoscale model. The concentration axial line of cloud seeding line BC, DE and EF are parallel to that of cloud trace B'C', D'E' and E'E", respectively, the distances between axial lines BC and B'C', DE and D'E', EF and E'E" are 13.0, 6.5 and 11.4 km. The concentration axial line of CD is cross with that of C'D', and FG is almost coincides with F"G'. The transporting and diffusing positions of seeding material agree with the positions of the cloud trace, each segment of seeding line is corresponded with the each segment of the cloud trace, which suggested that the cloud trace is caused by cloud seeding, and the model has a good simulation of the line source of seeding materials, and the mesoscale model can rather correctly simulates the dynamical fields.

The shapes and the widths of concentration greater than $10L^{-1}$ or less than $1L^{-1}$ are greatly different from that of the cloud trace, the maximum widths corresponding to concentrations 1, 4, 5 L^{-1} are 18.3 km (near the point B), 11.4 km (near the point C), and 10.6 km (near the point C), their average widths are 12.9, 8.6, and 7.9 km. The widths and the shapes of

concentration 4 and $5L^{-1}$ are similar to that of the cloud trace, and the ones of concentration $4L^{-1}$ is more similar.

The concentration $4L^{-1}$ (the shadow in the Fig. 2) is wide at the middle and narrow at the ends. It agrees well with the width variation of the cloud trace, the concentration widths of seeding line AB, FG, GH are rather narrow, and ones of BC, CD, DE are rather wide. Correspondingly, the fore parts A'B', B'C' and whole F"G' of the cloud trace are narrow, the rear parts of B'C', and whole C'D' E'E" are wide.

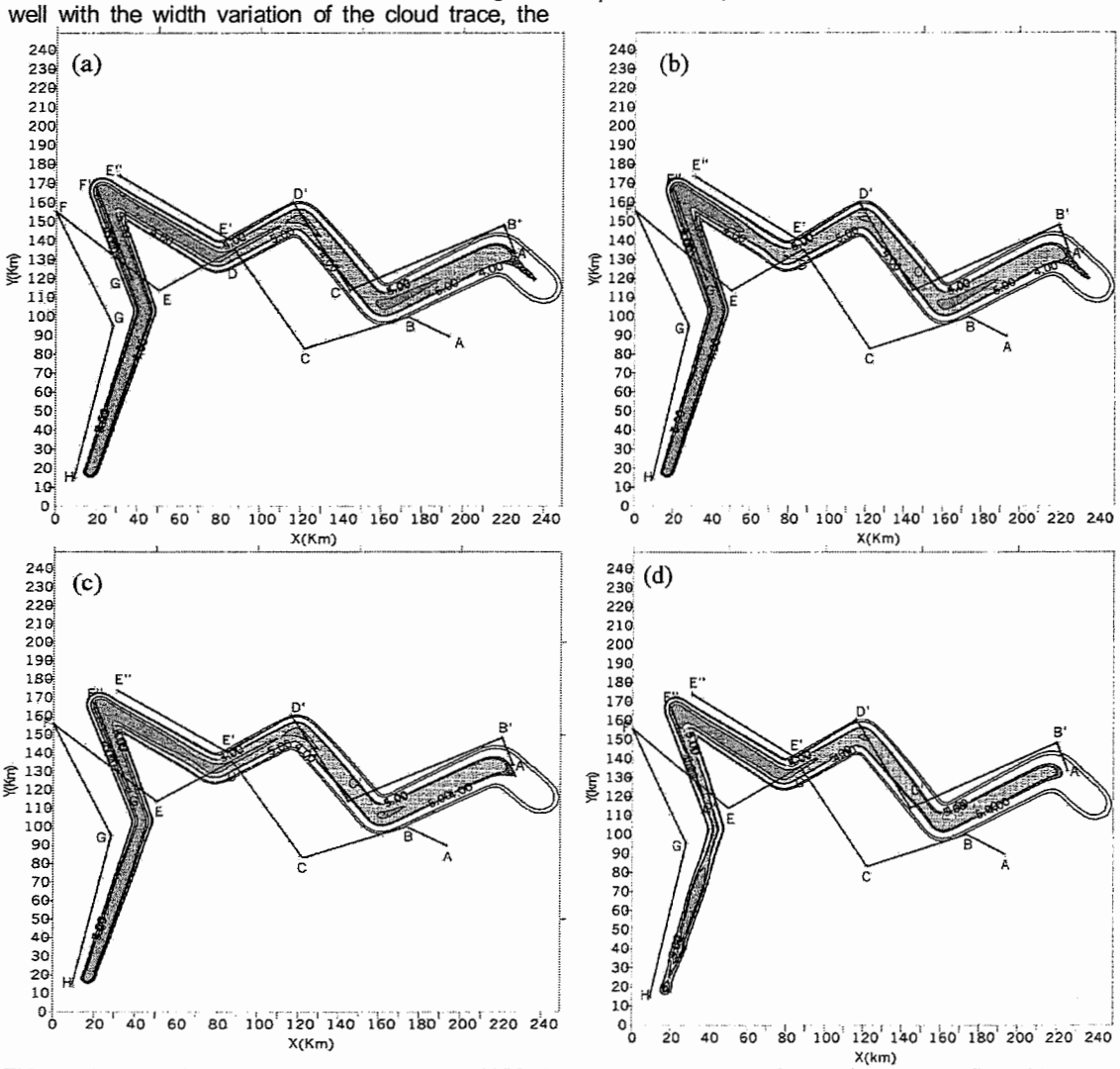

FIG. 2. Simulated concentration shape at 0735UTC: (a) projected on the surface, (b) at the seeding altitude 4.35 km, (c) at 4.55 km, and at 4.75 km. ABCDEFGH is seeding line, A'B'C'D'E'E"F"G' is axial line of the cloud trace. The intervals of concentration contour are 0.5, 1, 4, 5, 10 100, 500 L^{-1}.

TABLE 1. Lengths of the actual seeding line, of the cloud trace and of the modeling line

Seeding line	AB	BC	CD	DE	EF	FG	GH	total
Actual line length(km)	22.8	48.8	62.4	41.1	67.2	67.0	81.7	391.0
Seeding time(min)	4	14	9	6	11	9	13	66
NOAA line length (km)	14.7	83.3	55.5	36.7	61.2	49.8		301.2
Modeling line length (km)	22.0	65.3	60.4	44.1	63.7	63.7	93.1	412.3

Table 1 displays the lengths of the actual seeding line, of the cloud trace and of the modeling line for concentration $4L^{-1}$.The actual line length is calculated by flight distance between two points, and the seeding time is the flight time between them., the lengths of seeding line segments CD, DE and EF are close to the length of the actual line and of the cloud trace. The modeling line lengths of CD and EF are shorter than the actual seeding line, but DE is longer, three all together are shorter than by 2.5 km (1.5 per cent). How-

ever, they are longer than the cloud trace, and three all together are longer than by 14.8 km (8.4 per cent). The length of the cloud trace is shorter by 17.3 km (10.1 per cent) than the actual seeding line.

However, the modeling line length of AB, BC and FG are different greatly from the ones of the actual line and of the cloud trace. The modeling length of AB is 22.0 km. The length of the cloud trace A'B' is 14.7 km, shorter by 8.1 km (35.5 per cent) than its actual length. One of the reasons may be that physical effect acted on the cloud top caused by AB seeding line is decreasing.

The length of the cloud trace and the modeling length corresponding to the seeding line BC are longer by 34.5 km (70.7 per cent) and 16.5 km (33.8 per cent) than its actual length. Because there was no measurement of Globe Position System (GPS), the seeding parameter was based on the record of the flight. The recorded time of BC line was 14 minutes, the flight speed was 400 kmh^{-1}, but the actual length was only 48.8 km (should be 93.3 km), so there existed a great difference and had an uncertainty among them. Due to lack the factor enlarging the seeding line, the actual length of seeding line might reach to 80 km. The possible fact was that the aircraft flew westwards 30 km after arriving the point C. The simulation describes the seeding process according to the record and not to the baseless correction.

There exists a broken part on the cloud image corresponding to the turning point F (see Fig. 1), which leads to a great length difference 17.2 km (25.7 per cent) between cloud trace F"G' and the actual seeding line FG. However, the modeling FG length is only shorter by 3.3 km (4.9 per cent) than its actual length.

Comparisons between the simulating results and the cloud trace show that the position, shape, width and length of seeding material concentration are rather agreed with that of the cloud trace. The cloud trace is caused by the cloud seeding, is physical effect reflected on the cloud top. The model can reveal the main characteristics of transport and diffusion of seeding material.

5. COCLUSION

The transport and diffusion of every segment of seeding line is well corresponding to every segment of the cloud trace. The distributions of concentration, the turning points of seeding line entering the cloud, the movements of seeding material, the diffusive width all reveal that the cloud trace is resulted from the cloud seeding and physical respond of cloud on the cloud top. The feature comparisons between the simulating spatial and temporal distributions of concentrations and the cloud trace suggest that the three-dimensional model can simulate the transporting and diffusive characteristics of seeding material, and the model is reasonable and reliable.

It is noted that the particle of seeding material is assumed to be inert in the model. This should be paid attention, and it is what we will improve in the future. Also, two points must be noted. First, the cloud trace is the reflection of cloud top, but not of obvious effect of cloud seeding within the cloud. Second, the satellite resolution determines the size of the cloud trace.

Acknowledgments

We would first like to thank all those who participated in the preparation and filed phases of cloud seeding operation. The satellite data were supplied by Agricultural Remote Sensing Information Center of Xianyang City, Meteorological Bureau of Xianyang City. This work was supported by Chinese ministry of science and technology Grant 2001BA901A41.

References

Bruintjes, R. T., G. L. Kok, D. W. Breed and V. Salazar, 1999: Hygroscopic seeding: theory and practice. Seventh WMO scientific conference on weather modification. WMO/TD-No. 936, 65-68.

Bruintjes, R. T., T. L. Clark and W. D. Hall, 1995: The dispersion of tracer plumes in mountainous regions in central Arizona: comparisons between observations and modeling results. *J. Appl. Meteor.*, **34**, 971~988.

Holroyd E. W., J. T. McPartland and A. B. Super, 1988: Observations of silver iodide plumes over the Grand Mesa of Colorado. *J. Appl. Meteor.*, **27**, 1125-1144.

Huang, C. Y., and S. Raman, 1989: Application of the E-ε closure model to simulations of mesoscale topographic effects. *Boundary-Layer Meteor.*, **49**, 169-195.

Levin, Z., S. O. Krichak, and T. Reisin, 1997: Numerical simulation of disposal of inert seeding material in Israel using a three-dimensional mesoscale model. *J. Appl. Meteor.*, **36**, 474-484.

Ludwig F. L., L. S. Gasiorek and R. E. Ruff, 1977: Simplification of a Gaussian puff model for real-time minicomputer use. *Atmos. Environ.*, **11**, 431-436

Ludwig F. L., R. Salvador and R. Bornstein, 1989: An adaptive volume plume model. *Atmos. Environ.*, **23**, 127-138

Pielke, R. A., and C. L. Martin, 1981: The derivation of a terrain-following coordinate system for use in a hydrostatic model. J. Atmos. Sci., **38**, 1707-1713.

Warburton J. A, R. H. Stone and B. L. Marler, 1995: How the transport and dispersion of AgI aerosols may affect detectability of seeding effects by statistical methods. *J. Appl. Meteor.*, **34** 1929-1947.

Yu Xing, Fan Peng, Wang Xiaoling, Dai Jin, and Li Zhaoyuan, 1998: Numerical simulation of multiple line source diffusion of seeding agent within stratus. *Acta Meteorologica Sinica*, **56**, 190-197.

Yu Xing, Dai Jin, Jiang Weimei and Fan Peng, 2000: A three-dimensional model of transport and diffusion of seeding material within stratus. *Advances in Atmospheric Sciences*, **4**, 617-635.

THE RESEARCH OF SEEDING AGENT DIFFUSION TRAIL

Zhang Jinghong Gu Shufang Chen Zhixin Wang Xiaomei

JiLin Weather Modification Office, ChangChun, 130062, China

1. INTRODUCTION

With the further development of large-scale weather modification experiments in our country and abroad, the effects of them come to attract more and more attention. In our country's weather modification field, more and more scientific achievements have been applied into practice. At present, the numerical simulator system of our country's weather modification technology still lacks a mode of seeding agent's operational distribution trail, and there are few people doing research in this respect. However, the results of this study are of inestimable significance in the course of artificial rain enhancement.

2. MODE STRUCTURE

The Mode assumes that the rain enhancement airplane operates in steady sheet cloud, the atmosphere in the sheet cloud is isotropic, and the flow in the cloud is stationary, even, and flat. Not considering the vertical wind shear, i.e., the vertical (X-Z phase or Y-Z phase) diffusion also overlooked presently, if the rain enhancement airplane spreads seeding agents in a direction vertical (line source direction) to the wind direction in the upper air spreading level, then, the seeding agents will be diffused along the principal wind direction (X-Y phase). Taking X axis as the average wind direction, and Y axis as the airplane's operation direction, we put the origin of the coordinates at the place where the airplane starts to work. Here the transmission and diffusion range of the seeding agents are in the same direction with the principle wind direction, thus, the seeding agents' horizontal diffusion will reach the farthest distance. By level transmission distance, we can roughly determine the rainfall range of the rain enhancement.

According to the gradient transmission theory in free air, the diffusion equation is as follows:

$$\frac{dq}{dt} = \frac{\partial}{\partial x}(kx\frac{\partial q}{\partial x}) + \frac{\partial}{\partial y}(ky\frac{\partial q}{\partial y}) + \frac{\partial}{\partial}(kz\frac{\partial q}{\partial z}) \qquad \text{-------(1)}$$

that is

$$\frac{\partial q}{\partial t} + u\frac{\partial q}{\partial x} + v\frac{\partial q}{\partial y} + w\frac{\partial q}{\partial z} = kx\frac{\partial^2 q}{\partial^2 x} + ky\frac{\partial^2 q}{\partial^2 y} + kz\frac{\partial^2 q}{\partial^2 z} \qquad \text{------(2)}$$

In the above equation, "q" represents the density of diffused material, number/L;

"u", "v" and "w" respectively represents the wind speed on X, Y and Z axis, km/h;

"k_x", "k_y" and "k_z" respectively represents the turbulence coefficient on X, Y and Z axis, making $k_x = k_x = k_x = k$ (isotropic), m^2/s;

"t" represents time, min;

"w" represents the descending speed caused by the mass of the seeding agents themselves, m/s.

Considering the possible fusion of seeding agent particles and their interaction with the cloud droplets, the above equation can be rewritten as:

$$\frac{\partial q}{\partial t} + u\frac{\partial q}{\partial x} + v\frac{\partial q}{\partial y} + w\frac{\partial q}{\partial z} = kx\frac{\partial^2 q}{\partial^2 x} + ky\frac{\partial^2 q}{\partial^2 y} + kz\frac{\partial^2 q}{\partial^2 z} - aNcq - \frac{1}{2}Bq^2 \qquad \text{-------(3)}$$

In the above equation, "N_c" is the density of cloud droplet, number/cm^2;

"a" is the cloud droplets' capture coefficient;

"B" is the fusing coefficient of different seeding agent particles. According to document[1], the fusion of seeding agent particles can be ignored here.

In addition, the "v" and "w" are generally at the level of several cm/sec in sheet clouds, also can be ignored, therefore, we get the equation that:

$$\frac{\partial q}{\partial t} + u\frac{\partial q}{\partial x} + v\frac{\partial q}{\partial y} + (w - w')\frac{\partial q}{\partial z} = \frac{\partial}{\partial x}\left(k_x\frac{\partial q}{\partial x}\right) + \frac{\partial}{\partial y}\left(k_y\frac{\partial q}{\partial y}\right) + \frac{\partial}{\partial z}\left(k_z\frac{\partial q}{\partial z}\right) - aNcq - \frac{1}{2}\beta q^2 \qquad \text{------(4)}$$

Taking incipient boundary conditions into account:

When t=0,q=Qõ (x) õ (y) õ (z-H)

When z=0,q=0

When $\sqrt{x^2 + y^2 + z^2} \to \infty$, q=0

------(5)

In the equation, Q is the production rate of unit point source core.

Hence we get the equation for unit point source density diffusion as follows:

$$q = \frac{Q}{8\sqrt{(\pi kt)^3}}\exp\left[-\frac{w^2 t}{4k} - \frac{w(z-H)}{2k} - \frac{w(x-ut)^2}{4kt} - \frac{y^2}{4kt}\right] \times\left\{\exp\left[-\frac{(z-H)^2}{4kt}\right] - \exp\left[-\frac{(z+H)^2}{4kt}\right]\right\}\exp(-aNct) \qquad \text{------(6)}$$

Corresponding author's address: No.653, HePing Street, ChangChun City, JiLin Province,130062,China; E-Mail: zhangjh8070@sina.com.cn

As line source is the accumulation of the density of point sources along the spreading line, we get the equation for line source diffusion in sheet clouds:

$$q=\frac{Q_L}{4\pi kt}\exp\left[-\frac{w^2t}{4k}-\frac{w(z-H)}{2k}-\frac{(x-ut)^2}{4kt}\right]$$
$$\times\left\{\exp\left[-\frac{(z-H)^2}{4kt}\right]-\exp\left[-\frac{(z+H)^2}{4kt}\right]\right\}\exp(-aNct)$$
------(7)

In the above equation, Q represents the production rate of unit line source core, number/m.

3. CASE ANALYSIS

3.1 Combining our 2001 spring rain enhancement operation, we choose 4 flying cases to make analog calculations of AgI transmission trail.

(1) In the first flying operation of May 10, 2001, the operation temperature T= -5.2℃, wind speed u=11km/h, operation height H=3000m, AgI amount=500g, cloud seeding time=90min. Now the line source production rate is 6.67×10^8/m. See the analog results in Form1, unit=number/L.

(2) In the first flying operation of May 24, 2001, the operation temperature T= -3℃, wind speed u=100km/h, operation height H=4200m, AgI amount=500g, cloud seeding time=90min. Now the line source production rate is 6.67×10^8/m. See the analog results in Form1, unit=number/L.

(3) In the first flying operation of May 15, 2001, the operation temperature T= -9℃, wind speed u=21km/h, operation height H=3500m, AgI amount=500g. Now the line source production rate is 6.67×10^9/m. See the analog results in Form1, unit=number/L.

(4)At May 8, 2001, the operation temperature T= -13℃, wind speed u=28km/h, operation height H=5000m, AgI amount=500g, cloud seeding time=90min. Now the line source production rate is 4.44×10^{11}/m. See the analog results in Form1, unit=number/L.

form1 Seeding Agent Transmission Distribution Table

Operation Time (Year 2001)	May 10	May 24	May 15	May 8
Operation Temperature (℃)	−5.2	−3	−9	−13
Operation Wind Speed (km/h)	11	100	21	28
Operation Height (m)	3000	4200	3500	5000
AgI Amount (kg)	0.5	0.5	0.5	0.5
Cloud Seeding Time (min)	90	90	90	90
Diffusion Time (min)	17	17	90	180
Maximum Diffusion Distance (km)	3	28	35	90

3.2 Calculation Result

According to [1][2], we treat Nc、a and k as constants. From the Form we know that:

(1) When operation temperature is higher than –7℃, and the wind speed is comparatively slow, the horizontal diffusion distance of seeding agent is comparatively short, and its transmission time on X-Y phase after seeding operation is short.

(2) When operation temperature is higher than –7℃, and the wind speed is comparatively fast, the horizontal diffusion distance of seeding agent is also comparatively short (but longer than the above-mentioned case); the maintenance time after seeding operation is also comparatively short.

In the above two circumstances, the airplane's zigzag seeding operation should choose a shorter distance between each turning. For instance, in the operation of May 10, 2001, after 6 min.'s cloud seeding, the number of ice cores formed by AgI in the cloud has added to less than 5/L.

(3) When operation temperature is lower than -8℃, and the wind speed is lower, the horizontal diffusion distance of seeding agent is comparatively long, and the maintenance time after seeding operation is comparatively long.

(4) When operation wind speed is rather high, and the temperature is comparatively low (lower than –8℃), the horizontal diffusion range in the same direction of the wind becomes quite large, and the operation time effect is very long. Such as, in the operation of May 5, 2001, (see Form 1), we should choose a wider distance between each zigzag of the airplane in the course of cloud seeding.

Moreover, in the circumstances that the wind speed and other conditions keep the same, the larger is the turbulence coefficient k, the quicker the seeding agent fades, and the horizontal diffusion range in the same direction of the wind will become smaller. We'll not cite examples to expound this point.

Here the cloud seeding line in our analog is in accordance with our real flying operation line. Therefore, to consider the trail of seeding agent's diffusion is to grasp the method of controlling the distance of cloud seeding. It is helpful to increase the effect of rain enhancement, to bring the effect of seeding agent into full play in potential rainfall area, avoid waste of fund or repetitive operation in the same region, so as to provide guidance to artificial rain enhancement more scientifically and effectively, and to make greater contribution to the cause of draught resisting and striving for good harvest.

References:

Shen Yiming: The Diffusion of Seeding Agent in Cloud, Meteorological Press, 1994.

Huang Meiyuan, Xu Huaying: Cloud and Precipitation Physics, Scientific Press, 2001.

Sang Jianguo, Wen Shigeng: The Numeric Calculation of Atmosphere Diffusion, Meteorological Press, 1992.

Zhou Xiuji and others: Advanced Atmospheric Physics, Meteorological Press

American Society of Civil Engineer: Advanced Atmospheric Physics, translated by Mu Haixing, Zhong Zhiwu, "National Coordinating Conference of Weather Modification" Office, China Meteorological Administration Bureau Science Education Section, 1997.

AN EXPERIMENTAL STUDY OF THE EFFECTS OF EXPLOSION ON A CONVECTIVE ECHO

Hesheng Zhou[1], Qing Luo[1], Huanbin Xu[1], Jianxin Li[2], Can Xu[3], Gang Liu[4]
Liyun Yin[2], Wei Wei[3], Libing Liu[3], Qing Wang[3], and Shuguang Meng[2]

[1]Institute of Plateau Meteorology, CMA, Chengdu, Sichuan, 610071, P. R. China
[2]Weather Modification Centre of Yunnan, Kunming, Yunnan, 650034, P. R. China
[3]Chengdu Weather Modification Headquarters, Chengdu, Sichuan, 610071, P. R. China
[4]Yuxi Weather Modification Headquarters, Yuxi, Yunnan, 653100, P. R. China

1. INTRODUCTION

Explosions produce gas, splashing shrapnel, blasts, sound vibration, strong disturbance airflow, and gravity waves. Many studies have examined the effects of those products of explosions on the cloud-precipitation microphysical and dynamic processes. Vittori (1960) suggests that the cavum in water drops caused by explosions can generate soft hail. Goyer (1965) finds that thunders can freeze supercooled water droplets. His experiments also show that explosions can break water drops. Huang et al. (1979) finds that 0.2 to 0.3 seconds after an explosion the flue starts to swing and its ascending speed decreases, but the flue reverts to normal after one second. Xu et al. argue that (1) the mechanical effect of a blast on an airflow can restrain updraft whose speed is up to 3 m/s (Xu, 1979); (2) the lubricating effect of sound vibration accelerates the descending speed of precipitation particles (Xu et al., 1984); (3) the effects of gas and splashing shrapnel generated by explosions on the development of clouds are negligible (Xu et al., 1989); (4) the strong disturbance airflow caused by explosions and the break-down of gravity waves can significantly affect the mean airflow of clouds (Xu, 2001). In a field study, Zhou (1999) finds that precipitation is observed after shooting strong convective clouds with shells that do not contain silver iodide. He hypothesizes that this is because the disturbance caused by the explosions in the clouds breaks the equilibrium between precipitation particles and updraft in clouds, and hence causes the precipitation particles to precipitate. Extending prior research, this paper examines the effects of explosions on a convective echo using data collected from field experiments and numerical simulation of the effect of an explosion on an airflow field.

2. FILED EXPERIMENTS

To study the effects of explosions on a convective echo, we shoot strong convective clouds using 37-mm anti-aircraft guns and observe the variations of convective echoes using radar. We compare the echoes before and after the experiments. We also compare the echoes of the clouds we operate with those we do not.

Corresponding author's address: Hesheng Zhou, Institute of Plateau Meteorology, CMA, Chengdu, Sichuan, 610071, P. R. China; E-Mail: zhouhs@mail.sc.cninfo.net

2.1 Time periods and locations of the experiments

Our field experiments were conducted in two areas: Chengdu, Sichuan province and Yuxi, Yunnan province. We started our experiments in Longquanyi district (104°10'E-104°24'E, 30°29'N-30°43'N) and Pengzhou city (103°56'E-104°08'E, 30°55'N-31°07'N) of Chengdu in the summer of 2001. We had conducted experiments in this area for three years till 2003. From 2002 to 2003, we had conducted experiments in Jiangchuan county (102°37'E-102°52'E, 24°15'N-24°24'N), Huaning county (102°54'E-102°58'E, 24°12'N-24°16'N) and Yimen county (102°09'E-102°13'E, 24°37'N-24°41'N) of Yuxi.

2.2 Experiment Design

Experiment equipment: We used 37-mm anti-aircraft guns, the effective height of shooting of which is about 4000 meters, and two types of shells, one with silver iodide and the other without.

Observatory equipment: In Chengdu area, we used an X-band digital radar (known as XDR). The revolving speed of its antenna is about 4 rounds per minute. It takes approximate 4 minutes to complete a three-dimensional scan with 17 elevations. In Yuxi area, we used a C-band Doppler radar (known as CINRAD-CC). The revolving speed of its antenna is about 3 rounds per minute. It takes approximate 5 minutes to complete a three-dimensional scan with 14 elevations.

Experiment conditions: The maximum echo intensity should be at least 30 dbz, and the height of the echoes should be at least 4 kilometers above the height of the radar.

When an echo met the experiment conditions in the experiment areas and within the shooting range of the anti-aircraft guns, we immediately sought approval from the air traffic regulatory agency to conduct experiments. We randomly chose the types of shells to be used. We were constantly performing three-dimensional scans using radar till the echo did not meet the experiment conditions. We name the convective echoes under the influence of explosions "experiment echoes" and similar echoes that are not under the influence of explosions "control echoes". We study the effects of explosions on a convective echo by analyzing variations of the evolution of convective echoes between "experiment echoes" and "control echoes".

2.3 Doppler radar imaging

When an isolated convective echo is in an area without obvious convergence of radial velocity, no matter the shell contains iodide or not, we find that the explosions causes the area of the echo to diminish, split, or even disappear. For instances, at 14:08 PM on August 15, 2002 (Beijing time) we observed a strong convective echo to the Southwest of Jiangchuan county. The area of the convective echo whose intensity was no less than 20 dbz was 13 square kilometers. The echo was moving towards the radar station. The echo's central radial velocity was -2.6m/s, and it had no obvious convergence of radial velocity (Color figures omitted). At 14:19 PM, we shot 10 shells that did not contain silver iodide at the convective echo. At 14:21 PM, the PPI scope showed that the experiment echo disappeared while control echoes in nearby area continued to develop (Color figures omitted). However, when a similar convective echo is in an area with obvious convergence of radial velocity, the explosions have insignificant effect on the change of the area of the echo.

2.4 Statistical analysis of the results of the experiments

The results of the statistical analysis of the experiment data are reported below. We perform statistical analysis only on the experiment data collected from Chengdu because the sample collected from Yuxi is too small. Besides, the two types of radar used in the two areas have different parameters, which makes the comparison of data collected from the two areas difficult. The statistic we examine is the rate of change of the areas of CAPPI echoes. Our sample meets the following criteria: first, the intensity of the echo is no less than 20 dbz; second, the height of the echo is at least 4 kilometers above the height of the radar; third, the area of the echo is no larger than 100 square kilometers; fourth, the time lag between two consecutive observations is no more than 15 minutes. Since our sample is relatively small and we focus on the effect of explosions, rather than silver iodide, on convective echoes, we do not separately analyze the effects of explosions with or without silver iodide.

Variable ECHO in table 1 is defined as the rate of change of the areas of CAPPI echoes. GROUP 1 refers to the control echoes and GROUP 2 refers to the experiment echoes. We use the Mann-Whitney U test to test the difference between the two groups. Table 1 and 2 summarize statistical test results.

Table 1 Ranks

	GROUP	N	Mean Rank	Sum of Ranks
ECHO	1	130	77.29	10048.00
	2	17	48.82	830.00
	Total	147		

Table 2 Test Statistics

	ECHO
Mann-Whitney U	677.000
Wilcoxon W	830.000
Z	-2.592
Asymp. Sig. (2-tailed)	.010

Our experiment echo GROUP has 17 observations and our control GROUP has 130 observations. The Mann-Whitney U is 677.000, and is asymptotically significant at 0.01 level. Therefore, our statistical analysis confirms our visual observations that explosions significantly reduce the area of an echo whose intensity is no less than 20 dbz.

3. NUMERICAL SIMULATION OF THE EFFECT OF EXPLOSION ON THE AIRFLOW FIELD

We use a three-dimensional cloud scale model (Xu et al., 1990) to simulate the effect of an explosion on an airflow field. The intensity of the perturbation center caused by explosions is $5\times5m^2/s^2$, the perturbation radius is about 150 meters, and the perturbation lasting time is 60 seconds (Xu, 2001). The grid length in the model is 20 meters. For simplicity, we assign 50 grid points horizontally and vertically. The area of the simulation is thus 1000m×1000m×1000m. Since the area of the simulation is relatively small, the results of the simulation should be interpreted with cautions. The shell explodes in the center of the simulated area. The time step for computations is 0.5 second. An explosion is simulated sixty seconds after the simulation starts, and the lasting time of the disturbance caused by the explosion is 60 seconds. The simulation results are reported in the figures below. The figures on the left show the airflow field at the horizontal section of 400 meters height, and the figures on the right show the airflow field at the vertical section of 500 meters from the origin along the y-axis. Figure 1 shows the airflow field sixty seconds after simulation starts, namely,

immediately before the explosion. Figure 2 shows the airflow field 120 seconds after simulation starts when there is no explosion. Figure 3 shows the airflow field 120 seconds after simulation starts when there is an explosion. The figures show that, after explosion, (1) horizontally, there is an abruption in formerly single divergence airflow, and (2) vertically, the updraft is twisted and moving to the top and right. Those changes could break the continuous evolution of the echo, prevent the natural precipitation process from developing, and lead to the decay of the clouds.

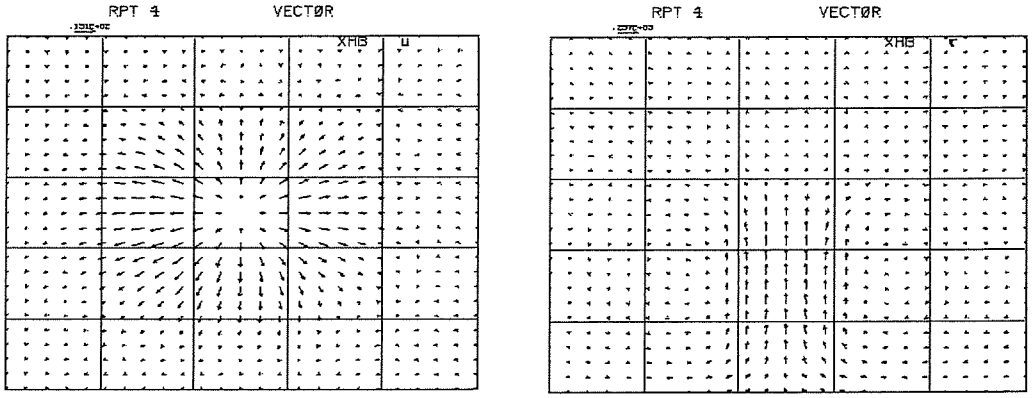

Figure 1. The airflow field 60 seconds after simulation starts, namely, immediately before the explosion.

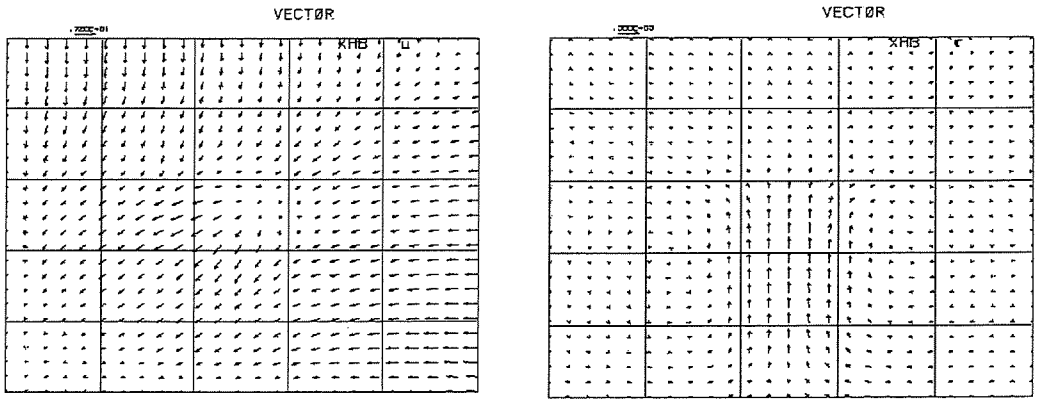

Figure 2. The airflow field 120 seconds after simulation starts when there is no explosion.

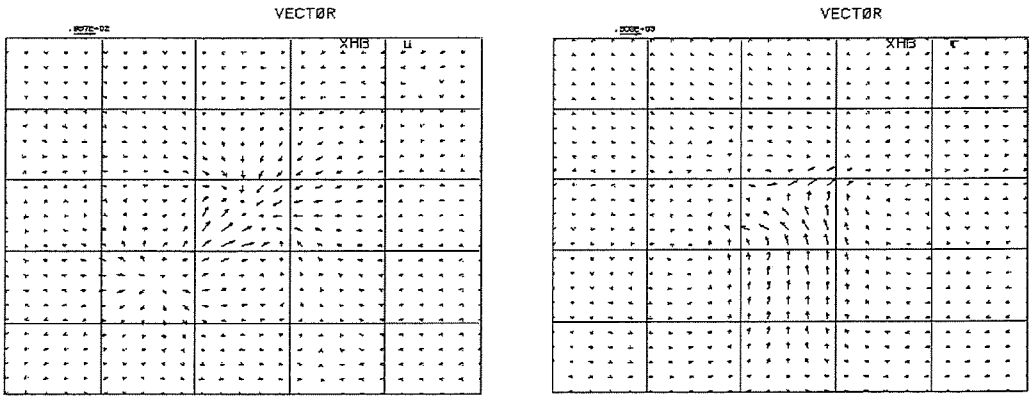

Figure 3. The airflow field 120 seconds after simulation starts when there is an explosion.

4. CONCLUSIONS

1) When an isolated convective echo whose intensity is no less than 20 dbz is in an area without obvious convergence of radial velocity, no matter the shell contains iodide or not, we find that explosions cause the area of the echo to diminish, split, or even disappear.

2) When an isolated convective echo whose intensity is no less than 20 dbz is in an area with obvious convergence of radial velocity, the explosions have insignificant effect on the change of the area of the echo.

3) Mann-Whitney U test result suggests that the rate of change of the areas of CAPPI echoes whose intensity is no less than 20 dbz is statistically different between echoes that are under the influence of explosions and those that are not. The difference between the two groups is statistically significant at 0.01 level.

4) Simulation results show that explosions have significant effects on the evolution process of the airflow field in a convective cloud. Specifically, explosions break horizontal airflow and twist the vertical airflow of the clouds. The maximum updraft's horizontal position shifts to the side and its vertical position moves upward.

5. ACKNOWLEDGEMENTS

The authors thank the financial support from the Ministry of Science and Technology of P. R. China. We are also grateful for the help from Weather Modification Centre of Yunnan Province, Chengdu Weather Modification Headquarters, and Yuxi Weather Modification Headquarters. Kunming Doppler radar station and Chengdu radar station provide many original data. Without their help, this research cannot be completed. We therefore devote our sincere appreciation to them.

6. REFERENCES

Goyer, G. G., 1965: Effects of lightning on hydrometeors, Nature, 206(19): 1203-1209.

Goyer, G. G., 1965: Mechanical effects of a simulated lightning discharge on the water droplets of 'Old Faithful' Geyser, Nature, 206 (26): 1302-1304.

Huang, Meiyuan et al. 1979: Studies of influence on development of convective clouds by explosion, Sci. Atmos. Sinica, 3 (3): 280-288 (in Chinese).

Vittori, O., 1960: Preliminary note on the effects of pressure wave upon hailstorms, Nubila, No. 1, 34-52.

Xu, Huanbin, 1979: Fundamentals of mechanics on the effects of explosion on the airflow, Meteorological Monthly, 5 (10): 26-29 (in Chinese).

Xu, Huanbin and Siwei Wang, 1984: On the influence of acoustic vibration on the regime of air motion in the boundary layer of spherical precipitation particle falling, Acta Meteor. Sinica, 42 (4): 431-439 (in Chinese).

Xu, Huanbin and Siwei Wang 1989: Some issues on hail suppression by explosion, Collected works on hail suppression and hailstorm physics, Meteorology Press, 214-236 (in Chinese).

Xu, Huanbin, 2001: The possible dynamic mechanism of explosion in hail suppression, Acta Meteor. Sinica, 59 (1): 66-76 (in Chinese).

Xu, Huanbin and Siwei Wang, 1990: A three-dimensional cloud-scale model that is suitable for compressible atmosphere, Acta Meteor. Sinica, 48 (1): 80-90 (in Chinese).

Zhou, Hesheng, 1999: The impact of shell explosion in severe convective clouds on precipitation, WMO/TD – No. 936, 431-434.

THE EFFECTS OF ADDING SMALL CRYSTALS IN THE ICE PARTICLE SIZE DISTRIBUTION ON THE EVOLUTION OF MIXED-PHASE CLOUD

Faisal S. Boudala [1] and George A. Isaac [2],
[1] Department of Physics and Atmospheric Science, Dalhousie University, Halifax, Nova Scotia, Canada
[2] Cloud Physics Research Division, Meteorological Service of Canada, Toronto, Ontario, Canada

1. INTRODUCTION

Simulation of mixed-phase clouds and estimation of their phase fraction (ice or liquid) require a reasonable representation of ice crystal size distributions. This is because most large-scale cloud models do not predict the ice crystal size distribution, and as a result they assume a certain functional shape to represent the distribution. Ice crystal size distributions are used to formulate a bulk microphysics parameterization to simulate cloud processes such ice crystal growth by riming and vapor deposition, and gravitational settling of ice particles. Many large-scale and weather prediction models use such parameterization of ice crystal size distribution in their schemes to parameterize these processes (e.g., *Tremblay et al.* 1996; *Levkov et al.* 1992; *Zawadzki et al.* 1993; *Lin et al.* 1983). In most cases small crystals (L<100μm) are ignored, largely because of the uncertainty of their in-situ measurements. In this paper, various cloud processes mentioned earlier will be derived using parameterized ice crystal size distributions based on observations. For small ice particles, a parameterization developed by *Boudala et al.* (2002a) will be applied. Using these results, the evolution of mixed-phase cloud and the sensitivity to small ice particles and temperature will be explored using a single prognostic equation developed by *Tremblay et al.* (1996).

2. MEASUREMENTS

The data used for derivation of various parameters were based on four projects. The Beaufort and Arctic Storms Experiment (BASE) was conducted in October 1994 over the Canadian Western Arctic (*Gultepe et al.* 2000). The FIRE Arctic Cloud Experiment (FIRE.ACE) project began in April 1998 and ended in July 1998, with the Convair-580 measurements being made in April (*Curry et al.* 2000). The First Canadian Freezing Drizzle Experiment (CFDE I) was conducted in March 1995 over Newfoundland and the Atlantic Ocean. The Third Canadian Freezing Drizzle (CFDE III) started in December 1997 and ended in February 1998. During CFDE III, the aircraft flew over Southern Ontario and Quebec, Lake Ontario and Lake Erie (*Isaac et al.* 2001a).

Corresponding author address: Faisal S. Boudala, Cloud Physics Research Division, Meteorological Service of Canada, Toronto, Ontario, Canada M3H 5T4; e-mail: faisal.boudala@ec.gc.ca.

The instrumentation used in these projects are described in *Isaac et al.* (2001a, 2001b). The instruments used for this work are the Nevzorov liquid water content (LWC) and total water content (TWC), FSSP, and the PMS 2D-C and 2D-P probes, which measure size, shape and concentration of hydrometers. The temperature has been measured with a Rosemount temperature probe.

3. MODELING APPROACH

The evolution of ice fraction (f_i) following *Tremblay et al.* (1996) is given by equation

$$\frac{df_i}{dt}=\frac{-wGf_i[1+\xi(1-f_i)]+D_i+R}{TWC} \tag{1}$$

where D_i is the vapor deposition rate on ice crystals, R is the riming rate, w is vertical velocity, G is the vertical gradient of saturation mixing ratio, TWC is the total water content, and ξ is the sedimentation parameter which varies from 1 to –1 (*Tremblay et al.* 1996). Tremblay et al. (1996) have also shown that the mixed-phase cloud is not very sensitive to ξ. In this work ξ is set to unity.

4. THE DETERMINATION OF D_i AND R

The vapor deposition rate can be given as

$$D_i=4u\pi S_{si}\sum_{L=L_{min}}^{L=L_{max}} CN(L) \tag{2}$$

where $S_{si}=e/e_{si}-1$ is the supersaturation with respect to ice, e is the ambient vapor pressure, e_{si} saturation vapor pressure with respect to ice, L is the particle dimension, N is the ice particle concentration at size L, C is the capacitance given here as $C=L/\pi$ assuming a hexagonal plate, u is given by relation

$$u=\left(\frac{l^2_s}{k_vR_vT^2}+\frac{R_vT}{e_{si}D_v}\right)^{-1} \tag{3}$$

where l_s is the latent heat of sublimation, k_v is the coefficient of thermal conductivity of air, D_v is the vapor diffusion coefficient, and e_{si} is saturation vapor pressure with respect to ice.

The riming rate is calculated as

$$R=\frac{\pi}{4}E\,LWC\sum_{L=L_{min}}^{L=L_{max}} L^2V(L)N(L) \qquad (4)$$

where E is the collection efficiency (assumed to be unity), LWC is the liquid water content and V is the terminal velocity which is related to particle dimension as $V=aL^b$ where a and b are 147 cm $^{1-b}$ s^{-1} and 0.27 respectively (*Locatelli and Hobbs* 1974). Inspecting equations 2 and 4 reveals that both D_i and R depend on a term represented here by $M^{(n)}$ with moment n given as

$$M^{(n)}=\sum_{L=L_{min}}^{L=L_{max}} L^nN(L)\,. \qquad (5)$$

In this case n is 2+b and 1 for riming and vapor deposition rate respectively. Using PMS 2D-C and 2D-P probe measurements for large ice crystals and the *Boudala et al.* (2002a) approach for small ice particles (L<100μm), $M^{(1)}$ and $M^{(b+2)}$ are derived with and without small ice particles. Figure 1 shows $M^{(1)}$ (panel A) and $M^{(b+2)}$ (panel B) with and without small particles plotted against IWC derived based on Cunningham area to mass coefficients (*Cunningham* 1978) and small ice particles as described in *Boudala et al.* (2002a). The addition of small ice particles significantly increase $M^{(1)}$ but has no effect on $M^{(b+2)}$. Since both $M^{(1)}$ and $M^{(b+2)}$ are well correlated with IWC, power law relationships in a form $M^{(n)} = \alpha_n IWC^{\beta_n}$ are derived and the coefficients are given in Table 1.

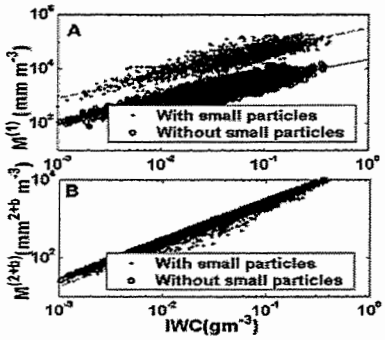

Figure 1. Comparisons of $M^{(1)}$ (panel A) and $M^{(b+2)}$ (panel B) with and without small ice particles.

Table 1. Coefficients determined as $M^{(n)} = \alpha_n IWC^{\beta_n}$ with and without small ice particles (in the closed bracket)

Moments	$M^{(1)}$		$M^{(b+2)}$	
Coefficients	α_1	β_1	α_{2+b}	β_{2+b}
$\alpha_n IWC^{\beta_n}$	2.4x10^5 (2.22x10^4)	0.71 (0.74)	2.58x10^4 (2.78x10^4)	1.05 (1.00)

5. NUMERICAL SIMULATION OF ICE FRACTION

Figure 2 shows numerically simulated ice fraction in a water saturated atmosphere for a given TWC, temperature, pressure and vertical velocity and this is plotted against time. The cloud glaciates rapidly within a few minutes. This can be compared to Fig. 3 when the small ice particles are ignored. In this case, the cloud approaches equilibrium. Complete glaciation does not occur if w is greater than 0.1 ms^{-1}, particularly at warmer temperatures (panel A). Generally the vertical velocities in stratiform clouds are believed to be near 0.1 ms^{-1} and may contain super-cooled droplets at cold temperatures (*Pruppacher and Klett* 1997). These clouds may last for several hours. According to Figs. 2 and 3, when w is near 0.1 ms^{-1}, only if small ice particles are present one can expect the cloud not to glaciate within 35 min. However, it is now well recognized that small ice particles exist in the natural clouds (e.g., *Gultepe et al.* 2000; *Boudala et al.* 2002a) and thus their effects should be parameterized in cloud models.

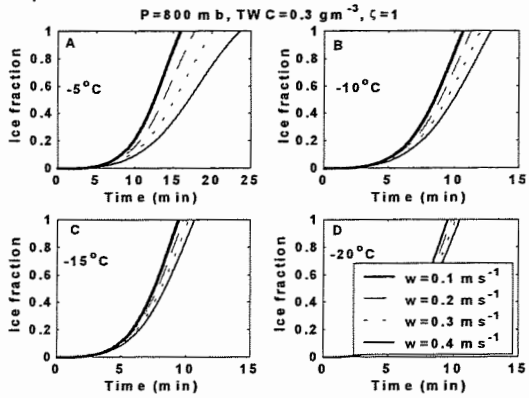

Figure 2. The evolution of ice fraction calculated using coefficients in Table 1 that includes small ice particles.

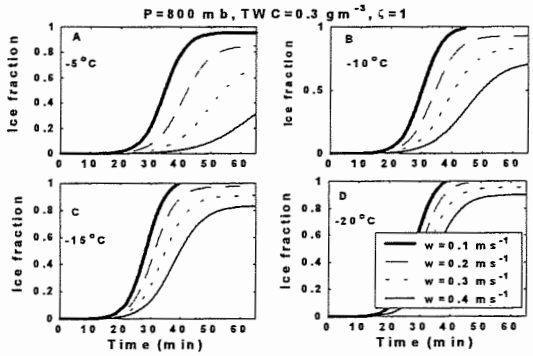

Figure 3. The evolution of ice fraction calculated using the coefficients in Table 1 without small ice particles.

Microphysical processes in mixed-phase cloud are very complex and such an idealized model may not adequately capture them. However, the ice crystal growth term is very sensitive to ice crystal concentration and supersaturation, and these parameters are not well parameterized in mixed-phase clouds. There is some evidence based on observations that the mean ice mass in ice cloud is larger by a factor of 3 as compared to mixed-phase clouds (*Boudala* and Isaac 2004). Therefore, the application of a parameterization based on ice particle spectra measured in ice clouds for mixed-phase clouds may overestimate the ice mass. Nevertheless, even a factor of 3 difference in ice mass may not fully explain the rapid glaciation of the simulated mixed-phase cloud even when the small ice particles are ignored.

It should also be noted that these numerical calculations were based on the assumption that the atmosphere is saturated with respect to water. However, when air is assumed to be saturated with respect to water, it is supersaturated with respect to ice (*Pruppacher and Klett* 1997), which enhances the Bergeron-Findeisen process. As a result, a mixed phase cloud becomes unstable unless there is a sustained supply of moisture from below that may increase the ambient water saturation. Therefore, the assumption that a mixed-phase cloud is always saturated with respect to water is not strictly correct. The recent aircraft observations within mixed-phase clouds also seems to indicate that the assumption of water saturation overestimates the ambient relative humidity on average by 15% as compared to observations (*Fu and Hollars* 2003). Such conditions are consistent with small-scale inhomogeneities within the cloud with the results that a large-scale region of a mixed-phase cloud appears sub-saturated with respect to water. The description of such clouds in a model is very difficult and certain assumptions have to be made. One way to account for the mixed-phase condition in cloud is by modifying the saturation water vapor pressure in a form

$$e_{mix}=(1-f_i)e_{sw}+f_i e_{si}\ , \qquad (6)$$

where e_{sw} and e_{si} are the saturation vapor pressure over water and ice respectively, and f_i is the ice fraction (*Lord et al.* 1984; *Fu and Hollars* 2003).

Figure 4 shows the evolution of the mixed-phase cloud after modification using Eq. 6. In this case, the mixed-phase cloud approaches equilibrium within a few minutes and may last for several hours if the condition is right. This is because the new formalism slows down the ice enhancement due to the Bergeron-Findeisen process when the ice fraction is significant. However, at low vertical velocities and temperatures colder than –5°C, the cloud is still dominated by ice (panels B, C, and D).

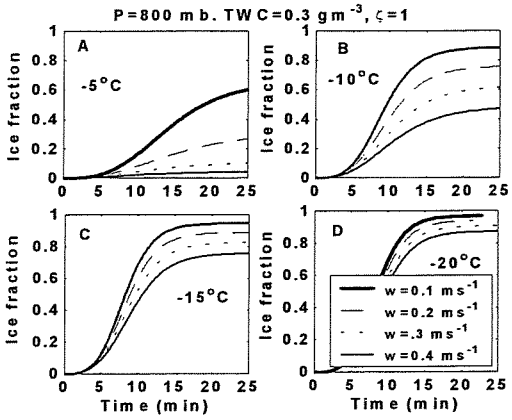

Figure 4. The evolution of ice fraction calculated using coefficients in Table 1 that includes small ice particles.

As discussed earlier, derived $M^{(1)}$ and $M^{(b+2)}$ (see Table 1) were obtained from measurements in glaciated clouds and the appropriate values of α_1 and α_{2+b} should be 8×10^4 mm m^{-3} and 9.27×10^3 mm^{2+b}m^{-3} respectively for mixed-phase clouds with small ice particles. Using these values, and measured TWC and temperature (*Boudala et al.* 2002b), the ice fraction for a given TWC and temperature is numerically calculated and the results are plotted in Fig. 5. The ice fraction exhibit a maximum at –15 °C where the ice growth rate maximum is observed (e.g., *Fukuta* and *Takahashi* 1999). The equilibrium values of ice fractions simulated here are very similar to the one reported by *Boudala et al.* (2002b) based on observations in stratiform clouds. The conclusions made based on this simulation do not change if a different value for atmospheric pressure other than 800 mb is used or a standard atmosphere is assumed.

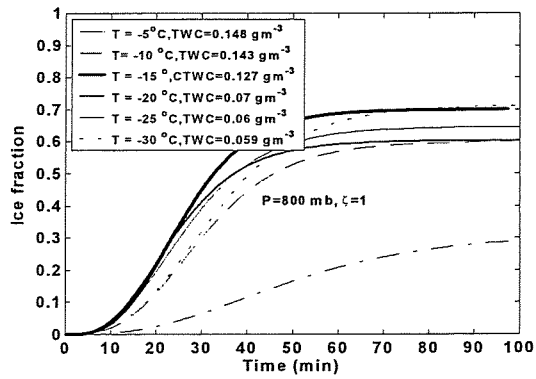

Figure 5. The evolution of ice fraction calculated using $\alpha_1=8\times10^4$ mm m^{-3} and $\alpha_{2+b}=9.27\times10^3$ mm^{2+b} m^{-3}, w=0.1 ms^{-1}, and based on measured T and TWC.

6. SUMMARY AND CONCLUSION

Using a large data set of in-situ aircraft observations collected in mid and high latitude regions, a parameterization of the ice crystal size distribution that can be used to simulate cloud microphysical processes, such as ice crystals growth by riming and vapor deposition, and its removal by sedimentation, has been developed. This parameterization includes small ice particles and its validity has been tested based on independent measurements (*Boudala et al.* 2002a).

Using a single prognostic equation developed by *Tremblay et al.* (1996) and the new parameterization, it was shown that the addition of small ice crystals significantly increases the vapor deposition rate which makes the cloud unstable in a water saturated atmosphere. It has been suggested that that saturation vapor pressure should be parameterized as a function of ice fraction in order to simulate physically meaningful stable mixed-phase clouds. After including this parameterization, it was shown that the simulated mixed-phase cloud exhibits a maximum in ice fraction at –15°C, which is consistent with the in-situ observations reported by *Boudala et al.* (2000b). The effects of radiative heating and turbulent mixing in the development and stability of mixed-phase cloud have not been included in this work. These effects will be considered in the next stage of this research.

7. ACKNOWLEDGEMENTS

This work was partially funded by the National Search and Rescue Secretariat, Transport Canada, the Panel on Energy Research and Development, the Meteorological Service of Canada, the National Research Council of Canada as well as Boeing, NASA and the FAA. Faisal Boudala also received support from NSERC, the Climate Action Fund, and the Canadian Foundation for Climate and Atmospheric Sciences. The data were collected using the Canadian National Research Council Convair-580 and the authors are grateful to their NRC colleagues for their assistance.

8. REFERENCES

Boudala, F. S., A. G. Isaac, Q. Fu, and S. G. Cober, 2002a: Parameterization of effective particle sizes for high latitude clouds. *Int. J. Climatology* (accepted).

Boudala, F. S., G.A. Isaac, S. G. Cober, Q. Fu, and A.V. Korolev, 2002b: Parameterization of liquid fraction in terms of temperature and cloud water content in stratiform mixed-phase clouds. *11th Conference on Cloud Physics*, June 3-7, Ogden, UT.

Boudala, F.S and G.A. Isaac, 2004: Parameterization of stratiform mixed-phase clouds for climate model: Theoretical modeling. In preparation.

Cober, S. G., G. A. Isaac, A.V. Korolev, and J.W. Strapp, 2001: Assessing cloud-phase conditions *J. Appl. Meteor.*, **40**, 1967-1983.

Curry, J. A., P. V. Hobbs, M. D. King, D. A. Randall, P. Minnis, G. A. Isaac, J. O. Pinto, T. Uttal, A. Bucholtz, D. G. Cripe, H. Gerber, C. W. Fairall, T. J. Garrett, J. Hudson, J. M. Intrieri, C. Jakob, T. Jensen, P. Lawson, D. L. Marcotte, L.Nguyen, P. Pilewskie, A. Rangno, D. Rogers, K. B. Strawbridge, F. P. J. Valero, A. G. Williams, and D. Wylie, 2000: FIRE Arctic Clouds Experiment. *Bull. Am.Meteorol. Soc.*, **81**, 5-29.

Fu, Q., and S. Hollars, 2003: Test of in-cloud water vapor parameterization using SHEBA/ FIRE.ACE observations. Accepted in Journal of climate.

Fukuta, N., and T. Takahashi, 1999: The growth of atmospheric ice crystals: A summary of findings in vertical supercooled cloud tunnel studies. *J. Atmos. Sci.,* **56**, 1963-1979.

Gultepe, I., G. A. Isaac, and S. G. Cober, 2001: Ice crystal number concentration versus temperature. *Int. J. Climatology*, **21**, 1281-1302.

Gultepe, I., G. A. Isaac, D. Hudak, R. Nissen, and J. W. Strapp, 2000. Dynamical and microphysical characteristics of Arctic clouds during BASE. *J. Climate*, **13**, 1225-1254.

Isaac, G. A., S. G. Cober, J. W. Strapp, A.V. Korolev, A. Tremblay, D. Marcotte, 2001a: Recent Canadian research on aircraft in-flight icing. *Canadian Aeronautics and Space Journal*, 47-3, 213-221.

Isaac, G. A., S.G. Cober, J. W. Strapp, and D. Hudak 2001b: Preliminary Results from Alliance Icing Research Study (AIRS). 39th Aerospace Sciences Meeting and Exibit, 8-12, January 2001.

Levkov, B. Rockel, H. Kapitza , and E. Raschke, 1992: 3D mesoscale numerical studies of cirrus and stratus clouds by their time and space evolution. *Beitr. Phys. Atmosph.*, 65, 35-58.

Locatelli, J. D. and P. V. Hobbs, 1974. Fall speeds and masses of solid precipitation particles. *J. Geophys. Res.*, **79**, 2185-2197.

Lord, J. S., W. E. Hugh, and J. M. Piotrowicz, 1984: Role of parameterized ice phase microphysics in an axisymmetric, non hydrostatic tropical cyclone model. *J. Atmos. Sci.*, **41**, 2836-2848.

Lin, Y. L., R. D. Farley, and H. D. Orville, 1983: Bulk parameterization of the snow field in a cloud field. *J. Climate Appl. Meteorol.*, **22**, 1065-1092.

Pruppacher, H. R. and J. D. Klett. *Microphysics of Clouds and Precipitation,* Kluwer Academic Publisher, 1997.

Tremblay, A., A. Glazer, W. Yu, and R. Benoit, 1996: A mixed phase cloud scheme based on a single prognostic equation. *Tellus*, **48A**, 483-500.

Zawadzki, I, L. Ostiguy, and J.P.R. Laprise, 1993: Retrieval of the microphysical properties in a CASP storm by integration of a numerical kinematic model. *Atmosphere Ocean*, **31**, 202-233.

A long term comparison of cloud properties observed by vertically pointing radar and lidar with their representation in operational NWP models

M.E.Brooks[1], R.J.Hogan[1] and A.Illingworth[1]

[1]Department of Meteorology, University of Reading, Reading, UK

1. INTRODUCTION

The representation of clouds is one of the major uncertainties in the predictions of future climate change (Mitchell 2000, Stocker, 2001), due to the complex effects of clouds on the earths radiative and hydrological balances. Much of this uncertainty stems from the lack of adequate and objective observations.

The CLOUDNET project aims to use data obtained from near-continuously operating cloud observing sites for the development and implementation of cloud remote sensing synergy algorithms. The data is obtained from a network of three cloud remote sensing stations, Chilbolton (UK,) Cabauw (Netherlands), and Paris (France). The data presented in this abstract used appromximately 8 months of data, but data collection is ongoing and should last for 2 years.

The use of active instruments (lidar and radar) results in detailed vertical profiles of important cloud parameters which cannot be derived from current satellite sensing techniques. These can be compared with the cloud parameters produced from a range of Numerical Weather Prediction (NWP) models which are outputting profiles of cloud and other parameters over the cloud remote sensing stations from the operational forecast runs. At present outputs are archived from the the ECMWF, Meteo France, the Met Office (Mesoscale and Global models) and the KNMI RACMO model.

2. METHOD

The data used in this paper are primarily the cloud radar and lidar. The exact configuration of each of these instruments varies from site to site, but generally speaking the cloud radars are able to detect most cloud, except thin Cirrus and thin StratoCumulus (which has yet to develop drizzle droplets), although the cloud radar cannot meaningfully distinguish the cloud base when precipitation is falling from the clouds, however the lidar is ideally suited to this task .The presence of cloud is determined (as Hogan 2000), where there is a radar return. For ice cloud, this is unambiguous in that falling ice is treated as cloud in most NWP models. Cloud warmer than the wet-bulb 0°C (as determined from the model profiles) isotherm is considered to be cloud if it is above a cloud base detected the lidar.

This results in a time-height section through the clouds, at the radars high temporal and vertical resolution. This is then averaged onto the same grid as the model outputs to be compared with the model profiles of cloud parameters. The model clouds are filtered to remove cloud which have Ice Water Contents (*IWC*) lower than the sensitivity of the radar would be able to predict. In the ECMWF output cloud is added below clouds precipitating significant amounts of ice, as at present this is not included in the ECMWF model as cloud.

3. RESULTS

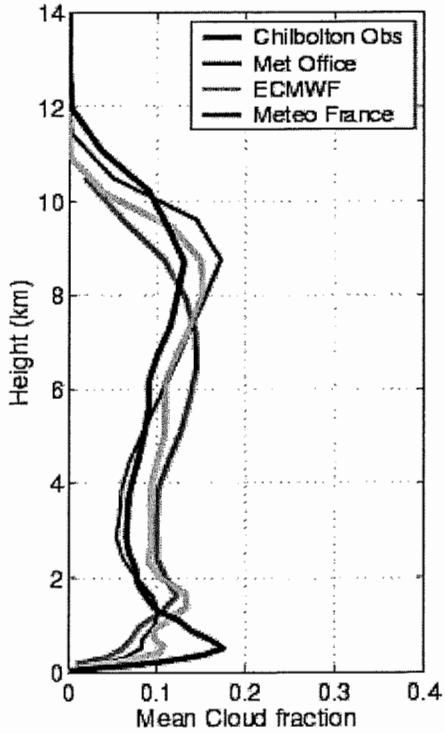

Figure 1. Mean cloud fraction over the Chilbolton site for the Met Office (Mesoscale), ECMWF and MeteoFrance models, for the period April-September 2003.

Figure 1. shows a a general underestimate of cloud fraction below 8 km, by all three of the models shown,

although the ECMWF appears to have a mean cloud fraction closest to the observations at all heights. In the full poster, these results will be expanded, and displayed for more models, and more sites.

4. ACKNOWLEDGEMENTS

The authors would like to acknowledge the CLOUDNET project. More information is available at: http://www.met.rdg.ac.uk/radar/cloudnet/

5. REFERENCES

Hogan, R.J. and Illingworth, A.J. (2000): Deriving Cloud Overlap Statistics from Radar Observations. Quart. J. Roy. Meteor. Soc. **126**, 1-7.

Mitchell, J.F.B. (2000): Modelling Cloud-Climate Feedbacks in the Predixction of Human induced Climate Change. World Climate Research Program Workshop on Cloud Processes and Cloud Feebacks in Large-Scale models. WCRP-110.

Stocker, T.F. 2001: Physical Climate Processes and Feedbacks, in IPCC, Climate Change 2001: The Scientific Basis.

PARAMETERIZATION OF THE STRATOCUMULUS CLOUD TOPPED BOUNDARY LAYER: EVALUATION OF THE ECHAM BOUNDARY LAYER SCHEME AGAINST LARGE-EDDY SIMULATIONS

Andreas Chlond,* Frank Müller and Igor Sednev

Max-Planck-Institut für Meteorologie, Hamburg, Germany

1. INTRODUCTION

The European Project on Cloud Systems in Climate Models (EUROCS) aimed to improve the treatment of cloud systems in global and regional climate models. In this paper we concentrate our efforts on a major and well identified deficiency of climate models, namely the representation of subtropical marine stratocumulus. The purpose of this paper is to evaluate and improve methods of representing shallow cloud systems in global climate models of the atmosphere.

2. APPROACH

This paper addresses the full diurnal cycle of stratocumulus based on FIRE I observations. The methodology adopted rests upon the use of the single-column model (SCM) version of the ECHAM climate model (Roeckner et al., 2003) and the MPI-LES model (Chlond, 1992, 1994). The strategy applied here requires a two-stage procedure: In the first step the MPI-LES model is used to explicitly model the cloud topped boundary layer and to produce comprehensive 4-D datasets of marine stratocumulus. The second step of the strategy is to evaluate and improve turbulent mixing scheme in the ECHAM-GCM. A powerful tool in this context is the use of the ECHAM-SCM representing a single column of the GCM with the same physical package as the full GCM. The intercomparison of the SCM results against the LES results enables the validation of the standard parameterization package and allows to quantify the deficiencies in the various schemes.

3. MODEL INITIALIZATION AND FORCING

In this paper we consider a simulation of the diurnal variation of stratocumulus. The simulation is defined in the EUROCS model-intercomparison project (Duynkerke et al., 2004), and is based on measurements during the FIRE I stratocumulus experiment performed off the coast of California in July 1987 (Albrecht el al., 1988). The case consists of a 37-h long simulation, starting at 0800 UTC (= 00 LT) 14 July 1987 with idealized initial profiles and large-scale forcings. The initial and boundary conditions are based on observations described in Blascovic et al. (1991), Betts (1990), Hignett (1991) and Duynkerke and Teixera (2001) and are specified in Duynkerke et al. (2004).

4. RESULTS

4.1 LES and SCM results

4.2.1 Standard model

The LES and SCM simulations were started on 14 July 0800 UTC (= 00 LT) lasting for 37 hours. Figure (1) shows the variation of the simulated LWPs as function of time which are compared with the retrievals of a microwave radiometer from 14 and 15 July 1987, and the hourly monthly mean diurnal variation. The LES model reproduces the strong diurnal variation in LWP due to the forcing imposed by the shortwave heating of the cloud layer. In accord with the observations, the maximum LWP is found during the late night (around sunrise which occurs at 0500 LT), and the minimum of the LWP occurs shortly after local noon (which is at 1200 LT). The SCM also predicts a solid cloud cover and reproduces a fair representation of the diurnal cycle as the liquid water path varies between 100 g m^{-2} around sunrise to about 20 g m^{-2} some hours before sunset. However, compared to the observations the SCM predicts a too low LWP and thus tends to thinnen the stratocumulus layer to quickly. Subsequently, in the SCM this leads to a much larger amount of downwelling shortwave radiation absorbed at the sea surface causing an erroneous warming bias of the sea surface temperature. Realizing the large sensitivity of the LWP with cloud thickness, this implies that even small errors due to the coarse vertical resolution of current operational GCMs or due to an incorrect description of the entrainment fluxes at cloud top can give rise to large errors in the modelled LWP and subsequently to large errors in the surface energy balance.

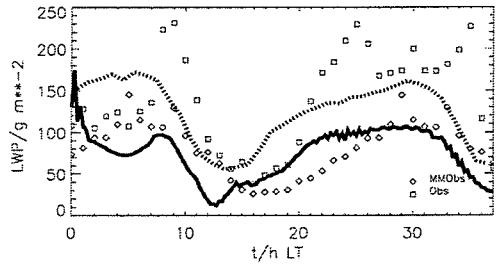

Fig. 1: Time series of observed and simulated LWPs generated by the LES-model (dashed line) and the standard SCM (full line) for the stratocumulus case. Open squares refer to hourly mean observations during 14 and 15 July 1987, whereas the open diamonds represent the hourly monthly mean diurnal variation.

4.2.2 Revised model

Based on the findings described above, we modified the standard SCM. In this section we will show that the behaviour of the model for this case can be significantly improved. The applied modifications basically concerned the implementation of an explicit entrain-

* Corresponding author's address: Andreas Chlond, Max-Planck-Institut für Meteorologie, Bundesstr. 53, D-20146 Hamburg, Germany, E-mail: chlond@dkrz.de

ment parameterization to specify the vertical fluxes of heat and moisture at the boundary layer top. This approach permits a realistic treatment of a stratocumulus topped boundary layers even in a SCM/GCM with coarse vertical resolution and combines the ordinary 1.5-order turbulent closure model with an explicit entrainment formulation. To represent the entrainment interface on a discrete vertical grid we applied a numerical front tracking/capturing method which allows the computation of propagating phase boundaries in fluids (Zhong et al., 1996). The advantage of this formulation is that it permits the stratocumulus top to lie between grid levels and continuously evolving with time. This is a desirable feature for the simulation of stratocumulus clouds because cloud feedbacks on turbulence and radiation can be captured despite the coarseness of the grid. A comprehensive description of the scheme is given in Chlond et al. (2004).

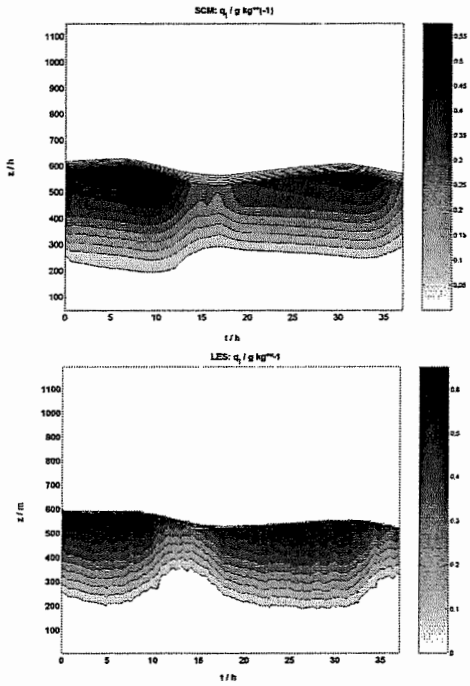

Fig 2: Time evolution of the liquid water content obtained using the revised SCM (upper panel) and the LES model (lower panel) for the reference case.

Results of this revised model are displayed in Figure (2) (upper panel) showing the time evolution of the liquid water content. For comparison also the liquid water field generated by LES for the same case is shown (lower panel). The modified SCM captures the diurnal variation of the liquid water content profiles due to the forcing imposed by the shortwave radiation. Like the LES, the maximum cloud thickness is found during the night, and cloud deck gradually thins until the afternoon. In both models the computed liquid water content increases with height in the cloud and reaches a maximum at $z/z_i = 0.9$. This shows that entrainment leads to a decrease in the liquid water content just below cloud top. A peak value in the liquid water content of about 0.60 g kg^{-1} was predicted by both models during the night whereas during the afternoon peak values around 0.20 g kg^{-1} were produced by LES as well as by the SCM.

5. ACKNOWLEDGEMENTS

This work has received financial support by the CEC contract EVK2-CT95-1999-00051 EUROCS (European Project on Cloud Systems in Climate Models).

6. REFERENCES

Albrecht, B. A., Randall, D.A. and Nicholls, S., 1988: Observations of marine stratocumulus clouds during FIRE. *Bull Amer. Meteor. Soc.*, **69**, 618-626.

Betts, A.K., 1990: The diurnal variation of California coastal stratocumulus for two days of boundary layer soundings. *Tellus*, **42A**, 302-304.

Blascovic, M.R., Davies, R. and Snider, J.B, 1991: Diurnal variation of marine stratocumulus over San Nicolas Island during July 1987. *Mon. Wea. Rev.*, **119**, 1469-1478.

Chlond, A., 1992: Three-dimensional simulation of cloud street development during a cold air outbreak. *Bound.-Layer Meteor.*, **58**, 161-200.

Chlond, A., 1994: Locally modified version of Bott's advection scheme. *Mon. Wea. Rev.*, **122**, 111-125.

Chlond, A., Müller, F. and Sednev, I., 2004: Numerical simulation of the diurnal cycle of marine stratocumulus during FIRE - A LES and SCM modelling study. Submitted to *special issue Quart. J. Roy. Met. Soc*

Duynkerke, P.G. and Teixeira, J., 2001: Comparison of the ECMWF Re-analysis with FIRE I observations: Diurnal variation of marine stratocumulus. *J. of Climate*, **14**, 1466-1478.

Duynkerke, P. G., de Roode, S. R. + case participants, 2004: Observations and numerical simulations of the diurnal cycle of the EUROCS stratocumulus case. Submitted to *special issue Quart. J. Roy. Met. Soc.*

Hignett, P., 1991: Observations of the diurnal variation in a cloud-capped marine boundary layer. *J. Atmos. Sci.*, **48**, 1474-1482.

Roeckner, E., Bäuml, G., Bonaventura, L., Brokopf, R., Esch, M., Giorgetta, M., Hagemann, S., Kirchner, I., Kornblueh, L., Manzini, E., Rhodin, A., Schlese, U., Schulzweida, U. and Tompkins, A., 2003: The atmospheric general circulation model ECHAM5. PART I: Model description. Max-Planck-Institut für Meteorologie Report No. 349, Hamburg. [Available from Max Planck Institute for Meteorology, Bundesstr. 53, 20146 Hamburg, Germany]

Zhong, X., Hou, T.Y. and LeFloch, P.G., 1996: Computational methods for propagating phase boundaries. *J. Comp. Phys.*, **124**, 192-216.

PARAMETERIZATION OF MICROPHYSICAL PROCESSES IN A NON HYDROSTATIC PREDICTION MODEL

O.V. Drofa and P. Malguzzi

Institute of Atmospheric and Climate Sciences of the Italian National Research Council (ISAC-CNR), Via Piero Gobetti, 101, I-40129, Bologna, Italy

1. INTRODUCTION

Due to the rapid increase of computing power, the horizontal scale explicitly resolved by regional numerical prediction models has gone beyond the limit of validity of the hydrostatic approximation. Even though some turbulent processes still need to be parameterized (like entrainment in strong updrafts), the explicit description of atmospheric moist convection is in the reach of non-hydrostatic prediction models having horizontal grid distances of the order of one kilometer. In devising such models, particular attention must be paid to the parameterization of the microphysical processes responsible for the formation of clouds and precipitation.

In this paper, following a brief highlight of the ISAC-CNR non-hydrostatic model (section 2), the parameterization of the microphysical processes are described in detail in section 3. The scheme presented here is original in many respects; in particular, the parameterization of fast processes (see section 3) takes into account the size distribution of cloud particles. The model is used to simulate well documented episodes of cumulonimbus development. Simulated and observed quantities like maximum vertical velocity and temperature fluctuations are compared. Results are discussed in the final section 4.

2. MODEL DESCRIPTION

The numerical model used in the present study (MOLOCH), developed at the ISAC-CNR, integrates in time the fully compressible set of equations governing the atmospheric motion. The basic dynamical variables are pressure, temperature, specific humidity, and the three dimensional velocity. The model terrain following vertical coordinate ζ is related to the geometric height z according to the implicit formula:

$$\zeta = H\left(1 - e^{-\frac{z-h(1-\zeta/H)^S}{H}}\right) \qquad (2.1)$$

where h is the orographic height and H is the density scale height ($R_D\ T_0\ /\ g$) computed at the reference temperature T_0. Equation (2.1) transforms the semi-infinite z-axis into the finite interval [0, H]. The parameter S is introduced to smoothly relax ζ-coordinate surfaces to horizontal ones above the orography, in order to reduce the error in the computation of the pressure gradient force at higher levels. Numerical discretization is based on the Arakawa C-grid and on equally spaced vertical intervals. Time integration is splitted with a forward-backward scheme for horizontally propagating waves and implicit for vertically propagating sound waves. Advection terms are computed with the second order FBAS scheme (Malguzzi and Tartaglione, 1999). The physical package of MOLOCH consists in radiation, vertical diffusion, and soil water and energy budgets. No convective parameterization schemes are applied. The MOLOCH simulations can be nested in runs of the hydrostatic limited area model BOLAM.

Corresponding author's address: Drofa Oxana V., ISAC-CNR, Via Piero Gobetti, 101, I-40129, Bologna, Italy; E-mail: o.drofa@isac.cnr.it.

3. MICROPHYSICAL PARAMETERIZATION

The microphysical scheme used in the MOLOCH model is the evolution of the methods proposed by Drofa (2003) and partly based on Marecal et al. (1993) and Rutledge and Hobbs (1983). The scheme predicts the time evolution of the specific concentration of four microphysical species: cloud water, cloud ice, precipitating liquid water (rain), and precipitating ice. Precipitating ice is formed by crystal hydrometeors having physical properties depending on temperature. Physical processes involving transformations between the atmospheric specific humidity q_V and cloud species (see fig. 1) occur on a very short time scale and are therefore computed every model time step. The time evolution of hydrometeors is characterized by a longer scale and is computed over a longer time interval. Slow processes are summarized in fig. 2.

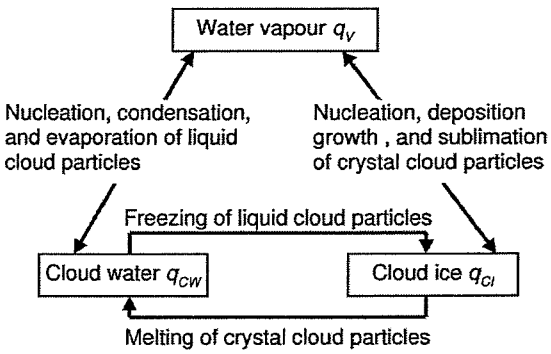

Fig.1. Schematic representation of fast processes.

All parameterized processes, apart from auto-conversion of precipitation, are based on the computation of the mass tendency of a particle of diameter D. The tendency of the specific

concentration, say q, of a given microphysical specie is then obtained by the general formula:

$$\partial q/\partial t = \frac{1}{\rho_{air}} \int_0^\infty dm/dt\, N(D)\, dD \qquad (3.1)$$

where $N(D)$ is the volumetric concentration of particles per unit size D. For cloud particles, the gamma-distribution is used (Oblaka i Oblachnaja Atmosfera, 1989, and Volkovitzkiy et al., 1983):

$$N(D) = \frac{2N_0\beta^{\alpha+1}}{\Gamma(\alpha+1)} D^\alpha e^{-\beta D} \qquad (3.2)$$

where the parameter β is determined by the integral:

$$\frac{1}{\rho_{air}} \int_0^\infty m(D)N(D)dD = q\,, \qquad (3.3)$$

$m(D)$ being the mass of a cloud particle, defined by:

$$m = aD^b \qquad (3.4)$$

This gives:

$$\beta = \left[\frac{2N_0 a\,\Gamma(\alpha+b+1)}{\rho_{air}\, q\,\Gamma(\alpha+1)}\right]^{\frac{1}{b}} \qquad (3.5)$$

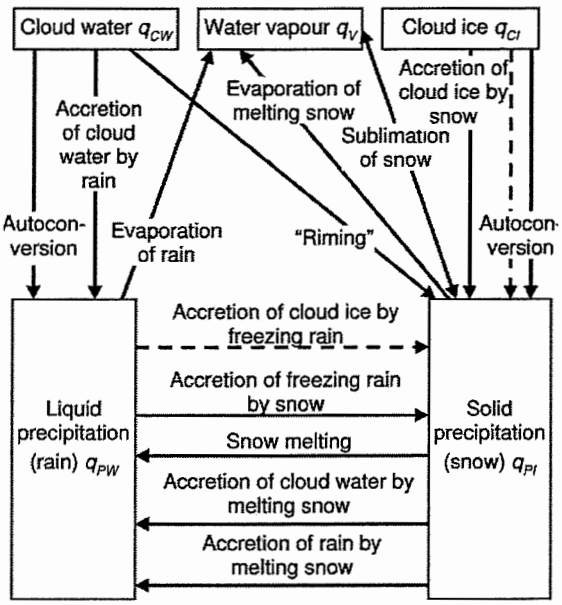

Fig.2. Schematic view of slow processes.

In the previous expressions, the parameters N_0, α, a, and b depend on the particle phase. N_0 is in the range 10^6-10^7 (10^7-10^8) for cloud water (cloud ice); α is set to 6.0 (3.0); $a = \pi\rho_W/6$ (100.0); and b =3.0 (2.5).

It is clear from (3.2) and (3.5) that the actual particle distribution depends, for a fixed N_0, on the specific concentration of cloud species. In particular, for small quantities of cloud water or ice, the size distribution becomes peaked towards large amounts of small diameter particles. Hence, the particle distribution has a dynamical evolution.

Similar considerations apply to the parameterization of processes involving precipitation. Liquid (rain) and solid (snow / ice) hydrometeors are distributed according to the Marshall-Palmer (1948) distribution:

$$N(D) = N_0\, e^{-\lambda D}\,, \qquad (3.6)$$

where

$$\lambda = \left[\frac{N_0\, a\,\Gamma(b+1)}{\rho_{air}\, q}\right]^{1/(b+1)} . \qquad (3.7)$$

As done in the derivation of (3.5), expression (3.4) has been used here. For iced hydrometeors, the parameters N_0, a, and b depend on temperature T according to the following Table I (after Drofa, 2003). For liquid precipitation, the parameters a and b assume the same values defined for cloud water while N_0 is set to $8.0 \cdot 10^6$ m^{-4}. In the following of this section, the mass tendency associated to all of the above physical processes is given.

Table I. Values of the parameters N_0, a, b, k, and n (see text) used for iced hydrometeors (Drofa, 2003).

T (° C)	N_0 (m^{-4})	a	b	k	n
$T > -10$	$8 \cdot 10^6$	232.	3.06	144.	0.66
$-10 < T < -20$	$2 \cdot 10^7$	157.	3.31	156.	0.86
$-20 < T < -30$	$4 \cdot 10^7$	1.43	2.79	18.	0.62
$T < -30$	$5 \cdot 10^7$	0.145	2.59	7.3	0.55

Most of the microphysical processes described below are associated to heat exchanges. The corresponding temperature variations are computed from entropy conservation (its expression is given in the Appendix). The entropy of the mixture of air, ice, and water is exactly conserved by the numerical code.

3.1 Condensation/evaporation and sublimation

Condensation of water vapor starts over nuclei when supersaturation conditions are present. Subsequent condensation occurs over cloud droplets. Its rate is determined by assuming equilibrium between diffusive fluxes of water vapor and heat and obeys the following law, which stems out from a second order Taylor expansion of the saturation humidity with respect to temperature (Srivastava and Coen, 1992):

$$\frac{dm}{dt} = D \cdot \frac{2\pi F\left(q_V/q_{SW,SI} - 1\right)\rho_{air}}{\dfrac{1}{q_{SW,SI}\,\chi} + \dfrac{L^V_{w,i} M_W}{K_A T}\left(\dfrac{L^V_{w,i}}{R_V T} - 1\right)} \cdot$$

$$\cdot \left\{1 - \frac{1}{2}\left(\frac{q_V}{q_{SW,SI}} - 1\right)\left[\frac{\rho_{air}\left(\dfrac{L^V_{w,i}}{R_V T} - 1\right)}{\dfrac{K_A T}{q_{SW,SI}\,\chi\, L^V_{w,i}} + \rho_{air}\left(\dfrac{L^V_{w,i}}{R_V T} - 1\right)}\right]^2 \right\} .$$

$$\cdot\left[1+\left(1-2\frac{L^v_{w,i}}{R_V T}\right)\Big/\left(\frac{L^v_{w,i}}{R_V T}-1\right)^2\right]\Bigg\}, \qquad (3.8)$$

where K_A = $2.43\cdot10^{-5}$ $Jkg^{-1}K^{-1}s^{-1}$ is the thermal conductivity of air; M_W, the molecular weight of water; R_V, the gas constant of water vapor; $\chi=2.26\cdot10^{-5}$ m^2s^{-1}, the coefficient of molecular diffusion of vapour into air; and where the ventilation coefficient F is equal to 0.8 for cloud particles and

$$F = 0.78 + Sc^{1/3}(\rho_{air} D\, u(D)/\mu)^{1/2} \qquad (3.9)$$

for hydrometeors, Sc=0.6 being the Schmidt number, and μ =$1.178\cdot10^{-5}$ kg $m^{-1}s^{-1}$, the dynamical molecular viscosity of air. In (3.9) $u(D)$ represents the terminal velocity of a precipitating particle that depends on pressure P and is approximated by:

$$u = kD^n (P_0/P)^{0.4} \qquad (3.10)$$

The parameters k and n hold 842.0 and 0.8, respectively, for rain. For solid hydrometeors, the values of k and n are given in Table I. The formula (3.8) also applies to evaporation of cloud droplets, rain, melting snow, and to sublimation of cloud and precipitating ice. In the latter case, the latent heat of sublimation L^v_i and the saturation specific humidity over ice q_{SI} are used.

3.2 Melting and freezing

When temperature is below (above) the freezing temperature of water T_{TR} , freezing (melting) of cloud water (cloud and precipitating ice) occurs (see fig. 1 and 2). These processes are governed by the diffusion of heat and are parameterized according to:

$$\frac{dm}{dt} = D\cdot\frac{2\pi K_A F\,|T-T_{TR}|}{L^w_i} \qquad (3.11)$$

where the coefficients are as in (3.8).

3.3 Accretion of cloud by hydrometeors

There are 5 slow processes involved (see fig. 2). If temperature is greater than T_{TR}, accretion of cloud water by melting snow occurs. This process actually consists in the contribution to the melting of a particle of precipitating ice due to the interception of cloud water during its fall. When temperature is below T_{TR}, cloud ice is intercepted by precipitating ice, and sudden freezing of precipitating water is triggered by particles of cloud ice. This process is splitted into the sweep-out effect, described by the following equation (3.12), and the sudden freezing of the rain involved (dashed arrows in fig.2). Independently on temperature, accretion of cloud water by rain will occur. Finally, the fifth process of this group consists in the sudden freezing of super cooled cloud water on the surface of crystals of precipitating ice (riming). All these processes are governed by the following law:

$$\frac{dm}{dt} = \rho_{air}\frac{\pi}{4}D^2 u(D) E q_{CW,CI}\cdot \left\{C_W(T-T_{TR})/L^w_i\right\} \qquad (3.12)$$

where E is the accretion coefficient, C_W the specific heat of water, and where the last factor must be taken into account in the case of melting snow only. The accretion coefficient holds, for the 5 processes listed above, 1.0, 0.1, 1.0, 0.6, 1.0, respectively.

3.4 Interaction between hydrometeors

If T is less than T_{TR}, sudden freezing of super cooled rain occurs when a raindrop encounters a snowflake. Applying the geometric swept out concept, the mass increase of an iced hydrometeor is given by:

$$\frac{dm_{PI}}{dt} = \rho_{air}\frac{\pi}{4}(D_{PW}+D_{PI})^2|U_{PI}-U_{PWi}|Eq_{PW}, \qquad (3.13)$$

where E=1.0 and where U denotes the mass weighted mean terminal velocity of precipitation defined as

$$U = \int_0^\infty N(D)m(D)u(D)dD \Big/ \int_0^\infty N(D)m(D)dD. \qquad (3.14)$$

In this case, a double integral over the size distributions of solid and liquid precipitating particles must be performed in place of (3.1) in order to obtain the tendency of the specific mass.

Above freezing, a contribution to melting snow comes from the heat capacity of the intercepted rain. This is computed by multiplying (3.13) by the extra factor appearing in (3.12).

3.5 Autoconversion of precipitation

Autoconversion is the only way in which the microphysical scheme can create precipitation from clouds. This is not really a physical process, being simply a conventional redefinition of some cloud particles as hydrometeors when the specific concentration of cloud exceeds a threshold q^{TH}. This is done according to the following formulas:

$$\partial q_{PW}/\partial t = \alpha_{AC}\, max\left\{0, q_{CW} - q^{TH}_{CW}\right\} \qquad (3.15)$$

$$\partial q_{PI}/\partial t = \alpha_{AC}\, e^{[0.025 min\{0, T-T_0\}]}\, max\left\{0, q_{CI} - q^{TH}_{CI}\right\}$$

The autoconversion coefficient α_{AC} is an important parameter that has a strong influence upon ground precipitation. Its value is set in the range from 1.0 to 3.0 10^{-3} s^{-1}. The threshold values are 5.0 10^{-4} and 10^{-3} kg/kg for cloud water and cloud ice, respectively.

4. DISCUSSION AND CONCLUSIONS

The results obtained with the scheme described in the previous section has been tested by simulating real episodes of strong convection and cumulonimbus development.

The data used to initialize the simulations of cumulonimbus development is obtained from radio-sounding profiles of temperature and dew-point measured before strong episodes of convection. These cases have been studied in detail and are listed in Drofa (2003). To initiate convection, a saturated bubble is defined in the model initial condition in the vertical layer where near saturation conditions are

observed. Model runs are performed with 250 m of horizontal and vertical resolution on a 20 by 20 km horizontal domain, and extend one hour in time. Axial symmetry around the domain center is imposed in order to obtain well organized developments. For each simulation, the maximum value of updraft and downdraft vertical velocity, temperature fluctuations (with respect to the initial temperature profile), total water content, and simulated radar echo are computed and compared with observations. Some results are summarized in fig. 3, where observed and simulated maximum vertical velocity (triangles) and temperature anomaly (stars) are reported in a scatter plot. It can be readily seen that the model performs satisfactorily especially for very strong convective episodes. There is, nevertheless, the tendency to somewhat underestimate updrafts in relatively weak cases. However, the limited number of cases analyzed here does not allow to draw any firm conclusion.

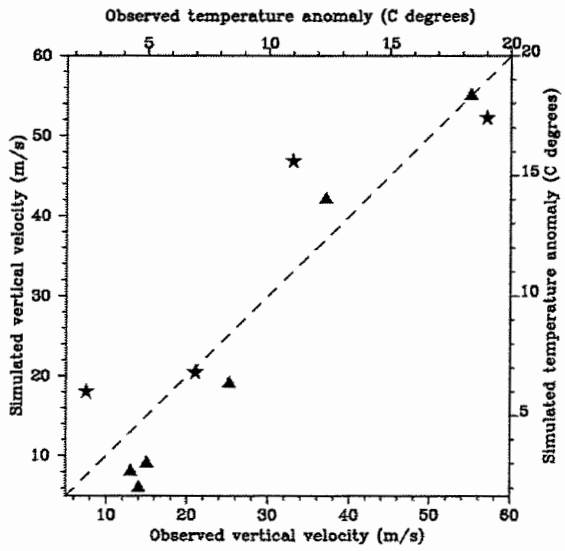

Fig3. Scatter plot of observed and simulated maximum vertical velocity in updraft (triangles) and maximum temperature fluctuations (stars). Left and bottom axis: vertical velocity in m/s. Right and top axis: temperature in ^{0}C.

The above results are just preliminary ones. A more exhaustive comparison of the present scheme with more classical parameterizations, especially for what concerns microphysical variables, should be performed in order to assess the validity of the hypotheses made here. Moreover, the proposed scheme can be improved in several ways, for instance by inserting a new prognostic variable for hail. Research on these topics is under way.

APPENDIX

The exact expression for entropy is:

$$E = C_P \ln\frac{T}{T_0} - (1-q_0)R_D \ln\frac{P-e}{e} - q_V R_V \ln\frac{e}{e_0} + q_V \frac{L_i^v}{T_0} + (q_{PW} + q_{CW})\frac{L_i^w}{T_0}$$

where q_0 denotes the total amount of water per kg of air; C_P, the total heat capacity at constant pressure of the mixture of air and water; e, the partial pressure of water vapor; and e_0, its saturation value computed at the reference temperature T_0.

REFERENCES

Drofa, O.V., 2003. The parameterization of microphysical processes for atmospheric numerical models. Il Nuovo Cimento, 26, N.3, pp. 233-262.

Malguzzi, P., and N. Tartaglione, 1999: An economical second order advection scheme for numerical weather prediction. Q.J.R.Meteorol.Soc., 125, 2291-2303.

Marecal V., D. Hauser, and F. Roux, 1993. The12/13 January 1988 narrow cloud-frontal rainband observed during MFDP/FRONT 87. Part II: Microphysics. J.Atm.Sci., 50, 975-998.

Marshall J.S., and W. Palmer, 1948. The distribution of raindrops with size. J.Meteor., 5, 165-166.

Oblaka i Oblachnaja Atmosfera (Clouds and cloudy atmosphere), 1989. *Spravochnik pod red.* (Handbook edited by) Mazina I.A., A.KH. KHrgiana. L., Gidrometizdat, 648pp., in Russian.

Rutledge S.A., and P.V. Hobbs, 1983. The mesoscale and microscale structure and organisation of clouds and precipitation in midlatitude cyclones. VIII: A model for the «Seeder-Feeder» process in warm-frontal rainbands. J.Atm.Sci., 40, 1200-1206.

Srivastava P.C., and J.L. Coen, 1992. New explicit equations for the accurate calculation of the growth and evaporation of hydrometeors by the diffusion of vapour. J.Atmos.Sci., 49, 1643-1651.

Volkovitzkiy O.A. et al., 1983. Issledovanie spektral'nogo propuskaniya kristallicheskih tumanov (Study of spectrum transparency of crystal fogs). Izvestiay of Sciences Academy of USSR, 19, N.5, pp. 497-503.

PARAMETRIZATION OF MICROPHYSICS FOR CONVECTIVE-SCALE NUMERICAL WEATHER PREDICTION

R. M. Forbes

Met Office, Joint Centre for Mesoscale Meteorology, U.K.

1. INTRODUCTION

The performance of the next generation of short range forecast systems, based upon use of high resolution Numerical Weather Prediction (NWP) models, will depend, in part, on the accuracy and suitability of the cloud and precipitation microphysics parametrization. An appropriate representation of the complex liquid and ice phase microphysical processes that occur in the atmosphere is therefore required, not only for the direct prediction of cloud and precipitation, but also for the effect on atmospheric dynamics through condensation heating and evaporative cooling (Forbes and Clark 2002). If the parametrization is too simple, then many of the important processes may be mis-represented. On the other hand, a parametrization that is too complex may be inappropriate for the model resolution and too computationally expensive for implementation in an operational NWP system. This paper explores the level of complexity required in order to adequately forecast convective (and frontal) precipitation using the Met Office Unified Model (UM) (at high resolution (1 km grid spacing). An example of the representation of rain in high resolution NWP models is described.

2. MICROPHYSICS PARAMETRIZATION

The current microphysics parametrization in the Unified Model (UM) used in operational forecasts at the Met Office is based on the scheme described by Wilson and Ballard (1999). The model has three predicted (i.e. prognostic) variables to represent the grid-box mean specific humidities for (1) water vapour, (2) cloud liquid water droplets and (3) snow particles. These variables are stored in the model between timesteps and advected by the three-dimensional wind field. Rain is diagnosed every timestep from the predicted variables (i.e. it is a diagnostic variable) and is not advected by the wind.

There are many aspects of the microphysics parametrization that could be improved for higher resolution NWP using knowledge from observations, including the way in which certain microphysical processes are represented, the assumptions about particle size distributions, fall speeds and densities, and the number of variables in the model that are used to represent the hydrometeors in the atmosphere. For example, for NWP at convective scale resolution, it is likely that a prognostic representation of rain is required along with some form of parametrization of graupel and possibly multiple prognostic variables to represent different types or moments of ice crystal / snow aggregate particle distributions, (similar to the parametrizations in Cloud Resolving Models used in research applications).

To indicate at what model grid resolution it may be desirable to have a prognostic rather than diagnostic representation for a particular hydrometeor type (e.g. snow, rain, graupel) the relative magnitude of the terms in the budget equation can be examined:

$$\frac{\partial q}{\partial t} = \nabla.\left(\rho(\bar{u} + \bar{w} + \bar{v}_t)q\right) + S$$

$$\approx \underset{(1)}{\rho\bar{u}\nabla q} + \underset{(2)}{\rho w\frac{\partial q}{\partial z}} + \underset{(3)}{\frac{\partial(\rho v_t q)}{\partial z}} + S$$

where q is the hydrometeor mixing ratio, ρ is the density or air, u is the velocity of the horizontal wind, w is the vertical wind speed, v_t is the grid box mean mass-weighted fallspeed of the hydrometeor, and S represents the source and sink terms for q.

For a particular model grid resolution and hydrometeor type, if terms (1) or (2) in the above equation are small compared to term (3), then the advection terms can be neglected and the hydrometeor *within a grid box* can be assumed to be in steady state and can be represented diagnostically in the model. As the size of grid boxes is reduced (i.e. higher horizontal resolution) then the length scale of horizontal variations of q decreases and term (1) increases. Also, the magnitude of the resolved vertical component of the wind increases with increasing resolution which will increase term (2). Taking rain as an example, at 12 km grid resolution, terms (1) and (2) are small compared to term (3) and so rain can be treated diagnostically. At 1 km resolution, the first two terms can be much larger and a prognostic representation of rain that includes the 3D advection by the wind may be more appropriate. However, additional prognostic variables in the model also increases the computational expense and complexity of the microphysical parametrization, so any changes should be justified in improved forecast skill of the cloud and/or precipitation fields.

Corresponding author's address: Richard. M. Forbes, Met Office JCMM, Meteorology Building, University of Reading, PO Box 243, Reading, RG6 6BB, U.K.;
E-Mail: richard.forbes@metoffice.com

3. EXAMPLE: DIAGNOSTIC VS. PROGNOSTIC REPRESENTATION OF RAIN

This section provides an example of how an increase in the complexity of the microphysics parametrization can be assessed to determine whether it can improve high resolution NWP forecasts. Three results are shown here indicating the beneficial impact of including prognostic rain in a high resolution NWP model.

3.1 Longevity of Deep Convective Cells

An idealised case study of the diurnal cycle of convection over land is used to assess the impact of the prognostic representation of rain on the development and evolution of deep convective cells. Figure 1 shows the surface precipitation over the 150 km square domain at six hour intervals during the forecast for two runs of the UM (1 km resolution) with diagnostic and prognostic rain respectively. Relatively small-scale deep convective cells develop around midday over the whole domain and as the day progresses there is an evolution upscale to fewer larger cells. The rainfall field in the prognostic rain model is more diffuse, as expected from the additional advection of rainfall by the wind. However, the lifetime of the convective cells is also increased in the prognostic rain run, particularly for the large cells in the evening. This suggests there is more organization in the convection in the prognostic rain run, in which rain can be advected away from the location of the convective updraught.

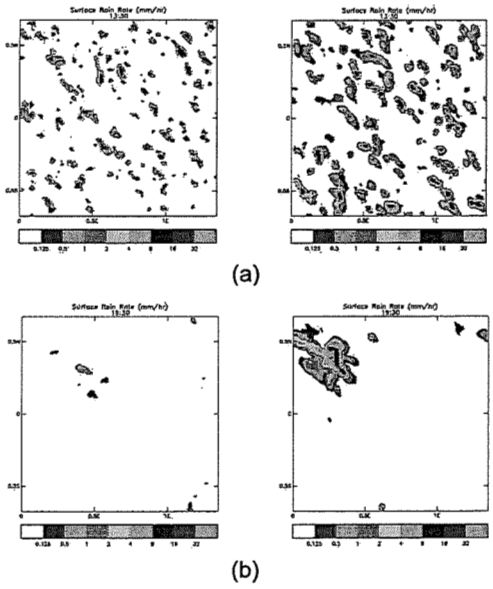

Figure 1 Plan view of surface precipitation rate (mm/hr) for the reference UM run with diagnostic rain (left hand side) and for the UM with prognostic rain (right hand side) at (a) 13:30 (6 hour forecast) (b) 19:30 (after 12 hours).

3.2 Orographic Rainfall

The benefit of a prognostic representation of rain may be particularly significant when rainfall is stationary over a prolonged period, leading to large rain accumulations and potential flooding in individual river catchments. Orographic enhancement of rainfall is one meteorological situation where the seeder-feeder mechanism can lead to significant rainfall tied to the location of the orography. River catchment boundaries are also associated with orography and so small displacement errors in the model forecast of orographic rainfall could lead to the rain falling into the wrong river catchment.

An orographic rainfall case study (19 Nov 2001) is used here to test the hypothesis that it is important to include a prognostic representation of rain in high-resolution models to improve surface precipitation forecasts. Some results are shown in Figures 2 and 3 which highlight the beneficial impact of including horizontal advection of rain in a 2 km grid version of the UM on river catchment rainfall totals.

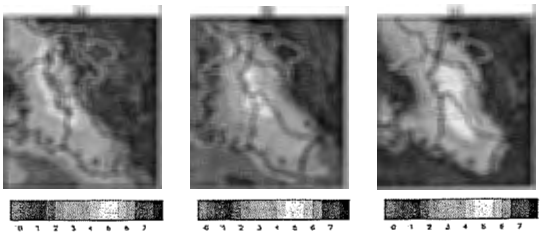

Figure 2 Accumulated rainfall (mm) from 01Z to 12Z on 21/11/2001 over Dartmoor in south-west England from (a) model with diagnostic rain., (b) model with prognostic rain and (c) radar. The river catchment boundaries are indicated by the black lines. The orogaphy contours at 100m intervals are indicated by white contours. The rainfall accumulations for the two model runs have been normalised to give the same total rainfall as the radar data, but it is the improved spatial distribution of the rainfall in (b) that is the key result.

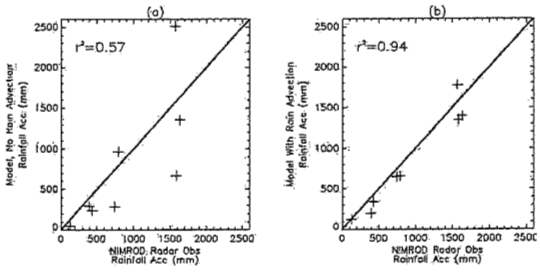

Figure 3 Correlations between model and radar catchment rainfall accumulations shown in Fig. 2 for (a) the model with diagnostic rain and (b) the model with prognostic rain. The r^2 correlation (which is independent of any rainfall normalization) is significantly improved for the prognostic rain run..

3.3 Comparison with Radar Reflectivities

The effect of prognostic rain on the prediction of a band of convective cells advecting southwards across Southern England on 01 Jul 2003 is described. As for the previous case studies, two model simulations are performed with a high resolution (1km) version of the UM; one with diagnostic rain and one with prognostic rain. The results are compared with radar data from the 3GHz research radar based at Chilbolton in Hampshire.

The 3GHz scanning radar at Chilbolton has a radial resolution of 300m and an azimuth resolution decreasing with distance (at a rotation rate of 1\textdegree~per second the resolution is 1 km at 60 km range). The Chilbolton radar thus provides a detailed view of the structure of the precipitation.

A comparison of radar reflectivity from the Chilbolton radar (interpolated to 1 km resolution) with the model calculated reflectivity after a six hour forecast shows the similar scales and spatial distribution of the convective cells in the model and the observations (Fig. 4). The overall evolution of the band of convection for the two model runs is similar but the prognostic rain run has significantly less of the undesirable grid point structure in the precipitation pattern and different evolution of individual convective cells. A quantitative comparison of the reflectivity values in the 90 km radius circle is shown in Figure 5 as probability densities. The diagnostic rain run under-predicts the frequency of points in the 10-30 dBZ range and over-predicts the frequency in the 35-50 dBZ range. Although other assumptions about the rain drop size distribution will affect the reflectivity, the prognostic rain run does improve on the overall representation of the relative frequency of different reflectivity values.

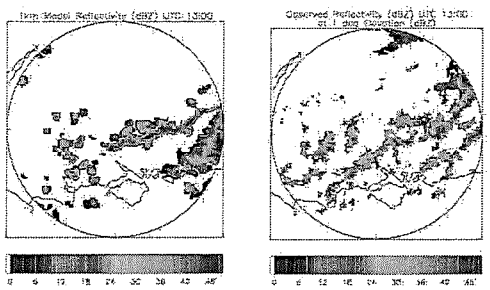

(a) (b)

Figure 4 *360 degrees PPI scans of reflectivity (dBZ) out to 90km range from (a) the model with prognostic rain and (b) the Chilbolton 3GHz radar at 1 degree elevation interpolated to a 1 km grid.*

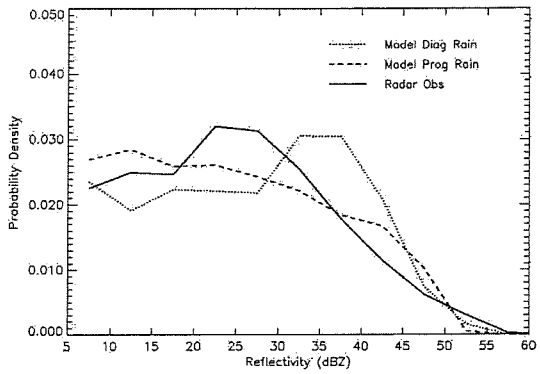

Figure 5 *Probability density distribution of reflectivity from the radar and models with diagnostic and prognostic rain for the fields shown in Figure 4.*

4. SUMMARY

There is a trend towards higher resolution for operational Numerical Weather Prediction models as available computing power increases and such models require an appropriate but computationally efficient parametrization of cloud and precipitation microphysics for accurate prediction of cloud and precipitation. There are many aspects of the microphysics parametrization that could be improved, but the impact of any changes needs to be assessed. This paper has described one example of assessing the benefit of increased complexity of the microphysics parametrization.

Acknowledgements

The author would like to thank a number of colleagues at the Met Office for their contributions to this work including Peter Clark, Carol Halliwell, Humphrey Lean, Nigel Roberts and Jon Petch. I would also like to thank Robin Hogan at Reading University and the Radiocommunications Research Unit at the Rutherford Appleton Laboratory for the data from the Chilbolton 3GHz radar.

References

Forbes, R. M., and Clark, P. A., 2003: Sensitivity of extra-tropical cyclone mesoscale structure to the parametrization of ice microphysical processes. *Quart. J. Roy. Meteorol. Soc.*, **129**, 1123-1148.

Wilson, D. R., and Ballard, S. P., 1999: A microphysically based precipitation scheme of the UK Meteorological Office Unified Model. *Quart. J. Roy. Meteorol. Soc.*, **125**, 1607-1636.

TEST AND IMPROVEMENTS OF GCM CLOUD PARAMETERIZATION USING THE CCCMA SCM WITH SHEBA DATASET

Q. Fu[1], J. Yuan[1], and N. McFarlane[2]

[1]Department of Atmospheric Sciences, University of Washington, Seattle, Washington, USA
[2]Canadian Center for Climate Modeling and Analysis, Victoria, British Columbia, Canada

1. INTRODUCTION

Cloud feedbacks, particularly in the Arctic region, represent one of the major uncertainties in global climate model (GCM) predictions of future climate change (e.g., *Tao et al.* 1996; *Houghton* 2001). The Surface Heat Budget of the Arctic Ocean (SHEBA) field project from the late of 1997 to the early of 1999 at the Arctic ocean ice pack provides an integrated observational dataset to improve our understanding of the Arctic cloud processes (*Uttal et al.* 2002). In this study, we apply the current version of the Canadian Center for Climate Modeling and Analysis (CCCMa) single-column model (SCM) (*Lohmann et al.* 1999) to the SHEBA observational year to test and improve the GCM cloud parameterizations in the Arctic region.

2. MODEL DESCRIPTION

The CCCMA SCM (CSCM) used in this study is adapted from the second generation CCCMA GCM. It predicts horizontal wind components, temperature, water vapor and total condensed water. The turbulence scheme contains a prognostic equation for the turbulent kinetic energy (TKE) [*Abdella and McFarlane* 1997]. Other second-order quantities are determined diagnostically through a parameterization of the third-order moments based on a convective mass-flux argument. Cumulus clouds are represented by a bulk model including the effects of entrainment and detrainment on the updraft and downdraft convective mass fluxes [*Zhang and McFarlane* 1995]. The radiation code is based on two-stream solutions of the radiative transfer equation with six spectral intervals in the infrared spectrum and two in the solar spectrum. Gaseous absorption due to water vapor, CO_2, O_3, CH_4, N_2O, and CFCs is included.

Two kinds of cloud schemes are available as options in this CSCM. One is an explicit cloud scheme, another is statistical cloud scheme. The explicit cloud scheme is used in this study, which is described in detail by *Lohmann and Roecker* (1996) and *Lohmann et al.* (1999). It has prognostic variables for LWC (q_l) and IWC (q_i) and uses an explicit approach for condensation and cloud cover based on *Sundqvist* (1978).

Corresponding author's address: Qiang Fu, Dept. of Atmospheric Sciences, Univ. of Washington, Seattle, WA 98195, USA. Email: qfu@atmos.washington.edu.

3. DATA

The data needed to drive the CSCM are large scale forcing data and surface observations. Also to test the model's ability to predict properties of clouds based on a realistic atmospheric state, we use the technique of nudging for horizontal velocities, temperature and water vapor profiles toward the profiles obtained from objective analysis of observed data. The simulated period is from November 1997 to September 1998.

The forcing data is produced by the ECMWF's reanalysis hourly output including the total adiabatic tendency profiles of horizontal velocities, temperature and water vapor for the SHEBA site (Beesley et al. 2000). The surface data is also based on ECMWF's reanalysis hourly output. We used the surface temperature and surface relative humidity.

The observational data at the SHEBA site which we use to validate model's prediction for cloud cover, liquid water path and ice water path, are derived from a combined ground-based cloud radar, lidar, microwave radiometer retrievals (Shupe et al. 2001). The surface precipitation data are provided by Moritz (personal communication, 2000) based on a nipher shielded snow gauge system. We also used the SHEBA rawinsonde data in this study.

4. NUDGING USING ECMWF REANALYSIS H_2O PPOFILES WITH MODIFICATION

The nudging technique we used in the CSCM is based on Newtonian relaxation (*Jeuken et al.* 1996). We relax the model predicted horizontal velocities toward ECMWF's reanalysis data for given relaxation time, and relax temperature and water vapor toward ECMWF's reanalysis profiles based on the relaxation time associated with mean horizontal velocities.

Figure 1a shows that the simulated total cloud cover is much lower than the radar observations. The simulated precipitation is also too low compared to the SHEBA surface observations (Fig.1b). Note that the simulated surface precipitation is largely determined by the large-scale forcing and nudging but not sensitive to the detail microphysical processes.

Due to the predicted cloud cover and surface precipitation being much lower than observed, microphysics parameterizations can not be evaluated by comparing observed and predicted cloud liquid and ice water paths. Therefore our first focus is to attempt to improve the prediction of the total cloud and precipitation for the SHEBA year.

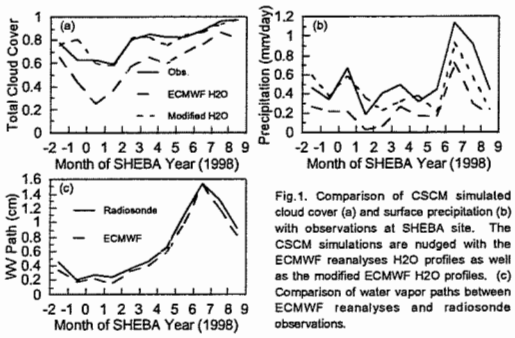

Fig.1. Comparison of CSCM simulated cloud cover (a) and surface precipitation (b) with observations at SHEBA site. The CSCM simulations are nudged with the ECMWF reanalyses H2O profiles as well as the modified ECMWF H2O profiles. (c) Comparison of water vapor paths between ECMWF reanalyses and radiosonde observations.

An obvious possibility for the underprediction of the total cloud cover is that the parameterization, which was developed in middle latitude or tropic region simulations, is not suitable in the Arctic Region. However, because we use the nudging based on ECMWF's profiles for temperature and water vapor mixing ratio, underprediction of both cloud cover and surface precipitation could likely be due to the humidity profiles used for nudging being dryer than observed atmosphere. Figure 1c shows that the ECMWF reanalysis underestimates the water vapor path systematically during the SHEBA year.

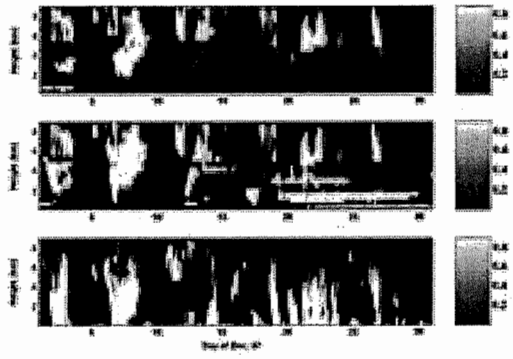

Fig.2. Comparison of simulated cloud cover with radar observations (lower panel) in the December of 1997 at the SHEBA site. The upper and middle panels are CSCM simulations using the original and modified ECMWF reanalyses H_2O profiles for nudging, respectively.

Since radiosonde observations were only carried out once every 6 or 12 hours at the SHEBA site, we cannot directly use these observations to nudge the CSCM. By considering that the model predicted cloud cover is determined by the relative humidity, we develop the following scheme to scale the ECMWF reanalyses H_2O profiles using the radiosonde data (*Yuan and Fu* 2002): (i) Calculate the relative humidity with respect to liquid water based on ECMWF's data and radiosonde measurements separately and obtain their ratio for each level at time when the radiosonde measurement is available; (ii) linearly interpolate the ratio to those times when sonde data is not available; (iii) use those ratios to scale the ECMWF's water vapor mixing ratio at each time and each level.

Also shown in Fig. 1a&b are the CSCM simulated cloud cover and precipitation using the nudging with modified ECMWF H_2O profiles, which agree with observations well. These results indicate that the cloud cover parameterization used in CSCM is valid in the Arctic region, and the ECMWF large-scale forcing along with the nudging is also justified. Figure 2 shows the comparison of the cloud cover as a function of time and height for the Dec. 1997 between the simulations and radar observations.

Now we can evaluate the microphysical processes grounded on reasonable cloud cover and precipitation simulations. In the following, for the CSCM simulations with nudging, the modified ECMWF H_2O profiles are always used. Note that in some sensitivity studies, the CSCM is also run without nudging.

5. TESTING & IMPROVING GCM MICROPHYSICS PARAMETERIZATIONS

The cloud microphysics parameterizations used in this CSCM (*Levkov et al.* 1992; *Beheng* 1994; *Lohmann and Roeckner* 1996; *Lohmann et al.* 1999) are the same as those used in current CCCMa GCM. It is found that the cloud liquid and ice water paths simulated from the CSCM are much larger than those derived from observations during the SHEBA year. In this section, the parameterizations of microphysical processes are tested and improved by comparing CSCM simulations and observations.

5.1 Accretions

The accretional growth of rain (collecting cloud drops) and snow (riming and collecting ice crystals) are parameterized in term of q_l, q_i, and rain (q_r) and snow (q_s) mixing ratios (*Lohmann and Roecker* 1996) where q_r and q_s are not prognostic variables. *Lohmann and Roecher* (1996) and *Lohmann* et al. (1999) used $q_r=F_r/(\rho\Delta z/\Delta t)$ and $q_s=F_s/(\rho\Delta z/\Delta t)$ where F_r and F_s are the rain and snow precipitation fluxes, ρ the air density, and Δz and Δt are the model layer-thickness and time step, respectively. These relations between precipitating mixing ratios and fluxes have little physical bases, and obviously depend on the vertical resolution. In this scheme, the change of the model vertical resolution is equivalent to the change of the mean terminal velocities of rain and snow.

Figure 3 shows the CSCM simulated liquid water path (LWP) and ice water path (IWP) using the original microphysics parameterizations, which are extremely sensitive to the vertical resolutions used in the model.

Here we modify the paramterizations by relating the accretional growth rates directly to the product of cloud water mixing ratios and precipitation fluxes following *Lekov et al.* (1992), *Rotstayn* (1997) and *Lin et al.* (1983). Consequently we have the equation for growth of precipitation flux in the form

$$dF/dz = a(q_x) + bFq_x$$

where F is the precipitation flux, $a(q_x)$ is the increase of flux caused by either autoconversion or aggregation, q_x is the cloud water content, and the second term of the right hand side accounts for the

accretion effect. The above equation can be solved analytically to obtain

$$F_1 = F_0 exp(bq_x\Delta z) + a(q_x)[exp(bq_x\Delta z)-1]/(bq_x)$$

where F_1 and F_0 are the fluxes at the top and bottom of the layer, respectively. In this way, for the first time, we explicitly consider the accumulation effect of accretion through each model layer, i.e., the accretion between the cloud water and the precipitations generated in the same model layer.

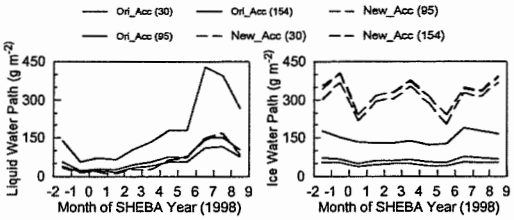

Fig.3. Sensitivities of CSCM simulations of LWP and IWP to the model vertical resolutions. The number of layers used are 30 (default), 95, and 154. The results in solid and dashed lines are based on original and new parameterizations of accretion processes, respectively. In those simulations we release the nudging on water vapor and directly use the ECMWF temperature in order to isolate the layer effects. Using the original scheme, the simulated LWP and IWP decrease with the increase of the vertical resolution.

Also shown in Fig.3 are the CSCM simulations with our new parameterizations of accretion processes, which are not sensitive to the vertical resolutions. It should be noted that without considering the accumulation effects, the simulated LWP and IWP will still depend on the vertical resolutions, which will overestimate the LWP and IWP by more than 25% for typical GCM vertical resolutions.

5.2 Ice Nucleation Number Concentration

Ice nucleation number concentration in the atmosphere is not well known, which introduces large uncertainties in the GCM simulations of clouds. In the CSCM, the rate for which new ice crystals nucleate is given by *Lohmann et al.* (1999) in the form

$$Q_{nuci} = 3\rho q_i^{dep} /(4\pi\rho_i r_{iv}^3 \Delta t)$$

where ρ_i is the ice crystal density, and r_{iv} is the mean ice crystal volume radius. Note that most of GCMs and cloud resolving models use the parameterization of the number concentration of ice nuclei based on observations (Meyers et al. 1992) instead.

Figure 4 shows the sensitivity of CSCM simulations to the ice nucleation number concentrations. It is suggested that using the parameterization by Meyers et al. (1992) reduces the simulated IWP by more than a factor of 2 as compared to using *Lohmann et al.* (1999). This is because the original parameterization produces a much larger number of ice nuclei and then much more ice particles with smaller sizes, which is less efficient to be converted to snow through the aggregation process. The comparison of simulated IWP with observations seems support the parameterization developed by *Meyers et al.* (1992).

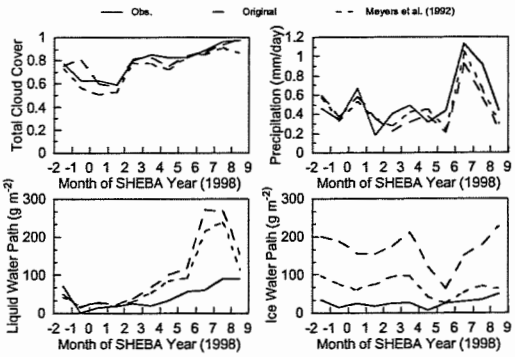

Fig.4. Sensitivities of CSCM simulations to the parameterization of ice nucleation number concentration. The original parameterization follows *Lohmann et al.* (1999). The CSCM is nudged with the modified ECMWF reanalyses profiles.

5.3 Autoconversion

In CSCM, the parameterization of autoconversion process is based on *Beheng* (1994), which is highly nonlinear function of in-cloud liquid water content ($\sim q_l^{4.7}$). *Pincus and Klein* (2000) pointed out that this kind of nonlinear parameterizations based on mean cloud water content would underestimate the autoconversion rate due to the cloud sub-grid scale variability. To consider the effect of cloud horizontal inhomogeneity, we can express the autoconversion rate in the form

$$Q_{aut} = R_{aut} Q_{aut}(\overline{q}_l)$$

where $\overline{q}_l$ is the grid mean in-cloud water content. By applying a Gaussian distribution function to *Beheng* (1994)'s parameterizations, we can derive a R_{aut} in the form

$$R_{aut} = -40C^3 + 89C^2 - 93C + 47$$

where C is the cloud fraction.

With consideration of the sub-grid variability effect on the autoconversion parameterization, the simulated LWP is reduced by about 10% in July and August during the SHEBA year. But it has little effects on LWP in other months.

In summary, Fig.5 shows the CSCM simulation with the original microphysics parameterizations, and that with the modified parameterizations including the new accretion treatment, ice nucleation number concentration from *Meyers et al.* (1992), and the consideration of inhomogeneity effect on autoconversion. Observational results are also shown for the comparison purpose. The simulated IWP with modified microphysics parameterizations agree with the observations within observational uncertainties (*Shupe*, personal communication, 2002). The simulated LWP is also greatly improved. But it is noted that there still exist significant discrepancies between the simulated LWP and observation in July and August. Further efforts are under way to understand these discrepancies.

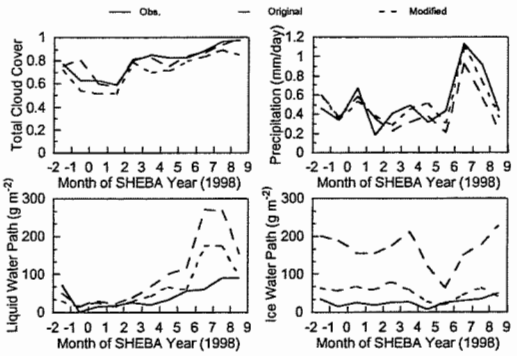

Fig.5. Comparison of CSCM simulations with observations. Here shown are the CSCM results using the original microphysics parameterization and using modified microphysics parameterizations including accretion processes, ice nucleation number concentration, and cloud horizontal inhomogeneity effect on auroconversion. The CSCM is nudged with the modified ECMWF reanalyses profiles.

6. SIMMARY

In this study, a SCM along with the integrated SHEBA data is used to test and improve GCM cloud microphysics parameterizations. Results of the SHEBA annual simulation using the CSCM are discussed.

We find that the ECMWF reanalyses water vapor profiles at the SHEBA site are too dry compared with observations, which are not suitable to nudge the SCM simulations. We develop a simple scheme to adjust the ECMWF water vapor profiles with radiosonde observations. The CSCM simulations based on the nudging using the modified water vapor profiles lead to reasonable predictions of cloud cover and surface precipitation. But the simulated LWP and IWP are much larger than those derived from observations.

It is found that in the CSCM there are several unphysical and inconsistent treatments related to the accretion processes. We modify the parameterizations of these processes where we consider the accumulation effect of accretion in each model layer so that the parameterizations are independent of model vertical resolution.

By comparing the original treatment of ice nucleation number concentration in the CSCM with that developed by *Meyers et al.* 1992, we find that the original scheme produces much larger ice nucleation number concentration. By replacing the original treatment with *Meyers et al.* [1992], the CSCM produces much smaller IWP, which is closer to the observations.

It is also found that that the CSCM uses *Beheng* [1994]'s parameterization for autoconversion, which is highly nonlinear to the in-cloud liquid water content. We develop a simple parameterizations to consider the cloud inhomogeneity effect on the autoconversion.

With modified cloud microphysics parameterizations including improved treatments for accretion processes, ice nucleation number concentration, and autoconversion, the CSCM simulated LWP and IWP are much improved as compared with observations. Further research efforts are under way to understand the remaining discrepancies between model and observations.

7. ACKNOWLEDGEMENTS

This study is supported by NSF Grant OPP-0084259, and partly by the Canadian CCAF fund, and DOE Grant (Task Order 355043-AQ5 under Master Agreement 325630-AN4).

8. REFERENCES

Abdella, K., and N. McFarlane, A new second-order turbulence closure scheme for the planetary boundary layer, *J. Atmos. Sci.*, **54**, 1850–1867,1997.

Beesley, T. A., C. S. Bretherton, C. Jakob, E. L Andreas, J. M. Intrieri, and T. A. Uttal, A comparison of the ECMWF forecast model with observations at SHEBA, *J. Geophys. Res.*, **105**, 12337-12349, 2000.

Beheng, K. D., A parameterization of warm cloud microphysical conversion processes, *Atmos. Res.*, **33**, 193–206, 1994.

Bretherton, C. S., S. R. de Roode, C. Jakob, E. L Andreas, J. Intrieri, R. E. Moritz, and P. O. G. Persson, A comparison of the ECMWF forecast model with observations over the annual cycle at SHEBA, *J. Geophys. Res.*, (in press).

Houghton, J.T. et al. (eds), *Climate change 2001: The scientific basis*, Cambridge University Press, London, 2001.

Jeuken, A. B. M., P. C. Siegmund, L. C. Heijboer, J. Feichter, and L. Bengtsson, On the potential of assimilating meteoro-logical analyses in a global climate model for the purpose of model validation, *J. Geophys. Res.*, **101**, 16 939–16 950, 1996.

Levkov, L., B. Rockel, H. Kapitza, and E. Raschke, 3D mesoscale numerical studies of cirrus and stratus clouds by their time and space evolution, *Beitr. Phys. Atmos.*, **65**, 35–57, 1992.

Lin, Yuh-Lang, Richard D. Farley, and Harold D. Orville, Bulk Parameterization of the Snow Field in a Cloud Model, *J. Appl Meteorol*, **22**, 1065–1092, 1983.

Lohmann, U., and E. Roeckner, Design and performance of a new cloud microphysics scheme developed for the ECHAM general circulation model, *Clim. Dynamics*, **12**, 557-572, 1996.

Lohmann, U., N. McFarlane, L. Levkov, K. Abdella, and F. Albers, Comparing Different Cloud Schemes of a Single Column Model by Using Mesoscale Forcing and Nudging Technique, *J. Clim.*, **12**, 438–461, 1999.

Moritz, R. E., and D. K. Perovich (eds), Surface Heat Budget of the Arctic Ocean Science Plan, *ARCSS/OAII Report Number 5, University of Washington, Seattle*, 64pp, 1996

Pincus, Robert, and Stephen A. Klein, Unresolved spatial variability and microphysical process rates in large-scale models, *J. Geophys. Res.*, **105**, 27059-27065, 2000.

Randall, David A., Kuan-man Xu, Richard J.C. Somerville, Sam Iacobellis, Single-Column Models and Cloud Ensemble Models as Links between Observations and Climate Models, *J. Clim.*, **9**, 1683–1697, 1996.

Rotstayn, Leon D., A physically based scheme for the treatment of stratiform clouds and precipitation in large-scale models Part I: Description and evaluation of the microphysical processes, *Q. J. R. Meteorol. Soc.*, **123**, 1227-1282, 1997.

Shupe, M.D., T. Uttal, S.Y. Matrosov, A.S. Frisch, Cloud Water Contents and Hydrometeor Sizes During the FIRE-Arctic Clouds Experiment, *J. Geophys. Res.*, **106**, 15,015-15,028, 2001.

Sundqvist, H., A parameterization scheme for non-convective condensation including prediction of cloud water content, *Q. J. R. Meteorol. Soc.*, **104**, 677–690,1978.

Tao, X., J.E. Walsh, and W.L. Chapman, 1996: An assessment of global climate model simulations of arctic air temperatures. *J. Climate*, **9**, 1060-1076.

Uttal, T., et al., The surface Heat Budget of the Arctic Ocean, *Bull. Am. Meteorol. Soc.*, **83**, 255-275, 2002.

Zhang, G. J., and N. A. McFarlane, Sensitivity of climate simulations to the parameterization of cumulus convection in the Canadian Climate Centre General Circulation Model, *Atmos.–Ocean*, **33**, 407–446, 1995.

MODEL DYNAMIC AND MICROPHYSICAL VERIFICATION OF THE 13-14 DECEMBER 2001 IMPROVE 2 CASE

M.F. Garvert[1], C. P. Woods[1], B. Colle[2], C.F. Mass[1], and, P.V. Hobbs[1]

[1]Department of Atmospheric Sciences, University of Washington, Seattle, WA, 98195, USA
[2]Institute for Terrestrial and Planetary Atmospheres, State University of NY, Stony Brook, NY, 11794, USA

1. INTRODUCTION

While numerical models have become increasingly capable of simulating synoptic and mesoscale features associated with baroclinic waves, quantitative precipitation forecasts (QPF) generally have not shown corresponding improvements due, in part, to deficiencies in the bulk microphysical parameterization (BMP) schemes used in the models.

The IMPROVE-2 field experiment, which took place in November and December 2001 over the Oregon Cascades, collected a unique set of observations that provide a detailed depiction of the thermodynamic and kinematic structure of many precipitation events (Stoelinga et al. 2003). Comprehensive microphysical data were also obtained, thereby providing an opportunity to diagnose the representations in the BMP of important microphysical processes.

An overview of the goals, facilities, mode of operation, and case studies for IMPROVE is given by Stoelinga et al. (2003). Papers in an upcoming special issue of the *Journal of the Atmospheric Sciences* present the synoptic and mesoscale evolution, precipitation processes, mesoscale simulations, and a radar analysis for the 13–14 December 2001 case study (Garvert et al. 2005a; Woods et al. 2005; Colle et al. 2005; Houze and Medina 2005). This paper presents a summary of the results given by Garvert et al. 2005b, which compares the MM5 microphysical fields and processes with detailed airborne measurements obtained during a period of heavy precipitation from 2200 UTC 13 December 2001 through 0130 UTC 14 December 2001. For detailed information on the IMPROVE project and related papers, the reader is referred to *http://improve.atmos.washington.edu*

2. METHODOLOGY

The IMPROVE-2 study area was positioned over the central Oregon Cascades (Fig. 1a). The 13-14 December 2001 storm system that moved across the Oregon Cascades was characterized by the passage of a mid-level baroclinic zone followed by a cold front. A broad area of heavy precipitation was associated with synoptic-scale lifting ahead of the mid-level baroclinic zone that interacted with low-level orographic forcing to produce heavy precipitation over the elevated terrain of the Cascades [see Fig. 15 of Garvert et al. (2005a)]. The wind field was relatively steady state during the event, with strong (30-40 m s^{-1}), stable southwesterly flow below 4 km. The relatively uniform precipitation and low-level wind fields simplified the microphysical analysis and the comparisons of the model with observations.

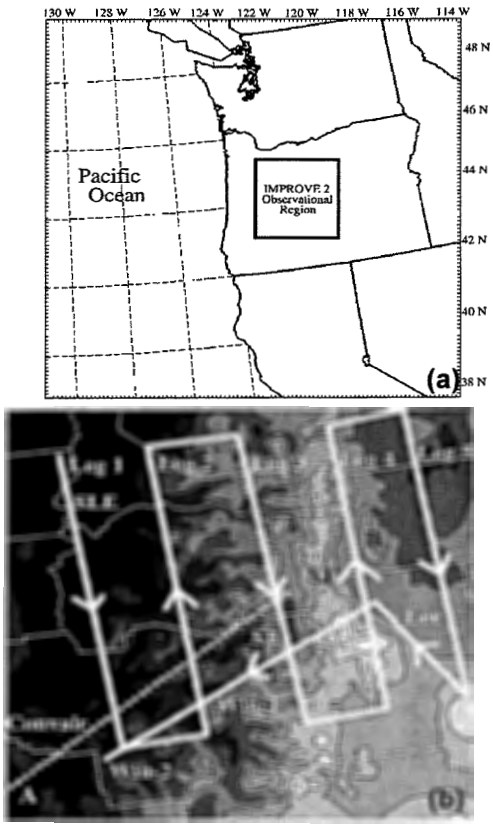

Figure 1. (a) Map of the Pacific Northwest with the study area delineated by the box. (b) P-3 (solid white) and Conviar-580 (dotted white line) flight tracks plotted over the terrain of the study area. Terrain is contoured every 300m; the intensity of shading decreases with increasing height.

During 13-14 December 2001, two research aircraft (the University of Washington's (UW) Convair-580 and NOAA's P-3) collected a variety of basic state and microphysical data. The UW Convair-580 flew vertically stacked horizontal flight legs and gathered

Corresponding author's address: Matthew Garvert, University of Washington Seattle, WA, 98195,USA; E-Mail: mgarvert@atmos.washington.edu

microphysical data at a number of altitudes, thereby providing detailed depictions of precipitation growth within the storm (Fig 1b). The NOAA P-3 performed a 'lawnmower' flight track, consisting of five north-south (N-S) flight legs at various elevations beginning over the Willamette Valley and concluding downwind of the Oregon Cascade Mountains. The P-3 also performed a cross-mountain transect at minimum allowable altitudes, providing detailed measurements in the lee of the mountain ("Lee" in Fig. 1b), above the windward slopes ("Win-1" in Fig. 1b), and above the windward foothills ("Win-2" in Fig. 1b).

Here we will compare the microphysical measurements collected by the two aircraft with those simulated by the Penn State/National Center for Atmospheric Research (PSU-NCAR) mesoscale model (MM5) version 3.5. A 1.33-km MM5 simulation was found to accurately simulate most of the synoptic and mesoscale structures associated with the 13-14 December 2001 system (Garvert et al 2005a). Yet, despite the relatively accurate portrayal of the larger scale dynamics of the system, significant QPF errors were present in the simulation, including pronounced overpredictions of precipitation amounts over the windward and immediate leeward slopes of the Oregon Cascades. The overprediction was most pronounced during the passage of the stratiform precipitation band (see Fig. 16 in Garvert et al. 2005).

3. MICROPHYSICAL COMPARISONS

3.1 Cloud Liquid Water Comparisons

Table 1 shows the cloud liquid water (CLW) measured by a Johnson-Williams (JW) probe aboard the P-3 and the modeled CLW averaged along the five north-south flight legs of the P-3. The first P-3 leg was flown at a height of 2 km above the relatively flat terrain of the Willamette Valley (Fig 1b). Along this flight leg vertical velocities were <150 cm s^{-1} [see Fig. 12 of Garvert et al. (2005a)]. Cloud liquid water measurements varied between 0-0.3 g m^{-3}, with an average along the leg of 0.12 g m^{-3}. Both the 4-km and 1.33-km resolution model simulations overpredicted CLW with average values of 0.25 g m^{-3} along the flight leg.

Variations in the vertical velocity were most pronounced during the second P-3 leg, which was flown at 2.5 km over the windward Cascades slopes. Radar and in-situ observations indicated accretional processes were occurring along the leg as the snow became rimed with supercooled CLW (Houze and Medina 2005, Garvert 2005b). Table 1 shows that the 1.33-km resolution simulation overpredicted the amount of CLW by almost a factor of two along the leg. However, the 4-km resolution model simulation accurately reproduced the measured CLW, with a leg average value of 0.25 g m^{-3}.

A north-south cross-section of CLW, vertical velocity, and underlying terrain for leg 2 is shown in Fig. 2. Measured upward vertical velocities were located where strong low-level southerly winds

Average CLW values in g m^{-3} along P-3 Legs				
P3	Height (km)	Measured	MM5 4-km	MM5 1.33-km
Leg 1	2.0	0.12	0.25	0.25
Leg 2	2.5	0.24	0.25	0.41
Leg 3	3.5	0.18	0.07	0.12
Leg 4	4.0	0.10	0.01	0.02
Leg 5	3.0	0.02	0.01	0.09

Table 1. Average measured, MM5 4-km resolution forecasted and MM5 1.33-km resolution forecasted CLW values for the 5 legs of the P3 flight track.

impinged on the higher terrain of the Cascade foothills. Measurements along leg 2 indicated that the CLW amounts were closely related to the variations in vertical velocity, where areas of high (low) CLW coincided with or were just upwind of upward (downward) vertical air motions. In many areas along leg 2, the 1.33-km resolution simulation appeared to depict correctly the perturbations in vertical air motions, yet it drastically overpredicted the amount of CLW; this suggests a possible error within the BMP. The 4-km resolution model run better simulated the amount of CLW, but it underpredicted the amplitude of vertical velocity forcings. This indicates the lower CLW amounts from the 4-km simulation were a result of unrealistically weak vertical motions in the model.

Leg 3 of the P-3 was flown at a height of 3.5 km about 20 km west of the Cascade crest. Substantial variations in vertical velocities and CLW were measured, although the amplitudes of the fluctuations were much less than for leg 2. The 1.33-km resolution model run slightly underpredicted the CLW along the crest, with average values of ~0.12 g m^{-3}, compared to the measured average of 0.18 g m^{-3} (Table 1). The underprediction problem was worse in the 4-km

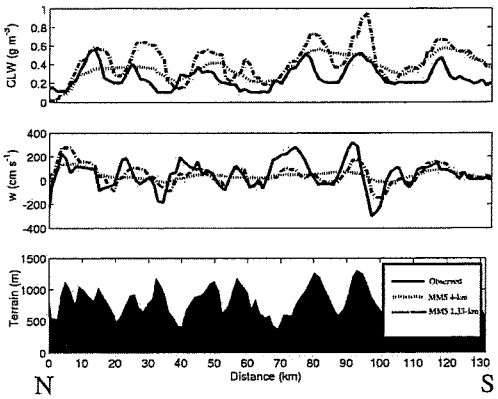

Figure 2. Comparison of cloud liquid water (CLW) and vertical velocity (w) for leg 2 of the P-3 flight track. The solid line shows the measured values. The dotted lines are values from the 4-km resolution MM5 simulation and the dashed lines are from the 1.33-km resolution MM5 simulation. The last panel shows the elevation of the underlying terrain.

resolution simulation, with the model CLW values significantly lower than measured.

Over the lee slopes of the Cascades, legs 4 and 5 of the P-3 were flown at heights of 4 and 3 km, respectively (Fig. 5). Measured CLW values were much lower than those in the earlier legs, averaging <0.15 g m^{-3}. Along leg 4, both the 4-km and 1.33-km resolution model simulations showed almost no CLW, which is a significant. Along the final P-3 flight leg (leg 5), which was flown on the lee side of the Cascade Range, very little CLW was measured. The 4-km resolution model run accurately predicted low CLW (~0.01 g m^{-3}), while the 1.33 km resolution model run overpredicted CLW, averaging 0.09 g m^{-3} over the leg.

3.2 Ice Verification

The measured mass concentrations and size distributions of snow particles obtained in the stacked flight legs of the Convair-580 between 4.9 km and 6 km in the upper-level altostratus cloud were compared with the model simulations for the three horizontal flight legs (legs 1, 2, and 3). The measured mass concentrations were determined using the method described by Woods et al. (2005). The measured snow mass concentrations increased from an average of 0.12 g m^{-3} along the highest leg flown at 6 km to 0.25 g m^{-3} as the Convair descended to 4.9 km (Table 2). In comparison, the model simulations of snow mass concentrations were 2 to 3 times larger than the measured values at these levels. Despite the ability of the model to accurately predict the correct region of enhanced depositional snow growth aloft (see Fig. 3 of Garvert et al 2005b), the failure of the model to correctly simulate the snow mass concentrations resulted in excessive spillover of snow to the lee of the Cascades.

A comparison of modeled versus measured snow particle size distribution also exposed potential errors in the model's BMP. The model BMP uses a slope (λ_s) and a temperature dependent ordinate intercept ($N_{0,S}$) to represent the snow size distribution. The motivation behind a temperature-dependent value for N_{os} is to parameterize the effects of aggregation (Thompson 2004). Thus, in a stably stratified environment, as temperature increases with

Convair	Height (km)	q_s Meas.	q_s Mod	q_g Meas.	q_g Mod
Leg 1	6.0	0.12	0.33	0.00	0.00
Leg 2	5.4	0.16	0.45	0.00	0.00
Leg 3	4.9	0.25	0.55	0.00	0.00
P3	**Height (km)**	**q_s Obs**	**q_s Mod**	**q_g Obs**	**q_g Mod**
Lee	4.1	0.06	0.22	0.00	0.00
Win 1	4.1	0.09	0.73	0.31	0.08
Win 2	3.2	0.13	0.60	0.15	0.18

Table2. Comparison between measured and modeled mass concentrations (in g m^{-3}) of snow (q_s) and graupel (q_g) along the Convair and P-3 flight tracks. See Fig. 1b for position of flight tracks.

Convair	Height (km)	$N_{o,s}$ Meas.	$N_{o,s}$ Mod	λ_s Meas.	λ_s Mod
Leg 1	6.0	2.7e7	2.3e7	2670	2251
Leg 2	5.4	2.4e7	1.5e7	2309	2075
Leg 3	4.9	4.9e7	1.0e7	2555	1567

Table 3. Comparison of measured and modeled fitted parameters for the size spectra of particles for snow along the Convair flight track. Values of the slope intercept ($N_{o,s}$ in m^{-4}) and the slope values (λ_s in m^{-1}) for snow are given. See Fig. 1b for position of Convair flight track.

decreasing height the value of N_{os} decreases. Along the UW Convair-580 flight route, snow size spectra were determined using measurements described by Woods et al. (2005). Interestingly, the measured values of N_{os} increased as the temperature increased from -20 to -17 °C between the first Convair flight leg at 6 km and the third horizontal leg at 4.9 km (Table 3). In contrast, the model predicts decreasing N_{os} values with increasing temperature. Total ice particle (including both snow and graupel species) size spectra along the P-3 cross-mountain transect [see Fig. 12 of Woods et al. (2005)], which was flown below the Convair at 3.2 to 4 km, show a decrease in N_{os} compared to those spectra measured aloft by the Convair, which is consistent with the model assumption of a temperature dependent N_{os}. These findings indicate that the value of N_{os} depends on factors other than temperature; if N_{os} is assumed to depend on temperature alone, these effects there is a misrepresentation of snow size spectra at low temperatures.

In the MM5, the slope of the snow particle size distribution curve is defined by the variable λ_s (Reisner 1998). While the model accurately produced a decrease in the value of λ_s with decreasing altitude (i.e., increasing temperature) (Table 3), the combination of erroneous values for N_{os} and λ_s results in marked discrepancies between the measured size distribution curves and those simulated by the model (Fig. 4). The measured number distributions are primarily exponential, which supports the assumption of a Marshall-Palmer distribution for snow. However, direct comparison of the measured versus modeled size spectra aloft shows an underprediction of the concentration of small snow crystals and a significant overprediction for snow particles >1.5 mm in diameter.

Comparisons of snow mass concentrations measured at lower levels aboard the P-3 during its cross-mountain transect and the model simulations are shown in Fig. 3 and Table 2. Above the lee slopes, the predominant observed precipitation type was snow, with only minimal amounts of graupel. The model overpredicted the amount of snow in this area, particularly close to the crest where strong downward vertical motions were present (Fig. 3). Over the windward Cascade slopes (labeled Win 1 in Table 2), the model also overpredicted the amount of snow, while underpredicting the amount of graupel. As the P-3 progressed to the windward foothills and descended to 3.2 km, the model continued to

overpredict snow amounts, but provided a relatively accurate portrayal of the graupel field.

4. CONCLUSION

The results in this paper suggest that the excessive mass concentrations of snow aloft in the model simulations contributed to the overprediction of precipitation to the immediate lee of the Cascades. The excessive snow may have been due to errors in the representation of the depositional growth of snow and sensitivity to the temperature dependent slope intercept used in the model. The transition from a model overprediction of CLW over the windward slopes to an underprediction over the crest and lee, indicates the possibility that an excessive amount of snow was produced in the model at the expense of liquid water near the crest. An overprediction of cloud liquid water amounts over the lower windward slopes indicated that QPF errors in these regions might be related to the BMP.

5. REFERENCES

Colle, M. F. Garvert, J. B. Wolfe, C. F. Mass, and P. V. Hobbs, 2005: Microphysical budgets and sensitivity studies for the 13-14 December 2001 IMPROVE-2 Event. *J. Atmos. Sci.* (IMPROVE Special Issue).

Garvert, M. F., B. A. Colle, and C. F. Mass, 2005a: Synoptic and mesoscale evolution of the 13-14 December 2001 IMPROVE II storm system and comparison with a mesoscale model simulation. *J. Atmos. Sci.* (IMPROVE Special Issue).

Garvert, M. F., C. P. Woods, B. Colle, C. F. Mass, and P.V. Hobbs, 2005b: Comparison of MM5 Model Simulations of Clouds and Precipitation with Observations for the 13-14 December 2001 IMPROVE-2 Event. *J. Atmos. Sci.* (IMPROVE Special Issue).

Houze, R. A., and S. Medina, 2005: Turbulence as a mechanism for orographic precipitation enhancement. *J. Atmos. Sci.* (IMPROVE Special Issue).

Reisner, J., R. M. Rasmussen and R..T. Bruintjes, 1998Explicit forecasting of supercooled liquid water in winter storms using the MM5 mesoscale model.*Quart. J. Roy. Meteor.* , **124** ,1071-1107.

Stoelinga, M., P. V. Hobbs, C. F.Mass, J. D.Locatelli, B. A. Colle, and co-authors, 2003: Improvement of microphysical parameterizations through observational verification experiments (IMPROVE). *Bull. Amer. Meteor. Soc.*, **84**, 1807-1826.

Thompson, G., R. M., Rasmussen, and K. Manning, 2004: Explicit forecasts of winter precipitation using an improved bulk microphysics scheme. Part I: Description and Sensitivity Analysis. *Mon Wea. Rev.* **132**, 519-542.

Woods, C. P., M. T. Stoelinga, J. D. Locatelli, and P. V. Hobbs, 2005: Cloud structures, microphysical processes and synergistic interaction between frontal and orographic forcing of precipitation during the December 13, 2001 IMPROVE-2 event over the Oregon Cascades. *J. Atmos. Sci.* (IMPROVE Special Issue)

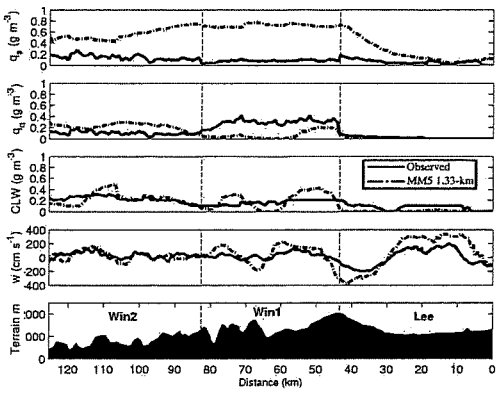

Figure 3. Snow (q_s), graupel (q_g), cloud liquid water (CLW), vertical velocity (w), and terrain along the P-3 flight track as depicted in Fig. 1b. The solid lines are the measurements and the dashed lines are values from the 1.33-km resolution MM5 simulation.

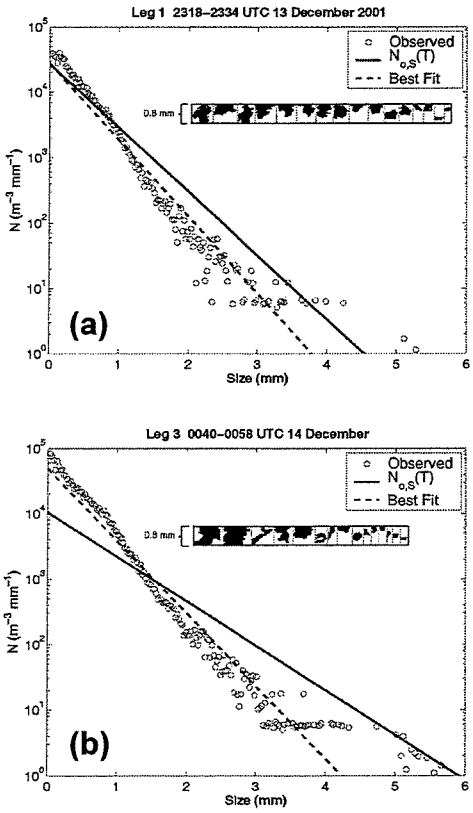

Figure 4. Measured and modeled number distributions of snow for (a) leg 1 and (b) leg 3 of Convair flight track. Circles are the measured distribution, dashed lines are best fit to the measurements, and solid lines are 1.33-km resolution MM5 distributions. Sample images of ice crystals from the in situ 2D-C probe are also shown.

RELATIONSHIP BETWEEN SOLAR RADIATIVE BIASES AND DEEP CONVECTION ANVIL DIMENSIONS

Francesca Di Giuseppe[a],[1] and Adrian Tompkins[b]

[a] ARPA Servizio IdroMeteorologico, Bologna, Italy
[b] European Centre for Medium–Range Weather Forecasts, Reading, RG2 9AX, UK

1. INTRODUCTION

This study focuses on the interaction between short-wave radiation and a field of tropical deep convective clouds generated using a cloud resolving model to assess the significance of three dimensional radiative transport effects. The comparisons of a three-dimensional (3D) solution with an independent column approximation approach (ICA) is used to quantify the bias due to unresolved sub-grid scale variability.

To document the evolution of radiative biases in a systematic manner, a series of cloud scenes generated by a cloud resolving model undergo modification by an idealized function, that allows the cirrus anvil coverage to be progressively enlarged without affecting the realism of the scene produced. In addition to offering controlled phase space investigation with a realistic complex cloud geometry, the method is also computationally efficient, since only one cloud resolving model integration is required to generate a complete series of cloud scenes.

The documented bias is then explained in term of two contributions: the *geometrical shading* effects of clouds at low sun angles and the true *3D effect* of photon scattering from the original path direction.

2. METHODOLOGY

2.1 Radiation model

The investigation uses the Monte Carlo code outlined by Scheirer and Macke (2001). A multi spectral band calculation is used, according to the K-distribution model of Fu and Liou (1992). Six bands cover the solar part of the spectrum (0.2-4 microns). Gaseous absorption for ozone, CO_2, CH_4,and N_2O is included as horizontally homogeneous. Layer mean water vapour and temperature values are obtained from the CRM, while above the CRM domain seven additional atmospheric levels are placed between 20 km to 100 km which are interpolated using tropical standard profiles (McClatchey et al., 1972). Rayleigh scattering is also included.

For each cloud scene two radiative calculations are conducted: a full 3D solution, and an independent column approach in which horizontal photon transport is inhibited. The ICA calculation is performed by imposing local periodic boundary conditions for each separate column of the CRM domain. Investigations are performed for a range of solar declination angles of 0, 30, 60 and 75 degrees.

2.2 Cloud scenes

Four CRM fields are used from the CRM simulation of Tompkins (2001), which are separated by 6 hours in time (denoted EXP6, EXP12, EXP18, EXP24). To control the anvil cloud coverage of the CRM scenes an idealized function, (F_w), is added to the mean total water, and then the cloud water is diagnosed at each grid-point assuming no supersaturation can exist. At each height the cloud water q_c (the sum of cloud ice q_i and liquid water q_l) at each grid point in the horizontal is given by

$$q_c = \underbrace{\mathcal{H}(z-z_1)\mathcal{H}(z_2-z)K sin^2\left(\frac{(z-z_1)}{(z_2-z_1)}\pi\right)}_{F_w} + q_v^{crm} + q_l^{crm} + q_i^{crm} - q_{sat}^{crm}, \quad (1)$$

where the superscript "crm" signifies an input quantity from the cloud resolving model field. The first term on the right is the idealized perturbation, which is a function of height only. In this term $\mathcal{H}$ is the Heavyside function, which restricts the idealized perturbation to the layer between $z = z_1$ and $z = z_2$. The constant K determines the maximum amplitude of the perturbation.

For each of the four CRM input scenes, an ensemble of 5 cloud scenes is generated by using a value of K ranging from $-1\frac{q_s(z)}{10}$ (a cloud cover

[1]Corresponding author address: F. Di Giuseppe
ARPA-SIM, Viale Silvani,6. I-40128 Bologna
e-mail: fdigiuseppe@smr.arpa.emr.it

reduction) through zero to $3\frac{q_s(z)}{10}$ (overcast) and imposing $z_1 = 8km$ and $z_2 = 12km$. The maximum cloud cover obtained with the application of eqn. 1 is 99.8% and the minimum is 3.3 %. The increase in the cloud cover is only due to an increase in the anvil dimension. The lower level shallow convection is untouched by the application of eqn. 1. This is evident from fig. 1 where the X-Y column integrated cloud water content and the projection on the Y=0 plane for four additional cloud scenes generated from the original CRM simulation (EXP24:0) are shown.

3. SOLAR BIAS

The ICA biases (defined as the ratio (3D-ICA)/ICA) are presented as a function of cloud cover and solar declination in figure 2, and are stated in terms of a relative bias in percent. The ICA bias is assumed in all cases to be zero for clear sky conditions. For all other points the bias is presented as a function of the mean cloud fraction for a given value of K, with error bars representing one standard deviation of the bias over the four input cases.

The first notable feature of the bias curves is the strong dependence on cloud cover. From a zero bias for a clear sky scene, the bias increases strongly with cloud cover to reach a maximum at a cloud cover of around 30% for reflectance. The maximum value of the bias is around 20% when the sun is overhead, but is larger when the sun is low, reaching as much as 46% for a SZA of 75 degrees. After the peak bias is reached, it begins to fall off more slowly with cloud cover, approaching zero as the scene becomes overcast. The transmission and absorption profiles are similar to those of the reflectance.

The obvious question that arises from fig 2 is why the bias peaks at a cloud cover of 30% rather than at higher or lower values. Since the bias is such a strong function of cloud cover, it is likely that cloud geometry is playing a role, and more specifically, the number, organization and interaction between clouds inside the domain. Varnai and Davies (1999) systematically itemized the variety of photon interaction mechanisms such as trapping and escape effects that can play a role in 3D radiative transfer. It is apparent from their analysis that two clouds of a certain dimension separated by a clear sky gap are likely to have a larger 3D effect than one single cloud of a size equivalent to their sum. Therefore, most of the 3D bias effects can be connected with the gap filling produced by the oblique photon trajectories.

With this systematic documentation of the bias as a function of cloud cover, it is possible to place the previous investigations using cloud resolving model input into context. Di Giuseppe and Tompkins (2003) documented biases of 16 % for a scene with cloud cover peaking at around 15% in the anvil region. On the other hand, the investigations of Barker et al. (1998, 1999); Fu et al. (2000) documented significantly smaller biases of less than 5 percent for scenes approaching overcast conditions, even for low sun angles. Here it is revealed that for a SZA of 60 degrees, the bias is also less than 5% when the cloud cover exceeds 80%.

Figure 2 highlights, therefore, the dangers of studying isolated scenes and generalizing these results to wider dynamical scenarios.

4. BIAS CORRECTION

The previous section established that the dependence of the ICA bias on the cloud cover is mainly controlled by the geometry ('shading') and a series of effects such as photon trapping and escape mechanisms that can not be appreciated in a 1D calculation. The former accounts for the fact that, even in the absence of scattering events, when the sun is low a photon will encounter a different cloud history to that assumed by a 1D calculation using a rescaled calculation with the sun overhead.

Unlike the complication of representing the consequences of scattering in a 1D framework, the 'shading' effect outlined above can be tackled relatively simply by the use of a variant of the ICA calculation, termed the "tilted ICA" or TICA, where each column of an ICA calculation is given the profile of cloud condensate and clear sky gaps encountered by a direct ray from the sun. Practically this is simply the equivalent of applying a lateral translation of the cloud field by a distance equivalent to the tangent of the solar declination angle. In this way, it is clear that at least in terms of this effect, a declining sun angle is no different radiatively than a physical translation of a cloud deck by vertical wind shear.

The TICA approximation is applied here to assess by how much, if any, it reduces the bias of the orthodox ICA methodology. The calculation is accomplished for all sun angles and cloud covers for the single case of EXP24. The general results as a function of cloud cover and sun angle are given in Fig. 3 where the percentage correction to the ICA bias by the TICA approach is shown. The TICA is able to correct the bias in reflection for a wide range of cloud covers. If we assume that the TICA

bias is entirely due to photon scattering, and the ICA bias is the consequence of both scattering and sun-angle geometry, then the ratio of the TICA to the ICA bias gives an estimate of the relevance of photon scattering to 1D biases. It is clear that the all the bias is due to scattering when the sun is overhead and therefore the TICA does not correct the 1D bias. However as the sun lowers, the contribution to the 1D biases due to the increase in cloud cover is evident. In this regime the TICA approach is able to correct for most of the bias. An important feature is that the TICA approach is able to correct for the increase in the cloudy area due to the three dimensional geometry showing also that the contribution due to the *true scattering* is limited and mostly independent of the cloud cover and the sun zenith angle. In fact, Fig. 3 shows that at 75 SZA angles the scattering effect accounts for around 5 % of the bias at a cloud cover of 30 %.

From these results it is clear that the most of the contribution to the ICA bias comes from the inexact cloud cover estimation performed by a 1D radiative calculation, when in presence of broken clouds. In a simple one dimensional calculation the cloud surface that interact with the radiation is underestimated. The error produced increases as the sun lowered and it will be maximum when the number of clouds (and thus of gaps) is maximum!

5. CONCLUSIONS

By systematically examining the relation of the solar bias in deep convective regimes to the anvil cloud coverage it is found that the bias in scene albedo can reach as much as 22 % when the sun is over head and 46% at low sun angles. This maximum bias is attained at cirrus anvil cloud cover of approximately 30 to 40%. The bias is an asymmetrical function of cloud cover. For cloud cover of around 15% the bias is half its maximum value, while it is limited for coverage exceeding approx 80%.

These findings corroborate all earlier works for deep convective situations, where small biases were found in deep convective scenes with high cloud cover, while scenes with 20% coverage produced much more significant biases. Additionally we have shown that the documented bias consists of two contributions: the geometrical shading effects of clouds at low sun angles and the true 3D effect of photon scattering from the original path direction. Since the former contribution is related to the increase in the effective cloud cover in low sun angle conditions due to the 'filling' of clear sky regions between individual clouds, an attempt to correct it is made by performing a simple technique, whereby the field rotated by the tangent of the solar declination angle. This technique was previously suggested and implemented by Varnai and Davies (1999) with mixed results. Here the TICA technique is able to greatly reduce the 1D bias at low sun angles. The residual bias, indicating the true 3D effect of scattering, is almost independent of SZA for this scene. This is likely to lie with the fact that the cirrus cloud shield has a small aspect ratio. This is encouraging, since deeper cloud systems, such as frontal cloud, tend not to be broken, and will also have limited ICA biases.

ACKNOWLEDGMENTS
The Met Office (U.K.) supplied the cloud resolving model used to generate the cloud field. Part of this work was performed while the first author was at the Environmental System Science Centre, University of Reading supported by NERC Studentship GT/4/00/217

References

Barker, H. W., J. J. Morcrette, and G. D. Alexander, 1998: Broadband solar fluxes and heating rates for atmospheres with 3D broken clouds, *Quart. J. Roy. Meteor. Soc.*, **124**, 1245–1271.

Barker, H. W., G. L. Stephens, and Q. Fu, 1999: The sensitivity of domain-averaged solar fluxes to assumptions about cloud geometry, *Quart. J. Roy. Meteor. Soc.*, **125**, 2127–2152.

Di Giuseppe, F. and A. M. Tompkins, 2003: Three dimensional radiative transfer in tropical deep convective clouds, *J. Geophy. Res.*, In press.

Fu, Q., M. C. Cribb, H. W. Barker, S. K. Krueger, and A. Grossman, 2000: Cloud geometry effects on atmospheric solar absorption, *J. Atmos. Sci.*, **57**, 1156–1168.

Fu, Q. and K. N. Liou, 1992: On the correlated k-distribution method for radiative-transfer in nonhomogeneous atmospheres, *J. Atmos. Sci.*, **49**, 2139–2156.

McClatchey, R. A., R. W. Fenn, J. E. A. Selby, F. E. Volz, and J. S. Garing, 1972: Optical properties of the atmosphere, Technical Report AFCRL-72-0497, Hanscom Air Force Base, Bedford, Mass.

Scheirer, R. and A. Macke, 2001: On the accuracy of the independent column approximation in calculating the downward fluxes in the UVA, UVB and PAR spectral ranges., *J. Geophy. Res.*, **106**, 14 301–14 312.

Tompkins, A. M., 2001: Organization of tropical convection in low vertical wind shears: The role of coldpools, *J. Atmos. Sci.*, **58**, 1650–1672.

Varnai, T. and R. Davies, 1999: Effects of cloud heterogeneities on shortwave radiation: Comparison of cloud top variability and internal heterogeneity, *J Atmos. Sci.*, **56**, 4206–4224.

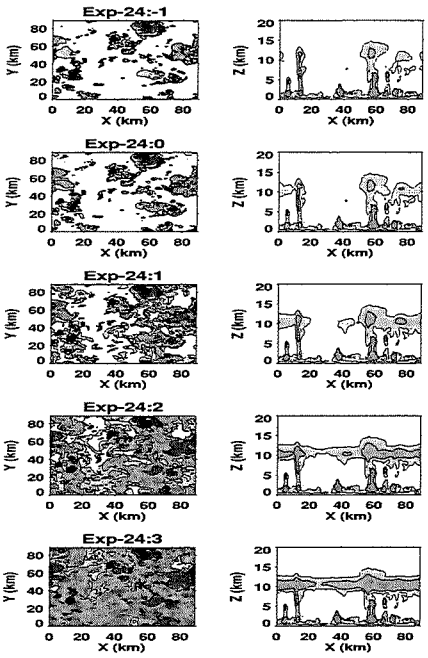

Figure 1: Additional cloud scenes generated from the original CRM simulation (EXP24:0). Left panel: X-Y column integrated cloud water content (grey levels corresponding to 10, 100 and 1000 gm^{-2}). Right panel: Cloud water content field projected on the Y=0 plane (grey levels corresponding to 10^{-2}, 10^{-1}, 10^{0} gm^{-3}).

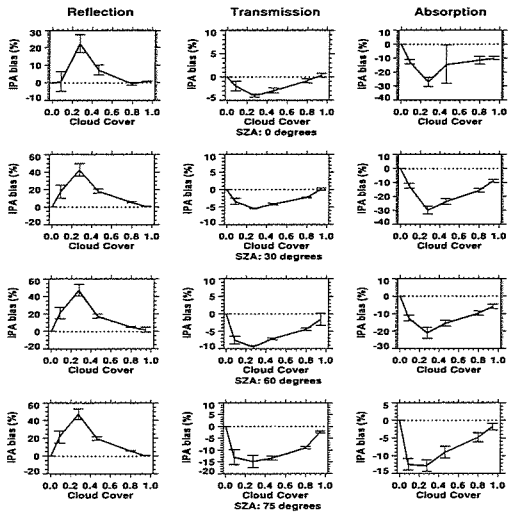

Figure 2: Relative ICA biases as a function of cloud cover and solar declination angle. The error bars represent one standard deviation of the bias over the four input cases

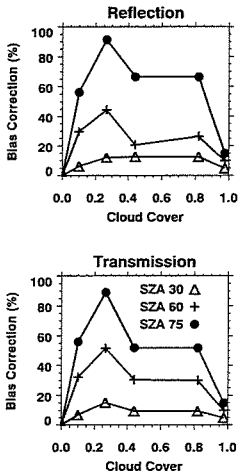

Figure 3: Percentage of 1D bias correction due to the TICA approach as a function of the cloud cover and for different solar zenith angles.

FORECASTING ICING CONDITIONS DURING ALLIANCE ICING RESEARCH STUDY II WITH THE CANADIAN METEOROLOGICAL CENTRE GLOBAL ENVIRONMENTAL MULTISCALE MODEL

Anna Glazer[1] and George A. Isaac[2]

[1]Meteorological Service of Canada, Dorval, Québec, H9P 1J3, Canada
[2]Meteorological Service of Canada, Toronto, Ontario, M3H 5T4, Canada

1. INTRODUCTION

The second Alliance Icing Research Study (AIRS2) was conducted in the Ottawa (Ontario) - Mirabel (Québec) region in Canada (Fig. 1).

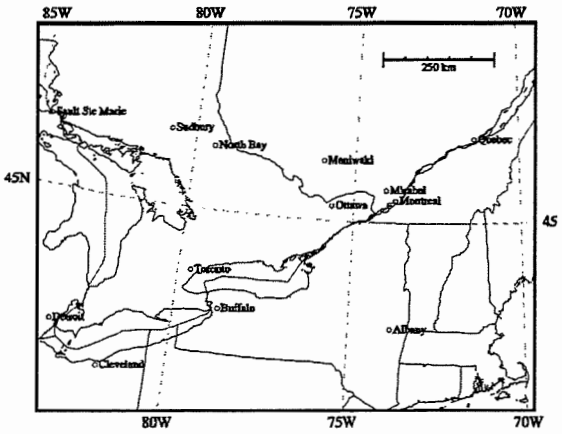

Fig. 1 AIRS2 project area

It took place between 3 November 2003 and 11 February 2004 and included two intensive observation periods (IOP). The IOP1 extended from 4 November until 12 December and the IOP2 from 19 January until 11 February. AIRS2, an international field project, involved over 50 people and numerous research organizations from Canada, United States and Europe. The aim of this study was to get a better understanding, and improve forecasts, of hazardous winter weather conditions with a particular focus on icing. To achieve project objectives five instrumented research aircraft flew over an ensemble of ground-based in-situ and remote-sensing meteorological measurement systems that were installed at Mirabel, Québec. The Mirabel site was available during the whole study period. The measurements were taken continuously, with balloon atmospheric soundings done from Mirabel during interesting periods.

Corresponding author's address: Anna Glazer, Meteorological Service of Canada, Dorval, Québec, H9P 1J3, Canada; E-mail: anna.glazer@ec.gc.ca

A detailed description of the project and its objectives can be found in the "AIRS II Science Plan" available on the AIRS Web site: http://www.airs-icing.org.

2. PREPARING PROJECT FLIGHTS

To plan the project flights a thorough analysis of weather conditions had to be made daily. This was the purpose of weather briefings during which special attention was paid to clouds, their distribution, phase and possible evolution during the day, as well as to the observed and predicted precipitation amount and type. The clouds with supercooled liquid droplets were of a particular interest because the existence of supercooled liquid water (SLW) aloft is a prerequisite of in-fight icing, as freezing rain and drizzle at the surface entails ground icing. From the meteorological perspective **forecasting icing conditions** means forecasting the distribution of SLW in the atmosphere. During weather briefings the forecasts for Mirabel were analyzed with special interest, because flying over Mirabel had many advantages. Real-time observations were available at Mirabel allowing frequent weather updates before flight, and readjustment of flight trajectory once in the air. Data collected over Mirabel could be compared not only with model predictions but with the ground-based instruments data as well. But still, if there were no clouds at this particular location, any other destination was worth of considering. To prepare a weather briefing, surface and upper air observations, satellite and radar data, pilot reports and public forecasts, were analyzed together with output from standard numerical models and special products prepared for the project. Some of these other special products have been described in the Science Plan. The Canadian products that helped evaluate the weather conditions will be presented below.

3. CANADIAN NUMERICAL MODELS FORECASTS

Twice a day, starting from 00 and 12 UTC data, at the Canadian Meteorological Centre (CMC) the Global Environmental Multiscale (GEM) model (Côté et al., 1998) in its global and regional configurations are being run. The main purpose of the runs is to provide a medium range forecast (up to 10 days) with the global

model and a high resolution (24 km) short range forecast (2 days) for the North American continent and adjacent oceans with the regional model. These model outputs were consulted during the project to provide an outlook of future conditions. To plan the flights for the same day, the regional aviation GEM (AVN) predictions were utilized. The operational forecasts of aviation products (AVN) are available twice a day with the 00 and 12 UTC runs. The aviation package diagnoses the supercooled cloud base and top heights and gives the position of freezing level (at 6-h intervals). The product is based on regional GEM model runs.

For the purpose of the AIRS2 project two special products were prepared: an additional output of the HIgh Resolution Model Application Project (HIMAP) version of GEM model and a CMC Trajectory Model special output (http://iweb.cmc.ec.gc.ca/~afsrweb/airquality/smog/) for Cleveland and Mirabel. One of the project aircraft, the NCAR C-130 was stationed at Cleveland, which is the reason for selecting this site.

Model predicted forward, and particularly backward, trajectories at four levels (500, 700, 850 and 925 mb), available twice daily, were looked at to infer the type of air mass that was expected to arrive over these places. An example of a backward trajectories ending at Mirabel on 30 January 2004 is given on Fig. 2. This is a 24-h prediction issued on 29 January 2004.

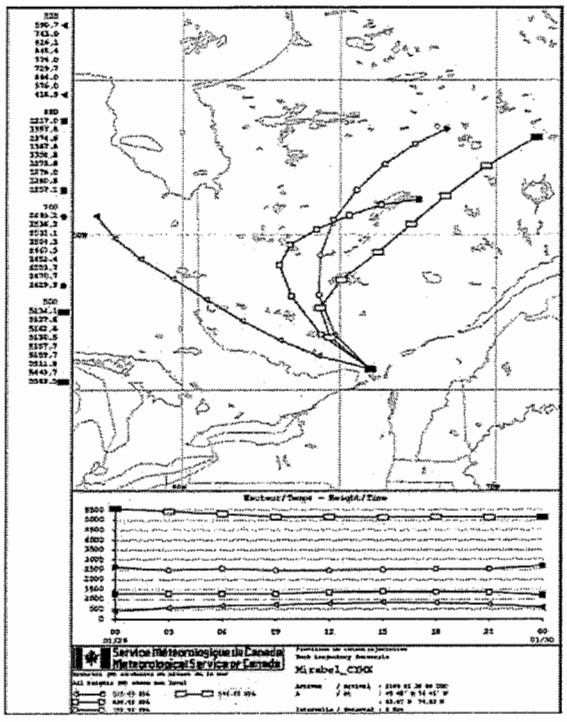

Fig. 2 Backward trajectories for Mirabel

The HIMAP model is being executed at CMC over two sub-domains covering Western and Eastern Canada. HIMAP East is centered on the Québec-Windsor corridor. Its output was modified to include special products that facilitate flight planning. The choice of HIMAP East as a predictive tool for AIRS2 was justified by its high resolution (this is the model with the highest resolution - 10km - that is currently operationally run at CMC) and employed cloud scheme. A lot of research has been dedicated to identify weather scenarios propitious to the sustained presence of SLW in the atmosphere. A few numerical meteorological models have integrated the results of this research in order to predict the SLW distribution. The HIMAP model offers such a possibility. The mixed-phase cloud scheme (Tremblay and Glazer, 2000), now available within the CMC physics library and implemented into HIMAP, forecasts the occurrence of SLW.

4. SPECIAL PRODUCTS WITH HIMAP MODEL

Normally there are two HIMAP runs daily starting from 06 and 18 UTC data. The frequency of HIMAP output (at 3-h) was judged too coarse for the project requirements. This is why, for 101 model points'

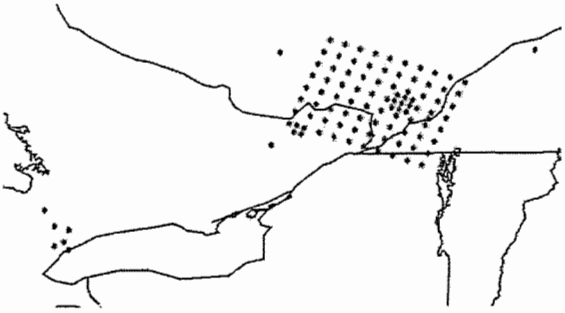

Fig. 3 The 101 HIMAP grid points for time series output

covering the project region (Fig. 3) and for a few variables the time series were generated at 6 minutes, which is at each model time step. The 3D fields of temperature, dew point temperature (that allowed getting model predicted tephigrams at Mirabel as the one presented on Fig. 4b), relative humidity and liquid water content, and 2D fields of integrated vapor, SLW and precipitation rate were among output variables. All these fields were also available for the whole domain, but at 3-h only.

During the project the field of supercooled liquid water path (SLWP), which is a vertical integral of SLW content, was the most frequently consulted model output. Both 2D fields for the whole model domain displayed using CMC software vizaweb (http://iweb.cmc.ec.gc.ca/~afsipaf/vizaweb.html) and time series at high temporal frequency for Mirabel and other locations were consulted.

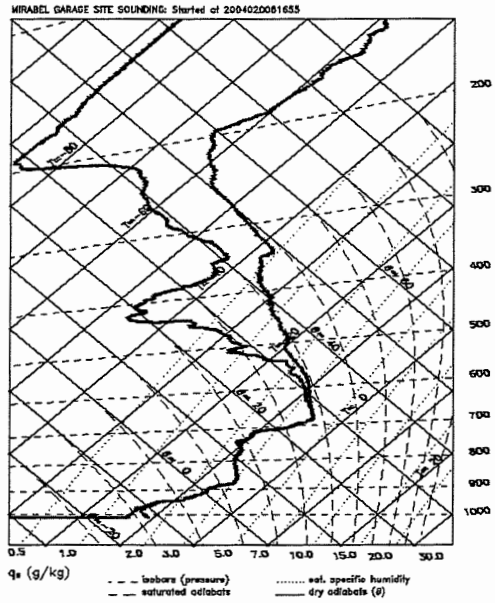

a)

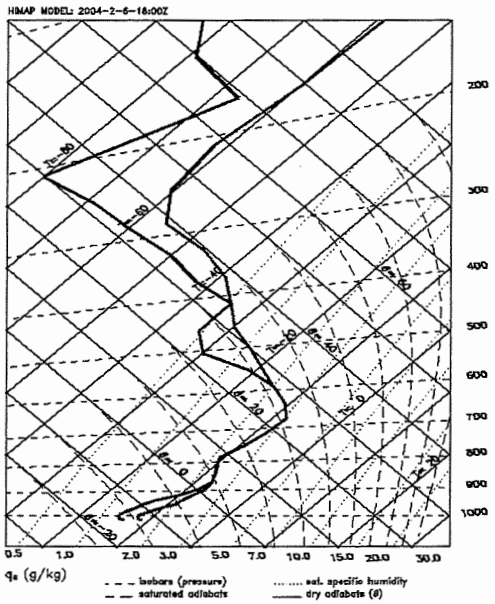

b)

Fig. 4 Temperature profile at Mirabel, (a) observed and (b) model predicted

Figure 5 shows the time series of SLWP over Mirabel measured and predicted for 12-h period starting at 12 UTC on 06 February 2004. There are three curves on the figure: SLWP forecast with HIMAP (squares) superimposed with the GEM (circles) regional predictions of liquid water path (LWP) and radiometer (triangles) measurements of LWP. The LWP is truly the SLWP, because for this day the temperature was below freezing around Mirabel, as can be deduced both from the temperature profiles available as model output, soundings, and surface measurements. An example of temperature sounding done over Mirabel at 16:55 UTC is displayed at Fig. 4a. The model forecasts for 06 February (Fig. 5) were available early in the morning; the radiometer readings were available in real time. Consequently, the figure including all three curves (Fig. 5) was ready only on 07 February, although model forecasts were ready for early briefing on 06 February.

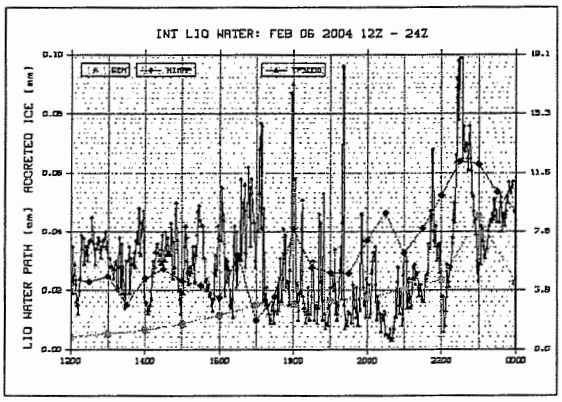

Fig. 5 SLWP over Mirabel

During the briefings the SLWP was consulted to infer the possibility and importance of model predicted icing. The regions characterized by a zero value were rarely considered for flight missions unless there was a strong belief that model was wrong.

5. RESULTS

To provide an assessment of HIMAP capability to predict icing conditions, a preliminary evaluation of project missions with Convair-580 was done. The model predicted time series of SLWP and flight reports of icing were analyzed conjointly. The maximum value of model predicted SLWP for the period of flight (*SLWP max*) was chosen to be an indicator of model predicted icing. For the flight on 06 February this value is 0.65 mm (Fig. 5).

The NRC instrumented research aircraft Convair-580 flew 22 missions during AIRS2, with 12 during IOP1 and 10 during IOP2. The majority of flights (16) were over Mirabel the remaining were over Lake Ontario (3), Erie (1) and Georgian Bay (2). Severe icing was reported on 5, moderate on 6 and light on 9 flights.

There were two flights with no icing reported, both over Mirabel area. For these flights the model predicted SLW content was small. For the first flight (no 8, on 27 November), the model predicted a thin supercooled cloud at about 500 mb over Mirabel thickening and lowering with time during flight, with a maximum liquid

water content of about 0.03 g/kg. For the second flight (no 16, on 30 January) with no icing reported, the model predicted cloud was almost glaciated with a shallow layer of a short duration of SLW patch around 700 mb. The quantity of locally predicted SLW content was never bigger than 0.02 g/kg. In other words, guided by the SLWP forecast alone, one would normally not recommend a research flight in these situations.

On the other extreme there were two project flights over Mirabel, both reporting light icing, with observed SLW content of about 0.26 g/m3 (flight no 2 on 12 November) and 0.08 g/m3 (flight no 4 on 14 November), when model predicted cloud over Mirabel was thin and completely glaciated. The *SLWP max* was zero (no icing). These were the model worst forecasts of icing conditions.

For the 18 remaining Convair-580 missions the icing was both observed and predicted. For each flight the observed icing intensity was assessed and the model predicted *SLWP max* was calculated.

With the exception of two flights, one with light icing when the model predicted *SLWP max* was relatively large (flight no 9 on 28 November, *SLWP max* = 0.7 mm) and another with severe icing and low *SLWP max* (flight no 21 on 7 February, *SLWP max* = 0.25 mm), the reported icing intensity was correlated with model predicted *SLWP max*. For flights with light icing, *SLWP max* was below 0.25 mm, for moderate between 0.3 and 0.5 mm and for severe it was over 0.65 mm. Next, for all flights with reported light icing, a mean value of *SLWP max* was calculated. The same was done for all flights reporting moderate and then severe icing. The results are presented in Table 1.

Icing intensity	<*SLWP max*> Mirabel	<*SLWP max*> all
L	0.23	0.22
M	0.49	0.45
S	0.53	0.58

Tab. 1 Icing intensity and mean value of *SLWP max* for Convair-580 flights

The mean value of *SLWP max* for all flights is slightly different when Mirabel flights only are analyzed. The model results for missions outside Mirabel should be however considered with caution, as these regions were not covered with the high temporal resolution of model output and less confidence should be given to these results.

6. CONCLUSION

The preliminary analysis of AIRS2 aircraft missions confirm the utility of SLWP, calculated with HIMAP, as a planning tool for research flights. For 18 of the 22 analyzed project flights, model forecasts of icing (SLWP>0) were confirmed during flights, and for 16 of them the value of predicted *SLWP max* could have been used as an indicator of expected icing intensity.

The presence of Supercooled Large Drops (SLD), or drops larger than 50 µm, is also a critical variable for making icing forecasts, because some accidents have been attributed to the presence of these drops. However, the Canadian numerical models cannot currently predict this variable.

This is a preliminary analysis and further work will be done to determine the best method(s) for predicting icing using either numerical model output or a combination of model and data from other sources (e.g. radiometers, radars, satellites, etc). Other recent Canadian papers comparing model predicting icing fields, and mixed cloud properties with aircraft data can be found in Guan et al. (2002), Tremblay et al. (2003) and Vaillancourt et al. (2003).

7. ACKNOWLEDGMENTS

The authors are grateful to Janti Reid for Figure 5. The radiometer data was possible through the use of the Communication Research Center equipment. The main funding for AIRS2 was provided by Transport Canada, the Canadian National Search and Rescue Secretariat, the Meteorological Service of Canada and the National Research Council. U.S. funding sources includes the Federal Aviation Administration, NASA Glenn and Langley, and the National Science Foundation. There were many participants and a complete list can be found in the Science Plan on the AIRS Web site.

8. REFERENCES

Côté, J., J. G. Desmarais, S. Gravel, A. Méthot, A. Patoine, M. Roch, and A. Staniforth, 1998: The operational CMC-MRB Global Environmental Multiscale (GEM) Model. Part I: Design considerations and formulation. *Mon. Wea. Rev.*, **126**, 1373-1395.

Guan, H., S. G. Cober, G. A. Isaac, A. Tremblay and A. Méthot, 2002: Comparison of three cloud forecast schemes with in-situ aircraft measurements. *Wea. and Forecasting*, **17**, 1226-1235.

Tremblay, A. and A. Glazer, 2000: An Improved Modeling Scheme for Freezing Precipitation Forecasts. *Mon. Wea. Rev.*, **128**, 1289-1308.

Tremblay, A., P. A. Vaillancourt, S. G. Cober, A. Glazer, and G. A. Isaac, 2003: Optimization of a mixed-phase cloud scheme using aircraft observations. *Mon. Wea. Rev.*, **131**, 672-686.

Vaillancourt, P. A., A. Tremblay, S. G. Cober, and G. A. Isaac, 2003: Comparison of aircraft observations with mixed-phase cloud simulations. *Mon. Wea. Rev.*, **131**, 656-671.

CLOUDS AND CLIMATE: PROGRESS AND PROSPECTS

Wojciech W. Grabowski

National Center for Atmospheric Research, Boulder, CO 80307 USA

Clouds play a key role in atmospheric general circulation through their impact on radiative fluxes and their role in the water and energy cycles. The globally- and annually-averaged cloud radiative forcing [defined as the difference between radiative fluxes at the top of the atmosphere (TOA) for the case of the atmosphere with clouds and a hypothetical situation where all clouds are removed] is estimated at about 30 W m^{-2} and -50 W m^{-2} for longwave (i.e., Earth's thermal) and shortwave (i.e., solar) radiation, respectively. The net impact of clouds (a sum of the shortwave and longwave cloud forcings) is a cooling of about -20 W m^{-2}. Moreover, cloud processes contribute significantly to the poleward energy transport in the atmosphere, which (together with the oceanic transport) balances the TOA net (i.e., solar minus longwave) radiative energy flux on the global scale. The net TOA flux is positive near the equator (up to 70 W m^{-2}) and negative at high latitudes (down to about -120 W m^{-2} near the poles), see Kiehl et al. (1998). The latent energy is a significant part of total energy that the atmosphere carries from warm low latitudes toward the cold high latitudes. The latent energy is released when water vapor condenses within frontal clouds associated with midlatitude weather systems. The mean surface precipitation associated with these weather systems is in the range of 1 to 3 mm day^{-1} (depending on whether a model or surface observations are used, e.g., Chahine 1992). Such a surface precipitation results in the latent heating of the atmospheric column in the range of about 30 to 90 W m^{-2} (energy flux of 100 W m^{-2} is equivalent to about 3.4 mm day^{-1} of the surface precipitation). This is a substantial fraction of the TOA radiative imbalance between low and high latitudes.

Representing clouds in atmospheric general circulation models (AGCMs) is challenging. At a very basic level, this is because clouds are typically subgrid-scale horizontally (e.g., convective clouds) and often vertically (e.g., stratocumulus, cirrus). AGCMs simply cannot afford resolving small- and mesoscale motions which underlie the evolution of clouds and cloud systems. Even the highest-resolution AGCMs run nowadays (e.g., at the European Centre for Medium-range Weather Forecasts with horizontal resolutions of several tens of kilometers) must rely on sophisticated subgrid-scale parameterization schemes (Gregory et al. 2000; see also a review in Fowler et al. 1996). The inadequacy of the parameterization approach is especially evident for the tropical moist convection that requires horizontal gridlength of the order of 1 km to capture transport properties of clouds that are in quantitative agreement with observations. Even higher resolutions are required for boundary-layer cloudiness in subtropics.

Clouds, unlike trace gases, are dynamically active. This means that treating clouds merely as passive features that reflect shortwave radiation, absorb and emit longwave radiation, and leave behind latent heat once precipitation develops and falls out, offers an incomplete picture of the role of clouds in the climate system. The issue of cloud dynamics and its coupling with cloud microphysics is particularly relevant for the anthropogenic impacts on cloud processes, such as the indirect impact of atmospheric aerosols, and their role in the climate change. The indirect aerosol impact is associated with individual clouds and its impact on the climate system can be addressed with very low confidence in traditional climate models where cloud dynamics and microphysics are parameterized.

Cloud-resolving models (i.e., nonhydrostatic small-scale models with horizontal grid spacing of about 1 km), hereafter CRMs for brevity, represent small-scale and mesoscale processes explicitly. CRMs still have to parameterize subgrid-scale processes such as turbulence and cloud microphysics, but these parameterizations are better posed when atmospheric dynamics is resolved down to a few-kilometer scale. A global CRM is 5 to 6 orders of magnitude more computationally demanding than traditional

Corresponding author's address: Wojciech Grabowski, National Center for Atmospheric Research, PO Box 3000, Boulder, CO 80307 USA; E-Mail: grabow@ncar.ucar.edu

climate models and can only be applied to short simulations within the near future.

The role of CRMs in the clouds-in-climate problem was highlighted by the creation of the World Climate Research Programme's GEWEX (Global Energy and Water Cycle Experiment) Cloud System Study (GCSS), a long-term program designed to develop better understanding of the impact of cloud processes on the large scales and to improve representation of clouds in climate and weather prediction models. CRMs were envisioned to play a critical role in the GCSS strategy. The GEWEX Cloud System Science Team (1993) stated: "Observations from field programs will be used to develop and validate the cloud-resolving models, which in turn will be used as test-beds to develop the parameterizations for the large-scale models. The cloud-resolving models provide synthetic datasets representing rather complete descriptions of entire cloud systems, from which it will also be possible to develop algorithms for remote-sensing observations". Moncrieff et al. (1997) present an extensive discussion of the "GCSS process" from the perspective of a GCSS working group devoted to the precipitating convective cloud systems. Randall et al. (2003a) provide a recent review of the GCSS accomplishments.

As far as field programs are concerned, the Atmospheric Radiation Measurement (ARM) Program is likely the most significant effort to quantify the role of clouds in the climate system using ground-based observations. ARM Program, created in 1989 with funding from the U.S. Department of Energy (DOE), operates field research sites located in climatologically-sensitive locations, such as the Southern Great Plains in the U.S., tropical western Pacific warm pool, and northern slope of Alaska. These sites provide essential datasets needed for development, testing, and validation of CRMs and improving traditional parameterizations used in AGCMs (e.g., Xie et al. 2002, Xu et al. 2002).

As a result of model evaluation and intercomparison projects within GCSS, there exists a large body of evidence that CRMs, even when applied in a simplified two-dimensional (2D) slab-symmetric geometry, provide observationally validated representations of cloud-scale processes and interactions among them. This result led Grabowski and Smolarkiewicz (1999) and Grabowski (2001) to suggest an approach where a 2D CRM is applied in each column of a large-scale model to represent subgrid-scale processes associated with deep convection. Such an approach was termed the cloud-resolving convection parameterization (CRCP) and it is often referred to as "super-parameterization". A 2D CRM is applied in each column of a large-scale model to represent explicitly small-scale and mesoscale processes and interactions among them. The 2D CSRM works as a sophisticated parameterization (hence the name) and it can, in principle, include all subgrid-scale atmospheric processes that are parameterized in traditional climate models (e.g., dry and moist convection, precipitation processes, land-surface processes, radiative transfer, atmospheric chemistry, etc.). This approach is 2 to 3 orders of magnitude more expensive than current climate models, but 3 orders of magnitude less expensive than a global CRM. Ideal for parallel computations, it can easily be implemented on thousands of processors and can be applied to decadal-to-centennial climate simulations on today's computers. As discussed in Randall et al. (2003b), the main advantage of the super-parameterization is its explicit representation of the latent heating by cloud-scale processes (because of the coupling between cloud dynamics and cloud microphysics) and realistic spatial distribution of clouds (cloud overlap in particular), which is crucial for the radiative transfer.

The potential of CRCP in the clouds-in-climate problem was illustrated in idealized simulations of planetary-scale organization of moist convection, relevant to the Madden-Julian Oscillation (MJO); see Grabowski (2001, 2003) for detailed discussions. Previous studies have suggested a wide range of physical processes, such as coupling between moist convection and the large-scale dynamics (e.g., CISK-related ideas), radiative transfer, equatorial waveguide dynamics, and atmosphere-ocean interactions, to explain the fundamental mechanism behind the MJO. However, despite vigorous research in the past decades, MJO remains an enigmatic feature of the large-scale dynamics in the tropics. Traditional approaches, which involve convective parameterizations in one way or another, show a frustrating sensitivity of MJO simulations to not only the convective scheme selected, but often to the scheme parameters.

Sensitivity simulations discussed in Grabowski (2003) suggest a new mechanism essential for development and maintenance of large-scale MJO-like coherent structures. This mechanism involves feedback between moist convection and free-tropospheric moisture (cf. Tompkins, 2001). This feedback causes spatial perturbations of

moist convection to strengthen perturbations of the free-tropospheric moisture, which, in turn, affect the spatial distribution of moist convection. By moistening its immediate environment, convection renders it more favorable for future convection because clouds growing in a more humid environment lose their positive buoyancy (as a result of entrainment of dry environmental air) more slowly than clouds growing in a drier environment. Moreover, environmental relative humidity also affects the evaporation of precipitation and thus the net convecting heating. The large-scale circulation, which develops in response to spatial fluctuations of convective heating, plays an important role in this feedback because, through the effect of the large-scale subsidence, it makes areas with suppressed convection even drier. Moreover, interactive radiation enhances this convection-moisture feedback because of the impact of water vapor and clouds on radiative transfer. In general, differential heating due to radiative transfer tends to strengthen large-scale circulations created by spatial fluctuations of convective heating. An extensive discussion of the moisture-convection feedback is given in Grabowski and Moncrieff (2004).

CRCP has also been applied in realistic climate simulations using the Community Climate System Model (CCSM), see Khairoutdinov and Randall (2001), Randall et al. (2003b), and Khairoutdinov et al. (2004). Due to computational expense, CRCP applied in the CCSM uses relatively small computational domain and low horizontal resolution (64 columns with 4 km horizontal gridlength). By comparing several-hundred day long simulations using CCSM in its standard configuration and with CRCP, Khairoutdinov et al. (2004) concluded that many aspects of the simulated climate system were dramatically improved, such as global distributions of surface precipitation and cloudiness, temporal variability of precipitation, clouds, winds, radiative fluxes, etc. on temporal scales ranging from diurnal to intraseasonal. Perhaps the most important result of these simulations is that realistic energy budgets (at the surface as well as at the top of the atmosphere) were obtained without any tuning of the model. This is in dramatic contrast to traditional climate models where considerable model tuning is required for realistic simulations of the energy budget (radiative fluxes in particular).

The super-parameterization approach for modeling climate and climate change is still in its infancy. Further enhancements of this approach have been proposed, such as Arakawa's idea to allow cloud-scale super-parameterization models to exchange cloud-scale information between neighboring columns (see Randall 2003b) or this author's formulation of the coupling between cloud-scale and large-scale models (cf. Grabowski 2004). There is no doubt, however, that climate models featuring super-parameterization will significantly enhance climate research in the future. A simple estimate suggests that a *decade-long* simulation with a super-parameterization climate model has a comparable cost to a *millennium-long* simulation using a traditional climate model, and about a *few-day-long* simulation using a cloud-resolving global model. It follows that super-parameterization offers an attractive compromise between a high-cost cloud-resolving global model, where all scales from cloud to global are resolved and coupled, and a low-cost traditional climate model, where representation of cloud-scale and mesoscale processes is questionable at best.

REFERENCES

Chahine, M. T., 1992: The hydrological cycle and its influence on climate. Nature, 359, 373-380.

Fowler, L. D., D. A. Randall, and S. A Rutledge, 1996: Liquid and ice cloud microphysics in the CSU General Circulation Model. Part I: Model description and simulated microphysical processes. J. Climate, 9, 489-529.

GEWEX Cloud System Science Team, 1993: The GEWEX Cloud System Study (GCSS). Bull. Amer. Meteor. Soc., 74, 387-400.

Grabowski, W. W., 2001: Coupling cloud processes with the large-scale dynamics using the Cloud-Resolving Convection Parameterization (CRCP). J. Atmos. Sci., 58, 978--997.

Grabowski, W. W., 2003: MJO-like coherent structures: Sensitivity simulations using the Cloud-Resolving Convection Parameterization (CRCP). J. Atmos. Sci., 60, 847--864.

Grabowski, W. W., 2004: An improved framework for super-parameterization. J. Atmos. Sci. (in press).

Grabowski, W. W., and P. K. Smolarkiewicz, 1999: CRCP: A Cloud Resolving Convection Parameterization for Modeling the Tropical Convecting Atmosphere. Physica D, 133, 171--178.

Grabowski, W. W., and M. W. Moncrieff, 2004: Moisture-convection feedback in the Tropics. Quart. J. Roy. Met. Soc. (EUROCS Special Issue, in press).

Gregory, D., J. J. Morcrette, C. Jakob, A. C. M Beljaars, and T. Stockdale, 2000: Revision of convection, radiation and cloud schemes in the ECMWF Integrated Forecasting System. Quart. J. Roy. Met. Soc., 126, 1686-1710.

Khairoutdinov, M. F., and D. A. Randall, 2001: A cloud resolving model as a cloud parameterization in the NCAR Community Climate System Model: Preliminary results. Geophys. Res. Let., 28, 3617-3620.

Khairoutdinov, M.F., D.A. Randall, and C. DeMotte, 2004: Simulations of the atmospheric general circulation using a cloud-resolving model as a super-parameterization of physical processes. J. Atmos. Sci. (submitted).

Kiehl, J. T., J. J. Hack, and J. W. Hurrell, 1998: The energy budget of the NCAR Community Climate Model: CCM3. J. Climate, 11, 1151-1178.

Moncrieff M. W., and Coauthors, 1997: GEWEX Cloud System Study (GCSS) Working Group 4: Precipitating Convective Cloud Systems. Bull. Amer. Meteor. Soc., 78, 831-845.

Randall, D., and Coauthors, 2003a: Confronting models with data: The GEWEX Cloud Systems Study. Bull. Amer. Meteor. Soc., 84, 455-469.

Randall, D., M. Khairoutdinov, A. Arakawa, and W. Grabowski, 2003b: Breaking the cloud-parameterization deadlock. Bull. Amer. Meteor. Soc., 84, 1547-1564.

Tompkins, A. M., 2001: Organization of tropical convection in low vertical wind shears: The role of water vapor. J. Atmos. Sci., 58, 529-545.

Xie, S.-C., and Coauthors, 2002: Intercomparison and evaluation of cumulus parameterizations under summertime midlatitude continental conditions. Quart. J. Roy. Met. Soc., 128, 1095-1135.

Xu, K.-M., and Coauthors, 2002: An intercomparison of cloud-resolving models with the ARM summer 1997 IOP data. Quart. J. Roy. Met. Soc., 128, 593-624.

QUANTITATIVE PRECIPITATION FORECASTING OF WINTERTIME STORMS IN THE SIERRA NEVADA: SENSITIVITY TO THE MICROPHYSICAL PARAMETERIZATION

Vanda Grubišić,* Ramesh K. Vellore, and Arlen W. Huggins
Desert Research Institute, Reno, Nevada, 89512, USA

1. SUMMARY

Quantitative Precipitation Forecasting (QPF) remains one of the foremost challenges in numerical weather prediction, in spite of advances in computing power and the degree of sophistication of atmospheric numerical models. In this study, a statistical approach was adopted to study the skill of a mesoscale numerical model in predicting orographic precipitation in the Sierra Nevada, and the sensitivity of that skill to the choice of the microphysical parameterization and horizontal resolution. The performance of four existing bulk microphysical parameterization schemes (DUDH, Dudhia 1989; SCHUL, Schultz 1995; GSFC, Tao and Simpson 1993; REIS, Reisner et al. 1998) was examined in the PSU/NCAR Mesoscale Model MM5 high-resolution simulations of a group of high-impact precipitation events. The finest grid increment in these simulations was 1.5 km. The verification data set consists of ground precipitation measurements from a selected number of wintertime storms in

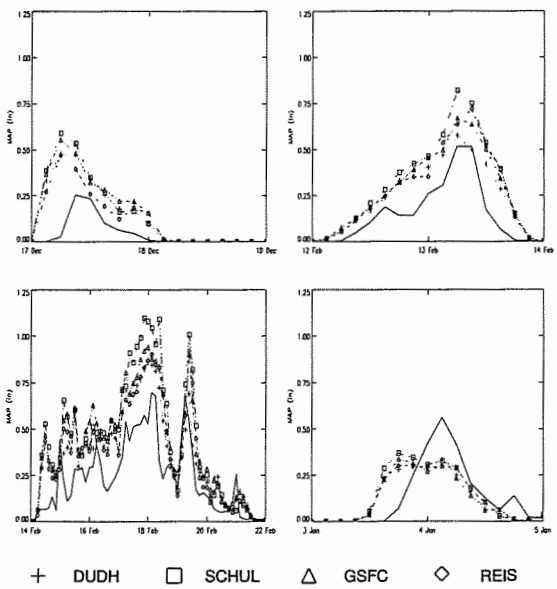

Figure 1: Mean Areal Precipitation (MAP) computed from 3-h precipitation accumulations (inches) using the predicted amounts at the gauge locations of the Sierra Co-operative Pilot Project for the winter storms: (a) 17–19 December 1982, (b) 12–14 February 1986, (c) 14–22 February 1986, and (d) 3–5 January 1987. Solid line indicates MAP computed from observations.

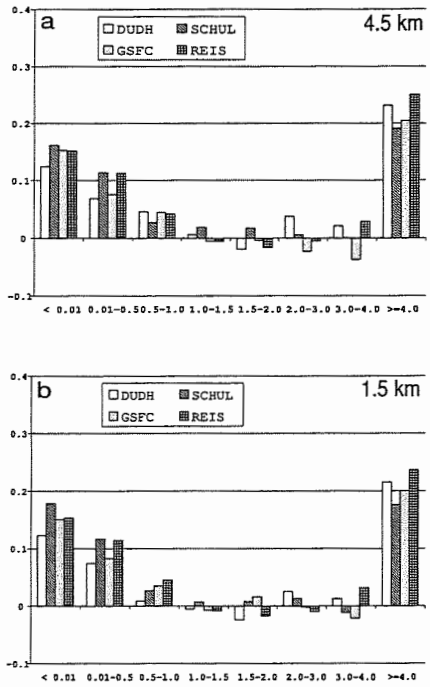

Figure 2: (a) Histogram of the Equitable Treat Score for the defined precipitation intervals (inches) for the four examined microphysical schemes for the 4.5-km model domain. (b) As in the top panel but for the 1.5-km domain.

*Corresponding author's address: Dr. Vanda Grubišić, Desert Research Institute, Division of Atmospheric Sciences, 2215 Raggio Pkwy, Reno, NV 89512–1095; E-mail: Vanda.Grubisic@dri.edu

the Sierra Nevada documented during the Sierra Cooperative Pilot Project (Reynolds and Dennis 1986) in the 1980's (Fig. 1). The results show a tendency for the existing microphysical schemes in MM5 to produce an over-prediction of precipitation on both the windward and lee slopes of the Sierra Nevada. Examination of the statistical skill scores reveals that the MM5 QPF skill for the Sierra Nevada orographic precipitation is fairly low, that the skill is not improved by increasing the horizontal resolution (Fig. 2), and that on average the QPF skill is better on the windward than on the lee side (Fig. 3). Results of a statistical significance test show that the differences in skill scores obtained for different microphysical schemes are not statistically significant (Grubišić et al. 2004).

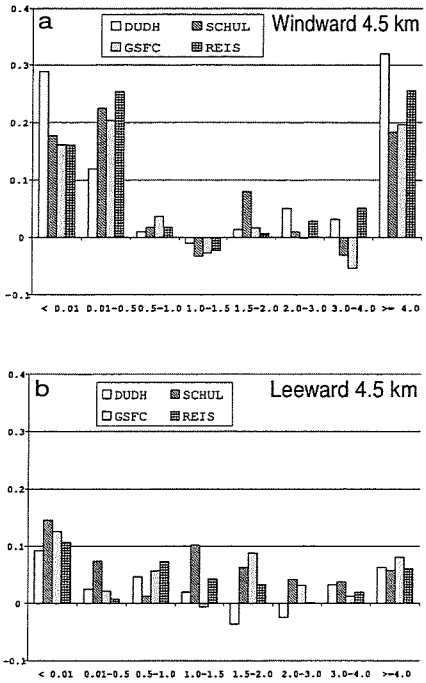

Figure 3: (a) Equitable Treat Scores for the defined precipitation intervals (inches) for the four examined microphysical schemes on the windward side of the 4.5-km model domain. (b) As in the top panel but for the lee side of the model domain.

2. ACKNOWLEDGMENTS

This research has been supported in part by the NSF US Weather Research (ATM–9908995) and DOE ARM programs.

3. REFERENCES

Dudhia, J, 1989: Numerical study of convection observed during the winter monsoon experiment using a mesoscale two-dimensional model. *J. Atmos. Sci.*, **46**, 3077–3107.

Grubišić, V., R. K. Vellore, and A. Huggins, 2004: Quantitative precipitation forecasting of wintertime storms in the Sierra Nevada: Sensitivity to the microphysical parameterization. Submitted to *Mon. Wea. Rev.*

Reisner, J., R. M. Rasmussen, and R. T. Bruintjes, 1998: Explicit forecasting of supercooled liquid water in winter storms using MM5 mesoscale model. *Quart. J. Roy. Meteor. Soc.*, **124**, 1071–1107.

Reynolds, D. W., and A. S. Dennis, 1986: A review of the Sierra Cooperative Pilot Project. *Bull. Amer. Meteor. Soc.*, **67**, 513–523.

Schultz, P, 1995: An explicit cloud physics parametrization for operational numerical weather prediction. *Mon. Wea. Rev.*, **123**, 3331–3343.

Tao, W-K, and J. Simpson, 1993: Goddard Cumulus Ensemble Model, Part I: Model Description. *Terrestrial, Atmospheric and Oceanic Sciences*, **4**, 35–72.

MICROPHYSICAL PARAMETERIZATION AND VARIABILITY FOR MIXED PHASE CLOUDS USING IN-SITU OBSERVATIONS

I.Gultepe[1] and G. A. Isaac
Meteorological Service of Canada, Toronto, Ontario, M3H 5T4, Canada

1. INTRODUCTION

Mixed phase clouds contain both liquid and ice particles at various scales along which the liquid fraction are highly variable. The variability in liquid water content (LWC) and ice water content (IWC) for a given temperature (T) range is very large, so that derived relationships can only be used in a model with larger averaging scales in both time and space. Because of the smaller saturation vapor pressure over ice crystals, as compared to liquid droplets, ice crystals glaciate clouds in short time periods at the expense of droplets, depending on physical and dynamical processes. A detailed summary of LWC and LWC fraction (k_L=LWC/(LWC + IWC)) versus T for climate studies was given by Gultepe and Isaac (1997). The liquid fraction versus temperature was studied for mixed phase clouds by Cober et al. (2001) and Korolev et al. (2003). Unfortunately, these studies only considered LWC or liquid fraction versus temperature. As suggested by Randall et al (1998), parameterizations should represent realistic atmospheric conditions. In the present work, a parameterization is developed using in-situ observations that include LWC, IWC, effective radius (r_{eff}), and droplet number concentration (N_d). The resulting equation is then tested by comparing observed LWC_{obs} with predicted LWC_{pre}, and with previous studies of LWC fraction versus T.

2. IN-SITU OBSERVATIONS

The in-situ observations were collected with instruments mounted on the National Research Council (NRC) Convair-580 during the Alliance Icing Research Study (AIRS1, Isaac et al. 2001) that took place over southerm Ontario and Quebec regions during the winter of 1999-2000. The LWC and N_d were obtained from hot wire probes (Nevzorov and King probes) and FSSP probes, respectively. N_d and ice crystal number concentration (N_i) were obtained at a standard size range of 2-47 μm and an extended size range of 5-95 μm from two Particle Measuring Systems (PMS) Forward Scattering Spectrometer Probes (FSSP) and from PMS two-dimensional cloud (2D-C; 25-800 μm) and precipitation (2D-P; 200-6400 μm) probe measurements. FSSP measurements were corrected for probe dead-time and coincidence. Uncertainties in LWC and N_d, can be about 15% and 30%, respectively. Discrimination between the ice and liquid regions within the cloud was accomplished by using 1) a Rosemount icing detector (RID) which clearly responds to the liquid phase present within the cloud, and 2) FSSP and Nevzorov Probe measurements (Cober et al. 2001). Under most circumstances, the Nevzorov probe LWC and total water content (TWC) measurements are accurate to 10-15%. The T measurements were obtained from both Rosemount and reverse flow T probes with an accuracy of about ±1°C.

[1]*Corresponding author: Ismail Gultepe, Meteorological Service of Canada, Toronto, Ontario, M3H5T4, Canada; E-mail: ismail.gultepe@ec.gc.ca*

3. METHOD AND RESULTS

3.1 Method

A new parameterization was generated using the in-situ data collected at various level flights over path lengths that were at about 20 km long with at least 90% of time being in mixed conditions. The 30 constant altitude legs selected are used in this analysis. Then, all data are combined to represent winter mixed phase clouds at temperatures between 0 and –30°C. The clouds are defined when IWC>0.001 g m^{-3} and LWC>0.005 g m^{-3}, and N_d>1 cm^{-3} along a constant altitude flight leg where the Rosemount icing detector measurements were used for mixed phase cloud detection. In the analysis, first, LWC versus N_d, r_{eff}, IWC, and T were investigated in pairs. Then, based on physical concepts that relate LWC [g m^{-3}] with r_{eff}^3 [μm] and N_d [cm^{-3}], and assuming that LWC decreases with increasing IWC for a constant volume, the following parameterization, representing a scale of about 20 km, is suggested:

$$LWC = 0.012 + 1.69x10^{-5}\left[\frac{N_d}{IWC}\log\left(\frac{r_{eff}^3}{|T|}\right)\right]. \qquad (1)$$

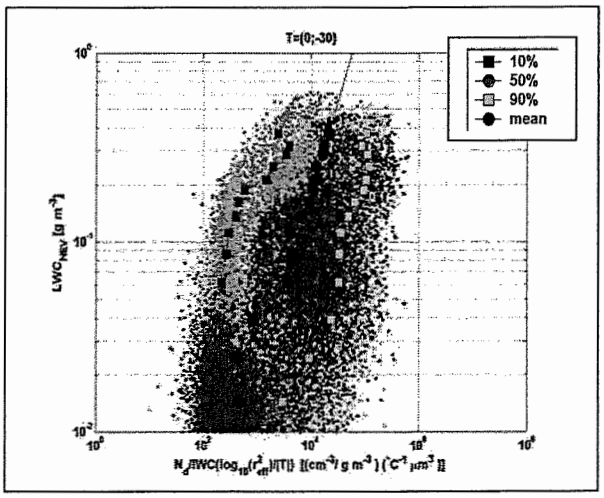

Fig. 1: The red and yellow squares are for 10% and 90% values, respectively. Scatter Plot of observed and calculated LWC values for 30 flight segments. Each flight leg is represented by a different color dot. Large black dots are the average values. The best fit to the average values is given by equation 1 (black line).

Eq. 1 represents the best fit to the filled black circles in Fig. 1. The averages of the x-axis values at specific LWC intervals (0.01 g m^{-3}) are well represented by the fit. This equation is valid when the estimated value in the brackets is between 20000 and 100, and for droplet sizes not larger than about 100 μm. The colored dots are for individual flight legs.

3.2. LWC versus r_{eff}

Fig. 2 shows LWC measurements versus r_{eff} for all flights. It is seen that LWC increases with increasing r_{eff}, and the variability is large for a given r_{eff} value, indicating that a single equation cannot be a unique solution for a relationship between LWC and r_{eff}. At least, a relationship between LWC and r_{eff} exists when LWC values are averaged, suggesting that r_{eff} should also be considered in the LWC parameterization for mixed phase clouds.

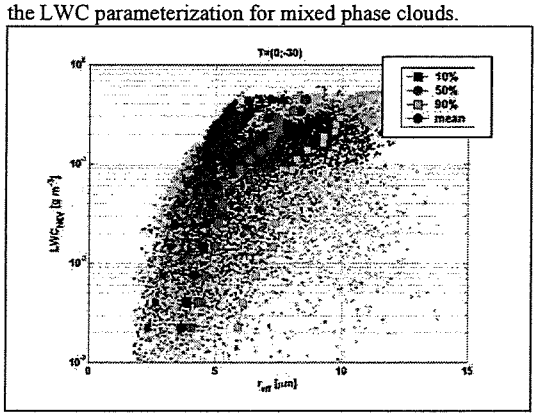

Fig. 2: Each colored dot is for a specific flight segment out of 30 flights. The filled black circles (blue circles) are for median values (mean values). The red (yellow) squares are for 10% (90%) values.

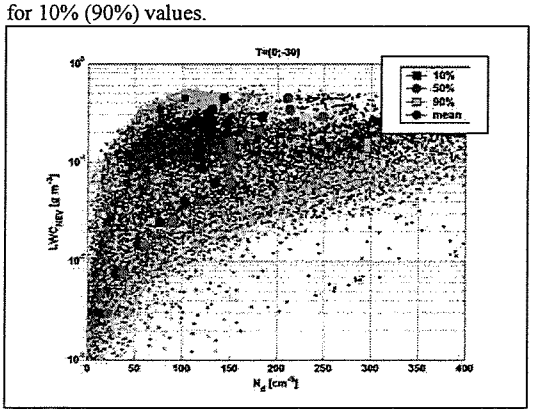

Fig. 3: Same as Fig. 2 except for N_d.

3.3 LWC versus N_d

Fig. 3 shows LWC versus N_d obtained using the in-situ data from each flight segment. The 1-s LWC values increase sharply with N_d when N_d<100 cm^{-3}, then gradually increases with increasing N_d. The variability in LWC is very large for a given N_d, suggesting that variability should be considered in future parameterizations. The general trend between LWC and N_d in Fig. 3 suggests that the use of N_d in Eq. 1 is justified.

3.4 LWC versus IWC

Fig. 4 shows LWC versus IWC. Obviously, the relationship is not clear between these two variables. Mean values (blue circles) of LWC increase with increasing IWC when the mean IWC<~0.1 g m^{-3} and the mean LWC<0.1 g m^{-3} but, when the LWC>0.1 g m^{-3}, LWC decreases with increasing IWC, although the variability is very large. In the consideration of mixed phase conditions for a specific cloud volume, one should see decreasing LWC with increasing IWC. The scatter of data points in Fig. 4 suggests that uncertainties in the measurements can be significant when mixed phase conditions exist or LWC increases in the saturated environment at the same time IWC continues to increase.

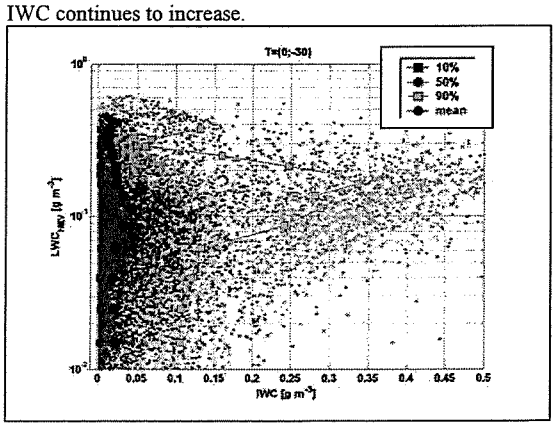

Fig. 4: Same as Fig. 2 except for IWC.

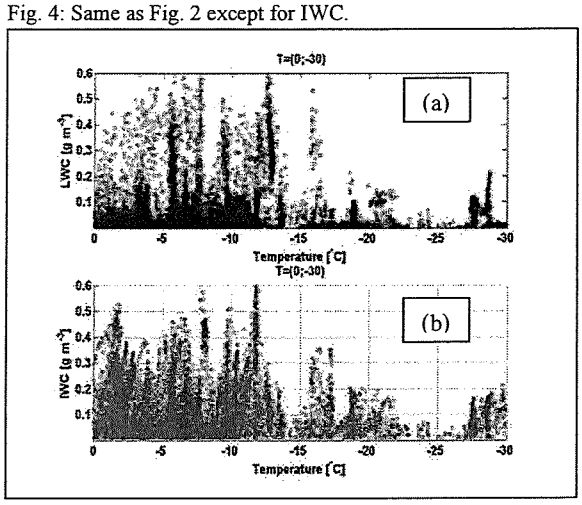

Fig. 5: LWC and IWC versus temperature.

3.5 LWC and IWC versus T

Fig. 5 shows LWC versus T in (a) and IWC versus T in (b). Although there is no clear relationship between IWC and LWC (see Fig. 4), they show a much better correlation with decreasing T. Both parameters decrease with decreasing T, since not enough moisture is available at cold T for particle growth. The variability for a given T is so large that any derived relationship between LWC fraction and T cannot be unique. As shown in earlier studies and in the present work, LWC decreases with decreasing T, and for this reason, T is included in Eq. 1.

3.6 LWC_{obs} versus LWC_{pre}

Fig. 6 shows how the results obtained from Eq. 1 compare with observations. The black line is for the observed LWC, and the red line is for the predicted LWC. Comparisons for a 200 sec (20 km) flight segment from Dec. 10 2004 case show that LWC_{pre} follows LWC_{obs} values closely, but for individual points, the uncertainty in the mean LWC_{pre} can be very large. Overall, the mean LWC_{pre} is found to be about 0.034 g m^{-3} and mean LWC_{obs}=0.056 g m^{-3} for the 200 s segment.

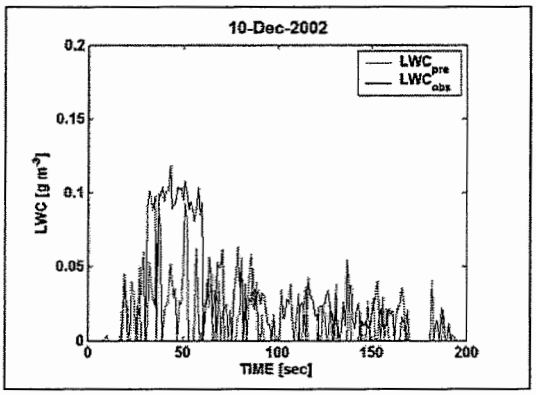

Fig. 6: Time series of observed and predicted LWC.

4. DISCUSSIONS

The results indicate that for individual data points (1-s data), the uncertainty in LWC can be as high as 50%. This is a significant value, but previous studies also had similar uncertainties. For example, using observed ice water contents, Fig. 7 shows a time series with calculated LWC using various parameterizations of liquid fraction such as Smith (1990) $LWC_{Sm.}$, Moss and Johnson (1994) LWC_{MJ}, Sun (1995) LWC_{Su}, Rockel et al. (1991) LWC_{Ro}, and. Korolev et al. (2003) LWC_{Ko}. An exponential fit to the Korolev et al data, with R=0.90, was obtained for mixed phase conditions. Fig. 8 shows the various parameterizations plotted against each other, along with the 1-s observations. These comparisons also indicate that LWC fraction versus T is not unique, and it is likely that some other parameters should be considered in the parameterizations.

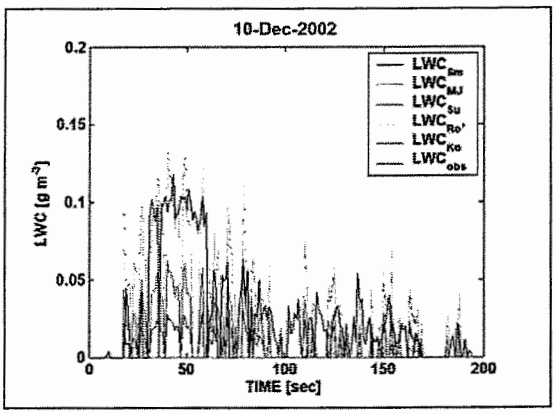

Fig. 7: Time series of observed LWC and LWC estimated using previous studies.

In order to verify the differences among the parameterizations, they are applied to observations collected at 20 km segments for various T levels, and the results are shown in Table 1. Table 1 indicates that the derived LWC amounts can be significantly different as compared to LWC_{obs}, depending on T. The last column in Table 1 shows the relative uncertainty as compared to the observed LWC_{obs}, indicating that the methods given by Rockel et al (1991) and the present work (shown as LWC_{GI}) resulted in less uncertainty (~37%).

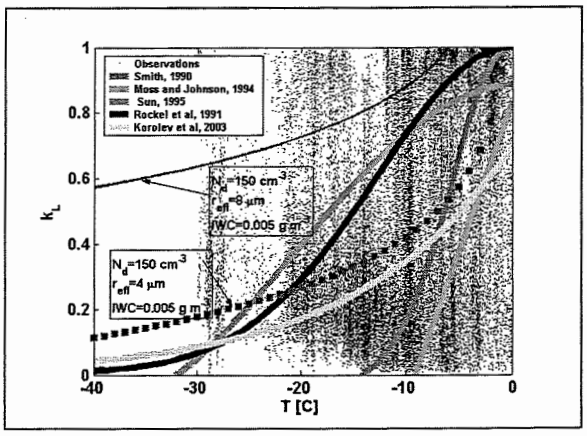

Fig. 8 The liquid fraction (LWC/TWC) versus temperature from observations (red dots), previous studies, and current work (blue lines) using fixed N_d, r_{eff}, and IWC values.

The variability as seen in Fig. 8 is very large. This suggests that the use of mean values for fits should be clearly explained, and the scales they represent, should be given. Future parameterizations should also include an indication of the variability. Because of nonlinearities in the relationships among microphysical parameters, large variability exists. Because of this it is possible that

overestimates or underestimates of LWC may occur when Eq. 1 is applied to specific cases.

Table 1: LWC values at various T levels. The last column shows mean LWC values from each parameterization and observations. The percentile shows the difference as compared to the mean observed LWC_{obs}.

T[C]→ [g m^{-3}]↓	-2.5	-5.2	-9.5	-14.3	-28.2	Mean LWC [g m^{-3}]
LWC_{obs}	0.084	0.192	0.056	0.028	0.023	0.128
LWC_{GI}	0.102	0.197	0.034	0.025	0.047	0.081(37%)
LWC_{Sm}	0.017	0.074	0.017	0.001	0	0.022(83%)
LWC_{Su}	0.092	0.168	0.067	0.043	0.004	0.075(41%)
LWC_{Ko}	0.062	0.096	0.032	0.019	0.004	0.043(66%)
LWC_{Ro}	0.104	0.183	0.067	0.039	0.004	0.079(38%)
LWC_{MJ}	0.063	0.064	0.001	0	0	0.026(80%)

Currently, LWC or TWC in general circulation models (GCMs) is obtained from either prognostic equations or diagnostically defined parameterizations. Then, IWC in mixed phase clouds is estimated from the LWC fraction versus T relationships and the model calculated TWC. Using bulk formulas, LWC can be obtained as a function of N_d, and r_{eff}. N_d, if it is not specified, can be obtained from aerosol number concentrations (N_a) measurements (Gultepe and Isaac, 2004). The new parameterization in this paper uses N_d, r_{eff}, TWC, and T to estimate LWC and IWC in mixed phase clouds. It should be noted that IWC in Eq. 1 can be replaced by TWC-LWC if TWC is known. Then, Eq. 1 can be easily used in GCMs, allowing microphysical parameters to interact at each time step. It also appears to be more physically realistic.

5. CONCLUSIONS

The main conclusions derived from the present work are summarized as follows:

♦The significant relationships between LWC and N_d, and r_{eff}, and T indicated that LWC fraction parameterization for mixed phased clouds should include N_d, r_{eff}, and T.

♦Inclusion of IWC in the new parameterization is important physically but the measurement accuracy for IWC still is a challenge (Gultepe et al., 2000). This may cause a large variability in LWC obtained from this new parameterization and from the fraction rate parameterizations in earlier studies.

♦The new parameterization is better than LWC fraction parameterizations that use only T because it potentially includes more microphysical processes.

♦The variability in the present results indicates that the derived relationships are not unique and should be used cautiously.

♦The scale issues are still major problems that need to be resolved.

6. ACKNOWLEDGEMENTS

The main funding for the AIRS1 project was provided by the National Search and Rescue Secretariat of Canada, Boeing Commercial Airplane Group, Transport Canada, Federal Aviation Administration (FAA), and NASA Glenn. The aircraft data were obtained using the National Research Council of Canada Convair-580 and the scientific and technical efforts of many National Research Council and Meteorological Service of Canada staff.

7. REFERENCES

Cober, G., G. A. Isaac, A. V. Korolev, and J. W. Strapp, 2001: Assessing cloud-phase conditions, ***J. Appl. Meteor.***, **40**, 1967-1983.

Gultepe, I., and Isaac, G. A., 1997: Relationship between liquid water content and temperature based on aircraft observations and its applicability to GCMs. ***J. Climate.*** **10**, 446-452.

Gultepe, I., G. Isaac, D. Hudak, R. Nissen, and W. Strapp, 2000: Dynamical and Microphysical characteristics of arctic clouds during BASE. ***J. of Climate***, **13**, 1225-1254.

Gultepe, I., and and G. A. Isaac, 2004: An analysis of cloud droplet number concentration (N_d) for climate studies: Emphasis on constant N_d. ***Q. J. Royal Met. Soc.***, conditionally accepted.

Isaac, G.A., S.G. Cober, J.W. Strapp, A.V. Korolev, A. Tremblay, and D.L. Marcotte, 2001: Recent Canadian research on aircraft in-flight icing. ***Canadian Aeronautics and Space Journal***, **47**, 213-221.

Korolev, A. V., G. A. Isaac, S. G. Cober, J. W. Stratt, and J. Hallet, 2003: Microphysical characterization of mixed phase clouds. ***Q. J. R. Meteorol. Soc.***, **129**, 39-65.

Moss, S. J., and D. W. Johnson, 1994: Aircraft measurements to validate and improve numerical model parameterizations of ice to water ratios in clouds. ***Atmos. Res.*** **34**, 1-25.

Randall, D., J. Curry, D. Battisti, G. Flato, R. Grumbine, S. Hakkinen, D. Martinson, R. Preller, J. Walsh, and J. Weatherly, 1998: Status of and outlook for large-scale modelling of atmosphere-ice-ocean interactions in the Arctic. ***Bull. Amer. Meteor. Soc.***, **79**, 197-219.

Rockel, B., E. Raschke, and B. Weyres, 1991: A parameterization of broadband radiative transfer properties of water, ice, and mixed clouds, ***Beitr. Phyiscs.***, **64**, 1-12.

Smith, R. N. B., 1990: A scheme for predicting layer clouds and their water content in a general circulation model. ***Q. J. Royal Meteor. Soc.***, **116**, 407-426.

Sun, Z., 1995: Comparison of observed and modeled radiation budget over the Tibetian plateau using satellite data. ***Inter. J. Climatology***, **15**, 423-445.

HIERARCHY OF MICROPHYSICAL PARAMETERIZATIONS SUITABLE FOR CLOUD AND MESOSCALE MODELS.

William D. Hall*and Roy M. Rasmussen
National Center for Atmospheric Research†, Boulder, Colorado

1. Introduction

There has been a considerable amount of research on the modeling of microphysical processes that lead to the formation of precipitation within dynamical frameworks. This research has been concerned with many time and spatial scales, and physics mechanisms. While the most general theme often is to understand the role of natural and anthropogenic aerosols to precipitation formation, other purposes such as the prediction of specific physical phenomena such as rain, snow, and hail on the ground, aircraft icing conditions aloft, and precipitation enhancement potential remain important goals. This paper will present a hierarchy of microphysical parameterizations schemes to represent the major physical process characteristics of precipitation development in wintertime mid-latitude storms. The present approach utilizes classical spectral functions to represent each hydro-meteor class (i.e. cloud water, rain water, pristine ice, snow ,and graupel) in an explicit equation set. The hierarchy of schemes range from more complex two parameter functions to simplified one parameter representations of each class. The present work examines the suitability of the spectral assumptions commonly used to reduce the number of variables from two parameter to one parameter representations.

The bulk physical microphysical parameterization scheme for the ice phase generally follows the work of Reisner *et. al.* (1998) that is based upon the earlier works of Rutledge and Hobbs (1983,1984), Lin, Farley and Orville (1983), and Murakami (1990). For the liquid water phase (cloud droplets and rain), the Cohard *et. al.* (1998) analytical treatment of cloud condensation nucleation and the Khairoutdinov and Kogan (2000) stochastic collision-coalescence bulk parameterization are included. Several other variations of the microphysical processes that have been suggested by Thompson *et. al.* (2004) have also be included. The purpose of this hierarchy is to systematically compare different microphysical approaches within the identical dynamical framework.

*Corresponding author address: William D. Hall NCAR, PO Box 3000, Boulder, CO 80307; e-mail: hallb@ncar.ucar.edu.

†NCAR is sponsored by the National Science Foundation.

2. Model Description

The present dynamical framework is the non-hydrostatic Weather Research and Forecast Model (WRF), (WRF,2003). The hierarchy of microphysical schemes contains a number of different treatments of the microphysical processes for both liquid and ice phase processes. The warm rain processes include cloud condensation nucleation activation from a background activation spectrum to be used when the vertical motions can be explicitly resolved and a simple cloud number concentration prescription method to be used at larger scales. The coalescence of rain or drizzle include treatments by Kessler (1969), Berry and Reinhardt (1974), and Khairoutdinov and Kogan (2000). The ice phase includes separate bulk parameterization spectral treatments for small ice particles, graupel particles, and snow. The small ice particles are represented by a two parameter function (number and mass concentration) and graupel particles are represented by a one parameter mass concentration following the work of Thompson et. al. (2004). The snow field contains several different approaches that include a two parameter function, (number and mass concentration) and three other one parameter methods. The different treatments of the warm rain and snow field will be the focus of the present paper.

The snow field is represented by a traditional Gunn-Marshall distribution in the form, $N_s e^{-\lambda_s D}$. The two variable parameterization uses the field variables N_s and Q_s to completely describe the function. The one variable, Q_s, parameterization

can close the system by one of the following three methods:

1. Based upon the observational results of Sekhon and Srivastava (1970) Reisner *et. al.* (1998) approximated N_s to be a function of Q_s.

2. Based upon the observational results of House *et. al.* (1979) Thompson *et. al.* (2004) approximated N_s to be a function of Temperature.

3. Ryan (2000) suggests λ_s to be a function of Temperature.

3. DEC 13-14, 2001 Improve 2 Field Study

The present hierarchy of microphysical schemes is currently being employed in the WRF, MM5, and RUC models. This paper will present results using the WRF model on the well documented case study of Dec 13-14,2001 from the IMPROVE 2 field experiment, Garvert *et. al.* (2004), Woods *et. al.* (2004). A rather coarse 20 km resolution was chosen in order to match the RUC model resolution and test the suitability of microphysical parameterization assumptions to forecast the predominate microphyiscal processes at this scale. The present results show a snap shot of east-west vertical cross-sections of several microphysical fields that intersect the intense observational area where in situ aircraft data was collected during the field experiment in souther Oregon. The present results are for the case using the 2 parameter rain and 2 parameter snow parameterization assuming a 25 /cc cloud droplet concentration. The results illustrate characteristic results for both frontal and post frontal times during the Dec 13-14 storm. These results will be compared with the other parameterization approaches and presented at the conference.

4. Future Work

Many questions remain as to the suitability of using explicit bulk parameterization schemes where the dynamical representation may not be adequately caapturing the dominant motions controlling precipitation development. Work continues to test the hierarchy of bulk microphysical schemes for cases where verification observational data is availiable. Improvements to the spectral functions representation are planned. A complete analysis of this case, including finer resolution studies, will be reported at the conference.

5. REFERENCES

Berry, E.X., and R. L. Reinhardt, 1974: An analysis of cloud drop growth by collection. Part II: Single initial distributions. *J. Atmos. Sci.* , **31**, 2127-2135.

Cohard, Jean-Martial, Jean-Pierre Pinty, Carole Bedos, 1998: Extending Twomey's Analytical Estimate of Nucleated Cloud Droplet Concentrations from CCN Spectra. *J. Atmos. Sci.* , **55**, 3348-3357.

Cohard, Jean-Martial, Jean Pierre Pinty 2000: A Comprehensive two moment warm microphysical bulk scheme. I: Description and tests. *Quart. J. Roy. Meteor. Soc.*, **126**. 1815-1842.

Cohard, Jean-Martial, Jean Pierre Pinty 2000: A Comprehensive two moment warm microphysical bulk scheme. II: 2D experiments with a non-hydrostatic model. *J. Atmos. Sci.* , **55**, 1843-1859.

Dudhia, Jimy, 1993: A Nonhydrostatic Version of the Penn State-NCAR Mesoscale Model: Validation Tests and Simulation of an Atlantic Cyclone and Cold Front. *Mon. Wea. Rev.*, **121**, 1493-1513.

Garvert, M., C.P. Woods, B.A. Colle, C.F. Mass, P.V. Hobbs, J.B. Wolfe, 2004: Comparisons of MM5 Model Simulations of Clouds and Precipitation with Observations for the 13-14 December 2001 IMPROVE-2 Event. *J. Atmos. Sci.* , , submitted.

Kessler, E. 1969: On the distribution and continuity of water substance in atmospheric circulations. *Meteorol. Monogr.* No. **10**, American Meteorological Society, Boston, USA.

Khairoutdinov, Marat, Yefim Kogan, 2000: A New Cloud Physics Parameterization in a Large-Eddy Simulation Model of Marine Stratocumulus. *Mon. Wea. Rev.*, **11** ,229-243.

Lin, Yuh-Lang, Richard D. Farley, Harold D. Orville, 1983: Bulk Parameterization of the Snow Field in a Cloud Model. *J. Appl. Meteor.*, **22**, 1065-1092.

Murakami, M. 1990: Numerical modeling of dynamical and microphysical evolution of an isolated convective cloud - the 19 July 1981 CCOPE cloud. *J. Meteorol. Soc. Japan***68**, 107-128.

Rasmussen, Roy M., Ben C. Bernstein, Masataka Murakami, Greg Stossmeister, Jon Reisner, Boba Stankov, 1995: The 1990 Valentine's Day Arctic Outbreak. Part I: Mesoscale and Microscale Structure and Evolution of a Colorado Front Range Shallow Upslope Cloud. *J. Appl. Meteor.*, **34**, 1481-1511.

Reisner, J., R. M. Rasmussen, R. T. Bruintjes, 1998: Explicit forecasting of supercooled liquid water in winter storms using the MM5 mesoscale model. *Quart. J. Roy. Meteor. Soc.*, **124**, 1071-1107.

Rutledge, Steven A., Peter V. Hobbs, 1983: The Mesoscale and Microscale Structure and Organization of Clouds and Precipitation in Midlatitude Cyclones. VIII: A Model for the "Seeder-Feeder" Process in Warm-Frontal Rainbands. *J. Atmos. Sci.* , **40**, 1185-1206.

Rutledge, Steven A., Peter V. Hobbs, 1984: The Mesoscale and Microscale Structure and Organization of Clouds and Precipitation in Midlatitude Cyclones. XII: A Diagnostic Modeling Study of Precipitation Development in Narrow Cold-Frontal Rainbands. *J. Atmos. Sci.* , **41**, 2949-2972.

Ryan, B.F. 2000: A Bulk Parameterization of the Ice Particle Size Distribution and the Optical Properties in Ice Clouds. *J. Atmos. Sci.* , **57**, 1436-1451.

Sekhon,R.S., R.C. Srivastava, 1970: Snow apectra and radar reflectivity. *J. Atmos. Sci.* , **27**. 299-307.

Thompson, Gregory, R. M. Rasmussen, K. Manning, 2004: Explicit Forecasts of Winter Precipitation Using an Improved Bulk Microphysics Scheme. Part 1: Description and Sensitivity Analysis. *Mon. Wea. Rev.*, **132**,519-542.

Woods, C.P., M.T. Stoelinga, J.D. Locatelli, and P.V. Hobbs, 2004: Cloud Structures, Microphysical Processes and Synergistic Interaction between Frontal and Orographic Forcing of Precipitation during the December 13, 2001 IMPROVE-2 Event over the Oregon Cascades.*J. Atmos. Sci.* , , submitted.'

WRF, Weather Research and Forecasting (WRF) Model, available online at http://www.wrf-model.org

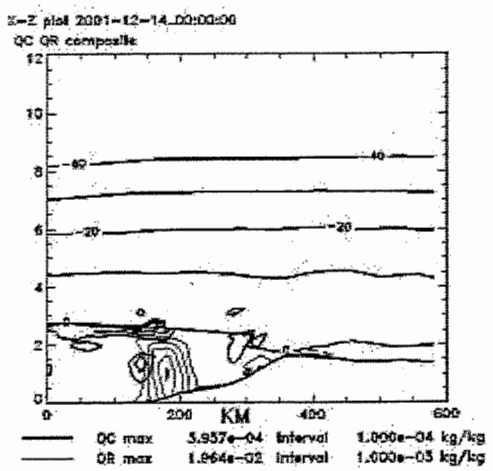

Figure 1: Cloud and Rain mixing ratio during the frontal passage at 0Z UTC.

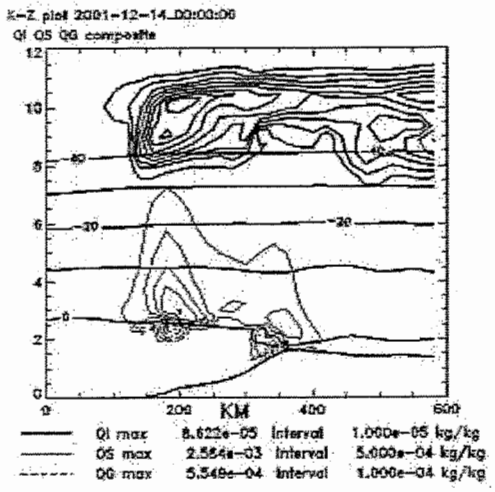

Figure 2: Ice Crystal, Snow and Graupel mixing ratio during the frontal passage at 0Z UTC.

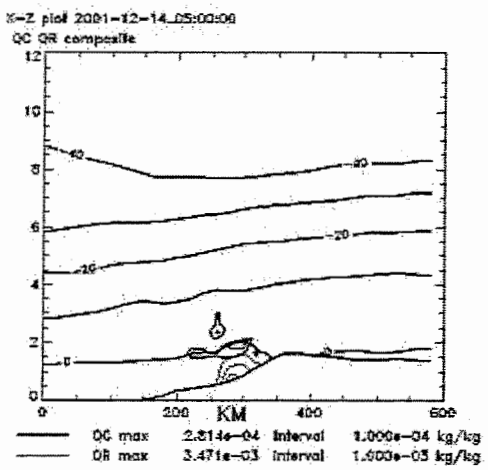

Figure 3: Cloud and Rain mixing ratio after frotal passage at 5Z UTC.

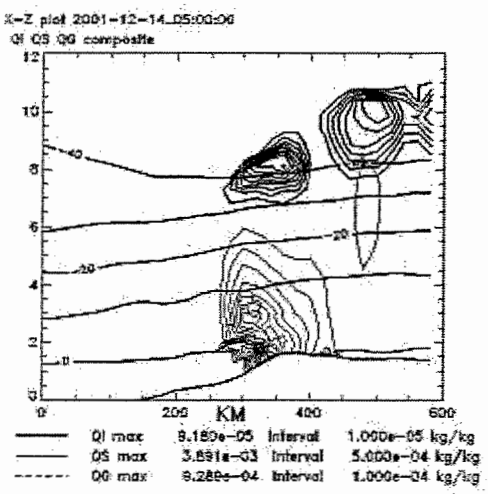

Figure 4: Ice Crystal, Snow and Graupel mixing ratio after frotal passage at 5Z UTC.

COMPARISON OF OBSERVED CLOUD PROPERTIES AT THREE GROUND BASED SITES WITH THEIR REPRESENTATION IN OPERATIONAL MODELS: THE EU CLOUDNET PROJECT

Anthony J.Illingworth[1], and the CloudNET team[2].

[1]Department of Meteorology, University of Reading, Reading, Berkshire, United Kingdom
[2]IPSL, CNRS, France; KNMI, The Netherlands; University of Reading, UK; RCRU, RAL, UK; The Met Of?ce, UK; TUD, The Netherlands; ECMWF, UK; MeteoFrance, France; Vaisala Oyj, Finland

1 INTRODUCTION

The correct representation of clouds is crucial to models used to provide short term weather forecasts and predict future climate change. Such models now typically have one or two prognostic variables to simulate the clouds, such as cloud fraction and ice/liquid water content. The EU CloudNET project has three aims: a) to develop cloud radar and lidar instrumentation and appropriate algorithms to derive the variables used to represent clouds in such models, b) to obtain a two year continous record of these cloud variables over three sites within Europe and then, c) to compare these observations with the representation of clouds over these three sites in four operational forecast models of ECMWF, the Met Of?ce, MeteoFrance and Racmo. The CloudNET project will terminate in the summer of 2005. In this paper we describe the progress made in the ?rst three years of the project. The instrumentation and sites are outlined in section 2 and a summary of the algorithms development is provided in section 3, the data sets in section 4, and some early results of comparisons with the models are described in section 5. Several papers in these proceedings provide further details. The 17 refereed CloudNET papers are too lengthy to list in this short article but can be found along with the data set quicklooks at http://www.met.rdg.ac.uk/radar/cloudnet/ .

2 CLOUDNET REMOTE SENSING STATIONS.

2.1 Observation Sites

The three sites are located at Chilbolton UK (51.14N -1.44E), Palaiseau, Paris, France (48.24N 2.16E) and Cabuaw, The Netherlands (51.97N 4.92E). At each site a variety of ground based remote sensing instruments is deployed, most of which have been operating 24 hours a day and 7 days a week since the start of the two year intensive period of observations on 1 October 2002. The most important instruments are the vertically pointing Dopplerised cloud radars (94/95 Ghz at Chilbolton and Palaiseau, and 35 GHz at Cabauw) and 905 nm lidar ceilometers which provide pro?les with 60m vertical resolution every 30 seconds. In addition there are downwelling broadband SW and LW radiometers, several microwave radiometers for providing water vapour and liquid water information and a 3 GHz radar at Cabauw. Other instruments such as 355 nm UV Raman lidar at Chilbolton and a polarimeteric lidar at Palaiseau have been run on an event basis.

Corresponding author address: Anthony J Illingworth, Department of Meteorology, University of Reading, Earley Gate, PO Box 243, Reading RG6 6BB, UK; E-mail: a.j.illingworth@reading.ac.uk.

2.2 Instrument Calibration

Accurate calibration is crucial when deriving cloud properties from the lidar and radar backscatter pro?les.

Lidar Calibration Traditionally lidars are calibrated by comparison with molecular Rayleigh scattering but this is not possible at wavelengths greater than 600 nm. Instead we use thick stratocumulus clouds to provide a self-calibration technique by adding up the backscatter (in m^{-1} sr^{-1}) at each gate until the signal is extinguished. This gives us the 'integrated backscatter' which should have a theoretical value of 15 sr in liquid water clouds. The calibration factor is adjusted until this value is achieved and provides an absolute calibration accurate to about 10%.

Radar Calibration Absolute calibration via link-budget calculations is error prone. Instead we use the fact that at 94GHz Mie scattering leads to a radar re?ectivity in rain above 2 mm hr^{-1} which is virtually constant and close to 19 dBZ. The re?ectivity is measured at a range of 250 m to minimise any attenuation affects and provides an absolute calibration to within 1 dB.

3 DATA QUALITY AND ALGORITHMS

3.1 Categorisation and Quality Control

If the products are to be used for evaluating NWP model performance then the data must be rigorously quality controlled to avoid spurious artifacts being falsely identi?ed as cloud.

Categorisation The ?rst stage is to examine the lidar backscatter and Doppler data together with the temperature pro?le from the operation models and classify the targets into nine categories of targets: i) aerosols, ii) insects, iii) aerosols and insects, iv) ice and supercooled droplets, v) ice, vi) drizzle/rain and cloud

droplets, vii) drizzle or rain, viii) cloud droplets only, and ix) clear sky.

Quality control This categorisation information is accompanied by a status ?ag. Firstly, the 94GHz radar must be corrected for attenuation by water vapour and oxygen which is straightforward using the operational model. Cloud liquid water attenuation can be corrected if good radiometer data is present, but very dif?cult for attenuating rain. Low level water cloud will extinguish the lidar return completely. This leads to nine status ?ags: i) Radar ground clutter, ii) Radar corrected for liquid attenuation, iii) No radar echo but known attenuation iv) Good radar echo only v) No radar but unknown attenuation (rain), vi) Good radar and lidar echo, vii) Radar echo but uncorrected attenuation, viii) Lidar echo only, and ix) Clear sky.

3.2 Retrieval Algorithms

The next stage is to derive the products which will be compared to the values held in the operational model output which is available every hour with a vertical resolution ranging from 100 m to 500 m. Below is a summary of some of the algorithms which have been developed. Note the philosophy whereby operational model variables are used in some of the algorithms.

Cloud Fraction. The categorisation information can be used to identify which of the 60m/30second pixels contain a cloud, as opposed to, for example, a radar signal indicating drizzle below the lidar cloud base. A typical model grid box will contain over a hundred pixels so cloud fraction can be estimated to a few per cent. The spatial distribution of pixels within the grid box can be used to examine cloud overlap properties.

Ice Water Content from Z and T. The re?ectivity values of those pixels within a model grid box categorised as ice can be converted into ice water content (IWC) either by a straightforward empirical IWC-Z relationship, or, for increased accuracy, an IWC-(Z,T) relationship using T from the operational model. A value of mean IWC within a grid box or a pdf of IWC within the grid box can then be derived together with its error. The error has two components, one associated with the IWC-Z or IWC-(Z,T) retrieval, and an additional error arising from the attenuation of Z and the con?dence with which that attenuation has been corrected. During heavy rain we reject all data as being too error prone.

Ice Water Content and Size from Radar and Lidar When the categorisation indicates ice and the quality ?ag signals that there are good radar and lidar echoes, then a radar/lidar algorithm is invoked which uses the radar signal to correct for lidar attenuation, and then derives the ice particle size from the ratio of the radar backscatter to the attenuation corrected lidar backscatter. Once the size is known then a more accurate IWC can be calculated from the value of Z (see van Zadelhoff and Donovan, these proceedings).

Ice particle Density. The density of ice particles tends to fall with increasing size and the precise form of this density-size relationship can change the IWC derived from Z by 50%. The variation of the ratio of the re?ectivities at 35 and 94 GHz as a function of the ratio of the observed mean Doppler at the two frequencies can be used to infer the optimum density-size relationship (see Gaussiat et al, these proceedings).

Stratocumulus with and without drizzle. It is dif?cult to derive liquid water content (LWC) of clouds from Z because the presence of occasional drizzle droplets dominates Z but contributes little to LWC. Techniques have been developed which use the Doppler and re?ectivity radar observations with the lidar to isolate the drizzle component and derive the concentration and size of the droplets together with the drizzle ?ux. In the absence of drizzle the lidar and radar signal are used to derive the size and concentration of the cloud droplets and hence ?nd the LWC and the degree to which mixing leads to subadiabatic values. These ?ndings con?rm the validity of assuming a pro?le with a constant drop concentration in the lower half of stratocumulus clouds (see O'Connor et al, these proceedings).

Turbulence. The rate of dissipation of turbulent kinetic energy (TKE) is derived from a new radar parameter: the variance of the mean Doppler velocities recorded every second over a period of thirty seconds. This new approach uses the wind, U m s^{-1}, from the operational model, so that the two limits for the spatial scale of the motions sensed by the variance of the mean Doppler are 30U m and (U+beamwidth) m. These two limits are within the inertial subrange, so by integrating an expression involving the variance of the mean doppler between these two spatial scales, we can derive the dissipation rate of TKE in terms of the observed variance in the mean Doppler. The values of TKE in stratocumulus are found to be three orders of magnitude higher than in cirrus.

4 DATA SETS

The raw observations taken every 30 seconds with 60 m resolution are displayed on quick looks for each site every day in near real time together with monthly composite quick looks. The derived model quantities are plotted on the hourly model grid with the appropriate vertical resolution and displayed on the web together with parameters from the four operational models hour-by-hour at each site. All data are recorded in standard netCDF format for ease of subsequent processing.

The raw data plotted are pro?les of i) radar re?ectivity, ii) mean Doppler, iii) spectral width, iv) variance of the mean Doppler, v) lidar backscatter; integrated values of vi) rainrate , vii) liquid water path from the radiome-

ters; pro?les of viii) the 94GHz attenuation from oxygen and water vapour, ix) 94GHz attenuation due to lwp, x) broad band SW and LW downward ?uxes. Then the derived pro?les of xi) target classi?cation xii) target status, xiii) cloud fraction calculated by area and volume, and for one hour or for a time equivalent to 60km estimated using the model winds. xiv) Integrated cloud cover computed four ways as for the cloud fraction pro?les xv) Pro?les of Ice water content from Z and T and associated errors and status xvi) Pro?les of Ice water content, ice particle size and extinction coef?cient calculated from simultaneous radar and lidar and associated errors xvii) Pro?les of dissipation rates of TKE derived from the variance of the mean Doppler and its associated error.

These observed quantities can then be compared with the hourly pro?les from the four operational models. The following values are archived for the grid point above the three stations: T, q_v, RH, LWC, IWC, u, v, w, and cloud fraction.

5 RESULTS

The common NetCDF data format makes comparing model and observations relatively straightforward. We now report on three example comparisons.

5.1 Fractional cloud cover and ice water content

Analysis of one years data over Chilbolton reveals that the ECMWF and Met Of?ce mean fractional cover for the whole year tended to be overestimated above 6km and underestimated below 6km. This was principally due to an error in the fractional cloud cover when cloud was present. The values of pro?les of IWC in the two models were about half the value observed, but this difference was within the error of the observed IWC arising from uncertainty in the IWC-(Z,T) relationship. In addition, the data were split up into six weather regimes, depending whether there was ascent at 500 and 700mb and if the atmosphere was stable at 900mb. An example of the conclusions is that the Met Of?ce diagnostic cloud fraction scheme found it dif?cult to produce 100% cloud cover when there was low level stability, whereas such complete cloud cover was frequently observed and well captured by the prognostic cloud cover scheme used by ECMWF. More detail is provided by Brooks et al (these proceedings).

5.2 Climatology of supercooled clouds

Supercooled cloud layers can be easily identi?ed by the very high lidar backscatter leading to total extinction of the signal at cold temperatures which is not accompanied by a signi?cant increase in radar re?ectivity. This inference has been validated by simultaneous in-situ aircraft observations of cloud particle type. Analysis of one year's data at Chilbolton and Cabauw reveals that such layers are relatively common, for example on 20% of the occasions when there is cloud at -10C then a supercooled layer is present. Such layers are often thin and contain relatively low amounts of condensed water but have a large effect on the radiation, but the same amount of water in the form of ice would have a much smaller radiative impact. The models are not able to produce these supercooled layer clouds in a realistic manner.

5.3 Parameterisation of ice cloud inhomogeneities

Analysis of the spatial distribution and variability of individual pixels of ice water content within a model grid box has revealed that the pdf of the iwc is well represented by either a log-normal or gamma function. Expressions have been derived on how the fractional variance of the iwc varies within the grid box as a function of grid box size and wind shear. In addition the degree to which inhomogeneities in ice water content overlap in the vertical has been quanti?ed as a function of grid box size and wind shear; currently the ice is assumed ?ll the grid box uniformly but the degree of overlap in?uences the radiative transfer.

5.4 De?ning cloud fraction by volume or by area

Models implicitly assume that the fraction of the grid box ?lled by cloud is equal to the projected area of the grid box ?lled by cloud, and use this fraction for computing radiative effects. Analysis of the precise distribution of cloudy pixels within a grid box shows that clouds usually slope to some degree so that the cloud fraction by area is always higher than that by volume. For example, for a grid box with a height of 720m if the volume is half ?lled with cloud, then the horizontally projected area of cloud is about 80%. Analytical expressions have been derived for the mean difference between the two values of cloud cover as a function of grid box size and wind shear.

6 CONCLUSION

A unique quality controlled data set of observed pro?les of cloud properties with errors at three ground stations and coincident pro?les of the representation of clouds in four operational models is being obtained. The data is all stored in a common format to facilitate comparison of the observations with the model representation and the ?rst results are being produced. With this infrastructure it is a simple step from comparing one algorithm product at one site with one model output to testing the product at all sites for all models. Such comparisons will be available over the next twelve months.

6.1 Acknowledgements

This work has been carried out with the ?nancial support of the EU CloudNET action contract EVK2-2000-00065.

Tropical Cirrus Parameterization for Trimodal Size Spectra

Dorothea C. Ivanova[1], David L. Mitchell[1], Greg M. McFarquhar[2]

1) Desert Research Institute, Reno, NV; 2) University of Illinois at Urbana-Champaign, IL

The role of small ice crystals in cirrus and the use of the FSSP (Forward Scattering Spectrometer Probe) to characterize the concentration and sizes of small crystals continues to be controversial, although new evidence in recent studies indicate that the FSSP may approximate the size distributions (SD) of small ice crystals (D < 100 micrometers). Efforts to parameterize the SD in tropical anvil cirrus should thus take advantage of existing FSSP data to evaluate the potential impact of small ice crystals. This study describes a parameterization for trimodal size spectra in tropical cirrus, based on 5,546 SD taken from 3 flights on April 1, April 4 and March 17 1993, during the Central Equatorial Pacific EXperiment (CEPEX). FSSP and 2DC probe measurements were used to parameterize the SD. This parameterization provides three gamma SD parameters for each mode of the trimodal distribution: very small, small and large.

The parameters are expressed in terms of cloud ice water content (IWC) and/or temperature (T). SD behavior in the tropical cirrus is quite different from the SD behavior in the mid-latitude cirrus. This leads to differences in the cloud radiative properties. The resulting parameterization predicts the full trimodal SD in terms of three gamma functions, based on knowledge of T and total IWC. The simple inputs make the parameterization useful for Global Climate Models (GCMs).

Accuracy of the FSSP in Cirrus

There is now mounting evidence that the FSSP does a reasonable job at measuring the concentration and size of small ice crystals. Figure1 compares size distribution (SD) measurements from various probes, including the Cloudscope (CS) and the FSSP. The operating principle of the CS is impaction at high collision efficiency, yet it agrees relatively well with the FSSP.

Courtesy of Pat Arnott and students

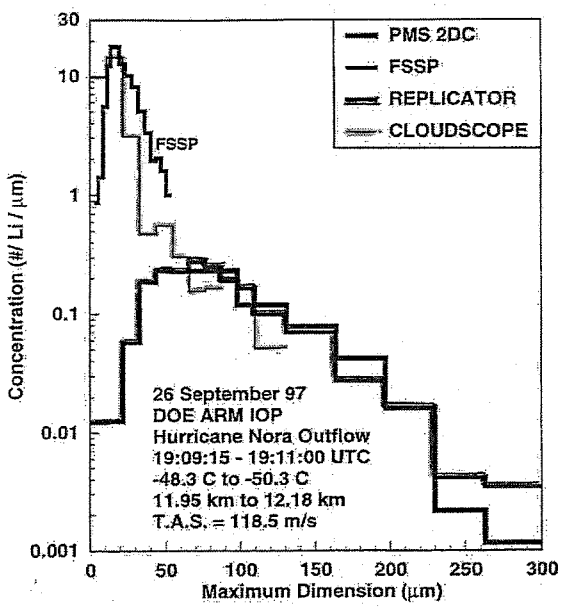

Fig.1 Comparison of replicator, 2DC, FSSP, and cloudscope data for the indicated time interval. The 2DC and replicator data are in excellent agreement for maximum dimension greater than 66 µm. The FSSP and cloudscope data are in reasonable agreement. Replicator data for particle sizes less than 50 µm 'rolls off' in comparison with the FSSP and cloudscope results.

A Trimodal SD parameterization for tropical Cirrus clouds:

We used CEPEX cases of March 17, April 1 and April 4. We parameterize SDs as trimodal (see Fig. 2 a), b) and c)), with all three modes: 1. very small, 2. small and 3. large mode, expressed as a gamma distribution having the form:

$$N(D) = N_0 D^{\nu} \exp(-\lambda D)$$

5,546 CEPEX size distributions were used in this parameterization. Every SD analyzed in this study exhibited three distinct populations as illustrated in Fig. 2 a) b) and c).

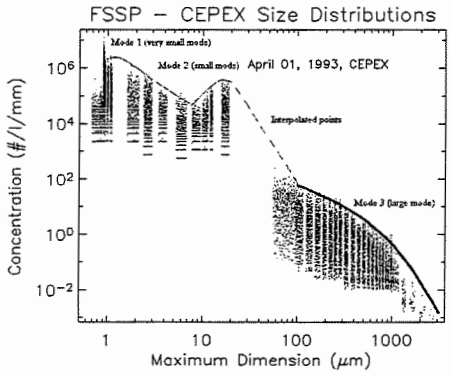

Fig. 2 a) CEPEX data for March 17,1993

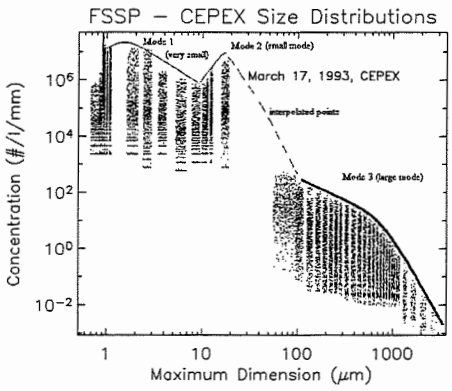

Fig. 2 b) CEPEX data for April 01, 2003.

The SD parameters D, λ and ν in Table 1 were determined from the probe measurements, using the formulas, given in Mitchell(1991).

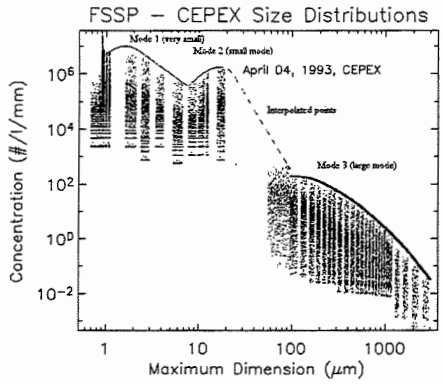

Fig. 2 c) CEPEX data for April 17, 2003.

Naturally, the three modes: 1.very small, 2. Small and 3. Large are present. Mode 1 (very small) has been ignored in the previous parameterization studies.We use linear interpolation (10 additional data points are created) between the last FSSP and the first usable 2-DC bins to approximate better Mode 2 and to estimate more-accurately the IWC amounts.

Parameter	*Value*	*St.deviation*
D1	**2.47384**	**1.1672**
Lambda 1	**28130.4112**	**13093.315**
Nju 1	**6.02121**	**3.67834**
D2	**18.06**	**4.3218**
Lambda 2	**2779.81**	**757.50810**
Nju 2	**4.02**	**1.38143**

Table 1. Trimodal distribution parameters, which are approximated as constants.The crystal shape assumed is Planar polycrystals.

The description of the parameterization methodology and procedure is given next as a Flow chart of methodology. Note: planar polycrystals are assumed for the shape of mode

2 and mode 3 ice crystals and spheres are assumed for the very small mode 1 crystals.

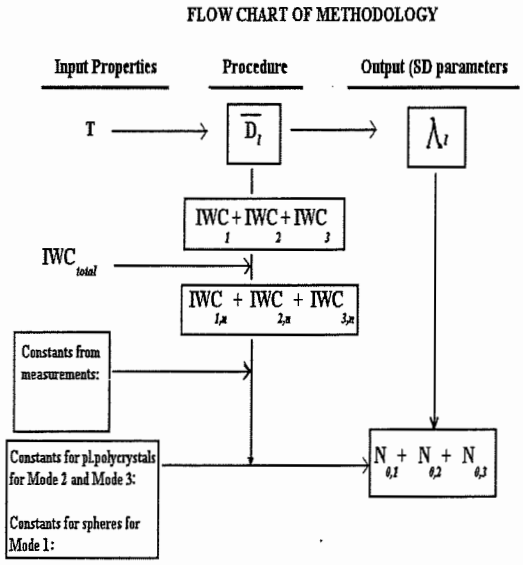

This methodology illustrates the procedure for acquiring all nine of the gamma parameters for trimodal size spectra The SD constant values were obtained directly from measurements and are listed in Table 1.

Normalized IWC calculated from the FSSP and 2-DC related to the large mode (mode 3) mean size D. Here:

$$F_{iwc} = -1.633\text{x}10^{-4}T - 0.005453$$
$$IWC_1 = F_{iwc}(IWC_{total}) \quad F_{iwc} > 0.0001$$
$$IWC_2 = 0.04 + 0.96(\exp(-D_3/55)^{3.7})$$

and $IWC_3 = 1.0 - (IWC_1 + IWC_2)$

Main Findings:

As temperature decreases beyond -35 C, the magnitude of the small mode is enhanced with the tropical scheme, but the opposite occurs with the mid-latitude scheme. This is a fundamental finding, and indicates that the radiative properties of tropical and mid-latitude cirrus are considerably different for the same IWP. For example, tropical cirrus should reflect considerably more sunlight at colder temperatures for the same IWP.

This finding may also point to the different mechanisms by which convective and non-convective cirrrus are generated. The temperature dependence of their size spectra may yield important clues for unraveling the underlying physics that determine the evolution of size spectra in these different cloud systems.

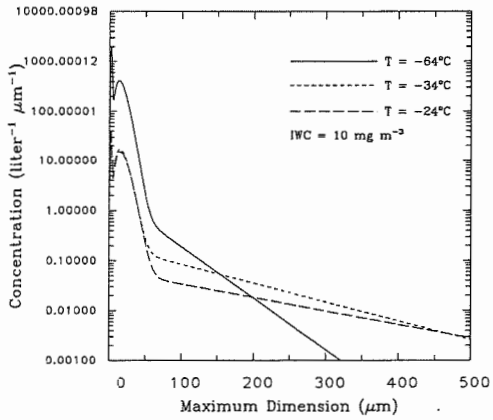

Fig.3. Size spectra predicted by the new tropical trimodal parameterization.

SUBGRID-SCALE ACTIVATION OF CCN

Hongli Jiang* and William R. Cotton

Department of Atmospheric Science, Colorado State University, Ft. Collins, CO 80523

1 A PDF MODEL

A one-dimensional probability distribution function (PDF) based boundary layer parameterization has been recently developed (Golaz et al., 2002a,b). The PDF model is a higher-order closure model with a closure based on a double Gaussian family of PDFs. It can accurately represent a variety of non-precipitating boundary layer regimes without the need for trigger functions. In the PDF model, the subgrid-scale, higher-order vertical velocity moments such as second and third moments are predicted. These velocity scales provide information that can be used to diagnose subgrid-scale variations of supersaturation.

In this paper the PDF model is extended to include precipitation processes which will permit cloud microphysical/dynamic/radiative response to varying concentrations of cloud condensation nuclei (CCN), giant CCN (GCCN), and ice forming nuclei (IFN). In this paper we focus on calculation of subgrid-scale supersaturation , which is of utmost importance to investigations of aerosol indirect effects on clouds. The inclusion of the subgrid-scale activation in the PDF model is referred to as the coupled PDF model.

Our guiding principle in this work is to develop parameterizations of subgrid-scale effects on nucleation, condensation, collection, and precipitation formation without adding a large number of prognostic variables. A number of previous studies have used an empirical formulation to estimate average droplet concentrations due to nucleation (e.g. Ghan et al. 1993; Lohmann et al. 1999a). The estimated droplet concentrations are dependent on total soluble aerosol number concentration, vertical velocity, and parameters related to aerosol composition, geometric standard deviation of log-normal aerosol size distribution, and the mode radius. We seek similar simpli?ed approaches to parameterize activation of CCN. We use large eddy simulations (LESs) of a number of observed boundary layer cases as benchmark data sets to aid our development and to verify the performance of the coupled PDF model.

Six cases are chosen all based on the Global Energy and Water Experiment (GEWEX) Cloud Study System (GCSS) boundary layer cloud intercomparison working group. They represent a broad range of boundary layer regimes including trade-wind cumulus (BOMEX), cumulus over land (ARM), stratocumulus (ASTEX, FIRE, DYCOMS II), and intermediate case (ATEX). ATEX represents an intermediate case between stratocumulus and cumulus with cloud fraction greater than 50%.

2 INTERFACE THE PDF TO RAMS ACTIVATION SCHEME

2.1 RAMS activation scheme

The Regional Atmospheric Modeling System is a multi-purpose modeling system that has been used to simulate a wide variety of cloud systems. The newest version of bulk microphysics in RAMS is designed to emulate a bin-resolving microphysics model including, prediction of cloud droplet number from a fully prognosed CCN ?eld (Cotton et al. 2003). The number of CCN that activate are a function of air temperature, Lagrangian supersaturation production rate (related to vertical velocity and other factors), number concentration of CCN, and median radius of the CCN distribution. Other factors such as CCN chemistry, mean radius, and spectral width are considered ?xed for a given simulation since these produce the least relative variability. Based on the above CCN characteristics and environmental factors, the fraction of CCN that nucleate into cloud droplets is accessed in RAMS from a lookup table that was previously generated from a detailed bin-parcel model (Saleeby and Cotton 2003).

The lookup tables are essentially data tables with four-dimensional arrays containing percentage values of CCN that activate and grow to cloud droplet sizes.

*Corresponding Author's Address, Hongli Jiang, Department of Atmospheric Science, Colorado State University, Fort Collins, CO 80523; E-Mail: jiang@atmos.colostate.edu.

The table values vary with air temperature, vertical velocity, CCN concentration, and median radius of CCN distribution. Figure 1 displays droplet numbers activated vs vertical velocity at a selected median radius and CCN concentration over a range of air temperature. To interface the PDF model to the RAMS activation scheme, each of these four variables is either provided by the PDF model directly if available or derived from other prognostic or diagnostic variables in the PDF model.

2.2 Subgrid scale vertical velocity

The w diagnosed in the PDF model is a grid mean, and will be so small to be meaningless. We therefore seek w-moments predicted from the PDF model that yield appropriate subgrid-scale vertical velocity. Detailed procedure on how to identify the relationship between higher-moments and subgrid-scale vertical velocity are described in the following.

Using the bulk microphysics with its CCN activation parameterization, large eddy simulations (LESs) of the six observed boundary layer cases are performed with an initially uniform CCN spectra. In the LES various clouds activate the CCN to form cloud droplets with a concentration N_d. The simulated cloud layer is sampled to obtain an average droplet concentration $\overline{N_d}$. Given the CCN spectra and the computed average $\overline{N_d}$ we can identify the w-scale that has yielded a $\overline{N_d}$ for the pressure and temperature at the sample level from the activation scheme (see Fig. 1). From the PDF of w derived from the LES data, we determine whether there exists a w-moment corresponding to the w that yielded $\overline{N_d}$. Our approach is to repeatedly sample the LES data for all six cases to evaluate the appropriate w-scale.

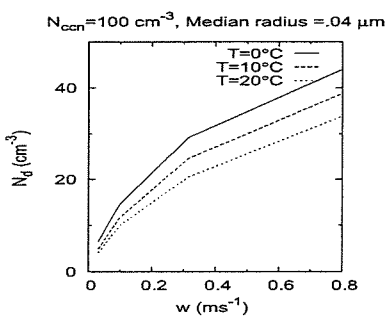

Figure 1: Number concentration of droplets activated from RAMS activation scheme.

We have found that the subgrid-scale w is dominated by the root-mean-square (rms) value of $\sqrt{\overline{w'^2}}$. Table 1 lists values of $\overline{N_d}$ averaged over the cloudy layer, the maximum value of $\sqrt{\overline{w'^2}}$ over the cloudy layer, and the corresponding w identi?ed from the activation scheme (Fig. 1) from all six cases of LES simulations. The parameter C is determined by assuming $w = C \times \sqrt{\overline{w'^2}}$. As can be seen in Table 1, C ranges from 0.166 to 0.387 with an average value of 0.226 among all six cases. A similar relationship is used in Lohmann et al. (1999b) who assumed that the subgrid-scale w is dominated by the turbulent transport, and is related to the rms value of TKE as $w = \overline{w} + c\sqrt{TKE}$ with $c = 0.7$. The vertical velocity used throughout this study will be the sum of the grid mean, $\overline{w}$, and the subgrid-scale vertical velocity as $w = \overline{w} + c\sqrt{\overline{w'^2}}$ with $C = 0.226$.

Table 1. Values of $\overline{N_d}$, maximum of $\sqrt{\overline{w'^2}}$, and w

EXP	$\overline{N_d}$ (cm^{-3})	$\sqrt{\overline{w'^2}}$ (ms^{-1})	w (ms^{-1})	C*
ARM	11.	0.626	0.12	0.192
ASTEX	11.	0.310	0.12	0.387
ATEX	10.5	0.524	0.11	0.210
BOMEX	7.	0.329	0.065	0.198
DYCOMS II	12.	0.685	0.14	0.204
FIRE	10.	0.602	0.1	0.166

* C is de?ned through $w = C\sqrt{\overline{w'^2}}$, see text for details.

2.3 The coupled PDF model vs LES

Liquid water potential temperature (θ_{il}) and total water mixing ratio (r_t) are predicted, while liquid water mixing ratio (r_l) is diagnosed in the PDF model. The variables of $w = \overline{w} + C\sqrt{\overline{w'^2}}$, T, r_v either diagnosed or predicted in the PDF model are used to drive the supersaturation calculations in the RAMS bulk microphysics.

The variables discussed in the following are averaged over the horizontal $(x-y)$ planes and then time-averaged over the last two or four hours of simulations depending on the simulation length for each individual cases. Comparison between the results of LES and the coupled PDF model will be shown for selected cases. The coupled PDF model is con?gured and initialized similarly to the LES.

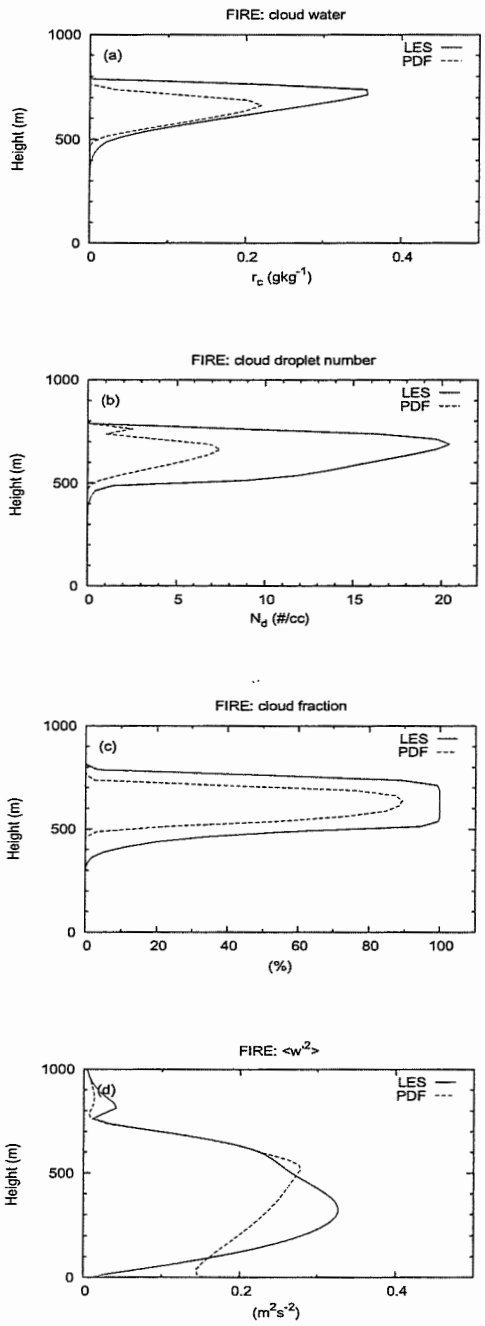

Figure 2: Pro?les of cloud water, cloud droplet number, $\overline{w'^2}$, and cloud fraction for the FIRE case. Solid lines are LES results, dashed lines are the coupled PDF model results time-averaged over the last 2 hours of simulations.

For the nocturnal stratocumulus FIRE case, the coupled PDF model produced a slightly thinner cloud layer that has a similar vertical pro?le and is located at the same height as the LES. The maximum cloud water (Fig. 2a) is about 61.7% and the cloud droplet number (Fig. 2b) is about 36.5% of that LES. The maximum of cloud fraction (the fraction of grid columns that contain cloud water) is 100% in the LES, and is 90% in the PDF model (Fig. 2c). Large differences in the variance of vertical velocity $\overline{w'^2}$ (Fig. 2d) are shown near surface and in the subcloud layer, suggesting different turbulent structure between the two models.

For the ATEX case, larger differences in cloud layer location and vertical distribution are demonstrated between the two models (Fig. 3a,b). Notice that the LES simulated a partial cloudiness below the major cloud layer (Fig. 3c), while the PDF model produced a single, deep layer. The reduced cloud cover beneath the major cloud layer is indicative of the presence of penetrating cumulus below the major cloud layer, a feature often observed in stratocumulus to cumulus transition regime (e.g. Miller and Albrecht, 1995). The variance of vertical velocity $\overline{w'^2}$, however, has a typical distribution of cumulus cloud with a secondary maximum in the subcloud layer due to dry convection, but the cloud layer values is twice as large in the PDF model as in LES. The maximum cloud water and cloud droplet number are about 45.8% and about 37.3% of that LES, respectively.

3 SUMMARY

We have presented preliminary results of the coupled PDF model for stratocumulus regime and alike. The results from these model diagnostics suggest that the coupled model can predict an average droplet concentration as high as 37% and cloud liquid water content as high 62% of that produced in a LES. The coupled PDF model has produced a similar turbulent structure as in LES.

For a cumulus population in which we have diagnosed the mean concentration of droplets using empirical methods we have developed, and then attempted to input it into the micro module. Naturally the grid-mean temperature, T, and total water mixing ratio, r_t, do not yield supersaturated conditions needed to calculate vapor deposition growth of droplets. A new sampling technique is being developed to sample the supersaturated portion of the r_t PDF space only. More complete results will be reported in a journal article.

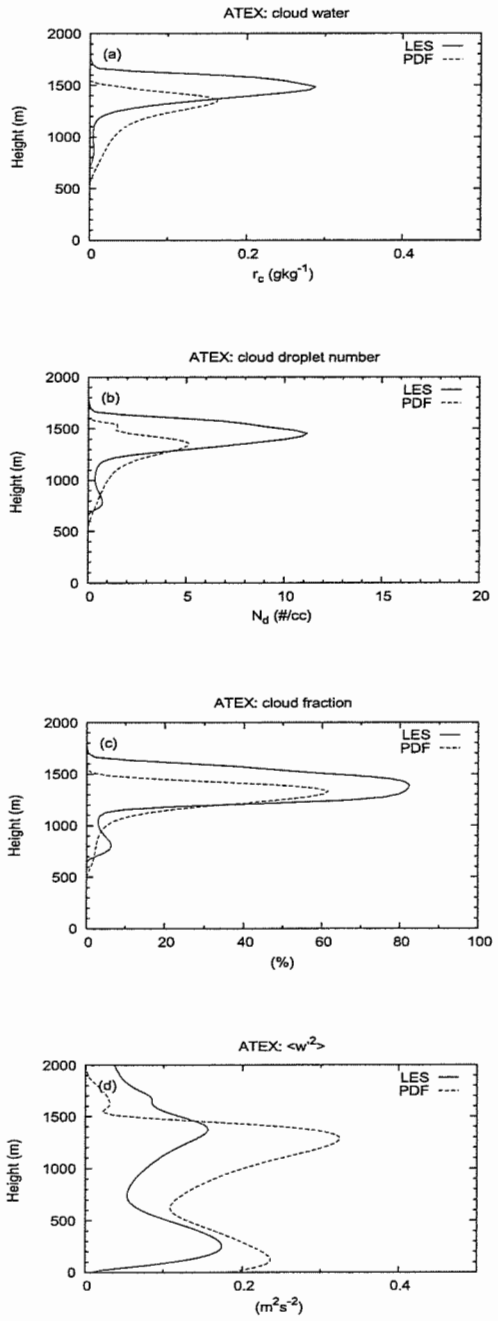

Figure 3: Similar to Fig. 2 except for ATEX case.

4 ACKNOWLEDGMENTS

This research was supported by NSF under Grant ATM-0215367.

5 REFERENCES

Cotton, W.R., R. Pielke, R. Walko, G. Liston, C. Tremback, H. Jiang, R.L. McAnelly, G.Y. Harrington, M. Nicholls, G.G. Carrio, and J.P. McFadden, 2003: RAMS 2001: Current status and future directions. *Meteor. And Atmos. Physics*, 82, 5-29.

Ghan, S. J., L. Ruby Leung, and R. C. Easter, 1997: Prediction of cloud droplet number in a general circulation model. *J. Geophys. Res.*, **102**, 21,777–21794.

Golaz, J-C, V. E. Larson, and W. R. Cotton, 2002a: A PDF-based model for boundary layer clouds. Part I: Method and model description. J. Atmos. Sci., **59**, 3540–3551.

Golaz, J-C, V. E. Larson, and W. R. Cotton, 2002b: A PDF-based model for boundary layer clouds. Part II: Model results. J. Atmos. Sci., **59**, 3552–3571.

Lohmann, U., J. Feichter, C. C. Chuang, and J. E. Penner, 1999a: Prediction of the number of cloud droplets in the ECHAM GCM. J. Geophys. Res., **104**, 9169-9198.

Lohmann, U., N. McFarlance, L. Levkov , K. Abdella, and F. Albers, 1999b: Comparing different cloud schemes of a single column model by using mesoscale forcing and nudging technique. *J. climate*, **12**, 348-461.

Miller, M.A. and B.A. Albrecht, 1995: Surface-based observations of mesoscale cumulus-stratocumulus interaction during ASTEX, *J. Atmos. Sci.*, **52**, 2809–2826.

Saleeby, M. S., and W. R. Cotton, 2004: A large-droplet mode and prognostic number concentration of cloud droplets in the Colorado State University Regional Atmospheric Modeling System (RAMS). Part I: Module descriptions and supercell test simulations. *J. Appl. Meteor.*, **43**, 182-195.

REPRESENTING STRATOCUMULUS CLOUDS IN NUMERICAL MODELS: SENSITIVITY TO MODEL PHYSICS AND VERTICAL RESOLUTION

Colin G. Jones

Rossby Centre, Swedish Meteorological and Hydrological Institute,
Norrköping, S601 76, Sweden

1. INTRODUCTION

Stratocumulus clouds are a key component of the climate system playing a crucial role in the surface radiation budget. The presence of subtropical stratocumulus clouds can reduce the mean surface radiation flux by up to 300Wm^{-2} through reflection of incoming solar radiation (Duynkerke and Teixeira(2001). The albedo of stratocumulus clouds is a complex function of the liquid water path (LWP), droplet size distribution and spatial variability of the water field. The LWP of stratocumulus clouds is often in the range 50-300 gm^{-2}, small variations in the LWP can therefore lead to large changes in cloud albedo. It is important that climate models accurately simulate stratocumulus LWP and associated radiative effects for a realistic prediction of the tropical Sea Surface Temperature (SST).

In this paper we explore the balance between various physical parameterizations controlling the LWP and albedo of model stratocumulus clouds. In particular we assess the sensitivity of liquid water amounts to model vertical resolution and to the parametric representation of drizzle and cloud top mixing. The relative balance between competing parameterizations, acting to control the cloud water content, changes as the model vertical resolution increases. Cloud top mixing becomes an increasingly important term controlling the water balance of the cloud as vertical resolution is increased. We introduce a parameterization of cloud top entrainment into the model in order to simulate this important sink of water at lower vertical resolutions.

2. CASE DESCRPITION AND MODEL

A problem in simulating stratocumulus clouds is the need for an accurate specification (or simulation) of the large scale subsidence rate directly above the clouds. This term, along with the associated thermodynamic jumps at the boundary layer top, play a key role in determining the stratocumulus cloud depth and water content. To avoid this problem the EUROCS project designed a one dimensional (1D) case, based on the FIRE 1987 Stratocumulus campaign (Albecht etal. 1988).

Corresponding author's address: Colin G. Jones, Rossby Centre, SMHI, S60176 Norrköping, Sweden
E-Mail: Colin.Jones@smhi.se.

In the 1D case, the subsidence rate, large scale advection, SST and surface pressure are all prescribed in a manner consistent with observations. The case is 40 hours in duration, allowing an analysis of the diurnal cycle. Use of prescribed large scale forcing in a 1D setting allows single column versions of climate models (SCMs) to be run with identical forcing to 3D Large Eddy Simulation Models (LES models). LES models explicitly resolve most of the cloud scale turbulence and mixing, thereby offering a relatively accurate reference against which SCM results can be compared (Duynkerke etal 2004). In this manner improved parameterizations may be developed using LES as guidance.

Results are presented from a single column version of the SMHI Rossby Centre Regional Climate Model (RCA1D) (Jones etal. 2004). RCA1D uses a prognostic, moist conservative turbulent kinetic energy (TKE) scheme (Lenderink and Holtslag 2004) coupled to a statistical cloud scheme to simulate boundary layer turbulence and cloud processes. The cloud scheme is embedded within the turbulence scheme and uses the parameterized turbulent length scale and saturation deficit to estimate both cloud fraction and cloud liquid water. The resulting cloud fraction and water are then used in the parameterizations of radiation and precipitation.

3. RESULTS AND SENSITIVITY TESTS.

The standard configuration of the RCA1D model has 40 levels in the vertical with a vertical resolution of ~100m in the boundary layer. Figure 1 shows a timeseries of the RCA1D simulated precipitation rate, LWP and surface solar radiation flux. Also shown is the MESO-NH LES results. (Note that both LES and RCA1D simulated overcast conditions throughout all the simulations). All LES models participating in the intercomparison assumed the case to be non-precipitating. This may not necessarily be a valid assumuption, in fact recent observations of stratocumulus in the DYCOMS II experiment off California (Stevens 2003) indicate frequent precipitation from stratocumulus clouds of order ~0.5mm/day. RCA1D simulates a diurnal cycle in LWP and drizzle, but overestimates the LWP by some 50-100 gm^{-2}. This causes a significant underestimate in the surface solar radiation flux of ~200Wm^{-2} relative to the LES results. There is minimal compensation for this error by increased long wave emission from clouds, due to the low cloud base and high cloud

emissivity. This type of surface flux error would lead to a severe underestimate of the sea surface temperatures in a coupled climate model.

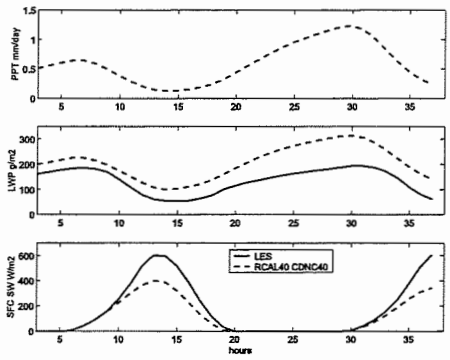

Figure 1 Timeseries of simulated precipitation (mm/day), LWP (gm^{-2}) and surface solar radiation flux (Wm^{-2}) from RCA1D with 40 levels and CDNC=$40cm^{-3}$ Also shown are MESO-NH LES results. The x-axis shows hours after model start (00Z local time??)

Figure 1 indicates that drizzle rates and LWP are correlated. This is not too surprising as the parameterization of drizzle in RCA1D requires cloud water to exceed a certain threshold value before autoconversion of cloud water to precipitation can begin The figure also suggests that drizzle controls the amount of LWP (i.e. LWP increases are limited by increasing drizzle removal of water). The parameterization of autoconversion follows the ideas of Chen and Cotton (1987). An assumed cloud droplet number concentration (CDNC) is specified and combined with the prognostic liquid water content (LWC), determines the mean droplet size distribution in the simulated clouds. The cloud water content must increase so that the parameterized droplet radius exceeds a prescribed threshold (9μm) before autoconversion can begin.

A large CDNC will lead to a given LWC being distributed amongst many, small droplets, limiting the onset of drizzle. In contrast, a small CDNC, will give, for the same LWC, relatively fewer droplets of larger radius. Drizzle will therefore begin at a lower LWC for clouds with a lower assumed CDNC. In the standard integration CDNC was set to 40 cm^{-3} for the stratocumulus clouds. Figure 2 shows results when CDNC is increased to 150 cm^{-3}. The change in the parameterized droplet size changes the balance between LWP and drizzle. LWP increases and drizzle rates decrease. Also shown in figure 2 is the RCA1D results when precipitation is disabled. This model configuration is most directly comparable with the LES set up. Non-precipitating, stratocumulus clouds in RCA1D greatly overestimate LWP and the resulting surface solar radiation flux is underestimated by some $300Wm^{-2}$. The results suggest that the primary mechanism for water removal in the standard RCA1D simulation is drizzle. When drizzle is disabled RCA1D LWP values rise to unrealistically high amounts, compromising the surface energy budget. We contend the RCA1D model run at ~100m vertical resolution, lacks a key mechanism for removal of liquid water from clouds, namely entrainment at cloud top.

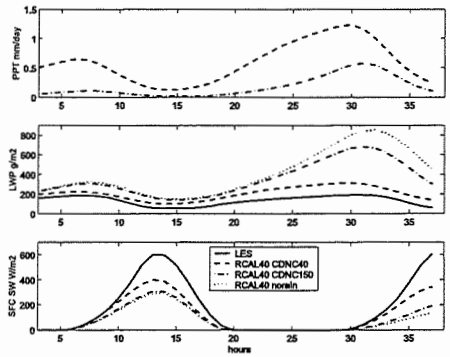

Figure 2 As in figure 1, with RCA1D 40L using CDNC=150 cm^{-3} and with precipitation disabled.

The MESO-NH LES model was run with a vertical level spacing of 10m in the boundary layer. We have repeated the RCA1D integration with the vertical resolution increased to 25m (150 vertical levels), to determine if increased vertical resolution leads to higher turbulent mixing at cloud top. Figure 3 shows the results for the standard 40 level RCA1D and the identical model run with 150 levels.

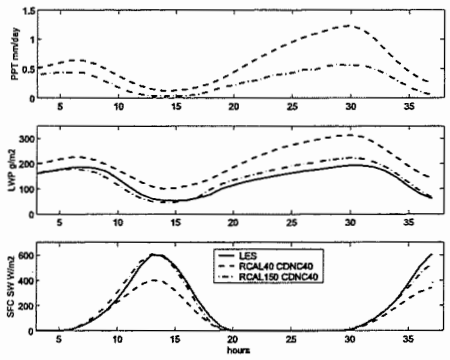

Figure 3 As in figure1, for RCA1D 40L and 150L, both with CDNC=$40cm^{-3}$.

LWP amounts are greatly reduced, being much closer to the LES values. Also the drizzle rate is reduced. We note that drizzle rates are not zero as assumed in the LES set up, but are ~0.25mm/day, a rate comparable to the DYCOMS II estimates. Increasing the vertical resolution leads to greater mixing at cloud top directly from the turbulence scheme. As a result dry air is mixed into the cloud. The turbulence scheme uses

total water (q_t) and liquid water potential temperature (θ_l) as mixing variables, both conserved in non-precipitating moist adiabatic processes. Hence entrainment of dry, high θ air into the cloud will directly lead to a reduction in cloud water to conserve θ_l and q_t

Increasing the vertical resolution changes the balance between terms controlling the water content of the simulated cloud. Drizzle is no longer the single dominant sink term for liquid water, cloud top mixing is now a second removal mechanism. Both mechanisms become more efficient as liquid water increases. As a result of the increased cloud top mixing, LWP and drizzle rates come into balance at a lower level. The resulting surface solar radiation flux is also greatly improved. To accurately simulate the evolution of stratocumulus clouds, inclusion of all terms in the water budget is clearly necessary.

Figure 4 shows the RCA1D results using 150 levels with the CDNC value increased to 150cm^{-3}. LWP and precipitation rates again increase, analogous to the results with 40 levels. But, the sensitivity to this microphysical assumption is greatly reduced in the 150 level model. LWP now only increases to ~300gm^{-2} compared to 600gm^{-2} in the 40 level model. Likewise the precipitation rates are less than half those in the equivalent 40 level model.

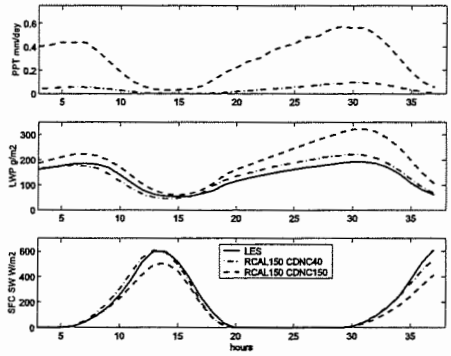

Figure 4. As in figure1, but for RCA1D 150L with CDNC equal to 40cm^{-3} and 150cm^{-3}, respectively.

The overall water balance in the cloud has changed due to the increased cloud top mixing. With CDNC equal to 150cm^{-3} drizzle will not start until LWC values are quite high (as seen in figure 2). As cloud water increases, in-cloud θ_l will decrease and q_t increase. Both changes increase the gradient of the respective quantities across the cloud top. The direct result is increased vertical mixing at cloud top, reducing the cloud water amounts and the vertical gradients of the two conserved variables. Cloud top mixing therefore limits the mixing ratio of liquid water in the cloud and by implication drizzle rates from the cloud.

The standard version of RCA1D does not include an explicit parameterisation of cloud top entrainment, rather mixing at cloud top is handled by the prognostic TKE turbulence scheme The subgrid scale vertical flux of variable χ is given by:

$$\overline{\omega'\chi'} = l\overline{e^{\frac{1}{2}}}\rho g\frac{\partial\overline{\chi}}{\partial z} \qquad (1)$$

where l is a diagnosed mixing length and e is the TKE value. We have tested replacing this approach to subgrid scale vertical mixing, at the cloud top inversion, by a parameterisation of cloud top entrainment following the ideas of Grenier and Bretherton (2001). In this approach we search for the sharpest jump in θ_v between a saturated (cloudy) layer and an unsaturated layer above, searching from the surface upward. The level of maximum jump is defined as the inversion level (KINV). At KINV we replace the subgrid scale flux given by (1) with a flux derived from a parameterized entrainment velocity.

$$\overline{\omega'\chi'} = -w_e\Delta\chi \qquad (2)$$

$$w_e = (a_1(1+a_2E))\frac{\overline{e^{\frac{3}{2}}}}{l\frac{g}{\theta_{v0}}(\Delta\theta_v)} \qquad (3)$$

$$E = \left(1-\frac{\Delta_m b}{\Delta b}\right) \qquad (4)$$

w_e is an entrainment velocity at the inversion level and $\Delta\chi$ is the jump in a prognostic variable across the inversion. E is referred to as the evaporative enhancement of entrainment and represents the increased energy, available for mixing at the cloud top, due to the generation of negatively buoyant mixtures of cloudy and clear air. E increases as the jumps in θ_l and q_t across the inversion increase. E will also be higher for larger values of cloud water. Δb is the linearized average buoyancy of all possible mixtures of cloudy air and free-tropospheric air, relative to the pure cloudy air (for more details see Grenier and Bretherton 2001).

Figure 5 shows the result of including this parameterization, for the subgrid scale vertical flux at KINV, in the 40 level version of RCA1D. The left column shows results with CDNC=150cm^{-3} and the right column with CDNC=40cm^{-3}. Comparison is made between the standard 40 level results and those with cloud top entrainment included. Clearly inclusion of parameterized cloud top entrainment leads to a marked reduction in both LWP and drizzle in the 40 level model, analogous to the results with 150 levels. In particular, the sensitivity of drizzle rates to the specification of CDNC is greatly reduced, again indicating that cloud top mixing puts a constraint on the build up of cloud water and as a result also directly limits precipitation production. The overall balance of the water budget changes due to the increased entrainment at cloud top and appears more similar to the 150 level model. As a direct result of the reduced LWP, the surface flux of solar radiation is increased in RCA1D being much closer to the LES results.

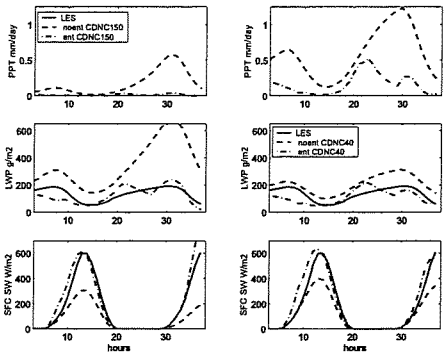

Figure 5, As in figure 1 but with RCA1D 40L, with (ent) and without (noent) parameterized cloud top entrainment. Left column is with CDNC=150cm^{-3} and right column with CDNC=40cm^{-3}

More work is needed to tune the entrainment parameterization particularly in determining the across inversion gradients used in equation (2). Nevertheless, these results suggest this is a promising avenue for improving the representation of stratocumulus clouds in RCA1D.

4. CONCLUSIONS

We have presented results from RCA1D simulations of the diurnal cycle of stratocumulus clouds, based on the FIRE campaign of July 1987. The model successfully simulates the diurnal cycle of LWP and precipitation and remains completely overcast throughout the simulation, in accordance with the LES results. The standard 40 level RCA1D overestimates LWP and drizzle leading to a poor simulation of the surface solar radiation flux. The 40 level model appears to have a single dominant liquid water sink, namely precipitation. The only means by which a reasonable LWP can be achieved is through an onset of drizzle at unrealistically low LWC values, leading to both excessive drizzle occurrence and accumulations.

Increasing the model vertical resolution to 25m from the standard 100m, improves the results. Mixing of dry air from above the inversion into the cloud increases and acts as a second sink for liquid water. As a result, both LWP and drizzle rates decrease in RCA1D, becoming closer to the LES results. The reduced LWP has a profound influence on the surface radiation budget. Introduction of a parameterization of cloud top entrainment into the 40 level model also increases cloud top mixing, analogous to the 150 level model. The extra sink of water leads to a reduction of both LWP and drizzle and an improved surface radiation budget.

An accurate simulation of the radiative effect of stratocumulus clouds requires the inclusion of all physical processes influencing the cloud water budget. The relationship between drizzle production and cloud water amount is changed if cloud top mixing is active or not. This sensitivity is of great importance in the context of modeling the indirect aerosol effect in clouds where drizzle rates are coupled to changing aerosol and cloud condensation nuclei concentrations.

5. ACKNOWLEDGMENTS

This work was formed part of the EU project EUROCS (http://www.cnrm.meteo.fr/gcss/EUROCS/EUROCS.html) under contract number EVK-CVT-1999-00051. I would like to acknowledge fruitful discussions with Geert Lenderink and Sander Tijm (KNMI).

6. REFERENCES

Albrecht B A, D.A.Randall and S.Nicholls 1988. Observations of marine stratocumulus during FIRE. Bull. Am. Met. Soc. 69, 618-626

Chen C and W.R. Cotton 1987. The physics of the marine stratocumulus-capped mixed layer. J. Atmos Sci 44, 2951-2977

Duynkerke P.G and J.Teixeira 2001. Comparison of the ECMWF reanalysis with FIRE I observations: Diurnal variation of marine stratocumulus. J.Climate 14, 1466-1478.

Duynkerke P.G. and co-authors 2004. Observations and numerical simulations of the diurnal cycle of the EUROCS stratocumulus case. Submitted to Q.J.R.Met. Soc. EUROCS special issue.

Grenier H and C.Bretherton 2001. A Moist PBL Parameterisation for Large Scale Models and ite Application to Subtropical Cloud-Topped Marine Boundary Layers. Mon. Wea. Rev. 129, 357-377.

Jones C.G, U Willén A.Ullerstig and U.Hansson 2004 The Rossby Centre Regional Atmospheric Climate Model (RCA Part I: Model climatology and performance for the present climate over Europe. Submitted to Ambio SWECLIM special issue 2004.

Stevens B. and co-authors 2003. Dynamics and Chemistry of Marine Stratocumulus-DYCOMSII Bull. Am. Met. Soc. 84, 579-595

Lenderink G. and A.A.M Holtslag 2004. An Updated Length Scale Formulation for Turbulent Mixing in Clear and Cloudy Boundary Layers. Accepted Q.J.R.Met. Soc. EUROCS special issue

USING REMOTE SENSING DATA TO EVALUATE THE LOKAL-MODELL PERFORMANCE

Christian Keil

Institut für Physik der Atmosphäre, DLR Oberpfaffenhofen, D - 82234 Wessling, Germany

1. INTRODUCTION

Remote sensing observations from satellite and radar represent rich sources of data that can be potentially used to improve weather forecasts through data assimilation or to evaluate the forecast quality. However, a direct comparison between observation and model forecast is complicated because of the different nature of measured and simulated quantity, *i.e.* satellites measure brightness temperature (BT in K) while the corresponding forecast quantity is cloud cover (in %). This comparability problem can be solved applying a forward radiative transfer model that uses forecast model fields to simulate measurements obtained by remote sensing instruments. Such a model-to-observation approach allows a direct comparison of observation and model and will be used to evaluate the forecast quality. Here, this approach is used to reveal deficiencies in the parameterization of physical processes governing the generation of upper-tropospheric clouds in LM.

2. MODEL AND OBSERVATIONAL DATA

The non-hydrostatic Lokal-Modell (LM) (Doms and Schättler, 1999) has been the operational short range weather forecasting tool at Deutscher Wetterdienst (DWD) since December 1999. In the operational configuration with a horizontal mesh size of 7 km the model domain encompasses all of Central Europe. The resolution will be increased in the near future to 2.8 km. The LM has a generalized terrain-following vertical coordinate, which divides the atmosphere in 35 layers from the bottom up to 20 hPa. The prognostic variables are the wind vector, temperature, pressure perturbation, specific humidity, and cloud liquid water, while the geopotential height, rain and snow flux are currently diagnostic variables. The model physics include a level-2 turbulence parameterization, a delta-2-stream radiation scheme, and a multi-layer soil model. The model includes a grid-scale cloud and precipitation scheme as well as a parameterization of moist convection (Tiedtke, 1989). The LM distinguishes between water in clouds and precipitation. To parameterize the conversion terms, cloud water is treated as a bulk phase without spectral distribution, whereas size distribution functions are specified for rain and snow.

Satellite data from the geostationary satellite METEOSAT 7 is used in the present study. METEOSAT 7 is positioned at the equator on the Greenwich meridian. The infrared window channel (IR; 10.1 – 13.0 μm) considered in the present study is mainly sensitive to the vertical distribution of cloud amount and to surface characteristics. The uncertainty caused by calibration error amounts to 2 –4 K (Köpken, 2001) and is significantly smaller than the cloud signals investigated in the present study. The satellite's spatial resolution is 5 km at nadir and about 8 km at 50 °N, comparable to the resolution of the LM.

Synthetic satellite imagery is generated using RTTOV-7, a development of the fast radiative transfer model for TIROS Operational Vertical Sounder (RTTOV), originally developed at European Centre for Medium Range Weather Forecast (ECMWF) in the early 90 s (Eyre, 1991). Subsequently the original code has gone through several developments (e.g. Saunders et al., 1999; Chevallier et al., 2001; Chevallier and Kelly, 2002; Matricardi et al., 2001), more recently within the EUMETSAT NWP Satellite Application Facility (SAF), of which RTTOV-7 is the latest version. The model allows fast simulation of brightness temperatures for satellite infrared or microwave nadir scanning radiometers given an atmospheric profile of temperature, variable gas concentrations (specific humidity, ozone), cloud (cloud liquid water, cloud ice, cloud cover) and surface properties (skin temperature, temperature and specific humidity at 2 m, land-sea mask). RTTOV-7 plays a key role in the assimilation of satellite data at ECMWF. Recently, the forward calculation necessary to generate synthetic brightness temperature was implemented into the LM (version 3.7) for evaluation purposes (Keil and Tafferner, 2003).

3. CASE STUDY RESULTS AND DISCUSSION

On 11 September 2003 a well-evolved mesoscale cyclone was slowly moving across Europe. Observation of METEOSAT 7 shows a striking, cyclonically curving cloud pattern at 6:00 UTC (Fig. 1). The corresponding synthetic satellite image forecast by LM (00:00 UTC + 6 h) is also displayed in Fig. 1. The cloud vortex across eastern Germany and the Czech Republic, the key feature of the cyclone *Veit*, is correctly forecast in position and strength.

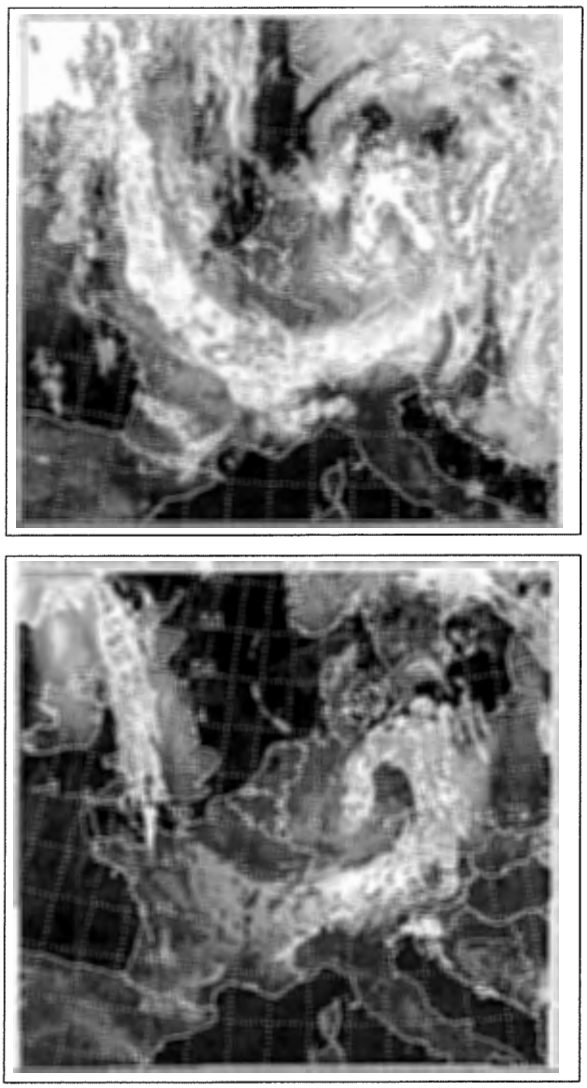

Fig. 1. METEOSAT 7 (above) and LM synthetic satellite image (below) at 06:00 UTC 11 September 2003 (t + 6 h LM forecast) in the IR channel.

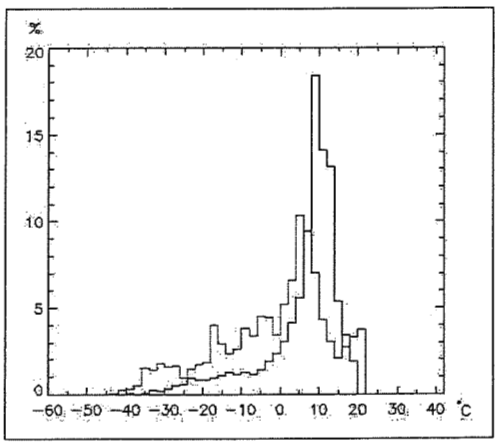

Fig. 2. Histogram of METEOSAT 7 (gray) and LM synthetic satellite image (black) in the IR channel at 06:00 UTC 11 September 2003.

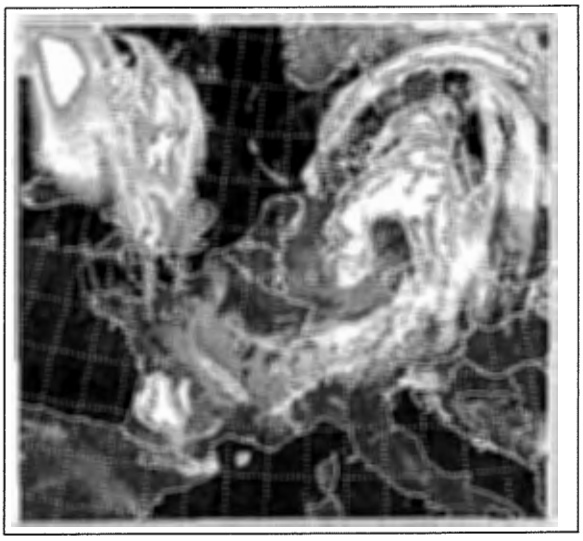

Fig. 3. Same as Fig. 1 but for experiment NA4 with changed critical ice mixing ratio of $5 \times 10^{-5}\ kg kg^{-1}$.

However, LM underestimates the amount of clouds, especially the amount of high clouds. Clouds across the Baltic Sea, Poland, France and Ireland are largely absent in the LM forecast. This model deficiency also becomes evident in the histogram that shows the frequency distribution of BT retaining only information on the vertical structure of clouds (Fig. 2). Low BTs correspond to radiation coming from the upper troposphere while high BTs mark the portion emitted by clouds in the lower troposphere or the ground. The BT histogram shows a warm bias of the LM in that BT peak at 10 °C, *i.e.* roughly 5 K warmer than METEOSAT 7. The cloud-free and low cloudiness regions dominate the LM forecast, which is already apparent in the visual comparison of observed and synthetic satellite imagery in Fig. 1, resulting in the warm bias. Since there are less higher clouds forecast, BTs below -5 °C are underestimated in LM. This discrepancy is especially evident for upper-tropospheric clouds (BTs lower -25 °C).

A better agreement of the observed and forecast cloud (BTs, respectively) amount is an essential requirement for a further objective usage of satellite imagery to evaluate forecast quality. Therefore, additional experiments were performed to investigate the sensitivity of high clouds to changes in the cloud microphysics scheme.

The upper–tropospheric cloud amount in LM is primarily governed by the balance between cloud-ice generation by water vapor deposition in regions with ascending motion, and cloud-ice removal by the au-

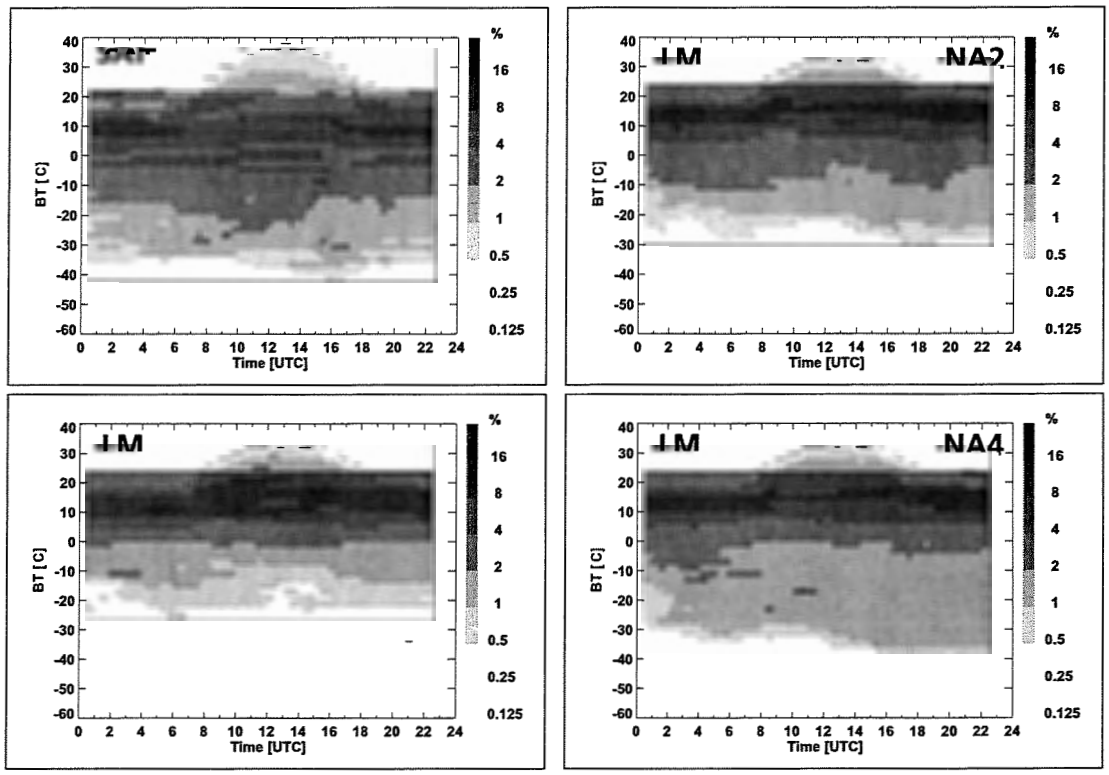

Fig. 4. Evolution histogram of METEOSAT 7 (top, left) and LM synthetic satellite images (operational LM forecast (bottom, left), experiment NA2 (top, right) and NA4 (bottom, right) in the IR channel on 11 September 2003.

toconversion process. The autoconversion process is parameterized following Lin et al. (1983) and converts non-precipitating cloud-ice to precipitating snow when a cloud-ice threshold (critical ice mixing ratio) is reached. Using a cloud resolving model Lin et al. (1983) suggested a critical ice mixing ratio of $1 \times 10^{-3}\ kgkg^{-1}$. A profound impact of the ice-to-snow autoconversion threshold on forecast BTs of mid-latitude cyclones was shown in mesoscale model (Meso-NH) experiments suggesting a value of $2 \times 10^{-5}\ kgkg^{-1}$ (Chaboureau et al., 2002). However, in the current operational forecasting system at DWD, the critical ice mixing ratio is set to zero because of an overestimation of high clouds in the tropics in DWD's global model (Doms, personal communication). Following earlier LM experiments for mid-latitude winter storms (Keil et al., 2003) the impact of the critical ice mixing ratio on BT is investigated for this cyclone. In experiment NA2 the critical ice mixing ratio is set to $2 \times 10^{-5}\ kgkg^{-1}$, in experiment NA4 to $5 \times 10^{-5}\ kgkg^{-1}$.

In Fig. 3 the corresponding synthetic satellite image of experiment NA4 is displayed. The positioning of the cloud system is similar to the original LM forecast as a result of the strong dynamical organization of the flow. However, changing the critical ice mixing ratio has a large impact on the cloud generation leading to a strong increase in upper-tropospheric clouds (e.g. across the Baltic Sea, southwest France and the British Isles).

The impact of changes in the critical ice mixing ratio on the vertical distribution of clouds is further depicted using evolution histograms (Fig. 4). These are constructed by stringing together hourly histograms of observed and forecast synthetic BT binned in 2 K increments (e.g. Fig. 2) covering 24 hours on 11 September 2003. Increasing the critical ice mixing ratio leads to a steady growth of mid- and upper-level clouds (BT between -5 and -40 °C). The distribution of clouds of experiment NA2 compares better with satellite observations than the original LM forecast. Experiment NA4 shows a rather uniform frequency distribution of BTs less than -5 °C and overestimates the upper-tropospheric clouds (BT < -40 °C). The overestimation of BTs around 10 °C is, as expected, not affected by the changes in the cloud scheme. Here inconsistencies of surface temperatures between satellite and model cause the differences. Moreover, the daily cycle of surface temperature is less pronounced in LM than observed by satellite (BT larger 20 °C between 10:00 and 18:00 UTC). Comparison of daily rainfall sums only shows a weak impact of the ice-

to-snow autoconversion process on precipitation (less than 1.5 %, not shown).

4. CONCLUSIONS AND OUTLOOK

The new diagnostic LM option (LMSynSat) generating synthetic satellite imagery allows direct comparisons of model forecasts with satellite observations. LMSynSat produces model forecast BTs for different satellites (presently METEOSAT 7 and Meteosat Second Generation (MSG-1)) in GRIB format and will be operationally at DWD in spring 2004. In the present study, changes of the critical ice mixing ratio in the microphysics scheme show a strong impact on the realistic representation of upper-tropospheric clouds in LM. A better agreement is found using a critical ice mixing ratio of $2 \times 10^{-5}\ kg kg^{-1}$. Daily precipitation accumulations show hardly any impact of the modified critical ice mixing ratio. However, the impact on other model variables (like surface heat flux) has to be investigated more extensively. Systematic experiments taking into account these results are necessary to support the findings.

A realistic representation of clouds is a crucial requirement for plans constructing an objective algorithm to evaluate the forecast quality using remote sensing data based on pattern recognition techniques at DLR.

ACKNOWLEDGEMENTS

Meteosat data are copyrighted by EUMETSAT. The author thanks Ulrich Schättler (DWD) for his support implementing LMSynSat into the LM code.

References

Chaboureau, J.-P., Cammas, J.-P., Mascart, P. and Pinty, J.-P.: 2002, Mesoscale model cloud scheme assessment using satellite observations., *J. Geophys. Res.* **107**, doi:10.1029/2001JD000714.

Chevallier, F. and Kelly, G.: 2002, Model clouds as seen from space: comparison with geostationary imagery in the 11 microns window channel, *Mon. Wea. Rev.* **130**, 712–722.

Chevallier, F., Bauer, P., Kelly, G., Jakob, C. and McNally, T.: 2001, Model clouds over oceans as seen from space: Comparison with HIRS/2 and MSU radiance, *J. Climate* **14**, 4216–4229.

Doms, G. and Schättler, U.: 1999, The nonhydrostatic limited–area model LM (Lokal–Modell) of DWD, *Technical report*, Deutscher Wetterdienst, Offenbach am Main. 172 pp.

Eyre, J. R.: 1991, A fast radiative transfer model for satellite sounding systems, *ECMWF, Technical Memorandum No. 176*. Available from ECMWF, Shinfield Park, Reading RG2 9AX, UK.

Keil, C. and Tafferner, A.: 2003, LMSynSat Users Guide. 7pp., available from DLR.

Keil, C., Tafferner, A. and Schättler, U.: 2003, Evaluating high-resolution model forecasts of European winter storms by use of satellite and radar observations, *Weather and Forecasting* **18**, 732–747.

Köpken, C.: 2001, Monitoring of METEOSAT WV radiances and solar stray light effects, *EUMETSAT/ECMWF Fellowship Programme, Research Report No.10*. 46 pp. Available from ECMWF, Shinfield Park, Reading RG2 9AX, UK.

Lin, Y.-L., Farley, R. D. and Orville, H. D.: 1983, Bulk parameterization of snow field in a cloud model, *J. Climate Appl. Meteor.* **22**, 1065–1092.

Matricardi, M., Chevallier, F. and Tjemkes, S.: 2001, An improved general fast radiative transfer model for the assimilation of radiance observations, *ECMWF, Technical Memorandum No. 345*. 40 pp. Available from ECMWF, Shinfield Park, Reading RG2 9AX, UK.

Saunders, R., Matricardi, M. and Brunel, P.: 1999, An improved radiative transfer model for assimilation of satellite radiance observations, *Quart. J. Roy. Meteor. Soc.* 1407–1425.

Tiedtke, M.: 1989, A comprehensive mass flux scheme for cumulus parameterization in large-scale models, *Mon. Wea. Rev.* **117**, 1779–1800.

CLOUD-RESOLVING MODEL AS A PARAMETERIZATION OF CLOUDS IN A GENERAL CIRCULATION MODEL

Marat F. Khairoutdinov and David A. Randall
Department of Atmospheric Science, Colorado State University, Fort Collins, Colorado, U.S.A.

1.INTRODUCTION

Since the onset of global climate modeling, various statistical theories of clouds called parameterizations have been developed to account for the effects of clouds in general circulation models (GCMs). These semi-empirical parameterizations are generally extrapolate the unresolved or subgrid-scale (SGS) information from the grid-resolved fields using some simple general rules. Numerous parameterizations have been developed over the past decades; nevertheless, the problem of cloud parameterization still remains largely unsolved and in some sense "deadlocked", as discussed by Randall *et al.* (2003) and Arakawa (2004).

Unlike parameterizations, cloud-resolving models (CRMs) use the first-principle approach to modeling the dynamics of clouds with the exception of cloud microphysics which is still highly simplified. A global CRM could take at least a million times more total computation than current GCMs, to resolve the scales on the order of a few kilometers. However, even at such resolution, only deep convective towers and storms would be resolved.

Recently, a new approach has emerged. It has its roots in the so-called single-column modeling (SCM), where a package of parameterizations from a GCM is forced by the prescribed tendencies representing large-scale advection. CRMs have also been used in a similar manner. In order to control sinks and sources of momentum, mass, and energy, and, simply, because there is no associated large-scale grid, the domain is usually chosen to have no lateral boundaries, that is to be periodical, and the forcing tendencies are applied horizontally uniform. In such a framework, CRM acts exactly as a conventional parameterization, that is the input is the large-scale tendencies due to large-scale (or resolved-scale) processes, and the output is the large-scale tendencies due to 'unresolved' or 'sub-large-scale' processes. The important difference though is that unlike conventional parameterizations, the CRM actually resolves the 'sub-large-scale' dynamics and physics down to some scale defined by the CRM grid.

The next logical step is to embed a CRM in the manner similar to the SCM approach into each grid-column of a GCM replacing conventional cloud parameterizations, with the large-scale tendencies computed by a GCM. This was first implemented by Grabowski (2001).The SP in the experiments performed by Grabowski was embedded into a simplified global model representing an aqua-planet with globally uniform sea-surface temperatures (SSTs), no topography, etc. To limit the computational cost, a two-dimensional (2-D) SP was applied with the results shown to be, to some extent, orientation-dependent.

Khairoutdinov and Randall (2001; hereafter KR) took the next step by adopting a 2-D version of their three-dimensional (3-D) CRM as parameterization of clouds in the NCAR Community Atmosphere Model (CAM). CAM has all the attributes of a true GCM, with realistic SSTs, continents with topography, a sophisticated land-surface model, convective and stratiform parameterizations, radiative transfer parameterization, etc. As the initial test, KR performed a single two-month (December-January) simulation using the T42 (2.8x2.8 deg) global-grid resolution and 26 vertical levels. The simulated January-mean distribution of precipitation and precipitable water among others looked very reasonable. KR also proposed the term "super-parameterization" (SP) to be used for CRMs embedded in GCMs.

The results of KR have encouraged us to perform an annual-cycle simulations with a relatively low-resolution T21 SP-CAM. The main goal was to see if the SP-CAM could simulate the Madden-Julian Oscillation (MJO). The results showed (Randall *et al.*, 2003) that the SP-CAM can indeed produce a vigorous MJO that has many features of the observed phenomenon, in contrast to the standard CAM which produces virtually no MJO. Further encouraged by the results from the T21-resolution run, we have recently performed a series of 500-day long T42 runs. Some results from these computationally expensive experiments will be presented during the ICCP 2004 oral presentation.

2. THE SP-CAM MODEL

The SP component of the SP-CAM model is based on a 3-D CRM described in detail by Khairoutdinov and Randall (2003). A copy of the SP was embedded in each of the 8192 grid-columns of the T42 L26 CAM. Both 2-D and 3-D SP have been used in this study, with the 2-D SP using 64x24 and 3-D SP using 8x8x24 grid point domain. Both used rather course 4 km horizontal grid spacing and the vertical levels identical to the lowest 24 levels of CAM. The domain was periodical and aligned in the west-east direction in the case of the 2D SP. The SP was forced by large-scale tendencies updated every CAM time step, and providing its own horizontally averaged tendencies as a feedback. Due to incorrect vertical momentum transport by the 2-D SP, no feedback to large-scale winds was allowed. However, the resolved convective momentum transport was allowed in the case of 3-D SP.

The CRM was continuously subcycling within a GCM's time step with its own time step of 20 sec. Only the CRM forcing was updated once per GCM time step

Corresponding author address: Marat Khairoutdinov, Dept. of Atmospheric Science, Colorado State University, Fort Collins, CO 80523, U.S.A.

(1800-3600 sec). The radiative transfer computations were performed every 15 minutes on a CRM grid, that is independently for every CRM column using no explicit cloud overlap assumption.

The SP-CAM is more than 200 times more expensive to run than the standard CAM. In the early tests of the prototype SP-CAM in 2001, it took us about 20 wall-clock days to simulated one year on 64 processors of NCAR's IBM-SP "Blackforest". Recently, due to both software and software improvements, we achieved nearly linear scaling (92% efficiency) out to 1024 processors of the NERSC's "Seaborg" IBM-SP supercomputer, which allows us to simulate one year in less than 44 wall-clock hours.

3. RESULTS

The space of this publication does not allow for extensive presentation of the results. The following major results have been obtained:

- In terms of the mean state, the SP model produces quite reasonable geographical distributions of precipitation, precipitable water, top-of-atmosphere radiative fluxes, cloud- radiative forcing, and high-cloud fraction (Fig.1) for both seasons;
- Small-scale cloud-radiation interactions resulting from computation of radiative transfer within the SP domain change the global cloud cover geographical distribution quite notably, specifically increase low-cloud fraction (see the extended abstract by Grabowski *et al* "Super-Parameterization..."). A comprehensive study on the subject has recently been done by Cole *et al* (2004);
- It is apparent that the SP model exhibits much improved diurnal variability of non-drizzle precipitation frequency in terms of the diurnal cycle over the standard model. Over the summer time land masses, the control model tends to precipitate most frequently around local solar noon, which is a few hours earlier than observations suggest. In contrast, the SP model tends to peak precipitation frequency during late afternoon hours, in accord with observations. Over the ocean, both models precipitate most frequently in the early morning hours as observed;
- The SP model global distribution of the percentage of days with non-drizzle precipitation compares to observed distribution most favorably, while the standard model tends to precipitate by about 20-30% more frequently;
- There is a rather dramatic improvement in intraseasonal oscillation such as the MJO;
- Explicit momentum transport (MT) in SP-CAM with 3-D SP dries the atmosphere out compared to control 3-D SP with no explicit convective MT allowed. It also seems to mitigate the double-ITCZ problem.

Acknowledgments The sponsorship and computing resources provided by the U.S. National Energy Research Scientific Computing Center (NERSC) and the National Center for Atmospheric Research (NCAR) are greatly appreciated. This research was supported in part by the U.S. Department of Energy Grant DE-FG03-95ER61968 to Colorado State University as part of the Atmospheric Radiation Measurement Program, and by National Science Foundation Grant ATM-9812384 to Colorado State University.

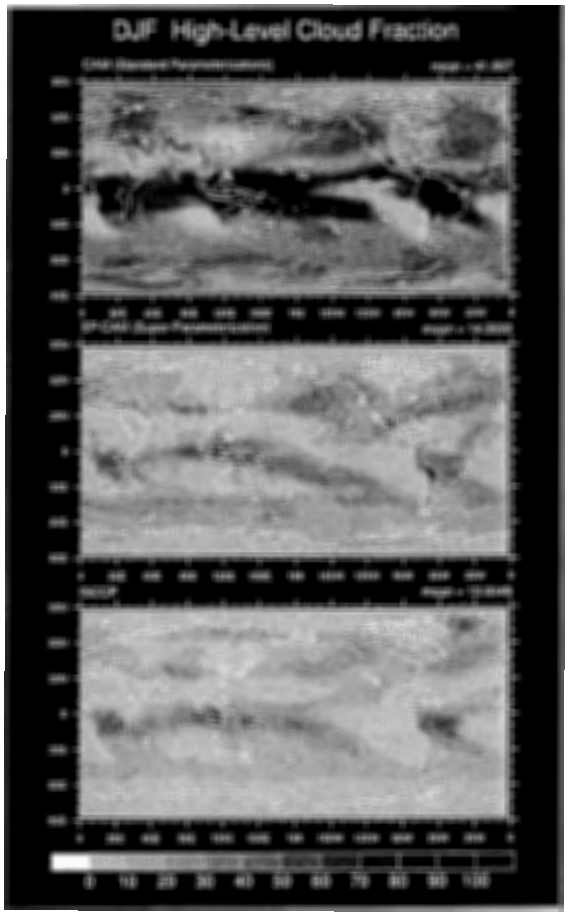

Figure 1: December-January-February mean high-cloud fraction as simulated with the standard CAM (top), CAM with super-parameterization, (middle), and as observed.

References

Arakawa, A., 2004: The Cumulus Parameterization Problem: Past, Present, and Future. *J. Climate* (in press).

Cole, J. N., H. W. Barker, D. A. Randall, M. F. Khairoutdinov, and E. Clothiaux, 2004: Interactions between Clouds and Radiation at Scales Unresolved by Global Climate Models. Submitted for publication.

Grabowski, W. W., 2001: Coupling cloud processes with the large-scale dynamics using the cloud-resolving convection parameterization (CRCP). *J. Atmos. Sci.*, **58**, 978-997.

Khairoutdinov, M. F., and D. A. Randall, 2001: A cloud resolving model as a cloud parameterization in the NCAR Community Climate System Model: Preliminary Results. *Geoph. Res. Letters*, 28, 3617-3620.

Khairoutdinov, M.F., and D.A. Randall, 2003: Cloud resolving modeling of the ARM summer 1997: Model formulation, results, uncertainties, and sensitivities. *J. Atmos. Sci.*, 60, 607-625.

Randall, D. A., M. Khairoutdinov, A. Arakawa, and W. Grabowski, 2003: Breaking the cloud-parameterization deadlock. *Bull. Amer. Meteor. Soc.*, 84, 1547-1564.

On characterization of sub-grid variability in stratiform clouds based on MMCR data

Zena N. Kogan, David B. Mechem, and Yefim L. Kogan

Cooperative Institute for Mesoscale Meteorological Studies, University of Oklahoma, Norman OK

1. INTRODUCTION[1]

Parameters of cloud variability over NWP or GCM grid cells are crucial in determining areal averages of cloud radiative and microphysical properties. Neglecting variability can lead to substantial underestimates of microphysical process rates (see, e.g. Kogan 1998, Pincus and Klein 2000). The Atmospheric Radiation Measurement Program (ARM) operates a millimeter wave cloud radar (MMCR) at the ARM Climate Research Facility (ACRF) at Southern Great Plains site (SGP) that provides a unique opportunity to obtain continuous observations to address issues of cloud system variability. The objective of this study is to develop a formulation of low cloud system variability based on statistical moments of radar reflectivity's PDF.

2. APPROACH

We analyzed more than 1100 hours of radar reflectivity observations of overcast low stratiform clouds over the ARM SGP site during two winter seasons (December-February 1997-1998 and January-March of 2001), and the month of the March 2000 IOP. The database consists of time series of radar reflectivity measured within the middle portion of the cloud by the vertically pointed MMCR with a 45 m vertical spacing and a 10 s time interval. A cloudy period was included in the analysis if it was continuously captured by radar for more than 8 min. Cases of overlapping clouds were also included, except for the periods when precipitation from them contaminated the lower layers.

All clouds were divided into two distinct categories – boundary layer stratocumulus with tops below 1.5 km and a depth of several hundred meters (BL), and low altitude stratiform clouds with bases below 2 km and a depth of up to about 3 km (LA). Precipitation significantly affects cloud dynamics and therefore variability of cloud parameters. To address this issue, BL and LA categories were further discriminated into precipitating[2] and non-precipitating subcategories (further referred to as BLpr, BLnp, LApr, and LAnp). Observations suggest a -17 dBZ value as a threshold for such discrimination which, according to LES simulations, corresponds to the 24 μm drop size threshold. The term 'drizzle' is used to account for the liquid water content in the tail of cloud drop spectra (r> 24 μm).

To study variability on specific scales, we further divide all segments into 20 and 60 min sub-segments, corresponding to NWP- and large-scale model grid sizes of 10 and 30 km, respectively (assuming the "frozen turbulence" hypothesis with an advection velocity of ~ 9 mc^{-1}, typical for the analyzed seasons).

3. DATA SET

Table 1 shows statistics on duration and occurrence of cloud segments. About 90% of the segments have a life span less than two and a half hours (about 80 km when translated to the spatial scale). Some of the remaining segments, however, exist surprisingly long (17 hours). The average duration of all BL segments is about one and a half hour (~50 km). It is remarkable, however, that because of their two times greater numbers, the non-precipitating segments significantly dominate in total duration: the ratio of non-precipitating to precipitating BL clouds is about 7:3. Half of precipitating clouds are only very lightly drizzling (Z<-14 dBZ), thus about 85% of all observed BL clouds are either non-precipitating or have a very light drizzle. It is also interesting that there is a greater number of longer duration and thus, of a larger scale, segments in the BLnp category.

TABLE 1. Duration and occurrence of segments

Cloud type	Precip	# of Segm.	Cloud segment duration [h]				
			Total	*Mean*	σ	*Med*	*75th perc.*
BL	No	324	538.6 (69%)	1.7	1.9	0.97	2.2
	Yes	158	236.8 (31%)	1.5	2.1	0.69	1.7
LA	No	112	77.6 (30%)	0.69	1.0	0.34	0.85
	Yes	114	178.2 (70%)	1.56	2.0	0.69	2.1

Low altitude clouds, on the contrary, occur less frequently and are predominantly precipitating. The duration ratio of LAnp to LApr (3:7) is reverse to the BL case. Thus, LA clouds are mostly precipitating, while BL clouds are mostly non-precipitating. The less frequent non-precipitating LA segments last only half as long (~40 min) and thus, are of a significantly

[1] *Corresponding author address*: Dr. Zena Kogan, Cooperative Institute for Mesoscale Meteorological Studies, University of Oklahoma, Norman OK 73019
email: zkogan@ou.edu

[2] Precipitating (drizzling) clouds are defined by the presence of drizzle *within* the cloud layer.

smaller size relative to their non-precipitating counterparts. It is interesting that the LAnp segments have the shortest average life span among all categories.

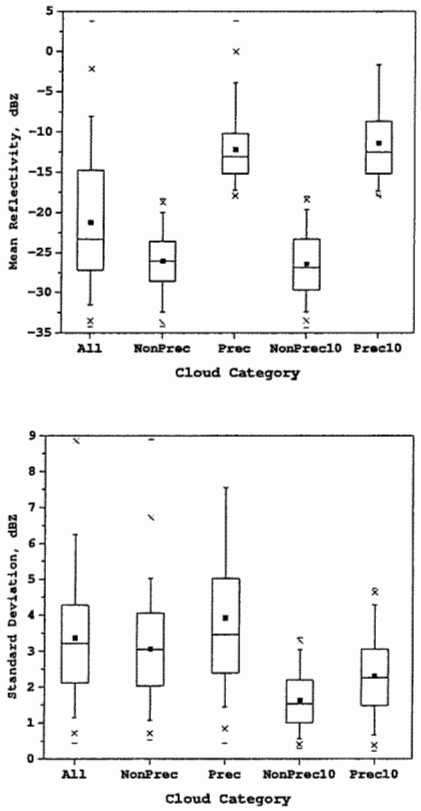

Fig. 1. Box-plots of first (top) and second (bottom) moments of reflectivity distributions shown for five data sets (see text for explanation).

4. CHARACTERIZATION OF VARIABILITY

Comparative statistics related to reflectivity distributions of BL segments is shown in Fig. 1 (the results for LA category are qualitatively similar; however, due to lack of space they are not shown here). The box-plots[3] show distributions of the first and second moments of the segments' reflectivity PDF (i.e., mean and standard deviation σ) for five datasets: 'All' for all segments; 'NonPrec' and 'Prec' for non-precipitating and precipitating segments, respectively; 'NonPrec10' and 'Prec10' for non-precipitating and precipitating 10 km sub-segments, respectively.

[3] Box and whisker range is 25-75% and 5-95%, respectively.

The results demonstrate that the 'All' segments category has the largest variability[4] range for both moments. Clearly, a probability distribution function that may be applicable for all boundary layer clouds will have quite uncertain mean and standard deviation values.

As we divide all cloud segments into separate non-precipitating and precipitating categories, the range of variability for the mean reflectivity (Fig.1, top) is substantially reduced, meaning that a separate PDF designed for each of these categories will be more representative. However, as Fig. 1, bottom shows, the σ scatter in both 'NonPrec' and 'Prec' categories is still quite large, indicating that the width of such PDF will still be unacceptably large. It is interesting to note that the precipitating clouds show substantially larger variability than non-precipitating ones especially in the LA case. The increase in variability in the 'Prec' category compared to the 'All' category is due to the fact that the number of non-precipitating segments is larger in the 7:3 ratio (see Table), therefore their contribution to the variability in the 'All' category dominates over the contribution of the precipitating segments.

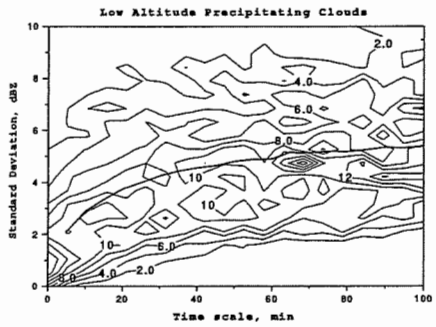

Fig. 2. Probability distribution function for the standard deviation of reflectivity as a function of segment duration. The thick solid line depicts the mean value of σ.

Not surprisingly, the variability strongly depends on the scale of the segment. Fig. 2 shows PDF of variability as a function of segment scale. The thick solid line depicts the mean variability. These results were obtained by varying sub-segment duration with a 5 min increment in the 5 - 100 min range. The results clearly demonstrate a substantial increase of variability with scale (almost a doubling increase in the 20 - 100 min range). The steepest increase in variability occurs at the smallest scales.

The dependence of radar reflectivity variability on scale is an interesting topic but is beyond the scope of current investigation. Our goal is to develop a parameterization of variability on certain fixed scales,

[4] The term variability used throughout the paper refers to the standard deviation σ of the corresponding parameter.

namely on scales equal to the grid sizes currently used in NWP and climate models. Having this in mind, we define (from the original segments) sets of 20 and 60 min sub-segments corresponding to 10 and 30 km scales as a proxy for NWP and climate model grid sizes. The statistics for the 10 km set shown in Fig. 1 separately for 'NonPrec' and 'Prec' category is quite encouraging in the sense that it clearly demonstrates that on a fixed scale the variability in mean and σ is substantially reduced. Thus a basis for a parameterization of variability on a fixed scale is much more substantiated.

Due to the lack of space, results for LA clouds are not shown; we briefly note that for all LA segments σ is 1.4 times that of BL segments. Precipitating segments have σ which is 1.6 times larger than non-precipitating segments.

5. PARAMETERIZATION OF VARIABILITY

Traditionally, parameterization of variability in clouds is cast as a PDF, usually a Gamma, Gaussian or log-normal type that depends on 2-3 parameters. The parameters of analytical distribution may be expressed through statistical moments of the PDF. In our formulation we consider only the first two moments of the PDF (mean and standard deviation).

We illustrate the formulation of cloud variability in terms of radar reflectivity, which is continuously measured at the ACRF SGP site and can be analyzed statistically for long climatological periods. Although current numerical models do not include radar reflectivity as a prognostic variable, it is possible to deduce with reasonable accuracy the PDF of predicted cloud variables, such as, e.g., cloud liquid water from the PDF of the directly observable radar reflectivity (see, e.g., Frisch et al, 1995).

In Fig. 3 we present results of reflectivity variability for fixed 10 and 30 km scales. This analysis does not discriminate between non- and precipitating segments because our intention is to derive a relationship valid in the whole range of reflectivity. The entire dataset provides 2150 BL 10-km sub-segments and 700 LA 10-km sub-segments. There are fewer 30 km sub-segments: 520 for the BL and 210 for the LA category. Standard deviation of reflectivity is presented in Fig. 3 as a function of its mean in a 1 dBZ bins.

In addition to the standard deviation σ, Fig. 3 also shows the standard deviation of σ (σ_σ) inside each bin and the number of sub-segments in each bin. The main result of Fig. 3 is that the standard deviation may be defined as a function of mean reflectivity Z_m with an error on average of about 30-40%. In the precipitation range of reflectivity, the number of sub-segments decreases and the relationship is more noisy, but, nevertheless, the parameterization $\sigma = f(Z_m)$ may be well represented by a linear function:

$$\sigma = \alpha + \beta \times Z_m$$

where parameters α and β depend on the scale and cloud category (BL or LA). For the BL case α=3.45 (4.61) and β=0.058 (0.093) for the 10 km (30 km) grid correspondingly.

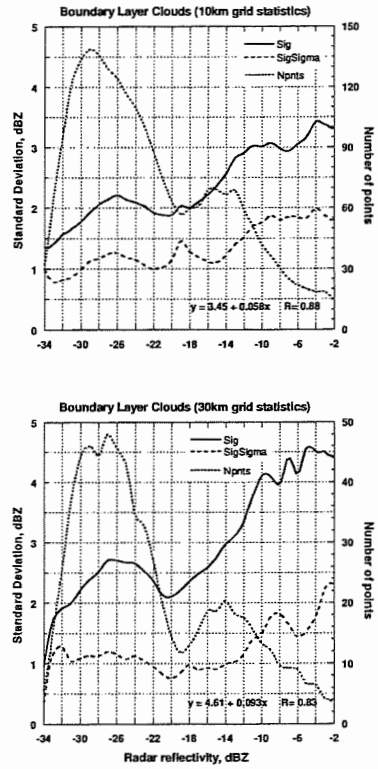

Fig. 3. Standard deviation (thick solid), its standard deviation (thin), and the number of sub-segments per bin (dotted) as a function of a bin's mean reflectivity Z_m.

6. BIAS OF A TWO-MOMENT PDF PARAMETERIZATION

The importance of sub-grid variability has been demonstrated in many previous studies (see, e.g. Pincus and Klein, 2000). We have evaluated the bias introduced by neglecting of sub-grid variability, as well as the one introduced by using a two-moment, analytical PDF instead of the exact PDF. As an illustration, we calculate for each segment the mean precipitating flux R from the Z-R relationship $Z = a R^b$. The bias (negative in this case, as the Z-R function is concave) is estimated by comparing the true value of R using the exact PDF for each segment and a biased value of R calculated using the mean reflectivity. The results for the BL category (Fig. 4) show that unresolved variability leads to a significant underestimation of calculated mean precipitating flux. We estimated that for $b=1.2$ (Comstock et al, in press) the relative bias can be as large as 70 % for the BL

category (90 % for LA category, not shown). The bias is even higher for smaller *b* (greater non-linearity of the Z-R function).

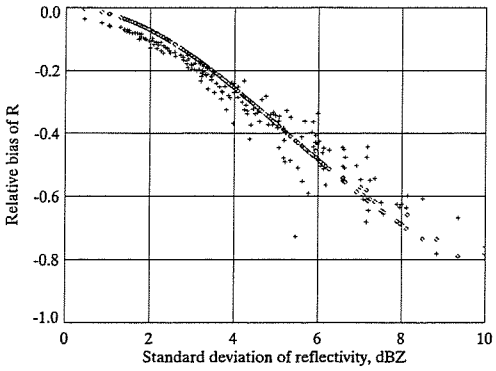

Fig. 4. Relative bias of the mean precipitating flux as a function of standard deviation. The bias is calculated using the exact PDF (pluses) and the two-moment Gaussian PDF (diamonds).

We also calculated the bias B_{2m} using a two-moment Gaussian function instead of the exact PDF. The parameters of Gaussian function were calculated from the mean and standard deviation of the exact PDF. The normalized difference between the 'exact' biases, B_e, and the B_{2m} is a measure of accuracy of the two-moment PDF formulation. As Fig. 4 shows, the difference is on the order of 4-8%, demonstrating that the two-moment PDF is a very reasonable formulation for the sub-grid variability.

7. CONCLUSIONS

We have analyzed radar reflectivity variability based on more than 1100 hours of MMCR observations of overcast boundary layer and low altitude stratiform clouds over the ACRF SGP site. A unified PDF for the whole data set is unable to represent the wide variability of PDF shapes, means and standard deviations. Distinct differences exist between PDFs of precipitating and non-precipitating clouds, as well as between PDFs of boundary layer and low altitude stratiform cloud categories. Specific conclusions are:

1. Low altitude clouds have much larger variability compared to boundary layer clouds (on average 1.4 times larger standard deviation).
2. Precipitating clouds exhibit significantly greater variability compared to non-precipitating clouds.
3. Variability strongly depends on scale.
4. Reasonably accurate parameterizations of sub-grid variability can be formulated for fixed scales of 10 km and 30 km, representative for NWP and large scale model grid sizes.
5. The PDF characterizing sub-grid variability can be accurately defined based on two moments, the mean and the standard deviation. We have shown that the use of a simple Gaussian type PDF is justified, as long as the mean and the standard deviation are known.
6. On a fixed 10 km and 30 km scale, the standard deviation can be reasonably well parameterized as a function of the mean; the latter would be represented by a resolved model variable.

Acknowledgement. This research was supported by the Environmental Sciences Division of the U. S. Department of Energy (through Battelle PNR Contract 144880-A-Q1 to the Cooperative Institute for Mesoscale Meteorological Studies) as part of the Atmospheric Radiation Measurement Program and the ONR Grants N00014-96-1-0687 and N00014-03-1-0304. Data were obtained from the Atmospheric Radiation Measurement (ARM) Program sponsored by the U.S. Department of Energy, Office of Science, Office of Biological and Environmental Research, Environmental Sciences Division.

REFERENCES

Comstock, K.K., R. Wood, S.E. Yuter, and C.S. Bretherton, 2003: Reflectivity and rain rate in and below drizzling stratocumulus. *Quart. J. Roy. Meteor. Soc.*, submitted.

Frisch, A. S., C. W. Fairall, and J. B. Snider, 1995: Measurements of stratus cloud and drizzle parameters in ASTEX with K_a-band Doppler radar and microwave radiometer. *J. Atmos. Sci.*, **52**, 2788-2799.

Kogan, Y.L., 1998: Parameterization of cloud physics processes in mesoscale models of stratocumulus cloud layers. Preprints, *AMS Conference on Cloud Physics,* 17-21 August 1998, Everett, WA.

Pincus, R., and S. A. Klein, 2000: Unresolved spatial variability and microphysical process rates in large-scale models. *J. Geophys. Res.*, **105**, 27059-27065.

DEVELOPMENT OF THE PARAMETERIZATIONS TO PREDICT THE INITIAL SIZE DISTRIBUTION OF CLOUD DROPLETS FOR THE CLOUD MICROPHYSICAL MODEL IN THE GLOBAL OR REGIONAL MODELS

– Numerical simulation with a hybrid cloud microphysical model –

Naomi Kuba

Frontier Research System for Global Change, Yokohama, Kanagawa, 236-0001, Japan

1. INTRODUCTION

Identifying the effect of aerosol particles on the atmospheric radiative budget and the hydrological cycle is one of the keys to understanding and predicting global climate change. However, it is difficult to deal with this effect in the global climate models and regional climate models. Therefore, the parameterizations of the effect of aerosol particles on the microstructure and optical properties of clouds are needed.

These parameterizations can be developed by using the results of numerical experiments and observations.

2. PARAMERTERIZATION TO PREDICT CLOUD DROPLET CONCENTRATION

The parameterizations to predict cloud droplet concentration (N_d cm^{-3}) were proposed (Kuba and Iwabuchi, 2003, Kuba, 2003) as a function of the updraft velocity at the cloud base (V_{base} m s^{-1}) and the cumulative number of aerosol particles, which can play the role of cloud condensation nuclei (CCN) that can be activated at S % supersaturation ($N_c(S)$ cm^{-3}), as follows.

$$N_d = A\, N_c(S) \,/\, (N_c(S) + B) \qquad (1)$$

$V_{base} \leq 0.24$ m s^{-1} : $S = 0.2$ %

$$A = 4710\, V_{base}^{\ 1.19}$$
$$B = 1090\, V_{base} + 33.2$$

$0.24 < V_{base} \leq 0.5$ m s^{-1} : $S = 0.4$ %

$$A = 11700\, V_{base} - 1690$$
$$B = 10600\, V_{base} - 1480$$

$0.5 < V_{base} \leq 1.0$ m s^{-1} : $S = 0.5$ %

$$A = 4300\, V_{base}^{\ 1.05}$$
$$B = 2760\, V_{base}^{\ 0.755}$$

$1.0 < V_{base} \leq 3.0$ m s^{-1} : $S = 1.0$ %

$$A = 7730 - 15800 \exp(-1.08\, V_{base})$$
$$B = 6030 - 24100 \exp(-1.87\, V_{base})$$

$3.0 < V_{base} \leq 10.0$ m s^{-1} : $S = 2.0$ %

$$A = 1140\, V_{base} - 741$$
$$B = 909\, V_{base} - 56.2$$

The critical supersaturations of 0.2 %, 0.4 % , 0.5 %, 1.0 % and 2.0 % correspond to radii of 0.036 μm (0.048 μm), 0.023 μm (0.031 μm), 0.019 μm (0.027 μm), 0.012 μm (0.017 μm) and 0.0077 μm (0.011 μm) for the dry nucleus of NaCl ($(NH_4)_2SO_4$), for example. These were derived from the numerous numerical experiments with cloud microphysical model. Figure 1 shows the results of numerical simulation using cloud-microphysical parcel model and approximations using eq. (1).

3. PARAMETERIZATION TO PREDICT THE CLOUD DROPLET SIZE DISTRIBUTION

Gamma distributions have been used in many studies to express the cloud droplet size distribution and they are written as follows;

$$n(r) = C\, r^{\beta} \exp(-Dr)\, dr \qquad (2)$$

$$C = N_d (4\pi(\beta+3)(\beta+2)(\beta+1)\, N_d / 3Q)^{(\beta+1)/3} / \beta!$$

$$D = (4\pi(\beta+3)(\beta+2)(\beta+1) N_d / 3Q)^{1/3}$$

$n(r)$ is the number density of cloud droplet (cm^{-4}), N_d is the cloud droplet concentration (cm^{-3}), Q is the cloud water (g cm^{-3}). β is integer (2 or 4 in this study).

Corresponding author's address: Naomi Kuba, Frontier Research System for Global Change, Yokohama, 236-0001, Japan; E-Mail: kuba@jamstec.go.jp

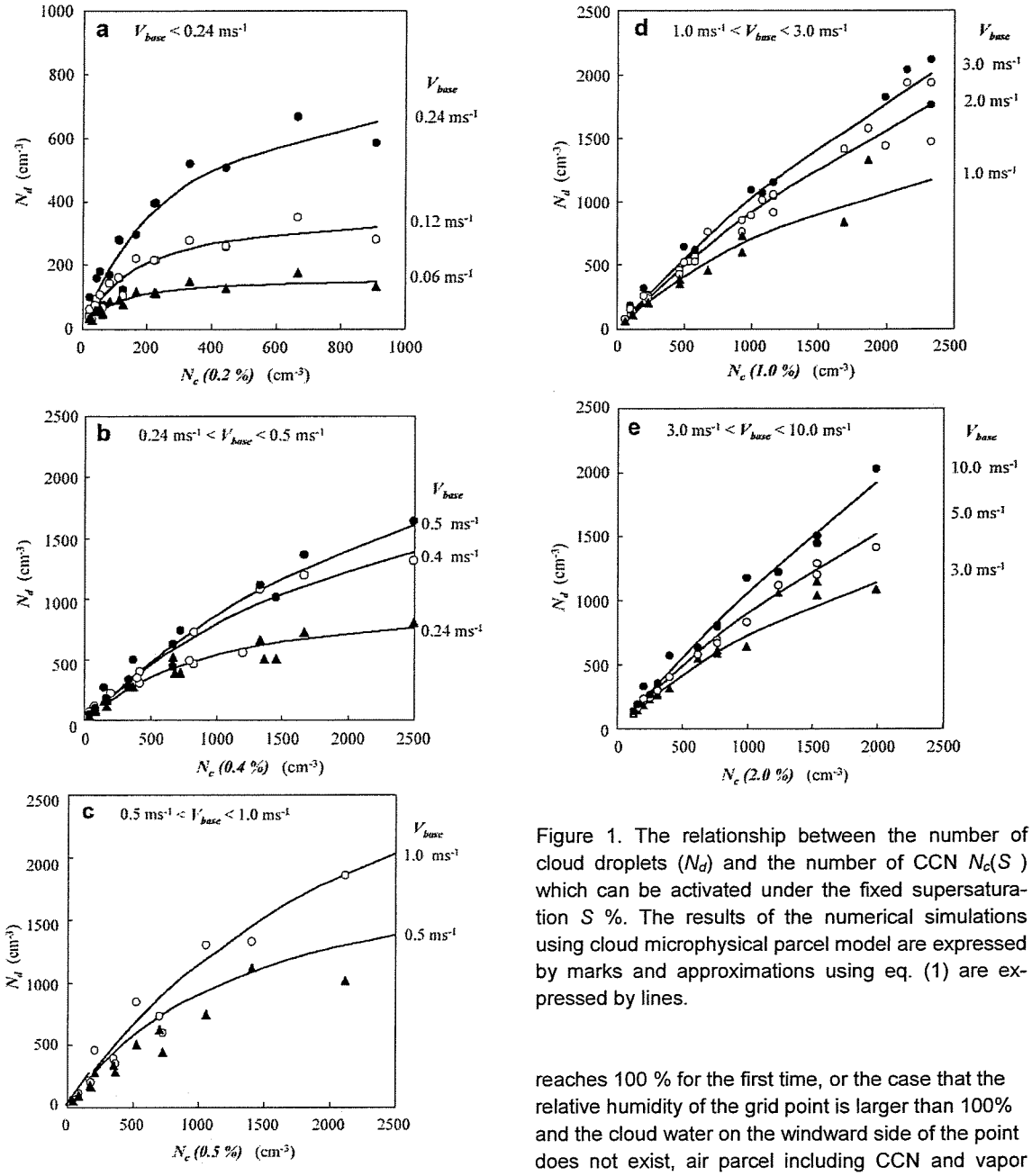

Figure 1. The relationship between the number of cloud droplets (N_d) and the number of CCN $N_c(S)$ which can be activated under the fixed supersaturation S %. The results of the numerical simulations using cloud microphysical parcel model are expressed by marks and approximations using eq. (1) are expressed by lines.

4. CLOUD MODEL WITH CLOUD MICROPHYSICAL MODEL

To compare the derived parameterizations with detail cloud microphysical model, the hybrid cloud model are developed. In this model, each grid point has a parcel model to estimate the activation of nuclei. In the case that the relative humidity of the grid point reaches 100 % for the first time, or the case that the relative humidity of the grid point is larger than 100% and the cloud water on the windward side of the point does not exist, air parcel including CCN and vapor starts to rise from the windward side of the point. In each parcel, the condensation growth of CCN is estimated in Lagrangian framework using the microphysical model described in Takeda and Kuba (1982) and Kuba et al. (2003). When droplets condensed on CCN grow enough to be distinguished from embryo, which can not become cloud droplets, the cloud droplets size distribution, the mixing ratio of vapor and potential temperature in the parcel are given to the grid point.

The cloud droplet size distribution on the grid point is formulated using bins of fixed radii, and their growth by condensation and coalescence are calculated in the Eulerian framework with special attention to prevent numerical diffusion of cloud droplet size distribution. The time change of cloud droplet size distribution caused by condensation and coalescence is estimated by using two moment bin method developed by Chen and Lamb (1994). Sedimentation and advection of droplets are estimated in the Eulerian framework among grid points.

The dynamical framework was designed to test the warm rain microphysical model in the Case 1 of the fifth WMO Cloud Modeling Workshop by Szumowski et al. (1998). The dynamical cloud model prescribes an evolving flow (0-50 min) and performs 2D advection of the temperature and water variables (domain: 9km x 3km, dx and dz: 50m, dt: 3sec). Figure 2 shows the wind field at 25 min., which corresponds to the peak stage of the updraft.

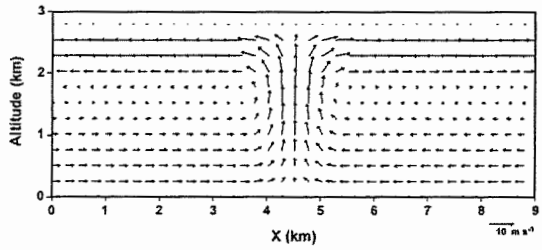

Figure 2. The wind field at 25 min..

5. REPLACEMENT OF THE PARCEL MODEL WITH THE PARAMETERIZATIONS

The parameterizations to predict the number and the initial size distribution of cloud droplets given to the bin model can be used instead of the parcel model belonging to the grid points. When the supersaturation at the grid point is estimated that the adjusted condensed cloud water reaches 1.0 e-7, N_d derived by eq. (1) and the adjusted condensed cloud water as Q are used in eq. (2). Using eq. (2) with derived C and D, the number and mass of droplets included in each bin are calculated.

6. RESULTS OF NUMERICAL EXPERIMENTS

Figure 3 shows the CCN size distribution used in this study. The difference between the three cases is the number of small particle CCN (radius < 0.1 μm).

Figure 4 shows the cloud droplet size distribution estimated by using parcel model precisely and those

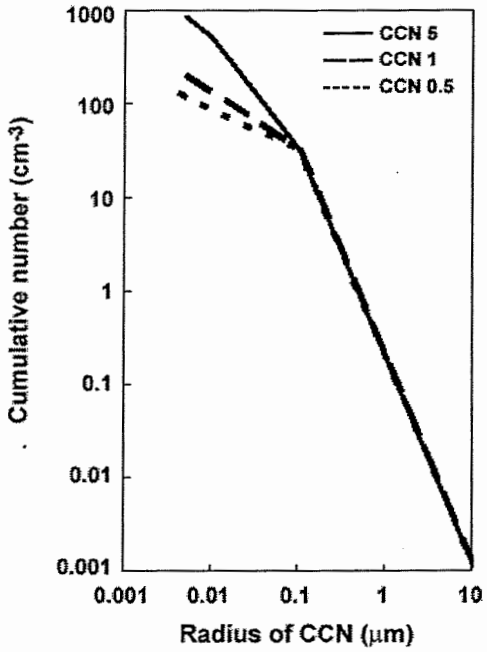

Figure 3. The three size distributions of CCN used in this study.

derived by the parameterization eqs. (1) and (2) in the case of CCN1.

The widths of Gamma distributions are wider than that derived by using parcel model in the Lagrangian framework. Besides, Gamma distributions can not express the large cloud droplets condensed on large CCN.

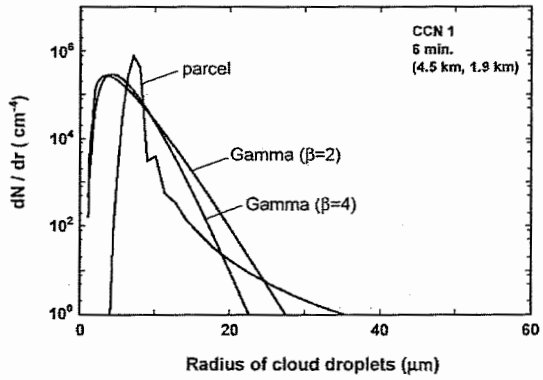

Figure 4. The initial size distributions of cloud droplets for the bin method derived by using parcel model and derived by using parameterization. β of the Gamma distribution is 2 or 4 here.

Figure 5 shows the accumulated rainfall for 50 min. at the surface for three cases. The difference between the results of parcel model and parameterizations is not so large (mean values in the domain are shown in Fig.5). The overestimate of width of size distribution leads to the overestimate of rainfall in the case with Gamma distribution.

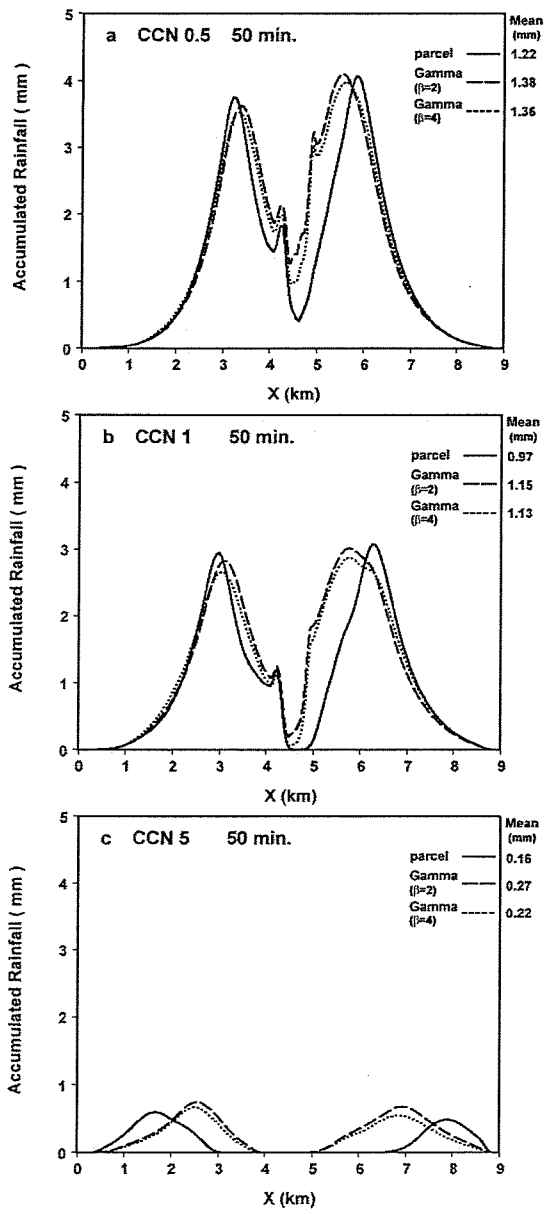

Figure 5. Accumulated rainfall for 50 min. at the surface for three cases. **a**: case with CCN0.5. **b**: case with CCN1. **c**: case with CCN5.

7. CONCLUDING REMARKS

The parameterization to predict number of cloud droplets were derived from the numerous numerical experiments with cloud microphysical model. Using these estimated number of cloud droplets and Gamma distributions are used to give the initial size distribution of cloud droplets for the bin method. It is found that the widths of Gamma distributions are wider than that derived by using parcel model in the Lagrangian framework. Besides, Gamma distributions can not express the large cloud droplets condensed on large CCN. These errors lead to the overestimate of rain water. However, this method can estimate the effect of CCN number concentration (see the difference in the results of numerical experiments between cases of CCN0.5, CCN1 or CCN5).

For verification and improvement of these parameterizations, simultaneous data of cloud condensation nuclei (CCN), updraft velocity at the cloud base, cloud droplet concentration, optical thickness and effective radius are useful.

Updraft velocity in a cloud is not easy to measure, especially for stratus cloud, but it is expected that a Doppler lidar will be able to measure ascent velocity. The combination of remote sensing and in situ measurement make these parameterizations useful.

8. REFERENCES

Chen, J. –P. and D. Lamb, 1994: Simulation of cloud microphysics and chemical processes using a multi-component framework. Part I Description of the microphysical model. J. Atmos. Sci., **51**, 2613-2630.

Kuba, N and T. Takeda, 1982: Numerical study of the effect of CCN on the size distribution of cloud droplets. Part I. Cloud droplets in the stage of condensation growth. J. Meteorol. Soc. Japan, **60**, 978-993

Kuba, N., H. Iwabuchi, K. Maruyama, T. Hayasaka, T. Takeda and Y. Fujiyoshi, 2003: Parameterization of the effect of cloud condensation nuclei on the optical properties of a non-precipitating water layer cloud. J. Meteorol. Soc. Japan, **81**, 393-414.

Kuba, N and H. Iwabuchi, 2003: Revised parameterization to predict cloud droplet concentration and a retrieval method to predict CCN concentration – Supplement–, J. Meteorol. Soc. Japan, **81**, 1485-1487.

Kuba, N.,2003: Parameterizations of cloud microphysical processes for non-hydrostatic model, 5th Non-hydrostatic model Workshop, Yokohama, Japan.

DERIVING PROGNOSTIC EQUATIONS FOR CLOUD FRACTION AND LIQUID WATER CONTENT

Vincent E. Larson[1] *
[1] Atmospheric Science Group, Dept. of Mathematical Sciences, University of Wisconsin — Milwaukee, Milwaukee, Wisconsin.

1. INTRODUCTION

A weather or climate model must prognose accurate moisture and temperature ?elds in part because these ?elds are used to drive parameterizations in the model. Driving the parameterizations is dif?cult because many microphysical and radiative processes are both nonlinear and highly variable. An example is autoconversion of cloud droplets to drizzle drops. For such processes, grid box *mean* quantities often lack suf?cient information to accurately drive the parameterizations. Rather, the host model needs to provide information to the parameterization about subgrid-scale variability.

One approach to doing this is to formulate prognostic equations for the grid box mean of speci?c liquid water content, $\langle q_l \rangle$, and cloud fraction, C. This provides information about partial cloudiness. Tiedtke (1993) presented modeled equations for $\langle q_l \rangle$ and C, but he did not derive them from ?rst principles. Wang and Wang (1999) did derive equations for C and $\langle q_l \rangle$, but they assumed a Gaussian family of FDFs. An FDF is the spatial average of a probability density function over a grid-box-sized volume (Colucci et al. 1998). The FDF, P_s, has all the properties of a PDF (Pope 2000, p. 59); that is, the FDF is non-negative everywhere and is normalized. Gregory et al. (2002), Wilson and Gregory (2003), and Bushell et al. (2003) derived equations for C and $\langle q_l \rangle$, but they were not completely general. For instance, the ?rst two papers assume that forcings are applied uniformly across the grid box.

This paper derives prognostic equations for C and $\langle q_l \rangle$ that are valid for any FDF shape and for non-uniform forcing. The derivation starts from the evolution equation for the FDF of moisture. The FDF equation is a prognostic equation that can be derived from the conservation of moisture. This FDF equation and others like it have been widely studied by combustion engineers since the pioneering work of Lundgren (1967, 1969); see, for example, Pope (2000).

Deriving equations for C and $\langle q_l \rangle$ is useful because these equations contain exact but unclosed terms that can in principle be estimated by large eddy simulation and compared with parameterizations of the terms. Deriving C and $\langle q_l \rangle$ shows that closure of terms in the equations for C and $\langle q_l \rangle$ depends on and requires information about the relevant FDF. In addition, the C and $\langle q_l \rangle$ equations contain an unclosed dissipation term that does not appear in equations for conserved scalars. For this term, this paper compares a closure due to (Tiedtke 1993) versus another called the linear mean-square estimation (LMSE) model.

Interested readers may ?nd more details about this research in Larson (2004).

*Corresponding author address: Vincent E. Larson, Department of Mathematical Sciences, University of Wisconsin — Milwaukee, P. O. Box 413, Milwaukee, WI 53201-0413; vlarson@uwm.edu; http://www.uwm.edu/~vlarson

2. THE STARTING POINT: THE EVOLUTION EQUATION FOR THE FILTERED DENSITY FUNCTION

We choose to study the one-dimensional FDF of a variable s that was introduced by Mellor (1977) and Sommeria and Deardorff (1977). The variable s has several useful properties. First, when $s > 0$, $s \cong q_l$ (although s can be negative, whereas q_l cannot). Second, s is conserved during condensation (although not during adiabatic pressure changes). Third, s is a single variable that accounts for how liquid water varies with both total water content and temperature. The variable s has the same units as q_l, e.g. g kg^{-1}. The conservation equation for s is an advection-diffusion equation with a source term, S_s.

A prognostic transport equation for the FDF, P_s, can be rigorously derived from the conservation equation for s and other fundamental equations and de?nitions (Colucci et al. 1998; Klimenko and Bilger 1999; Pope 2000; Larson 2004). We assume the diffusivity of s, κ, is constant and that the ?uid is Boussinesq. The ?nal result is

$$\underbrace{\frac{\partial P_s}{\partial t}}_{\text{Time tendency}} + \underbrace{\frac{\partial}{\partial x_i}\left(\langle u_i|\psi\rangle P_s\right)}_{\text{Advection}} = \underbrace{\kappa \nabla^2 P_s}_{\text{Diffusion}} - \underbrace{\frac{\partial^2}{\partial \psi^2}\left(\left\langle \kappa \frac{\partial s}{\partial x_i}\frac{\partial s}{\partial x_i}\middle|\psi\right\rangle P_s\right)}_{\text{Dissipation}} - \underbrace{\frac{\partial}{\partial \psi}\left[\langle S_s|\psi\rangle P_s\right]}_{\text{Source}}. \quad (1)$$

We write an unconditional average or ?ltered value of a function $f(x_i, t)$ as $\langle f(x_i, t)\rangle$. The conditional average,

$\langle f|\psi\rangle$, is the average of $f(x_i,t)$ over those points for which $s(x_i,t)=\psi$.

In this equation, $P_s = P_s(\psi;x_i,t)$ depends on ?ve independent variables: the usual ones of space (x_i) and time (t), plus the so-called "sample-space" variable, ψ, corresponding to s. The addition of the sample-space variable adds an extra dimension to the equation: the equation tracks how the ?ltered density $P_s(\psi;x_i,t)$ at each value of ψ evolves in space and time. In this sense, Eq. (1) differs from the conservation equation for $s(x_i,t)$ and resembles more the equation for bin microphysics, which bins hydrometeors according to radius and transports the bins individually in space and time.

We now comment on the terms in the FDF equation (1), starting from the left.

- The time tendency term quanti?es how the FDF of s within the ?ltered region near x_i changes shape in sample space (ψ-space) with time.
- The advection term transports the ?ltered density P_s in physical space (x_i space), not by the full averaged velocity $\langle u_i\rangle$, but by $\langle u_i|\psi\rangle$, the velocity conditionally averaged with respect to the condition that $s=\psi$.
- The diffusion term diffuses P_s in physical space. Although the diffusion term cannot change the shape of P_s averaged over the whole domain, it can change the shape of P_s in a particular grid box.
- The dissipation term does change the shape of the domain-integrated FDF of s, unlike the aforementioned diffusion term. In fact, one can see that the dissipation term has the form of a Laplacian diffusion term in *sample space* (ψ-space) with a non-positive diffusivity, $-\langle\kappa(\partial s/\partial x_i)(\partial s/\partial x_i)|\psi\rangle$ (Chen and Kollmann 1994; Dopazo 1994). A negative diffusivity, rather than broadening the domain-integrated FDF, tends to narrow it in ψ-space by mixing ?uid parcels with different values of s. Therefore the dissipation term, acting unopposed, homogenizes s.

3. DERIVING A PROGNOSTIC EQUATION FOR CLOUD FRACTION

We now derive a prognostic equation for the cloud fraction within a ?ltered region near x_i, e.g., within a grid box.

If all vapor in excess of saturation is converted immediately to liquid, then cloud fraction, C, is given by:

$$C(x_i,t)=\int_{-\infty}^{\infty} d\psi\; P_s(\psi;x_i,t)H(\psi)=\langle H(s)\rangle\,, \qquad (2)$$

where H is the Heaviside step function. This formula states that the cloud fraction equals that portion of the area under P_s that corresponds to q_t in excess of saturation, i.e. the area with $s>0$.

The derivation proceeds simply by integrating the FDF equation over the cloudy portion of the domain. That is, we apply the operator

$$\int_{\psi=0}^{\psi=\infty} d\psi = \int_{\psi=-\infty}^{\psi=\infty} d\psi H(\psi) \qquad (3)$$

to the FDF equation (1). We assume here that the ?uid is Boussinesq and that the diffusivity κ is constant. Recalling that $C=\langle H(s)\rangle$, we ?nd

$$\begin{aligned}\underbrace{\frac{\partial C}{\partial t}}_{\text{Time tendency}} &+ \underbrace{\frac{\partial}{\partial x_i}\langle u_i H(s)\rangle}_{\text{Advection}} \\ &= \underbrace{\kappa\nabla^2 C}_{\text{Diffusion}} \\ &\quad + \underbrace{\left[\frac{\partial}{\partial\psi}\left(P_s\left\langle\kappa\,\frac{\partial s}{\partial x_i}\frac{\partial s}{\partial x_i}\middle|\psi\right\rangle\right)\right]_{\psi=0}}_{\text{Dissipation}} \\ &\quad + \underbrace{\left(\langle S_s|\psi\rangle\, P_s\right)_{\psi=0}}_{\text{Source}}\,. \qquad (4)\end{aligned}$$

A similar equation for generic intermittent ?elds was obtained by Chen and Kollmann (1994). Several of the terms in the equation merit discussion.

- The advection term shows that cloud is advected by the within-cloud velocity, not the average full velocity $\langle u_i\rangle$ that is typically prognosed by a model.
- The dissipation term describes how mixing affects C by narrowing P_s. Mixing can either increase or decrease C. Consider the simple case in which $\langle\kappa(\partial s/\partial x_i)(\partial s/\partial x_i)|\,\psi\rangle$ is constant. Then the sign of the dissipation term depends on the slope of P_s at $\psi=0$, that is, at saturation. For instance, suppose P_s is a single Gaussian in ψ and that it narrows in time because of mixing (see Fig. 1). If $\langle s\rangle>0$, so that C is large ($C>1/2$), then $\partial P_s/\partial\psi|_{\psi=0}>0$, implying that mixing tends to increase C. This is because mixing causes the unsaturated tail ($\psi<0$) to decrease in area. Likewise, if $\langle s\rangle<0$, then C is small and mixing tends to decrease C.
- Computing the source term requires that we determine the average strength of the source at saturated points within the grid box, $(\langle S_s|\psi\rangle)_{\psi=0}$; knowledge of the grid box average source, $\langle S_s\rangle$, is not suf?cient.

Both the dissipation and source terms depend explicitly on the FDF, P_s; the advection term depends implicitly on P_s. Therefore the equation for C cannot be closed without an explicit or implicit model for P_s. Hence if one chooses to predict cloud fraction by prognosing C, one does not thereby circumvent the dif?culties involved in predicting P_s.

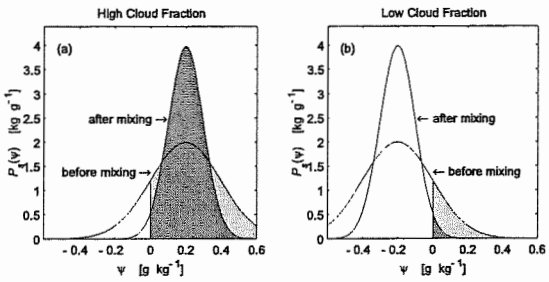

Figure 1: Gaussian FDFs of s, $P_s(\psi)$, before and after a hypothetical dissipative mixing process occurs for (a) high cloud fraction, and (b) low cloud fraction. The light grey shading indicates the cloud fraction before mixing, and the dark grey, the cloud fraction after mixing. For high cloud fraction, the mean of P_s is at $\psi > 0$. Then mixing, which narrows the FDF, *increases* cloud fraction. For low cloud fraction, however, the opposite is true.

4. THE DISSIPATION TERM IN THE CLOUD FRACTION EQUATION: A DIFFICULT PARAMETERIZATION PROBLEM

The dissipation term alters C by decreasing the variance of s. Teixeira (2001) found that in subtropical boundary layers, the dissipation term is one of the largest terms in Tiedtke's (1993) modeled equation for C.

One simple closure, widely used in the turbulence and combustion literature, is the linear mean-square estimation (LMSE) model (Villermaux and Devillon 1972; Dopazo and O'Brien 1974; Pope 2000, Eq. 12.326). The LMSE closure has the defect of preserving the shape of the FDF as it narrows, rather than relaxing it to a Gaussian (Pope 2000, p. 550). If the LMSE diffusion model acts on a skewed FDF, the FDF does not become symmetrical. The LMSE closure for both the diffusion and dissipation terms in the equation for C is

$$\underbrace{\kappa\nabla^2 C}_{\text{Diffusion}} + \underbrace{\left[\frac{\partial}{\partial\psi}\left(P_s\left\langle\kappa\frac{\partial s}{\partial x_i}\frac{\partial s}{\partial x_i}\middle|\psi\right\rangle\right)\right]_{\psi=0}}_{\text{Dissipation}} = \left(P_s\frac{1}{2}c_s\frac{\epsilon}{e}\langle s\rangle\right)_{\psi=0}. \quad (5)$$

This parameterization leaves C unaltered if $P_s|_{\psi=0} = 0$, that is, if there are no parcels just at saturation. Otherwise, C increases if $\langle s\rangle > 0$, and C decreases if $\langle s\rangle < 0$. This conforms to the expected effect of mixing on Gaussian FDFs shown in Fig. 1. The expression $(1/2)c_s\epsilon/e$ may be thought of as an inverse time scale that depends on the turbulent dissipation and in?uences the rapidity with which C dissipates.

Tiedtke (1993, Eq. 32) has proposed another expression for the dissipation of cloud fraction:

$$\text{Dissipation} \cong \frac{C^2}{\langle q_l\rangle}K(\langle q_s\rangle - \langle q\rangle) \geq 0, \quad (6)$$

where q is the speci?c humidity, q_s is the saturation speci?c humidity, and $K = 10^{-6}\ \text{s}^{-1}$ is an inverse time constant. We can pass from the LMSE model of dissipation of C, (5), to Tiedtke's model, (6), if we change the following. We assume that P_s is a uniform (rectangular) FDF. We equate timescales, so that $K = (1/4)c_s\epsilon/e$. Finally we replace $\langle s\rangle$ by $(q_s - q)$. The last change, however, is signi?cant, since the LMSE model allows dissipation to either increase or decrease C, depending on the cloud fraction, the relative humidity of unsaturated air, and the liquid water content of cloudy air (see Fig. 1). Tiedtke's (1993) formula, in contrast, only permits dissipation to decrease C. Although this is a drawback, we note that in the cases in which dissipation increases cloud fraction, q approaches q_s, so that Tiedtke's expression (6) diminishes C weakly, not strongly.

5. DERIVING A PROGNOSTIC EQUATION FOR LIQUID WATER

We now use the FDF equation (1) to derive a prognostic equation for the ?ltered speci?c liquid water content, $\langle q_l\rangle$. We again assume that any supersaturation is immediately converted to liquid. Then q_l is given, in terms of s, as $q_l = sH(s)$, and $\langle q_l\rangle$ is

$$\langle q_l\rangle = \int_{-\infty}^{\infty} d\psi\ P_s(\psi; x_i, t)\psi H(\psi) = \langle sH(s)\rangle. \quad (7)$$

We can derive an equation for $\langle q_l\rangle$ by applying the operator

$$\int_{\psi=0}^{\psi=\infty} d\psi\ \psi = \int_{-\infty}^{\infty} d\psi\ H(\psi)\psi \quad (8)$$

to Eq. (1) for P_s. Assuming a Boussinesq ?ow, and making the questionable assumption that the diffusivity κ is constant, we obtain

$$\underbrace{\frac{\partial\langle q_l\rangle}{\partial t}}_{\text{Time tendency}} + \underbrace{\frac{\partial}{\partial x_i}\langle u_i q_l\rangle}_{\text{Advection}} = \underbrace{\kappa\nabla^2\langle q_l\rangle}_{\text{Diffusion}} - \underbrace{\left(P_s\left\langle\kappa\frac{\partial s}{\partial x_i}\frac{\partial s}{\partial x_i}\middle|\psi\right\rangle\right)\Big|_{\psi=0}}_{\text{Dissipation}} + \underbrace{\langle S_s H(s)\rangle}_{\text{Source}}. \quad (9)$$

The terms are somewhat analogous to their counterparts in the prognostic equation for C (4). We only note that the dissipation term describes how diffusive mixing, which tends to homogenize the ?uid, affects

$\langle q_l \rangle$ via evaporation or condensation. Since both P_s and the scalar dissipation, $\kappa(\partial s/\partial x_i)(\partial s/\partial x_i)$, are nonnegative, the dissipation term cannot increase $\langle q_l \rangle$. This is a consequence of the fact that we have assumed that s mixes linearly. In contrast, dissipation or mixing can either increase or decrease C readily (recall Eq. 4); therefore, mixing has different effects on $\langle q_l \rangle$ and C. This is an important consideration for modeling purposes.

6. CONCLUSIONS

The main result of this paper is the derivation of the prognostic equation (4) for cloud fraction, C, and equation (9) for ?ltered speci?c liquid water content, $\langle q_l \rangle$. These equations were derived from the prognostic equation for the ?ltered density function (FDF) of s, (1). An extra term emerges in the C and $\langle q_l \rangle$ equations, a term that does not appear in equations for variables that are conserved with respect to condensation, such as total speci?c water content, q_t. The extra term arises from the tendency of dissipation or diffusive mixing to homogenize a ?uid. From inspection of the dissipation term, we see that it always diminishes $\langle q_l \rangle$ with the diffusive model we use. In contrast, dissipation can either increase or decrease C.

We have compared a closure for dissipation used by combustion engineers with the closure used by Tiedtke (1993). Perhaps the biggest difference is that the engineers' linear mean-square estimation (LMSE) model can either increase or decrease C, but Tiedtke's parameterization can only decrease C. In nature, either an increase or decrease in C is possible (see Fig. 1). The dissipation term in Tiedtke's equation for C is a dominant term in many situations (Teixeira 2001), although the term tends to zero as the grid box average speci?c humidity approaches saturation.

Should modelers prognose moments of s and diagnose C and q_l based on an assumed FDF, or should they prognose C and q_l directly? Each method has disadvantages. However, many of the terms in the C and $\langle q_l \rangle$ equations depend explicitly or implicitly on the FDF; therefore, prognosing C and $\langle q_l \rangle$ does not evade the problem of prognosing or diagnosing the FDF.

Acknowledgements The author is grateful for ?nancial support provided by subcontracts G-7420-2, G-7470-2, and G-7424-1 from the DoD Center for Geosciences at Colorado State University, and grant ATM-0239982 from the National Science Foundation.

References

Bushell, A. C., D. R. Wilson, and D. Gregory, 2003: A description of cloud production by non-uniformly distributed processes. *Quart. J. Roy. Meteor. Soc.*, **129**, 1435–1455.

Chen, J.-Y. and W. Kollmann, 1994: Comparison of prediction and measurement in non-premixed turbulent ?ames. *Turbulent Reacting Flows*, P. A. Libby and F. A. Williams, Eds., Academic Press, 211–308.

Colucci, P. J., F. A. Jaberi, P. Givi, and S. B. Pope, 1998: Filtered density function for large eddy simulation of turbulent reacting ?ows. *Phys. Fluids*, **10**, 499–515.

Dopazo, C., 1994: Recent developments in Pdf methods. *Turbulent Reacting Flows*, P. A. Libby and F. A. Williams, Eds., Academic Press, 375–474.

Dopazo, C. and E. E. O'Brien, 1974: An approach to the autoignition of a turbulent mixture. *Acta Astronaut.*, **1**, 1239–1266.

Gregory, D., D. Wilson, and A. Bushell, 2002: Insights into cloud parametrization provided by a prognostic approach. *Quart. J. Roy. Meteor. Soc.*, **128**, 1485–1504.

Klimenko, A. Y. and R. W. Bilger, 1999: Conditional moment closure for turbulent combustion. *Prog. Energy Combust. Sci.*, **25**, 595–687.

Larson, V. E., 2004: Prognostic equations for cloud fraction and liquid water, and their relation to ?ltered density functions. *J. Atmos. Sci.*, **61**, 338–351.

Lundgren, T. S., 1967: Distribution functions in the statistical theory of turbulence. *Phys. Fluids*, **10**, 969–975.

Lundgren, T. S., 1969: Model equation for nonhomogeneous turbulence. *Phys. Fluids*, **12**, 485–497.

Mellor, G. L., 1977: The Gaussian cloud model relations. *J. Atmos. Sci.*, **34**, 356–358.

Pope, S. B., 2000: *Turbulent Flows*. Cambridge University Press, 771 pp.

Sommeria, G. and J. W. Deardorff, 1977: Subgrid-scale condensation in models of nonprecipitating clouds. *J. Atmos. Sci.*, **34**, 344–355.

Teixeira, J., 2001: Cloud fraction and relative humidity in a prognostic cloud fraction scheme. *Mon. Wea. Rev.*, **129**, 1750–1753.

Tiedtke, M., 1993: Representation of clouds in large-scale models. *Mon. Wea. Rev.*, **121**, 3040–3061.

Villermaux, J. and J. C. Devillon, 1972: *Proc. Second Int. Symp. on Chemical Reaction Engineering*, New York: Elsevier.

Wang, S. and Q. Wang, 1999: On condensation and evaporation in turbulence cloud parameterizations. *J. Atmos. Sci.*, **56**, 3338–3344.

Wilson, D. and D. Gregory, 2003: The behaviour of large-scale model cloud schemes under idealized forcing scenarios. *Quart. J. Roy. Meteor. Soc.*, **129**, 967–986.

NEW PARAMETERIZATIONS FOR THE AUTOCONVERSION PROCESS AND THE DISPERSION EFFECT

Yangang Liu[1], Peter H. Daum and Robert McGraw

[1] Environmental Sciences Department, Brookhaven National Laboratory, Upton, NY 11973-5000

1. INTROCUTION

Representation of cloud and precipitation processes is crucial for improving atmospheric models of various scales ranging from large eddy simulations (LES) to cloud resolving models (CRMs) to global climate models (GCMs) (Stokes and Schwartz 1994). A key process that must be parameterized is the so-called autoconversion process whereby large cloud droplets collect small ones and become embryonic raindrops (Kessler 1969; Manton and Cotton 1977; Tripoli and Cotton 1980; Liou and Ou 1989; Baker 1993; Boucher et al. 1995; Liu and Daum 2004). Accurate parameterization of this process is especially important for studies of the second indirect aerosol effect (Boucher et al. 1995; Lohmann and Fleichter 1997; Rotstayn 2000).

Kessler (1969) proposed a simple parameterization that linearly relates the autoconversion rate to the cloud liquid water content (L), and assumes a critical value for L below which no autoconversion occurs. One major improvement in later Kessler-type parameterizations is explicitly accounting for the droplet concentration (N) as well as L (Manton and Cotton 1977; Tripoli and Cotton 1980; Liou and Ou 1989; Baker 1993; Liu and Daum 2004). The inclusion of N in the autoconversion parameterization allows for modeling studies of the second indirect aerosol effect. It has also been recognized that the threshold process should be determined by a critical radius (r_c) rather than by a critical L as conceived by Kessler. Considering autoconversion as a threshold process is a distinctive feature that sets Kessler-type parameterizations apart from other types of autoconversion parameterizations (e.g., Berry 1968; Beheng 1994; Khairoutdinov and Kogan 2000).

Without loss of generality, all the improved Kessler-type parameterizations can be generically written as

$$P = fH(r_m - r_c), \tag{1}$$

where P is the autoconversion rate; f is a function of L and N; r_m is the control radius; the Heaviside function $H(r_m - r_c)$ is introduced to describe the threshold process such that there is no autoconversion when the control radius is less than r_c. The control radius is the volume-mean radius in Manton and Cotton (1977), Tripoli and Cotton (1980), Liou and Ou (1989), and Baker (1993), the mean radius of the 4th moment in Boucher et al. (1995), and the mean radius of the 6th moment in the parameterization that we have recently derived (Liu and Daum 2004; hereafter Liu-Daum parameterization). The function f is also different for different parameterizations.

Furthermore, although model results are very sensitive to the value of r_c (Boucher et al. 1995; Rotstayn 1999), the idea of threshold process embedded in Kessler-type parameterizations have been used rather loosely, and r_c has been largely considered an empirical parameter that is arbitrarily tuned to match model simulations with observations. Liu et al. (2004) have derived an analytical expression for r_c by coupling a new theory on the rain formation that we have recently formulated (McGraw and Liu 2003) with the Liu-Daum parameterization. Here we first briefly discussed the Liu-Daum parameterization and the derivation of the expression for r_c, and then introduce a new Kessler-type parameterization by coupling Liu-Daum parameterization with the expression for r_c. Implications of the new parameterizations for the evaluation of the autoconversion rate and the second indirect aerosol effect are discussed.

2. LIU-DAUM PARAMETERIZATION

As detailed in Liu and Daum (2004), the Liu-Daum parameterization is given by

[1] Corresponding author: Yangang Liu, Brookhaven National Laboratory, Bldg. 815E, Upton, NY 11973 lyg@bnl.gov

$$P = \eta N^{-1} L^3 H(r_6 - r_c), \quad (2a)$$

$$\eta = \left(\frac{3}{4\pi\rho_w}\right)^2 \kappa\beta_6^6 \quad (2b)$$

$$\beta_6 = \left[\frac{(1+3\varepsilon^2)(1+4\varepsilon^2)(1+5\varepsilon^2)}{(1+\varepsilon^2)(1+2\varepsilon^2)}\right]^{1/6}, \quad (2c)$$

where $\kappa = 1.1 \times 10^{10}$ $cm^{-3}s^{-1}$ is an empirical coefficient in the Long collection kernel for $r < 50$ μm (Long 1974), ρ_w is the water density, ε is the relative dispersion of the cloud droplet size distribution, and r_6 is the mean radius of the 6th moment of the droplet size distribution. Heaviside function $H(r_6 - r_c)$ is introduced to consider the threshold process such that the autoconversion rate is negligibly small when $r_6 < r_c$.

Rewritten in the form of the commonly used previous Kesser-type parameterizations (e.g., Boucher et al. 1995), the Liu-Daum parameterization becomes

$$P = \alpha N^{-1/3} L^{7/3} H(r_6 - r_c), \quad (3a)$$

$$\alpha = \left(\frac{3}{4\pi\rho_w}\right)^2 \kappa\beta_6^6 \left(\frac{L}{N}\right)^{2/3}. \quad (3b)$$

The following points should be emphasized. First, the Liu-Daum parameterization exhibits stronger dependence of the autoconversion rate on both the liquid water content (L^3), the droplet concentration (N^{-1}) and the relative dispersion; this change affects the evaluation of the precipitation and the indirect aerosol effect after the onset of the autoconversion Second, the control radius is the mean radius of the 6th moment instead of 3rd or 4th moments; this change affects the evaluation of the onset of the autoconversion. These improvements comes from the elimination of the incorrect assumption of fixed collection efficiency inherent in the previous parameterizations (Liu and Daum 2004) Examination of the Liu-Daum parameterization provides an explanation for a number of long-standing issues associated with previous parameterizations. For example, such a wide range of values have been assigned to the coefficient a_k in studies using the original Kessler parameterization that, in practice, it has been often considered to be arbitrarily tunable (e.g., Kessler 1969; Liu and Orville 1969; Ghosh et al. 2000). It is evident from the Liu and Daum parameterization that the wide range of values assumed for a_k may stem from the variabilities in the liquid water content, droplet concentration and relative dispersion that are not properly accounted for in the original Kessler parameterization. Similar to the arbitrary tunability of the coefficient a_k in the original Kessler parameterization, a wide range of values have been also assigned to the α coefficient in modeling studies using the traditional R_4 parameterizations (Baker 1993; Boucher et al. 1995). The Liu-Daum parameterization again suggests that the wide range of the coefficient α in the early parameterizations may be largely due to the variability of droplet concentration, liquid water content and relative dispersion. This is demonstrated in Fig.1. The result also suggests that the substantial effects of variation of the liquid water content and droplet concentration are masked by the tunable coefficient α in the previous Kessler-type parameterization that has been commonly used.

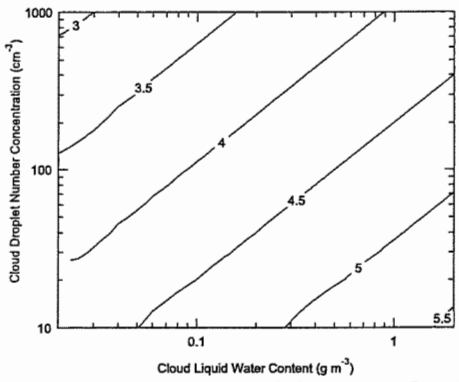

Figure 1. The empirical coefficient α as a function of the liquid water content and droplet concentration as calculated from Eq. (3) for a monodisperse cloud droplet size distribution. The contour value denotes the log(α). The α coefficient varies by three orders of magnitude depending on the combination of the droplet concentration and the liquid water content. The effect of the liquid water content and droplet concentration on the conversion coefficient in the original Kessler scheme is even larger, depending the choice of the threshold liquid water content Lc.

3. EXPRESSION FOR THE CRITICAL RADIUS

3.1. Kinetic Potential Theory

Although it has been well established that three physical processes (condensation, evaporation and collection) are involved in the formation of warm rain, many issues regarding the initiation of warm rain remain unsolved (Beard and Ochs 1993; Telford 1996). McGraw and Liu (2003) have recently developed a new theory on rain formation by extending the theory of statistical crossing of a kinetic potential barrier in nucleation to the processes of condensation, evaporation and collection occurring in warm clouds. Briefly, by analogy to the kinetic theory on nucleation, the kinetic potential $\Phi(j)$ for a droplet consisting of j water molecules is given by

$$\Phi(j) \equiv -\ln\left[\prod_{g=1}^{j-1} \frac{\beta_{con}(g)+\beta_{col}(g)}{\gamma_{eva}(g+1)}\right] \quad (4a)$$

$$\beta_{col}(g) = \frac{\kappa v}{\rho_w^2} g^2 L, \quad (4b)$$

$$\gamma_{eva}(g) = \exp\left(\frac{vN}{L}\right)\beta_{con}(g), \quad (4c)$$

$$g = \frac{4\pi\rho_w}{3v} r^3, \quad (4d)$$

where β_{con} (s^{-1}), β_{col} (s^{-1}), and γ_{eva} (s^{-1}) denote the condensation, collection, effective evaporation rate constants, respectively; $v = 3.0 \times 10^{-23}$ (g) is the mass per water molecule; s^{-1} is a constant in the Long collection kernel; ρ_w is the water density (g cm^{-3}). The kinetic potential as a function of droplet radius (r) can be then calculated using Eq. (4). Figure 2 shows a typical example of the change of the kinetic potential with the droplet radius. The kinetic potential first increases with increasing droplet radius and then decreases after reaching a peak.

The point where the kinetic potential reaches its maximum is worth emphasizing because it physically defines a critical point. As in nucleation theory, the maximum kinetic potential is referred to as the "barrier"; the corresponding droplet radius defines r_c. Before reaching the critical point, the droplet system is in a stable state because more potential is needed to climb the "hill". Once the barrier is passed, the system becomes unstable down the "hill", and embryonic raindrops spontaneously form. Therefore, the idea of threshold process and r_c inherent in Kessler-type parameterizations of the autoconversion process emerges naturally from the kinetic potential theory.

3.2. Analytical Expression for Critical Radius

In state-of-the art GCMs, L and N are predicted/diagnosed. It is therefore desirable to have an analytical expression that relates r_c to these two variables. It is known from McGraw and Liu (2003) that at the critical point, the forward and reverse rate constants are equal, i.e.,

$$\beta_{con} + \beta_{col} = \gamma_{eva} \quad (5)$$

Therefore, the critical radius is given by

$$r_c = \left\{\left(\frac{3}{4\pi}\right)^2 \frac{v}{\kappa}\beta_{con}\left[\exp\left(\frac{vN}{L}\right)-1\right]\frac{1}{L}\right\}^{1/6} \quad (6a)$$

Because $(vN/L) << 0$, Eq. (6a) can be simplified to

$$r_c = \left\{\left(\frac{3}{4\pi}\right)^2 \frac{v^2}{\kappa}\beta_{con}\frac{N}{L^2}\right\}^{1/6} \approx 4.09\times10^{-4}\beta_{con}^{1/6}\frac{N^{1/6}}{L^{1/3}} \quad (6b)$$

In general, β_{con} is a complex function of cloud turbulence that is unknown at present (McGraw and Liu 2003). The mean condensation rate constant of $\beta_{con} = 1.15 \times 10^{23}$ s^{-1} estimated in Liu et al. (2004) from microphysical measurements is used in this work.

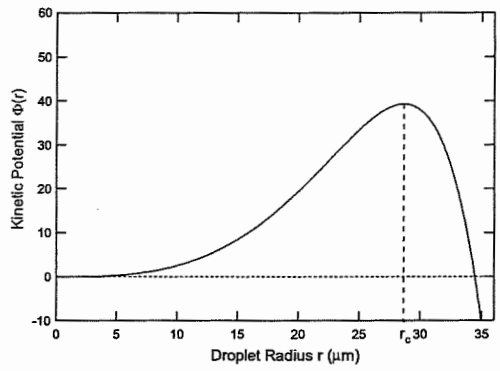

Figure 2. An example of the kinetic potential as a function of the droplet radius. The results are for a cloud liquid water content L = 0.5 g m^{-3}, the cloud droplet number concentration N = 300 cm^{-3}, and the condensation rate constant $\beta_{con} = 9 \times 10^{24}$ s^{-1}

3.3. Critical Radius of Ambient Clouds

Equation (6b) indicates that r_c is a function of L and N, varying from cloud to cloud, even from place/time to place/time in the same cloud. To demonstrate this, Figure 3 shows r_c calculated from Eq. (6b) using the mean β_{con} and the data on L and N from stratiform clouds given in *Miles et al.* [2000]. It

is clear that r_c varies significantly, from ~ 6 μm to 40 μm. Note that since each point in Figure 3 actually represents an average of many samples, variation in r_c is expected to be even larger for individual clouds. This suggests that prescribing r_c as a constant is more troublesome in small-scale models than in GCMs.

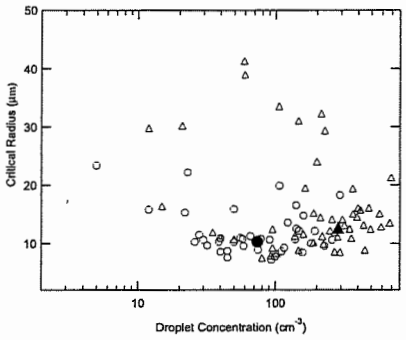

Figure 3. Relationship of the critical radius to the droplet concentration. The open triangles and dots denote continental and marine clouds, respectively. The solid triangle and dot denote the average of continental and marine clouds, respectively

4. NEW PARAMETERIZATION AND IMPLICATIONS

A new parameterization for the autoconversion rate is readily obtained by substituting the expression for r_c into the Liu-Daum parameterization. In the form of Eq. (1), the new parameterization is

$$f=\left(\frac{3}{4\pi\rho_w}\right)^2\kappa\left[\frac{(1+3\varepsilon^2)(1+4\varepsilon^2)(1+5\varepsilon^2)}{(1+\varepsilon^2)(1+2\varepsilon^2)}\right]N^{-1}L^3H(r_6-r_c), \tag{7a}$$

$$r_6=\left(\frac{3}{4\pi\rho_w}\right)^{1/3}\left[\frac{(1+3\varepsilon^2)(1+4\varepsilon^2)(1+5\varepsilon^2)}{(1+\varepsilon^2)(1+2\varepsilon^2)}\right]^{1/6}\left(\frac{L}{N}\right)^{1/3} \tag{7b}$$

$$r_c=4.09\times10^{-4}\beta_{con}^{1/6}\frac{N^{1/6}}{L^{1/3}}. \tag{7c}$$

The new parameterization has the following important implications for the evaluation of the second indirect aerosol effect. First, anthropogenic aerosols inhibit the onset of embryonic raindrops by decreasing the control radius r_6 and by increasing the critical radius. This phenomenon is self-evident from the relation between r_6 and r_c, (Liu et al. 2004)

$$r_c=\left[\left(\frac{3}{4\pi}\right)^3\frac{\nu^2\beta_{con}}{\kappa\rho_w L}\right]^{1/6}\frac{\alpha^{1/2}}{r_6^{1/2}}\approx\frac{23.72}{L^{1/6}r_6^{1/2}}, \tag{8a}$$

or from the equation

$$\Delta=r_6-r_c=r_6-\frac{23.72}{L^{1/6}r_6^{1/2}} \tag{8b}$$

Second, an increase in aerosol loading also decreases the conversion rate from cloud water to rain water after the onset of the autoconversion process. This phenomenon is evident from Eq. (7a).

5. CONCLUSIONS

The Liu-Daum parameterization for the autoconversion rate is briefly introduced, and is used to explain the wide range of the empirical coefficient α that has been commonly used in previous Kessler-type parameterizations. An analytical expression for r_c is introduced and discussed by coupling the kinetic potential theory on the formation of warm rain with the Liu-Daum parameterization. A new parameterization for the autoconversion rate is presented by substituting the expression for r_c into the Liu-Daum parameterization It is shown that anthropogenic aerosols have the effect of increasing r_c but decreasing the control radius concurrently, inhibiting the onset of embryonic raindrops. An increase in aerosol loading also decreases the conversion rate from cloud water to rain water after the onset of the autoconversion.

The effect of the relative dispersion on the autoconversion rate after the onset of this process manifest itself in Eq. (7a). Part of the effect of the relative dispersion on the onset of the autoconversion process is embodied in the equation for the control radius [Eq. (7b)]. However, a complete solution is awaiting the inclusion of the relative dispersion in the formulation of the expression for r_c.

ACKNOWLEDGEMENTS

This research was supported by the Environmental Sciences Division of the US Department of Energy, as part of the Atmospheric Radiation Measurement Program and was performed under contract DE-AC02-98CH10886.

REFERENCES (Omitted)

CLOUD PROPERTIES SIMULATED BY A SINGLE-COLUMN MODEL

Yali Luo[1] and Steven Krueger[2]

[1]National Institute of Aerospace, Hampton, VA 23666, USA [2]University of Utah, Salt lake City, Utah 84112, USA

1. INTRODUCTION

Cirrus macrophysical properties such as cloud boundaries are observed by millimeter cloud radar (MMCR) located at the central facility (CF) of Atmospheric Radiation Measurement program (ARM; Stokes and Schwartz, 1994) Southern Great Plains (SGP) site. The bulk microphysical properties for optically thin single layer cirrus events since December 1996 were retrieved by Mace et al. (2001; hereafter MCA). Cirrus clouds are important in GCMs due to their significant radiative effects (e.g. solar reflection and greenhouse effect, redistribution of water vapor). However they are represented poorly and differently in GCMs because of insufficient knowledge about their formation, maintenance and decay, too large vertical grid size, and representation of detrainment and microphysics in the models. A NWP model, such as the National Centers for Environmental Prediction (NCEP) global model, allows testing of cloud parameterization that could be used in GCMs. Cirrus clouds form only in particular situation (large-scale ascent, convective detrainment, orographic ascent, mesoscale ascent, etc) and their properties depend on temperature, humidity, vertical velocity, cloud depth, cumulus detrainment, microphysics, et al., so that errors in model cirrus properties may indicate other model problems. We use MCA's observations and a CRM simulation here to evaluate the cirrus representation in the SCM version of the NCEP MRF model, which is relatively neglected due to the secondary-importance of cirrus clouds to short-to-medium-range weather prediction. Our major purpose is demonstrating a new method that could be used to find possible problems in the representation of a large-scale model's cloud physical processes.

A Single-Column Model (SCM) is one grid column taken from a 3-D General Circulation Model (GCM), which can be used to predict climate or used as a numerical weather prediction (NWP) model. A SCM is run in isolation from the other parts of the 3-D GCM. One obvious advantage of using a SCM instead of a 3-D GCM for evaluation is saving computer time. A SCM can be driven using observational analyses as well as large-scale advective tendencies from a global model. If observational analyses are used for the large-scale advective tendencies information, the discrepancies found between the results of a SCM simulation and observations (or an explicit simulation) could indicate problems in the ways that physical processes are parameterized in the model, if the large-scale information is accurate. This is another advantage of a SCM over a GCM since it can be difficult to separate the effects of physical parameterizations from the effects of the 3-D model simulated large-scale dynamics. In addition, the same observational analyses can be used to run more detailed models than SCMs, such as large eddy simulation (LES) models and cloud-resolving models (CRMs). The superiority of CRMs over SCMs in the simulation of most model fields has been demonstrated by the ARM Program (e.g. Xu et al. 2003, Ghan et al. 2000). The results from a SCM can be compared to not only observations but also results from an explicit simulation. Because of these advantages, SCMs have been used as prime tools for parameterization testing and development starting in the 1980's.

The demanding large-scale observational data necessary to "drive" a SCM and a CRM are available from the ARM and other field experiments. For this study, we ran a SCM based on the NCEP MRF model (Kalnay et al. 1998) and the UCLA/CSU CRM (Krueger 1988, Krueger et al. 1995) for a 29-day intensive operational period (IOP). The large-scale analyses based on measurements at the ARM SGP site produced by the variational analysis method (Zhang et al. 2001) were used to run the two models. We evaluated the CRM simulated cirrus properties using MCA's datasets (Luo et al. 2003). We analyzed the SCM's results in a way that produces the simulated cirrus cloud properties on the scale of radar observations and the CRM resolution. We then compared the SCM's cirrus properties with the radar observations and the CRM results. We also used the CRM to evaluate the cumulus detrainment and microphysics parameterizations in the SCM because they are probably two of the most important physical processes determining ice cloud properties.

We describe our study in two papers. As the first part, this paper contains the evaluation of the SCM's cirrus properties (Luo and Krueger, 2004).

2. ANALYSIS OF SCM RESULTS

The SCM predicts cloud condensate (liquid water or ice) which represents a large-scale grid mean value, i.e. on the scale of the ARM SCM domain (300 km scale). The cirrus properties from cloud radar observations and retrievals represent values on kilometer scale. The SCM results can not be compared directly to the cloud radar observations and retrievals because

Corresponding author's address: Yali Luo, National Institute of Aerospace, 144 Research Drive, Hampton, VA 23666, USA. E-Mail: yali@nianet.org

of this scale discrepancy. To produce cirrus statistics from the SCM results that are comparable to the cloud radar observations, the SCM predicted cloud condensate profile was horizontally distributed into 100 sub-grid-scale columns basically following the method described by Klein and Jakob (1999). Different overlap assumptions generate different cloud configurations. Maximum/random and random overlap assumptions are most commonly used in current large-scale models for radiation calculation. The random overlap assumption is used in the SCM, which means the positions of cloudy cells at each level is determined randomly. The maximal/random overlap means that when clouds occur in adjacent layers, they are maximally overlapped but the excess portion is positioned at random across the layer. In addition, if a clear layer separates two cloudy layers, they are assumed to be randomly overlapped. In our analysis both maximal/random and random overlap assumptions were used. In-cloud horizontal homogeneity of cloud condensate is assumed.

For comparison to the cloud radar observations, the cloud boundaries in the model are defined as reflectivity greater than -40 $dbZe$. In our study, two extreme situations are analyzed. In one, snow and rain are neglected completely, so that the SCM cirrus clouds consist of cloud ice only and only cloud ice or cloud liquid water is used to calculate the reflectivity. This is called *NOSNOW* case. In the other extreme, the SCM cirrus clouds are assumed to consist of both cloud ice and snow. In addition to cloud ice and cloud water, snow and rain are included for reflectivity calculation. This is called *SNOW* case.

MCA defined cirrus and thin cirrus based on temperature and reflectivity. To be qualified as cirrus layer, the temperature at radar echo top must be less than -35°C and the temperature at the level of maximum reflectivity must be less than -20°C. MCA defined thin cirrus clouds to be a subset of cirrus events which occur with no lower cloud layers and have IR emissivity less than 0.85.

For each subcolumn, we calculated the equivalent radar reflectivity factor profile from cloud ice/liquid water content profile and effective size of ice crystal/water droplet following Beesley et al. (2000). We calculated the IR emissivity of a cirrus layer for each subcolumn from the mixing ratios and effective sizes of cloud ice. The cloud layer IR emissivity at a particular wavelength is calculated using the parameterization developed by Fu and Liou (1993).

We then sampled cirrus and thin cirrus at the 100 subcolumns, using nearly the same definition of cirrus and thin cirrus as MCA, and analyze their properties. The SCM results from *NOSNOW* analysis using random overlap assumption are called *NOSNOW random*, while those using maximum/random overlap assumption are called *NOSNOW max/rand*.

For *SNOW* analysis, the random overlap assumption was used to get the sub-column cloud field every hour. We then determined the sub-grid distribution of snow and rain at each time as described. We used the resulting hydrometeor field, including the cloud ice, cloud liquid water, snow and rain, to determine cirrus and thin cirrus occurrence for each of the 100 subcolumns each hour using nearly the same definition of cirrus and thin cirrus as MCA, and analyzed their properties. The SCM results from this analysis are called *SNOW random*.

3. COMPARISON OF CIRRUS PROPERTIES

3.1 Cirrus Macro-Scale Statistics

In the SCM analyses, regardless of the assumptions about cloud overlap and snow, the depth of the thinnest SCM cirrus and thin cirrus clouds is about 1.1 km. This is determined by the vertical grid size of the SCM at the cirrus levels. The SCM *NOSNOW* cirrus clouds have modes at the minimum possible depth (Figs. 1c and 1d). About 75% (*random*) and 50% (*maximum/random*) of the *NOSNOW* cirrus clouds are thinner than 2 km because they occur at a single model level. The SCM *SNOW random* cirrus clouds have normalized frequency distribution of depths similar to the CRM: too many large depths and too few small depths compared to observations, because snow extends too low and subgrid-scale horizontal inhomogeneity of snow is neglected in the SCM.

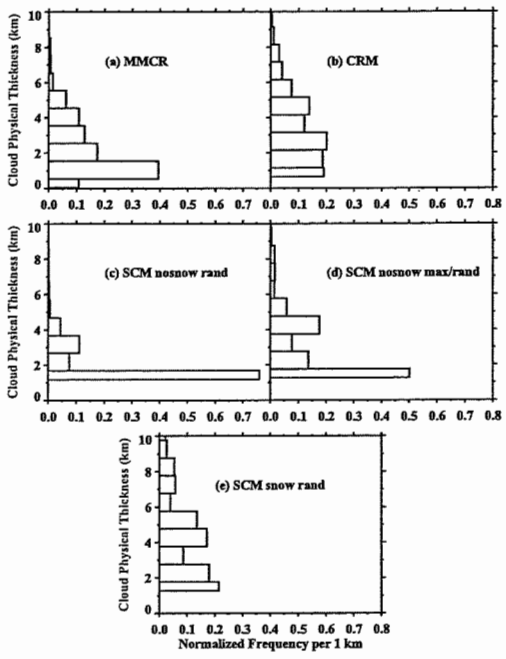

FIG. 1. Normalized frequency distributions of cirrus cloud physical thickness. (a) The cloud radar observations; (b) the CRM results; (c) the SCM *NOSNOW* random results; (d) the SCM *NOSNOW* max/random results; (e) the SCM *SNOW* random results.

The *NOSNOW* cirrus cloud base heights, when random overlap assumption is used, are too high compared to observations because snow is not considered. When the maximum/random overlap assumption was used, the SCM *NOSNOW* cirrus clouds have lower cloud base heights, and they were physically thicker, compared to the SCM *NOSNOW* cirrus when the random overlap assumption was used. These results are due to the tendency that the maximum/random overlap assumption generates thicker clouds, when there are clouds existing at contiguous levels, than the random overlap assumption.

SNOW random cirrus layers had too many low cloud base heights and too few high cloud base heights due to snow extending too low.

3.2 Thin Cirrus Micro-Scale Statistics

Fig. 2 show that for thin cirrus clouds the SCM IWP normalized frequency distributions depend little on overlap assumption or whether snow is considered or not: the normalized frequencies are generally too large except at low values of IWP. In other words, thin cirrus with large IWP occur too often relative to thin cirrus with low IWP. The same results are found for the SCM thin cirrus layer-mean IWC.

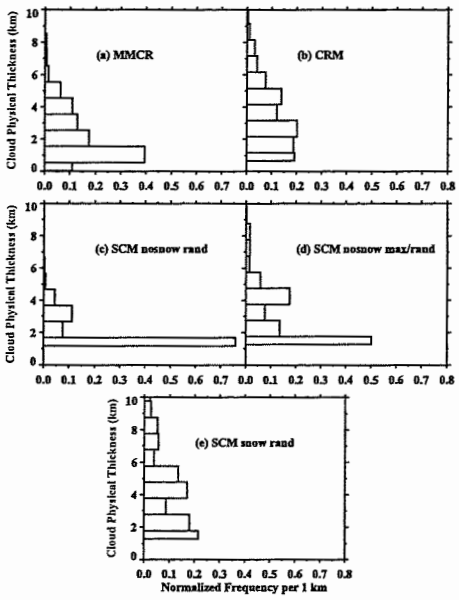

FIG. 2. Normalized frequency distributions of thin cirrus cloud ice water path. (a) MCA's results; (b) the CRM results; (c) the SCM *NOSNOW* random results; (d) the SCM *NOSNOW* max/random results; (e) the SCM *SNOW* random results.

We evaluated the SCM's ability to reproduce the observed relationship between the thin cirrus IWP/IWC and temperature. The layer-mean IWC and IWP values of the SCM thin cirrus clouds were divided into 8 temperature categories using a 5 K bin size. The mean values of the IWC and IWP in each temperature bin and their 90 percent confidence intervals were calculated and compared to the retrievals. Figure 3 provides these results from the cloud radar retrievals, the SCM *NOSNOW random*, *NOSNOW max/rand*, and *SNOW random*. As shown by Fig. 3, the SCM thin cirrus IWP and IWC both increase too rapidly with temperature, no matter whether snow is considered or not and regardless of the overlap assumption used. As a result, the mean IWCs and IWPs in the SCM thin cirrus clouds are larger than the cloud radar retrievals for temperature > 217.5 K.

The CRM thin cirrus IWP temperature dependence is very close to the retrievals, but its IWC is too low because the CRM thin cirrus cloud layer thickness is too large.

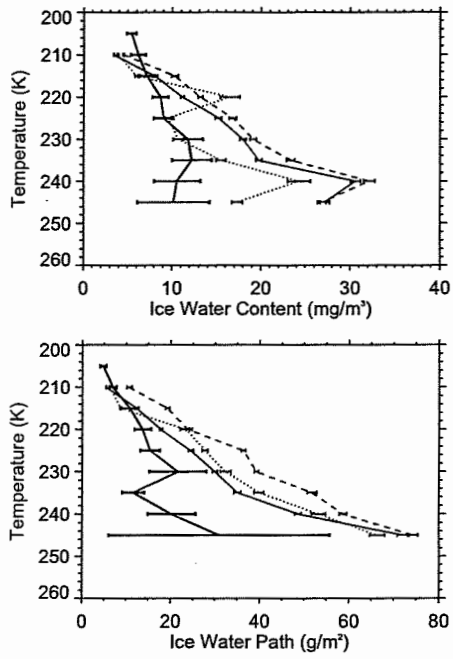

FIG. 3. The mean values of thin cirrus layer-mean ice water content (a) and ice water path (b) as function of temperature. Thick solid line: cloud radar retrievals; thin solid line: the SCM *NOSNOW random*; thin dashed line: the SCM *NOSNOW max/rand*; thin dotted line: the SCM *SNOW random*. The bars represent the 90% confidence intervals of the means.

We examined the dependence of thin cirrus IWC on cloud-layer depth in the SCM simulation though comparing with that revealed by the cloud radar retrievals. The retrieved (and the CRM) thin cirrus layer-mean IWCs and IWPs for warm ($\bar{T}$ > 230 K), neutral (220 K < $\bar{T}$ < 230 K), and cold ($\bar{T}$ < 220 K) cloud layers were segregated by cloud physical depth into 3 classes: 0 - 1km, 1 -2 km, 2 - 4 km. Similarly, for the SCM's warm, neutral, and cold thin cirrus clouds, the layer-mean

IWCs were divided into 3 different classes by the cloud physical depth: thin (1 - 2 km), neutral (2 - 4 km), and thick (4 - 6 km). Note that the vertical resolution of the SCM at thin cirrus levels is about 1.1 km so the cloud depth can not be less than 1 km. Figure 4 shows the cloud depth dependence of layer-mean IWC for the SCM *NOSNOW random* and retrieved thin cirrus. The results from the SCM *NOSNOW max/random* and *SNOW random* (not shown) are similar to those from the SCM *NOSNOW random*.

We concluded from Fig. 4 that although the IWCs increase with temperature as revealed by the SCM, CRM and observation, the rate of increase is too large in the SCM. This results in too large IWCs for the SCM warm thin cirrus clouds. Fig. 4 also shows that the SCM thin cirrus IWCs *decrease* with cloud thickness, which is opposite to the retrievals (and the CRM results) which show that layer-mean IWCs *increase* with cloud thickness. The mean IWCs of the SCM *NOSNOW random* thin cirrus clouds with depths less than 2 km are about 2 times as large as those contained in thick (4 - 8 km) SCM *NOSNOW random* thin cirrus clouds, in all three temperature classes. Further analysis revealed that the physically thin cirrus containing large IWCs were generated by cumulus detrainment in the SCM. Further analysis of detrainment in the SCM will be contained in the Part 2.

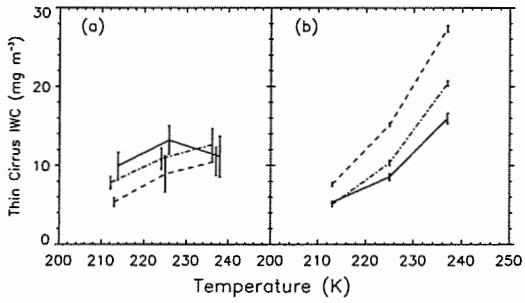

FIG. 4. Thin cirrus layer-mean ice water content in three temperature categories and three cloud thickness classes. (a) The cloud radar retrievals; (b) The SCM *NOSNOW random* results. The solid/dash-dotted/dashed lines represent thick/medium/thin thin cirrus clouds, respectively.

4. DISCUSSION

A large-scale forcing analysis for the ARM SGP CART site during the summer 1997 IOP was used to run a SCM based on the NCEP MRF model and also the UCLA/CSU CRM. The SCM's cloud fields were analyzed to obtain cirrus properties that are on scale comparable to the MMCR observations and the resolution of the CRM grid. Results from the SCM *NOSNOW (random and max/rand)* and *SNOW (random)* analyses were compared to both the MMCR observations and the results from the CRM simulation.

The SCM cirrus cloud base heights and layer depths depend on overlap assumption used and more significantly on whether snow is included or not. Compared to the MMCR observations, the SCM *NOSNOW random* cirrus clouds have too high cloud base height, and too many of *NOSNOW (random and max/rand)* cirrus occur at a single model level, *SNOW (random)* cirrus clouds have too low cloud base height and too large cloud thickness. The SCM cirrus cloud-top heights depend little on the overlap assumption and whether snow is considered or not. They have higher tops than the radar observations.

Compared to the radar observations and the CRM simulation, regardless of the overlap assumption used, for the SCM *NOSNOW (random and max/rand)* and *SNOW (random)* thin cirrus clouds:

(1) large IWP and large layer-mean IWC occur too often relative to small IWP and IWC resulting in too large mean IWP and IWC, and hence too large cloud optical depth.

(2) the IWP and layer-mean IWC are too large at most temperatures considered and they increase with temperature too fast.

(3) the layer-mean IWCs decrease with cloud physical thickness, in opposition to the retrievals and CRM results.

As concluded above, the SCM simulated cirrus statistics are very different from the cloud-scale radar observations. Which physical processes in the SCM contribute significantly to the differences found: the representation of cumulus detrainment and cloud ice microphysics, and/or the treatment of snow? Using the results from the simulations for the IOP and from some idealized simulations of anvil clouds performed by the CRM and the SCM, we explored the possible reasons and methods to improve. We will present our results in the Part 2.

ACKNOWLEDGMENTS

This research was supported by the Environmental Sciences Division of the U.S. Department of Energy (DOE) as part of the Atmospheric Radiation Measurement program, under grant DE-FG03-94ER61769.

REFERENCES

Krueger, S. K., 1988: Numerical simulation of tropical cumulus clouds and their interaction with the subcloud layer. *J. Atmos. Sci.*, **45**, 2221-2250.

Luo, Y.-L., S. K. Krueger, G. G. Mace, and K.-M. Xu, 2003: Cirrus cloud statistics from a cloud-resolving model simulation compared to cloud radar observations. *J. Atmos. Sci.*, **60**, 510-525.

–, and –, 2004: Cloud properties simulated by a single-column model. Part I: Comparison to cloud radar observations of cirrus clouds. Submitted to *J. Atmos. Sci.*.

Mace, G. G., E. E. Clothiaux, and T. P. Ackerman, 2001: The composite characteristics of cirrus clouds; bulk properties revealed by one year of continuous cloud radar data. *J. Climate*, **14**, 2185-2203.

Stokes, G. M. and S. E. Schwartz, 1994: The Atmospheric Radiation Measurement (ARM) Program: Programmatic background and design of the Cloud and Radiation Testbed. *Bull. Amer. Meteor. Soc.*, **75**, 1201-1221.

SIMULATION OF A SQUALL LINE CONVECTIVE SYSTEM USING SPECTRAL (BIN) MICROPHYSICS AND BULK PARAMETERIZATIONS

B. Lynn[1], A. Seifert[2] and A. Khain[1]

(1) The Institute of Earth Sciences, the Hebrew University of Jerusalem, Israel
(2) National Center for Atmospheric Research, Boulder, USA

1 INTRODUCTION

Signi?cant efforts have been directed towards improving the simulation of bulk microphysics in mesoscale models (e.g.,Thompson et al. 2004; Seifert and Beheng 2004). These models are either improved versions of existing schemes or use two-moments, i.e. number and mass concentrations, to better represent the evolution of microphysics. Moreover, they have been benchmarked with results obtained from cloud models with spectral (bin) microphysics (Rasmussen et al. 2002, Seifert et al. 2004). The use of two-moment schemes provides for greater accuracy in the simulation of microphysics through the better representation of the size spectra of liquid and ice particles.

The new scheme by Seifert and Beheng (2004) adds another layer of sophistication. It takes into account the effects of cloud condensation nuclei (CCN) on the droplet spectrum by predicting nucleation of cloud droplets explicitly. Higher concentrations of CCN lead to more cloud droplets, which delays the onset of raindrop formation. This can also affect the formation of ice, as well as stratiform rain.

This abstract presents results of simulations of a mesoscale rain event using a mesoscale model with either spectral microphysics or bulk parameterization of both Thompson et al. and Seifert&Beheng.

2 MODEL DESCRIPTION

Model dynamics: The non-hydrostatic Mesoscale Modeling System, Generation 5, MM5 (Dudhia 1993) was chosen as the dynamical platform for the spectral (bin) microphysics and bulk model parameterization tests. The standard model predicts the three-dimensional wind components, temperature, mixing ratios for water vapor, cloud water/ice and rain/snow, and a pressure perturbation. The model uses a terrain-following sigma coordinate in the vertical, and a stretched vertical coordinate with the highest vertical resolution closest to the ground surface.

Spectral (bin) microphysics (SBM): The spectral (bin) microphysical package is described in an accompanying abstract entitled 'Simulation of a Convective Systems using a Mesoscale Model with Spectral (bin) Microphysics' by Lynn et al. The model simulates the size distributions of water droplets, three types of ice crystals, graupel, snow (aggregates), hail/frozen drops, as well as aerosol particles. A speci?c feature of the model is the existence of an aerosol budget. The concentration of CCN decreases during the process of droplet formation and precipitation.

Bulk-microphysics schemes: Two new schemes have recently been implemented into MM5. The Thompson et al. scheme is a signi?cant modi?cation of the scheme commonly referred to as Reisner2 (option 4 of Reisner et al. 1998). This bulk, mixed-phase microphysics scheme uses prognostic variables for the mixing ratios of cloud water, rain, cloud ice, snow, and graupel, plus the number concentration of ice. One signi?cant change is the implementation of the Berry and Reinhardt (1974) autoconversion scheme instead of Kessler (1969). The Seifert and Beheng (2004, S&B hereafter) scheme is a full two-moment scheme and includes ?ve particle types (cloud, rain, ice, snow, graupel/hail); ?ve mass variables and corresponding ?ve number concentration variables. In S&B, size distributions are parameterized by generalized gamma distributions, and nucleation of cloud ice is parameterized explicitly as a function of super-saturation similar as in SBM. The model also has consistently formulated integral growth equations that have been derived from the corresponding spectral collection equations, and mean collision ef?ciencies for ice-ice and ice-cloud interaction formulated as functions of the mean particle diameters. The S&B scheme uses the autoconversion scheme of Seifert and Beheng (2001), which is based on the results of a spectral (bin) model. In addition, the full mixed-phase S&B scheme has recently been calibrated and veri?ed using the SBM scheme in the Hebrew University Cloud Model (Seifert et al. 2004).

Corresponding author's address: Axel Seifert, National Center for Atmospheric Research; P.O. Box 3000 Boulder, CO 80307, E-Mail: seifert@ucar.edu. NCAR is sponsored by the National Science Foundation.

3 CASE STUDY AND EXPERIMENT DESIGN

The convective development that occurred on 27th of July 1991 over Florida was accompanied by squall line formation. Figure 1 shows the observed radar re?ectivity ?eld on this day for three hours in the late afternoon. The purpose of the simulations described here was to compare the spectral (bin) model results with those of the bulk parameterization results. The model was run on a 3 km grid domain centered over the Florida Peninsula. Calculations with spectral microphysics were performed for low (maritime) CCN concentrations (SBM Mar), while S&B was simulated with both maritime and a slightly more continental aerosol concentration (referred to as: Sei Mar and Sei Con). In Sei Con, the upper bound of the droplet number concentration was increased from 200 cm^{-3} to 300 cm^{-3} (note that the Sei Con shown here uses a different, much more maritime CCN as the SBM Con of the accompanying Lynn et al. abstract). Reisner2 was set to run with parameters in the autoconversion equation appropriate to a maritime simulation (referred to as: Rei Mar).

4 RESULTS OF SIMULATIONS

Figure 2 shows the simulated radar re?ectivity from the four simulations described above. The SBM Mar simulation produced the most realistic radar re?ectivity. In particular, it captured best the development of short line convection at 21 UTC, the squall line at 22 UTC, and the formation of stratiform cloud at 23 UTC. Of the remaining simulations, Rei Mar and Sei Con produced somewhat more realistic radar crosssections than Sei Mar. Note, however, that neither the Reisner2 nor the S&B scheme simulate the squall line correctly, although Rei Mar simulated better the development of the stratiform clouds.

Figure 3 shows observed and simulated average rainfall obtained each hour from 15 UTC to 25 UTC. The observations are from a number of rain gauges in central Florida, while the model results are from the nearest grid-element. The Sei Con scheme produced the most realistic rainfall regarding amounts and timing. The rainfall obtained from SBM Mar was much too early, in association with unrealistic rainfall amounts along the east-coast sea-breeze. The Rei Mar simulated the peak rainfall amount later than observed.

Figure 4 shows the maximum rainfall amounts from observations and from model simulations at each hour. None of the models captured the timing and amount of maximum rainfall exactly. Generally, the S&B simulations produced their ?rst peak too early and their sec-

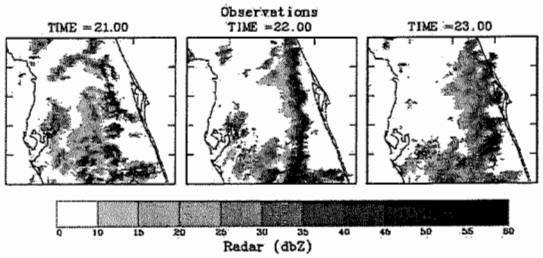

Fig. 1: *Observed radar re?ectivity on 27 July 1991*

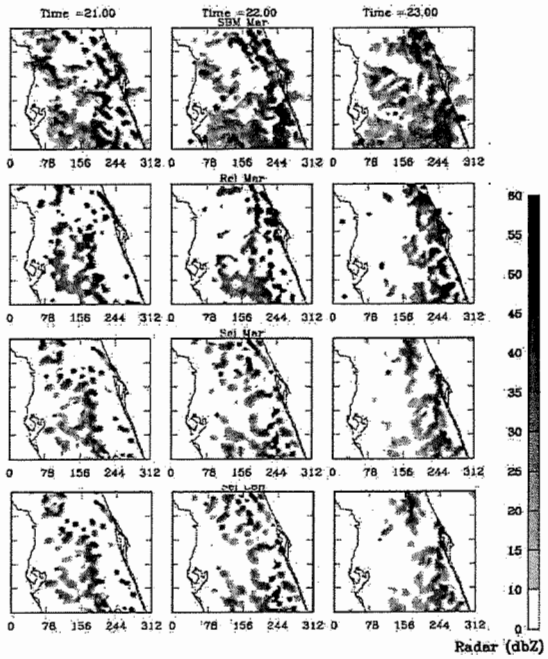

Fig. 2: *Calculated radar re?ectivity from SBM Mar, Rei Mar, Sei Mar, and Sei Con at the times shown.*

ond peak 'on-time'. The Reisner2 simulation produced peaks that were late and too large. The SBM reproduced very well the ?rst peak, but the second peak was weaker than observed.

Here we don't show results from simulations with SBM (or S&B) assuming a continental aerosol (with CCN concentration about 1000 cm^{-3}). However, the rainfall obtained with SBM developed more slowly in the continental case compared to SBM Mar, although a larger maximum hourly rainfall amount of 7.5 mm/h is simulated (compared to 4.3 mm/h in the maritime case). The CCN effects are discussed in detail in the accompanying abstract by Lynn et al. and results of the bulk schemes assuming continental CCN will be presented at the conference.

Figure 5a and 5b shows a three-dimensional picture

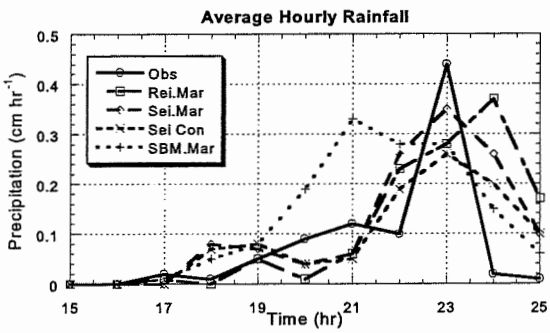

Fig. 3: *Observed and simulated rainfall obtained from rain gauges and closest grid elements.*

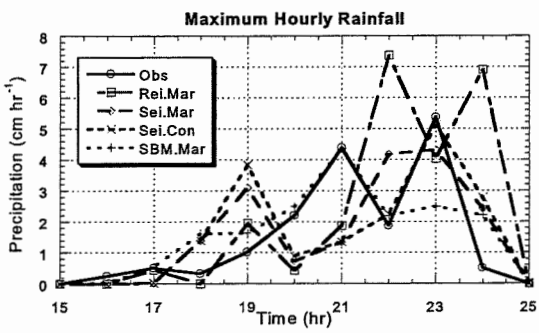

Fig. 4: *Maximum observed and simulated rainfall hourly amounts.*

of total cloud mass from SBM Mar and Rei Mar with the original Kessler Scheme. Figure 6 shows Rei Mar with the Berry and Reinhardt autoconversion. Note that SBM Mar produced more realistic cloud structure than either the old or the new Reisner2 scheme. In fact, both Reisner2 schemes produced clouds that were unnaturally upright with ice particles having formed at very high levels in the troposphere - a typical problem with Kessler type schemes and now apparently with some of the newer schemes as well.

5 SUMMARY AND CONCLUSIONS

A comparison has been presented using a mesoscale model with spectral (bin) microphysics and with bulk model parameterization. The bulk model parameterizations used are improved 'state-of-the-art' schemes that e.g. have more sophisticated autoconversion schemes than their predecessors. In fact, important improvements in rainfall simulations were obtained (compare results here with those of Lynn et al. in this abstract compendium).

However, in this case study the bulk parameteriza-

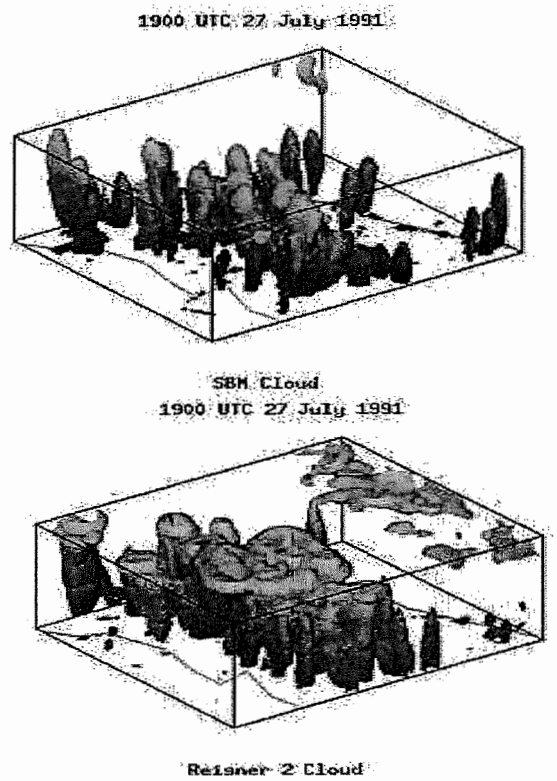

Fig. 5: *Total cloud mass content in SBM Mar (above) and Reisner2 (below, with the Kessler autoconversion).*

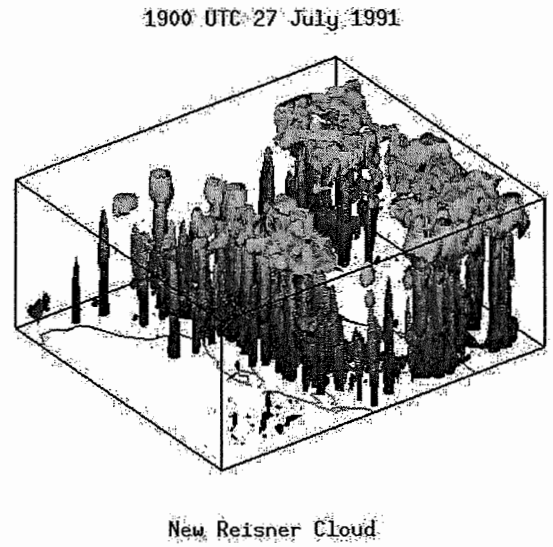

Fig. 6: *Total cloud mass content obtained with Rei Mar (with the Berry Reinhardt autoconversion scheme).*

tion did not well simulate the spatial distribution of cloud cover, the squall line formation and the development of stratiform precipitation regions. The new Reisner2 scheme still shows unnaturally upright clouds with ice extending unrealistically high into the troposphere.

The successful use of bulk parameterization in mesoscale models appears to be limited by their need to represent the particle spectra by one or two moments (e.g. mass and number or mass and mean diameter). In the simulations shown here, these limitations are most apparent in the lack of development of stratiform rain, probably due to the use of a mean sedimentation velocity. Although two-moment bulk schemes do in fact use two different mass resp. number weighted mean sedimentation velocities, this, obviously, did not improve the simulation of the stratiform regions in this case. In addition, the bulk schemes seem to show a delay in the freezing of liquid drops, leading to the advection of too much ice to upper troposphere levels. These problems need to be addressed in future studies e.g. by using the more accurate SBM results to improve the assumptions made in the bulk schemes.

Acknowledgements: Thanks go to Derek Posselt for preparing Figs. 5 and 6. B. Lynn was supported by Binational US-Israel Science foundation (grant 2000215) and the European Project SMOCC. A. Seifert was supported by the German - Israeli cooperation in water technology (BMBF grant 02WT0249) and the Advanced Study Program of NCAR.

REFERENCES

Berry, E. X. and R. L. Reinhardt, 1974: An analysis of cloud drop growth by collection: Part II. Single initial distributions, *J. Atmos. Sci.*, **31**, 1825–1831.

Dudhia, J., 1993: A nonhydrostatic version of the penn state/ncar mesoscale model: Validation tests and simulation of an atlantic cyclone and cold front, *Mon. Wea. Rev.*, **121**, 1493–1513.

Kessler, E., *On the distribution and continuity of water substance in atmospheric circulations*, Meteor. Monogr. 32, Amer. Meteor. Soc., Boston, 1969.

Rasmussen, R., I. Geresdi, G. Thompson, K. Manning and E. Karplus, 2002: Freezing drizzle formation in stably strati?ed layer clouds: The role of radiative cooling of cloud droplets, cloud condensation nuclei, and ice initiation, *J. Atmos. Sci.*, **59**, 837–860.

Reisner, J., R. M. Rasmussen and R. T. Bruintjes, 1998: Explicit forecasting of supercooled liquid water in winter storms using the MM5 mesoscale model, *Quart. J. Roy. Met. Soc.*, **124**, 1071–1107.

Seifert, A. and K. D. Beheng, 2001: A double-moment parameterization for simulating autoconversion, accretion and selfcollection, *Atmos. Res.*, **59-60**, 265–281.

Seifert, A. and K. D. Beheng, 2004: A two-moment cloud microphysics parameterization for mixed-phase clouds. Part I: Model description, *submitted to Meteorol. Atmos. Phys.*

Seifert, A., A. Khain, A. Pokrovsky and K. D. Beheng, 2004: Aerosol effects on simulated convective storms using spectral bin and two-moment bulk mixed-phase cloud microphysics, *submitted to Atmos. Res.*

Thompson, G., R. M. Rasmussen and K. Manning, 2004: Explicit forecasts of winter precipitation using an improved bulk microphysics scheme. Part 1: Description and sensitivity analysis, *Mon. Wea. Rev.*, **132**, 519–542.

Convective cloudy boundary layer parameterization using a mass flux approach

A. Mathieu[1]*, F. Hourdin[1], A. Lahellec[1], M. Haeffelin[1], P. Drobinski[2], C. Rio[1]
(1)Laboratoire de Météorologie Dynamique - IPSL - France
(2)Service d'Aérologie - IPSL - France

1 INTRODUCTION

The stratocumulus-topped Boundary Layer (BL) plays an important role in climate, due to its radiative impacts on the Earth's energy balance. On the ocean, large sheets of Stratocumulus (Sc) are being observed over eastern borders. In general, large scale atmospheric models have difficulties in correctly representing such clouds (Jakob 1999). In global models, the boundary layer is classically parameterized by a K-diffusion scheme (Louis 1979) based on local Richardson number. The lack of water in the upper layers of the boundary layer in models may be attributed to the inadequacy of the diffusion scheme to represent the effect of meso-scale flows on vertical fluxes. Present day research activity focuses on this problem of representing the effect of meso-scale motions of the BL: non-local models (Holtslag and Boville 1992) and mass flux schemes (Lappen and Randall 2001; Lock et al. 2000) among others.

The existence and importance of the organized vertical motions in the boundary layer are known for a long time. If one simplifies these motions considering a single cell with an updraft (thermal) supplied by unstable air coming from the surface layer and compensated by downdraft motions, one adopts the mass-flux representation of meso-scale air motions. We adopt these views but we do not oppose K-diffusion schemes and non-local processes. The K-diffusion scheme has to take into account small scale turbulence that mainly concerns the surface layer and the cloud layer. In addition to the small scale, BL flows are structured by secondary motions. One of the limitations of the mass-flux approach until now is the so called closure problem. As mentioned by several authors, no definite closure has been found to match the GCM grid resolution so far (i.e. Lappen and Randall 2001). Hourdin et al. (2002) have proposed a solution to this question for dry boundary layer. They developed a mass flux parameterization in the climate model, LMDZ. This parameterization has been validated against LES results and campaign observations. We pursue this approach considering the modifications due to the introduction of the cloud phase to design a mass flux parameterization of the cloud-topped BL.

In the following, we describe the dry BL parameterization. We discuss how BL clouds are introduced in the parameterization. In the future (not discuss here) we plan to take into account the cloud dissipation by entrainment processes as well following Mathieu and Lahellec (2004).

2 THE THERMAL MASS FLUX MODEL

A typical profile of dry convective BL can be define by an unstable surface layer (SL) of height z_s, a neutral mixed layer (ML) topped by an inversion layer at the altitude z_i. In this idealized frame, the thermal is introduced as a simple plume of buoyant air originating from the surface layer. If the plume does not mix with its environment nor condensate, its virtual potential is that of surface layer Θ_{vSL}. If, in addition, the thermal is assumed

*Corresponding author: Anne Mathieu, Laboratoire de Météorologie Dynamique. Ecole Polytechnique - 91128 Palaiseau Cedex, France. E-mail: amathieu@lmd.polytechnique.fr fax: +33 01 69 33 30 05

to be stationary and frictionless, the vertical velocity inside the plume is given by :

$$\frac{dw}{dt} = w\frac{\delta w}{\delta z} = g\frac{\Theta_{vSL} - \Theta_{vML}}{\Theta_{vML}} \quad (1)$$

if one neglects the horizontal pressure difference between the plume and its environment. The thermal is uniformly accelerated in the mixed layer until the level where the buoyancy of the environment exceeds Θ_{vSL} is reached. This level is defined as z_i. The square of vertical velocity w_{max} obtained by vertically integrating the preceding equation over the BL depth is twice the convective available potential energy (CAPE) defined as

$$CAPE = \int_0^{z_i} g\frac{\Theta_{vSL} - \Theta_{vML}}{\Theta_{vML}}dz \quad (2)$$

Above z_i, w is still positive (overshooting) but decreases to finally vanish at the height z_t (top). After reaching z_t, air parcels coming from the plume are heavier than the environment and sink again. This will not be considered in the parameterization for the moment.

What is required for transport computations is not the vertical velocity but rather the mass flux per unit area, $f = \alpha\rho w$, where α is the fraction of the horizontal surface covered by ascending plumes and ρ is the air density. As a first step, f is assumed to be constant within the mixed layer. In order to determine its value, Hourdin et al. invoke the geometry of the thermal cell, considering a 2D configuration like typical BL rolls with an invariant horizontal direction x. The air in the thermal is supplied by horizontal convergence in the surface layer. If friction and rotation effects are neglected, and if the cell is stationary, the equation for the horizontal acceleration in the surface layer reduces to

$$v\frac{\delta v}{\delta y} = -\frac{1}{\rho}\frac{\delta p_s}{\delta y} \quad (3)$$

where p_s is the surface pressure. Integrated over the width of a single cell and considering that the pressure is identical in the plume and environment at z_i, one obtain to first order

$$v_{max}^2 = \frac{2}{\rho_s}\Delta\int_0^{z_i} g\rho dz\, 2\int_0^{z_i} g\frac{\rho}{\rho_s}\frac{\Theta_{vSL} - \Theta_{vML}}{\Theta_{vML}}dz \quad (4)$$

Δ denotes the difference between the conditions within the plume and its environment. The equation is obtained assuming that $\Delta\rho/\rho_s \sim \Delta\Theta_v/\Theta_v$. Except for the density factor, the computation is that of the maximum vertical velocity w_{max} at height z_i. Although this presentation is far from the real situation, $v_{max} = w_{max}$ is used for the parameterization.

In a 2D geometry, the vertical mass flux in the thermal must equal the horizontal convergence of air in the surface layer

$$w_{max}l(z_i)\rho(z_i) = v_{max}z_s\rho(z_s/2) \quad (5)$$

where $l(z)$ is the width of the plume at height z. In this simple view, the width of the thermal at the inversion is roughly the height of the SL. The fact that near-surface horizontal converging winds are of the order of magnitude of vertical winds further implies that the width of a cell L is comparable to its height z_t. In reality, the aspect ratio, $r = L/z_t$, typically ranges from 1 to 10 according to Atkinson and Wu Zhang 1997. Hourdin et al. (2002) introduce r as a tunable parameter and obtain the minimum fractional area at level z_i as $\alpha(z_i) = l(z_i)/(rz_t)$ resulting in

$$f = \frac{\rho(z_s/2)z_s\sqrt{2CAPE}}{rz_t} \quad (6)$$

Observations suggest that for a 2D geometry r is about 2-3 (LeMone 1973). We retained $r = 2$. Based on this analysis one can introduce mixing process with the environment as the detrainment proposed by Hourdin et al. (2002).

3 MODEL EVALUATION AT SIRTA

To test the ability of the preceding approach to reproduce realistic diurnal cycles of the boundary layer, we compared outputs of the climate model, LMDZ ran with this parameterization to the observations of the SIRTA (Site Instrumental de Recherche par Télédétection), in a version zoomed on the SIRTA site, and nudged by NCAR analyzes. For dry cases, the BL depth and its diurnal cycle are derived from the aerosol lidar. Ceilometer observations are used to detect the presence of clouds, the cloud base height and BL clouds diurnal cycle of the BL. Comparison on the BL depth between model

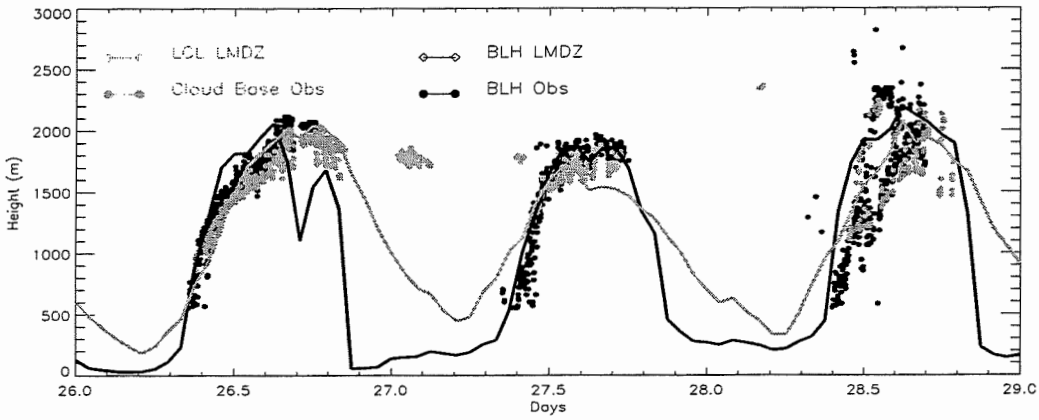

Figure 1: Observations (dots) and diagnostics (lines) of the BLH (black) and the cloud base height or equivalently, the LCL (grey) during the 26-27-28 of Mai 2003 over the SIRTA.

and observations show that LMDZ with the thermal scheme reproduces well the diurnal cycle of dry convective BL. The comparisons between model and observations have been extended to convective days with occurrence of small boundary layer cumulus. The end of the month of May 2003 corresponds to such occurrence and has been taken as a test period to evaluate the ability of LMDZ with the thermal scheme to reproduce such boundary layer types.

Following Mathieu et al. (2004) a diagnostic approach is used to estimate the contribution from meso-scale motions to the vertical structure of the BL and to the development of clouds. The boundary layer height (BLH) is derived from model output. The derivation is based on the method proposed by Troen and Mahrt (1986). The physical idea behind this algorithm is that, under unstable situations, some parcels of air (characterized by an excess of buoyancy) can detach from the surface layer. They rise until they reach their equilibrium level which is then associated with the boundary layer height. The equilibrium level takes into account both thermodynamic and dynamic stability. In numerical terms, the boundary layer is defined by a bulk Richardson number reaching a critical value. We can also look at the lifting condensation level (LCL) of the parcel, which is virtually lifted from the near surface layers. In physical terms, the condensation level can be linked to cloud base height of BL clouds resulting from surface driven processes. Hence the cloud base height should be representative of what is observed in reality when processes are driven by the surface. When the LCL is found above the BLH the level of condensation cannot be reached by parcels detaching from the surface layer and no cumulus should occur.

Figure 1 shows 3 days of comparison at the end of Mai 2003, between the above mentioned parameters and SIRTA observations. During the day, the BLH (black line) matches approximately with aerosol lidar detection (black dots). Ceilometer observation indicates the occurrence of BL Cumulus (the altitude of their base is plotted with grey dots). The condensation level of air parcels originating from the surface layer diagnosed using LMDZ outputs is plotted with grey lines. Considering convective mixing, the thermal scheme should be able to create clouds in coherence with the observations if one would consider water phase modifications as introduced in the diagnostics.

4 TOWARD A MASS FLUX MODEL FOR CLOUDY CONVECTIVE BL

Based on those results, we introduce in the thermal scheme the condensation process. It means that the virtual potential temperature of the thermal is no more constant. All the scheme is now designed to insure the conservation of the liquid potential temperature and the total water content. In case of conden-

sation, $\Theta_v(plume) > \Theta_{vSL}$, and the CAPE value and thus the vertical speed of the plume become sensibly greater than what was obtained in the dry configuration. In coherence with results discuss by Siebesma et al. (2003), the vertical speed is then found greater than what it should be in reality by a factor of 3 or 4.

In the thermal algorithm, the vertical speed is strongly influenced by the air characteristics in the first unstable layer of the model. The dry configuration closure is not coherent with the interpretation proposed by Randall and Shao (1992), whose description is based on the existence of a ventilation layer from where plumes originate. The ventilation layer is defined as the area near the ground where parcels of air are in equilibrium with the surface and we should take its thermodynamic characteristics to define the plumes. We will discuss during the ICCP conference how we concretely introduce this notion in the thermal algorithm.

This approach is actually evaluated using a double approach. On one hand we use the classical climatic approach to validate the parameterization running the model on a global mode and comparing results with ISCCP data. On the other hand we run the zoomed and nudged version of LMDZ to validate the parameterization with ground-based observations from the European project CLOUDNET.

5 ACKNOWLEDGMENT

One of us (A.M.) was supported by the European project CLOUDNET.

References

Atkinson, B. W., and J. Wu Zhang, 1997: Mesoscale shallow convection in the atmosphere, *Reviews of Geophysics*, **34,4**, 403–431.

Holtslag, A. A. M., and B. A. Boville, 1992: Local versus nonlocal boundary-layer diffusion in a global climate model, *J. Climate*, **6**, 1825–1842.

Hourdin, F., F. Couvreux, and L. Menut, 2002: Parameterization of the dry convective boundary layer based on a mass flux representation of thermals, *J. Atmos. Sci.*, **59**, 1105–1123.

Jakob, C., 1999: Clouds in the ecmwf reanalysis, *J. Climate*, **12**, 947–959.

Lappen, C. L., and D. A. Randall, 2001: Toward a unified parameterization of the boundary layer and moist convection. part i: A new trype of mass-flux model, *J. Atmos. Sci.*, **58**, 2021–2036.

LeMone, M. A., 1973: The structure and dynamics of horizontal roll vortices in the planetary boundary layer, *J. Atmos. Sci.*, **30**, 1077–1091.

Lock, A. P., A. R. Brown, M. R. Bush, G. M. Martin, and R. N. B. Smith, 2000: A new boundary layer mixing scheme. part i: Scheme description and single-column model tests, *Mon. Wea. Rev.*, **128**, 3187–3199.

Louis, J. F., 1979: A parametric model of vertical eddy fluxes in the atmosphere, *Boundary-Layer Meteorol.*, **17**, 187–202.

Mathieu, A., and A. Lahellec, 2004: Comments on a DYCOMS-II analysis of stratocumulus stability, *Q. J. R. Meteorol. Soc.*, **submitted.**

Mathieu, A., A. Lahellec, and A. Weill, 2004: Evaluation of a numerical weather forecast model using boundary layer cloud top temperature retrieved from AVHRR, *Mon. Wea. Rev.*, **132**, 915–928.

Randall, D. A., and Q. Shao, 1992: A second-order bulk boundary-layer model, *J. Atmos. Sci.*, **49**, 1903–1923.

Siebesma, A. P., C. S. Bretherton, A. Brown, A. Chlond, J. Cuxart, P. G. Duynkerke, H. Jiang, M. Khairoutdinov, D. Lewellen, C. Moeng, E. Sanchez, B. Stevens, and D. E. Stevens, 2003: Large eddy simulation intercomparison study of shallow cumulus convection, *J. Atmos. Sci.*, **60**, 1201–1219.

Troen, I., and L. Mahrt, 1986: A simple model of the atmospheric boundary-layer; sensitivity to surface evaporation, *Bound. Layer Meteor.*, **37**, 129–148.

EXPLICIT PREDICTION OF HAIL USING A TRIPLE-MOMENT BULK MICROPHYSICS SCHEME

Jason A. Milbrandt and M. K. Yau

Department of Atmospheric and Oceanic Sciences, McGill University, Montreal, Quebec, Canada

1. INTRODUCTION

With increasing computer power, explicit microphysics schemes are playing an increasingly important role in atmospheric models. Because of the prohibitive computational cost of bin-resolving schemes, the bulk method continues to be used for parameterizing cloud microphysics in NWP models. Many schemes use a Kessler-type parameterization in which one moment of the hydrometeor size distribution – proportional to the mass content (Q) – is predicted. More recently, the two-moment method has been used in which both the mass content and the total number concentration (N_T) of the hydrometeor categories are independently predicted.

The size spectrum of each hydrometeor category is often described by a three-parameter gamma distribution function of the form

$$N_x(D) = N_{0x} D^{\alpha_x} e^{-\lambda_x D},$$

where N_{0x}, α_x, and λ_x are distrubtion parameters of category x. Two-moment schemes generally treat N_{0x} and λ_x as the prognostic variables while holding the shape parameter, α_x, constant. In this study, the role of the shape parameter in bulk schemes is investigated and its effects on sedimentation and microphysical growth rates are examined. Comparisons are made between various bulk approaches – a one-moment, a two-moment, and a three-moment scheme – and an analytic bin model. A method is proposed to extend the double-moment approach by allowing the shape parameter to vary as a diagnostic parameter. Results from 3D simulations of a severe hailstorm using various versions of a new bulk scheme, including a triple-moment version, are discussed.

Corresponding author's address: Jason A. Milbrandt, Department of Atmospheric and Oceanic Sciences, McGill University, Montreal, Quebec, H3A 2K6, Canada
E-mail: jason@zephyr.meteo.mcgill.ca

2. ANALYZING THE ROLE OF THE SHAPE PARAMETER

The shape parameter affects the prediction of the various moments in two ways. First, α affects the redistribution of the predicted moments in the vertical due to hydrometeor sedimentation since the moment-weighted fall velocities used to compute sedimentation rates depend on all of the size distribution parameters. Second, the microphysical growth rates also depend on the values of the distribution parameters. We examine the role of α in the bulk method by comparing below the following approaches: a single-moment scheme (SM), a double-moment scheme with a constant $\alpha = 0$ (FIX0), a double-moment scheme with a constant $\alpha = 3$ (FIX3), a double-moment scheme with a diagnosed value of α (DIAG), and a triple-moment scheme (TM). In DIAG, α is diagnosed as a monotonically increasing function of the mass-weighted mean diameter, D_m, which is proportional to the ratio of the predicted moments, Q/N_T. In TM, the radar reflectivity Z (the sixth moment of the particle distribution) is predicted in addition to Q and N_T, thus making α a prognostic parameter. For details on the formulations in DIAG and TM, see Milbrandt and Yau (2003). For the analysis in this section, the schemes are compared to an analytic (Lagrangian) bin model (ANA). The schemes are summarized in Table 1.

Symbol	Predicted moments	Treatment of α
SM	Q	$\alpha = 0$
FIX0	Q and N_T	$\alpha = 0$
FIX3	Q and N_T	$\alpha = 3$
DIAG	Q and N_T	$\alpha = f(D_m)$
TM	Q, N_T and Z	prognostic
ANA	*Analytic bin model*	

Table 1 List of symbols used to refer to the bulk schemes tested.

Differences between the methods in the computation of the fall velocities and growth rates, are due to the ability of the schemes to represent the particle size distribution. Fig. 1 shows an example of the size distribution from the different schemes. Values of Q, N_T and Z are computed from the number of particles in each size bin from the analytic model for the size spectrum of hail shown in Fig. 1. From these moments, the appropriate distribution parameters (N_0, λ, and α) are computed for each of the schemes and the size distributions are plotted. With different treatments of α, there are obvious differences in the abilities of the various schemes to match the distribution of ANA. In this example, the FIX0 distribution (which is inverse-exponential) is clearly unable to capture the narrowness of the ANA distribution. The distribution of FIX3 is somewhat closer while those of DIAG and TM are much better. Note that the DIAG distribution is quite similar to the TM distribution which implies that in this particular example, the value of α diagnosed from Q and N_T by DIAG is similar to the value computed from Q, N_T, and Z by TM.

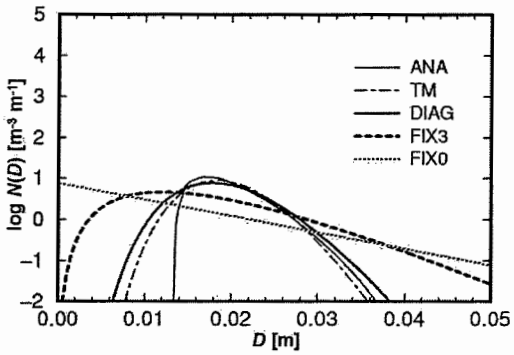

Fig. 1 Representations of a particle size distirbution by various bulk schemes.

To investigate the role of α in a bulk scheme and assess the importance of treating α appropriately, we examine independently in the following subsections the effects of α on hydrometeor sedimentation and on the instantaneous growth rates.

2.1 Sedimentation

A 1D model is used to investigate pure sedimentation in bulk schemes. In the bulk method, the predicted moments of the size distribution sediment at the appropriate moment-weighted bulk fall velocities. For the following calculations, hail is used to avoid confusion regarding particle coalescence and breakup, but the same conclusions apply to all sedimenting hydrometeor categories. An initial population of hail particles is defined by specifying the hail mass content Q_h to vary sinusoidally between heights (z) of 8 and 10 km above ground with a maximum value of 5 g m^{-3} at z = 9 km. Values of $N_{0h} = 4 \times 10^4$ m^{-4} and $\alpha_h = 0$ are used to compute the initial values of N_{Th} and Z_h at each level. A constant updraft of 10 m s^{-1} is imposed throughout the column. Fig. 2 shows profiles of Q_h, N_{Th}, Z_{eh} (the equivalent radar reflectivity of hail) and D_{mh} after 40 min. These profiles can be interpreted as the results of pure sedimentation of particles starting near the top of a deep convective system with the cloud base and top at 0 and 12 km respectively. For all parameters, the predicted profiles of TM are the closest to those of the analytic model. The profiles of DIAG are all closer than those of FIX3.

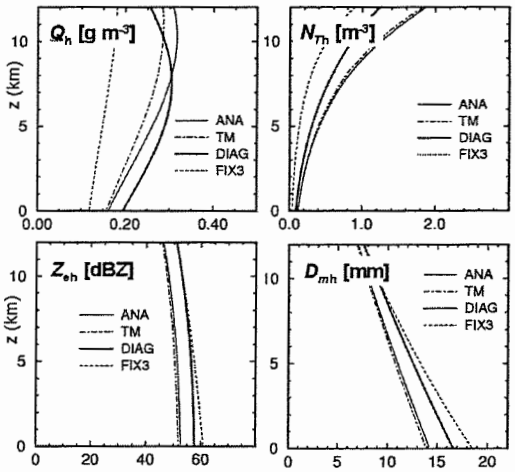

Fig. 2 Vertical profiles of Q_h, N_{Th}, Z_{eh}, and D_{mh} after 40 min calculated by the indicated bulk schemes and the analytic bin model (ANA).

Based on the results of these and other experiments, we conclude that the shape parameter does indeed play a significant role in affecting the prediction of the various moments by sedimentation. For a double-moment scheme, introducing a diagnostic relation for α based on the mean particle size represents a distinct improvement over holding α constant at even the optimal value (which we deemed to be 3 based on our calculations of sedimentation). Including a prognostic equation for α (the triple-moment method) yields the best results.

2.2 Microphysical Source/Sink Terms

For the microphysical processes, collection, diffusional growth/decay, and melting have the greatest impact on the prediction of the moments of the hydrometeor size spectra. It can be readily shown that the mass growth rates of a given particle type are proportional to certain moments of its size spectrum. For example, for a frozen hydrometeor category x growing by continuous collection of cloud water, the accretion rate is proportional to $M_x(2 + b_x)$, the $2+b_x^{th}$ moment of $N_x(D)$, where b_x is the fall velocity parameter in the relation $V_x(D) = a_x D^{b_x}$. Thus for hail ($x = h$) with $b_h = 0.6$, the continuous accretion rate is pro-portional to $M_h(2.6)$. [For stochastic collection, the mass growth rate is directly proportional to $M_x(2+b_x)$ as well as to $M_x(1+b_x)$ and $M_x(b_x)$.] Examining the role of α in determining the instantaneous growth rates is therefore equivalent to examining the sensitivity of specific moments (those on which the growth rates depend) on the value of α.

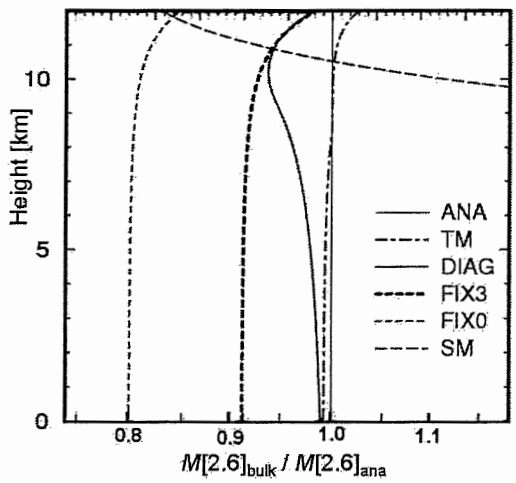

Fig. 3 Vertical profile of the ratios of $M(2.6)$ computed by various bulk schemes to $M(2.6)$ from the analytic model after 8 min of sedimentation through a constant updraft of 10 m s^{-1}.

Figure 3 depicts the ratio $M(2.6)_{bulk}/M(2.6)_{ana}$. $M(2.6)_{ana}$ is computed from the analytic bin model after 8 min of sedimentation. The moments $M(2.6)_{bulk}$ for the various bulk schemes are computed from N_0, λ, and α determined from the values of Q, N_T, and Z in the analytic bin model at this time. As indicated in the figure, all schemes underestimate the growth rate (except for TM above 11 km and SM below that level). FIX0 underestimates the rate by 20% for most of the column and FIX3 by nearly 10%. There is considerable improvement for DIAG for a deep part of the column (below ~9 km) and TM is within a few percent of the analytic growth rate everywhere. Similar under/over-predictions exist for other moments important to growth rates. We conclude, therefore, that the shape parameter also play a significant role in affecting the instantaneous microphysical growth rates.

3. HAIL PREDICTION USING A TRIPLE-MOMENT SCHEME

A new bulk microphysics scheme has been developed and implemented into the fully compressible, nonhydrostatic Canadian MC2 mesoscale model (Benoit et al., 1997). The scheme consists of six hydrometeor categories: cloud, rain, ice, snow, graupel and hail. Various versions of the scheme have been implemented. The fully double-moment (for all categories) version combines the warm-rain scheme of Cohard and Pinty (2000a) with aspects of the ice-phase schemes of Ferrier (1994), Meyers et al. (1997), and others. A single-moment version of the scheme was also implemented for comparison. The double-moment version includes separate diagnostic relations for α_x of all sedimenting categories (rain and all frozen categories). The triple-moment version includes predictive equations for Z_x for these five hydrometeor categories. (See Milbrandt and Yau, 2003 for a full description of the scheme).

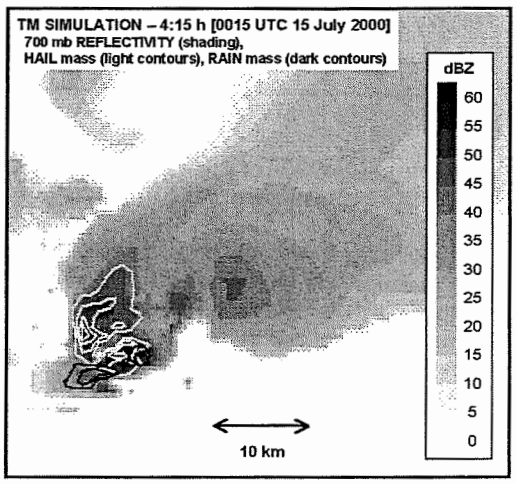

Fig. 4 Horizontal cross-section (700 mb) from the TM simulation showing total equivalent radar reflectivity (shading interval 5 dBZ); hail mass content (light contours, inteval is 1 g m-3); rain mass content (dark contours, interval is 1 g m-3).

Using only synoptic data (with no nudging or thermal perturbations), the model has been used to conduct high-resolution (1-km) simulations of a high-precipitation supercell storm which produced large hail (14 July 2000 in Alberta, Canada). The control run, using the triple-moment scheme, does remarkably well in reproducing a realistic, long-lived supercell, conforming closely to radar observations. The simulated storm had similar propagation speed, accumulated precipitation amounts, radar reflectivity values, and storm structures (including a hook echo and mesocyclone) as those observed. Fig. 4 shows a 700 mb "CAPPI" (at approximately 2 km AGL) of the total Z_e along with hail and rain mass concentrations from the TM simulation. Radar observations at this time (not shown) also indicate the presence of a hook echo and a mesocyclone. The simulation is hence deemed sufficiently realistic to allow investigation of the effects of using the various versions of the microphysics scheme.

Sensitivity experiments on the predicted precipitation using the various versions of the scheme were conducted. The simulation using the SM scheme considerably overpredicted (compared with the TM run) the surface hail (solid), as well as the total (liquid + solid), precipitation rates. The total precipitation rates of all the double-moment runs were similar to those of the TM run but with different biases in the phase of the surface precipitation. The FIX0 run was biased towards higher solid and lower liquid precipitation compared to the TM run. The solid and liquid precipitation rates in the FIX3 run were closer to those of the TM run than those of the FIX0 run, but the closest double-moment run to the TM run was the DIAG run. The treatment of α in the double-moment scheme can therefore significantly effects the type of simulated precipitation at the ground (as well as other aspects such as radar reflectivity and particle sizes distributions).

4. CONCLUSION

The shape parameter in a bulk scheme using a three-parameter gamma distribution function was shown to play an important role in the prediction of hydrometeor sedimentation and on microphysical growth rates. Based on these results, we conclude that introducing a diagnostic relation for the shape parameter as a monotonically increasing function of the mean-mass diameter represents an important improvement in the double-moment method. However, a triple-moment scheme results in the best representation of particle size distributions and the best prediction of sedimentation and growth rates.

ACKNOWLEDGEMENTS

This research was supported by the Canadian Foundation for Climate and Atmospheric Sciences.

REFERENCES

Benoit, R., J.M. Desgagné, P. Pellerin, S. Pellerin, Y. Chartier, and S. Desjardins, 1997: The Canadian MC2: A semi-Lagrangian, semi-implicit wideband atmospheric model suited for finescale process studies and simulation. *Mon. Wea. Rev.*, **125**, 2382-2415.

Cohard, J.-M. and J.-P. Pinty, 2000a: A comprehensive two-moment warm microphysical bulk scheme. I: Description and tests. *Quart. J. Roy. Meteor. Soc.*, **126**, 1815-1842.

Ferrier, B.S., 1994: A two-moment multiple-phase four-class bulk ice scheme. Part I: Description. *J. Atmos. Sci.*, **51**, 249-280.

Meyers, M.P., R.L. Walko, J.Y. Harrington and W.R. Cotton, 1997: New RAMS cloud microphysics. Part II: The two-moment scheme. *Atmos. Res.*, **45**, 3-39.

Milbrandt, J.A. and M.K. Yau, 2003: Analysis of the role of the shape parameter in bulk microphysics parameterizations and a proposed triple-moment approach. Submitted to *J. Atmos. Sci.*

NUMERICAL MODELLING OF RISING THERMAL: APPLICATION FOR CUMULUS CLOUDS PARAMETERIZATION

G.V. Mostovoy[1] and Pat J. Fitzpatrick

GeoResources Institute, Mississippi State University, Stennis Space Center, Mississippi, USA

1. INTRODUCTION

Cumulus clouds play an important role in a vertical transport of heat and moisture. It is well-known that current schemes of convective parameterization have a number of shortcomings manifested in global numerical weather forecasting (Tiedke 1988) and in climate modelling (Slingo et al. 1994). These are: biased location and intensity of the trade wind inversion and systematic overheating and excessive moistening of the lowest 4-km layer in the subtropics. Similar shortcomings are also reported in studies with regional/mesoscale models (Liu et al. 2001) using Kain-Fritsch cumulus parameterization scheme (Kain and Fritsch 1990). Parameterized convective heating and moistening of the atmosphere are proportional to the difference of thermodynamic properties between a cloud and the environment. Therefore all these deficiencies are mostly originated from a simplified description of a cumulus cloud by a steady plume or column. In this way thermodynamic profiles within a cloud are reduced to the moist adiabatic which essentially characterizes temperature and humidity changes within a rising parcel having a prescribed mixing rate with the environment. It is evident that cumulus parameterizations can be improved due to more accurate representation of the cloud thermodynamic properties.

Despite a progress of using a numerical tracer technique in cloud modelling studies in recent years (e.g., Bretherton and Smolarkiewicz 1989; Cohen 2000) our knowledge about cumuli thermodynamic properties remains incomplete. This paper is an attempt to clarify some features of cloud thermodynamics from Lagrangian viewpoint which makes more clear a description of any cloud variable field in terms of parcel history (parcel age and level of origin).

2. NUMERICAL MODEL AND EXPERIMENTS

Simulations of a thermal developing into a small cloud have been performed with the COAMPS numerical model (Hodur 1997). A quasi slab-symmetric configuration of the model with 9 points along y-axis were used. The integration domain was 2.56-km in vertical and 4.05-km along x-axis. The grid spacing was equal to 45 m and 40 m along horizontal and vertical axis, respectively. Potential temperature of the air, water vapour (q_v) and liquid water content (LWC) mixing ratios were used in the model to describe thermodynamics of non-precipitating cumulus convection. Rigid lid condition was adopted at the model top and periodicity was used at lateral boundaries. The model was integrated with a 0.1 second time step during 50-min period. This period was long enough to reproduce an entire life-cycle of the small cloud cell.

The thermal was initiated as a heated semi-circular spot placed at the bottom of the integration domain. Within the spot the temperature decreased from its centre, having a Gaussian distribution with a typical half-width Γ which was specified in grid steps, and with an amplitude A. The mixing ratio of the water vapour was also perturbed in the same way, but the amplitude of perturbation was equal to $\beta(q_{sat} - q_v)$, where is a saturation mixing ratio and is a number between 0 and 1. Numerical simulations were performed with different values of Γ (5 - 15), A (0.5K - 1.0K), and β (0 -1). Numbers in brackets indicate a typical parameters range used in experiments.

[1] Corresponding author address: GeoResources Institute, MSU, Stennis Space Center, MS, 39529-6000 (e-mail: mostovoi@gri.msstate.edu)

Initial large-scale vertical profiles used for numerical experiments were taken from BOMEX data (Siebesma and Cuijpers 1995), except for winds and external forcing which were set to zero.

3. RESULTS

Simple tracer technique is used for the analysis of numerical simulation results. To trace deformations associated with convection one can use any conservative variable. We choose the total moisture content $q_T = q_v + LWC$ for this purpose. The isosurfaces of q_T are quasi-material surfaces consisting of the same air parcels because q_T is a conservative quantity in the absence of sub-grid mixing. As an example figure 1 shows such isosurfaces produced by temporal variations of q_T on y-centreline of the integration domain (The simulation have been done with Γ = 10, A = 1K, and β = 0.8). Their configuration reflects the deformation of initially horizontal layers caused by the ascending thermal.

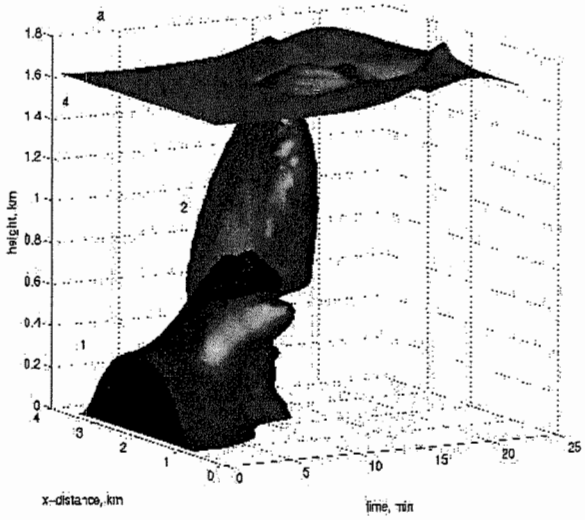

Figure 1. Temporal variations of total moisture content q_T and LWC on y-centreline of the integration domain. Simulation with Γ = 10, A = 1K, and β = 0.8. (a) Isosurfaces of q_T marked by 1, 3, and 4 stand for 17 g/kg, 14 g/kg, and 9 g/kg values, respectively. Isosurface of LWC with 0.05 g/kg value is denoted by number 2. (b) The same as in (a) but for rear view.

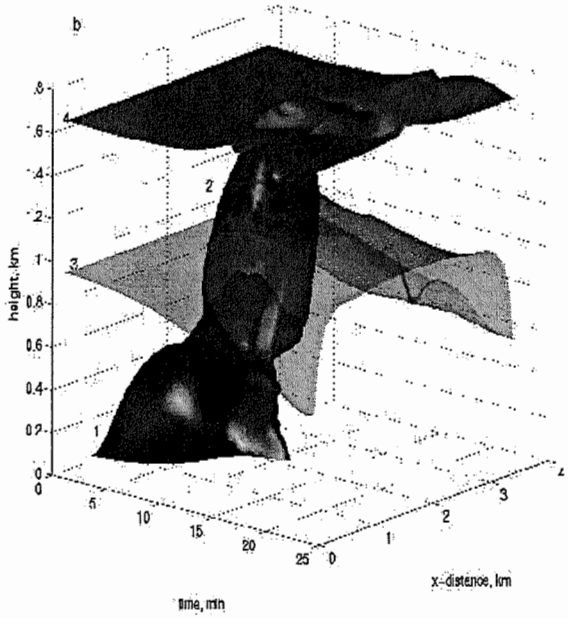

Figure 1. (continued)

The evolution of the thermal is readily seen in figure 1. The maximum value of q_T in the environment is 17.0 g/kg, so the isosurface with q_T = 17 g/kg confine from above the thermal domain occupied by initially heated and moisten particles. This domain rise and then dissapear loosing individual property of q_T > 17.0 g/kg in about 12 min due to the distortion and sub-grid mixing. Figure 1 also proves that thermal particles are not involved in a developing cloud.

Figure 2 shows that q_T values within thermal protected core are conceptually different from that of rising parcel (undiluted and diluted). This principal distinction does not broadly recognized. The difference is due to the fact that atmospheric buoyant convection makes air layers of a certain depth move, so that air parcels start simultaneously from various levels having different velocities.

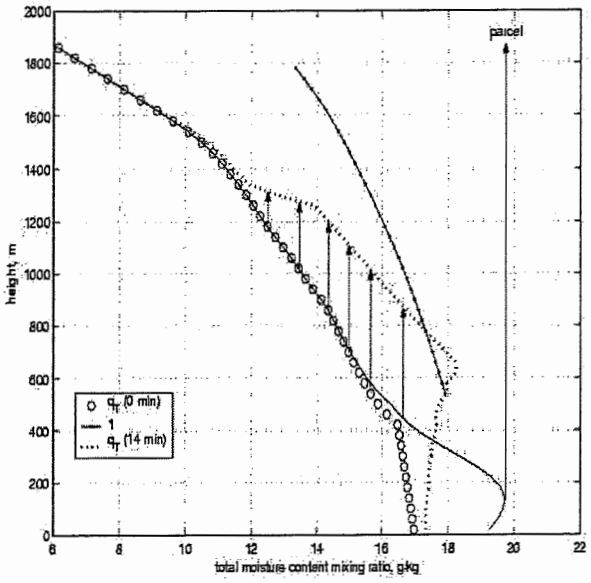

Figure 2. Distribution of total moisture content q_T with height at the centre of integration domain for the same experiment as in figure 1. This sampling point is away from thermal/cloud boundary therefore representing adiabatic or non-mixed cloud core. Large arrow shows q_T within undiluted ascending parcel. Small arrows indicate displacements from the origin level for 14 min of thermal development. Circles stand for initial q_T stratification and solid line shows initial q_T disturbance. Line 1 marks q_T within diluted by lateral entrainment parcel with 0.2-km radius r, which corresponds to the fractional entrainment rate $\lambda = 0.2/r$ (Arakawa and Shubert 1974).

4. CONCLUDING REMARKS

The above results suggest that a classic parcel method to represent a cloud adiabat can be refined to account for terminal sizes of convective elements. The work is in progress.

References

Arakawa, A., and W.H. Shubert, 1974: Interaction of a cumulus cloud ensemble with the large-scale environment, Part I, J. Atmos. Sci., **31**, 674-701.

Bretherton, C.S., and P.K. Smolarkiewicz, 1989: Gravity waves, compensating subsidence and detrainment around cumulus clouds. J. Atmos. Sci., **46**, 740-759.

Cohen, C., 2000: A quantitative investigation of entrainment and detrainment in numerically simulated cumulonimbus clouds. J. Atmos. Sci., **57**, 1657-1674.

Hodur, R.M., 1997: The Naval Research Laboratory's Coupled Ocean/Atmosphere Mesoscale Prediction System (COAMPS). Mon. Wea. Rev., **125**, 1414-1430.

Kain, J.S., and J.M. Fritsch, 1990: A one-dimensional entraining/detraining plume model and its application in convective parameterization. J. Atmos. Sci., **47**, 2784-2802.

Liu, C., M.W. Moncrieff, and W.W. Grabowski, 2001: Explicit and parameterized realizations of convective cloud systems in TOGA COARE. Mon. Wea. Rev., **129**, 1689-1703.

Siebesma, A.P., and J.W.M. Cuijpers, 1995: Evaluation of parametric assumptions for shallow cumulus convection. J. Atmos. Sci., **52**, 650-666.

Slingo J., et al., 1994: Mean climate and transience in the tropics of the UGAMP GCM: Sensitivity to convective parameterization. Q. J. Roy. Meteorol. Soc., **120**, 881-922.

Tiedtke M., Heckley W.A., and Slingo J.M., 1988: Tropical forecasting in ECMWF: The influence of physical parameterization on the mean structure of forecasts and analyses. Q. J. Roy. Meteorol. Soc., **114**, 639-664.

RESULTS FROM A NEW MAXIMUM SIMPLICATION MODEL OF CLOUD PROPERTIES BENEATH THE MARINE BOUNDARY LAYER

Sungsu Park[1], Conway B. Leovy[2], and Margaret A. Rozendaal[2]

[1]Advanced Study Program, National Center for Atmospheric Research, Boulder, CO 80307, USA
[2]Department of Atmospheric Sciences, University of Washington, Seattle, WA 98195, USA

1. INTRODUCTION

The global net radiation budget at the top of the atmosphere is sensitive to the coverage and optical properties of stratiform clouds in the MBL, but the properties of these clouds are notoriously difficult to simulate in climate models (*e.g.*, Slingo, 1990; Hartmann *et al.,* 1992). Thus, for reliable simulation of the climate system with cloud feedback, there is need for improved cloud model representations of the MBL and for better understanding of the sensitivities of MBL properties to controlling variables such as SST, subsidence, and humidity above the MBL.

In this study, we develop a new heuristic single column model to obtain simple but physically reasonable insights into the feedback mechanisms responsible for the variations of diurnally averaged stratiform clouds in a steady state inversion-topped marine boundary layer (MBL). Our model aims to predict the statistical properties of inversion base air (and so cloud fraction and cloud optical properties) for a given set of boundary conditions (SST, divergence, inversion top potential temperature and specific humidity, wind speed).

2. MODEL STRUCTURES

Following the approach of Betts (1985), total specific humidity (q_t) and liquid potential temperature (θ_l) at the inversion base (z_h) are assumed to be determined by the weighted averages of inversion top (z_f) and mixed layer (ML) values (z_m. See Fig.1) :

$$q_{t,h}(i) = q_{t,m} + \alpha_{q_t}(i) \cdot (q_{t,f} - q_{t,m}) \quad (1a)$$

$$\theta_{l,h}(i) = \theta_{l,m} + \alpha_{\theta_l}(i) \cdot (\theta_{l,f} - \theta_{l,m}) \quad (1b)$$

where α_{q_t} and α_{θ_l} are decoupling parameters, and subscripts m, h, and f correspond to ML top, inversion base and inversion top respectively, and (i) is an index of position in the probability distribution.

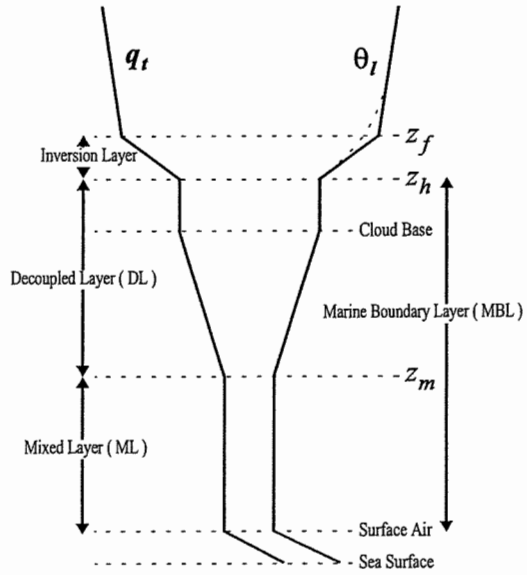

Fig.1. Structure of a new heuristic single column MBL cloud model. In a typical sounding, variations of θ_l, but not necessarily q_t, are smoother through the inversion layer as depicted by the dashed line.

Decoupling parameters are assumed to share a common standard deviation (σ) and a common normal Gaussian probability density function with a stan-

Corresponding author's address : Sungsu Park, Advanced Study Program / NCAR, 1850 Table Mesa Dr. P.O. 3000, Boulder, CO 80307; Email : sungsup@ucar.edu

dardized decoupling parameter, $X(i)$,

$$X(i) \equiv (\alpha_{q_t}(i) - \hat{\alpha}_{q_t})/\sigma = (\alpha_{\theta_l}(i) - \hat{\alpha}_{\theta_l})/\sigma \quad (2)$$

where $\hat{\alpha}_{q_t}$ and $\hat{\alpha}_{\theta_l}$ are median decoupling parameters.

Based on the analyses of soundings, we assume

$$\hat{\alpha}_{q_t} = (\Delta z_{DL}/2750)^{1.3} \quad (3)$$

where $\Delta z_{DL}(=z_h - z_m)$ is the thickness of the decoupled layer (DL) in meter.

Considering buoyancy reduction due to strong cloud top radiative cooling, $\hat{\alpha}_{\theta_l}/\hat{\alpha}_{q_t}$ is parameterized as a linear function of stratocumulus cloud fraction, *fsc* :

$$\hat{\alpha}_{\theta_l}/\hat{\alpha}_{q_t} = 1 - 0.2 \cdot fsc \quad (4)$$

From the analysis of soundings and LES data, σ is parameterized as a linear function of Δz_{DL} :

$$\sigma = 6 \cdot 10^{-5} \cdot \Delta z_{DL} \quad (5)$$

After calculating cloud liquid water path $[Q(i)]$, *fsc* is assumed to be the same as the cumulative probability of $Q(i)$ larger than a cut-off LWP, $Q_c = 3$ gm^{-2} where $Q(i_c) = Q_c$:

$$fsc = 0.5 \cdot [1 + erf(2^{-0.5} \cdot X(i_c))] \quad (6)$$

ML properties $(q_{t,m}, \theta_{l,m})$ are determined by simplified steady state MBL moisture (advection in MBL $\approx$ surface flux + entrainment flux + subsidence moistening) and ML heat balance constraints (advection in ML $\approx$ surface flux), respectively. Inversion top properties $(q_{t,f}, \theta_{l,f})$ are obtained from input linear free air profiles. z_m is tied to the lifting condensation level (LCL) of ML air and z_h is obtained from steady state MBL mass budget constraint (advection of z_h = entrainment rate - subsidence) where MBL top entrainment (*Ee*) is calculated from simplified steady state DL heat budget constraint (entrainment flux $\approx$ radiation across DL + advection in DL). Radiative flux divergence across DL is parameterized as a linear function of MBL cloud fraction.

3. RESULTS

Our model is applied to downstream trajectory in the autumn eastern tropical Pacific Ocean in which two different climate regimes - cold and warm advection - coexist in association with the SST cold tongue.

As observed in Fig.2, warm advection region exists (Trajectory 6~17) between upstream cold advection region and stronger downstream cold advection region, SST front (Fig.2b). Stratocumulus cloud fraction rapidly decreases downstream across the warm advection region, reaching a minimum near the cold tongue axis and a local maximum over the SST front (Fig.2b). Enhanced stratification and moistening of the lower MBL within the warm advection region are observed in atmospheric soundings (Figs.2c,d).

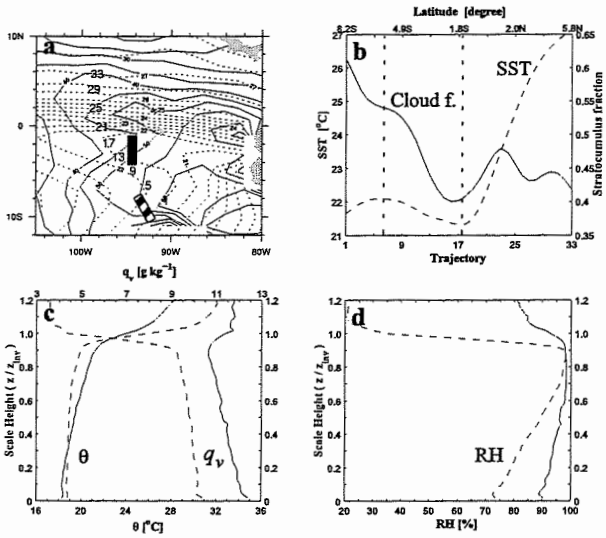

Fig.2. Observations. (a) Ship observed 40-year ('56-'95) August-October climatologies of stratocumulus (*CL6584*) amount (solid contours, absolute %) and SST (dashed contours, 0.5°C). A 5-day backward trajectory at 3 hour intervals is shown by numerics. Locations of average soundings displayed in Figs.2c,d are shown by heavy solid and dashed bars. (b) Stratocumulus amount (solid) and SST (dashed) following the trajectory in Fig.2a. Climatological SST warm advection region is indicated by two vertical dotted lines. (c),(d) Composited soundings of (c) θ and q_v, and (d) relative humidity in the cold tongue (solid) and south of the cold tongue (dashed) plotted against normalized height of the mid-point of the inversion layer. Soundings are from the East Pacific Investigation of Climate (EPIC) 2001 field campaign (Bretherton *et al.*, 2004) during Oct.10.2001 ~ Oct.21.2001.

Figure 3 shows model simulated downstream MBL variations along the idealized SST profile (dashed line in Fig.3a). Other input boundary conditions (divergence, free air profiles, wind speed) are fixed throughout the trajectory. Thin and thick lines correspond to full and static equilibrium (without horizontal advection) model results respectively.

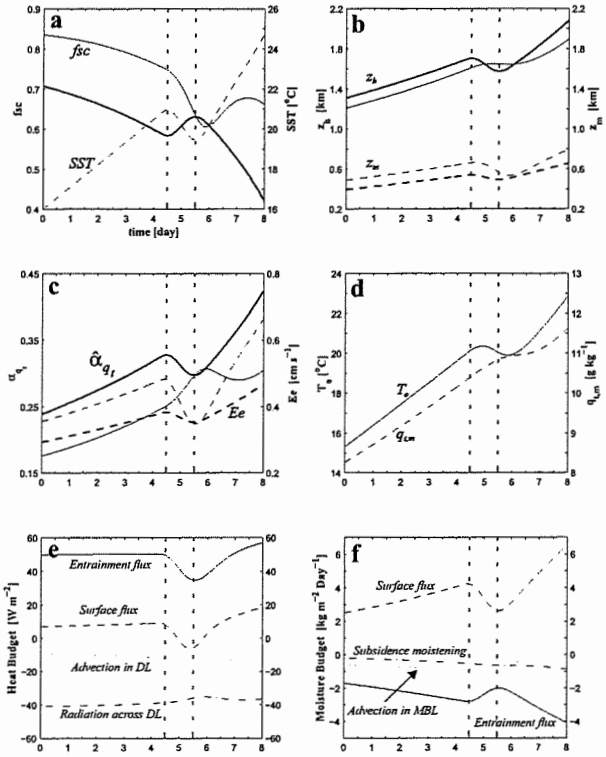

Fig.3. Idealized SST cold tongue simulation. (a) Stratiform cloud fraction (solid) and SST (dashed) with static equilibrium stratiform cloud fraction (heavy line), (b) inversion base height (solid) and mixed layer height (dashed) with static equilibrium solutions (heavy lines), (c) humidity decoupling parameter (solid) and entrainment velocity (dashed) with static equilibrium solutions (heavy lines), (d) surface air temperature (solid) and specific humidity (dashed), (e) MBL heat balance components, (f) MBL humidity balance components.

In the upstream cold advection region (day 0~4.5), simulated downstream variation behavior - MBL deepening and decoupling, and decreased cloudiness - is similar to the observations and LES results. Consistent with observed behavior in the cold tongue region, *fsc* in the full model drops rapidly across the warm advection region to a minimum just beyond the cold tongue axis, and rises again to a maximum in the SST frontal region (Fig.3a). Variations in *fsc* largely reflect variations in the decoupling parameters which increase rapidly across the warm advection region, reach a local maximum just beyond the cold tongue axis, and decline downstream to a minimum in the SST frontal region ($\hat{\alpha}_{q_t}$ in Fig.3c).

Variations in $\hat{\alpha}_{q_t}$ reflect in turn variations in DL thickness and its components, ML and MBL thicknesses (Fig.3b). The key is ML thickness, reflecting the influence of lower MBL processes. ML thins to a local minimum just downstream of the cold tongue axis while MBL thickness variation is much smoother, responding primarily to the integrated effects of entrainment velocity variations (Fig.3c). It is the stronger response of the ML that leads to the local maxima in DL thickness and decoupling parameters, and the corresponding local minimum in stratiform cloud fraction. The strong cold tongue variation of ML thickness is in turn a response to the variations of temperature and specific humidity in the ML. Because thermal response time is shorter than humidity response time, ML temperature variations are stronger and occur sooner than humidity variations (Fig.3d), resulting in maximum relative humidity and minimum z_m just beyond the cold tongue.

Model fluxes reflect the behavior of observed fluxes across the cold tongue region (Figs.3e,f). Positive surface and entrainment heat fluxes and surface moisture flux decline to minima near the cold tongue axis, while the entrainment flux drying effect reaches a minimum there. All of these are consistent with the MBL stabilization shown in the soundings (Fig.2c).

The difference between the full model and the static equilibrium model is striking. In the static equilibrium model, the instantaneous responses to SST change produce a large variation in z_h and a smaller variation in z_m in phase with SST variations. As a result, decoupling parameters reach minima and *fsc* reaches a maximum near the cold tongue axis. The key ingredient is the difference in response times of z_h, ML humidity, and ML temperature.

4. CONCLUSION

We have here a kind of maximum simplification model of the MBL in that complex internal processes, such as the total kinetic energy budget, are not explicitly represented, but omission of any major model component would cause it to fail badly. Key assumption is that decoupling parameters are increasing func-

5. ACKNOWLEDGEMENTS

We are grateful to C. S. Bretherton and R. Wood for encouragement and helpful discussion.

6. REFERENCES

This abstract is a partial summary of the following paper by Park *et al.* (2004)

Table 1. Characterization of the Eight ACE-2 Cases

	pristine		intermediate			polluted		
	26 June	25 June	17 July	19 July	16 July	18 July	8 July	9 July
H (m)	202	262	272	272	222	192	182	167
N (cm^{-3})	51	75	114	134	134	178	208	167

stant in ACE-2 cases, since the temperature and pressure at cloud base did not vary signi?cantly. The following formulae result for the cloud layer vertically av-

a result, the drizzle concentration stays below $2\,cm^{-3}$ in the polluted case, but it increases to $6\,cm^{-3}$ in the pristine case. The most interesting feature is the location of the peak values of drizzle concentration. In

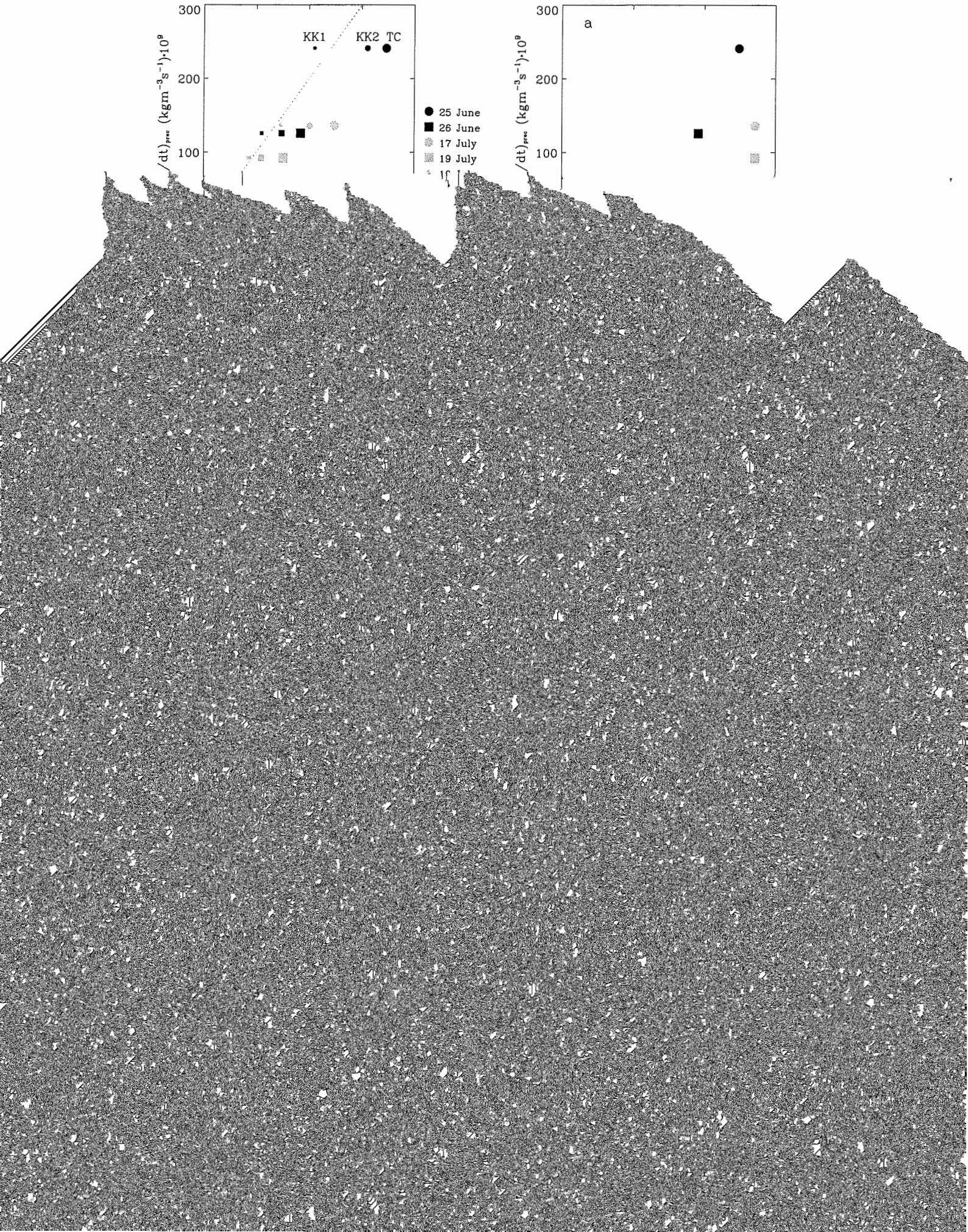
300
200
100
KK1
KK2
TC
25 June
26 June
17 July
19 July
a

stratocumulus clouds where spatial variability of the cloud LWC is less pronounced than in deep cumulus clouds.

[illegible]

for the onset of precipitation, and for calculating the precipitation rate in the layer.

6. REFERENCES

[illegible]

Param.	r_c	r_r	r_i	r_s	r_g
α, ν	3,1	1,2	3,3	1,1	1,1
a	524	524	0.82	0.02	196

Graupels are formed in the case of heavy riming of snow and by rain freezing when supercooled raindrops come in contact with pristine ice crystals.

model top to damp vertically propagating gravity waves. 3D Turbulence has a 1.5 level closure with prediction of the tubulent kinetic energy (TKE).

3.1 Time series

The time evolution of the maxima of some fields is given in Fig. 1. Convection is well developped even with a small buoyant impulse. The main updraft reaches 9.2 ms^{-1} at 2.8 km after 18 min. The formation and growth of the cloud droplets follow w, up to 4.4 gkg^{-1} at 3.7 km (-3.5° C height level). Downdrafts ($w_{min} \sim -8.5$ ms^{-1} at 2.3 km) occur when a copious amount of rain begins to evaporate during its fall after 37 min. Ice nucleation starts after 15 min. Pristine ice is rapidly converted into snow at 5 km. Due to the large quantity of supercooled cloud droplets, snow is efficiently converted into graupels (up to 6 gkg^{-1}). It is worth to notice that rain is produced by melting graupels and not by autoconversion of cloud droplets. The origin of the pristine ice concentration is well depicted on the CI/CN plot. Ice is first produced by heterogeneous nucleation (~ 2 l^{-1}) but as environmental conditions are very favourable, an explosive increase of n_i (≤ 180 l^{-1}) is obtained via the Hallett-Mossop process. In contrast with OK2000, this high value of n_i does not persist for more than 10 min due to the strong depletion of the cloud droplets (and ice

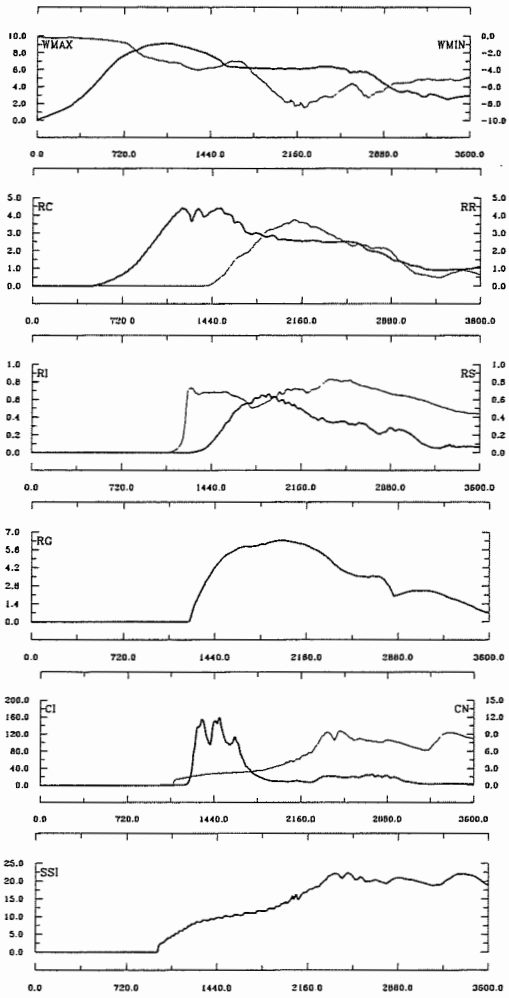

Figure 1: Time series of domain maxima. From top to bottom, the vertical speed (with WMIN minima), the liquid water r_c (bold) and r_r, the un(or lightly)rimed ice r_i (bold) and r_s, the graupel r_g, the ice n_i (bold) and nucleated IN n_n concentrations (l^{-1}) and ice supersaturation SS_i (%).

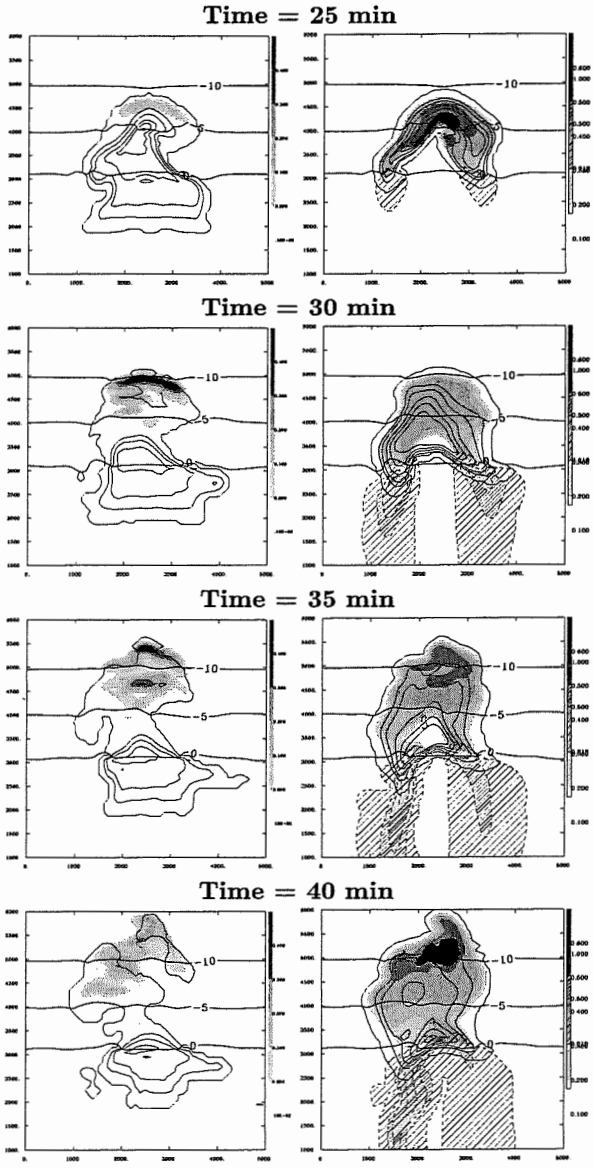

Figure 2: Vertical cross sections through domain center: r_i ([10^{-3}, 0.05, 0.1, 0.2, 0.3, 0.4 gkg^{-1}] grey scale) and r_c ([10^{-2}, 0.5, 1, 2, 3, 4 gkg^{-1}] (left) and r_s ([0.1, 0.2, 0.3, 0.4, 0.5, 0.6 gkg^{-1}] grey scale), r_g and r_r (hatched areas) with r_c contours (right). Labelled curves are isotherms in ° C.

particles) by wet riming on the graupels. However small ice crystals are still produced by IN nucleation ($n_i < 10\ l^{-1}$) at cloud top where SS_i attains 20%.

3.2 Time sequence analysis

Figure 2 presents the 5 min evolution of the same vertical cross section passing through the center of the domain. The field asymmetry is a consequence of the SEI technique of initialization (OK2000). At 25 min, the updraft sustains the supercooling of the cloud droplets at -5 ° C. The presence of graupel at this level is optimal for the Hallett-Mossop ice crystal multiplication. Rain begins to form on the edges of the updraft from the melting graupels and not in the updraft core from the "warm" pathway although r_c is large enough there. The reason is that the BR autoconversion parameterization of the scheme do not produce many raindrops because the cloud droplets are too small (vol. diameter $D_c < 23$ μm). Five min later, the freshly nucleated ice crystals have grown (a r_i increase) and are transported upwards to the -10 ° C level. The cloud droplets are clearly depleted to the advantage of the graupels. The narrow rainbands develop and reach the ground (the plots are cut at 1 km high). At 35 min, the cloud continues its ascent by carrying cloud ice and a small amount of cloud droplets. The small ice crystals are slowly converted into snow crystals at 40 min leading to a significant increase of r_s at 5000 m. As the updraft starts to decline, less supercooled water is available for the graupel growth.

3.3 Sensitivity to CCN and to IN changes

A twin experiment is performed but with a drastic reduction of the initial CCN concentration now divided by a factor 10. The CCN maximum value is 60 cm^{-3}. The maximum precipitation rates of the "CCN" and the "CCN/10" cases are compared in Fig. 3. Both cases lead to a similar amount of cumulated precipitation (max value of 6 mm). As expected for the "CCN/10" case, an early precipitation peak is fund because warm microphysical processes are active. The second peak corresponds to precipitation formed through ice processes, as for the "CCN" case. The other difference is that no ice enhancement is possible for the "CCN/10" simulation because droplets are depleted for $T < -3°$ C.

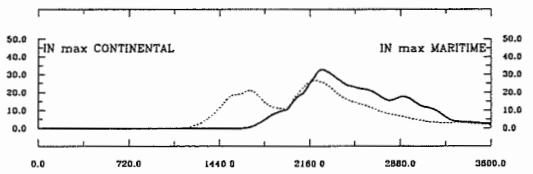

Figure 3: Maximum precipitation rate (mmh^{-1}) for the "CCN" (bold) and the "CCN/10" (dashed) cases.

The last series of simulation is made after multiplying and dividing by a factor 10 the nominal IN concentration. The result is that no significant change is observed in the simulated cloud and precipitation.

4. CONCLUSION

This study reports results obtained by a quasi 2-moment microphysical scheme which explicitly incorporates activation and nucleation of the aerosols. The New-Mexico cumulus cloud test case shows that the cloud evolution compares reasonnably well with that of OK2000's bin model. The study underlines the importance of the CCN concentration at cloud base to select the warm or cold microphysical chain process of precipitation. In contrast, a dramatic change of IN concentration is much less sensitive.

5. REFERENCES

Banta, R., and K. R. Hanson, 1987: Sensitivity studies on the contientality of a numerically simulated cumulonimbus. *J. Climate Appl. Meteor.*, **26**, 275-286.

Cohard, J.-M., and J.-P. Pinty, 2000: A comprehensive two-moment warm microphysical bulk scheme. Part I: Description and selective tests. *Quart. J. Roy. Meteor. Soc.*, **126**, .

DeMott, P. J., M. P. Meyers and W. R. Cotton, 1992: Parameterization and impact of ice initiation processes relevant to numerical model simulations of cirrus clouds. *J. Atmos. Sci.*, **51**, 77-90.

Ferrier, B. S., 1994: A double-moment multiple phase four-class bulk ice scheme. Part I: description. *J. Atmos. Sci.*, **51**, 249-280.

Harrington, J. Y., M. P. Meyers, R. L. Walko, and W. R. Cotton, 1995: Parameterization of ice crystal conversion processes due to vapor deposition for mesoscale models using double-moment basis functions. Part I: Basic formulation and parcel model results. *J. Atmos. Sci.*, **52**, 4344-4366.

Kärcher, B., and U. Lohmann, A parameterization of cirrus cloud formation: Homogeneous freezing of supercooled aerosols.*J. Geophys. Res.*, **107**, 10.1029/2001JD000470.

Khvorostyanov, V. I., and K. Sassen, 1998: Cirrus cloud simulation using explicit microphysics nad radiation. Parts I and II. *J. Atmos. Sci.*, **55**, 1808-1845.

Meyers, M. P., P. J. DeMott, and W. R. Cotton, 1992: New primary ice-nucleation parameterization in an explicit cloud model. *J. Appl. Meteor.*, **31**, 708-721.

Mossop, S. C., 1976: Production of secondary ice particles during the growth of graupel by riming. *Quart. J. Roy. Meteor. Soc.*, **102**, 45-57.

Ovtchinnikov, M., Y. L. Kogan, and A. M. Blyth, 2000: An investigation of ice production mechanisms in small cumuliform clouds using a 3D model with explicit microphysics. Part II: Case study of New Mexico cumulus clouds. *J. Atmos. Sci.*, **57**, 3004-3020.

Pinty, J.-P. and P. Jabouille, 1998: A mixed-phase cloud parameterization for use in a mesoscale non-hydrostatic model: simulations of a squall line and of orographic precipitation. In *Conf. on Cloud Physics*, Everett, WA. Amer. Meteor. Soc., 217-220.

Reisin, T., Z. Levin, and S. Tzivion, 1996: Rain production in convective clouds as simulated in an axisymmetric model with detailed microphysics. Parts I: description of the model. *J. Atmos. Sci.*, **53**, 497-519.

STOCHASTIC CONVECTIVE PARAMETERIZATION WITH MULTIPLE PLUMES

R.S. Plant[1] and G.C. Craig[2]

[1]Department of Meteorology, University of Reading, RG6 2BB, UK
[2]DLR-Institut fuer Physik der Atmosphaere, Oberpfaffenhofen, Germany

1. CHARACTER OF THE SCHEME

We have produced a stochastic parameterization of cumulus clouds, suitable for use at both climate and NWP resolutions. The scheme does not relax model profiles towards an assumed state, but attempts to represent cumulus elements directly (as in Gregory and Rowntree, 1990; Kain 2004). Unlike many such schemes, however, its conceptual basis is not some "representative plume", nor an "ensemble plume" obtained from a weighted sum over a variety of cloud types. Rather, the approach encompasses a variable number of plumes, each plume being launched randomly with properties selected from a pdf. In the deterministic limit where there are very many plumes present, our method is equivalent to a true spectral scheme, as envisaged by Arakawa and Schubert (1974).

2. THE CASE FOR A STOCHASTIC SCHEME

The need for stochastic representations of parameterized small-scale flows has been increasingly recognized over recent years. The argument stems from the manifest difficulties of trying to struggle along without them. Determinism is fundamentally unrealistic, and is also a seriously flawed approximation in practice.

2.1 Determinism is Unrealistic

A deterministic scheme takes as input the instantaneous resolved-scale flow and produces as a unique output the feedbacks to that flow from the sub-grid convective motions. However, an element of small-scale variability arises naturally in convection because instability is released by discrete cumulus clouds, with some distribution of sizes. It is straightforward to demonstrate explicitly that the convective states consistent with resolved flows are wide-ranging. Figure 1 shows the distribution of updraft mass fluxes near cloud base that were obtained from a cloud-resolving-model (CRM) simulation (Cohen, 2001) of radiative-convective equilibrium. The fluxes are averaged over various areas, representative of possible grid-box sizes in a larger-scale model.

Corresponding author's address: Robert S. Plant, Department of Meteorology, University of Reading, PO Box 243, Reading, Berkshire. UK. RG6 2BB; E-Mail: r.s.plant@rdg.ac.uk

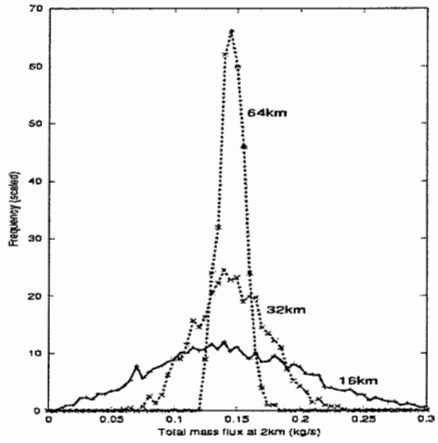

Figure 1. Histogram of total convective mass flux obtained from a CRM simulation. The total flux is averaged over different-sized areas and binned into intervals of 0.01kg/s. The vertical axis is scaled to account for the larger number of suitable averaging areas that become available as the unit averaging area is reduced in size.

Even with strong and uniform forcing, there is considerable convective variability at a mesoscale gridlength of 16km. At a global resolution of 64km, one might hope that the increased averaging would reduce the variability to tolerable levels. However, the width of the pdf is still ~30% of the mean flux, so that fluctuations about the ensemble mean remain a notable feature of the system.

2.2 Determinism is a Problematic Approximation

A deterministic scheme aims to determine the ensemble mean effect of the sub-grid states. Thus, it neglects convective fluctuations, which as we have seen, are potentially large. Moreover, the fluctuations are capable of interacting strongly with non-linearities in the convective system and with model dynamics. It is clear that the missing convective variability is a serious problem that cannot simply be dismissed. There are good indications that the lack of high-frequency, small-scale variability damages the ability of numerical models to capture important low-frequency, large-scale features of interest. Variations

in moist convection are known to provoke mesoscale simulations to evolve in qualitatively diverse ways (Zhang et al., 2003). However, variations in the initial conditions are often not able to produce ensembles with sufficient spread. Similarly, there is a systematic tendency to produce insufficient variability in many aspects of GCMs, particularly in the tropics. Insufficient variability has been implicated in the inability of models to predict features such as the equatorial quasi-biennial oscillation (Horinouchi et al., 2003).

3. A PHYSICALLY-BASED STOCHASTIC SCHEME

A number of groups have investigated parameterizations with a stochastic element (e.g., Buizza, 1999; Majda and Khouider, 2002; Lin and Neelin, 2003). Results have been encouraging, demonstrating positive impacts for a variety of approaches. However, an obvious objection to current stochastic schemes is the rather arbitrary character of the variability introduced. Justifications for particular schemes are no stronger than appeals to plausibility. We contend that the benefits of stochastic representations are now demonstrated, and so we should look beyond toy models. Small-scale variability included in models should have as much solid physical support as is possible, and our scheme is designed with this consideration to the fore.

3.1 Outline of Scheme

Exploiting an analogy with the ideal gas, Cohen (2001) showed that an ensemble of weakly-interacting convective cells in statistical equilibrium has a pdf of mass flux per cloud that is exponential,

$$p(m) = \frac{1}{\langle m \rangle} \exp\left(\frac{-m}{\langle m \rangle}\right) dm$$

Here m is the mass flux of a single cloud, and the angled brackets denote ensemble averages. The distribution has been verified in CRM simulations of radiative-convective equilibrium. It is remarkably robust, the exponential shape holding for a wide range of forcings and over most of the troposphere.

In our stochastic parameterization, we launch convective plumes with the above distribution of fluxes imposed at the LCL. The assumptions leading to the exponential distribution include a statement of equilibrium that enables one to link the destabilizing forcing mechanisms with the convective response. The strength of the response is can be characterized by the ensemble mean mass flux of the full cumulus field, $\langle M \rangle = \langle N \rangle \langle m \rangle$, where $\langle N \rangle$ is the mean number of cumulus elements present. $\langle M \rangle$ is a normalization factor that can be regarded as some function of processes operating on the large scale. It is calculated with a CAPE closure method, in which the CAPE is based on the full ensemble of entraining plumes. The closure itself operates on an equilibrium spatial scale that is dependent upon the forcing (it uses an averaging distance related to the mean inter-cloud separation).

Each individual convective plume is parameterized as a distinct entity, which may persist in the model over multiple timesteps. We must specify the properties and behaviour of each plume, given m, the mass flux at the LCL. A one-dimensional plume model is required for this purpose. We use the plume model of the Kain-Fritsch scheme (Kain, 2004): this contains a buoyancy sorting algorithm and has been chosen because it is designed to be responsive in a realistic way to details of its environment. Thus, when used in a stochastic framework, it allows convective fluctuations in the history of the local environment to influence the properties of individual plumes at the present time. The plume model is linked to the stochastic pdf by assuming that the plume radius is proportional to the square root of the randomly-chosen mass flux. The radius parameter of the plume model is a controlling factor in the entrainment calculations.

4. TESTING THE SCHEME

We have tested the scheme in radiative-convective equilibrium using the UM single column model (SCM). The aim is to replicate in a statistical sense the behaviour of the CRM subject to the same forcing. A variety of results from the tests will be presented at the conference. Here we outline some of the salient points, contrasting the stochastic scheme with the standard, deterministic, implementation of the Kain-Fritsch scheme, which has only a single cloud type with a single radius.

Similar mean equilibrium states are achieved. However, the number of cumulus elements present in the stochastic scheme fluctuates significantly around a mean of ~30, for a nominal grid-box size of 128km. Of course, this number scales with the grid-box area. By contrast, regardless of the grid size, the original Kain-Fritsch parameterization gives a single plume, which is present around 50% of the time. A pdf of the total mass flux $\langle M \rangle$ produced by the stochastic scheme is shown in Figure 2. This is in good agreement with both theory (Cohen, 2001) and the pdf found in the CRM (not shown). By contrast, the pdf for a deterministic scheme has a spike at zero flux (no plume present), together with an extremely narrow spike at some fixed value of flux (plume present, with weak spread from variations in the environmental conditions).

The mass fluxes above the LCL are unconstrained and there is no reason a priori to expect the stochastic scheme to agree with details of the CRM. However, some agreement is obtained, and in particular, exponential mass flux distributions have been achieved at other heights.

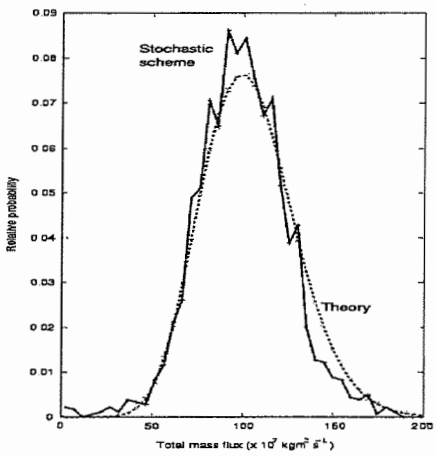

Figure 2. Pdf for the total mass flux, *M*: theoretical result and distribution in the SCM from the stochastic scheme.

5. CONCLUSIONS

We have constructed a stochastic convection scheme, which introduces grid-scale variability in a form that has a sound physical basis. The character of the variability is both verifiable and verified. Single-column tests have shown that the scheme can produce a good representation of the mean convective state and the statistical variations about that state. We are currently exploring the behaviour of the scheme in a full 3D model.

6. ACKNOWLEDGEMENTS

R. Plant acknowledges funding from the UWERN programme, supported by NERC. We are grateful to B. Cohen for providing us with data from her CRM simulations.

7. REFERENCES

Arakawa, A. and Schubert, W. H., 1974: Interaction of a Cumulus Cloud Ensemble with the Large-Scale Environment. Part I. J. Atmos. Sci., **31**, 674-701.

Buizza, R., Miller, M. and Palmer, T. N., 1999: Stochastic Representation of Model Uncertainties in the ECMWF Ensemble Prediction System, Quart. J. Roy. Met. Soc., **125**, 2887-2908.

Cohen, B. G., 2001: Fluctuations in an Ensemble of Cumulus Clouds. PhD thesis, University of Reading.

Gregory, D. and Rowntree, P. R., 1990: A Mass Flux Convection Scheme with Representation of Cloud Ensemble Characteristics and Stability-Dependent Closure. Mon. Wea. Rev., **118**, 1483-1506.

Horinouchi, T. et al., 2003: Tropical Cumulus Convection and Upward-Propagating Waves in Middle-Atmospheric GCMs. J. Atmos. Sci., **60**, 2765-2782.

Kain, J. S., 2004: The Kain-Fritsch Convective Parameterization: An Update. J. Appl. Meteorol., **43**, 170-181.

Lin, J. W. B. and Neelin, J. D., 2003: Toward Stochastic Deep Convective Parameterization in General Circulation Models. Geophys. Res. Lett., **30** (4), 1162-1165.

Majda, A. J. and Khouider, B., 2002: Stochastic and Mesoscopic Models for Tropical Convection, Proc. Nat. Acad. Sci., **99**, 1123-1128.

Zhang, F., Snyder, C. and Rotunno, R., 2003: Effects of Moist Convection on Mesoscale Predictability. J. Atmos. Sci., **60**, 1173-1185.

SENSITIVITIES IN MODEL RESULTS DUE TO CHANGES IN THE PARAMETERIZATION OF CLOUD MICROPHYSICS

Thorsten Reinhardt* and Ulrike Wacker

Alfred-Wegener-Institut für Polar- und Meeresforschung, D-27515 Bremerhaven, Germany

1 INTRODUCTION

Atmospheric ice particles show a great variety of shapes. A compilation of natural shapes can be found e. g. in the classification of Magono and Lee (1966) or in the paper of Locatelli and Hobbs (1974).

In atmospheric prediction models the effects of cloud microphysical processes are considered in parameterized form. Usually only a few categories of ice particles are taken into account and their shape parameters are prescribed. E. g. Walko et al. (1995) use in their model RAMS five categories of ice particles (pristine ice crystals, snow, aggregates, graupel, and hail) while the operational forecast models of the British (Wilson and Ballard, 1999) and German (Doms and Schättler, 1999) weather services consider only one respectively two species of ice particles. Thereby the natural variety of ice particle types cannot be considered.

In this contribution we study the influence of assumptions for ice particle properties on model results. To this end we start with the derivation of generalized expressions of the transformation rates for accretion/riming, deposition, and the sedimentation flux. Based on sensitivity studies with the Lokal-Modell (LM) of Deutscher Wetterdienst (DWD) we will then evaluate the sensitivity of simulated fields of condensate concentration and precipitation rate to the prescribed properties of the ice particles.

2 GENERALIZED PARAMETERIZATION EQUATIONS

In LM, the effects of cloud microphysical processes are parameterized, similar to other numerical weather prediction models, by a scheme considering the H_2O categories water vapor, cloud water, rain, and ice. In such schemes each species is characterized by one moment of the particle size distribution. Such concepts inevitably require certain relationships between mass and size and between sedimentation velocity and size. It is common practice to use relationships which are fits to observations in the form of power laws:

$$m(D_*) = aD_*^x \qquad \text{and} \qquad v(D) = v_0 D^y \ , \quad (1)$$

with D_*: characteristic particle diameter, D: equivalent diameter of a spherical water drop with same mass, a, v_0, x, y: fitted parameters. The relationships (1) used in this study are taken from Locatelli and Hobbs (1974) for ice particles and from Kessler (1969) for rain drops. With assumptions familiar in parameterization theory and the given relationships from Eq. (1), expressions for the mass sedimentation flux and the conversion rates are derived. This finally yields the following equations for the sedimentation flux:

$$F = \tilde{d} P_{\mathrm{i,r}}^{\delta} \ , \quad (2)$$

for the riming rate:

$$S_{\mathrm{rim}} = bCP_{\mathrm{i,r}}^{\beta} \ , \quad (3)$$

and for the vapor deposition rate:

$$S_{\mathrm{dep}} = \alpha_1(1+\alpha_2 P_{\mathrm{i}}^{\gamma_1})(q_{\mathrm{v}} - q_{\mathrm{v,sat}})P_{\mathrm{i}}^{\gamma_2} \ , \quad (4)$$

with C and P: mass fractions of cloud water and precipitation species (ice/rain), q_{v}: mass fraction of water vapor, $q_{\mathrm{v,sat}}$: saturation mass fraction of water vapor with respect to ice.

The coefficients $\tilde{d}$, b, and $\alpha_{1,2}$, and the exponents β, δ, and $\gamma_{1,2}$ are uniquely determined. They depend on, among other things, the parameters a, v_0, x, y from Eq. (1) and hence, carry the information on the particular particle type. For the melting rate, we yield an expression analogous to Eq. (4). A detailed derivation of Eqs. (2) and (3) can be found in Wacker (2000).

In Fig. 1 we compare the riming/accretion rates, and the deposition rates as functions of the mass

* Present Affiliation: Deutscher Wetterdienst, D-63067 Offenbach, Germany

Corresponding author's address: Ulrike Wacker, Alfred-Wegener-Institut für Polar- und Meeresforschung, Postfach 120161, D-27515 Bremerhaven, Germany; E-Mail: uwacker@awi-bremerhaven.de.

fractions of ice and rain for several ice particle types and for rain drops. Note the logarithmic scaling of the axes. The transformation rates related to the different particle types can differ at a given precipitation mass fraction by a factor of up to ten. Thus it can be expected that these large differences in the transformation rates for different particle types also affect model results when choosing different precipitating ice particle types in the parameterization.

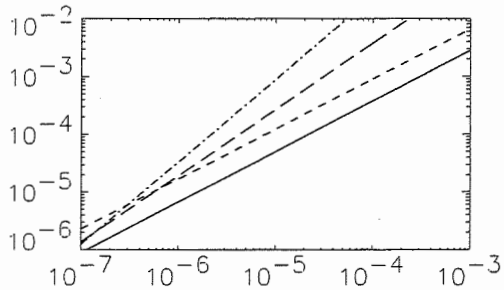

Fig. 1: Riming and accretion rates per mass fraction of cloud water, $S_{rim/acc}/C$, in s^{-1}, as functions of mass fraction of ice and rain, resp., for the following particle types: rain drops (———), unrimed aggregates (- · - · - ·), densely rimed aggregates (— — —), lump graupel (- - - - -).

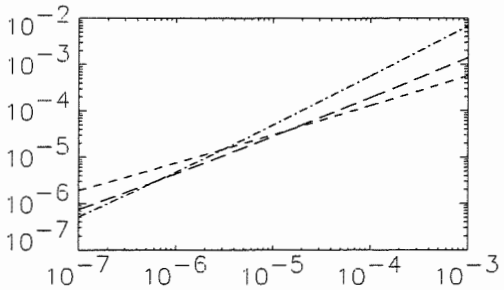

Fig. 2: Deposition rates normalized to ice supersaturation, $S_{dep}/(q_v - q_{v,\,sat})$, in s^{-1}, as functions of mass fraction of ice. Ice particle types as in Fig. 1.

3 SENSITIVITY STUDIES WITH LM

In this section we present sensitivity studies carried out with the Lokal-Modell (LM) with respect to different prescribed precipitation ice particle types. The grid-scale cloud parameterization in LM is a Kessler-type scheme extended by the ice phase (Doms and Schättler, 1999). The condensate categories considered are cloud water, rain, precipitating ice, and—optionally—(non-precipitating) cloud ice. For the precipitation species—like in many models—equilibrium within vertical columns is assumed, i. e. the cloud physical source rates always balance the divergence of the sedimentation flux, and the tendency term and advective effects are all neglected.

The transformation rates for precipitating ice collecting cloud droplets or cloud ice crystals, for deposition, and for melting, and the magnitude of the mass sedimentation flux depend explicitly on the assumptions on the particular ice particle type, as shown in Section 2.

To show the impact of the assumptions about the ice particle type on the model results, we discuss case studies of a stationary two-dimensional flow over a bell-shaped mountain. The forcing is a geostrophic flow of 20 m/s from the left. A horizontal mesh size of 7 km and 40 vertical levels are used.

These simulations are carried out in two versions of the parameterization scheme. They either treat non-precipitating condensate as one single category cloud water or as two categories cloud water and cloud ice. In the scheme neglecting cloud ice, precipitating ice is initiated from cloud water, whereas, in the scheme including cloud ice, cloud ice is nucleated from water vapor and precipitating ice is initiated by growth of cloud ice particles due to deposition and aggregation.

Fig. 2 shows the mass fraction of cloud water in simulations neglecting cloud ice, for precipitation ice particles interpreted as graupel and as unrimed aggregates, respectively. Precipitation falls out only from the primary cloud formed at the windward side of the mountain.

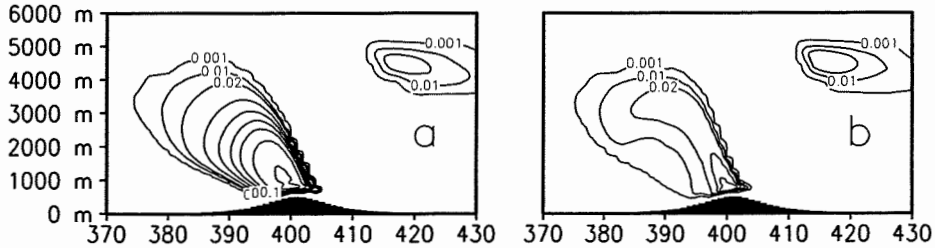

Fig. 2: Vertical cross section of cloud water massfraction in g/kg. Isolines: 0.001, 0.01, 0.02, 0.04, 0.06, 0.08, 0.10, 0.13, 0.18. Precipitation ice particles interpreted as a) graupel, b) unrimed aggregates. Abscissa labeled as distance from inflow boundary in gridpoints (mesh size: 7 km).

	cloud ice	no	no	yes	yes
	precip. ice particle type	graupel	unr. agg.	graupel	unr. agg.
	cloud water	27.462	7.460	11.387	1.281
	cloud ice	-	-	3.423	1.562
	precipitation ice	7.319	11.341	11.663	18.806
	rain water	1.925	1.530	2.325	1.696
CW→PI	riming	3.74 (0.44)	10.22 (0.82)	4.22 (0.27)	8.49 (0.51)
CW→RW	shedding	0.00 (0.00)	0.10 (0.01)	0.01 (0.00)	0.18 (0.01)
CW→RW	cloud water autoconv.	2.55 (0.30)	0.63 (0.05)	4.76 (0.31)	0.71 (0.04)
CW→PI	nucleation	1.58 (0.19)	0.69 (0.05)	-	-
WV→PI	deposition	1.24 (0.15)	2.93 (0.23)	2.28 (0.15)	7.39 (0.45)
CW→RW	accretion	0.78 (0.09)	0.05 (0.00)	0.61 (0.04)	0.03 (0.00)
PI→RW	melting	5.75 (0.67)	12.89 (1.02)	9.72 (0.63)	16.53 (1.00)
RW→PI	freezing	0.33 (0.04)	0.11 (0.01)	0.36 (0.02)	0.03 (0.00)
RW→WV	evaporation	1.16 (0.14)	1.40 (0.11)	1.28 (0.08)	1.52 (0.09)
PI→WV	sublimation	0.21 (0.02)	0.63 (0.05)	0.23 (0.02)	0.80 (0.05)
CI→PI	aggregation	-	-	0.17 (0.01)	0.35 (0.02)
WV→CI	cloud ice deposition	-	-	6.10 (0.40)	2.46 (0.15)
CI→PI	cloud ice autoconv. (agg.)	-	-	1.07 (0.07)	0.22 (0.01)
WV→PI	cloud ice autoconv. (dep.)	-	-	3.76 (0.24)	1.45 (0.09)
CI→CW	cloud ice melting	-	-	0.00 (0.00)	0.00 (0.00)
CI→WV	cloud ice sublimation	-	-	1.04 (0.07)	0.43 (0.03)
(RW+CI)→PI	rain cloud ice coag.	-	-	0.24 (0.02)	0.00 (0.00)
	precipitation rate	8.53 (1.00)	12.59 (1.00)	15.38 (1.00)	16.50 (1.00)

Table 1: Totals over primary (windward side) cloud. Condensate content in 10^3 kg per m in y-direction, conversion rates and precipitation rates in kilogram per meter in y-direction and second and (in brackets) relative to precipitation rate. First column shows the categories involved in the conversions. WV stands for water vapor, RW for rain water, CW for cloud water, CI for cloud ice, and PI for precipitating ice. Cloud ice nucleation does not occur in this stationary situation, because it is only considered at gridpoints where cloud ice is not there.

Table 1 gives a list of the totals of the condensate species and of the microphysical conversion rates (integrated over the primary cloud) for simulations with precipitating ice either interpreted as graupel or unrimed aggregates, and either using the parameterization scheme version including or neglecting cloud ice.

From Fig. 2 (for simulations without cloud ice) and from Table 1 we can see that with precipitating ice interpreted as graupel the cloud water content is everywhere higher than in the simulation assuming the precipitating ice particles to be unrimed aggregates. Table 1 shows that this finding is independent, whether cloud ice is considered or not; moreover, cloud ice concentration is also larger in the "graupel" case.

Due to their larger surface area, unrimed aggregates grow more efficiently than graupel by water vapor deposition and by collecting water droplets (riming) and cloud ice crystals (aggregation). On the other hand, due to their lower sedimentation velocity, the same mass fraction of precipitating particles is associated with a smaller sedimentation flux. For these reasons, we find in the "unrimed aggregates" cases less cloud water and cloud ice, but more precipitating ice than in the "graupel" cases. Despite the lower cloud water content, the riming and aggregation rates are still significantly higher in the "unrimed aggregates" cases than in the "graupel" cases.

With respect to surface precipitation, in the simulations without cloud ice we find a significantly higher value in the "unrimed aggregates" cases than in the "graupel" cases. In the simulations considering cloud ice there is a much smaller difference. This can be explained by the reduced importance of collection processes (riming/aggregation) which strongly depend on the assumed ice particle type. Instead, in the simulations with cloud ice the precipitating ice particle mass grows very efficiently due to cloud ice processes which do not explicitly depend on the precipitating ice particle type.

There is also a difference in the precipitation rate for liquid and solid particles: The "unrimed aggregates" case provides all surface precipitation as rain whereas in the "graupel" case a small portion of the precipitation reaches the ground as ice particles (not shown). This finding is not surprising: Compared to unrimed aggregates, graupel particles have a smaller melting rate, therefore in the "graupel" case some portion of solid precipitation is not melted before reaching the ground.

The impact of the prescribed ice particle type on model results can also be found in simulations of real weather situations. A series of 12 consecutive days of LM forecasts for a domain covering Germany was run. Precipitating ice particles were either interpreted as unrimed aggregates or graupel. Cloud ice was not considered. The main findings from that comparison were the following: Mean area precipitation over a large area like Germany did not depend significantly on the assumed ice particle type. However, comparing individual grid points, larger differences between the two cases were found. In particular, the precipitation maxima in the "unrimed aggregates" cases were higher than in the "graupel" cases whereas in areas with low precipiation quite often in the "graupel" cases more precipitation was found. In contrast to the low sensitivity in simulated area mean precipitation, simulated condensate contents were—like in the twodimensional simulations—found to be quite sensitive to the prescribed ice particle types: Mean simulated cloud water content was more than twice as high in the "graupel" cases as in the "unrimed aggregates" cases while the simulated precipitation ice content was about 50 % higher in the "unrimed aggregates" than in the "graupel" cases.

4 DISCUSSION

It has been shown that in strongly idealized two-dimensional model studies as well as in the simulation of real weather situations the choice of the particular ice particle type in the cloud microphysics parameterization can have great impact on simulated fields of condensate contents and of surface precipitation. To document this effect, two very different particle types were chosen, i. e. graupel and unrimed aggregates. Of course, unrimed ice particles will change their habits towards those of rimed particles when growing by riming. On the other hand, particles consisting mostly of rime like graupel can occur only *after* heavy riming. So in general the uncertainty caused by prescribing a somehow "mean" ice particle type should be smaller than the range of model results shown in this study.

In current parameterization schemes, it is unavoidable to prescribe the ice particles' properties. The results shown in this contribution make clear that in these schemes the choice of just these ice particle types and their properties are relevant for simulated fields of condensate contents and (to a lower extent) precipitation rates. Remedy to that uncertainty would be the development of parameterization schemes which specify the ice particle type depending on the particles' history.

5 ACKNOWLEDGEMENTS

The authors are grateful to the staff of DWD's Geschäftsbereich Forschung und Entwicklung for providing LM and for their support. This research was supported by the Deutsche Forschungsgemeinschaft (grant WA 1334/1-1,2).

References

Doms, G. and U. Schättler, 1999: *The nonhydrostatic Limited-Area Model LM (Lokal-Modell) of DWD. Part I: Scientific Documentation.* DWD, GB Forschung und Entwicklung.

Kessler, E., 1969: *On the Distribution and Continuity of Water Substance in Atmospheric Circulations. Meteor. Monogr.*, **10**, Nr. 32, Amer. Meteor. Soc., Boston, 84 S.

Locatelli, J. D. and P. V. Hobbs, 1974: Fall speeds and masses of solid precipitation particles. *J. Geophys. Res.*, **79**, 2185–2197.

Magono, C. and C.V. Lee, 1966: Meteorological classification of natural snow crystals. *J. Fac. Sci. Hokkaido Univ. Ser. 2, 1*, 321–362.

Wacker, U., 2000: Influence of the type of condensate particles on cloud physical quantities. *Phys. Chem. Earth (B)*, **25**, 91–99.

Walko, R. L. , W. R. Cotton, M. P. Meyers and J. Y. Harrington, 1995: New RAMS cloud microphysics parameterization. Part I: The single-moment scheme. *Atmos. Res.*, **38**, 29–62.

Wilson, D. R. and S. P. Ballard, 1999: A microphysically based precipitation scheme for the UK Meteorological Office Unified Model. *Q. J. R. Meteorol. Soc.*, **125**, 1607–1636.

MODELLING CIRRUS CLOUDS IN THE TROPICAL TROPOPAUSE LAYER

C. Ren and A. R. MacKenzie

Environmental Science Department, Lancaster University, Lancaster LA1 4YQ, UK

1. INTRODUCTION

Recent observations have shown that optically thin cirrus clouds are ubiquitous below the cold point tropopause over the tropical zone. These clouds contribute to the dehydration of air entering the stratosphere, a crucial process in determining the global distribution of lower stratospheric water vapour. Observations also show that stratospheric water vapour has increased in recent decades, providing more ozone-destroying HOx radicals, and more condensate for polar stratospheric clouds, and so influencing ozone depletion and climate change.

However, the formation, evolution, and dissipation of tropical cirrus clouds are not well quantified, especially for those clouds not connected with convection. Nor is it clear by how much they dehydrate air entering the stratosphere. In this study, assuming ice particles form from homogeneous freezing of aerosol droplets, we develop a particle-size-resolving microphysical model and a parameterisation suitable for large-scale models. We also combine the microphysical modelling with trajectories to assess the dehydration of air parcels.

2. A DETAILED MICROPHYSICAL MODEL

A detailed microphysical model is set up and run as the following. An offline trajectory model (Methven, 1997) is run using the ECMWF analysis data to provide the histories of temperature T, pressure p, temperature lapse rate, Γ, and position of air parcels. Knowing the thermodynamic history of an air parcel, its microphysics is simulated in a partial-column framework following the trajectory (figure 1). A parameter, called the cloud-top reference height, is introduced for use in calculating dehydration.

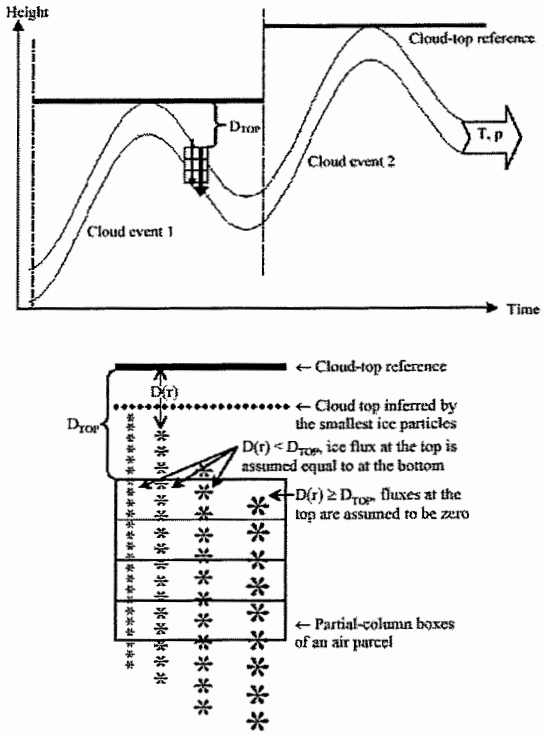

Figure 1. Sketch of the model structure. **(Above)** A partial-column microphysical model following a trajectory in the upper troposphere and lower stratosphere. Cloud events, which only take place below the cold-point tropopause, are determined by the vertical movement of an air parcel. Corresponding to each cloud event, the cloud-top reference is given as the highest point of the trajectory. D_{TOP} is the distance from the upper box of the model to the cloud-top reference. The thinner downward arrow represents smaller ice particles, which do not dehydrate the uppermost box because of "top-up" from above; the thicker downward arrow represents bigger ice particles, which do dehydrate the uppermost box because they have fallen more than the distance D_{TOP} since they were formed. This is shown in more detail below. **(Below)** The estimation of ice fluxes at the top of the uppermost box for different ice particle sizes.

Corresponding author's address: Chuansen Ren, Department of Environmental Sciences, Lancaster University, Lancaster LA1 4YQ, U.K; E-Mail: c.ren@lancaster.ac.uk.

For a given total water content (usually determined by synoptic conditions), every other property will be reasonable if the ice number is reasonable in our model. The model agrees with existing box models in the ice number in test scenarios without sedimentation. With sedimentation, the model shows some features of APE-THESEO observations, such as the number and size of ice crystals in tropopause cirrus clouds (figure 2 and 3). The model is also run along typical trajectories to investigate the dehydration ability of various cirrus clouds, and to study the microphysical mechanism linking total entry water with the temperature.

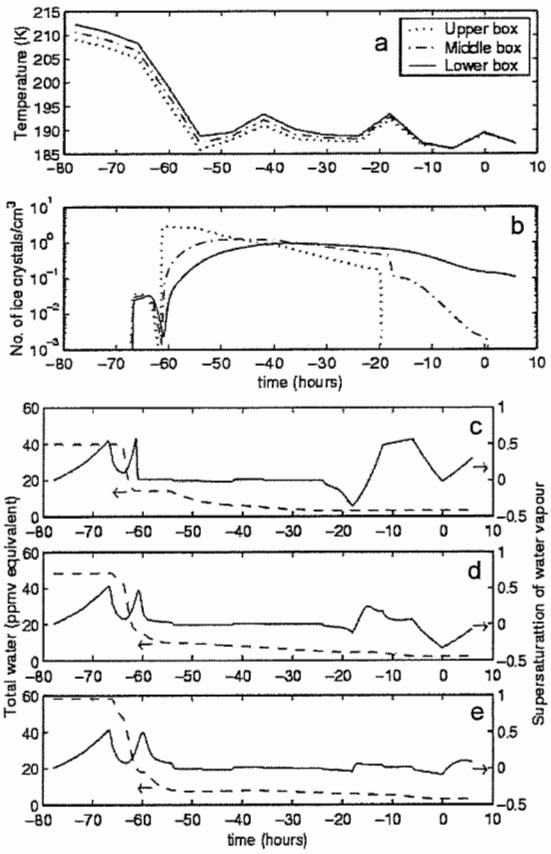

Figure 2. A case study of cirrus clouds. Dehydration takes place in the lower tropical tropopause layer from –65 hour, continues to near the cold-point tropopause. **(a)** Temperatures inputted into the three boxes; **(b)** Ice particle numbers in each box; Supersaturation (to the right-side coordinate) and total water (to the left-side coordinate) in the upper box **(c)**; in the middle box **(d)**; and in the lower box **(e)**. Comparison with data (see figure 3) is at 0 hours.

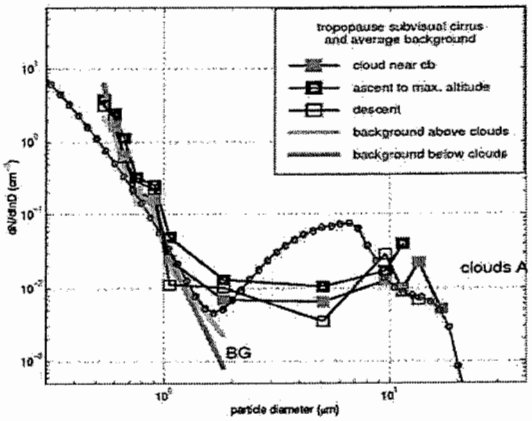

Figure 3. Comparison of modelled size distribution (marked with dense circles) with APE-THESEO in-situ measurements on February 24, 1999 (see legend, Thomas et al., 2002) near the tropopause.

3. A PARAMETERISATION

A simplified version of the model has been developed, which can be used as a parameterisation in large-scale model. In the parameterisation, ice particles are formed only when the homogeneous-nucleation-required supersaturation has been reached, then water vapour relaxes towards the saturated condition in the cloud according to a diagnostic e-folding time. The fall-speed of ice particles is calculated assuming monodisperse ice crystals. The dehydration is, then, calculated using the fall-speed of ice particles, the position of the air parcel, and the cloud-top reference, which is introduced in last section. The dehydration behaviour of the parameterisation is compared with other dehydration schemes and the detailed model (figure 4). The instantaneous dehydration scheme includes no size-resolving cloud microphysics. An earlier parameterisation by Gettelman et al. (2002) prescribes three time-scales and fixes the supersaturation hurdle at 10%. In our scheme, all microphysical variables are determined by the thermodynamic history of an air parcel, so the parameterisation maintains more of the essential cloud physics, without significantly increasing calculation-time. Ensemble runs of large (e.g. space-filling) trajectory sets are carried out to estimate the influence of large-scale condensation on the transport and distribution of water vapour in the tropical tropopause region. Figure 5 shows the occurrence of cirrus clouds.

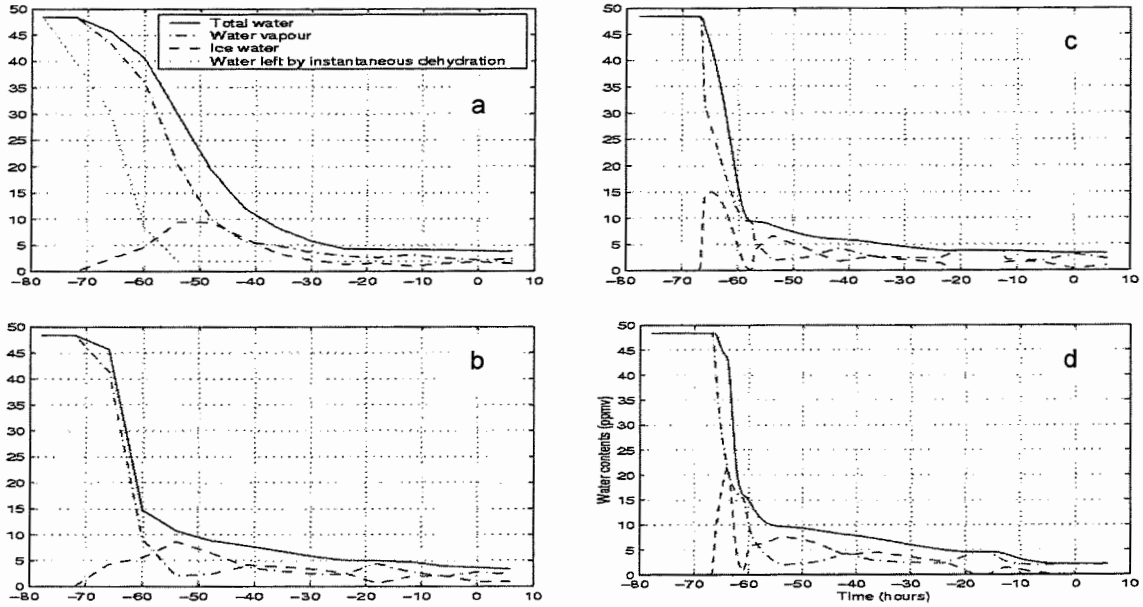

Figure 4. Comparison of dehydration behaviour for different calculation schemes. **(a)** Gettelmann et al. (2001) scheme; **(b)** our parameterisation with 6-hour time-step, the same as (a); **(c)** our parameterisation with 20-minute time-step, typical for a large-scale model; **(d)** results from the middle box of the detailed microphysical model. For each scheme, total water (solid lines, the uppermost), water vapour (dashdotted lines, close to total water at the beginning), and ice water (dashed lines) are given in ppmv. The instantaneous dehydration scheme has only one output, water vapour, which is given in (a) by the dotted line.

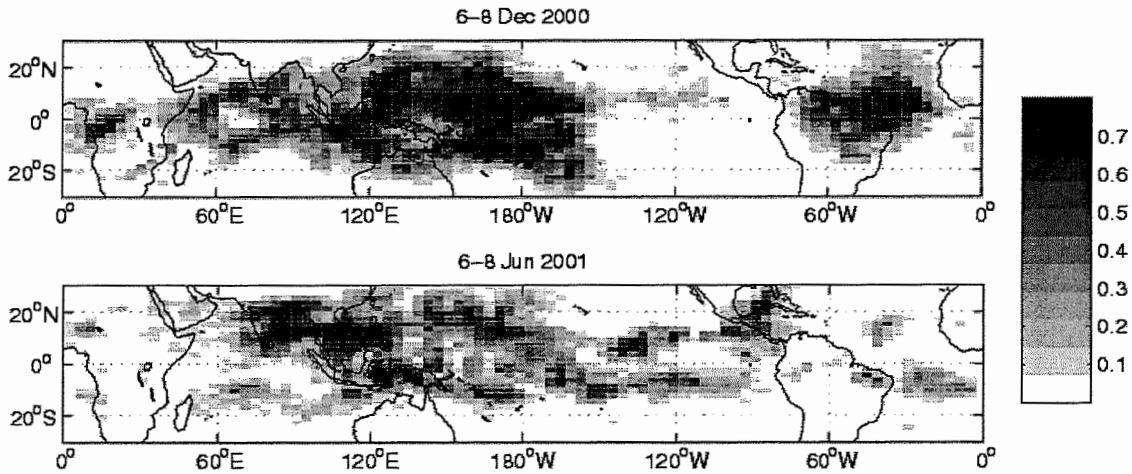

Figure 5. The frequencies of optically thin clouds in the tropical tropopause layer. For each case, 12 sets of space-filling backward trajectories, upon which the Ci-dehydration parameterisation was applied, were generated at 6hr-intervals. The frequency at a point was calculated by counting how many times there was ice water out of the 12 snapshots. The dark regions in the figure represent the regions where cirrus clouds are most likely to appear, while the white means no appearance of clouds on any of the three levels of 360, 370, and 380 Kelvin potential temperatures. The frequencies shown in this figure generally match those in figure 2 of Dessler and Yang (2003), which is not shown here. Since both studies are "first attempts", the results support each other. Please note, the blank areas in the Dessler and Yang figure mean that no reliable data are available.

4. CONCLUSIONS

A Lagrangian, partial-column, microphysical model has been established, which can be used to simulate the nucleation, growth, and sedimentation of ice crystals in an air parcel. The model agrees well with existing box models in test scenarios without sedimentation, and, with sedimentation, shows some features of APE-THESEO observations, such as the number and size of ice crystals in tropopause cirrus clouds. Model runs show that homogeneous nucleation appears to provide a sufficient number of ice particles to match cirrus cloud observations, even though supersaturation of about 0.6 with respect to ice is required (Koop et al., 2000). The supersaturation produced by internal waves can dwarf the supersaturation hurdle for homogeneous nucleation, and consequently influences later cloud events.

A simple, but physically sound, parameterisation has been developed. The parameterisation is based on the e-folding time for a cloud to relax water vapour towards saturated conditions assuming a uniform size of ice crystals. All microphysical variables are determined by the thermodynamic history of an air parcel, so the parameterisation maintains more of the essential cloud physics, without significantly increasing calculation-time, than current parameterisations. The parameterisation has dehydration behaviour similar to the detailed model. Using this parameterisation, ensemble runs of large (i.e. space-filling) trajectory sets are carried out to estimate the influence of large-scale condensation on the transport and distribution of water vapour in the tropical tropopause layer. A boreal winter case and a summer case compare well with MODIS satellite results retrieved by Dessler and Yang (2003). In the winter case, the stratospheric 'fountain' region shows high occurrences of cirrus clouds. In contrast, in the summer case, the high-frequency region is less well defined. In summer, more water is allowed to enter the stratosphere than in winter, but dehydration has removed more water from the tropical tropopause layer.

Ensemble runs to estimate the annual cycle 'tape recorder' and the stratospheric water content trend are going to be carried out next.

Acknowledgements

Funded by NERC CWVC project NER/T/S/2000/00977, and EC TroCCiNOx project EVK2-CT-2001-00122.

Thanks to: P. Haynes, and V. M. Bonazzola, Cambridge University; J. Methven, University of Reading; B. Luo, and T. Koop, Swiss Federal Institute of Technology.

References

Dessler, and Yang, 2003: The distribution of tropical thin cirrus clouds inferred from Terra MODIS data. *J. Climate*, **16**, 1241-1247.

Gettelman, A., W. J. Randel, F. Wu, and S. T. Massie, 2002: Transport of water vapour in the tropical tropopause layer. *Geophys. Res. Lett.*, **29,** 10.1029/2001GL013818.

Koop et al., 2000: Water activity as the determinant for homogeneous ice nucleation in aqueous solutions. *Nature*, **406**, 611-614.

Methven, J., 1997: *Offline trajectories: Calculation and accuracy.* UGAMP Tech. Rep. 44, 18 pp. [Available from CGAM, University of Reading, Early Gate, Reading RG6 6BB, United Kingdom.]

Thomas, A. et al., 2002: In-situ measurements of background aerosol and subvisible cirrus in the tropical tropopause region. *J. Geophys. Res.*, **107,** 10.1029/2001JD001385.

Retrieving Inhomogeneous Clouds

Ronald Scheirer[1] and Sebastian Schmidt[2]

[1]Institut für Physik der Atmosphäre, German Aerospace Center, Wessling, D-82234, Germany
[2]Leibniz-Institut für Troposphärenforschung, Leipzig, D-04318, Germany

1. INTRODUCTION

According to IPCC (2001), the parameterization of the cloud-radiation interaction is one of the largest sources of uncertainty in our prediction of future climate. To improve such parameterizations, detailed three-dimensional (3D) radiative transfer studies are required, to quantify the impact of cloud inhomogeneity on the radiation budget.

A great challenge in 3D radiative transfer is the generation of realistic clouds as input to the sophisticated radiative transfer models (e.g. Petty, 2002 or Borde and Isaka, 1996). Currently, it is not possible to derive the required distribution of liquid water content and droplet sizes from observations of a single instrument. Passive satellite remote sensing instruments may provide a detailed horizontal distribution but fail to give any information about vertical profiles (e.g. Crewell et al., 1999). In-situ observations, on the other hand, may give data for any location but are usually restricted to only a few point measurements, e.g. along an aircraft flight track. Physical cloud-models (e.g. LES) on the other hand can provide the full 3D information of all needed microphysical properties but they do not necessarily represent real or even realistic cloud fields (Stevens and Lenschow, 2001). This study presents a method to retrieve 3D inhomogeneous clouds (described by liquid water content and effective radius) from aircraft measurements.

2. RETRIEVAL ALGORITHM

Clouds vary significantly in the three spatial dimensions and in time. It is only possible to retrieve clouds from aircraft observations if the clouds stay reasonably constant for the measuring time period but even then it remains a challenge to derive 3D cloud structures from measurements along a flight leg.

For this purpose, an automated algorithm, CLABAUTAIR (cloud liquid water content and effective radius retrieval by an automated use of aircraft measurements) was developed which scans aircraft measurements of liquid water content (LWC) and effective radius (R_{eff}) for characteristic patterns and extrapolates them to a complete 3D field. The method is illustrated in Figure 1a-f. Starting with measurements in a single horizontal layer (Figure 1a) the first step is to identify the main directions sampled by the aircraft (Figure 1b). This identification is necessary to avoid aliasing due to the connection of different flight legs, or in other words, to correlate only data collected within a reasonably small time interval during which the cloud may be considered constant. The next step is to calculate the autocorrelation functions along these directions (Figure 1c). Then the measured LWC and R_{eff} are filled into the model grid (Figure 1d). To extrapolate the observations, individual empty boxes are selected by random. The requested parameters (LWC and R_{eff}) for each of these boxes are calculated by a weighted (by the autocorrelation coefficient) average over filled boxes along the main directions (Figure 1e). Adjacent boxes from the next layer above and below the chosen one are taken into account with a fixed weight. This step is repeated until all boxes are filled. Finally, the probability density functions (PDF) of the measurements (including the cloud-free parts to permit cloud fractions less than 1) are mapped onto the thus derived spatial distributions. This is done for all cloudy layers separately. Figure 1f shows the final cloud field.

3. DATA AND APPLICATION

The first application of the algorithm to in-situ microphysical data was performed for a cloud situation which was measured during the first field experiment of the EC project INSPECTRO (influence of clouds on the spectral actinic flux in the lower troposphere) on September 14, 2002, on the coast of East Anglia, United Kingdom. On this day, a stable stratus layer which was moving into land at a speed of about 10 m/sec was observed between 500 and 1100 m altitude. The microphysical measurements used for this study were performed with a two-propeller research aircraft, a Partenavia P68B, which was equipped with meteorological, microphysical, and radiation instrumentation. The microphysical cloud properties were measured with a Fast Forward Scattering Spectrometer Probe (Fast-FSSP, Brenguier et al., 1998) and a Particle Volume Monitor (PVM-100, Gerber et al., 1994). The Fast-FSSP measures the cloud drop size distribution by detecting the forward scattering signal of each

Corresponding author's address: Ronald Scheirer, Institut für Physik der Atmosphäre, German Aerospace Center (DLR), Oberpfaffenhofen, D-82234 Wessling, Germany; E-Mail: ronald.scheirer@dlr.de

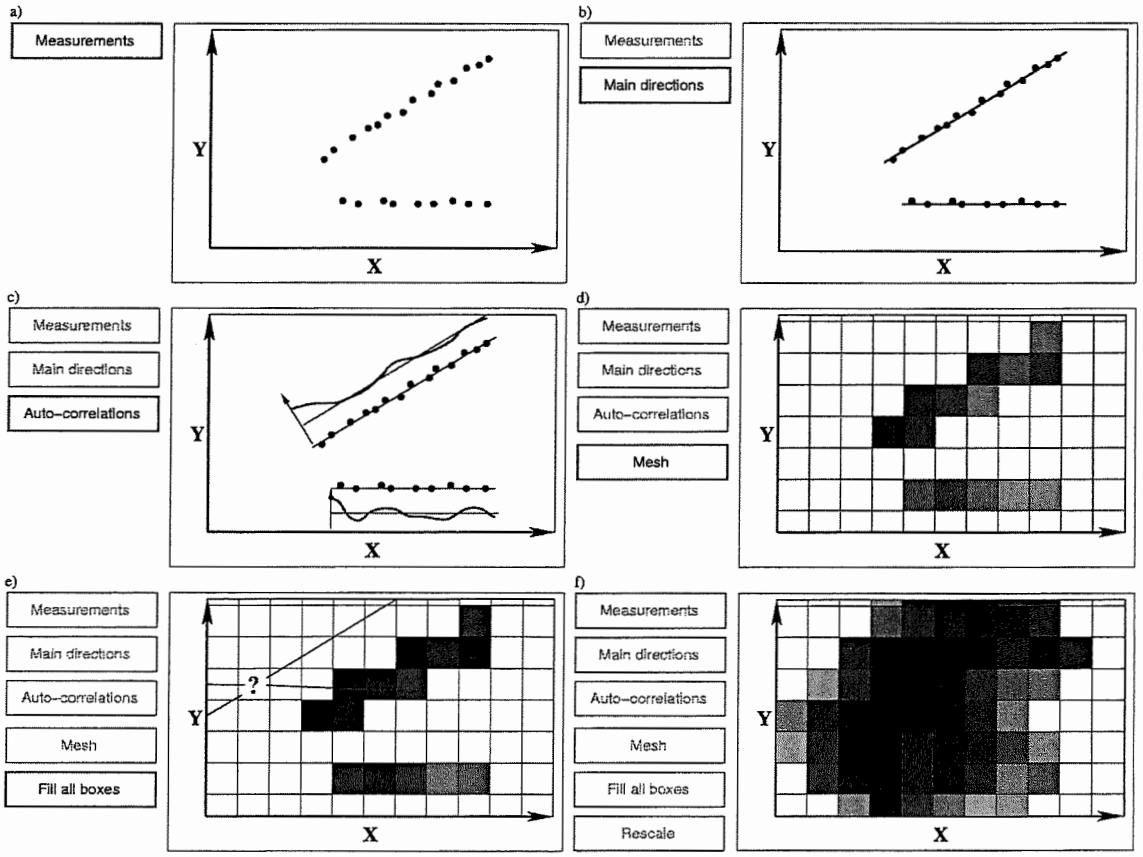

Figure 1: The six main steps of CLABAUTAIR. This Figure illustrates an approach to retrieve 3D clouds from aircraft measurements.

individual droplet passing a laser beam. From the drop size distribution, bulk parameters such as the LWC, the drop concentration, and R_{eff} can be derived. In contrast, the PVM-100A measures the LWC directly by detecting the scattering signal of an ensemble of droplets. For this study, the LWC measurements by the PVM-100A were used because of the high accuracy and temporal resolution of the data. The effective droplet radius R_{eff} was derived from the FSSP measurements because of its higher accuracy for size distributions.

In order to examine the three-dimensional cloud structure, several ascents and descents through the cloud layer were flown by the aircraft. In addition, one triangular flight pattern within the layer was performed. Figure 2 shows the two-dimensional PDFs of the LWC and R_{eff} for three different altitudes. They were determined by combining the measurements of the PVM-100A and the Fast-FSSP, and binning them into several height levels. The gray-scale in the plots corresponds to the probability of a particular LWC and R_{eff} at the respective level. These two-dimensional PDFs reflect the microphysical properties accumulated throughout the cloud layer. The layer cloud fraction as a macro-physical property is also deduced from the microphysical measurements. The horizontal structure is contained in the autocorrelation functions which are calculated for the three legs of the triangle.

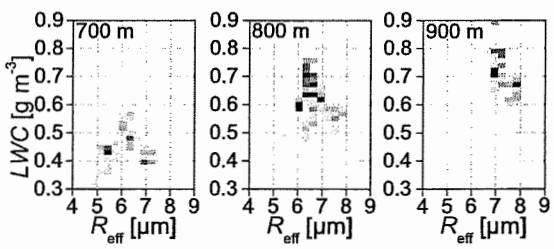

Figure 2: Two-dimensional PDF of the measured liquid water content and the effective drop radius at three altitudes.

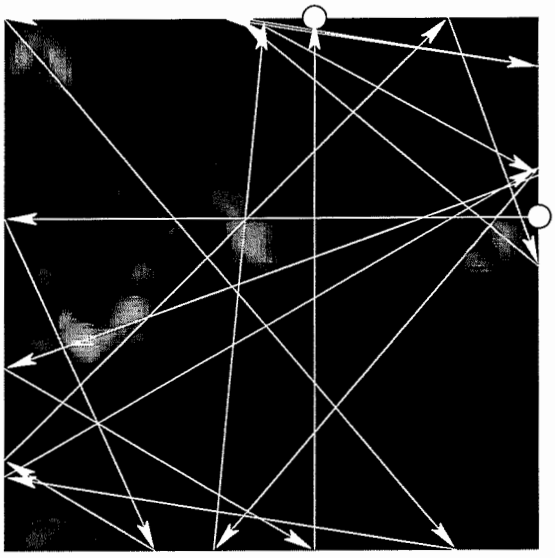

Figure 3: Liquid water path (LWP) for and flight legs within the selected LES cloud. Bright pixels denote large LWPs.

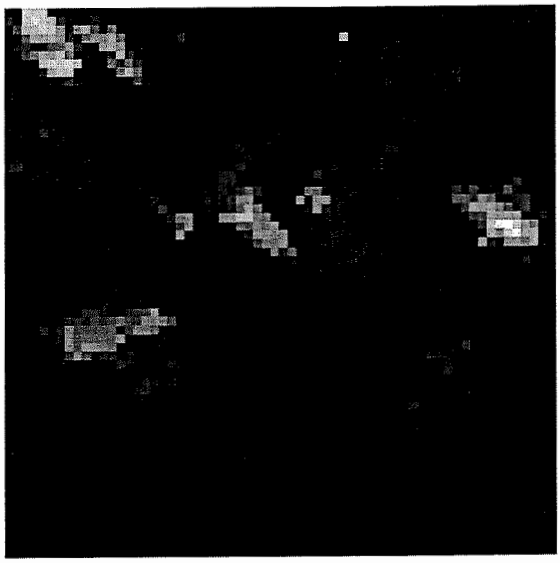

Figure 4: Liquid water path for the reproduced cloud.

4. RESULTS

As a first trial, the algorithm was tested with a well-known cloud field. Sampling a very inhomogeneous model cloud realization (a large eddy simulation (LES) Figure 3) along almost arbitrary flight tracks, we tested if CLABAUTAIR was able to reproduce the clouds in a statistically reasonable way. The LES cloud field provides a horizontal resolution of about 33m. With 192 times 192 boxes the length of both sides results in about 6.4km. The clouds are located between altitudes of 1130m and 2200m. For the retrieved cloud the horizontal resolution is reduced to about 100m. The measurements were simulated by taking local data of LWC and R_{eff} along strait lines at different altitudes, simulating real flight legs. The reproduced field (Figure 4) shows a promising agreement to its origin, so application to real measurements started.

In Figure 5, measured and reconstructed profiles of the LWC are compared, and the reconstructed layer cloud fraction is displayed (bars). The dashed lines show all PVM-100A measurements. At 800 m, the horizontal flight pattern was performed. The range of LWC values measured at this altitude reflects the high variability which prevails even in a stratus layer. The solid line shows the mean reconstructed LWC profile. The error bars indicate the standard deviation throughout the grid. It reproduces well the range of LWC values which were measured during the horizontal leg. The dash-dotted lines correspond to the maximal or minimal LWC values which are generated at the respective level. The layer cloud fraction is the portion of cloudy pixels at each level. From 700 to 900 m, nearly all pixels are occupied. Below and above, some cloud gaps occur. The cloud top and base heights vary approximately within 200 m.

The horizontal structure of the measured and reconstructed cloud is compared in Figure 6 by means of power spectra P_n which are shown here as a function of the wavenumber n. The dotted line with open circles shows the power spectrum which was calculated from PVM-100A measurements along one of the legs of the triangular pattern within the cloud layer (about 20 km length). The measurements are conform with the $n^{-5/3}$ scaling law (thin solid line) which is typically found for real clouds (Davis et al.,1996). The variability within the measured power spectrum is due to the short length

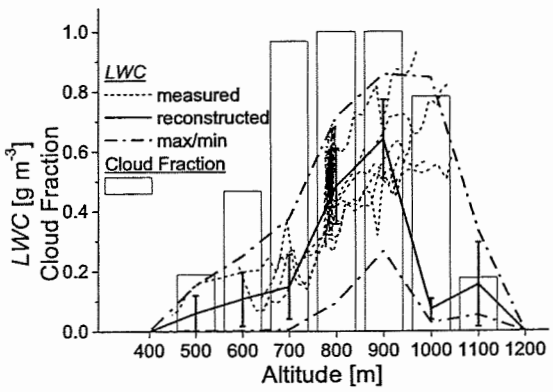

Figure 5: Measured and reconstructed LWC profile and reconstructed cloud fraction.

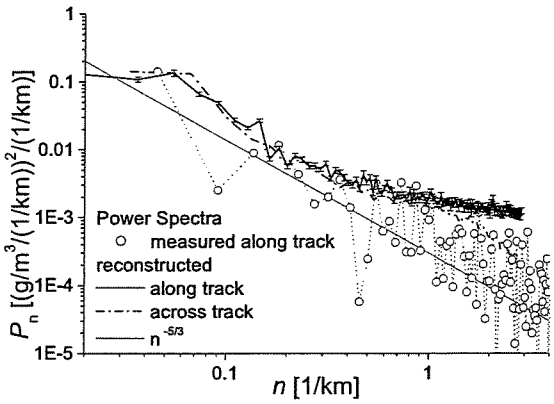

Figure 6: Measured and reconstructed Power Spectrum of the LWC.

of the leg. The power spectra from the reproduced cloud were obtained by calculating power spectra over horizontal lines throughout the grid and by subsequent averaging. The direction of the lines was chosen along and across the flight leg whose power spectrum is displayed. The solid line shows the averaged power spectrum of lines parallel to the leg direction. In general the $n^{-5/3}$ scaling is well reproduced. However, the variability is slightly overestimated by the generator for large wavenumbers. The dash-dotted line shows the averaged power spectrum from lines across the flight direction. In this case, the variability is more conform with the measurements. The power spectra for the PVM-100A data measured along the other legs of the in-cloud pattern are similar to the power spectrum which is displayed in Figure 6. Thus, the differences between power spectra along different directions of the reproduced cloud field cannot be explained by the measurements. However, the power spectra and the total variability of the reproduced cloud field (integrated power spectrum) agrees with the observations within the range of measurement uncertainty.

5. CONCLUSION

We found the characteristics of the simulated clouds to fit well to the observed counterparts. It can not be expected to match the real clouds in three dimensions with CLABAUTAIR because the input field is by no means complete. Nevertheless, the measured statistic is represented as well as the characteristic in spatial structure. This should be valid also for the spiky behavior (the intermittency, e.g. Davis et al., 1994) of natural clouds, if found within the measurements, i.e. if the database is really representative.

ACKNOWLEDGEMENTS

This work was funded by the European project INSPECTRO (Influence of clouds on the spectral actinic flux in the lower troposphere), contract EVK2-2001-00135. Enviscope GmbH, Frankfurt, Germany, operated the aircraft during the experiment: Thanks to R. Maser, D. Schell, and H. Franke, and to the pilot B. Schumacher.

REFERENCES

Borde, R., and H. Isaka, 1996, Radiative transfer in multifractal clouds, *J. Geophys. Res.*, **101(D23)**, 29461-29478.

Brenguier, J. L., T. Bourrianne, A. Coelho, J. Isbert, R. Peytavi, D. Trevarin, and P. Wechsler, 1998: Improvements of droplet size distribution measurements with the Fast-FSSP (Forward Scattering Spectrometer Probe). *J. Atmos. Oceanic Technol.*, **15**, 1077–1090.

Crewell, S., G. Hasse, U. Löhnert, H. Mebold, and C. Simmer, 1999, A Ground Ased Multi-Sensor System for the Remote Sensing of Clouds, *Phys. Chem. Earth (B)*, **24**, 207-211.

Davis, A., A. Marshak, W. Wiscombe, and R. Cahalan, 1994, Multifractal characterizations of nonstationarity and intermittency in geophysical fields: Observed, retrieved, or simulated, *J. Geophys. Res.*, **99(D4)**, 8055-8072.

Davis, A., A. Marshak, W. Wiscombe, and R. Cahalan, 1996, Scale Invariance of Liquid Water Distributions in Marine Stratocumulus. Part I: Spectral Properties and Stationarity Issues, *J. Atmos. Sci.*, **53**, 1538-1558.

Gerber, H., B. G. Ahrends, and A. S. Ackerman, 1994: New microphysics sensor for aircraft use. *Atmos. Res.*, **31**,, 235–252.

IPCC, 2001: *Climate Change 2001: The Scientific Basis. Contribution of Working Group I to the Third Assessment Report of the Intergovernmental Panel on Climate Change*, Houghton, J.T., Y. Ding, D.J. Griggs, M. Noguer, P.J. van der Linden, X. Dai, K. Maskell, and C.A. Johnson (eds.), Cambridge University Press, Cambridge, United Kingdom and New York, NY, USA, 881pp.

Petty, G.W., 2002, Area-Average Solar Radiative Transfer in Three-Dimensionally Inhomogeneous Clouds: The Independently Scattering Cloudlet Model, *J. Atmos. Sci.*, **59**, 2910-2929.

Stevens, B., and D.H. Lenschow, 2001, Observations, experiments and large eddy simulation, *Bull. Amer. Meteor. Soc.*, **82**, 283-294.

A COMPARISON OF SPECTRAL BIN AND TWO-MOMENT BULK MIXED-PHASE MICROPHYSICS

A. SEIFERT[1], A. KHAIN[2], A. POKROVSKY[2] AND K. D. BEHENG[3]

[1] National Center for Atmospheric Research, Boulder, USA

[2] Institute of the Earth Sciences, The Hebrew University of Jerusalem, Israel

[3] Institut für Meteorologie und Klimaforschung, Universität/Forschungszentrum Karlsruhe, Germany

1 Introduction

Quantitative precipitation forecast (QPF) and the investigation of aerosol-cloud interations are among of the most challenging research topics for the next decade and beyond. It is obvious that an improved representation of the cloud microphysical processes plays a key role for future aerosol-cloud-climate studies as well as for reaching the goals of mesoscale cloud-resolving QPF.

The most rigorous approach to describe cloud microphysical processes in cloud resolving models is the spectral bin formulation, which represents the size distributions by a number of discrete size bins and solves the corresponding budget equations, for as many hydrometeor types as considered. Compared to bulk schemes this method has the clear advantage of being the most detailed representation of the relevant physical processes and the different physical properties of particles of different sizes. Since aerosol particles acting as cloud condensation or ice nuclei are basic for initiation of hydrometeors a spectral bin model should be able to describe aerosol-cloud effects properly. Unfortunately, this approach suffers from a large computational effort, especially in three-dimensional models. But the spectral bin approach can be used as a benchmark to prove the validity of the much more ef?cient bulk schemes.

Representatives of advanced bulk schemes are so-called two-moment parameterizations which use, in addition to mass variables, also the number concentrations of the liquid and ice hydrometeors (Cotton et al. 1986; Murakami 1990; Reisner et al. 1998) as prognostic variables. At present, two-moment schemes are the most promising microphysical compromise, since they show a forecast skill superior to commonly used one-moment cloud microphysical schemes (Reisner et al. 1998).

Using the Hebrew University Cloud Model (HUCM), which includes the most detailed spectral bin microphysics module available today, we present a comparison of the two different modeling approaches.

Corresponding author's address: Axel Seifert, National Center for Atmospheric Research; P.O. Box 3000 Boulder, CO 80307, E-Mail: seifert@ucar.edu. NCAR is sponsored by the National Science Foundation.

2 Model description

The spectral bin microphysics model and the dynamical framework of this study is the Hebrew University Cloud Model (HUCM). The dynamical and thermodynamical equations solved in HUCM have been described by Khain and Sednev (1996) as well as Khain et al. (2000, 2001). The spectral bin microphysics of HUCM is based on solving prognostic equations for size distributions of seven hydrometeor types: water drops, three types of ice crystals, snow?akes, graupel and hail/frozen drops. To take into account the effects of atmospheric aerosols on cloud development and precipitation formation a size distribution for atmospheric aerosol particles, playing the role of cloud condensation nuclei (CCN), is considered. All relevant microphysical processes/interactions including droplet nucleation, primary and secondary ice generation, condensation/evaporation of drops, deposition/sublimation of ice particles, freezing/melting, and mutual collisions between the various hydrometeors are calculated explicitly.

The bulk scheme used here is a two-moment scheme. In contrast to previous ones, this scheme relies on a sophisticated parameterization of the warm phase coagulation processes autoconversion and accretion and deals with number and mass densities of cloud droplets

and raindrops (Seifert and Beheng 2001). Together with this warm phase scheme a two-moment mixed-phase cloud scheme has been developed that predicts the evolution of number as well as mass concentration of cloud ice, snow and graupel (Seifert and Beheng 2004). The nucleation of cloud droplets is treated explicitly using empirical CCN relations for maritime and continental conditions. This mixed-phase two-moment scheme has been implemented into HUCM so that the identical dynamical framework is used with both microphysical schemes.

3 Results

The study is based on two very different test cases: the simulation of a single deep convective cloud and a squall line system. In addition, the sensitivity of these cloud systems to changes of the CCN spectrum is investigated.

The ?rst case for the comparison is the well documented case of an isolated deep convective cloud based on the sounding from 13 August 1999, Midland/Texas (Khain et al. 2001). Assuming realistically continental CCN this is an example of a deep convective cloud sustaining a high amount of supercooled liquid water at upper levels and developing precipitation mostly via rather inef?cient ice phase processes.

For all simulations a high model resolution has been chosen with 250 m grid spacing in the horizontal and 125 m in the vertical. Convection has been initiated by arti?cial differential heating in the boundary layer.

All results are obtained by using, on one hand, the spectral bin microphysics scheme and, on the other hand, the two-moment bulk scheme mentioned above.

For brevity, here only the time series of the accumulated surface precipitation and the maximum updraft velocities are shown for maritime and continental CCN (Figures 1).

To elaborate differences related to CCN-effects also maritime CCN are prescribed. In this case surface precipitation starts after 35 min model time with maximum rainrates about 50 mm/h for both microphysics schemes. After 2 hours the accumulated surface precipitation amounts to 0.95 mm with the spectral bin model vs. 0.75 mm with the bulk model.

For continental CCN the onset of precipation is at about 50 min and the rainrates are much lower reaching only about 3 mm/h. In contrast to the maritime case, most precipitation originates from melted graupel and snow. The accumulated surface precipitation reaches only 0.1 mm with the bin scheme and 0.06 mm with the bulk

a) accumulated precipitation

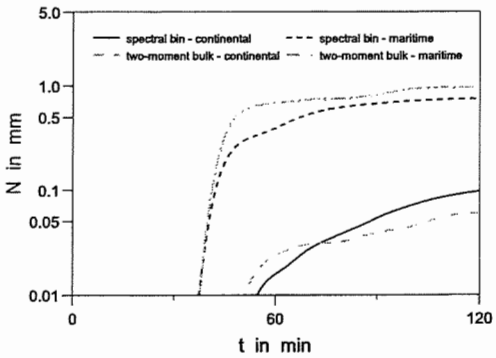

b) maximum vertical velocities

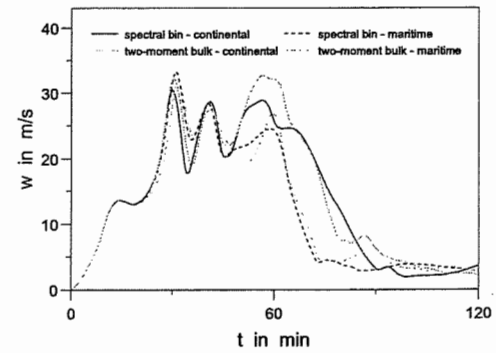

Figure 1: Time series of grid averaged accumulated surface precipitation in mm (a) and maximum vertical velocity in m/s (b) from the 4 Texas case simulations applying spectral bin (black lines) vs. two-moment bulk (grey lines) microphysics and assuming continental vs. maritime CCN as indicated.

scheme. Considering the differences in the details of both schemes the agreement is remarkable.

An almost perfect agreement of the maximum updraft velocities shown in Fig. 1b is found in the early stage of cloud development. Later on the differences between maritime and continental CCN assumptions are larger than the disagreement between the spectral bin and the two-moment bulk scheme. Both microphysical models show a longer lifetime of the updraft core in the continental case.

The second case is the formation of a typical maritime convective system observed on day 261 of the GATE ?eld experiment. For the simulations typical pro-?les from the 1200 UTC sounding aboard the Canadian ship *Quadra* have been taken. This sounding has been used in many previous modeling studies devoted

to maritime convection. In contrast to the Texas cloud, this convective system is to a large extent dominated by warm phase processes with secondary convection playing an important role. To study the sensitivity of the microphysical models for that case besides a maritime also a continental CCN relation is applied.

A major difference between the HUCM bin microphysics and the current version of two-moment bulk scheme is that the latter does not include a budget equation for CCN, but assumes a quasi-stationary background CCN. The spectral bin scheme explicitly predicts activation, nucleation and the depletion of CCN.

The simulations of the GATE case reveal that the spectral bin scheme predicts a strong decrease of the CCN concentration in secondary clouds, especially when assuming maritime CCN. Since evaporation of cloud droplets is currently not considered as a source in the CCN budget of the HUCM spectral bin microphysics, the decrease of CCN might be overestimated. To investigate the sensitivity of the bin model to the treatment of nucleation, we performed a second simulation with the bin microphysics and maritime CCN, but now assuming an abundant 'bulk' background concentration (as it is done in the bulk model).

Figure 2 shows the spatio-temporal evolution of surface precipitation from the 3 model runs using spectral bin vs two-moment bulk microphysics and maritime CCN. In all cases a ?rst precipitation event occurs after about 30 min with instantaneous rainrates exceeding 100 mm/h. After this ?rst event the surface precipitation rate decreases while the region of weak precipitation expands in up- and down-wind direction. The simulation using spectral bin microphysics (Fig. 2a) leads to a complete suppression of secondary deep convection and no squall line-like structures develop, instead only weak precipitation occurs dying out after about two hours simulation time. Applying the two-moment bulk scheme (Fig. 2b) results in a remarkably different evolution since secondary deep convection appears after about 70 minutes. To demonstrate that this is in fact caused by the different nucleation schemes a third simulation with maritime CCN has been performed changing the nucleation treatment of the spectral bin microphysics to an simple diagnostic 'bulk CCN' scheme as it is used in the bulk model. The results are depicted in Fig. 2c showing secondary convection very similar to the maritime two-moment bulk case.

In Figure 3 timeseries of the accumulated surface precipitation are depicted for different model schemes and maritime as well as continental CCN. It is recognized that the GATE squall line is to a large extent a dynamically forced system, since four of the ?ve simulations

a) spectral bin: maritime CCN

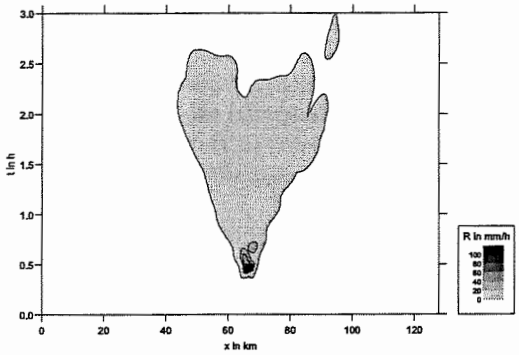

b) two-moment bulk: maritime CCN

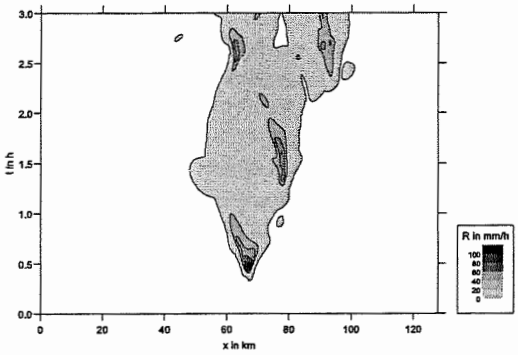

c) spectral bin: maritime 'bulk' CCN

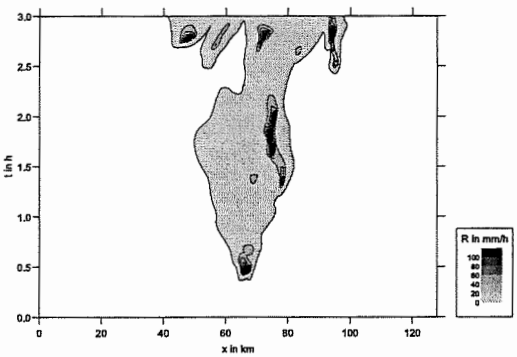

Figure 2: Hovmöller-diagrams showing the surface precipitation in mm/h from the 3 GATE case simulations applying spectral bin vs. two-moment bulk microphysics and assuming maritime CCN.

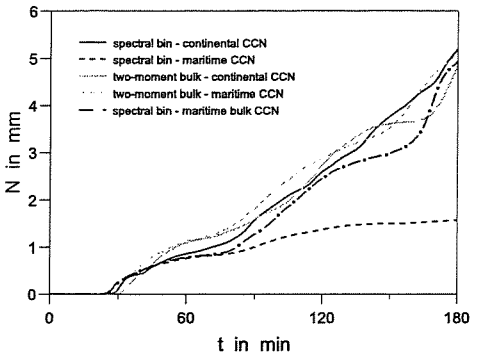

Figure 3: Time series of grid averaged accumulated surface precipitation in mm from the 5 GATE case simulations.

show a very similar rain accumulation. Only the spectral bin model assuming maritime CCN with its strong decrease of available CCN, which leads to the suppression of any secondary deep convection, changes the structural evolution of total precipitation. The continental CCN leads to even stronger secondary convection as the maritime simulations shown in Fig. 2b and 2c.
In effect, it can be stated that different CCN assumptions can result in a different temporal and spatial distribution of precipitation. And, as in the Texas case, both microphysical schemes have a similar sensitivity to CCN variations, but in the GATE case the main effect is that the more continental CCN leads to higher rainrates and stronger secondary convection (not shown here, but visit the poster!).
Finally, it can be concluded that the overall agreement between the results obtained with the bin scheme and those applying the bulk scheme is more than satisfactory. This proves the ability of the bulk scheme to simulate cloud microphysics closely to the most detailed formulation.

4 Conclusions

The comparison shows that the two-moment bulk-scheme is able to describe the development of deep convective clouds in good agreement with the spectral bin approach, but reveals also some limitations of the bulk scheme as, e.g., raindrops freeze too slowly and snow formation is slightly different leading to less snow in the bulk scheme.
Our conclusion is that the advanced two-moment bulk-scheme applied here is a very attractive compromise being much more detailed than simple one-moment schemes and also at least an order of magnitude less expensive than the spectral bin approach.
In addition, the study has shown the importance of CCN for the precipitation formation and cloud dynamics: A conclusion which goes far beyond the purposes of a comparison of two microphysical schemes.

References

Cotton, W. R., G. J. Tripoli, R. M. Rauber, and E. A. Mulvihill (1986). Numerical simulation of the effects of varying ice crystal nucleation rates and aggregation processes on orographic snowfall. *J. Clim. Appl. Met. 25*, 1658–1680.

Khain, A., M. Ovtchinnikov, M. Pinsky, A. Pokrovsky, and H. Krugliak (2000). Notes on the state-of-the-art numerical modeling of cloud microphysics. *Atmos. Res. 55*, 159–224.

Khain, A. P., D. Rosenfeld, and A. Pokrovsky (2001). Simulating convective clouds with sustained supercooled liquid water down to -37.5 °C using a spectral microphysics model. *Geophys. Res. Lett. 28*, 3887–3890.

Khain, A. P. and I. L. Sednev (1996). Simulation of precipitation formation in the eastern mediterranean coastal zone using a spectral microphysics cloud ensemble model. *Atmos. Res. 43*, 77–110.

Murakami, M. (1990). Numerical modeling of dynamical and microphysical evolution of an isolated convective cloud - The 19 July 1981 CCOPE cloud. *J. Met. Soc. Jap. 68*, 107–128.

Reisner, J., R. M. Rasmussen, and R. T. Bruintjes (1998). Explicit forecasting of supercooled liquid water in winter storms using the MM5 mesoscale model. *Quart. J. Roy. Met. Soc. 124*, 1071–1107.

Seifert, A. and K. D. Beheng (2001). A double-moment parameterization for simulating autoconversion, accretion and selfcollection. *Atmos. Res. 59-60*, 265–281.

Seifert, A. and K. D. Beheng (2004). A two-moment cloud microphysics parameterization for mixed-phase clouds. Part I: Model description. *submitted to Meteorol. Atmos. Phys.*

NUMERICAL SIMULATION OF THE 16TH JULY CRYSTAL-FACE STORM AND COMPARISON WITH OBSERVATIONS

Axel Seifert, Andrew J. Heyms?eld and Aaron Bansemer

National Center for Atmospheric Research, Boulder, USA

1 Introduction

Many microphysical processes within mixed-phase deep convection are still not well understood. Especially our knowledge of the various ice nucleation processes and other microphysical interactions affecting the ice particle size distribution is still very limited. Other open questions are the amount of liquid water existing in the strong updrafts or the importance of small-scale dynamical processes like lateral entrainment and upper level downdrafts. In addition, most of these processes interact with the atmospheric aerosol resulting in a very complex and nonlinear system which can, on one hand, hardly be understood in all details from observations alone. Cloud modeling, on the other hand, has also its limitations since it relies on parameterizations of exactly these processes which are poorly understood, like heterogeneous nucleation, ice sticking ef?ciencies, particle shapes or, least known, ice particle fragmentation.

The present approach combines advanced microphysical cloud-resolving modeling with in-situ and radar observations. The aim is to achieve a reliable interpretation of the dynamical and microphysical evolution during the development of deep convection.

The modeling side is based on a sophisticated two-moment mixed-phase cloud scheme, which predicts not only the mass contents of cloud droplets, raindrops, ice crystals, snow and graupel, but also their number concentrations (Seifert and Beheng 2001,Seifert and Beheng 2004, S&B hereafter). Explicitly predicting the number concentrations results in a consistent representation of mean particle sizes and e.g. allows the direct application of Mie theory to calculated the radar re?ectivity. Furthermore, applying Mie theory it is possible to derive radar images at different wavelength including attenuation effects for ice and liquid water. This makes the model a valuable tool to guide the interpretation of the multi-wavelength radar observations and to test retrieval methods. The in-situ observations, on the other hand, can be used to chose the particle properties and other tunable parameters assumed in the model. Statistical relations between in-situ measured variables are utilized to verify the representation of microphysical processes in the model. Finally, since a 3-d high resolution model with grid spacing below 500 m is applied, most small-scale dynamical processes like entrainment are explicitly resolved.

Corresponding author's address: Axel Seifert, National Center for Atmospheric Research; P.O. Box 3000 Boulder, CO 80307, E-Mail: seifert@ucar.edu. NCAR is sponsored by the National Science Foundation.

2 Cloud resolving simulations (preliminary results)

To simulate the development of an isolated convective cell, which was observed on July 16th 2002 during CRYSTAL-FACE, we apply the Weather Research and Forecast model (WRF) at a isotropic resolution of 250 m. The model is initialized using a single sounding based on the 1800 UTC measurements at Miami, Florida (Figure 1). Convection is initiated by a randomized warm bubble. We apply an improved version of the S&B two-moment microphysics with some changes in the treatment of the snow particles. Namely the mass-size and mass-velocity relations have been changed to new empirical relations (mass m in g, diameter D in cm, fall velocity v in cm/s)

$$m = 5.13 \times 10^{-3} D^{2.1}$$
$$v = 427 D^{0.7}$$

which have recently been derived from in-situ measurements during CRYSTAL-FACE.

Fig. 2 shows isosurfaces of the radar re?ectivity calculated from the model results for different times of the cloud evolution. The initially small cloud develops

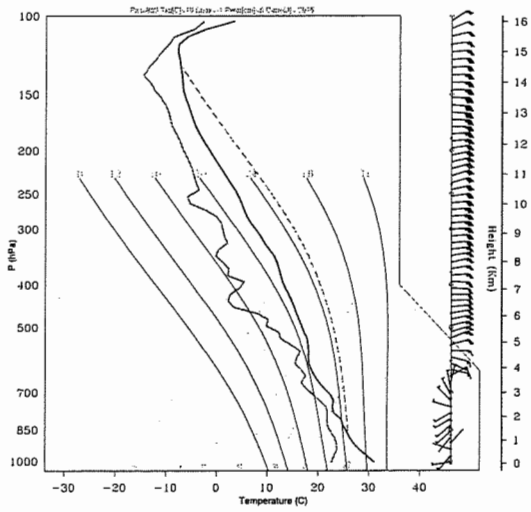

Fig. 1: *Skew-T-log-p diagram of the sounding used as initial condition for the WRF simulation.*

quickly into a strong deep convective cell with high re-?ectivities (>60 dBZ) and a cloud top reaching about 17 km height. Later on a large anvil cloud is formed. Overall, the cloud development and structure looks very realistic, obviously a result of the high spatial resolution which is able to resolve many of the turbulent eddies at the cloud boundary. This gives at least some hope, that the entrainment of mid-level air is also explicitly resolved and well simulated.

3 Comparison with dual-wavelength cloud radar measurements

The most valuable observations for the veri?cation of advanced cloud resolving models are high-resolution radar measurements, if available, multi-wavelength or polarization radar. During CRYSTAL-FACE a dual-wavelength cloud radar was operated on the NASA ER-2 looking downward from about 16 km height. The dual-wavelength radar uses X-band (3.21 cm) and W-band (3.18 mm) wavelength (Heyms?eld et al. 1996) and an example of the measurements of 16th July storm is depicted in Fig. 3. It shows the mature stage of the deep convective cell and cloud top is at 14 km. Horizontally the cloud extends over about 100 km and the highest re?ectivities of 50 dBZ are observed in the melting layer of the in?ow region. The W-Band shows strong attenuation in the same region, probably due to the large liquid water content.

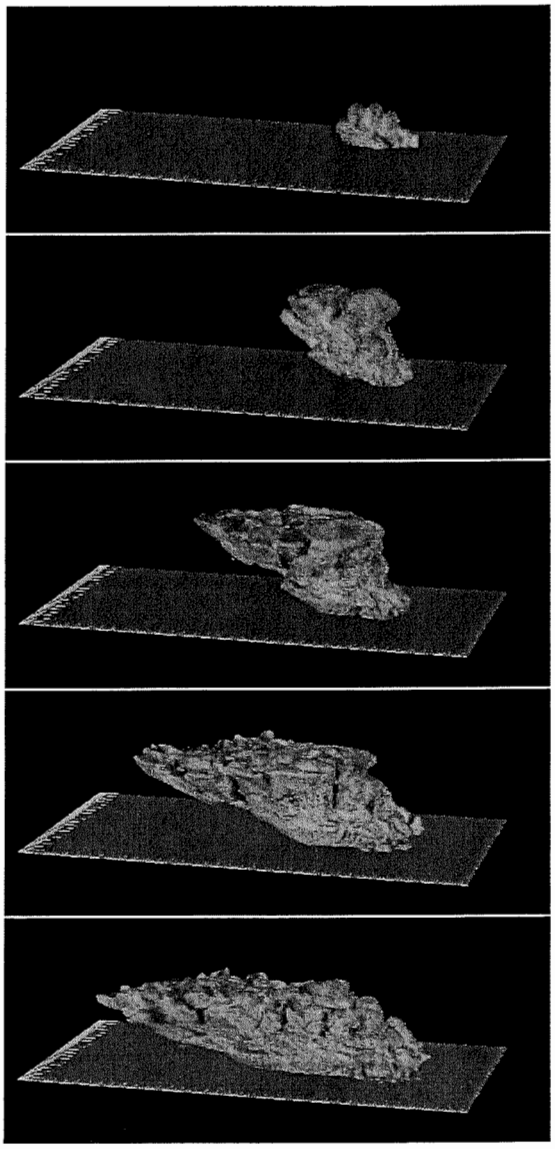

Fig. 2: *Evolution of the simulated deep convective cloud shown as isosurfaces of the radar re?ectivity at 0 dBZ at different times after model initialization (10, 20, 30, 40 and 50 min, from top to bottom). The depicted surface area is 75 km × 40 km.*

Figure 4 shows similar vertical cross sections derived from the model results. To calculate the radar re?ectivity we apply Mie theory using the predicted mass and number concentrations, as well as the particle geometries and size distributions from the two-moment mi-

crophysics parameterization. Downward attenuation is calculated for both, X- and W-band. Qualitatively the model simulations show similar structures in the re?ectivity ?eld e.g. the mid-level maximum in the stratiform region and also the higher X-band re?ectivity and strong W-band attenuation in the updraft region. Some differences are obvious too, e.g. the much smaller horizontal size of the simulated cell, the higher re?ectivities at mid- and upper-levels and too low X-band re?ectivities in the updraft core.

Using the model results, the regions of strong attenuation in the W-band can easily be identi?ed as mixed-phase updraft regions with high liquid water content (shown in Fig. 4) and the differential re?ectivity gradient of the W-band might be used as a detection parameter for the liquid water content (not shown here). Fig. 4 shows also the total ice water content, which reaches high values in the updraft and decreases in the stratiform region.

4 Comparison with in-situ measurements

A preliminary comparison of the model predicted mass and number concentrations of snow (aggregates) with in-situ observations shows some interesting differences e.g. the model predicts a signi?cant growth of snow aggregates in the anvil, while the CRYSTAL-FACE measurements give no clear evidence of snow aggregation (in contrast to some previous ?eld experiments). Further analysis is necessary and the results will be presented at the conference.

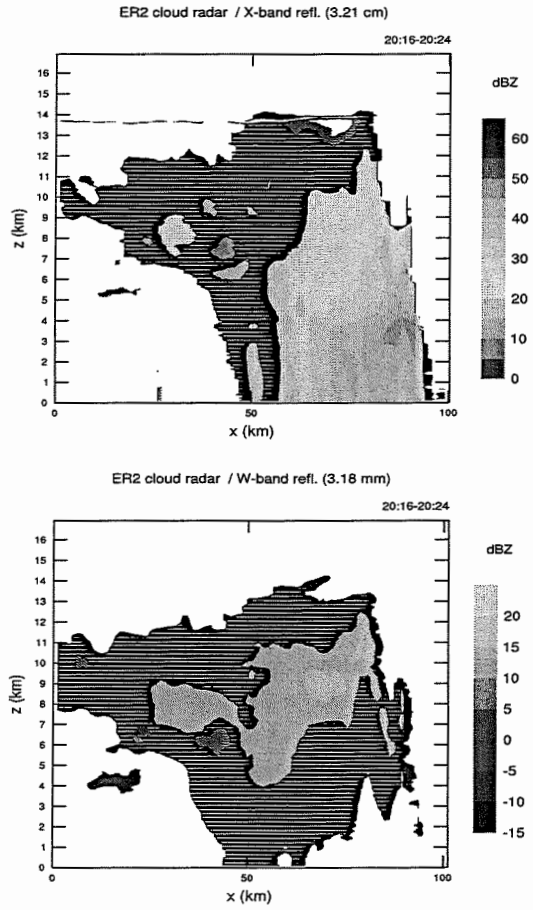

Fig. 3: *Vertical cross section of the radar re?ectivity in dBZ measured by the ER-2 cloud radar (top: X-band, bottom: W-band; data provided by G. Heyms?eld, NASA).*

5 Conclusions

We have presented preliminary results of a cloud-resolving WRF simulation of the CRYSTAL-FACE 16th July 2002 storm. Using a two-moment microphysical scheme the model is able to reproduce some, but not all features, in a reasonable way.

The comparison with the dual-wavelength cloud radar measurements have shown that the model overestimates the upper-level re?ectivity and underestimates the re?ectivity in the updraft core. These problems can have many reasons e.g. the oversimpli?ed model set up using only a homogeneous environment and a warm bubble to force convection. Another (or related?) problem of the WRF simulation is that it develops very strong updrafts ($w > 50$ m/s), which are not observed by the doppler radar measurements. This can also cause the errors in the microphysical ?elds like upper level ice content and low re?ectivities in the updraft core, since the graupel particles do not have enough time to grow but are rapidly transported into the anvil instead. Another de?ciency of the model might be the lack of a special hail class in the S&B microphysical scheme. And even at the high-resolution used here, the

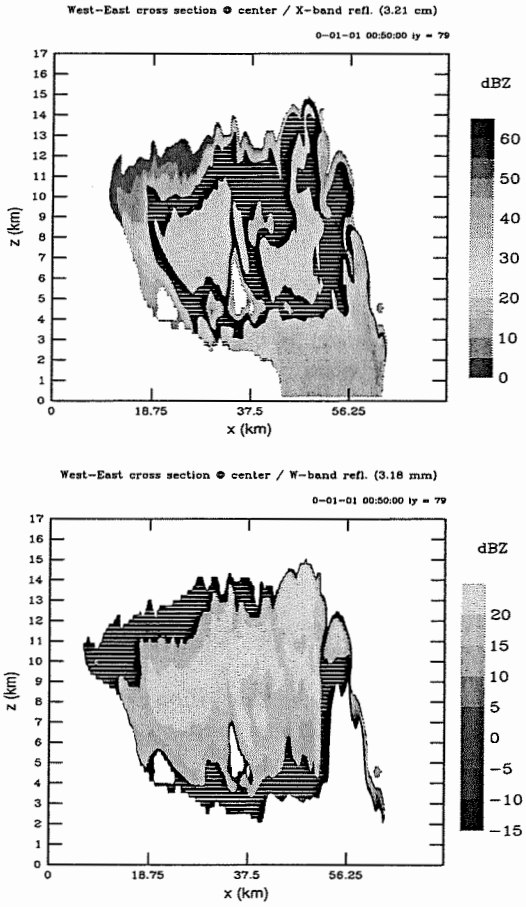

Fig. 4: *Vertical cross section of the radar re?ectivity in dBZ calculated from WRF simulations (top: X-band, bottom: W-band). Note the different scale of the x-axis compared to Fig. 3.*

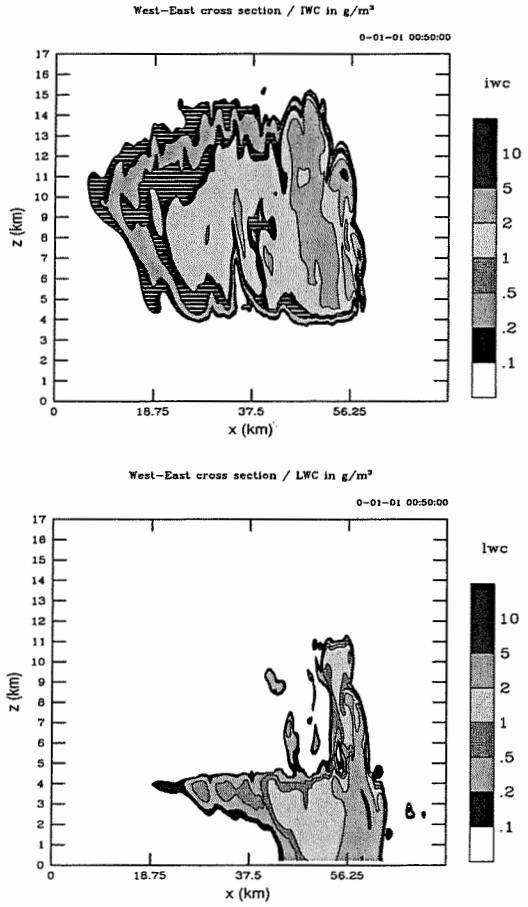

Fig. 5: *Vertical cross section of the total ice water content (top) and the liquid water content (bottom) in* gm^{-3}.

question whether the lateral entrainment is suf?ciently resolved remains unanswered.

Future modeling work will have to address these and other questions in more detail e.g. by using nested domains or extending the microphysical scheme to full hail microphysics.

References

Heyms?eld, G., S. Bidwell, I. Caylor, S. Ameen, S. Nicholson, W. Boncyk, L. Miller, D. Vandemark, P. Racette and L. Dod, 1996: The EDOP radar system on the high-altitude NASA ER-2 aircraft., *J. Atmos. Oceanic Tech.*, **17**, 795–809.

Seifert, A. and K. D. Beheng, 2001: A double-moment parameterization for simulating autoconversion, accretion and selfcollection, *Atmos. Res.*, **59-60**, 265–281.

Seifert, A. and K. D. Beheng, 2004: A two-moment cloud microphysics parameterization for mixed-phase clouds. Part I: Model description, *submitted to Meteorol. Atmos. Phys.*

USING SUBGRID CLOUD VARIABILITY IN NON LINEAR PRECIPITATION PROCESSES

Adrian M Tompkins[a],[1] and Robert Pincus[b]

[a] European Centre for Medium–Range Weather Forecasts, Reading, UK
[b] NOAA-CIRES Climate Diagnostics Center, USA

1. INTRODUCTION

Many cloud microphysical processes are nonlinear. Authors have previously pointed out that biases can thus occur when cloud schemes use grid-mean cloud water (ice+liquid) values and neglect any subgrid variability Pincus and Klein (2000); Rotstayn (2000); Larson et al. (2001); Wood et al. (2002).

Here we examine the magnitude of this bias for the microphysics of the ECMWF cloud scheme. This is accomplished using a modi?ed version of the ECMWF cloud scheme, that parameterizes cloud cover using a simple statistical approach representing subgrid ?uctuations of liquid water and humidity. Two column model experiments for a deep convective case are compared: the ?rst uses mean in-cloud values, while the second takes cloud variability into account.

2. METHODOLOGY

2.1 Cloud scheme

The experiment is conducted using a column model version of the ECMWF IFS forecast model. In order to gain information concerning the cloud water ?uctuations, knowledge of the underlying probability density function (PDF) for total water is required. One could accomplish this by ?tting a 3 moment distribution to the water vapour, cloud water and cloud cover information provided by the operational Tiedtke (1993) scheme. The disadvantage of this approach is that the Tiedtke scheme can produce combinations of these three variables that result in unreasonable or even unphysical PDFs, due to the fact that the sources and sinks of cloud cover and cloud water are not always derived self-consistently with an assumed underlying PDF.

Alternatively, we take the approach of disabling the prognostic cloud cover, and ?tting at each time step a 2-moment symmetrical distribution to the liquid water and water vapour mass mixing ratios. The cloud cover is then obtained by integrating the saturated part of the PDF.

The Beta PDF is used, as in Tompkins (2002); a bounded, unimodal, 4-moment distribution. The PDF of total water mixing ratio $G(r_t)$ is

$$G(r_t) = \frac{1}{B(p,q)} \frac{(r_t - a)^{p-1}(b - r_t)^{q-1}}{(b-a)^{p+q-1}} \quad (1)$$

where a and b are the distribution bounds ($a \leq r_t \leq b$) and, $B(p,q)$ represents the Beta function, and can be de?ned in terms of the Gamma function, Γ, as follows:

$$B(p,q) = \frac{\Gamma(p)\Gamma(q)}{\Gamma(p+q)}. \quad (2)$$

In order to reduce the distribution to a 2-moment distribution, the two de?ning shape parameters p and q are speci?ed.

Tompkins (2002) ?xed one shape parameter to 2, restricting the Beta distribution to a bell shaped regimes with skewness values between 0 and $\sqrt{2}$, in other words to positively skewed distributions only.

Here we abandon this in favour of a new closure which relates p and q as follows:

$$(p-1)(q-1) = K \quad (3)$$

where K is a constant. This allows the skewness to take its maximum possible range (for the Beta PDF), namely $\varsigma \in (-2, 2)$. Thus both positive and negative skewness values are possible with one combined shape parameter. The constant K determines the kurtosis of the limiting case symmetrical Beta distribution. The choice of K is based on pragmatism. We select $K = 2$. This choice of K gives $pq = p+q+1$ which allows the full relationship between p, q and skewness ς

$$\varsigma = \frac{2(q-p)}{p+q+2}\sqrt{\frac{p+q+1}{pq}}, \quad (4)$$

to be reduced to

$$q = \frac{(\varsigma+2) + \sqrt{2(\varsigma^2+4)}}{2-\varsigma}. \quad (5)$$

Once q is known, p is given by $p = \frac{q+1}{q-1}$.

To reduce the distribution further to a 2-moment distribution, we simply enforce symmetry by setting $p = q$

[1] Corresponding author address: Adrian Tompkins, ECMWF, Shin?eld Park, Reading, RG2 9AX, UK.
e-mail: tompkins@ecmwf.int

which, given K, are equal to a value of $1 + \sqrt{2}$. However, the framework outlined above facilitates the move to a ?exible 3 moment distribution in future.

In overcast or clear sky situations only one moment is known; the distribution mean. We thus resort to a ?xed distribution width of $MIN\{2r_c, 0.1r_s\}$ in overcast situations and $MIN\{2(r_s - r_v), 2r_v, 0.4r_s\}$ for clear sky, where r_l, r_v and r_s represent the cloud water, water vapour and saturation mixing ratios, respectively. The larger limit of $0.4r_s$ in the latter case re?ects the fact that precipitation processes tend to reduce total water variance, however, the prevalence of partially cloudy conditions in this test results in a limited sensitivity to these imposed values.

2.2 variability in microphysics

It is necessary to take the variability given by the PDF of cloud water outlined above into account in the microphysics. Ideally one would perform an analytical solution for each process, integrating across the PDF. However, this is an involved procedure, and it is questionable if a tractable solution can be found for all processes. We instead use a numerical solution, by splitting up the column into a number of sub-columns, where the cloud properties in each column overlap according to the maximum-random overlap assumption used in the radiation scheme. This is similar to the approach of Jakob and Klein (1999), except that here we also take sub-cloud variability into account in addition to the cloud cover mask. In order to resolve the PDF we use 100 sub-columns. This implementation is ?exible, but unlike the McICA approach for radiation (Pincus et al., 2003), (which does not increase cost by performing each sub-column calculation once for a different radiative band), it is numerically more expensive. It is affordable in this column model determination of biases, but would be currently infeasible for the full GCM.

The integration of the column model using the 100 sub-columns is compared to a control experiment where the microphysical processes operate on the mean in-cloud water content as usual. The integration simulates a 6 day period during the TOGA-COARE campaign in the tropical Western Paci?c, during which prevalent deep convection occurs in the model.

3. RESULTS

Figure 1 gives the timeseries of vertically integrated liquid water path (LWP) and ice water path (IWP) for the two integrations. It is immediately clear that the two experiments differ substantially. The integration that takes subgrid variability into account increases IWP and LWP by over a factor of 3, and reduces the temporal variability of the clouds. This is also apparent if the cloud cover is examined (not shown).

Are these changes as expected? The autoconversion from liquid cloud water into rain is parameterized according to Sundqvist et al. (1989) as

$$\frac{dr_l}{dt} = r_l c_0 \left(1 - exp\left[-\left(\frac{r_{cl}}{r_{cl}^{crit}}\right)^p\right]\right), \qquad (6)$$

where r_{cl}^{crit} is the critical value of the in-cloud water content at which precipitation generation becomes ef?cient. The constant C_0 is adjusted by a function of the precipitation ?ux entering the layer from above to crudely account for accretion processes, as is r_{cl}^{crit} (Tiedtke, 1993). Compared to some of the precipitation forms discussed by Pincus and Klein (2000), this equation is only weakly nonlinear; indeed for cloud water contents reasonably exceeding the critical threshold, the autoconversion is approximately linear. Nevertheless, the nonlinearity at small cloud water contents would tend to *decrease* the cloud water when sub-cloud ?uctuation are accounted for. This is opposite to the observed sensitivity. The answer lies with the ice autoconversion to snow. This is currently parameterized as a side-effect of the ice-sedimentation process, where ice falling into clear sky regions is treated as snow (Jakob, 2002). The ice sedimentation rate follows Heyms?eld and Donner (1990) giving an effective autoconversion rate from ice to snow that is

$$\frac{dr_i}{dt} \propto r_i^{0.16} \qquad (7)$$

This is quite a weak nonlinearity. However, it is found to dominate the response of the model in deep convective situations. The reason is related to the signi?cant non-diagonal Jacobian sensitivity documented by Fillion and Mahfouf (2003). The precipitation ?ux generated at higher levels in the model is able to strongly in?uence the autconversion rates in warm and mixed phase clouds through the adjustments made to account for accretion processes. Thus the nonlinearity of this ice-phase process accumulates throughout the column and produces larger cloud water amounts when variability is accounted for.

Can we reasonably assume that this sensitivity accurately re?ects nature? It is probably safe to state that this is not the case. While the relationship for ice fall speeds has been observationally determined, it is clear that it does not represent the physics of the snow generation process. Indeed, many models such as Lin et al. (1983) represent snow generation in a similar way to rain, and thus the sensitivity would be of the opposite sign. This study thus underlines the importance of gaining a more accurate understanding of complex ice microphysics, which becomes more crucial when sub-cloud variability is accounted for.

4. CONCLUSIONS

Many cloud microphysical processes are nonlinear. Authors have previously pointed out that biases can thus occur when cloud schemes use grid-mean cloud water values and neglect any subgrid variability. Here we examine a modi?ed version of the ECMWF cloud scheme, that parameterizes cloud cover using a simple statistical approach representing subgrid ?uctuations of liquid water and humidity. Two column model experiments for a deep convective case are compared: the ?rst uses mean in-cloud values for precipitation generation, while the second takes cloud variability into account by dividing the column model pro?les into 100 sub-columns.

It is found that the surface rainfall differs by a factor of three between the cases. Moreover, the ice microphysics dominates, ?rstly due to its nonlinearity, and secondly due to feedbacks through the accretion processes in lower troposphere.

We acknowledge that the snow generation in the model is likely to be a poor representation of the process in nature, and that the sensitivity to subgrid variability could even be of the opposite sign. This study underlines the importance of increasing our knowledge of ice microphysical processes, especially if sub-cloud ?uctuations are to be accounted for in future microphysical schemes.

ACKNOWLEDGMENTS
Steve Klein is thanked for many useful discussions on this topic.

References

Fillion, L. and J.-F. Mahfouf, 2003: Jacobians of an operational prognostic cloud scheme, *Mon. Wea. Rev.*, **131**, 2838–2856.

Heyms?eld, A. J. and L. J. Donner, 1990: A scheme for parameterizing ice-cloud water content in general circulation models, *J. Atmos. Sci.*, **47**, 1865–1877.

Jakob, C., 2002: Ice clouds in numerical weather prediction models: Progress, problems and prospects, in D. K. Lynch, K. Sassen, D. Starr, and G. Stephens, eds., *Cirrus*, Oxford University Press, pp. 327–345.

Jakob, C. and S. A. Klein, 1999: The role of vertically varying cloud fraction in the parametrization of microphysical processes in the ECMWF model, *Q. J. R. Meteorol. Soc.*, **125**, 941–965.

Larson, V. E., R. Wood, P. R. Field, J.-C. Golaz, T. H. VonderHaar, and W. R. Cotton, 2001: Systematic biases in the microphysics and thermodynamics of numerical models that ignore subgrid-scale variability, *J. Atmos. Sci.*, **58**, 1117–1128.

Lin, Y. L., R. D. Farley, and H. D. Orville, 1983: Bulk parameterization of the snow ?eld in a cloud model, *J. Climate Appl. Meteor.*, **22**, 1065–1092.

Pincus, R., H. W. Barker, and J. J. Morcrette, 2003: A fast, ?exible, approximate technique for computing radiative transfer in inhomogeneous cloud ?elds, *J. Geophy. Res.*, **108**, 10.1029/2002JD003322.

Pincus, R. and S. A. Klein, 2000: Unresolved spatial variability and microphysical process rates in large-scale models, *J. Geophy. Res.*, **105**, 27059–27065.

Rotstayn, L. D., 2000: On the "tuning" of autoconversion parameterizations in climate models, *J. Geophy. Res.*, **105**, 15495–15507.

Sundqvist, H., E. Berge, and J. E. Kristjansson, 1989: Condensation and cloud parameterization studies with a mesoscale numerical weather prediction model, *Mon. Wea. Rev.*, **117**, 1641–1657.

Tiedtke, M., 1993: Representation of clouds in large-scale models, *Mon. Wea. Rev.*, **121**, 3040–3061.

Tompkins, A. M., 2002: A prognostic parameterization for the subgrid-scale variability of water vapor and clouds in large-scale models and its use to diagnose cloud cover, *J. Atmos. Sci.*, **59**, 1917–1942.

Wood, R., P. R. Field, and W. R. Cotton, 2002: Autoconversion rate bias in stratiform boundary layer cloud parameterizations, *Atmos. Res.*, **65**, 109–128.

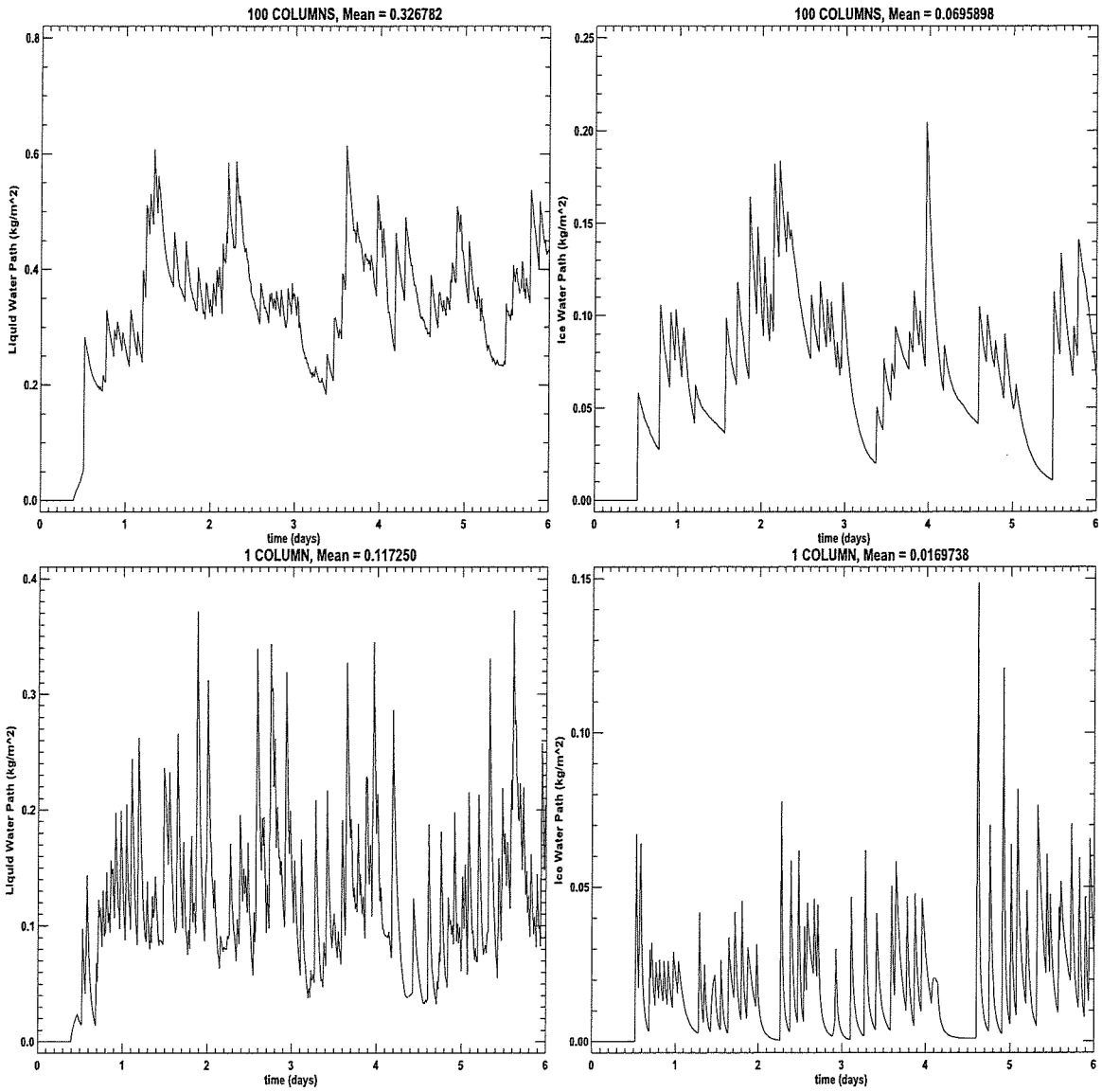

Figure 1: Top panels: timeseries of LWP and IWP when subgrid variability is taken into account using 100 sub-columns. Bottom panels: timeseries of LWP and IWP when subgrid variability is neglected

A 3D SPECTRAL ICE HABIT PREDICTION SYSTEM FOR IMPROVING CLOUD RADIATION SIMULATIONS

G. J. Tripoli[1], T. Hashino[1], G. Panegrossi[1], S. Di Michele[2] , S. Dietrich[2], and A. Mugnai[2]

[1]Department of Atmospheric and Oceanic Sciences, University of Wisconsin, Madison, Wisconsin, 53706, USA
[2]Institute of Atmospheric Sciences and Climate, CNR, Roma, Italy

1 Introduction

The standard Kessler/Orville approach to ice bulk microphysics parameterization used in most 3D cloud resolving models is based on the premises that ice hydrometeors can be naturally divided into distinct categories such as cloud ice, crystals (of various labels), aggregates, graupel, hail and so on (e.g, Kessler, 1969, and Lin et al., 1983). Each of these categories can be predicted over an assumed or explicitly simulated (bin) size distribution. Veri?cation studies of this basic framework for ice microphysics models conducted over the past three decades have often been successful in predicting the surface quantitative precipitation while at the same time, unsuccessful simulating the precise process observed to lead to that precipitation. These results have been noted but often brushed aside in the past, due to the success in the primary goal of precipitation predictions.

In recent years, new studies of microphysical process in support of remote sensing instruments such as space, aircraft and ground based radar, lidar and radiometers have provided a new urgent need to improve microphysics models in order to properly relate the radiance observations to conventional observations of temperature, moisture, wind, cloud physics and precipitation. These relationships occur in the form of both retrieval algorithms and forward models used in data assimilation. The errors in process simulation become readily apparent when comparing cloud radiation simulations to actual observed radiance from space borne platforms.

Corresponding author's address: Gregory J. Tripoli, Department of Atmospheric and Oceanic Sciences, University of Wisconsin, Madison, Wisconsin, 53706, USA; E-Mail: tripoli@meteor.wisc.edu

Our investigations into the causes of these errors suggest a strong sensitivity of simulated radiance to the model categorization of ice. Under close scrutiny, it can be argued that the modeled conversion tendencies between ice categories under the Orville paradigm are arbitrary as are the categories themselves. To improve the situation, we have proposed a new type of microphysics model that replaces ice categorization with a self-evolving ice particle scheme. In the past, a few researchers have worked on explicit simulation of ice crystal shape by vapor deposition. Millar and Young (1979) numerically simulated ice crystal growth under ?xed conditions by de?ning three principal growth modes: isometric growth, constant axial ratio growth, and limited growth. Chen and Lamb (1994a) developed more general theoretical framework that allows one to simulate ice crystals in non-?xed temperature, and they simulated a steady-state orographic storm with a bin model that includes self-evolving ice particles scheme (1994b, and 1999).

This research modi?es and extends Chen and Lamb's framework to a 3-D cloud resolving model, University of Wisconsin - Nonhydrostatic Modeling System (UWNMS) (Tripoli, 1992). The model currently uses bulk water parameterization. Instead, the possibility of a single solid hydrometeor spectrum that consists of bins with representative particles is investigated. Each solid hydrometeor is comprised of explicitly predicted variables that effectively de?nes its primary habit and type. The hydrometeors interact each other, depending on the habit and type. Thus, this approach is capable of giving more physical-based information on density and shape that have responded to the surrounding environment.

2 Bin Model with Self-Evolving Solid Hydrometeor

2.1 Strategy

In order for the bin model to be usable in a 3-D mesoscale model it is required that one 1) minimize required memory over the domain of simulation , and 2) minimize computational time, while keeping accuracy of cloud microphysics required for comparison with in-situ or satellite observations. As for the ?rst point, we attempt to limit the prognostic variables by assuming that the solid hydrometeor mass spectrum has one representative (most probable) habit for a given mass interval. This can also be interpreted that the solid hydrometeor sorts its habit by mass.

For this initial study, a bulk water parameterization similar to Flatau et al. (1989) is used for liquid hydrometeors. The time-step for the scheme must also be reasonable for use in a mesoscale model. Therefore, the supersaturation is not explicitely predicted, but diagnosed based on the assumption that the supersaturation with respect to water will remain zero as proposed by Cotton et al. (1986). As a result, the excess vapor, not consumed by vapor deposition, have to go to the cloud water category at the beginning of a time-step. In other words, the nucleation occurs instantaneously and forms cloud droplets, which is reasonable since the time-step used in the simulation is typically an order of $10^1 \sim 10^2$ seconds.

2.2 Bin Model

The bin model developed is based on a detailed bin model proposed by Chen and Lamb (1994b). They call it a *hybrid bin method*, which calculates the total growth of particles in each bin using its mean mass. The linear distribution is determined inside of a bin to conserve total concentration and mass.

This research uses only ice mass as the independent variable. Chen and Lamb (1994b) used three independent variables to describe the ice spectrum, which are solute mass, ice mass, and axis ratio of ice crystals $\phi = c/a$ with 20, 45, and 11 bins, respectively. However, it may not be feasible to build the same bin model to 3-D mesoscale model. In order to represent the shape of an ice particle, it is divided into different parts of ice; the mass of an ice crystal m is assumed to consist of the mass components on a-axis m_a, c-axis m_c, and dendritic axis m_d of a ice crystal, mass m_R by riming process, and mass m_A by aggregation process:

$$m = m_a + m_d + m_c + m_R + m_A. \quad (1)$$

The concentration of each component is assumed to be the same, i.e., one bin represents one shape:

$$n = n_a = n_d = n_c = n_R = n_A. \quad (2)$$

In addition, volumes produced by riming and aggregation, v_R and v_A, are predicted or diagnosed. The lengths along a-axis and c-axis of an ice crystal, a and c, are necessary to keep track in order to ensure the vapor deposition growth based on Chen and Lamb's theory. The concentration variable, ?ve mass variables, two volume variables, and two length variables in a bin can be simulated and transferred to other bins based on physical processes, namely vapor deposition/evaporation, aggregation, and riming.

For example, in case of vapor deposition the growth of length a and c are calculated based on the inherent growth ratio given temperature (Chen and Lamb, 1994b), and then the mass change is distributed into m_a and m_c by differentiation of the mass of a spheroid with respect to a and c. If the environment satis?es the two following conditions, the mass change on a-axis, δm_a is moved to dendritic axis mass δm_d: 1) The ambient air temperature is in between of -16 and -12 Celsius, and 2) The ambient excess vapor density is greater than 0.20×10^{-6} g/cm^3.

Since one bin has one representation of ice crystal, the ratio of each mass component to the total mass is ?xed to one value. Therefore, once the ratio is calculated for the jth bin grown by the vapor deposition, transferred total mass from the jth bin into the ith bin times the ratio gives mass components transferred into the ith bin, so that the mass is conserved. The new length of a-axis in an original bin may be given by weighting the length in the grown bin based on the transfered concentration into the bin. The same method is applied for the other non-mass prognostic variables.

2.3 Ice Crystal Model

The ice crystal model proposed here consists of a hexagonal column and six dendritic arms as shown in Figure 1. The mass components on a-axis, c-axis and dendritic axis have the following

geometric relationship:

$$m_a = A_a(a')h_a\rho_0 \quad (3)$$
$$m_c = A_a(a')c'\rho_0 \quad (4)$$
$$m_d = A_d(a', d)h_d\rho_0 \quad (5)$$

where A_a (A_d) are the hexagonal (dendritic) area projected from the top (see the right in Figure 1), h_a is the thickness with which the prism faces grow, the dendritic arm has the thickness h_d, and ρ_0 is the bulk density of the ice. The radial length of the hexagonal prism along the a-axis, a', and the length of the dendritic arm, d, sum up to total length a. c' indicates the part of the ice crystal possessed by two basal faces. Given ?ve variables, m_a, m_c, m_d, a and c, those dimensions will be determined. The geometric information is used for calculation of terminal velocity with general formula by Bohm (1989, 1992), ventilation coef?cient, and categorizing the habit and type of hydrometeor. Currently, the spheroid model with a and c lengths as Chen and Lamb (1994a) is used for growth by vapor deposition since more theoretical work has to be done to predict the growth only by the mass components.

The habit and type of hydrometeor is essential information because the collision ef?ciency available was calculated for collectors with different habits and types (aggregates or graupels). In case of riming of ice crystals this research uses the collision ef?ciency calculated for hexagonal ice plates, broad-branch crystals, and columnar ice crystals by Wang and Ji (2000). In cases where relatively large, supercooled cloud drops collecting a small columnar ice crystal or planar crystal, the collection ef?ciencies calculated by Lew and Pruppacher (1983) and Lew et al. (1985) are used. For the collision between graupels (or hailstones) and cloud drops Pinsky et al. (2001) have calculated the ef?ciency which depends on the ambient pressure. This pressure dependence of the ef?ciency should be taken account in the simulation of cumulus clouds with signi?cant vertical development.

The solid hydrometeor is assumed to change from the lightly rimed and/or aggregated ice crystal mode to the graupel mode in the following condition: 1) if total volume taken by riming ?lls the space between the ice crystal model with aggregation and circumscribing spheroid, and 2) if the maximum dimension is larger than 500 μm.

2.4 Level of Complexity

The prognostic variables passed from cloud microphysics routine are mixed by the 3-D dynamic model. As discussed before, the number of prognostic variables becomes a critical problem in terms of memory usage when one simulates a storm over a large domain or with high resolution. This research proposes a framework called *the level of complexity* in the simulation where one can select the desirable detail of cloud microphysics as shown in Table 1.

Level 1 uses the same method in growth of a and c lengths as Chen and Lamb (1994b) described, and does not use the ice crystal model. Level 2 and Level 3 have m_a, m_c, and m_r rime mass components to utilize the ice crystal model, which describes an aggregate by one crystal shape. Level 4 and Level 5 are somewhat different from Level 2 and Level 3; the ice crystal model is used to represent one ice crystal in an aggregate. Since the total mass is known, the dimension of the aggregate can be calculated based on empirical mass-dimensional relation.

3 Ongoing Work

The authors plan to test the microphysics scheme on two orographic storms including 1) the Sierra Cooperative Pilot Project (SCPP), and 2) the Steamboat Orographic Storm Experiment (SOSE). Results of cloud radiation simulations using the current bulk water parameterization and the new approaches with different level of complexity will be compared and presented at the poster presentation.

REFERENCES

Bohm, H.P., 1989: A general equation for the terminal fall speed of solid hydrometeors. *J. Atmos. Sci.*, **46**, 2419-2427.

Bohm, 1992: A general hydrodynamic theory for mixed-phase microphysics. Part I: Drag and fall speed of hydrometeors. *Atmos. Res.*, **27**, 253-274.

Chen, J.-P., and D. Lamb, 1994a: The Theoretical Basis for the Parameterization of Ice Crystal Habits: Growth by Vapor Deposition. *J. Atmos. Sci.*, **51**, 1206-1221.

Chen, J.-P., and D. Lamb, 1994b: Simulation of Cloud Microphysical and Chemical

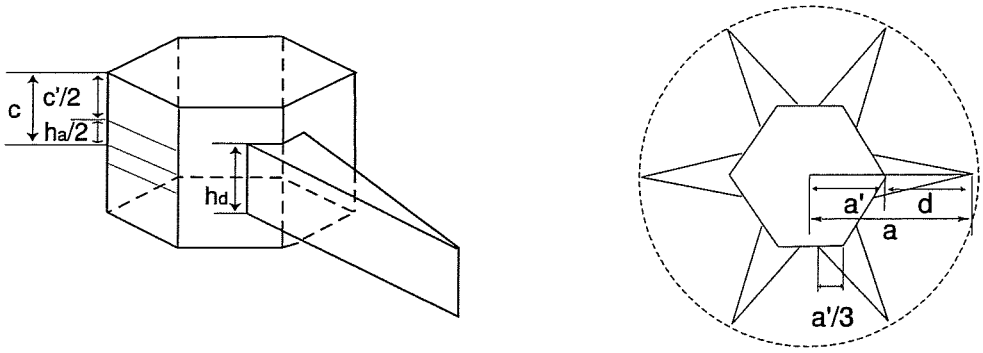

Figure 1: Ice Crystal Model.

Table 1: Level of Complexity. P, D, and N/A denote prognostic variable, diagnostic variable, and not available, respectively. N_p is the number of prognostic variables for one solid hydrometeor bin.

Level	n	m	a	c	m_a	m_c	m_d	m_R	m_A	v_R	v_A	N_p
5	P	D	P	P	P	P	P	P	P	P	P	10
4	P	D	P	P	P	P	P	P	P	D	D	8
3	P	D	P	P	P	P	P	P	N/A	D	N/A	7
2	P	D	P	P	P	P	N/A	P	N/A	D	N/A	6
1	P	P	P	P	N/A	N/A	N/A	N/A	N/A	N/A	N/A	4

Processes Using a Multicomponent Framework. Part I: Description of the Microphysical Model. *J. Atmos. Sci.*, **51**, 2613–2630.

Chen, J.-P., and D. Lamb, 1999: Simulation of Cloud Microphysical and Chemical Processes Using a Multicomponent Framework. Part II: Microphysical Evolution of a Wintertime Orographic Cloud. *J. Atmos. Sci.*, **56**, 2293–2312.

Cotton, W. R., G. J. Tripoli, R. M. Rauber, and E. A. Mulvihill, 1986: Numerical simulation of the effects of varying ice crystal nucleation rates and aggregation processes on orographic snowfall. *J. Climate Appl. Meteor.*, **25**, 1658-1680.

Flatau, P. J., G. J. Tripoli, J. Verlinde, and W. R. Cotton, 1989: The CSU-RAMS Cloud Microphysics Module: General Theory and Code Documentation. Technical Report 451, Colorado State University, 88pp.

Kessler, E., 1969: On the distribution and continuity of water substance in atmospheric circulations. *Meteor. Monogr.*, No 32, Amer. Meteor. Soc., 84pp

Lew, J.K., and and H. R. Pruppacher, 1983: A theoretical determination of the capture ef?-ciency of small columnar ice crystals by large cloud drops. *J. Atmos. Sci.*, **40**, 139-153.

Lew, J.K., D. E. Kingsmill, and D. C. Montague, 1985: A theoretical study of the collision ef-?ciency of small planar ice crystals colliding with large supercooled water drops. *J. Atmos. Sci.*, **42**, 857-862.

Lin, Yuh-Lang, Farley, Richard D., Orville, Harold D. 1983: Bulk Parameterization of the Snow Field in a Cloud Model. *J. Appl. Meteor.*, **22**, 1065–1092.

Miller, T. L., and K. C. Young, 1979: A numerical simulation of ice crystal growth from the vapor phase. *J. Atmos. Sic.*, **36**, 458-469.

Pinsky, A. K., M. Shapiro, and A. Pokrovsky, 2001: Collision rate of small graupel and water drops. *J. Atmos. Sci.*, **58**, 2571-2595.

Tripoli, Gregory J. 1992: A Nonhydrostatic Mesoscale Model Designed to Simulate Scale Interaction. *Monthly Weather Review*, **120(7)**, 1342-1359.

Wang, P.K. and W. Ji, 2000: Collision Ef?ciencies of Ice Crystals at Low-Intermediate Reynolds Numbers with Supercooled Cloud Droplets: A Numerical Study. *J. Atmos. Sci.*, **57**, 1001-1009.

A Statistical Activation Scheme for Turbulence Closure Models

Shouping Wang[1] and Jean-Christophe Golaz[2]

[1] Naval Research Laboratory, Monterey, California
[2] National Research Council, Research Associateship Programs

1. INTRODUCTION

Turbulence closure models have been widely used for simulation of stratocumulus clouds in the atmospheric boundary layers. Recently, efforts have been made to couple this type of models to a detailed cloud microphysical representation to predict the temporal evolution of the droplet-size spectrum. One major difficulty in this efforts is the parameterization of the droplet activation since the turbulence closure models cannot provide information on instantaneous local super-saturation and vertical motion, which are essential for the activation process. We propose to couple the well-known Twomey equation with the vertical velocity statistics predicted by the turbulence model to formulate the activation tendency.

2. TURBULENCE-MICROPHYSICS MODEL

The model basically follows that of Wang and Wang (2000) in which all the relevant 2nd and 3rd order turbulence statistics are predicted. The model assumes lognormal droplet size distribution and predicts liquid water content ($\overline{q_l}$), droplet number concentration ($\overline{N}$) and their turbulence fluxes. Readers are referred to that paper for more details of the formulation. Activation and evaporation parameterizations are summarized below.

3. ACTIVATION AND EVAPORATION

Our statistical activation approach is based on the approach of Twomey (1959), which is

$$N^* = C(100 \cdot S^*)^k \tag{1}$$

where C and k are parameters depending on the CCN spectrum and S^* is

$$S^* = \left[\frac{A(T,P)\, w^{3/2}}{Ck\beta(3/2, k/2)} \right]^{1/(k+2)} \tag{2}$$

Corresponding Author: Shouping Wang
wang@nrlmry.navy.mil

where A is a thermodynamic function, β is the complete beta function. If the turbulence vertical velocity is known, activated droplet number can be obtained from (1) and (2). However, a turbulence closure model cannot predict instantaneous vertical velocity. Rather it predicts the statistics of vertical velocity such as its variance. Assuming that the probability density function of vertical velocity [*pdf(w)*] is known, then we can write the ensemble mean droplet number as follows

$$\overline{N}^* = \int_0^\infty pdf(w)\, C \cdot (100 \cdot S^*)^k \, dw. \tag{3}$$

Therefore, the activation tendency used in the model can be formulated as

$$\left(\frac{\partial \overline{N}}{\partial t}\right)_{act} = \frac{1}{\Delta t} \int_{w_{\min}}^{\infty} pdf(w) \left(C \cdot (100 \cdot S^*)^k - N_u\right) dw \tag{4}$$
$$for\ \overline{S} \geq -0.01$$

where w_{min} is the minimum vertical velocity that maintains the integrant positive, N_u is the droplet number density in updrafts and calculated following the approach of Wang and Wang (2000). A corresponding term is included in the $\overline{q_l}$ equation:

$$\left(\frac{\partial \overline{q_l}}{\partial t}\right)_{act} = \frac{\rho_l}{\rho_0} \frac{4}{3} \pi\, r_{cri}^3 \left(\frac{\partial \overline{N}}{\partial t}\right)_{act} \tag{5}$$

where r_{cri} = 1 μm. When $\overline{S}$ < 0, the droplets with radius less than the critical value (r_{cri} = 1 μm) completely evaporate. We further assume the evaporation only occurs in the downdraft, leading to

$$\left(\frac{\partial \overline{N}}{\partial t}\right)_{eva} = -\frac{\int_{-\infty}^{0} pdf(w)\, dw \int_0^{r_{cri}} n(r, r_g, \sigma)\, dr}{\Delta t} \tag{6}$$

where n is lognormal distribution, r_g is mean geometric radius and σ is breath parameter. A similar term is also included in the $\overline{q_l}$ equation. Because the activation only occurs in the updrafts and the droplet evaporation in downdrafts, these processes should have a significant impact on the turbulent droplet number flux (Wang *et al.* 2003).

To complete the above activation-evaporation parameterization, we need to assume probability density function for vertical velocity *w*. In general, *pdf* of *w* varies significantly for different cloud regimes due to the different dynamic nature. For stratocumulus clouds, Gaussian distribution is an acceptable approximation. For computational simplicity, we choose triangular distribution for *pdf (w)*, in which the variance of *w* is predicted by the turbulence closure model. Therefore, the integrals in (4) and (6) can be easily derived analysitcally.

It should be emphasized that although the activation scheme is coupled with the third-order turbulence model, (4) and (6) is applicable to any other low-order models as long as *pdf(w)* is provided and the relevant statistics are calculated.

4. RESULTS

We tested the activation scheme by simulating the case of stratocumulus clouds as discussed by Bechtold et al. (1996), who give a detailed description of the initial and large-scale conditions. The background CCN number concentration is set to be 100 cm^{-3}. The model is integrated for 5 hours and all the results shown here are the averaged over last hour.

As shown in Fig. 1, the mean liquid water content increases to 0.35 gkg^{-1} at the cloud top and the droplet number is quasi-constant within the cloud layer, leading to an increase of mean droplet radius $\bar{r}_m$ with $z^{1/3}$. However, it is noticed that $\bar{N}$ does not reach the maximum value of 100 cm^{-3}.

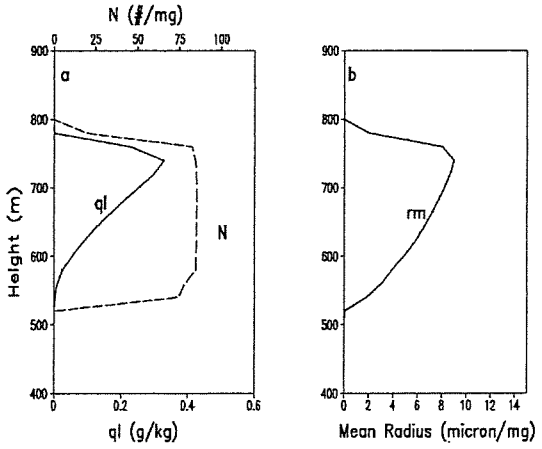

Fig. 1. a: liquid water content (solid), the droplet number concentration (dashed); b: mean radius.

The droplet number activation and evaporation profiles (Fig. 2) demonstrate the maximum values at the cloud base, a feature very similar to that simulated by a coupled LES-Bin microphysics (e.g., Wang *et al*, 2003). It is important to notice that the maximum activation occurs at the cloud base where the mean supersaturation is negative. This result clearly verifies that the parameterized

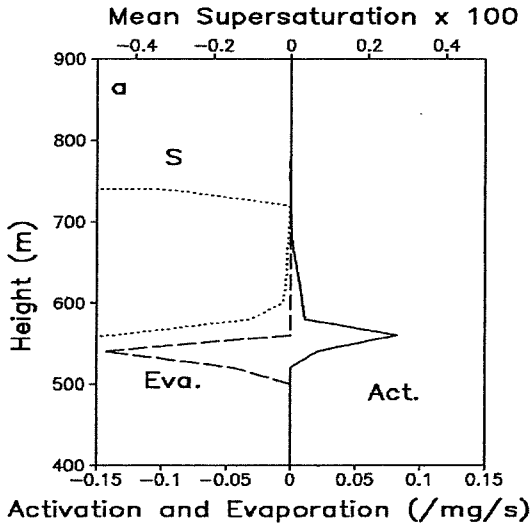

Fig. 2. Solid line represents activation rate, dashed the evaporation, and the dotted the mean supersaturation.

activation is not driven by the mean supersaturation. Rather it depends on the turbulent vertical velocity spectrum. This, again, is consistent with our basic understanding of the cloud microphysics and the results of LES studies.

ACKNOWLEDGEMENTS

Shouping Wang was supported by the Office of Naval Research and the Naval Research Laboratory through CBLAST. This work was performed while J-C Golaz held a National Research Council Research Associateship Award at NRL, Monterey, CA.

REFERENCES

Bechtold, P. and others, 1996: Modeling a stratocumulus-topped PBL: Intercoparison among different 1 D codes and with LES. *Bull. Amer. Meteor. Soc.*, 77, 2033-2042.

Twomey, S., 1959: The nuclei of natural formation. Part II: The supersaturation in natural clouds and the variation of clouds droplet concentration. *Geophy. Pure Appl.*, 43, 243-249.

Wang, S., and Q. Wang, 2000: A cloud microphysical parameterization for higher-order turbulence closure models. 13th International Conference on Clouds and Precipitation, Proceedings, 557-560, Reno, Nevada USA, 14-18 August 2000.

Wang, S., Q. Wang and G. Feingold, 2003: Turbulence, condensation and liquid water transport in numerically simulated non-precipitating stratocumulus clouds. *J. Atmos. Sci.*, **60**, 262-278.

COMPARISON OF MODEL AND RADAR DERIVED CLOUD VERTICAL STRUCTURE AND OVERLAP

U. Willén[1] and S. Crewell[2]

[1]Rossby Centre, Swedish Meteorological and Hydrological Institute, 601 76 Norrköping, Sweden
[2] Meteorological Institute University München, Theresienstr. 37, 80333 München, Germany

1. INTRODUCTION

The vertical distribution of clouds has a large impact on the radiative heating and cooling rates of the atmosphere and the surface. Assumptions regarding the vertical cloud overlap in a grid column are required in climate models for the radiative transfer calculations. These various assumptions can lead to large differences in subsequent radiative heating rates of the atmosphere and the surface. The cloud overlap assumption can be evaluated by comparing the model output with ground based cloud profiling radar data for particular locations and limited time periods. In this study, we assess the cloud vertical structure and cloud overlap of four atmospheric models using two ground-based cloud profiling radars for the BALTEX BRIDGE Campaign (BBC) of CLIWA-NET.

2. DATA AND MODELS

The BBC campaign took place at Cabauw, the Netherlands, in August and September 2001. A full description of the CLIWA-NET project can be found at www.knmi.nl/samenw/cliwa-net. In this study, we use observational data from two radars operating at different frequencies (35 and 95 GHz). For evaluating the model vertical cloud distributions we create radar grid box values by averaging the high frequency radar observations over different time intervals to mimic the different horizontal resolutions of the models, and over different numbers of range gates to account for the model vertical levels. The ratio of the number of cloud filled pixels to the total number of pixels in each 'grid box' give a volume fraction which corresponds to the model plane-parallel cloud fraction.

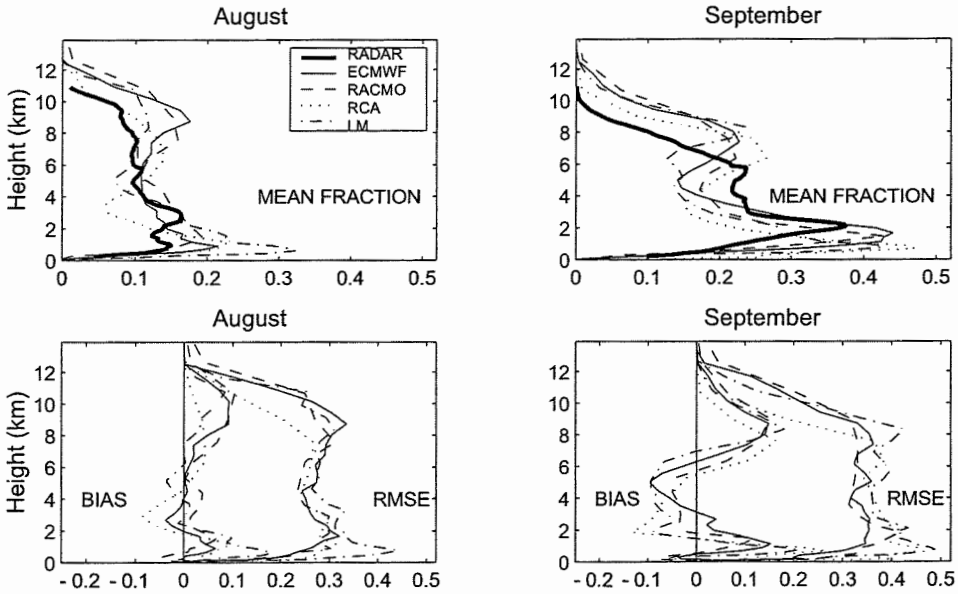

Figure 1: Mean cloud fraction (top row) for the 35 GHz radar on the original 90m resolution. The model values are given at their specific layer resolution. The bias and RMSE between model predicted and observed time series of cloud fraction is shown in the bottom row.

Corresponding author's address: Ulrika Willén, Rossby Centre, SMHI, SE-610 76 Norrköping, E-mail: ulrika.willen@smhi.se

Because the wind speed varies with time and height, in principal the temporal average should vary accordingly. For simplicity, we choose to calculate the radar cloud fractions for three fixed timescales for each model depending on the mean observed wind speed at three height intervals.

Model data from four European institutes, the ECMWF (European Centre for Medium range Weather Forecasts), KNMI (Royal Netherlands Meteorological Institute), SMHI (Swedish Meteorological and Hydrological Institute) and DWD (Deutscher Wetterdienst) were used. The ECMWF global forecast model was run with 55km horizontal resolution and 60 vertical eta levels, the regional climate models from KNMI and SMHI, RACMO and RCA respectively, were run with 18km horizontal resolution and 24 vertical eta levels. Finally, the non-hydrostatic local model, LM, from DWD was run at 7 km horizontal resolution and 35 vertical levels.

3. RESULTS

3.1 Cloud vertical distribution

The mean vertical cloud fractions for each model grid column closest to Cabauw and the occurrence of hydrometeors in each 90-m vertical range bin from the 35 GHz radar are shown in figure 1. The models capture some of the vertical structure and especially the difference between the two periods. August was a fairly sunny month with convective activity at Cabauw, while September was more overcast with persistence low level cloudiness. All models overestimate the occurrence of high clouds (above 7km) and underestimated clouds at mid-levels (mainly for September), similar to what Beesley et al (2000) and Hogan et al (2001) found for the ECMWF model for the Arctic and England, respectively. Below 2km all models overestimate the cloud occurrence.

In order to look at the forecast skill of the models, we calculated the mean error and the root-mean square error for the model compared to the radar derived time series of cloud fraction (Fig. 1). For this purpose the radar volume cloud fractions were calculated for each model vertical layer assuming the mean mid-tropospheric advective time-scale. The bias structure is fairly similar for all models, although the strong underestimation of clouds at mid-levels occurs at slightly higher altitudes for the ECMWF model than for the other models. In addition, the latter models show a narrower, and lower level maxima than the radar.

There are many possible explanations why the model and radar fractions could differ, such as, co-location errors due to the time-averaging approach, problems of the radar sensitivity, the model not representing everything detected by the radar, and what we really want to evaluate, any errors due to poor model performance. Hogan et al (2001) modified the model fractions to account for some of the known discrepancies between the measurements and the model variable. High thin clouds may be undetected by the radar and can be excluded from the model output. The underestimation at mid levels could be due to precipitating ice crystals or snowflakes, which are included in the radar derived cloud fraction but not in the model fractions.

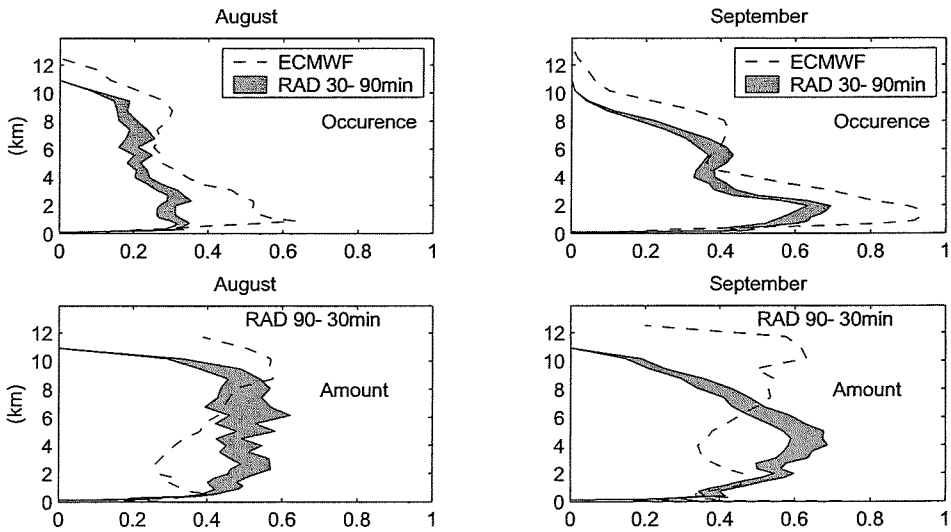

Figure 2: Frequency of cloud occurrence and amount when present (>5%) for ECMWF and for the radar at the corresponding vertical resolution. The bandwidth (grey shaded area) of the observation indicates the possible variation due to changes in advection speed.

Here, we have left the model output unchanged to compare the unaltered statistics. However, we used the minimum and maximum time averages to obtain a bandwidth of probable realizations from the observations as the time averages were chosen to represent maximum and minimum advection speeds for each model. We calculated the 'frequency of occurrence' and the 'amount when present' from the observations and the models (shown for ECMWF in Figure 2). It turns out that the occurrence and amount are fairly insensitive to the length of time intervals. Because longer time averages are more likely to contain more clear-sky the longer time averages give less amount and slightly higher frequency of occurrence. The models overestimate the occurrence of clouds at high and low levels and underestimate the amount of cloud from 1 km to 6 km. The errors above 7 km appear to be due to both a too high occurrence and too high amounts when present.

In figure 3 we compare the frequency distributions of cloud fractions for the ECMWF model with the distributions for the minimum and maximum radar advective time scales. Ideally, the model distribution should fall inside this 'uncertainty range' of the time-average approach. Generally, the model distributions are skewed and the occurrence of smaller cloud fractions (<50-60%) were overestimated at all heights by all models. On the other hand, the models underestimate clear-sky conditions and the occurrence of overcast.

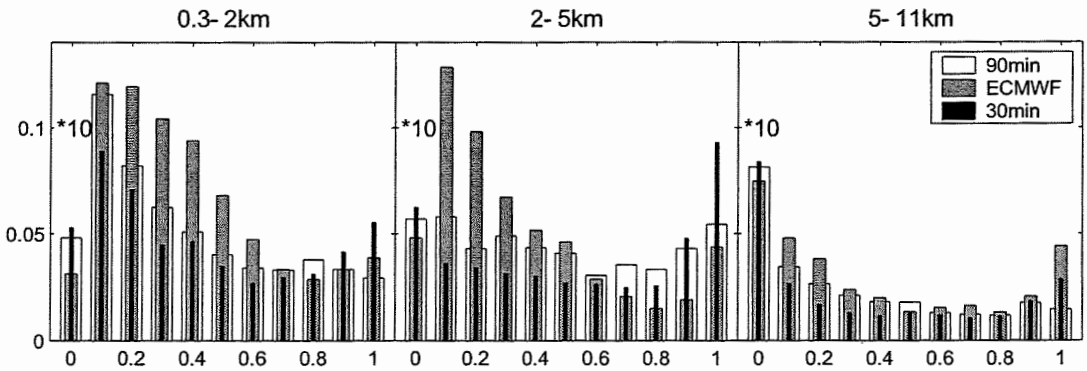

Figure 3: Frequency distribution of the cloud fraction for ECMWF, with the corresponding radar observations for low, mid and high clouds. The model distribution (grey bars) are compared to the observations averaged according to their minimum (white bars) and maximum (black columns) advective time scales. The first group of bars, the clear-sky values should be multiplied by 10.

3.2 Cloud overlap

For the overlap statistics we need to know the cloud cover at each level, i.e. the sub-grid scale overlap or 'the area fraction'. We derived the area fraction for the radar, by calculating the horizontal projection of cloud elements in each grid box. The area fraction is always equal to or larger than the volume fraction. It is important to know the typical thickness of the observed clouds, if they are thinner than the model vertical resolution, they will deviate from the plane-parallel (PP) assumption. This could lead to an underestimation of cloud cover and overestimation of the model cloud overlap even if the volume fractions were well predicted.

The difference between the volume and area fraction is fairly small at 60 vertical levels as illustrated in figure 4a, and therefore the overlap calculated from the ECMWF PP clouds was comparable to the radar overlap. Most cloud-radiation schemes are based on maximum-random (M-R) overlap, adjacent cloud layers have maximum overlap and clouds which are not in direct vertical connection have random overlap. Since the ECMWF model overestimated high clouds and underestimated at mid levels the mean value for maximum-random was fairly close to the observed value. This illustrates how error in the vertical cloud distribution might be concealed if only the ground or top of the atmosphere values are validated with observations.

We compared the radar true overlap with different cloud overlap assumptions calculated from the radar area fractions (figure 4b). The mean true overlap diverged from maximum overlap near the position of the maxima in cloud cover. Therefore, we tried a new simple version of M-R overlap, whereby random overlap was used also for continuous clouds when the cloud cover gradient was above a certain value. This improved the agreement with the true overlap for the whole BBC periods for all the tested resolutions. The M-R gradient overlap is also shown for the ECMWF model (Fig 4a). It is closer to the observations at the surface, but still for the wrong reasons.

In many large-scale models a cloud overlap matrix is used in the radiation scheme. The matrix contains the accumulated cloud covers between any two levels in the atmosphere and thereby the amount of clear and cloudy sky above and below any layer can be determined for the longwave and shortwave calculations. The accumulated cloud fractions in figure 4 are part of the cloud matrix. We derived the cloud matrix from the radar data for the BBC period and compared with different overlap assumptions. The mean bias and RMSE were smallest for M-R gradient overlap.

Other radar overlap studies have shown that continuous clouds are maximum overlap but tend to random at certain de-correlation lengths, Hogan and Illingworth (2000). However, Mace and Benson (2002) did not find a general expression for the overlap of two separate layers. A possible explanation to why the maximum-random gradient overlap worked so well also for different resolutions could be since it was a way of obtaining a 'general' de-correlation length, applicable for different thick clouds. Continuous clouds could be in maximum overlap in the interior, but near edges (top or bottom) where there is larger change in cloud cover they could be in random overlap even at small separations.

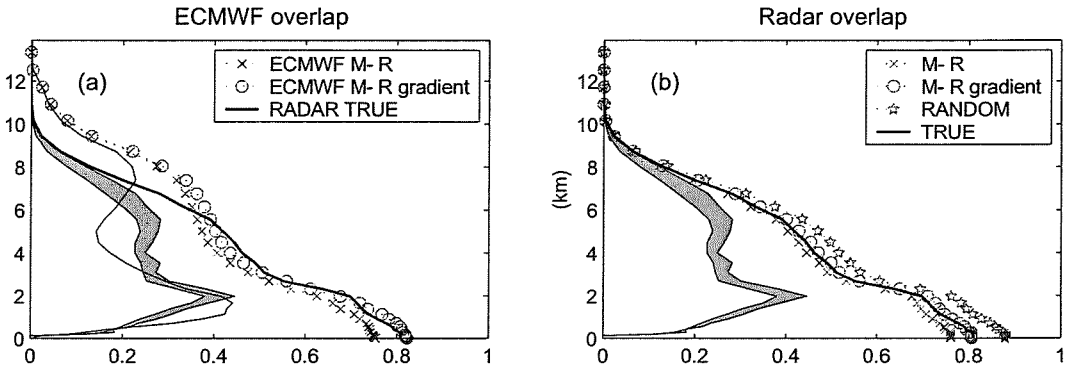

Figure 4: Accumulated cloud fraction as observed from above (top) and below (bottom) for different types of overlap assumptions for September and for the true overlap (bold line). The thin line (4a) is the ECMWF cloud fractions and the grey areas show the radar volume and area fractions.

4. CONCLUSIONS

We found that the cloud vertical distributions of the four models of different horizontal and vertical resolutions performed fairly well for the BBC period. However, the models overestimated high and low clouds and under estimated at mid-levels. Clouds occurred more frequently in the models, but with less amounts when present. The cloud fraction frequency distributions were more skewed for the models, and the observations more binary. The results were fairly independent of the assumed advection speed for the radar derived fractions.

The accumulated cloud fractions, or cloud overlap matrix was found to be in between maximum-random and random overlap. Using random also for continuous clouds when the cloud cover gradient was high improved the agreement with the true overlap.

5. ACKNOWLEDGEMENTS

We are grateful to our CLIWA-NET colleagues for providing us with all observational data and model results.

6. REFERENCES

Beesely J. A., C.S.Bretherton, C. Jakob, E.L. Andreas, J.M. Intreri and T. A. Uttal 2000: A comparison of cloud and and boundary layer variables in the ECMWF forecast model with observations at the SHEBA ice camp. *J. Geophys. Res.*, 105, 12337-12349.

Hogan R.J, C. Jakob and A.J. Illingworth 2001: Comparison of ECMWF winter-season Cloud fraction with radar-derived values. *J. Appl. Meteorol.*, 40, 513-525.

Hogan R.J and A.J. Illingworth 2000: Deriving Cloud overlap statistics from radar. *Quart. J. Roy. Meteor. Soc.*, 126, 2903-2909.

Mace, G.G., and S. Benson-Troth, 2002. Cloud-layer overlap characteristics derived from long-term cloud radar data. *J. Climate*, 15, 2505-2515.

THE BEHAVIOUR OF DIFFERENT CLOUD PROCESS PARAMETRIZATIONS IN A LARGE-SCALE MODEL

Damian R. Wilson, Amanda M. Kerr-Munslow, Andrew C. Bushell
Met Office, Exeter, EX1 3PB, UK

1. INTRODUCTION

In this paper we compare the results from two, very different, general circulation model (GCM) large-scale cloud schemes. These are run in the Met Office Unified Model (UM). The first scheme is a diagnostic cloud scheme, based on Smith (1990) and Wilson and Ballard (1999). The second scheme is a prognostic cloud scheme, following on from the work of Gregory et al (2002). We briefly describe the essential differences between the schemes, then present more detailed analysis of simulations of tropical convective cloud and mid-latitude stratocumulus cloud. We note that:

a) the simulation of high tropical cirrus cloud is primarily determined not by the phase or cloud fraction parametrization of the detrained water, but simply by the amount of water detrained. It is the large-scale scheme that controls the cloud fraction and ice content of the cloud;

b) the simulation of stratocumulus cloud is much improved by allowing the width of the assumed, underlying probability density function (PDF) of moisture to vary. Specifically, the width should decrease as cloud fraction increases, and this can be achieved through parametrization of the physical processes involved.

2. THE LARGE-SCALE MODEL CLOUD SCHEMES

2.1 The diagnostic (control) scheme

The control scheme represents the condensation and evaporation of liquid water with the PDF method of Smith (1990). Here a specified distribution of total moisture ($q_T=q+l$) and liquid water temperature ($T_L=T - l\,L/c_p$) is assumed across a gridbox, with the mean values given by the large-scale prognostic variables. q represents vapour, l represents liquid water, T, the dry-bulb temperature, L is the latent heat of condensation and c_p is the heat capacity of air. The width of this distribution is specified, and does not change with the action of cloud processes. Instantaneous condensation is assumed so that, at any point in the gridbox,

$$l = \max\{ q_T - q_{sat\,water}(T),\ 0 \}$$

where $q_{sat\,water}$ is the saturation specific humidity with respect to liquid water. Integrating across the PDF will retrieve the gridbox mean values of q and l from q_T.

The rest of the parametrized microphysics uses the scheme of Wilson and Ballard (1999), which represents the transfer of water between four categories: ice; liquid water; vapour and rain. Within this scheme there is an implicit subgrid-scale parametrization of the deposition / sublimation process that allows deposition to start occurring before the gridbox becomes completely saturated.

2.2 The PC2 (Prognostic Cloud, Prognostic Condensate scheme).

The PC2 scheme describes liquid and ice contents and cloud fractions in a prognostic way. This is similar in concept to Tiedtke (1993), although the formulation of each term is different. Condensation is represented by formulating equations for dq/dt. dl/dt and dC_l/dt, where C_l is the liquid cloud fraction, for each process that is represented in the model. For l, for example,

$$dl/dt = dl/dt|_{advection} + dl/dt|_{adiabatic\ warming}\ dl/dt|_{radiation} + dl/dt|_{boundary\ layer} + dl/dt|_{convection} + dl/dt|_{microphysics}.$$

The formulation for the convection is discussed in Bushell et al (2003). Condensation can also be forced by adiabatic warming or cooling as a result of the advection, the radiative warming or cooling and the change in temperature and moisture due to the boundary layer. This is currently represented as if the forcing was uniform across the gridbox, described in more detail by Wilson and Gregory (2003).

The microphysics scheme is that of Wilson and Ballard (1999) and is modified to give liquid cloud fraction and ice cloud fraction changes as well as changes to liquid and ice contents (as in the control). In particular, the autoconversion parametrization (representing the collision coalescence mechanism of warm rain production) does *not* alter the cloud fractions, but does adjust the liquid water content. This may allow optically thin, but extensive, layer clouds to exist more readily.

3. HIGH ICE CLOUD

Typically, deep convection detrains moisture at high levels in the troposphere. This behaviour is modelled by convection schemes, for example, the mass-flux based convection scheme used in the UM. The detrained moisture causes large anvil clouds to form, which may extend over hundreds of kilometres and persist long after the convective source of the moisture

Corresponding author's address: Damian R. Wilson, Met Office, FitzRoy Road, Exeter, EX1 3PB, UK;
E-Mail: Damian.Wilson@metoffice.com

has declined. Aircraft observations of ice particles in these anvil clouds demonstrate that the ice particles have usually not been detrained from the convective core, but have formed and evolved as a result of circulations in the moist anvil itself.

In the control simulation considered here, detrainment is entirely in the form of vapour, and it is the microphysics scheme that determines its conversion into ice, which will persist over several timesteps. Figure 1 shows a slice of instantaneous large-scale cloud fraction through convection. The control also has a representation of convective tower and anvil cloud directly linked to the convection scheme, when convection is active this cloud will be diagnosed.

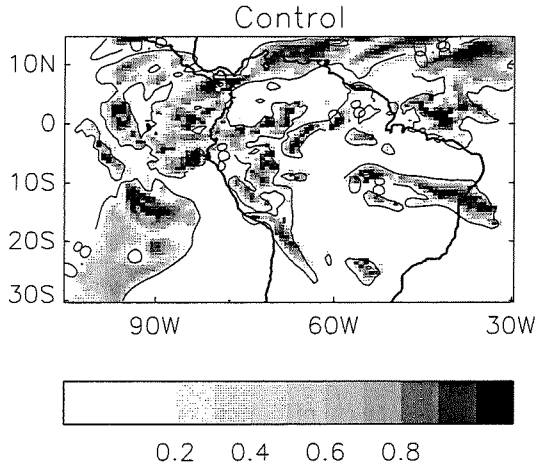

Figure 1. Cloud fraction at 12.5 km altitude for a T+6 run of the control scheme, VT 12Z 19/3/02. The solid line is the 0.8 relative humidity wrt ice contour.

The equivalent PC2 simulation (figure 2) allows convection to directly detrain (and entrain) condensate and cloud fraction. Hence we might expect significant differences between the two simulations. Although there are differences on the grid-points in the immediate vicinity of a convective core, the phase of the detrainment (vapour or ice) does not give significant differences further away, although we note that low values of cloud fraction are more extensive (see next section). In particular, the highest cloud, which is fed by moisture from only a few, very strong, convective sources, shows almost no sensitivity to the phase of the detrained moisture. *It is simply the amount of moisture detrained and the details of the microphysics scheme that affect the predicted cloud.*

3.1 The subgrid-scale ice microphysics model.

The representation of the distribution of vapour across a gridbox is, not surprisingly, a key factor in the simulations. In a prognostic ice microphysics scheme (used in both the control and PC2), it is not possible to use the concept of instantaneous condensation, since the timescale for the depositional growth or sublimation of ice is significant (of order 30 minutes). Notably, an assumption of instantaneous condensation for ice will preclude the existence of any liquid water.

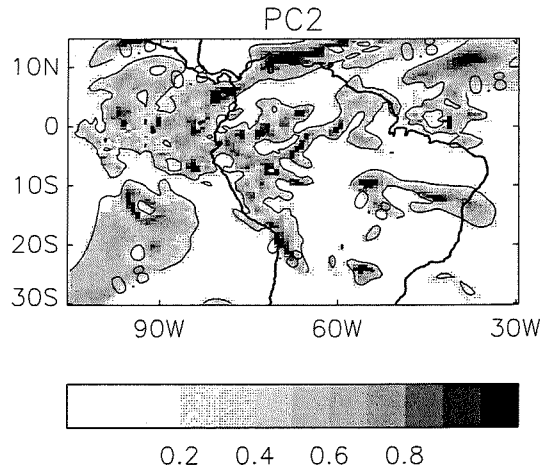

Figure 2. Like figure 1 but for the PC2 scheme.

For PC2 we have proceeded by first calculating the mean vapour content across the part of the gridbox covered by ice cloud (but not by liquid cloud). We now assume that the vapour in this partition of the gridbox has a uniform distribution. By specifying its width and assuming that the ice is located where the vapour content is largest, we are able to calculate the average deposition rate across the whole gridbox. Figure 3 demonstrates the effect of applying this change *on its own* to the control simulation shown in figure 1. *Small cloud fractions are now closer to those predicted by the PC2 scheme.*

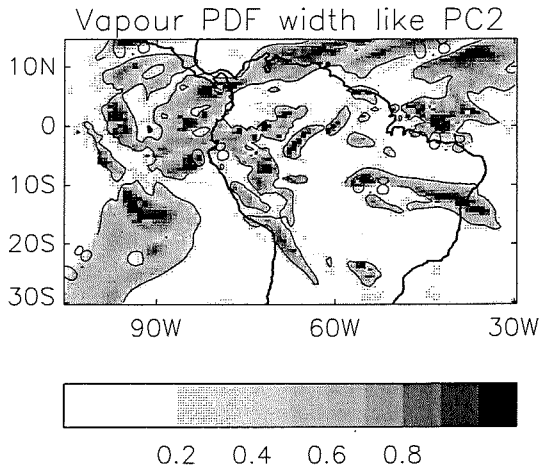

Figure 3. Like figure 1 but for the adjusted width of the vapour distribution in ice-cloud.

This change in this parametrization of vapour distribution gives very significant differences in results of a full atmospheric GCM. Notably, the cold and moist bias in upper levels in midlatitudes is removed when a large width is chosen for the parametrization. Figure 4

shows the difference between PC2 (which includes, amongst others, the change that is demonstrated in figure 3) and the control simulation for zonal mean temperature and relative humidity (RH). The change in the midlatitudes (but not the tropics) can be shown to be attributable to the parametrization of the vapour distribution by running an equivalent simulation to that shown in figure 3.

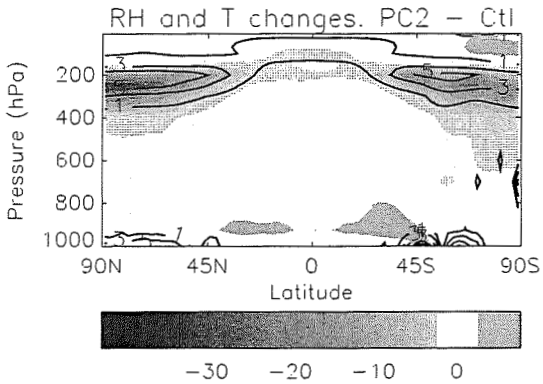

Figure 4. Annnual mean relative humidity changes wrt ice (shaded) and temperature changes (contours) between the PC2 and control simulations for a 5 year simulation.

These changes are a significant improvement in the simulation of mean temperature and relative humidity. Figure 5 shows the mean errors of the PC2 simulation when it is compared with ECMWF reanalysis data.

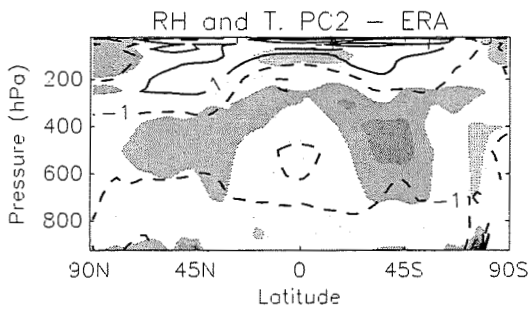

Figure 5. Zonal mean annual differences between PC2 and ERA for temperature (contours, values +1 and +3 are solid, -1 and -3 are dashed) and relative humidity (shaded as in figure 4).

We hypothesize that the changes in RH are caused by more ice being produced when the parametrized width of the vapour distribution is greater. This ice can fall to lower levels, so drying the upper troposphere. The temperature change is a radiative response to the drying; although the relative humidity response in the model is immediate, the temperature response requires several months to appear in full.

4. STRATOCUMULUS CLOUD

The ready breakup of stratocumulus sheets over land in operational models is a principal reason for developing the PC2 scheme. Figure 6 shows a satellite image of a typical UK stratocumulus case.

Figure 6. Visible satellite image, 1209Z 6/4/03.

The representation of autoconversion (representing the collision coalescence mechanism of drizzle production) should remove water from the moistest parts of a gridbox. In a scheme (like PC2) where cloud fraction is not reduced in response, this will effectively reduce the width of the underlying PDF of moisture (although the scheme does not need to know this width). In contrast, removal of liquid content by autoconversion in the fixed PDF-width control (Smith, 1990) scheme, will, in general, result in the reduction of cloud fraction and some extra condensation.

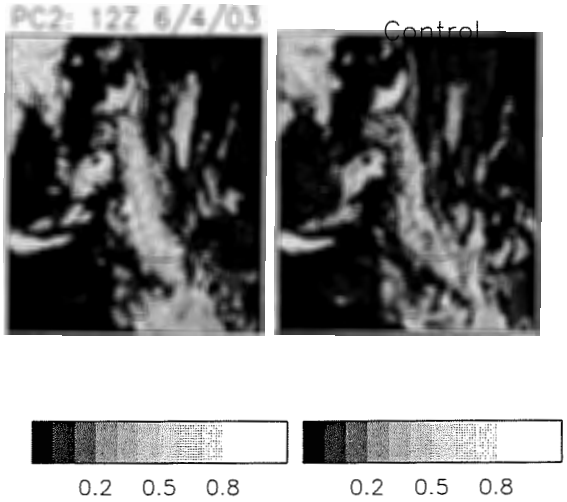

Figure 7. Liquid cloud fractions (looking down) for a T+11 run, VT 12Z 6/4/03. PC2 (left) and control (right).

The narrowing the PDF, as PC2 allows, will result in cloud fractions of 1 being reached for lower gridbox mean relative total humidities. This allows stratocumulus to be more prevalent in PC2, as shown in figure 7.

The satellite image (figure 6) shows that the sheet of cloud exists in an almost unbroken state across most of the UK, more in accordance with the PC2 predictions. Note that, in this example, the PC2 cloud scheme has produced substantial icing of the sheet in its eastern part (probably due to the greater overlap of ice and liquid cloud in PC2), which may have contributed to thinning of the liquid cloud in this region.

Wood and Field (2000) presented aircraft data from decoupled and coupled stratocumulus cases and showed relationships between cloud fraction and water contents that were not consistent with currently used cloud parametrization schemes. In particular, cloud fractions reached 1 for gridbox mean moisture only a little above saturation. Figures 8 and 9 show that the PC2 results compare favourably with the Wood and Field relationships.

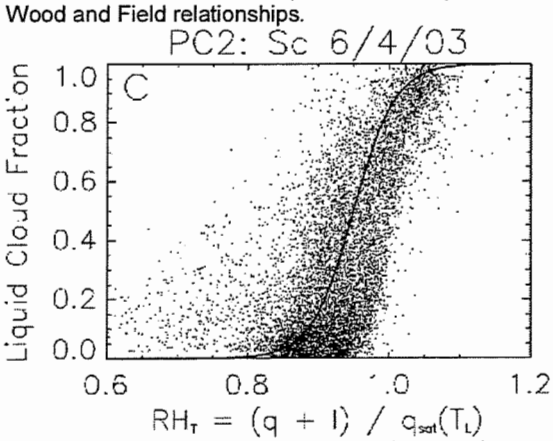

Figure 8. Liquid cloud fraction against total water content normalised by the saturation specific humidity for the PC2 simulation. The solid line is the WFI relationship from Wood and Field (2000).

Relationships from a Smith-like scheme for the RH_T – C_l plot will always be anti-symmetric, passing through the point $RH_T = 1$, C_l=0.5.

Climate simulations with PC2 show that the increased stratocumulus cloud is also visible in the semi-permanent stratocumulus sheets off western continental landmasses.

5. SUMMARY

The representation of clouds by a prognostic scheme can offer considerable advantage over a diagnostic scheme, but improvements may come for reasons that are quite subtle. In this paper we have seen that the PC2 scheme improves the simulation of stratocumulus cloud by effectively decreasing the width of the underlying PDF of moisture. The behaviour of the high ice cloud, even in strongly convective regions, is more affected by the parametrization of the PDF of moisture than by the details of the detrainment of ice cloud fraction.

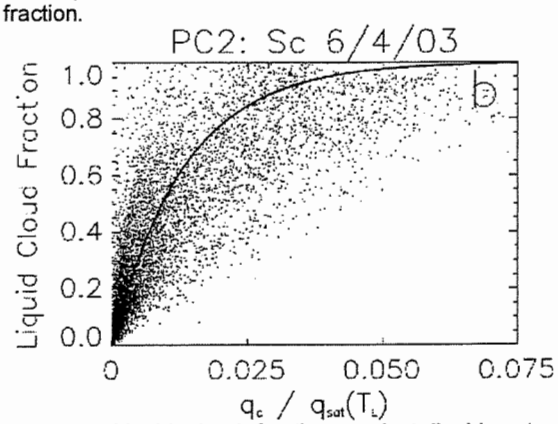

Figure 9. Liquid cloud fraction against liquid water content normalised by the saturation specific humidity for the PC2 simulation. The solid line is the WFII relationship from Wood and Field (2000).

6. ACKNOWLEDGEMENTS

We would like to thank David Gregory for initial parametrization ideas for the PC2 scheme.

7. REFERENCES

Bushell, A.C., Wilson, D.R. and Gregory, D. (2003). A description of cloud production by non-uniformly distributed processes. *Quart. J. Roy. Meteorol. Soc.*, **129**, 1435-1455

Gregory, D., Wilson, D. and Bushell, A. (2002). Insights into cloud parametrization provided by a prognostic approach. *Quart. J. Roy. Meteorol. Soc.*, **128**, 1485-1504

Wilson, D. and Gregory, D. (2003). The behaviour of large-scale model cloud schemes under idealized forcing scenarios. *Quart. J. Roy. Meteorol. Soc.*, **129**, 967-986

Wilson, D.R. and Ballard, S.P. (1999). A microphysically based precipitation scheme for the Meteorological Office Unified Model. *Quart. J. Royal Meteorol. Soc.*, **125** 1607-1636

Smith, R.N.B. (1990). A scheme for predicting layer clouds and their water contents in a general circulation model. *Quart. J. Royal Meteorol. Soc.*, **116** 435-460

Tiedtke, M. (1993). Representation of clouds in large-scale models. *Mon. Weather Rev.*, **121**, 3040-3061

Wood, R. and Field, P.R. (2000). Relationships between total water, condensed water, and cloud fraction in stratiform clouds examined using aircraft data. *J. Atmos. Sci.*, **57**, 1888-1905

MODELLING CLOUDS AND RADIATION IN THE ARCTIC

K. Wyser , C.G. Jones and U. Willen

Rossby Centre, Swedish Meteorological and Hydrological Institute, 601 76 Norrköping, Sweden

1. INTRODUCTION

Recent observations and climate modelling results have highlighted the Arctic region as particularly vulnerable to potential anthropogenic climate change. Global model projections of the future climate show the largest surface warming over sea ice covered regions of the Arctic Ocean, where an initial climate warming is hypothesized to lead to sea ice melt, a reduction in the surface albedo and further melting and warming through increased absorption of solar radiation (i.e positive feedback). However, Global Climate Model simulations of the Arctic vary widely in quality and many of the key physical processes that must be parameterized are poorly understood.

One of the areas with the largest uncertainties concerns the interaction between clouds and radiation. The radiation schemes of today's climate models have often been developed with mid-latitude or tropical clouds in mind. In this study we will evaluate clouds and radiation from existing regional climate models that have participated in the Arctic Modeling Intercomparison project (ARCMIP, Curry and Lynch 2002). Model results are compared against observations from the SHEBA site.

2. MODELS AND DATA

Eight models have participated in ARCMIP (Table 1). All models have used a similar domain in the Western Arctic with approximately 50 km horizontal resolution and roughly 60 by 80 gridpoints. Lateral and lower boundary forcing was prescribed for the 13 month long simulation. Details of the setup can be found at the ARCMIP homepage (see references). Each modelling group has extracted cloud and radiation variables at the location of the SHEBA station.

The Surface Heat Budget of the Arctic Ocean (SHEBA) experiment has collected a large amount of observational data on clouds and radiation (beside other valuable datasets). A vessel was frozen into the pack ice north of Alaska and drifted with the ice for a year. Here, we use timeseries from SW and LW radiometers for solar and terrestrial radiation, and from microwave radiometers for liquid water path. Cloud base temperature has been derived from interpolated radiosoundings with the cloud base height from a combined lidar/radar system. Cloud cover is taken from the AVHRR Polar Pathfinder (APP) program.

Corresponding author's address: Klaus Wyser, Rossby Centre, SMHI, SE-610 76 Norrköping, E-mail: klaus.wyser@smhi.se

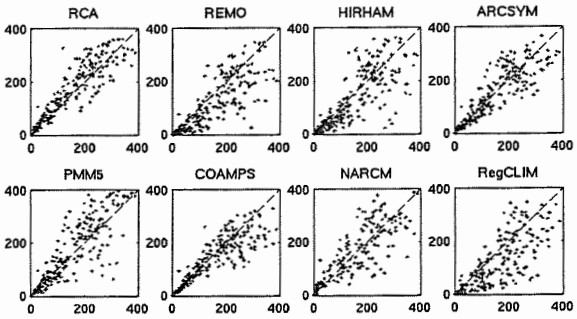

Figure 1: Downwelling shortwave radiation at the SHEBA site, daily averages in W m^{-2}. Observations are displayed on the x-axis, and model data on the y-axis. The dashed line indicates a perfect agreement.

3. RESULTS

3.1 Surface radiation

Figure 1 displays diurnally averaged downwelling SW radiation at the surface from the eight models, compared to observations. Some of the models show a fair agreement with the observations, while others reveal considerable scatter. The linear correlation coefficient is above 0.8 for all models. The bias is lowest for ARCSYM and NARCM (around 1 W m^{-2}) and highest for REMO and REGCLIM (-25 W m^{-2}). It is

Model	Reference
RCA	Jones et al. (2004)
REMO	Jacob (2001)
HIRHAM	Christensen at al. (1996), Dethloff et al. (1996)
ARCSYM	Lynch et al. (1995)
PMM5	Bromwich et al. (2001)
COAMPS	Hodur (1997)
NARCM	http://airquality.tor.ec.gc.ca
RegCLIM	http://regclim.met.no

Table 1: ARCMIP models and references

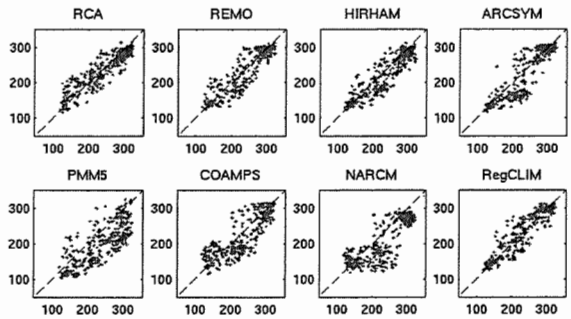

Figure 2: As Fig.1, but for longwave radiation.

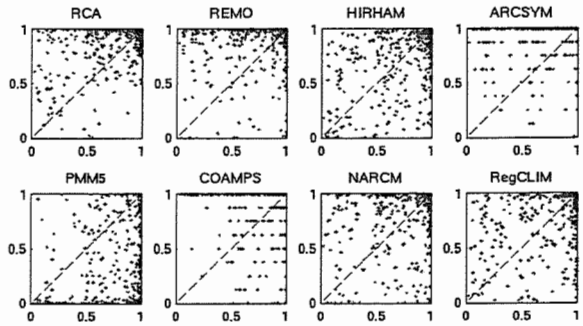

Figure 3: As Fig. 1, but for cloud cover.

interesting to note the intermodel differences at low values: RCA and NARCM overestimate, and REMO, HIRHAM and REGCLIM underestimate the downwelling SW at the surface. This is an important difference as the incoming solar radiation in spring (when insolation is low) is important for the snow melt and the albedo feedback.

Figure 2 shows a similar plot for the downwelling LW radiation at the surface. The scatter in the plots is much less than for SW, but there are large differences between the different models. Some of the plots show a tendency for two clusters, most notably for ARCSYM or NARCAM. These models don't have fractional cloudiness, a column is either clear-sky or overcast, and the computed LW radiation thus jumps between two states. The other models compute clear-sky and overcast radiation and weigh it with the fractional cloud cover, which results in a better agreement with the observation. About half of the models overestimate the downwelling LW at very cold temperatures when the observed LW radiation is low. The reason for this could be an overestimated cloud cover, or a too high emissivity from water vapour below clouds.

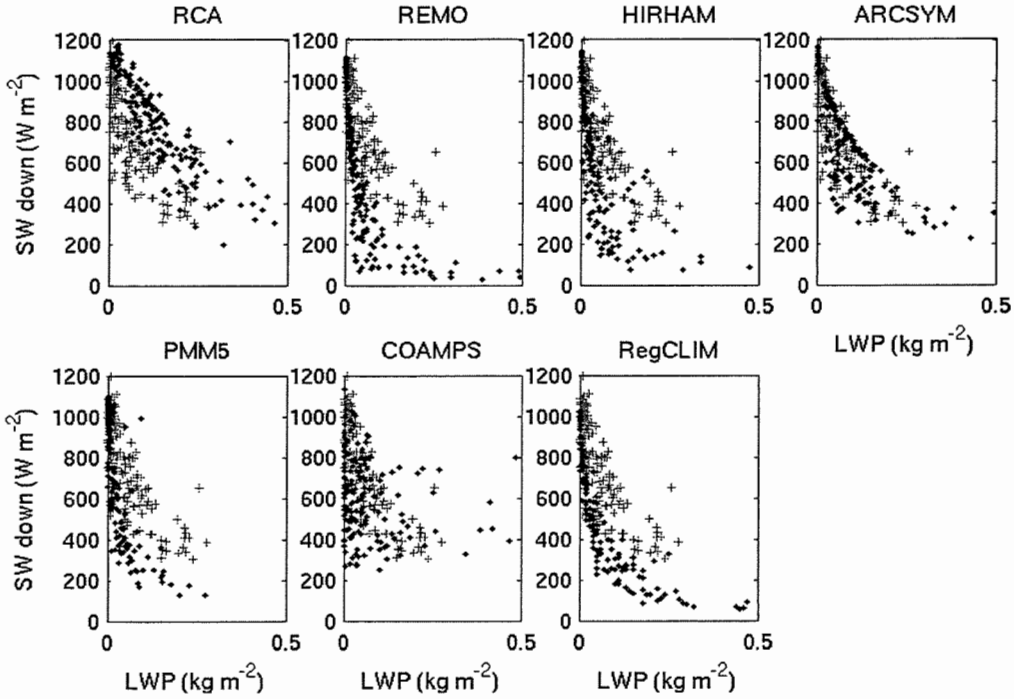

Figure 4: Downwelling SW radiation vs. Vertically integrated cloud condensate. Black dots are model data and gray crosses observations. The observed LWP contains only the contribution from liquid water clouds, while model data includes both liquid and ice. To remove the diurnal and annual variation of SW, we only display data from 0 UTC (local noon), corrected with a solar zenith angle dependent airmass factor.

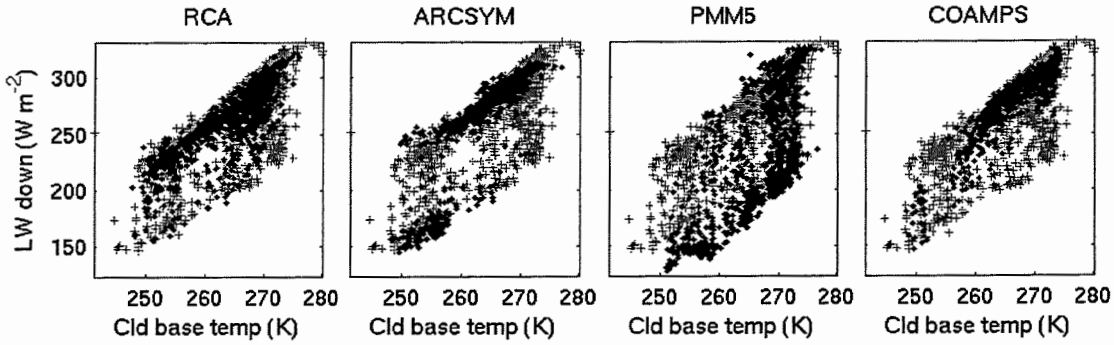

Figure 5: Downwelling LW radiation vs. cloud base temperature, 3-hourly instantaneous values. Model results are shown as black dots, observations as gray crosses.

3.2 Cloud cover

In contrast to the fair agreement between observed and modelled radiation, we find almost no correlation at all when comparing cloud cover (Fig. 3). Clearly, the representation of clouds in models needs an improvement. Since clouds are a strong modulator of the radiation, and we find such a poor agreement between modelled and observed clouds, the question remains whether or not compensating errors may cause the fair agreement in SW and LW radiation. If this is true, we conclude that a better parameterisation for cloud cover may not necessarily lead to an improvement in the radiation.

3.2 SW radiation and cloud condensate

The amount of cloud condensate has a strong impact on the radiation that reaches the ground. In Fig. 4 we plot the downwelling SW vs. the vertically integrated of cloud condensate. From the models we use both liquid water and ice clouds, but the radiometer only gives information about the liquid water path. The observed LWP values are thus a low estimate for the true amount of cloud condensate. Most models show a too strong sensitivity of the incoming solar radiation to the amount of cloud condensate. The transmissivity in most models decreases too fast with growing clouds. A possible explanation is a wrong assumption about the effective radius in the model. A too small effective radius increases optical thickness and reduces transmission for the same amount of cloud condensate. The distribution between liquid water and ice clouds could play a role, too.

3.2 LW radiation and cloud base temperature

The downwelling LW radiation at the surface is strongly influenced by the presence of clouds and the temperature of the cloud base. We compare these two variables from four of the models against observations (Fig. 4). All observations lie in a wide band whose limits are given by the Stefan-Boltzman law. The upper limit is for a blackbody with emissivity 1. The lower limit can be obtained from the clear-sky emissivity at the cloud base temperature and assuming 100% relative humidity. All points between these two limits have an emissivity that is between that of clear-sky and overcast.

The models easily reproduce the upper limit of the band structure that is given by a fundamental physical law. The other characteristics of the observations are not very well captured; PMM5 for example has a wrong emissivity under clear conditions. None of the models is able to reproduce the right mix between clouds with emissivity 1 and those with lower emissivity. In contrast to the observations, clouds in the various models are predominantly blackbodies.

4. CONCLUSIONS

The simulation of a full Arctic year with 8 different regional climate models has provided us with many interesting results. Here, we evaluate modelled clouds and radiation at the SHEBA site and find a reasonable agreement. However, if we look into the details, we find large discrepancies between models and observations. For example, all models poorly reproduce cloud cover; there is basically no correlation between simulated and observed cloudiness. Other problems have been identified with the sensitivity of radiation to the amount of cloud condensate, or to the cloud base temperature. With these deficits in mind, we believe that the fair agreement between simulated and observed radiation follows from compensating errors. The difference between models and observations clearly demonstrate the need for improvements of the parameterisations, preferentially based on physical laws and realistic observations.

5. ACKNOWLEDGEMENTS

We are grateful to our ARCMIP colleagues for providing us with their model results and the SHEBA project office for the observation data.

6. REFERENCES

ARCMIP, http://curry.eas.gatech.edu/ARCMIP

Bromwich, D.H., J.J. Cassano, T. Klein, G. Heinemann, K.M. Hines, K. Steffen, and J.E. Box, 2001: Mesoscale modeling of katabatic winds over Greenland with the Polar MM5. *Mon. Wea. Rev.*, **129**, 2290 – 2309.

Christensen J.H, O.B. Christensen, P. Lopez, E. Van Meijgaard and M. Botzet, 1996: *The HIRHAM4 regional atmospheric climate model*, DMI Sci. Rep. 96-4, Danish Met. Inst. Copenhagen, 51pp.

Curry J.A. and A.H. Lynch, 2002: Comparing Arctic Regional Climate Models. *EOS Trans. Amer. Geophys. Union.* , **83**, 87.

Dethloff K, A. Rinke, R. Lehmann, J.H. Christensen, M. Botzet andB. Machenhauer, 1996: A regional climate model of the Arctic atmosphere. *J. Geophys. Res.*, 101,23401-23422.

Hodur R. M., 1997: The Naval Research Laboratory's coupled ocean/atmosphere mesoscale prediction system (COAMPS). *Mon. Wea. Rev.*, **125**, 1414 – 1430.

Jacob D., 2001: A note to the simulation of annual and interannual variability fo the water budget over the Baltic Sea drainage basin. *Meteorol. Atmos. Phys.*, 77, 61 –73.

Jones C.G., K. Wyser, A. Ullerstig and U. Willen, 2004: The Rossby Center regional atmospheric climate model. Part II: Application to the Arctic. *Ambio*, Accepted.

Lynch A. H., W. L. Chapman, J. E. Walsh, G. Weller, 1995: Development of a Regional Climate Model of the Western Arctic. *J. Clim.*, **8**, 1555 – 1570.

SHEBA, http://sheba.apl.washington.edu

A QUASI-IMPLICIT CALCULATING SCHEME OF CLOUD MODEL

Shi Yueqin Hu Zhijin

Chinese Academy of Meteorological Sciences, Beijing, 100081, China

1. INTRODUCTION

The cloud physical variable (A) is always positive. It cannot be calculated in cloud model If $A<0$, because its term A^{α}, where α may be not an integer.

In cloud models a cloud physical process (Fi) usually is the sink term of one physical variety (j), at the same time it is the source term of another physical variety, which means

$$F_{ijk} = -\frac{\delta A_j}{\delta t} = \frac{\delta A_k}{\delta t} \qquad (1)$$

Its value at the moment t+1 may be calculated by,

$$A_n^{t+1} = A_n^t + (ADVn + DIFn)Dt + \sum_{ij} F_{ijn} \cdot Dt - \sum_{ik} F_{ink} \cdot Dt + FALn \cdot Dt \qquad (2)$$

where $ADVn$, $DIFn$, and $FALn$ are the advection, mixing and fallout terms of A_n. F_{ijk} is the source term of the cloud variable k and the sink term of variable j due to cloud physical process i. If $\sum_{ik} F_{ink} \cdot Dt$ is big enough, the value of A_n^{t+1} may be impositive, the calculation cannot be continued, because F_{ijk} usually related to A^{α}, where α may be not an integer.

In some models (Reisner 1998) the negative value is set to zero. But this method can cause the problem of unconservation.

In this paper a quasi-implicit calculating scheme is developed to solve the difficult problem.

2. QUASI-IMPLICIT CALCULATING SCHEME OF CLOUD PHYSICS SOURCE-SINK TERMS

The values of source-sink terms of cloud physical processes are usually positively related to the quantity of being consumed. So we can write out,

$$F_{ijk} = H_{ijk} \cdot A_j \qquad (3)$$

H_{ijk} means the relatively changing rate, its unit is s^{-1}.

We suggest using the following quasi-implicit difference scheme.

$$A_n^{t+1} = A_n^t + (ADV_n^t + DIF_n^t + FAL_n^t - \sum_{ik} H_{ink}^t \cdot A_n^{t+1} + \sum_{ij} H_{ijn}^t \cdot A_j^{t+1}) \cdot Dt \qquad (4)$$

$$A_n^{t+1} = [A_n^t + (ADV_n^t + DIF_n^t + FAL_n^t + \sum_{ij} H_{ijn}^t \cdot A_j^{t+1}) \cdot Dt]/(1 + \sum_{ik} H_{ink}^t \cdot Dt) \qquad (5)$$

A specific calculation sequence is used to calculate the cloud physical varieties with more sink

Corresponding author's address: Chinese Academy of Meteorological Sciences, 46 Zhongguancun South Street, Haidian District, Beijing, 100081, China; E-mail: shiyq@cams.cma.gov.cn

terms and less source terms in prior, which can make the right terms in the formula (4) be known, thus can simplify the calculation.

The specific calculating sequence, in the warm region is cloud water, ice crystals, snow flakes, graupels and rain droplets, otherwise in the cold region is ice crystals, cloud water, snow flakes, rain droplets and graupels.

3. CONDENSATION, EVAPORATION AND DEPOSITION

The diffusion growth has the most intense latent heat release and the biggest changing rate. So we calculate condensation, evaporation and deposition terms after we obtain the transient value of Q_v^*, T^* and $Q_{sw}^* = Q_{sw}(T^*)$ by calculating other physical processes in advance.

For liquid-gas cloud,

$$F_{svc} = H_{svc} \cdot (Q_v^* - Q_{sw}^*) / [1 + H_{svc} \cdot (1 + \frac{L_v}{C_p} \frac{dQ_{sw}}{dT}) \cdot Dt] \quad (6)$$

where svc means cloud condensation.

For solid-liquid-gas cloud,

$$Q_v^{**} = Q_v^* - (H_{svc} + H_{svs} + H_{svg}) \cdot (Q_{sw}^* - Q_{si}^*)] \cdot Dt \quad (7)$$

$$T^{**} = T^* + L_s / C_p \cdot (H_{svc} + H_{svs} + H_{svg}) \cdot (Q_{sw}^* - Q_{si}^*) \cdot Dt \quad (8)$$

$$(Q_v - Q_{sw})^{***} = (Q_v^{**} - Q_{sw}^{**}) / \{1 + [H_{svc} \cdot (1 + \frac{L_v}{C_p} \frac{dQ_{sw}}{dT}) + (H_{svc} + H_{svs} + H_{svg}) \cdot (1 + \frac{L_s}{C_p} \frac{dQ_{sw}}{dT})] \cdot Dt\} \quad (9)$$

$$F_{svc} = H_{svc} \cdot (Q_v - Q_{sw})^{***} \quad (10)$$

$$F_{svi} = H_{svi} \cdot [(Q_v - Q_{sw})^{***} + (Q_{sw}^* - Q_{si}^*)] \quad (11)$$

$$F_{svs} = H_{svs} \cdot [(Q_v - Q_{sw})^{***} + (Q_{sw}^* - Q_{si}^*)] \quad (12)$$

$$F_{svg} = H_{svg} \cdot [(Q_v - Q_{sw})^{***} + (Q_{sw}^* - Q_{si}^*)] \quad (13)$$

where svi, svs, svg mean the sublimation of ice crystals, snow flakes and graupels.

4. TEST IN A ONE-DIMENSIONAL TIME-DEPENDENT STRATIFORM MODEL

A dual-moment model is used for testing the scheme, in which the specific contents and the specific concentration of ice crystals, snow flakes, rain drops and graupels, as well as the specific content of vapor and cloud water are calculated. In addition, to calculate the autoconversion of cloud water to rain drops, ice crystals to snow flakes and to graupels, 3 parameters are used to describe the cloud spectra width (Fc) and the droplets of ice crystals and snow flakes riming rate (Fi,Fs).

The prognostic formula of all varieties in the model is,

$$\frac{\partial A}{\partial t} = -w \frac{\partial A}{\partial z} + K \frac{\partial^2 A}{\partial z^2} + \frac{1}{\rho} \frac{\partial \rho V A}{\partial z} + \frac{\delta A}{\delta t} \quad (14)$$

Where $\frac{\partial A}{\partial t}$ is the cloud physical term. 31 microphysical processes are considered, including sublimation (evaporation), coalescence, riming, aggregation, nucleation, multiplication and autoconversion (in detail see Hu 1986,1988).

The model is tested in a one-dimensional time-dependent framework. The initial values are that the surface temperature is 287.10 K, the surface pressure is 1002.0 hPa, Vapor occupies 80 percent of the saturation water vapor. The temperature declined with the wet-adiabatic lapse rate. The vertical grid scale is 240 m and its number is 50. The ascending velocity (w) is assumed to be unchanged in the simulation and to have a parabolic profile and the biggest ascending velocity (wm) of 0.1 m/s, 0.2 m/s, 0.48 m/s and 2.0 m/s are used to simulate the microphysical processes and precipitation under different dynamic condition. To study the stability and accuracy of the model, a sensitivity test was done for different time steps. The time steps (Dt) of 5, 10, 20, 40, 100, 200 and 400 sec were used for small wm and the time steps (Dt) of 0.5, 1, 2, 5, 10, 20, 40 and 100 sec were used for big ones.

The calculation results showed that in the case of $wm = 0.1m/s$ and $wm = 0.2m/s$, the simulated rainfall intensity for Dt=5, 10, 20, and 40 sec coincided and agreed very well for Dt=100 sec after 5 h when rainfall became stationary. The simulated rainfall intensity for Dt=400 sec had the same changing tendency but less value after 4 h (Fig. 1).

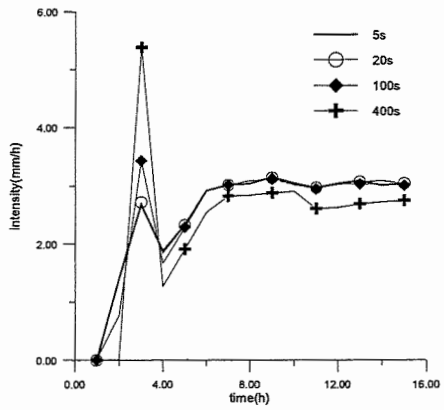

Fig.1. Rainfall intensity at wm=0.20m/s

In the case of $wm = 2.0m/s$, the simulated rainfall intensity for Dt=5, 10, 20 and 40 sec were in good accordance, and indicated a wave variation with a period of 3-4 h. The rain rate for Dt=100 sec had the same periodic variation till the 9th simulation hour, but became different after then (Fig. 2).

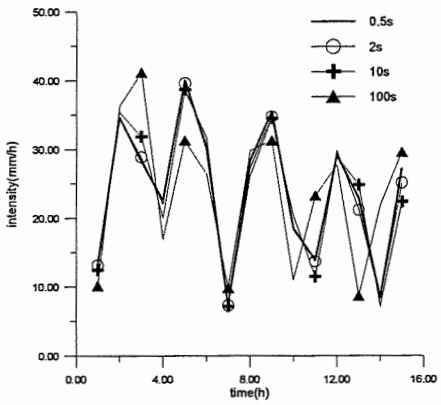

Fig.2. Rainfall intensity at wm=2.0m/s

5. CONCLUSION

The quasi-implicit cloud model could assure the positiveness, conservation and stability of calculation. The one-dimensional time dependent framework with different ascending velocities was shown to be stable, positive and conservative by using different time steps from 0.5 sec to 400 sec. The results were in good accordance by using small time steps and the differences grew bigger while time steps increased.

6. REFERENCE

Hu Zhijin, Yan Caifan, Numerical Simulation of Microphysical Processes in Stratiform Clouds (I): Microphysical Model, *Journal of Academy of Meteorological Science, China,* 1986,1(1): 37-53(in Chinese).

Hu Zhijin, He Guanfang, Numerical Simulation of

Microprocesses in Cumulonimbus Clouds (I): Microphysical Model, *ACTA Meteorologica Sinica,* 1988, 2, 471-489.

Reisner J., R. M. Rasmussen and R. T. Bruintjes, Explicit forecasting the MM5 mesoscale model, *Q.J.R. Meteor. Sci.*, 1998, 124, 1071-1107.

A MICROPHYSICAL PARAMETERIZATION FOR CONVECTIVE CLOUDS IN THE ECHAM GCM: DESCRIPTION AND FIRST RESULTS

Junhua Zhang and Ulrike Lohmann

Department of Physics and Atmospheric Science, Dalhousie University, Halifax, NS, B3H 3J5, Canada

1. INTRODUCTION

Convective clouds act like an engine in atmospheric systems transporting energy and water vapor from the surface to the free troposphere. In this process, they produce large amounts of precipitation and drive global-scale circulations. Proper representation of convective clouds in general circulation models (GCMs) is a very important issue when conducting global climate simulations. The aerosol effect on clouds and climate is another importance issue that influences the global climate through direct (e.g., Hobbs et al., 1997), indirect (e.g., Lohmann et al., 2000) and semi-direct effects (e.g., Ackerman et al., 2000). So far, aerosol effects on clouds are mainly studied in the framework of large-scale stratiform clouds in climate models. However, observations show that aerosol effects on precipitation formation in deep convection clouds are also important (e.g., Rosenfeld, 1999).

Using the ECHAM4 GCM, Nober et al. (2003) studied the aerosol effect on convective clouds by simply decreasing the conversion rate of cloud water to precipitation for higher cloud droplet number concentrations (CDNC). Although the microphysical parameterization for convective clouds is based on a very simple assumption in ECHAM4, they found a definite perturbation of the global circulation. A more sophisticated cloud microphysical parameterization, however, is applied for stratiform clouds in the recent ECHAM 5 GCM (Lohmann and Rockner, 1996). In this model the cloud liquid and ice water contents are prognostic variables. In this study, we will implement this stratiform cloud microphysical para-meterization also into convective clouds. Then we will evaluate it at the Atmospheric Radiation Measurement (ARM) Southern Great Plain (SGP) site using the single column model (SCM) of ECHAM5. Preliminary results from global simulations will also be shown.

2. MODEL DESCRIPTION

2.1 Convective Scheme

In ECHAM5, the cumulus parameterization is based on the mass flux concept (Tiedtke, 1989) with modifications for penetrative convection according to Nordeng (1994). In this assumption, cumulus clouds are considered to be embedded in the large-scale environment with a common cloud base but different heights. They are defined by upward and downward mass flux, and by heat, moisture and cloud water content. The scheme treats the bulk properties of cumulus updrafts and downdrafts separately. The bulk properties, such as cloud base mass flux and entrainment/detrainment rates are specified differently for penetrative, midlevel and shallow convection.

Updraft associated precipitation, G_p , is crudely represented in the scheme. It is assumed to be proportional to the cloud water content:

$$G_p = K(p)l \quad (1)$$

where G_p is the conversion rate from cloud water to precipitation, l is cloud water content in the convective clouds, and $K(p)$ is an empirical function that varies with height in pressure coordinate p.

Cloud water content, l, is calculated as the amount of water vapor that exceeds the saturation specific humidity:

$$l = q - q_s \quad (2)$$

where q is the specific humidity and q_s is the saturation specific humidity over water or ice depending on the temperature, T. If $T \geq 0°C$, the saturation specific humidity is assumed to be with respect to water, otherwise, it is with respect to ice.

Downdrafts are associated with convective precipitation formed in the updrafts. In the downdrafts, some rain and snow is evaporated/sublimated to maintain a saturated descent. The environmental air injected at the level of free sinking (LFS) is moisturized and cooled by the evaporation of precipitation.

2.2 Microphysical parameterization for stratiform cloud

The microphysical parameterization for stratiform clouds is based on the work by Lohmann and Roeckner (1996) with modifications by Tompkins (2002). Parameterized microphysical processes include: condensational growth of cloud droplets, depositional growth of ice crystals, homogeneous, heterogeneous and contact freezing of cloud droplets, autoconversion of cloud droplets, aggregation of ice crystals, accretion of cloud ice and cloud droplets by snow, accretion of cloud droplets by rain, evaporation of liquid water and rain, sublimation of cloud ice and snow, melting of cloud ice and snow.

Corresponding author's address: Junhua Zhang, Department of Physics and Atmospheric Science, Dalhousie University, Halifax, NS, B3H 3J5, Canada; E-Mail: zhang@mathstat.dal.ca

Details of the governing equations for the mass mixing ratios of water vapor, cloud water and cloud ice can been found in Lohmann and Roeckner (1996). Ice clouds are formed by homogeneous and heterogeneous freezing processes. Below -35°C, all cloud droplets freeze within one time step. Between -35°C and 0°C, cloud droplets have to form first and then ice crystals form by heterogeneous freezing. After the ice water content exceeds a threshold, the Bergeron-Findeisen process sets in, allowing ice crystals to grow at the expense of cloud droplets (Lohmann and Roeckner, 1996).

3. SCM SIMULATIONS

In order to investigate aerosol effects on convective clouds, microphysical parameterizations for stratiform clouds in ECHAM5 are implemented in convective clouds to replace the rather simple assumption described in Section 2.1. The performance of the new parameterization is first evaluated by using a SCM at the ARM SGP site.

3.1 Data

Data used in this study are obtained from the ARM SGP Intensive Operational Periods (IOPs). Observations available at the ARM site include radiosonde soundings every 3 hours, surface data from the meteorological network, wind profiler data, radar rainfall and cloud reflectivity and satellite data. Description of the ARM SGP clouds and radiation testbed (CART), observations, forcing data and experiment design for SCM simulations are detailed by Ghan et al. (2000).

Three datasets are used in this study for the evaluation purpose: 1995 Summer IOP (Jul. 18 - Aug. 4), 1997 Summer IOP (Jun. 18 - Jul. 17) and 2002 Spring IOP (May 25 - Jun. 15). 1995 Summer IOP was used as the first effort to conduct comparisons of SCMs using ARM data (Ghan et al., 2000). The 1997 Summer IOP was chosen for another model comparison of SCMs and Cloud-Resolving Models (CRMs). This was conducted jointly by ARM and the GEWEX Cloud System Study (GCSS) as a convectively driven period, which contained a wide range of summertime weather conditions (Xie et al., 2002; Xu et al., 2002). The aim of the 2002 Spring IOP is to study convective initiation and test the convective cumulus parameterizations in GCMs.

3.2 Results of SCM Simulations

The SCM has 19 vertical levels and uses a time step of 30 minutes. The forcing data to drive the SCM simulations are interpolated from the observations of horizontal and vertical advective tendencies of temperatures and moisture, surface fuxes, and the surface temperatures for each model time step. Two simulations are conducted in this study. ORIG uses the original model setup and CONV uses the new microphysical parameterization for convective clouds. Results from the two simulations are shown below.

3.2.1 Precipitation and Liquid Water Path

The microphysical parameterization is closely related to the precipitation and cloud water content, so an examination of the SCM simulated precipitation and liquid water path (LWP) follows. Figure 1 shows the daily mean surface precipitation, and Table 1 summarizes the accumulated precipitation during the three IOPs. The accumulated precipitation agrees well with the observed values for both ORIG and CONV (Table 1). Figure 1 shows that SCM simulations capture almost all of the major precipitation events, but that there are some spurious events during non-precipitation periods, such as in days 18 and 25 of the 1997 Summer case and in day 14 of the 2002 Spring case. The spurious events were also found in several other model simulations when a large number of SCMs were tested using the 1997 Summer case by Xie et al. (2002). These spurious precipitation events may relate to an overly active triggering mechanism for cumulus as discussed in Xie et al. (2002).

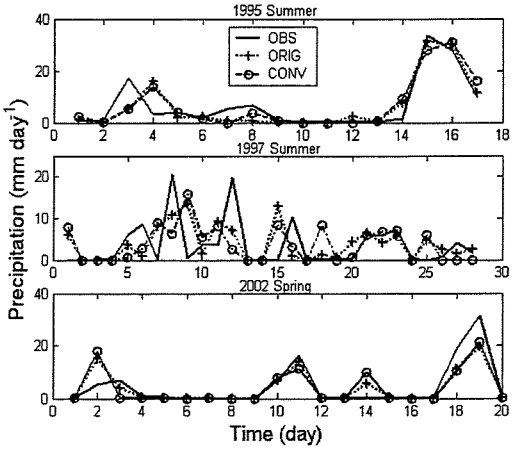

Figure 1. Comparison of daily mean precipitation rate

The comparison of LWP is shown in Figure 2, and the averaged LWP during the IOPs are summarized in Table 1. Values in Table 1 show that both ORIG and CONV overestimate the mean LWP for the 1995 Summer IOP, but CONV produces only about half the LWP of ORIG and, thus, agrees better with the observations. ORIG significantly overestimates LWP for 1997 Summer IOP while CONV only slightly underestimates it. Both experiments underestimate LWP for 2002 Spring IOP, but ORIG agrees better with the observations during this IOP.

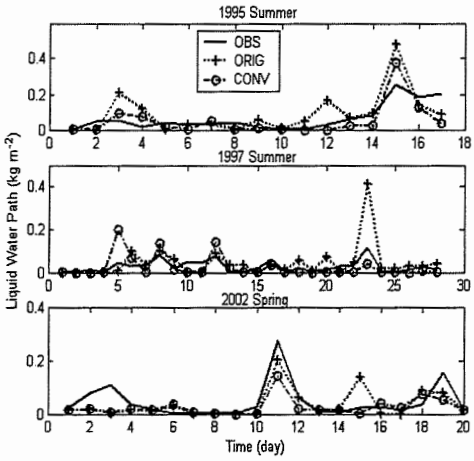

Figure 2. Comparison of daily mean LWP

3.2.2 Cloud Fraction

The mean vertical profiles of cloud fraction are shown in Figure 3 and the mean total cloud covers are summarized in Table 1. The black stars in Figure 3 represent the GOES satellite observed low (P>631 hPa), middle (400 hPa<P<631 hPa) and high (P>400 hPa) cloud fraction during these periods. We can see that the model simulated mean profiles of cloud fraction agree well with the satellite observations. Generally CONV produces less cloud cover than ORIG does as shown in Figure 1 and Table 1. The mean total cloud cover in Table 1 suggests that CONV agrees better with the observations.

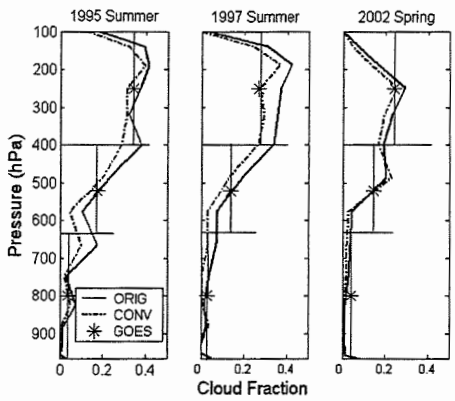

Figure 3. Comparison of meanly profile of cloud cover fraction

3.2.3 Radiation

Comparisons of the mean outgoing longwave radiation (OLR) and surface net downward radiation (F_{sfc}^{-}) are also included in Table 1. It shows that both experiments significantly underestimate OLR. With the original model setup, OLR is underestimated by as much as 40 Wm^{-2} during the 1995 and 1997 summer IOPs. The new microphysical parameterization improves the SCM simulation dramatically, increases OLR by 15 – 20 Wm^{-2} for the 1995 and 1997 summer IOPs as compared to ORIG and , thus, agreeing better with the observations. ORIG underestimates F_{sfc}^{-} by as much as 17 W m^{-2} during the 1995 and 1997 summer IOPs, while F_{sfc}^{-} simulated by CONV deviates less than 6 W m^{-2} from the observations in all IOPs, agreeing better with observations.

The radiation results suggest that the SCM generally produces more clouds than observed as shown in the total cloud cover fraction in Table 1. Underestimation of OLR suggests that more high clouds are simulated by the SCM than there should be. ORIG underestimates OLR more than CONV because it simulates more high clouds as shown in Figure 3.

Table 1. Comparison of Mean precipitation, LWP,CF and radiation

	IOPs	OBS	ORIG	CONV
Precipitation (mm)	1995 Summer	7.57	6.28	6.60
	1997 Summer	4.26	3.76	3.91
	2002 Spring	4.80	3.82	3.88
LWP ($g\ m^{-2}$)	1995 Summer	21.1	87.4	46.9
	1997 Summer	29.7	47.8	25.0
	2002 Spring	45.0	34.9	25.4
CF (%)	1995 Summer	55.1	66.3	54.7
	1997 Summer	42.8	76.4	64.2
	2002 Spring	42.7	56.8	57.4
OLR ($W\ m^{-2}$)	1995 Summer	251.8	211.8	228.7
	1997 Summer	262.2	213.1	233.8
	2002 Spring	253.7	231.6	235.8
F_{sfc}^{-} ($W\ m^{-2}$)	1995 Summer	147.6	129.5	153.5
	1997 Summer	162.3	145.8	166.2
	2002 Spring	161.2	155.3	160.2

4. INITIAL GCM RESULTS

Figure 4 shows the initial comparisons of the global cloud cover distribution among satellite observations

from the International Satellite Cloud Climatology Project (ISCCP) and ECHAM5 simulations using the original and new parameterizations. The GCM is run for one year at T31 resolution after a 3 months spin up. Generally, the model produces less cloud cover with the new parameterization than with the original setup in agreement with the SCM conclusions. However, it underestimates the cloud cover over the tropics and subtropics. A detailed analysis of the GCM results will be conducted in the future to improve the simulation.

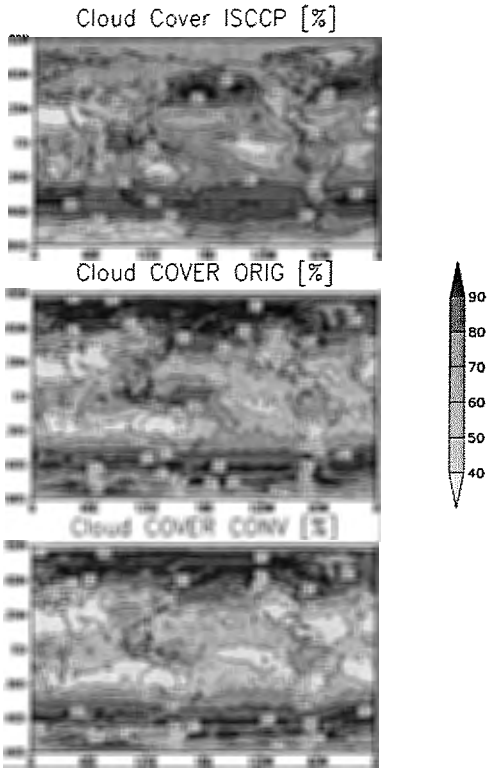

Figure 4. Comparison of annual mean cloud cover

5. CONCLUSIONS

SCM simulations of the 3 ARM SGP IOPs show that the new parameterization performs at least as well as the original model setup. For some fields, such as radiation, the new parameterization performs better than the original one. This new parameterization offers the possibility to study aerosol effects on convective clouds in climate models. An initial evaluation of cloud cover from simulations with the ECHAM5 GCM show agreement with the SCM study. However, less cloud cover is simulated using the new parameterization than observed by ISCCP. It suggests that some parameters may need to be adjusted for convective cloud systems. This will be addressed in future studies.

ACKNOWLEDGEMENTS

This research is supported by the Modeling of Clouds and Climate (MOC2) project funded by the National Science and Research Council of Canada (NSERC) and the Canadian Foundation for Climate and Atmospheric Science (CFCAS). We thank Peter Klages for his comments.

REFERENCES

Ackerman, A.S., et al., 2000: Reduction of tropical cloudiness by soot. *Science*, 228, 1042-1047.

Hobbs, V.P., et al., 1997: Direct radiative forcing by smoke from biomass burning. *Science*, 275, 1777-1778.

Ghan. S., et al., 2000: An intercomparison of single column model simulations of summertime midlatitude continental convection. *J. Geophys. Res.*, 105, 2091-2124.

Lohmann, U. and E., Roeckner, 1996: Design and performance of a new cloud microphysics scheme developed for the ECHAM general circulation model. *Climate Dyn.*, 12, 557-572.

Lohmann, U., et al., 2000: Indirect effects of sulfate and carbonaceous aerosols: a mechanistic treatment. *J. Geophys. Res.*, 105, 13685-13700.

Nober, F. J., et al., 2003: Sensitivity of the global circulation to the suppression of precipitation by anthropogenic aerosols. *Global and Planetary Change*, 37, 57-80.

Nordeng, T., 1994: Extended versions of the convective parameterization scheme at ECMWF and their impact on the mean and transient activity of the model in the tropics. *Technical Memorandum*, 206, ECMWF, Reading, UK.

Rosenfeld, D., 1999: TRMM observed first direct evidence of smoke from forest fires inhibiting rainfall. *Geophys. Res. Lett.*, 20, 3105-3108

Tiedtke, M., 1989: A comprehensive mass flux scheme for cumulus parameterization in large-scale models. *Mon. Wea. Rev.*, 117, 1779-1800.

Tompkins, A.M., 2002: A prognostic parameterization for the subgrid-scale variability of water vapor and clouds in large-scale models and its use to diagnose cloud cover. *J. Atmos. Sci.*, 59, 1917-1942

Xie S.C., et al., 2002: Intercomparison and evaluation of cumulus parametrizations under summertime midlatitude continental conditions, *Q. J. R. Meteorol. Soc.*, 128, 1095-1135.

Xu KM., et al., 2002: An intercomparison of cloud-resolving models with the atmospheric radiation measurement summer 1997 intensive observation period data. *Q. J. R. Meteorol. Soc.*, 128, 593-624.

THE DEVELOPMENT OF A NEW EXPLICIT MICROPHYSICAL SCHEME USING IN MM5

ZHEN ZHAO, HENG-CHI LEI and YU-XIA WU

Institute of Atmospheric Physics, Chinese Academy of Sciences

1.INTRODUCTION

The production of realistic clouds and precipitation forecasts with detailed mesoscale models is a difficult task. Increasing the microphysics complexity implies the specification of a number of adjustable parameters and processes, which requires extensive research and numerical experimentation. Furthermore, a large number of predictive equations and microphysical processes significant increase computational time and thus limit the use of complex cloud microphysics schemes in operational applications.

A complex mixed-phase explicit microphysical parameterization scheme was developed for use in the NCAR/Penn State Mesoscale Model Version5 (MM5). The single-moment schemes, in which the mixing ratio of ice species are predicted and number concentration specified, performed reasonably well if a diagnostic equation for $N_{0,s}$, the Y-intercept of the assumed exponential snow distribution, is allowed to vary with snow mixing ratio. The scheme assumes a Marshall-Palmer distribution law for rain, snow and graupel. In its essence, the scheme predicts only the mixing ratios (third-order moments) of drops.

The research presented in this paper aims at developing a new double-moment microphysical scheme, in which both the mixing ratios and number concentrations of cloud water, rain water, cloud ice, snow and graupel were predicted. Besides its impact in the formation of the first raindrops by autoconversion, the prediction of cloud-droplet number concentration is especially important in cloud chemistry and radiative transfer. The results obtained by running the new scheme are not discussed in this paper.

2.THE LIQUID WATER IN THE SCHEME

The new scheme is based upon the drop size distributions are assumed to follow the gamma distribution form:

$$n_x = N_{0x} D^{\alpha_x} \exp(-\lambda_x D) \qquad (1)$$

where the index x∈[i, r, s, g] stands for ice, rain, snow and graupel, respectively. Our strategy is to predict only two of the most significant moments of Eq. (1) that posses a clear physical meaning, namely the zeroth, number concentration N_x

$$N_x = \int_0^\infty n_x dD$$

and third-order moments, mixing ratio q_x

$$\rho q_x = \int_0^\infty \frac{\pi}{6} \rho_x D^3 n_x(D) dD .$$

As these two moments are determined from Eq. (1), the variable slope parameter λ_x and the slope intercept N_{0x} can be deduced from

$$\lambda_x = \left[\frac{\pi \rho_x N_x \Gamma(4+\alpha_x)}{6 \rho q_x \Gamma(1+\alpha_x)} \right]^{1/3} \qquad (2)$$

$$N_{0x} = \frac{N_x \lambda_x^{1+\alpha_x}}{\Gamma(1+\alpha_x)}, \qquad (3)$$

whereas the remaining parameters α_x are mostly related to the spectral breadth of Eq. (1), are held fixed for the moment. The parameters α_x are setting

as follows: $\alpha_i=1$, $\alpha_r=2$, $\alpha_s=1$ and $\alpha_g=0$.

3. THE MODIFIED MICROPHYSICAL SCHEME

3.1 CCN nucleation for production terms of cloud water

The CCN activation and the condensation growth of cloud droplets are the dominant processes distinctly affecting the number concentration, N_c, and the mixing ratio, q_c, of cloud liquid water at the early stage of the cloud lifetime. The nucleating properties of CCN are described with an activation spectrum of the form:

$$N_{CCN}=CS_{vw}^{k}F(\mu,k/2,k/2+1;-\beta S_{vw}^{2}) \quad (4)$$

where N_{CCN} is the number concentration of the activated CCN at supersaturation S_{vw}, F(a,b,c;x) is the hypergeometric function and C, k, μ and β are adjustable parameters. Here the following settings are used corresponding to a maritime case: C=2.01 $\times 10^{11}$ m^{-3}, k=3.50, μ =3.76 and β =44.1. To continental case: C=8.04$\times 10^{11}$ m^{-3}, k=3.50, μ =3.76 and β =44.1.

Nucleation of cloud-droplet is parameterized as follows:

$$N_{cdsn}=\frac{N_{CCN}-N_c}{2\Delta t} \quad (5)$$

The increase in mass of cloud-droplet associated with this process is given as:

$$P_{cdsn}=\frac{m_{co}}{\rho}N_{cdsn} \quad (6)$$

where m_{co} is the mass of the smallest cloud-droplet.

3.2 Conversion from cloud water into rain water

The collision and coalescence of cloud droplets to form raindrops has been parameterized as follows:

$$P_{ccnr}=a_1(10^3\rho q_c^2)^2/[5+a_2(\frac{N_b}{D_b})/(\rho q_c)]$$

$$D_b=0.146-5.964\times 10^{-2}\ln\frac{N_b}{2000} \quad (7)$$

where D_b is the cloud-droplet relative dispersion. The constant coefficients of a_1 and a_2 is 1.67×10^{-5}, 3.6×10^{-5},respectively. The unit of ρ is kg m^{-3} and the initial cloud-droplet number concentration N_b takes the value of 100 cm^{-3}.

3.3 Coalescence

In the continuous coalescence equation, the particles fall velocity difference $|U_i - U_j|$ is not moved out from the integral, but is integrated in the equation as the function of diameter D to avoid the error of using particles average fall velocity.

$$P_{iacj}=\frac{1}{\rho}\int_0^\infty\int_0^\infty\frac{\pi}{4}(D_i+D_j)^2|U_i-U_j|E_{ij}m_jn_jn_idD_jdD_i \quad (8)$$

In the new scheme, generation rate of graupel due to the collection of snow by graupel P_{gacs} and the collection of cloud ice P_{gaci} by graupel are included.

3.4 Equation set

Corresponding to the gamma size distribution, microphysical equations in the new scheme are rewritten which including 19 microphysical processes.

The new developed double-moment microphysical scheme has the prognostic equations for the mixing ratios and number concentrations, in which both the mixing ratios and number concentrations of cloud water, rainwater, cloud ice, snow and graupel are predicted.

4.CONCLUSION

A new complex mixed-phase explicit microphysical parameterization scheme was developed for using in the NCAR/Penn State Mesoscale Model Version 5 (MM5). The new double-moment microphysical scheme, in which both the mixing ratios and number concentrations of cloud water, rain water, cloud ice, snow and graupel were predicted, uses the more reasonable gamma law as basis functions for the hydrometeor drop size distribution. The scheme is incorporated in the three-dimensional non-hydrostatic model MM5 and becomes a new option in its explicit microphysical scheme.

5.ACKNOWLEDGEMENTS

The authors would like to thank Professor Meiyuan HUANG for helpful advice concerning the work.

6.REFERENCES

Reisner J., Rasmussen R. M. and Bruintjes R. T., 1998: Explicit forecasting of supercooled liquid water in winter storms using the MM5 mesoscale model. Quart. J. Roy. Meteor. Soc., 124, 1071~1107.

Xu Huanbin, Duan Ying, 1999: Some questions in studying the evolution of size-distribution spectrum of hydrometeor particles. Acta Meteorolgica Sinica, 57, 450~460.

Rutledge, S.A. and Hobbs, P.V., 1983: The mesoscale and microscale structure and organization of clouds and precipitation in midlatitude cyclones. Part Ⅷ: A model for the 'seeder–feeder' process in warm–frontal rainbands. J. Atmos. Sci., 40, 1185~1206.

Rutledge, S.A. and Hobbs, P.V., 1984: The mesoscale and microscale structure and organization of clouds and precipitation in midlatitude cyclones. Part XⅡ: A diagnostic modeling study of precipitation development in narrow cold–frontal rainbands. J. Atmos. Sci., 41, 2949~2972.

Lin, Y.–L., Farley, R.D. and Orville, H.D., 1983: Bulk parameterization of the snow field in a cloud model. J. Clim. Appl. Meteorol., 22, 1065~1092.

Cohard J.-M. and Pinty J.-P., 2000: A comprehensive two-moment warm microphysical bulk scheme. Ⅱ: 2D experiments with a non-hydrostatic model. Quart. J. Roy. Meteor. Soc., 126, 1843~1859.

Grabowski, W.W., 1999: A parameterization of cloud microphysical for long-term cloud-resolving modeling of tropical convection. Atmos. Res., 52, 17~41.

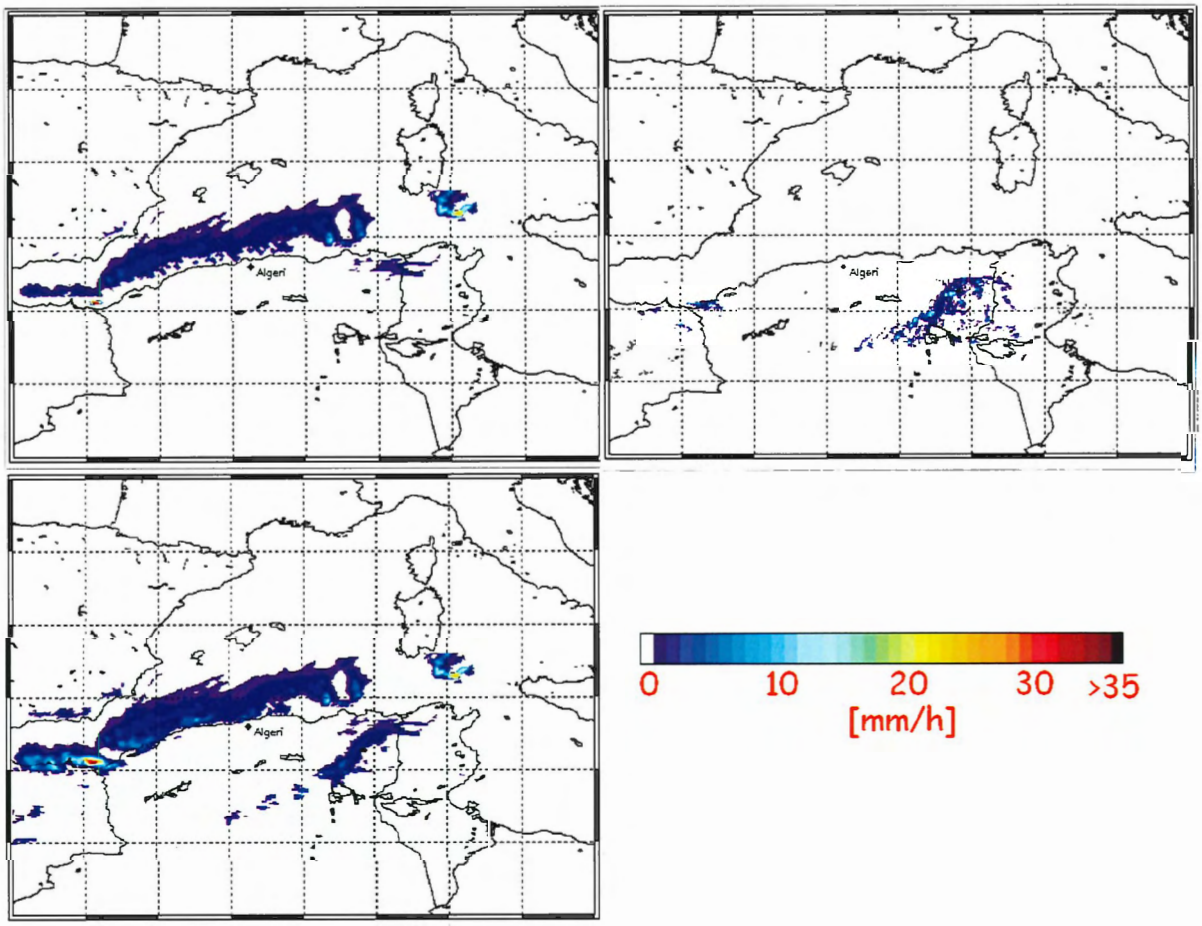

10 November 2001, 0032 UTC. Flood event in Algiers and Algerian coastal area as seen from the Tropical Rainfall Measuring Mission (TRMM). Top left: rainfall estimation using the Goddard Profiling Algorithm v.6 (GPROF6) and microwave data from the TRMM Microwave Imager (TMI). Top right: rainfall measurements of the Precipitation Radar (PR). Bottom left: rainfall estimation using GPROF6 after modification of the ice screening procedure of overland and coastal pixels. Note the precipitation now detected inland in accordance with the radar. Courtesy of F. Torricella.

International Conferences on Clouds and Precipitation

1954	I	4-6 October	Zürich, ETH
1960	II	9-13 August	Verona
1961	III	September	Canberra, Sydney
1965	IV	24 May- 1 June	Tokyo, Sapporo
1968	V	26-30 August	Toronto, University of Toronto
1972	VI	August	London, Royal Society
1976	VII	26-30 June	Boulder
1980	VIII	15-19 July	Clermont-Ferrand
1984	IX	21-28 August	Tallinn
1988	X	15-20 August	Bad Homburg
1992	XI	17-21 August	Montreal, McGill
1996	XII	19-23 August	Zürich, ETH
2000	XIII	14-18 August	Reno, DRI
2004	XIV	19-23 July	Bologna, CNR